

# Thermal Remote Sensing of Active Volcanoes

A USER'S MANUAL

Andrew Harris

CAMBRIDGE

CAMBRIDGE

more information – [www.cambridge.org/9780521859455](http://www.cambridge.org/9780521859455)



# THERMAL REMOTE SENSING OF ACTIVE VOLCANOES

## A User's Manual

Active volcanoes emit heat through lava flows and erupting vents. Remote measurements of heat emission from such active features can provide insights into the physical processes governing volcanic activity. Development of thermal remote sensing, and improved data-processing techniques, have enabled operational use of infrared instruments to perform volcano radiometry and to quantify the thermal flux from eruptions and volcanic systems, leading to better detection and measurement of volcanic activity.

This book encapsulates over 100 years of research developments, forming a comprehensive manual for measurements of Earth surface temperatures and heat fluxes. With a particular focus on volcanic hot spots, the book explores methodologies and principles used with satellite, radiometer and thermal-camera data. It presents traditional applications using satellite- and ground-based sensors as well as modern applications that have evolved for use with hand-held thermal cameras, and is fully illustrated with case studies, data bases and worked examples. Chapter topics include techniques for thermal mixture modeling and heat flux derivation, and methods for data collection, mapping, and time series generation. Appendices covering specific sensors and their deployment, plus an extensive reference list, provide the reader with a rigorous background. Online supplements present additional specific notes on areas of sensor application and data processing.

This book is an invaluable resource for academic researchers and graduate students in the fields of thermal remote sensing, volcanology, geophysics and planetary studies. It is also of interest to anyone involved in the fields of Earth and space science.

ANDREW HARRIS is a professor at Université Blaise Pascal (Clermont Ferrand, France) and holder of the Chaire d'Excellence for the Auvergne region. He is a member of the Remote Sensing Society, IAVCEI and AGU, and has worked with a variety of ground- and satellite-based thermal data sets, having deployed experimental equipment at active volcanoes in Africa, Europe, Central America, South America and Hawaii. Dr. Harris has published over 130 publications in international scientific journals dedicated to thermal remote sensing and volcanology. His work has been recognized by several awards, including IAVCEI's Wager medal (2004) and the University of Hawaii Regents' Medals for both excellence in research (2003) and teaching (2005).



# THERMAL REMOTE SENSING OF ACTIVE VOLCANOES

A User's Manual

ANDREW HARRIS

*Université de Clermont-Ferrand II  
(Université Blaise Pascal)*



CAMBRIDGE UNIVERSITY PRESS  
Cambridge, New York, Melbourne, Madrid, Cape Town,  
Singapore, São Paulo, Delhi, Mexico City

Cambridge University Press  
The Edinburgh Building, Cambridge CB2 8RU, UK

Published in the United States of America by Cambridge University Press, New York

[www.cambridge.org](http://www.cambridge.org)  
Information on this title: [www.cambridge.org/9780521859455](http://www.cambridge.org/9780521859455)

© Andrew Harris 2013

This publication is in copyright. Subject to statutory exception  
and to the provisions of relevant collective licensing agreements,  
no reproduction of any part may take place without the written  
permission of Cambridge University Press.

First published 2013

Printed and bound in the United Kingdom by the MPG Books Group

*A catalog record for this publication is available from the British Library*

*Library of Congress Cataloging in Publication data*

Harris, Andrew, 1967–

Thermal Remote Sensing of Active Volcanoes : A User's Manual / Andrew Harris.

p. cm.

ISBN 978-0-521-85945-5 (hardback)

1. Volcanic ash, tuff, lava, etc. – Temperature – Remote sensing. 2. Volcanological research. 3. Terrestrial radiation – Measurement. 4. Volcanic activity prediction. I. Title.

QE527.55.H37 2013

551.21028'4–dc23

2012026276

ISBN 978-0-521-85945-5 Hardback

Additional resources for this publication at [www.cambridge.org/radiometry](http://www.cambridge.org/radiometry)

Cambridge University Press has no responsibility for the persistence or accuracy of URLs for external or third-party internet websites referred to in this publication, and does not guarantee that any content on such websites is, or will remain, accurate or appropriate.

# Contents

	<i>page</i>
<i>Acknowledgments</i>	ix
0 Introduction: Background, motivation and essential definitions	1
0.1 Remote sensing of terrestrial volcanic hot spots: a brief history	1
0.2 Thermal remote sensing: What it is and what we have	5
0.3 Reviews to date and the value of thermal remote sensing	6
0.4 Thermal remote sensing of volcanic hot spots on other planets	10
0.5 Aim and use of this book	11
0.6 Structure and content of this book	11
0.7 Supporting material and companion texts	15
0.8 Waveband definitions	16
0.9 A final note: hot spots and thermal anomalies – what do we mean?	16
<b>Part I Introduction and underlying principles</b>	19
1 History of thermal remote sensing of active volcanism	21
1.1 Nimbus, Surtsey and subsequent work	23
1.2 A history of satellite infrared sensors	27
1.3 A history of the discipline	42
1.4 Ground-based and airborne sensors	54
2 Thermal remote sensing of active volcanism: principles	70
2.1 The Planck Function, Wein's Displacement Law and Stefan–Boltzmann	70
2.2 Emissivity	78
2.3 Atmospheric effects	90
2.4 Brightness temperature and surface temperature: how to obtain surface temperature	109
2.5 Summation	111

3	Satellite orbits and sensor resolution	113
3.1	Orbits and temporal resolution	113
3.2	The sensor: the basic acquisition system	125
3.3	Spatial resolution	130
3.4	Spectral resolution and response	146
3.5	Selection of an appropriate sensor	150
<b>Part II</b>	<b>Space-based volcano radiometry</b>	153
4	The mixed pixel, the dual-band technique, heat loss and volume flux	155
4.1	The problem of the thermally mixed pixel	155
4.2	The dual-band method	166
4.3	Three-component solutions	183
4.4	Heat flux	212
4.5	Mass and volume	248
5	Hot spot detection	274
5.1	Detection by eye	274
5.2	Detection: physical basis	275
5.3	Automated hot spot detection algorithms	292
5.4	How can we detect eruption termination?	317
5.5	Cool anomalies	322
5.6	Operational volcano hot spot detection systems	324
6	Mapping, classification, time series and profiles	331
6.1	Hot spot maps	331
6.2	Hot spot classification	346
6.3	Types of time series	367
6.4	Time series generation	373
6.5	Case studies	377
6.6	Trends and smoothing	404
6.7	Spatial profiles	407
6.8	Use of multiple platform data for validation	408
6.9	Inventories: the current status of satellite remote sensing	410
<b>Part III</b>	<b>Ground-based volcano radiometry and thermography</b>	411
7	Broad-band radiometers I: instrumentation and application	413
7.1	Detector types	413
7.2	Broad-band radiometers: capabilities and operation	419
7.3	Review of radiometer measurements of volcanic phenomena	432
7.4	Permanent deployment	447
8	Broad-band radiometers II: data collection and analysis principles	453
8.1	Lava flows and lakes	453

8.2	Vents and fumarole fields	462
8.3	Explosive eruptions	475
8.4	Thermal waveforms associated with bomb-dominated emission	483
8.5	Slope of the waveform and velocity	494
8.6	Response time and slew rate	495
8.7	Radiometers versus imagers	498
9	Broad-band thermal imaging cameras	500
9.1	Thermal camera: general texts	500
9.2	The hand-held thermal camera	501
9.3	Thermal camera applications in volcanology: history and classification	527
9.4	Measurement principles	539
9.5	Deployment principles: making the measurement	577
9.6	Methodologies	584
9.7	Methodologies II: temperature measurements	591
9.8	Methodologies III: dimensional and volume/mass measurements	606
9.9	Surveillance and monitoring	623
9.10	End note	625
<b>Appendix A</b>	<i>Collation and summary of satellite-volcano radiometry: a literature data base</i>	627
<b>Appendix B</b>	<i>Estimation of solar zenith angle and contribution of reflected radiation to at-satellite radiance</i>	639
<b>Appendix C</b>	<i>TM-class sensors</i>	646
<b>Appendix D</b>	<i>AVHRR-class sensors</i>	651
<b>Appendix E</b>	<i>GOES-class sensors</i>	661
<b>Appendix F</b>	<i>Scan and satellite location geometry</i>	666
<b>Appendix G</b>	<i>Automated volcano hot spot detection: worked example</i>	669
<b>Appendix H</b>	<i>Optical pyrometers</i>	680
<b>Appendix I</b>	<i>Thermal camera options</i>	684
<i>References</i>		688
<i>Index</i>		717

**Electronic supplements – available at [www.cambridge.org/radiometry](http://www.cambridge.org/radiometry)**

<b>ES 1</b>	<i>Detection capabilities of thermal sensors</i>
<b>ES 2</b>	<i>Calibration</i>
<b>ES 3</b>	<i>Surface temperature retrieval</i>
<b>ES 4</b>	<i>Notes on application of emissivity, atmospheric and surface reflection corrections</i>
<b>ES 5</b>	<i>The dual-band method: A history of its application to volcanic hot spots</i>
<b>ES 6</b>	<i>The dual-band method: worked examples</i>

- ES 7** *Conversion from spectral radiance to lava area, heat flux and discharge rate*
- ES 8** *Fire detection algorithms, 1985–1995*
- ES 9** *Fixed threshold algorithms used for volcano hot spot detection*
- ES 10** *Image sharpening and density slicing: An example using an AVHRR image*
- ES 11** *Etna 2008–2010 eruption: MODIS-derived time series data*

Color plate section is found between pages

[344](#) and [345](#)

## Acknowledgments

This book was initially an effort led by the thermal remote sensing group of the Hawaii Institute of Planetology and Geophysics (HIGP) at the University of Hawaii. It resulted from a proposal, made to Cambridge University Press in 2005, by Robert Wright, and also involved Luke Flynn and Peter Mouginis-Mark. Figure drafting was completed by Lucia Gurioli, supported by funding provided by the Hawaii Space Grant Consortium. Andrew Harris wrote this book while a faculty member at HIGP and, from 2009 onwards, at the Laboratoire Magmas et Volcans (Université Blaise Pascal). The author is most grateful to Thomas and Daniel Harris for giving up valuable playing time to allow book completion, as well as for making useful suggestions. I am also extremely grateful for the time, effort and careful edits made by each of the chapter reviewers, these being: Dave Rothery ([Chapters 0 and 1](#)), Martin Wooster ([Chapters 2 and 3](#)), Clive Oppenheimer, Laszlo Keszthelyi and Steve Baloga ([Chapter 4](#)), Tania Ganci ([Chapter 5](#)), Mike Ramsey ([Chapter 6](#)), Harry Pinkerton ([Chapter 7](#)), Mike James ([Chapter 8](#)), and Letizia Spampinato and Matthew Patrick ([Chapter 9](#)). Finally, I thank Fran Van Wyk de Vries for helping with a thorough final check of the delivered text. This work was supported by the Région Auvergne (Chaire d'Excellence) and is ClerVolc Center of Excellence contribution no. 41.



# 0

## Introduction

### *Background, motivation and essential definitions*

From a geophysical point of view, volcanic eruptions produce earthquakes, deformation, gas, sound and heat. As magma ascends it fractures rock, and flows to produce seismic shocks and tremors. With ascent and intrusion the magma also deforms the Earth's surface. Exsolution of volatiles generates gas emission through the edifice flanks, fumaroles and (if present and open) from the central conduit. Upon eruption, the explosion or effusion produces sound as well as a cloud of ash and gas, and/or emission of lava. With ascent, intrusion and eruption, the magma also loses heat to the Earth's crust and atmosphere ([Figure 0.1](#)). In the case of effusion, heat loss occurs by direct radiation from the lava surface to space and convection due to wind blowing over the lava surface or, in still air conditions, generation of convection cells due to heating of the overlying air. In the case of intrusion, heat loss occurs by permeable convection across the overlying country rock, so that the heat is then lost from the surface across a geothermally heated zone or fumarole field.

Consequently, volcanoes tend to be monitored using instruments that can measure seismicity, deformation, gas emission, sound and/or heat. Thus seismometers are deployed to monitor tremor, tilt-meters for deformation, spectrometers for gas, infrasonic sensors for sound, and thermocouples or radiometers for heat. Of these quantities, volcano seismology and deformation have two dedicated texts, these being *Introduction to Volcano Seismology* by Zobin ([2003](#)) and *Volcano Deformation* by Dzurisin ([2007](#)). Gas has a number of texts, which together cover the exsolution, emission, dispersion and measurement processes (e.g., Carroll and Holloway, [1994](#); Oppenheimer *et al.*, [2004](#); Williams-Jones *et al.*, [2008](#)). However, such manuals for infrasonic measurements at active volcanic systems or thermal remote sensing of hot volcanic phenomena are lacking. The aim of this book is to fill the thermal remote sensing gap, with our focus being on remote sensing of thermal emission during volcanic activity.

### **0.1 Remote sensing of terrestrial volcanic hot spots: a brief history**

Since 1985, a growing body of literature has demonstrated how remote measurements of heat emitted by active lava flows, lava domes, lava lakes and erupting, or degassing, vents can provide insights into the physical processes that are both the cause and consequence of

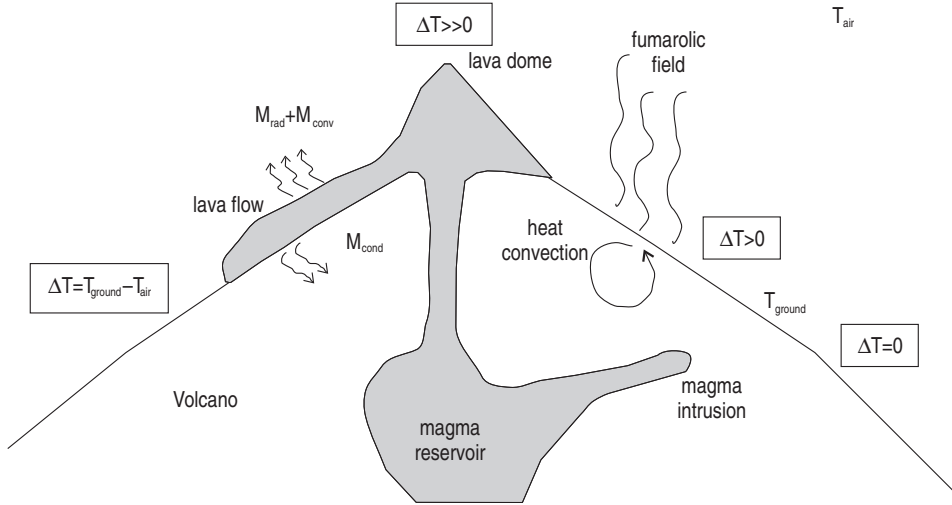


Figure 0.1 Sketch of the main sources of thermal emission that can be detected by a satellite or airborne sensor [modified from Bonneville and Gouze (1992, Fig. 1); reproduced by permission of American Geophysical Union]. In normal conditions ground ( $T_{\text{ground}}$ ) and air temperature ( $T_{\text{air}}$ ) are approximately equal, so that  $\Delta T = T_{\text{ground}} - T_{\text{air}} \approx 0$ . Over a subsurface heat supply, such as a magmatic intrusion, above which natural convection in porous, or fractured, rock carries heat to the surface,  $\Delta T$  becomes positive. Over a high-temperature surface heat source, such as an active lava,  $\Delta T$  becomes strongly positive. Given data collected at the correct wavelengths and spatial resolution, both anomalies can be detected by a satellite infrared sensor. The schematic diagram also shows the main sources of heat loss from an active lava body which are typically calculated using infrared data; these being radiation ( $M_{\text{rad}}$ ), convection ( $M_{\text{conv}}$ ) and conduction ( $M_{\text{cond}}$ ).

volcanic eruptions. Although much in the field of satellite volcano-radiometry is relatively new, the first paper describing satellite observations of active volcanism was published as long ago as 1965 (Gawarecki *et al.*, 1965), just five years after the first satellite dedicated to observing the Earth's surface for peaceful means, TIROS-1, was launched. However, although several papers describing serendipitous satellite observations of volcanic eruptions were published in the years following this landmark paper, it was not until the mid 1980s that serious attention was devoted to the question of what quantitative data for eruptive products and processes could be extracted from remotely sensed thermal data. We summarize the developments, themes and landmark years in thermal remote sensing of volcanic hot spots in the flow chart of Figure 0.2 (based on the literature collation of Appendix A).

A group of four papers published between 1985 and 1988 (Bonneville *et al.*, 1985; Bonneville and Kerr, 1987; Francis and Rothery, 1987; Rothery *et al.*, 1988) did much to establish the technique of satellite remote sensing as a viable source of data for estimating the temperatures of, and heat flux from, active lava bodies. These studies also gave impetus to a wider group of researchers who began to build upon this initial work. The work of

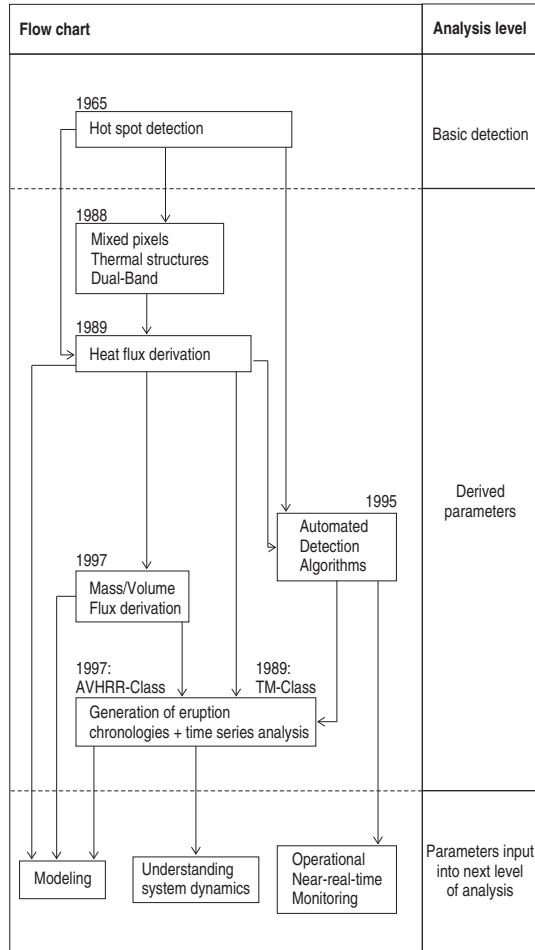


Figure 0.2 Flow chart tracing the key developments and landmark years in satellite-based thermal remote sensing of volcanic hot spots. Four main themes have developed out of the initial discovery, by Gawarecki *et al.* (1965), that hot spots related to volcanic activity could be detected in infrared data provided by satellite-flown sensors. These themes are: (1) analysis of mixed pixels to extract surface thermal structures, (2) derivation of heat and mass fluxes, (3) development of eruption chronologies, and (4) automated hot spot detection. Landmark years relate to the papers of Rothery *et al.* (1988) and Glaze *et al.* (1989) for themes (1) and (2), respectively, and to the publication of the first automated hot spot detection algorithm by Harris *et al.* (1995) for theme (4). For theme (3) we trace the first high spatial, but low temporal, resolution time series to the TM-based work of Glaze *et al.* (1989). For high temporal resolution time series, we use the development of the AVHRR- and ATSR-based work by Harris *et al.* (1997) and Wooster and Rothery (1997) as the starting point.

Rothery *et al.* (1988), for example, was mainly focused on demonstrating techniques by which the temperature of active lava domes, flows, and lakes could be determined from space at the sub-pixel scale, using high-spatial-resolution (30 to 120 m pixel) satellite data acquired by Landsat's Thematic Mapper (TM) sensor. A series of papers followed that showed how such temperature extractions could be used to derive other heat-loss parameters, and estimate the thermal budgets, for a variety of active volcanic systems (Glaze *et al.*, 1989), the temperature of lava flow interiors (Pieri *et al.*, 1990), and the variation in surface temperature and crust thickness with distance from the vent (Oppenheimer, 1991). These papers marked the development of a new emphasis which went beyond simply applying and testing detection and temperature retrieval techniques but, instead, also derived higher-level physical parameters.

Beginning in the mid 1990s a new developmental direction began to evolve. This began to address the fact that the dynamic nature of volcanic eruptions benefits from regular collection of thermal data at a high frequency. As a result, workers began to look towards low-spatial-resolution meteorological satellites which, out of necessity, acquire data on an hourly to daily basis. Using the Advanced Very High Resolution Radiometer (AVHRR) and the Along-Track Scanning Radiometer (ATSR) workers showed that by adapting the techniques developed using Landsat TM data, these low-spatial-resolution satellite sensors could be used to compile complete eruption chronologies and perform retrospective analyses of entire eruptive episodes (Harris *et al.*, 1997a; Wooster and Rothery, 1997a). Parallel with this work, efforts to use satellite thermal data to contribute to routine, real-time monitoring efforts developed rapidly during the 1990s. This resulted in the development of algorithms to automatically detect, and give notice of new effusive activity, or to flag changes in on-going activity. This was driven largely by the increasing use of AVHRR data in an operational setting as part of the volcano monitoring efforts at the University of Alaska Fairbanks (Dean *et al.*, 1996).

The start of the new millennium saw a major advance in the range of resources available for the analysis of the thermal signatures of erupting volcanoes, with the launch of several NASA spacecraft under the banner of Earth Observing System (EOS). The Terra, Landsat-7, Aqua and EO-1 (Earth Observing) spacecraft all carried sensors that allowed the thermal emission from an active volcano to be studied from space. As a result, the first truly global satellite volcano monitoring system became established, which monitored all the Earth's active and potentially active volcanoes on a daily basis (Wright *et al.*, 2004). This system began operation in February 2000, and constituted an archive of the heat flux from all of the Earth's erupting volcanoes (Wright and Flynn, 2004).

The progression culminated in the use of parameters derived from satellite thermal data to drive higher-level modeling, such as flow emplacement simulations, and integration with other geophysical and physical volcanology data sets to allow improved constraint of system dynamics. Such themes thus form the current terminus to our Figure 0.2 flow chart.

Likewise, initial advances in ground-based radiometry made during the 1960s were followed up with a series of studies which steadily increased in number during the 1990s, and more rapidly after 2000. While portable spectrometers have been used to obtain point

measurements of lava flows and lava lakes at hundreds of wavelengths (e.g., Flynn *et al.*, 1993), radiometers have been adapted and exploited to measure thermal flux from erupting volcanoes, at intervals of a second or less, for time periods spanning weeks to years (e.g., Marchetti and Harris, 2008). A recent development has been the use of hand-held Forward Looking Infrared (FLIR) thermal-imaging cameras to acquire spatially and temporally detailed measurements of lava surface temperatures (e.g., Oppenheimer and Yirgu, 2002) and explosive events emitting high-temperature ejecta (e.g., Patrick *et al.*, 2007). We will return in more detail to the development of satellite thermal remote sensing of volcanic hot spots in Chapter 1, and to ground-based approaches in Part III.

## 0.2 Thermal remote sensing: What it is and what we have

Chapter 1 of Curran (1985) provides a brief review of the development of remote sensing as a technique and discipline. In addition, Chapter 2 of the *Manual of Remote Sensing* provides a detailed history, tracing developments in remote sensing since the (first, or) earliest surviving photographs taken by Niepce in 1825–26 and Daguerre in 1838–39 (Fischer *et al.*, 1975). First coined as a term by Evelyn L. Pruitt at the US Office of Naval Research in the 1960s, remote sensing can be defined as “the observation and measurement of an object without touching it” (p. 1, Curran, 1985). Such a definition spans many disciplines including geography, geology, botany, zoology, civil engineering, forestry, meteorology, agriculture and oceanography. This definition also spans a variety of techniques, meaning that volcanological measurements made using seismometers, infrasonic sensors, even a microprobe, fall under the banner of remote sensing. Thus, a more specific definition has been developed, this being: “the use of electromagnetic radiation sensors to record images of the environment which can be interpreted to yield useful information” (p. 1, Curran, 1985). One modification to this definition would be to replace “images” with “data,” thereby including the use of spot-based temperature measurements using thermal infrared thermometers or radiometers. This definition also spans the full electromagnetic spectrum, spanning wavelengths from 3 Ångströms (X-ray-based measurements) to 3 km (radio frequencies). Thus, to narrow the definition further, we are here strictly interested in the thermal infrared portion of the spectrum. Thus, the definition, for our purposes, can be modified to: “the use of electromagnetic radiation sensors operating in the thermal infrared portion of the spectrum to record data for active volcanic phenomena which can be interpreted to yield useful information.”

No satellite or commercially available ground-based thermal sensor has ever been designed primarily for a volcanological use, and no satellite mission dedicated to volcanology has ever been launched. However, there are many thermal sensors designed for military, civilian and industrial applications that can be adapted for volcanological applications. Volcanologists have thus had to use sensors and data that were never intended for volcanological roles. The data are not always perfect. Data from weather satellites, for example, provide data at wavebands and frequencies suitable for examining volcanic hot

spots. However, because the meteorologist is typically interested in low temperatures associated with cloud tops and ambient temperatures associated with the ground surface, the upper limit of these sensors (in terms of temperature detection) is often rather low, meaning that they typically saturate over even quite small volcanic hot spots. The remote sensing volcanologist has to work within these limits, as well as be highly imaginative in the way he adapts to the limits of the available data. Until an appropriately designed sensor, with suitable wavebands, gain settings, spatial resolution and orbit configuration becomes available, we will have to continue to adapt data intended for other applications. The aim of this book is to provide a thorough review of technologies and methodologies that should allow continued application of remotely sensed thermal data in volcanology.

### 0.3 Reviews to date and the value of thermal remote sensing

Although no one book has been written which focuses entirely on remote sensing of active volcanism, a number of short reviews do exist which give the state of the discipline at the time of each review. These include the following (in chronological order).

- 1974: Cassinis, R. and Lechi, G. I. (1974). The use of infrared radiometry in geothermal areas. In *Physical Volcanology*, ed. Civetta, Gasparini, Luongo and Rapolla. Amsterdam: Elsevier, pp. 117–131.
- 1979: Francis, P. W. (1979). Infra-red techniques for volcano monitoring and prediction – a review. *Journal of the Geological Society London*, **136**, 355–359.
- 1989: Mouginis-Mark P. J., Pieri, D. C., Francis, P. W. et al. (1989). Remote sensing of volcanoes and volcanic terrains. *EOS*, **70**(52), 1567–1575.
- 1989: Rothery, D. A. (1989). Volcano monitoring by satellite. *Geology Today*, July–August 1989, 128–132.
- 1992: Francis, P. and Oppenheimer, C. (1992). Applications of satellite remote sensing techniques to volcanology. In *Understanding the Terrestrial Environment – the Role of Observation from Space*, ed. Mather, London: Taylor & Francis, pp. 37–52.
- 1992: Mouginis-Mark, P. J. and Francis, P. W. (1992). Satellite observations of active volcanoes: prospects for the 1990's. *Episodes*, **15**(1), 46–55.
- 1992: Rothery, D. A. (1992). Monitoring and warning of volcanic eruptions by remote sensing. In *Geohazards Natural and Man-Made*, ed. McCall, Laming and Scott, London: Chapman & Hall, pp. 25–32.
- 1992: Rothery, D. A. and Lawrence, G. (1992). Remote sensing for the study of volcanoes and earthquakes. *Geoscientist*, **3**(6), 10–11.
- 1993: Oppenheimer, C. (1993c). I spy with my infrared eye. *New Scientist*, **1876**, 26–31.
- 1996: Francis, P. W., Wadge, G. and Mouginis-Mark, P. J. (1996). Satellite monitoring of volcanoes. In *Monitoring and Mitigation of Volcano Hazards*, ed. Scarpa and Tilling. Berlin: Springer-Verlag, pp. 257–298.
- 1997: Oppenheimer, C. (1997c). Surveillance and mapping of volcanoes and their emissions by satellite remote sensing. *Geography*, **82**(4), 317–333.

- 2000: Francis, P. and Rothery, D. (2000). Remote sensing of active volcanoes. *Annual Review of Earth and Planetary Sciences*, **28**, 81–106.
- 2008: Ernst, G. G. J., Kervyn, M. and Teeuw, R. M. (2008). Advances in remote sensing of volcanic activity and hazards, with special consideration to applications in developing countries. *International Journal of Remote Sensing*, **29**(22), 6687–6723.

Following the listing of Kervyn *et al.* (2007), four main volcanological remote sensing application themes can be identified in these reviews.

- (1) Detection, analysis and monitoring of thermal phenomena associated with active volcanic systems, including active lava flows, lava lakes, lava domes, degassing vents, fumarole fields, crater lakes and geothermally heated ground.
- (2) Detection, analysis and monitoring of clouds of volcanic ash and gas.
- (3) Mapping of volcanic deposits and morphological analysis, including spectrally based identification of mineralogical, textural and compositional differences between different units.
- (4) Assessment of ground deformation, derivation of digital elevation models, volumetric assessment, and surface roughness mapping using radar.

Several of the reviews listed above consider all four of these themes, although here we are strictly concerned only with the first: remote sensing of volcanic thermal phenomena associated with active volcanic systems. Of the thirteen reviews listed, seven were written during the 1990s, with three appearing in the popular scientific literature (*Geology Today*, *Geoscientist* and *New Scientist*). This trend marks the take-off and establishment of satellite-based remote sensing as a volcanological technique during the same decade.

The most visionary of the reviews was that of Francis (1979). Published at a time when just two papers had been published dealing with volcanological applications of satellite data, Francis (1979) recognized the potential value of yet-to-be launched sensors such as Landsat's Thematic Mapper. More specific reviews focusing on satellite remote sensing of active lavas, volcanic gas plumes and ash clouds, as well as airborne scanner applications to geothermal areas, have also been provided, these being the reviews of Rothery and Pieri (1993), Symonds *et al.* (1994), Sparks *et al.* (1997), and Cassinis and Lechi (1974), respectively. In addition, reviews have been written focusing on volcanological applications of specific sensors, these being the reviews of AVHRR applications to volcanology by Oppenheimer (1998) and of Landsat TM/ETM+ by Flynn *et al.* (2000; 2001). Radar applications have also been covered by Gens and Van Genderen (1996), with uses of satellite data for deformation and digital elevation model derivation being reviewed by Dzurisin (2007) and Kervyn *et al.* (2007). Volcanological applications of sensors flown as part of NASA's Earth Observing System have been previewed by Mouginis-Mark *et al.* (1991) and reviewed by Ramsey and Flynn (2004), with Drury (2001) covering geological mapping (including volcanic terrains). For our purposes, the most relevant text to date is the review of ground- and space-based thermal infrared techniques for measuring and monitoring high and low temperature volcanic hot spots by Rothery *et al.* (1995).

What all of these reviews highlight are the five main benefits thermal remote sensing offer to volcanology. These being:

- (1) Measurements that extend beyond the visible range of the electromagnetic spectrum and into the thermal infrared.
- (2) Regular and fixed return periods, with sensors mounted on polar orbiting and geostationary satellites allowing repeat monitoring of a given point on the Earth's surface at a known and reliable frequency.
- (3) Synoptic capability, with satellite-based sensors allowing entire volcanoes and volcanically active regions to be examined with a single image.
- (4) Continuity of data acquisition, where satellite missions that operate over several decades guarantee provision of time series data in a standard and consistent format.
- (5) Global capability, where polar orbiting satellites and constellations of geostationary platforms allow coverage of the entire planet, and all active and dormant sub-aerial volcanoes within their image footprints.

In addition, thermal data from satellite sensors are becoming increasingly cheap, and in many cases freely available. The fixed, calibrated, digital format data also suits automation and allows routine processing, with the data format for most satellite sensors being detailed in dedicated user manuals, such as the *Polar Orbiters User Manual* written to support unpacking of AVHRR data (e.g., Kidwell, 1991; 1995). Availability of easy-to-use, off-the-shelf image processing software also makes data analysis and interpretation straightforward. For example, MODIS data are available in a variety of calibrated and georectified formats at no cost from NASA within a few hours of acquisition and TM and ETM+ data are now also freely available in GEOTIFF format. Both data types can be read by any off-the-shelf image processing package.

Even the cost of a receiving station, which allows free, direct data reception and real-time access, can be less than US\$ 5000, with system costs varying depending on sophistication of the reception system ([Table 0.1](#)). As early as 1992, Gower *et al.* (1992) detailed a receiving station comprising a 1.2 m dish (US\$ 200) and steering device (US\$ 400), a receiver and down-converter (US\$ 1000), and a PC interface (US\$ 1150) with 200 Mbytes of disk storage (US\$ 2000). The entire station thus cost just US\$ 4750 at 1992 prices ([Table 0.1](#)).

As a result, by the early 1990s, direct reception for volcanological analysis had even been achieved by some schools. Matthews *et al.* (1994), for example, reported use of a satellite receiving station purchased and installed at Ulverston Victoria High School in the United Kingdom. Images were received using a VHF aerial and an aimed dish. Software, provided by Dartcom (see [Table 0.1](#)) and running on a desktop computer, then allowed AVHRR, GOES and Meteosat images to be downloaded as they were transmitted, allowing the 1993 eruptions of Llaima (Southern Chile) and Rinjani (Indonesia) to be observed and reported by the students. Today satellite thermal data can also be obtained via the internet within hours of image acquisition. For example, MODIS Level 1b data can currently (October 2011) be downloaded from <http://ladsweb.nascom.nasa.gov/>. In addition, for more than a decade

Table 0.1. *Costs and details of commercially available AVHRR receiving stations in 1996 (from Harris, 1996).*

System hardware and software details	Company address	Cost (date of quote)
Bradford University Research Limited	Bradford University, Bradford, UK	US\$ 2700 upwards (1994)
Hardware:	Motorized antenna to track satellite, cable to PC, PC card to convert data to PC readable format.	
Software:	Automatic tracking and reception software included. (HRPT and SEAWiFs compatible.)	
System installed at the Institute of Ocean Sciences	Institute of Ocean Science, Sidney V8L 4B2, Canada	US\$ 4750 (Gower <i>et al.</i> , 1992)
Hardware:	PC interface board, receiver feed, combiner . . . pre-amplifier/down-converter, PC, 1.2 m dish, antenna steering device.	
Software:	Real time display of central strip of image and data archiving. (Chinese Feng-Yun satellite FY-1 compatible.)	
Timestep PROsat II system	Timestep, Newmarket, CB8 8XB, UK	US\$ 4800 (1995)
Hardware:	PC, 170 Mb hard drive, HR color monitor, dish antenna with all cables and associated hardware and software.	
Software:	Live display, saves full pass in full resolution, calibration, geo-referencing, satellite track prediction, image processing. (GOES/Meteosat compatible.)	
SeaSpace TeraScan system	SeaSpace, San Diego, CA 92126, USA	>US\$ 20 000 (1995)
Hardware:	1.0 m antenna, 1.5 m protective dome (survival conditions: -30 to +55 °C, 162 km/h winds, 22 kg/m <sup>2</sup> ice loading), amplifier and down-converter, cable, Sun-4/50 SPARC work station, DAT archive tape drive.	
Software:	Antenna control and data acquisition (includes automatic unattended operation), calibration, geo-location, cloud screening and image processing.	

Table 0.1. (*cont.*)

System hardware and software details	Company address	Cost (date of quote)
Dartcom winHRPT system	Dartcom, Yelverton, PL20 6SP, UK	US\$ 38 000 – 62 000 (1996)
Hardware:	Pentium PCI, 1 Gb fast SCSI II hard disk, archiving drives, FST monitor, 1.2–1.8 m antenna (survival conditions: −35 to +63 °C, 210 km/h winds), down-converter and receiver, built-in GPS.	
Software:	Antenna control, image acquisition and quick look, image processing including reflectance and temperature calibration and geo-location.	

now, location and spectral radiance data for hot spots detected by the University of Hawaii's MODVOLC hot spot detection system have been downloadable from <http://modis.higp.hawaii.edu/> within hours of hot spot detection. Modern, internet-based capabilities mean that, if a user wants to obtain data for a volcanic hot spot, they do not need a receiving station, just access to the internet.

#### 0.4 Thermal remote sensing of volcanic hot spots on other planets

An excellent book has recently been published by Cambridge University Press authored by Ashley Davies and covering thermal remote sensing of active volcanic phenomena on Jupiter's moon Io (Davies, 2008). Io is the only known body in the solar system to exhibit on-going high temperature volcanism beyond Earth. As a result, Io has witnessed two thermal remote sensing missions and programs designed to measure and examine this activity (namely Galileo and the New Horizons flyby). These are reviewed by Davies (2008), as are the techniques and applications developed to measure and track active volcanism on Io using remotely sensed thermal data. However, no similar text is available for this planet.

Thus, although we originally planned to include a chapter on extra-terrestrial remote sensing of volcanic hot spots, the publication of Davies (2008) makes such a chapter redundant. In fact, that thermal remote sensing of Io required a book to adequately cover the full body of knowledge regarding missions to Io, and the science completed, shows that relegating this subject to a chapter in this book would have done Io a disservice. Here, we solely consider terrestrial thermal remote sensing of volcanic hot spots, and refer the reader to Davies (2008) for the state-of-the-art regarding extra-terrestrial remote sensing of active volcanic hot spots. We note, though, that the principles and techniques described here are equally transferable to extra-terrestrial scenarios.

## 0.5 Aim and use of this book

Thermal remote sensing of active volcanoes, as a discipline, is relatively new and has expanded rapidly in the past 30 years, so that thermal remote sensing has become established as a viable discipline in volcanology. To support this new discipline, our aim has been to consolidate descriptions of all of the techniques that have been developed for space- and field-based investigations of the thermal manifestations of active volcanism. To achieve this our material will focus on a number of themes, including the following.

- The instruments that can be utilized to perform volcano radiometry, i.e., which satellite- and ground-based sensors provide appropriate data, how do they operate and what are their limits?
- A review of those methodologies that can be applied to the data acquired by these instruments in order to derive higher-level physical parameters, i.e., what techniques are appropriate to detect volcanic hot spots and extract thermal structures?
- Define what volcanological information can be extracted from the results, i.e., how can thermal measurements be used to estimate magma budgets at persistently active volcanoes, the mass flux of magma and gas at open-vent volcanic systems or the discharge rate of lava at effusive systems?

As a result, this book is designed to be more than a simple distillation of published research papers. Instead, it is a review of the principles, techniques and methodologies applied in thermal remote sensing for active volcanoes. As such, it is designed as a user's manual for any student or professional interested in selecting, using and applying satellite- and ground-based thermal remote sensing data for the analysis of active volcanic phenomena.

## 0.6 Structure and content of this book

Remote sensing texts tend to separate discussion of the technology and techniques from the science and applications. We will adopt this convention, with the book being divided into three main parts.

- **Part I** considers the origins and early history of the discipline, the underlying physical principles of thermal measurements, and the factors controlling temporal, spatial and spectral resolution.
- **Part II** deals with methods applied to, and results obtained from, satellite-based data.
- **Part III** deals with technologies available for ground-based thermal remote sensing, and reviews methods that can be applied to, and results obtained from, radiometer and thermal camera data.

The chapters that comprise each of these sections, and main themes covered in each chapter, are outlined in [Table 0.2](#).

Table 0.2. *Structure and contents of this book with summary of themes covered in each chapter.*

Part / chapter number	Part / chapter title and contents
<b>Part I</b>	<b>Introduction and underlying principles</b>
<i>Chapter 1</i>	<p><i>History of thermal remote sensing of active volcanism</i></p> <ul style="list-style-type: none"> <li>• The development of suitable satellite missions.</li> <li>• Milestones in the establishment of satellite-based thermal remote sensing of active volcanism.</li> <li>• A history of the development of ground-based thermal sensors (radiometers and imagers) and their establishment in volcanology.</li> </ul>
<i>Chapter 2</i>	<p><i>Thermal remote sensing of active volcanism: principles</i></p> <ul style="list-style-type: none"> <li>• Terminology and physics for thermal remote sensing of active volcanism: the Planck function, Wein's Law and Stefan–Boltzmann.</li> <li>• Kinetic temperature and emissivity.</li> <li>• Atmospheric effects in the SWIR, MIR and TIR.</li> <li>• Conversion of at-satellite radiance to brightness and surface temperature.</li> </ul>
<i>Chapter 3</i>	<p><i>Satellite orbits and sensor resolution</i></p> <ul style="list-style-type: none"> <li>• Commonly used satellite sensors, orbits and temporal resolution.</li> <li>• The sensor and generic issues of data calibration/pre-processing.</li> <li>• Spatial resolution, calculation of pixel size and the point spread function.</li> <li>• Temporal resolution and latitudinal coverage.</li> <li>• Spectral resolution.</li> </ul>
<b>Part II</b>	<b>Space-based volcano radiometry</b>
<i>Chapter 4</i>	<p><i>The mixed pixel, the dual-band technique, heat loss and volume flux</i></p> <ul style="list-style-type: none"> <li>• The mixed-pixel problem.</li> <li>• Un-mixing the pixel using the dual-band thermal mixture model.</li> <li>• Three component solutions, reality and worked examples.</li> <li>• Heat flux models for active volcanic systems, and constraints using IR data.</li> <li>• Heat balance, and relation with mass, volume and volume flux.</li> </ul>
<i>Chapter 5</i>	<p><i>Hot spot detection</i></p> <ul style="list-style-type: none"> <li>• Physical basis and underlying concepts.</li> <li>• Detection algorithms.</li> <li>• Cool anomalies.</li> <li>• Operational volcano hot spot detection systems.</li> </ul>
<i>Chapter 6</i>	<p><i>Mapping, classification, time series and profiles</i></p> <ul style="list-style-type: none"> <li>• Hot spot mapping.</li> <li>• Hot spot classification.</li> <li>• Types of time series.</li> <li>• Time series generation.</li> <li>• Case studies using TM-, AVHRR- and GOES-class data.</li> <li>• Spatial profiles.</li> </ul>

Table 0.2. (cont.)

Part / chapter number	Part / chapter title and contents
<b>Part III</b>	<b>Ground-based volcano radiometry and thermography</b>
<i>Chapter 7</i>	<i>Broad-band radiometers I: Instrumentation and application</i> <ul style="list-style-type: none"> <li>• Detector types, capabilities and operation.</li> <li>• Viewing geometry and atmospheric correction.</li> <li>• A review of volcanological applications of ground-based radiometers.</li> <li>• Development of autonomous radiometer packages, logistics of installation/maintenance, and permanent deployment design.</li> </ul>
<i>Chapter 8</i>	<i>Broad-band radiometers II: data collection and analysis principles</i> <ul style="list-style-type: none"> <li>• Data processing and applications for (i) lava flows and lakes, (ii) vents and fumarole fields, and (iii) explosive eruptions.</li> <li>• Response time issues.</li> </ul>
<i>Chapter 9</i>	<i>Broad-band thermal imaging cameras</i> <ul style="list-style-type: none"> <li>• Characteristics of instruments and sensors, available instruments and selection of a suitable model.</li> <li>• A review of volcanological applications of ground-based imagers.</li> <li>• Measurement principles (pixel size and image geometry).</li> <li>• Measurement accuracy and atmospheric effects.</li> <li>• Modes of use in the field (deployment principles).</li> <li>• Application to studying (i) lava flow temperatures, (ii) lava flow dynamics, and (iii) explosive eruptions.</li> <li>• Surveillance and monitoring.</li> </ul>
<b>Appendices</b>	
<i>Appendix A</i>	<i>Collation and summary of satellite-volcano radiometry: a literature data base</i> <ul style="list-style-type: none"> <li>• Literature data base for satellite-based thermal remote sensing of volcanic hot spots: 1960–2005.</li> </ul>
<i>Appendix B</i>	<i>Estimation of solar zenith angle and contribution of reflected radiation to at-satellite radiance</i> <ul style="list-style-type: none"> <li>• Equations to achieve theoretical calculation of reflected solar radiation.</li> </ul>
<i>Appendix C</i>	<i>TM-class sensors</i> <ul style="list-style-type: none"> <li>• Descriptions and characteristics of TM, ETM+ and ASTER.</li> </ul>
<i>Appendix D</i>	<i>AVHRR-class sensors</i> <ul style="list-style-type: none"> <li>• Descriptions and characteristics of AVHRR, ATSR and MODIS.</li> </ul>
<i>Appendix E</i>	<i>GOES-class sensors</i> <ul style="list-style-type: none"> <li>• Descriptions and characteristics of GOES, SEVIRI and MTSAT.</li> </ul>
<i>Appendix F</i>	<i>Scan and satellite location geometry</i> <ul style="list-style-type: none"> <li>• Definitions of scan and satellite geometry terminology.</li> </ul>
<i>Appendix G</i>	<i>Automated volcano hot spot detection: worked example</i> <ul style="list-style-type: none"> <li>• TIR and MIR image of Etna containing a hot spot, with two hot spot detection methodologies applied.</li> </ul>

Table 0.2. (cont.)

Part / chapter number	Part / chapter title and contents
<i>Appendix H</i>	<i>Optical pyrometers</i> • Pyrometer operation and application in volcanology.
<i>Appendix I</i>	<i>Thermal camera options</i>
<b>Electronic supplements</b>	
<i>Supplement 1</i>	<i>Detection capabilities of thermal sensors</i> • Detection capabilities and limits. • Thermal properties of the active lava targets and pixel-integrated temperature. • Detection of volcanic hot spots. • Saturation.
<i>Supplement 2</i>	<i>Calibration</i> • Calibration of satellite sensors (conversion of DN to spectral radiance, and non-linearity corrections).
<i>Supplement 3</i>	<i>Surface temperature retrieval</i> • Worked example of convolution of spectral radiance, response, up-welling radiance, transmissivity and emissivity functions. • Comparison with surface temperature retrieval using band-averaged values.
<i>Supplement 4</i>	<i>Notes on application of emissivity, atmospheric and surface reflection corrections</i> • Definition of MODTRAN, and other commonly used reflection and atmospheric correction routines. • Tables of MODTRAN-derived correction values.
<i>Supplement 5</i>	<i>The dual-band method: a history of its application to volcanic hot spots</i> • History of the dual band applied to TM- and AVHRR-class data (an essay). • A history of attempts to derive heat and mass/volume flux from satellite data.
<i>Supplement 6</i>	<i>Dual-band method: worked examples</i> • Support for Sections 4.1, 4.2 and 4.3 of Chapter 4. • Application of a range of dual-band solutions to AVHRR and TM data.
<i>Supplement 7</i>	<i>Conversion from spectral radiance to lava area, heat flux and discharge rate</i> • Example for anomalous pixel location, atmospheric correction and application of the dual-band method. • Conversion to heat and volume flux, and cross-check with ground-truth. • Worked exercise using an AVHRR image of Mt. Etna containing a lava-flow related hot spot.
<i>Supplement 8</i>	<i>Fire detection algorithms, 1985–1995</i> • A review and collation of fire detection algorithms published during the decade spanning 1985 through 1995.

Table 0.2. (cont.)

Part / chapter number	Part / chapter title and contents
Supplement 9	<i>Fixed threshold volcano hot spot detection algorithms</i> • A review and collation of fixed threshold volcano hot spot detection algorithms published through 2005.
Supplement 10	<i>Image sharpening and density slicing: example</i> • Example application of the image sharpening methodology of <a href="#">Chapter 6</a> . • Uses an AVHRR image acquired during the first hours of Krafla's 1984 eruption.
Supplement 11	<i>MODIS-derived time series data</i> • Data tables used for the time series examples given in <a href="#">Chapter 6</a> . • Large format versions of the panels that comprise <a href="#">Figure 6.14</a> . • Detail of time series construction methodology, with assumptions and parameters used in converting between each time series level. • Case using all cloud-free MODIS hot spot data extracted during Etna's 2008–2009 eruption.

## 0.7 Supporting material and companion texts

In completing this book I drew heavily on the following remote sensing texts, each of which provide excellent and complete groundings in remote sensing, satellites, orbits, sensors and detectors, and which are referenced herein from the chapters to which they are most relevant.

- Curran, P. J. (1985). *Principles of Remote Sensing*, Harlow: Longman Scientific and Technical, 282 p.
- Cracknell, A. P. (1997). *The Advanced Very High Resolution Radiometer*, London: Taylor & Francis, 534 p.
- Cracknell, A. P. and Hayes, L. W. B. (1991). *Introduction to Remote Sensing*, London: Taylor & Francis, 293 p.
- Dereniak, E. L. and Boreman, G. D. (1996). *Infrared Detectors and Systems*, New York: John Wiley & Sons, 561 p.
- Janza, F. J., Blue, H. M. and Johnston, J. E. (1975). *Manual of Remote Sensing, Volume I: Theory, Instruments and Techniques*, Falls Church (VA): American Society of Photogrammetry, 867 p.
- Lillesand, T. M. and Kiefer, R. W. (1987). *Remote Sensing and Image Interpretation*, New York: John Wiley & Sons, 721 p.
- Mouginis-Mark, P. J. and Domergue-Schmidt, N. (2000). Acquisition of satellite data for volcano studies. In *Remote Sensing of Active Volcanoes*, AGU Geophysical Monograph, **116**, pp. 9–24.
- Schott, J. R. (2007). *Remote Sensing: The Image Chain Approach*, New York: Oxford University Press, 666 p.

- Schowengerdt, R. A. (2007). *Remote Sensing: Models and Methods for Image Processing*, Burlington: Academic Press, 515 p.
- Singh, S. M. and Warren, D. E. (1983). Sea surface temperature from infrared measurements. In *Remote Sensing Applications in Marine Science and Technology*, ed. A. P. Cracknell, D. Reidel Publishing Company, pp. 231–262.

## 0.8 Waveband definitions

We need to define the thermal infrared region in which we are interested, as well as the nomenclature that will be used throughout this book. We use the general term infrared (IR) to cover any measurement within the 0.7 to 20  $\mu\text{m}$  waveband, with the techniques we describe falling under the umbrella term *infrared radiometry*. However, this broad waveband has several windows, each of which is useful for examining volcanic thermal phenomena of different temperature, from high-temperature surfaces in the shortwave infrared region (1.1 to 3.0  $\mu\text{m}$ ) to low-temperature surfaces in the longwave infrared region (5.0 to 20  $\mu\text{m}$ ). Following Figure 3.4 of Schott (p. 64, 2007), we define the following abbreviations and limits to the regions of the electromagnetic spectrum within the IR waveband.

Visible	VIS	0.4 to 0.7 $\mu\text{m}$
Near infrared	NIR	0.7 to 1.1 $\mu\text{m}$
Shortwave infrared	SWIR	1.1 to 3.0 $\mu\text{m}$
Midwave infrared	MIR	3.0 to 5.0 $\mu\text{m}$
Longwave infrared	TIR	5.0 to 20 $\mu\text{m}$

The exact “windows” within these regions that we can use for measurements of Earth surface temperature and heat flux depend on the placement of zones of atmospheric absorption of surface-leaving spectral radiance within each waveband, as will be detailed in Chapter 2.

## 0.9 A final note: hot spots and thermal anomalies – what do we mean?

The term *hot spot* is here used to denote a thermally anomalous feature on the Earth’s surface resulting from volcanic activity. The hot spot may thus be related to, for example, the eruption of lava onto, or the presence of hot open vents at, the surface, or from heating of land (or water) surfaces due to a flux of volcanic energy from a deeper magmatic source. A *thermal anomaly* is, in turn, defined as a feature that differs in temperature when compared with typical surface temperatures observed for a particular location over space or time. The surface can thus be spatially or temporally anomalous, and can often be both spatially and temporally anomalous at the same time. The sudden emplacement of a lava flow onto cold, ambient ground, for example, will mean that the inundated area will be much hotter than it was previously (i.e., it is

temporally anomalous), and will also be much hotter than its ambient surroundings (i.e., it is also spatially anomalous). In our case, we are considering positive thermal anomalies, i.e., phenomena that have temperatures that are substantially higher than those of surrounding surfaces, or that are higher than those previously observed for the given location. Both the terms *hot spot* and *thermal anomaly* will be used extensively throughout this book.



## **Part I**

Introduction and underlying principles



# 1

## History of thermal remote sensing of active volcanism

Late in the evening of 4 October 1957, a Soviet R-7 rocket carried the Sputnik-1 satellite into a successful Earth orbit. Although Sputnik transmitted little more than a stream of location data, its launch heralded a new era of satellite remote sensing of the Earth's surface: a man-made satellite was finally in Earth orbit.

The launch of Sputnik-1 was the climax of a 35 year period of rapid developments in rocket technology, culminating in the generation of a vehicle capable of carrying a satellite into orbit. In his book *Countdown*, Heppenheimer (1997) traces the advent of modern rocketry to the post-World War I work of Oberth and the 1923 publication of his book, *Die Rakete zu den Planetenräumen (The Rocket into Interplanetary Space)*. As part of his work, Oberth suggested that, by burning modern fuels such as petrol or liquid oxygen, a rocket could outperform traditional gunpowder-fired missiles thereby making space flight possible. From this starting point, modern rocketry developed through the wonder-weapons of World War II, such as Germany's V-1 and V-2 bombs as well as the Me262 jet fighter, to close with the Cold War space race between the United States and the Soviet Union. The first lap of the race was completed by the Soviet Union with the October 1957 launch of Sputnik-1.

Sputnik-2 (carrying the unfortunate dog Laika) was launched (not quite so successfully) a month later in November 1957. At the end of January 1958, the USA sent Explorer-1 into Earth orbit. Two years later, on 1 April 1960, the first satellite dedicated to observing the Earth's surface for peaceful means, TIROS-1 (Television and Infrared Observation Satellite), was launched carrying the Vidicon instrument. This, in effect, was a TV camera system that provided visible data with a pixel size of 3.8 km. With TIROS-1, the era of satellite-based Earth remote sensing had truly begun.

It was with the launch, from Cape Canaveral on 23 November 1960, of TIROS-2 that the first infrared radiometer attained Earth orbit. Five years later, Garawecki *et al.* (1965) reported the detection of thermal anomalies in infrared data collected by a satellite-based sensor over an active lava flow field. Then, in 1970, Williams and Friedman published "Satellite observation of effusive volcanism" in the *Journal of the British Interplanetary Society*. This paper reported the results from an analysis of infrared data for the 1966 eruption of Surtsey (Williams and Friedman, 1970). These were the first uses of satellite thermal data for volcanological purposes published in the mainstream literature, and, as such, marked the beginning of satellite remote sensing of active volcanism as a discipline.

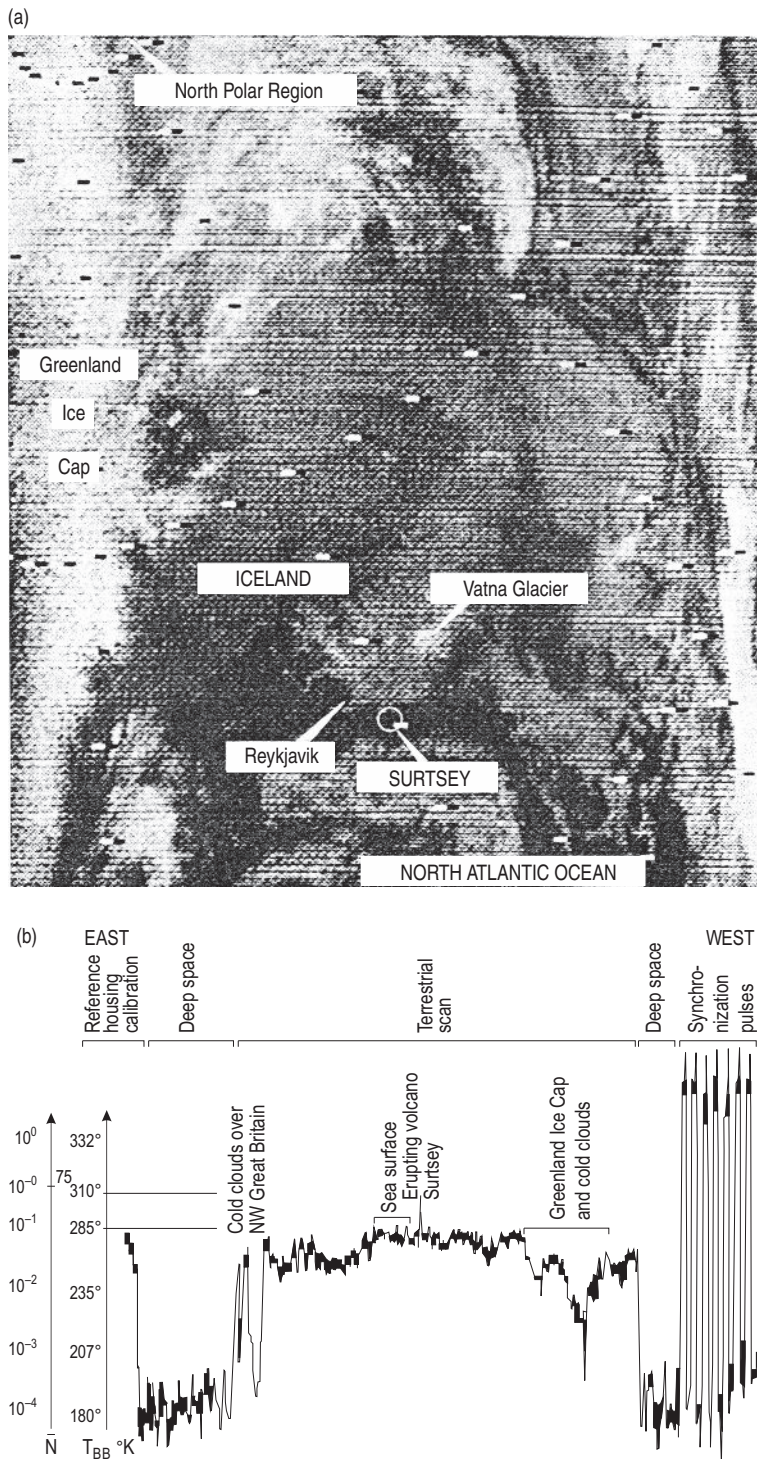


Figure 1.1 (a) Low-spatial-resolution (8 km pixel) infrared (3.45 to 4.07  $\mu\text{m}$ ) image of the North Atlantic Ocean acquired on 22 August 1966 by the HRIR sensor aboard Nimbus II. This was one of the

### 1.1 Nimbus, Surtsey and subsequent work

The first Nimbus satellite was launched on 28 August 1964, with Nimbus-2 being launched two years later on 15 May 1966. Both carried the High Resolution Infrared Radiometer (HRIR) into a near-polar orbit at an altitude of 1114 km. In a review of potential geological applications of space-based infrared imagery, Gawarecki *et al.* (1965) demonstrated the potential of HRIR data from Nimbus-1 to detect volcanic hot spots using data for an effusive eruption at Kilauea (Hawaii, USA). However, it was not until the launch of Nimbus-2 that a study focusing on the full potential of space-based infrared data was published.

Three months after the launch of Nimbus-2, on 19 August 1966, an effusive eruption began at Surtsey (Vestmannaeyjar, Iceland). HRIR successfully detected the associated thermal emission, the image published by Williams and Friedman (1970) being given here in [Figure 1.1a](#). Initially reported in a 1967 progress report (Friedman *et al.*, 1967), as well as in an extended abstract for the 5th Symposium on Remote Sensing of Environment at the University of Michigan (Friedman and Williams, 1968) and a 1969 US Geological Survey research paper (Friedman *et al.*, 1969), the seminal work of Williams and Friedman (1970) used seven Nimbus-2 HRIR images acquired between 20 August and 3 October 1966 to show how the eruption was apparent as a thermal spike, or hot spot, in HRIR's mid-infrared band, as shown in [Figure 1.1b](#). Williams and Friedman (1970) went on to calculate the total radiant heat flux from the entire  $64 \text{ km}^2$  pixel area, this being 30 GW. As traced in [Figure 1.2](#), a total of seven satellites were launched in the Nimbus series. Together, these satellites carried four sensors capable of infrared imaging, these being, in addition to HRIR, the Medium Resolution Infrared Radiometer (MRIR), the Temperature-Humidity Infrared Radiometer (THIR) and the Surface Composition Mapping Radiometer (SCMR). However, only infrared data from HRIR flown on Nimbus-1 and -2 were ever explored for volcano hot spot applications.

Although pre-dated by Gawarecki *et al.* (1965), the work of Williams and Friedman (1970) can be viewed as a landmark because it defined the basic utility of satellite infrared data for analysis of volcanic hot spots. This being two-fold: (1) detection of the hot spot, and (2) constraint of its heat flux. As traced in the flow chart of [Figure 1.3](#), research using satellite thermal data over the 35 years since Williams and Friedman (1970) has focused on, and

---

Caption for Figure 1.1 (cont.)

images used by Williams and Friedman (1970). Through the noise, the shape of Iceland can just be made out with the black spot in the white circle below Iceland marking the Surtsey hot spot. Darker tones relate to higher temperatures. The hot spot, in fact, cannot really be seen in the grainy and noisy original image as reproduced from Williams and Friedman (1970). However, the scan-line data of [Figure 1.1b](#) are somewhat more compelling [from Williams and Friedman (1970), Fig. 3]. (b) Nimbus II thermal record for one HRIR scan cycle for the same image as given in (a). It shows 3.45 to 4.07  $\mu\text{m}$  radiance ( $\bar{N}$ ,  $\text{W m}^{-2}\text{sr}^{-1}$ ) and brightness temperature ( $T_{\text{BB}}$ ) along the scan. The hot spot at Surtsey is apparent as a spike in the record. It is also the pixel with the highest temperature in the scan [from Williams and Friedman (1970), Fig. 4].

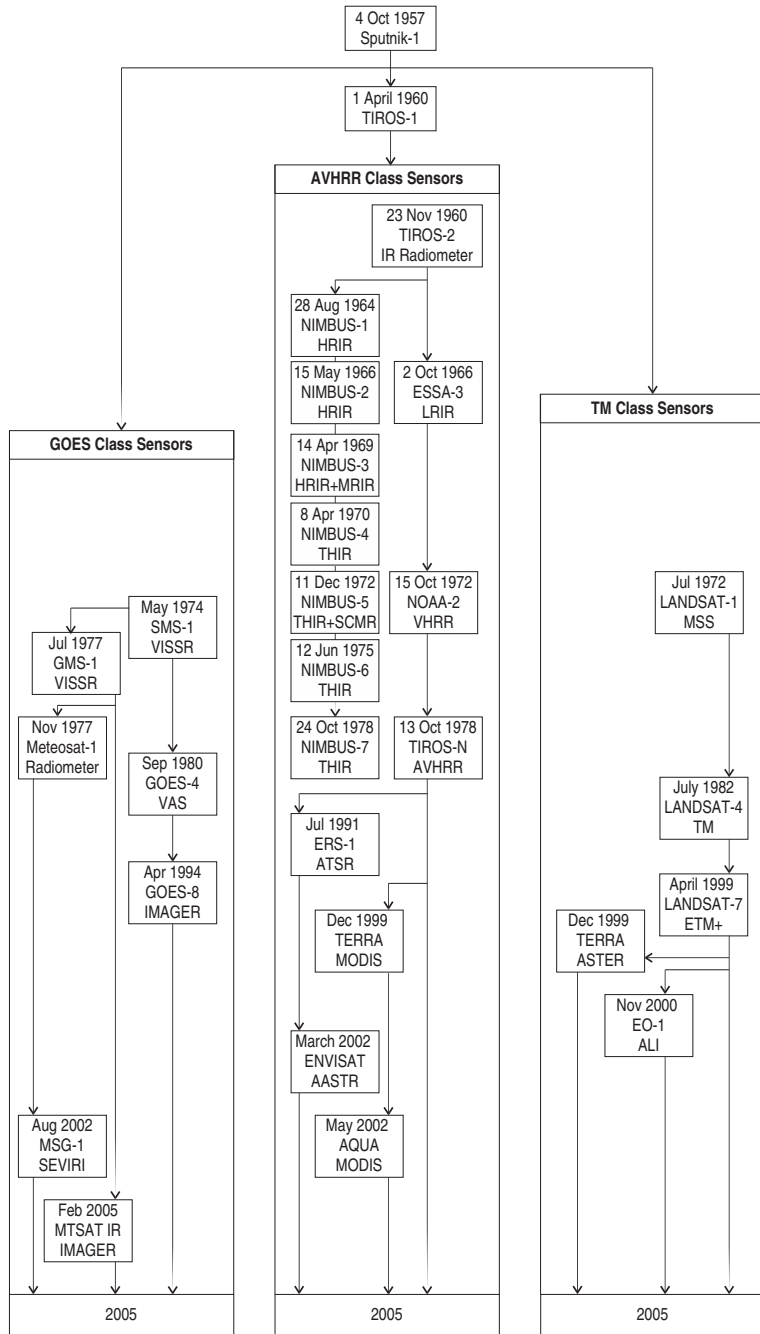


Figure 1.2 Flow chart tracking the availability of each satellite-flown sensor commonly used for thermal remote sensing of active volcanism. Sensors are split into their three main classes (TM-, AVHRR- and GOES-class), as will be defined in Chapter 3.

(a)

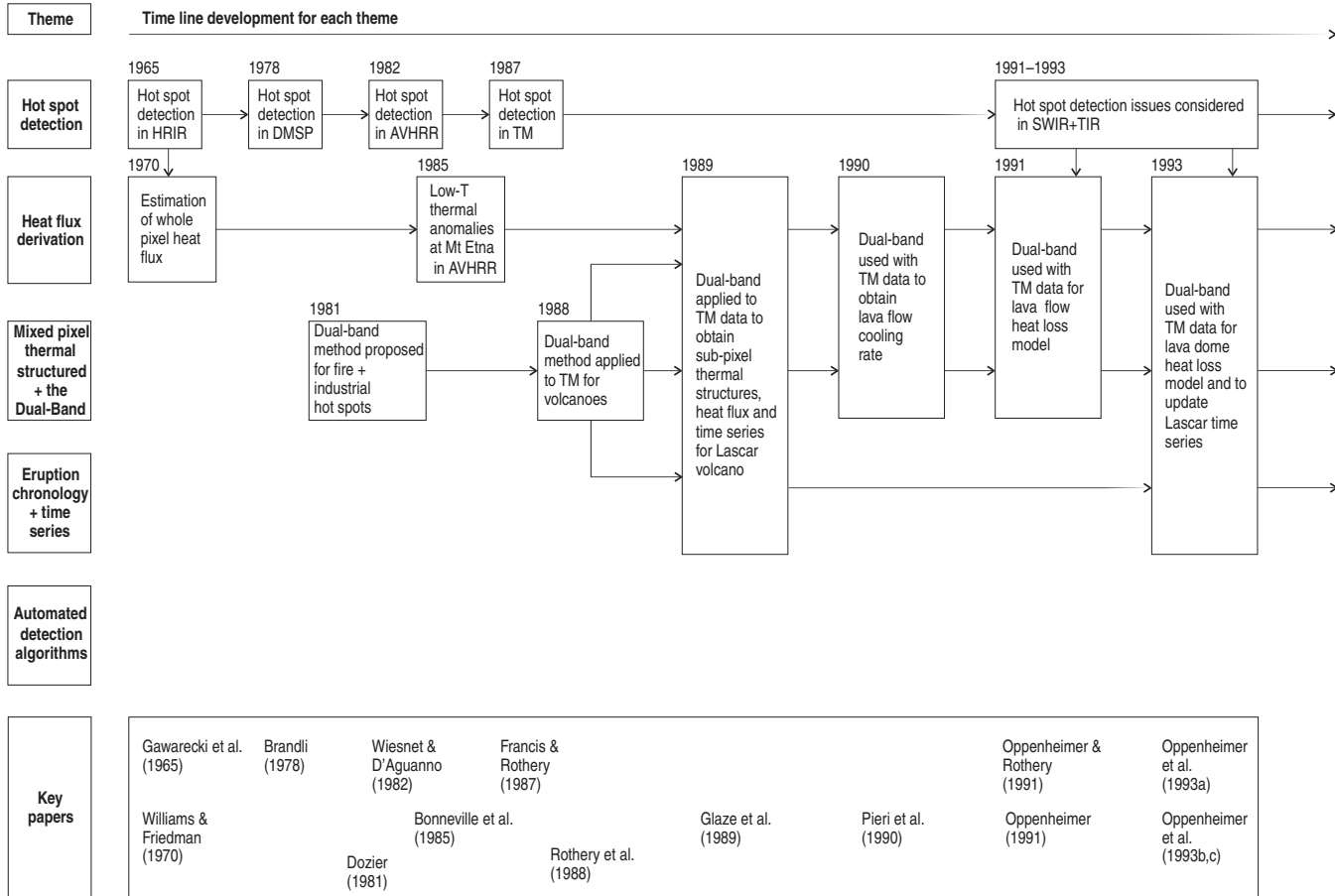


Figure 1.3(a) Flow chart detailing the key advances in each of the six main theme areas in satellite-based thermal remote sensing of active volcanism between 1965 and 1993. The key paper marking each advance is referenced at the base of the chart.

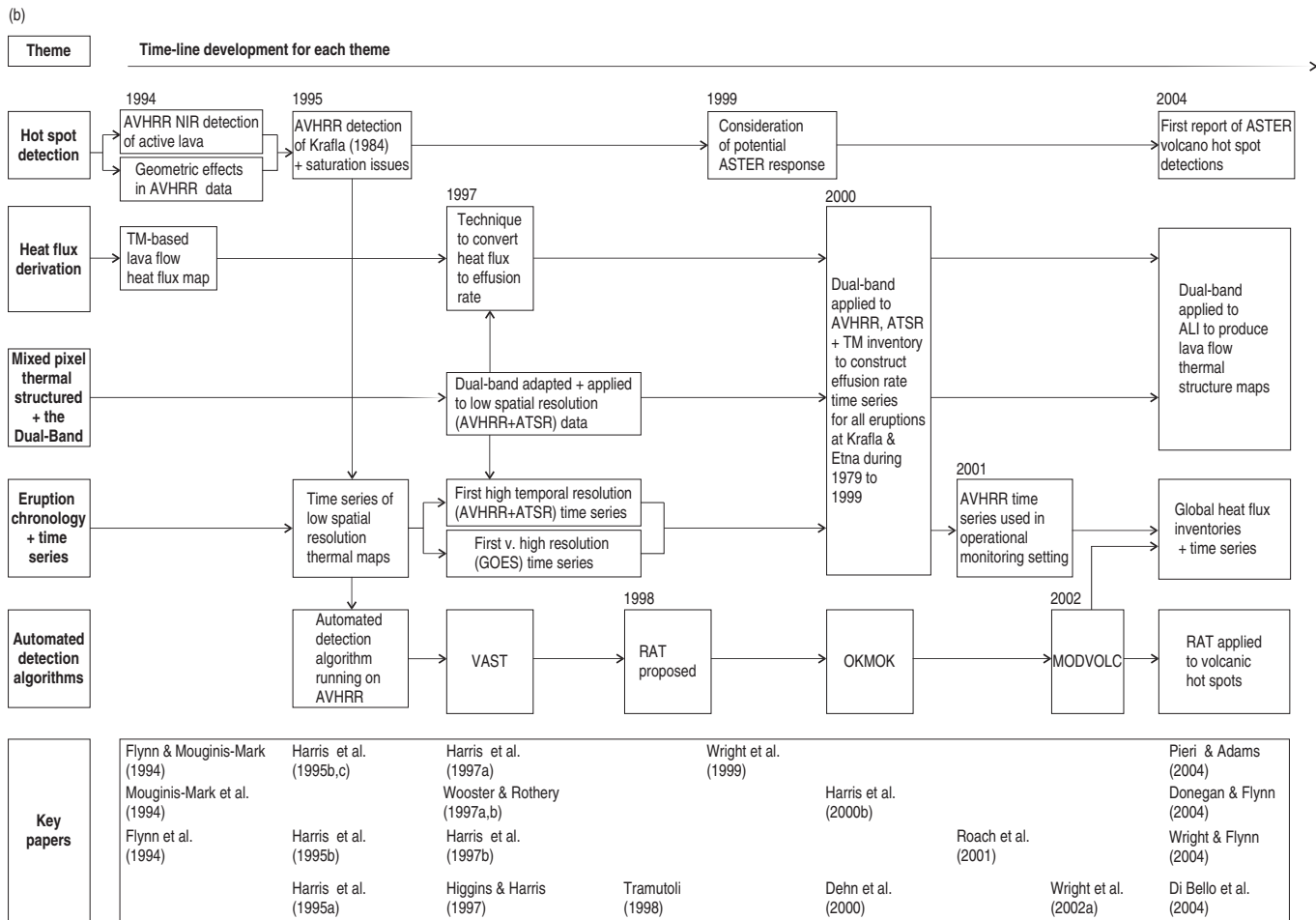


Figure 1.3(b) Flow chart detailing the key advances in each of the six main theme areas in satellite-based thermal remote sensing of active volcanism between 1994 and 2004. The key paper marking each advance is referenced at the base of the chart.

developed from, these two basic themes. Since 1970, more than 100 scientific papers have been published that use satellite thermal data to examine volcanic hot spots associated with active lava flows, lava domes, lava lakes, active vents, fumaroles and crater lakes. [Appendix A](#) provides a full collation and content summary of these works, as well as details regarding the satellite sensor(s) used. If we plot the number of publications per year between 1965 and 2005, as done in [Figure 1.4a](#), we see that work really picked up during the mid 1980s, supported by data primarily from AVHRR and TM ([Figure 1.4b](#)), with the two basic themes of detection and heat flux measurement being rapidly developed ([Figure 1.4c](#)).

Before we explore the history of satellite-based thermal remote sensing of active volcanism, we first need to consider the satellites and sensors that allowed this progress, for it was their availability that dictated the rate of progress. As explained in [Chapter 0](#), a dedicated satellite mission with a primarily volcanological role has yet to be launched. The initiation and development of satellite programs that supported the operation of infrared-capable sensors for weather and Earth observation purposes has thus been fundamental in the evolution of thermal remote sensing of active volcanism. However, as is already apparent from the 10-year-long lag between the first launch of an infrared-capable satellite sensor, aboard TIROS-2, and the publication of Williams and Friedman ([1970](#)), the history has been characterized by a lag between data availability and volcanological application.

## 1.2 A history of satellite infrared sensors

### 1.2.1 The workhorses: AVHRR and TM

The time-line for the launch of those satellite-based infrared sensors used for volcano hot spot analysis is given in [Figure 1.2](#). [Figure 1.2](#) shows that three main types of sensor have been used, these being AVHRR-, TM- and GOES-class, with each coming on-line in 1960, 1972 and 1974, respectively. Subsequently, although the number and type of sensor in each class has evolved, data availability within each class has been continuous.

Data from two of these sensors, the Advanced Very High Resolution Radiometer (AVHRR) and the Thematic Mapper (TM), have been the main data sources for satellite-based thermal studies of volcanic hot spots. As plotted in [Figure 1.4b](#), of the 120 satellite-based studies of volcanic hot spots listed in [Appendix A](#), 47 (39%) have relied wholly, or in part, on AVHRR data. Another 51 (43%) have relied on TM or ETM+ data. Thus, 82% of the studies published between 1965 and 2005 relied on AVHRR or TM data. Of these two sensors, AVHRR was flown on a weather satellite and was thus designed primarily to obtain meteorological, as well as sea-surface reflection and temperature, data. The primary function of TM, flown on NASA's Landsat satellite series, was to allow vegetation discrimination, land classification and surface mapping. Although neither sensor was designed with the detection and measurement of volcanic hot spots in mind, both provided SWIR, MIR and/or TIR data that could be used for such an application.

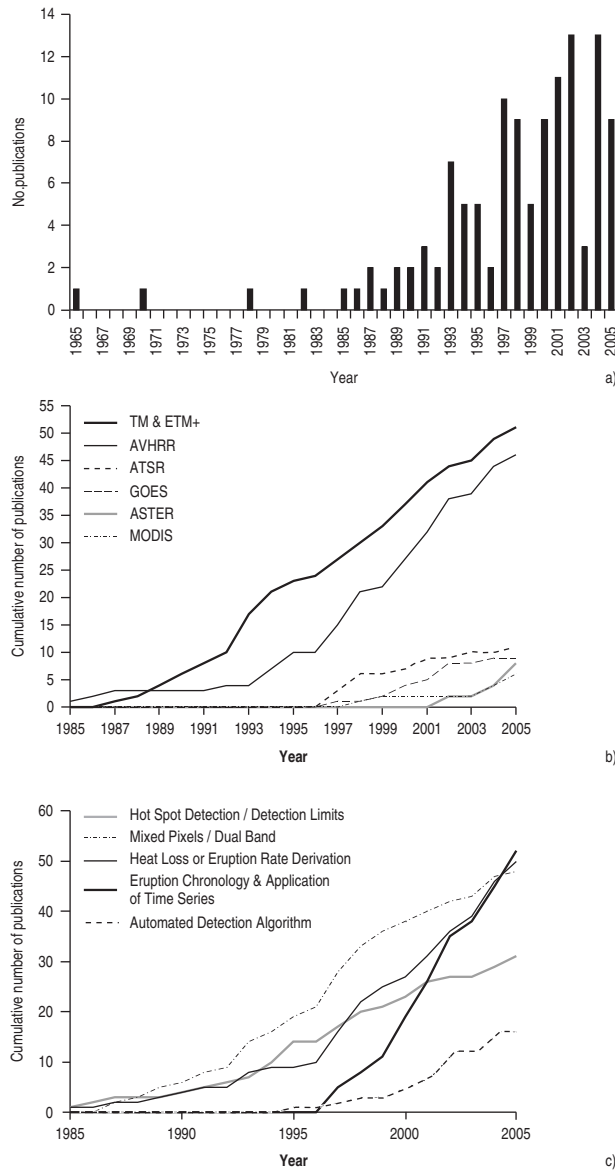


Figure 1.4 Statistics for publications dealing with satellite-based thermal remote sensing of active volcanism. (a) Total number of publications per year, 1965–2005; (b) cumulative number of publications by sensor used, 1985–2005; (c) cumulative number of publications by theme considered, 1985–2005. The full data base on which these plots are based, and other statistics taken from the same data base, are given in [Appendix A](#).

### 1.2.1.1 The NOAA-satellite series and the AVHRR

The AVHRR was flown on a series of polar orbiting satellites operated by the National Oceanic and Atmospheric Administration (NOAA). Between 1960 and 2005, 34 satellites were launched in this series. Their launch, orbit, and sensor package history is summarized in [Table 1.1](#). The NOAA satellite series began with the launch of TIROS-1 in 1960. A series of ten TIROS satellites carried Vidicon in a polar orbit between April 1960 and April 1966, with TIROS-2, -4, and -7 also carrying an IR radiometer. The second series of polar orbiters were those of the Environmental Science Services Administration (ESSA) and began with the launch of ESSA-1 in February 1966. ESSA-1 carried the Advanced Vidicon Camera System (AVCS), with odd numbered satellites (ESSA-3, -5, -7 and -9) also operating a Low Resolution IR Radiometer (LRIR) until November 1972.

The second generation of polar orbiters in the NOAA series began with the launch of the Improved TIROS Operational System (ITOS-1) in January 1970 and continued with the launch of NOOAs -1 through -5 between December 1970 and July 1976. ITOS-1 and NOAA-1 carried a scanning radiometer (SR) which provided infrared data with an 8 km spatial resolution. The predecessor to AVHRR, the VHRR (Very High Resolution Radiometer), was added to the payloads of NOOAs -2 through -5. The VHRR provided 1 km data in two channels, one in the visible and one in the TIR. The third generation of NOAA satellites began with the launch of TIROS-N in October 1978 and was followed by 12 satellites (NOOAs -6 through -18, minus NOAA-13 which failed shortly after launch). These carried the AVHRR. This advanced version of the VHRR was equipped with four-to-five channels located in the visible, MIR and TIR.

Thus, as is apparent from a review of [Table 1.1](#), an instrument with an infrared capability has been flown on the NOAA-satellite series since November 1960, with the LRIR being flown continuously between 1966 and 1972, and the VHRR between 1972 and 1978. Since 1978, the AVHRR has been in continuous operation. The first journal-published analysis of a volcanic hot spot using IR data from the NOAA-satellite series occurred in 1982. This was the publication of Wiesnet and D'Aguanno ([1982](#)) and reported the detection of a hot spot in AVHRR data at Mt. Erebus. Three papers published between 1985 and 1987 subsequently reported detection of volcanic hot spots in AVHRR data at Mt. Etna, these being those of Bonneville *et al.* ([1985](#)), Scorer ([1986](#)) and Bonneville and Kerr ([1987](#)) – see Tables A1 and A2 of [Appendix A](#). As is apparent from [Figure 1.4b](#), use of AVHRR for volcano hot spot detection and analysis did not, however, take off until after 1994. This take-off was possibly heralded by a statement in Bhattacharya *et al.* ([1993](#)). This was an otherwise TM-focused analysis of volcanic thermal structures apparent in TM images of Barren Island volcano (Indian Ocean), but a short statement was included that read “in order to further narrow down the exact commencement date of the volcanic eruption, AVHRR images acquired on a daily basis have been checked back through 4 April 1991.” This hints at the ease with which volcanic hot spots can be detected using AVHRR’s MIR band, and the value of such high-temporal-resolution data in tracking and logging volcanic activity.<sup>1</sup> However, application

<sup>1</sup> Note, though, that the fire community had long since recognized the value of AVHRR for detecting and tracking wild fires, as well as the presence of industrial hot spots (see [Chapter 5](#)).

Table 1.1. *History of the NOAA polar orbiting satellite series (modified and updated from Cracknell, 1997).*

Satellite series / letter		No.	Launch date	VIS/IR imager	Status as of October 2008
TIROS	1	01/04/60	Vidicon	Data: 01/04/60 – 14/06/60	
TIROS	2	23/11/60	Vidicon, IR Radiometer	Data: 23/11/60 – 27/09/61	
TIROS	3	12/07/61	Vidicon	Data: 12/07/61 – 23/01/62	
TIROS	4	08/02/62	Vidicon, IR Radiometer	Data: 08/02/62 – 18/06/62	
TIROS	5	19/06/62	Vidicon	Data: 19/06/62 – 14/05/63	
TIROS	6	18/09/62	Vidicon	Data: 18/09/62 – 21/10/63	
TIROS	7	19/06/63	Vidicon, IR Radiometer	Data: 19/06/63 – 26/02/66	
TIROS	8	21/12/63	Vidicon	Data: 21/12/63 – 12/02/66	
TIROS	9	22/01/65	Vidicon	Data: 23/02/65 – 09/09/66	
TIROS	10	02/07/65	Vidicon	Data: 02/07/65 – 02/04/66	
ESSA	1	03/02/66	Advanced Vidicon Camera System (AVCS)	Data: 04/02/66 – 06/10/66	
ESSA	3	02/10/66	AVCS, Low Resolution IR Radiometer (LRIR)	Data: 04/10/66 – 01/06/67	
ESSA	5	20/04/67	AVCS, LRIR	Data: 01/06/67 – 03/12/68	
ESSA	7	16/04/68	AVCS, LRIR	Data: 16/04/69 – 31/03/69	
ESSA	9	26/02/69	AVCS, LRIR	Data: 01/04/69 – 15/11/72	
ITOS	1	23/01/70	Scanning Radiometer (SR)	Data: 28/04/70 – 17/06/71	
NOAA	1	11/12/70	SR	Data: 28/04/70 – 17/06/71	
NOAA	2	15/10/72	SR, Very High Resolution Radiometer (VHRR)	Data: 16/11/72 – 19/03/74	
NOAA	3	06/11/73	SR, VHRR	Data: 26/03/74 – 17/12/74	
NOAA	4	15/11/74	SR, VHRR	Data: 17/12/74 – 15/09/76	
NOAA	5	29/07/76	SR, VHRR	Data: 15/09/76 – 16/03/78	
TIROS-N		13/10/78	Advanced Very High Resolution Radiometer (AVHRR)	Operational: 11/06/78 – 01/11/80	
NOAA-A	6	27/06/79	AVHRR, Version 1	Operational: 17/07/79 – 09/07/86	
NOAA-B	-		AVHRR	Failed to achieve orbit	
NOAA-C	7	23/06/81	AVHRR, Version 2	Operational: 24/06/81 – 08/01/85	
NOAA-E	8	28/03/83	AVHRR, Version 1	Operational: 20/06/82 – 17/10/85	
NOAA-F	9	12/12/84	AVHRR, Version 2	Operational: 17/12/84 – 19/01/95	
NOAA-G	10	17/09/86	AVHRR, Version 1	Operational: 08/10/86 – 06/10/94	
NOAA-H	11	24/09/88	AVHRR, Version 2	Operational: 21/10/88 – 15/09/94	

Table 1.1. (cont.)

Satellite series / letter	No.	Launch date	VIS/IR imager	Status as of October 2008
NOAA-D	12	14/05/91	AVHRR, Version 2	Operational: 16/07/91 – 10/08/07
NOAA-I	13	09/08/93	AVHRR, Version 2	Out of service: 21/09/93*
NOAA-J	14	30/12/94	AVHRR, Version 2	Operational: 19/01/95 – 23/06/07
NOAA-K	15	13/05/98	AVHRR, Version 3	Operational: 13/05/98 – present
NOAA-L	16	21/09/00	AVHRR, Version 3	Operational: 21/09/00 – present
NOAA-M	17	24/06/02	AVHRR, Version 3	Operational: 24/06/02 – present
NOAA-N	18	20/05/05	AVHRR, Version 2	Operational: 20/05/05 – present

\* Screw damaged power supply.

of AVHRR rapidly increased through the remainder of the 1990s to a point, in 1998, when Clive Oppenheimer could provide a review of volcanological applications using AVHRR (Oppenheimer, 1998). The “thermal surveillance” section of Oppenheimer (1998) comprised 14 pages of the 35 page review, the introduction, plume studies and references comprising the remainder. Data from the IR radiometer and LRIR, however, have never been used, and reports considering use of VHRR for volcano hot spot detection are limited to a single conference proceeding abstract: that of Archambault *et al.* (1979).

#### 1.2.1.2 The Landsat-satellite series, TM and ETM+

The Landsat satellite series began in July 1972 with the launch of Landsat-1 from the Western Test Range of Vandenberg Air Force Base, California (USA). As of 2005, a total of seven Landsat satellites had been launched by NASA. Their launch, orbit history and sensor payload history is summarized in Table 1.2. Initially, Landsats-1, -2 and -3 carried the Multispectral Scanner (MSS). This sensor had four bands spanning the visible with a spatial resolution of ~80 m, with the MSS on Landsat-3 having a fifth band in the TIR with a 240 m spatial resolution. This fifth TIR channel, however, failed shortly after launch. With the launch of Landsat-4 in July 1982 the Thematic Mapper was added to the Landsat payload. The TM was also flown on Landsat-5 and had four bands in the visible, two in the SWIR and one in the TIR. While the visible and SWIR bands had a spatial resolution of 30 m, that of the TIR band was 120 m. Although Landsat-4 was decommissioned in June 2001, the hardy TM aboard Landsat-5 was still capable of providing TM images as of January 2008, after 24 years of service.

Table 1.2. History of the Landsat program: RBV = Return Beam Vidicon, MSS = Multispectral Scanner, TM = Thematic Mapper, ETM = Enhanced Thematic Mapper. RBV consisted of three television-like cameras sensitive at 0.475–0.575 μm (green), 0.580–0.680 μm (red) and 0.690–0.830 (NIR).

Satellite & no.	Launched	Decommissioned	Sensors	Spatial resolution (m)	Satellite altitude (km)	Satellite return period (days)
Landsat-1	23 July 1972	6 January 1978	RBV	80	917	18
			MSS	80		
Landsat-2	22 January 1975	25 February 1982	RBV	80	917	18
			MSS	80		
Landsat-3	05 March 1978	31 March 1983	RBV	40	917	18
			MSS	80 (VIS-SWIR) 240 (TIR)		
Landsat-4	16 July 1982	TM failed: August 1993	MSS	80	705	16
			TM	30 (SWIR) 120 (TIR)		
Landsat-5	01 March 1984	Operational as of January 2008	MSS	80	705	16
			TM	30 (SWIR) 120 (TIR)		
Landsat-6	05 October 1993	Launch Failure	ETM	15 (panchromatic) 30 (SWIR) 60 (TIR)	705	16
Landsat-7	April 1999	Operational as of January 2008	ETM+	15 (panchromatic) 30 (SWIR) 60 (TIR)	705	16

With the launch of Landsat-7 in April 1999 an improved version of the TM gained orbit, the Enhanced Thematic Mapper Plus (ETM+). An eighth panchromatic (visible) band with a spatial resolution of 15 m was added, and the spatial resolution of the TIR band was increased to 60 m. Previously, an ETM sensor had been launched on Landsat-6 during October 1993, but the satellite failed to achieve orbit after a ruptured rocket fuel chamber meant that the spacecraft failed to attain the velocity necessary to obtain orbit, so that the spacecraft fell into the Pacific.

Thus, a high-spatial-resolution infrared capability, represented by the IR band of MSS, has been in orbit since 1972, with high-spatial-resolution SWIR data being continuously available from TM since the launch of Landsat-4 in 1982. Although the TIR band of MSS was only rarely utilized for analysis of volcano hot spots, TM and ETM+ became the mainstay of high-spatial-resolution thermal analysis of volcanic hot spots from space. Reports of the potential use of MSS for analysis of volcano hot spots lagged behind the first MSS launch by 10 years, with the first mention of thermal emission in MSS data over a volcano hot spot appearing in Wiesnet and D'Aguanno (1982) and then in Rothery *et al.* (1988). It is noteworthy, though, that Heiken and Pitts (1975) used MSS images of Sakurazima volcano (Japan), as well as Stromboli (Italy), obtained just five months after the first launch of MSS, to detect and describe plumes of ash and gas at both volcanoes. They concluded that, “with continued research on sensors and an increasing number of satellites in stationary orbit, volcanologists might well use satellites to identify and measure the extent and characteristics of eruption clouds in areas with inclement weather.”

Francis and Rothery (1987) provided the first consideration of TM data for a volcano hot spot, so that there was a five year lag between the launch of TM and the first TM-based volcano hot spot manuscript. As plotted in [Figure 1.4b](#), after 1988 use of TM and ETM+ for volcano hot spot detection and analysis increased steadily, the number of publications between 1988 and 2005 having increased in a near-perfect linear fashion at a rate of 2.6 publications per year.

#### 1.2.1.3 Other sensors: Geostationary, ATSR and the EOS-program

As traced in [Figure 1.2](#), infrared data from six other satellite-based sensors have been used for volcano hot spot studies: ALI, ASTER, ATSR, GOES-Imager, JERS-OPS and MODIS. Of these, one, the GOES-Imager, has been in a geostationary orbit since 1994, and three (ALI, ASTER and MODIS) were launched as part of NASA's Earth Observing System (EOS) between December 1999 and November 2000.

**Geostationary infrared sensors** The Synchronous Meteorological Satellites (SMS) and Geostationary Operational Environmental satellite (GOES) series have been in orbit since 1974. Like the NOAA satellite series, they are primarily weather satellites used, for example, to track weather systems, severe storms and hurricanes (e.g., [Figure 1.5](#)), as well as local weather events including thunderstorms, tornadoes, flash floods, and snow storms. However, as can be seen in [Figure 1.5](#), hot spots due to volcanoes and fires are also readily apparent in their data. SMS/GOES is a cooperative venture between NOAA and NASA, with SMS/GOES being part

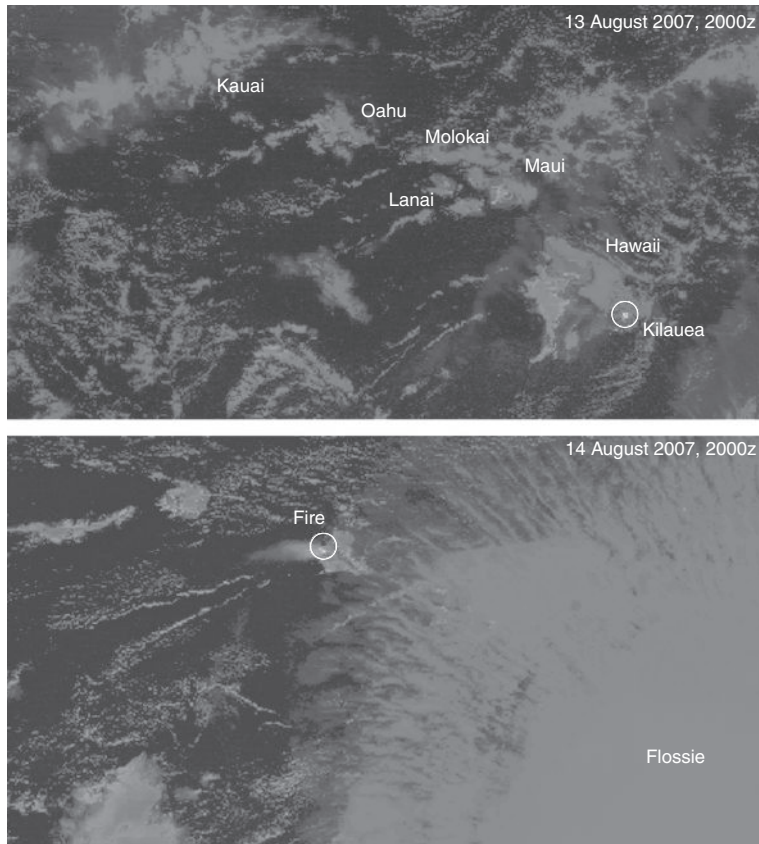


Figure 1.5 GOES true color composites of the Hawaiian Island Chain at 20:00 UT on 13 August 2007 (top) and 24 hours later (bottom). In the top image the hot spot due to active lava at Kilauea is apparent. In the bottom image the hot spot has become masked by the thick cloud (light blue) ahead of an approaching hurricane, Flossie. However, a hot spot due to a fire burning in NW Oahu is now apparent ahead of the approaching cloud mass. See also color plates section.

of a global network of geostationary satellites, spaced about  $70^{\circ}$  apart above the Equator and including the European Space Agency's Meteosat and Japan's Geostationary Meteorological Satellites (GMS). Together, sensors aboard this satellite constellation provide a near-continuous view of global weather patterns.

To date, a total of 15 satellites have been launched in the SMS/GOES series, with the launch, orbit and sensor payload history being summarized in [Table 1.3](#). Typically, two satellites are operational at any one time, with back-up craft being placed in storage orbits. The two operational satellites are located over the Equator at  $135^{\circ}$  W (GOES-West) and  $75^{\circ}$  W (GOES-East). From these geostationary locations, the whole Earth disk can be imaged

Table 1.3. History of the SMS/GOES satellite series (collated and summarized from the NASA web-site: <http://goes.gsfc.nasa.gov/>).

Satellite-letter	No.	Launch date	Instrument	Orbit designation	Orbit location	Notes	Status as of October 2008
SMS	1	17/05/74	VISSR	Central Atlantic	45 W	Covered the Eastern USA and Atlantic	Deactivated on 21/01/81
SMS	2	06/02/75	VISSR	E-Central Pacific	135 W	Complement to SMS-1: covers Western USA and Pacific basin	Deactivated on 05/08/82
GOES-A	1	16/10/75	VISSR	Indian Ocean	W of SMS-1 135 W	Moved to replace SMS-2 when GOES-3 launched in June 1978	Deactivated on 07/03/85
GOES-B	2	16/06/77	VISSR	West	60 W	Replaced SMS-1	Operational 1975–1993. Re-activated in 1995 to broadcast NSF transmissions from S. Pole
GOES-C	3	16/06/78	VISSR	East	135 W	Replaced GOES-1	Operational 1978–1993. Re-activated in 1995 to transmit educational programming from the University of Hawaii
GOES-D	4	09/09/80	VAS	West	135 W	Replaced GOES-3	Deactivated 22/11/88
GOES-E	5	22/05/81	VAS	East	75 W	Replaced GOES-2	Deactivated 18/07/90
GOES-F	6	28/04/83	VAS	West	136 W	Replaced GOES-4	VAS failed on 21/01/89
GOES-G	—	03/05/86	VAS	—	—	Launch vehicle exploded during launch	Failed to attain orbit
GOES-H	7	26/02/87	VAS	East	75 W	Originally a GOES-5 replacement at	(See Note a)
				Prime	108 W	GOES-E, operation began 02/89 as	
				West	135 W	“GOES Prime”, a one-GOES system following the 01/89 failure of GOES-6. Operations began as GOES-W 01/95 after deployment of GOES-8 to GOES-E	

Table 1.3. (cont.)

Satellite-letter	No.	Launch date	Instrument	Orbit designation	Orbit location	Notes	Status as of October 2008
GOES-I	8	13/04/94	Imager SN03	East	75 W	Operations as GOES-E began: 09/06/95	Active
GOES-J	9	23/05/95	Imager SN04	West	135 W	Operations as GOES-W began: 22/01/96 (See Note b)	
GOES-K	10	25/04/97	Imager SN05	West	135 W	Replaced GOES-9: 09/07/98	Active
GOES-L	11	03/05/00	Imager SN06	West	135 W	Replaced GOES-10: 28/06/06	Active
GOES-M	12	23/07/01	Imager SN07	East	75 W	Replaced GOES-8: 01/04/03	Active
GOES-N	13	24/05/06	Imager SN08	Storage	105 W	In orbit storage	In storage until needed to replace GOES-12 or GOES-11

<sup>a</sup> GOES-7 was moved to: (i) 98 W in 07/89 for hurricane season, (ii) 108 W in 11/89 for the Pacific storm season, (iii) 98 W in 07/90, (iv) 108 W in 11/90, (v) 98 W in 07/91, (vi) 112 W in 04/92 when Meteosat-3 was brought to 75 W, and (vii) finally to 135 W in 01/95 following the commissioning of GOES-8.

<sup>b</sup> On 22/05/03, GOES-9 completed repositioning to 155 E, and became the operational meteorological satellite over the West Pacific and Eastern Asia, replacing the Japan Meteorological Agency's GMS-5 satellite. Deactivated 14/06/07.

every 30 minutes, with GOES-West covering the Atlantic and Eastern USA, and GOES-East covering the Eastern-Central Pacific and Western USA. In this way, the two satellites provide regular coverage of ~60% of the Earth's surface.

The first satellite in the series (SMS-1) was launched in May 1974, with a satellite from this series being maintained in the GOES-West and -East orbits ever since. This was broken by a six year period spanning February 1989 to January 1995 when only one satellite was operational, with GOES-7 operating as GOES-Prime. The two SMS satellites, and GOES-1 through -3, carried the Visible Infrared Spin Scan Radiometer (VISSR). This provided visible data at a 1.25 km pixel resolution and TIR data at a 5 km resolution. GOES-4 to -7 carried the VAS (Visible Infrared Spin Scan Radiometer Atmospheric Sounder). This instrument added an Atmospheric Sounder to the VISSR. However, imaging and sounding could not be carried out at the same time. GOES-8 through -13 all carried an imager, which provided 4 km data in the MIR and TIR every 15 minutes without interruption for sounding.

Similar sensors have been flown by the European Space Agency (ESA) on Meteosat, providing images that cover Europe and Africa from an orbit location above the Equator at 0° E. In total, nine Meteosat satellites have been launched since 1977, providing continuous thermal coverage since that date, as collated in [Table 1.4](#). Meteosats-1 through -7 carried an imager which provided visible data at a 2.5 km pixel resolution and 5 km resolution TIR data. Beginning with the launch of Meteosat-8 in 2005, the Meteosat Second Generation (MSG) satellite carried the Spinning Enhanced Visible and Infrared Imager (SEVIRI). This now provides 3 km data in the NIR, MIR and TIR every 15 minutes.

The first GMS satellite was also launched in 1977, with a total of five satellites being launched between 1977 and 1995 carrying the VISSR. The launch, orbit, and sensor payload history for the GMS series is also summarized in [Table 1.4](#). Operated by Japan's National Space Development Agency (NASDA), GMS was located above the Equator at 140° E, from where it covered a hemispherical sector including Australia and Japan. MTSAT, a joint venture between Australia's Ministry of Land, Infrastructure and Transport and the Japanese Meteorological Agency, carried a new imager into the 140° E orbit in 2005, providing 4 km data in one MIR band and two TIR bands every 30 minutes.

Thus, thermal data for the whole Earth disk have been available from SMS/GOES since 1974, and from Meteosat and GMS since 1977. Such data allow regular monitoring of most of the world's active volcanoes. The value of TIR data provided from these geostationary sensors every 15 to 60 minutes for detecting and tracking ash plumes from explosive eruptions was soon recognized, with Arlin Kreuger publishing a Science paper in 1982 in which he used hourly TIR data from SMS-1 to track ash plumes erupted during the April 1979 eruption of St. Vincent's Soufriere volcano ([Kreuger, 1982](#)). In the same year, Robock and Matson ([1982](#)) used TIR data from the GOES-E and -W satellites to track the stratospheric ash cloud from the 4 April 1982 El Chichon (Mexico) eruption, finding that the cloud took three weeks to travel around the world. Later, Holasek and Self ([1995](#)) used GOES-3 VISSR data to track the 18 May 1980 eruption cloud of Mount St. Helens at one hour steps.

Table 1.4. History of the Meteosat, GMS and MTSAT satellite series.

Satellite	Number	Launch date	Orbit	Instrument
Meteosat	1	23/11/77 (10/84)	0°E (1977–1981)	METEOSAT Radiometer
Meteosat	2	16/06/81 (12/91)	0°E (1981–1988)	METEOSAT Radiometer
Meteosat	3	15/06/88 (11/95)	0°E (06/88–06/89) <sup>a</sup>	METEOSAT Radiometer
Meteosat	4 (also called MOP 1)	06/03/89 (11/95)	0°E (03/89–02/95) <sup>b</sup>	METEOSAT Radiometer
Meteosat	5 (also called MOP 2)	02/03/91 (04/07)	0°E (1993–1997) <sup>c</sup>	METEOSAT Radiometer
Meteosat	6 (also called MOP 3)	20/11/93	0°E (03/96–06/98) <sup>d</sup>	METEOSAT Radiometer
Meteosat	7	02/10/97	0°E (10/01–03/07) <sup>e</sup>	METEOSAT Radiometer
Meteosat	8 (also called MSG-1)	28/08/02	0°E (2002–2005) <sup>f</sup>	SEVIRI
Meteosat	9 (also called MSG-2)	21/12/05	0°E (2005–2008) <sup>f</sup>	SEVIRI
GMS	1 (also called Himawari 1)	14/07/77	140°E	VISSR
GMS	2 (also called Himawari 2)	10/08/81	140°E	VISSR
GMS	3 (also called Himawari 3)	02/08/84 (07/95)	140°E	VISSR
GMS	4 (also called Himawari 4)	05/10/89 (03/00)	140°E	VISSR
GMS	5 (also called Himawari 5)	03/17/95 (06/05) <sup>g</sup>	140°E	VISSR
MTSAT	1R	26/02/05	140°E	MTSAT Imager
MTSAT	2	18/02/06	145°E (on stand-by)	MTSAT Imager

<sup>a</sup> Then (i) 50°W (06/89), (ii) 0°E(01/90), (iii) 5°W (04/90), (iv) 50°W (07/91), (v) 75°W (12/92), (vi) 72.8°W (04/93) and (vii) 70°W (02/95).

<sup>b</sup> Then (i) 7.7°W (02/95) and (ii) 10°E (08/95).

<sup>c</sup> Then (i) 9°W (05/97) and (ii) 62.9°E (06/98).

<sup>d</sup> Then (i) 9°W (07/98) (ii) 9°E (10/02), and (iii) 67°E (05/07).

<sup>e</sup> As of 03/07 located at 57°E.

<sup>f</sup> As of 10/08, Meteosat-8 is in backup mode, -9 is operational at ~0°E.

<sup>g</sup> Replaced in 05/03 by GOES-9.

Likewise data from GMS were being used to track ash plumes as early as 1977, with Sawada (1989) collating examples of ash plumes apparent in GMS imagery from 31 eruptions at 23 different volcanoes over the period 1977 to 1985, including those from Mayon's September 1984 eruption (see also Sawada (1985)). Most famously, GMS time series were used to track the eruption plumes from the 1982 eruptions of Galunggung, which were responsible for two damaging aircraft encounters (Hanstrum and Watson, 1983) and to track the giant umbrella cloud from the 15 June 1991 eruption of Mt. Pinatubo (Koyaguchi and Tokuno, 1993; Holasek *et al.*, 1996). Meteosat has been less commonly used, with Bertrand *et al.* (2003) and Aloisi *et al.* (2002) reporting use of TIR data acquired every 30 minutes by Meteosat-7 to track and model the dispersion of the plumes erupted from Mt. Etna (Italy) during 2001 and 1998.

The first study to examine the use of infrared data from a geostationary platform to detect a volcano hot spot was not until 1997 when Harris *et al.* (1997b) produced a detailed chronology of the January 1997 effusive eruption at Napau crater (Kilauea) using MIR data available every 15 minutes from the imager aboard GOES-9. To be fair, a MIR sensor in which volcano hot spots are likely to be detected had only been carried on GOES since the launch of GOES-8 in 1994, and a MIR capability has only been carried on Meteosat since the launch of Meteosat-8 in 2002, and on GMS since the launch of MTSAT in 2005. Thus, the gap between the first MIR-capable geostationary sensor and first publication was only three years. As charted in Figure 1.4b, between 1997 and 2005 a total of nine papers reported the use of GOES data for either hot spot detection and/or production of effusive event chronologies. With the launch of MTSAT and SEVIRI in 2002 and 2005, respectively, the high-temporal-resolution MIR and TIR capability offered by the GOES imager is now available for most of the globe, and we are beginning to see manuscripts exploring its utility to document short-lived, rapidly evolving, effusive events, such as fountain-fed lava flows (e.g., Calvari *et al.*, 2011; Ganci *et al.*, 2012a; Gouhier *et al.*, 2012).

**NASA's Earth Observing System** In 1991, NASA launched a comprehensive program to study the Earth as one environmental system, the aim being to provide a scientific baseline from which to monitor and understand Earth systems (Ramsey and Flynn, 2004). Later called the Earth Science Enterprise (ESE), this effort focused on a satellite component known as the Earth Observing System (EOS). As of 2003, there were 12 EOS-designated satellites carrying 36 instruments, as summarized in Figure 1.6. Discounting ETM+, those sensors with thermal capabilities slated for volcano hot spot applications were MODIS, ASTER and ALI. Launched between 1999 and 2000, by 2005 data from these three sensors had been used to support a total of 15 studies (MODIS = 8; ASTER = 6; ALI = 1).

The Moderate Resolution Imaging Spectroradiometer (MODIS) was first launched on NASA's EOS Terra (EOS AM-1) satellite on 18 December 1999, with a second being launched on the Aqua (EOS PM-1) spacecraft on 4 May 2002. MODIS provided 36 spectral bands covering the 0.4  $\mu\text{m}$  to 14.4  $\mu\text{m}$  portion of the spectrum at spatial resolutions of 250 m to 1 km. ASTER (Advanced Spaceborne Thermal Emission and Reflection Radiometer) was also launched in December 1999 on Terra. Although ASTER was designed to provide the

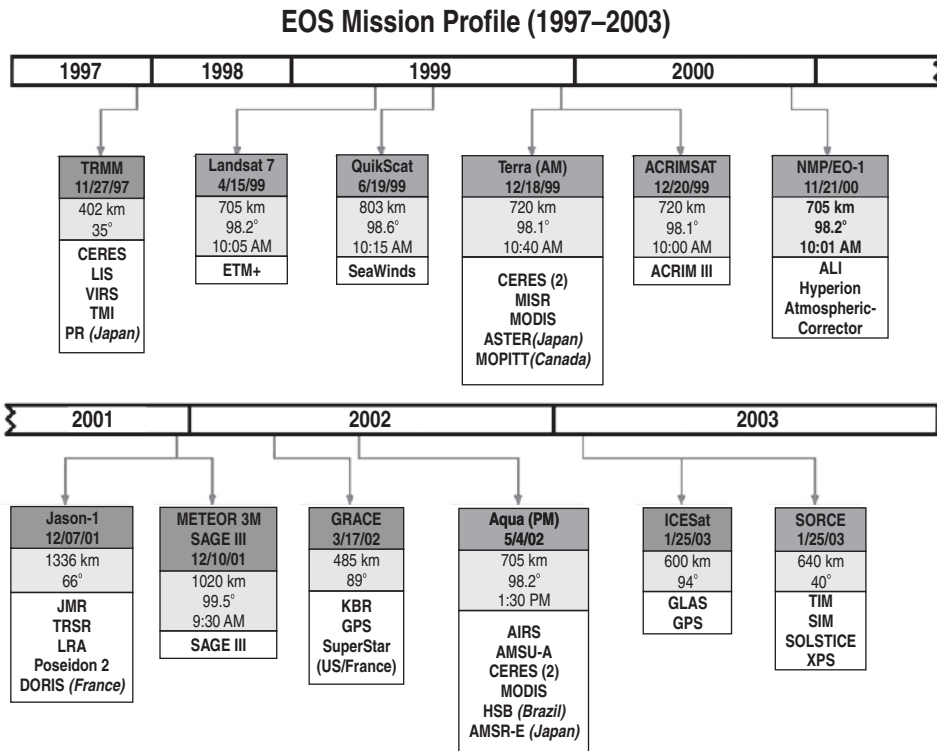


Figure 1.6 NASA Earth Observing System platforms launched between 1997 and 2003 showing orbit configuration and sensor payload. Not all missions and sensors were designed for volcanic observations, with the key sensors for thermal remote sensing of volcano hot spots being ETM+, MODIS, ASTER, ALI and Hyperion [reprinted from Ramsey and Flynn (2004, Fig. 1): with permission from Elsevier].

next generation in remote sensing imaging capabilities (TM and JERS-OPS being the first generation), there are currently no plans for a follow-on mission. ASTER provides six bands of SWIR data at a 30 m spatial resolution and five bands of TIR data at 90 m. Owing to limited onboard storage capacity, ASTER acquires data during just 8 % of each orbit (Yamaguchi *et al.*, 1998). This limited acquisition time, coupled with adjustable pointing and gain settings has required daily scheduling of the instrument for volcanic, as well as all other, applications (Ramsey and Dehn, 2004). Thus, efforts have been made to trigger acquisitions using hot spot detections from other sensors (e.g., AVHRR) to build high-spatial-resolution thermal data sets for active volcanic hot spots (Ramsey and Dehn, 2004). The Earth Observing-1 (EO-1) mission was developed as part of the NASA New Millennium Program (NMP) and was launched on 21 November 2000. It carried the Advanced Land Imager (ALI) and Hyperion. ALI provides nine bands of 30 m data spanning the VIS and SWIR. Like ASTER, it was designed to be an improved version of TM. EO-1 also carried Hyperion, a spectrometer providing data in 172 spectral bands spanning the SWIR.

**The Along Track Scanning Radiometer** The Along Track Scanning Radiometer (ATSR) provided SWIR, MIR and TIR data at a spatial resolution of 1 km. The first ATSR was launched on board the European Space Agency’s (ESA) European Remote Sensing Satellite (ERS-1) in July 1991 as part of ESA’s Earth Observation Program. ATSR-2 was launched in April 1995, with the AATSR (Advanced Along Track Scanning Radiometer) being launched on board the ENVISAT satellite in March 2002. As shown in Figure 1.4b, publications examining volcanic hot spots using ATSR took off in 1997, with Martin Wooster leading three papers in 1997 (Wooster *et al.*, 1997; Wooster and Rothery, 1997a; 1997b) and another three in 1998 (Wooster and Kaneko, 1998, Wooster *et al.*, 1998a; 1998b). ATSR-based efforts between 1998 and 1999 were driven by the Empedocles project. This project was outlined by Rothery *et al.* (2001), and followed heightened seismicity at Mt. Etna in January 1998. This led to speculation that a flank eruption might be imminent. This, in turn, led the Italian Civil Protection to ask ESA to advise on how remote sensing could contribute to monitoring efforts. In response, ESA commissioned the Empedocles project to investigate the utility of synthetic Aperture Radar and thermal infrared remote sensing data from ERS-2 for monitoring Etna’s activity.

**JERS-OPS, CZCS, and DMSP** Use of the optical sensor (OPS) flown on the Japanese Earth Resources Satellite (JERS) sums up the state of utilization of the remaining satellite-based thermal sensors. JERS-OPS provided SWIR data with an 18 m spatial resolution between November 1992 and October 1999. However, data from JERS-OPS only supported three publications, two of which were led by Anthony Denniss (Denniss *et al.*, 1996; 1998). Both revealed sensor problems, but yielded data in which activity levels at the hot spot due to lava dome extrusion at Lascar (Chile) could be detected and tracked.

Two other sensors with thermal infrared capabilities have remained under-utilized. These are the Coastal Zone Color Scanner (CZCS) and Defense Meteorological Satellite Program (DMSP) sensors. The CZCS was launched on Nimbus-7 in October 1978, remained in service until June 1986, and provided five bands of visible data and one band of TIR data at a spatial resolution of 825 m. No volcano-oriented analysis was ever published. DMSP data have been available to civilian users on an unclassified basis since April 1973 and comprise images in the 0.4  $\mu\text{m}$  to 1.1  $\mu\text{m}$  and 8  $\mu\text{m}$  to 13  $\mu\text{m}$  bands at a spatial resolution of 0.55 km to 2.7 km. Currently, data from four satellites are added to the DMSP archive each day.

Lillesand and Kiefer (1987) point out that a unique capability of the DMSP Operational Linescan System is night-time imaging in the NIR. This comes through the ability to tune the amplifiers to obtain images under low illumination conditions, allowing “vivid images of phenomena such as urban light patterns” as well as “auroral displays, volcanoes, oil and gas fields” (Lillesand and Kiefer, 1987). Indeed, Henry Brandli in a short note in PE&RS (Brandli, 1978) gave a figure showing detection, in a 28 December 1970 DMSP image of Hawaii, of a “bright light with haloed rings around it” due to “the erupting volcano of Kilauea.” The city lights of Honolulu could also be seen shining brightly against a dark ocean. Brandli (1978) concluded, “volcanic eruptions, both explosive and effusive, can easily be seen in remote areas with this nighttime visible and near-infrared sensor.”

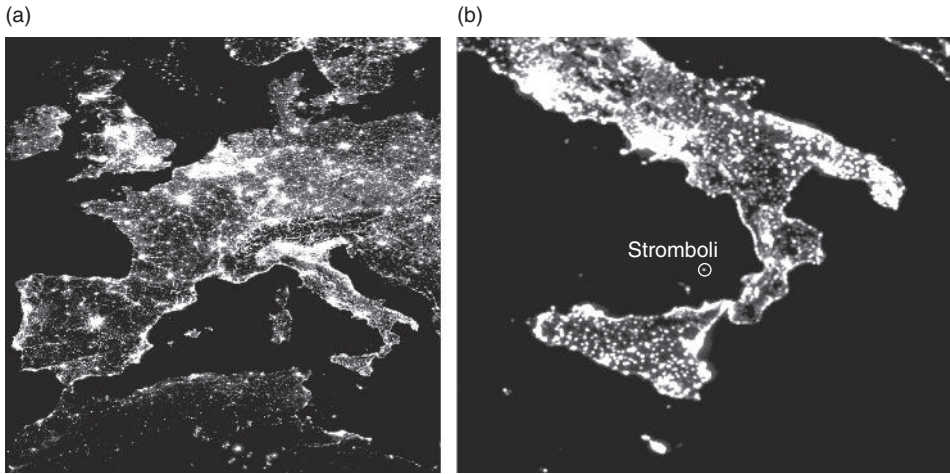


Figure 1.7 DMSP composite image for 2003 showing light sources over Western Europe (left) and Southern Italy (right). The image is dominated by light sources associated with centers of population. However, in the left-hand image the location of oil platforms in the North Sea are also apparent due to the sensitivity of the DMSP sensor to flares of burning gas active at the platforms. Stromboli volcano (Italy) is also apparent as a light source in the bottom image. Given that there are few street lights on Stromboli, the source must be incandescence from lava flows active during the effusive activity that persisted at Stromboli between January and July 2003.

Elvidge *et al.* (1997) also used DMSP data to produce inventories of human settlements using nocturnal radiant emissions, and in doing so mapped locations of streetlight emission, an example of which is given in Figure 1.7. The maps of Elvidge *et al.* (1997) also picked-up glow from fires, oil and gas field flares, and lights from fishing fleets, plus glow from active high-temperature volcanic sources, as shown in Figure 1.7. However, although DMSP data have been shown to be capable of monitoring and mapping forest fires (e.g., Badarinath *et al.*, 2007; Chand *et al.*, 2006), no further work examining the potential use for volcano hot spot detection has been carried out since the short report of Brandli in 1978.

### 1.3 A history of the discipline

#### 1.3.1 A history of satellite remote sensing of volcano hot spots

The full literature data base for satellite remote sensing of volcano hot spots is collated in Appendix A, with the development time-line being detailed in Figure 1.3. Examination of the Appendix A data base shows that, following the work of Williams and Friedman (1970), there was an inexplicable gap in progress, as recorded by a 12-year-long break in the Figure 1.4a plot of publication number per year. The gap was interrupted by a single publication in 1978. In this, Brandli (1978) completed his short review of the DMSP capability to detect low-light sources, including volcanoes, as described above.

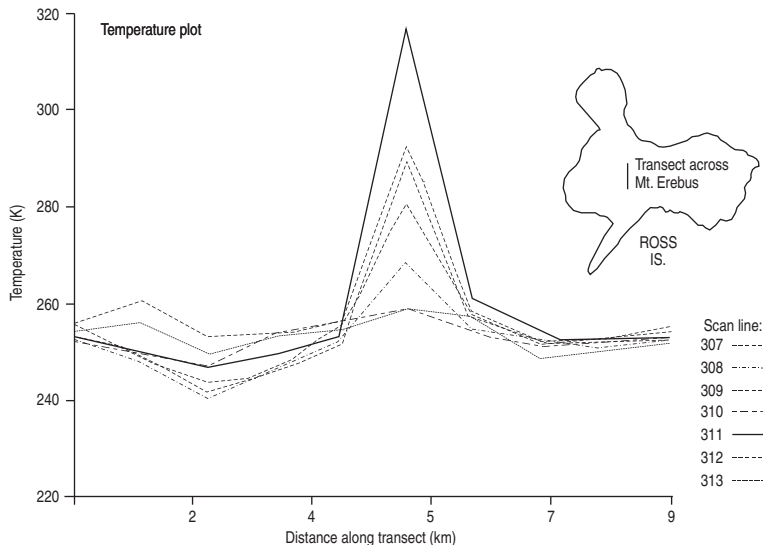


Figure 1.8 Transects of pixel-integrated temperature in 1 km AVHRR data over the [active] lava lake at the summit of Mount Erebus (Antarctica) in February 1980. The lava lake is apparent as a spike in the transect and affects five transects across the image (i.e., five rows of image data). As explained by Wiesnet and D'Aguanno (1982), “the pixel that includes the crater is about 50 K warmer than the area surrounding the crater. As the pixel is larger in diameter than the crater (1100 meters compared with 250 meters), the cooler rocks and ice surrounding the crater also contribute to the measured temperature of the pixel. The temperature determined by the satellite sensor is thus less than the actual temperature of the crater area” [from Wiesnet and D'Aguanno (1982, Fig. 3)].

Despite the promise of DMSP, and the availability of MSS and VHRR data after 1972, the next publication was not until that of Wiesnet and D'Aguanno (1982). This was published in 1982 as a short note in the *Antarctic Journal* entitled “Thermal imagery of Mount Erebus from the NOAA-6 satellite.” Like Brandli (1978), Wiesnet and D'Aguanno (1982) did little more than report the presence of a hot spot due to volcanic activity associated with an active lava lake at Mount Erebus (Antarctica). This was apparent from a spike in AVHRR MIR band brightness temperature profiles drawn across Erebus’ summit, as reproduced in Figure 1.8. We can reduce the gap in the publication record by three years if we include the one page paper presented by Archambault *et al.* in 1979 at the *7th Reunion Annuelle des Sciences de la Terre* in Lyon (France). In this abstract they reported results from an analysis of a NOAA-5 VHRR image of Mt. Etna (Italy) acquired on 16 September 1978, in which thermal anomalies covering a total pixel area of  $50 \text{ km}^2$  could be identified. These could be associated with the cooling lava flows from eruptions in 1974, 1975–76, 1977 and 1978 (Archambault *et al.*, 1979).

However, following Wiesnet and D'Aguanno (1982), there was a further gap of four years until Scorer's 1986 short report in the journal *Weather* entitled “Etna: the eruption of Christmas 1985 as seen by meteorological satellite.” Despite the promise of the title,

the article did little more than present a series of images acquired by the AVHRR flown on NOAA-9. Hot spots, associated with active lava at Etna, were again apparent. However, this discovery appeared to be of less interest than the cloud patterns that the same images showed, with Scorer (1986) stating that “the eruption was not exciting, but there are many points of meteorological interest.” Scorer himself seemed underwhelmed by the volcanological significance of the data, summing up by recommending a source of further reading “not about volcanoes, but about interpretation of pictures from meteorological satellites.”

### 1.3.1.1 Four pivotal publications: 1985–1988

The publication on 10 July 1988 of “Volcano monitoring using short wavelength infrared data from satellites” in the *Journal of Geophysical Research* by David Rothery, Peter Francis and Charles Wood is widely recognized as the real start of regular use of satellite infrared data for analysis of volcanic hot spots. In their paper, Rothery *et al.* (1988) completed a thorough review of the potential use of high spatial resolution SWIR and TIR data acquired by TM and MSS for thermal analysis of a variety of volcanic hot spots, these being:

- a lava dome at Lascar (Chile),
- lava lakes at Erta Ale (Ethiopia) and Erebus (Antarctica),
- hot pyroclastic flows at Augustine (Alaska), and
- a lava flow at Sierra Negra (Galapagos).

The down-flow surface temperature profile extracted for the Sierra Negra lava flow by Rothery *et al.* (1988) is reproduced here in Figure 1.9. In completing their review, Rothery

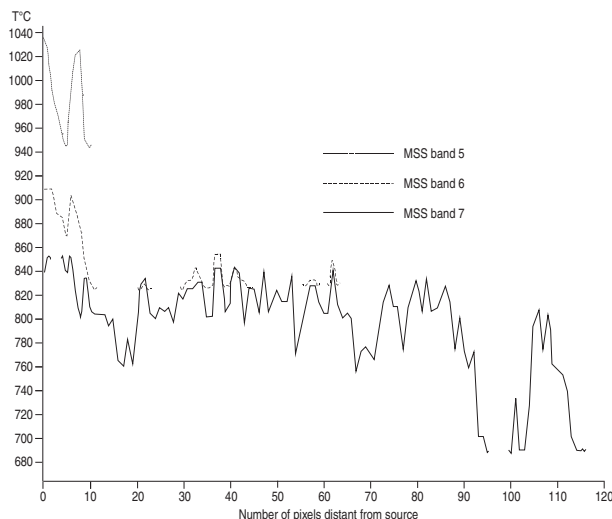


Figure 1.9 Landsat MSS pixel-integrated temperature transect down the center line of a lava flow active at Sierra Negra (Galapagos Islands) on 19 November 1979 [from Rothery *et al.* (1988, Fig. 7): reproduced by permission of American Geophysical Union].

*et al.* (1988) explored the likely sources of error in making satellite-based measurements of volcanic thermal phenomena, including a consideration of pixel size, the point spread function, atmospheric effects, and re-sampling problems resulting from geometric rectification. Most importantly, Rothery *et al.* (1988) introduced the volcanological community to the dual-band method. This method, initially proposed for use with AVHRR data containing industrial hot spots and fires by Dozier (1981), allowed estimation of the size and temperature of a sub-pixel heat source. The introduction of this new “dual-band” methodology defined the basis of a major theme in satellite-based high-spatial-resolution thermal analysis that developed over the following two decades. The publication frequency plot (by theme) of Figure 1.4c shows that this theme dominated the literature into the mid 2000s. Its history will be reviewed further in Chapter 5.

**Three other papers** Three excellent (but rarely cited) papers actually preceded Rothery *et al.* (1988) by between one and three years: Bonneville *et al.* (1985), Bonneville and Kerr (1987) and Francis and Rothery (1987). The first two of these studies took a slightly different track to Rothery *et al.* (1988), examining low temperature thermal anomalies in AVHRR data. The studies of Bonneville *et al.* (1985) and Bonneville and Kerr (1987) both analyzed AVHRR data for Mt. Etna to identify thermally anomalous (warm) pixels for three cases. The first case covered a region of the persistently active summit craters, the second case included anomalous pixels in the vicinity of the cooling lava flow field from Etna’s 1981 eruption (Bonneville *et al.*, 1985), and the third took into account anomalies in images acquired in the three months prior to Etna’s 1983 effusive eruption (Bonneville and Kerr, 1987). The location of these latter pixels was consistent with surface heating above an intrusion that preceded the eruption, as reproduced in Figure 1.10. The third study in the series was published by Peter Francis and David Rothery in *Geology* in July 1987. It was the prelude to the study of Rothery *et al.* (1988) of the following year and explored TM data for Lascar to demonstrate the response of TM’s SWIR bands to a high-temperature volcanic source. Although yet to apply the dual-band method, Francis and Rothery (1987) stated that the most important conclusion of their work was that, “the TM, a remote sensing instrument not specifically designed for volcanological work, provides a means whereby even rather small (< 100 m), cool (< 400 °C) volcanic manifestations can be confidently identified (Francis and Rothery, 1987).”

**Plus two abstracts** Then, in 1989, two telling conference abstracts were published. The first was that of Jaskolla and Arnason (1989). Presented at a workshop held in Frascati (Italy) in December 1987, it gave the results from analyses of three Landsat-TM scenes collected over Iceland during 1984 and 1985. Analyses showed how SWIR and TIR data could be used to identify zones of hydrothermal alteration, geothermal heating and cooling lava. The second was that of Oppenheimer (1989). Presented at the *Fourth AVHRR data users’ meeting* in Rothenberg (Sweden) in September 1989, it used AVHRR data collected for

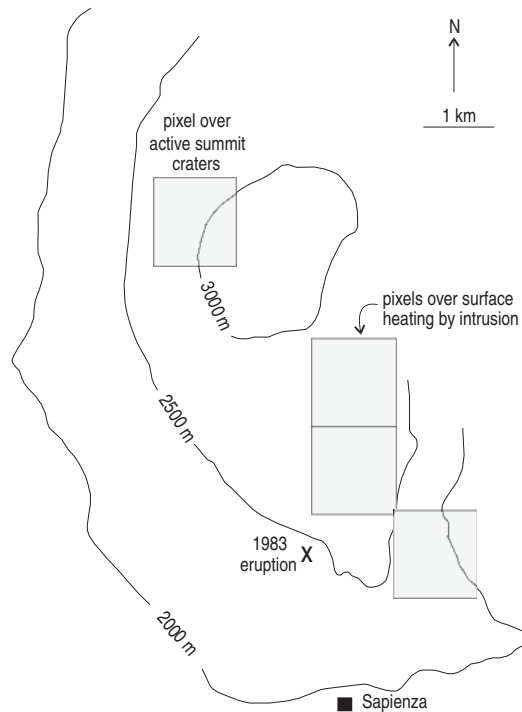


Figure 1.10 Map of Etna's summit area showing those 1 km pixels identified as being thermally anomalous in a March 1983 AVHRR image. In this figure, two zones of low-temperature thermal anomaly are located across which temperatures are about 3 °C hotter than the surroundings. These relate to the location of the summit craters, where hot open vents are active, and a zone of flank warming assumed to be the result of intrusion prior to the 1983 flank eruption. This eruption began from a location near the flank anomaly a few days after the image was acquired [reprinted from Bonneville and Kerr (1987, Fig. 14) with permission from Elsevier].

Stromboli, Vulcano and Etna volcanoes (Italy) to test the dual-band method on 1-km spatial resolution data. It also pointed to the difference in brightness temperature recorded between the mid-infrared ( $\sim 3.9 \mu\text{m}$ ) and thermal infrared ( $10\text{--}12 \mu\text{m}$ ) experienced when data are collected for pixels containing small, but high-temperature, volcanic hot spots. Both abstracts heralded the *discoveries* that were soon to follow.

**The IAVCEI Remote Sensing Commission** This pivotal period culminated with the founding of the IAVCEI Remote Sensing Commission. Instigated by Peter Francis, David Pieri and David Rothery, the commission originated as a Working Group set up following discussions at the Osservatorio Vesuviano 150th anniversary conference in Naples (Italy) in August 1991. The commission was formally established in January 1997 at the IAVCEI General Assembly in Puerto Vallarta (Mexico). It remains one of IAVCEI's commissions set

up to serve as “groups of individuals who work together towards common goals in support of science” (<http://www.iavcei.org/>).

### 1.3.1.2 The growth period: 1985–2005

The five publications of 1985–1988 triggered a change. Prior to 1985, although thermal remote sensing instruments capable of detecting volcanic hot spots had been in orbit since 1960, only four papers dealing with satellite based studies of volcano hot spots had been published. [Figure 1.4a](#) shows that, beginning in 1985, the frequency of publication suddenly increased. It never again dropped below one publication per year, with momentum really picking up after 1990. Another turn around occurred in 1997. Between 1990 and 1996, satellite-based studies of volcano hot spots averaged 2.6 publications per year. This increased to 14 publications per year during 1997 to 2005, with 50% (58) of all publications in the [Appendix A](#) data base occurring between 2000 and 2005. This second turn around marked the take-off in the use of AVHRR, GOES and ATSR, as well as TM, to support volcano hot spot studies, as is apparent from [Figure 1.4b](#).

The current body of research, as collated in [Appendix A](#), comprises 115 papers published between 1985 and 2005, and 119 since 1970 (120 since 1965). Of these, 37% have been published in volcanological journals, 24% in remote sensing journals, and 19% in American Geophysical Union journals. Work focusing on thermal analysis of active lava flows and domes comprises the majority of the studies (45% and 25% of all studies, respectively), with studies of lava lakes comprising another 12%. Studies that examine hot pyroclastic flows, open vents, fumaroles, crater lakes and low temperature anomalies account for the remaining 18% (hot pyroclastic flows: 1%, open vents: 9%, fumaroles: 3%, crater lakes: 2%, low temperature anomalies: 2%).

**The take-off: 1990** Following the flow chart for the development of satellite-based volcano radiometry given in [Chapter 0](#), and further developed here in [Figure 1.3](#), we can split the work of 1990–2005 into five main theme areas:

- (1) examination and demonstration of satellite sensor detection capabilities;
- (2) examination of mixed pixel issues, sub-pixel thermal structures, and application of the dual-band technique;
- (3) derivation of heat loss and eruption rates;
- (4) automated hot spot detection;
- (5) generation of high-temporal-resolution eruption chronologies and time series analysis.

As can be seen from [Figure 1.3](#), these study directions began to proliferate rapidly following the publication of Rothery *et al.* (1988). In a *Nature* paper of the following year, Glaze *et al.* (1989) showed how the dual-band technique could be used with TM data to estimate the radiant heat flux for an active lava dome at Lascar, as well as the lava lakes at Erebus and Ertá Ale. They also showed how multiple TM images could be used to produce time series, presenting an energy flux time series for Lascar comprising ten data points spanning 1984 to 1987. Next, Pieri *et al.* (1990) used a TM scene for an active lava flow at Etna to show

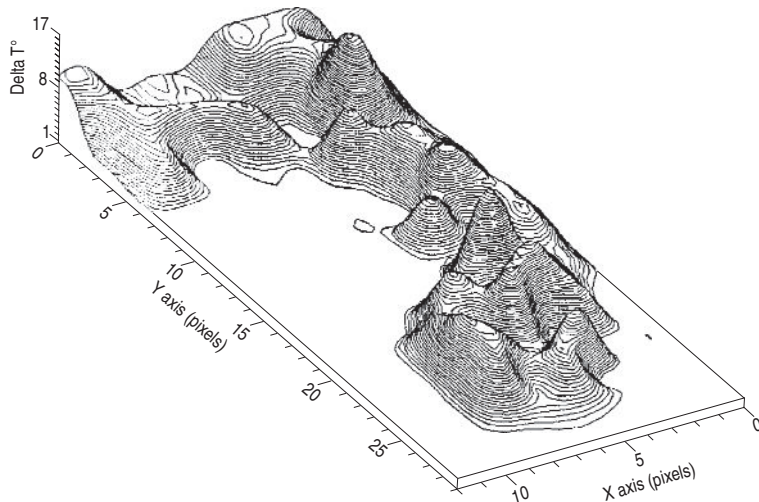


Figure 1.11 Map of core cooling for a lava flow active at Etna's SE Crater during June 1984 drafted by Pieri *et al.* (1990) using Landsat TM thermal data. Model calculations of the flow's internal temperature and core cooling are based on heat loss estimated from TM data. Results are presented in terms of core cooling, this being the temperature difference between the assumed eruption temperature and calculated internal temperature at any point in the lava flow. The methodology that needs to be applied to achieve such a result is given in Chapter 4 [from Pieri *et al.* (1990, Fig. 3)].

how the dual-band method could be used to estimate lava flow heat loss and core cooling, as reproduced here in Figure 1.11, with Clive Oppenheimer further developing the application of the dual-band method and its output to allow improved lava flow heat loss estimations (Oppenheimer, 1991) and time series analysis of active lava domes (Oppenheimer *et al.*, 1993a) using TM data. The themes of detection, application of the dual-band technique and heat loss were further developed through the 1990s, so that by the end of the decade a total of 38 papers had been written presenting use application of the dual-band method to satellite IR data containing volcano hot spots (see Figure 1.4c). While the history of developments within the theme of detection will be covered further in Chapter 5 (Hot spot detection), Chapter 4 will cover the mixed pixel, the dual-band technique, heat loss and volume flux. The theme of time series analysis will be reviewed in Chapter 6.

This take-off had been predicted by Peter Francis in a 1979 review of infrared techniques, in which he wrote “once satellites equipped with high-resolution scanning systems are available, it will then be possible to keep a thermal watch over almost all the volcanoes in the world” (Francis, 1979). Francis (1979) concluded, “it is hard to imagine that such thermal data will not be a great help in predicting volcanic eruptions, particularly when supplemented with other lines of evidence.” Why this sudden post-1990 growth? Certainly the work of the late 1980s had triggered it, but other factors were at work to give the wave real momentum.

**Preparation for EOS** Work was given a boost through the 1990s as preparations were made for the launch of NASA's Earth Observing System (EOS). This thrust was driven by the volcanology interdisciplinary science (IDS) team. At the inception of EOS, a series of interdisciplinary science teams were set up, each having specific scientific objectives to be addressed using data from EOS instruments. The volcanology interdisciplinary science team was one of 28 such teams selected by NASA for the EOS project (Mouginis-Mark *et al.*, 1991). The team was led by Peter Mouginis-Mark and initially included ~20 volcanologists and remote sensing specialists from the USA and the UK. Mouginis-Mark and Francis (1992) described the project as encompassing a consideration of:

- (i) long- and short-term monitoring of selected volcanoes,
- (ii) detection and analysis of precursory activity associated with eruptions, and
- (iii) monitoring of on-going eruptions.

In terms of volcanic hot spots, the main objectives were stated as being:

- (i) to use MODIS for detection of new eruptions through identification of thermal anomalies, and
- (ii) to use ASTER to study lava flow temperatures, as well as to study changes in fumarole temperatures and distributions as potential precursors.

At a team meeting held at NASA Goddard Space Flight Center in July 1992 the potential of MODIS and ASTER for thermal anomaly detection began to be explored further, with the meeting report concluding:

Although explosive eruptions formed the focus of the Goddard Volcanology Meeting, other aspects of volcanism and its effects on the atmosphere are also being investigated by the IDS Volcanology team. In particular, new nighttime spectroradiometer measurements of active lava flows and lava lakes are being used to develop algorithms for ASTER and MODIS" (Mouginis-Mark, 1992).

By 1996, a series of draft reports were available detailing the algorithms that would be applied to generate the various volcanology products. Product MOU81-3292 entitled "Thermal anomaly – low spatial resolution" (Flynn, 1996), for example, dealt with plans to produce "a chronological image record which will show the large scale (1 km) thermal evolution of eruptive areas and provide a catalog of data." The efforts of the EOS-IDS volcanology team culminated in a special session at the Annual Fall Meeting of the American Geophysical Union (AGU) in 1997 entitled "Remote Sensing of Active Volcanism." The session, featuring two poster sessions and one oral session, attracted 51 abstracts. An AGU Monograph based on the session was subsequently put together entitled *Remote Sensing of Active Volcanism* (Mouginis-Mark *et al.*, 2000a). This contained 14 chapters, three of which dealt with volcanic hot spots, these being those of Schneider *et al.* (2000), Harris *et al.* (2000a) and Flynn *et al.* (2000). A second AGU special session was held at the AGU Fall 2001 meeting. Entitled "Volcanic observations from space: New results from the EOS satellite instruments," it featured 22 papers split between one oral and one poster session. This time, the papers resulted in the publication of a special issue of the *Journal of Volcanology and Geothermal*

*Research*, published in 2004 (Volume 135, Issues 1–2). This contained ten papers, six of which dealt with volcano hot spots (Pieri and Adams, 2004; Wright *et al.*, 2004; Dean *et al.*, 2004; Donegan and Flynn, 2004; Ramsey and Dehn, 2004; Harris *et al.*, 2004).

**The beginnings of operational use of satellite data** Enormous headway was also made during the 1990s by the volcano remote sensing group at the University of Alaska Fairbanks (UAF) led by Ken Dean. Work at UAF was particularly significant because it marked the first use of satellite thermal data in an operational volcano monitoring role. As part of the Alaska Volcano Observatory function, over 100 volcanoes across Alaska, the Aleutians, Kamchatka and the northern Kurile islands were monitored in as close-to-real-time-as-possible using direct reception of AVHRR, GOES and GMS data at a receiving station installed at UAF in 1990 (Dean *et al.*, 1996; 1998). The primary concern was detection and tracking of ash clouds emitted by explosive eruptions, and assessing the hazard these posed to air traffic. Hot spots, mostly detected using AVHRR, provided useful information for activity levels at these remote and largely un-observed (from the ground) volcanoes, thereby allowing an assessment of likely hazard. During the 1996 eruption of Pavlof, for example, an increase in the pixel size of the AVHRR-recorded hot spot, along with the presence and altitude of AVHRR-recorded ash plumes and volcano seismicity, all served to determine the color code assigned to the eruption (as logged in Table 1.5). The need to deal, on a 24 hour basis, with satellite data for volcano hot spots at erupting, and about-to-erupt, volcanoes resulted in a rapid increase in understanding at AVO about how to detect and interpret volcanic hot spots in remotely-sensed thermal data, and led to a series of contributions including those from Wyatt and Dean (1995), Dean *et al.* (1996), Schneider *et al.* (2000), Roach *et al.* (2001), Dehn *et al.* (2000; 2002) and Dean *et al.* (2002; 2004). All showed how AVHRR data could be used to detect and track volcano hot spots. The weight of data, and the need for a timely alert, also led to the development of an operational AVHRR-based hot spot detection algorithm at UAF, this being the OKMOK algorithm (see Chapter 5), as well as the development of a model for internal monitoring procedures, report dissemination, archival and response protocols.

As a result of these efforts, by 2000 the volcano remote sensing community was firmly established, with well-populated volcano remote sensing special sessions regularly being held at international volcanological and geophysical meetings. These were coupled with workshops focusing on the potential of satellite data for volcano monitoring. On 23 July 2000, a volcano remote sensing workshop was held as part of the International Association of Volcanology and Chemistry of the Earth's Interior (IAVCEI) General Assembly in Bali. The workshop, entitled “Real-time volcano monitoring from space – principles, tools and issues,” attracted around 30 participants and resulted in a special issue of *Advances in Environmental Monitoring and Modeling* (Vol. 1, No. 3). The special issue went by the same title and contained six papers dealing with near-real-time satellite monitoring of volcanic hot spots using GOES, AVHRR, MODIS and ATSR (Dean *et al.*, 2002; Flynn *et al.*, 2002; Harris *et al.*, 2002a; 2002b; Kaneko *et al.*, 2002a; Wooster and Rothery, 2002). A volcano remote sensing workshop was also organized in June 2005 by the Italian Istituto Nazionale di

Table 1.5a. Chronology of the 1996 eruption sequence of Pavlof volcano and hazard code assigned using AVHRR-based hot spot and plume observations, plus seismicity (from Tables 1 and 4 of Roach et al., 2001).

Date(s) / time (UT)	AVHRR thermal anomaly (thermal anomalies given as number of MIR pixels >30 °C)	Seismicity (tremor amplitudes given as 3-station reduced displacement averages)	Plume (length from AVHRR, height from ground & pilot observations)	Color code (See Table 1.5b for definition)
Sept. 11 (15:25)		Anomalous seismicity at station PV6 (4.6 km distant from summit)		Green
Sept. 11 (17:37)		Anomalous seismicity at station PVV (8.1 km distant from summit)		Green
Sept. 13 (13:09)	First anomaly: 2 pixels	Anomalous seismicity		Green
Sept. 13 (18:32)	Anomaly persists	Anomalous seismicity		Green
Sept. 16 (02:23)		Detection of airwave		Orange
Sept. 16 (16:30)			First observation of ejecta & steam plume	Orange
Sept. 17–24	Cloudy		Plumes extending >50 km	Orange
Sept. 25–Oct. 5	Steady increase: 6–8 pixels	Tremor increase to >3 cm <sup>2</sup>	Plumes extending 100–150 km	Orange
<b>Oct. 3</b>				<b>FAA imposes flight level restrictions</b>
Oct. 6–10	Continued increase	Increase in tremor & triggers		Orange
Oct. 10–15	Peak: ~15 pixels	Continued increase		Orange
<b>Oct. 18</b>	<b>Begin Decline</b>	<b>Tremor &gt;10 cm<sup>2</sup></b>	<b>Plume to altitude of 6705 m</b>	<b>Red</b>
Oct. 19–Nov. 3		Tremor >3 cm <sup>2</sup> and increasing		Orange
<b>Nov. 4</b>		<b>Tremor &gt;10 cm<sup>2</sup></b>	<b>Plume to altitude of 7315 m</b>	<b>Red</b>
Nov. 5–9		Tremor >3 cm <sup>2</sup>	Occasional plumes extending >100 km	Orange
Nov. 10		Begins to decline		Orange
Nov. 18–26	Receiving station lost	Second period of increase		Orange
<b>Nov. 23</b>	<b>Receiving station down</b>	<b>Tremor &gt;10 cm<sup>2</sup></b>	<b>Plume to altitude of 9150 m</b>	<b>Orange: NWS alerted</b>

Table 1.5a. (cont.)

Date(s) / time (UT)	AVHRR thermal anomaly (thermal anomalies given as number of MIR pixels >30 °C)	Seismicity (tremor amplitudes given as 3-station reduced displacement averages)	Plume (length from AVHRR, height from ground & pilot observations)	Color code (See Table 1.5b for definition)
Dec. 4	Receiving station down	Abrupt decline to pre-eruption level		Orange
Dec. 6–9	Receiving station down			Yellow
<b>Dec. 10</b>	<b>Receiving station down</b>	<b>Burst in triggers &amp; tremor</b>		<b>Orange then red</b>
<b>Dec. 11</b>	<b>Receiving station down</b>	<b>Tremor peaks at 12 cm<sup>2</sup></b>	<b>Steam plume to 8687 m, ash to 5180 m</b>	<b>Red</b>
Dec. 12	Receiving station down	Tremor decreases		Orange
Dec. 13	Receiving station down	Tremor below detection limits		Orange
Dec. 15	Receiving station down			Yellow
Dec. 26	Receiving station replaced	Burst in triggers & tremor		Orange
<b>Dec. 27</b>		<b>Tremor peaks at 20 cm<sup>2</sup></b>	<b>Probable plume</b>	<b>Red</b>
Dec. 28		Tremor decreases to ~7 cm <sup>2</sup>	Plumes extending <100 km for several days	Orange
Dec. 29		Seismicity decreases abruptly		Yellow
Jan. 1		Seismicity at background		Yellow
Jan. 3			Last observation of ash plume	Yellow
Jan. 17	Last anomaly: 2 pixels		Occasional steam plume for several months	Yellow
Apr. 4				Green

<sup>1</sup> FAA = Federal Aviation Administration, NWS = National Weather Service.<sup>2</sup> Bold = Major aviation warning and ash emission events.

**Table 1.5b.** *Alaska Volcano Observatory level-of-concern color code as used for the 1996 Pavlof eruption and given by Roach et al., 2001 (Table 5 of Roach et al., 2001). Color codes are assigned based on an assessment of seismic activity, as well as plume and hot spot activity as evident from AVHRR data.*

Color code	Intensity of unrest at volcano	Forecast
Green	Volcano is quiet	No eruption anticipated
Yellow	Small earthquakes detected locally and/or increased gas emission	An eruption is possible in the next few weeks and may occur with little or no additional warning
Orange	Increased numbers of local earthquakes, lava (flow or dome) extrusion may be occurring	Explosive eruption is possible within a few days and may occur with little or no additional warning. Ash plumes not expected to reach 7620 m
Red	Strong earthquake activity detected even at distant stations. Explosive eruption may be in progress	Large explosive eruption expected within 24 h. Large ash plumes expected to reach at least 7920 m

Geofisica e Vulcanologia (INGV), the Naples-based Istituto per il Rilevamento Elettromagnetico dell'Ambiente (IREA) and the European Space Agency (ESA). This workshop, held at the Vesuvius Observatory (Ercolano, Italy), was entitled “Use of remote sensing techniques for monitoring volcanoes and seismogenic areas” and attracted 40 oral presentations. Of these, 36 dealt with satellite or airborne remote sensing data, of which seven considered infrared applications for monitoring volcano hot spots. Most recently, volcano remote sensing research efforts culminated in a vibrant volcano remote sensing poster session at the August 2008 IAVCEI General Assembly, at which 56 posters were presented.

**The role of improved technology** Beyond the influence of developing satellite capabilities coupled with evolving research and monitoring programs, a third important factor was at work in driving remote sensing of volcano hot spots forward. This was the enormous advances in reception, processing and storage capacity made between 1990 and 2008. Massive advances in computing capabilities made it easier to receive, process and archive large volumes of satellite data. Compare the reception, storage and processing capabilities of 1988 with those of 2008. In 1988, uncalibrated TM data, for example, were usually stored on bulky and slow-to-access magnetic tapes (which could also be wiped by electric-drill-wielding technicians installing phone systems next to the tape archive). Data typically required calibration by the user, and ordering delays would cause a lag between data acquisition and analysis of up to a few months. By 2008, terra-bytes of data could be stored on small, fast, cheap, solid-state hard-drives. Data were typically calibrated, rectified and ready-to-use in automated processing algorithms. For example, calibrated ETM+ data in GEOTIFF format could be ordered from the USGS, or fully calibrated MODIS data from

NASA, with a delay of 24–48 hours. Data were usually downloadable via the internet. In addition, data purchase costs were greatly reduced, with availability, access and length of available time series undergoing a parallel increase. The TM data used by Rothery *et al.* (1988), for example, cost \$1650 for a quarter scene, or \$140 000 for a full scene. Most TM, AVHRR, GOES and MODIS data in 2008 were freely available via various web-sites. For example, in January 2009, MSS, TM and ETM+ data spanning 1972 to 2009, became freely available from the USGS' EROS data center, and MODIS data for 2000 to 2008 were freely available from NASA. The free availability of vast amounts of easy-access thermal data had, without a doubt, facilitated a proliferation in the incidence of use.

This revolution in storage media and web-based data availability coincided with a decrease in the price of computers and image processing software, as well as an increase in computing power (i.e., hard-disk sizes and processor speeds). This facilitated the use of software installed on desktops and laptops to achieve work once only done in specialist remote sensing laboratories. For example, in the 1980s, and through most of the 1990s, image processing of satellite images meant that the user had to buy a stand-alone image processing system, costing around \$100k, and invest in image processing laboratories that included, for example, banks of dedicated workstations. By 2008, the same processing could be carried out on a desktop PC using relatively cheap image processing software packages, such as ENVI, or even free ware. This made use and application of remote sensing data accessible to a much wider population.

## 1.4 Ground-based and airborne sensors

### 1.4.1 *Ground-based thermal remote sensing of volcanic hot spots*

Ground-based thermal remote sensing of active volcano hot spots can be divided into two groups; the first includes work carried out using radiometers, the second uses thermal imagers. The difference between the two is that radiometers collect temperature for a single point, whereas an imager records temperature for all points, or pixels, across the image array. The full history of the use of radiometers and imagers in volcanology will be reviewed in Part III. Here, we review the development of the thermal sensor technology that allowed us to reach a point where the technology could be applied to allow measurement of volcanic thermal phenomena. Being ground-based, such thermal sensors do not require the launch vehicle (i.e., a rocket) necessary to carry a satellite-based sensor into orbit. Thus, the timeline for application of ground-based thermal remote sensing is not constrained by developments in rocketry and satellite technology. Instead, constraint lies in the development of sensor technology.

Krutikov (2002) traces the history of thermal sensor technology back to 1703 and the invention of the gas thermometer by Amonton. This was the first instrument that met the definition of a remote thermal sensor, this being a sensor which detects emitted radiation on the basis of a change in the detector's own temperature. Since 1703, a large number of

different thermal sensor types have been invented which can be divided into two main classes on the basis of detector response:

- thermal radiation detectors, which react to a change in incident radiation by a change in detector temperature, and
- photon radiation detectors, which react to a change in incident radiation by generating an electrical response proportional to the intensity of the at-sensor radiation.

As will be explained in [Chapter 7](#), thermal detectors are the most commonly used detector type in ground-based volcanological applications. Photon detectors are extremely sensitive and have fast response times. However, they tend to require cooling and have heavy power requirements, making them not very field portable, the cooling system itself being rather bulky. They also commonly have detection cut-off points in the SWIR, so that low-to-moderate ( $100\text{ }^{\circ}\text{C}$  to  $500\text{ }^{\circ}\text{C}$ ) temperature sources cannot be detected. Thermal sensors, on the other hand, can extend the measurement range to ambient temperatures, do not require cooling and are power efficient. However, they usually require long exposure times to the radiator (thus the response time is slow) and require large lenses to collect and focus the radiation. The same problem is encountered in military applications. Here, photon sensors are extremely useful for applications which require fast response, such as missile guidance, tracking and interception. However, they are too bulky for portable (battle-field) applications, such as night vision, use in rifle sights and deployment for surveillance missions, for which thermal sensors are more useful ([Nothwang \*et al.\*, 2004](#)). Given that thermal sensors are predominantly used in volcanology, we focus here on the development of thermal detector technology. [Krutikov \(2002\)](#) does a superb job of tracing the time-line of development for both detector types. His chronology tree for the development of thermal detectors is reproduced here in [Figure 1.12](#) and forms the basis of the following chronology.

#### 1.4.1.1 Development of radiometers

The development of infrared (non-thermometer-based) radiometry can be traced to William Herschel's discovery, in 1800, that heat is radiated in the infrared portion of the spectrum. Using a mercury thermometer with a blackened bulb as a radiation detector, and splitting the colors of the spectrum using a Newton prism, Herschel tested the heating effect of each portion of the visible spectrum. He found a steady increase in the heating effect as he moved from the violet end of the spectrum to the red end, and concluded that there must be a point outside the visible portion of the spectrum where heating reaches a maximum, i.e., he had discovered thermal infrared radiation. Thermometers remained in use as radiation detectors until the invention of the thermocouple by Nobili in 1830, an invention which relied on the 1826 discovery by Seebeck of the thermal response that occurs when a junction of wires is heated. Then, in 1840, Melloni connected a number of thermocouples together in series to create the first thermopile. The thermopile remains one of the main thermal detectors used in commercial broad-band ( $8\text{--}14\text{ }\mu\text{m}$ ) radiometers, as used widely in volcanology today (see [Chapter 7](#)).

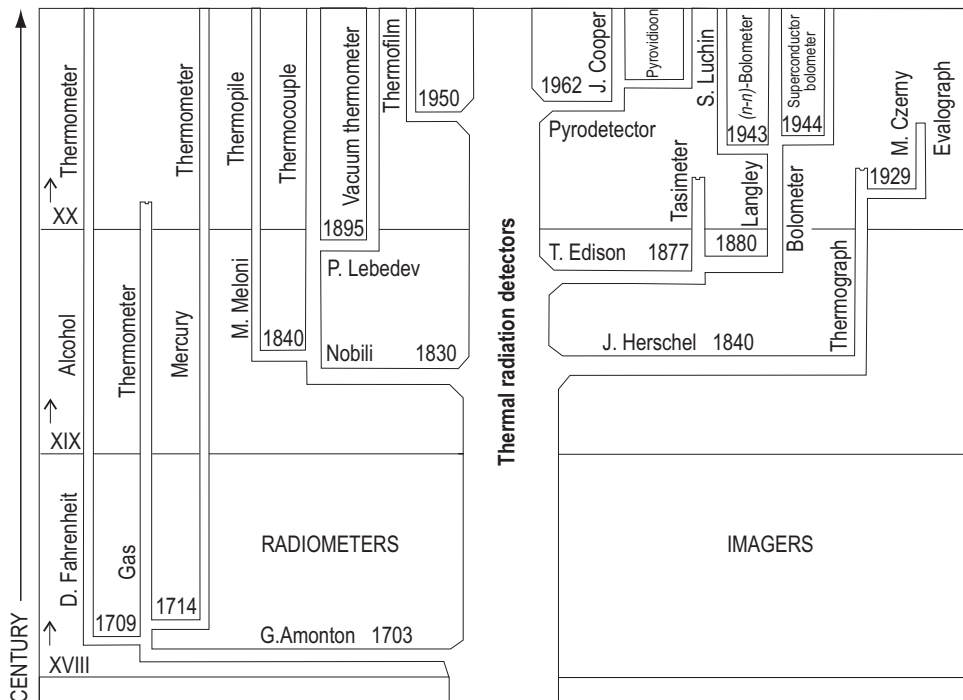


Figure 1.12 Chronological tree for the development of thermal radiation detectors given by Krutikov (2002) [from Krutikov (2002, Fig. 1), with kind permission from Springer Science and Business Media].

As will be reviewed in Chapter 7, technological advances in radiometer design coupled with increased demand, has resulted in a wide range of low-cost radiometers being commercially available. As with meteorological satellite-based sensors, no radiometer-based sensor has been designed specifically for volcanology, and demand from volcanology alone is insufficient to drive technological advances. The driver for the widespread provision of affordable radiometers has largely been industrial. The Williamson Corporation, for example, provides a six-page summary sheet that deals with the application of, and required specifications for, radiometers installed for a variety of functions at aluminium smelting plants (Williamson Corporation, 2004). In addition, the use of non-contact, infrared detectors has become widespread in the medical profession, where sensors such as the Braun Thermoscan make body temperature measurements easier, quicker to obtain and more accurate than those obtained using traditional mercury thermometers (Chamberlain *et al.*, 1995; Nimah *et al.*, 2006). Although not designed specifically for volcanological applications, the range of models now available means that radiometer specifications can be selected for any volcanological application. Thus, as with satellite sensors, volcanology can use and adapt the technology designed for other purposes.

**Use in volcanology** Given that the invention of the thermopile dates back to 1840, it is not too surprising that the first recorded use of a ground-based thermal sensor on an active volcano easily predates the first use of a satellite-flown sensor. Macdonald (1972) provides

a tabulation of temperature measurements made at active lava flows, lakes, domes and fountains for the period 1900 to 1966. Updating this tabulation to 1970 and adding some entries that were not repeated from his earlier collation in 1963 (Macdonald, 1963), as done here in [Table 1.6](#), shows that at least 47 temperature measurements were reported at active volcanoes between 1900 and 1970. The collation shows that the first temperature measurement can be traced to that of a lava flow active on Stromboli (Italy), as made by Brun in 1901. This first measurement was obtained through contact, i.e., using a thermocouple. The first non-contact measurements were made eight years later at Kilauea (Hawaii) by Daly in 1909, who used an optical pyrometer to obtain temperatures at Halemaumau's active lava lake. In fact we see that, of the [Table 1.6](#) collation, 18 measurements were thermocouple-based, 19 were obtained using optical pyrometers, and eight were made using radiometers. All of these radiometer deployments occurred during the 1960s.

At the point of Macdonald's collation, the optical pyrometer was "the instrument most commonly used to measure temperatures at volcanoes" (Macdonald, 1972). [Table 1.6](#) shows that thermocouple measurements were dominant prior to 1938. The use of optical pyrometers became dominant after Zeis' (1941) measurements at Santiaguito (Guatemala) in 1940, with optical pyrometers subsequently being used extensively on Kilauea. However, the optical pyrometer is neither a thermal detector nor a photon detector. Instead it

consists essentially of a telescope in which a wire filament is mounted in such a way that it is visible in the telescope field at the same time as the glowing object, the temperature of which is being measured. Passing electrical current through the filament causes it to glow, its color changing from dull to bright red, orange, yellow, and white as the strength of the current is increased. At some point the color of the filament is exactly the same as that of the glowing object, and viewed against the object the filament completely disappears (Macdonald, 1972, pp. 55–56).

The amount of current necessary to cause the filament to acquire the same color as the incandescent background allows the temperature of the object to be calculated. It is, thus, purely an optical device.

The first ground-based use of a radiometer to obtain volcano surface temperatures did not occur until 1964, just one year prior to the satellite-based observations of thermal emission from an active lava by Gawarecki *et al.* (1965), and was reported by Decker and Peck (1967). Their application involved the use of a radiometer to obtain a surface temperature profile across the cooling lava lake within Kilauea's Alae crater during 1964. In the same year, Moxham *et al.* (1965) used an airborne radiometer to obtain temperature profiles for transects crossing the summit of Mt. Rainier (USA). A ground-based radiometer was subsequently used by Birnie (1973) to map surface temperature anomalies at Pacaya and Santiaguito in Guatemala during 1969 and 1970. Tazieff (1970) first reported deployment of a continuously recording radiometer to log the thermal signals generated by hot gas exiting an active vent on Etna in 1969. The following year, Shimozuru (1971) presented thermal waveforms acquired using continuously logging radiometers targeted at explosions from Akita-komaga-take (Japan) in 1970.

Application of ground-based radiometry to volcanology thus, surprisingly, began at roughly the same time as space-based radiometers were being developed. Even more surprisingly, and as we will see from [Chapter 7](#), the progression in use of ground-based radiometry for volcanic studies actually lagged behind the development of satellite-based

Table 1.6. Table 4.2 of Macdonald (1972, p. 58) listing “some of the better” temperature measurements made at active lavas (lakes, flows, fountains and domes) from 1900 to 1966, updated to 1970, sorted by year-of-measurement, and with method of measurement added.

Volcano	Date	Temp, °C	Investigator	Rad	OP	Thm	Other	Notes
Stromboli	1901	1150	Brun		✓			Lava flow close to vent
Kilauea	1909	1000	Daly		✓			Surface of lava lake in Halemaumau
Etna	1910–1957	940–1150	Cucuzza-Silvestri		✓			Lava issuing from vents
Etna	1910	900–1000	Perret		✓			Lava flows at vent
Kilauea **	1911	1050	Perret		✓			Active lava lake
Kilauea	1912	1000	Day & Shepherd		✓			Surface of lava lake in Halemaumau
Vesuvius	1913	1200	Perret		✓			Flowing lava
Vesuvius	1916–1918	1015–1040	Perret		✓			Flowing lava
Kilauea	1917	1000	Jaggar			✓		Surface of lava lake in Halemaumau
Kilauea	1917	860	Jaggar			✓		1 m below surface of lava lake
Kilauea	1917	1170	Jaggar			✓		Bottom of lake (depth 13 m)
Vesuvius	1929	1150	Rittmann		✓			Lava fountain at vent
Klyuchevskaya	1938	865	Popkov		✓			Lava flow 800 m from vent
Klyuchevskaya	1938	690	Popkov		✓			Lava flow 2400 m from vent
Nyamлагира	1938	1040–1075	Verhoogen		✓			Lava at vents
Santa Maria	1940	725	Zies		✓			Dacite dome
Paricutin	1943	1135	Bullard		✓			Lava flow at vent
Nyiragongo	1948–1959	987–1080	Tazieff		✓			Fountains in lava lake
Mauna Loa*	1949	745	Macdonald & Orr		✓			Barely moving aa flow (~1 m below surface)
Mauna Loa **	1950	1030–1110	Finch & Macdonald		✓			Vents, flows near vents
Mauna Loa **	1950	850–980	Finch & Macdonald		✓			Flow fronts, edges
Mauna Loa	1950	1070	Macdonald		✓			Lava fountain at vent
Oshima	1950	1060	Murauchi			✓		Lava flow near vent
Oshima	1951	1125	Minakami			✓		Lava flow near vent

Kilauea	1952	1095–1130	Macdonald		✓			Lava fountains in Halemaumau
Kilauea	1955	1080–1100	Macdonald & Eaton		✓			Lava fountains at vents, flank eruption
Kilauea	1959	1120–1190	Eaton & Murata		✓			Lava fountain at vent in Kilauea Iki
Kilauea **	1959	1065–1190	Richter & Murata		✓			Lava fountains (Kiluea Iki)
Kilauea **	1960	1020–1125	Richter & Murata		✓			Lava fountains (East Rift)
Kilauea *	1960	1064	Rawson			✓		Lava below crusted lake surface (Kilauea Iki)
Kilauea	1960	1050–1130	Eaton & Murata		✓			Lava fountain, flank eruption
Kilauea *	1961	1064–1100	Ault <i>et al.</i>		✓	✓		Lava below crusted lake surface (Kilauea Iki)
Kilauea **	1961	1095–1125	Richter <i>et al.</i>		✓			Lava fountains at Halemaumau
Kilauea **	1961	1096–1114	Richter <i>et al.</i>		✓			Lava fountains at Halemaumau
Kilauea **	1961	1085–1127	Richter <i>et al.</i>		✓			Lava fountains at Halemaumau
Kilauea	1963	1140	Peck <i>et al.</i>			✓		Lava fountain and lake in Alae Crater
Kilauea	1964		Decker & Peck	✓				Cooling (inactive) lake in Alae Crater
Rainier	1964		Moxham <i>et al.</i>	✓				Ground temperature profiles (airborne)
Kilauea	1965	1085–1190	Wright <i>et al.</i>		✓			Surface of lava lake in Makaopuhi Crater
Etna	1966	880–1050	Tanguy & Biquand			✓		Lava flows near vents
Kilauea **	1967–1968	1110–1125			✓			Lava fountains at Halemaumau
Fuji	1968		Fujita <i>et al.</i>	✓				
Surtsey	1968		Williams <i>et al.</i>	✓				
Santiaguito	1969–1970		Birnie	✓				Surface of edifice flank
Erta Ale	1969		Tazieff & Jatteau	✓				
Etna	1969		Tazieff	✓				Waveforms for gas puffing
Akita-komaga-take	1970		Shimozuru	✓				Waveforms for explosive eruptions
Total	47			8	19	18	3	

Entries marked \* are added from Table 1 of Macdonald (1963); those marked \*\* are added from Table 1 of Helz *et al.* (1995).

Key: Rad = Radiometer, OP = Optical Pyrometer, Thm = Thermocouple, Other = measurements by Jaggar using Seger cones.

applications, radiometer-based studies not really taking off until 2000, there being six published studies in the 1960s, eight during the 1970s, four during the 1980s, 11 during the 1990s, and then 24 between 2000 and 2005 (31 for 2000 to 2007). A post-1995 increase in the availability of cheap, portable and robust off-the-shelf radiometers contributed to this increase in the reported use of radiometers to measure volcanic thermal phenomena. We carry out a full review of these developments and consider the history of ground-based radiometry in [Chapter 7](#).

#### *1.4.1.2 Development of thermal imagers*

In the same year as Melloni's invention of the thermopile, William Herschel's son, John Herschel, made a discovery that led to the development of the thermal imager. His means of visualizing the spatial distribution of infrared radiation relied on the evaporation of a material sensitive to heating. The device consisted of a carbon-coated sheet of paper impregnated with alcohol. When the alcohol was heated, spots appeared on the paper, the distribution of which corresponded to the distribution of thermal radiation intensity across the sheet. The result was a thermograph: the first thermal image. Czemy, in 1929, improved on Herschel's design by using camphor oil as the working (evaporating) material. However, although sensitive and having high spatial resolution, they were not convenient in practice (Krutikov, 2002), thus their use died out so that their development is not taken further in Krutikov's chronology tree of [Figure 1.12](#).

In 1877, Edison invented the tasimeter. Composed of compressed carbon, the electrical resistance of the tasimeter varied when heated. Three years later, in 1880, Langley developed a more sensitive instrument, consisting of a blackened platinum strip which operated on the same principle as the tasimeter, i.e., its electrical resistance varied when heated. This was the bolometer, with Langley's bolometer being able to detect the heat from a cow over a distance of 400 m. Like rocketry, the development of the thermal resistive (bolometric) principle of detecting radiation progressed considerably during World War II, with Luchin designing the first semiconductor bolometer in the USSR, and the superconducting bolometer being invented in the USA ([Figure 1.12](#)). Today the bolometer forms the basis of most portable thermal imagers, as will be reviewed in [Chapter 9](#).

The main thermal imager currently used in volcanology is based on the Forward Looking Infrared (FLIR) detector, a focal plane array of bolometers (see [Chapter 9](#)). This was mostly developed thanks to its utility to military applications. Infrared detectors have been an increasingly important part of the US Army's arsenal since the early 1960s when a cooled FLIR was first developed as a night vision system (Nothwang *et al.*, 2004). In 1978, uncooled thermal imaging was demonstrated to the US Army, and in 1985 the first battery-operated night vision system went into operation. Three years later, in 1988, the first commercial infrared camera became available with the focal plane size, and resolution, increasing to  $256 \times 256$  pixels in 1990, and to  $512 \times 512$  pixels in 1992 (Nothwang *et al.*, 2004).

Most of the advances in thermal imaging continue to be driven by military requirements. Nothwang *et al.* (2004), in their review of detector materials for enhanced military night

vision and targeting capabilities for the US Army materials research journal, *AMPTIAC*, point out that

small uncooled thermal sensors offer the army medium-performance alternatives that are cost effective, light weight, and low powered (uncooled FLIRs are specifically either pyroelectric or microbolometer devices) (Nothwang *et al.*, 2004).

They go on to point out that such sensors are used in rifle sights and vehicle (e.g., tank) driver viewers. In April 2008, FLIR Systems Inc. (the manufacturer of the most commonly used hand-held thermal cameras in volcanology) received two contracts from the US Army for a total of \$18.4 million to install their Star SAFIRE multisensor imaging system in H-60 Black Hawk helicopters. The Star SAFIRE HD comprises an 8–5  $\mu\text{m}$  thermal imager, a color zoom camera and a low light camera, all with a  $1280 \times 720$  pixel image resolution. The system outputs merged visible and thermal images, weighs 10.4 kg, has dimensions of  $254 \times 191 \times 318$  mm, and consumes 200 W (22 to 29 Vdc) of power. Likewise, ICx Technologies won a contract worth \$1.13 million in January 2008 to deliver its DefendIR infrared cameras for use by the US Army to support operations in urban terrain. Like the Star SAFIRE HD, the camera outputs merged thermal and visible images, with the thermal camera using an uncooled vanadium oxide microbolometer to provide  $320 \times 240$  thermal images at frame rates of up to 60 images per second.

Such ground-based imaging technology, developed not only for the army but also for industrial and search-and-rescue purposes, is transferable to volcanology, with recent advances being reflected in a take-off in the use of off-the-shelf hand-held thermal cameras in volcanology. This has been apparent from the proliferation of publications reporting the use of ground-based thermal imagers in volcanology since 2000. The number of publications has increased from none during 2000 and 2001, to 20 between 2002 and 2004, and 93 between 2005 and 2010 (see [Table 9.3 of Chapter 9](#)). At the same time, the installation of thermal infrared cameras as part of permanent monitoring networks has also taken off, with (in Italy alone) permanently recording thermal cameras being installed on Etna, Vulcano, Stromboli, Campi Flegrei and Vesuvius in 2003 and 2004. There is a full review of the history of ground-based thermal imaging of volcanic hot spots in [Chapter 9](#).

#### **1.4.2 *The role of airborne remote sensing***

Use of airborne scanners to obtain thermal infrared imagery of active volcanic phenomena has been relatively common since the 1960s. Moxham (1971) cites the first use of an infrared scanner as occurring at Yellowstone National Park in 1961. Subsequent surveys of geothermal and volcanically active areas included flights over Kilauea (Fischer *et al.*, 1964), Mount Rainier (Moxham *et al.*, 1965), Taal (Moxham, 1967), Mono Lake (Friedman, 1966; 1968), Surtsey, Hekla and Myvatn (Friedman *et al.*, 1969), the Geysers geothermal field (Moxham, 1969; 1970; Boynton and Moxham, 1969) and the Cascades (Moxham, 1970).

Moxham (1971) provides a complete review of airborne scanner surveys completed during the 1960s, as do Friedman and Williams (1968) and Williams (1972). During this

surge of activity, Friedman and Williams (1968) highlighted the widespread application of airborne thermal remote sensing at active volcanoes during the 1960s by writing

a literature review indicates that the most numerous and definitive examples of detection of active geologic processes on the Earth's surface by airborne infrared line-scanning techniques have been of volcanic and geothermal activity ... more than 22 volcanoes, in various stages of activity and repose, have been surveyed by infrared techniques (Friedman and Williams, 1968).

Their literature review in support of this statement is repeated here in [Table 1.7](#). In fact, a review of Friedman and Williams (1968) reveals that many of the approaches applied today, including conversion to heat and volume flux (see [Chapter 4](#)), were already in place by 1968 thanks to the early impetus provided by the airborne survey efforts of the 1960s. A review of [Table 1.7](#) also reveals the great variety of volcanoes and volcanic processes that had been targeted by thermal infrared sensors by 1968, spanning detection and mapping of active lava flows, lakes and tubes, through analyses of structural, fumarolic and crater lake features. In fact, although drafted in 1967, [Table 1.7](#) provides an excellent and thorough tabulation of most potential applications of high spatial resolution thermal infrared data to volcanology.

#### *1.4.2.1 A review of airborne scanner studies: 1970–2000*

Scanners are flown on aircraft flying at a fixed altitude. Those flown in the 1960s typically collected data at one or two wavebands located in the mid-infrared and/or thermal infrared. Since the 1960s, development of sensors with 10s to 100s of wavebands, extending into the NIR and SWIR, has allowed increasingly sophisticated analysis. This development is apparent from a review of the main airborne studies of volcanic thermal phenomena published between 1970 and 2000.

Studies in the 1970s and 1980s tended to rely on data from scanners collecting data in one or two wavebands. Cassinis and Lechi (1974) reviewed infrared radiometry in geothermal areas, presenting airborne-scanner-derived maps of radiant power and 3.5–5.0  $\mu\text{m}$  radiance for Vulcano and Solfatara (Italy). Over-flights of Rabaul (Papua New Guinea) were made during May 1973 by Perry and Crick (1976) to complete an infrared survey of land-based and shallow-water hot spots. In this deployment a two-band Daedalus line scanner, operating in the 3.5–5.5  $\mu\text{m}$  and 8–14  $\mu\text{m}$  regions, was used. Kieffer *et al.* (1981) next reported the use of a range of single-band aircraft-mounted scanners, as well as hand-held imagers, to complete a series of thermal surveys at Mt. St. Helens (USA) between 1966 and August 1980. This was followed up by Friedman *et al.* (1981) who used a single band (8–14  $\mu\text{m}$ ) scanner to complete thermal surveys of the extruding domes and eruption deposits following the 18 May 1980 eruption of Mt. St. Helens.

In Italy, Geraci *et al.* (1985) used a helicopter-mounted Airborne AGA Thermovision System (AATS) to obtain 100-pixel-wide images in the 3–5.6  $\mu\text{m}$  waveband along a short flight path flown on Mt. Etna's south flank during May 1983. This enabled detection of active lava flows and ground fractures. Brivio *et al.* (1989) reported data for Vulcano collected during a series of over-flights spanning May 1970 to August 1980. These deployments used scanners operating in two wavebands: 1–2  $\mu\text{m}$  and 9–11  $\mu\text{m}$  (by day) and

Table 1.7. *Table 1 of Friedman and Williams (1968, pp. 789–792) listing “infrared imagery studies of active volcanoes through 1967.” All studies involve use of airborne scanner data, except that marked (E) which used aerial Ektachrome infrared photography to confirm the presence of molten lava. Entries marked (I) and (II) also report eruption detection by HRIR aboard Nimbus I and II, respectively. Apart from a few minor edits, chronological sorting, and entry of full reference listings, I have not amended, corrected or updated this table from the original.*

Volcano	Type of volcano, type of activity and composition of products erupted	State of activity during airborne surveys	Geologic processes represented	Contribution of infrared imagery in geologic interpretation of anomalies	Reference
Kilauea, Hawaii (I)*	– Shield volcano – Effusive	Intereruptive	– Caldera and Alae lava lake formation and cooling; – Convecting fractures and fissures.	– Delineation of warm vent areas and convecting fracture systems; – Identification of pneumatolytic alteration and deposition zones; – Kapoho (lava) flow details; – Order of magnitude of apparent surface temperatures.	Fischer <i>et al.</i> (1964) Infrared surveys of Hawaiian volcanoes.
Mauna Loa, Hawaii	– Basalt				<i>Science</i> <b>146</b> (3645):733–742
Mt. Rainier, USA	– Stratovolcano – Explosive & effusive – Hypersthene & Pyroxene Andesites	Late- or post-volcanic	– Thermal convection from concentric fracture system; – Prehistoric caldera collapse; – Fumarolic activity on North rim of East and West summit craters.	– Confirms reported thermal emission; – Shows relation of thermal sources to structure and area of greatest intensity of emission in relation to central plug of volcano.	Moxham <i>et al.</i> (1965) Thermal features at Mount Rainier, Washington, as revealed by infrared surveys. <i>USGS Prof Pap</i> <b>525D</b> :D93-D100
Irazu, Costa Rica	– Stratovolcano – Pyroclastic – History of explosive & effusive activity – Vitric basaltic-andesitic ash	Active pyroclastic eruptions & interparoxysmal activity	– Eruption of vitric ash; – Ejection of bombs; – Thermal emission from fumaroles and hot springs.	– Delineation of lava pit; – Configuration and identification of septum; – Relative temperatures of hot springs NW of Irazu; – Alignment of hot springs.	Gawarecki <i>et al.</i> (unpublished data)

Table 1.7. (cont.)

Volcano	Type of volcano, type of activity and composition of products erupted	State of activity during airborne surveys	Geologic processes represented	Contribution of infrared imagery in geologic interpretation of anomalies	Reference
Turrialba, Costa Rica	– Stratovolcano – Pyroclastic	Intereruptive	– Fumarolic activity.	– Relative temperature and degree of activity at venting fumaroles; – Alignment of points of thermal emission.	Gawarecki <i>et al.</i> (unpublished data)
Poas, Costa Rica	– Basaltic andesite				
Taal, Philippines	– Pyroclastic – Explosive	Active pyroclastic	– Fumaroles on N. flank of main crater; – Anomalies around summit and on SE flank of Mt. Binintiang on NW tip of island; – Hydrothermal activity in lake	– Documents changing patterns of hydrothermal activity and suggests hydrothermal activity is controlled by pre-existing fault system that controlled the major pyroclastic eruption of 1965.	Moxham & Alcarez (1965) Infrared survey of Taal volcano. <i>Proc of the 4th Symposium of Remote Sensing of Environment</i>
Mt. Shasta, USA	– Stratovolcano – Solfataric activity – Pyroxene andesite to andesite basalt	Probably late-volcanic	– Some thermal emission.	– Identification of thermal anomalies	Moxham (unpublished data) <sup>4</sup> 1966 survey
Mt. St. Helens, USA	– Stratovolcano with small domes – Pyroclastic and effusive – Pyroxene andesite and olivine basalt	Probably late-volcanic	– Some thermal emission.	– Identification of thermal anomalies	Moxham (unpublished data) <sup>4</sup> 1966 survey
Mt. Adams, USA	– Stratovolcano	Probably late-volcanic	– Some thermal emission.	– Identification of thermal anomalies	Moxham (unpublished data) <sup>4</sup> 1966 survey

Lassen Peak, USA	<ul style="list-style-type: none"> <li>– Endogenous dome</li> <li>– Explosive &amp; effusive &amp; mudflows</li> <li>– Mostly dacite</li> </ul>	Intereruptive or late volcanic	<ul style="list-style-type: none"> <li>– Some thermal emission.</li> </ul>	<ul style="list-style-type: none"> <li>– Identification of thermal anomalies</li> </ul>	Moxham (unpublished data) <sup>4</sup> 1966 survey
Crater Lake, USA	<ul style="list-style-type: none"> <li>– Caldera (stratovolcano)</li> </ul>	Last great activity > 6000 years ago	<ul style="list-style-type: none"> <li>– Some thermal emission.</li> </ul>	<ul style="list-style-type: none"> <li>– Identification of thermal anomalies</li> </ul>	Moxham (unpublished data) <sup>4</sup> 1966 survey
Taal, Philippines Canlaon, Philippines Mayon, Philippines	<ul style="list-style-type: none"> <li>– Stratovolcano</li> <li>– Effusive &amp; pyroclastic</li> <li>– Augite andesite to basalt</li> </ul>	Intereruptive			Moxham (1967) Changes in surface temperature of Taal volcano. <i>Bull. Volcanol.</i> <b>31</b> :215–234
Mt. Etna, Italy (I)	<ul style="list-style-type: none"> <li>– Polygenetic stratovolcano over shield volcano</li> <li>– Fissure type</li> <li>– Effusive &amp; explosive</li> <li>– Trachyandesitic basalt</li> </ul>	Active effusive eruption	<ul style="list-style-type: none"> <li>– Flank eruption and parasitic crater offset in relation to main crater;</li> <li>– Lava flows;</li> <li>– Ejection of “fragmental lava”;</li> <li>– Gas emission.</li> </ul>	<ul style="list-style-type: none"> <li>– Lava flow configuration at time of survey;</li> <li>– Relative intensity of main crater and subsidiary crater anomalies</li> </ul>	Williams & Del Bono (unpublished data)
Mt. Vesuvius, Italy	<ul style="list-style-type: none"> <li>– Stratovolcano within caldera rim (Mt. Somma)</li> <li>– Explosive &amp; effusive</li> <li>– Trachyte to tephritic leucitite</li> </ul>	Intereruptive	<ul style="list-style-type: none"> <li>– Fumarolic activity emanating from walls and floor of main crater.</li> </ul>	<ul style="list-style-type: none"> <li>– Delineation of crater rim and floor anomalies;</li> <li>– Detection of curvilinear, convecting fractures in crater floor.</li> </ul>	Williams & Del Bono (unpublished data)
Surtsey, Iceland (II)	<ul style="list-style-type: none"> <li>– Shield volcano of submarine origin (with early tephra ring phase)</li> <li>– Linear fissure type</li> <li>– Initially explosive, “currently” effusive</li> </ul>	<ul style="list-style-type: none"> <li>– Active effusive (Surtur I)</li> <li>– Late-volcanic stage (Surtur II)</li> </ul>	<ul style="list-style-type: none"> <li>– Effusive fissure eruption (19 August 1966) from floor of Surtur I;</li> <li>– Formation of active crater row along en echelon fault;</li> <li>– Fumarolic stage activity from earlier flows.</li> </ul>	<ul style="list-style-type: none"> <li>– Configuration of Surtur I (lava flow at time of survey);</li> <li>– Convecting fracture alignment along pressure ridges and collapse features;</li> <li>– Identification of sub-surface lava course from Surtur II;</li> </ul>	Friedman <i>et al.</i> (1967) <sup>1</sup> Williams <i>et al.</i> (1967) <sup>2</sup> Williams <i>et al.</i> (1968) <sup>3</sup>

Table 1.7. (cont.)

Volcano	Type of volcano, type of activity and composition of products erupted	State of activity during airborne surveys	Geologic processes represented	Contribution of infrared imagery in geologic interpretation of anomalies	Reference
	– Olivine basalt			– Detection of radiant emission from orbital altitude.	
Jolnir, Iceland	– Tephra cone of submarine origin – Explosive (phreatic) – Olivine basalt tephra	Late-volcanic	– Last pulses and termination of phreatic tephra eruption following emergence of submarine volcano (related to Surtsey volcano and mainland Iceland's neovolcanic zone.	– Documents main crater lake and tectonic graben lagoon anomalies and last hydrothermal activity before destruction of island by wave action.	No reference given
Hekla, Iceland	– Linear stratovolcano (eruptive fissure) – Effusive & explosive – Rhyolitic tephra ranging to basalt lavas & scoria	Intereruptive	– Thermal and gas emission from 1947–48 eruption fissure.	– Documents relative intensity of emission from aligned thermal points in eruption fissure; – Greatest emission from flanks of shoulder crater and subsidiary explosion crater, secondarily from summit crater.	Friedman <i>et al.</i> (1967) <sup>1</sup>
Askja, Iceland	– Caldera within ring remnant of large stratovolcano ring (Dyngjufjoll ring) – Effusive & explosive – Rhyolitic tephra to basalt flows & tuff – Probably effusive	Intereruptive	– Thermal activity within caldera; – Thermal emission from Vikraborgir crater row (formed in 1961); – Fumarolic and solfatara activity elsewhere within caldera.	– Identification of most intense emission from solfatara activity in 1875 explosion crater, Viti; – Alignment of thermal anomalies around and within subsided caldera lake, Oskjuvatn.	Friedman <i>et al.</i> (1967) <sup>1</sup>
		Intereruptive(?)			Friedman <i>et al.</i> (1967) <sup>1</sup>

Kverkfjoll, Iceland	<ul style="list-style-type: none"> <li>– Subglacial crater row</li> <li>– Possible basalt-hyaloclastite composition</li> </ul>		<ul style="list-style-type: none"> <li>– Subglacial thermal and volcanic field localized along NE-trending dilation fissures of neovolcanic median zone;</li> <li>– Apparent continuation of fracture system which includes Grimsvotn and Eldgja.</li> </ul>	<ul style="list-style-type: none"> <li>– Identification of thermal emission from subglacial lineament;</li> <li>– Thermal anomalies around periphery of subglacial volcano (possible fumarole or solfatara activity).</li> </ul>	
Erebus, Antarctica (E)	<ul style="list-style-type: none"> <li>– Dome-shaped stratovolcano</li> <li>– Pyroclastic &amp; effusive</li> <li>– Trachyte to olivine basalt</li> </ul>	Intereruptive or pre-eruptive	<ul style="list-style-type: none"> <li>– Active thermal and steam emissions;</li> <li>– Possible pre-eruptive movement of lava in central vent of summit crater.</li> </ul>	<ul style="list-style-type: none"> <li>– Identification of possibly fluid lava in throat of main crater.</li> </ul>	Parker (unpublished data) 1967 survey
Mt. Melbourne, Antarctica	<ul style="list-style-type: none"> <li>– Effusive &amp; pyroclastic</li> <li>– Trachyandestite</li> </ul>	Fumarolic activity		<ul style="list-style-type: none"> <li>– Defines anomalously warm area.</li> </ul>	Parker (unpublished data) 1967 survey
Volcanoes of Kamchatka Peninsular, USSR	<ul style="list-style-type: none"> <li>– Aggregated lava-rich stratovolcanoes with overlying pyroclastic volcanoes</li> <li>– Predominantly explosive</li> <li>– Andesite to trachyandesite</li> </ul>	Intereruptive	<ul style="list-style-type: none"> <li>– Thermal and gas emission;</li> <li>– Hot spring activity.</li> </ul>	<ul style="list-style-type: none"> <li>– Identification of exit points of hot water and gases;</li> <li>– Some structural details.</li> </ul>	Komarov <i>et al.</i> (1968) The methods of applications of infrared aerial photography when studying the volcanoes and thermal activities of Kamchatka Peninsula. <i>5th Symposium of Remote Sensing of Environment</i>

\* Observations of hot spots in HRIR data are not mentioned by Fischer *et al.* (1964). Thus I assume this is the authors', i.e., Friedman and Williams' (1968), own observation. It cannot be an observation of the eruption at Kapoho for this occurred during January–February 1960, four years before the first Nimbus satellite was launched (28 August 1964). Nor can it be for activity at Alae in 1963. Hence my assumption that, it is for activity during the Mauna Ulu eruption of 1969–1974.

<sup>1</sup> Infrared surveys in Iceland in 1966. *Trans AGU* **48**(1):228.

<sup>2</sup> Analysis of 1966 infrared imagery of Surtsey, Iceland. *IUGG XIV<sup>th</sup> General Assembly*:61.

<sup>3</sup> Analysis of 1966 infrared imagery of Surtsey, Iceland. *Surtsey Research Progress Report IV*, The Surtsey Research Society, Reykavik, May 1968.

<sup>4</sup> The results of the Cascades surveys were later published by Moxham (1970).

4.5–5.5  $\mu\text{m}$  and 9–11  $\mu\text{m}$  (by night). Imagery was used to map and examine thermal inertia features. Likewise, Tabbagh *et al.* (1987) used a two-band (7.6–9.6  $\mu\text{m}$  and 10.5–12.5  $\mu\text{m}$ ) scanning radiometer to map thermal features at Etna and Vulcano during a September 1983 over-flight. Next, Pieri *et al.* (1984) used an aircraft-mounted scanner operating in the 8–12  $\mu\text{m}$  band to map active lava flows during Mauna Loa's 1984 eruption. Likewise, Mongillo and Wood (1995) used a video thermal infrared scanner to allow mapping of White Island (New Zealand) during an April 1992 over-flight.

During the 1990s instrument sophistication began to improve, with analysis beginning to involve exploration of multispectral and hyperspectral data. These developments were heralded by the test flight of two multispectral imagers over the volcanoes of southern Italy in July 1986 (Bianchi *et al.*, 1990a). The two instruments were NASA's Thermal Infrared Multispectral Scanner (TIMS), which operated in six bands in the TIR, and the Thematic Mapper Simulator (TMS), which had seven bands in the VIS, NIR, SWIR and TIR. Over-flights of Mount Etna carrying TMS were subsequently completed during October 1989, allowing the collection of infrared data for cooling lava flows and warm fractures (Bianchi *et al.*, 1990b). Data from 1991 over-flights of Mount Etna, Vulcano and Stromboli by an aircraft carrying TMS were later used by Oppenheimer (1993a) and Harris and Stevenson (1997a) to examine lava thermal structures at Etna and to map vent heat fluxes at Vulcano and Stromboli, respectively.

Hyperspectral instruments were also flown during the 1990s. These included the Airborne Visible/Infrared Spectrometer (AVIRIS) which collected data in 224 bands spanning 0.4–2.5  $\mu\text{m}$ . Data from a July 1991 over-flight of Etna were examined by Oppenheimer *et al.* (1993b) to determine the value of hyperspectral data for temperature retrievals over high temperature volcanic phenomena. This paralleled the development of multispectral analysis of active lava lakes and flows using ground-based multispectral sensors by Flynn and Mouginis-Mark (1992; 1994) and Flynn *et al.* (1993). Test deployment of a second hyperspectral imager, the multispectral infrared visible imaging spectrometer (MIVIS), occurred during a July 1994 over-flight of Sicily (Abrams *et al.*, 1997). MIVIS had 102 bands spanning 0.4–12.7  $\mu\text{m}$ , and was later used in over-flights of the lava flow field active during Etna's 2001 eruption to examine lava surface thermal structures (Lombardo and Buongiorno, 2006).

During the 2000s, the increased commercial availability and use of thermal cameras led to the use of FLIR cameras in a hand-held mode from aircraft and helicopters. Such deployments were initially reported alongside fixed airborne scanner campaigns during the 1980 eruption of Mt. St. Helens by Kieffer *et al.* (1981) and Friedman *et al.* (1981). However, as will be reviewed more thoroughly in Chapter 9, only since 2000 has use of hand-held cameras from an aerial vantage point really taken off.

#### *1.4.2.2 A note on aircraft campaigns*

Reports detailing the use of airborne scanners are not as prevalent in the literature as those reporting use of satellite-based and/or ground-based radiometers. There are two main reasons for this. First, the cost of mounting an airborne operation usually makes them

prohibitively expensive to carry out. This means that, second, deployments tend to be few and far between. They tend to be one-off events, or become clustered during times of crisis. As a result, two main types of studies can be identified in the airborne scanner literature.

- (1) Those that are experimental in nature and which focus on exploring the capability of the technology (e.g., Bianchi *et al.*, 1990a; Abrams *et al.*, 1997) and/or the data (e.g., Oppenheimer *et al.*, 1993b; Lombardo and Buongiorno, 2006).
- (2) Those that provide one-off thermal maps of a volcano, or volcano sector (e.g., Perry and Crick, 1976; Tabbagh *et al.*, 1987).

Exceptions to the rule occur during times of crisis, when multiple, repeat over-flights may be possible at high frequencies as, for example, during the 1980 eruption of Mt. St. Helens (e.g., Kieffer *et al.*, 1981; Friedman *et al.*, 1981) or the 2002 to 2003 eruption of Stromboli (e.g., Calvari *et al.*, 2005; Harris *et al.*, 2005c). During both crises multiple (daily-to-weekly) over-flights were necessary for monitoring purposes, and allowed temporally detailed time series of airborne thermal imagery to be built. In addition, some volcano observatories, with access to a thermal camera and flight time, complete regular (weekly-to-monthly) over-flights for monitoring purposes, as at the INGV-Catania and USGS Hawaiian Volcano Observatory.

We should draw a line here between the more difficult to deploy airborne scanner missions, and the simple deployment of personnel pointing a thermal camera from a helicopter. The latter deployment is integral to the principles and applications considered in Chapter 9, in which we focus on hand-held thermal camera deployments. However, because of the more common usage of satellite, radiometer and thermal camera data in volcanology, we have detailed the application of airborne scanners here, and will now focus on satellite- and ground-based technologies and applications. However, all principles and methodologies that we consider herein are equally transferable to airborne scanner data.

# 2

## Thermal remote sensing of active volcanism: principles

The physical basis of thermal remote sensing of active volcanoes is the Planck Function. An understanding of this function allows any methodology applied in this book to be understood, adapted and applied. We thus focus here on the application of the Planck Function, as well as complications when using the function to deal with at-sensor spectral thermal radiance emitted by a graybody source located on the Earth's surface. Example images, and pictures of the surface types, to which we apply these principles are given later in the book (especially across [Chapters 4, 6 and 9](#), as well as in Electronic Supplement 1).

### 2.1 The Planck Function, Wein's Displacement Law and Stefan–Boltzmann

In this book we use the nomenclature defined for all radiative terms by the *Manual of Remote Sensing* (Janza *et al.*, 1975). These definitions are given in [Table 2.1](#). We first deal with spectral radiant exitance from the radiator which, in our case, is the Earth's surface. Published by Max Planck in 1901, the Planck Function describes how spectral radiant exitance,  $M(\lambda, T)$ , from a blackbody varies with temperature ( $T$ ) and wavelength ( $\lambda$ ). The function is given by:

$$M(\lambda, T) = 2\pi hc^2 \lambda^{-5} \left[ \exp^{\frac{hc}{\lambda kT}} - 1 \right]^{-1} (\text{W m}^{-2} \text{m}^{-1}) \quad (2.1a)$$

in which  $h$  is Planck's constant ( $6.6256 \times 10^{-34}$  J s),  $c$  is the speed of light ( $2.9979 \times 10^8$  m s $^{-1}$ ), and  $k$  is the Boltzmann gas constant ( $1.38 \times 10^{-23}$  J K $^{-1}$ ). Because temperature and wavelength are the only variables, Equation (2.1a) can be simplified by combining the constants that contribute to the first and second terms of (2.1a), so that:

$$c_1 = 2\pi hc^2 = 3.741 \times 10^{-16} \text{ W m}^2$$

and

$$c_2 = hc/k = 1.4393 \times 10^{-2} \text{ m K}.$$

Table 2.1. Summary and definition of radiative terms [modified from Table 3–3 of Suits et al. (1975)].

Name	Symbol	Units	Definition
Radiant energy	$Q_{\text{rad}}$	Joules (J)	Capacity of radiation (integrated across a given spectral band) to do work.
Radiant flux	$\Phi_{\text{rad}}$	Watts ( $\text{W} = \text{J s}^{-1}$ )	Time rate of radiative energy flow on to, or off of, a surface.
Radiant flux density	$M_{\text{rad}}$	Watts per square meter ( $\text{W m}^{-2}$ )	Time rate of radiative energy flow on to, or off of, a surface per unit area of that surface.
<u>Radiant flux density at the surface</u>			
Irradiance	$E$	Watts per square meter ( $\text{W m}^{-2}$ )	Radiant flux incident upon a surface per unit area of that surface.
Radiant exitance	$M$	Watts per square meter ( $\text{W m}^{-2}$ )	Radiant flux leaving a surface per unit area of that surface.
Radiant intensity	$I$	Watts per steradian ( $\text{W sr}^{-1}$ )	Radiant flux leaving a small source per unit solid angle in a specified direction.
Radiance	$L$	Watts per steradian per square meter ( $\text{W sr}^{-1} \text{ m}^{-2}$ )	Radiant intensity per unit area of a small source per unit solid angle.

Note.

Adding the term “spectral” before each term means that the measurement is a spectral quantity. That is, it is measured at a particular wavelength ( $\lambda$ ). In this case, the quantity becomes a function of  $\lambda$ , and the measurement is thus given per unit wavelength. Radiant exitance, for example, becomes:

Spectral radiant exitance:  $M(\lambda)$  in Watts per square meter per micron ( $\text{W m}^{-2} \mu\text{m}^{-1}$ ). That is, radiant flux leaving a surface per unit area of that surface, measured per unit wavelength.

This allows a simplified version of (2.1a) to be written:

$$M(\lambda, T) = c_1 \lambda^{-5} \left[ \exp^{\frac{C_2}{\lambda T}} - 1 \right]^{-1} \quad (\text{W m}^{-2} \text{ m}^{-1}). \quad (2.1b)$$

Dividing the result by  $10^{-6}$  gives spectral radiant exitance in the more commonly used units of watts per meter squared per micron ( $\text{W m}^{-2} \mu\text{m}^{-1}$ ).

If we hold the temperature of the emitting body constant, the Planck Function can be used to show how spectral radiant exitance from a blackbody varies with wavelength. The resulting Planck curves for a series of typical ambient and active lava temperatures are plotted in Figure 2.1. The plot illustrates three key principles.

- (1) Planck curves for two blackbodies at two different temperatures will not cross.
- (2) In the shortwave infrared, spectral radiant exitance from blackbodies at ambient temperature becomes very small.

Table 2.2. Spectral exitance at  $1.1\text{ }\mu\text{m}$ ,  $2.5\text{ }\mu\text{m}$ ,  $3.5\text{ }\mu\text{m}$ ,  $10\text{ }\mu\text{m}$  and  $12\text{ }\mu\text{m}$  for blackbodies at a range of Earth ambient and lava temperatures, with wavelength of peak emission for each temperature.

Blackbody temperature (°C)	Spectral exitance ( $\text{W m}^{-2}\text{ m}^{-1}$ )					Wavelength of peak emission ( $\mu\text{m}$ )
	1.1 $\mu\text{m}$	2.5 $\mu\text{m}$	3.5 $\mu\text{m}$	10 $\mu\text{m}$	12 $\mu\text{m}$	
-50	7.96E-12	2.39E+01	7.07E+03	5.92E+06	7.00E+06	13.0
0	3.65E-07	2.69E+03	2.06E+05	1.94E+07	1.89E+07	10.6
50	6.04E-04	7.01E+04	2.12E+06	4.40E+07	3.77E+07	9.0
100	1.37E-01	7.63E+05	1.17E+07	8.07E+07	6.29E+07	7.8
250	3.19E+03	6.37E+07	2.75E+08	2.55E+08	1.69E+08	5.5
500	1.04E+07	2.24E+09	3.51E+09	6.88E+08	4.04E+08	3.7
800	1.18E+09	1.80E+10	1.58E+10	1.32E+09	7.31E+08	2.7
1000	7.99E+09	4.21E+10	2.93E+10	1.78E+09	9.60E+08	2.3
1100	1.69E+10	5.88E+10	3.75E+10	2.02E+09	1.08E+09	2.1
1200	3.23E+10	7.85E+10	4.65E+10	2.26E+09	1.20E+09	2.0

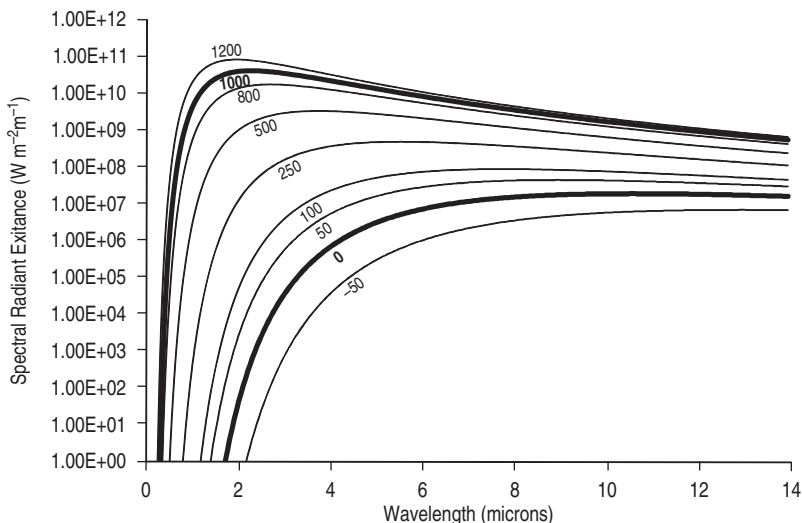


Figure 2.1 Planck curves plotted using Equation (2.1b) for blackbody surfaces at temperatures between  $-50\text{ }^{\circ}\text{C}$  and  $1200\text{ }^{\circ}\text{C}$ .

- (3) Spectral radiant exitance for a high-temperature blackbody is greater than that for a low-temperature blackbody at all wavelengths, but the difference is greatest in the shortwave infrared and least in the thermal infrared.

These three principles mean that, as detailed in Table 2.2, the following rules apply.

- At  $1.1\text{ }\mu\text{m}$ , spectral radiant exitance from a blackbody at ambient temperature ( $0\text{ }^{\circ}\text{C}$ ) is small. However, exitance for a blackbody at magmatic temperature ( $1000\text{ }^{\circ}\text{C}$ ) is 16 orders of magnitude larger.

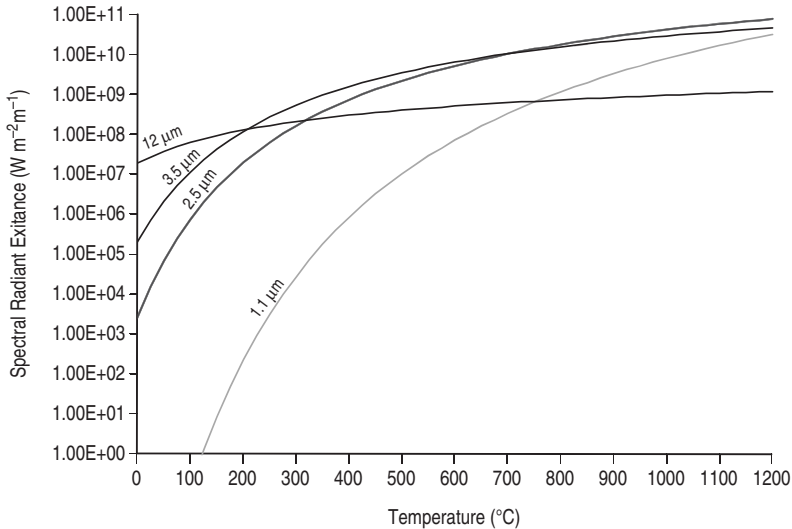


Figure 2.2 Increase in spectral radiant exitance with temperature for a blackbody surface emitting in the NIR (at 1.1  $\mu\text{m}$ ), SWIR (at 2.5  $\mu\text{m}$ ), MIR (at 3.5  $\mu\text{m}$ ) and TIR (at 12  $\mu\text{m}$ ).

- Between 1.1  $\mu\text{m}$  and 3.5  $\mu\text{m}$ , spectral radiant exitance from the blackbody at 0  $^{\circ}\text{C}$  increases by 12 orders of magnitude. That emitted by the blackbody at 1000  $^{\circ}\text{C}$  remains higher, but increases by just a single order of magnitude between the two wavelengths.
- At 12  $\mu\text{m}$  spectral radiant exitance from the blackbody at 0  $^{\circ}\text{C}$  is still less than that for the 1000  $^{\circ}\text{C}$  blackbody, but the difference is now the smallest of the three cases.

By holding wavelength constant we can also use the Planck Function to see how, at a given wavelength, spectral radiant exitance will increase with the temperature of the blackbody. The relationships between spectral radiant exitance and temperature for measurements made in the shortwave infrared, the mid-infrared and thermal infrared are given in Figure 2.2. This plot illustrates three other key points:

- (1) for a given wavelength, spectral radiant exitance increases with temperature;
- (2) the rate of change in spectral radiant exitance with temperature is greater for short wavelengths than for long wavelengths; so that
- (3) as temperature increases the wavelength of dominant emission decreases.

From Figure 2.2 we see that, for a blackbody at 0  $^{\circ}\text{C}$ , spectral radiant exitance is greatest at 12  $\mu\text{m}$  and least at 1.1  $\mu\text{m}$ . However, as temperature increases, so the spectral radiant exitance recorded at shorter wavelengths overtakes that recorded at longer wavelengths. As a result, spectral radiant exitance is greater at 12  $\mu\text{m}$  than at 3.5  $\mu\text{m}$  until 200  $^{\circ}\text{C}$ . At this point, the 3.5  $\mu\text{m}$  plot crosses the 12  $\mu\text{m}$  plot, so that spectral radiant exitance at 3.5  $\mu\text{m}$  exceeds that at 12  $\mu\text{m}$ . At 750  $^{\circ}\text{C}$ , maximum spectral radiant exitance shifts to 2.5  $\mu\text{m}$ . If the plot was extended to 1530  $^{\circ}\text{C}$ , then peak emission would be recorded at 1.1  $\mu\text{m}$ . In short, as temperature increases, so the wavelength at which peak spectral radiant exitance is recorded decreases. This is Wein's Displacement Law.

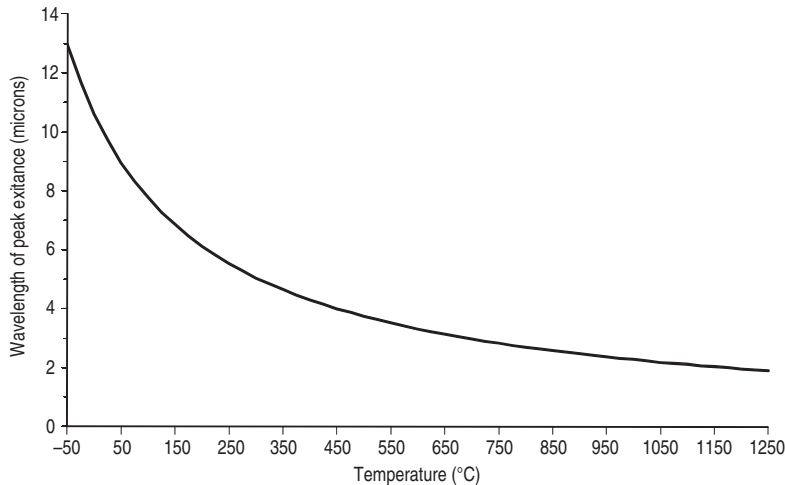


Figure 2.3 Variation in wavelength of peak emission with temperature plotted following Wein's Displacement Law.

### 2.1.1 Wein's Displacement Law

As temperature increases, so the wavelength of peak spectral radiant exitance moves to shorter wavelengths. This behavior is described by Wein's Displacement Law, which relates the wavelength at which the blackbody radiation curve reaches a maximum ( $\lambda_m$ ) to the temperature of the blackbody ( $T$ , in Kelvin) through:

$$\lambda_m = \frac{A}{T} \quad (\mu\text{m}), \quad (2.2)$$

$A$  being Wien's constant (2898  $\mu\text{m K}$ ).

The wavelengths of peak spectral radiant exitance for blackbodies radiating at typical ambient and active lava temperatures are plotted in Figure 2.3 and given in Table 2.2. These show the following.

- Peak spectral radiant exitance for Earth ambient surfaces is recorded in the thermal infrared.
- For crusted lava surfaces at between 250 °C and 800 °C, the wavelength of peak spectral radiant exitance shifts towards the mid-infrared.
- For bodies at magmatic temperatures (1000 °C to 1200 °C), peak spectral radiant exitance is recorded in the shortwave infrared.

Hence, measurements of these three thermal surface types suit measurements in the thermal, mid- and shortwave infrared, respectively.

### 2.1.2 Stefan–Boltzmann

If we integrate the spectral radiant exitance from a blackbody over all wavelengths we obtain radiant flux density ( $M_{\text{rad}}$ ):

$$M_{\text{rad}} = \int_0^{\infty} M(\lambda, T) d\lambda = \int 2\pi h c^2 \lambda^{-5} \left( \exp^{\frac{hc}{kT}} - 1 \right)^{-1} d\lambda = \frac{2\pi^5 k^4 T^4}{15 c^2 h^3} \quad (\text{W m}^{-2})$$

so that  $M_{\text{rad}}$  can be written,

$$M_{\text{rad}} = \frac{2\pi^5 k^4}{15 c^2 h^3} T^4. \quad (2.3a)$$

This allows us to isolate and combine constants  $k$ ,  $c$  and  $h$ , so that,

$$\frac{2\pi^5 k^4}{15 c^2 h^3} = \frac{(2)(3.14)^5 (1.38 \times 10^{-23} \text{JK}^{-1})^4}{(15)(6.6256 \times 10^{-34} \text{Js})^2 (2.9979 \times 10^8 \text{m s}^{-1})^3} = 5.67 \times 10^{-8} \text{ Wm}^{-2}\text{K}^{-4}.$$

This is the Stefan–Boltzmann constant ( $\sigma$ ), which allows us to reduce Equation (2.3a) to:

$$M_{\text{rad}} = \sigma T^4 \quad (\text{W m}^{-2}). \quad (2.3b)$$

This relation defines the radiated heat flux density from a blackbody, i.e., heat flux per unit area, and shows that spectral radiant exitance from a blackbody increases with temperature following a power-law relationship. The  $T^4$  dependency of  $M_{\text{rad}}$  means that spectral radiant exitance from a blackbody at 1000 °C is three orders of magnitude higher than that from a blackbody at 0 °C,  $M_{\text{rad}}$  being  $2 \times 10^5 \text{ W m}^{-2}$  and  $3 \times 10^2 \text{ W m}^{-2}$  respectively.

Multiplying Equation (2.3b) by the surface area ( $A_{\text{surf}}$ ) of the body emitting at temperature  $T$  now gives the radiant flux, i.e.,

$$M_{\text{rad}} A_{\text{surf}} = \Phi_{\text{rad}} \quad (\text{W or J s}^{-1}). \quad (2.3c)$$

Finally, integrating through time ( $t$ ) gives radiant energy, i.e.,

$$\Phi_{\text{rad}} t = Q_{\text{rad}} \quad (\text{J}). \quad (2.3d)$$

### 2.1.3 Lambertian radiation and the steradian

Radiation from a blackbody is Lambertian or diffuse. That is, there is little or no directional character to the emission so that radiation is distributed uniformly over the entire hemisphere above the surface. As a result, radiance from the Lambertian surface is equal in all directions, as sketched in Figure 2.4. Given such emission properties, spectral radiant exitance from a point source will be projected onto the surface of the hemisphere over an area defined by the solid (three-dimensional) angle ( $d\Omega$ ). This is the steradian (sr), which is otherwise defined as the “angle formed when the area ( $A$ ) delimited on the surface of a sphere is equal to the square of the radius ( $r$ ) of the sphere” (Mather, p.6, 1987). As shown in Figure 2.5, this means that the angle defining the steradian ( $d\Omega$ ) is equal to  $A/r^2$ . As a result, the steradian is

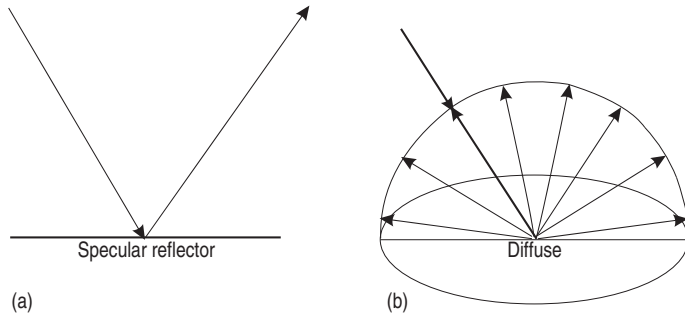


Figure 2.4 Reflectance characteristics of idealized surfaces: (a) a specular reflector and (b) a diffuse reflector [from Schott (2007 Fig. 4.7), by permission of Oxford University Press, Inc].

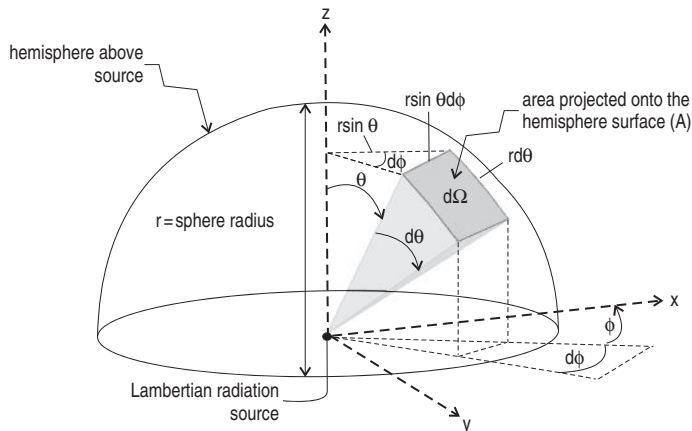


Figure 2.5 Schematic showing the projection of radiation from a point source onto the surface of a hemisphere above that point, illustrating the concept of the solid angle [from Schott (2007, Fig. 3.14) by permission of Oxford University Press, Inc].

dimensionless, being  $\text{m}^2/\text{m}^2$ . Thus, as defined in Figure 2.5, spectral radiance measured by the sensor (in  $\text{W sr}^{-1} \text{ m}^{-2}$ ) can be defined as the proportion of the radiant exitance (in  $\text{W m}^{-2}$ ) from a blackbody that would be measured at the edge of the hemisphere. The geometry for Lambertian blackbody radiant exitance means that the relationship between spectral radiance [ $L(\lambda, T)$ ] and radiant exitance [ $M(\lambda, T)$ ] is

$$L(\lambda, T) = M(\lambda, T)/\pi. \quad (2.4a)$$

Thus,  $M(\lambda, T)$  obtained from the Planck Function can be expressed in terms of spectral radiance,  $L(\lambda, T)$ , following:

$$L(\lambda, T) = \frac{M(\lambda, T)}{\pi} = 2hc^2\lambda^{-5} \left[ \exp \frac{hc}{\lambda kT} - 1 \right]^{-1} \quad (\text{W sr}^{-1} \text{ m}^{-2} \text{ m}^{-1}), \quad (2.4b)$$

which can be simplified to

$$L(\lambda, T) = \frac{M(\lambda, T)}{\pi} = c_3 \lambda^{-5} \left[ \exp^{\frac{c_2}{\lambda T}} - 1 \right]^{-1} \quad (\text{W sr}^{-1} \text{ m}^{-2} \text{ m}^{-1}) \quad (2.4c)$$

in which

$$c_3 = 2hc^2 = 1.19 \times 10^{-16} \text{ W sr}^{-1} \text{ m}^{-2},$$

this being constant  $c_1$  of Equation (2.1b) divided by  $\pi$ .

#### 2.1.4 Temperature and radiance conversion

The Planck Function allows us to convert spectral exitance from a blackbody at wavelength  $\lambda$  to the temperature ( $T$ ) of that blackbody. Because the units in Equation (2.1) are in meters, wavelengths must be input into Equation (2.1) in units of meters, so that (for example)  $3 \mu\text{m}$  will be  $3 \times 10^{-6} \text{ m}$ . Now, for a temperature of  $290 \text{ K}$ , inputting a wavelength of  $3 \times 10^{-6} \text{ m}$  into Equation (2.1b) gives a spectral radiant exitance of

$$M(\lambda, T) = \frac{(3.741 \times 10^{-16} \text{ W m}^{-2})}{(3 \times 10^{-6} \text{ m})^5} \left( \exp^{\frac{(1.4393 \times 10^{-3} \text{ mK})}{(3 \times 10^{-6} \text{ m})(290 \text{ K})}} - 1 \right)^{-1} = 1.01 \times 10^5 \text{ W m}^{-2} \text{ m}^{-1}.$$

This converts to a spectral radiance of

$$L(\lambda, T) = \frac{M(\lambda, T)}{\pi} = \frac{(1.01 \times 10^5 \text{ W m}^{-2} \text{ m}^{-1})}{(3.14)} = 3.20 \times 10^4 \text{ W sr}^{-1} \text{ m}^{-2} \text{ m}^{-1}.$$

Dividing by  $10^6$  gives wavelength in units of  $\mu\text{m}$ . That is,

$$\frac{(3.20 \times 10^4 \text{ W sr}^{-1} \text{ m}^{-2} \text{ m}^{-1})}{10^6} = 3.20 \times 10^{-2} \text{ W sr}^{-1} \text{ m}^{-2} \mu\text{m}^{-1}.$$

Inversion of the Planck Function now allows spectral exitance to be converted back to temperature:

$$T = \frac{c_2}{\lambda \ln \left( \frac{c_1 \lambda^{-5}}{M(\lambda, T)} + 1 \right)}. \quad (2.5)$$

In solving these equations, all we have to do is to check that the input units are correct. For example, constants  $c_1$  and  $c_2$  used in Equation (2.5) are  $3.741 \times 10^{-16} \text{ W m}^{-2}$  and  $1.4393 \times 10^{-2} \text{ m K}$ . Thus, temperature and  $M(\lambda, T)$  must be entered in units consistent with the constants' units, i.e., temperature must be input in Kelvin (= centigrade plus 273.15) and  $M(\lambda, T)$  in  $\text{W m}^{-2} \text{ m}^{-1}$ . If, instead, spectral radiance is input in units of  $\text{W sr}^{-1} \text{ m}^{-2} \text{ m}^{-1}$ , then either  $L(\lambda, T)$  must first be divided by  $\pi$ , so as to convert to units of  $\text{W m}^{-2} \text{ m}^{-1}$ , or  $c_1$  must be replaced by  $c_3$ . Likewise, if  $M(\lambda, T)$  is in wavelength units of per micron ( $\text{W m}^{-2} \mu\text{m}^{-1}$ ), then  $M(\lambda, T)$  must be multiplied by  $10^6$  to convert to  $\text{W m}^{-2} \text{ m}^{-1}$ .

#### 2.1.4.1 Worked example

For the AVHRR, sensor spectral radiances are recorded in units of milliwatts/m<sup>2</sup>-steradian-cm<sup>-1</sup> (Kidwell, 1991). In this case, wavelength will have to be entered into the Planck Function as a wavenumber in cm<sup>-1</sup>. Constant  $c_3$  will be  $1.191 \times 10^{-5}$  mW sr<sup>-1</sup> cm<sup>-4</sup> (so that  $c_1 = c_3/\pi = 3.791 \times 10^{-6}$  mW cm<sup>-4</sup>), and  $c_2$  will be 1.439 cm K. The Planck Function for spectral radiance also needs to be modified to

$$L(v, T) = c_3 v^3 \left[ \exp \frac{c_2 v}{T} - 1 \right]^{-1} \quad (\text{mW sr}^{-1} \text{ m}^{-2} \text{ cm}^{-1}), \quad (2.6a)$$

$v$  being wavenumber (in cm<sup>-1</sup>). Thus, three microns becomes 1/0.0003 cm or 3333 cm<sup>-1</sup>. Now, for a temperature of 290 K, we obtain a spectral radiance of

$$\begin{aligned} L(\lambda, T) &= (1.191 \times 10^{-5} \text{ mW sr}^{-1} \text{ cm}^{-4}) (3333 \text{ cm}^{-1})^3 \left( \exp \frac{(1.439 \text{ cm K})(3333 \text{ cm}^{-1})}{(290 \text{ K})} - 1 \right)^{-1} \\ &= 0.0289 \text{ mW sr}^{-1} \text{ m}^{-2} \text{ cm}^{-1}, \end{aligned}$$

which converts to a spectral radiant exitance of

$$M(l, T) = \pi L(\lambda, T) = (3.14) (0.0289 \text{ mW sr}^{-1} \text{ m}^{-2} \text{ cm}^{-1}) = 0.091 \text{ mW m}^{-2} \text{ cm}^{-1}.$$

Inversion of Equation (2.6a) allows conversion of spectral radiance back to temperature, that is,

$$T = \frac{c_2 v}{\ln \left( 1 + \frac{c_3 v^3}{L(v, T)} \right)} \quad (\text{kelvin}), \quad (2.6b)$$

so that

$$T = \frac{(1.439 \text{ cm K})(3333 \text{ cm}^{-1})}{\ln \left( 1 + \frac{(1.191 \times 10^{-5} \text{ mW sr}^{-1} \text{ cm}^{-4})(3333 \text{ cm}^{-1})^3}{(0.0289 \text{ mW sr}^{-1} \text{ m}^{-2} \text{ cm}^{-1})} \right)} = 290 \text{ K}.$$

These relationships are essential in converting pixel radiances to temperature, and temperature back to radiance. They thus underpin many of the mathematical operations applied in processing and applying thermal data acquired over active volcanic targets.

## 2.2 Emissivity

So far we have assumed blackbody behavior. This assumption means that the surface is considered to be an ideal radiator which totally absorbs and then reemits all energy incident upon it. In such cases reflectivity is zero and absorptivity is one.

In reality, most surfaces do not display blackbody behavior and instead emit only a fraction of the energy emitted from a blackbody. The emitting ability of such a non-blackbody surface is described by emissivity,  $\epsilon(\lambda)$ . This will vary with wavelength and viewing angle. Emissivity can thus be defined as the ratio of spectral exitance,  $M(\lambda, T)$ , from

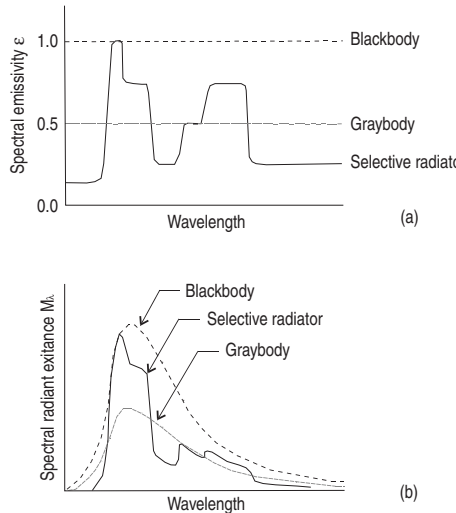


Figure 2.6 (a) Variation in emissivity with wavelength for a blackbody, graybody and selective radiator, and (b) the effect that each of these spectral emissivity curves have on the spectral radiant exitance from a blackbody, graybody and selective radiator [from Lillesand and Kiefer (1987, Fig. 7.3)]. This material is reproduced with permission of John Wiley & Sons, Inc.].

an object at wavelength  $\lambda$  and temperature  $T$ , to that from a blackbody at the same wavelength and temperature,  $M_{\text{BB}}(\lambda, T)$ :

$$\varepsilon(\lambda) = \frac{M(\lambda, T)}{M_{\text{BB}}(\lambda, T)}. \quad (2.7)$$

A graybody has an emissivity of less than 1, i.e.,  $M(\lambda, T) < M_{\text{BB}}(\lambda, T)$ . For a graybody, emissivity is also constant at all wavelengths, so that at any given wavelength the spectral exitance from the graybody is a constant fraction of that from the blackbody at the same temperature. If emissivity varies with wavelength, then the body is a selective radiator. In this case the spectral exitance from the graybody is a variable fraction of that from the blackbody at the same temperature, with the fraction varying with wavelength as shown in Figure 2.6a.

### 2.2.1 The Kirchoff Radiation Law

All energy incident upon a body ( $E_I$ ) must either be absorbed by it ( $E_A$ ), reflected from it ( $E_R$ ), or transmitted through it ( $E_T$ ) so that:

$$E_I = E_A + E_R + E_T. \quad (2.8a)$$

If we assume that no radiation is transmitted through the body (i.e., the body is opaque to thermal radiation), then  $E_T = 0$  and Equation (2.8a) reduces to:

$$E_I = E_A + E_R. \quad (2.8b)$$

Dividing by  $E_I$  allows the equation to be expressed as a ratio of the energy incident upon the surface of the body to that either absorbed or reflected by it:

$$\frac{E_I}{E_I} = \frac{E_A}{E_I} + \frac{E_R}{E_I}. \quad (2.8c)$$

The right-hand terms now comprise ratios that can be used to describe the absorptance,  $\alpha(\lambda)$ , and reflectance,  $\rho(\lambda)$ , of the body:

$$\alpha(\lambda) = \frac{E_A}{E_I} \quad (2.8d)$$

$$\rho(\lambda) = \frac{E_R}{E_I} \quad (2.8e)$$

so that Equation (2.8c) can also be written:

$$\alpha(\lambda) + \rho(\lambda) = 1. \quad (2.8f)$$

In other words, all energy available to the body is either absorbed into it, or reflected by it. In the case of a blackbody,  $\rho(\lambda) = 0$ , so  $\alpha(\lambda)$  must be 1. Kirchoff's Radiation Law states that the spectral emissivity of a body equals its spectral absorptance, i.e.,  $\varepsilon(\lambda) = \alpha(\lambda)$ . Thus, replacing  $\alpha(\lambda)$  with  $\varepsilon(\lambda)$  in Equation (2.8f) results in:

$$\varepsilon(\lambda) + \rho(\lambda) = 1. \quad (2.8g)$$

Thus, we have a direct relationship whereby, in the thermal infrared region of the spectrum:

$$\varepsilon(\lambda) = 1 - \rho(\lambda). \quad (2.8h)$$

That is, the higher the spectral reflectance of a surface, the lower the emissivity. This now allows emissivity to be calculated from spectral reflectance measurements. Simply, we place the measurement for  $\rho(\lambda)$  into Equation (2.8h) and we have  $\varepsilon(\lambda)$ . Spectral reflectance (measured across the 8–14  $\mu\text{m}$  waveband) and the  $\varepsilon(\lambda)$  that these yield are given, for a range of volcanic surface types, in Table 2.3.

### 2.2.2 Emissivity, radiation and kinetic temperature

The Planck Function, as given in Equation (2.1), applies to a blackbody radiator and yields spectral radiant exitance for a blackbody,  $M_{\text{BB}}(\lambda, T)$ . We can estimate spectral radiant exitance from a non-blackbody,  $M(\lambda, T)$ , by reducing  $M_{\text{BB}}(\lambda, T)$  by the spectral emissivity of the body, that is:

$$M(\lambda, T) = \varepsilon(\lambda)M_{\text{BB}}(\lambda, T) = \varepsilon(\lambda)2\pi hc^2\lambda^{-5} \left[ \exp^{\frac{hc}{kT}} - 1 \right]^{-1}, \quad (2.9)$$

Table 2.3. Broad-band (8–14  $\mu\text{m}$ ) spectral reflectance [ $\rho(\lambda)$ ], and the emissivity [ $\varepsilon(\lambda)$ ] that this yields, for the range of volcanic surfaces for which the spectral emissivity are plotted in Figure 2.7. First, the blackbody spectral exitance,  $M_{BB}(\lambda, T)$ , is given for a range of kinematic temperatures ( $T_{kin}$ ) typical of each active volcanic surface. Next, the actual spectral exitance for each non-blackbody source,  $M(\lambda, T)$ , is given. This is obtained by multiplying the spectral exitance expected from a blackbody at temperature  $T$  ( $= T_{kin}$ ) by the emissivity of that body [i.e.,  $M(\lambda, T) = \varepsilon(\lambda) M_{BB}(\lambda, T)$ ]. Finally, the radiative temperature ( $T_{rad}$ ) that each  $M(\lambda, T)$  yields is given. The radiative temperature is, for all non-blackbody cases where  $\varepsilon(\lambda) < 1$ , always less than the kinematic temperature (i.e.,  $T_{kin} - T_{rad}$  is negative). This a result is the object being an imperfect emitter.

Body	$\rho(\lambda)$ 8–14 $\mu\text{m}$	$\varepsilon(\lambda)$ 8–14 $\mu\text{m}$	$T_{kin}$ , K ( $^{\circ}\text{C}$ )	$M_{BB}(\lambda, T)$ (W $\text{m}^{-2} \text{m}^{-1}$ )	$M(\lambda, T)$ (W $\text{m}^{-2} \text{m}^{-1}$ )	$T_{rad}$ , K ( $^{\circ}\text{C}$ )	$T_{kin} - T_{rad}$ K or $^{\circ}\text{C}$
BLOCK 1: Basalt at constant temperature (1000 $^{\circ}\text{C}$ ) and increasing emissivity							
Basalt: Kilauea, glassy pahoehoe (2 months old)	0.1	0.9	1273 (1000)	1.29E+09	1.16E+09	1193 (920)	-80
Basalt: Kilauea, ropey pahoehoe (2 months old)	0.057	0.943	1273 (1000)	1.29E+09	1.22E+09	1228 (955)	-45
Basalt: Kilauea, 'A'a (26 years old)	0.046	0.954	1273 (1000)	1.29E+09	1.23E+09	1236 (963)	-37
Basalt: Etna slabby (spiney) pahoehoe (2 months old)	0.043	0.957	1273 (1000)	1.29E+09	1.24E+09	1239 (966)	-34
Basalt: Etna 'A'a (3 years old)	0.029	0.971	1273 (1000)	1.29E+09	1.26E+09	1250 (977)	-23
Blackbody at 1000 $^{\circ}\text{C}$	0	1	1273 (1000)	1.29E+09	1.29E+09	1273 (1000)	0
BLOCK 2: Sulfur at constant temperature (100 $^{\circ}\text{C}$ ) and increasing emissivity							
Fresh sulfur surface: Vulcano	0.14	0.86	373 (100)	7.18E+07	6.18E+07	358 (85)	-15
Weathered sulfur surface: Vulcano	0.091	0.909	373 (100)	7.18E+07	6.53E+07	364 (90)	-10
Blackbody at 100 $^{\circ}\text{C}$	0	1	373 (100)	7.18E+07	7.18E+07	373 (100)	0
BLOCK 3: Trachytic-rhyolitic lava at decreasing temperature and constant emissivity (0.975)							
Trachytic-rhyolitic: Vulcano (erupted in 1888–90)	0.025	0.975	1273 (1000)	1.29E+09	1.26E+09	1253 (980)	-20
Trachytic-rhyolitic: Vulcano (erupted in 1888–90)	0.025	0.975	1023 (750)	8.96E+08	8.74E+08	1009 (736)	-14
Trachytic-rhyolitic: Vulcano (erupted in 1888–90)	0.025	0.975	773 (500)	5.24E+08	5.11E+08	764 (491)	-9
Trachytic-rhyolitic: Vulcano (erupted in 1888–90)	0.025	0.975	523 (250)	2.07E+08	2.02E+08	518 (245)	-5
Trachytic-rhyolitic: Vulcano (erupted in 1888–90)	0.025	0.975	373 (100)	7.18E+07	7.00E+07	371 (97)	-3

$M_{\text{BB}}(\lambda, T)$  being the radiant exitance for a blackbody at temperature  $T$  and wavelength  $\lambda$ . The emissivity effect on the Planck curve for spectral radiant exitance for a graybody and a selective radiator is shown graphically in [Figure 2.6b](#).

The radiant flux density from a non-blackbody source also needs to be reduced by the emissivity factor, so that the Stefan–Boltzmann relation needs to be written:

$$M_{\text{rad}} = \varepsilon \sigma T^4 \quad (\text{W m}^{-2}). \quad (2.10)$$

In this case  $\varepsilon$  is emissivity integrated over all wavelengths.

A thermal sensor will record the radiation temperature ( $T_{\text{rad}}$ ) of a surface, without taking into account emissivity effects, that is:

$$T_{\text{rad}} = \frac{c_2}{\lambda \ln \left( \frac{c_1 \lambda^{-5}}{M(\lambda, T)} + 1 \right)}. \quad (2.11a)$$

Because emissivity has not been taken into account, this will provide an underestimate of the true, kinetic, temperature of the surface if emissivity is less than one. To obtain kinetic temperature ( $T_{\text{kin}}$ ), the emissivity of that surface must be accounted for, i.e.,

$$T_{\text{kin}} = \frac{c_2}{\lambda \ln \left( \frac{\varepsilon(\lambda) c_1 \lambda^{-5}}{M(\lambda, T)} + 1 \right)}. \quad (2.11b)$$

Thus, for non-blackbody sources, we need to divide the spectral exitance recorded by the sensor [ $M(\lambda, T)$ ] by emissivity to obtain the blackbody-equivalent spectral exitance or kinetic temperature:

$$M(\lambda, T)/\varepsilon(\lambda) = M_{\text{BB}}(\lambda, T) = 2\pi h c^2 \lambda^{-5} \left[ \exp^{\frac{hc}{\lambda T}} - 1 \right]^{-1}. \quad (2.11c)$$

The expected difference between the kinetic and radiation temperature for a number of volcanic surfaces is given in [Table 2.3](#). Note that  $T_{\text{kin}}$  is only equal to  $T_{\text{rad}}$  for a blackbody where  $\varepsilon(\lambda) = 1$ . From [Table 2.3](#) we see that emissivities in the 8–14  $\mu\text{m}$  waveband for active volcanic surfaces are always less than 1, so that none of the [Table 2.3](#) surfaces are blackbodies. [Table 2.3](#) shows that, by making the assumption that the surface is a blackbody emitter (and thus not correcting for emissivity) will result in an error (underestimate) in the assessment of true surface (kinematic) temperature by 10 to 80 °C. This underestimate is revealed by the difference between the body's kinematic and radiative temperature calculated for the 8–14  $\mu\text{m}$  waveband, as given in the final column of [Table 2.3](#). As can be seen from the first block of basaltic surface types given in [Table 2.3](#), for an active lava at 1000 °C, the difference between  $T_{\text{kin}}$  and  $T_{\text{rad}}$  decreases as emissivity increases. The same effect is apparent in the second block of [Table 2.3](#) where typical emissivities for sulfur are used to calculate the expected  $T_{\text{rad}}$  for a sulfur-encrusted fumarole at 100 °C. The final (third) block of [Table 2.3](#) shows, using the emissivity for a trachytic-rhyolitic lava flow, how the difference between  $T_{\text{kin}}$  and  $T_{\text{rad}}$  will also decrease (for a constant emissivity) with kinematic temperature.

Table 2.4. Summary statistics for the maximum, minimum and mean emissivities across the 2–15  $\mu\text{m}$  waveband for a range of volcanic surface types, with wavelength location of maximum ( $\lambda_{\max}$ ) and minimum ( $\lambda_{\min}$ ) emissivity. The reflectance spectra from which these statistics are derived are given in Figure 2.7. All samples were measured between 2.08  $\mu\text{m}$  and 14.98  $\mu\text{m}$  using a Nicolet system FTIR spectrometer by J. Salisbury (Johns Hopkins University) during December 1995.

Surface composition, location and type (sample age, at time of measurement, is given in parentheses)	Maximum $\varepsilon$	$\lambda_{\max}$ ( $\mu\text{m}$ )	Minimum $\varepsilon$	$\lambda_{\min}$ ( $\mu\text{m}$ )	Mean $\varepsilon$
Basalt: Kilauea, glassy pahoehoe (2 months old)	0.995	8.2	0.822	10.2	0.91
Basalt: Kilauea, ropey pahoehoe (2 months old)	0.992	8.3	0.903	10.5	0.96
Basalt: Kilauea, 'A'a (26 years old)	0.993	14.9	0.904	9.1	0.95
Basalt: Etna slabby (spiney) pahoehoe (2 months old)	0.988	8.2	0.932	10.8	0.95
Basalt: Etna 'A'a (3 years old)	0.987	8.0	0.956	10.3	0.97
All basalts	0.995	8.2	0.956	10.3	0.95
Trachytic-rhyolitic: Vulcano (erupted in 1888–90)	0.991	6.0	0.813	2.2	0.95
Fresh sulfur surface: Vulcano	0.924	11.8	0.450	2.2	0.74
Weathered sulfur surface: Vulcano	0.927	14.9	0.577	2.1	0.80

### 2.2.3 Emissivity of lavas

Between 2  $\mu\text{m}$  and 15  $\mu\text{m}$ , emissivity of basalt is generally between 0.9 and 0.99, with a mean of 0.95 (see Table 2.4). Thus, basaltic surfaces are not blackbody sources. From Figure 2.7 we also see that, although there is not much variation in emissivity with wavelength, there is some. Thus basalts are selective radiators, and an appropriate emissivity should be selected depending on wavelength. For comparison with the basalts, the spectral emissivity of trachyte-rhyolite and sulfur (a common surface at fumarole fields) is also given in Figure 2.7. We see that these too are selective radiators.

The main variation in the spectral emissivity of fresh basalt is due to a broad reflectance feature between 8  $\mu\text{m}$  and 12  $\mu\text{m}$ . As found by Crisp *et al.* (1990), this reflectance feature typically has a peak between 10.3  $\mu\text{m}$  and 10.5  $\mu\text{m}$  in basalts. As a result, and as is apparent from Table 2.4, lowest emissivities for basalts are encountered within the 9–11  $\mu\text{m}$  waveband.

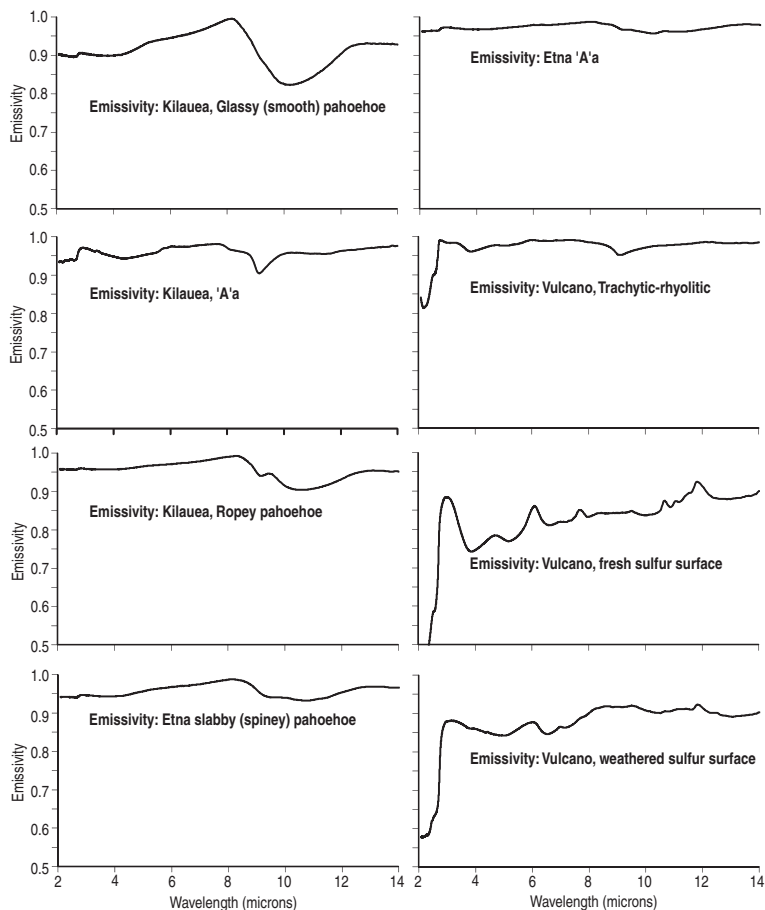


Figure 2.7 Spectral emissivity for a range of common volcanic surface types. Spectral emissivity was calculated from reflectance spectra obtained for samples collected at Kilauea, Etna and Vulcano.

This is due to a strong degree of disorder in volcanic glass, which is made up a variety of silicate units with a variety of bond angles, strengths and arrangements that vibrate at different frequencies (Crisp *et al.*, 1990; Kahle *et al.*, 1995). With time, the unstable configuration breaks down as the silica tetrahedra become organized into sheet-like and chain-like units. This causes the 8–12  $\mu\text{m}$  feature to decay, and the spectra to flatten, with time (Kahle *et al.*, 1995). Again, we see this effect in Table 2.4 where the emissivities in the older silicate samples are typically higher than those for younger samples, meaning that reflection is decaying with time.

#### 2.2.4 What emissivity to use?

We are interested in active features, thus the spectra from (and hence emissivity for) fresh, glassy samples, before aging and/or weathering, are of interest to us. However, most

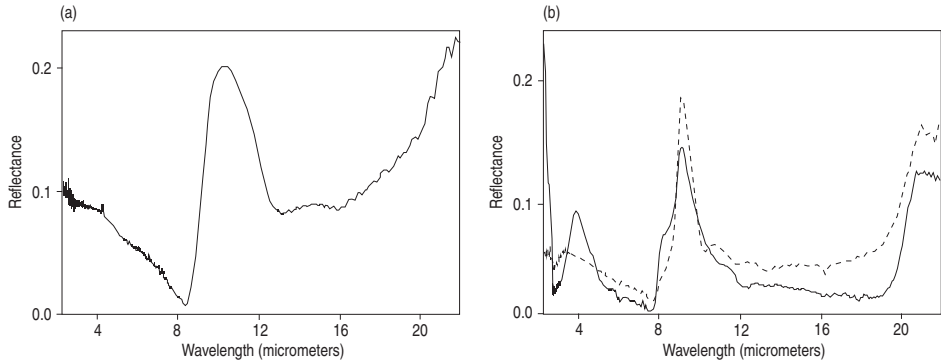


Figure 2.8 (a) Reflectance spectrum for a sample of basalt collected from an active lava flow at Kilauea in May 1989 [from Crisp *et al.* (1990, Fig. 2): reproduced by permission of American Geophysical Union]. (b) Reflectance spectrum for a sample of rhyolite obsidian (solid line) and basalt glass (1984 Mauna Loa basalt collected in May 1989, dashed line) [from Crisp *et al.* (1990, Fig. 15): reproduced by permission of American Geophysical Union].

emissivity measurements to date have been made on solid lava at ambient temperatures, after (at best) a few minutes or (at worst) a few years of emplacement. Measurements on such solid lava samples at ambient temperature indicate that emissivities are high in the 2–15  $\mu\text{m}$  waveband, as shown in Figure 2.7 and summarized in Table 2.4. Reflectance spectra measurements made by Pollack *et al.* (1973), Walter and Salisbury (1989), Crisp *et al.* (1990), Kahle *et al.* (1995), Realmuto *et al.* (1992) and Wells and Cullinane (2007), as well as emissivity values reported by Moxham (1971), are all consistent with the emissivities given in Table 2.4.

Reflectance spectra for Hawaiian lavas, as well as rhyolite obsidian, obtained by Crisp *et al.* (1990), and given here in Figure 2.8, show a strong reflectance feature between 8  $\mu\text{m}$  and 12  $\mu\text{m}$ . This translates to a minimum  $\varepsilon(\lambda)$  of  $\sim 0.8$  for basaltic glass and 0.85 for rhyolite obsidian between 8  $\mu\text{m}$  and 12  $\mu\text{m}$ . Reflectance spectra of Crisp *et al.* (1990) are also consistent with  $\varepsilon(\lambda)$  of 0.90–0.95 (for basalt) and  $\sim 0.96$  (for rhyolite) above 12  $\mu\text{m}$  and below 8  $\mu\text{m}$ . Spectral emissivity obtained by Realmuto *et al.* (1992) for Hawaiian pahoehoe flows of a few months in age are given in Figure 2.9. Like the results of Crisp *et al.* (1990), these give  $\varepsilon(\lambda)$  in the 8.5  $\mu\text{m}$  to 11.5  $\mu\text{m}$  waveband of 0.9–0.95. We note also that the increase in emissivity with age, as predicted from the discussion above, can be seen in the spectra-time series given for the Hawaiian (Kilauea) basaltic pahoehoe flow in Figure 2.9, so that the emissivity should also be set depending on the age of the sample. Figure 2.9 shows that an emissivity of  $\sim 0.90$  may be appropriate at 10.5  $\mu\text{m}$  for basaltic pahoehoe surfaces that are  $\sim 5$  months old, and  $\sim 0.95$  for the same surface after two years.

Measurements by Walter and Salisbury (1989) allow consideration of other igneous rock types, as given here in Figure 2.10. These reflectance spectra yield emissivity for andesite of

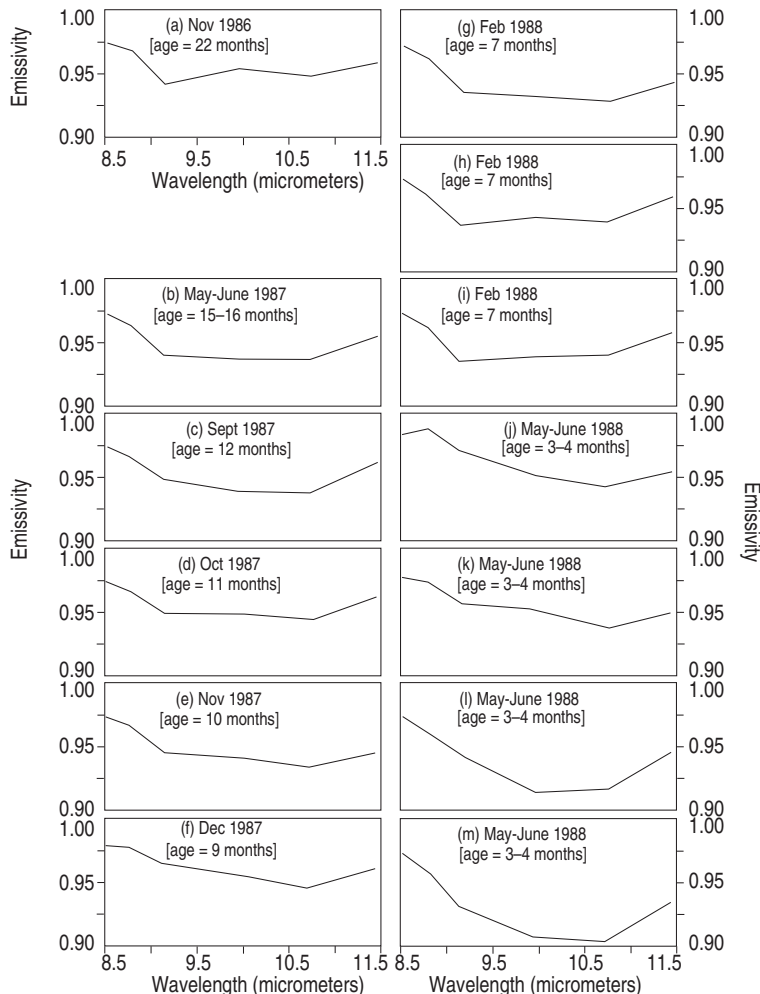


Figure 2.9 Emissivity variation between  $8.5\text{ }\mu\text{m}$  and  $11.5\text{ }\mu\text{m}$  for basaltic surfaces at Kilauea. Measurement was made on 1 October 1988 using the TIMS sensor, so that the surfaces are between 5 and 48 months old. Spectra decrease in age from the spectra given in (a) through that given in (m), where we see that the emissivity increases with age [from Realmuto *et al.* (1992, Fig. 6); with kind permission from Springer Science and Business Media]. Date given on each graph is that of lava flow emplacement

between 0.91 and 0.95 in the  $8\text{--}12\text{ }\mu\text{m}$  waveband. For the  $8\text{--}14\text{ }\mu\text{m}$  waveband, Moxham (1971) provides a nice summary of  $\varepsilon(\lambda)$  for different compositions, giving:

- 0.90 for polished basalt,
- 0.95 for rough basalt,
- 0.93–0.95 for olivine basalt,
- 0.91–0.94 for andesite,
- 0.94–0.95 for rhyolite, and
- 0.87–0.90 for rhyolitic obsidian.

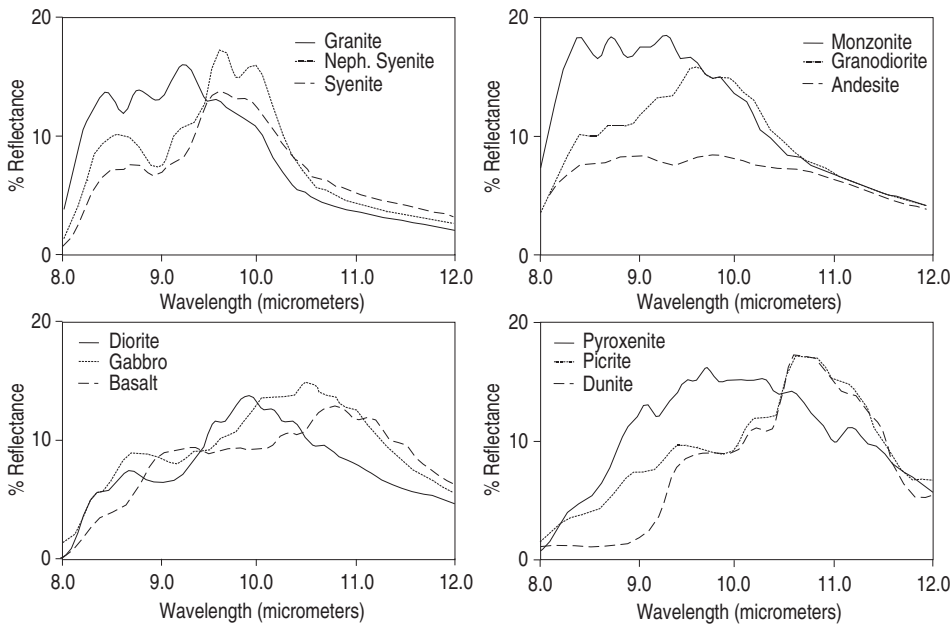


Figure 2.10 Thermal infrared reflectance spectra for a range of igneous rocks [from Walter and Salisbury (1989, Fig. 3); reproduced by permission of American Geophysical Union].

Emissivities for a range of other terrestrial surface types are given (tabulated) in Salisbury and D'Aria (1992), Salisbury and D'Aria (1994) and Salisbury *et al.* (1994).

#### 2.2.4.1 Changes in emissivity between molten and solid lava samples

There is some evidence that, at short wavelengths, lava reflectance may decrease over the first 24 hours of its lifetime from relatively high values upon emplacement to lower values after a few hours. This means that emissivity will increase from a relatively low value upon emplacement, to higher values for solidified surfaces after a few hours. Using a spectrometer operating in the 1.1–2.5  $\mu\text{m}$  waveband at pahoehoe lava active on Kilauea, we collected reflectance spectra during emplacement of an active lava. These revealed relatively high reflectances of ~25 %, giving an emissivity of ~0.75 (L. Flynn, unpublished data). Reflectance, however, decreased to more typical values with time and cooling, reflectance being less than 10% (giving an emissivity of greater than 0.9) within 24 hours. The high starting reflectance was, however, not always encountered. This means that, in some cases, spectral emissivity between 1.1  $\mu\text{m}$  and 2.5  $\mu\text{m}$  may increase from a low level upon emplacement to levels more typical of those given in Figure 2.7 after a few hours. This may result from highly reflective and coherent glass rinds developing on fresh lava. The presence of such surfaces has been observed to cause reflectance anomalies over fresh pahoehoe flows in satellite (ETM+) data obtained in the 0.52–0.9  $\mu\text{m}$  waveband by Flynn *et al.* (2001). A subsequent decrease in reflectance would result from spalling of this glassy

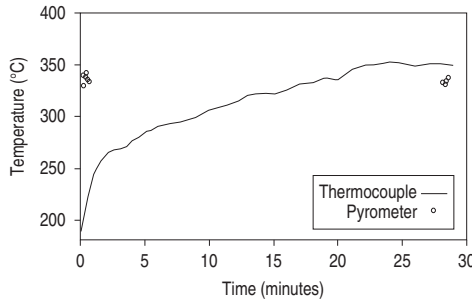


Figure 2.11 Thermocouple-derived temperatures for the surface of Erta Ale's active lava lake as a function of time. Open circles represent the infrared measurements made at the beginning of the experiment and after thermal equilibrium of the thermocouple [from Burgi *et al.* (2002, Fig. 4); with kind permission from Springer Science and Business Media].

rind, to expose an underlying, rougher, vesicular surface, where shedding of the glassy rind during, or shortly after, emplacement is a commonly observed phenomenon on Hawaiian pahoehoe.

By comparing  $T_{\text{rad}}$  obtained using an optical pyrometer with  $T_{\text{kin}}$  obtained from a thermocouple in contact with active lava surfaces at the Erta Ale lava lake (Ethiopia), Burgi *et al.* (2002) also obtained low emissivities of 0.74 for a crusted, but active, lava surface (at 350 °C) in the 1.1–1.7 μm waveband. The results of their experiment are given in Figure 2.11. The method applied by Burgi *et al.* (2002) allows emissivity to be calculated from the difference between the kinematic and radiation temperatures obtained for the active lava surface from:

$$\log \varepsilon(\lambda) = \log(\varepsilon_a) + \frac{hc}{\lambda k} \left( \frac{1}{T_{\text{kin}}} - \frac{1}{T_{\text{rad}}} \right). \quad (2.12a)$$

Here,  $\varepsilon_a$  is the arbitrary emissivity used when making the measurement of  $T_{\text{rad}}$  with the pyrometer, in the case of Burgi *et al.* (2002) the instrument was set to an emissivity ( $\varepsilon_a$ ) of 0.9. This, essentially, is the same as the approach suggested by Brivio *et al.* (1989), whereby the difference between the kinematic and radiation temperatures are used to obtain emissivity in:

$$\varepsilon(\lambda, T) = \frac{\exp(c_2/\lambda T_{\text{kin}}) - 1}{\exp(c_2/\lambda T_{\text{rad}}) - 1}. \quad (2.12b)$$

Given the  $T_{\text{kin}}$  of 350 °C and  $T_{\text{rad}}$  of 342 °C, as measured at Erta Ale's lava lake surface by Burgi *et al.* (2002), and using the mid-point wavelength of their pyrometer (1.4 μm), Equation (2.12a) yields:

$$\begin{aligned} \log \varepsilon(\lambda) &= \log(0.9) + \frac{(6.6256 \times 10^{-34} \text{ J s})(2.9979 \times 10^8 \text{ m s}^{-1})}{(1.4 \times 10^{-6} \text{ m})(1.38 \times 10^{-23} \text{ J K}^{-1})} \left( \frac{1}{(623 \text{ K})} - \frac{1}{(615 \text{ K})} \right) \\ &= \log(-2.606) = 0.77. \end{aligned}$$

Application of the Equation (2.12b) approach gives a slightly higher value:

$$\varepsilon(\lambda, T) = \frac{\exp^{(0.014\ 393\ \text{mK})/[(1.4 \times 10^{-6}\text{m})(623\ \text{K})]} - 1}{\exp^{(0.014\ 393\ \text{mK})/[(1.4 \times 10^{-6}\text{m})(615\ \text{K})]} - 1} = 0.81.$$

Such low emissivities are also consistent with Le Guern *et al.* (1979), who cited a value of 0.7 as being appropriate for basalt in the 9.1–11.2 μm waveband. These measurements thus indicate that, under certain conditions and at certain wavelengths, emissivities of ~0.8 may be appropriate for active (basaltic) lava surfaces.

However, laboratory-based comparisons between radiometer-obtained  $T_{\text{rad}}$  (in the 0.8–1.1 μm waveband) and thermocouple-obtained  $T_{\text{kin}}$  for a Hawaiian pahoehoe lava sample by Pinkerton *et al.* (2002) showed best agreement using an emissivity of 1.0 for temperatures between 600 °C and 1000 °C. Likewise, furnace-based measurements on Erta Ale samples by Burgi *et al.* (2002) failed to replicate the low value obtained in the field, with the closest match between the pyrometer- and thermocouple-measured temperatures being obtained using  $\varepsilon(\lambda)$  of between 0.87 and 0.89. In addition, application of a low emissivity (0.74) to spectral exitance measurements made at 8–14 μm can yield kinetic temperatures that are unrealistically high. For example, the radiation temperature measured for the surface of the Erta Ale lava lake by Oppenheimer and Yirgu (2002) gave a maximum of 1174 °C which, being obtained using a thermal camera operating in the 8–14 μm waveband, is a radiative temperature. Converting this to radiant exitance using Equation (2.1), correcting for an emissivity of 0.74 and then converting back to kinetic temperature using Equation (2.11b), yields a kinetic temperature of 1500 °C. This is somewhat higher than the expected maximum liquidus temperature at Erta Ale of 1125–1225 °C (from Bizouard *et al.*, 1980), and therefore improbable.

As already argued, one explanation for different emissivities between two surfaces of the same type and at the same temperature is variation in surface roughness. Such a suggestion was made by Burgi *et al.* (2002) to explain the low emissivities at Erta Ale, where the presence of a glassy crust may increase the reflectance over a lava characterized by a rough, vesicular surface. Measurements by Ramsey and Fink (1999) show how the emissivity of rhyolite increases with vesicularity at all wavelengths. The measurements, given here in Figure 2.12, show the minimum emissivity (recorded at ~9 μm) increasing from 0.70 for a surface composed of rhyolite glass to 0.89 for a coarsely vesicular surface. Thus, we would expect emissivity for a lava flow with a glassy surface to be lower than that for a lava with a rough, vesicular surface.

The results reviewed here point to the need to obtain an improved understanding of the variation in emissivity with (1) surface type (and roughness), (2) temperature and (3) wavelength. Measurements thus need to be made through the phase change from molten to solid, and as thin, high-reflective glass coatings and/or rough vesicular surfaces develop. Clearly there are conditions under which emissivity at an active, basaltic lava can be quite low (such as at active flows with a glassy crust), but there are also conditions under which emissivities are high (as is typical for rougher surfaces). For now, the difficulty in replicating

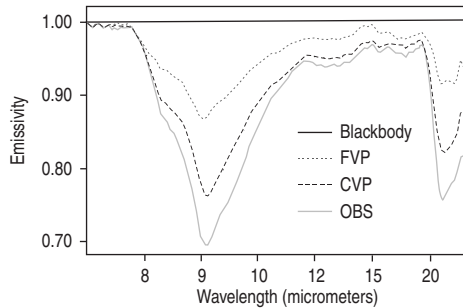


Figure 2.12 Thermal infrared emissivity spectra for a rhyolite glass (OBS), finely vesicular pumice (FVP) and coarsely vesicular pumice (CVP). Spectra are averages of at least ten samples and show how emissivity decreases with increased surface roughness. The absorption band, diagnostic of glass, is observed at  $9.25\text{ }\mu\text{m}$  [from Ramsey and Fink (1999, Fig. 1): with kind permission from Springer Science and Business Media].

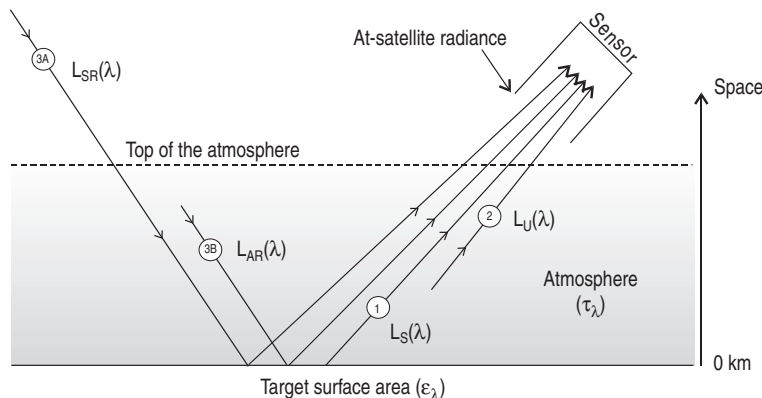


Figure 2.13 Cartoon showing the contributions to satellite-received radiance [based on Cracknell and Hayes (1991, Fig. 8.2)].

our low-reflectance measurements at Kilauea and Erta Ale with commonly measured  $\epsilon(\lambda)$  in the range 0.9–0.99, lead us to suggest that the values of Figure 2.7 are typical. However, emissivity must be selected carefully, and set depending on surface type (and rock composition), temperature, age, roughness, and wavelength of the measurement.

### 2.3 Atmospheric effects

While the atmosphere will both absorb and emit radiation of its own, the surface will also reflect radiation, so that the radiation arriving at the satellite will be an integrated radiance comprising both the surface and atmospheric components, as sketched in Figure 2.13. If this integrated radiance is converted to a temperature using Planck's Formula, it will thus not yield

the surface temperature, but instead a value termed the brightness temperature. Here we deal with the unwanted atmospheric and reflection components, and examine means of obtaining surface temperature from the brightness temperature through atmospheric correction.

**Transmissivity** The atmosphere is not perfectly transparent to infrared radiation. As a result, a portion of the radiance emitted by a surface will be absorbed and back-scattered by the atmosphere. This attenuation effect is described by atmospheric transmissivity,  $\tau(\lambda)$ . This has a value in the range of one, for a perfectly transparent atmosphere, to zero, for a perfectly opaque atmosphere. Thus, for a surface at temperature  $T_s$ , surface-leaving radiance,  $\varepsilon(\lambda)L(\lambda, T_s)$ , will be related to the radiance arriving at the sensor,  $L_S(\lambda)$ , by:

$$L_S(\lambda) = \tau(\lambda) \varepsilon(\lambda) L(\lambda, T_s). \quad (2.13a)$$

That is, the radiance emitted by the surface and arriving at the sensor will be reduced by a factor described by the atmospheric transmissivity.

### 2.3.1 Atmospheric windows

As shown in [Figure 2.14a](#), transmissivity varies with wavelength. Hence, the degree of attenuation experienced by surface emitted radiance will vary with wavelength. The resulting effect on the spectral radiant exitance from a blackbody at 1000 °C is illustrated in [Figure 2.14b](#). Across some portions of the spectrum, the atmosphere will absorb most (if not all) of the emitted radiance. However, there are seven atmospheric windows across which emitted radiance suffers less than 10% attenuation (i.e., regions within which  $\tau(\lambda)$  is greater than 0.9). As listed in [Table 2.5](#), two of these windows are located in the NIR, three are in the SWIR and one is in the MIR. A broad window also occurs between 8.6 μm and 12.2 μm, i.e., in the TIR. Within these windows, the atmosphere is semi-transparent to emitted radiation. Sensor wavebands for instruments designed to make measurements of emitted radiance by the Earth's surface are thus located within these windows. However, even within these windows, transmissivity is not zero, and ranges from 0.9 at worst, to 0.98 at best (see [Table 2.5](#)). Thus, some of the radiance emitted by a surface, will always be attenuated on arrival at the sensor. As a result, some correction will have to be made to the at-sensor radiance to take into account this attenuation effect and to allow the surface-leaving radiance to be retrieved.

#### 2.3.1.1 Correction for transmissivity, and variation with altitude and scan angle

Correction for the attenuation effect can be achieved using  $\tau(\lambda)$  in:

$$L(\lambda, T_s) = L_S(\lambda) / \tau(\lambda) \varepsilon(\lambda). \quad (2.13b)$$

For a given wavelength, transmissivity will vary with path length, altitude and scan angle. Longer path lengths traverse more atmosphere, so that more of the emitted radiance will be

**Table 2.5.** Locations of, and average transmissivities across, the seven main atmospheric windows in the NIR, MIR and TIR. Values obtained using MODTRAN (see Electronic Supplement 4 for a definition and description of the MODTRAN model and its uses for atmospheric correction). MODTRAN was run using a 1976 US Standard atmosphere with a vertical path from sea-level to space (zenith = 180°, observer height = 100 km), and a CO<sub>2</sub> mixing ratio of 380 ppm·v.

Window location	Waveband (μm)	Width (μm)	Average $\tau(\lambda)$	Max $\tau(\lambda)$	Location of Max $\tau(\lambda)$ (μm)
NIR	0.7–0.89	0.19	0.90	0.93	0.89
NIR	1.0–1.1	0.1	0.94	0.95	1.07
SWIR	1.18–1.31	0.13	0.94	0.96	1.25
SWIR	1.51–1.76	0.25	0.96	0.97	1.68
SWIR	2.03–2.36	0.33	0.96	0.98	2.14
MIR	3.44–4.13	0.69	0.94	0.97	3.96
TIR	8.6–12.2	3.6	0.92	0.96	10.11

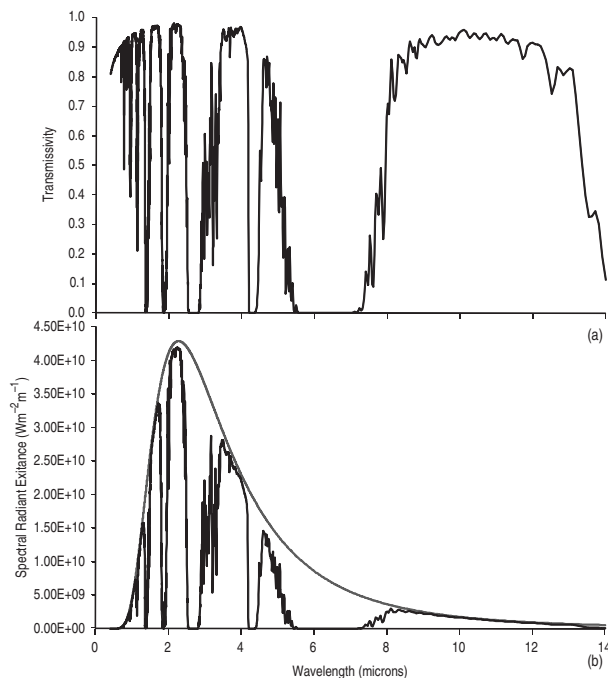


**Figure 2.14** (a) Variation in atmospheric transmissivity with wavelength for a MODTRAN US Standard atmosphere (model is run using the same input conditions as used for the simulations of Table 2.5). (b) Effect of atmospheric transmissivity on at-satellite spectral radiance curve for a surface radiating at 1000 °C. See Electronic Supplement 4 for a definition and description of the MODTRAN model and its uses for atmospheric correction.

absorbed as the path length increases, while measurements made at higher altitudes are made in a thinner atmosphere than those at lower altitudes, so that atmospheric attenuation effects decrease with altitude. Path length and altitude effects are significant for ground-based sensors set at variable distances from the source and/or operated at different altitudes, and are considered further in Part III. Here we consider surface altitude and scan angle effects for a satellite-based sensor.

The satellite is at a fixed altitude, typically located several hundred kilometers above the surface. Thus the distance to sea-level remains constant. However, as the satellite passes over terrain of variable elevation, so the path length between the satellite and the surface changes. As elevation of the surface increases, so the path length to the satellite decreases, so that the transmissivity will increase. More importantly, the atmosphere becomes rapidly thinner at higher altitudes, so that attenuation diminishes for satellite observations over surfaces located at higher elevations. For example, 85% of the absorbing gases are found in the lowermost 5 km of the atmosphere (a calculation that excludes O<sub>2</sub>), with ~90% of atmospheric H<sub>2</sub>O being located in this lowermost layer. Thus, although a change in 3 km (the difference in making a measurement at sea-level or Etna's summit) over a surface-to-satellite path length of 800–900 km may not seem like much, the effect of cutting out the lowermost, and least transmissive, layer of the atmosphere is significant. As plotted in [Figure 2.15](#), for a satellite sensor viewing the surface from a vantage point vertically above the surface, transmissivity will increase (i.e., the degree of attenuation will decrease) with surface elevation since the surface at a high elevation has a thinner atmosphere between it and the satellite sensor, so less absorption of the surface-leaving emission occurs.

On the other hand, as the scan angle ( $\alpha$ ) increases (for any given surface elevation), so the atmospheric path length ( $L$ ) will also increase, following  $L = \cos(\alpha)/S_h$ ,  $S_h$  being the sensor height above the ground. As a result, to a first approximation (ignoring refraction and scattering), transmissivity will decrease (i.e., the degree of attenuation will increase) with

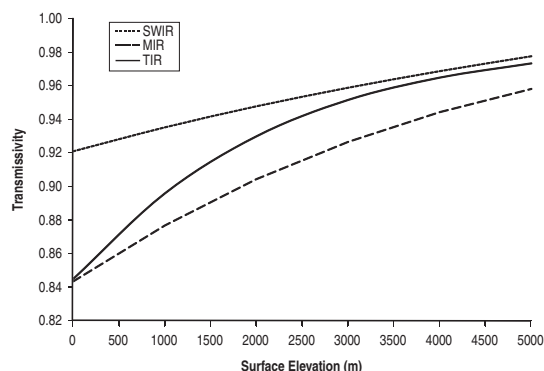


Figure 2.15 Increase in atmospheric transmissivity with surface elevation for a satellite viewing the surface from space in (i) the SWIR (2.1–2.5 μm) (ii) the MIR (3.5–4.0 μm) and (iii) the TIR (10–12 μm). The same MODTRAN US Standard atmosphere as used in [Figure 2.14](#) is applied.

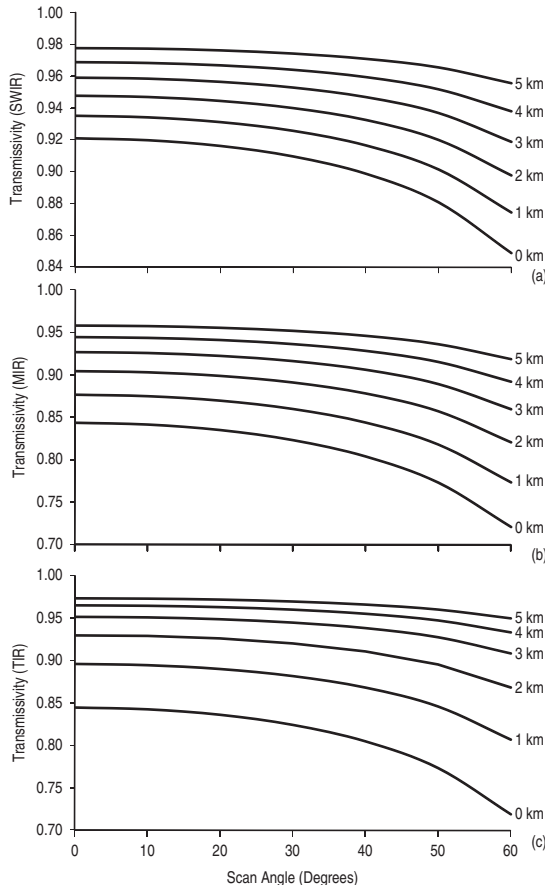


Figure 2.16 Variation in atmospheric transmissivity with scan angle and surface elevation for a satellite viewing the surface from space in (a) the SWIR (2.1–2.5  $\mu\text{m}$ ), (b) the MIR (3.5–4.0  $\mu\text{m}$ ) and (c) the TIR (10–12  $\mu\text{m}$ ). The same MODTRAN US Standard atmosphere as used in Figure 2.14 is applied.

scan angle, as plotted in Figure 2.16 since the thickness of the atmosphere through which the surface is viewed increases as the scan angle increases.

### 2.3.2 Atmospheric emission and surface reflection

As well as attenuating surface-emitted radiance, the atmosphere will also emit radiation. In addition, the surface will reflect radiance. Thus, the at-sensor radiance is actually composed of the radiance emitted from, and reflected by, both the surface and the atmosphere.

Singh and Warren (1983) and Cracknell and Hayes (1991) provide excellent reviews of how the radiance recorded by an infrared sensor is not just the result of surface emission, but

is a complex product of the emission (and attenuation) effects of the intervening atmosphere, as well as the reflective (and hence emissive) properties of the targeted surface. As summarized in [Figure 2.13](#), radiation arriving at the sensor will thus be composed of radiance from three different sources:

- (1) radiance emitted by the surface itself,  $L_S(\lambda)$ ,
- (2) radiance emitted by (i.e., up-welling from) the atmosphere,  $L_U(\lambda)$ , and
- (3) radiance reflected by the surface,  $L_R(\lambda)$ .

Hence the make-up of sensor-received radiance,  $R_{\text{in}}^*$ , can be written:

$$R_{\text{in}}^* = L(\lambda)^* = L_S(\lambda) + L_U(\lambda) + L_R(\lambda). \quad (2.14a)$$

As a result, the temperature value obtained by converting the sensor-arriving radiance to temperature is not the surface temperature ( $T_s$ ), but a brightness temperature ( $T^*$ ). That is,

$$L(\lambda)^* = L(\lambda, T^*) = \varepsilon(\lambda) \tau(\lambda) L_S(\lambda) + L_U(\lambda) + L_R(\lambda), \quad (2.14b)$$

where  $\tau(\lambda)$  needs to be added to describe the attenuating effect of the atmosphere on the surface-leaving radiance. Brightness temperature is thus the sum of radiance from all sources of emitted and reflected radiance that contribute to the sensor-arriving radiance. However, we are interested in the surface temperature. Thus, the quantity that we are interested in is  $L_S(\lambda)$ , rather than the quantity that we have actually measured, i.e.,  $L(\lambda)^*$ . To obtain  $L_S(\lambda)$  we must define, constrain and remove the unwanted components, i.e.,

$$L_S(\lambda) = [L(\lambda, T^*) - L_U(\lambda) - L_R(\lambda)] / \varepsilon(\lambda) \tau(\lambda). \quad (2.14c)$$

Executing the corrections necessary to eliminate the unwanted quantities,  $L_U(\lambda)$  and  $L_R(\lambda)$ , is not so straightforward, as can be understood by examining the source of each of these quantities.

### 2.3.2.1 Sources of emission

The sensor will be responding to two main sources of emitted radiation. The first is the radiance emitted by the targeted surface,  $L_S(\lambda)$ . As already shown, this is attenuated as it passes upwards towards the sensor such that, by the time it reaches the sensor, surface-leaving radiance is related to sensor-arriving radiance by  $L_S(\lambda) = \tau(\lambda)\varepsilon(\lambda)L(\lambda, T_s)$ . The same atmosphere also emits radiation upwards towards the sensor, so that the second source of sensor-arriving radiance is that up-welling from (i.e., emitted towards the sensor by) the atmospheric column,  $L_U(\lambda)$ .

### 2.3.2.2 Sources of reflection

Surface-reflected radiance has three sources:

- (1) solar radiation reflected by the surface towards the sensor,  $L_{SR}(\lambda)$ ,
- (2) radiance from space reflected by the surface,  $L_{SP}(\lambda)$ , and
- (3) radiation emitted by the atmosphere that down-wells to the surface to then be reflected back towards the sensor,  $L_{AR}(\lambda)$ .

Thus surface-reflected radiance arriving at the satellite can be written as

$$L_R(\lambda) = L_{SR}(\lambda) + L_{AR}(\lambda) + L_{SP}(\lambda). \quad (2.15)$$

Of these sources, reflected solar radiation ( $L_{SR}$ ) will depend on the solar radiance incident upon the Earth's surface,  $E_{in}(\lambda)$ , and the reflectivity of that surface,  $\rho(\lambda)$ .  $E_{in}(\lambda)$  can be determined from the solar irradiance arriving at the top of the atmosphere (TOA),  $\bar{E}_{TOA}(\lambda)$ . For the mean Sun–Earth distance this can be estimated from:

$$\bar{E}_{TOA}(\lambda) = M(\lambda, T_{\text{sun}}) (R_S/D_{E-S})^2, \quad (2.16a)$$

in which  $M(\lambda, T_{\text{sun}})$  is the radiant exitance from the Sun,  $T_{\text{sun}}$  is the temperature of the Sun (6000 K),  $R_S$  is the radius of the Sun ( $695.3 \times 10^6$  m) and  $D_{E-S}$  is the mean Sun–Earth distance ( $149.6 \times 10^9$  m). Because the Earth's orbit is elliptic with eccentricity ( $e' = 0.0167$ ), solar radiance arriving at the top of the atmosphere changes slightly from day to day. Actual solar irradiance arriving at the top of the atmosphere,  $E_{TOA}(\lambda)$ , can thus be obtained from the mean value ( $\bar{E}_{TOA}(\lambda)$ ) using a Julian Day (JD) dependent-correction in Singh and Warren (1983):

$$E_{TOA}(\lambda) = \bar{E}_{TOA}(\lambda) \{1 + e' \cos [2\pi(JD - 3)/365]\}^2. \quad (2.16b)$$

The incoming solar radiance will be attenuated (absorbed and scattered) by the atmosphere during its downward passage to the surface. The radiance incident upon the surface thus depends on the solar zenith angle ( $\theta_S$ ) and the transmissivity of the atmosphere along the incoming path length [ $\tau(\lambda, \theta_S)$ ], so that

$$E_{in}(\lambda) = \tau(\lambda, \theta_S) \cos(\theta_S) E_{TOA}(\lambda). \quad (2.17)$$

The incident solar radiance is then reflected from the surface upwards towards the sensor. As the reflected solar radiation passes upwards through the atmosphere towards the sensor it is again attenuated. Thus, reflected solar radiation arriving at the sensor is described by:

$$L_{SR}(\lambda) = \tau(\lambda) \rho(\lambda) E_{in}(\lambda). \quad (2.18a)$$

Because  $\rho(\lambda) = 1 - \varepsilon(\lambda)$ , this can also be written

$$L_{SR}(\lambda) = \tau(\lambda) [1 - \varepsilon(\lambda)] E_{in}(\lambda) \quad (2.18b)$$

or, writing  $E_{in}(\lambda)$  in full,

$$L_{SR}(\lambda) = \tau(\lambda) [1 - \varepsilon(\lambda)] \tau(\lambda, \theta_S) \cos(\theta_S) E_{TOA}(\lambda). \quad (2.18c)$$

As detailed in [Appendix B](#), since solar zenith angle (i.e., solar incidence angle) depends on the time of year, time of day, and latitude, so too does  $E_{in}(\lambda)$  and, hence also  $L_{SR}(\lambda)$ .

The second component of surface reflected radiation is reflected atmospheric down-welling radiance. Radiation will be emitted downwards from the atmosphere to the Earth's surface. This, like solar radiation, undergoes reflection upwards towards the sensor. Thus, the amount of down-welling atmospheric radiation,  $E_a(\lambda)$ , reaching the sensor will depend on the reflectivity of the surface and the transmissivity of the atmosphere through which it passes before arriving at the sensor. That is:

$$L_{AR}(\lambda) = \tau(\lambda) \rho(\lambda) E_a(\lambda) \quad (2.19a)$$

or, writing  $1 - \varepsilon(\lambda)$  for  $\rho(\lambda)$ ,

$$L_{\text{AR}}(\lambda) = \tau(\lambda) [1 - \varepsilon(\lambda)] E_a(\lambda). \quad (2.19\text{b})$$

Following Singh and Warren (1983), a crude estimate of  $E_a(\lambda)$  can be obtained from the up-welling radiance, so that replacing  $E_a(\lambda)$  with  $L_U(\lambda)$  in Equation (2.19b) gives:

$$L_{\text{AR}}(\lambda) = \tau(\lambda) [1 - \varepsilon(\lambda)] L_U(\lambda). \quad (2.19\text{c})$$

The final source of reflected radiation is that from space,  $L_{\text{SP}}(\lambda)$ . Space has a background temperature of  $\sim 3$  K. This component,  $E_{\text{sp}}(\lambda)$ , passes down through the atmosphere, is reflected by the surface and passes back up through the atmosphere to reach the sensor (Cracknell and Hayes, 1991). Thus, this quantity is given by:

$$L_{\text{SP}}(\lambda) = \tau(\lambda) \rho(\lambda) \tau_{\text{in}}(\lambda) E_{\text{sp}}(\lambda) \quad (2.20\text{a})$$

or

$$L_{\text{SP}}(\lambda) = \tau(\lambda) [1 - \varepsilon(\lambda)] \tau_{\text{in}}(\lambda) E_{\text{sp}}(\lambda), \quad (2.20\text{b})$$

$\tau_{\text{in}}$  being the atmospheric transmissivity experienced by the radiation during its in-coming journey downwards through the atmosphere and  $\tau(\lambda)$  being that experienced during its out-going journey upwards to the sensor.

### 2.3.3 Variation of each term between the SWIR, MIR and TIR

The relative contribution of each emission and reflection component to the at-sensor radiance is assessed in Table 2.6a. This considers the atmospheric upwelling and surface reflected contributions to the at-satellite radiance in the SWIR, MIR and TIR from a surface, located at sea-level, to a satellite located vertically overhead. The model is run using a high-emissivity (low-reflection) surface typical of basalt, i.e.,  $\varepsilon(\lambda)$  is 0.95 at all wavelengths. Two points can be made from the model calculations completed in Table 2.6a.

- (1) As we move from the SWIR to the TIR, so the dominant reflected or atmospheric source of emission moves from reflected and back-scattered solar radiation in the SWIR to atmospheric up-welling radiance in the TIR.
- (2) By night, with no solar contribution, reflected and scattered solar radiation is zero.

Table 2.6b adds the contribution of an ambient surface radiating at 15 °C to the model. The radiance from such a source in the SWIR is trivial. In fact, the at-sensor radiance is utterly dominated by solar reflected and scattered radiation, so that converting the at-sensor radiance to a brightness temperature is meaningless. By night, the only source in the SWIR is surface emission, but the intensity of the emission is so weak that it would not register a measurable signal at the sensor (see Electronic Supplement 1). Thus, we apply a more realistic (high-temperature) surface emission model for the SWIR in Table 2.6c. This shows that, by day, as we move to a surface temperature of 100 °C the contribution of surface emitted radiance to the total increases to 7%. The contribution of the reflected component, as well as atmospheric attenuation and emissivity effects, result in a brightness

Table 2.6a. Contribution of atmospheric up-welling and surface reflected components to at-sensor radiance. Contributions are assessed for the SWIR (2.1–2.5  $\mu\text{m}$ ), MIR (3.5–4.0  $\mu\text{m}$ ) and TIR (10–12  $\mu\text{m}$ ) during the day when reflection and scattering of solar radiation occurs, and at night, when the solar contribution is absent. Transmissivities,  $\tau(\lambda, \theta_S)$  and  $\tau(\lambda)$ , as well as atmospheric down-welling and up-welling components,  $E_a(\lambda)$  and  $L_U(\lambda)$ , are obtained using MODTRAN. MODTRAN was run using a 1976 US Standard atmosphere with a vertical path from sea-level to space (zenith = 180°, observer height = 100 km), a CO<sub>2</sub> mixing ratio of 380 ppm·v and a flat emissivity for basalt. Radiance values given in bold are the dominant components within each waveband.

Contribution of atmospheric up-welling and surface reflected radiance to at-sensor radiance									
Source	Term/derivation	Day-time (W cm <sup>-2</sup> sr <sup>-1</sup> $\mu\text{m}^{-1}$ )			Night-time (W cm <sup>-2</sup> sr <sup>-1</sup> $\mu\text{m}^{-1}$ )				
		SWIR	MIR	TIR	SWIR	MIR	TIR		
<u>Inputs</u>									
Solar zenith angle (°)*	$\theta_S$		23°			No Sun			
Surface emissivity	$\epsilon(\lambda)$		0.95			0.95			
Surface albedo	$\rho(\lambda)$		0.05			No reflection (night-time)			
<u>Surface-incident radiance</u>									
TOA solar irradiance	$E_{\text{TOA}}(\lambda)$	2.21E-03	3.94E-04	6.66E-06	No solar irradiance (night-time)				
Transmissivity for in-coming $E_{\text{TOA}}(\lambda)$	$\tau(\lambda, \theta_S)$	0.92	0.84	0.84	n/a				
Surface-incident solar radiance	$E_{\text{in}}(\lambda)$	1.87E-03	3.04E-04	5.18E-06	No surface-incident solar radiance				
Surface-incident down-welling radiance**	$E_a(\lambda)$	1.08E-09	1.93E-06	9.52E-05	1.57E-09	2.37E-06	9.52E-05		
<u>At-sensor radiance components</u>									
Transmissivity for up-welling radiance	$\tau(\lambda)$	0.92	0.84	0.84	0.91	0.85	0.84		
Atmospheric up-welling (at-sensor)	$L_U(\lambda)$	1.08E-09	1.93E-06	<b>9.52E-05</b>	<b>1.08E-09</b>	<b>1.93E-06</b>	<b>9.52E-05</b>		
Surface-reflected solar (at-sensor)	$L_{\text{SR}}(\lambda)$	<b>8.62E-05</b>	<b>1.29E-05</b>	2.19E-07	0.00E-00	0.00E-00	0.00E-00		
Surface-reflected down-welling (at-sensor)	$L_{\text{AR}}(\lambda)$	4.98E-11	8.13E-08	4.02E-06	4.98E-11	8.13E-08	4.02E-06		
Solar radiance scattered to the sensor	$L_{\text{scat}}(\lambda)$	<b>1.97E-05</b>	1.71E-06	1.33E-08	0.00E-00	0.00E-00	0.00E-00		

\* At mid-day, on 1 January at 0° N, 0° E.

\*\* Following Singh and Warren (1983),  $E_a(\lambda) = L_U(\lambda)$ .

Table 2.6b. Assessment of total radiance arriving at the sensor, the brightness temperature that this gives, and the contribution of each of the radiance sources to  $L(\lambda)$ . Assessment is made for the SWIR (2.1–2.5  $\mu\text{m}$ ), MIR (3.5–4.0  $\mu\text{m}$ ) and TIR (10–12  $\mu\text{m}$ ), during the day and night. The model is run for emission from a surface with an emissivity of 0.95 and at a temperature of 15 °C, with the atmospheric up-welling and surface reflected contributions of Table 2.6a.

Day- and night-time emission: surface temperature = 15°C, emissivity = 0.95							
Source	Term/derivation	Day-time ( $\text{W cm}^{-2} \text{ sr}^{-1} \mu\text{m}^{-1}$ )			Night-time ( $\text{W cm}^{-2} \text{ sr}^{-1} \mu\text{m}^{-1}$ )		
		SWIR	MIR	TIR	SWIR	MIR	TIR
Surface temperature (°C)	$T_s$		15 °C			15 °C	
Blackbody radiance	$L(\lambda, T_s)$	6.85E–08	2.64E–05	7.97E–04	6.85E–08	2.64E–05	7.97E–04
Surface-emitted radiance	$\varepsilon(\lambda)L(\lambda, T_s)$	6.50E–08	2.50E–05	7.57E–04	6.50E–08	2.50E–05	7.57E–04
At-sensor radiance from surface emission	$L_S(\lambda)$	5.99E–08	2.11E–05	6.39E–04	5.99E–08	2.12E–05	6.39E–04
Total at-sensor radiance	$L(\lambda)$	1.06E–04	3.77E–05	7.39E–04	6.10E–08	2.31E–05	7.38E–04
Brightness temperature (°C)	$T^*$	162.3 °C	23.0 °C	10.3 °C	13.5 °C	12.2 °C	10.3 °C
<u>At-sensor radiance contributions (%)</u>							
At-sensor radiance from surface emission	$L_S(\lambda)$	0.1	56.0	86.6	98.1	91.3	86.6
Atmospheric up-welling (at-sensor)	$L_U(\lambda)$	0.0	5.1	12.9	1.8	8.3	12.9
Surface-reflected solar (at-sensor)	$L_{SR}(\lambda)$	81.4	34.2	0.0	0.0	0.0	0.0
Surface-reflected down-welling (at-sensor)	$L_{AR}(\lambda)$	0.0	0.2	0.5	0.1	0.4	0.5
Solar radiance scattered to the sensor	$L_{scat}(\lambda)$	18.6	4.5	0.0	0.0	0.0	0.0

Table 2.6c. Assessment of total radiance arriving at the satellite, the brightness temperature that this gives, and the contribution of each of the radiance sources to  $L(\lambda)$ . Model is run for day-time emission in the SWIR for surfaces at a range of temperatures emitting in the SWIR (2.1–2.5  $\mu\text{m}$ ) between 100 °C and 1000 °C. We use an emissivity of 0.95 with the atmospheric up-welling and surface reflected contributions of Table 2.6a.

Day-time emission in the SWIR							
Source	Term/derivation	Radiance ( $\text{W cm}^{-2} \text{ sr}^{-1} \mu\text{m}^{-1}$ )					
		SWIR	SWIR	SWIR	SWIR	SWIR	SWIR
Surface temperature (°C)	$T_s$	100 °C	250 °C	375 °C	500 °C	750 °C	1000°C
Blackbody radiance	$L(\lambda, T_s)$	9.64E-06	1.18E-03	1.19E-02	5.65E-02	4.09E-01	1.37E+00
Surface-emitted radiance	$\epsilon(\lambda)L(\lambda, T_s)$	9.16E-06	1.12E-03	1.13E-02	5.37E-02	3.89E-01	1.30E+00
At-sensor radiance from surface emission	$L_S(\lambda)$	8.43E-06	1.03E-03	1.04E-02	4.94E-02	3.58E-01	1.20E+00
Total at-sensor radiance	$L(\lambda)$	1.14E-04	1.14E-03	1.05E-02	4.95E-02	3.58E-01	1.20E+00
Brightness temperature (°C)	$T^*$	164.6	248.4	366.8	487.6	728.2	966.5
<u>At-sensor radiance contributions (%)</u>							
At-sensor radiance from surface emission	$L_S(\lambda)$	7.4	90.7	99.0	99.8	100.0	100.0
Atmospheric up-welling (at-sensor)	$L_U(\lambda)$	0.0	0.0	0.0	0.0	0.0	0.0
Surface-reflected solar (at-sensor)	$L_{SR}(\lambda)$	75.4	7.6	0.8	0.2	0.0	0.0
Surface-reflected down-welling (at-sensor)	$L_{AR}(\lambda)$	0.0	0.0	0.0	0.0	0.0	0.0
Solar radiance scattered to the sensor	$L_{scat}(\lambda)$	17.2	1.7	0.2	0.0	0.0	0.0
<u>Basic correction for <math>\epsilon(\lambda)</math> and <math>\tau(\lambda)</math></u>							
Emissivity	$\epsilon(\lambda)$	0.95	0.95	0.95	0.95	0.95	0.95
Transmissivity	$\tau(\lambda)$	0.92	0.92	0.92	0.92	0.92	0.92
Corrected radiance ( $\text{W cm}^{-2} \text{ sr}^{-1} \mu\text{m}^{-1}$ ) <sup>a</sup>	$L(\lambda)/[\epsilon(\lambda) \tau(\lambda)]$	1.31E-04	1.30E-03	1.20E-02	5.66E-02	4.09E-01	1.37E+00
Temperature (°C) <sup>b</sup>	$T^*$	168.7	254.2	375.7	500.2	750.0	1000.0

<sup>a</sup> Radiance obtained by correcting at-sensor radiance by just  $\epsilon(\lambda)$  and  $\tau(\lambda)$ .

<sup>b</sup> Temperature obtained from correcting at-sensor radiance by just  $\epsilon(\lambda)$  and  $\tau(\lambda)$ .

Table 2.6d. Assessment of total radiance arriving at the satellite, the brightness temperature that this gives, and the contribution of each of the radiance sources to  $L(\lambda)$ . Model is run for day-time conditions for surfaces at a range of temperatures (from 50 °C to 500 °C) emitting in the MIR (3.5–4.0  $\mu\text{m}$ ) and TIR (10–12  $\mu\text{m}$ ). We use an emissivity of 0.95 with the atmospheric up-welling and surface reflected contributions of Table 2.6a.

Source	Daytime emission in the MIR & TIR (radiance in $\text{W cm}^{-2} \text{sr}^{-1} \mu\text{m}^{-1}$ )							
	$T_s = 50 \text{ }^\circ\text{C}, \varepsilon(\lambda) = 0.95$		$T_s = 100 \text{ }^\circ\text{C}, \varepsilon(\lambda) = 0.95$		$T_s = 250 \text{ }^\circ\text{C}, \varepsilon(\lambda) = 0.95$		$T_s = 500 \text{ }^\circ\text{C}, \varepsilon(\lambda) = 0.95$	
	MIR	TIR	MIR	TIR	MIR	TIR	MIR	TIR
Surface temperature (°C)	50 °C	50 °C	100 °C	100 °C	250 °C	250 °C	500 °C	500 °C
Blackbody radiance	1.12E-04	1.31E-03	5.48E-04	2.29E-03	1.05E-02	6.60E-03	1.13E-01	1.67E-02
Surface-emitted radiance	1.06E-04	1.25E-03	5.20E-04	2.17E-03	9.94E-03	6.27E-03	1.07E-01	1.58E-02
At-sensor radiance from surface emission	8.94E-05	1.05E-03	4.39E-04	1.83E-03	8.39E-03	5.30E-03	9.05E-02	1.34E-02
Total at-sensor radiance	1.06E-04	1.15E-03	4.56E-04	1.93E-03	8.40E-03	5.40E-03	9.05E-02	1.35E-02
Brightness temperature (°C)	48.6	40.1	93.4	83.4	234.8	213.6	467.2	426.7
<u>At-sensor radiance contributions (%)</u>								
At-sensor radiance from surface emission	84.3	91.4	96.4	94.9	99.8	98.2	100.0	99.3
Atmospheric up-welling (at-sensor)	1.8	8.3	0.4	4.9	0.0	1.8	0.0	0.7
Surface-reflected solar (at-sensor)	12.2	0.0	2.8	0.0	0.2	0.0	0.0	0.0
Surface-reflected down-welling (at-sensor)	0.1	0.3	0.0	0.2	0.0	0.1	0.0	0.0
Solar radiance scattered to the sensor	1.6	0.0	0.4	0.0	0.0	0.0	0.0	0.0
<u>Basic correction for <math>\varepsilon(\lambda)</math> and <math>\tau(\lambda)</math></u>								
Emissivity	0.95	0.95	0.95	0.95	0.95	0.95	0.95	0.95
Transmissivity	0.84	0.84	0.84	0.84	0.84	0.84	0.84	0.84
Corrected radiance ( $\text{W cm}^{-2} \text{sr}^{-1} \mu\text{m}^{-1}$ ) <sup>a</sup>	1.32E-04	1.44E-03	5.69E-04	2.41E-03	1.05E-02	6.73E-03	1.13E-01	1.68E-02
Temperature (°C) <sup>b</sup>	54.7	57.2	101.4	105.5	250.1	253.6	500.0	502.8

<sup>a</sup> Radiance obtained by correcting at-sensor radiance by just  $\varepsilon(\lambda)$  and  $\tau(\lambda)$ .

<sup>b</sup> Temperature obtained from correcting at-sensor radiance by just  $\varepsilon(\lambda)$  and  $\tau(\lambda)$ .

temperature that is  $\sim 65$  °C higher than the actual surface temperature (c.f.,  $T_s$  and  $T^*$  in [Table 2.6c](#)). As we move to 250 °C, the contribution of surface-emitted radiance to the total increases to 91%. The contribution of the reflected component is no longer sufficient to balance the effect of atmospheric attenuation, so the brightness temperature is now lower than the actual surface temperature by  $\sim 2$  °C. As we move to higher temperatures, so the contribution of the reflected component to the total continues to decline, to approach 0% of the total at a surface temperature of 500 °C. As a result, attenuated surface-emitted radiance becomes the dominant source, attenuation meaning that the brightness temperature continues to be somewhat ( $\sim 34$  °C) less than the actual surface temperature.

For an ambient surface radiating at 15 °C in the MIR, the same model shows that 56% of the at-sensor radiance will be due to emission from the surface ([Table 2.6b](#)). Of the remainder, reflected and scattered solar radiation together contribute  $\sim 39\%$  and atmospheric up-welling radiance contributes  $\sim 5\%$ . The result is a brightness temperature that is  $\sim 8$  °C higher than the actual surface temperature (c.f.,  $T_s$  and  $T^*$  in [Table 2.6b](#)). By night, the solar source is absent, with surface emission accounting for more than 90% of the total at-sensor radiance, with atmospheric up-welling radiance contributing the remainder. Attenuation effects now dominate, so that the brightness temperature is  $\sim 3$  °C lower than the actual surface temperature by night. As we increase the surface temperature, as in the [Table 2.6d](#) model, so the contribution of surface emission to the total at-sensor radiance becomes increasingly dominant, to approach 100% at a source temperature of 250 °C. However, the ever-present attenuation effect continues to modify the sensor-arriving radiance, so that the brightness temperature remains lower than the actual surface temperature by up to 33 °C (as in the 500 °C case of [Table 2.6d](#)).

In the TIR, [Table 2.6b](#) shows that the contribution of reflected and scattered solar radiation is small, having a combined contribution of  $< 0.5\%$  in all cases. The contribution of reflected down-welling radiance is also trivial in this low-reflectivity model. Instead, surface emission contributes more than 90% of the at-sensor radiance by both day and night, with atmospheric up-welling radiance contributing the remainder. Attenuation effects thus dominate so that the brightness temperature is lower than the surface temperature in all cases (c.f.,  $T_s$  and  $T^*$  in [Table 2.6d](#)). As we increase the surface temperature, as in the [Table 2.6d](#) model, so the contribution of surface emission to the total at-sensor radiance becomes increasingly dominant, to exceed 99% at a source temperature of 500 °C. However, as in the MIR, attenuation effects result in brightness temperatures that are lower, by up to 73 °C, than the actual surface temperature.

Comparison of the surface temperature with the brightness temperature in [Tables 2.6b](#) and [2.6c](#) shows that, if we use brightness temperature, we tend to under- or over-estimate true surface temperature. Atmospheric correction must, therefore, be completed if we are to extract surface temperature.

### **2.3.4 Variation in atmospheric up-welling and reflected solar radiation with altitude and scan angle**

The Table 2.6 model was run for a fixed path length, from a satellite vertically over the measurement point to sea-level. However, as with transmissivity, the quantity of up-welling

radiance and reflected solar radiance varies with path length, altitude and scan angle. For up-welling radiances, while longer path lengths contain a greater amount of atmosphere, so that more emitted radiance can be produced, thinner atmospheres above surfaces at higher altitudes result in lower amounts of atmospheric emission. At the same time, increased path lengths will result in increased absorption of surface arriving, and reflected, solar radiation, hence reducing the reflected solar radiation component arriving at the sensor. On the other hand, solar radiation passing through thinner atmospheres at higher altitudes will experience decreased absorption, hence increasing the amount of reflected solar radiation arriving at the sensor.

As plotted in [Figure 2.17a](#), for a satellite sensor viewing the surface from a vantage point vertically above the surface, up-welling radiance will decrease with increased surface

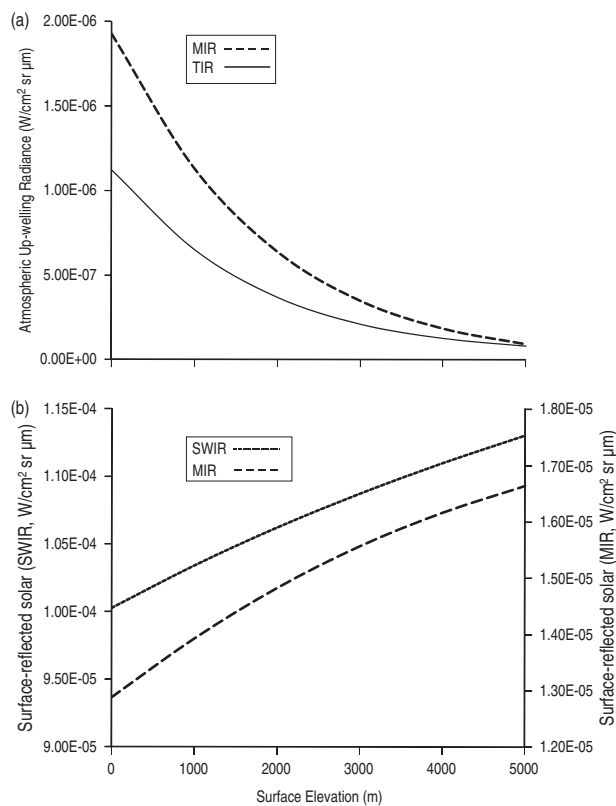


[Figure 2.17](#) (a) Decrease in atmospheric up-welling radiance with surface elevation for a satellite viewing the surface from space in (i) the MIR (3.5–4.0  $\mu\text{m}$ ), and (ii) the TIR (10–12  $\mu\text{m}$ ). (b) Increase in surface-reflected radiance with surface elevation for a satellite viewing the surface from space in (i) the SWIR (2.1–2.5  $\mu\text{m}$ ), and (ii) the MIR (3.5–4.0  $\mu\text{m}$ ). The same MODTRAN US Standard atmosphere as used in [Figure 2.14](#) is applied, and reflection is calculated (for mid day, on 1 January at 0° N, 0° E) following the procedure detailed in [Appendix B](#).

elevation. This is a result of a reduction in the length of the atmospheric column between the surface and the sensor with elevation. Conversely, reflected solar radiation will increase with surface elevation ([Figure 2.17b](#)), a result of increased transmissivities with shorter path lengths and a thinner atmosphere. For a given surface elevation, although up-welling radiance will increase with scan angle, as the path length increases ([Figure 2.18](#)), reflected solar radiation will decrease due to increased absorption along the longer path length ([Figure 2.19](#)).

So far we have considered reflection from a high-emissivity (basaltic) surface. Of course, reflected solar radiation will increase with surface reflection in the SWIR and MIR, i.e., as emissivity decreases, reflected solar radiation increases ([Figure 2.20a](#)). Reflected atmospheric down-welling radiance in the MIR and TIR will also increase as surface reflection increases ([Figure 2.21](#)). At the same time, reflected solar radiation will decrease with solar

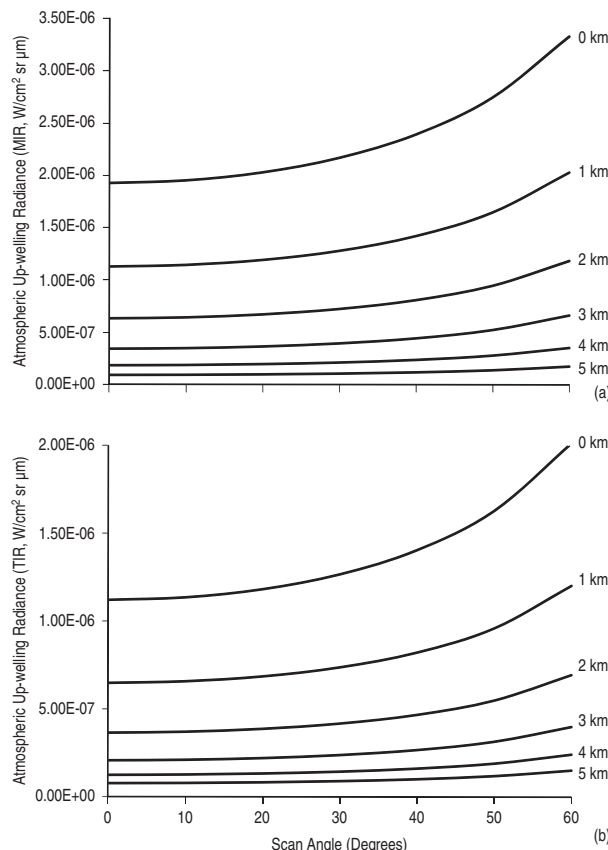


[Figure 2.18](#) Variation in atmospheric up-welling radiance with scan angle and surface elevation for a satellite viewing the surface from space in (a) the MIR (3.5–4.0  $\mu\text{m}$ ), and (b) the TIR (10–12  $\mu\text{m}$ ). The same MODTRAN US Standard atmosphere as used in [Figure 2.14](#) is applied.

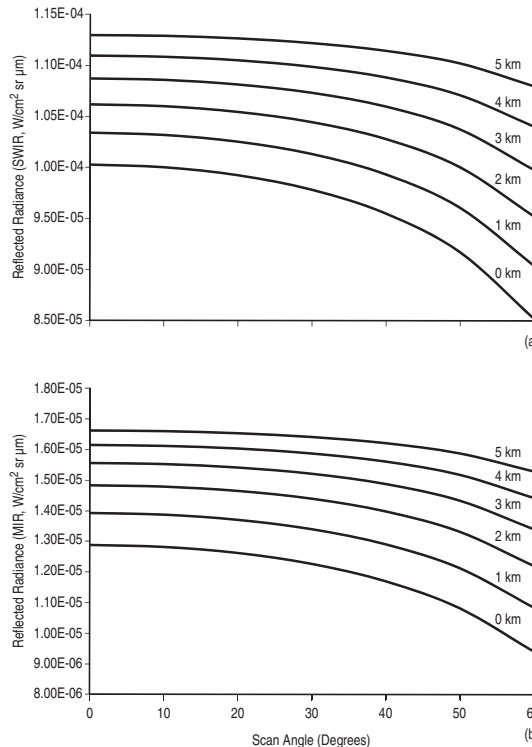


Figure 2.19 Variation in surface-reflected radiance with scan angle and surface elevation for a satellite viewing the surface from space in (a) the SWIR (2.1–2.5  $\mu\text{m}$ ), and (b) the MIR (3.5–4.0  $\mu\text{m}$ ). The same MODTRAN US Standard atmosphere as used in Figure 2.14 is applied.

zenith angle, declining from a maximum when the Sun is directly overhead, so that  $\theta_S = 0$ , to a minimum when the Sun is lower in the sky ( $\theta_S > 0$ ) (Figure 2.20b).

### 2.3.5 Atmospheric correction

If we consider the transmissive and emissive effects of the atmosphere, as well as the reflective and emissive properties of the surface, an equation for the effects of atmospheric emission, absorption and surface reflection on the sensor-arriving radiance can be written. Taking Equation (2.14b) and writing  $L_S(\lambda)$  in full we obtain:

$$L(\lambda)^* = L(\lambda, T^*) = \tau(\lambda) \varepsilon(\lambda) L(\lambda, T_s) + L_U(\lambda) + L_R(\lambda). \quad (2.21a)$$

Re-arranging shows that surface temperature ( $T_s$ ) can be obtained from the brightness temperature through:

$$L(\lambda, T_s) = [L(\lambda, T^*) - L_U(\lambda) - L_R(\lambda)] / [\tau(\lambda) \varepsilon(\lambda)]. \quad (2.21b)$$

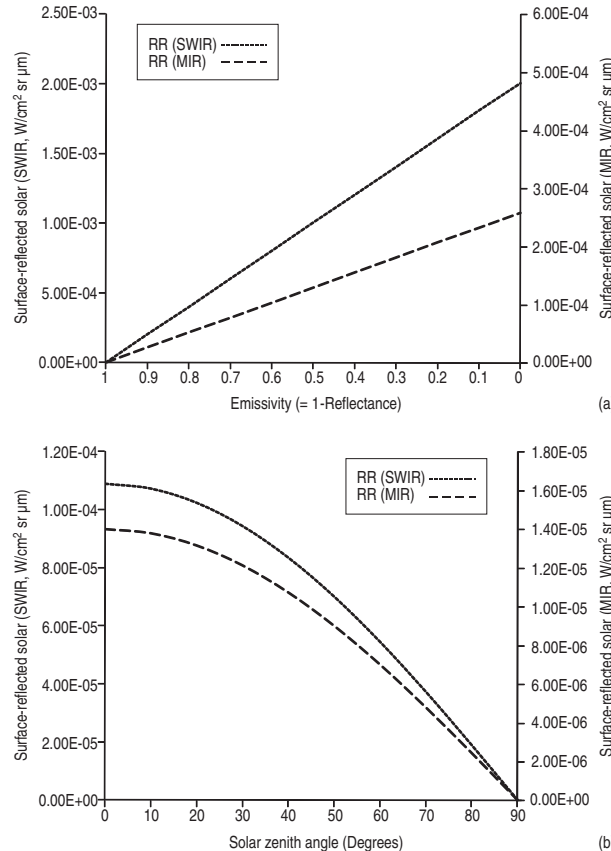


Figure 2.20 Variation in surface reflected radiance in the SWIR (left-hand axis) and MIR (right-hand axis) with (a) surface emissivity and (b) solar zenith angle. The same MODTRAN US Standard atmosphere as used in Figure 2.14 is applied, and reflection is calculated following the procedure detailed in Appendix B.

As we know, parameter  $L_R(\lambda)$  is composed of three components. Writing each of the terms of Equation (2.15) in full shows that the reflected component of the sensor-arriving radiance is itself described by:

$$L_R(\lambda) = \tau(\lambda) [1 - \varepsilon(\lambda)] \{ \tau(\lambda, \theta_S) [E_{TOA}(\lambda) + E_{sp}(\lambda)] + L_U(\lambda) \}. \quad (2.21c)$$

Equations (2.21b) and (2.21c), in effect, describe the atmospheric correction that we need to apply to the sensor-recorded radiance if we are to isolate the quantity we require, i.e.,  $L(\lambda, T_s)$ . That is, if we are to arrive at the true surface kinetic temperature, we have to subtract the atmospheric up-welling and reflected components from the at-satellite radiance, and then divide by transmissivity and emissivity.

We can simplify matters if we consider the importance of each term within each of the atmospheric windows of interest, and reject those that do not significantly contribute to the

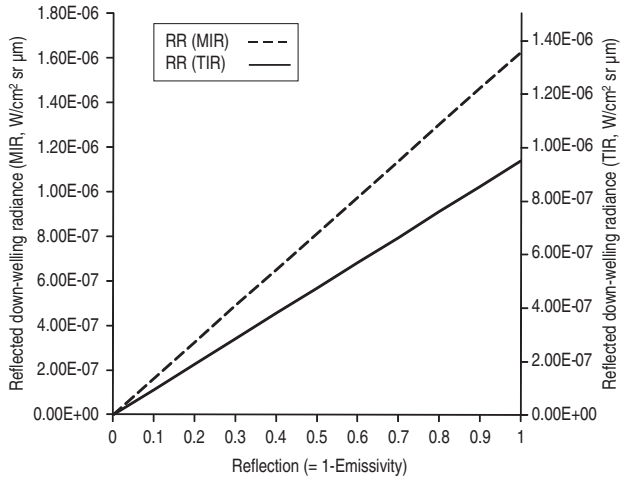


Figure 2.21 Increase in surface-reflected down-welling radiance in the MIR (left-hand axis) and TIR (right-hand axis) with surface reflection. The same MODTRAN US Standard atmosphere as used in Figure 2.14 is applied.

total at-sensor radiance. First, though, we can remove one component. Reflected space radiance is extremely small at all infrared wavelengths. Thus we can discount  $E_{\text{sp}}(\lambda)$  for all cases and simplify Equation (2.21c) to:

$$L_R(\lambda) = \tau(\lambda) [1 - \varepsilon(\lambda)] [\tau(\lambda, \theta_S) E_{\text{TOA}}(\lambda) + L_U(\lambda)]. \quad (2.22)$$

### 2.3.5.1 Atmospheric correction in the SWIR

As can be seen by examining the cases in Table 2.6c, reflection of atmospheric down-welling radiance makes a negligible contribution to the total at-satellite radiance in the SWIR, as does atmospheric up-welling radiance. As a result, Equation (2.21b) can be simplified to

$$L(\lambda, T_s) = [L(\lambda, T^*) - L_R(\lambda)] / [\tau(\lambda)\varepsilon(\lambda)] \quad (2.23a)$$

and (2.22) to:

$$L_R(\lambda) = \tau(\lambda) [1 - \varepsilon(\lambda)] [\tau(\lambda, \theta_S) E_{\text{TOA}}(\lambda)]. \quad (2.23b)$$

In other words, we only have to correct the at-sensor signal for reflection of solar radiation and atmospheric attenuation. However, solar radiance scattered upwards towards the sensor by the atmosphere contributes up to 15% of the total at-sensor radiance, so that the contribution of back-scattered radiation,  $L_{\text{scat}}(\lambda)$ , needs to be added to Equation (2.23b):

$$L_R(\lambda) = \tau(\lambda) [1 - \varepsilon(\lambda)][\tau(\lambda, \theta_S) E_{\text{TOA}}(\lambda)] + L_{\text{scat}}(\lambda). \quad (2.23c)$$

Thus, the atmospheric correction in the SWIR involves making an estimate for, and subtracting, the contributions of reflected and scattered solar radiation, as well as atmospheric transmissivity, in:

$$L(\lambda, T_s) = [L(\lambda, T^*) - L_R(\lambda) - L_{\text{scat}}(\lambda)] / [\tau(\lambda)\varepsilon(\lambda)]. \quad (2.24a)$$

Typical values for  $L_R(\lambda)$ ,  $L_{\text{scat}}(\lambda)$  and  $\tau(\lambda)$  are given, for a path length from space to sea-level, in [Table 2.6a](#). Of course, as shown in [Table 2.6a](#), at night there is no solar reflected or scattered contribution, so that the correction reduces to:

$$L(\lambda, T_s) = L(\lambda, T^*) / [\tau(\lambda)\varepsilon(\lambda)]. \quad (2.24b)$$

In fact, examination of [Table 2.6c](#) shows that by day, for low-reflectivity surfaces ( $\rho(\lambda) < 5\%$ ), once the temperature of the surface exceeds 350 °C, surface emission accounts for more than 99 % of the total at-sensor radiance. As a result, under such conditions, Equation (2.24b) may be applied to day time data to approximate surface temperature from brightness temperature. This correction is sufficient to retrieve surface temperatures to within 0.2 °C for surfaces at 500 °C. However, for cooler surfaces the failure to remove the reflected component will result in an over-estimate of surface temperature by between 1 °C and 68 °C, as can be seen by comparing  $T_s$  and  $T^*$  in [Table 2.6c](#).

### *2.3.5.2 Atmospheric correction in the TIR*

As can be seen by examining the cases in [Table 2.6d](#), reflection and scattering of solar radiation makes a negligible contribution to the total at-satellite radiance in the TIR. Instead, atmospheric up-welling radiance can contribute as much as 13% to the total at sensor radiance. As a result, Equation (2.21b) can be simplified to

$$L(\lambda, T_s) = [L(\lambda, T^*) - L_U(\lambda)] / [\tau(\lambda)\varepsilon(\lambda)] \quad (2.25)$$

In other words, we only have to correct the at-sensor signal for atmospheric up-welling radiation and atmospheric attenuation. Typical values for  $L_U(\lambda)$  and  $\tau(\lambda)$ , for a path length from sea-level to space are given in [Table 2.6a](#). [Table 2.6d](#) shows that the relative contribution of  $L_U(\lambda)$  to the total at-satellite radiance decreases as surface temperature increases, declining to 0.7% of the total when considering emission from surfaces at 500 °C. However, even at 500 °C, failure to remove the atmospheric up-welling component will result in an over-estimate of surface temperature by ~3 °C (compare  $T_s$  and  $T^*$  in [Table 2.6d](#)).

### *2.3.5.3 Atmospheric correction in the MIR*

The at-sensor radiance in the MIR is complicated by solar radiance reflected from the surface and back-scattered by the atmosphere, as well as by the presence of atmospheric up-welling radiance. As can be seen from [Table 2.6b](#), reflected solar radiation is the

dominant radiance contribution to the total at-sensor radiance after surface emission, representing ~34% of the total at-sensor radiance over ambient surfaces. However, scattered and up-welling radiance contribute ~4% and 6% of the total, respectively. Thus, correction in the MIR is the most complicated of the three cases, requiring correction for the contributions of reflected, scattered and up-welling radiance, while taking into account the effects of attenuation, so that:

$$L(\lambda, T_s) = [L(\lambda, T^*) - L_U(\lambda) - L_R(\lambda)] / [\tau(\lambda)\varepsilon(\lambda)], \quad (2.26a)$$

in which

$$L_R(\lambda) = \tau(\lambda) [1 - \varepsilon(\lambda)] [\tau(\lambda, \theta_S) E_{TOA}(\lambda)] + L_{scat}(\lambda). \quad (2.26b)$$

Examination of [Table 2.6b](#) shows that, over ambient surfaces, only the contribution of reflected down-welling atmospheric radiance can be neglected. By night, the solar-reflected and scattered components can also be neglected ([Table 2.6b](#)), so that Equation (2.26) simplifies to:

$$L(\lambda, T_s) = [L(\lambda, T^*) - L_U(\lambda)] / [\tau(\lambda)\varepsilon(\lambda)]. \quad (2.26c)$$

[Table 2.6c](#) shows that, by day, the same is true once the surface temperature exceeds 100 °C, if the reflectivity of the surface is low ( $\rho(\lambda) < 5\%$ ). Also, as the temperature of the surface reaches ~250 °C, so the contribution of  $L_U(\lambda)$  declines to less than 0.5% of the total. Over low-reflectivity (basaltic) surfaces, and at surface temperatures of greater than 250 °C,  $T_s$  can therefore be approximated from:

$$L(\lambda, T_s) = L(\lambda, T^*) / [\tau(\lambda)\varepsilon(\lambda)]. \quad (2.27)$$

Comparing  $T_s$  and  $T^*$  in [Table 2.6d](#) shows that, for a surface temperature of 250 °C, this will return a corrected temperature of 250.1 °C.

## 2.4 Brightness temperature and surface temperature: how to obtain surface temperature

An overview of the steps required to determine a surface temperature from satellite sensor data is given in Cracknell (1997). It is given, in modified form, here in [Figure 2.22](#).

### 2.4.1 A summary of the physical processes controlling at-sensor radiance

The left-hand side of [Figure 2.22](#) illustrates the physical principles involved in transmitting the radiance from the surface to the satellite sensor. These are as follows.

- (1) Radiation is emitted by the surface, its spectral distribution being governed by the Planck Function, modified by emissivity. Radiation is also reflected from the surface, the intensity depending on the wavelength of the measurement, the level of incoming solar radiation and the reflectivity of the surface.

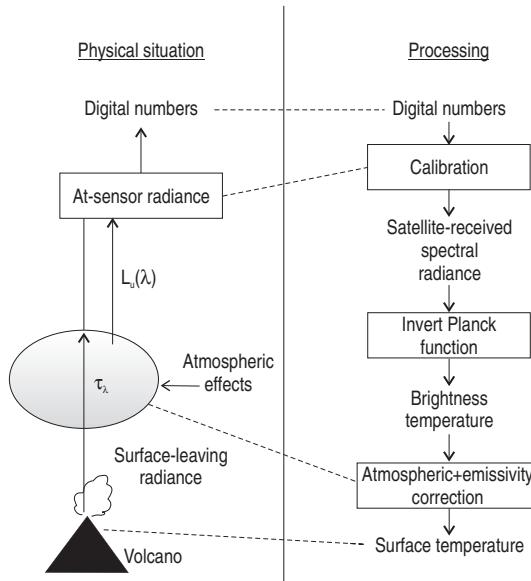


Figure 2.22 Summary of the physical processes affecting surface-leaving spectral radiance during its passage from the surface to the space-based sensor (left-hand side), with the processing required to retrieve the surface kinematic temperature from the satellite-sensor recorded digital number on the right-hand side [modified from Cracknell (1997, Fig. 4.3)].

- (2) The radiation travels upwards to the space-based sensor, passing through the entire atmospheric column. The atmosphere itself emits further radiation, while absorbing some of the surface-emitted and -reflected radiation.
- (3) The radiation arrives at the satellite where it registers a voltage on the detector proportional to the level of at-sensor radiance. The voltage is converted to a digital number (DN), which is usually related to incident, at-sensor, radiance ( $R^*$ ) through a linear relationship, whereby:

$$R^* = a \text{ DN} + b, \quad (2.28)$$

in which  $a$  and  $b$  are known calibration coefficients (see Electronic Supplement 2).

- (4) This, through inversion of the Planck Function, can be converted to a brightness temperature ( $T^*$ ) through

$$T^* = \frac{c_2}{\lambda \ln \left( \frac{c_1 \lambda^{-5}}{R^*} + 1 \right)}. \quad (2.29)$$

#### 2.4.2 Processing of at-sensor radiance to obtain surface-leaving radiance

The right-hand side of Figure 2.22 outlines the processing operations required to invert the process and thereby convert the satellite-recorded value (the DN), back to the desired quantity (surface temperature). The main steps are as follows.

- (1) Cloud detection and elimination.
- (2) Conversion of the DN to at-sensor radiance through application of Equation (2.28).
- (3) Correction of the at-satellite radiance ( $R_{\text{in}}^*$ ) for atmospheric and emissivity effects using, for the SWIR:

$$L(\lambda, T_s) = [R_{\text{in}}^* - L_R(\lambda) - L_{\text{scat}}(\lambda)] / [\tau(\lambda) \varepsilon(\lambda)] \quad (2.30\text{a})$$

for the MIR:

$$L(\lambda, T_s) = [R_{\text{in}}^* - L_U(\lambda) - L_R(\lambda)] / [\tau(\lambda) \varepsilon(\lambda)] \quad (2.30\text{b})$$

and for the TIR:

$$L(\lambda, T_s) = [R_{\text{in}}^* - L_U(\lambda)] / [\tau(\lambda) \varepsilon(\lambda)]. \quad (2.30\text{c})$$

- (4) Finally, the Planck Function is inverted and the atmospherically and emissivity corrected radiance [ $R = L(\lambda, T_s)$ ] is used (with the appropriate wavelength) to obtain surface temperature from:

$$T_s = \frac{c_2}{\lambda \ln \left( \frac{c_1 \lambda^{-5}}{R} + 1 \right)}. \quad (2.30\text{d})$$

This process is considered in more detail in Electronic Supplement 3 where, to obtain an exact temperature for a selective radiator, the sensor spectral response function may have to be convolved with spectral emissivity and transmissivity. However, as shown in Electronic Supplement 3, a good approximation of surface temperature (theoretically to within 0.1 °C) can be obtained by following the above steps and inputting appropriate band-averaged values. Band-averaged emissivity, atmospheric and reflection correction values for some commonly used sensors and wavebands are given in Electronic Supplement 4.

## 2.5 Summation

Here we define precision and accuracy. Precision is the degree of refinement with which we can make a measurement, i.e., to how many significant figures can we make the measurement? For a remote sensing sensor this can be defined by the noise equivalent temperature difference ( $NE\Delta T$ ), i.e., the variation in measured temperature due to detector noise (see [Section 3.4.2 of Chapter 3](#)). This is typically less than 0.5 °C for most satellite-based thermal detectors. This contrasts with accuracy, which is the degree to which the measurement conforms to the truth. In our case, we need to ask how close is the measurement of surface temperature, as derived from the integrated radiance recorded by the detector, to the actual surface temperature?

Over a surface of homogeneous temperature (at pixel scale), it is unlikely that we can execute emissivity and atmospheric correction to allow estimation of surface temperature to

an accuracy any greater than 1 °C. Over an active lava the problem can be exacerbated by extreme heterogeneity in surface temperature at the scale of the pixel, requiring application of mixture models to extract actual surface temperature (see [Chapter 4](#)). The presence of volcanic gas will also complicate the problem (see [Section 9.4.6.7 of Chapter 9](#)). Thus, in the absence of precise atmospheric and emissivity data specific to the time and location of the measurement, accuracies of a few degrees centigrade are (have to be) acceptable. Comparisons between actual surface temperature and those obtained from a satellite-based measurement are given in [Electronic Supplement 4](#).

# 3

## Satellite orbits and sensor resolution

Satellite-flown sensors used to obtain thermal data over active volcanoes can be split into three classes depending on their temporal and spatial resolutions. We name these classes after the principal sensor used to develop the discipline in each class, i.e., the sensor most commonly used for infrared radiometry at active volcanic phenomena (see [Chapter 1](#)).

The classes are as follows.

- Low-temporal but high-spatial-resolution sensors: *TM-class sensors*
- Moderate-temporal and -spatial resolution sensors: *AVHRR-class sensors*
- High-temporal but low-spatial-resolution sensors: *GOES-class sensors*

The specifications of the main sensors used for volcanological thermal applications (as of 2008) within each of these three classes are given in [Appendix C](#) (for *TM-class sensors*), [Appendix D](#) (for *AVHRR-class sensors*) and [Appendix E](#) (for *GOES-class sensors*). In addition, images of different types of volcano hot spot, as imaged by sensors in each class, are collated in Electronic Supplement 1, where the detection capabilities of each class are also assessed. In the following sections we do not dwell on the characteristics of individual sensors. Instead we consider the way in which these sensors orbit and acquire their data, thereby covering the main factors controlling the temporal, spatial and spectral capabilities of satellite-flown sensors. Understanding these factors is crucial for two reasons. First, data of appropriate spatial, spectral and/or temporal resolutions need to be identified depending on the size and temperature, as well as the rate of change, of the eruptive phenomena targeted. Second, selection of appropriate data processing and reduction methodologies (i.e., applications of the methods detailed in [Chapters 4, 5 and 6](#)) requires an understanding and precise definition of the sensor temporal, spatial and spectral characteristics.

### 3.1 Orbit and temporal resolution

Upon launch, a satellite system comprises three components: the launch vehicle, the satellite and the sensor. The launch vehicle or rocket carries the satellite into space and is thus used only for launch of the satellite. The satellite is the structure on which the sensor is mounted. It therefore carries the sensor, allows for orbital adjustments, provides power through solar

panels and carries the transmitter which returns data to Earth. Finally the sensor includes the infrared detector and scanning system which allows acquisition of data. The sensor thus collects the data, and the satellite controls the orbit.

The orbital characteristics for the satellite which carries the sensor will control the overpass frequency or temporal resolution of a given point on the Earth's surface. The sensor itself will then collect spectral radiance emitted from that point, with the sensor design characteristics determining the surface area (spatial resolution) and wavelength (spectral resolution) across which the measurement is made.

### **3.1.1 Satellite height and orbit period**

The height of the satellite above the Earth's surface will determine the time it takes the satellite to complete one orbit of the Earth. This can be shown using Newton's Second Law of Motion, which states that the force ( $F$ ) on an object will be equal to the object's mass multiplied by its acceleration ( $a$ ). For a satellite of mass  $m$  in a circular orbit of radius  $r$  around the Earth of mass  $M$ , the satellite will experience a gravitational force of:

$$F = GMm/r^2 = ma = mr\omega^2, \quad (3.1a)$$

in which  $G$  is Newton's gravitational constant ( $6.67428 \times 10^{-11} \text{ N m}^2 \text{ kg}^{-2}$ ) and  $\omega$  is the satellite angular velocity (radians per second). Because the units of a newton can also be written as  $\text{kg m s}^{-2}$ , the units of the gravitational constant can be written as  $\text{m}^3 \text{ kg}^{-1} \text{ s}^{-2}$ . Since the units of radians are dimensionless, the units of angular velocity are  $\text{s}^{-1}$ . Thus, dimensionally, Equation (3.1a), reduces to  $\text{kg m s}^{-2}$ , or newtons.

Equation (3.1a) can be re-arranged to give angular velocity:

$$\omega = \sqrt{GM/r^3}. \quad (3.1b)$$

The period of revolution of the satellite ( $P$ , in seconds) is then given by:

$$P = 2\pi/\omega = 2\pi\sqrt{r^3/GM}. \quad (3.1c)$$

This equation can now be used to assess the satellite height required to give a certain orbital period, as done in [Figure 3.1](#). For satellites in low-Earth orbits, i.e., between 700 km and 900 km above the Earth's surface, the orbital period will thus be  $\sim 100$  minutes. Re-arranging Equation (3.1c) also shows that, to obtain the orbital period required for a geostationary orbit, i.e., 24 hours, the satellite needs to be stationed 35 900 km above the Equator, a location that allows the satellite to exactly track the Earth's rotation. Equation (3.1c) is solved for a number of typical satellite heights in [Table 3.1](#), where we can group the satellites carrying sensors used for volcanological thermal applications into one of two different orbit types: low-Earth orbits and geostationary orbits.

Table 3.1. Acceleration and orbital period calculated for the satellite heights of Landsat, NOAA, GOES and the Moon.

Satellite	Landsat (TM)	NOAA (AVHRR)	NOAA (AVHRR)	GOES (Imager)	Moon
Satellite height ( $S_h$ , km)	705	833	870	36 000	384 400
Satellite height ( $S_h$ , m)	7.05E+05	8.33E+05	8.70E+05	3.60E+07	3.84E+08
Radius of Earth ( $R$ , m)	6.37E+06	6.37E+06	6.37E+06	6.37E+06	6.37E+06
Radius of orbit ( $r = R + S_h$ , m)	7.08E+06	7.20E+06	7.24E+06	4.24E+07	3.91E+08
Gravitational constant ( $G$ , N m <sup>2</sup> kg <sup>-2</sup> )*	6.67E-11				
Mass of the Earth ( $M$ , kg)	5.98E+24				
Angular velocity ( $\omega$ , Equation (3.1b), m s <sup>-1</sup> )	1.06E-03	1.03E-03	1.03E-03	7.24E-05	2.59E-06
Acceleration ( $a = r \omega^2$ , m s <sup>-2</sup> )	8.0	7.7	7.6	0.2	0.003
Period of revolution (seconds)	5919	6080	6127	86 747	2 429 688
Period of revolution (minutes)	99	101	102	1446	40495
Period of revolution (hours)	1.65	1.68	1.7	24	675

\* See Mohr *et al.* (2008, pp. 688–689) for measurement collation for, and uncertainty in, Newton’s gravitational constant; the 2006 National Institute of Standards and Technology recommended value is  $6.67428 \times 10^{-11} \text{ m}^3 \text{ kg}^{-1} \text{ s}^{-2}$ .

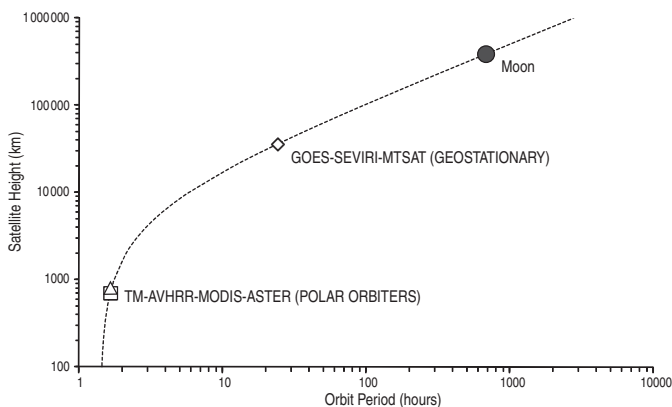


Figure 3.1 Increase in orbital period with satellite height. The satellite height – orbital period loci for polar orbiters (at heights of between 700 km and 800 km) and geostationary platforms (at 35 000 km) are given, as is that of the Moon.

### 3.1.2 Low-Earth orbits

As illustrated in Figure 3.2, low-Earth orbits (LEOs) are typically Sun-synchronous, pass over the poles and are near-circular. LEOs are thus also known as polar orbits. Low-Earth orbits are designed to keep pace with the Sun’s westward progress as the Earth rotates, the

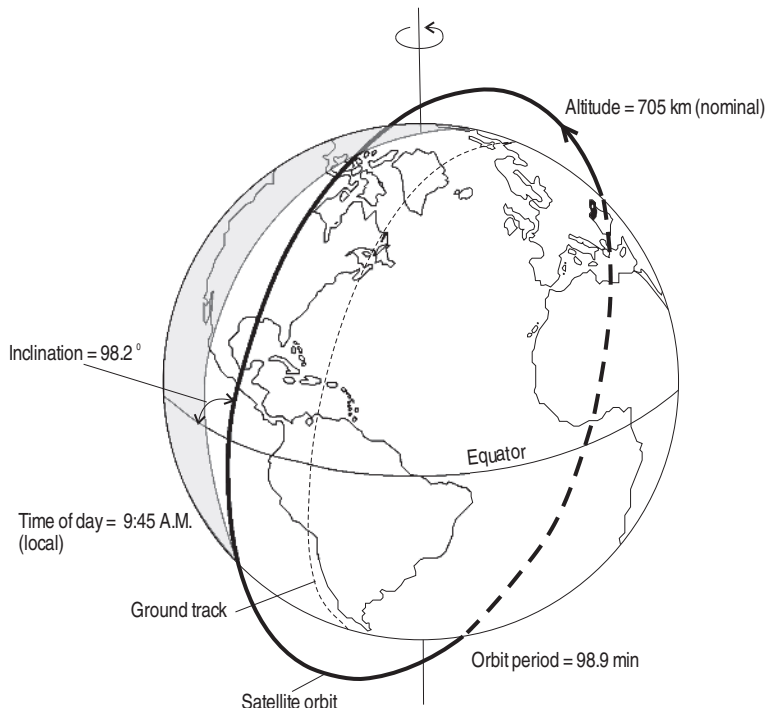


Figure 3.2 Polar orbit of the Landsat satellite [from USGS/NOAA (1984, Fig. 5.1), and NASA (1998, Fig. 5.1)]: Example of a LEO.

orbit being orientated so that the satellite passes over the Equator at the same local time during every orbit. As shown in Figure 3.2, using Landsat's low-Earth orbit by way of example, each orbit involves a north-to-south descent of the illuminated portion of the planet. This is followed by a south-to-north ascent of the planet's dark side. As listed in Table 3.2a, the LEO satellites considered here (i.e., those commonly used for thermal remote sensing of volcanism) have an orbital period of  $\sim 100$  minutes so that they can complete  $\sim 14$  full Earth orbits in 24 hours.

As shown in Table 3.2a, low-Earth orbits for satellites flying sensors used for volcanological thermal applications are all inclined at a high angle, typically  $\sim 98^\circ$ , to the Equator. This allows the orbit to move (precess) around the Earth at almost the same rate that the Earth rotates around the Sun. An inclination of  $>90^\circ$  means that the satellite orbits the Earth in the opposite direction to the planet's rotation, thereby maintaining a retrograde orbit. This means that the satellite effectively back steps, with respect to the Earth's rotation, during each orbit so as to maintain the same position relative to the Sun. Thus, the satellite is able to cross the Equator from north-to-south (in descending mode) at the same local time during each orbit. Likewise, they cross from south-to-north (in ascending mode) at the same

Table 3.2a. Orbital and angular field of view characteristics for LEO orbiting satellites used for thermal remote sensing of volcanism.

Satellite series	Name	Sensor	Altitude (km)	Inclination (degrees)	Orbital period (minutes)	Equatorial crossing time		Field of view (± degrees from nadir)
						Descending (local time)	Ascending (local time)	
NOAA	6, 8, 10, 12	AVHRR	833	98.7	101.58	7:30	19:30	55.4
NOAA	7, 9	AVHRR	870	98.9	102.37	2:30	14:30	55.4
NOAA	11, 13, 14	AVHRR	870	98.9	102.37	1:30	13:30	55.4
Landsat	4, 5	TM	705	98.2	98.8	9:45	21:45	7.5
	7	ETM+	705	98.2	98.8	10:00	22:00	7.5
EOS	Terra	MODIS/ ASTER	705	98.7	98.9	10:30	22:30	55 (MODIS)
ERS	1, 2	ATSR	780	98.5	100	10:30	22:30	23.45

Table 3.2b. *Orbital, swath width and repeat period characteristics of LEO orbiting satellites calculated using data given in Table 3.2a. Note that ATSR has a curved scan geometry (see Prata et al., 1990), so the overlapping swath width calculated for a non-curved swath will be an over-estimate. The swath width of 500 km is taken from Prata et al. (1990).*

Satellite series	Name	Sensor	Orbits per day	Swath width (km)		No. orbits for complete coverage	Time required or repeat coverage (Days)	
				Overlapping	Non-overlapping		Descending	Descending + ascending
NOAA	6, 8, 10, 12	AVHRR	14.2	2925	2840	14	1	0.5
NOAA	7, 9	AVHRR	14.1	3094	2840	14	1	0.5
NOAA	11, 13, 14	AVHRR	14.1	3094	2840	14	1	0.5
Landsat	4, 5	TM	14.6	185	171.5	234	16	8.0
	7	ETM+	14.6	185	171.5	234	16	8.0
EOS	Terra	MODIS	14.6	2330	2330	17	1.2	0.6
ERS	1, 2	ATSR	14.4	685	500	80	5.6	2.8

local time every night. For example, Landsat-7 crosses the Equator during its descent at 10:00 local time during every orbit. It crosses the Equator on the dark side half an orbit (49.45 minutes) later at 22:00 local time. This maintains a reliable and predictable overpass time and image-acquisition frequency. In addition, the images will have the same shadows and degrees of solar heating in them from year to year, if taken on the same date. As a result, any changes will be due to surface changes, rather than changes in illumination or solar heating differences throughout a 24 hour period.

### 3.1.3 LEO-based sensor swath width, return period and temporal resolution

Satellite return period can be defined as the time needed for a satellite to return to a location over a given point on the Earth's surface. The duration of this period is determined by the satellite orbital period and the sensor swath width. Take two low-Earth-orbit satellites with the same orbital period. The first has a wide swath and the second a narrow swath. The narrow-swath sensor will require a greater number of orbits to achieve complete coverage of the Earth's surface than the wide-swath sensor. The satellite equipped with the narrow-swath sensor will thus take longer to return to the starting point. As a result, the satellite return period will be longer in the second case than in the first.

Repeat coverage can now be defined as the time required to obtain one day-time (ascending) and one night-time (descending) image for every point of the Earth's surface. This determines the temporal resolution of the sensor carried by the satellite. Thus, to understand temporal resolution, the satellite orbital period must be defined, as in [Section 3.1.1](#), as well as the sensor swath width.

Sensor swath width ( $W_{\text{swath}}$ ) can be defined as the along-scan width of the ground sector imaged during an overpass. Swath width can be calculated using the satellite altitude ( $S_h$ ), radius of the Earth ( $R = 6374 \text{ km}$ ) and total angular field of view of the sensor ( $\alpha_{\text{tot}}$ ) in:

$$W_{\text{swath}} = 2 \left\{ R \left[ \sin^{-1} \left( \Omega \sin \frac{\alpha_{\text{tot}}}{2} \right) - \frac{\alpha_{\text{tot}}}{2} \right] \right\} \quad (3.2a)$$

in which

$$\Omega = (S_h + R)/R. \quad (3.2b)$$

Note that  $\alpha_{\text{tot}}/2$  is the angular field of view from nadir to the edge of the scan. The total angular field of view for an AVHRR image is, for example,  $110.8^\circ$ . This extends  $\pm 55.4^\circ$  either side of nadir, so that  $\alpha_{\text{tot}}/2$  is  $55.4^\circ$  (see [Appendix F](#) for full definition of satellite scan notation). Angular fields of view for AVHRR, TM/ETM+, MODIS and ASTER, and the swath widths that these yield, are given in [Table 3.2b](#).

Swath width can be used to estimate the number of orbits ( $n_{\text{complete}}$ ) required to image every point around the Earth's equator, of circumference  $C$  ( $40\,050 \text{ km}$ ), in:

$$n_{\text{complete}} = C/W_{\text{swath}}. \quad (3.3a)$$

This can be converted to the time required for full Earth coverage at the equator ( $t_{\text{complete}}$ ) by multiplying by orbit period ( $P$ ),

$$t_{\text{complete}} = P n_{\text{complete}}. \quad (3.3b)$$

This now allows us to define the repeat coverage, or temporal resolution, of the sensor as given in [Table 3.2b](#).

### *3.1.3.1 Wide-swath example: AVHRR (Table 3.2b)*

Given a non-overlapping AVHRR swath of 2840 km, and the orbital period of the NOAA satellite on which AVHRR flies (~102 minutes), the full 40 000 km equatorial circumference of the Earth can be imaged in 14 orbits, or once in 24 hours. Because each point on the surface is imaged once every 24 hours during the descending mode of the orbit, and once every 24 hours during the ascending mode, the effective return period is 12 hours. The first (descending) overpass will occur prior to the local noon, and the second (ascending) pass will occur after local noon. It is the policy of NOAA to keep at least two satellites in-orbit at any one time, each separated by 12 hours. Using two satellites in tandem decreases the equatorial return period to six hours, so that any point on the Equator is imaged four times per day by sensors flown on the two satellites. However, it is important to note that while imaging of a particular point may occur every 12 hours, each image will have widely varying view angles (and thus pixel sizes and atmospheric effects). Images of the same point at the same viewing angle will occur far less frequently, i.e., every few days to weeks.

### *3.1.3.2 Narrow-swath example: TM (Table 3.2b)*

In comparison, the narrower non-overlapping TM swath of 171.5 km means that the complete coverage of the equatorial circumference requires 233 orbits or, given the 99 minute orbital period, 16 days to be imaged. As shown in [Figure 3.3a](#), rotation of the Earth between two sequential Landsat orbits means that the center points of the two 185-km-wide TM image swaths obtained during those consecutive orbits will be separated by an equatorial distance of 2752 km. As can be seen from [Figure 3.3b](#), it will take 16 days to fill the gap. Thus, the daytime return period of TM is typically quoted as 16 days. However, as with the AVHRR, each sub-orbital point on the Earth's surface is imaged once during the descending mode of each orbit and once during the ascending mode. If the nighttime (ascending) Landsat overpasses are also considered, the effective return period for TM reduces to 8 days.

### *3.1.3.3 The effect of polar orbit convergence*

Orbit convergence towards the poles mean that regions towards the poles can be imaged more frequently. Erebus at 78° south, for example, can be imaged five times every day by any single NOAA-based AVHRR sensor. Given two orbiting satellites, this means that 10 images per day are available at this latitude. Likewise, as shown in [Table 3.3](#), TM images increase in overlap from 7.3% at the equator to 83.9% at 80° north and south. Imaging frequency for points within overlapping regions will be twice as high as in non-overlapping

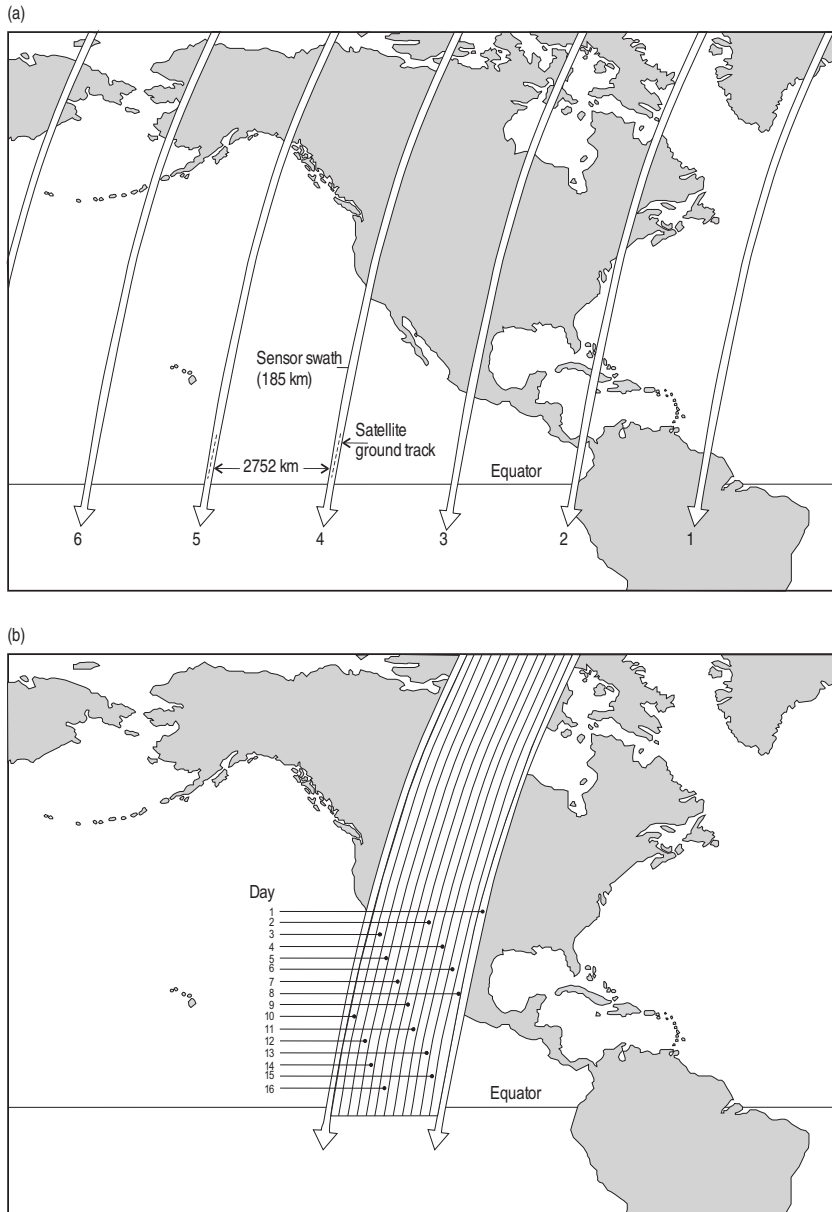


Figure 3.3 (a) Spacing between adjacent Landsat orbit tracks at the equator. The Earth revolves 2 752 km to the east at the equator between each overpass, so that a 2 567 km gap is left between each 185-km-wide image swath. (b) Timing of adjacent Landsat coverage swaths. Adjacent swaths are imaged seven days apart. We see that it takes 16 days to fill the gap between two adjacent swaths (as marked with the two arrowed swaths) so that it takes 16 days to re-image swath 1; it also takes 16 days to achieve full global coverage. This period can be reduced by increasing the swath width, thereby reducing the size of the gap that needs to be filled [from USGS/NOAA (1984, Figs. 5.2 and 5.3); as reproduced in Lillesand and Kieffer (1987, Figs. 9.20 and 9.21): this material is reproduced with permission of John Wiley & Sons, Inc].

Table 3.3. Percent side-lap in TM images with latitude, and resulting overlapping and non-overlapping swath widths [side-lap from Table 5.1 of NASA (1998)].

Latitude (degrees)	Image side-lap (%)	Overlapping swath width (km)	Non-overlapping swath width (km)	Width of overlap (km)
0	7.3	185	171.5	13.5
10	8.7	185	168.9	16.1
20	12.9	185	161.1	23.9
30	19.7	185	148.6	36.4
40	29.0	185	131.4	53.7
50	40.4	185	110.3	74.7
60	53.6	185	85.8	99.2
70	68.3	185	58.6	126.4
80	83.9	185	29.8	155.2

regions, occurring on the seventh day, as well as the first day, of each 16-day-long return period cycle. Thus, above 80° north or south the day-time repeat coverage for TM is eight days for ~84% of the surface, i.e., within the 155-km-wide zone of overlap. This increases to four days if ascending and descending passes are considered.

### 3.1.4 Geostationary orbits

Geostationary platforms are stationed above the equator. They move with the Earth's rotation, having an orbital period of exactly 24 hours. As a result, they keep track with the same sub-orbital point on the Earth's surface, thus remaining fixed directly above a point on the equator. Following the calculations completed in Table 3.1, to achieve this the satellite must be placed at an altitude of 35 900 km at 0° inclination. A series of weather satellites, that provide data suitable for volcanological thermal applications (see Chapter 1), have been placed around the equator about every 60° to 75°. These are GOES-E (at 75° W), GOES-W (at 135° W), MTSAT (at 140° E) and METEOSAT (at 0° E). From these locations the satellites can provide imagery of the entire Earth disk, the coverage provided by GOES-W and -E being given in Figure 3.4 by way of example, with the spacing of the four satellites allowing complete Earth coverage. Only regions towards the poles cannot be imaged due to problems of Earth curvature (see Figure 3.4). As described next, geostationary orbits allow rapid, repeat observations of large, fixed areas covering almost the entire Earth disk.

### 3.1.5 Geostationary sensor swath width, return period and temporal resolution

Given that sensors flown on geostationary platforms are maintained in fixed positions, the repeat coverage, or temporal resolution, is not determined by the orbital period and swath width, but instead by the scanning rate. To view a surface area with a radius equal to that of

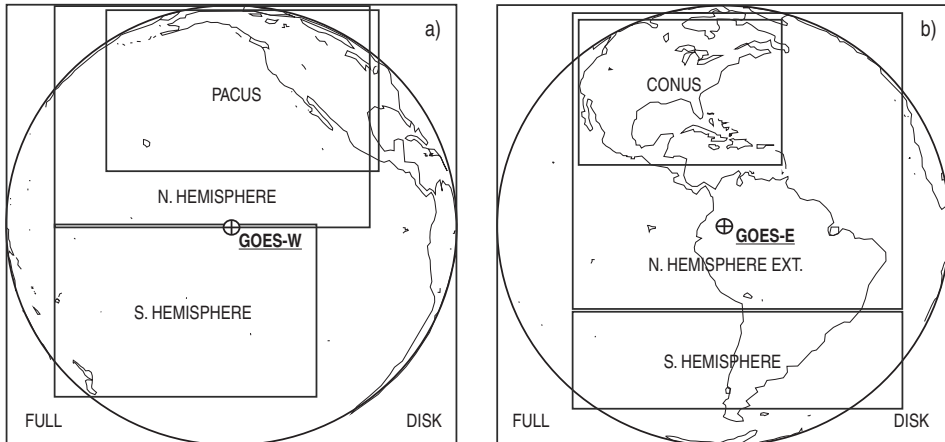


Figure 3.4 Hemispherical views of (a) GOES-West and (b) GOES-East [from NOAA Satellite Services Division]. The imaging frequency of each of the labeled zones is given in Tables 3.4 and 3.5 (credit to NOAA).

the Earth, from a geostationary satellite altitude of 35 900 km, Equation (3.2a) indicates that the total angular field of view for the image needs to be  $\sim 16^\circ$  to cover the entire Earth disk. Thus, the Imager flown on GOES covers an angular field of view which is  $19.2^\circ$  (east-to-west) by  $20.8^\circ$  (north-to-south). The sampling rate for the GOES Imager is  $183.3 \mu\text{sec}$  per pixel (or 5456 samples per second) in the IR and  $45.8 \mu\text{sec}$  per pixel (or 21 840 samples per second) in the VIS. Thus, a single line of visible data (5236 pixels long) spanning the full  $19.2^\circ$  angular field of view, can be collected in:

$$5236 \text{ pixels per line} \times 4.58 \times 10^{-6} \text{ seconds per pixel} = 0.24 \text{ seconds per line.}$$

If the full disk is covered in 6530 lines, then it takes

$$6530 \text{ lines} \times 0.24 \text{ seconds per line} = 1566 \text{ seconds.}$$

That is, 26 minutes and 6 seconds to scan the full disk. Thus, the return period (or temporal resolution) for the full Earth disk is nominally  $\sim 30$  minutes.

Instead, Meteosat spins at a rate of 100 rpm (= rotations of the satellite per minute) about an axis parallel to the north–south axis of the Earth, with a new line of data being collected with each rotation of the satellite. In other words, with each satellite spin the thermal sensor aboard Meteosat (SEVIRI) performs an east-to-west scan of the Earth’s surface. Each revolution nominally lasts 0.6 s. To ensure the necessary north-to-south coverage, the scan mirror is stepped south-to-north in steps of 9 km at the end of each spin. The mirror thus has to complete 100 steps every minute, so that 100 image lines are acquired in one minute. The full Earth disk image is obtained in 1250 steps, so that full disk coverage takes

$$1250 \text{ steps}/100 \text{ steps per minute} = 12.5 \text{ minutes.}$$

At the end of the acquisition of the full disk image, the scan mirror is driven back to its initial starting point and the next scan begins. This retrace takes about 2 minutes, which results in a maximum return period of 15 minutes for the entire disk.

### *3.1.5.1 Rapid geostationary scanning*

Higher temporal resolutions can be achieved by targeting small sectors within the full disk, and repeatedly scanning just that sector. GOES temporal resolution for certain sectors is, for example, increased by scanning smaller sectors within the Earth's disk during certain scans. These sectors are identified in [Figure 3.4](#). The sectors, being smaller than the full Earth disk, require shorter scanning times of between 5 minutes and 14 minutes, with the scan duration and return period for each sector being given in [Tables 3.4](#) and [3.5](#).

### *3.1.5.2 Time of acquisition*

Because of the high temporal resolution, geostationary data are often used for precise event timing. The acquisition time for a given pixel is thus an important parameter. The exact time of acquisition ( $t_{\text{acquisition}}$ ) for a given pixel in a geostationary satellite image (at sample number  $s_{\text{samp}}$  in line number  $y$ ) can be obtained using the scan start time ( $t_{\text{start}}$ ) in

$$t_{\text{acquisition}} = t_{\text{start}} + r_{\text{samp}} [(y - 1) \times n_{\text{samp}} + s_{\text{samp}}], \quad (3.4)$$

*Table 3.4. Sectors covered by the GOES-West and -East imagers, with sector acquisition duration and return period. For map location of each sector, see [Figure 3.4](#) (from NOAA Satellite Services Division: Credit to NOAA).*

Satellite	Sector name	Sector extent	Acquisition duration (mm:ss)	Sector return period
GOES-West	Full Disk	Earth Edge	26:06	3 hours
	N. Hemisphere (incl. PACUS)	70N-0N, 160E-100W	10:15	30 minutes
	PACUS	70N-14N, 180W-95W	06:35	15 minutes
	S. Hemisphere	0N-50S, 160E-115W	07:00	30 minutes
GOES-East	Full Disk	Earth Edge	26:06	3 hours
	N. Hemisphere Extended (incl. CONUS)	65N-20S, 120W-30W	14:13	30 minutes
	CONUS	60N-14N, 115W-68W	04:49	15 minutes
	S. Hemisphere	20S-57S, 122.5W-26.5W	04:48	30 minutes

*Table 3.5a. Example of GOES-West routine scanning schedule (from NOAA Satellite Services Division: Credit to NOAA). The schedule for the first three hours of the day are given. The cycle begins and ends with a full disk scan and then repeats itself for the rest of the day. On occasion, the routine schedule is departed from, and rapid or super-rapid scan schedule applied. This achieves more frequent imaging of smaller sectors and is typically used for hurricane and severe storm tracking.*

Scan start time (UTC)	Scan start time: minutes past the hour	Scan sector	Scan duration (mm:ss)
00:00:00	00	Full Disk	26:06
00:30:00	30	N. Hemisphere (incl. PACUS)	10:15
00:45:00	45	PACUS	06:35
00:51:55	52	S. Hemisphere	07:00
01:00:00	00	N. Hemisphere (incl. PACUS)	10:15
01:15:00	15	PACUS	06:35
01:21:55	22	S. Hemisphere	07:00
01:30:00	30	N. Hemisphere (incl. PACUS)	10:15
01:45:00	45	PACUS	06:35
01:51:55	52	S. Hemisphere	07:00
02:00:00	00	N. Hemisphere (incl. PACUS)	10:15
02:15:00	15	PACUS	06:35
02:21:55	22	S. Hemisphere	07:00
02:30:00	30	N. Hemisphere (incl. PACUS)	10:15
02:45:00	45	PACUS	06:35
02:51:55	52	S. Hemisphere	07:00
03:00:00	00	Full Disk	26:06

in which  $r_{\text{samp}}$  is the pixel sampling rate and  $n_{\text{samp}}$  is the number of samples per line. For the GOES infrared bands,  $r_{\text{samp}}$  is 183.3  $\mu\text{sec}$  per pixel. Thus, for a scan starting at 01:45:00.0Z, pixel 500 in line 700 will be collected after:

$$183.3 \mu\text{sec per pixel} \times [(700 - 1) \times 5236 \text{ pixels per line} + 500 \text{ pixels}] = 671 \text{ seconds.}$$

This is 11.2 minutes after the scan began, meaning that the time of pixel acquisition is 01:51:10.2Z.

### 3.2 The sensor: the basic acquisition system

Most satellite sensors used for volcanological thermal analyses operate in the same basic way, with the primary components of a typical satellite-flown sensor being summarized in [Figure 3.5](#). Operation of such a system involves scanning of the Earth's surface so that energy from discrete areas (or pixels) on the Earth's surface are focused by the sensor optics, through a spectral filter (that cuts out the wavelength of interest), onto a series of detectors.

**Table 3.5b.** Example of GOES-East routine scanning schedule (from NOAA Satellite Services Division: Credit to NOAA). The schedule for a three hour period is given. The cycle begins and ends with a full disk scan and then repeats itself for the rest of the day.

Scan start time (UTC)	Scan start time: minutes past the hour	Scan sector	Scan duration (mm:ss)
02:45:00	45	Full Disk	26:06
03:15:00	15	N. Hemisphere Extended (incl. CONUS)	09:44
03:31:30	32	CONUS	04:48
03:39:10	39	S. Hemisphere	04:49
03:45:00	45	N. Hemisphere Extended (incl. CONUS)	09:44
04:01:30	02	CONUS	04:48
04:09:10	09	S. Hemisphere	04:49
04:15:00	15	N. Hemisphere Extended (incl. CONUS)	09:44
04:31:30	32	CONUS	04:48
04:39:10	39	S. Hemisphere	04:49
04:45:00	45	N. Hemisphere Extended (incl. CONUS)	09:44
05:01:30	02	CONUS	04:48
05:09:10	09	S. Hemisphere	04:49
05:15:00	15	N. Hemisphere Extended (incl. CONUS)	09:44
05:31:30	32	CONUS	04:48
05:39:10	39	S. Hemisphere	04:49
05:45:00	45	Full Disk	26:06

*Note.* On occasion, the routine schedule is departed from and rapid or super-rapid scan schedule applied. This achieves more frequent imaging of smaller sectors and is typically used for hurricane and severe storm tracking.

Each detector produces a continuous electrical signal that is proportional to the in-coming energy. This electrical signal (voltage) is then amplified and converted from an analog to a digital signal by the Analog/Digital (A/D) converter. The digital signal is then sampled in time to output a discrete digital number (DN) for each spatial element, or pixel, of the image. Calibration allows the DN to be converted back to spectral radiance (see Electronic Supplement 2). As sketched in [Figure 3.5](#), rotation of the scanning mirror builds the image pixel-by-pixel in the scan (E–W) direction, and motion of the satellite builds the image line-by-line in the satellite track (S–N) direction (see [Appendix F](#) for further details).

As a result, energy emitted by each discrete unit area on the Earth’s surface is measured in terms of an energy distributed across a detector footprint. This footprint is the equivalent of an image pixel. Thus, energy is recorded by each detector in terms of power (watts) per unit area ( $\text{m}^2$ ) per unit wavelength ( $\mu\text{m}$ ) per solid angle (steradian). We next detail this data acquisition sequence with special reference to two standard sensors, these being the AVHRR, as reviewed by Cracknell (1997), and the GOES Imager, as documented by the GOES I-M data book (NASA, 1996).

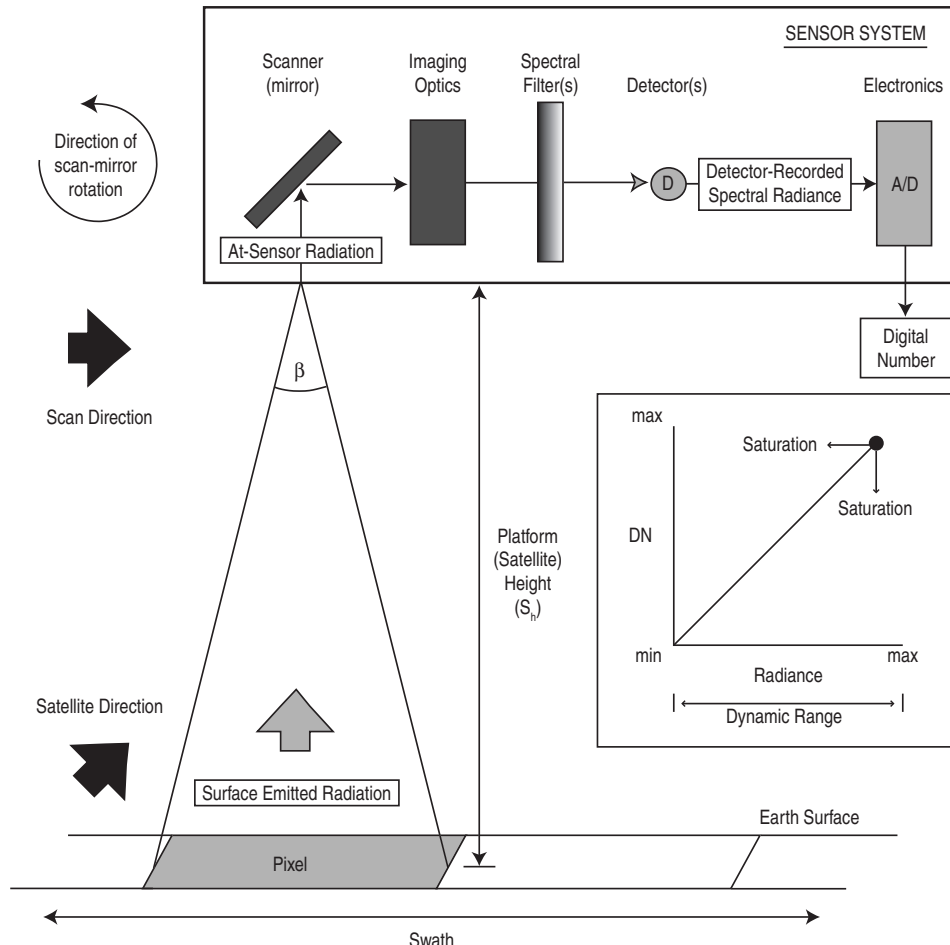


Figure 3.5 The primary components of a sensor system. A scanner equipped with a rotating scanning mirror is depicted here. The detector has an angular field of view that opens at an angle of  $\beta$  radians. At-detector radiance is converted to a Digital Number (DN) by the Analog-to-Digital (A/D) converter. DN can be converted to radiance using a linear conversion (as inset). Marked on the conversion is the dynamic range of the detector and the saturation point (i.e., the upper limit of the dynamic range).

### 3.2.1 Scanning and data acquisition

The AVHRR scans using a continuously rotating mirror which rotates in a clockwise direction. The mirror rotates at 360 rpm, sweeping a  $110.8^\circ$  wide swath of the Earth's surface. The clockwise rotation means that the surface is scanned from east-to-west. One rotation of the scan mirror allows one scan of the Earth's surface, plus collection of in-flight calibration data, so that one line of image data is collected with each scan. Such a scanning mode is typical of LEO-based sensors.

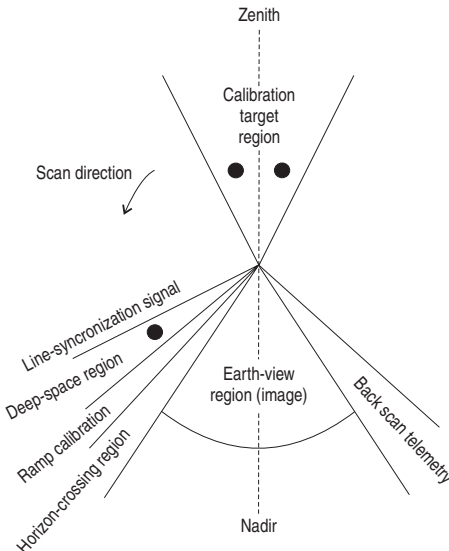


Figure 3.6 Data collected during a single rotation of AVHRR’s scanning mirror [from Cracknell (1997, Fig. 1.10)]. The 2048 pixel swath of image data is marked using the curved line, where the three black dots mark the location of the calibration points used to define the  $y = mx + c$  form of the DN-to-radiance conversion as inset in Figure 3.5. While the two black dots of the “calibration target region” mark the calibration measurement provided by the onboard blackbody of known temperature, that of the “deep-space region” marks the radiance measurement of deep space used to define the conversion coefficients (see Electronic Supplement 2 for details as to how these measurements are used to achieve calibration).

As shown in Figure 3.6, at the beginning of each AVHRR scan the mirror passes a physical location where a magnetic signal marks the beginning of the scan line. Next, the mirror looks to deep space, before receiving a ramp calibration signal. The ramp signal increases in steps of 6.26 mV with each scan line so that the calibration ramps from zero to the maximum extent of the radiometer output (6.41 volts) in 1024 scan lines. The ramp is then reset to zero. During the Earth scan portion of the mirror rotation the ground data are collected. Finally, internal calibration data are collected during the mirror back sweep. These calibration data are included at the beginning of each image line, along with various housekeeping data. The scanning mirror rotation rate means that 360 lines of image and calibration data are collected every minute.

In the case of a LEO-based sensor, the scanning mirror sweeps east-to-west to obtain an image line, with the south-to-north (in ascending mode) motion of the satellite building the image in the latitudinal direction. Differences from this standard scanning mode are highlighted in Appendix E. ATSR, for example, features a conical scanning geometry, allowing a nadir swath and forward-looking swath to be collected with each scan. As a result, the ATSR scan geometry is somewhat curved, but includes a forward and nadir sweep allowing two measurements of the same point on the Earth’s surface separated by 137 seconds. MODIS has

a standard east-to-west scanning geometry, but scans each swath in banks of 10, 20 or 40 pixels (for the 1.0, 0.5 and 0.25 km resolution bands, respectively). Thus, each MODIS image line is collected in 10–40-pixel-wide strips, a feature which increases the pixel dwell time.

Because geostationary satellites sit in a fixed location above an unchanging sub-equatorial point, if the scanning motion was just east-to-west, geostationary sensors would solely collect data for a single east–west strip of the Earth’s surface located along the equator immediately below the satellite. Thus the sensor must also step north-to-south at the end of each scan to acquire the full disk. In the case of GOES, this is achieved by rotating the mirror in an east-to-west direction to collect each line of data. At the end of each sweep the scan mirror elevation is stepped south. The next scan line is then obtained by rotating the mirror in the opposite (west-to-east) direction. In the case of Meteosat, the satellite spinning motion allows each east–west sweep. This collects each image line. The scan mirror is then rotated south-to-north in steps of  $125.8 \mu\text{rad}$  at the end of each sweep, across a total scan range of  $11^\circ$ . This allows the image to be built in the south-to-north dimension.

### 3.2.2 Imager optics and acquisition of in-coming signal

Radiance arriving at the satellite is directed onto the detectors via the imager optics. In the case of the AVHRR and GOES-Imager, the optical elements are similar. Those for the GOES-Imager are given in Figure 3.7. Incoming radiance is directed by the scanning mirror

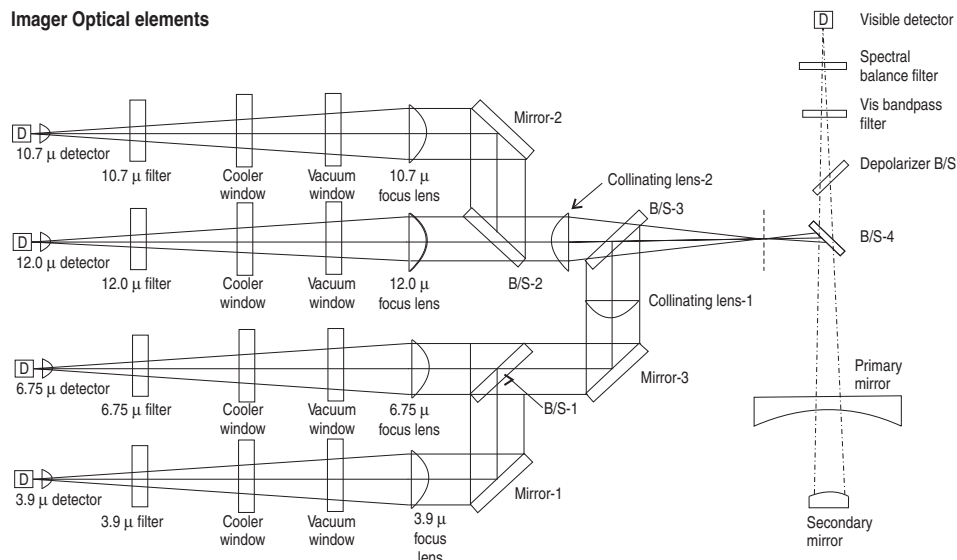


Figure 3.7 Schematic of the GOES Imager [From *GOES I-M Data Book*, NASA (1996), Fig. 28], showing how incoming radiance is split into five beams, filtered (to isolate the waveband of interest) and focused onto five detectors (marked “D”). B/S = beam splitter (credit to NOAA).

onto a telescope which collects the radiance and focuses the beam. Next, beam splitters separate the radiance into the spectral bands of interest. The IR energy is split and deflected onto a series of detectors that reside within a radiative cooler. For the GOES-Imager, the IR energy is separated into the 3.9  $\mu\text{m}$ , 6.75  $\mu\text{m}$ , 10.7  $\mu\text{m}$ , and 12  $\mu\text{m}$  wavebands. The four beams are then directed into the radiant cooler and onto the appropriate detector. While the 3.9  $\mu\text{m}$  detector is InSb (indium antimonide), the 6.75  $\mu\text{m}$ , 10.7  $\mu\text{m}$  and 12  $\mu\text{m}$  detectors are HgCdTe (mercury cadmium telluride). To reduce dark current noise, these sensors must be cooled to  $\sim 100$  K. While detector cooling reduces noise levels and increases the precision of the detectable signal, the detectors themselves define the pixel size and shape; the detectors for the four GOES-Imager bands are square with a 112  $\mu\text{rad}$  field of view. Between them, the beam splitter and detectors thus determine the sensor spectral and spatial resolutions.

### **3.2.3 A/D conversion and calibration**

In the case of the AVHRR and GOES-Imager, the detector signal for each band is amplified, filtered and then converted from an analog signal to a 10-bit digital signal by an A/D converter which, for the AVHRR, samples all detectors every 25  $\mu\text{sec}$ . This sampling rate is set to match the sampling rate of the sensor. We see this from the following series of calculations.

- The scanning mirror, rotating at 360 rpm, collects 360 image lines every minute, or one line every 0.1667 seconds.
- During each scan, the image swath occupies  $110.8^\circ$ , or 31%, of the full  $360^\circ$  mirror sweep. Thus it takes  $0.31 \times 0.167 \text{ s} = 0.051 \text{ s}$ , to obtain the image swath.
- Given that the swath is composed of 2048 pixels, this means that the acquisition time per pixel is  $0.051 \text{ s} / 2048 \text{ pixels}$ , or  $2.5 \times 10^{-5} \text{ seconds per pixel}$ .
- Hence the sampling rate of the A/D converter is also 25  $\mu\text{sec}$ .

The output is a digital number (DN) which, for 10-bit data, will be in the range of 0 to 1024. Calibration allows this to be converted back to the sensor recorded radiance ( $R^*$ ), typically through a linear conversion which has the form given in [Chapter 2](#). However, calibration sometimes diverges from a linear form, with the exact calibration routine varying from sensor to sensor (as explored in Electronic Supplement 2).

## **3.3 Spatial resolution<sup>1</sup>**

The sensor spatial resolution is determined by the height of the satellite above the Earth's surface ( $S_h$ ) and the detector instantaneous field of view (IFOV,  $\beta$ ). The IFOV is defined as the “cone angle within which incident energy is focused on the detector” (Lillesand and

<sup>1</sup> Note that all scan geometry terminology used here is defined in [Appendix B](#).

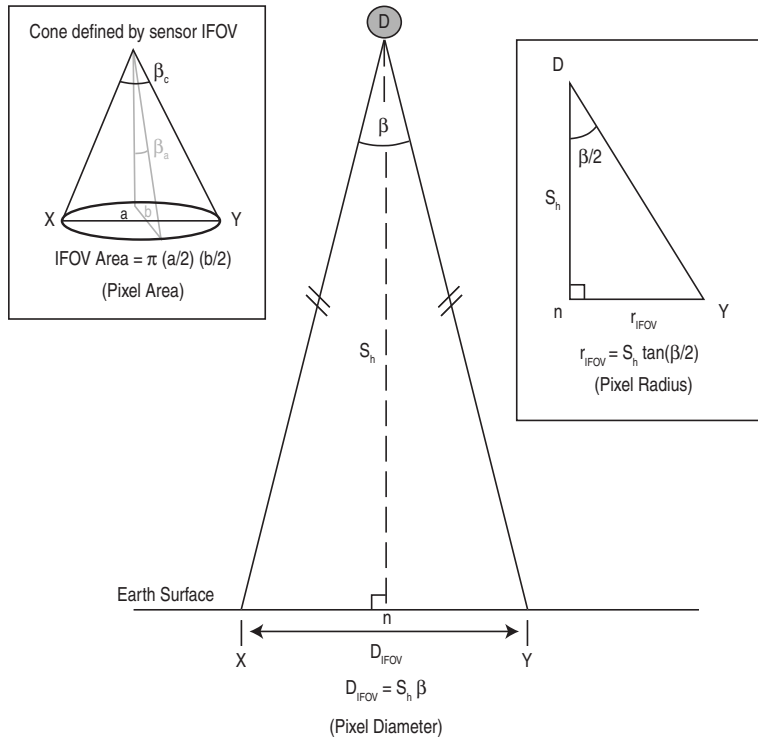


Figure 3.8 Pixel diameter for a detector with an angular field of view opening at angle  $\beta$  and flown on a satellite at height  $S_h$ , plus the geometry required to estimate pixel radius and area at nadir.

Kiefer, p. 408, 1987). Its size is determined by the instrument's optical system and the size of the detector element.

As shown in Figure 3.8, simple geometry dictates that the ground surface area covered by the IFOV will have a diameter ( $D_{\text{IFOV}}$ ) of:

$$D_{\text{IFOV}} = 2[S_h \tan(\beta/2)] \quad (3.5a)$$

which reduces to

$$D_{\text{IFOV}} = S_h \beta. \quad (3.5b)$$

Thus, the spatial resolution for a sensor with a 1.4 milliradian IFOV, and flown on a satellite orbiting 850 km above the Earth's surface, will be:

$$D_{\text{IFOV}} = (850\,000 \text{ m}) \times (1.4 \times 10^{-3} \text{ rad}) = 1190 \text{ m.}$$

In other words, the ground cell across which radiance is being integrated and measured, i.e., the pixel, will have a diameter of 1.19 km.

This geometry applies to a pixel at nadir, i.e., directly beneath the sensor. For off-nadir viewing, scan angle and Earth curvature effects will have to be taken into account. The arc-length distance ( $L$ ) between the sub-satellite point at nadir and the point on the Earth's surface being viewed at scan angle  $\alpha$  can be calculated using the geometry given in Figure 3.9, so that:

$$L = r \left\{ \sin^{-1} \left[ \frac{(S_h + r)}{r} \sin \alpha \right] - \alpha \right\} \quad (3.6)$$

in which  $r$  is the radius of the Earth (6378 km). This can now be used to estimate the along-scan pixel dimension ( $L_a$ ) at scan angle  $\alpha$ . To do this we first need to estimate the angle between the nadir point and the pixel outer and inner edges ( $\alpha_2$  and  $\alpha_1$ , respectively). These can be calculated from:

$$\alpha_2 = \alpha + \beta/2 \quad (3.7a)$$

$$\alpha_1 = \alpha - \beta/2, \quad (3.7b)$$

$\alpha$  being the scan angle to the center of the pixel. Substituting these angles into Equation (3.6) now allows the arc-length distance to the pixel outer edge ( $L_2$ ) and the pixel inner edge ( $L_1$ ) to be calculated, i.e.,

$$L_2 = r \left\{ \sin^{-1} \left[ \frac{(S_h + r)}{r} \sin \alpha_2 \right] - \alpha_2 \right\} \quad (3.8a)$$

and

$$L_1 = r \left\{ \sin^{-1} \left[ \frac{(S_h + r)}{r} \sin \alpha_1 \right] - \alpha_1 \right\}. \quad (3.8b)$$

Subtracting the two will give the difference in distance between the pixel inner and outer edges, or the pixel width in the along-scan direction, i.e.,

$$L_a = L_2 - L_1 = r \left\{ \sin^{-1} \left[ \frac{(S_h + r)}{r} \sin \alpha_2 \right] - \alpha_2 \right\} - r \left\{ \sin^{-1} \left[ \frac{(S_h + r)}{r} \sin \alpha_1 \right] - \alpha_1 \right\}. \quad (3.9)$$

For example, take a pixel at the extreme edge of an AVHRR image. This will be located at scan angle  $55.7^\circ$ , i.e.,  $1024 \text{ pixels} \times 0.95 \text{ mrad}$  from nadir ( $0.95 \text{ mrad}$  being the AVHRR scan increment angle and  $1024 \text{ pixels}$  being the number of pixels between the image center and the image edge). Now, for a nominal AVHRR IFOV of  $1.4 \text{ mrad}$ , angles  $\alpha_2$  and  $\alpha_1$  will be:

$$\alpha_2 = 0.9721 \text{ radians} + (0.0014 \text{ radians}/2) = 0.9728 \text{ radians}$$

and

$$\alpha_1 = 0.9721 \text{ radians} - (0.0014 \text{ radians}/2) = 0.9714 \text{ radians}.$$

Thus the distance to the pixel outer edge will be:

$$L_2 = 6378\,000 \text{ m} \left\{ \sin^{-1} \left[ \frac{(850\,000 \text{ m} + 6378\,000 \text{ m})}{6378\,000 \text{ m}} \sin 0.9728 \right] - 0.9728 \right\}$$

$$= 1531\,120 \text{ m} = 1531.12 \text{ km}$$

and the distance to the pixel inner edge will be:

$$L_1 = 6378\,000 \text{ m} \left\{ \sin^{-1} \left[ \frac{(850\,000 \text{ m} + 6378\,000 \text{ m})}{6378\,000 \text{ m}} \sin 0.9714 \right] - 0.9714 \right\}$$

$$= 1523\,826 \text{ m} = 1523.83 \text{ km.}$$

Thus the along-scan pixel dimension will be:

$$L_a = L_2 - L_1 = 1531.12 \text{ km} - 1523.83 \text{ km} = 7.29 \text{ km.}$$

In the cross-scan (track) direction, the pixel dimension ( $L_c$ ) can be calculated from the geometry given in [Figure 3.9b](#), so that:

$$L_c = 2 \left[ \left( \frac{r \sin \delta}{\sin \alpha} \right) \tan \left( \frac{\beta}{2} \right) \right] \quad (3.10a)$$

in which  $\delta$  is the angle from the center of the Earth to the pixel center. This is given by:

$$\delta = \sin^{-1} \left[ \frac{(S_h + r)}{r} \sin \alpha \right] - \alpha. \quad (3.10b)$$

In our AVHRR scan edge example, we obtain

$$\delta = \sin^{-1} \left[ \frac{(850\,000 \text{ m} + 6378\,000 \text{ m})}{6378\,000 \text{ m}} \sin 0.9721 \right] - 0.9721 = 0.2395 \text{ radians}$$

so that

$$L_c = 2 \left[ \left( \frac{6378\,000 \text{ m} \sin 0.2395}{\sin 0.9721} \right) \tan(0.0014/2) \right] = 2564 \text{ m} = 2.56 \text{ km.}$$

Now, the pixel area can be approximated by multiplying  $L_a$  and  $L_c$ .

Thus, we find that the AVHRR image covers a ground swath which extends 1530 km either side of nadir. Across this swath the pixel size increases from  $1.19 \text{ km} \times 1.19 \text{ km}$  at nadir ( $1.4161 \text{ km}^2$ ) to  $7.29 \text{ km} \times 2.56 \text{ km}$  ( $18.6624 \text{ km}^2$ ) at the scan edge. The variation in pixel dimension with scan angle is plotted in [Figure 3.10](#) and shows that distortion is more extreme in the scan direction than in the cross-scan direction. For narrower swaths, with smaller scan angles, the pixel distortion effect is less extreme. Landsat TM, for example, has a satellite height of 705 km, an IFOV of 0.0425 mrad and a scan which extends  $7.46^\circ$  either side of nadir. For this geometry we find that the image covers a ground swath which extends 92 km either side of nadir, and that the along-scan pixel dimension is

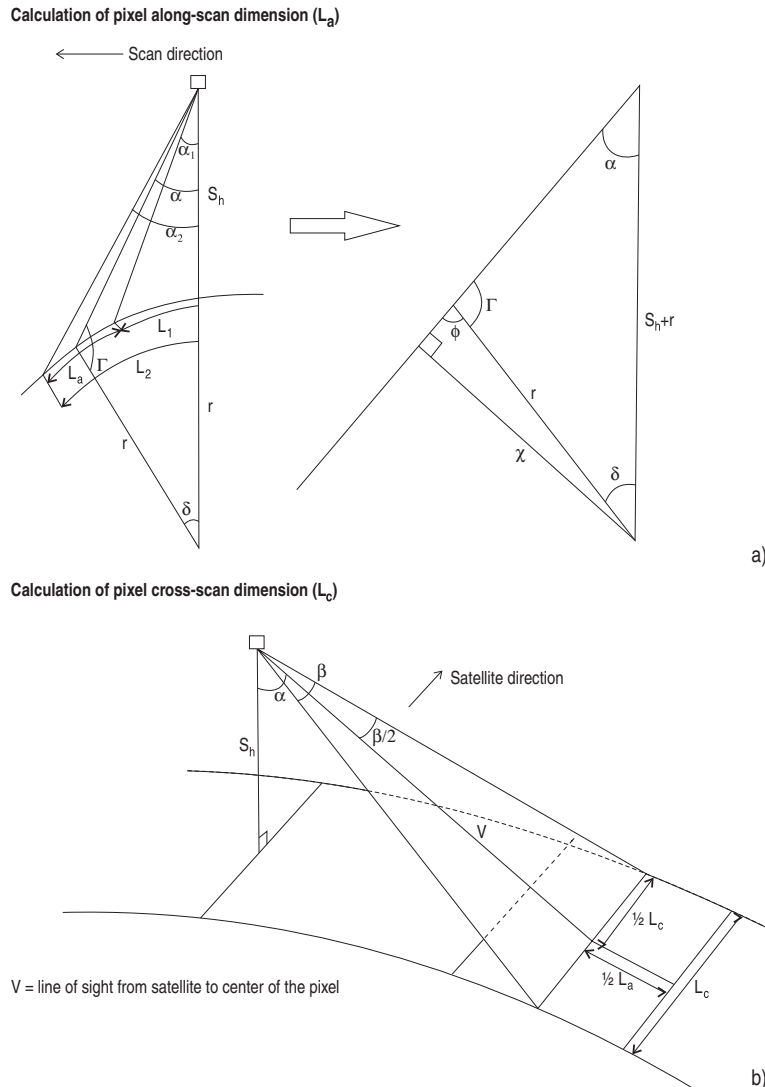


Figure 3.9 Geometrical relationships used to estimate pixel dimension in (a) the along-scan and (b) cross-scan directions.

29.96 m × 29.96 m (897.75 m<sup>2</sup>) at nadir, increasing to 30.57 m × 30.25 m (924.54 m<sup>2</sup>) at the scan edge.

### 3.3.1 Pixel overlap, rotation and shape

With increased scan angle, two other effects must be taken into account: pixel overlap and rotation. Because the pixel IFOV is greater than the scan increment angle, there will be a degree of overlap in both the along- and cross-scan directions.

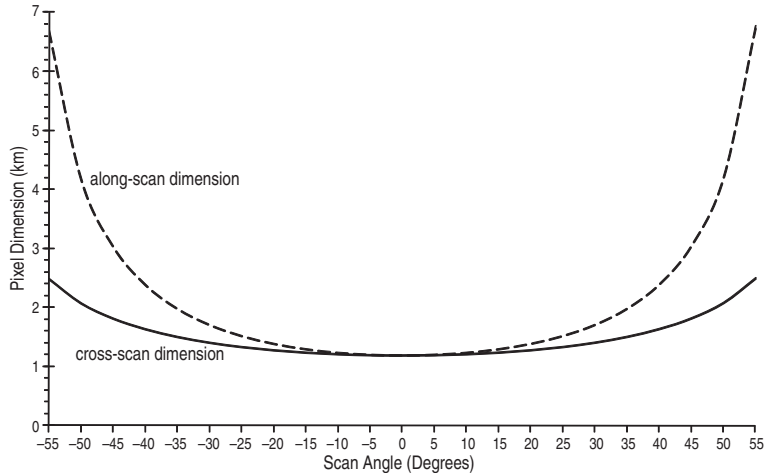


Figure 3.10 Increase in pixel dimension in the along-scan and cross-scan directions as a function of scan angle. Calculation is for a detector with an IFOV of 1.4 mrad, flown on a satellite operating 850 km above the Earth's surface, and covering a swath that extends 55° either side of nadir (i.e., the NOAA-AVHRR scan geometry).

The overlap in the scan direction can be calculated using the angle to the outer edge of pixel  $n$  [ $\alpha_2(n)$ ] centered at angle  $\alpha(n)$  and the angle to the inner edge of pixel  $n + 1$  [ $\alpha_1(n + 1)$ ] centered at angle  $\alpha(n + 1)$ . In this case,

$$\alpha_2(n) = \alpha(n) + \beta/2 \quad (3.11a)$$

and

$$\alpha_1(n + 1) = \alpha(n + 1) - \beta/2. \quad (3.11b)$$

Inserting these angles into Equation (3.6) yields the distance to the outer edge of pixel  $n$ ,  $L_2(n)$ , and the distance to the inner edge of pixel  $n + 1$ ,  $L_1(n + 1)$ . The difference between these two values [i.e.,  $L_2(n) - L_1(n + 1)$ ] is the width of the overlap, with the fractional overlap for pixel  $n$  ( $P_o$ ) being obtained from its along-scan dimension,  $L_a(n)$  in:

$$P_o = [L_2(n) - L_1(n + 1)]/L_a(n). \quad (3.12)$$

For an AVHRR pixel, the nominal IFOV of 1.4 mrad compares with a scan increment angle of 0.95 mrad. At nadir, the relevant angles will thus be:

$$\alpha_2(n) = 0 \text{ radians} + (1.4 \text{ mrad}/2) = 0.7 \text{ mrad}$$

and

$$\alpha_1(n + 1) = (0 \text{ radians} + 0.95 \text{ mrad}) - (1.4 \text{ mrad}/2) = 1.65 \text{ mrad}.$$

Use of these values in Equation (3.6) results in  $L_2(n)$  of 595 m and  $L_1(n+1)$  of 213 m, so that the pixels overlap by  $595 \text{ m} - 213 \text{ m} = 383 \text{ m}$ . Given that the pixel is 1190 m wide, this is equivalent to an overlap of 32%. The pixel will be overlapping by 32% in both the scan and back scan directions, so that only 36% of the pixel is non-overlapping in the scan direction. Although the overlap at the scan edge increases to 2155 m, in percentage terms the relative amount of overlap remains the same at 32%.

Overlap in the cross-scan, or satellite track, direction can be calculated using the difference between the pixel cross-scan dimension and the distance moved by the satellite between consecutive scans. If the distance moved by the satellite between scans is less than the pixel diameter, then there will be overlap. To calculate the distance the satellite has moved between two scans we first need to know the Earth surface distance traveled by the satellite during one orbit ( $D_{\text{earth}}$ ):

$$D_{\text{earth}} = 2\pi r, \quad (3.13)$$

which will be:

$$2 \times \pi \times 6378 \text{ 000 m} = 40\ 074\ 156 \text{ m.}$$

For AVHRR, the time required to complete one orbit is 102 minutes. Thus the velocity at which the satellite tracks across the surface is:

$$40\ 074\ 156 \text{ m}/6120 \text{ s} = 6548 \text{ m s}^{-1}.$$

Now, the AVHRR scan mirror rotates at a speed of 360 revolutions per minute, so that one sweep takes 1/6 of a second to complete. Thus, each scan is separated by a distance of

$$6548 \text{ m s}^{-1} \times 0.1667 \text{ s} = 1091 \text{ m.}$$

The difference between the cross-scan pixel dimension and the scan distance separation yields the overlapping pixel distance, which at nadir will be:

$$1190 \text{ m} - 1091 \text{ m} = 99 \text{ m.}$$

In terms of the fraction of the 1190 m pixel which is overlapping, we obtain

$$99 \text{ m}/1190 \text{ m} = 0.08.$$

In other words the AVHRR pixel overlaps its neighbor in the following row by 8%. There will also be an 8% overlap in the back track direction. In this case, as shown in [Figure 3.11](#), overlap increases with scan angle to 1400 m, or 56%, at 55°.

The effect of viewing angle on pixel dimension, distortion and overlap is sketched in [Figure 3.12](#). We see that, with increased scan angle, the pixel becomes (i) larger and (ii) increasingly elongated in the scan direction, with (iii) the overlap problem becoming worse with scan angle.

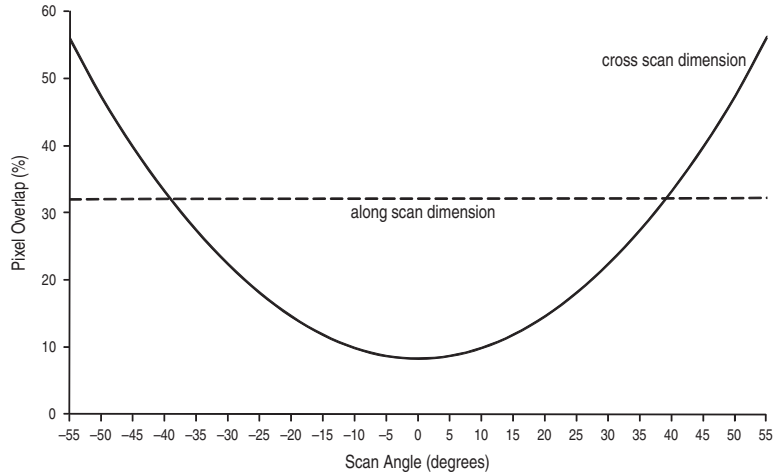


Figure 3.11 Pixel overlap in the along-scan and cross-scan directions as a function of scan angle. The detector characteristics of Figure 3.10 are used, with a scan increment angle of 0.95 mrad (i.e., the NOAA-AVHRR scan geometry).

### 3.3.1.1 Pixel rotation

This treatment is over-simplistic because it does not take into account pixel rotation, where pixels will also become rotated with scan angle. The angle of rotation will be equal to the scan angle, so that at a scan angle of 55° pixels undergo rotation by 55°. This effect is given in Figure 3.12, in which pixels are sketched without and with rotation. We see that, by introducing rotation, we complicate (accentuate) distortion and overlap problems.

### 3.3.1.2 A note on pixel shape

Because pixels are displayed in the image in a square format, it is tempting to assume that the ground area sampled by the pixel is also square (or rectangular for off-nadir imaging). However, the pixel shape depends on diffraction by the optics and detector shape, which can be oval or lozenge shaped. As sketched in Figure 3.12, for example, AVHRR pixels sample an oval-shaped ground area. Thus, to estimate pixel area in this case we need to assume an oval, rather than a square/rectangular shape. Take the AVHRR pixel in the example followed thus far in this chapter. The nadir pixel size is 1.19 km × 1.19 km so that, with the square pixel assumption, the pixel area is

$$1.19 \text{ km} \times 1.19 \text{ km} = 1.4161 \text{ km}^2.$$

However, at nadir the sampled area ( $A_{\text{pixel}}$ ) will be circular, so that  $A_{\text{pixel}} = \pi r^2$ , i.e.,

$$A_{\text{pixel}} = \pi \left( \frac{1.19 \text{ km}}{2} \right)^2 = 1.1122 \text{ km}^2.$$

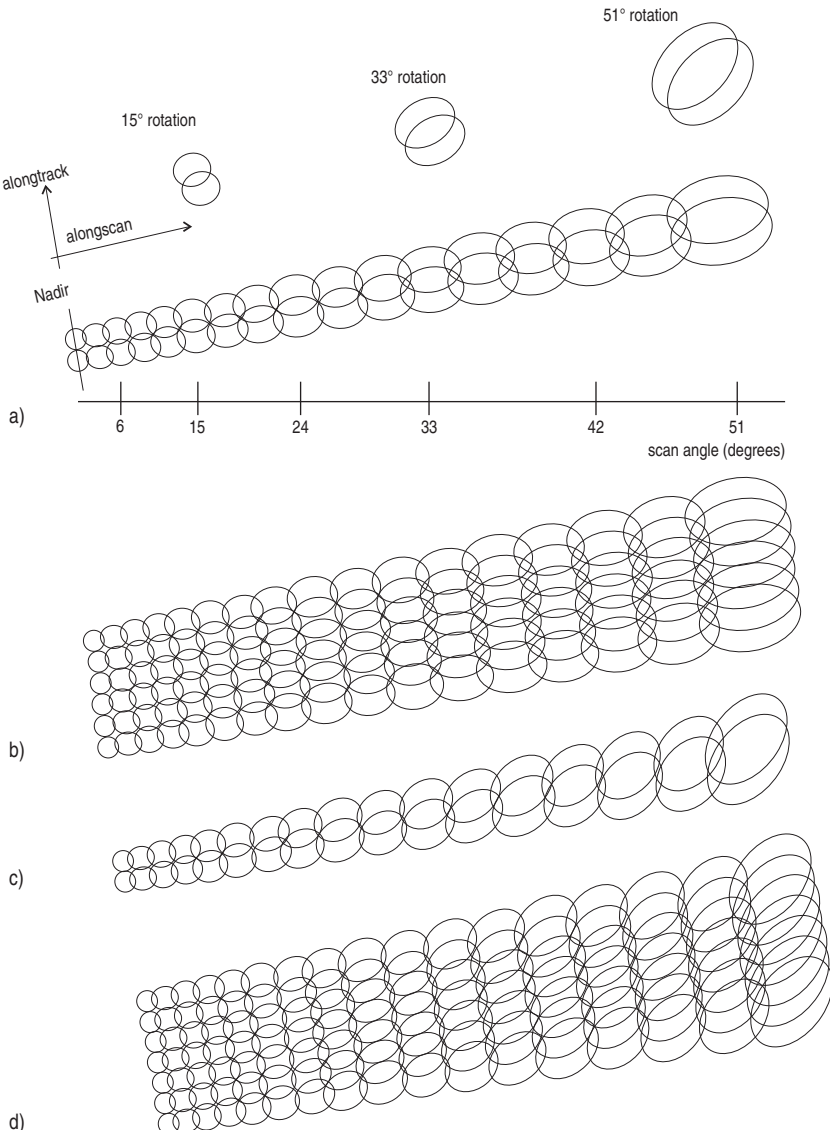


Figure 3.12 Sketch of pixel geometry for (a) two and (b) six adjacent AVHRR scan lines showing change in pixel shape, dimension and overlap with increasing scan angle. The geometry is that given by Breaker (1990) and is for lines of unrotated pixels. The effect of rotating pixels at scan angles of 15°, 33° and 51° is given at the top of the figure, with the rotated pixel geometry for the same image strips being given in (c) and (d).

The scan-edge pixel size is  $7.29 \text{ km} \times 2.56 \text{ km}$  so that, with the square pixel assumption, the pixel area is

$$7.29 \text{ km} \times 2.56 \text{ km} = 18.6624 \text{ km}^2.$$

However, an oval shape assumption yields:

$$A_{\text{pixel}} = \pi ab$$

$a$  and  $b$  being the radii of the oval long and short axes, respectively, so that we have (see Figure 3.8):

$$A_{\text{pixel}} = \pi \left( \frac{7.29 \text{ km}}{2} \right) \left( \frac{2.56 \text{ km}}{2} \right) = 14.6574 \text{ km}^2.$$

Thus, care must be taken to use the correct pixel shape or else, especially at extreme viewing angles, the actual ground area over which the radiance has been sampled will be over-estimated.

### 3.3.2 Topographic adjustments

For pixels on a steep slope, a correction may be necessary to take into account the fact that the satellite has a vertical view of a sloping surface. The geometry for this correction can be assessed using the slope of the terrain ( $\sigma_s$ ) and the pixel dimension calculated assuming a horizontal surface ( $L$ ), so that the adjusted pixel dimension ( $L_{\text{adjust}}$ ) =  $L \cos(\sigma_s)$ . If the direction of the slope is in the scan direction, the adjustment will have to be made to the pixel dimension in the along-scan direction, so that  $L = L_a$ . Alternatively, if the direction of the slope is in the cross-scan direction, the adjustment will have to be made to the pixel dimension in the along-scan direction, so that  $L = L_c$ . For a TM-class 30 m pixel, this correction gives the following results.

- $\sigma_s = 5^\circ$ ,  $L_{\text{adjust}} = 30.1 \text{ m}$ ;  $\sigma_s = 10^\circ$ ,  $L_{\text{adjust}} = 30.5 \text{ m}$
- $\sigma_s = 15^\circ$ ,  $L_{\text{adjust}} = 31.1 \text{ m}$ ;  $\sigma_s = 20^\circ$ ,  $L_{\text{adjust}} = 31.9 \text{ m}$
- $\sigma_s = 25^\circ$ ,  $L_{\text{adjust}} = 33.1 \text{ m}$ ;  $\sigma_s = 30^\circ$ ,  $L_{\text{adjust}} = 34.6 \text{ m}$

For an AVHRR-class 1.1 km pixel, this correction gives the following results.

- $\sigma_s = 5^\circ$ ,  $L_{\text{adjust}} = 1.11 \text{ km}$ ;  $\sigma_s = 10^\circ$ ,  $L_{\text{adjust}} = 1.13 \text{ km}$
- $\sigma_s = 15^\circ$ ,  $L_{\text{adjust}} = 1.15 \text{ km}$ ;  $\sigma_s = 20^\circ$ ,  $L_{\text{adjust}} = 1.18 \text{ km}$
- $\sigma_s = 25^\circ$ ,  $L_{\text{adjust}} = 1.22 \text{ km}$ ;  $\sigma_s = 30^\circ$ ,  $L_{\text{adjust}} = 1.28 \text{ km}$

Thus, where steep ( $>15^\circ$ ) slopes are maintained throughout the pixel, a topographic adjustment may be required. Wooster and Rothery (1997b) argue that, where slopes are small enough (less than  $10^\circ$ ), a constant value (derived for a horizontal surface) may be assumed.

### 3.3.3 Image distortion and geometric correction

For our purposes, exact knowledge of pixel area is essential for quantitative applications that aim to extract lava flow area and heat flux from satellite IR imagery, as will be reviewed in

[Chapter 4](#). However, the variation in pixel size with scan angle also induces image distortion. As shown in [Figure 3.13](#), the effect of preferentially increasing the pixel dimension in the along-scan direction causes features to become increasingly compressed in the along-scan dimension with increased scan angle. This can also cause an apparent elongation in the cross-scan direction, as well as feature rotation. To restore the correct geometry, geometric correction is required. We will not detail geometric correction techniques here; suffice to say, geometric correction allows projection of the distorted image onto a map projection. This can be achieved using standard routines in most image processing packages and usually involves selection of common ground control points evenly distributed across the distorted (slave) image and the undistorted map (master) image. The slave is then warped to fit the master. Other correction routines involve use of satellite header data in an appropriate geometric model for the satellite orbit and scan geometry. Such corrections are often carried out as part of data pre-processing as detailed, for example, in Nishihama *et al.* (1997) for MODIS Level 1A data. MODIS Level 1A data come geometrically corrected with pixel location errors in the along-scan direction of less than  $\sim 300$  m at nadir and less than  $\sim 1420$  m at a scan angle of  $55^\circ$  (i.e., location is good to a precision of  $\sim 0.3$  pixels). In the cross-scan direction the errors are the same at nadir, but reduce to  $\sim 590$  m at  $55^\circ$ . Such small location errors are essential for precise hot spot location, as well as for feature mapping. Further details regarding the mechanics of geometric correction routines are given in most remote sensing texts, as listed in [Chapter 0](#), as in *Image Registration for Remote Sensing* edited by Le Moigne *et al.* (2011).

### 3.3.3.1 Do we need geometric correction?

For many quantitative methodologies presented in this book, such as the heat and mass flux extraction routines of [Chapter 4](#), or spectral radiance time series generation of [Chapter 6](#), geometric rectification may not be necessary. All that is necessary is that we know the exact position of the pixel(s) in the image, so that the precise pixel area can be calculated to allow feature area (and heat flux) estimation. In addition, we need to know that the pixel radiances are original and unaltered. In this regard, it is possible that some geometric correction routines can alter the pixel radiance values over their original values and may, thus, not be welcome. For example, until 1992 TM data were available either in a radiometrically processed format (CTT-A format) or in a radiometrically and geometrically corrected format (CTT-P format). Geometric correction of the CTT-P format data was achieved either by cubic convolution (CC) or nearest neighbor (NN) resampling. Oppenheimer *et al.* (1993a) noted that, while such processing produced “nicer looking” images, it reduced the “radiometric fidelity of individual pixels.” In particular Oppenheimer *et al.* (1993a) noticed that, in CTT-P format TM images of Lascar’s lava dome, the geometric correction routine:

- (i) increased the number of saturated pixels;
- (ii) introduced duplicate “fill” pixels,
- (iii) added fill pixels to some bands, but not others, to result in
- (iv) band-to-band misregistration for individual pixels.

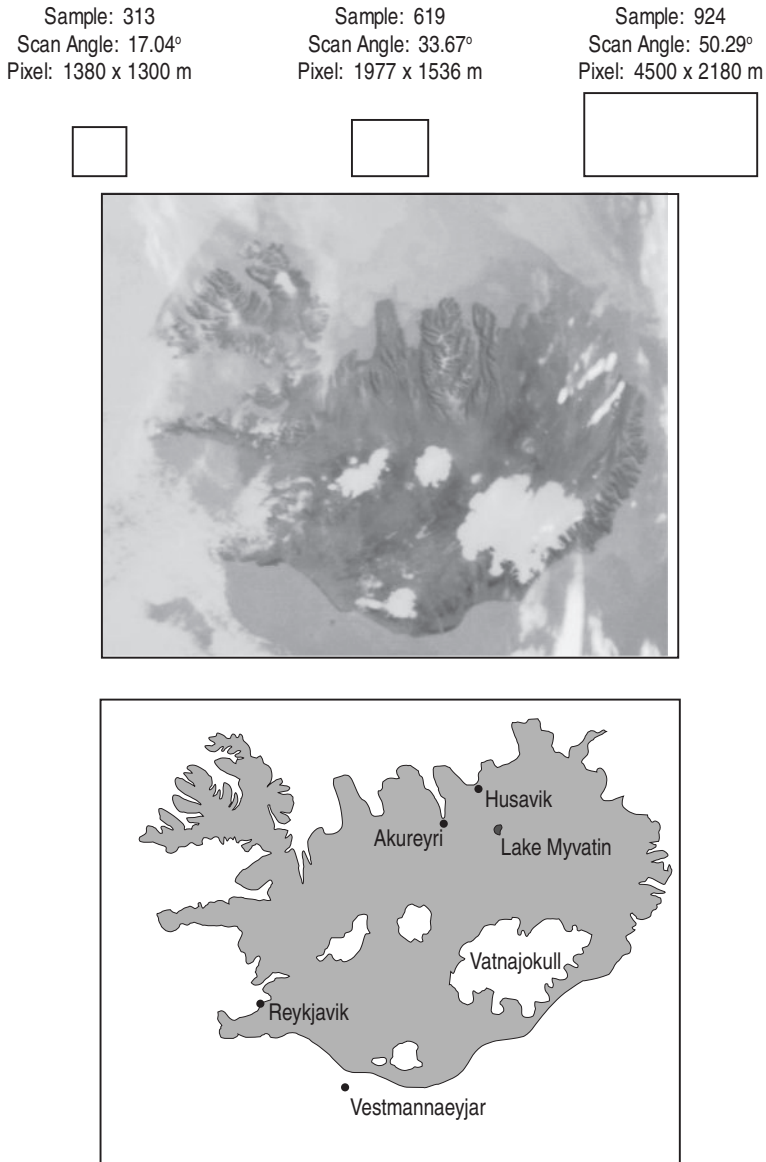


Figure 3.13 Band 4 (TIR) sub-image of Iceland acquired at 16:48Z on 3 September 1984 with Iceland's outline (with main ice caps – in white – plus population centers and Lake Myvatn marked) for comparison. Along the top of the figure is the pixel dimension at the west-edge, middle, and east-edge of the image, showing how pixels elongate from west-to-east across the image. The distortion effect that this introduces can be seen by examining the eastern edge of Vatnajökull and Iceland's eastern coast, both of which have a steeper SW–NE orientation in the image than in the map.

In the following chapter we consider the dual-band method to extract the size and temperature of sub-pixel hot spots. For such data-reduction techniques the band-to-band pixel registration problem is a particularly worrying issue since we rely on the pixel being perfectly registered in a spatial (and radiometric) sense across all wavebands.

If precise quantitative measurements are required, inclusion of fill pixels or deletion of real data (pixels), required to allow the image to look “nice,” or the modification of original pixel values, is obviously not useful. The image may look nicer, but the pixel values are corrupted so that the data cannot be trusted for quantitative applications. If there is concern that geometric post-processing has altered the radiometric fidelity of the pixel values, it is better to work with the original radiometrically calibrated, but geometrically uncorrected, data so that the numeric data are in their original (as received by the detector) form.

### **3.3.4 Image blurring and the point spread function**

The sensor optics, detectors and electronics will modify the spatial properties of the image to induce blurring. As shown in [Figure 3.14](#), a perfect spatial response would be represented by a square wave which switches from a response of 0% to a response of 100% precisely at the pixel edge. However, blurring results in a radiance distribution which can be modeled as a Gaussian distribution which has tails that extend beyond the edge of the nominal pixel boundary. This means that radiance is collected from a larger area than that defined by the detector IFOV.

Blurring is defined by the sensor point spread function (PSF). As described by Markham ([1985](#)) and Schowengerdt ([2007](#)), the PSF consists of three main components.

- (1) Optical: the optical system is not perfect so that radiance from a point source will become spread over a small area on the focal plane due to optical diffraction and aberrations.
- (2) Detector-based: the detectors will induce blurring due to variations in the detector response across its spatial area.
- (3) Electronic: electronic blurring results from filtering of the signal to reduce noise.

Blurring will also occur in two dimensions. While blurring in the first dimension is caused by the scanning motion of the mirror, the motion of the spacecraft causes blurring in the second dimension. Obtaining the point spread function thus requires convolution, this being an operation whereby two or more functions, or sets of inputs, are combined to create a new function, or output set. An asterisk is used to represent convolution, so that for two input sets,  $f(x)$  and  $f(y)$ , we can create an output set,  $f(z)$ , from

$$f(x) * f(y) = f(z). \quad (3.14a)$$

In our case, the two image dimensions can be analyzed separately to define the line spread function (LSF) in the scan ( $x$ ) and track ( $y$ ) directions. These can then be combined to define the total point spread function for the sensor in the two dimensions,  $\text{PSF}(x, y)$ :

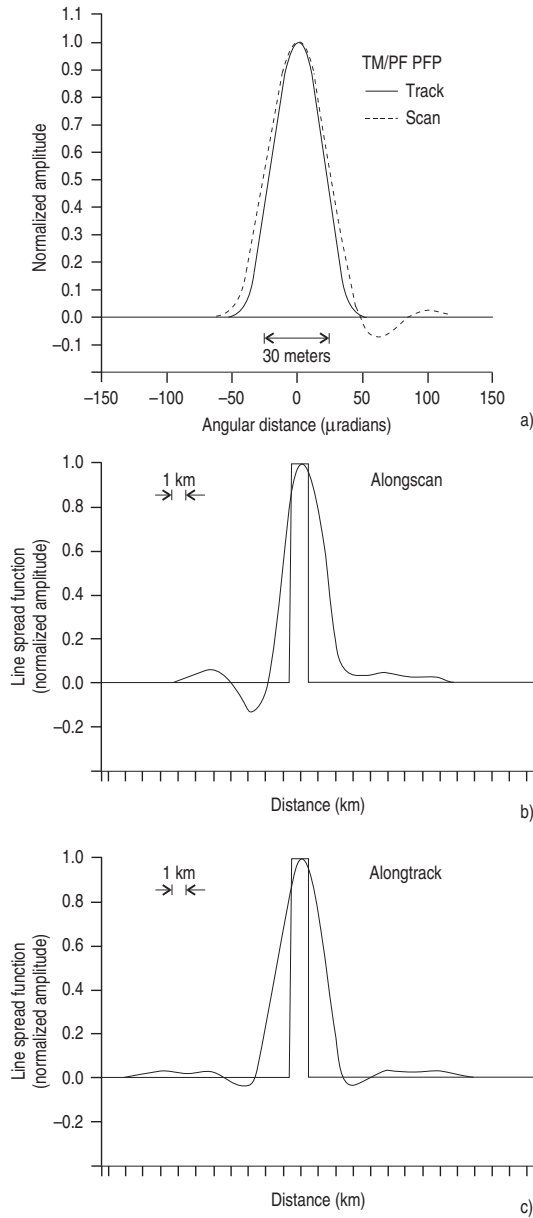


Figure 3.14 Point spread functions for (a) Thematic Mapper [modified from Markham (1985, Fig. 10)], (b) AVHRR in the along-scan direction [from Breaker (1990, Fig. 5): reproduced by permission of American Geophysical Union], and (c) AVHRR along-track direction [from Breaker (1990, Fig. 6): reproduced by permission of American Geophysical Union]. The square (top hat) function represents the perfect response.

$$\text{PSF}(x, y) = \text{LSF}(x) * \text{LSF}(y). \quad (3.14\text{b})$$

The line spread function in the scan direction [ $\text{LSF}(x)$ ] is, itself, described by three inputs: the optics line spread function [ $\text{OSF}(x)$ ], the detector line spread function [ $\text{DSF}(x)$ ] and the electronics line spread function [ $\text{ESF}(x)$ ]. Convolution of these three functions now gives the line spread function in the scan direction:

$$\text{LSF}(x) = \text{OSF}(x) * \text{DSF}(x) * \text{ESF}(x). \quad (3.14\text{c})$$

In the track direction the electronics response has negligible effect because the effective scanning velocity induced by the satellite forward motion is much slower than the scan velocity of the mirror in the scan direction. Thus, the line spread function in the track direction [ $\text{LSF}(y)$ ] is solely a function of the optics and the detectors:

$$\text{LSF}(y) = \text{OSF}(y) * \text{DSF}(y). \quad (3.14\text{d})$$

As a result, blurring tends to be reduced in the track direction as opposed to the scan direction, where the amount of sensor blur for AVHRR, MSS and MODIS is about twice as great in the scan direction than in the track direction (Schowengerdt, 2007).

Blurring means that all systems have a cross-track spatial response that is broader than that of the detector. As a result, the effective IFOV (EIFOV) is typically larger than the commonly given geometric IFOV. As will be shown in the following chapters, many quantitative studies of active volcanism examine small, sub-pixel thermal phenomena. These applications thus depend on accurate estimation of the area over which the radiance measurement has been integrated. Precise measurement of the effective pixel dimension is therefore essential. In short, the volcano thermal remote sensor cannot rely on nominal resolutions and pixel dimensions, but must calculate the entire area over which radiance has been integrated from first principles (as given in [Section 3.3](#)) and using the EIFOV.

By way of example, EIFOVs for AVHRR and TM, and the effective pixel dimensions that these yield, are given in [Tables 3.6](#) and [3.7](#). For both the AVHRR and TM we see that the EIFOV varies by band as well as by instrument. AVHRR's along-scan pixel EIFOV, for example, varies from 1.05 mrad to 1.48 mrad depending on the sensor and waveband. This results in an along-scan effective pixel dimension that varies, at nadir, between 1.05 km and 1.48 km. This compares with a nominal spatial resolution of 1.19 km, as calculated using the nominal IFOVs given for AVHRR ([Table 3.6b](#)). For TM, the effective pixel dimensions vary from 33 m to 36 m in bands 5 and 7. This compares with a nominal value of 30 m. In band 6 the effective pixel dimensions of 124 m by 141 m compare with a nominal value of 120 m.

In terms of the image, blurring and pixel-overlap will cause radiance to be spread into pixels where the radiance does not belong. In a simple case where a small hot spot is located within a single pixel, the along- and cross-scan PSF can transform what should be a single pixel thermal anomaly into a cross-shape, an example being given in [Figure 3.15](#). Because of severe pixel overlap problems at the scan edge, single pixel anomalies can become

Table 3.6a. *AVHRR effectiveIFOVs (EIFOV) and pixel dimensions that these give in the along- and cross-scan directions ( $L_a$  and  $L_c$ ), along with the resulting pixel area [calculated using an oval shape assumption so that  $P_a = \pi (L_a/2) (L_c/2)$ ]. Sensor EIFOVs are those given by ITT Aerospace (the manufacturers of the AVHRR).*

NOAA	Band	EIFOV		Nadir			Scan Edge		
		Scan (mrad)	Track (mrad)	$L_a$ (km)	$L_c$ (km)	$P_a$ (km <sup>2</sup> )	$L_a$ (km)	$L_c$ (km)	$P_a$ (km <sup>2</sup> )
6	1	1.2995	1.2954	1.08	1.08	0.92	6.5	2.31	11.79
	2	1.2751	1.2792	1.06	1.07	0.89	6.38	2.28	11.42
	3	1.3299	1.066	1.11	0.89	0.78	6.65	1.9	9.92
	4	1.2448	1.2954	1.05	1.08	0.89	6.28	2.31	11.39
7	1	1.443	1.433	1.26	1.25	1.24	7.92	2.71	16.86
	2	1.433	1.423	1.25	1.24	1.22	7.86	2.69	16.61
	3	1.28	1.463	1.11	1.27	1.11	7.02	2.76	15.22
	4	1.423	1.423	1.24	1.24	1.21	7.81	2.69	16.50
	5	1.32	1.31	1.15	1.14	1.03	7.24	2.47	14.05
8	1	1.362 53	1.366 65	1.13	1.14	1.01	6.81	2.44	13.05
	2	1.357 32	1.363 38	1.13	1.14	1.01	6.79	2.43	12.96
	3	1.388 84	1.108 97	1.16	0.92	0.84	6.95	1.98	10.81
	4	1.218 78	1.188 63	1.02	0.99	0.79	6.1	2.12	10.16
9	1	1.301	1.359	1.13	1.18	1.05	7.14	2.57	14.41
	2	1.295	1.37	1.13	1.19	1.06	7.1	2.59	14.44
	3	1.067	1.47	0.93	1.28	0.93	5.85	2.78	12.77
	4	1.165	1.222	1.01	1.06	0.84	6.39	2.31	11.59
	5	1.159	1.257	1.01	1.1	0.87	6.36	2.37	11.84
10	1	1.137 06	1.3401	0.95	1.12	0.84	5.69	2.39	10.68
	2	1.051 78	1.275 13	0.88	1.06	0.73	5.26	2.28	9.42
	3	1.143 15	1.228 43	0.95	1.02	0.76	5.72	2.19	9.84
	4	1.055 84	1.289 34	0.88	1.07	0.74	5.28	2.3	9.54
11	1	1.22	1.26	1.06	1.1	0.92	6.69	2.38	12.51
	2	1.3	1.27	1.13	1.1	0.98	7.13	2.4	13.44
	3	1.34	1.46	1.17	1.27	1.17	7.35	2.76	15.93
	4	1.14	1.24	0.99	1.08	0.84	6.25	2.34	11.49
	5	1.197	1.38	1.04	1.2	0.98	6.57	2.61	13.47
12	1	1.32	1.34	1.1	1.12	0.97	6.6	2.39	12.39
	2	1.32	1.32	1.1	1.1	0.95	6.6	2.36	12.23
	3	1.38	1.42	1.15	1.18	1.07	6.9	2.54	13.76
	4	1.24	1.28	1.03	1.07	0.87	6.2	2.29	11.15
	5	1.32	1.26	1.1	1.05	0.91	6.6	2.25	11.66
14	1	1.4	1.42	1.17	1.18		7	2.54	13.96
	2	1.4	1.42	1.17	1.18	1.08	7	2.54	13.96
	3	1.38	1.48	1.15	1.23	1.08	6.9	2.24	12.14
	4	1.28	1.34	1.07	1.12	1.11	6.4	2.39	12.01
	5	1.48	1.242	1.23	1.03	0.94	7.4	2.22	12.90

Table 3.6b. Comparison of pixel dimension statistics obtained using the EIFOVs for all AVHRR sensors with the nominal values given by Kidwell (1995).

Band	EIFOV		Nadir			Scan edge		
	Scan (mrad)	Track (mrad)	$L_a$ (km)	$L_c$ (km)	$P_a$ ( $\text{km}^2$ )	$L_a$ (km)	$L_c$ (km)	$P_a$ ( $\text{km}^2$ )
Data from all sensors given in Table 3.6a								
Min.	1.05	1.07	0.88	0.89	0.73	5.26	1.90	9.42
Max.	1.48	1.48	1.26	1.28	1.24	7.92	2.78	16.86
Mean	1.28	1.32	1.09	1.12	0.96	6.67	2.41	12.66
$\sigma$	0.11	0.10	0.10	0.09	0.14	0.63	0.21	1.97
1	1.39	1.39	1.16	1.16	1.06	6.95	2.48	13.54
Nominal values of Kidwell (1995)								
2	1.41	1.41	1.17	1.17	1.08	7.05	2.52	13.95
3	1.51	1.51	1.26	1.26	1.25	7.55	2.7	16.01
4	1.41	1.41	1.17	1.17	1.08	7.05	2.52	13.95
5	1.3	1.3	1.08	1.08	0.92	6.5	2.32	11.84
Generic	1.4	1.4	1.19	1.19	1.11	7.29	2.56	14.66

Table 3.7. TM effective IFOVs (EIFOV) and pixel dimensions that these give in the scan and track directions [EIFOVs taken from Table IV of Markham (1985)].

TM spatial resolution	Bands 1 to 4		Bands 5 & 7		Band 6	
	Track	Scan	Track	Scan	Track	Scan
(1) Protoflight (PF) instrument flown on Landsat-4 EIFOV (mrad)	0.0455	0.0508	0.0473	0.0508	0.1758	0.2005
Nadir pixel dimension (m)	32.1	35.8	33.3	35.8	123.9	141.4
(2) Flight (F) instrument flown on Landsat-5 EIFOV (mrad)	0.0455	0.0509	0.0473	0.0505	0.1758	0.2001
Nadir pixel dimension (m)	32.1	35.9	33.3	35.6	123.9	141.1

increasingly large image anomalies, as in the scan-edge example of Figure 3.15. PSF-induced blurring can thus cause halos surrounding the parental thermal anomaly.

### 3.4 Spectral resolution and response

Sensor spectral resolution is defined by the number, width and location of the sensor wavebands. This, in turn, is determined by the number and spectral sensitivity of the

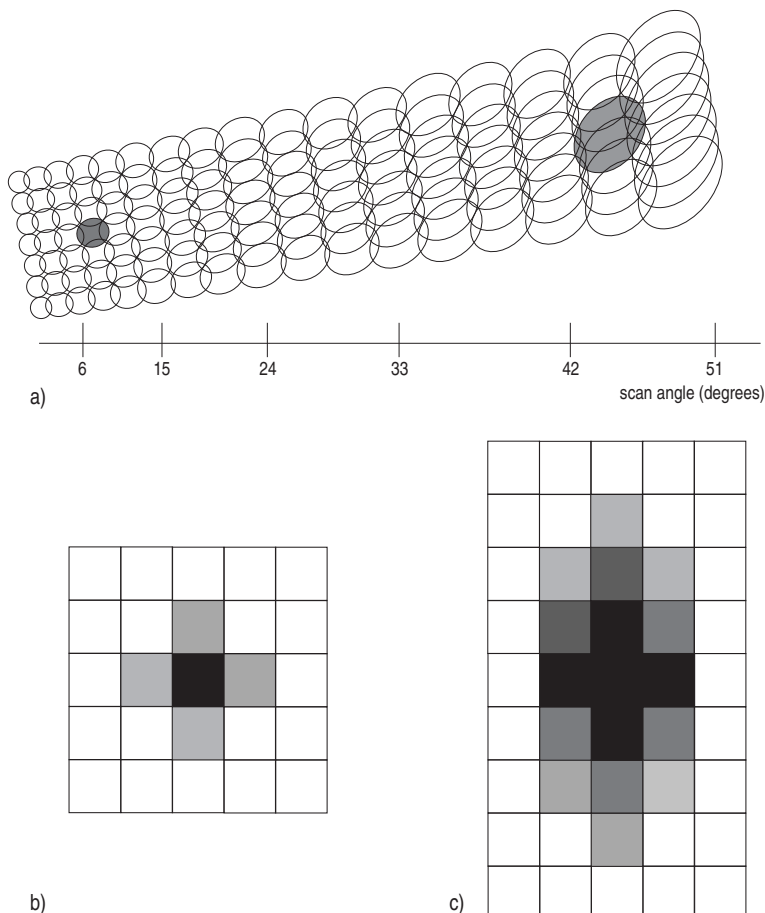


Figure 3.15 Theoretical radiance spreading due to pixel overlap. Hot pixels have been placed in the scan line of Fig. 3.12d at scan angles within  $10^\circ$  of nadir and  $10^\circ$  of the scan edge. We see from (a) that, near-nadir, the effect of pixel overlap will cause the single-pixel hot spot to spread its radiance into at least four other pixels in the cardinal directions. When re-projected onto a square pixel grid (as done in (b)) this will cause a cross-shaped thermal anomaly. At the scan edge we see that pixel distortion, coupled with pixel overlap, causes the single-pixel hot spot to be spread into 16 overlapping pixels. This, when re-projected onto a square pixel grid (as done in (c)), results in a large, N–S elongated anomaly.

detectors carried by the sensor. The number and spectral ranges of each detector for the main TM-, AVHRR- and GOES-class sensors used for analyses of volcano hot spots are defined in Appendices C, D and E, respectively. However, each waveband will also have a unique response and dynamic range, both of which need to be understood when making measurements of high temperature targets (as is explored further Electronic Supplement 1).

### 3.4.1 Spectral response

As explained in [Section 3.2.2](#), radiance arriving at the sensor is split and filtered onto each detector, the filter focussing on the appropriate spectral region. Radiance in the selected waveband is thus directed, by the sensor beam splitters and filters, onto the appropriate detector (see [Figure 3.7](#)). The spectral radiance arriving on the detector is modified by the filter and the sensor optics, so that the responsivity of the detector varies with wavelength across the waveband in which the detector is responding.

The effect of the spectral filter transmittance and detector spectral sensitivity can be described by the spectral responsivity of the detector,  $R_b(\lambda)$ , or the spectral response function. This defines the detector spectral responsivity for each wavelength increment ( $d\lambda$ ) across the waveband from its lower sensitivity limit ( $\lambda_{\min}$ ) to its upper limit ( $\lambda_{\max}$ ). The response functions for the NIR, SWIR and TIR bands of ETM+ are given in [Figure 3.16](#) by

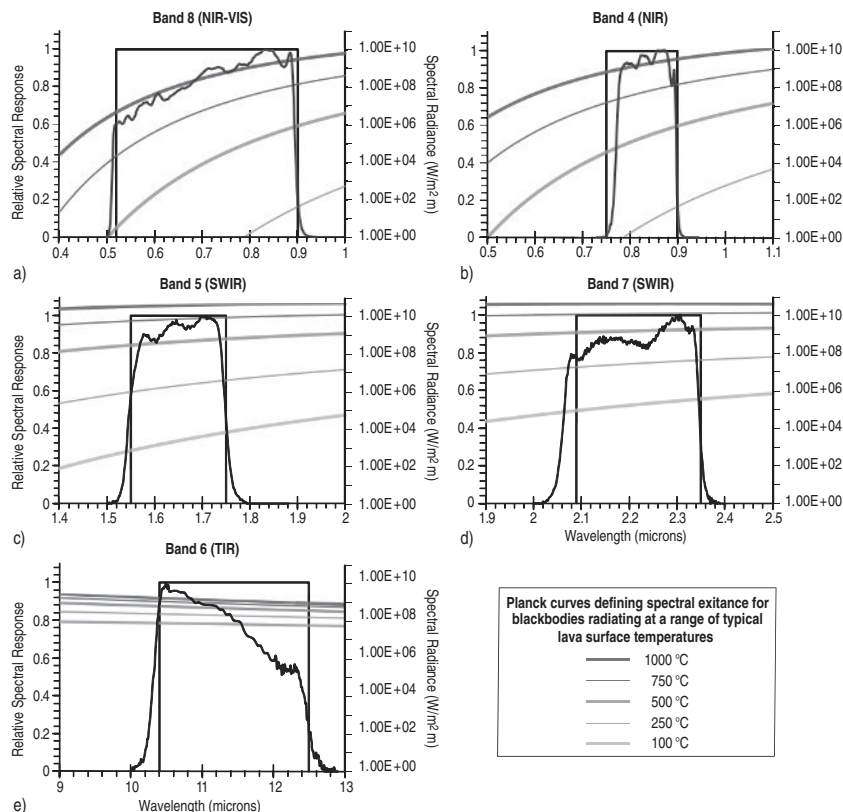


Figure 3.16 Relative spectral response for each of the NIR, SWIR and TIR bands of ETM+ (blue) compared with a perfect “top hat” function where response is 100% within the waveband and 0% outside of it (black). Spectral radiance curves for blackbodies at a range of temperatures have been placed over the response functions to show the variation in emitted spectral radiance across each waveband. See also color plates section.

way of example. As with the spatial response considered in Section 3.3.4, a perfect spectral response would be represented by a square function which switches from a response of 0% to a response of 100% precisely at the waveband limits. This is plainly not the case, with the response extending beyond the waveband limits and being variable, and typically less than 100%, across each waveband.

Convolving the detector response function with the spectral radiance arriving at the sensor ( $R_{\text{in}}^*$ ) yields the radiance actually recorded by the detector ( $R^*$ ) in  $\text{W m}^{-2}$ :

$$R^* = \int_{\lambda_{\min}}^{\lambda_{\max}} R_{\text{in}}^* R_b(\lambda) d\lambda \quad (\text{W m}^{-2}). \quad (3.15a)$$

Dividing by the integral of the spectral increments multiplied by the spectral responsivity yields units of  $\text{W m}^{-2} \text{ m}^{-1}$ , i.e.,

$$R^* = \frac{\int_{\lambda_{\min}}^{\lambda_{\max}} R_{\text{in}}^* R_b(\lambda) d\lambda}{\int_{\lambda_{\min}}^{\lambda_{\max}} R_b(\lambda) d\lambda} (\text{W m}^{-2} \text{ m}^{-1}). \quad (3.15b)$$

As a result, the recorded, at-detector, brightness temperature will be somewhat different to arriving, at-sensor, brightness temperature. Convolution of the spectral response with the spectral radiance allows the at-detector brightness temperature to be converted to an at-sensor brightness temperature. This can be achieved following the procedure detailed in Electronic Supplement 3.

As argued at the end of Electronic Supplement 3, for narrow wavebands and portions of the spectrum across which the Planck curves are fairly flat, the difference between the at-detector brightness temperature and at-sensor brightness temperature is minimized. This is apparent in the case followed through in Electronic Supplement 3 for MODIS Band 22 where the at-sensor brightness temperature of 11.4 °C compares with an at-detector brightness temperature of 12.0 °C. As already argued at the end of Chapter 2, in such cases satisfactory temperature retrievals can be obtained by simply converting the detector derived radiance to a brightness temperature using the Planck Function and the mid-point wavelength of the waveband.

In cases where the waveband is particularly wide and/or where Planck curves rise steeply across the waveband, differences between at-detector brightness temperature and at-sensor brightness temperature will be large, and convolution of the response function will be necessary. This is particularly true of measurements made in the NIR. Across this waveband Planck curves ascend steeply. From Figure 3.16 we see that the spectral radiance from sources at 800–1100 °C increases substantially across ETM+ band 8, which is particularly broad. Likewise, the radiance from the 1000 °C and 1100 °C sources ascends relatively steeply across the narrower waveband range of band 3. In both of these cases, convolution of

the spectral response function will be necessary to obtain at-sensor brightness temperature. Otherwise the effect of the response function will cause the at-sensor brightness temperature to be lower than the actual kinetic temperature. However, spectral radiance variation with wavelength is flatter for bands 4, 5, 6 and 7 (Figure 3.16), although the spectral response function is still in no way perfect. If the spectral response function shows a high degree of variation across the waveband of measurement, and/or the expected spectral radiance response is not approximately flat across the waveband, the spectral response and Planck Functions should thus be convolved in order to extract precise brightness temperature.

### **3.4.2 Detector limits: signal-to-noise and saturation**

The dynamic range of the sensor defines the detection limits. It is effectively the range of radiances that the sensor can record (see Figure 3.5). Radiance from the source must exceed the lower radiance limit of the dynamic range in order to be detected. It must also exceed the noise level which is defined by the signal-to-noise ratio ( $S/N$ ) or the noise equivalent temperature difference ( $NE\Delta T$ ), where the  $NE\Delta T$  gives the variation in temperature due to noise.

The sensor will also have an upper limit beyond which radiance from the source may increase, but no higher value can be registered. Instead, the maximum recordable radiance is given for all radiance levels above the upper measurement limit, a point termed saturation. This defines the highest measurable radiance or temperature. At this point, all that we know is that the source temperature is greater than, or equal to, the saturation temperature.

Of course, for examination of high temperature volcanic sources, a broad dynamic range with low  $NE\Delta T$  and high saturation temperatures is desirable. These limits are given for the main sensors considered here in Appendices C, D and E. We see that, for the meteorological satellites (AVHRR and GOES), saturation levels are typically quite low, being around 50 °C–60 °C for most detectors operating in the MIR and TIR. This means that data collected over active lavas are frequently saturated.

## **3.5 Selection of an appropriate sensor**

None of the available Earth observing thermal sensors reviewed in Appendices C, D or E are perfect for detecting, tracking and measuring volcanic thermal phenomena. Most importantly there is a trade-off between spectral, spatial and temporal resolution. The main trade-off is between spatial and temporal resolution: we cannot have both high-temporal and high-spatial-resolution data at the same time.

### **3.5.1 Spatial and temporal resolution trade-off**

Sensors operating at high temporal resolutions tend to have poor spatial resolution. For example, GOES is flown at a high altitude (36 000 km) in a geostationary orbit above the equator. From here it is able to scan the Earth's disk every 15–30 minutes. However, the

same high, orbital height that allows this high temporal resolution, coupled with the detector IFOV, means that data are of a low spatial resolution of 4 km. GOES data are thus excellent for timely event detection and generation of detailed radiance time series, but not for detailed feature mapping and thermal structure analysis. In contrast, TM is flown in a relatively low altitude (705 km) polar orbit from which it obtains 30-m-pixel data for a relatively narrow (185-km-wide) ground swath. This, though, means that the sensor requires 16 days to cover the entire globe, meaning that the temporal resolution (or return period) is 16 days. TM data are thus not good for timely detection and detailed time series generation, but are excellent for detailed mapping and thermal structure analysis.

### 3.5.2 Incomplete spectral coverage

In addition, while some sensors are equipped with MIR and TIR bands (e.g., AVHRR and GOES), some are equipped with SWIR and TIR bands (e.g., TM and ASTER), and others with SWIR, MIR and TIR bands (e.g., ATSR and MODIS). As detailed in Electronic Supplement 1, different wavelengths are suitable for detection of active volcanic features at different temperatures. Sensors equipped with SWIR detectors are best suited for detection of high-temperature features, such as overturning lava lakes, active lava fountains, or lava flows across which high-temperature surfaces are well exposed. However, TIR sensors are better suited for measurements of well-crusted lava flows and crater lakes of warm acidic water. MIR sensors can cover the full range of phenomena, but suffer from saturation problems, as do many SWIR sensors operating in low-gain mode. In addition, satellites carrying high-spatial-resolution SWIR sensors capable of detailed high-temperature analysis are typically carried on low-temporal-resolution sensors (e.g., TM, ETM+, ASTER), whereas high-temporal-resolution platforms typically carry low-spatial-resolution sensors operating in the MIR and TIR (e.g., AVHRR and GOES). As reviewed in Electronic Supplement 1, the temperature and structure of the volcanic surface under consideration will also influence the selection of sensor, for we need a spectral and spatial sensitivity that is capable of (i) detecting the phenomena, while (ii) not saturating, and, if the thermal structure is highly complex over spatial scales that are smaller than the pixel, we need (iii) data in multiple wavebands. These issues are considered in the following chapter ([Chapter 4](#)) where we examine mixed pixels and methodologies to un-mix the thermal structure of the pixel using multiple wavebands of thermal sensor data.

### 3.5.3 Sensor selection

Owing to the above trade-offs, sensor selection has to be made according to application.

- TM-class sensors offer high-spatial-resolution data in the NIR, SWIR and TIR, but at a low temporal resolution. They thus provide data well suited to hot spot mapping as well as for well-constrained quantitative (thermal structure and heat flux) studies, saturation permitting. However, any time-series analysis will have a relatively poor (16 day)

temporal resolution and may thus miss some short, but important, events (e.g., short-lived fire fountains), and can suffer from saturation problems.

- AVHRR-class sensors offer moderate-spatial-resolution data in the NIR, MIR and TIR at a moderate temporal resolution. Note, though, that the hot spot has to be particularly hot and large to register in the NIR (see Electronic Supplement 1). Sensors such as AVHRR and MODIS thus provide data suited to 1 km spatial resolution hot spot location and mapping, and can provide data for quantitative (thermal structure and heat flux) studies. They also offer moderately timely detection capabilities and moderately detailed time series showing radiance variation developing over time scales greater than 6–12 hours.
- GOES-class sensors offer low-spatial-resolution data in the MIR and TIR, but at a very high temporal resolution. They thus provide data suitable for no more than general (poorly constrained) hot spot location, i.e., hot spot location to within 4 km and radiance assessment for the  $16 \text{ km}^2$  pixel area. However, they do offer excellent alerting and temporal detection capabilities, as well as the most detailed time series possible, providing an observation of the hot spot every 15 minutes. They can also provide a surprising quality of quantitative (heat and mass flux) data for larger hot spots (see examples in [Chapters 5 and 6](#)).

One of the best approaches is to combine all sensor classes to gain the best of all worlds: GOES- and AVHRR-class data can produce frequent assessments of feature radiance level, with TM-class data providing infrequent, high-precision, checks on the location and spatial distribution of the phenomena, plus well-constrained quantitative output for use with, and validation (cross-checks) of, extractions from the higher-spatial-resolution data sets. We explore methodologies to fully utilize these capabilities in the following three chapters.

## **Part II**

### Space-based volcano radiometry



# 4

## The mixed pixel, the dual-band technique, heat loss and volume flux

In [Chapter 2](#) the underlying assumption was that the pixel was thermally pure. That is, the surface occupying the pixel was assumed to be isothermal. In such cases the pixel-temperature (if corrected for emissivity, atmospheric and sensor response effects) should equate to the temperature of the targeted surface. Over the ocean, even 1–4 kilometer pixels may be approximately isothermal, with sea-surface temperature varying over a spatial scale that is greater than that of the pixel. On land, AVHRR- and GOES-class pixels will likely contain surfaces at a variety of ambient temperatures, with surface temperatures potentially varying by tens of degrees over spatial scales of hundreds of meters. As seen in [Electronic Supplement 1](#), over active volcanic surfaces not only will surface temperatures vary over spatial scales that are much less than the scale of even a 30 m TM-class pixel, but also the temperature differences across the pixel may range over hundreds of degrees. This means that the pixel collected over a volcano hot spot will be a mixture of many different thermal components. The resulting mixed pixel problem is fundamental to thermal remote sensing of volcano hot spots, having been the focus of around 36% of the work achieved up until 2005 (see [Appendix A](#)), with the development of this theme being reviewed in [Electronic Supplement 5](#). Understanding the mixed pixel problem over pixels containing active lavas and volcanic vents allows us to develop models to un-mix the pixel. To un-mix the thermally mixed pixel, one method remains fundamental: the dual-band method of [Dozier \(1980\)](#). This chapter explores first the problem of thermally mixed pixels in [Section 4.1](#), followed by the application of the dual-band method in [Sections 4.2](#) and [4.3](#). It then finishes by reviewing the use of extracted temperatures and hot feature areas to allow estimation of heat, mass and volume fluxes in [Sections 4.4](#) and [4.5](#).

### 4.1 The problem of the thermally mixed pixel

#### 4.1.1 *The mixed pixel problem*

An image will divide the Earth’s surface into discrete areas or pixels, typically with dimensions of meters to thousands of meters (see [Chapter 3](#)). If the pixel contains a homogeneous surface, such as the sea, then the brightness of the surface contained within the pixel will equate to the brightness of the pixel. A problem arises when surfaces of more than one brightness fall within a pixel. The problem was well stated by [Campbell \(1986\)](#), who wrote

when a pixel is composed of two or more areas that differ greatly in respect to brightness, then the average is composed of several very different values, and the single digital value that represents the pixel may not accurately represent any of the categories present.

As a result, over a mixed pixel, pure spectral responses will be integrated to form, using the terminology of Campbell (1986), a *composite signature* that does not match the pure signature of the sub-pixel features we wish to analyze.

As shown in [Figure 4.1a](#), the problem is usually viewed as an edge effect whereby a spectrally pure zone of pixels of brightness  $Y_i$  is surrounded by spectrally pure pixels of a second brightness ( $X_i$ ). As sketched in [Figure 4.1a](#), such a scenario may be encountered around a lava flow, for example. In such a case, the zone of pixels at the lava brightness of  $Y_i$  will be surrounded by pure (lava-free) pixels at brightness  $X_i$  separated by a ring of pixels for which the brightness is some weighted average ( $M_i$ ) of the two brightnesses  $X_i$  and  $Y_i$ . These are *mixed pixels*. The exact value of  $M_i$  will depend on the relative proportions of the two pure components present in the mixed pixel. The resulting brightness for the mixed pixel will be neither that of feature  $X$  nor feature  $Y$ , and may resemble that of a third feature not actually present in the pixel.

Campbell (1986) points out that “scattered occurrences of small parcels may produce special problems” because in such cases the scene will be composed “only by mixed pixels.” According to Campbell (1986), “an especially difficult situation can be created by many parcels that are small relative to the spatial resolution of the sensor,” as shown in [Figure 4.1d](#). As explored in Electronic Supplement 1, surface temperatures over volcanic hot spots, such as active lava bodies or fumarole fields, will be highly variable over spatial scales of millimeters-to-centimeters, which is much smaller than the spatial scale of even TM-class pixels. Thus, over an active volcanic hot spot we usually have Campbell’s (1986) worst-case scenario, and all pixels will be mixed. For example, the schematics of [Figure 4.1](#) are drawn to resemble the situation we would expect for data with a meter-scale spatial resolution collected over an active lava flow, or over a fumarole field.

The simple starting point of [Figure 4.1a](#), is complicated because (in many cases) we cannot assume that pixels occupied by feature  $Y$  (in this case the active lava flow) are thermally pure. Instead the surface will be represented, in its most simple form, by a hot crust broken by even hotter cracks (see Electronic Supplement 1). Thus, in the schematic of [Figure 4.1c](#), pixels across feature  $Y$  are actually mixed and contain a third feature of brightness  $Z_i$ . Pixels within the core of feature  $Y$  are now two component mixtures ( $Y_i + Z_i$ ) and those at the edge are three component mixtures ( $X_i + Y_i + Z_i$ ) (see [Figure 4.1e](#)).

Campbell (1986) also shows how the problem changes with spatial resolution, with the number of spectrally pure pixels decreasing with spatial resolution, and the number of spectrally mixed pixels increasing. As shown in [Figure 4.1b](#), as spatial resolution becomes coarser, the proportion of mixed pixels increases at the expense of pure background or interior pixels (Campbell, 1986). Thus the problem is particularly acute for AVHRR- and GOES-class sensors, although the reality of the situation over active lavas means that, usually, even TM-class pixels are thermally mixed.

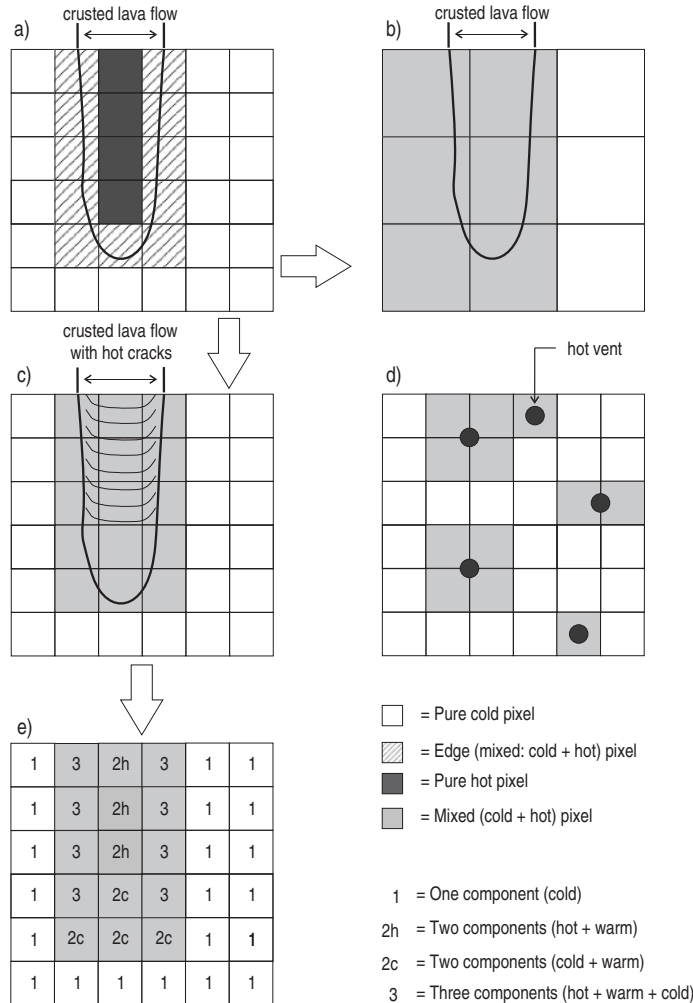


Figure 4.1 The mixed pixel problem. (a) Schematic showing isothermal lava flow advancing across a pixel grid of isothermal ambient pixels. In this scenario we have four thermally pure lava flow pixels, surrounded by 11 edge pixels that are mixtures of the hot lava flow and cold background thermal components. (b) Effect of increasing pixel size: now all pixels across the lava flow are mixed. (c) Complicating the problem by modeling the lava flow surface as a warm crust occupied by hot cracks. Now, as shown in (e), all pixels central to the lava flow are mixtures of two thermal components (warm crust + hot cracks), and edge pixels are mixtures of three components (warm crust + hot cracks + cold background). (d) Mixed pixel possibilities when small hot vents are scattered across the pixel grid, with the vents either falling within a pixel or straddling two or more pixels depending on the placement of the grid with respect to the scattered hot spots.

#### *4.1.1.1 The two-component, weighted average, mixture model of Marsh et al. (1980)*

For a simple case where two different brightnesses are present in a pixel, the brightness of the mixed pixel can be modeled using the weighted average method of Marsh *et al.* (1980). Developed to resolve sub-pixel mixtures over geological terrains containing vegetation, soil, talus and tuff, it was applied by Marsh *et al.* (1980) to single bands of reflected data with a spatial resolution of 80 m collected by Landsat's Multispectral Scanner. The method is based on a simple linear weighting equation for a two component mixture, whereby the spectral reflectance for the mixed pixel ( $M_i$ ) can be described by:

$$M_i = p_y Y_i + (1 - p_y) X_i \quad (4.1)$$

in which:

$Y_i$  = the mean brightness of surface  $Y$  in band  $i$ ;

$X_i$  = the mean brightness of surface  $X$  in band  $i$ ;

$p_y$  = proportion of component  $Y$  in the two-component mixed pixel; and

$M_i$  = the mean spectral brightness for the pixel in band  $i$ .

By writing Equation (4.1) in full we arrive at,

$$M_i = p_y Y_i + X_i - p_y X_i. \quad (4.2a)$$

This can be simplified to

$$M_i = p_y (Y_i - X_i) + X_i. \quad (4.2b)$$

If we now re-arrange Equation (4.2b), we can solve for the proportion of component  $Y$  within the mixed pixel:

$$p_y = \frac{M_i - X_i}{Y_i - X_i}. \quad (4.2c)$$

This equation can now be solved if the spectral reflectance of surface  $X$  and  $Y$  is known or can be obtained from spectrally pure pixels around the mixed pixel zone.

Marsh *et al.* (1980) also pointed out that the weighted average equation can be reduced to a simple linear regression. Rewriting Equation (4.1) shows that this linear regression is given by:

$$M_i = (Y_i - X_i)p_y + X_i \quad (4.3)$$

in which the slope is the difference between the component spectral signatures ( $Y_i - X_i$ ) and the intercept is the pure reflectance of one component (in this case  $X_i$ ). However, application of this method requires use of pixels within which the proportions of the component terrains are known, so that the slope can be defined. Such an appraisal may not be possible, meaning that use of the weighted average method is more straightforward.

Marsh *et al.* (1980) also noted that, if different bands are used in the weighted average method, each band may yield a slightly different proportion estimate, depending on the spectral sensitivity of each band to the surface under consideration. Thus, Equation (4.2) needs to be applied to all available bands, and the band for which the best result is obtained used (i.e., the band with the highest sensitivity). If the band is selected appropriately, Marsh *et al.* (1980) found that the weighted average method could be used to estimate the total area occupied by component terrains to within  $\pm 6\%$  of the true area covered.

**Example to estimate the island area of Vulcano and Stromboli** Application of the method to AVHRR data for Vulcano and Stromboli bears these points out. In VIS and NIR AVHRR images, the volcanic islands of Vulcano and Stromboli are apparent as higher reflectance anomalies against a dark (low reflectance) background of sea. The resulting AVHRR pixel map looks very much like that given in Figure 4.1a, where a core of dark island pixels, with brightness  $Y_i$ , are separated from the surrounding bright sea pixels, with brightness  $X_i$ , by a ring of mixed pixels with a moderate brightness  $M_i$ .

If we characterize the spectral reflectance of the sea using the minimum reflectance from the surrounding water, and use the mean reflectance of pure island pixels (i.e., pixels central to the island and entirely surrounded by other island pixels) we can apply Equation (4.2c) to all of the mixed pixels surrounding the island interior. The area of each mixed pixel occupied by island ( $A_y$ ) can now be obtained by multiplying the resulting pixel portion occupied by island ( $p_y$ ) by pixel area ( $A_{\text{pixel}}$ ), i.e.,

$$A_y = p_y A_{\text{pixel}}. \quad (4.4)$$

Summing  $A_y$  calculated for each mixed pixel, and adding in the area of the whole pixels which are entirely island-occupied, should yield the total island area. Applying this to a cloud-free AVHRR image acquired on 25 July 1995 yields the following results.

- In AVHRR band 1 (VIS: 0.58 – 0.68  $\mu\text{m}$ ), Vulcano is apparent as a 44 pixel anomaly. If we apply the Marsh *et al.* (1980) approach to all mixed pixels around the periphery of the island, and add in all whole island pixels, we obtain an island area of  $19.6 \text{ km}^2$ .
- In AVHRR band 2 (NIR: 0.725 – 1.1), Vulcano is apparent as a 46 pixel anomaly which converts to an island area of  $25 \text{ km}^2$ .
- In AVHRR band 1, Stromboli is apparent as a 26 pixel anomaly which converts to an island area of  $11 \text{ km}^2$ .
- In AVHRR band 2, Stromboli is apparent as a 28 pixel anomaly which converts to an island area of  $10.7 \text{ km}^2$ .

The island areas obtained from a Thematic Mapper image (acquired on 3 August 1994) are  $21.2 \text{ km}^2$  for Vulcano and  $12.9 \text{ km}^2$  for Stromboli. Thus the difference between the AVHRR-estimated (mixture-model-derived) areas and TM-derived areas are as follows.

- AVHRR band 1, Vulcano:  $19.6 \text{ km}^2 - 21.2 \text{ km}^2 = -1.6 \text{ km}^2 = -7.5\%$
- AVHRR band 2, Vulcano:  $25.0 \text{ km}^2 - 21.2 \text{ km}^2 = 3.8 \text{ km}^2 = +17.9\%$

- AVHRR band 1, Stromboli:  $11.0 \text{ km}^2 - 12.9 \text{ km}^2 = -1.6 \text{ km}^2 = -14.7\%$
- AVHRR band 2, Stromboli:  $10.7 \text{ km}^2 - 12.9 \text{ km}^2 = -2.2 \text{ km}^2 = -17.0\%$

Thus, AVHRR band 1 provides the best result, likely due to this waveband coinciding with the peak reflectance for the island surfaces. If the correct waveband is used, an accuracy of 7.5% is possible, but this decreases with feature size, and thus also with number of mixed pixels used, so that accuracy is poorer for the smaller target of Stromboli.

**Feature size required to ensure a spectrally pure (un-mixed) pixel** Following Oppenheimer (1993b), if we have a circular isothermal feature, the feature radius needs to exceed  $i\sqrt{2}$ ,  $i$  being the pixel width in meters, to ensure at least one thermally pure pixel. Thus, for a 1 km AVHRR-class pixel, the required feature radius to ensure a thermally pure pixel is 1.41 km, increasing to 5.66 km for a 4 km GOES-class pixel. For a TM-class pixel it is 42 m (for pixels in the SWIR) or 85 m to 170 m (for a 60 m and 120 m pixel, respectively, in the TIR).

#### 4.1.1.2 A two-component, weighted average, mixture model for the thermal infrared

So far we have assessed the mixed pixel problem in terms of brightness and reflection. By using the Planck Function, Marsh *et al.*'s (1980) weighted average method can be expressed in terms of temperature, whereby the spectral exitance for a mixed pixel containing two thermal components can be described by

$$M(\lambda, T_{\text{int}}) = p M(\lambda, T_h) + (1 - p) M(\lambda, T_c) \quad (4.5)$$

in which:

$T_h$  = temperature of the high-temperature surface;

$T_c$  = temperature of the low-temperature surface;

$p$  = proportion of the pixel covered by surfaces at temperature  $T_h$ ; and

$T_{\text{int}}$  = the pixel-integrated temperature for the pixel in band  $\lambda$ .

Now Equation (4.2a) becomes:

$$M(\lambda, T_{\text{int}}) = p M(\lambda, T_h) + M(\lambda, T_c) - pM(\lambda, T_c) \quad (4.6a)$$

which simplifies to

$$M(\lambda, T_{\text{int}}) = p [M(\lambda, T_h) - M(\lambda, T_c)] + M(\lambda, T_c). \quad (4.6b)$$

This can be re-arranged to solve for the portion of either thermal component within the mixed pixel, where for the portion occupied by the high-temperature we have:

$$p = \frac{M(\lambda, T_{\text{int}}) - M(\lambda, T_c)}{M(\lambda, T_h) - M(\lambda, T_c)}. \quad (4.6c)$$

This is the two-component thermal mixture model of Dozier (1980).

**Example for estimating areas of scoria and snow on Etna** We can test the validity and limits of this model by using thermal infrared data collected on the ground during a satellite overpass of a mixed pixel. On 3 June 1994 I made 44 temperature measurements across Etna's 1990 scoria field, immediately to the west of the Bocca Nuova summit crater. Measurements were made over a  $100 \times 100$  m ( $10\,000$  m $^2$ ) area using a Minolta/Land Compac 3 thermal infrared thermometer operating in the 8–14  $\mu\text{m}$  waveband (see Chapter 7 for instrument details and operation). Data were corrected for an emissivity of 0.97 (see Table 8.1) to yield a mean surface temperature of  $52.9^\circ\text{C}$  (min =  $39.3^\circ\text{C}$ , max =  $68.9^\circ\text{C}$ ,  $\sigma = 6.7^\circ\text{C}$ ). Within this area was a  $3800$  m $^2$  snow patch with a typical surface temperature of  $-1.0^\circ\text{C}$ . The snow patch thus occupied 38 % of the measurement area ( $p = 0.38$ ). Such surface cover was typical of the larger ( $1\,000\,000$  m $^2$ ) AVHRR-class pixel area within which my control area was centered.

A simultaneous overpass of AVHRR (at 15:06Z) yielded pixel temperatures<sup>1</sup> for the pixel within which the ground-based measurements were made of  $34.3^\circ\text{C}$  (band 3) and  $34.9^\circ\text{C}$  (in both bands 4 and 5). We can now apply Equation (4.6c) to see what portion of the pixel occupied by scoria (at  $T_h = 52.9^\circ\text{C}$ ) and snow (at  $T_c = -1.0^\circ\text{C}$ ) the weighted average method yields when applied to ambient surfaces imaged in the thermal infrared.

- Band 3:

$$p = \frac{M(3.75\mu\text{m}, 34.3^\circ\text{C}) - M(3.75\mu\text{m}, -1.0^\circ\text{C})}{M(3.75\mu\text{m}, 52.9^\circ\text{C}) - M(3.75\mu\text{m}, -1.0^\circ\text{C})}$$

or

$$p = \frac{1.88 \times 10^6 \text{ W m}^{-2} \text{ m}^{-1} - 3.69 \times 10^5 \text{ W m}^{-2} \text{ m}^{-1}}{3.82 \times 10^6 \text{ W m}^{-2} \text{ m}^{-1} - 3.69 \times 10^5 \text{ W m}^{-2} \text{ m}^{-1}},$$

resulting in

$$p = 0.44 (1 - p) = 0.56, \text{ i.e., snow portion} = 56\%.$$

- Band 4:

$$p = \frac{M(10.8 \mu\text{m}, 34.9^\circ\text{C}) - M(10.8 \mu\text{m}, -1.0^\circ\text{C})}{M(10.8 \mu\text{m}, 52.9^\circ\text{C}) - M(10.8 \mu\text{m}, -1.0^\circ\text{C})}$$

or

$$p = \frac{3.41 \times 10^7 \text{ W m}^{-2} \text{ m}^{-1} - 1.91 \times 10^7 \text{ W m}^{-2} \text{ m}^{-1}}{4.35 \times 10^7 \text{ W m}^{-2} \text{ m}^{-1} - 1.91 \times 10^7 \text{ W m}^{-2} \text{ m}^{-1}},$$

resulting in

$$p = 0.62 (1 - p) = 0.38, \text{ i.e., snow portion} = 38\%.$$

<sup>1</sup> Corrected for emissivity and atmospheric effects.

- Band 5:

$$p = \frac{M(12.0 \text{ } \mu\text{m}, \text{ } 34.9 \text{ } ^\circ\text{C}) - M(12.0 \text{ } \mu\text{m}, \text{ } -1.0 \text{ } ^\circ\text{C})}{M(12.0 \text{ } \mu\text{m}, \text{ } 52.9 \text{ } ^\circ\text{C}) - M(12.0 \text{ } \mu\text{m}, \text{ } -1.0 \text{ } ^\circ\text{C})}$$

or

$$p = \frac{3.13 \times 10^7 \text{ W m}^{-2} \text{ m}^{-1} - 1.85 \times 10^7 \text{ W m}^{-2} \text{ m}^{-1}}{3.90 \times 10^7 \text{ W m}^{-2} \text{ m}^{-1} - 1.85 \times 10^7 \text{ W m}^{-2} \text{ m}^{-1}}$$

resulting in

$$p = 0.62 \ (1 - p) = 0.38, \text{ i.e., snow portion} = 38\%.$$

Given that the expected snow coverage for this pixel was around 38%, the difference between the AVHRR-estimated snow portion and the expected portion is as follows:

- AVHRR band 3:  $0.56 - 0.38 = + 0.18 = + 47\%$
- AVHRR band 4:  $0.38 - 0.38 = 0.00 = 0\%$
- AVHRR band 5:  $0.38 - 0.38 = 0.00 = 0\%$

Thus, AVHRR bands 4 and 5 provide the best results, providing an estimation of the feature area that matches the expected value. This is likely because these wavebands are located at, or close to, the peak of spectral radiant exitance for surfaces at ambient Earth temperatures (see Section 2.1.1 of Chapter 2). The point of peak emission for a surface at  $35 \text{ } ^\circ\text{C}$ , for example, is  $9.4 \text{ } \mu\text{m}$  (see Equation 2.2). This compares with the AVHRR band 3 waveband range of  $3.55\text{--}3.93 \text{ } \mu\text{m}$  and the band 4 range of  $10.3\text{--}11.3 \text{ } \mu\text{m}$ . Hence, the wavelength point of peak emission is much closer to the band 4 waveband range than to the band 3 range.

#### *4.1.1.3 Pixel-integrated temperature and effects over volcanic hot spots*

Equation (4.5) introduces the concept of the pixel-integrated temperature ( $T_{\text{int}}$ ). When a pixel is occupied by more than one thermal component, the pixel brightness temperature will be the result of integrating the radiance emitted by a number of thermal sources within the pixel. It is important to note that the pixel-integrated temperature will not be that of the coolest or hottest component within the pixel, but will be some weighted value that will fall between the two end-member temperatures.

Because the weighting of the value depends on the relative size of the two thermal components, as well as wavelength, the presence of a sub-pixel hot spot has an interesting effect on the recorded pixel-integrated temperature for bands spread across the thermal infrared. As is discussed further in Electronic Supplement 1, the presence of a sub-pixel hot spot will cause the pixel-integrated temperature for any single pixel to be different in the NIR, SWIR, MIR and TIR. This effect can be used to (i) tell that a pixel contains a sub-pixel hot spot, and (ii) un-mix the pixel.

**Volcano hot spot scenario** To illustrate this effect we use a volcanic hot spot scenario in which a  $2 \text{ m}$  radius circular vent at  $950 \text{ } ^\circ\text{C}$  is surrounded by ambient ground at  $25 \text{ } ^\circ\text{C}$ . We

Table 4.1. Pixel-integrated spectral exitances for a thermally mixed pixel containing a 2-m-radius circular hot spot at 950 °C against an ambient background at 25 °C. Relative radiance contributions for each component, plus the pixel-integrated radiance and temperature, are given for a 30 m TM-class pixel in the NIR (0.85 μm), SWIR (2.25 μm), MIR (3.75 μm) and TIR (11 μm), as well as for two wavebands in the TIR at 10.5 μm and 11.5 μm.

	NIR	SWIR	MIR	TIR	10.5 μm	11.5 μm
Hot spot temperature ( $T_h$ , °C)	950	950	950	950	950	950
Background temperature ( $T_c$ , °C)	25	25	25	25	25	25
Hot spot area ( $A_{\text{vent}}$ , m <sup>2</sup> )	12.57	12.57	12.57	12.57	12.57	12.57
Pixel area ( $A_{\text{pixel}}$ , m <sup>2</sup> )	900	900	900	900	121 000	121 000
Pixel portion occupied by hot spot ( $p$ , percent, %)	1.40	1.40	1.40	1.40	1.40	1.40
Pixel portion occupied by ground ( $1 - p$ , percent, %)	98.60	98.60	98.60	98.60	98.60	98.60
Radiance from hot source (W m <sup>-2</sup> m <sup>-1</sup> )	8.20E+08	3.49E+10	2.29E+10	1.21E+09	1.42E+09	1.04E+09
Radiance from ground (W m <sup>-2</sup> m <sup>-1</sup> )	1.82E-10	3.12E+03	1.29E+06	2.92E+07	2.98E+07	2.84E+07
$p M(\lambda, T_h)$ (W m <sup>-2</sup> m <sup>-1</sup> )	1.14E+07	4.88E+08	3.19E+08	1.69E+07	1.98E+07	1.46E+07
$(1 - p) M(\lambda, T_c)$ (W m <sup>-2</sup> m <sup>-1</sup> )	1.80E-10	3.08E+03	1.28E+06	2.88E+07	2.94E+07	2.80E+07
Integrated radiance (W m <sup>-2</sup> m <sup>-1</sup> )	1.14E+07	4.88E+08	3.21E+08	4.57E+07	4.92E+07	4.26E+07
Pixel-integrated temperature (°C)	662	400	248	58	61	56
Percent contribution of $p M(\lambda, T_h)$ to integrated radiance (%)	100.0	100.0	99.6	37.0	40.2	34.2

center this in a 30 m diameter (900 m<sup>2</sup>) pixel and apply the two-component mixture model of Equation (4.5):

$$M(\lambda, T_{\text{int}}) = 0.014M(\lambda, 950 \text{ °C}) + (1 - 0.014)M(\lambda, 25 \text{ °C}).$$

If we use typical waveband mid-points for the NIR, SWIR, MIR, and TIR, we can calculate the expected pixel-integrated spectral exitances for each waveband for such a thermally mixed pixel. These are given in Table 4.1. If we convert these spectral exitances to pixel-integrated temperatures we obtain 662 °C (in the NIR), 400 °C (in the SWIR), 248 °C (in the

MIR), and 58 °C (in the TIR). We thus see that the presence of a sub-pixel hot spot has two effects on the pixel-integrated temperature for the thermally mixed pixel:

- (i) The pixel-integrated temperature does not equal that of the two contributing components, but instead is a weighted average of the two and produces a temperature for a third, imposter, thermal feature that is not actually present on the ground.
- (ii) The pixel-integrated temperature decreases as we move from the NIR, through the SWIR and MIR, to the TIR, so that the temperature for the imposter feature is different in each waveband. In the TIR, for example, if the pixel portion occupied by the hot spot is sufficiently small, the pixel-integrated temperature for the hot spot can be very low. In this case the pixel-integrated temperature in the TIR is 58 °C when the actual temperature of the hot spot is 950 °C.

This is the classic mixed pixel problem and its effect on pixel-integrated temperature in the thermal infrared.

**Why do we have this effect?** As explained in Electronic Supplement 1, pixel-integrated temperatures for pixels containing two-component thermal mixtures are lower in the TIR than in the NIR. This is because of the differing relative contributions of the sub-pixel hot component to the pixel-integrated radiance for the two wavebands. This decreases as we move from the NIR to the TIR. As we see from [Figure 4.2a](#), while the absolute value for spectral radiant exitance for a hot component, in this case at 950 °C, decreases between the SWIR and the TIR, that for an ambient component increases. We also see that while the absolute value for spectral radiant exitance from the hot component decreases by one order of magnitude between the SWIR and the TIR, that for the cool component increases by four orders of magnitude. Consequently, the difference in spectral radiant exitance between the two components is seven orders of magnitude in the SWIR, but only two orders of magnitude in the TIR. Thus, as shown in [Figure 4.2b](#), while the relative contribution of the cool component to the pixel-integrated spectral exitance increases as we move towards the TIR, that of the hot component decreases. As we see from [Table 4.1](#), for this case the hot component contributes 100% of the pixel-integrated radiance in the NIR and SWIR, with the contribution of the cool component being extremely small. However, in the TIR the hot component contributes only 37% of the integrated radiance, with the cool component contributing the remaining 63%. As a result the pixel-integrated spectral radiant exitance, and hence so too the pixel-integrated temperature, becomes increasingly weighted towards the ambient temperature as we move towards the TIR.

We can also see this mixed pixel effect from the Planck curves, as plotted in [Figure 4.3](#). The mixed pixel has a hybrid Planck curve which crosses the Planck curves for pure cases (i.e., pixels containing a surface at a single, homogeneous temperature). We see that the position of the hybrid curve moves from a location near the Planck curve for the high-temperature (950 °C) component in the NIR, to a location near the Planck curve for the low-temperature (25 °C) component in the SWIR. Again, the increasing contribution of the cool component, along with the decreasing contribution of the hot component, pulls the pixel-integrated radiance, and hence temperature, towards that of the lower-temperature component as we move towards longer wavelengths. For example, at 1.65 μm, 3.7 μm and 7.1 μm the hybrid curve crosses the Planck

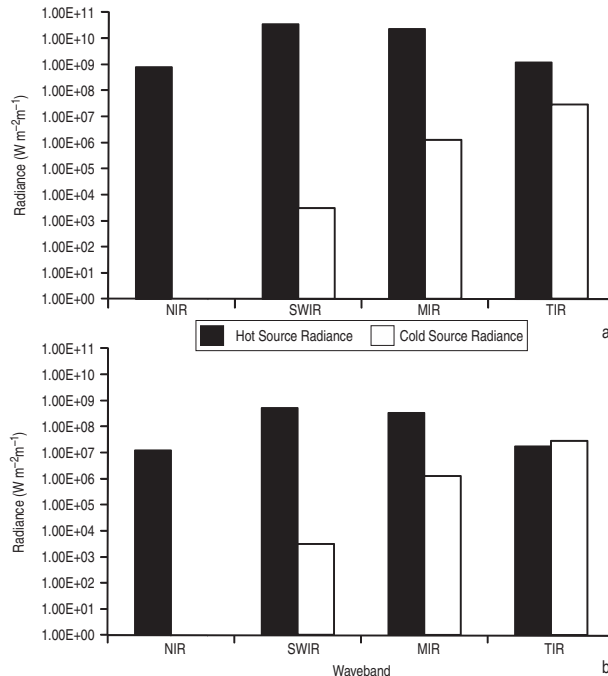


Figure 4.2 (a) Spectral radiance from a hot body at 950 °C and from a cold body at 25 °C in the NIR, MIR, SWIR and TIR. (b) Spectral radiance from a hot body at 950 °C and occupying 14% of a pixel (i.e., a 2-m-radius vent in a 30-m-square pixel) and for a cold body at 25 °C occupying the remainder (86%) of the pixel. Note that the difference between the hot and cold source radiance decreases as we move from the NIR to the TIR.

curves for bodies at 500 °C, 250 °C and 100 °C, respectively. As a result, the mixed pixel will have these pixel-integrated temperatures at each of these locations.

Thus, a thermally mixed pixel will be apparent from markedly different pixel-integrated temperatures in the NIR, SWIR, MIR and TIR. As discussed in Chapter 2, differential atmospheric and emissivity effects can cause brightness temperature to vary by a few degrees centigrade between these four wavebands, but the mixed pixel effect causes the temperature to vary by tens to hundreds of degrees centigrade.

#### 4.1.1.4 The thermally mixed pixel problem, and a solution

The problem is: *the pixel-integrated temperature for a mixed pixel is neither that of the hot source nor the cooler background*. Instead, it is a weighted mixture of the two. Because any pixel over a volcanic hot spot will likely contain more than one thermal surface, the pixel-integrated radiance, and hence also its pixel-integrated temperature, will not be representative of the actual surface temperatures within the mixed pixel. However, the underlying physics that causes a thermally mixed pixel to have different pixel-integrated temperatures in the NIR, SWIR, MIR, and TIR can be used to un-mix the pixel. We next address the problem of un-mixing the thermally mixed pixel over a volcanic heat source.

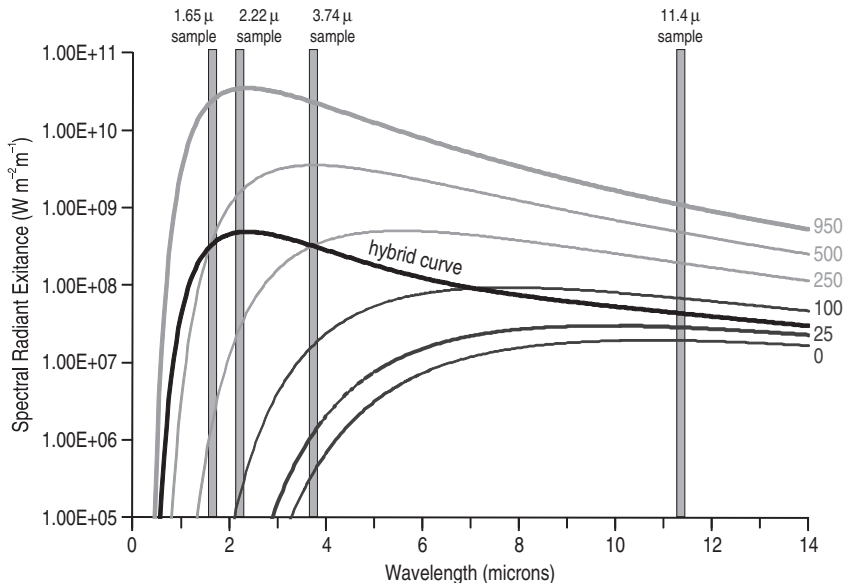


Figure 4.3 Planck curves for cold and hot surfaces at temperatures between 0 °C and 950 °C, plus the hybrid Planck curve for a mixed pixel where a 2-m-radius hot vent at 950 °C is centered in a 30-m-square pixel and is set against a background at 25 °C. We sample the curves in the NIR (1.6 μm), SWIR (2.22 μm), MIR (3.74 μm) and TIR (11.4 μm). Note that the hybrid Planck curve for the mixed pixel (i) crosses the Planck curves for thermally pure pixels, and (ii) is weighted towards the Planck curve for the high-temperature component of the mixed pixel in the NIR, and towards that for the low-temperature component in the TIR.

## 4.2 The dual-band method

For most satellite-sensor pixels containing an active volcanic feature we will have a multiple component surface. In such a case we have an  $n$ -component problem where the pixel-integrated temperature will be expressed by:

$$M(\lambda, T_{\text{int}}) = \sum_{i=1}^n p_i M(\lambda, T_i) \quad (4.7a)$$

or, written in the style followed here,

$$M(\lambda, T_{\text{int}}) = p_1 M(\lambda, T_1) + p_2 M(\lambda, T_2) \dots p_n M(\lambda, T_n). \quad (4.7b)$$

In these equations  $p_i$  and  $T_i$  are the pixel portion occupied by, and temperature of, thermal component  $i$ , and  $n$  is the total number of thermal components. We now have to solve Equation (4.7b) within two limits. The first limit is that of our data, i.e., how many wavebands do we have available, and what are the limits forced by saturation, non-detection and/or spatial resolution? The second limit is the confidence with which we can make realistic assumptions regarding the size and temperature of thermal components residing within the pixel, and/or

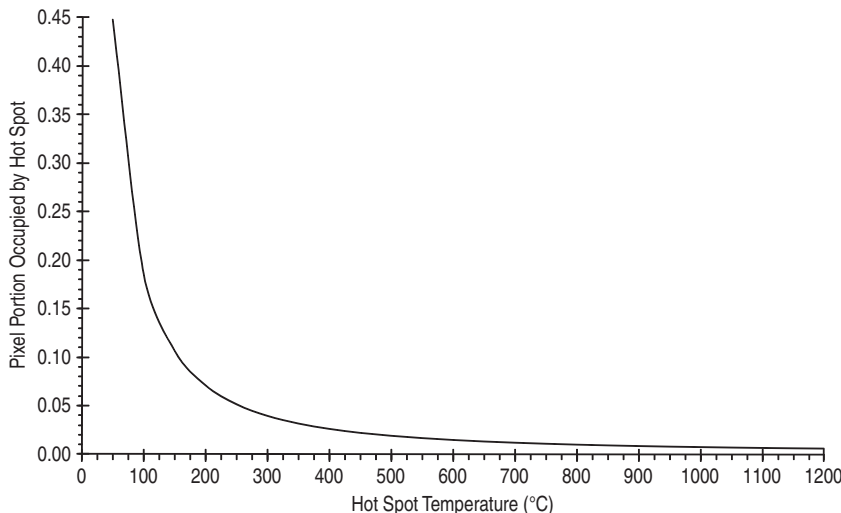


Figure 4.4 Hot spot pixel portion ( $p$ ) and temperature ( $T_h$ ) combinations that (when set against a background at 0 °C) will give a TIR pixel-integrated temperature of 25 °C. To maintain the pixel-integrated temperature we either need a small hot source, or a large cooler source. The relation follows a power law which has the form  $p = x T_h^{-y}$ .

decide how many components we have (i.e., what is the value for  $n$  in Equation (4.7b)). These limits result in a need for rationalization. That is, there are usually too many unknowns and too few useable spectral bands to allow a satisfactory solution of Equation (4.7a).

As reviewed in Electronic Supplement 5, methods to un-mix the thermally mixed pixel have evolved depending on (i) the type of feature examined, (ii) the number and location of available wavebands, and (iii) the spatial resolution of the data. Having presented the mixed pixel problem and classical solution in Section 4.1, we now consider the multitude of options that exist to un-mix the thermally-mixed pixel. We also consider the assumptions that need to be made when applying a mixture model. These will vary depending on the thermal character of the surfaces contained within the pixel, the number of available wavebands, their location in the spectrum, saturation issues and spatial resolution.

#### 4.2.1 Un-mixing the thermally mixed pixel

For a pixel containing a sub-resolution hot spot, an infinite combination of pixel portions occupied by that hot spot ( $p$ ) and potential hot spot temperatures ( $T_h$ ) can produce the same pixel-integrated temperature in any given waveband. If we take any given pixel-integrated temperature, use of Equation (4.6) allows us to plot the combinations of  $p$  and  $T_h$  that will give the pixel-integrated temperature in each waveband (Figure 4.4). From Figure 4.4 we see that, to maintain the integrated temperature, as  $T_h$  increases the pixel portion occupied by the sub-pixel hot spot must decrease. However, only one point on this line represents the actual combination of  $p$  and  $T_h$ .

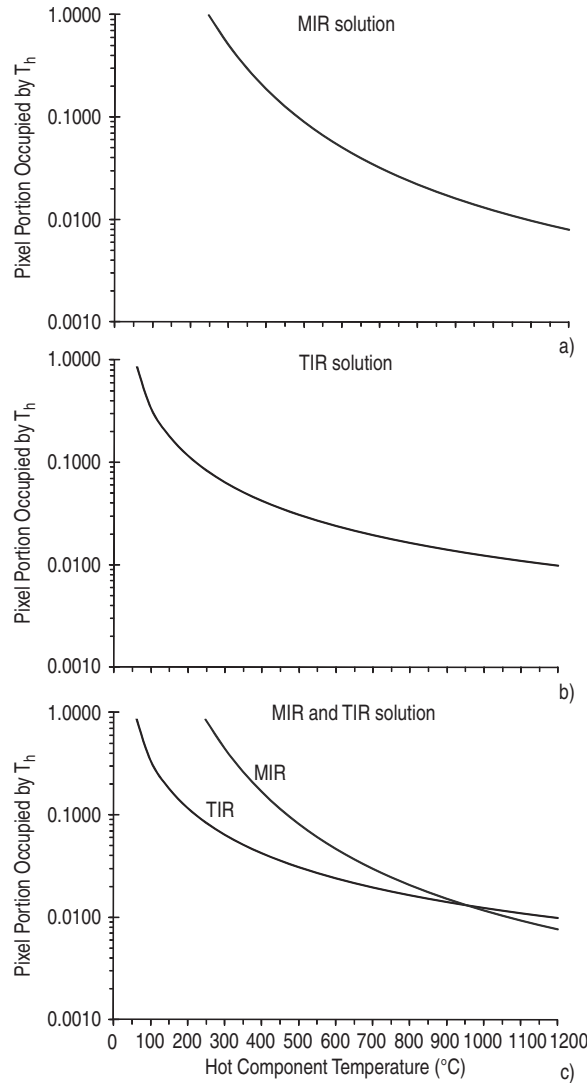


Figure 4.5 The dual-band solution. (a) Combinations of  $p$  and  $T_h$  that yield a MIR pixel-integrated temperature of 248 °C, and (b) a TIR pixel-integrated temperature of 58 °C (given an assumed background temperature of 25 °C). (c) The MIR and TIR  $p$  and  $T_h$  combinations plotted together showing convergence at the solution, i.e.,  $p = 0.0140$  and  $T_h = 950^\circ\text{C}$ , this being the size and temperature of the hot spot input into the hot vent pixel model.

For the sub-pixel hot spot scenario used earlier, where a 2-m-radius hot vent at 950 °C ( $= T_h$ ) against a background of 25 °C ( $= T_c$ ) was located in a 30-m pixel, we saw how the differing responses to the sub-pixel hot source yielded different pixel-integrated temperatures in the MIR and TIR. We can use this characteristic dual-band thermal response to un-mix the pixel.

The pixel-integrated temperature in the MIR ( $\lambda = 3.75 \mu\text{m}$ ) was  $248^\circ\text{C}$ . As plotted in Figure 4.5a, we see that any number of combinations  $p$  and  $T_h$  can now yield this pixel-integrated temperature in the MIR ranging from the lower  $T_h$  limit of  $248^\circ\text{C}$  for  $p = 1$ , to  $p = 0.0079$  at  $T_h = 1200^\circ\text{C}$ . We can do the same for the  $58^\circ\text{C}$  pixel-integrated temperature obtained for the TIR ( $\lambda = 11 \mu\text{m}$ ). Because the mixture model yields a lower pixel-integrated temperature in the TIR at  $p = 1$  (i.e., the pixel-integrated temperature of  $58^\circ\text{C}$ ), the combinations  $p$  and  $T_h$  that can yield this pixel-integrated temperature in the TIR extend to a lower  $T_h$  limit than in the MIR, this being  $T_h = 58^\circ\text{C}$  if  $p = 1$ , as plotted in Figure 4.5b. If we plot the two solution curves together (as in Figure 4.5c) we see that infinite combinations of  $p$  and  $T_h$  can yield the two pixel-integrated temperature curves in the two wavebands. However, for any given  $T_h$ , the  $p$  value required to yield the pixel-integrated temperature in the MIR has to be different to that required to yield the pixel-integrated temperature in the TIR. For example, a sub-pixel hot spot at  $250^\circ\text{C}$  against a background of  $25^\circ\text{C}$  can yield the required pixel-integrated temperatures of  $248^\circ\text{C}$  in the MIR and  $58^\circ\text{C}$  in the TIR, but it has to occupy a greater pixel portion in the MIR ( $p = 0.9752$ ) than in the TIR ( $p = 0.0927$ ). Only at one  $T_h$  are the values for  $p$  the same in both the MIR and TIR. At this point the two solution curves cross to locate the unique combination of  $p$  and  $T_h$  that yields the two pixel-integrated temperatures, i.e.,  $p = 0.0140$  and  $T_h = 950^\circ\text{C}$ . Identifying this unique solution point, where the two solution curves cross, is the basis of the dual-band method, a method that allows a thermally mixed pixel containing two thermal components to be un-mixed.

#### 4.2.1.1 The dual-band method

The dual-band method was developed by Dozier (1980; 1981), and was initially applied to AVHRR data containing sub-pixel hot spots due to steel mills and oil field gas flares by Matson and Dozier (1981). It was first applied to volcanic hot spots in TM data by Rothery *et al.* (1988), and to AVHRR data containing volcanic hot spots by Oppenheimer (1989), with Francis and Rothery (1987) having pointed to the differences in pixel-integrated temperatures between TM bands 5 and 7 caused by the presence of sub-pixel hot spots at Lascar's active lava dome. The history of the development and application of the method is detailed further in Electronic Supplement 5.

The method uses two points on the hybrid Planck curve associated with the thermally mixed pixel to find the unique combination of  $p$  and  $T_h$  that produces the hybrid curve. These two points are typically defined by the pixel-integrated spectral radiant exitances in the MIR and TIR (for AVHRR-type solutions) or in the SWIR (for TM-type solutions), i.e., the waveband zones marked on the hybrid Planck curve of Figure 4.3.

To apply the method we need to have:

- (i) two (and only two) distinct thermal components within the mixed pixel,
- (ii) knowledge of one of the three parameters:  $p$ ,  $T_h$  or  $T_c$ ,
- (iii) measurements at two widely separated wavebands,
- (iv) a thermal anomaly in both wavebands, and
- (v) unsaturated data.

Given these conditions we can use the pixel-integrated temperatures in the two wavebands to find (if  $T_c$  is known or can be assumed) the unique combination of  $p$  and  $T_h$  that produces the two pixel-integrated temperatures. This can be done either graphically or numerically. We demonstrated in Section 4.1.1.3 the hot spot scenario of a hot vent in a cool background, but the methodology can equally be applied to other scenarios, such as a two-component lava surface (with high-temperature cracks in a cooler crust). The hot spot demonstration used the MIR and TIR wavebands, but any combination of NIR, SWIR, MIR and/or TIR can also be used. Note, though, that although two SWIR bands can be used together (such as Landsat bands 5 and 7), two TIR bands can usually not be used together. This is because the method requires a difference in response between the two selected wavebands and, owing to the poor sensitivity of the TIR to sub-pixel hot spots, pixel-integrated temperatures obtained at two TIR wavebands (e.g., between bands operating at 10–11  $\mu\text{m}$  and 11–12  $\mu\text{m}$ ) are often similar. For example, for the hot spot scenario used here, the pixel-integrated temperature (for a 30 m pixel) will be 61 °C and 56 °C at 10–11  $\mu\text{m}$  and 11–12  $\mu\text{m}$ , respectively.

**Graphical solution** Graphical solution involves plotting all combinations of  $p$  and  $T_h$  that can yield the pixel-integrated temperatures in the two wavebands and finding the point at which the curves cross. This can be done, for example, by taking Equation (4.5) and starting at a reasonable upper limit for  $T_h$ , which may be ~1200 °C for a basaltic lava, and calculating the  $p$  in the two wavebands. We then decrease  $T_h$  by 50 °C and calculate again. We can carry on to a point where  $T_h$  is one degree above  $T_c$ . If we plot all of the points for both wavebands, as done in Figure 4.5c, we see that the curves cross. This is the solution point.

**Numerical solution** Numerical solution involves taking the pixel-integrated temperatures ( $T_{\text{int}}$ ) in the two wavebands centered at wavelengths  $\lambda_1$  and  $\lambda_2$ , converting them to spectral radiant exitances, and applying the following simultaneous equations:

$$M(\lambda_1, T_{\text{int}}) = p M(\lambda_1, T_h) + (1 - p)M(\lambda_1, T_c) \quad (4.8a)$$

$$M(\lambda_2, T_{\text{int}}) = p M(\lambda_2, T_h) + (1 - p)M(\lambda_2, T_c). \quad (4.8b)$$

Here we have two equations and three unknowns ( $p$ ,  $T_h$  and  $T_c$ ). We thus need to assume one of the three unknowns if we are to solve for the other two. One way to do this is to re-arrange the equations to isolate  $p$ , so that:

$$p_{\lambda 1} = \frac{M(\lambda_1, T_{\text{int}}) - M(\lambda_1, T_c)}{M(\lambda_1, T_h) - M(\lambda_1, T_c)} \quad (4.8c)$$

$$p_{\lambda 2} = \frac{M(\lambda_2, T_{\text{int}}) - M(\lambda_2, T_c)}{M(\lambda_2, T_h) - M(\lambda_2, T_c)}. \quad (4.8d)$$

If we now assume  $T_c$ , we can adjust  $T_h$  until  $p_{\lambda 1} = p_{\lambda 2}$ , or the ratio of  $p_{\lambda 1} / p_{\lambda 2} = 1$ . Take the earlier scenario where we have pixel-integrated temperatures for a sub-pixel hot spot of 248 °C in the MIR ( $=\lambda_1$ ) and 58 °C in the TIR ( $=\lambda_2$ ). If we know the ambient temperature (25 °C), we can start by assuming  $T_c$  (=25 °C) and by inputting a  $T_h$  that is one degree above the background (i.e.,  $T_c + 1$  °C = 26 °C). Converting these temperatures to spectral radiant exitances in the two wavebands and inserting them into Equations (4.8c) and (4.8d) gives:

$$p_{\lambda 1} = \frac{3.21 \times 10^8 \text{ W m}^{-2} \text{ m}^{-1} - 1.29 \times 10^6 \text{ W m}^{-2} \text{ m}^{-1}}{1.35 \times 10^6 \text{ W m}^{-2} \text{ m}^{-1} - 1.29 \times 10^6 \text{ W m}^{-2} \text{ m}^{-1}} = 5610$$

$$p_{\lambda 2} = \frac{4.57 \times 10^7 \text{ W m}^{-2} \text{ m}^{-1} - 2.92 \times 10^7 \text{ W m}^{-2} \text{ m}^{-1}}{2.96 \times 10^7 \text{ W m}^{-2} \text{ m}^{-1} - 2.92 \times 10^7 \text{ W m}^{-2} \text{ m}^{-1}} = 38$$

so that

$$p_{\lambda 1}/p_{\lambda 2} = 148.$$

Because the input  $T_h$  is lower than the pixel integrated temperature in both bands, the hot spot has to exceed the size of the pixel (i.e., the calculated  $p$  is greater than one) to yield the pixel-integrated temperature. This is plainly impossible. A more sensible starting point would thus be to input a  $T_h$  that is 1 °C greater than the highest pixel-integrated temperature (i.e., 248 °C + 1 °C = 249 °C). This now yields:

$$p_{\lambda 1} = \frac{3.21 \times 10^8 \text{ W m}^{-2} \text{ m}^{-1} - 1.29 \times 10^6 \text{ W m}^{-2} \text{ m}^{-1}}{3.24 \times 10^8 \text{ W m}^{-2} \text{ m}^{-1} - 1.29 \times 10^6 \text{ W m}^{-2} \text{ m}^{-1}} = 0.9891$$

$$p_{\lambda 2} = \frac{4.57 \times 10^7 \text{ W m}^{-2} \text{ m}^{-1} - 2.92 \times 10^7 \text{ W m}^{-2} \text{ m}^{-1}}{2.06 \times 10^8 \text{ W m}^{-2} \text{ m}^{-1} - 2.92 \times 10^7 \text{ W m}^{-2} \text{ m}^{-1}} = 0.0933$$

so that

$$p_{\lambda 1}/p_{\lambda 2} = 10.6.$$

The solution is now more sensible (i.e., the pixel portion occupied by the hot spot is less than one), but  $p_{\lambda 1}$  remains greater than  $p_{\lambda 2}$ , so that  $p_{\lambda 1}/p_{\lambda 2}$  is greater than one. We thus need to increase  $T_h$  to bring  $p_{\lambda 1}$  down. If, for example, we increase  $T_h$  to 500 °C we obtain

$$p_{\lambda 1} = \frac{3.21 \times 10^8 \text{ W m}^{-2} \text{ m}^{-1} - 1.29 \times 10^6 \text{ W m}^{-2} \text{ m}^{-1}}{3.55 \times 10^9 \text{ W m}^{-2} \text{ m}^{-1} - 1.29 \times 10^6 \text{ W m}^{-2} \text{ m}^{-1}} = 0.0901$$

$$p_{\lambda 2} = \frac{4.57 \times 10^7 \text{ W m}^{-2} \text{ m}^{-1} - 2.92 \times 10^7 \text{ W m}^{-2} \text{ m}^{-1}}{5.24 \times 10^8 \text{ W m}^{-2} \text{ m}^{-1} - 2.92 \times 10^7 \text{ W m}^{-2} \text{ m}^{-1}} = 0.0334$$

so that

$$p_{\lambda 1}/p_{\lambda 2} = 2.7.$$

We see that the increase in  $T_h$  has decreased both  $p_{\lambda 1}$  and  $p_{\lambda 2}$ , but  $p_{\lambda 1}$  has decreased to a greater degree, so that  $p_{\lambda 1}/p_{\lambda 2}$  is now lower. However,  $p_{\lambda 1}$  is still greater than  $p_{\lambda 2}$ , so that  $p_{\lambda 1}/p_{\lambda 2}$  remains greater than one. Thus we need to continue to increase  $T_h$  until  $p_{\lambda 1} = p_{\lambda 2}$ , so that  $p_{\lambda 1}/p_{\lambda 2} = 1$ . For this model, because the model input hot spot temperature is 950 °C, we reach this condition at a  $T_h$  of 950 °C, at which point:

$$p_{\lambda 1} = \frac{3.21 \times 10^8 \text{ W m}^{-2} \text{ m}^{-1} - 1.29 \times 10^6 \text{ W m}^{-2} \text{ m}^{-1}}{2.29 \times 10^{10} \text{ W m}^{-2} \text{ m}^{-1} - 1.29 \times 10^6 \text{ W m}^{-2} \text{ m}^{-1}} = 0.0140$$

$$p_{\lambda 2} = \frac{4.57 \times 10^7 \text{ W m}^{-2} \text{ m}^{-1} - 2.92 \times 10^7 \text{ W m}^{-2} \text{ m}^{-1}}{1.21 \times 10^9 \text{ W m}^{-2} \text{ m}^{-1} - 2.92 \times 10^7 \text{ W m}^{-2} \text{ m}^{-1}} = 0.0140$$

so that

$$p_{\lambda 1}/p_{\lambda 2} = 1.0.$$

If we start the process with a  $T_h$  that is too high, we have the reverse situation, in which  $p_{\lambda 1}$  is now less than  $p_{\lambda 2}$ , and  $p_{\lambda 1} / p_{\lambda 2}$  is less than one. For example, if we start by inputting  $T_h = 1200$  °C we obtain:

$$p_{\lambda 1} = \frac{3.21 \times 10^8 \text{ W m}^{-2} \text{ m}^{-1} - 1.29 \times 10^6 \text{ W m}^{-2} \text{ m}^{-1}}{4.02 \times 10^{10} \text{ W m}^{-2} \text{ m}^{-1} - 1.29 \times 10^6 \text{ W m}^{-2} \text{ m}^{-1}} = 0.0079$$

$$p_{\lambda 2} = \frac{4.57 \times 10^7 \text{ W m}^{-2} \text{ m}^{-1} - 2.92 \times 10^7 \text{ W m}^{-2} \text{ m}^{-1}}{1.62 \times 10^9 \text{ W m}^{-2} \text{ m}^{-1} - 2.92 \times 10^7 \text{ W m}^{-2} \text{ m}^{-1}} = 0.0140$$

so that

$$p_{\lambda 1}/p_{\lambda 2} = 0.77.$$

In this case we now need to decrease  $T_h$  until  $p_{\lambda 1} = p_{\lambda 2}$  and  $p_{\lambda 1} / p_{\lambda 2} = 1$ .

What we are doing is, in effect, pushing the solution point up and down the solution curves of Figure 4.5c until we meet the point at which the two curves converge. We have solved here for the case where  $T_c$  is known. Electronic Supplement 6 shows the rearrangements of the equations necessary if  $p$  and  $T_h$  are known, and also gives pieces of code written in IDL to execute each solution.

**Unique (assumption-free) solution using three bands and three equations** If we have a third waveband, at wavelength  $\lambda_3$ , we can obtain a unique solution to this two-component problem. The third waveband allows us a third equation, so that we now have three simultaneous equations and three unknowns ( $T_c$ ,  $T_h$  and  $p$ ):

$$M(\lambda_1, T_{\text{int}}) = p M(\lambda_1, T_h) + (1 - p) M(\lambda_1, T_c) \quad (4.9a)$$

$$M(\lambda_2, T_{\text{int}}) = p M(\lambda_2, T_h) + (1 - p) M(\lambda_2, T_c) \quad (4.9b)$$

$$M(\lambda_3, T_{\text{int}}) = p M(\lambda_3, T_h) + (1 - p) M(\lambda_3, T_c). \quad (4.9c)$$

We can now rewrite the third equation to eliminate, for example,  $p$ :

$$p = \frac{M(\lambda_3, T_{\text{int}}) - M(\lambda_3, T_c)}{M(\lambda_3, T_h) - M(\lambda_3, T_c)}. \quad (4.9d)$$

This allows us to solve the problem without making any assumptions.

An infinite number of combinations of  $T_c$ ,  $T_h$  and  $p$  can yield the pixel-integrated temperature in each of the three wavebands, each combination being defined by a plane of possible solutions. Our challenge is to find the combination of  $T_c$ ,  $T_h$  and  $p$  which makes the

three equations valid and which, when used in all three equations, will yield the required pixel-integrated temperature in each waveband.

Numerical solution requires iteration in two planes ( $T_c$  and  $T_h$ ) to find a value of  $p$  that is (i) greater than zero but less than one, and (ii) makes Equations (4.9a), (4.9b) and (4.9c) valid. That is, when we plug the value for  $p$  obtained using Equation (4.9d), along with the  $T_h$  used to obtain that value, into

$$M(\lambda_1, T_c) = \frac{M(\lambda_1, T_{\text{int}}) - pM(\lambda_1, T_h)}{(1 - p)} \quad (4.10\text{a})$$

and

$$M(\lambda_2, T_c) = \frac{M(\lambda_2, T_{\text{int}}) - pM(\lambda_2, T_h)}{(1 - p)} \quad (4.10\text{b})$$

the value for  $T_c$  in both equations is the same. It must also be equal to the value of  $T_c$  used to calculate  $p$  in Equation (4.9d). In other words, the same values of  $T_c$ ,  $T_h$  and  $p$  can be used in all three of the Equations (4.9a)–(4.9c) to obtain the three different pixel-integrated temperatures.

By way of example, take the Section 4.1.1.3 scenario where we have pixel-integrated temperatures for a sub-pixel hot spot of 248 °C in the MIR and 58 °C in the TIR, and add the pixel-integrated temperature from the SWIR of 400 °C. We now need to find the unique combination of  $T_c$  and  $T_h$  that allows all three equations to be solved. For this example, we will use the TIR for the third equation, the MIR for the second and the SWIR for the first. If we start with a hot-component temperature that is 100 °C ( $= T_h$ ), a cool-component temperature that is 0 °C ( $= T_c$ ), a TIR pixel-integrated temperature of 58 °C and convert all values to spectral exitances in the TIR, we arrive at

$$p = \frac{4.57 \times 10^7 \text{ W m}^{-2} \text{ m}^{-1} - 1.95 \times 10^7 \text{ W m}^{-2} \text{ m}^{-1}}{7.18 \times 10^7 \text{ W m}^{-2} \text{ m}^{-1} - 1.95 \times 10^7 \text{ W m}^{-2} \text{ m}^{-1}} = 0.5016.$$

If we now use the SWIR pixel-integrated temperature of 400 °C and the assumed  $T_h$  of 100 °C, along with the calculated  $p$  of 0.5016, converting the temperatures to spectral exitances in the SWIR we have:

$$\begin{aligned} M(\lambda_1, T_c) &= \frac{4.88 \times 10^8 \text{ W m}^{-2} \text{ m}^{-1} - 0.5016(2.33 \times 10^5 \text{ W m}^{-2} \text{ m}^{-1})}{(1 - 0.5016)} \\ &= 9.78 \times 10^8 \text{ W m}^{-2} \text{ m}^{-1}, \end{aligned}$$

which converts to a  $T_c$  of 454 °C. Doing the same for MIR (using the MIR pixel-integrated temperature of 248 °C) gives:

$$\begin{aligned} M(\lambda_2, T_c) &= \frac{3.21 \times 10^8 \text{ W m}^{-2} \text{ m}^{-1} - 0.5016(1.72 \times 10^7 \text{ W m}^{-2} \text{ m}^{-1})}{(1 - 0.5016)} \\ &= 6.26 \times 10^8 \text{ W m}^{-2} \text{ m}^{-1}, \end{aligned}$$

which converts to a  $T_c$  of 300 °C. The two  $T_c$  values are not the same and are different to that used in the TIR to estimate  $p$ , i.e., a different  $T_c$  is required in the SWIR, MIR and TIR to satisfy the equations using a  $p$  of 0.5016. We thus increase  $T_c$  and recalculate. After a  $T_c$  of 58 °C we find that  $p$  becomes negative, and a solution has still not been reached. Thus we now increase  $T_h$  to 150 °C and begin to increase  $T_c$  once more from the starting point of 0 °C. We finally reach solution at  $T_h = 950$  °C and  $T_c = 25$  °C. At this point, the TIR data yields:

$$p = \frac{4.57 \times 10^7 \text{ W m}^{-2} \text{ m}^{-1} - 2.92 \times 10^7 \text{ W m}^{-2} \text{ m}^{-1}}{1.21 \times 10^9 \text{ W m}^{-2} \text{ m}^{-1} - 2.92 \times 10^7 \text{ W m}^{-2} \text{ m}^{-1}} = 0.014.$$

In the SWIR this gives:

$$\begin{aligned} M(\lambda_1, T_c) &= \frac{4.88 \times 10^8 \text{ W m}^{-2} \text{ m}^{-1} - 0.014(3.49 \times 10^{10} \text{ W m}^{-2} \text{ m}^{-1})}{(1 - 0.014)} \\ &= 312 \times 10^3 \text{ W m}^{-2} \text{ m}^{-1}, \end{aligned}$$

which converts to a  $T_c$  of 25 °C. In the MIR this then gives:

$$\begin{aligned} M(\lambda_2, T_c) &= \frac{3.21 \times 10^8 \text{ W m}^{-2} \text{ m}^{-1} - 0.014(2.29 \times 10^{10} \text{ W m}^{-2} \text{ m}^{-1})}{(1 - 0.014)} \\ &= 1.29 \times 10^6 \text{ W m}^{-2} \text{ m}^{-1}, \end{aligned}$$

which also converts to 25 °C. Thus we have found the solution point.

**Applicability of the two-component model** Potential thermal mixture scenarios for a pixel containing an active lava are given in [Figure 4.6](#), where we see that as the thermal complexity of the surface, or the size of the pixel, increases, so we move away from a two-component scenario. For the two-component dual-band method to work, we need a situation where the pixel contains a single, isothermal hot spot against a cooler, isothermal background. For TM-, AVHRR- and GOES-class pixels this may apply to a case where a single hot vent is present against a cold ambient background, as envisaged in our test-case scenario. For TM-class pixels the two-component model may also apply to cases where the pixel is filled with active lava, so that the pixel thermal structure can be approximated by the model of Crisp and Baloga ([1990a](#)). This model describes an active lava surface using two thermal components whereby:

A cool crust at temperature  $T_c$  occupying fraction  $f$  of the surface is broken by high temperature cracks (at temperature  $T_h$ ) occupying  $(1-f)$  portion of the surface (Crisp and Baloga, [1990a](#)).

For active lava flows, lakes and domes, this may be a reasonable approximation for the thermal surface where incandescent cracks are apparent in a dark, cooled, surface crust, as in (b) of [Figure 4.6](#). As a result, such a scenario has commonly been assumed for application of the two-component dual-band method using TM-class data over active lava flows, lakes and domes (see Electronic Supplement 5).

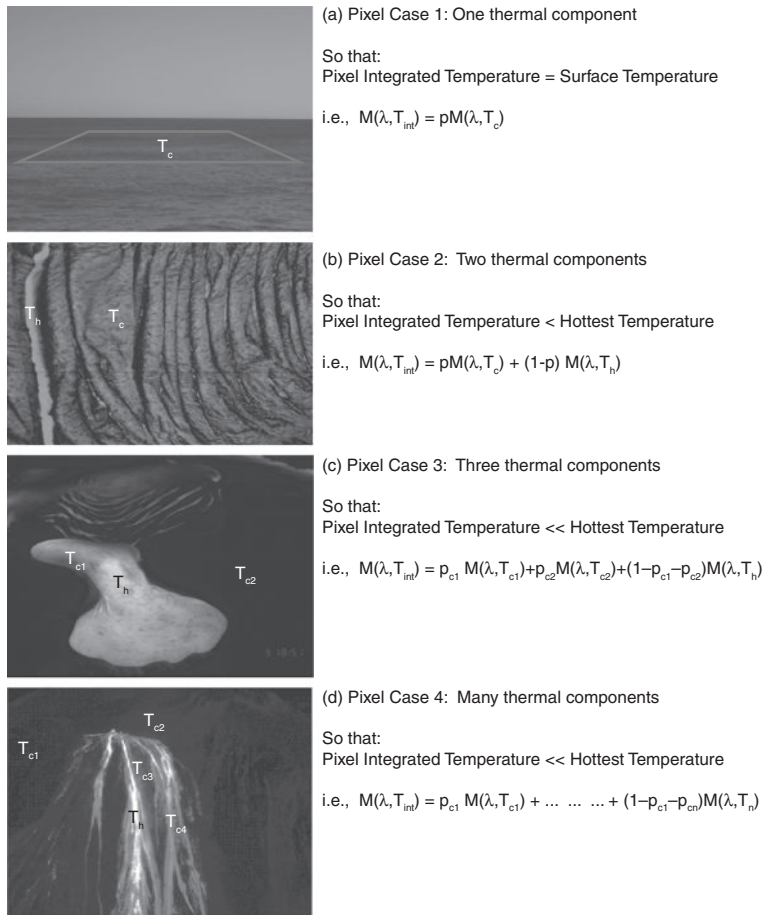


Figure 4.6 Pixel mixture models for (a) one-, (b) two-, (c) three-, and (d) multiple-thermal-component situations. Although there is actually a continuum of surface temperatures in (b)–(d), they can be approximated reasonably well with two or three thermal components. See also color plates section. Pixel width (also the picture width) is  $\sim 500$  m,  $\sim 1$  m, 5 m and 1000 m for (a), (b), (c) and (d), respectively.

If a third thermal component is present, then the two-component model will fail. This may occur where the hot feature is small, (c) of Figure 4.6, or the pixel large, (d) of Figure 4.6. In such cases the pixel will contain hot cracks at temperature  $T_h$ , cooler crust at temperature  $T_c$  and cold, ambient surfaces at temperature  $T_a$ . Here, to illustrate the problem, we take a  $2300\text{ m}^2$  lava lake that is centered in a  $1\text{ km}^2$  pixel. The lake itself has two thermal components (cool crust broken by hot cracks), and is set against an ambient background, thus the pixel contains three thermal components. Following Flynn *et al.*'s (1993) measurements for type 1 lava lake activity (see Electronic Supplement 1), these components are: hot crust

at 966 °C occupying  $5.61 \times 10^{-5}$  of the pixel, cooler crust at 385 °C occupying  $2.24 \times 10^{-3}$  of the pixel, and an ambient temperature of 25 °C for the remaining  $9.98 \times 10^{-1}$  of the pixel. Using these values in the three-component model of Electronic Supplement 1 gives a pixel-integrated temperature of 65.2 °C in the MIR and 26.9 °C in the TIR. If we take these pixel-integrated temperatures, assume the background temperature (25 °C) and apply a two-component model that assumes we have a lake at temperature  $T_h$  against a background at  $T_c$ , so that:

$$M(\lambda_{\text{MIR}}, 65.2 \text{ }^{\circ}\text{C}) = p M(\lambda_{\text{MIR}}, T_h) + (1 - p) M(\lambda_{\text{MIR}}, 25 \text{ }^{\circ}\text{C})$$

$$M(\lambda_{\text{TIR}}, 26.9 \text{ }^{\circ}\text{C}) = p M(\lambda_{\text{TIR}}, T_h) + (1 - p) M(\lambda_{\text{TIR}}, 25 \text{ }^{\circ}\text{C})$$

we reach a solution at  $T_h$  of 439 °C and  $p$  of  $2.02 \times 10^{-3}$ . Because we have not taken into account the radiant contribution of the hot cracks, we have reached a solution using a crust that is somewhat hotter than reality, and a pixel portion for that crust that is a little smaller.

Such a three-component situation may also occur over lava lakes and channels where the crust temperatures are variable over small (<30 m) spatial scales. For example, take a 30 m pixel filled by a lava channel where a hot central plug is composed of crust at 500 °C occupying 40% of the pixel, broken by cracks at 1000 °C occupying 10% of the pixel. The remaining 50% of the pixel is occupied by cooler crust residing at the channel margins at 250 °C. This three-component model gives a pixel-integrated temperature of 812 °C in the NIR ( $\lambda = 0.85 \text{ } \mu\text{m}$ ) and 618 °C in the SWIR ( $\lambda = 2.25 \text{ } \mu\text{m}$ ). If we then take these pixel-integrated temperatures, assume the lowest crust temperature (250 °C) and apply a two component model that assumes we have a crust at a single temperature,  $T_c$ , broken by cracks at  $T_h$ , so that

$$M(\lambda_{\text{NIR}}, 812 \text{ }^{\circ}\text{C}) = p M(\lambda_{\text{NIR}}, T_h) + (1 - p) M(\lambda_{\text{NIR}}, 250 \text{ }^{\circ}\text{C})$$

$$M(\lambda_{\text{SWIR}}, 618 \text{ }^{\circ}\text{C}) = p M(\lambda_{\text{SWIR}}, T_h) + (1 - p) M(\lambda_{\text{SWIR}}, 250 \text{ }^{\circ}\text{C})$$

we reach a solution at  $T_h$  of 979 °C and  $p$  of 13%. As in the lava lake example, because we have not taken into account the radiant contribution of the crust component at the moderate (500 °C) temperature, we have reached a solution using a high-temperature component that is somewhat cooler than reality, and have obtained a pixel portion that is a little larger. The pixel portion occupied by the coolest temperature component (250 °C) is also far too large, being 87%. Failure to take into account the moderate temperature component has thus pulled the temperature of the hottest component downwards, and the pixel portion occupied by the coolest component upwards. Unfortunately, if we apply a two-component model to a three-component scenario, we can reach a solution that looks plausible, but which is, in fact, wrong. We must thus only apply the two-component solution to scenarios in which we know the pixel thermal structure can be approximated by a two-component model.

Finally, we need to recognize that the dual-band equations may not be solvable, or may give an unrealistic solution. That is, solution may be achieved, but only when using a  $T_h$  that is unreasonably high. This may suggest that one of the assumptions is invalid, and application of the method to the case in hand is inappropriate. The problem is, we are attempting to retrieve the total shape of the Planck curve for a mixed pixel case where we have multiple components. However, we only have spectral-radiance measurements at one or two wavelengths that can be used to define that shape.

**Is it solvable?** As shown by Flynn *et al.* (1994), a point will be reached where, if the portion occupied by the hot component is too large, the radiance contributed by the cooler component will have to be negative to yield the integrated radiance. This is clearly not possible. This point-of-impossible solution marks the limit of the dual-band solution and is given by:

$$p_{\text{limit}} = M(\lambda, T_{\text{int}}) / M(\lambda, T_h) \quad (4.11\text{a})$$

where  $p_{\text{limit}}$  is the largest portion the hot component can attain before the background radiance has to become negative to allow solution. If we now solve the two-component form of the dual band and the resulting  $p$  is higher than  $p_{\text{limit}}$ , solution has been reached, but the solution is unreasonable since it requires a negative contribution from the cooler component. It can thus be rejected.

This relation also allows us to plot the range of hot component portions above which solution will not be possible for a given waveband and temperature assumption. This is done in [Figure 4.7](#), for a  $T_h$  of 1000 °C, for the wavelengths of TM's SWIR band 7 across a range of pixel-integrated temperatures between 0 °C and 1000 °C. We see that  $p_{\text{limit}}$  increases over six orders of magnitude between an integrated temperature of 100 °C and 1000 °C, reaching one at the pixel-integrated temperature that equals the assumed  $T_h$  value. Across TM band 7's dynamic range (as defined in Electronic Supplement 1),  $p_{\text{limit}}$  increases from  $2.78 \times 10^{-6}$  at the lower limit of detection (i.e., a pixel-integrated temperature of 94 °C) to  $1.00 \times 10^{-3}$  at band 7's saturation point (i.e., a pixel-integrated temperature of 277 °C).

Solution also requires that a thermal anomaly exists and/or that the data are not saturated. Thus, following the methodologies laid out in Electronic Supplement 1, “sensitivity” curves can be plotted using the lower and upper detection limits of the sensor. Using the lower response limit of the band (i.e., the minimum radiance that can be measured by the sensor,  $R_{\min}^*$ ) the combinations of  $p$  and  $T_h$  required to achieve this lower detection limit can be calculated from:

$$p_{\min} = \frac{R_{\min}^* - M(\lambda, T_c)}{M(\lambda, T_h) - M(\lambda, T_c)}. \quad (4.11\text{b})$$

In other words, the hot spot cannot be cooler or smaller than these  $p$  and  $T_h$  combinations if it is to be detected. The curves marking this limit for TM bands 5 and 7 are plotted in [Figure 4.7b](#). Likewise, the upper response limit of the band (i.e., saturation,  $R_{\max}^*$ ) can be used to find the combinations of  $p$  and  $T_h$  required to achieve this upper limit from:

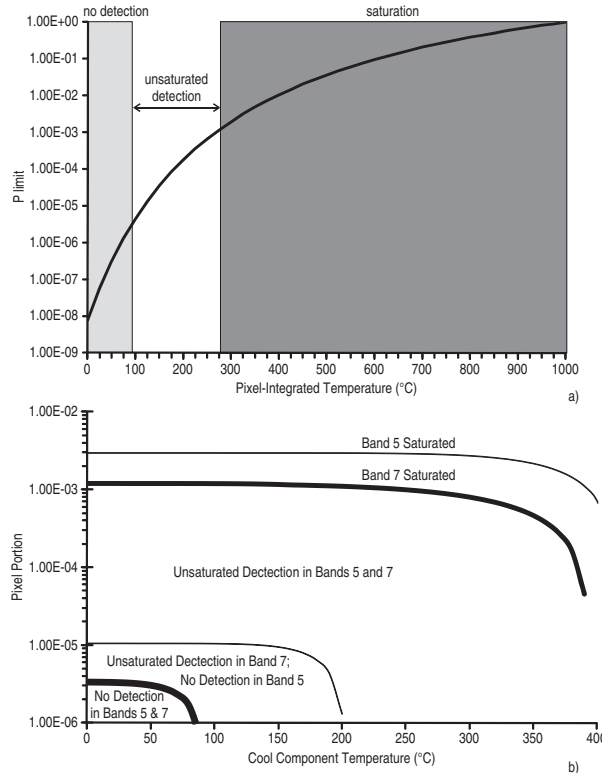


Figure 4.7 (a) Maximum pixel portion that a hot surface at 1000 °C can attain for SWIR pixel-integrated temperatures of between 0 °C and 1000°C. Also given are the zones within which (i) the hot spot will not be detected (i.e., pixel-integrated radiance is less than the lower end of the sensor dynamic range, which in this case is set equivalent to a pixel-integrated temperature of 97 °C) and (ii) the hot spot will saturate the sensor (for this case saturation is set to 277 °C). This is the dynamic range of Landsat TM's SWIR band 7. (b) Pixel portion and cool component temperature combinations that, for a hot component at 1000 °C, will (i) not be detectable in Landsat Thematic Mapper bands 5 and/or 7 (i.e., pixel-integrated temperature is less than 203 °C (band 5) or 94 °C (band 7)), or (ii) will saturate in Landsat Thematic Mapper bands 5 and/or 7 (i.e., pixel-integrated temperature is greater than 415 °C (band 5) or 277 °C (band 7)).

$$P_{\max} = \frac{R_{\max}^* - M(\lambda, T_c)}{M(\lambda, T_h) - M(\lambda, T_c)}. \quad (4.11c)$$

In other words, the hot spot has to be cooler or smaller than these  $p$  and  $T_h$  combinations if data are to be unsaturated. The curves marking this limit for TM bands 5 and 7 are also plotted in Figure 4.7b. Because solution of the dual band requires unsaturated data in two bands, solution is only possible for hot spot cases above the curve marking the lower detection limit of band 5, but below the saturation limit of band 7, i.e., within the zone marked “Unsaturated Detection in Bands 5 and 7” on Figure 4.7b. Below this zone, there will be no signal in band 5; above it band 7 will be saturated.

#### 4.2.1.2 One-component solutions in the NIR or SWIR

If the pixel is occupied by a hot source against a very cool (ambient) background then, as we can see from [Figure 4.2](#), the ambient background contributes a very small amount of radiance to the pixel-integrated spectral radiant exitance in the NIR and SWIR. In such cases we can assume that all of the radiance is coming from the hot source, so that we can reduce the problem to a one-component solution whereby the pixel-integrated spectral radiant exitance is described by:

$$M(\lambda, T_{\text{int}}) = pM(\lambda, T_h). \quad (4.12)$$

For such a case we can solve using one band of data if we have a measure of  $T_h$  or  $p$ . For example, given our working example where a 2 m radius ( $12.6 \text{ m}^2$ ) hot vent at  $950^\circ\text{C}$  is active against a background of  $25^\circ\text{C}$  and is located in a  $900 \text{ m}^2$  pixel, we have  $T_{\text{int}}$  of  $662^\circ\text{C}$  and  $400^\circ\text{C}$  in the NIR and SWIR, respectively. If we know the vent temperature, we can estimate  $p$  by (i) assuming  $T_h$ , (ii) converting all temperature values to the appropriate spectral radiant exitance values in the NIR or SWIR, and (iii) inserting these into a re-arranged form of Equation (4.12). In the NIR this results in:

$$p = 1.14 \times 10^7 \text{ W m}^{-2} \text{ m}^{-1} / 8.20 \times 10^8 \text{ W m}^{-2} \text{ m}^{-1} = 0.014$$

and, in the SWIR:

$$p = 4.88 \times 10^8 \text{ W m}^{-2} \text{ m}^{-1} / 3.49 \times 10^{10} \text{ W m}^{-2} \text{ m}^{-1} = 0.014$$

Given that the pixel area is  $900 \text{ m}^2$ , the vent area is  $0.014 \times 900 \text{ m}^2 = 12.6 \text{ m}^2$ . Alternatively, if we know the vent area, we can estimate  $T_h$  using  $p$ . In this case  $p$  is 0.014 (i.e.,  $12.6 \text{ m}^2 / 900 \text{ m}^2$ ). Using this in a suitably re-arranged form of Equation (4.12) gives a solution in the NIR of:

$$M(\lambda, T_{\text{int}}) = 1.14 \times 10^7 \text{ W m}^{-2} \text{ m}^{-1} / 0.014 = 8.20 \times 10^8 \text{ W m}^{-2} \text{ m}^{-1} = 950^\circ\text{C}$$

and, in the SWIR:

$$M(\lambda, T_{\text{int}}) = 4.88 \times 10^8 \text{ W m}^{-2} \text{ m}^{-1} / 0.014 = 3.49 \times 10^{10} \text{ W m}^{-2} \text{ m}^{-1} = 950^\circ\text{C}.$$

**Unique solution** If we have measurements in both the NIR and SWIR wavebands, we can arrive at a solution with no assumptions. In this case, the simultaneous equations that need to be solved are:

$$M(\lambda_{\text{NIR}}, T_{\text{int}}) = pM(\lambda_{\text{NIR}}, T_h) \quad (4.13a)$$

$$M(\lambda_{\text{SWIR}}, T_{\text{int}}) = pM(\lambda_{\text{SWIR}}, T_h). \quad (4.13b)$$

Solution should now be familiar and can be achieved either graphically, as done in [Figure 4.8](#), or numerically. Numerical solution involves either re-arranging Equations (4.13a) and (4.13b) to isolate  $p$  so that,

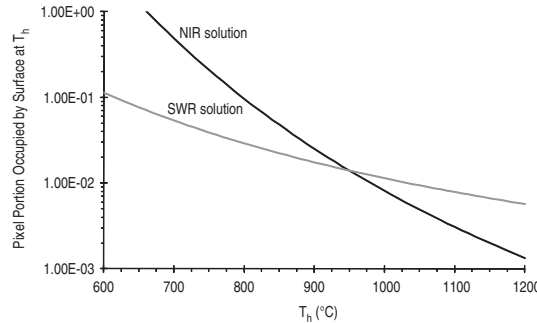


Figure 4.8 One-component dual-band (NIR and SWIR) solution for a hot spot set against a non-radiant background. Pixel-integrated temperature is 662 °C in the NIR and 400 °C in the SWIR. Solution occurs where the two curves, marking all combinations of hot spot pixel portion and temperature that can give the pixel-integrated temperatures in the two bands, cross.

$$p_{\text{NIR}} = M(\lambda_{\text{NIR}}, T_{\text{int}})/M(\lambda_{\text{NIR}}, T_h) \quad (4.13c)$$

$$p_{\text{SWIR}} = M(\lambda_{\text{SWIR}}, T_{\text{int}})/M(\lambda_{\text{SWIR}}, T_h) \quad (4.13d)$$

or by re-arranging to isolate  $T_h$  so that,

$$M(\lambda_{\text{NIR}}, T_h) = M(\lambda_{\text{NIR}}, T_{\text{int}})/p \quad (4.13e)$$

$$M(\lambda_{\text{SWIR}}, T_h) = M(\lambda_{\text{SWIR}}, T_{\text{int}})/p. \quad (4.13f)$$

Solution now involves either:

- (1) iterating on  $T_h$  until  $p_{\text{NIR}} = p_{\text{SWIR}}$ , or
- (2) iterating on  $p$  until  $T_h(\text{NIR}) = T_h(\text{SWIR})$ .

This can be achieved by following the numerical solution procedures detailed earlier.

**Applicability of the one-component model** Such a solution will fail if the background contributes to the pixel-integrated spectral exitance. In the NIR and SWIR, problems may occur over active lava lakes and flows. In such cases, the pixel may be filled by hot crust (the background) at temperatures in excess of 250 °C, broken by the hot cracks ( $T_h$ ) for which we are trying to find a solution. As a result, the background will contribute to the pixel-integrated spectral radiance, so that if we apply the single-component approach, solution will require the pixel portion occupied by the hot component to be too large in order to balance the spectral radiance. Take a case where, for example, we have hot cracks at 950 °C occupying 0.014 of the pixel against a crust at 500 °C. The pixel integrated temperatures for this case are 663 °C in the NIR and 524 °C in the SWIR. Assuming a one-component model, using a  $T_h$  of 950 °C, and converting to spectral exitances, in the NIR we obtain

$$p = 1.17 \times 10^7 \text{ W m}^{-2} \text{ m}^{-1} / 8.20 \times 10^8 \text{ W m}^{-2} \text{ m}^{-1} = 0.0143$$

and in the SWIR

$$p = 2.12 \times 10^9 \text{ W m}^{-2} \text{ m}^{-1} = 3.49 \times 10^{10} \text{ W m}^{-2} \text{ m}^{-1} = 0.0607$$

Thus we have an over-estimate on  $p$ . The same will apply if we assume  $p$  and solve for  $T_h$ , the result being 952 °C in the NIR and 1420 °C in the SWIR, the latter solution becoming unrealistic (1200 °C being the absolute maximum expected over a basaltic flow). The over-estimate is worse in the SWIR than in the NIR because the cool component contributes more to the pixel-integrated spectral radiance in the SWIR than in the NIR. For reasons of sensitivity (see Electronic Supplement 1) the relative contribution of the cool component is just 2% in the NIR, but 78% in the SWIR. The problem is thus (i) worse in the SWIR than in the NIR, and (ii) increases as the temperature of the background increases. Thus, if we are to apply the one-component approach, we must be sure that the hot component is the only source of radiance.

For the same reason, the one-component approach will never work when applied in the TIR as the background will always contribute, yielding  $p$  or  $T_h$  values that are too large. If, for example, we take the hot vent scenario, we have a TIR pixel-integrated spectral exitance of  $4.57 \times 10^7 \text{ W m}^{-2} \text{ m}^{-1}$ , which converts to a TIR pixel-integrated temperature of 58 °C, and to which the ambient component contributes 64%. Assuming  $p$ , and solving for  $T_h$ , the one-component model now gives a result that is ridiculous: 2168 °C.

For this scenario ( $T_h = 950$  °C,  $p = 0.014$ ,  $T_c = 25$  °C), the single-component solution works in the MIR. This mixture model yields a MIR pixel-integrated spectral exitance of  $3.21 \times 10^8 \text{ W m}^{-2} \text{ m}^{-1}$  in the MIR, which converts to a pixel-integrated temperature of 248 °C and to which the ambient component contributes just 0.4%. Assuming  $p$  and solving for  $T_h$  thus gives a result that is reasonable: 951 °C. However, as soon as we begin to increase  $T_c$ , or decrease  $T_h$ , the solution fails due to non-negligible contribution from the background:

- Increasing  $T_c$  to 50 °C gives a pixel-integrated spectral exitance of  $3.23 \times 10^8 \text{ W m}^{-2} \text{ m}^{-1}$ , which converts to a pixel-integrated temperature of 249 °C and to which the ambient component contributes 1%. Assuming  $p$  and solving for  $T_h$  begins to yield a  $T_h$  that needs to be a little too high (954 °C) in order to balance the pixel-integrated spectral exitance.
- Decreasing  $T_h$  to 500 °C gives a pixel-integrated spectral exitance of  $5.08 \times 10^7 \text{ W m}^{-2} \text{ m}^{-1}$ , which converts to a pixel-integrated temperature of 144 °C and to which the ambient component contributes 3%. Assuming  $p$  and solving for  $T_h$  again begins to yield a  $T_h$  that needs to be a little too high in order to balance the pixel-integrated spectral exitance: 504 °C.

The problem in the MIR thus increases with background temperature, and solutions become worse as the hot component temperature decreases. Again, if we are to apply the one-component approach in the MIR, we must be sure that the dominant source of radiance is from the hot component.

#### 4.2.1.3 No anomaly in the TIR?

If there is no thermal anomaly in the TIR, the dual-band solution cannot be solved. This is because if the temperature of the background is the same temperature as, or greater than, that of the target pixel, then the pixel portion occupied by the hot target will have to become negative to balance the equation. Look at the following mixture model, for example,

$$p = \frac{M(\lambda_{\text{TIR}}, T_{\text{int}}) - M(\lambda_{\text{TIR}}, T_c)}{M(\lambda_{\text{TIR}}, T_h) - M(\lambda_{\text{TIR}}, T_c)}. \quad (4.14a)$$

If  $M(\lambda_2, T_c)$  becomes greater than  $M(\lambda_2, T_{\text{int}})$ , as will be the case if  $T_c$  is greater than  $T_{\text{int}}$ , then the top line becomes negative. This means that the result ( $p$ ) will also be negative.

However, in this case we can use the fact that the sub-pixel hot spot is not emitting in the thermal infrared to our advantage; we can assume that the pixel-integrated temperature in the TIR equates to the temperature of the ambient ground in the pixel. If there is an anomaly in the MIR, this can now be used as  $T_c$  in

$$p = \frac{M(\lambda_{\text{MIR}}, T_{\text{int}}) - M(\lambda_{\text{MIR}}, T_c)}{M(\lambda_{\text{MIR}}, T_h) - M(\lambda_{\text{MIR}}, T_c)}. \quad (4.14b)$$

Solution now requires just one assumption: a value for  $T_h$ .

#### 4.2.1.4 Solution with one band of data

If only one band of data is available, a solution can only be achieved by assuming two values to estimate the third. A variety of options are available.

**Option 1** We can calculate the pixel portion occupied by the hot component ( $p$ ) by assuming the cool ( $T_c$ ) and hot component ( $T_h$ ) temperatures and solving:

$$p_{\lambda 1} = \frac{M(\lambda_1, T_{\text{int}}) - M(\lambda_1, T_c)}{M(\lambda_1, T_h) - M(\lambda_1, T_c)}. \quad (4.15a)$$

This may be possible in the case of a hot vent against an ambient background, where vent temperature is available from an independent source (e.g., field measurements) and the cool component temperature can be obtained from surrounding, ambient pixels. Alternatively a range of temperatures can be assumed for  $T_c$  (and/or  $T_h$ ) to output a range of likely hot feature areas. While the former approach was used to estimate skylight areas at Kilauea using one band of TIR data by Flynn *et al.* (1994), the latter approach was used by Gupta and Badarinath (1993) to estimate the possible range of vent areas and temperatures at Barren Island volcano using one band of NIR data. It was also applied by Oppenheimer and Francis (1997) to estimate the possible range of crack areas and crust temperatures at Erta Ale's lava lake using one band of NIR or SWIR data. In this case, a  $T_h$  was assumed and the range of all  $p$  and  $T_c$  temperatures that could give the pixel-integrated temperature in the NIR or SWIR

were plotted. This was done for two  $T_h$  cases, so that two solution graphs were output for each of the  $T_h$  cases (see Electronic Supplement 5).

**Option 2** Alternatively, we can calculate the temperature of the hot component ( $T_h$ ) by assuming the cool component temperature ( $T_c$ ) and pixel portion occupied by the hot component ( $p$ ) from:

$$M(\lambda_1, T_h) = \frac{M(\lambda_1, T_{\text{int}}) - (1-p)M(\lambda_1, T_c)}{p}. \quad (4.15\text{b})$$

This may again be possible in the case of a hot vent against an ambient background, where vent area ( $A_{\text{vent}}$ ) is available from an independent source (e.g., field measurement) and the cool component temperature ( $T_c$ ) can be obtained from surrounding, ambient pixels. Using the pixel area ( $A_{\text{pixel}}$ ),  $p$  is then calculated from  $A_{\text{vent}}/A_{\text{pixel}}$ .

**Option 3** We can also calculate the temperature of the cool component by assuming the hot component and pixel portion occupied by the hot component from:

$$M(\lambda_1, T_c) = \frac{M(\lambda_1, T_{\text{int}}) - pM(\lambda_1, T_h)}{(1-p)}. \quad (4.15\text{c})$$

It may be possible to apply such an approach when an active lava fills a pixel and the crack area ( $A_{\text{crack}}$ ) and temperature ( $T_h$ ) are available from an independent source (e.g., field measurement). Using the pixel area ( $A_{\text{pixel}}$ ),  $p$  is then calculated from  $A_{\text{crack}}/A_{\text{pixel}}$ .

### 4.3 Three-component solutions

In [Section 4.2](#) we considered simple two-component solutions. However, a review of [Figure 4.6](#) (and Electronic Supplement 1) reveals that, in many cases, three- or even four-component solutions may be necessary. We now consider these complex solutions, which require either further assumptions, or data availability at more numerous wavelengths so that multispectral methods can be applied.

#### 4.3.1 The three-component problem

As is apparent from [Section 4.2](#), if there are three distinct thermal components in a pixel, then the two-component dual-band method will fail, and instead a three-component model and solution will have to be applied.

More often than not, over an active lava body, a three-component solution is required. Take the active lava channel data of Flynn and Mouginis-Mark ([1994](#)), as given in Electronic Supplement 1. This shows that a TM-class pixel filled by such a source will be occupied by three thermal components, not two. These will be:

- (i) hot crust at the channel center, in this case at temperatures in the range 740–940 °C,
- (ii) cooler crust at the channel margins, in this case at temperatures in the range 200–570 °C,  
and
- (iii) hot cracks in the crust, in this case at temperatures in the range 900–1200 °C.

In other words, we have a surface composed of hot crust at temperature  $T_{c1}$  and cooler crust at  $T_{c2}$ , all broken by high-temperature cracks at  $T_h$ . In this case, the spectral exitance for the mixed pixel can be described by

$$M(\lambda, T_{\text{int}}) = p_{c1} M(\lambda, T_{c1}) + p_{c2} M(\lambda, T_{c2}) + p_h M(\lambda, T_h) \quad (4.16a)$$

in which:

- $T_h$  = the temperature of the high-temperature surface (cracks)
- $T_{c1}$  = the temperature of the moderate-temperature surface (high-temperature crust);
- $T_{c2}$  = the temperature of the low-temperature surface (low-temperature crust);
- $p_h$  = proportion of component at temperature  $T_h$ ;
- $p_{c1}$  = proportion of component at temperature  $T_{c1}$ ;
- $p_{c2}$  = proportion of component at temperature  $T_{c2}$ ;
- $T_{\text{int}}$  = the pixel-integrated temperature for the pixel in band  $\lambda$ .

We note that we cannot have more than 100% pixel fill, so that  $p_{c1} + p_{c2} + p_h$  must equal one and

$$p_h = 1 - p_{c1} - p_{c2}; \quad (4.16b)$$

writing  $(1 - p_{c1} - p_{c2})$  in Equation (4.16a) in place of  $p_h$  gives:

$$M(\lambda, T_{\text{int}}) = p_{c1} M(\lambda, T_{c1}) + p_{c2} M(\lambda, T_{c2}) + (1 - p_{c1} - p_{c2}) M(\lambda, T_h) \quad (4.16c)$$

and reduces the number of unknowns. However, we still have five:  $T_h$ ,  $T_{c1}$ ,  $T_{c2}$ ,  $p_{c1}$  and  $p_{c2}$ .

For AVHRR- and GOES-class data the larger pixel means that ambient ground surrounding the active lava body is often present in the pixel. An example of such a multiple-component scenario is given as case 4 in Figure 4.6. Such a scenario will also occur around the perimeter of an active lava body in TM-class pixels, these being the three-component edge pixels of Figure 4.1e. If the lava body within the pixel can be described by a two-component model, where a chilled crust is broken by hot cracks, then the spectral exitance for the mixed pixel can be described by

$$M(\lambda, T_{\text{int}}) = p_a M(\lambda, T_a) + p_c M(\lambda, T_c) + (1 - p_a - p_c) M(\lambda, T_h) \quad (4.17)$$

in which:

- $T_h$  = the temperature of the high-temperature cracks in the lava body;
- $T_c$  = the temperature of chilled crust;
- $T_a$  = the temperature of the ambient ground surrounding the lava body;
- $p_c$  = proportion of component at temperature  $T_c$ ;

$p_a$  = proportion of component at temperature  $T_a$ ;

$T_{\text{int}}$  = the pixel-integrated temperature for the pixel in band  $\lambda$ .

If we are lucky, and a two-component thermal structure can be assumed for the active lava body, then we can apply this mixture model. If we are unlucky, and the lava body itself is composed of more than two components, as is the case for the active lava channel described above, then the problem becomes more complex. This problem will be discussed later. For now we will consider cases where we can be satisfied that such a three-component model can be applied. This may apply, for example, to a lava lake, flow, or dome where the lava body comprises a mature and broadly isothermal crust broken by high-temperature cracks, and is surrounded by ambient ground. In this model we have five unknowns:  $T_h$ ,  $T_c$ ,  $T_a$ ,  $p_c$  and  $p_a$ .

#### 4.3.1.1 Three-component solutions

There are a number of ways to arrive at a three-component solution, depending on how many bands of data are available and how many assumptions can be made.

**One band of data, four assumptions** If we have just one band of data, we need to assume four values to solve for the fifth. However, because of the number of assumptions involved, such an approach is difficult to apply. For example, to apply Equation (4.16) to a TM-class pixel centered on an active lava channel, we may be able to assume value ranges for  $T_h$  (900–1200 °C),  $T_{c1}$  (740–940 °C), and  $T_{c2}$  (200–570 °C), but how can we confidently assume a value for  $p_{c1}$  or  $p_{c2}$ ?

Applying Equation (4.17) may be possible if enough information is available, such as the area of the active lava body in the pixel. Take, for example, an active lava lake centered in an AVHRR pixel. Such features are usually of known area; Kilauea's Kupaianaha lava lake, for example, had an area of 2300 m<sup>2</sup> when visited by Flynn *et al.* (1993). Thus it covered an AVHRR pixel portion of 2300 m<sup>2</sup> / 1 000 000 m<sup>2</sup> = 0.0023. This means that the pixel portion occupied by ambient ground surrounding the lake ( $p_a$ ) was 1 – 0.0023 = 0.9977. If, using data from surrounding lava-free pixels we can set a value for  $T_a$ , we may use field data to set plausible value ranges for  $T_c$  and  $T_h$ . We can now solve for the portion of the lake surface occupied by chilled crust from:

$$p_c = \frac{M(\lambda_1, T_{\text{int}}) - p_a[M(\lambda, T_a) - M(\lambda, T_h)] - M(\lambda, T_h)}{M(\lambda, T_c) - M(\lambda, T_h)}. \quad (4.18)$$

One way to solve could be to (i) assume a value for  $T_h$  of ~1000 °C, (ii) solve for two end-member crust temperature scenario's of 200 °C and 570 °C, and (iii) produce two end-member solutions for  $p_c$  which straddle the actual value.

**Two bands of data, three assumptions** The availability of a second band of data allows us to set up two equations which can be solved simultaneously:

$$M(\lambda_1, T_{\text{int}}) = p_{c1}M(\lambda_1, T_{c1}) + p_{c2}M(\lambda_1, T_{c2}) + (1 - p_{c1} - p_{c2})M(\lambda_1, T_h) \quad (4.19a)$$

$$M(\lambda_2, T_{\text{int}}) = p_{c1}M(\lambda_2, T_{c1}) + p_{c2}M(\lambda_2, T_{c2}) + (1 - p_{c1} - p_{c2})M(\lambda_2, T_h). \quad (4.19b)$$

This now allows us to solve with one less assumption. For example, if we have measurements in two NIR and/or SWIR wavebands we may be able to assume plausible values, or value ranges, for  $T_{c1}$ ,  $T_{c2}$  and  $T_h$  to solve for  $p_{c1}$  and  $p_{c2}$ , following:

$$p_{c1} = \frac{M(\lambda_1, T_{\text{int}}) - p_{c2}[M(\lambda_1, T_{c2}) - M(\lambda_1, T_h)] - M(\lambda_1, T_h)}{M(\lambda_1 - T_{c1}) - M(\lambda_1, T_h)} \quad (4.19c)$$

$$p_{c1} = \frac{M(\lambda_2, T_{\text{int}}) - p_{c2}[M(\lambda_2, T_{c2}) - M(\lambda_2, T_h)] - M(\lambda_2, T_h)}{M(\lambda_2 - T_{c1}) - M(\lambda_2, T_h)}. \quad (4.19d)$$

Solution can be achieved in the same way we solved the simultaneous equations set up for the two-component case in [Section 4.2.1.1](#), where we adjust  $p_{c2}$  until the result ( $p_{c1}$ ) is the same in both wavebands.

If instead, we have the [Equation \(4.17\)](#) scenario we may be able to use a band of MIR data with a band of TIR data to set up two equations

$$M(\lambda_1, T_{\text{int}}) = p_a M(\lambda_1, T_a) + p_c M(\lambda_1, T_c) + (1 - p_a - p_c) M(\lambda_1, T_h) \quad (4.20a)$$

$$M(\lambda_2, T_{\text{int}}) = p_a M(\lambda_2, T_a) + p_c M(\lambda_2, T_c) + (1 - p_a - p_c) M(\lambda_2, T_h). \quad (4.20b)$$

Given  $T_a$  from surrounding lava-free pixels, an assumed value for  $T_h$  (1000 °C) and a knowledge of the area of the active lava body (so that we can calculate  $p_a$ ), we can solve for  $p_c$  and  $T_c$ , these being the two values most difficult to pin down. Solution involves rearranging Equations [\(4.20a\)](#) and [\(4.20b\)](#) to isolate  $p_c$  or  $T_c$ , e.g.,

$$M(\lambda_1, T_c) = \frac{M(\lambda_1, T_{\text{int}}) - p_a[M(\lambda_1, T_a) - M(\lambda_1, T_h)] - M(\lambda_1, T_h) + p_c M(\lambda_1, T_h)}{p_c} \quad (4.21a)$$

$$M(\lambda_2, T_c) = \frac{M(\lambda_2, T_{\text{int}}) - p_a[M(\lambda_2, T_a) - M(\lambda_2, T_h)] - M(\lambda_2, T_h) + p_c M(\lambda_2, T_h)}{p_c}. \quad (4.21b)$$

Again, solution can be achieved in the same way we solved the simultaneous equations set up for the two-component case in [Section 4.2.1.1](#), where we adjust  $p_c$  until the result ( $T_c$ ) is the same in both wavebands. Alternatively, if we can pin down  $T_c$ , but have no data to allow  $p_a$  to be set, we may wish to solve in terms of  $p_a$  and  $p_c$ . In this case we can adjust  $p_c$  in:

$$p_a = \frac{M(\lambda_1, T_{\text{int}}) - p_c[M(\lambda_1, T_c) - M(\lambda_1, T_h)] - M(\lambda_1, T_h)}{M(\lambda_1, T_a) - M(\lambda_1, T_h)} \quad (4.22\text{a})$$

$$p_a = \frac{M(\lambda_2, T_{\text{int}}) - p_c[M(\lambda_2, T_c) - M(\lambda_2, T_h)] - M(\lambda_2, T_h)}{M(\lambda_2, T_a) - M(\lambda_2, T_h)} \quad (4.22\text{b})$$

until the result ( $p_a$ ) is the same in both wavebands.

**Three bands of data, two assumptions** The availability of three bands of data now allows a three equation system to be set up. The approach outlined by Oppenheimer (1993a) involves assuming the three-component case (case 3) of Figure 4.6, where a pixel contains a crusted lava broken by hot cracks, as well as ambient ground. Oppenheimer (1993a) ordered the components a little differently to our Equation (4.17), whereby the three-equation system was given by:

$$M(\lambda_1, T_{\text{int}}) = p_c M(\lambda_1, T_c) + p_h M(\lambda_1, T_h) + (1 - p_c - p_h) M(\lambda_1, T_a) \quad (4.23\text{a})$$

$$M(\lambda_2, T_{\text{int}}) = p_c M(\lambda_2, T_c) + p_h M(\lambda_2, T_h) + (1 - p_c - p_h) M(\lambda_2, T_a) \quad (4.23\text{b})$$

$$M(\lambda_3, T_{\text{int}}) = p_c M(\lambda_3, T_c) + p_h M(\lambda_3, T_h) + (1 - p_c - p_h) M(\lambda_3, T_a) \quad (4.23\text{c})$$

in which

$p_c$  = the pixel portion occupied by warm lava crust at temperature  $T_c$ ;

$p_h$  = the pixel portion occupied by hot cracks at temperature  $T_h$ ;

$T_{\text{int}}$  = the pixel integrated temperature for the pixel in band  $\lambda$ .

The number of unknowns that we have is five:  $p_c$ ,  $p_h$ ,  $T_c$ ,  $T_h$  and  $T_a$ . By re-arranging the first equation in the system to isolate  $p_h$ , i.e.,

$$p_h = \frac{M(\lambda_1, T_{\text{int}}) - p_c[M(\lambda_1, T_c) - M(\lambda_1, T_a)] - M(\lambda_1, T_a)}{M(\lambda_1, T_h) - M(\lambda_1, T_a)} \quad (4.24\text{a})$$

we can reduce the number of unknowns to four ( $p_c$ ,  $T_c$ ,  $T_h$  and  $T_a$ ). To simplify matters, Oppenheimer (1993a) wrote  $\Phi_1$  for  $[M(\lambda_1, T_h) - M(\lambda_1, T_a)]$  and  $\Psi_1$  for  $[M(\lambda_1, T_c) - M(\lambda_1, T_a)]$ . This simplifies Equation (4.24a) to:

$$p_h = \frac{M(\lambda_1, T_{\text{int}}) - p_c\Phi_1 - M(\lambda_1, T_a)}{\Psi_1}. \quad (4.24\text{b})$$

Inserting this term into Equations (4.23b) and (4.23c) removes one unknown ( $p_h$ ) from the remaining two equations, and re-arranging gives us two simultaneous equations in which  $p_c$  can be written in terms of the three remaining unknowns ( $T_c$ ,  $T_h$  and  $T_a$ ):

$$p_c = \frac{\Psi_1[M(\lambda_2, T_{\text{int}}) - M(\lambda_2, T_a)] - \Phi_2[M(\lambda_1, T_{\text{int}}) - M(\lambda_1, T_a)]}{\Psi_1[M(\lambda_2, T_c) - M(\lambda_2, T_a)] - \Phi_2[M(\lambda_1, T_c) - M(\lambda_1, T_a)]} \quad (4.25\text{a})$$

$$p_c = \frac{\Psi_1[M(\lambda_3, T_{\text{int}}) - M(\lambda_3, T_a)] - \Phi_3[M(\lambda_1, T_{\text{int}}) - M(\lambda_1, T_a)]}{\Psi_1[M(\lambda_3, T_c) - M(\lambda_3, T_a)] - \Phi_3[M(\lambda_1, T_c) - M(\lambda_1, T_a)]}. \quad (4.25b)$$

In these equations note that, to simplify matters,

$$\Phi_2 = M(\lambda_2, T_h) - M(\lambda_2, T_a),$$

and

$$\Phi_3 = M(\lambda_3, T_h) - M(\lambda_3, T_a).$$

Given that crust temperatures can be highly variable, the most sensible thing to do is to assume  $T_a$  and  $T_h$ , and adjust  $T_c$  until the same  $p_c$  is obtained in both bands. Graphical or numerical solution can be achieved in the same way we solved the simultaneous equations set up for the two-component case of [Section 4.2.1.1](#). In such a way we may estimate values for  $T_c$  and  $p_c$ . Having found  $T_c$  and  $p_c$ ,  $p_h$  can be obtained by using the derived values of  $T_c$  and  $p_c$  in Equation (4.24);  $p_a$  then equals  $1 - p_c - p_h$ . By way of example, the original solution of Oppenheimer ([1993a](#)) is given in Electronic Supplement 5.

#### *4.3.1.2 Three-component solutions in the TIR*

If the high-temperature component of an active lava body is of a sufficiently small area, it will contribute negligibly to the integrated radiance in the thermal infrared. Instead, radiance from the crusted component and the ambient background will dominate the contributions to the integrated value. In this case, the pixel contains three thermal components so that we have:

$$M(\lambda, T_{\text{int}}) = p_a M(\lambda, T_a) + p_c M(\lambda, T_c) + (1 - p_a - p_c) M(\lambda, T_h). \quad (4.26a)$$

However, negligible contribution of the high-temperature component means that we can reduce the problem to a two-component case:

$$M(\lambda, T_{\text{int}}) = p_c M(\lambda, T_c) + (1 - p_c) M(\lambda, T_a). \quad (4.26b)$$

Typically this model is applied to a pixel containing active lava surrounded by ambient ground so that  $T_c$  is the lava crust temperature and  $T_a$  is the ambient ground temperature. Solution now requires assuming two of the unknowns ( $p_c$ ,  $T_c$  or  $T_a$ ) to solve for the third. Typically  $T_a$  is set from background, lava-free, pixels and a value for  $T_c$  (the lava crust temperature) is assumed, so that  $p_c$  is calculated from:

$$p_c = \frac{M(\lambda_{\text{TIR}}, T_{\text{int}}) - M(\lambda_{\text{TIR}}, T_a)}{M(\lambda_{\text{TIR}}, T_c) - M(\lambda_{\text{TIR}}, T_a)}. \quad (4.26c)$$

Note that I have inserted the TIR subscript into this equation to stress that this solution can only be applied to a pixel containing active lava in the thermal infrared. Because solution requires assumption of  $T_c$ , which is not an easy number to pin down, solution is usually

completed over a range of  $T_c$  values to give two end-member solutions for  $p_c$ . The true  $p_c$  value is then assumed to lie between these two end-member solutions. Of course, if the area of active lava within the pixel is known, so that  $p_c$  can be calculated, then we can solve for  $T_c$ :

$$M(\lambda_{\text{TIR}}, T_c) = \frac{M(\lambda_{\text{TIR}}, T_{\text{int}}) - (1 - p_c)M(\lambda_{\text{TIR}}, T_a)}{p_c}. \quad (4.26d)$$

This may be applied, for example, to a large pixel centered on a small lava lake or dome where the area of that lake or dome is known.

**Applicability of the two-component TIR pixel model to a pixel containing active lava** Application of this model relies on the assumption that the high-temperature component does not contribute to the integrated radiance in the TIR. To assess whether this assumption holds, in [Table 4.2](#) I have collated available surface thermal structure data for active lava channels, flows and lakes. For each case, I selected the maximum and minimum hot and cool (crust) component temperatures measured in the field, and used the fractional coverage for the hot component appropriate to each case. I then used these values to obtain pixel-integrated radiance in the thermal infrared (at 11  $\mu\text{m}$ ) for a pixel containing such a thermal structure (following the methodology outlined in [Electronic Supplement 1](#)). Finally, I assessed the contribution of the hot component to the pixel-integrated value. We see that, for all cases apart from the hottest lava channel case, the contribution of the hot component to the integrated radiance is less than 4%. For the two lava flow cases, the hot-component contribution is less than 1%. For most cases the ratio of the crust-component radiance to the integrated value is greater than 0.96, meaning that the crusted component contribution dominates the lava-body contribution to the pixel-integrated value. Thus the assumption seems to hold for most of the cases considered here.

In a three-component case, the pixel also contains an area of lava-free ground at ambient temperature. In [Table 4.3](#), I have taken a case where the pixel is 50% filled with ambient ground at 25 °C (i.e.,  $p_a = 0.5$ ). The remainder of the pixel is filled with active lava with the end-member thermal structures of [Table 4.2](#). Now, the pixel integrated radiance can be calculated from:

$$M(\lambda, T_{\text{int}}) = p_a M(\lambda, T_a) + p_c M(\lambda, T_c) + p_h M(\lambda, T_h), \quad (4.27)$$

where  $p_a + p_c + p_h$  must all be positive and sum to one.

Now, we can make the assumption that the hot component does not contribute and use the integrated radiances to estimate  $p_c$  by inputting the crust and ambient temperatures used in the model into [Equation \(4.26c\)](#). We can use the result to assess the validity of the non-contribution of the hot-component assumption and the error induced by not taking into account this contribution. A review of the results in [Table 4.3](#) shows that for all cases, apart from the hottest lava channel case, the difference between the estimate of  $p_c$

Table 4.2. Summary of available data for the thermal structures of active lava flow and lake surfaces, with the pixel-integrated radiance at 11  $\mu\text{m}$  that these give. The top line for each case gives the maximum hot-component temperature ( $T_h$ ) and surface coverage ( $f$ ), with the maximum crust temperature ( $T_c$ ). The bottom line gives the minimum values. Also given are the pixel-integrated 11  $\mu\text{m}$  radiances for a pixel occupied by these two components ( $R_{int}$ ) as well as the spectral radiance contribution of the hot component [ $f L_{TIR}(T_h)$ ]. “Contrib.” is the percent contribution of the hot component [ $f L_{TIR}(T_h)$ ] to the total integrated radiance, and “Ratio” is the ratio of the radiance from the crust component [ $f_c L_{TIR}(T_c)$ ] to the total integrated radiance.

Location, case (Source reference)	$T_h$ (°C)	$f$	$T_c$ (°C)	$f_c$ (= 1 - $f$ )	$R_{int}$ (W/m <sup>2</sup> m)	$f L_{TIR}(T_h)$ (W/m <sup>2</sup> m)	Contrib. (%)	$f_c L_{TIR}(T_c)$ (W/m <sup>2</sup> m)	Ratio
Kilauea, lava channel (Flynn and Mouginis-Mark, 1994)	1120	6.00E-01	940	0.4	1.37E+09	8.95E+08	65	4.79E+08	0.35
	1100	5.90E-03	458	0.9941	4.72E+08	8.60E+06	1.8	4.63E+08	0.98
Etna, lava channel (Harris <i>et al.</i> , 2005a)	834	3.00E-02	760	0.97	9.15E+08	3.08E+07	3.4	8.84E+08	0.97
	932	3.00E-02	786	0.97	9.59E+08	3.55E+07	3.7	9.24E+08	0.96
Lonquimay, 'a'a lava flow (Oppenheimer, 1991)	1040	1.76E-04	258	0.999824	2.16E+08	2.39E+05	0.11	2.16E+08	1.00
	1040	1.40E-05	143	0.999986	1.05E+08	1.90E+04	0.02	1.05E+08	1.00
Kilauea, tube-fed pahoehoe (Harris <i>et al.</i> , 1998)	900	2.00E-04	150	0.9998	1.11E+08	2.27E+05	0.20	1.10E+08	1.00
	900	1.00E-04	259	0.9999	2.17E+08	1.13E+05	0.05	2.17E+08	1.00
Santiaguito, silicic lava flow (Harris <i>et al.</i> , 2003a)	830	2.00E-03	90	0.998	6.70E+07	2.04E+06	3.1	6.49E+07	0.97
	830	2.00E-05	250	0.99998	2.07E+08	2.04E+04	0.01	2.07E+08	1.00
Kilauea, lava lake (Flynn <i>et al.</i> , 1993)	1100	1.35E-02	572	0.9865	6.39E+08	1.97E+07	3.1	6.19E+08	0.97
	900	1.61E-05	210	0.999984	1.66E+08	1.82E+04	0.01	1.66E+08	1.00

Table 4.3. The left-hand side of the table gives a series of three component pixel models, based on the end-member lava surface thermal structures given in Table 4.2. In each case the pixel contains a portion of ambient ground at  $T_a$ , and a zone of active lava composed of a chilled crust at  $T_c$  broken by hot cracks at  $T_h$ . The right-hand side of the table begins with the pixel-integrated radiance ( $R_{int}$ ) that each model gives in the thermal infrared (11  $\mu\text{m}$ ). Next, I give the crust area solution obtained from assuming that the hot crack component does not contribute to  $R_{int}$  so that the two component solution of Equation (4.26c) can be applied. In the final column the difference between the solution and the value for crusted component portion input into the model is given. The greater this difference is, the less valid is the non-contribution assumption and the greater the error on calculated  $p_c$  when applying this method.

Location, case (Source reference)	$T_a$ (°C)	$T_c$ (°C)	$T_h$ (°C)	$p_a$ (%)	$p_c$ (%)	$p_h$ (%)	$R_{int}$ ( $\text{W m}^{-2} \text{m}^{-1}$ )	Solution ( $p_c$ , %)	Difference (%)
Kilauea, lava channel	25	940	1120	50.000	20.000	30.000	7.01E+08	57.550	37.55
(Flynn and Mouginis-Mark, 1994)	25	458	1100	50.000	49.705	0.295	2.50E+08	50.670	0.97
Etna, lava channel	25	760	834	50.000	48.500	1.500	4.72E+08	50.197	1.70
Harris <i>et al.</i> , 2005a)	25	786	932	50.000	48.500	1.500	4.94E+08	50.377	1.88
Lonquimay, 'a lava flow	25	258	1040	50.000	49.991	0.009	1.23E+08	50.054	0.06
(Oppenheimer, 1991)	25	143	1040	50.000	49.999	0.001	6.69E+07	50.012	0.01
Kilauea, tube-fed pahoehoe	25	150	900	50.000	49.990	0.010	6.99E+07	50.126	0.14
(Harris <i>et al.</i> , 1998)	25	259	900	50.000	49.995	0.005	1.23E+08	50.024	0.03
Santiaguito, silicic lava flow	25	90	830	50.000	49.900	0.100	4.81E+07	52.668	2.77
(Harris <i>et al.</i> , 2003a)	25	250	830	50.000	49.999	0.001	1.18E+08	50.005	0.01
Kilauea, lava lake	25	572	1100	50.000	49.325	0.675	3.34E+08	50.938	1.61
(Flynn <i>et al.</i> , 1993)	25	210	900	50.000	49.999	0.001	9.76E+07	50.006	0.01

(that excludes the hot component contribution) and the starting (required) value is less than 3%, and less than 0.1% for the two lava flow cases. In cases where the hot component contribution cannot be ignored (i.e., the hot channel case) the pixel portion occupied by crust is over-estimated. In these cases, to balance the integrated radiance, the estimated area of the crust component is increased to account for the missing hot-component radiance.

**Application of this model in the MIR and SWIR** The same exercise is completed for the MIR and SWIR in [Table 4.4](#). We see from [Table 4.4](#) that, in the MIR, the higher relative contribution of the hot component to the integrated radiance means that differences between the solved  $p_c$  and model-input  $p_c$  are greater than in the TIR cases. In some cases,

*Table 4.4. Pixel integrated radiance ( $R_{int}$ ) that each pixel model of Table 4.2 gives in the mid-infrared (3.75  $\mu\text{m}$ ) and SWIR (2.25  $\mu\text{m}$ ). Again, I give the crust area solution obtained from assuming that the hot crack component does not contribute to  $R_{int}$  so that the two-component solution of Equation (4.26c) can be applied. In the final column the difference between the solution and the value for the crusted component portion input into the model is given. The greater this difference, the less valid the non-contribution assumption and the greater the error on calculated  $p_c$ .*

Location, case (Source reference)	MIR			SWIR		
	$R_{int}$ (W $\text{m}^{-2} \text{m}^{-1}$ )	Solution ( $p_c$ , %)	Difference (%)	$R_{int}$ (W $\text{m}^{-2} \text{m}^{-1}$ )	Solution ( $p_c$ , %)	Difference (%)
Kilauea, lava channel (Flynn & Mouginis-Mark, 1994)	1.47E+10 1.42E+09	66.179 53.344	46.18 3.64	2.66E+10 6.95E+08	79.592 67.504	59.59 17.80
Etna, lava channel (Harris <i>et al.</i> , 2005a)	6.35E+09 7.03E+09	50.436 50.863	1.94 2.36	6.75E+09 8.00E+09	50.771 51.626	2.27 3.13
Lonquimay, 'a'a lava flow (Oppenheimer, 1991)	1.87E+08 25 757 098	50.681 50.413	0.69 0.41	2.35E+07 1.04E+06	61.543 75.680	11.55 25.68
Kilauea, tube-fed pahoehoe (Harris <i>et al.</i> , 1998)	31 646 772 1.88E+08	53.497 50.263	3.51 0.27	3.68E+06 2.09E+07	208.442 53.571	158.45 3.58
Santiaguito, silicic lava flow (Harris <i>et al.</i> , 2003a)	23 164 633 1.65E+08	187.391 50.048	137.49 0.05	1.98E+07 1.61E+07	13 933 50.620	13 883.12 0.62
Kilauea, lava lake (Flynn <i>et al.</i> , 1993)	2.9E+09 90 327 867	53.403 50.089	4.08 0.09	2.07E+09 5.99E+06	61.833 51.948	12.51 1.95

solution is close to required value, but in others the size of the crusted component has to be too high in order to account for the excess radiance from the (missing) hot component. In one case, the area occupied by the crusted temperature has to exceed the area of the pixel (i.e.,  $p$  is greater than one). Plainly this is unrealistic. Between the MIR and the SWIR the relative contribution of hot component to the integrated radiance increases even further, making solutions that ignore the contribution of the hot component even more unrealistic in the SWIR. The bottom line is, this approach should probably only be applied to the TIR in cases where we can be sure of negligible contribution of the hot component to the integrated radiance, otherwise solutions for the pixel portion occupied by the crusted component will be over-estimated.

#### 4.3.1.3 Using data of differing spatial resolutions

For some sensors, three wavebands of appropriate data may be available, but at different spatial resolutions. A good example of such a case is that of the ETM+, where two bands of SWIR data were available at a spatial resolution of 30 m, and one TIR band at 60 m. In this case, we can try to combine the radiances of the smaller pixels within the larger pixel using a weighted average method. In this method the integrated radiance for the smaller SWIR pixels ( $R_{\lambda\text{int}}$ ) can be obtained from,

$$R_{\lambda\text{int}} = \sum_{i=1}^n \left[ \frac{A_{\text{small}}}{A_{\text{big}}} R_{\lambda i} \right], \quad (4.28)$$

$n$  being the total number of small pixels of area  $A_{\text{small}}$  residing within the larger pixel of area  $A_{\text{big}}$ , and  $R_{\lambda i}$  being the radiance of pixel  $i$ . In other words, the radiance for each of the small SWIR pixels within the larger TIR pixel is weighted according to  $A_{\text{small}}/A_{\text{big}}$ , and summed. In our case, we will have four 30 m SWIR pixels within the larger 60 m TIR pixel, so that  $n = 4$ , and:

$$\frac{A_{\text{small}}}{A_{\text{big}}} = \frac{900 \text{ m}^2}{3600 \text{ m}^2} = 0.25.$$

Thus the radiance for each SWIR pixel will have to be multiplied by 0.25 and summed to make the weighted-average radiance.

Due to pixel mis-registration problems, a better approach may be to sum the radiances over the entire anomaly, so that

$$R_{\lambda\text{int}} = \sum_{i=1}^n \left( \frac{A_{\text{pixel}}}{A_{\text{anomaly}}} R_{\lambda i} \right). \quad (4.29)$$

Now  $n$  is the number of anomalous pixels,  $A_{\text{pixel}}$  is the pixel area and  $A_{\text{anomaly}}$  is the anomaly area. This operation should be done first for the large pixel radiances. Thus, if we have a thermal anomaly that covers three 60 m TIR pixels, the weighting factor for the TIR is:

$$\frac{A_{\text{pixel}}}{A_{\text{anomaly}}} = \frac{3600 \text{ m}^2}{3 \times 3600 \text{ m}^2} = \frac{3600 \text{ m}^2}{10800 \text{ m}^2} = 0.333.$$

The radiance for each anomalous TIR pixel then has to be multiplied by 0.333 and summed. Next we do the same for the smaller SWIR pixels. For the smaller 30 m pixels within the larger TIR anomaly, the weighting will be:

$$\frac{A_{\text{pixel}}}{A_{\text{anomaly}}} = \frac{900 \text{ m}^2}{3 \times 3600 \text{ m}^2} = \frac{900 \text{ m}^2}{10800 \text{ m}^2} = 0.083.$$

Thus the radiance for each anomalous SWIR pixel will have to be multiplied by 0.083 and summed.

For a case like ETM+, use of such a solution means that we now have three bands of data: one in the TIR and two in the SWIR. We may thus apply any of the two- or three-component approaches given in the preceding sections that work with three bands of data. That is, we can apply the two-component solution involving *unique (assumption-free) solution using three bands and three equations* of Section 4.2.1.1, or the three-component solution involving *three bands of data, two assumptions* of Section 4.3.1.1.

**Precision of integrated temperatures generated from weighted averages** McCabe *et al.* (2008) explored the difference between pixel-integrated brightness temperature obtained from the weighted-average method of Equation (4.28) and the actual pixel-integrated temperature recorded for a pixel. In effect, this method takes a number of sub-pixels and integrates them using the weighted average for the radiances of all sub-pixels. This is described by Equation (2) of McCabe *et al.* (2008):

$$M(\lambda, T_{\text{w-ave}}) = \frac{1}{n} \sum_{i=1}^n M(\lambda, T_i), \quad (4.30a)$$

in which  $n$  is the total number of sub-pixels,  $T_i$  is the emissivity and atmospherically corrected temperature of sub-pixel  $i$ , and  $T_{\text{w-ave}}$  is the pixel-integrated temperature obtained from the weighted-average method. McCabe *et al.* (2008) considered pixel mixtures involving up to  $100 \times 100$  sub-pixels (so that  $n = 10000$ ) and examined the difference between the actual pixel-integrated temperature ( $T_{\text{int}}$ ) and the fabricated pixel-integrated temperature ( $T_{\text{w-ave}}$ ), the difference being described here using annotation  $\Delta T_{\text{w-ave}}$  ( $= T_{\text{int}} - T_{\text{w-ave}}$ ). McCabe *et al.* (2008) found that  $\Delta T_{\text{w-ave}}$  increased with

- (i) decreased wavelength,
- (ii) increased standard deviation among the sub-pixels, and
- (iii) increased difference in the mean temperature across the surfaces comprising the mixed pixel.

The conclusions were drawn from 50:50 mixtures of two materials each with Gaussian temperature distributions. This means that, for such a condition, there will be a difference between the pixel-integrated temperature output by the weighted-average method and the

actual pixel-integrated temperature. The conclusions of McCabe *et al.* (2008) mean that this difference will be minimal in the TIR, but will increase towards the SWIR. It will also increase with the standard deviation of the temperature distribution for the sub-pixels within the parent pixel. McCabe *et al.* (2008) provided the following equation to allow  $\Delta T_{\text{w-ave}}$  to be appraised:

$$\Delta T_{\text{w-ave}} = \chi \left[ p(1-p)\Delta\bar{T}^2 + p\sigma_1^2 + (1-p)\sigma_2^2 \right]. \quad (4.30\text{b})$$

This applies to a binary combination of materials with two temperature distributions, where

$\sigma_1$  and  $\sigma_2$  = the standard deviations for the two temperature distributions,

$p$  = the proportion of one of the materials,

$\Delta T$  = the difference in the mean temperature of the two distributions, and

$\chi$  = the first and second derivatives of Planck's Function.

Parameter  $\chi$  is temperature dependent, and for a temperature of 290 K can be approximated as 0.016 098 K<sup>-1</sup> in the 3–5 μm band and 0.005 444 K<sup>-1</sup> in the 8–12 μm band (McCabe *et al.*, 2008). We must note that the actual value of  $\chi$  will vary with temperature, and was derived for two bodies at roughly ambient temperatures separated by, at most, a few tens of degrees centigrade. It will thus not work when applied to a 50:50 mixture of ambient rock at 50 °C and active lava at 250 °C, 500 °C or 1000 °C.

#### 4.3.1.4 Using saturation and non-response

Often three bands of NIR, SWIR and/or TIR data are available, but not all are *useable*. For example, a lava lake hot spot sufficient to give measurable radiance in Landsat TM SWIR band 5 will likely mean that the other SWIR band (band 7) and the TIR band (band 6) will be saturated. Alternatively, the hot spot may not be of sufficient size and/or temperature to generate detectable radiance in the NIR band. However, the saturated and unresponsive bands are *useable* in that they allow us to place limits on permissible solutions of two- or three-component solutions applied to a single band of *useable* data.

Take, for example, a case where we have three bands of data in the NIR, SWIR and TIR. We have one band of *useable* data, this being in the SWIR; the shorter-wavelength (NIR) band being non-responsive and the longer-wavelength (TIR) band being saturated. For this case, we can apply a two-component model to the SWIR data. By assuming  $T_h$  we can use the pixel-integrated radiance in the SWIR to calculate the range of hot-component pixel portions ( $p_h$ ) and cool-component temperatures that will give integrated radiance from

$$M(\lambda_1, T_c) = \frac{M(\lambda_1, T_{\text{int}}) - p_h M(\lambda_1, T_h)}{(1 - p_h)}.$$

Now, all solutions must meet the conditions that

- (i) the NIR waveband is unresponsive, and
- (ii) the TIR waveband is saturated.

Thus we can calculate the equivalent NIR and TIR pixel-integrated temperature that each combination of  $T_h$ ,  $T_c$  and  $p_h$  give, and test whether they are consistent with non-response in the NIR and saturation of the TIR. If the result forces the NIR value to a point that the hot spot would give a response, then we can reject all solutions above this point. Likewise, if the result forces the TIR value to a point that the hot spot would have caused this band not to saturate, then we can reject all solutions below this point.

**Example 1: Pixel-integrated temperature is towards the upper end of the dynamic range** For our first example, we take a night-time TM-class pixel filled with active lava so that  $T_c$  relates to the temperature of a chilled crust on the active lava,  $T_h$  to the portion occupied by hot cracks in the same lava and  $p_h$  to the pixel portion occupied by the cracks. Now, take a pixel-integrated temperature 410 °C in Landsat SWIR band 5, this being towards the top end of the dynamic range for this band (415 °C – see Electronic Supplement 1). If we assume a hot-component temperature of 1000 °C, we can calculate the full range of hot-component pixel portions and crust temperatures that will give the pixel-integrated temperature, as done in [Figure 4.9a](#). We see that the potential range of solutions extend from the  $p_h = 0$  (i.e., the pixel is filled with crust) so that the crust temperature equals the pixel-integrated temperature of 410 °C, to a crust temperature of 139 °C at  $p_h$  of 0.002 689. The next band up, in terms of wavelength, is SWIR band 7. If we calculate the pixel-integrated temperature that each combination of  $T_h$ ,  $T_c$  and  $p_h$  give, we find that band 7 will be saturated for all combinations plotted. For example, at the point where the [Figure 4.9a](#) solution curve begins to plunge towards the  $x$ -axis (i.e.,  $T_h = 1000$  °C,  $T_c = 139$  °C,  $p_h$  of 0.00 2689), the band 7 pixel-integrated temperature will still be 317 °C, that is 40 °C higher than the band 7 saturation temperature of 277 °C. The next band down, in terms of wavelength, is NIR band 4. The minimum pixel-integrated temperature that must be attained before detection is possible in this waveband is 595 °C. If we calculate the pixel-integrated temperature that each combination of  $T_h$ ,  $T_c$  and  $p_h$  give, we find that this band 4 limit will be reached at  $T_h = 1000$  °C,  $T_c = 360$  °C,  $p_h$  of 0.0017. At this point the hot component has become sufficiently large, that detectable emission will begin to be recorded in band 4. Thus, all points above this  $p_h$  point are inconsistent with non-response of band 4, so that the range on our  $T_c$  and  $p_h$  solution combination for the band 5 pixel-integrated radiance can be narrowed down, as marked in [Figure 4.9a](#).

**Example 2: Pixel-integrated temperature is towards the lower end of the dynamic range** Next, we take a night-time TM-class pixel filled with active lava, with a pixel-integrated temperature 300 °C in Landsat SWIR band 5, this being towards the lower end of the 203 °C to 415 °C dynamic range for this band. If we again assume a hot-component temperature of 1000 °C, we can calculate the full combination range of  $p_h$  and  $T_c$  that will give the pixel-integrated temperature, as done in [Figure 4.9b](#). We see that the potential range of solutions extends from the  $p_h = 0$  (i.e., the pixel is filled with crust), where the crust temperature equals the pixel-integrated temperature of 300 °C, to a crust temperature of 148 °C at  $p_h$  of 0.000 231. Now, if we calculate the band 4 pixel-integrated temperature for

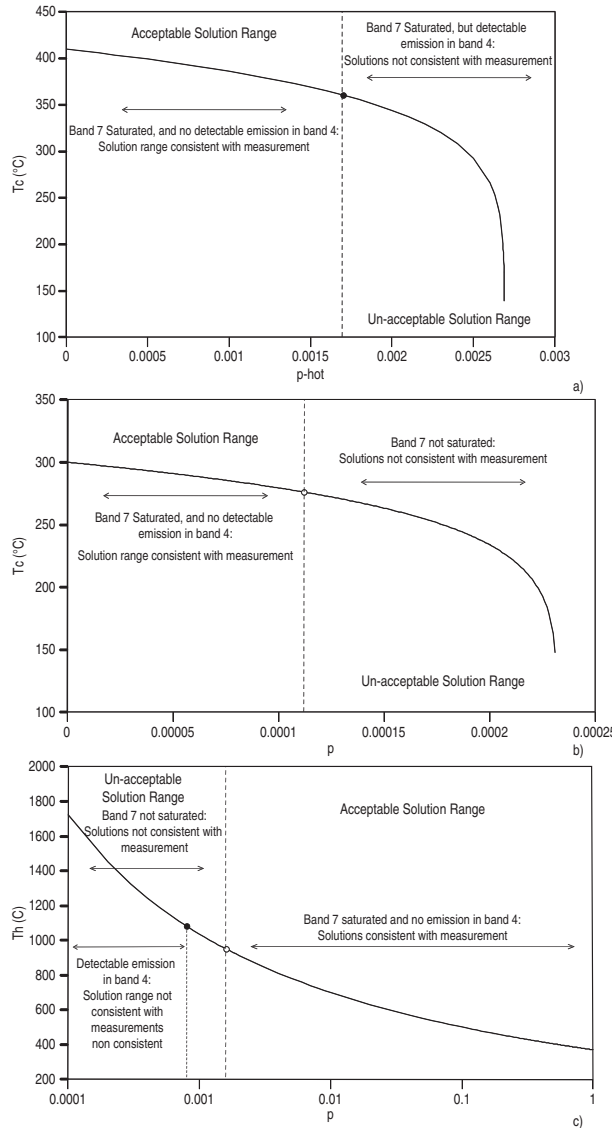


Figure 4.9 (a) Combinations of crust temperature and hot-component pixel portion (assuming a hot-component temperature of 1000 °C) that will give a pixel-integrated temperature in the SWIR (Landsat TM band 5) of 410°C. Also marked are solutions that are inconsistent with no detection in the NIR, i.e., the 1000 °C hot spot size will be such that the lower limit of Landsat TM band 4's dynamic range will be exceeded. (b) Combinations of crust temperature and hot-component pixel portion (assuming a hot-component temperature of 1000 °C) that will give a pixel-integrated temperature in the SWIR (Landsat TM band 5) of 300 °C. Also marked are solutions that are inconsistent with saturation of a second SWIR band, i.e., the 1000 °C hot spot size and crust temperature will be sufficiently low so as not to saturate Landsat TM band 7. (c) Combinations of hot spot temperature and size, when set against a non-radiant background, that will give a SWIR (Landsat TM band 5) pixel-integrated temperature of 370 °C. Also marked are sections of the curve for which solutions are inconsistent with non-response of Landsat TM NIR band 4 and saturation of Landsat TM SWIR band 7.

each combination of  $T_h$ ,  $T_c$  and  $p$  we find that no combination achieves the pixel-integrated temperature required for detection, the maximum being 515 °C (for  $T_h = 1000$  °C,  $T_c = 148$  °C,  $p_h$  of 0.000231) compared with the lower detection limit of this waveband of 595 °C. However, if we calculate the pixel-integrated temperature that each combination of  $T_h$ ,  $T_c$  and  $p_h$  will give in band 7 we find that we drop below the band 7 saturation limit at the point where  $T_h = 1000$  °C,  $T_c = 276$  °C and  $p_h = 0.000112$ . Thus, all  $p_h$  points above this point are inconsistent with non-saturation of band 7, so that the limit on the range of our  $T_c$  and  $p_h$  solutions using band 5 data can now be narrowed down using this constraint, as marked on Figure 4.9b.

**Example 3: Equation (4.12) solution** In Figure 4.9c I execute a one-component solution in the SWIR where we have an isothermal hot spot with an ambient (0 °C) background

$$M(\lambda, T_{\text{int}}) = p_h M(\lambda, T_h).$$

Again, I take a situation where we have a SWIR band 5 pixel-integrated temperature of 370 °C, non-response of NIR band 4, and saturation of band 7. In Figure 4.9c I have plotted all combinations of  $T_h$  and  $p_h$  that can give this band 5 pixel-integrated temperature. The hot spot will begin to be detectable in band 4 (i.e., the band 4 pixel-integrated temperature will begin to exceed the minimum limit of the band's dynamic range of 595 °C) when  $p_h = 0.0008$  and  $T_h = 1083$  °C. However, the band 7 threshold is met first. That is, we drop below the band 7 saturation limit when  $p_h$  reaches 0.0016 and  $T_h$  reaches 951 °C. Thus, this cut-off is used for the solution range of Figure 4.9c, because band 7 has to be saturated if the solution is to be valid.

#### 4.3.1.5 Conversion to area

Throughout this chapter we have worked in terms of pixel portion occupied by a thermal component. However, the more useful metric is area. That is, what we need to extract is the area covered by an active lava flow, lake, dome or vent. This requires multiplication of pixel portion by pixel area. Thus, for example, active vent area ( $A_{\text{vent}}$ ) can be obtained from multiplying the pixel portion occupied by the active vent at temperature  $T_h$  ( $p$ ), as obtained from solution of Equations (4.8a) and (4.8b), by pixel area ( $A_{\text{pixel}}$ ):

$$A_{\text{vent}} = p A_{\text{pixel}}. \quad (4.31a)$$

Here, pixel area must be calculated using the appropriate IFOV, scan angle and topographic adjustment if precise values are required, as can be achieved by following the pixel dimension calculation methods detailed in Section 3.3 of Chapter 3. Likewise, if lava area ( $A_{\text{lava}}$ ) is to be calculated from the results of Equation (4.23), pixel portion occupied by the crusted ( $p_c$ ) and high-temperature ( $p_h$ ) components of the flow must be summed and multiplied by pixel area, i.e.,

$$A_{\text{lava}} = (p_c + p_h) A_{\text{pixel}}. \quad (4.31b)$$

For the Equation (4.26c) approach this reduces to:

$$A_{\text{lava}} \approx p_c A_{\text{pixel}}. \quad (4.31c)$$

If the lava is spread across many pixels, so that we have a multiple pixel anomaly,  $A_{\text{lava}}$  values obtained for each anomalous pixel must be summed to obtain total lava flow, dome, or lake area.

#### 4.3.1.6 Which unknown to assume?

We usually need to assume a value to solve the dual band method. Probably the easiest value to set is that for the ambient ground surrounding the volcanic hot spot, followed by the temperature of the hottest component in the pixel (e.g., temperatures present at hot cracks in an active lava body or vent temperature). Crust temperatures across active lavas, and pixel portions occupied by each thermal component are, without a doubt, the most difficult values to set, or at least to ascribe a single value to, with any certainty.

**Background (ambient) temperature** The temperature for ambient surfaces within a mixed pixel can usually be set using the temperatures obtained from *cold* pixels immediately surrounding the hot spot pixel(s). Both the mean, or minimum, from the nearest ambient pixels have been used to characterize the background. The maximum should probably be avoided because this may have some contribution from the hot spot pixel due to point spread function, radiance bleeding and pixel overlap effects (see Chapter 3 for definition), as sketched in the illustrative example of Figure 4.10 (Case 3). Use of such pixels may result in the use of a background value that is too high, thereby forcing a dual-band solution that yields a hot spot area that is too small and/or too cool.

Use of the minimum background temperature ensures that we have probably chosen the least contaminated pixel. That is, the pixel least contaminated by point spread function, radiance bleeding and pixel overlap effects. However, if the temperature is biased by the presence of an anomalously cold body, such as ice or high cloud, that is present within the background pixel, but not in the target pixel, then the selected background temperature will be unrealistically low (Case 2 in Figure 4.10). There will also be a problem if the sensor responds to the hot spot by registering an anomalously low value just down scan of the hot spot, as is often the case in AVHRR data (see Electronic Supplement 1). This is Case 4 of Figure 4.10. With 1 km pixels spanning a great altitudinal range, as in Case 1 of Figure 4.10, use of the minimum may also weight the value towards high-altitude pixels when background temperatures for the target pixel are consistent with those experienced at lower altitudes. Alternatively, the mean from the nearest ambient background pixels could be used. However, inclusion of pixels contaminated by radiance spread into them by point spread function, radiance bleeding and pixel overlap effects may cause the average to be too high. Conversely, inclusion of sensor recovery, corrupt pixels or cold cloud pixels surrounding the anomaly may cause the average to be too low.

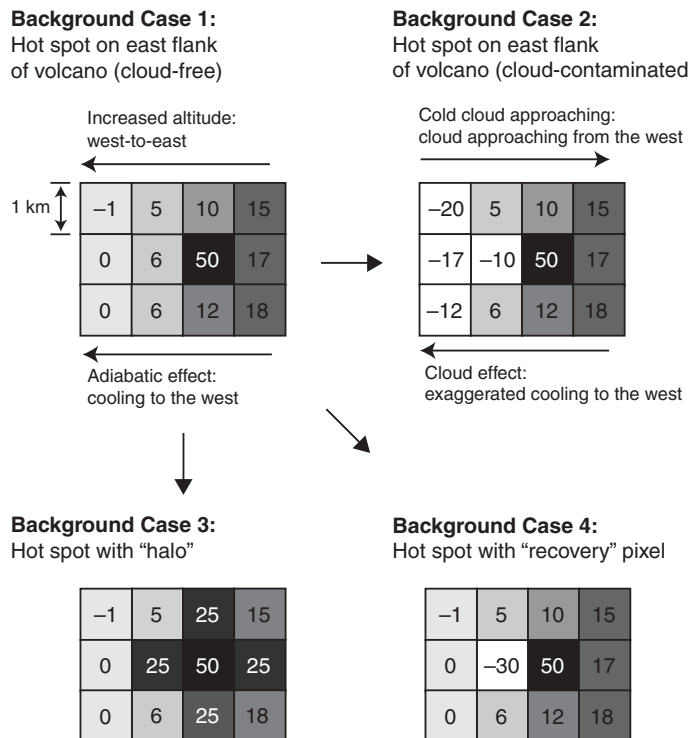


Figure 4.10 Temperatures for pixels surrounding a one-pixel hot spot at a pixel-integrated temperature of 50 °C. Examples show the effects on the hot spot background values of (1) altitudinal variation among the pixels surrounding the hot spot, (2) cold cloud contamination, (3) point-spread function effects, and (4) sensor recovery problems.

Probably the best approach is to select a pixel which is (1) the closest non-anomalous pixel in any of the cardinal directions to the target pixel that is (2) believed to be as free as possible from any source of contamination or corruption, and which is (3) composed of a similar surface type to the background within the target pixel, while being (4) located at a similar altitude and having a similar aspect. An example of such a selection procedure is given in Electronic Supplement 7.

**Hot-component temperature** Lava eruption and flow core (or interior) temperatures are relatively predictable and stable, and have thus been used to set the hot-component temperature, i.e., the hottest temperature “seen” by the sensor on an active lava surface. For example, at Kilauea the eruption temperature is typically around 1150 °C, and at Etna eruption temperatures are typically in the range 1060–1125 °C. However, the value we need is that encountered at the lava flow surface. Rapid radiative cooling, and the fact that most cracks often penetrate the cooler visco-elastic crust rather than the true flow core, mean that core temperatures are rarely encountered at the surface. Measurements by Hon *et al.* (1994a)

at pahoehoe sheet flows active on Kilauea, for example, give a temperature at the top of the visco-elastic layer of 800 °C and 1070 °C at its base. Thus cracks penetrating this layer will have temperatures in this range, so that the hot-component temperature may be expected to be in the range 800–1070 °C for such a case. The data of Hon *et al.* (1994a) also showed that lava surface temperatures typically cooled to ~800 °C within a second of exposure. Thus, maximum surface temperatures may be expected to be of a similar level.

These issues make setting of the hot-component temperature problematic, but measurements at Kilauea and Etna show that temperatures for the hot component may be fairly predictable. Thermal camera data of Wright and Flynn (2003), for example, showed that the highest temperature typically encountered on active pahoehoe lobes at Kilauea was ~1000 °C. Repeat radiometer measurements at Kilauea have also shown that the core temperature is rarely, if ever, encountered at the surface. Highest surface temperatures encountered are usually ~300 °C less than the core temperature for Hawaiian pahoehoe. During October and November 1999 I made 40 measurements of active pahoehoe surfaces, scanning the surface with a radiometer for up to 30 seconds and holding the maximum temperature. Results were in the range 710–990 °C, with a maximum of 1026 °C, a mean of 860 °C and a standard deviation of 70 °C. This compared with a thermocouple-measured core temperature of 1150 °C. Likewise, at an active lava channel on Etna, highest surface temperatures measured by Bailey *et al.* (2006) were 830–1040 °C, compared with a core temperature of 1065 °C.

Thus, at an active lava, the hot component temperature may be predictable over a relatively narrow range. However, care must be taken in setting this value, and use of the core (or eruption) temperature should probably be avoided. Instead a value that is 25–300 °C lower than the core temperature can often be used where, for example, a value of  $900 \pm 100$  °C may be defended for Hawaiian pahoehoe, and  $950 \pm 100$  °C for Etnean 'a'a. However, a review of the hot component values given in the Tables of Electronic Supplement 1 show that higher values may be justified for active lava lakes or fast-flowing lava channels. Ideally, a measurement simultaneous with image acquisition, or one which can be used to confidently defend selection of the hot component temperature, should be made and used, as was done at Lascar's lava dome by Oppenheimer *et al.* (1993a) and Lonquimay's lava flow by Oppenheimer (1991). In both cases, optical pyrometer or radiometer measurements of the hot cracks in the lava surface were made, and used to set the hot component temperature in a two-band, two-component application of the dual-band method to TM pixels.

**Crust component temperature** The temperature of the crust component can span hundreds of degrees centigrade depending on its age and distance from the source of emission. For example, the data of Hon *et al.* (1994a) indicate that crust temperatures for surfaces between 1 second and 10 minutes in age may span a temperature range of 800 to 410 °C. Hon *et al.*'s (1994a) data, as given here in Figure 4.11a, showed that crust temperature ( $T_{\text{crust}}$ , in centigrade) will decay logarithmically with time after exposure following the empirically-derived relation:

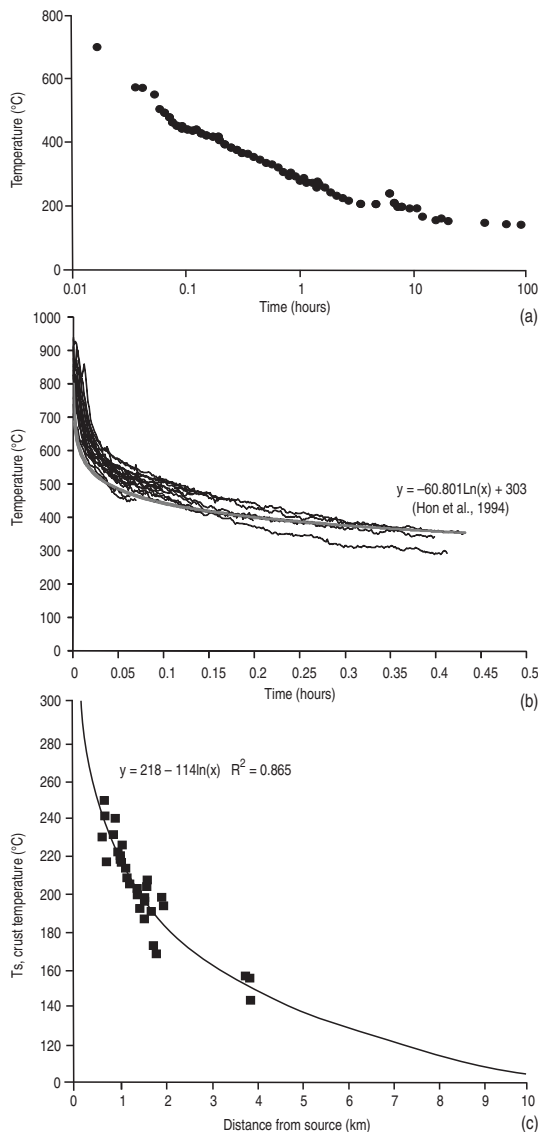


Figure 4.11 (a) Radiometer-derived surface temperature measurements of Hon *et al.* (1994) showing the logarithmic decay in pahoehoe surface temperature with time. (b) Forty radiometer-based cooling curves obtained for pahoehoe surfaces at Kilauea, with the best-fit surface temperature decay relation of Hon *et al.* (1994). (c) Decay in surface temperature ( $T_s$ ) with distance from source for Lonquimay's 'a'a flow as obtained from Landsat TM data by Oppenheimer (1991) [from Oppenheimer (1991, Fig. 4b); reproduced by permission of American Geophysical Union].

$$T_{\text{crust}} = a \log(t) + b, \quad (4.32a)$$

in which  $t$  is time (in hours). For surface cooling of Hawaiian pahoehoe, Hon *et al.* (1994a) gave values of  $-140$  for  $a$  and  $303$  for  $b$ . For a stable surface crust of between 1 minute and 12 hours in age this relation gives crust temperatures of  $550$  °C and  $150$  °C. The logarithmic decay in lava surface temperature with time means that crust temperatures are dominated by values of less than  $550$  °C. The set of 40 surface cooling measurements that I made at Kilauea are given in Figure 4.11b. The trend supports that found by Hon *et al.* (1994a), and shows typical temperatures of  $500$  °C after 5 minutes. Because a stable crust will age with distance down flow, crust temperature profiles will show the same trend. Down-flow crust temperature profiles extracted for Lonquimay's 1991 lava flow by Oppenheimer (1991), for example, showed the same logarithmic decay (see Figure 4.11c). This allowed Oppenheimer (1991) to set, for this lava flow, the following relation for crust temperature as a function of distance (*Distance*, in km),

$$T_{\text{crust}} = 218 - 114 \ln(\text{Distance}) \quad (R^2 = 0.865). \quad (4.32b)$$

We see from Figure 4.11c that the result is a flow surface dominated by crust temperatures between  $140$  °C and  $260$  °C.

The form of the lava flow surface cooling curve means that a stable lava flow surface will likely be dominated by crust temperatures in the range  $140$  to  $550$  °C, and possibly up to  $800$  °C for newly exposed crust. However, given that it will be difficult to guess the cooling history of the crust present within any single pixel, and that crust with a variety of different ages and temperatures will likely be present in the pixel, crust temperature can only reasonably be assumed over a range, where  $100$  to  $500$  °C may be a reasonable assumption range for most crusted 'a'a and pahoehoe lava cases. However, temperature data given in Electronic Supplement 1 show a great range in crust temperatures measured in the field, so that the safe assumption range may have to be extended up to  $950$  °C or even  $1000$  °C for particularly active channel-fed cases.

**Hot-component portion** Active lava flow area, or hot crack area, is very rarely known, and/or difficult to measure on a regular basis at the exact time of image acquisition. Likewise, areas of exposed high-temperature material will constantly change as cracks form and heal and flow fronts fail. Consequently the pixel portion occupied by the lava flow, or cracks within the flow, is exceedingly difficult to set or assume. The exception is where the feature area is relatively stable and predictable, as with a lava lake or hot vent, for example. In such cases pixel portion occupied by the lake or vent may be estimated using the routines given in Electronic Supplement 1.

**Crust temperature and pixel portion solution** Given the uncertainty in their actual value, crust temperature and/or coverage is usually solved for, as has tended to be the case using TM-class data (see Electronic Supplement 5). For example, crust temperature data of Oppenheimer (1991) for Lonquimay's 1989 'a'a lava flow were obtained by applying a two-component dual-band solution to two bands of TM SWIR data (bands 5 and 7). To

reach solution, Oppenheimer (1991) assumed a hot-component temperature of 1040 °C and solved for crust temperature and coverage. This hot-component temperature was set based on optical pyrometer measurements of incandescent regions exposed by flow front collapse and in deep cracks towards the flow front of the same lava flow. For Lascar's lava dome, Oppenheimer *et al.* (1993a) used TM bands 5 and 7 with a radiometer-constrained hot crack temperature of 800 °C, to solve for the temperature and area of crust in each pixel.

If crust temperature has to be assumed, setting a single value is probably impossible, unless the user has simultaneous measurements that show the value is valid and does not vary over the spatial scale of the pixel. For AVHRR data with only one useable TIR band, the approach of Section 4.3.1.2 has typically been applied. This requires solution of Equation (4.26c), i.e.,  $T_a$  is obtained from background pixels, and a crust temperature is assumed to characterize  $T_c$  allowing the pixel portion occupied by the crusted flow to be estimated,

$$p_c = \frac{M(\lambda_{\text{TIR}}, T_{\text{int}}) - M(\lambda_{\text{TIR}}, T_a)}{M(\lambda_{\text{TIR}}, T_c) - M(\lambda_{\text{TIR}}, T_a)}. \quad (4.33)$$

One solution is to solve for two end-member crust temperature conditions. The first condition assumes that the pixel is dominated by an active lava covered with a mature, cool crust, with a  $T_c$  of 100 °C usually being assumed for this condition. The second condition assumes that the pixel is dominated by an active lava covered by a young, hot crust. A  $T_c$  of 500 °C has been typically used to characterize this condition for 'a'a and pahoehoe surfaces, but values of up to 1000 °C have been used for vigorous fountain-fed lava flow. This range straddles the likely range of crust temperatures expected from field measurements, such as those plotted in Figure 4.11.

A comparison of AVHRR- extracted lava flow areas, with field measurements made during Etna's 1991–1993 eruption by Harris *et al.* (1997a), showed that the field measurements fell between the two area estimates given by such an end-member application of Equation (4.26c). However, as can be seen from Figure 4.12, the range of estimates produced by assuming end-member conditions of 100 °C and 500 °C is rather large. For this case, the central location of the field measurements in this wide envelope of solutions suggests that a narrower  $T_c$  assumption range of 250–350 °C may have been justified.

#### *4.3.1.7 How many thermal components?*

Most work has followed the lead of the classic two-component model for the surface of an active lava proposed by Crisp and Baloga (1990a), whereby a crusted surface is broken by high temperature cracks: Pixel Case 2 of Figure 4.6. Data given in Electronic Supplement 1 show that this model may hold, especially for a well-crusted 'a'a flow, dome or silicic flow where we have a warm, mature crust broken by hot cracks. A three-component model (that takes into account different crust temperatures at the channel center and margins) is likely to be more appropriate for lava channels.

For cases where crust moves smoothly away from its source, such as around a spreading center on an active lava lake or at an active pahoehoe, a continuum of temperatures may be

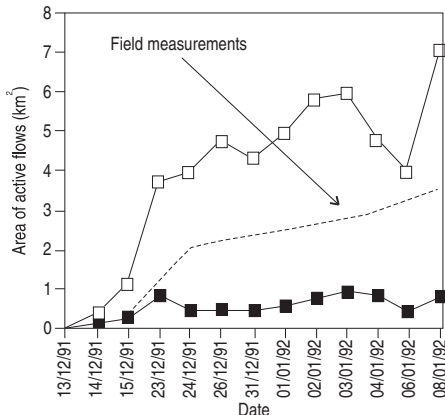


Figure 4.12 Range of active lava area obtained by applying the mixture model approach of Equation (4.26c) to AVHRR data. Results are plotted for the first four weeks of Etna's 1991–1993 effusive eruption. The upper bound (open squares) on the satellite-based derivation is obtained by assuming a characteristic lava surface temperature of 100 °C. The lower bound (black squares) on the satellite-based derivation is obtained by assuming a characteristic lava surface temperature of 500 °C. Field measurements of lava flow area were made by Calvari *et al.* (1994) [from Harris *et al.* (1997a, Fig. 4a); with kind permission from Springer Science and Business Media].

present across the lava surface over spatial scales of a few meters. In such a scenario  $T_h$  will be encountered at the crust source (i.e., the emission point or spreading center), away from which  $T_c$  will decrease logarithmically with time and distance following the relation of Equation (4.32). As a result, far more than two thermal components may be present in a pixel containing an active lava lake or pahoehoe.

This problem was well-illustrated using thermal camera data for active pahoehoe surfaces at Kilauea by Wright and Flynn (2003), who used the thermal camera images to create temperature histograms for the active pahoehoe surfaces, as given here in Figure 4.13. Their results confirm the points regarding setting of  $T_c$  and  $T_h$  values as made above, these being:

- (i) a higher-temperature ( $T_h$ ) component is typically located between 500 °C and 1000 °C, and
- (ii) a lower-temperature ( $T_c$ ) component is typically located between 200 °C and 500 °C.

The distributions of Wright and Flynn (2003) showed that pahoehoe surfaces were characterized by a continuum of temperatures between 200 °C and 1000 °C. Wright and Flynn (2003) tested the dual- and triple-band method, as well as three-, four-, five-, six- and seven-component fits obtained using Planck curve fitting approaches (see next section) on synthetic pixel-integrated temperatures obtained from these histograms. These model output temperatures and fractional coverages are over plotted on the Figure 4.13 temperature distributions. Using this comparison Wright and Flynn (2003) concluded the following.

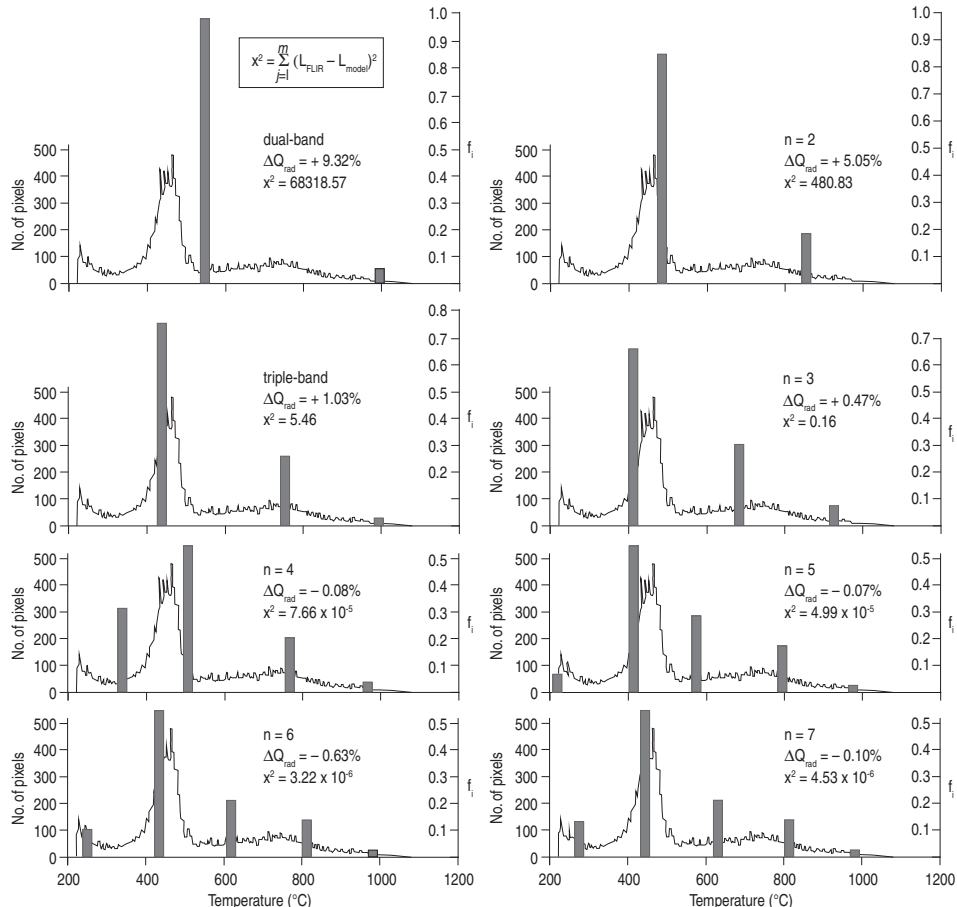


Figure 4.13. Frequency distribution of surface temperatures acquired by Wright and Flynn (2003) using a thermal camera pointed at an active pahoehoe surface on Kilauea. Temperatures were integrated across a synthetic pixel to create a pixel-integrated temperature. Results of dual- and triple-band solutions, as well as three-, four-, five-, six- and seven-component fits obtained using Planck curve fitting approaches applied to the synthetic pixel-integrated temperatures, are given using the vertical gray bars. Also given is the percent difference between the radiative heat flux obtain using the original data and various solutions, plus the chi-square fit between the spectral radiance given by integration of the original data and that predicted by the various solutions (modified from Wright and Flynn (2003, Fig. 1A)).

- A seven-component solution provides the most complete and accurate description of the actual temperature distribution, giving a good impression of the range and dispersion of the distribution.
- Six- and five-component fits are almost as reliable as the seven-component fit.
- Four-component fits provide a “fair indication” of the temperature ranges, but fail to identify the mode.

- Three-component fits correctly identify the mode, but do not have sufficient temperature resolution to give a good impression of the range.
- The problem becomes more acute with the two-component approach, which cannot give information regarding the temperature range.
- The dual-band approach can mis-identify the modal temperature by as much as 100 °C.

A five-to-six-component solution is probably appropriate for a pixel filled with Hawaiian pahoehoe.

**Multiple-component solutions** Multiple-component solutions have been developed in the mixture-modeling community to allow multiple surface types to be extracted from the pixel on the basis of their reflective properties. In such cases, the mixing equation for a number of different surface types can be written following Settle and Drake (1993):

$$\begin{aligned}x_1 &= f_1\mu_{1,1} + f_2\mu_{2,1} + \cdots f_c\mu_{c,1} \\x_2 &= f_1\mu_{1,2} + f_2\mu_{2,2} + \cdots f_c\mu_{c,2} \\&\vdots \\x_n &= f_1\mu_{1,n} + f_2\mu_{2,n} + \cdots f_c\mu_{c,n} \\f_1 + f_2 + \cdots + f_c &= 1\end{aligned}\tag{4.34}$$

where:

- $x_i$  = the spectral radiance in band  $i$ ,  
 $f_j$  = the fractional coverage of component  $j$ ,  
 $\mu_{i,j}$  = spectral radiance in band  $i$  of component  $j$ ,  
 $n$  = total number of bands, and  
 $c$  = total number of surface types (components).

The last equation in this system was termed the “sum-to-one constraint” by Settle and Drake (1993). That is, the fractional coverage by all surfaces must cover 100% of the pixel. Settle and Drake (1993) pointed out the following conditions.

- If the number of components ( $c$ ) is greater than the number of bands plus one (i.e.,  $c > n + 1$ ), then there will be an infinite number of exact solutions.
- If  $c = n + 1$ , that is there is one more component than there are bands, then the solution will be unique.
- If  $c < n + 1$ , that is there are fewer components than there are bands, then there may be no exact solution.

To achieve such multiple-component solutions in geological remote sensing, end-member spectra for “pure” surface types are usually mixed together in varying proportions until the target (hybrid or mixed) spectra is obtained. Bryant (1996), for example, used the method of Settle and Drake (1993) to un-mix pixels acquired over a Playa surface using six wavebands

of TM data and spectra for five, pure, end-member cover types (gypsum, halite, vegetation, alluvium and shade).

We can also write the mixing equation of Settle and Drake (1993) in terms of spectral radiance for a pixel containing a volcanic hot spot, where it will become

$$\begin{aligned} M(\lambda_1 T_{\text{int}}) &= p_1 M(\lambda_1, T_1) + p_2 M(\lambda_1, T_2) + \cdots p_c M(\lambda_1, T_c) \\ M(\lambda_2 T_{\text{int}}) &= p_1 M(\lambda_2, T_1) + p_2 M(\lambda_2, T_2) + \cdots p_c M(\lambda_2, T_c) \\ &\vdots \\ M(\lambda_n T_{\text{int}}) &= p_1 M(\lambda_n, T_1) + p_2 M(\lambda_n, T_2) + \cdots p_c M(\lambda_n, T_c) \\ p_1 + p_2 + \cdots + p_c &= 1 \end{aligned} \quad (4.35)$$

in which

$M(\lambda_i T_{\text{int}})$  = the pixel-integrated spectral radiance in band  $i$ ,

$p_j$  = the pixel coverage of component  $j$ ,

$M(\lambda_j T_j)$  = spectral radiance in band  $i$  of thermal component  $j$ ,

$n$  = total number of bands, and

$c$  = total number of thermal components.

Thus Planck curves for surfaces at different, end-member, pure temperatures can be mixed until a hybrid curve, which best fits the available data points, is obtained.

Take the simulated example given in Figure 4.14. Here, we have one band of unsaturated data in the NIR (band 1 at 0.82  $\mu\text{m}$ ), three in the SWIR (bands 2, 3, and 4 at 1.65  $\mu\text{m}$ , 2.205  $\mu\text{m}$ , and 2.395  $\mu\text{m}$ ), and two in the TIR (bands 5 and 6 at 9.1 and 11.3  $\mu\text{m}$ ). These are the waveband equivalents to ASTER bands 3, 4, 6, 9, 12 and 14 (see Table C2 of Appendix C). In each band we record the following pixel-integrated temperatures:

545 °C (band 1); 710 °C (band 2); 674 °C (band 3);

665 °C (band 4); 558 °C (band 5); 550 °C (band 6).

If we plot the spectral exitance equivalents for each of these pixel-integrated temperatures over the Planck curves of Figure 4.14a, we see that their trend does not follow any single curve, but instead crosses the plotted curves for pure (single) temperature emitters. This tells us that we have a thermally mixed pixel. By mixing the curves for the five pure temperature sources in varying proportions, we obtain a hybrid curve that plots through the six spectral exitance points with the following mix:

$$T_1 = 1000 \text{ °C} \quad p_1 = 0.0001$$

$$T_2 = 750 \text{ °C} \quad p_2 = 0.01$$

$$T_3 = 500 \text{ °C} \quad p_3 = 0.2$$

$$T_4 = 250 \text{ °C} \quad p_4 = 0.5$$

$$T_5 = 100 \text{ °C} \quad p_5 = 1 - p_1 - p_2 - p_3 - p_4 = 0.2899.$$

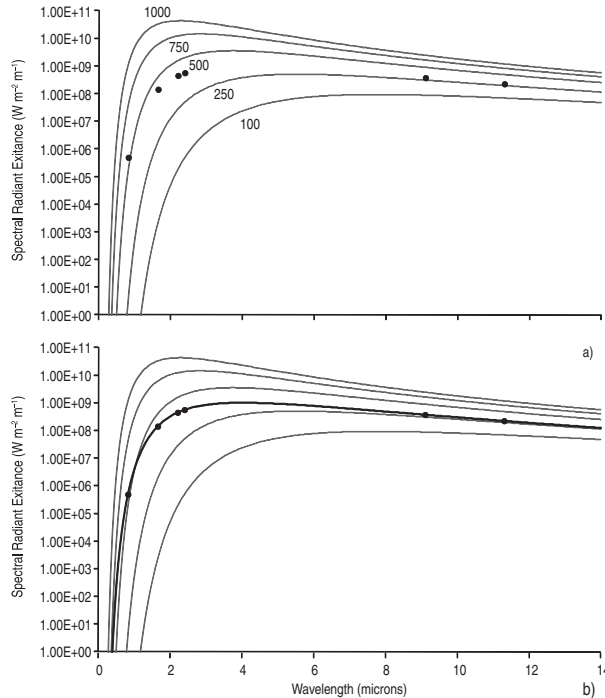


Figure 4.14 Curve fitting approach. (a) Planck curves for thermally pure surfaces at temperatures of between 100 °C and 1000 °C plus the ASTER pixel-integrated temperatures (filled circles) simulated for the NIR (band 1 at 0.82  $\mu\text{m}$ ), the SWIR (bands 2, 3 and 4 at 1.65  $\mu\text{m}$ , 2.205  $\mu\text{m}$  and 2.395  $\mu\text{m}$ ), and TIR (bands 5 and 6 at 9.1 and 11.3  $\mu\text{m}$ ). We see all the signs of a mixed pixel signature (i.e., the plots appear to move from one Planck curve to another, and do not fall on one curve – c.f. [Figure 4.3](#)). (b) Hybrid Planck curve best fit to the pixel-integrated temperatures as obtained using the mixture model given in the main text.

The fit with the hybrid curve that this mixture gives is plotted in [Figure 4.14b](#). Thus we need to adjust the temperature and pixel portion for each of the  $c$  components until the  $R^2$  fit between the hybrid curve and the available data points is minimized. Following this approach, three-to-seven-component fits may be achieved by:

- (i) setting  $T_i$  and  $p_i$  to starting values of 0 °C and 0.0;
- (ii) allowing  $T_i$  to float between 0 °C and 1200 °C, and  $p_i$  between 0 and 1;
- (iii) respecting the rule that the sum of all the  $p_i$ s must sum to one;
- (iv) iterating (to a maximum of 7000 iterations) until the chi-squared minima is obtained.

To achieve such fits, it is best to have between five and seven wavebands of data widely distributed across the NIR to TIR waveband range. Clustering of wavebands at points where the Planck curves change rapidly with wavelength (e.g., between 0.8  $\mu\text{m}$  and 4.0  $\mu\text{m}$ ) allows good characterization of the curve. Clustering of data points across sections where changes are less rapid and curves are closer together (e.g., between 10  $\mu\text{m}$  and 12  $\mu\text{m}$ ) makes solution

more difficult. Note, for example, how the hybrid curve of [Figure 4.14a](#) is easy to envisage using the four data points in the NIR and SWIR, but harder to project using the two points in the TIR, even though the two points in the TIR span a wider wavelength range (i.e., 2.2  $\mu\text{m}$  as opposed to 1.575  $\mu\text{m}$  for the NIR-SWIR points).

#### *4.3.1.8 A note on emissivity and atmospheric correction*

Throughout this chapter I have assumed that input values for pixel-integrated radiance have been corrected for emissivity, atmospheric and surface reflection effects. Of course, while emissivity will vary with surface type, emissivity, atmospheric and reflection effects will vary by wavelength, scan angle and surface elevation (see [Chapter 2](#)). Input values will thus have to be corrected for emissivity, atmospheric and reflection effects if we are to obtain realistic output temperatures and pixel portions. Following [Chapter 2](#), the form of this correction will vary by waveband. Correction procedures, as well as values typically used in these procedures, are given in Electronic Supplement 4.

#### *4.3.1.9 Reality*

An appraisal of Electronic Supplement 1 shows that, in reality, issues of non-response and saturation mean that we are often stuck with one or two bands of data. A surface sufficiently hot so as to emit spectral radiance in TM's NIR band will, for example, likely saturate TM's SWIR bands. Thus, the actual form of the dual-band method will have to be selected and applied according to the limits of the available data. In making this selection we need to ask the following questions.

- How many unsaturated bands are available?
- Which bands are saturated?
- Which bands are unresponsive?

A solution model then needs to be selected accordingly. If, for example, only one band of data is available, the one-band solutions of [Section 4.2.1.4](#). need to be considered. While availability of two or three bands of unsaturated data allows more sophisticated solutions to be applied, the presence of saturated and non-responsive bands allows application of solution constraints that test the consistency of the one-band solution with saturation, or non-response, of other bands, as done in [Section 4.3.1.4](#).

The solution model selected will also depend on the type of thermal feature present within the pixel. Again, an appraisal of Electronic Supplement 1 reveals the thermal complexity of real volcanic surfaces. This complexity means that it is essential to ask what type of feature is present (lava lake, lava dome, fountain-fed lava flow, channel-fed 'a'a, pahoehoe, open vent, etc.), followed by these questions.

- Do we have an isothermal hot surface against a non-radiant background?
- Is it a pixel-filling feature with a two-, three- or multiple-component surface?
- Is it a sub-pixel feature with a two-, three- or multiple-component surface against an ambient background?

- Are there some wavebands in which certain thermal components contribute little to the integrated spectral radiance?

For the first of these cases, the one-component NIR or SWIR solution model of [Section 4.2.1.2](#). may be appropriate. Otherwise we need to apply the classic two-component dual-band solution models of [Section 4.2.1.1](#), the three-component solutions of [Section 4.3.1.1](#) or the multiple-component solutions of [Section 4.3.1.7](#).

We also need to ask: what assumptions are we forced to make, and what are the most realistic values we can set for any assumed values? For example, we may ask the following.

- Do we have field constraints on the hot-component temperature?
- Do we have knowledge of the likely cool-component temperature or temperature range?
- Can we constrain the hot- and/or cool- component area?

Such considerations have led to modification, and case-specific adaptation, of the dual-band method. Consequently, a large number of different solution approaches are available, effectively creating a methodology menu from which the user can select an appropriate methodology depending on the answers to the questions posed above. This is apparent from the length of the preceding two sections, and the number of solution approaches presented. These methodologies comprise the core of the thermal-mixture model menu, and application of some of these un-mixing options, as developed through the 1990s, are given in the review of Electronic Supplement 5. Other worked examples are given in Electronic Supplement 6 and show how, and why, the mixture-modeling methodologies have had to be adapted depending on (i) the limits of the data, and (ii) the complexity of the thermal surface.

**Data limits, choices and multiple components** In some cases, many more than three thermal components may be present in the pixel. However, often only one band, and at most two or three bands, of unsaturated data are available. Thus, a two-to-three-component dual-band model often has to suffice. Although such models may be regarded as broadly realistic for many cases, appropriate assumptions and applications must be made. If, for example, we assume that an isothermal radiant vent is active in a 30 m SWIR pixel, against a non-radiant background, then the one-component solution of [Section 4.2.1.2](#) may be applied. If, instead, an active lava fills the pixel, comprising high-temperature cracks set in a hot radiant crust, then the one-component solution of [Section 4.2.1.2](#) will be invalid. Instead, a two-component model will have to be setup and applied, with selection of the model depending on the number of bands available, presence of unsaturated or unresponsive bands, and availability of field constraint to guide input of assumed values. Higher-level mixture modeling (involving more than three thermal components) is possible if unsaturated data are available at a sufficient number of wavebands. Such approaches may be required for cases where the two- or three-component assumption cannot be defended or approximated. This is the realm of multi- and hyper-spectral mixture modeling, as has typically been applied to airborne imaging spectrometer data (e.g., Oppenheimer *et al.*, 1993b). Such approaches require multiple bands of unsaturated data at appropriate waveband locations. The multispectral solution

of [Section 4.3.1.7](#), for example, requires six unsaturated measurements spanning the NIR, SWIR and TIR.

**Reality check** The potential complexity of thermal surfaces over active volcanic features, coupled with the limits of our measurement, may mean that we need to ask a more fundamental question: are our results valid? The type of radiometry presented here is bound to have substantial errors, so we need to be careful when extracting and using results from dual-band-based methodologies. As already discussed, the results may not be valid, but instead may be an artifact forced by having had to work with measurements at just one or two wavebands.

As a result, one question we may wish to consider before commencing an analysis is: what question do we really want to answer using our spaceborne data and, to obtain our answer, do we really need to apply a mixture model? If we do, we need to consider the limits of our data, and the potential complexity of the real thermal surface. For example, we might want to know if temperatures have increased significantly at a fumarole field, or if new fumaroles have opened up. In such a case, our test may be: has  $p$  increased? To obtain an answer, we may want to attempt to apply an appropriate variant of the dual-band method to extract  $p$ . However, while applying that method we need to ask “what are the limits of our assumptions and method” and “to what extent can we reach any confident conclusion”? In short, at what point do we begin to over-interpret the data?

In fact, if we can complete our analysis without extraction of sub-pixel thermal structures, we can avoid much uncertainty. In the case of our fumarole field, for example, we may be able to demonstrate opening of new fumaroles simply from changes (increases or decreases) in time series of integrated radiance (fast forward to [Chapter 6](#)). However, most of the heat and mass flux derivations that follow typically require application (and solution) of a mixture model as a first step.

#### 4.4 Heat flux

Given the surface temperature of a hot feature, the heat flux density (in  $\text{W m}^{-2} = \text{J s}^{-1} \text{m}^{-2}$ ) can be estimated. If area is also known, this can be converted to heat flux (in  $\text{W} = \text{J s}^{-1}$ ) by multiplying the heat flux density in  $\text{W m}^{-2}$  by the area of the emitting surface in  $\text{m}^2$ . As is apparent from the preceding sections and chapters, the main parameters that can be extracted from thermal infrared data collected by satellite-flown sensors are surface temperature and area. Satellite-based observations in the TIR are hence tailor made for heat flux assessments, so that 39% of the literature in thermal remote sensing of volcanic hot spots, as tabulated in Table A2 of [Appendix A](#), have some form of heat flux focus. The history of heat flux derivations from satellite data is charted in Electronic Supplement 5. Here we consider the main heat fluxes that can be measured using thermal sensors over active volcanic features, as well as the assumptions that need to be made to allow solution of the heat flux equations.

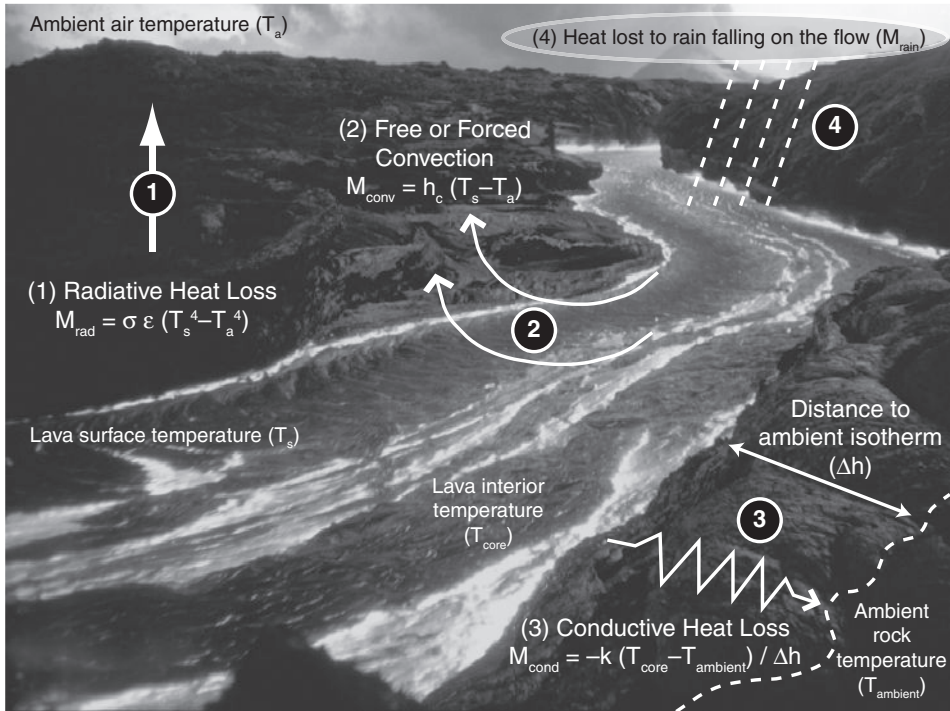


Figure 4.15 Heat losses from the surface of an active lava flow and parameters used in their calculation. We have, in order of magnitude for a surface at temperatures greater than 500 °C: (1) radiation, (2) convection, (3) conduction and (4) heat loss due to rain falling on the flow. See also color plates section.

#### 4.4.1 Estimation of heat fluxes over active lava bodies

Active lava lakes, flows and domes experience three main heat fluxes: radiation, convection and conduction. This model is sketched, for an active lava channel, in Figure 4.15.

##### 4.4.1.1 Radiation ( $M_{\text{rad}}$ and $\Phi_{\text{rad}}$ )

Radiation is the most straightforward heat flux to estimate, requiring a measurement of lava surface temperature ( $T_s$ ) and the temperature of the surrounding ambient environment ( $T_a$ ). If we raise both to the power of four, subtract one from the other and multiply the result by emissivity ( $\epsilon$ ) and the Stefan–Boltzmann constant ( $\sigma$ , see Chapter 2), we have the radiative heat flux density ( $M_{\text{rad}}$ , in  $\text{W m}^{-2}$ ):

$$M_{\text{rad}} = \epsilon \sigma (T_s^4 - T_a^4). \quad (4.36)$$

Now, multiplying by area ( $A$ ) yields the radiation flux ( $\Phi_{\text{rad}}$  in W)

$$\Phi_{\text{rad}} = A M_{\text{rad}} = A \epsilon \sigma (T_s^4 - T_a^4). \quad (4.37a)$$

Because the Stefan–Boltzmann constant is in units of  $\text{W m}^{-2} \text{K}^{-4}$ , temperature must be input into these equations in units of kelvin. If two or three thermal components are present across the lava surface, Equation (4.37a) needs to be written to take into account these components so that, for the two-component case,

$$\Phi_{\text{rad}} = A \sigma \varepsilon [f_c(T_c^4 - T_a^4) + (1 - f_c)(T_h^4 - T_a^4)]. \quad (4.37b)$$

In this two-component case,  $T_c$  is the crust temperature  $f_c$  is the fraction of the surface covered by crust and  $T_h$  is the temperature of the hot cracks in the lava body. If the lava body fills the pixel,  $A$  will be the pixel area. In cases where the lava body does not fill the pixel, the area will have to be the area of the active lava body, i.e.,  $A_{\text{lava}}$  of Equation (4.31b). When the thermal anomaly is spread across more than one pixel, the total heat flux from the lava body will be obtained by summing the fluxes obtained for each pixel.

**Effective radiation temperature** We can also define the effective radiation temperature ( $T_e$ ), which is the average surface temperature (weighted by area and radiant power) for two, or more, thermal surfaces present on an active lava flow surface (Pieri and Baloga, 1986; Crisp and Baloga, 1990a; Pieri *et al.*, 1990). For the two-component case where we have crust at temperature  $T_c$  broken by cracks at temperature  $T_h$ , the effective radiation temperature will be given by:

$$T_e = [f_c T_c^4 + (1 - f_c) T_h^4]^{1/4}, \quad (4.37c)$$

where all temperatures must be input in units of kelvin. In this case, the radiation flux can be approximated from:

$$\Phi_{\text{rad}} = A \sigma \varepsilon (T_e^4 - T_a^4). \quad (4.37d)$$

**Direct measurement of radiative heat flux from pixel-integrated radiance in the MIR** For sub-pixel fires emitting in the MIR (at around  $4 \mu\text{m}$ ), Kaufman *et al.* (1998) showed that the radiative heat flux density for a sub-pixel fire could be approximated by the empirical relation

$$M_{\text{rad}} = 4.34 \times 10^{-19} (T_{\text{MIR}}^8 - T_{\text{MIR-b}}^8). \quad (4.38a)$$

Here,  $T_{\text{MIR}}$  is the pixel-integrated temperature in the MIR for the hot spot pixel, and  $T_{\text{MIR-b}}$  is the temperature of the cold background surrounding the fire. Wooster *et al.* (2003) gave a similar relation for MODIS band 21 ( $3.96 \mu\text{m}$ ), but expressed the relation in terms of radiant heat flux from the fire and used spectral radiance of the hot spot pixel (in units of  $\text{W m}^{-2} \text{sr}^{-1} \mu\text{m}^{-1}$ ), giving

$$\Phi_{\text{rad}} = 1.89 \times 10^7 (L_{\text{MIR}} - L_{\text{MIR-b}}), \quad (4.38b)$$

$L_{\text{MIR}}$  now being the pixel-integrated spectral radiance in the MIR for the hot spot pixel, and  $L_{\text{MIR-b}}$  being the spectral radiance for the cold background in the pixel.

However, these relations can only be used for measurements in the MIR, and within strict temperature limits. Wooster *et al.* (2003) pointed out that this relation will fail for sub-pixel hot spots at temperatures less than 330 °C and greater than 1230 °C. Take, for example, a sub-pixel hot spot at 1000 °C occupying 25% of the pixel and set against a background at 25 °C. This will give a pixel-integrated temperature at 3.96 μm of 593 °C. The radiative heat flux density for such a hot spot is

$$M_{\text{rad}} = 5.67 \times 10^{-8} \text{ W m}^{-2} \text{ K}^{-4} \left[ (1273\text{K})^4 - (298\text{K})^4 \right] = 1.49 \times 10^5 \text{ W m}^{-2};$$

for a 1 km pixel this gives

$$\Phi_{\text{rad}} = (250\,000 \text{ m}^2)(1.49 \times 10^5 \text{ W m}^{-2}) = 3.71 \times 10^{10} \text{ W}.$$

For this hot spot temperature and pixel-integrated temperature, the relation of Kaufman *et al.* (1998) gives a result within 8% of  $M_{\text{rad}}$ , this being

$$M_{\text{rad}} = 4.24 \times 10^{-19} \left[ (866\text{K})^8 - (298\text{K})^8 \right] = 1.37 \times 10^5 \text{ W m}^{-2}.$$

The relation of Wooster *et al.* (2003) gives a result within 5% of  $\Phi_{\text{rad}}$ , this being

$$\Phi_{\text{rad}} = 1.89 \times 10^7 \left[ 1.87 \times 10^3 \text{ W m}^{-2} \text{ sr}^{-1} \mu\text{m}^{-1} - 0.62 \text{ W m}^{-2} \text{ sr}^{-1} \mu\text{m}^{-1} \right] = 3.53 \times 10^2 \text{ W}.$$

However, if the temperature of the sub-pixel hot spot declines, these relations begin to break down. Reducing the hot spot temperature to 500 °C, for example, yields

$$M_{\text{rad}} = 1.98 \times 10^4 \text{ W m}^{-2}$$

and

$$\Phi_{\text{rad}} = 4.95 \times 10^9 \text{ W}.$$

Using the pixel-integrated temperature of 325 °C in Kaufman *et al.* (1998) now yields,

$$M_{\text{rad}} = 7.06 \times 10^3 \text{ W m}^{-2}$$

giving an underestimate by 64%. The relation of Wooster *et al.* (2003), however, still performs well, giving an underestimate by just 7%:

$$\begin{aligned} \Phi_{\text{rad}} &= 1.89 \times 10^7 \left[ 2.81 \times 10^2 \text{ W m}^{-2} \text{ sr}^{-1} \mu\text{m}^{-1} - 0.62 \text{ W m}^{-2} \text{ sr}^{-1} \mu\text{m}^{-1} \right] \\ &= 5.29 \times 10^9 \text{ W}. \end{aligned}$$

Reducing the hot spot temperature further to 250 °C causes the relation of Wooster *et al.* (2003) to diverge, too, this case having

$$\Phi_{\text{rad}} = 9.50 \times 10^8 \text{ W}$$

compared with

$$\begin{aligned}\Phi_{\text{rad}} &= 1.89 \times 10^7 [2.99 \times 10^1 \text{ W m}^{-2} \text{ sr}^{-1} \mu\text{m}^{-1} - 0.62 \text{ W m}^{-2} \text{ sr}^{-1} \mu\text{m}^{-1}] \\ &= 5.53 \times 10^8 \text{ W},\end{aligned}$$

an underestimate by 42%. Such a short-cut negates the need for application of a pixel mixture model, but will not yield accurate results if applied to a sub-pixel lava with a surface temperature of less than  $\sim 350$  °C. A quick check of Figure 4.11 shows that typical crust temperatures across active lavas are, usually, less than this value.

**A note on total energy** In all heat flux cases that we will consider from herein, multiplying by time (in seconds) – or integrating the heat flux (in joules per seconds) through time (in seconds) – yields total energy in joules and is given by the notation  $Q$  or  $E_{\text{th}}$ . Following the definitions laid out in Table 2.1 of Chapter 2, for heat fluxes (in  $\text{J s}^{-1}$  or  $\text{W}$ ) we continue to use the notation  $\Phi$ , and for heat flux densities (in  $\text{J s}^{-1} \text{ m}^{-2}$  or  $\text{W m}^{-2}$ ) we use  $M$ .

#### 4.4.1.2 Convection ( $M_{\text{conv}}$ and $\Phi_{\text{conv}}$ )

On the face of it, convection appears even more straightforward than radiation to estimate, just requiring a measurement of active lava surface temperature ( $T_s$ ) and the ambient environmental temperature ( $T_a$ ), which is then multiplied by the convective heat transfer coefficient ( $h_c$ , in  $\text{W m}^{-2} \text{ K}^{-1}$ ). Thus the convective heat flux density ( $M_{\text{conv}}$ , in  $\text{W m}^{-2}$ ) can be obtained from:

$$M_{\text{conv}} = h_c(T_s - T_a). \quad (4.39a)$$

Multiplying by area ( $A$ ) yields the convective flux ( $\Phi_{\text{conv}}$  in  $\text{W}$ ), that is,

$$\Phi_{\text{conv}} = AM_{\text{conv}} = Ah_c(T_s - T_a). \quad (4.39b)$$

The problem is, obtaining a value for the convective heat transfer coefficient is not so straightforward. In some cases, attempts have been made to measure  $h_c$  in the field, with a value of 45–50  $\text{W m}^{-2} \text{ K}^{-1}$  being obtained over active pahoehoe with surface temperatures of 500 °C and at wind speeds of 10  $\text{m s}^{-1}$  by Keszthelyi *et al.* (2003). Likewise, Keszthelyi and Denlinger (1996) estimated  $h_c$  of  $70 \pm 25 \text{ W m}^{-2} \text{ K}^{-1}$  from field measurements over active pahoehoe in Hawaii. Patrick *et al.* (2005a) suggested values of between 50 and 100  $\text{W m}^{-2} \text{ K}^{-1}$  were appropriate for the cooling 'a'a flow emplaced during Okmok's 1997 eruption. In theory,  $h_c$  can also be calculated following methodologies laid out in text books such as *Heat Transfer* by Holman (1992), which we follow next.

**Heat transfer coefficient: free convection** In windless conditions, free convection occurs. In such cases, the heat transfer coefficient can be calculated using the Nusselt number ( $Nu$ ), where

$$Nu = h_c H/k_{\text{air}}, \quad (4.40)$$

in which  $H$  is the thickness of the layer of hot air overlying the lava flow (in m) and  $k_{\text{air}}$  is the thermal conductivity of the air in the overlying layer (in  $\text{W m}^{-1} \text{K}^{-1}$ ). Hence, the heat transfer coefficient can be calculated from:

$$h_c = (k_{\text{air}} Nu)/H. \quad (4.41)$$

Thus, to calculate  $h_c$ , we need to know the Nusselt number. For free convection, the Nusselt number is given by

$$Nu = 0.16 Ra^{1/3}, \quad (4.42)$$

in which  $Ra$  is the Rayleigh number. Thus, if we know the Rayleigh number, we can estimate the Nusselt number and hence solve Equation (4.41). The Rayleigh number depends on the buoyancy, viscosity and thermal conductivity of the air, and is the product of the Grashof number ( $Gr$ ) and the Prandtl number ( $Pr$ ), i.e.,

$$Ra = Gr Pr. \quad (4.43)$$

The Grashof number is the ratio of buoyancy to viscosity, and can be calculated from:

$$Gr = [g\beta (T_s - T_a) H^3] / \nu_{\text{air}}^2, \quad (4.44)$$

in which  $g$  is acceleration due to gravity ( $9.8 \text{ m s}^{-2}$ ),  $\beta = 1/T (\text{K}^{-1})$ , and  $\nu_{\text{air}}$  is the kinematic viscosity of the hot air ( $\text{m}^2 \text{s}^{-1}$ ). The Prandtl number can be written:

$$Pr = \nu_{\text{air}}/\alpha_{\text{air}}, \quad (4.45)$$

in which  $\alpha_{\text{air}}$  is the thermal diffusivity of the air overlying the lava ( $\text{m}^2 \text{s}^{-1}$ ). Thus, if we work backwards through these Equations, we can theoretically calculate the heat transfer coefficient for free convection, as done in Table 4.5. Note that the rheological properties for air are temperature dependent and need to be obtained from look-up tables, such as those given in Holman (1992). The required temperature for the look up in these tables is the temperature in the boundary layer above the lava flow ( $T_{\text{bound}}$ ) and is usually obtained from  $T_{\text{bound}} = (T_s + T_a)/2$ .

**Heat transfer coefficient: forced convection** In windy conditions, forced convection occurs. In such conditions the heat transfer coefficient can be calculated in the same way, i.e.,

$$h_c = (k_{\text{air}} Nu)/H. \quad (4.46)$$

However, the Nusselt number is now related to the Reynolds number ( $Re$ ) rather than the Rayleigh number. In this case, if  $RePr$  is between 0.6 and 50, the Nusselt number is given by:

$$Nu = 0.332 Pr^{0.3} Re^{0.5}. \quad (4.47)$$

However, if  $RePr$  is greater than 100,  $Nu$  is given by:

$$Nu = [0.3387 Pr^{0.3} Re^{0.5}] / \left[ (1 + (0.0468/Pr)^{0.67})^{0.25} \right]. \quad (4.48)$$

Table 4.5. Calculation of the convective heat transfer coefficient for free convection. Two cases are given: (1) an active lava flow or lava lake with a surface at a temperature of 600 °C, and (2) a silicic lava dome or silicic lava flow with a surface at a temperature of 100 °C.

Case 1: Active lava flow or lake Values used to calculate $h_c$ : free case	Case 2: Silicic lava dome or flow Values used to calculate $h_c$ : free case		
Values are set for air at $T_{\text{boundary}}$ using tables in Holman (1992)	Values are set for air at $T_{\text{boundary}}$ using tables in Holman (1992)		
$T_{\text{surface}} (\text{K})$	873	$T_{\text{surface}} (\text{K})$	373
$T_{\text{ambient}} (\text{K})$	298	$T_{\text{ambient}} (\text{K})$	298
$T_{\text{boundary}} (\text{K})$	586	$T_{\text{boundary}} (\text{K})$	336
[= $(T_{\text{surface}} + T_{\text{ambient}})/2$ ]		[= $(T_{\text{surface}} + T_{\text{ambient}})/2$ ]	
Kinematic viscosity ( $\text{m}^2 \text{s}^{-1}$ )	$5.13 \times 10^{-5}$	Kinematic viscosity ( $\text{m}^2 \text{s}^{-1}$ )	$2.08 \times 10^{-5}$
Thermal diffusivity ( $\text{m}^2 \text{s}^{-1}$ )	$7.51 \times 10^{-5}$	Thermal diffusivity ( $\text{m}^2 \text{s}^{-1}$ )	$2.98 \times 10^{-5}$
$Pr$	<b>0.68</b>	$Pr$	<b>0.70</b>
Gravity ( $\text{m s}^{-2}$ )	9.8	Gravity ( $\text{m s}^{-2}$ )	9.8
$\beta (1/T, \text{K})$	0.0017	$\beta (1/T, \text{K})$	0.0030
$H (\text{m})$	1.5	$H (\text{m})$	1.5
Kinematic viscosity ( $\text{m}^2 \text{s}^{-1}$ )	$5.13 \times 10^{-5}$	Kinematic viscosity ( $\text{m}^2 \text{s}^{-1}$ )	$2.08 \times 10^{-5}$
$Gr$	<b><math>1.23 \times 10^{10}</math></b>	$Gr$	<b><math>1.71 \times 10^{10}</math></b>
$Ra (= Gr Pr)$	<b><math>8.43 \times 10^9</math></b>	$Ra (= Gr Pr)$	<b><math>1.19 \times 10^{10}</math></b>
$Nu (= 0.16 Ra^{1/3})$	<b>326</b>	$Nu (= 0.16 Ra^{1/3})$	<b>366</b>
$H (\text{m})$	1.5	$H (\text{m})$	1.5
$k_{\text{air}} (\text{W m}^{-1} \text{K}^{-1})$	0.0046	$k_{\text{air}} (\text{W m}^{-1} \text{K}^{-1})$	0.030
$h_c (\text{W m}^{-2} \text{K}^{-1})$	<b>10</b>	$h_c (\text{W m}^{-2} \text{K}^{-1})$	<b>7.3</b>

Bold values are calculations; non-bold are input values.

To solve these equations, the Prandtl number can be calculated as in the free convection case (i.e., using [Equation \(4.45\)](#)). The Reynolds number is the ratio of inertial forces to viscous forces, and is given by

$$Re = (WL)/v_{\text{air}}, \quad (4.49)$$

in which  $W$  is wind speed and  $L$  is length scale. Length scale is the dimension of the body in question (i.e., the width of the lava channel, flow, dome or lake). If we can assume the values required to estimate  $Re$  and  $Pr$ , we can estimate  $Nu$  and hence constrain the convective heat transfer coefficient. Again, if we work backwards through these equations we can theoretically calculate the heat transfer coefficient for forced convection, as done in [Table 4.6](#).

The calculation in [Table 4.6](#) is for a flow width (length scale) of 100 m, which gives  $h_c$  of around  $40 \text{ W m}^{-2} \text{K}^{-1}$ . We note that decreasing the length scale to 1 m or 10 m decreases  $h_c$  to  $\sim 4 \text{ W m}^{-2} \text{K}^{-1}$  or  $\sim 12 \text{ W m}^{-2} \text{K}^{-1}$ . Increasing  $L$  to 1000 m increases  $h_c$  to  $\sim 126 \text{ W m}^{-2} \text{K}^{-1}$ .

Table 4.6. Calculation of the convective heat transfer coefficient for forced convection. Two cases are given: (1) an active lava flow or lava lake with a surface at a temperature of 600 °C, and (2) a silicic lava dome or silicic lava flow with a surface at a temperature of 100 °C.

<b>Case 1: Active lava flow or lake</b> Values used to calculate $h_c$ : Forced Case	<b>Case 2: Silicic lava dome or flow</b> Values used to calculate $h_c$ : Forced Case		
Values are set for air at $T_{\text{boundary}}$ using tables in Holman (1992)	Values are set for air at $T_{\text{boundary}}$ using tables in Holman (1992)		
$T_{\text{surface}} (\text{K})$	873	$T_{\text{surface}} (\text{K})$	373
$T_{\text{ambient}} (\text{K})$	298	$T_{\text{ambient}} (\text{K})$	298
$T_{\text{boundary}} (\text{K})$ [= $(T_{\text{surface}} + T_{\text{ambient}})/2$ ]	586	$T_{\text{boundary}} (\text{K})$ [= $(T_{\text{surface}} + T_{\text{ambient}})/2$ ]	336
Kinematic viscosity ( $\text{m}^2 \text{s}^{-1}$ )	$5.13 \times 10^{-5}$	Kinematic viscosity ( $\text{m}^2 \text{s}^{-1}$ )	$2.08 \times 10^{-5}$
Thermal diffusivity ( $\text{m}^2 \text{s}^{-1}$ )	$7.51 \times 10^{-5}$	Thermal diffusivity ( $\text{m}^2 \text{s}^{-1}$ )	$2.98 \times 10^{-5}$
$Pr$	<b>0.68</b>	$Pr$	<b>0.70</b>
Wind speed ( $\text{m s}^{-1}$ )	10	Wind speed ( $\text{m s}^{-1}$ )	10
Length scale (flow width, m)	100	Length scale (flow width, m)	100
Kinematic viscosity ( $\text{m}^2 \text{s}^{-1}$ )	$7.51 \times 10^{-5}$	Kinematic viscosity ( $\text{m}^2 \text{s}^{-1}$ )	$2.08 \times 10^{-5}$
$Re$	<b><math>1.95 \times 10^7</math></b>	$Re$	<b><math>4.82 \times 10^7</math></b>
$Re Pr$	<b><math>1.33 \times 10^7</math></b>	$Re Pr$	<b><math>3.35 \times 10^7</math></b>
$Nu$	<b><math>1.28 \times 10^3</math></b>	$Nu$	<b><math>2.03 \times 10^3</math></b>
$H (\text{m})$	1.5	$H (\text{m})$	1.5
$k_{\text{air}} (\text{W m}^{-1} \text{K}^{-1})$	0.0046	$k_{\text{air}} (\text{W m}^{-1} \text{K}^{-1})$	0.030
$h_c (\text{W m}^{-2} \text{K}^{-1})$ (Eqn. 4.46)	<b>39</b>	$h_c (\text{W m}^{-2} \text{K}^{-1})$ (Eqn. 4.46)	<b>41</b>
$h_c (\text{W m}^{-2} \text{K}^{-1})$ (Eqn. 5.50a)	<b>20</b>	$h_c (\text{W m}^{-2} \text{K}^{-1})$ (Eqn. 5.50a)	<b>20</b>
$h_c (\text{W m}^{-2} \text{K}^{-1})$ (Eqn. 5.50b)	<b>0.4</b>	$h_c (\text{W m}^{-2} \text{K}^{-1})$ (Eqn. 5.50b)	<b>0.4</b>
$h_c (\text{W m}^{-2} \text{K}^{-1})$ (Eqn. 5.50c)	<b>36</b>	$h_c (\text{W m}^{-2} \text{K}^{-1})$ (Eqn. 5.50c)	<b>36</b>

Bold values are calculations; non-bold are input values.

The effect of changing length scale on  $h_c$  is plotted in Figure 4.16. From Table 4.6 we see that the difference in thermal properties of the air between the two surfaces, one at 600 °C, the other at 100 °C, does not change  $h_c$  too much. However, as can be seen from Figure 4.16, increasing the length scale between a narrow feature (e.g. a 3 m wide channel) and a broad feature (e.g., a 500 m wide lava dome) can increase  $h_c$  from  $\sim 7 \text{ W m}^{-2} \text{ K}^{-1}$  to  $\sim 90 \text{ W m}^{-2} \text{ K}^{-1}$ . The heat transfer coefficient in the forced case should thus be set according to feature dimension. The measurement of  $45\text{--}50 \text{ W m}^{-2} \text{ K}^{-1}$  made by Keszthelyi *et al.* (2003) is consistent with a length scale of  $\sim 160 \text{ m}$ , which seems about right given that the measurement was made at the edge of a broad pad of pahoehoe. We also note that the calculation for  $h_c$  in the free convection case is independent of flow width, and hence plots as a horizontal line in Figure 4.16.

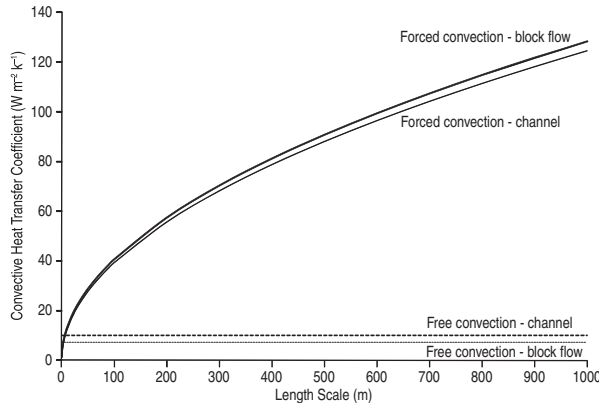


Figure 4.16 Variation in convective heat transfer coefficient with length scale for forced convection at (i) an active basaltic lava channel and (ii) an active silicic (block) lava flow (see Table 4.6 for parameters input into model). For both cases the heat transfer coefficient for free convection is also given. We see that this is independent of length scale.

**Heat transfer coefficient: other treatments using field measurements** Keszthelyi and Denlinger (1996) pointed out that solutions for the heat transfer problem are available from micrometeorological models for internal thermal boundary layers. Some require input of parameters that are difficult to measure or assume, but Keszthelyi and Denlinger (1996) took “three readily applicable” formulas from Arya (1998):

$$M_{\text{conv}} = 2 \times 10^{-3} \rho_{\text{air}} c_{\text{pair}} W (T_s - T_a) \quad (4.50a)$$

$$M_{\text{conv}} = \rho_{\text{air}} c_{\text{pair}} W \gamma H_{\text{air}}^2 / (2.25x) \quad (4.50b)$$

$$M_{\text{conv}} = C_H \rho_{\text{air}} c_{\text{pair}} W (T_s - T_a) \quad (4.50c)$$

and added a fourth:

$$M_{\text{conv}} = \rho_{\text{air}} c_{\text{pair}} W H_{\text{air}} \Delta T / x. \quad (4.50d)$$

Here, and using the values assumed by Keszthelyi and Denlinger (1996) for their “rough” calculations,

- $\rho_{\text{air}}$  = air density ( $1 \text{ kg m}^{-3}$ );
- $c_{\text{pair}}$  = heat capacity of air ( $1000 \text{ J kg}^{-1} \text{ K}^{-1}$ );
- $W$  = mean wind speed ( $\text{m s}^{-1}$ );
- $\gamma$  = adiabatic lapse rate ( $0.01 \text{ K m}^{-1}$ );
- $H_{\text{air}}$  = thickness of the boundary layer (i.e., the thickness of the zone of heated air over the lava flow,  $0.5\text{--}1.5 \text{ m}$ );
- $x$  = the down-wind distance across the active lava zone (m);

- $C_H = (W^*/W)^2$ , in which  $W^*$  is the friction wind speed, a value of 0.06 having been measured for  $W^*/W$  by Greeley and Iverson (1987) at the Amboy lava flow field; and
- $\Delta T$  = degree to which the air is heated during passage across the active lava.

Keszthelyi and Denlinger (1996) expressed concerns regarding the likely underestimation of the heat transfer coefficient, and hence  $M_{\text{conv}}$ , when Equations (4.50a)–(4.50c) were applied to an active lava, preferring Equation (4.50d). At the foot of Table 4.6 we provide the heat transfer coefficient derived from Equations (4.50a)–(4.50c) using the values given above with the wind speeds and length scales of Table 4.6. The results, when compared with the heat transfer coefficient derived theoretically in the previous section, show that although Equation (4.50a), and especially Equation (4.50b), give a value lower than the theoretical value, Equation (5.50c) gives a value of  $36 \text{ W m}^{-1} \text{ K}^{-1}$ , a value close to the theoretically derived value of  $\sim 40 \text{ W m}^{-1} \text{ K}^{-1}$ .

#### 4.4.1.3 Conduction ( $M_{\text{cond}}$ and $\Phi_{\text{cond}}$ )

Heat will also be lost by conduction through the base of a lava body to cause cooling at the flow base, as has been measured at the base of a pahoehoe lava flow during the first 8 minutes of cooling by Keszthelyi (1995a). Following Fourier's Law, conductive heat flux density ( $M_{\text{cond}}$ ) can be estimated by multiplying the thermal conductivity of the rock ( $k$ ) by the gradient in temperature between the lava body interior and the underlying country rock. The gradient can be obtained by dividing the temperature difference between the lava interior and the underlying surface ( $\Delta T$ ) by the distance over which this temperature difference applies ( $\Delta h$ ), so that:

$$M_{\text{cond}} = -k \frac{\Delta T}{\Delta h}. \quad (4.51\text{a})$$

The problem is, none of these measurements can be made from the satellite perspective. All that can be done is to use the satellite-data-derived flow area over which the conductive flux density applies ( $A$ ), with reasonable assumptions for  $k$ ,  $\Delta T$  and  $\Delta h$ , to convert to conductive heat flux ( $\Phi_{\text{cond}}$ ) following:

$$\Phi_{\text{cond}} = AM_{\text{cond}} = A - k \frac{\Delta T}{\Delta h}. \quad (4.51\text{b})$$

The difficulty of assuming  $\Delta h$  can be removed if the time since flow emplacement is known. In this case, following, for example, Turcotte and Schubert (2002), the thickness of the thermal boundary layer can be calculated as a function of time from:

$$\Delta h = \sqrt{\alpha \pi t}, \quad (4.52)$$

in which  $\alpha$  is the rock thermal diffusivity (in  $\text{m}^2 \text{ s}^{-1}$ ) and  $t$  is time (in seconds). Thermal diffusivity can, in turn, be calculated from the rock thermal conductivity ( $k$ , in  $\text{W m}^{-1} \text{ K}^{-1}$ ), density ( $\rho$ , in  $\text{J kg m}^{-3}$ ) and specific heat capacity ( $c_p$ , in  $\text{J kg}^{-1} \text{ K}^{-1}$ ) using

$$\alpha = k / \rho c_p. \quad (4.53)$$

Now, Equation (4.51a) becomes,

$$M_{\text{cond}} = -k \frac{\Delta T}{\sqrt{\alpha \pi t}} \quad (4.54)$$

However, we still need to know the time since emplacement, plus  $\Delta T$ , to solve.

#### 4.4.1.4 Crust thickness

Heat will also be conducted across the surface crust of an active lava flow, lake or dome. Heat conducted across the crust will then be lost from the surface by radiation and convection, as sketched in Figure 4.17. Thus, we may assume that the conductive flux density across the surface crust is equal to the sum of the radiative and convective flux densities leaving the same surface, so that

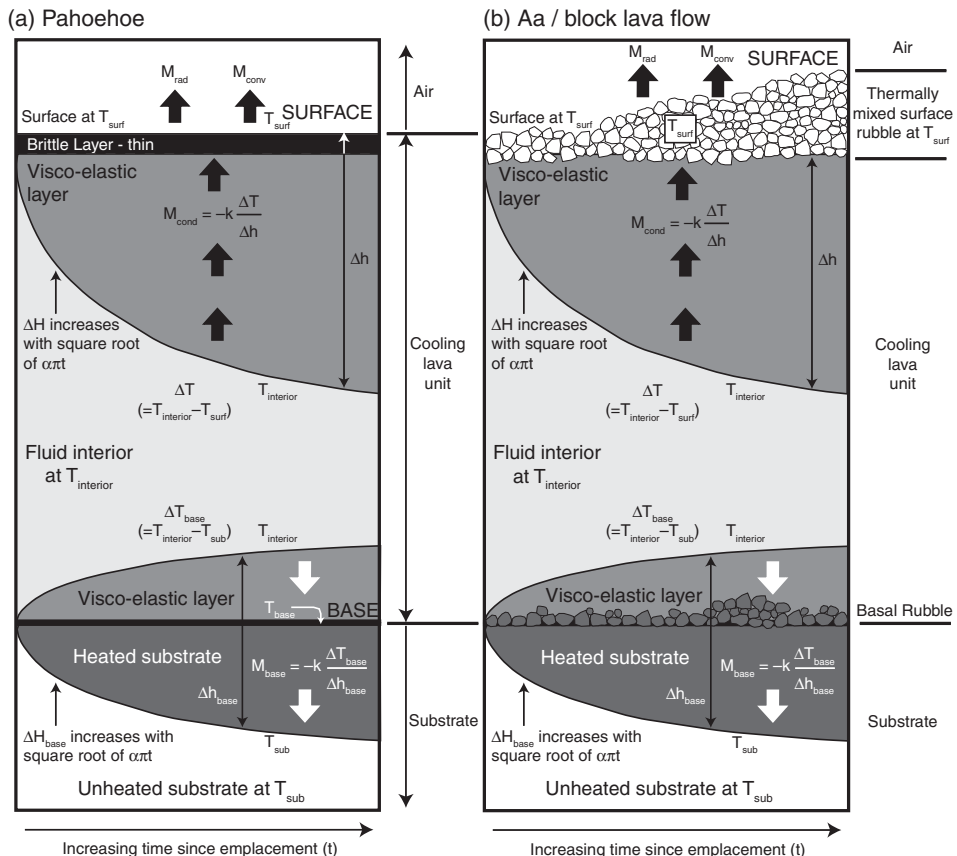


Figure 4.17 Model for heat loss through the surface and basal thermal boundary layers of (a) an active pahoehoe flow and (b) an active 'a'a lava flow.

$$M_{\text{cond}} = M_{\text{rad}} + M_{\text{conv}} = -k \frac{\Delta T}{\Delta h}. \quad (4.55)$$

If a satellite-based measure of radiative and convective flux densities is available, we can use these in a re-arranged version of Equation (4.55) to estimate surface crust thickness ( $\Delta h$ ), that is,

$$\Delta h = \frac{-k\Delta T}{M_{\text{rad}} + M_{\text{conv}}}. \quad (4.56)$$

Now, applying the equations of Sections 4.4.1.1 and 4.4.1.2 to estimate  $M_{\text{rad}}$  and  $M_{\text{conv}}$  using our satellite-derived flow temperatures, we can solve for  $\Delta h$ , given values for  $k$  and  $\Delta T$ . Because  $\Delta T$  is the temperature difference between the flow interior and surface, the satellite data may help further: if we have a satellite-derived estimate of flow surface temperature, we only need an assumption of flow interior temperature to estimate  $\Delta T$ . Oppenheimer (1991) was the first to attempt such a calculation using satellite data, using flow surface temperatures derived from TM data for Lonquimay's 1989 lava flow to estimate and plot down-flow changes in crust thickness using a field-measured core temperature of 1040 °C and a range of assumed conductivities of between 0.6 and 3.0 W m<sup>-1</sup> K<sup>-1</sup>. His results are reproduced here in Figure 4.18. The physical meaning of the  $\Delta h$  value is given in Figure 4.17. On an 'a'a flow it is probably the thickness of the thermal boundary beneath a thermally mixed surface

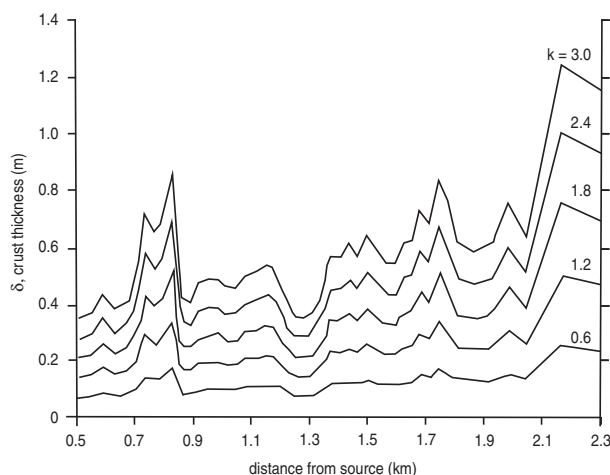


Figure 4.18 Down-flow variation in “crust” thickness ( $\Delta h$ ) obtained by Oppenheimer (1991) from Landsat-TM data for Lonquimay's 1989 'a'a flow using the approach of Equation (4.56). Solutions are given for a range of thermal conductivities ( $k$ ) between 0.6 and 3.0 W m<sup>-1</sup> K<sup>-1</sup> [from Oppenheimer (1991, Fig. 16); Reproduced by permission of American Geophysical Union]. Following Oppenheimer (1991)  $\Delta h$  is likely the thickness of the thermal boundary layer beneath a layer of thermally mixed rubble (see Figure 4.17b).

rubble (Oppenheimer, 1991), so that  $\Delta h$  is not equal to the complete thickness of crust (see right-hand box of Figure 4.17).

For a lava lake or pahoehoe flow where there is no surface rubble,  $\Delta h$  may equate to the thickness of crust between the molten core and the surface, as in the left hand box of Figure 4.17. Take a pahoehoe surface after 360 seconds of cooling and at a temperature of 443 °C, for example. Hon *et al.*'s (1994a) relation for the depth of the 1070 °C isotherm<sup>2</sup> predicts that the depth of the thermal boundary layer down to the 1070 °C isotherm (the base of the brittle and visco-elastic crusts) will be 2.5 cm by this time. Using the same surface temperature in Equations (4.36) and (4.39), with an emissivity of 0.98 and a convective heat transfer coefficient of 50 W m<sup>-2</sup> K<sup>-1</sup>, we obtain  $M_{\text{rad}}$  of  $1.42 \times 10^4$  W m<sup>-2</sup> and  $\Phi_{\text{conv}}$  of  $2.09 \times 10^4$  W m<sup>-2</sup>, which sum to  $3.51 \times 10^4$  W m<sup>-2</sup>. Putting this into Equation (4.56), with a thermal conductivity of between 1.25 W m<sup>-1</sup> K<sup>-1</sup> and 1.5 W m<sup>-1</sup> K<sup>-1</sup> and  $\Delta T$  of 627 K (equal to the difference in temperature between the 1070 °C isotherm and 443 °C surface temperature) yields  $\Delta h$  of between 2.2 cm and 2.7 cm. This is approximately the thickness of the surface crust expected from the empirical relation of Hon *et al.* (1994a).

#### *4.4.1.5 Heat loss due to rain falling on an active lava flow*

The heat flux due to rain falling onto an active lava surface can be calculated from

$$\Phi_{\text{rain}} = A M_{\text{rain}} = A \frac{dR}{dt} \rho_{\text{rain}} L_{\text{H}_2\text{O}}^+. \quad (4.57)$$

Here,

- $dR/dt$  = rainfall rate (in m s<sup>-1</sup>);
- $\rho_{\text{H}_2\text{O}}$  = density of water at 100 °C (958 kg m<sup>-3</sup>);
- $L_{\text{H}_2\text{O}}^+$  = latent heat of vaporization of water plus the heat needed to warm the water to boiling point (2.8 MJ kg<sup>-1</sup>; Keszthelyi, 1995b).

However, because our satellite image needs to be cloud-free if we are to view the thermal anomaly, we can assume that there will be no rain falling on the lava, so this flux will be zero during image acquisition.

**Heat flux: solution** To estimate the heat flux from an active lava body using satellite IR data, the following four-step methodology can be applied.

- (i) Extract all anomalous pixels from the satellite data, and apply all necessary atmospheric and emissivity corrections.
- (ii) Extract sub-pixel thermal structures (lava surface temperatures and areas) through dual-band modeling of the NIR, SWIR, MIR and/or TIR data.

<sup>2</sup> This relation is  $D_{1070} = 0.0779 * \text{SQRT}(t)$ , where  $D_{1070}$  is the depth of the 1070 °C isotherm, and  $t$  is time since emplacement in hours.

- (iii) Obtain radiative, convective and conductive heat flux densities (in  $\text{W m}^{-2}$ ) on a pixel-by-pixel basis and convert to heat flux (in W) for each pixel by multiplying by pixel area (in  $\text{m}^2$ ).
- (iv) Sum the heat fluxes for each pixel to obtain the total power output by the active lava body.

A worked example of this method is given in Electronic Supplement 7.

#### 4.4.1.6 Lava tubes

The above treatments apply to a lava body (flow, lake or dome) whose surface is exposed to the sky. For lava tubes, presence of a tube roof insulates the flowing lava so that a modified heat loss model needs to be applied. A complete heat loss model for a lava tube, containing skylights, is given by Keszthelyi (1995b), as sketched in Figure 4.19a. Keszthelyi (1995b) models the tube as a heated pipe buried in a cooler medium, so that heat is lost from the pipe by:

- heating of air circulating in fractures in the lava surrounding the pipe (i.e., convection),
- conduction from the hot pipe to the cooler surrounding rock, and
- heating and vaporization of rain water seeping into the rock surrounding the pipe.

We note that, in applying this model, we assume that the lava interior can be described by a single temperature, i.e., that of molten lava flowing down the tube that heats the interior of the tube (walls, roof and air) to the same temperature.

**Convection** Of these heat fluxes, the heat flux (in watts) due to convection ( $\Phi_{\text{tconv}}$ ) can be calculated from:

$$\Phi_{\text{tconv}} = L_{\text{tube}} \pi 0.565 \left( \frac{\rho_{\text{air}} \alpha_{\text{air}} g K_{\text{lava}} (T_{\text{tube}} - T_{\text{surf}}) D_{\text{tube}}}{\mu_{\text{air}} \beta_{\text{lava}}} \right)^{0.5} (T_{\text{tube}} - T_{\text{surf}}) k_{\text{lava}}. \quad (4.58)$$

This equation thus uses the dimensional and thermal properties of the tube:

- $L_{\text{tube}}$  = tube length (m);
- $D_{\text{tube}}$  = tube diameter (m);
- $T_{\text{tube}}$  = temperature of lava flowing in the tube (K);
- $T_{\text{surf}}$  = temperature of the surface above the tube (K);

along with the thermal properties of the air circulating in the rock around the tube,

- $\rho_{\text{air}}$  = air density ( $\text{kg m}^{-3}$ );
- $\alpha_{\text{air}}$  = air thermal diffusivity ( $\text{m}^2 \text{s}^{-1}$ );
- $\mu_{\text{air}}$  = air viscosity ( $\text{m}^2 \text{s}^{-1}$ ),

as well as those of the surrounding rock:

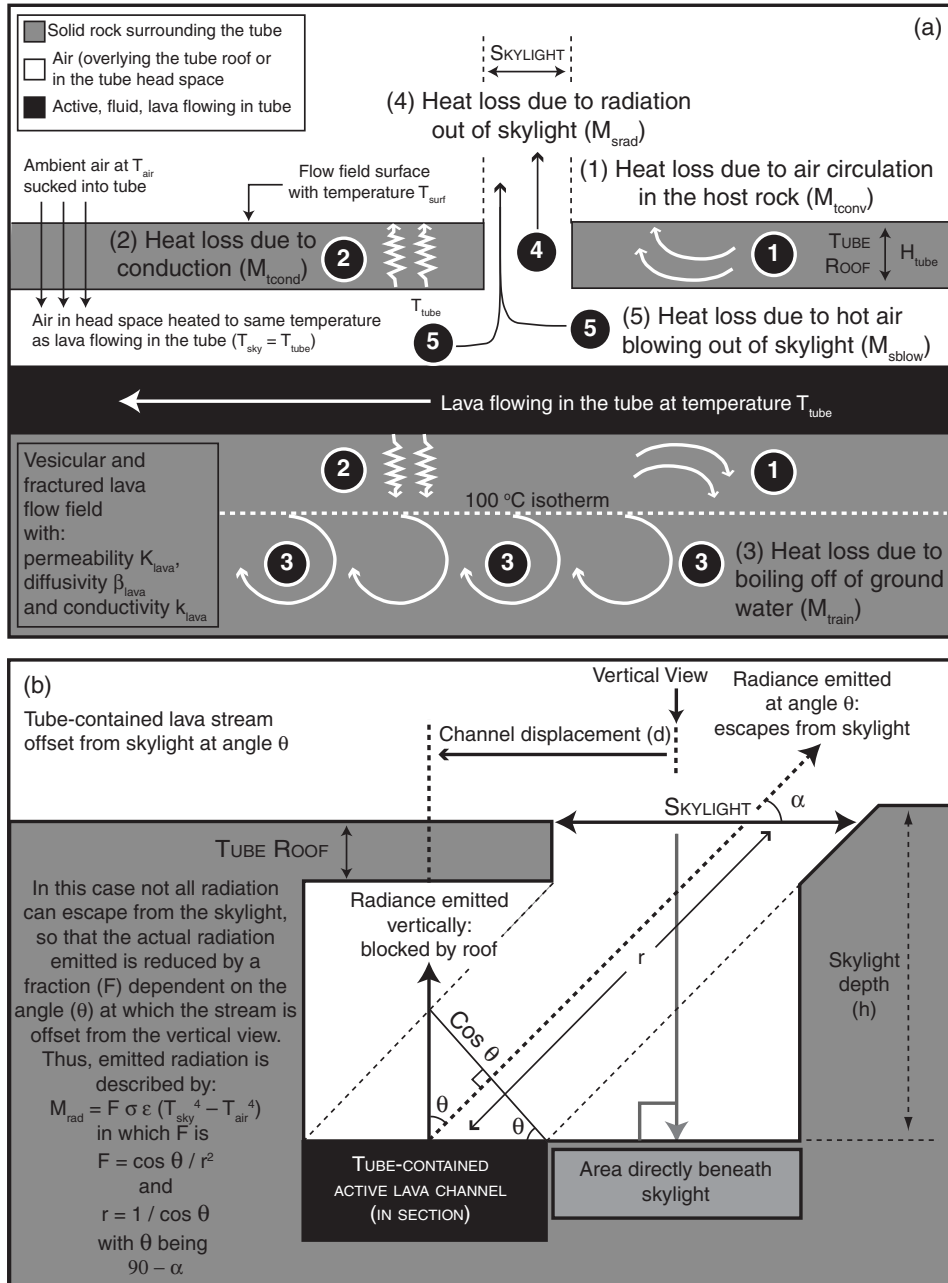


Figure 4.19 (a) Heat loss model for an active lava tube and the main parameters used for solution, giving the five main heat losses. (b) Geometry for shape factor correction applied to radiative heat losses from a lava stream not located directly beneath a skylight.

- $K_{\text{lava}}$  = rock permeability ( $\text{m}^2$ );
- $\beta_{\text{lava}}$  = rock thermal diffusivity ( $\text{m}^2 \text{s}^{-1}$ );
- $k_{\text{lava}}$  = rock thermal conductivity ( $\text{W m}^{-1} \text{K}^{-1}$ ).

As shown by Keszthelyi (1995b) this formulation is the result of combining the Nusselt number ( $Nu$ ) and the Rayleigh number ( $Ra$ ), where

$$\Phi_{\text{tconv}} = L_{\text{tube}} \pi Nu (T_{\text{tube}} - T_{\text{surf}}) k_{\text{lava}}, \quad (4.59\text{a})$$

in which

$$Nu = 0.565 Ra^{1/2}, \text{ for } Ra > 10 \quad (4.59\text{b})$$

and

$$Ra = \frac{\rho_{\text{air}} \alpha_{\text{air}} g K_{\text{lava}} (T_{\text{tube}} - T_{\text{surf}}) D_{\text{tube}}}{\mu_{\text{air}} \beta_{\text{lava}}}. \quad (4.59\text{c})$$

We see that, by writing the Rayleigh number in full in Equation (4.59b) and then inserting the result in place of the Nusselt number in Equation (4.59a), we obtain Equation (4.58).

**Conduction** Heat flux due to conduction ( $\Phi_{\text{tcond}}$ ) can be estimated using the thickness of the tube roof ( $H_{\text{tube}}$ ) and the tube radius ( $r_{\text{tube}}$ ) in:

$$\Phi_{\text{tcond}} = k_{\text{lava}} (T_{\text{tube}} - T_{\text{surf}}) \left[ \frac{2\pi L_{\text{tube}}}{\cosh^{-1}(H_{\text{tube}}/r_{\text{tube}})} \right]. \quad (4.60)$$

All other parameters are the same as those used for the calculation of the convective heat loss.

**Rain** Heat flux due to percolation of rain into the rock surrounding the tube and its subsequent heating and vaporization ( $\Phi_{\text{train}}$ ) can be estimated from

$$\Phi_{\text{train}} = \frac{\partial R}{\partial t} A_{\text{rain}} \rho_{\text{rain}} L_{\text{H}_2\text{O}}^+ . \quad (4.61)$$

Here, the terms are the same as those defined for Equation (4.57), with  $A_{100}$  being the area defined by the 100 °C isotherm. In this case it does not matter whether rain is falling or not. This is because we are considering an integrated heat flux, averaged over a long enough time period so as to include both rainy and dry days. Within this model, water (mostly supplied by rain) can percolate into the permeable (vesicular and cracked) lava to form a boil-off or wet zone (hydrothermal system) of area  $A_{100}$  surrounding the hot lava tube.

**Solution using satellite data** As shown in Electronic Supplement 1, the thermal expression of lava tubes can be detected in high-spatial-resolution (TM-class) data operating in the thermal infrared. This means that three of the main variables in Equations (4.58)–(4.60), i.e., tube length, surface temperature above the tube and area inside the 100 °C isotherm,

may be obtained from analysis of high-spatial-resolution satellite TIR data. However, solution of these equations also involves assumption, and/or calculation, of several air and lava thermal parameters, plus field measurement of unknowns such as tube diameter and depth, as well as rainfall rates. However, approaches have been applied that combine satellite-derived, calculated and field-measured values to complete heat flux inventories for tube-fed systems, with Harris *et al.* (1998) combining field data with analysis of a TM band 6 (TIR) image to apply the heat loss model of Keszthelyi (1995b) for an active lava tube on Kilauea.

#### *4.4.1.7 Skylights*

For tubes containing skylights, the heat loss from these openings also needs to be taken into account. The two main heat losses will be the following.

- That lost directly from the lava surface as it becomes exposed to the atmosphere as the lava passes through the skylight, i.e., radiation.
- Plus heat carried away by hot air blowing out of the skylight.

These heat losses have been assessed by Keszthelyi (1995b) and Witter and Harris (2007).

**Hot air blowing out of skylights** The hot air term takes into account the heat lost by heating cool air that is sucked into the tube. The heated air then gains in buoyancy and blows out of the skylight, carrying the heat with it. It can be described using (Keszthelyi, 1995b):

$$\Phi_{\text{sblow}} = A_{\text{sky}} U_{\text{air}} (T_{\text{sky}} - T_{\text{air}}) \rho_{\text{air}} c_{\text{air}}. \quad (4.62)$$

This equation thus uses:

- $A_{\text{sky}}$  = the skylight area ( $\text{m}^2$ );
- $U_{\text{air}}$  = the velocity at which the hot air blows out of the skylight ( $\text{m s}^{-1}$ );
- $T_{\text{sky}}$  = temperature of lava flowing past the skylight (K);
- $T_{\text{air}}$  = temperature of the ambient air sucked into the tube (K);
- $\rho_{\text{air}}$  = the density of the hot air ( $\text{kg m}^{-3}$ );
- $c_{\text{air}}$  = the specific heat capacity of the hot air ( $\text{J kg}^{-1} \text{ K}^{-1}$ ).

Note that the assumption is: the cool air sucked into the tube is heated to the same temperature as the lava flowing in the tube.

**Radiation from skylights** Radiation from skylights needs to take into account the radiation shape factor ( $F$ ), so that radiation is written using the area of the skylight and the temperature of the lava surface below it, as well as  $F$ :

$$\Phi_{\text{srad}} = F A_{\text{sky}} \sigma \varepsilon (T_{\text{sky}}^4 - T_{\text{air}}^4). \quad (4.63a)$$

The shape factor accounts for the fact that the lava surface may not be vertically below the skylight, so that not all of the radiation escapes vertically to the sky, as in [Figure 4.19b](#). Using the geometry given in [Figure 4.19b](#), the shape factor can be calculated from:

$$F = \cos \theta / r^2, \quad (4.63b)$$

$\theta$  being the angle of view out of the skylight (measured from the vertical), and  $r$  being the line of sight distance from the center of the skylight to the center of the lava stream surface. For a stream viewed vertically and situated directly below the skylight,  $\theta$  will be zero and so  $F$  will be one. As the stream becomes more offset in relation to the skylight,  $\theta$  and  $r$  in Equation (4.63b) will increase, so that  $F$  will decrease. Because  $F$  is a fraction which, when multiplied by radiation, decreases the radiation received according to viewing angle: as the line of sight distance and viewing angle increases,  $M_{\text{srad}}$  also decreases. We note, though, that if [as assumed in the Keszthelyi (1995b) model followed here] the whole interior of the tube is at lava temperature, then  $F = 1$ .

**Solution using satellite data** As shown by Flynn *et al.* (1994), two of the main parameters in determining the heat flux from skylights, skylight area and temperature, are relatively straightforward to calculate using TIR data if (i) there is anomalous radiance for the pixel containing the skylight, and (ii) the pixel is not saturated. Because the lava surface beneath the skylight can be considered to be broadly isothermal and close to the eruption temperature,  $T_{\text{sky}}$  can be assumed to be equal to, or close to, the lava eruption temperature. The temperature of the surrounding surfaces ( $T_{\text{surf}}$ ) can then be approximated by temperatures from surrounding ambient pixels. In this case, solution case (i) of [Section 4.2.1.4](#). of this chapter can be applied, so that the skylight area ( $A_{\text{sky}}$ ) can be calculated from:

$$A_{\text{sky}} = A_{\text{pixel}} \left[ \frac{M(\lambda, T_{\text{int}}) - M(\lambda, T_{\text{surf}})}{M(\lambda, T_{\text{sky}}) - M(\lambda, T_{\text{surf}})} \right]. \quad (4.64)$$

Recall that  $T_{\text{int}}$  is the pixel-integrated temperature at wavelength  $\lambda$ . We have simply applied a two-component mixture model to the pixel-integrated spectral radiance, re-arranged to isolate pixel portion occupied by the hot, skylight source, and multiplied by pixel area ( $A_{\text{pixel}}$ ) to convert to area in  $\text{m}^2$ .

In the TM image containing an active lava tube at Kilauea imaged on 23 July 1991 and presented in [Electronic Supplement 1](#), we see two hot spots due to skylights in the TIR (10.4–12.5  $\mu\text{m}$ ) band. These two hot spots have pixel-integrated temperatures in this band (band 6) of 49.6 °C and 53.6 °C.<sup>3</sup> The background temperature for both skylights was 46.6 °C. Assuming a lava temperature of 1150 °C and using a TM pixel area of 124 m × 141 m = 17 484  $\text{m}^2$  (see [Table 3.7](#) in [Chapter 3](#)) we obtain

<sup>3</sup> Corrected for atmospheric and emissivity effects following [Chapter 2](#) and [Electronic Supplement 4](#) (MODTRAN-corrected atmosphere using a US Standard and  $\varepsilon = 0.88$ ).

$$A_{\text{sky}} = 17\,484 \text{ m}^2 \left[ \frac{3.95 \times 10^7 \text{ W m}^{-1} \text{ m}^{-2} - 3.80 \times 10^7 \text{ W m}^{-1} \text{ m}^{-2}}{1.34 \times 10^9 \text{ W m}^{-1} \text{ m}^{-2} - 3.80 \times 10^7 \text{ W m}^{-1} \text{ m}^{-2}} \right]$$

$$= (0.001)(17\,484 \text{ m}^2) = 19.4 \text{ m}^2$$

for the first skylight, and

$$A_{\text{sky}} = 17\,484 \text{ m}^2 \left[ \frac{4.15 \times 10^7 \text{ W m}^{-1} \text{ m}^{-2} - 3.80 \times 10^7 \text{ W m}^{-1} \text{ m}^{-2}}{1.34 \times 10^9 \text{ W m}^{-1} \text{ m}^{-2} - 3.80 \times 10^7 \text{ W m}^{-1} \text{ m}^{-2}} \right]$$

$$= (0.003)(17\,484 \text{ m}^2) = 45.9 \text{ m}^2$$

for the second skylight. Assuming a circular skylight, these are equivalent to skylights between 4 m and 8 m across, which does not seem unreasonable. Assuming lava located directly below the skylight (i.e.,  $F = 1$ ), these results give

$$\Phi_{\text{srad}} = (19.4 \text{ m}^2)(5.67 \times 10^{-8} \text{ W m}^{-2} \text{ K}^{-4})[(1422)^4 - (320)^4] = 4.48 \text{ MW}$$

and

$$\Phi_{\text{srad}} = (45.9 \text{ m}^2)(5.67 \times 10^{-8} \text{ W m}^{-2} \text{ K}^{-4})[(1422)^4 - (320)^4] = 10.6 \text{ MW}.$$

Obtaining  $\Phi_{\text{sblow}}$  requires a measurement for the speed of the air blowing out of the skylight, plus calculation of the thermal properties of that air. This is beyond the scope of a satellite-based measurement in the IR. Procedures to derive or measure all parameters required to solve the skylight heat flux equations are given in Keszthelyi (1995b) and Witter and Harris (2007).

#### *4.4.1.8 Cooling rates*

Given a measure for the heat flux from an active lava body, and an estimate of the heat supplied from advection and crystallization, cooling rates can be calculated. In the most simple case, we can create an energy balance box model whereby all heat supplied by advection ( $\Phi_{\text{adv}}$ , in watts) and crystallization ( $\Phi_{\text{cryst}}$ , in watts) is lost by radiation, convection and conduction, so that

$$\Phi_{\text{adv}} + \Phi_{\text{cryst}} = \Phi_{\text{cond}} + \Phi_{\text{rad}} + \Phi_{\text{conv}}. \quad (4.65a)$$

The heat flowing into the box by advection can be given by:

$$\Phi_{\text{adv}} = V\rho c_p \text{ d}T/\text{d}t \quad (4.65b)$$

in which

- $V$  = lava volume ( $\text{m}^3$ );
- $\rho$  = lava density ( $\text{kg m}^{-3}$ );
- $c_p$  = lava specific heat capacity ( $\text{J kg}^{-1} \text{ K}^{-1}$ );
- $\text{d}T/\text{d}t$  = lava cooling rate ( $\text{K s}^{-1}$ ).

Heat generated by crystallization can be estimated from

$$\Phi_{\text{cryst}} = V\rho C_L (\mathrm{d}\phi/\mathrm{dT})(\mathrm{dT}/\mathrm{dt}) \quad (4.65\text{c})$$

in which

- $C_L$  = latent heat of crystallization ( $\sim 3.5 \times 10^5 \text{ J kg}^{-1}$ );
- $\mathrm{d}\phi/\mathrm{dT}$  = mass fraction of crystals grown per degree cooling ( $\text{K}^{-1}$ ).

Now, if we write  $\Phi_{\text{adv}}$  and  $\Phi_{\text{cryst}}$  in full and place them in Equation (4.65a), we obtain

$$V\rho c_p \mathrm{dT}/\mathrm{dt} + V\rho C_L (\mathrm{dT}/\mathrm{dt})(\mathrm{d}\phi/\mathrm{dT}) = \Phi_{\text{cond}} + \Phi_{\text{rad}} + \Phi_{\text{conv}}, \quad (4.65\text{d})$$

which simplifies to

$$V\rho \mathrm{dT}/\mathrm{dt} (c_p + C_L \mathrm{d}\phi/\mathrm{dT}) = \Phi_{\text{cond}} + \Phi_{\text{rad}} + \Phi_{\text{conv}}. \quad (4.65\text{e})$$

Writing  $\Phi_{\text{tot}}$  for  $\Phi_{\text{cond}} + \Phi_{\text{rad}} + \Phi_{\text{conv}}$  and re-arranging means that we can calculate the time-dependent cooling rate (cooling in degrees per second) from:

$$\frac{\mathrm{dT}}{\mathrm{dt}} = \frac{\Phi_{\text{tot}}}{V\rho(c_p + C_L \frac{\mathrm{d}\phi}{\mathrm{dT}})}. \quad (4.65\text{f})$$

Dimensionally this is

$$\frac{\text{J s}^{-1}}{\text{m}^3 \frac{\text{kg}}{\text{m}^3} \left( \frac{\text{J}}{\text{kg K}} + \frac{\text{J}}{\text{kg}} \text{K}^{-1} \right)} = \frac{\text{J s}^{-1}}{\text{kg} \frac{\text{J}}{\text{kg K}}} = \frac{\text{J s}^{-1}}{\text{J K}^{-1}} = \text{K s}^{-1}.$$

If instead we write advection and crystallization in terms of flow velocity ( $U_{\text{flow}}$ ) and depth ( $d$ ), we obtain,

$$M_{\text{adv}} = U_{\text{flow}} d \rho c_p \mathrm{dT}/\mathrm{dx} \quad (4.65\text{g})$$

and

$$M_{\text{cryst}} = U_{\text{flow}} d \rho C_L (\mathrm{d}\phi/\mathrm{dT})(\mathrm{dT}/\mathrm{dx}). \quad (4.65\text{h})$$

These are the advection and crystallization heat flux densities. We can show this dimensionally, where Equation (4.65g) is, for example,

$$\frac{\text{m}}{\text{s}} \frac{\text{kg}}{\text{m}^3} \frac{\text{J}}{\text{kg K}} \frac{\text{K}}{\text{m}} = \frac{\text{m kg JK}}{\text{s m}^3 \text{kg K}} = \frac{\text{J}}{\text{s m}^2} = \text{W m}^{-2}.$$

Now, if we write the energy balance equation in terms of heat flux densities, with advection and crystallization written in full, we have

$$U_{\text{flow}} d \rho c_p \mathrm{dT}/\mathrm{dx} + U_{\text{flow}} d \rho C_L (\mathrm{d}\phi/\mathrm{dT})(\mathrm{dT}/\mathrm{dx}) = M_{\text{cond}} + M_{\text{rad}} + M_{\text{conv}}, \quad (4.65\text{i})$$

which simplifies to

$$U_{\text{flow}} d \rho \mathrm{dT}/\mathrm{dx} [c_p + C_L (\mathrm{d}\phi/\mathrm{dT})] = M_{\text{cond}} + M_{\text{rad}} + M_{\text{conv}}. \quad (4.65\text{j})$$

Writing  $M_{\text{tot}}$  for  $M_{\text{cond}} + M_{\text{rad}} + M_{\text{conv}}$  and re-arranging means that we can calculate the distance-dependent cooling rate (cooling in degrees per meter) from:

$$\frac{dT}{dx} = \frac{M_{\text{tot}}}{U_{\text{flow}} d\rho (c_p + C_L \frac{d\phi}{dT})}. \quad (4.65k)$$

Dimensionally this is

$$\frac{\frac{J}{s} s^{-1} m^{-2}}{\frac{m}{s} m \frac{kg}{m^3} \left( \frac{J}{kg K} + \frac{J}{kg} K^{-1} \right)} = \frac{J s^{-1} m^{-2}}{\frac{kg}{s m} \frac{J}{kg K}} = \frac{J s^{-1} m^{-2}}{\frac{J}{s m K}} = \frac{W m^{-2}}{W m^{-1} K^{-1}} = \frac{m^{-1}}{K^{-1}} = K m^{-1}.$$

Thus:

- (i) if we have a satellite-based measure of  $\Phi_{\text{tot}}$  and an independent measure of flow volume, and can assume a temperature-dependent crystallization rate, we can calculate the time-dependent cooling rate; alternatively,
- (ii) if we have a satellite-based measure of  $M_{\text{tot}}$ , an independent measure of flow velocity and depth (or thickness), and can assume a temperature-dependent crystallization rate, we can calculate the distance-dependent cooling rate.

**Viscous dissipation ( $M_{\text{visc}}$ )** So far we have not considered viscous dissipation, or the conversion of potential energy into heat as the lava flows downhill, as a potential source of heat. For most basaltic eruptions, this term is small. But in highly viscous silicic lava flows or high shear environments, as well as during some extraterrestrial or ancient (rapid emplacement) eruptions, the term can be significant, and will thus have to be added to the formulations such as the energy balance box model of Equation (4.65). For a flowing lava, Keszthelyi and Self (1998) and Keszthelyi *et al.* (2000) give

$$M_{\text{visc}} = \rho g d U_{\text{flow}} \theta_s. \quad (4.66)$$

Here  $\theta_s$  is the ground slope, so that viscous dissipation increases with flow depth, velocity and slope.

#### 4.4.1.9 Lava flowing into water

Where lava enters water, it will heat and vaporize the water. The heat flux required to raise the temperature of a volume of water ( $\Phi_{H_2O-\text{heat}}$ ) can be obtained from:

$$\Phi_{H_2O-\text{heat}} = \frac{\rho_{H_2O} c_{H_2O} (T_{\text{plume}} - T_{H_2O-\text{ambient}}) V_{H_2O}}{R}. \quad (4.67a)$$

This equation thus uses:

- the density ( $\rho_{H_2O}$ ) and specific heat capacity ( $c_{H_2O}$ ) of the heated water which, for sea water, are  $1020 \text{ kg m}^{-3}$  and  $4005 \text{ J kg}^{-1} \text{ K}^{-1}$  for water temperatures of  $30\text{--}40^\circ\text{C}$ ;
- the degree of heating, as expressed by the temperature difference between the heated water plume at temperature  $T_{\text{plume}}$  and the surrounding, unheated water at  $T_{H_2O-\text{ambient}}$ ;

- the volume of water heated ( $V_{\text{H}_2\text{O}}$ ), and the residence time ( $R$ ) of water within the heated area.

Heat required to vaporize water ( $M_{\text{H}_2\text{O-vap}}$ ) can be obtained from:

$$\Phi_{\text{H}_2\text{O-vap}} = \frac{\rho_{\text{H}_2\text{O}} L_{\text{H}_2\text{O}^+} V_{\text{vap}}}{R} \quad (4.67\text{b})$$

in which  $L_{\text{H}_2\text{O}^+}$  is the latent heat of vaporization (plus heat needed to bring the water to boiling point) and  $V_{\text{vap}}$  is the volume of water vaporized.

**Solution using satellite data** As for lava tubes, the thermal expression of lava-heated water plumes can be detected in high-resolution (TM-class) data operating in the thermal infrared (see Electronic Supplement 1). For heated water plumes, high-spatial-resolution (TM-class) TIR data have been used to obtain  $T_{\text{plume}}$ ,  $T_{\text{H}_2\text{O-ambient}}$ ,  $V_{\text{H}_2\text{O}}$  and  $R$ , and hence solve Equations (4.65) (Harris *et al.*, 1998). We can obtain  $T_{\text{plume}}$  from water surface temperature derived from pixels inside the water thermal anomaly, and  $T_{\text{H}_2\text{O-ambient}}$  from pixels filled by water surfaces beyond the plume.  $V_{\text{H}_2\text{O}}$  can be obtained from the pixel area of the heated zone, although a thickness for the body of heated water must be assumed – which needs to be set from field data – to convert the area of heated water to a volume. Likewise the residence time for the water in the pixel can be set using the width of the pixel ( $L_{\text{pixel}}$ ), but an independent measure of the current velocity ( $U_{\text{H}_2\text{O}}$ ) also needs to be available if we are to calculate the transit time for water across the pixel. This is obtained from:

$$R = L_{\text{pixel}}/U_{\text{H}_2\text{O}}. \quad (4.68)$$

It is a little more difficult to see how satellite data can be used to solve Equation (4.67), although Harris *et al.* (1998) attempted this using TM data for an ocean entry lava flow at Kilauea. Here, they used the observation that heated water off-shore of Kilauea's ocean entry experienced a 1% increase in salinity to infer that 1% of the total volume of heated water was vaporized, so that Equation (4.66) became:

$$\Phi_{\text{H}_2\text{O-vap}} = \frac{\rho_{\text{H}_2\text{O}} L_{\text{H}_2\text{O}^+} 0.01 V_{\text{H}_2\text{O}}}{R}. \quad (4.69)$$

#### 4.4.1.10 Measurements at crater lakes

The utility of high-spatial-resolution TIR (TM-class) data for measuring the size, temperature and heat fluxes from volcanic crater lakes was developed by Clive Oppenheimer in a series of papers published in the 1990s (Oppenheimer, 1993b; 1996; 1997a; 1997b). As shown in Electronic Supplement 1, because crater lakes are relatively cool, only data acquired in the thermal infrared will be useable and will have to be corrected for atmospheric and emissivity effects accordingly.

**Lake temperature and area** To obtain a lake surface temperature, “pure” pixels that are entirely filled with lake water must be found; even then the temperature will be that

integrated over the pixel area and will not show any sub-resolution detail, such as meter-scale high-temperature zones over up-welling areas. To do this, Oppenheimer (1993b) recommends checking the coincident visible, NIR and/or SWIR data to find those thermal infrared pixels that are filled by water pixels. Alternatively, the maximum temperature pixel from within the crater lake thermal anomaly can be selected, or pixels from the core of the anomaly (entirely surrounded by other lake pixels) can be used. However, to ensure that the pixel does not contain a mixture of land and lake, the lake has to be sufficiently large, in relation to the size of the pixel, to fill at least one pixel. Following Oppenheimer (1993b), this criteria will be met if the lake radius exceeds  $i\sqrt{2}$ ,  $i$  being the pixel width in meters. Thus, for TM band 6, with a nominal spatial resolution of 120 m, the required lake radius is 170 m. For the smaller TIR pixel of ETM+ (60 m), this decreases to 85 m.

Area can be estimated from counting the number of lake pixels and multiplying by pixel area. For edge pixels, the pixel portion occupied by water will need to be calculated and multiplied by pixel area. This can be done in the visible, NIR or SWIR by applying the mixture model of Section 4.1.1.1, using the spectral reflectance of pure lake pixels for  $Y_i$  and pure land pixels for  $X_i$ . In applying this model, we have to assume that the lake shore is described by the same surface that characterizes the surrounding, barren, crater floor (an assumption that would be valid for, for example, a TM pixel acquired for Poas' crater lake, Costa Rica). In the, TIR the two-component thermal mixture model of Section 4.2.1.4 can be used with  $T_h$  (= the typical lake surface temperature) set using the temperature of pure lake pixels and  $T_c$  (= surface temperature for the surrounding land) from surrounding land pixels.

**Bulk versus skin temperature** Oppenheimer (1997a) showed that satellite-derived surface temperatures are typically 1 to 4 °C lower than measured temperatures for the lake interior (i.e., water temperatures made below the lake surface). Measurements made at Poas crater lake (Costa Rica) during February 2002 revealed just such an effect. A Minolta/Land Cyclops 300 radiometer was aimed at the lake surface for 45 minutes beginning at 11:45 am (local time) on 18 February; the mean surface temperature recorded was  $20.3 \pm 0.5$  °C. At the same time a K-type thermocouple was immersed ~30 cm below the lake surface; this gave a mean interior temperature over the same period of  $22.7 \pm 0.1$  °C. In all, 4300 samples were taken (at a rate of one sample every 0.6 seconds) and gave a difference ( $\Delta T$ ) between the bulk temperature ( $T_B$ ) and surface temperature ( $T_{lake}$ ), i.e.,  $\Delta T = T_B - T_{lake}$ , of  $-2.4 \pm 0.5$ , meaning that the interior of the lake was 2.4 °C warmer than the surface.

This difference is a result of the skin effect, a well known phenomena over ocean surfaces. As argued by Hasse (1963), strong temperature gradients exist across the surface boundary layer of a water body due to radiation, evaporation and heat transfer from the body interior. Heat is conducted across a surface boundary layer by molecular conduction so that, in cases where the surface is cooler than the interior, the surface is separated from the interior by a thermal boundary layer across which temperatures decline as modeled, for example, by Zülicke and Hagen (1998). As at an active lava flow this temperature difference can be described by Fourier's law so that, to use the notation of Saunders (1967), the flux density of

sensible heat within the water body ( $M_{\text{sens}}$ ) can be related to the temperature difference across the surface boundary layer ( $\Delta T$ ) by

$$M_{\text{sens}} = \frac{k\Delta T}{\delta}, \quad (4.70)$$

in which  $k$  is the thermal conductivity of the water and  $\delta$  is the thickness of the boundary layer. For an active lava flow we argued that surface-leaving heat losses can be used to approximate  $M_{\text{sens}}$  and solve for the boundary layer thickness; the same argument can be made for a water body where the surface leaving heat losses (due to evaporation) can be used to approximate  $M_{\text{sens}}$ . Saunders (1967) thus argued that  $\delta$  at the surface of a water body can be approximated from

$$\delta = \frac{\nu_{\text{H}_2\text{O}}}{(\tau'/\rho_{\text{H}_2\text{O}})^{1/2}}, \quad (4.71)$$

in which  $\nu_{\text{H}_2\text{O}}$  is the kinematic viscosity of the water,  $\tau'$  is the viscous stress due to wind blowing over the water surface, and  $\rho_{\text{H}_2\text{O}}$  is the water density. Inserting Equation (4.71) into (4.70) shows that the skin effect can now be described by

$$\Delta T = \frac{\lambda \nu_{\text{H}_2\text{O}} M_{\text{sens}}}{k U_*}, \quad (4.72)$$

in which

- $\lambda$  = an empirically determined non-dimensional constant, with a value of between 5 and 10 (Saunders, 1967). This value, though, will vary with wind speed from 2–3 for speeds of  $1\text{--}2 \text{ m s}^{-1}$ , to 4–5 for speeds of  $3\text{--}6 \text{ m s}^{-1}$ , up to a maximum of 6 at a wind speed of  $8 \text{ m s}^{-1}$  (see Table 1 of Grassl, 1976), with Simpson and Paulson (1980) obtaining  $\lambda$  of 5–9 for wind speeds of  $5.5\text{--}9.2 \text{ m s}^{-1}$ ;
- $U_*$  = the friction velocity as given by  $(\tau'/\rho_{\text{H}_2\text{O}})^{1/2}$ .

Paulson and Simpson (1981) provided an excellent review of the problem and pointed out that, when winds are very light, heat loss will cause buoyancy-driven convection so that, in such cases,

$$\Delta T = (Bk)^{-3/4} \left( \frac{D_{\text{H}_2\text{O}} \nu_{\text{H}_2\text{O}}}{g \alpha_{\text{H}_2\text{O}}} \right)^{1/4} M_{\text{sens}}^{3/4} \quad (4.73)$$

in which

- $B$  = a non-dimensional constant with a value of 0.2 (Saunders, 1967);
- $D_{\text{H}_2\text{O}}$  = thermal diffusivity of the water;
- $\alpha_{\text{H}_2\text{O}}$  = coefficient of thermal expansivity of the water.

It therefore needs to be recognized that, given the satellite perspective, we have a skin temperature rather than a bulk (lake interior) temperature, and operations that require use of bulk temperature should either not use the surface value, or correct the surface temperature

for the skin effect. On the other hand, the converse is true of surface temperature measurements; operations that use the bulk temperature, when surface temperature is required, will result in error. Oppenheimer (1997b), for example, showed that radiative, evaporative and conductive (sensible) heat losses, that depend on the surface temperature, may be overestimated by 10% if the bulk temperature is used.

Oppenheimer (1997b) suggests use of a thermal infrared thermometer (see Chapters 8 and 9) to obtain surface temperature; the interior temperature can then be obtained using a thermocouple inserted into the lake (as done at Poas), or by making a second thermal infrared thermometer measurement of the surface during vigorous stirring.

A number of empirical (regression) methods have also been applied to assess skin effects for ocean surfaces, which also allow lake bulk temperature to be estimated from a measurement of surface temperature. For example, Hasse (1971) used simultaneous measurements of water surface temperature ( $T_{\text{lake}}$ ), bulk temperature ( $T_B$ ), short wave radiation ( $M_{\text{rad}}^{\text{sun}}$ ), wind speed ( $U$ ), and sensible heat transfer ( $M_{\text{sens}}$ ) to obtain the empirical relation:

$$T_{\text{lake}} - T_B = c_1(M_{\text{sens}}/U) + c_2(M_{\text{rad}}^{\text{sun}}/U). \quad (4.74)$$

Likewise, Schluessel *et al.* (1990) completed a multiple regression between air temperature ( $T_{\text{air}}$ ), surface temperature ( $T_{\text{lake}}$ ), wind speed ( $U$ ), latent heat of evaporation ( $L$ ) and solar radiative flux density ( $M_{\text{rad}}^{\text{sun}}$ ), plus the water vapor mixing ratios of the water surface ( $q_s$ ) and atmosphere ( $q_a$ ). The resulting expression had the form

$$\Delta T = c_0 + c_1 U(T_{\text{lake}} - T_{\text{air}}) + c_2 U(q_s - q_a) + c_3 L \quad (4.75a)$$

by night, and

$$\Delta T = c_0 + c_1 M_{\text{rad}}^{\text{sun}}/U + c_2(q_s - q_a) + c_3 L \quad (4.75b)$$

by day. Of course, such empirical corrections require simultaneous measurement of all parameters and multivariate analysis if they are to be derived and applied.

**Heat fluxes** A number of crater lake heat balance models have been developed. These include those of Hurst *et al.* (1991) for Ruapehu's crater lake, Ohba *et al.* (1994) for Kusatsu-Shirane's crater lake and Fournier *et al.* (2009) for the Boiling Lake of Dominica. In addition, Pasternack and Varekamp (1997) developed a generic crater lake heat balance model, on which the model of Fournier *et al.* (2009) is based, and Oppenheimer (1996) based his remote-sensing-data driven analysis of crater lake heat losses on the model of Ohba *et al.* (1994). All of these models have evolved out of the energy budget analysis for the Poas crater lake completed, and published in *Nature*, by Brown *et al.* (1989), as well as the model for evaporation from a heated water body published by Adams *et al.* (1990) in *Water Resources Research*. A generic heat balance model based on these crater lake thermal studies is summarized in the schematic of Figure 4.20. This model can be expressed, following the *energy balance box model* and notation of Pasternack and Varekamp (1997), as:

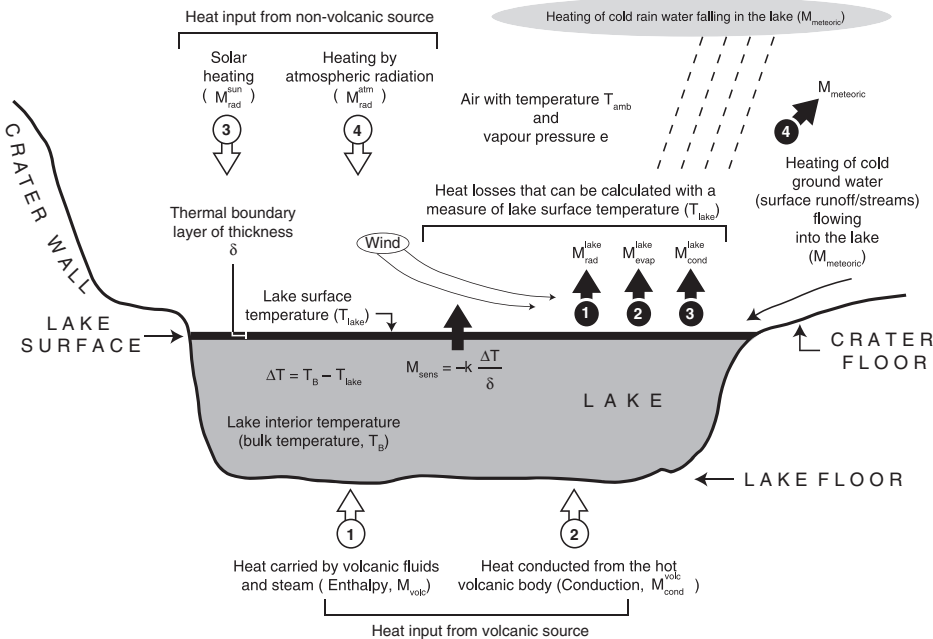


Figure 4.20 Heat loss model for a volcanic crater lake and the main parameters used for solution. Heat fluxes given in numbered black circles are the heat losses, and those given in numbered white circles are the heat sources.

$$\Phi_{\text{volc}}^{\text{vole}} + \Phi_{\text{volc}} + \Phi_{\text{rad}}^{\text{sun}} + \Phi_{\text{rad}}^{\text{atm}} = \Phi_{\text{rad}}^{\text{lake}} + \Phi_{\text{evap}} + \Phi_{\text{cond}}^{\text{lake}} + \Phi_{\text{meteoric}} \quad (4.76)$$

Terms on the left-hand side of this equation describe heat input into the lake system, with the first two terms being the inputs from volcanic sources, and the second two being inputs from the Sun and atmosphere, where

$\Phi_{\text{cond}}^{\text{vole}}$  = conductive heat input from a shallow magma body;

$\Phi_{\text{volc}}$  = enthalpy of the volcanic/hydrothermal flux;

$\Phi_{\text{rad}}^{\text{sun}}$  = shortwave solar flux;

$\Phi_{\text{rad}}^{\text{atm}}$  = longwave radiative input from the atmosphere.

Terms on the right-hand side are the heat losses (in watts), where:

$\Phi_{\text{rad}}^{\text{lake}}$  = radiation from the lake surface;

$\Phi_{\text{evap}}$  = heat loss due to evaporation;

$\Phi_{\text{cond}}^{\text{lake}}$  = heat loss due to conduction;

$\Phi_{\text{meteoric}}$  = energy spent heating meteoric influxes to the lake's temperature.

I consider here just the heat loss terms, these being the fluxes that can be calculated using satellite-sensor data. For estimation of the heat influx terms, I refer the reader to the references cited above, while noting that the solar and atmospheric fluxes can be estimated using the procedures outlined in Chapter 2 and Appendix B.

**Heat loss terms** Heat flux due to radiation from the water surface can be estimated using the lake area ( $A_{\text{lake}}$ ) and surface temperature ( $T_{\text{lake}}$ ) in the, now familiar, Stefan–Boltzmann relation:

$$\Phi_{\text{rad}}^{\text{lake}} = A_{\text{lake}} \varepsilon \sigma (T_{\text{lake}}^4 - T_{\text{amb}}^4). \quad (4.77)$$

Calculation of the heat flux due to evaporation can be achieved by applying the metric version of Equation (29) of Adams *et al.* (1990). This gives the heat flux from a heated water body, due to forced and free convection (i.e.,  $M_{\text{evap}}$ ), as:

$$\Phi_{\text{evap}} = A_{\text{lake}} \left\{ \left[ 2.7(T_{\text{lake}}^{\text{virtual}} - T_{\text{amb}}^{\text{virtual}})^{1/3} \right]^2 + \left[ 5.1 \left( \frac{A_{\text{lake}}}{1000} \right)^{-0.05} W \right]^2 \right\}^{1/2} (e_s - e_a), \quad (4.78)$$

here:

$A_{\text{lake}}$  = lake area ( $\text{m}^2$ );

$T_{\text{lake}}^{\text{virtual}}$  = the virtual temperature of the lake surface (K);

$T_{\text{amb}}^{\text{virtual}}$  = the virtual temperature of the overlying air (K);

$W$  = wind speed ( $\text{m s}^{-1}$ );

$e_s$  = saturation water vapor pressure at the lake surface temperature (mb); and

$e_a$  = saturation water vapor pressure at atmospheric temperature (mb).

Note that, as pointed out by Fournier *et al.* (2009), the  $\frac{1}{1000}$  conversion factor has been applied to lake area to convert from units of  $\text{m}^2$  to hectares; the units used by Adams *et al.* (1990) from whom we take this equation. The virtual temperatures for the lake surface and air can be calculated using measured (absolute) lake surface and air temperatures ( $T_x$ , in kelvin) in:

$$T_x^{\text{virtual}} = \frac{T_x}{1 - \frac{0.378e_x}{P}} \quad (4.79)$$

in which  $e_x$  is the water vapor pressure at  $T_x$ , and  $P$  is the ambient air pressure (in mb). Following the method laid out in the Appendix of Pasternack and Varekamp (1997), water vapor pressure can be set as a function of temperature in:

$$e_x = 2.71828(-0.00019899T_x^2 + 0.179064T_x - 32.23339). \quad (4.80)$$

Note,  $T_x$  used in this relation is in kelvin to give vapor pressure in mb.

The conductive heat flux from the lake surface can be calculated as a function of  $\Phi_{\text{evap}}$  following Brown *et al.* (1989), where

$$\Phi_{\text{cond}}^{\text{lake}} = c_B \frac{T_{\text{lake}} - T_{\text{amb}}}{e_s - e_a} \Phi_{\text{evap}}, \quad (4.81)$$

in which  $c_B$  is the Bowen constant ( $0.61 \text{ m K}^{-1}$ ).

Finally, the energy spent heating meteoric influxes (rain falling directly into the lake and run-off rain water entering the lake as sheet flow or in streams) to the lake's temperature, can

be estimated using the volumetric flow rate of meteoric water into the lake ( $V_{\text{meteoric}}$ , in  $\text{m}^3 \text{s}^{-1}$ ) in (Fournier *et al.*, 2009):

$$\Phi_{\text{meteoric}} = \rho_m V_{\text{meteoric}} (T_{\text{bulk}} - T_{\text{meteoric}}) C_{\text{p-water}}. \quad (4.82)$$

Here, following Pasternack and Varekamp (1997),

- $\rho_m$  = water molecular density ( $55555.9 \text{ mol m}^{-3}$ );
- $T_{\text{bulk}}$  = lake bulk temperature (K);
- $T_{\text{meteoric}}$  = temperature of the rain water falling and flowing into the lake (K);
- $C_{\text{p-water}}$  = water specific heat capacity ( $75.42 \text{ J mol}^{-1} \text{ K}^{-1}$ ).

**Solution using satellite data** Satellite data will provide the lake surface temperature ( $T_{\text{lake}}$ ) and area ( $A_{\text{lake}}$ ). As pointed out by Oppenheimer (1996), given that we have a surface rather than a bulk temperature, three of the four heat losses given above can be calculated, i.e., those due to outgoing radiation ( $\Phi_{\text{rad}}^{\text{lake}}$ ), evaporation ( $\Phi_{\text{evap}}$ ) and conduction ( $\Phi_{\text{cond}}^{\text{lake}}$ ). If assumptions for factors such as wind speed, air pressure, air (ambient) temperature, and humidity can be made, all of these equations can be solved. However, the equation for the heat loss due to heating of meteoric water entering the lake ( $\Phi_{\text{meteoric}}$ ) requires use of the lake interior or bulk temperature, and therefore cannot be solved with a lake surface temperature.

To estimate crater lake heat flux from satellite TIR data, the following four-step methodology, as modified from Oppenheimer (1997a), can be thus applied.

- (i) Extract all pure lake pixels from the TIR data, convert to brightness temperature and apply all necessary atmospheric and emissivity corrections.
- (ii) Apply a mixture model to all mixed pixels surrounding the “pure” lake pixels to obtain pixel portion occupied by lake water for all mixed pixels.
- (iii) Obtain radiative, evaporative and conductive heat flux densities (in  $\text{W m}^{-2}$ ) on a pixel-by-pixel basis and convert to heat flux (in W) by multiplying by pixel area (in  $\text{m}^2$ ).
- (iv) Sum the heat fluxes for each pixel (mixed and pure) to obtain the total power output.

The heat loss due to heating of meteoric fluids will have to be calculated using ancillary data.

#### 4.4.1.11 Measurements at open vents, fumarole fields and hot springs

Heat loss from an open vent will mostly be radiative, so that the heat flux density can be obtained from a measurement of the vent temperature ( $T_{\text{vent}}$ ) and ambient (air) temperature ( $T_a$ ),

$$M_{\text{vent}} = \varepsilon \sigma (T_{\text{vent}}^4 - T_a^4). \quad (4.83)$$

Multiplying this value by vent area ( $A_{\text{vent}}$ ) will give the heat flux ( $\Phi_{\text{vent}}$ ). Assuming that there is no expansion of the gas or air entrainment in the narrow pipe connecting the vent to the source, the other main heat loss will be conductive. That is, the walls of the pipe will be heated by the passage of the hot gas, and heat will then flow outwards, away from the pipe

and into the cooler zones of country rock. A simple way to measure this heat flux was given by Stevenson (Equation 14, 1993) as,

$$M_{\text{cond}} = \frac{h_t k (T_{\text{gas}} - T_{\infty})}{h_t r_0 (r_{\infty} - r_0) + k}, \quad (4.84)$$

in which

- $h_t$  is the heat transfer coefficient ( $\text{W K}^{-1}$ );
- $k$  is the thermal conductivity of the country rock ( $\text{W m}^{-1} \text{K}^{-1}$ );
- $T_{\text{gas}}$  is the gas temperature (K);
- $T_{\infty}$  is the country rock ambient temperature (K);
- $r_0$  is the conduit radius (in m);
- $r_{\infty}$  is the distance to the ambient temperature (m).

In an Appendix to his paper “Physical models of fumarolic flow,” Stevenson (1993) gives  $h_t$  for laminar flow (i.e., flow at Reynolds numbers  $< 100$ ) in a pipe, following Kay and Perkins (1973) as,

$$h_t = \frac{24}{11} \frac{k_g}{r_0}, \quad (4.85a)$$

in which  $k_g$  is the thermal conductivity of the gas. For turbulent flow in a long tube (i.e., flow at Reynolds numbers  $< 2100$ ), Stevenson (1993) uses Kay (1968) to give,

$$h_t = 0.023 \frac{k_g}{2r_0} Re^{0.8} Pr^{0.4}, \quad (4.85b)$$

in which the Reynolds number ( $Re$ ) is given by,

$$Re = \frac{2\rho_g v r_0}{\mu_g},$$

and the Prandtl number ( $Pr$ ) is

$$Pr = c_g \mu_g / k_g, \quad (4.85c)$$

in which,

- $\rho_g$  is the density of the ascending gas;
- $v$  is the velocity at which the gas is ascending;
- $\mu_g$  is the dynamic viscosity of the gas;
- $c_g$  is the gas specific heat capacity.

This method gives the heat flux density per meter length of pipe (i.e., units are  $\text{W m}^{-1}$ ) so that multiplying by pipe length will give the heat flux (in watts).

Although we have presented the problem so far in terms of heat losses due to gases flowing in a pipe, Bodvarsson (1983) gives a similar treatment for heat lost by hot water

ascending vertical pipes, as applied to obtain heat fluxes for geothermal zones containing hot springs in Iceland. The solution of Bodvarsson (1983) is based on Carslaw and Jaeger (1959) and is,

$$M_{\text{spring}} = 4 \pi k T_{\text{water}} / \ln(1.2 N) \quad (4.86a)$$

in which

$$N = 4 \alpha t / d^2. \quad (4.86b)$$

Here

- $k$  and  $\alpha$  are the conductivity and thermal diffusivity of the country rock;
- $T_{\text{water}}$  is the temperature of the water ascending the pipe;
- $t$  is the time the pipe has been active;
- $d$  is the diameter of the pipe.

Again, the solution gives the heat flux per unit length of pipe.

A simple steady-state approximation of the heat flux density for a hot pipe in cold ground can be made using Fourier's Law, i.e.,

$$M_{\text{spring}} = -k \frac{(T_g - T_\infty)}{r_\infty}. \quad (4.87a)$$

Distance  $r_\infty$  can be estimated from Equation (4.52). That is,

$$r_\infty = \sqrt{\alpha \pi t}, \quad (4.87b)$$

so that, for a thermal diffusivity of  $7 \times 10^{-7} \text{ m}^2 \text{ s}^{-1}$ ,  $r_\infty$  will be

- 8.3 m after 1 year;
- 26.3 m after 10 years;
- 83 m after 100 years; and
- 263 m after 1000 years.

This is the basis of the Bodvarsson (1983) solution which thus requires modification for the time the pipe has been active. Otherwise  $r_\infty$  needs to be constrained, which can be done using the diameter of the heated ground zone around the pipe. Conductive heat losses will decrease mostly with  $r_\infty$  and hence also time, so that solution requires measurement of these two properties, plus the temperature of the gas or fluid in the pipe.

**Solution using satellite data** Measuring vent temperature and area to aid in solving these equations may be a straightforward task if one or two large degassing vents are active. Solutions to obtain vent temperature and area from satellite data are the focus of Section 4.2 of this chapter and usually require application of a two-component mixture model to the pixel(s), containing the active vent. Obtaining a vent diameter or radius can then be

achieved using the derived vent area and applying a shape assumption. A circular vent, for example, will have a radius ( $r$ ) of,

$$r = \sqrt{\frac{A}{\pi}}.$$

AVHRR- and TM-class satellite data have thus been used to estimate open vent areas, dimensions, temperatures and heat fluxes at, for example, Stromboli by Harris and Stevenson (1997) and Shishaldin by Dehn *et al.* (2002).

However, a fumarole field may contain hundreds or thousands of active vents, some of which may be quite small (a single vent potentially being as narrow as a few mm), and potentially not being resolvable in satellite data (see Electronic Supplement 1). Each vent or vent zone will also likely have different areas and temperatures. In this case the size and temperature of each zone of hot vents will need to be characterized and the heat fluxes from each area summed to obtain the total heat lost from all vents and/or pipes active across the field. This is often best achieved using ground-based thermal methodologies, such as implementation of a radiometer-based survey. We will focus on methodologies applied to radiometer data to obtain such results in [Chapter 8](#). Another solution is to use a hand-held camera to collect a thermal image (or image mosaic) covering all vents, while ensuring that the vents more-or-less fill each pixel. Pixel temperatures in the image can be converted to vent temperatures and the pixel dimensions used to estimate vent area. These temperature and area derivations can then be converted to heat fluxes for each fumarole and summed to obtain the total heat loss for the field, or selected zones within the field. We will focus on methodologies that can be applied to characterize thermal surfaces and extract surface temperatures, feature areas and heat fluxes from thermal camera data in [Chapter 9](#).

#### *4.4.1.12 Measurements at geothermal fields and ground heated by intrusions*

At a fumarolic or geothermal system, heat will be generated by boiling and condensation of water at depth. This heat will then be transferred to the surface by convection or conduction. The heat transfer processes at such a system are sketched in [Figure 4.21](#). Above an active or cooling intrusion, heat will also be transferred to the surface in the same way. That is, it will flow from the hot source (the intrusion) to the cold surface. This situation is sketched in [Figure 0.1](#) of [Chapter 0](#).

In both cases this flow of heat to the surface will result in surface heating. The geothermal heating effect will thus cause surface temperatures above the hot source to be higher than those of adjacent (unheated) ambient areas. The heating effect can thus be described by the temperature difference ( $\Delta T_{\text{geothermal}}$ ) between a surface within the geothermal zone and an adjacent ambient surface (i.e., a point just outside the heated zone). However, this difference may be small, so that night-time measurements may need to be made to avoid obliteration or complication of the signal by solar heating effects. Also, because the heating effect is small, and anomalous surface temperatures low, such anomalies will only be apparent in the

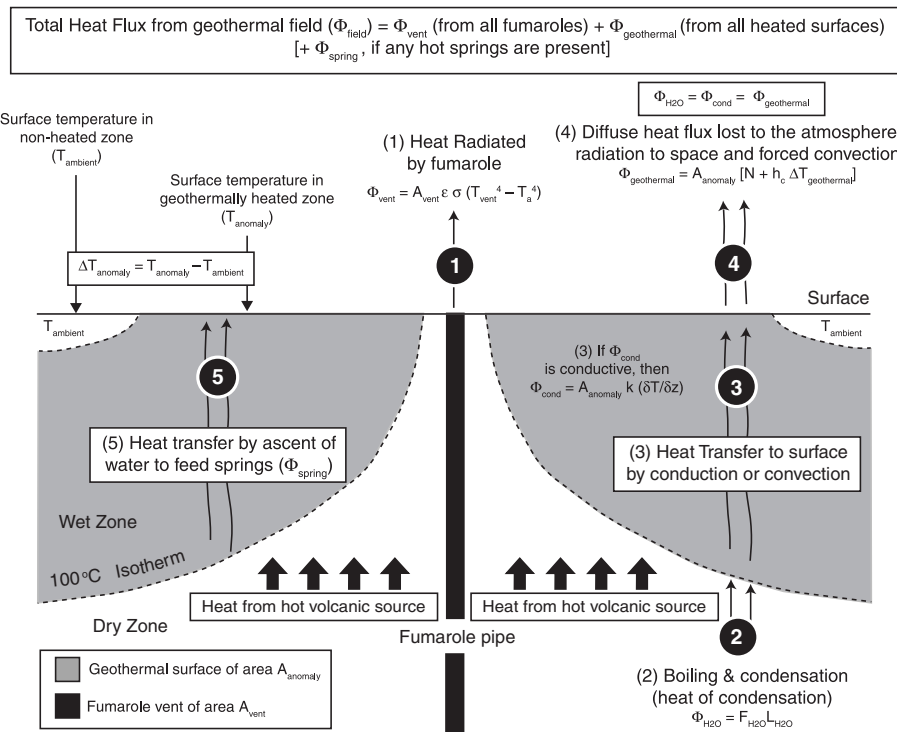


Figure 4.21 Heat loss model for an active fumarole, geothermal surface and/or hot spring. Note that heat fluxes 2, 3 and 4 should be the same, being subsurface heat carried to the surface by conduction and/or convection to be then lost from that surface. They are, thus, not additive.

longwave infrared, so that satellite, radiometer or hand-held camera sensors operating in the TIR will have to be used to measure  $\Delta T_{\text{geothermal}}$  and solve the following equations. The geothermal heat flux can be measured in one of three ways:

- using the water flux,
- using the thermal gradient in the soil,
- using the temperature of the surface over heated zones.

The measurements do not sum, because they are all the expression of the same (geothermal) flux, but should be approximately equal to one another, i.e., the heat flux measured from the water flux should be the same as that obtained from thermal gradients and surface heating.

**Water flux** If heating is due to boiling and condensation of water, the heat generated and transferred to the surface by this process ( $\Phi_{\text{H}_2\text{O}}$ ) can be calculated from,

$$\Phi_{\text{H}_2\text{O}} = F_{\text{H}_2\text{O}} L_{\text{H}_2\text{O}}, \quad (4.88)$$

$F_{\text{H}_2\text{O}}$  being the water or steam flux, and  $L_{\text{H}_2\text{O}}$  being the heat of condensation. Solution thus just requires a measurement of the steam flux. This method was applied by Chiodini *et al.* (2005) who used the steam flux obtained for Vulcano's Fossa crater in 1998, this being  $98.36 \text{ t d}^{-1}$ , to estimate a heat flux of

$$\Phi_{\text{H}_2\text{O}} = (8.08 \text{ kg s}^{-1})(2.6 \text{ MJ kg}^{-1}) = 21 \text{ MW.}$$

Assuming that of all of the heat generated in this way is transferred to the surface above the boiling zone, we can use this measurement to estimate the expected surface heating that the flux will cause from,

$$\Delta T_{\text{geothermal}} = \Phi_{\text{H}_2\text{O}} / h_c A_{\text{diffuse}}, \quad (4.89)$$

in which  $h_c$  is the heat transfer coefficient and  $A_{\text{diffuse}}$  is the area of surface heating. Given a heat transfer coefficient of  $35 \text{ W m}^{-2} \text{ K}^{-1}$  (from Matsushima *et al.*, 2003) and a heated area at Vulcano of  $415\,000 \text{ m}^2$  (from Chiodini *et al.*, 2005) we obtain,

$$\Delta T_{\text{geothermal}} = (21 \times 10^6 \text{ W}) / [(35 \text{ W m}^{-2} \text{ K}^{-1}) (415\,000 \text{ m}^2)] = 1.45 \text{ }^\circ\text{C.}$$

**Conductivity method** By burying a number of thermocouples in the ground within a heated zone, we can directly obtain the thermal gradient,  $dT/dz$ ; a methodology pioneered at active volcanic systems by Tabbagh and Trezeguet (1987). The methodology has since been applied to estimate geothermal heat flux at, for example, Etna by Aubert (1999), Vanuatu by Lardy and Tabbagh (1999), and Vulcano by Aubert and Alaprone (2005) and Aubert *et al.* (2008). The approach involves burying a series of thermocouples in the upper meter of the heated ground. The stack is arranged vertically, with each thermocouple placed one above the other. Because each thermocouple is separated by a known vertical distance ( $dz$ ), the temperature difference between each thermocouple ( $dT$ ) allows the temperature gradient ( $dT/dz$ ) to be defined. If the conductivity of the ground is known, this can be used to directly solve Fourier's Law and obtain the conductive heat flux density for the heated zone, from

$$M_{\text{cond}} = -k \frac{dT}{dz}. \quad (4.90)$$

Now, multiplying by the area of surface heating ( $A_{\text{diffuse}}$ ) will yield the conductive heat flux ( $M_{\text{cond}}$ ). Typical  $dT/dz$  values obtained by Aubert *et al.* (2008) in Vulcano's Fossa crater during 2004 were between  $50 \text{ }^\circ\text{C m}^{-1}$  and  $135 \text{ }^\circ\text{C m}^{-1}$ . Using a thermal conductivity calculated for Vulcano Fossa by Aubert *et al.* (2008) of  $0.8 \text{ W m}^{-1} \text{ K}^{-1}$  these temperature gradients yield heat flux densities of between

$$M_{\text{cond}} = (0.8 \text{ W m}^{-1} \text{ K}^{-1}) (50 \text{ K m}^{-1}) = 40 \text{ W m}^{-2}$$

and

$$M_{\text{cond}} = (0.8 \text{ W m}^{-1} \text{ K}^{-1}) (135 \text{ K m}^{-1}) = 108 \text{ W m}^{-2}.$$

Given a 415 000 m<sup>2</sup> area of diffuse degassing at Vulcano this multiplies to a heat flux due to heat conducted from the hot buried source to the cold surface of between

$$\Phi_{\text{cond}} = A_{\text{diffuse}} M_{\text{cond}} = (415 \ 000 \ \text{m}^2) (40 \ \text{W m}^{-2}) = 16.6 \ \text{MW}$$

and

$$\Phi_{\text{cond}} = A_{\text{diffuse}} M_{\text{cond}} = (415 \ 000 \ \text{m}^2) (108 \ \text{W m}^{-2}) = 44.8 \ \text{MW},$$

thus spanning the value for diffuse heat losses derived for Vulcano using the water flux approach.

**Surface temperature anomaly method** Sekioka and Yuhara (1974) provide a method that uses the degree of surface heating, as expressed by the difference in temperature between the geothermally heated surface and the adjacent ambient (non-heated) surface (i.e.,  $\Delta T_{\text{geothermal}}$ ), to obtain the geothermal heat flux density ( $M_{\text{geothermal}}$ ). This is the surface-leaving heat flux density due to the geothermal contribution and should equal the heat fluxes arriving at the surface, as calculated using the previous two methods. At first glance, the equation we need to solve appears simple, being

$$M_{\text{geothermal}} = N + h_c \Delta T_{\text{geothermal}}, \quad (4.91)$$

$N$  being an estimate of nocturnal radiation and  $h_c$  being the heat transfer coefficient. As always, it is obtaining these two values that complicates the problem.

However, following Sekioka and Yuhara (1974), nocturnal radiation is not too difficult to constrain, it being given by

$$N = (1 - 0.09 m) N_0 \quad (4.92a)$$

in which

$$N_0 = \varepsilon [0.52 + 0.065(e)^{1/2}] \sigma (T_0^4 - T_a^4) \quad (4.92b)$$

in which

- $m$  is cloudiness (0 = no cloud, 1 = complete cloud cover);
- $\varepsilon$  is the surface emissivity;
- $e$  is water vapor pressure;
- $\sigma$  is the Stefan Boltzmann constant;
- $T_0$  is the heated surface temperature; and
- $T_a$  is the ambient (non-heated) surface temperature.

so that  $N$  becomes,

$$N = \varepsilon (1 - 0.09 m) [0.52 + 0.065(e)^{1/2}] \sigma (T_0^4 - T_a^4). \quad (4.92c)$$

Thus, to estimate the contribution of the first component in Equation (4.91), i.e.,  $N$ , we need a measure of vapor pressure and the two surface temperatures  $T_0$  and  $T_a$ . Following Lawrence (2005), water vapor pressure ( $e$ ) can be obtained using a measurement of the relative humidity ( $RH$ ) and an estimate of the equilibrium, or saturation, vapor pressure ( $e_s$ ) in:

$$RH = 100 \frac{e}{e_s}. \quad (4.93a)$$

Saturation vapor pressure can be obtained using the air temperature measured above the surface in question ( $T_{\text{air}}$  in °C) from the empirical relation,

$$e_s = (610.94 \text{ Pa}) \exp\left(\frac{(17.625)T_{\text{air}}}{(243.04 \text{ }^{\circ}\text{C}) + T_{\text{air}}}\right). \quad (4.93b)$$

This relation gives almost the same result as the relation of Equation (4.80b).

Now, for their geothermal surface case, Sekioka and Yuhara (1974) give the heat transfer coefficient as,

$$h_c = \rho_{\text{air}} c_{\text{pair}} D(1 + r) \quad (4.94)$$

in which

- $\rho_{\text{air}}$  and  $c_{\text{pair}}$  are the density and specific heat capacity of air over the heated surface;
- $D$  is the transfer velocity;
- $r$  is the ratio of evaporative losses to sensible heat.

Sekioka and Yuhara (1974) derive a value of  $0.0159 \text{ m s}^{-1}$  for  $D$ , and 0.5 for  $r$ . Using these values in Equation (4.94) with an air density of  $1 \text{ kg m}^{-3}$  and a specific heat capacity of  $1000 \text{ J kg}^{-1} \text{ K}^{-1}$  we can approximate  $h_c$  from,

$$h_c = (1 \text{ kg m}^{-3})(1000 \text{ J kg}^{-1} \text{ K}^{-1})(0.0159 \text{ m s}^{-1})(1.5) = 24 \text{ W m}^{-2} \text{ K}^{-1}.$$

Now, taking our predicted  $\Delta T_{\text{geothermal}}$  for Vulcano of  $1.5 \text{ }^{\circ}\text{C}$ , and an ambient air temperature of  $20 \text{ }^{\circ}\text{C}$ , we obtain,

$$e_s = (610.94 \text{ Pa}) \exp\left(\frac{(17.625)(20 \text{ }^{\circ}\text{C})}{(243.04 \text{ }^{\circ}\text{C}) + 20 \text{ }^{\circ}\text{C}}\right) = 2333 \text{ Pa.}$$

For simplicity we assume, given the condensing atmosphere above a fumarole, relative humidity of 100%, so that,

$$RH = 100 \frac{e}{e_s}; \text{ so that } \frac{100}{100} = \frac{e}{2333 \text{ Pa}}; \text{ and thus } e = 2333 \text{ Pa.}$$

Now,

$$\begin{aligned} N &= (0.98)(1 - 0.09 \text{ m}) \left[ 0.52 + 0.065(2333 \text{ Pa})^{1/2} \right] (5.67 \times 10^{-8} \text{ W m}^{-2} \text{ K}^{-4}) \left[ (294.6 \text{ K})^4 - (293 \text{ K})^4 \right] \\ &= 31 \text{ W m}^{-2} \end{aligned}$$

and

$$\begin{aligned} M_{\text{geothermal}} &= (31 \text{ W m}^{-2}) + (24 \text{ W m}^{-2} \text{ K}^{-1})(1.5 \text{ K}) = (31 \text{ W m}^{-2}) + (36 \text{ W m}^{-2}) \\ &= 67 \text{ W m}^{-2}. \end{aligned}$$

Given a  $415\,000 \text{ m}^2$  area of diffuse degassing, this multiplies to a surface-leaving heat flux due to the geothermal contribution of

$$\Phi_{\text{geothermal}} = A_{\text{diffuse}} M_{\text{geothermal}} = (415\,000 \text{ m}^2)(67 \text{ W m}^{-2}) = 27.8 \text{ MW},$$

thus agreeing with the values for diffuse heat fluxes derived for Vulcano in our worked examples using the water flux and conductivity approaches.

**Solutions with radiometers and thermal cameras** Given the subtlety of the geothermal thermal anomaly, probably the easiest way to make the necessary measurements to constrain the geothermal heat flux is with a radiometer, as was done in the original experiment of Sekioka and Yuhara (1974) at the Owakudani geothermal area. A thermal camera could also be used, as was done to constrain both the fumarole vent and geothermal heat fluxes at Iwodake volcano by Matsushima *et al.* (2003).

Taking a surface temperature measurement within the zone of heating, and one just outside it (to define  $\Delta T_{\text{geothermal}}$ ), along with simultaneous atmospheric measurements at each point (wind speed, air temperature, pressure and humidity) allows the Sekioka and Yuhara (1974) solution to be applied. Making the measurement with a thermal camera has the advantage that any variation in surface temperature across the heated zone can be identified and accounted for. The area of heating can also be obtained using the thermal camera image allowing precise conversion from flux density to flux. The calculations can also be carried out on a pixel-by-pixel basis and summed to obtain the precise flux over the area.

To avoid solar heating and cloud complications, measurements are best made under a cloud-free sky and at night, preferably just before dawn so that the surface has had the maximum amount of time to cool following day-time solar heating. Making the measurements repeatedly (e.g., once a minute over a period of a few hours just before sunrise) also allows any variation due to, for example, changes in wind speed, air temperature, pressure or humidity, to be accounted for. Derivation of heated areas, and measurement of surface temperatures within those areas, at fumarole and geothermal fields using radiometer and thermal camera data will be detailed in Chapters 7, 8 and 9.

**Satellite measurements** If a thermal anomaly is present in the satellite TIR data, a ball-park estimate for the geothermal heat flux can be obtained by applying the method of Sekioka and Yuhara (1974). This has been done using, for example, TM data for Vulcano by Gaonac'h *et al.* (1994) and Harris and Stevenson (1997a), and involves the following steps.

- (i) Carry out all atmospheric and emissivity corrections.
- (ii) Extract all pixels within the anomaly (or the maximum value from within the anomaly) to set  $T_0$  and use adjacent ambient pixels to set  $T_a$ , and hence  $\Delta T_{\text{geothermal}} (= T_0 - T_a)$ .
- (iii) Use these values, with an assumed or in-situ air temperature, to solve Equation (4.91) and obtain the geothermal heat flux density ( $M_{\text{geothermal}}$ ).
- (iv) Multiply by anomaly area to obtain the geothermal heat flux ( $\Phi_{\text{geothermal}}$ ).

**System volume?** Italiano *et al.* (1984) opened up an interesting direction by suggesting that, at a fumarolic system, the system energy flux could be related to the rock volume involved in a heating event through application of a simple relation. Between August and October 1979 the measured gas temperature at Vulcano increased from 303 °C, on 15th August, to plateau at a new steady state of 318 °C by 8th October. Heating thus lasted 54 days and, from the water flux, was associated with a total energy ( $E$ ) release of  $6.42 \times 10^{14}$  calories,  $E$  being expressed, here, in terms of the units originally used. Using the total heating ( $\Delta T$ ) of 15 °C, and the specific heat capacity of the system ( $c_p$ ) of  $0.425 \text{ cal} \text{ } ^\circ\text{C}^{-1} \text{ cm}^{-3}$ , Italiano *et al.* (1984) estimated the volume of rock involved in the heating process ( $V$ ) from

$$V = \frac{E}{c_p \Delta T} = \frac{(6.42 \times 10^{14} \text{ cal})}{(0.425 \text{ cal} \text{ } ^\circ\text{C}^{-1} \text{ cm}^{-3})(15 \text{ } ^\circ\text{C})} = 10^{14} \text{ cm}^3 = 0.1 \text{ km}^3.$$

In other words,  $0.1 \text{ km}^3$  of reservoir rock were involved in the heating event. We next explore the development and application of such relations to volcanology.

## 4.5 Mass and volume

Efforts to extract active lava area and heat flux from spectral radiance data collected by satellite-based sensors resulted in the development of techniques to convert these values to lava mass, volume and/or volume flux. As of 2005, 23 papers (listed in the [Appendix A](#) literature collation) had attempted to achieve such conversions. We begin this section by reviewing the relation between thermal energy and system mass, as applied in volcanology. We then detail conversions between energy and mass that have been applied to satellite-based IR data. A history of attempts to extract energy and mass for active volcanic systems using satellite-based IR data is given in Electronic Supplement 5.

### 4.5.1 Relations between energy and mass: applications in volcanology

Because energy can be neither created nor destroyed, the first law of thermodynamics dictates that, if energy is added to a system due to heating, it will either:

- (1) be lost from that system, i.e., it will contribute to the heat loss experienced by the system, or
- (2) contribute to changing the internal energy of the system, i.e., it will heat the system, causing the internal temperature to increase.

Because the amount of energy added to the system ( $dQ$ ) needs to be balanced by the energy lost ( $dW$ ), or gained ( $dE$ ), by the system, the system's energy balance can be written as

$$dQ = dW + dE. \quad (4.95a)$$

While the energy lost can be assessed by the work done in terms of the pressure ( $P$ ) and the change in volume ( $dV$ ) experienced by the system, i.e.,

$$dW = P dV, \quad (4.95b)$$

the internal energy can be expressed in terms of the temperature ( $T$ ) and change in entropy ( $dS$ ) of the system,

$$dE = T dS. \quad (4.95c)$$

This simple relation is the basis for a multitude of applications in the Earth sciences, geophysics and volcanology.

#### 4.5.1.1 Application in linking rock mass and heat flow

Jeffreys (1962) used this approach in his book, *The Earth – Its Origin, History and Constitution*, to estimate temperature gradients below the Earth's surface. His approach provides a nice example of how Equation (4.95) can be applied to solve a problem in Earth sciences. First published in 1924, with the aim of discussing “the theories of the main problems of geophysics, and to exhibit their interrelations,” the book’s fourth edition was published in 1962 with an updated treatment of tidal heating. Jeffreys began Chapter 10, “The thermal history of the Earth,” with a consideration of the “method of solidification.” In this chapter, Jeffreys set out by estimating the Earth’s internal temperature distribution using, as a starting point, the following equations:

$$dQ = dE + dW \quad (4.96a)$$

$$= dE + P dV \quad (4.96b)$$

$$= d(E + PV) - V dP \quad (4.96c)$$

$$= c_p dT + m dP, \quad (4.96d)$$

in which

$dQ$  = inflow of heat

$dE$  = internal energy

$dW$  = heat lost

$P$  = pressure

$V$  = volume

$c_p$  = specific heat capacity at constant pressure

$dT$  = temperature change

$m$  = mass.

In other words, heat flowing into a given unit mass of rock ( $dQ$ ) will contribute to the internal energy of the rock mass ( $dE$ ) or will be lost to the surroundings through the process of doing work ( $dW$ ). Because  $dE$  can be described in terms of the temperature and change in entropy of the system,  $dE$  can be written in terms of the specific heat capacity ( $c_p$ ) of, and the change in temperature ( $dT$ ) experienced by, the rock mass. This is the first term of Equation (4.96d), i.e.,  $dE = c_p dT$ . Heat lost from the mass can be written in terms of the pressure ( $P$ ) and change in volume ( $dV$ ) experienced by the system, and hence can be written in terms of the rock mass ( $m$ ) and change in pressure ( $dP$ ) experienced by the rock. This is the second term of Equation (4.96d), i.e.,  $dW = mdP$ . Thus the flow of heat into the system can be related to the rock temperature and mass. Jeffreys (1962) used the approach to solve for the thermal gradient below the Earth's surface.

**Verhoogen (1946)** Application of the first law of thermodynamics to estimate the heat budget of a cooling lava flow on the basis of the mass or volume of the erupted lava can be traced to Verhoogen (1946). On page 747 of his study entitled "Volcanic heat" published in the *American Journal of Science*, Verhoogen (1946) wrote:

Take the total heat lost by 1 gram of lava crystallizing and cooling from 1000 °C to ordinary temperature to be 400 calories (300 cal. from specific heat, 100 cal. from latent heat). Then the total amount of heat required to account for all volcanic activity since the close of the Precambrian would be of the order of  $4 \times 10^{25}$  cal.

Although he did not write out the formula, what Verhoogen (1946) did was to take his estimate of lavas erupted since the Cambrian ( $= 10^{21} \text{ cm}^3 + 3 \times 10^{22} \text{ cm}^3$ , p. 746) and use this with a density of  $3 \text{ g cm}^{-3}$  (p. 767) to obtain a value for thermal energy carried by erupted lavas ( $E_{\text{th}}$ ). This, written with the non-SI units originally used, must have involved the following calculation:

$$E_{\text{th}} = (3.1 \times 10^{22} \text{ cm}^3)(3 \text{ g cm}^{-3})(300 \text{ cal} + 100 \text{ cal}) = 3.72 \times 10^{25} \text{ cal.}$$

Multiplying by 4.184 joules per calorie gives the result in SI units, i.e.,  $1.56 \times 10^{26}$  joules. The work of Verhoogen (1946) thus underpins the lava flow heat budget approaches and volume/mass conversions carried out today.

**The Yokoyama publication series** Izumi Yokoyama is generally regarded as the man who formalized the calculation of Verhoogen (1946) in volcanology. Yokoyama did this in the second of three papers published as a series in the University of Tokyo's *Bulletin of the Earthquake Research Institute* (Yokoyama, 1956; 1957a; 1957b). In the second paper of the series, "Energetics in Active Volcanoes papers 1, 2 and 3", Yokoyama (1957a) gave two equations. The first was for the "thermal energy carried away through the vent of the volcano." In this he used the specific heat for basalt ( $0.25 \text{ cal g}^{-1} \text{ °C}^{-1}$ ), lava temperature

above ambient ( $1000\text{ }^{\circ}\text{C}$ ) and heat of fusion ( $50\text{ cal g}^{-1}$ ) to obtain (again using the values and units originally used),

$$E_{\text{th}} = m(1000\text{ }^{\circ}\text{C} \times 0.25\text{ cal g}^{-1}\text{ }^{\circ}\text{C}^{-1} + 50\text{ cal g}^{-1}) J \text{ (ergs)},$$

in which  $m$  is mass of the ejecta in grams and  $J$  is a conversion factor, with a value of  $4.1855 \times 10^7$  ergs per calorie, that allows us to convert between calories and ergs. The second equation was for a lower temperature differential between the ejecta and ambient ( $500\text{ }^{\circ}\text{C}$ ) and was expressed by:

$$E_{\text{th}} = m(500\text{ }^{\circ}\text{C} \times 0.20\text{ cal g}^{-1}\text{ }^{\circ}\text{C}^{-1}) J \text{ (ergs)}.$$

Given the lower, sub-solidus, temperatures involved in the cooling of lava, his second formulation did not consider heat due to crystallization, and so considered a case where solid, non-crystallizing, ejecta was erupted. He next applied the equation to obtain the thermal energies for a series of eruptions, including the lava flow of Asama (yama), Japan, erupted in 1783. Given a lava flow volume of  $1.7 \times 10^{14}\text{ cm}^3$  he calculated that the heat carried by the flow was:

$$\begin{aligned} E_{\text{th}} &= (1.7 \times 10^{14}\text{ cm}^3) (2.5\text{ g cm}^{-3}) [1000\text{ }^{\circ}\text{C} \times (0.25\text{ cal g}^{-1}\text{ }^{\circ}\text{C}^{-1} + 50\text{ cal g}^{-1})] J \\ &= 5.4 \times 10^{24}\text{ ergs}. \end{aligned}$$

Multiplying by  $0.000\ 0001$  joules per erg gives the result in SI units, i.e.,

$$(5.4 \times 10^{24}\text{ ergs})(0.000\ 0001\ J\ \text{erg}^{-1}) = 5.4 \times 10^{17}\text{ joules}.$$

**Hérdervári (1963)** Hérdervári (1963), citing Yokoyama (1957a), wrote Yokoyama's equations formally, giving, for cases where temperature differential ( $dT$ ) was greater than  $1000\text{ }^{\circ}\text{C}$ ,

$$E_{\text{th}} = V\rho (dT c_p + L) J \text{ (ergs)} \quad (4.97\text{a})$$

in which

$V$  was lava volume (in  $\text{cm}^3$ ),

$\rho$  was mean lava density ( $2.7\text{ g cm}^{-3}$ ),

$dT$  was lava temperature above ambient ( $1100\text{ }^{\circ}\text{C}$ ),

$c_p$  was the specific heat of lava ( $0.25\text{ cal g}^{-1}\text{ }^{\circ}\text{C}^{-1}$ ),

$L$  was the latent heat of lava ( $50\text{ cal g}^{-1}$ ), and

$J$  was the calories to ergs conversion factor ( $4.1855 \times 10^7$  ergs  $\text{cal}^{-1}$ ).

Values given are those used by Hérdervári (1963) for Hawaiian lavas. For cases where  $T$  was less than  $500\text{ }^{\circ}\text{C}$ , Hérdervári (1963) gave

$$E_{\text{th}} = V\rho dT c_p J \text{ (ergs)}. \quad (4.97\text{b})$$

Hérdervári (1963) then used known erupted lava volumes, with appropriate lava temperatures and densities, to tabulate energy released by 94 eruptions, including effusive eruptions at Mauna Loa, Kilauea, Etna, Haleakala, Hualalai, Vesuvius, Nyirmuragira, and Paricutin.

**Scandone (1979): inclusion of heat carried by the volatile phase** Scandone (1979) was interested in estimating the thermal energy of Paricutin's 1943–1951 lava flow field. Using a total lava volume of  $700 \times 10^{12} \text{ cm}^3$  and a density of  $2.7 \text{ g cm}^{-3}$  he arrived at a total erupted lava mass ( $m$ ) of  $1.9 \times 10^{15} \text{ g}$ . Using this, Scandone (1979) wrote Equation (4.97a) in terms of mass to estimate the thermal energy released by lava in cooling to ambient, i.e., in cooling through the temperature interval  $\Delta T$ , in:

$$\begin{aligned}
 E_{\text{lava}} &= m (\Delta T c_p + L) J \\
 &= m (1000^\circ\text{C} \times 0.25 \text{ cal g}^{-1} \text{ }^\circ\text{C}^{-1} + 50 \text{ cal g}^{-1}) 4.1855 \times 10^7 \text{ ergs cal}^{-1} \\
 &= m (1.2 \times 10^{10} \text{ erg g}^{-1}) \\
 &= (1.9 \times 10^{15} \text{ g}) (1.2 \times 10^{10} \text{ ergs g}^{-1}) \\
 &= 2.4 \times 10^{25} \text{ ergs} \\
 &= (2.4 \times 10^{25} \text{ ergs})(0.000 0001 \text{ J erg}^{-1}) \\
 &= 2.4 \times 10^{18} \text{ joules.}
 \end{aligned} \tag{4.97c}$$

Scandone (1979) argued that the thermal energy carried by the volatiles contained within the lava, which in Scandone's case amounted to about 5% in weight (i.e.,  $0.05 \times 1.9 \times 10^{15} \text{ g} = 9.5 \times 10^{13} \text{ g}$ ) needed to be added. To calculate the energy carried by the volatile phase ( $E_{\text{volatile}}$ ), Scandone (1979) used the specific heat capacity of water ( $c_{\text{H}_2\text{O}}$ ) and latent heat of condensation ( $L_{\text{H}_2\text{O}}$ ) in:

$$E_{\text{volatile}} = m_w (\Delta T c_{\text{H}_2\text{O}} + L_{\text{H}_2\text{O}}) J, \tag{4.97d}$$

in which  $m_w$  was the volatile mass. This gave

$$\begin{aligned}
 E_{\text{volatile}} &= m 0.05 (900^\circ\text{C} \times 0.5 \text{ cal g}^{-1} \text{ }^\circ\text{C}^{-1} + 639 \text{ cal g}^{-1}) 4.1855 \times 10^7 \text{ ergs cal}^{-1} \\
 &= m(0.2 \times 10^{10} \text{ erg g}^{-1}) \\
 &= (1.9 \times 10^{15} \text{ g})(0.2 \times 10^{10} \text{ ergs g}^{-1}) \\
 &= 4.3 \times 10^{24} \text{ ergs} \\
 &= (4.3 \times 10^{24} \text{ ergs})(0.000 0001 \text{ J erg}^{-1}) \\
 &= 4.3 \times 10^{17} \text{ joules.}
 \end{aligned}$$

Thus, the total thermal energy released by the lava and its volatiles was:

$$\begin{aligned}
 E_{\text{lava(tot)}} &= E_{\text{lava}} + E_{\text{volatile}} \\
 &= 2.4 \times 10^{25} \text{ ergs} + 4.3 \times 10^{24} \text{ ergs} \\
 &= 2.8 \times 10^{25} \text{ ergs} \\
 &= 2.8 \times 10^{18} \text{ joules}
 \end{aligned}$$

or

$$\begin{aligned} E_{\text{lava(tot)}} &= m(1.2 \times 10^{10} \text{ erg g}^{-1} + 0.2 \times 10^{10} \text{ erg g}^{-1}) \\ &= m(1.4 \times 10^{10} \text{ erg g}^{-1}) \\ &= (1.9 \times 10^{15} \text{ g})(1.4 \times 10^{10} \text{ ergs g}^{-1})(0.000 0001 \text{ J erg}^{-1}) \\ &= 2.8 \times 10^{18} \text{ joules.} \end{aligned}$$

Thus, for the case of Scandone (1979), heat carried by the volatile phase contributed 15% of the  $2.8 \times 10^{18}$  joules of heat released by the lava in cooling to ambient.

**Friedman and Williams (1968): first application with satellite data** Equations (4.95) to (4.97) have many uses. However, our focus here is the history and heritage of application of these equations by the remote sensing community to

- (i) assess the energy budget of a lava flow, and then
- (ii) convert the energy budget to lava flow mass or volume.

The first attempt to apply a mass-to-energy conversion using satellite IR data was completed by Friedman and Williams (1968). The analysis involved Nimbus HRIR data, as well as data from airborne IR scanners, collected during the 1966 eruption of Surtsey (Iceland). Citing Yokoyama (1957a) and Hérdervári (1963), Friedman and Williams (1968) used Equation (4.97a), but wrote it in terms of volume flux ( $dV/dt$ ):

$$\Phi_{\text{th}} = dV/dt \rho (dT c_p + L) J \text{ (ergs per second)}$$

so that  $\Phi_{\text{th}}$  is the thermal energy flux. Friedman and Williams (1968) stated that the equation allowed relation of the “volcanic energy to the volume of the products erupted.” They proceeded by using the volume flux of erupted lavas during the Surtsey eruption ( $7 \times 10^6 \text{ cm}^3 \text{ s}^{-1}$ ) to estimate the thermal energy flux in ergs per second:

$$\begin{aligned} \Phi_{\text{th}} &= (7 \times 10^6 \text{ cm}^3 \text{ s}^{-1})(2.8 \text{ g cm}^{-3})[(1100 \text{ }^\circ\text{C} \times 0.25 \text{ cal g}^{-1} \text{ }^\circ\text{C}^{-1}) + 50 \text{ cal g}^{-1}] J \\ &= 2.67 \times 10^{17} \text{ ergs s}^{-1} \\ &= 2.67 \times 10^{10} \text{ J s}^{-1}. \end{aligned}$$

The results were compared with the thermal energies estimated from HRIR and other airborne IR data.

**Le Guern (1987): first application with radiometer data** Using radiometer-based measurements for the surface temperature of Niragongo’s lava lake made in 1972, Le Guern (1987) took the estimated energy flux ( $2.03 \times 10^9 \text{ cal s}^{-1}$ ), with cooling by  $400 \text{ }^\circ\text{C}$  and an assumed specific heat capacity of  $1 \text{ cal g}^{-1} \text{ }^\circ\text{C}^{-1}$ , to calculate the “amount of convective magma cooling” as

$$\begin{aligned} m &= (2.03 \times 10^9 \text{ cal s}^{-1}) / [(400 \text{ }^\circ\text{C})(1 \text{ cal g}^{-1} \text{ }^\circ\text{C}^{-1})] \\ &= (2.03 \times 10^9 \text{ cal s}^{-1}) / (400 \text{ cal g}^{-1}) \\ &= 5.08 \times 10^6 \text{ g s}^{-1} = 5.08 \times 10^3 \text{ kg s}^{-1}. \end{aligned}$$

This was for the crusted portion of the lake, with the heat loss, cooling and mass flux from “fountaining” portions being,

$$\begin{aligned} m &= (0.87 \times 10^9 \text{ cal s}^{-1}) / [(400 \text{ }^\circ\text{C})(1 \text{ cal g}^{-1} \text{ }^\circ\text{C}^{-1})] \\ &= (0.87 \times 10^9 \text{ cal s}^{-1}) / (400 \text{ cal g}^{-1}) \\ &= 2.18 \times 10^6 \text{ g s}^{-1} = 2.18 \times 10^3 \text{ kg s}^{-1} \end{aligned}$$

so that the total mass flux was:

$$\begin{aligned} 5.08 \times 10^3 \text{ kg s}^{-1} (\text{crusted portion}) + 2.18 \times 10^3 \text{ kg s}^{-1} (\text{fountaining portion}) \\ = 7.26 \times 10^3 \text{ kg s}^{-1}. \end{aligned}$$

We may argue that this, after the calculation of Italiano *et al.* (1984) given at the end of the previous section, was one of the first attempts to use measurements of surface temperature to convert to heat flux and then to mass flux at a volcanic system. However, in presenting his results, Le Guern (1987) appears to have omitted the  $dT$  term from his calculations, giving mass fluxes that were identical to the energy fluxes, i.e.,  $m$  of  $2.03 \times 10^9 \text{ g s}^{-1}$  for the crusted portion, and  $0.87 \times 10^9 \text{ g s}^{-1}$  for the fountaining portion. Such a result is only possible if the heat flux is divided by one, i.e., by  $1 \text{ cal g}^{-1} \text{ }^\circ\text{C}^{-1}$ , with  $dT$  either being omitted or also set to one, i.e.,  $1 \text{ }^\circ\text{C}$ , so that

$$\begin{aligned} m &= (2.03 \times 10^9 \text{ cal s}^{-1}) / [(1 \text{ }^\circ\text{C})(1 \text{ cal g}^{-1} \text{ }^\circ\text{C}^{-1})] \\ &= (2.03 \times 10^9 \text{ cal s}^{-1}) / [1 \text{ cal g}^{-1}] \\ &= 2.03 \times 10^9 \text{ g s}^{-1}. \end{aligned}$$

This result is three orders of magnitude greater than that given above which incorporates the  $400 \text{ }^\circ\text{C}$  of cooling recorded for the crusted portion of the lake, but is likely an error.

#### *4.5.1.2 Energy budget for a cooling lava*

Energy available to an active lava will come from the internal energy of the lava mass ( $dE$ ). This can be expressed in terms of the lava specific heat capacity ( $c_p$ ) and difference in temperature between the lava and ambient ( $\Delta T$ ) so that

$$dE = m c_p \Delta T. \quad (4.98a)$$

In addition, heat will be provided by latent heat of crystallization ( $L$ ). Thus the thermal energy available to a mass of lava ( $m$ ) can be written:

$$dE = m (c_p \Delta T + L). \quad (4.98b)$$

Dimensional analysis shows that this yields the total amount of energy available in units of joules, i.e.,

$$dE = \text{kg} \left( \frac{\text{J}}{\text{kg K}} \text{K} + \frac{\text{J}}{\text{kg}} \right) = \text{kg} \frac{\text{J}}{\text{kg}} = \text{joules.}$$

That is, it will yield the total heat available from a given mass of lava cooling to ambient from temperature,  $T$ . Take, for example,  $4.95 \times 10^{11}$  kg of lava at a temperature of  $1160^\circ\text{C}$  and cooling to  $0^\circ\text{C}$ . If we experience 100% crystallization and cooling through the same range, then the total energy available will be:

$$dE = (4.95 \times 10^{11} \text{ kg}) [(1130 \text{ J kg}^{-1} \text{ K})(1433 \text{ K}) + (3.5 \times 10^5 \text{ J kg}^{-1})] = 9.75 \times 10^{17} \text{ J.}$$

If lava density ( $\rho$ ) is known, Equation (4.98b) can also be written in terms of volume ( $V$ ),

$$dE = \rho V (c_p \Delta T + L).$$

Again, we can check this dimensionally, and find

$$dE = \frac{\text{kg}}{\text{m}^3} \text{m}^3 \left( \frac{\text{J}}{\text{kg K}} \text{K} + \frac{\text{J}}{\text{kg}} \right) = \text{kg} \frac{\text{J}}{\text{kg}} = \text{joules.}$$

Thus we can say that  $dE$  will be the total energy available from volume  $V$  of lava cooled by  $\Delta T$ . Take our working example, where we have  $2.35 \times 10^8 \text{ m}^3$  of lava with a bulk rock density of  $2100 \text{ kg m}^{-3}$  and cooling by  $1433 \text{ K}$ , now

$$\begin{aligned} dE &= (2100 \text{ kg m}^{-3}) (2.35 \times 10^8 \text{ m}^3) [(1130 \text{ J kg}^{-1} \text{ K}^{-1})(1433 \text{ K}) + (3.5 \times 10^5 \text{ J kg}^{-1})] \\ &= 9.75 \times 10^{17} \text{ J.} \end{aligned}$$

Following the first law of thermodynamics, this heat can either be retained or lost by the lava body. In cooling to ambient, a certain amount of heat must be lost or “carried away” ( $E_{\text{th}}$ ). This quantity should be equal to the amount of heat available, and can thus be estimated from:

$$E_{\text{th}} = dE = \rho V (c_p \Delta T + L \Delta \phi), \quad (4.98c)$$

in which:

$\Delta T$  = the temperature difference between eruption and ambient, and

$\Delta \Phi$  = the mass fraction of crystals grown in cooling through  $\Delta T$ .

If, for example, lava is erupted at  $1080^\circ\text{C}$ , cools to  $0^\circ\text{C}$  and, in cooling through this temperature range, undergoes 45% crystallization, then the thermal energy leaving the mass is:

$$\begin{aligned} E_{\text{th}} &= (4.95 \times 10^{11} \text{ kg}) [(1130 \text{ J kg}^{-1} \text{ K}^{-1})(1080 \text{ K}) + (3.5 \times 10^5 \text{ J kg}^{-1})(0.45)] \\ &= 6.82 \times 10^{17} \text{ J.} \end{aligned}$$

Thus  $6.82 \times 10^{17} \text{ J}$  of heat will be lost. Following Section 4.4.1, this is lost from the lava mass by radiation ( $Q_{\text{rad}}$ ), convection ( $Q_{\text{conv}}$ ) and conduction ( $Q_{\text{cond}}$ ), as well as by vaporization of rain and/or ground water ( $Q_{\text{H}_2\text{O}}$ ), so that

$$E_{\text{th}} = Q_{\text{tot}} = Q_{\text{rad}} + Q_{\text{conv}} + Q_{\text{cond}} + Q_{\text{H}_2\text{O}}.$$

Thus we can say that our lava mass will lose  $6.82 \times 10^{17}$  joules of heat in cooling to ambient. This will primarily be lost by radiation, convection, conduction and vaporization of water.

**Heat loss to lava mass relation** We have defined a balance whereby all heat released in cooling a lava mass through the temperature interval  $\Delta T$  will be lost from the lava body, so that

$$E_{\text{th}} = Q_{\text{tot}},$$

in which  $Q_{\text{tot}}$  is the sum of all the heat losses (i.e.,  $Q_{\text{rad}} + Q_{\text{conv}} + Q_{\text{cond}} + Q_{\text{H}_2\text{O}}$ ). If we write the right-hand side of this equation in full we have:

$$\rho V(c_p \Delta T + L \Delta \phi) = Q_{\text{tot}}. \quad (4.99\text{a})$$

Now, if we have a measure of the total energy released ( $Q_{\text{tot}}$ , in joules), we can use this to estimate the volume of lava that needs to be cooled through the temperature range  $\Delta T$  to generate the observed energy. Re-arrangement of Equation (4.99a) shows that this can be calculated from:

$$V = \frac{Q_{\text{tot}}}{\rho(c_p \Delta T + L \Delta \phi)}. \quad (4.99\text{b})$$

Alternatively, we can avoid the requirement of knowing lava density and convert between mass and energy:

$$m(c_p \Delta T + L \Delta \phi) = Q_{\text{tot}}. \quad (4.99\text{c})$$

In this case, if we have a measure of the total energy ( $Q_{\text{tot}}$ ), we can use this to estimate the mass of lava that needs to be cooled through the temperature range  $\Delta T$  to generate the observed energy, using:

$$m = \frac{Q_{\text{tot}}}{c_p \Delta T + L \Delta \phi}. \quad (4.99\text{d})$$

This is the basis of satellite-based attempts to

- (i) complete energy balance inventories, and
- (ii) convert derived heat losses to lava volumes and masses.

**Volatiles** These estimates do not take into account the energy carried by volatiles contained within the lava and heat released during condensation of these volatiles. Following Scandone (1979), this may add up to 15% to the total energy available to a cooling mass of lava. However, if we can assume that the lava is essentially degassed in water by the time it reaches the surface, so that heat due to condensation of the volatile phase does not

contribute to the heat budget for a cooling lava erupted onto the Earth's surface, we can neglect this contribution. For calculation of the potential volatile contribution to the heat budget of a cooling lava body, we need to apply Equation (4.97d).

#### 4.5.1.3 Application of the energy budget approach using satellite data

**Conversion to volume: the approach of Wooster *et al.* (1997)** Wooster *et al.* (1997) chose to use infrared data from the Along Track Scanning Radiometer to estimate the heat losses from Etna's 1991–1993 flow, with field-measured flow volumes being used to estimate the energy supplied. In this way Wooster *et al.* (1997) were able to approximate the energy budget of the lava flow field as follows.

- (1) First, the ATSR data were used to estimate the heat fluxes due to radiation, convection, conduction and vaporization of rain water, as plotted in Figure 4.22.
- (2) Next, heat fluxes (in  $\text{J s}^{-1}$ ) were integrated through time and summed to yield a value for total heat lost up to any given point in time ( $Q_{\text{tot}}$ , in joules), as done in Figure 4.23.
- (3) Finally, lava flow volumes measured in the field at points during the eruption were used to solve Equation (4.99a), and thus estimate the heat supplied ( $E_{\Delta T}$ ), at any point in time, as also done in Figure 4.23.
- (4) The difference between the two calculated values ( $Q_{\text{tot}} - E_{\Delta T}$ ) was used to estimate the energy balance during the eruption (Figure 4.23). The difference between the two values yielded the heat retained by the flow at the end of the eruption.

Given a total lava flow field volume of  $235 \times 10^6 \text{ m}^3$ , an eruption temperature of  $1080^\circ\text{C}$ , 45% post-eruption crystallization, a dense rock density of  $2700 \text{ kg m}^{-3}$ , and a specific heat capacity of  $1130 \text{ J kg}^{-1} \text{ K}^{-1}$ , Equation (4.98c) becomes

$$\begin{aligned} E_{\text{th}} &= (2700 \text{ kg m}^{-3})(235 \times 10^6 \text{ m}^3)[(1130 \text{ J kg}^{-1} \text{ K})(1080 \text{ K}) + (3.5 \times 10^5 \text{ J kg}^{-1})(0.45)] \\ &= 8.7 \times 10^{17} \text{ J}. \end{aligned}$$

Thus we can say that Etna's 1991–1993 flow field had the potential to release  $8.7 \times 10^{17} \text{ J}$  of heat in cooling from its eruption temperature of  $1080^\circ\text{C}$  to ambient. By the end of the eruption, Figure 4.23 shows that  $E_{\text{th}}$  and  $Q_{\text{tot}}$  had not balanced, with total heat lost being just  $\sim 2 \times 10^{17} \text{ J}$ . Thus the flow had lost just 23% of its thermal energy at the end of the eruption, and a further  $6.74 \times 10^{17} \text{ J}$  still needed to be lost before the flow reached ambient temperature. This meant that a considerable amount of heat was retained within the flow field at the end of the eruption, and a further 77% of the flow field's heat had to be lost before the condition  $E_{\text{th}} = Q_{\text{tot}}$  was met. This heat was lost during post-eruption cooling.

**Lava flow volume from satellite-derived heat loss** The approach of Wooster *et al.* (1997) can be used as the basis to estimate lava flow volume using satellite IR data. To do this, the total value for the heat lost, integrated throughout the entire cooling period ( $Q_{\text{tot}}$ ), needs to be used to estimate the volume of lava ( $V$ ) needs to cooled by  $\Delta T$  and crystallized by  $\Delta\Phi$  to yield the required  $Q_{\text{tot}}$ . That is, we use  $Q_{\text{tot}}$  to solve Equation (4.99a).

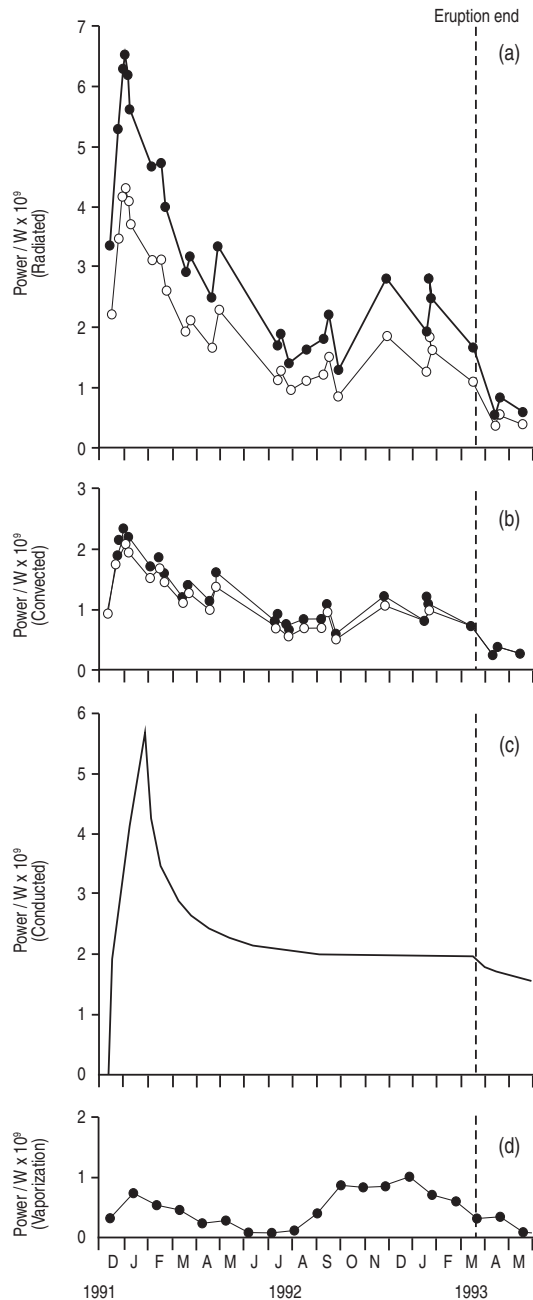


Figure 4.22 Heat losses due to (a) radiation, (b) convection, (c) conduction, and (d) vaporization of ground water calculated, using ATSR data, for Etna's 1991–1993 lava flow field during and immediately after effusion as calculated by Wooster *et al.* (1997) [from Wooster *et al.* (1997, Fig. 1); reproduced by permission of American Geophysical Union]. Closed and open circles represent the maximum and minimum bound on the estimates, respectively.

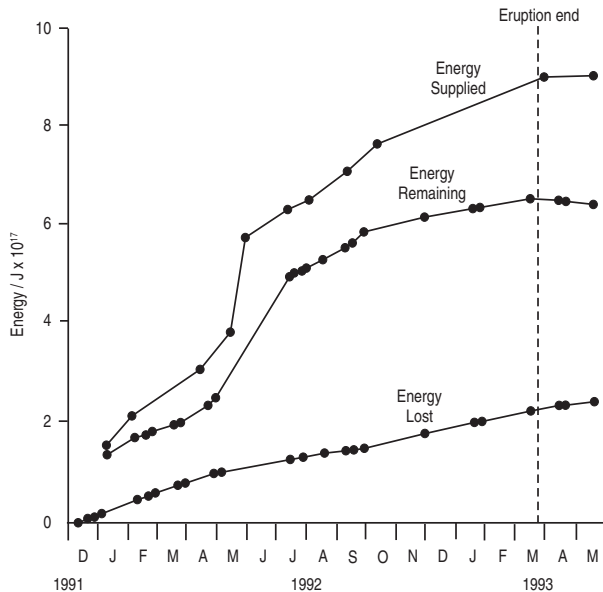


Figure 4.23 Calculations for energy supplied and energy lost, plus the resulting energy balance, for Etna's 1991–1993 lava flow field during and immediately after effusion as completed by Wooster *et al.* (1997) [from Wooster *et al.* (1997, Fig. 2): reproduced by permission of American Geophysical Union].

Application of this equation requires that our satellite-based measurements of heat flux (in units of  $\text{J s}^{-1}$ ) be integrated through time (in seconds) to obtain total heat loss in joules (i.e.,  $\text{J s}^{-1} \times \text{s} = \text{J}$ ). To do this we can use the trapezium rule. That is, the curve between each measurement point is treated as a trapezium and its area ( $A$ ) calculated from:

$$A = x_{n+1} - x_n \left( \frac{y_2 + y_1}{2} \right). \quad (4.100)$$

In our case, while  $x_n$  is the time at measurement point  $n$ ,  $x_{n+1}$  is the time of the next measurement point, with  $y_1$  and  $y_2$  being the heat flux measurements made at the two times, respectively. The area of each trapezium is then summed to obtain the area under the curve, or the integral of value  $x$ . In this case we obtain the time integral of heat flux, i.e., total heat lost. Although more sophisticated numerical integration algorithms could be considered, the trapezium rule is sufficient for our purposes, given the uncertainty in the data.

Take, for example, the following case where heat flux has been estimated for Etna's 2006 flow field at three points in time, over two days, using three AVHRR images. Derived heat fluxes ( $\Phi_{\text{th}}$ ) were:

- $2.17 \times 10^9 \text{ J s}^{-1}$  at 01:07 UT on 17 November,
- $2.12 \times 10^9 \text{ J s}^{-1}$  by 20:46 UT on the same day, and
- $2.34 \times 10^9 \text{ J s}^{-1}$  at 20:33 UT on 18 November.

The total heat lost between 01:07 UT and 20:46 UT on 17 November can thus be calculated as,

$$\begin{aligned} Q_{\text{tot}} &= 70\,740 \text{ s} - 0 \text{ s} \left( \frac{2.12 \times 10^9 \text{ J s}^{-1} + 2.17 \times 10^9 \text{ J s}^{-1}}{2} \right) \\ &= (70\,740 \text{ s})(2.14 \times 10^9 \text{ J s}^{-1}) = 15.52 \times 10^{14} \text{ J}. \end{aligned}$$

For the period spanning the 20:46 UT measurement on 17 November and the measurement of the following day, we have:

$$\begin{aligned} Q_{\text{tot}} &= 156\,360 \text{ s} - 70\,740 \text{ s} \left( \frac{2.34 \times 10^9 \text{ J s}^{-1} + 2.12 \times 10^9 \text{ J s}^{-1}}{2} \right) \\ &= (85\,620 \text{ s})(2.23 \times 10^9 \text{ J s}^{-1}) = 19.1 \times 10^{14} \text{ J}. \end{aligned}$$

Summing these values shows that a total of  $3.42 \times 10^{14}$  J were released by the lava over the 156 360 s (~43.5 h) period spanning the measurements. If we assume that, over this period, the lava cooled by 100 °C ( $= \Delta T$ ) and crystallized by 20% ( $\Phi = 0.2$ ) we arrive at a lava volume of

$$\begin{aligned} V &= \frac{3.42 \times 10^{14} \text{ J}}{2100 \text{ kg m}^{-3} (880 \text{ J kg}^{-1} \text{ K}^{-1} \times 100 \text{ K} + 3.5 \times 10^5 \text{ J kg}^{-1} \times 0.2)} = \frac{3.42 \times 10^{14} \text{ J}}{3.33 \times 10^8 \text{ J m}^{-3}} \\ &= 1.03 \times 10^6 \text{ m}^3. \end{aligned}$$

Field data available during the period show that, over the same period,  $9.87 \times 10^5 \text{ m}^3$  of lava was emplaced. Thus, given these cooling and crystallization assumptions, the calculation yields an appropriate volume.

The total energy released by the same lava volume in cooling to ambient (i.e.,  $\Delta T = 1080 \text{ K}$ ) would be:

$$\begin{aligned} E_{\text{th}} &= (9.87 \times 10^5 \text{ m}^3)(2100 \text{ kg m}^{-3})[(880 \text{ J kg}^{-1} \text{ K}^{-1})(1080 \text{ K}) + (3.5 \times 10^5 \text{ J kg}^{-1})(0.45)] \\ &= 2.31 \times 10^{15} \text{ J}. \end{aligned}$$

Thus we find that after cooling by 100 °C the lava has lost  $3.42 \times 10^{14}$  J, or 15% of the available heat. The remaining 85% must be retained by the flow. By the time the lava cools to ambient, the heat flux integration should reach  $2.31 \times 10^{15}$  J. At this point we can use the total value for the heat lost, integrated throughout the entire period of cooling to ambient, to estimate the lava volume required to yield  $2.31 \times 10^{15}$  J of heat where, reversing the calculation just made, we have,

$$\begin{aligned} V &= \frac{2.31 \times 10^{15} \text{ J}}{2100 \text{ kg m}^{-3} (880 \text{ J kg}^{-1} \text{ K}^{-1} \times 1080 \text{ K} + 3.5 \times 10^5 \text{ J kg}^{-1} \times 0.45)} \\ &= \frac{2.31 \times 10^{15} \text{ J}}{2.34 \times 10^9 \text{ J m}^{-3}} = 9.87 \times 10^5 \text{ m}^3. \end{aligned}$$

Of course, the problem is that we need a suitable measurement for  $\Delta T$  and  $\Delta\phi$ . In the case above the combination of  $\Delta T$  and  $\Delta\phi$  were obtained by virtue of best fit between the calculated volume and that derived from Digital Elevation Models obtained from synchronous LIDAR data. For this case,  $\Delta\phi$  is a plausible value for the amount of

crystallization experienced by a lava of Etna's composition in cooling by 100 °C from an eruption temperature of ~1080 °C (Harris *et al.*, 2010). If we do not have such control data sets to hand, or the capability to set the values by best-fitting, the best approach is to measure all heat lost during cooling to ambient, so that we can set  $\Delta T$  to eruption temperature minus ambient (which we approximate from 1080 °C – 0 °C = 1080 °C for this Etna case). To do this we need to continue measuring the heat losses until the flow has cooled to ambient, or until a thermal anomaly is no longer apparent in the IR imagery. This now raises a new set of problems, as we will explore in the following example.

**Application to Fernandina's 1995 lava flow field** Conversion of total heat loss to volume was attempted by Rowland *et al.* (2003) using ATSR data collected during Fernandina's 1995 eruption. If we integrate the heat losses from the eruption through time, we arrive at a value of  $Q_{\text{tot}}$  of  $3.6 \times 10^{16}$  J by the end of the eruption. Putting this into Equation (4.99b) yields:

$$V = \frac{3.6 \times 10^{16} \text{ J}}{(2100 \text{ kg m}^{-3})[(1130 \text{ J kg}^{-1} \text{ K}^{-1})(1080 \text{ K}) + (3.5 \times 10^5 \text{ J kg}^{-1})(0.45)]} \\ = 12 \times 10^6 \text{ m}^3.$$

This value is somewhat less than the total flow field volume expected from DEM subtraction ( $42 \times 10^6 \text{ m}^3$ ). Given that heat fluxes were only integrated until the end of the eruption, it suggests that not all of the heat had yet been released. In fact, if we invert our reasoning and use the measured lava volume to obtain the expected value for total heat loss in cooling to ambient ( $E_{\text{th}}$ ) we obtain

$$E_{\text{th}} = (2100 \text{ kg m}^{-3})(42 \times 10^6 \text{ m}^3)[(1130 \text{ J kg}^{-1} \text{ K}^{-1})(1080 \text{ K}) + (3.5 \times 10^5 \text{ J kg}^{-1})(0.45)] \\ = 1.22 \times 10^{17} \text{ J}.$$

In other words, only ~30 % of the heat available had been lost at the end of the eruption. The flow was thus still in the process of cooling, with ~70 % of the  $1.22 \times 10^{17}$  J available to the flow still having to be lost before the flow cooled to ambient. Because 70 % of the heat was retained, the flow interior had not yet fully cooled, so that the cooling experienced by the interior ( $\Delta T$ ) must have been less than 1080 K.

**Cooling rates** By re-arranging Equation (4.99b) we can isolate  $\Delta T$  to estimate the amount of cooling that the lava has undergone to liberate the measured quantity of heat:

$$\Delta T = \left( \frac{Q_{\text{tot}}}{\rho V} - L\Delta\phi \right) c_p^{-1}. \quad (4.101a)$$

Now, if we know volume, have a measure of the total heat lost to date, and can assume a value for the amount of crystallization the lava has undergone, we can solve for  $\Delta T$ . Assuming  $\Delta\phi = 0.2$  for the Fernandina case, we obtain

$$\begin{aligned}\Delta T &= \left( \frac{3.6 \times 10^{16} \text{ J}}{(2100 \text{ kg m}^{-3})(42 \times 10^6 \text{ m}^3)} - (3.5 \times 10^5 \text{ J kg}^{-1})(0.2) \right) \left( \frac{1}{1130 \text{ J kg}^{-1} \text{ K}^{-1}} \right) \\ &= 300 \text{ K.}\end{aligned}$$

Given an eruption temperature of 1080 °C, this would imply a core temperature of 780 °C. Given that this heat loss was based on an integration of heat flux over 80 days, we can estimate that the core had cooled by 300 °C by day 80, to give a time-averaged cooling rate of 3.75 °C per day over this period. Or, more realistically, a small amount of lava was cooled to near ambient temperature and the core barely cooled at all.

Likewise, if volume and  $\Delta T$  are known, the measurement of  $Q_{\text{tot}}$  may now allow the amount of crystallization to be calculated:

$$\Delta\phi = \left( \frac{Q_{\text{tot}}}{\rho V} - c_p \Delta T \right) L^{-1}. \quad (4.101b)$$

These re-arrangements may permit a satellite-derived inventory of thermal flux to be used to track cooling with time (i.e., to plot  $\Delta T$  as a function of time), if  $\Delta\phi$  can be assessed at any point in time, and lava volume is known. Alternatively, if volume and  $\Delta T$  are known for any point in time, the thermal flux inventory could be used to track crystallization with time (i.e., to plot  $\Delta\phi$  as a function of time).

**The problem of volume measurement with satellite data** This demonstration shows that, if this approach is to work as a volume measurement tool, thermal flux measurements must be completed, and integrated, through the entire cooling process, so that a correct value for  $Q_{\text{tot}}$  is used. This can be done if a cooling curve can be identified, and if the cooling curve can track through the entire cooling process.

The problem is, in AVHRR- and GOES-class, even for TM-class, data may not be capable of allowing this, the large pixel size causing the thermal anomaly to become unresolvable before the flow interior has completed cooling. As a result, a full inventory of the heat lost in cooling to ambient will not be completed (as the cooling process has not been traced through to completion). Thus the time-integral of  $Q_{\text{tot}}$  will be incomplete and volume will be under-estimated. This may mean that executing this approach is impossible. Interior temperatures for the lava lake within Kilauea's Kilauea Iki crater, for example, remain above ambient today (more than 50 years after its initial emplacement in 1959), and signs that the cooling process is underway remain apparent from the active steam vents on the lake surface. However, the thermal anomaly became unresolvable in AVHRR and GOES data long ago, preventing a satellite-based inventory of the full  $Q_{\text{tot}}$ . Maybe the value of satellite data is in using the estimated heat losses, with independent lava volume estimates, to build and interpret effective thermal budgets during, and immediately after, effusive eruptions, as shown by Wooster *et al.* (1997), as well as to estimate post-eruption core cooling rates.

#### 4.5.1.4 Conversion to volume flux

**The approach of Pieri and Baloga (1986)** We can also write the Equation (4.99b) in terms of volume flux ( $V_R$ , in  $\text{m}^3 \text{s}^{-1}$ ). This needs to be used with a measure of  $\Phi_{\text{tot}}$  ( $\text{J s}^{-1}$ ) in,

$$V_R \rho(c_p \Delta T + L \Delta \phi) = \Phi_{\text{tot}}, \quad (4.102a)$$

so that

$$V_R = \frac{\Phi_{\text{tot}}}{\rho(c_p \Delta T + L \Delta \phi)}. \quad (4.102b)$$

Dimensionally, this is now

$$V_R = \frac{\text{J s}^{-1}}{\frac{\text{kg}}{\text{m}^3} \left( \frac{\text{J}}{\text{kg K}} \text{K} + \frac{\text{J}}{\text{kg}} \right)} = \frac{\text{J s}^{-1}}{\frac{\text{kg}}{\text{m}^3} \left( \frac{\text{J}}{\text{kg}} + \frac{\text{J}}{\text{kg}} \right)} = \frac{\text{J s}^{-1}}{\text{J m}^{-3}} = \text{m}^3 \text{s}^{-1}.$$

This approach has largely been credited to Pieri and Baloga (1986) who, in exploring an empirical relation between volume flux and lava plan area in field data for Hawaiian lava flows, presented the following equation:

$$V_R = \frac{\varepsilon \sigma T_e^4}{\rho c_p (T_0 - T_f)} A(L). \quad (4.102c)$$

Here,

$T_e$  is the effective radiation temperature of the lava flow surface,

$T_0$  is the eruption temperature,

$T_f$  is the temperature at which flow stops, and

$A(L)$  is the flow area at the point at which flow ceases, this occurring at distance,  $L$ , from the vent at which point  $T(L) = T_f$ .

The assumptions, as stated by Pieri and Baloga (1986), were:

- (i) eruption temperature ( $T_0$ ) is constant for the duration of the flow;
- (ii) flow cools with distance from the vent, and flow is cooling-limited so that advance ceases at distance  $L$  from the vent, at which point the interior temperature has cooled to a temperature ( $T_f$ ) where forward motion is no longer possible;
- (iii) the final plan area of the flow is attained when the flow front stops.

**The method of Crisp and Baloga (1990b)** Crisp and Baloga (1990b) presented a similar equation with the aim of relating erupted volume flux ( $V_R$ ) to the following thermal parameters:

- fraction of flow core exposed ( $f$ );
- initial core temperature ( $T_0$ );
- flow plan area ( $A$ );

- core temperature when the flow stops advancing ( $T_f$ );
- crust thickness ( $\delta_0$ );
- flow thickness ( $h$ );
- lava density ( $\rho$ ) and specific heat capacity ( $c_p$ ).

Based on Equation (4.102c), the relation had the form

$$V_R = \frac{3f\epsilon\sigma T_0^3 A}{\rho c_p (1 - \frac{\delta_0}{h}) \left( \frac{T_0^3}{T_f^3} - 1 \right)}. \quad (4.103)$$

Crisp and Baloga (1990b) argued that this equation provided “a way to estimate average eruption rates of planetary lava flows if the total planimetric area of the flow is known.”

Take a 5 km long, 100 m wide ( $5 \times 10^5 \text{ m}^2$ ) flow unit which has reached its maximum length and plan area. Using typical values suggested by Crisp and Baloga (1990b), i.e.,  $f=0.001$ ,  $T_0 = 1120 \text{ }^\circ\text{C}$  and  $\delta_0/h = 0.2$ , with  $T_f = 900 \text{ }^\circ\text{C}$ , we obtain:

$$\begin{aligned} V_R &= \frac{3(0.001)(0.98)(5.67 \times 10^{-8} \text{ W m}^{-2} \text{ K}^{-4})(1433 \text{ K})^3 (5000 \text{ m})(100 \text{ m})}{(2100 \text{ kg m}^{-3})(1130 \text{ J kg}^{-1} \text{ K}^{-1})(1 - 0.2) \left( \frac{(1433 \text{ K})^3}{(1173 \text{ K})^3} - 1 \right)} \\ &= (2.45 \times 10^5 \text{ J s}^{-1} \text{ K}^{-1}) / (420 \text{ J m}^{-3} \text{ K}^{-1}) = 887 \text{ m}^3 \text{ s}^{-1}. \end{aligned}$$

That is, the flow needs to be fed at a volume flux of  $887 \text{ m}^3 \text{ s}^{-1}$  to attain the plan area of  $5 \times 10^5 \text{ m}^2$  under the assumed thermal conditions.

**Conversion to mass flux: the approach of Francis *et al.* (1993)** Francis *et al.* (1993) took heat fluxes ( $\Phi$ , in W or  $\text{J s}^{-1}$ ) derived from Landsat Thematic Mapper (TM) data for active lava lakes and domes to estimate the lava mass flux. The approach of Francis *et al.* (1993) essentially followed that of Friedman and Williams (1968) where, in using radiative heat flux rather than total heat lost (in joules), the conversion was between heat flux and mass flux ( $m_R$  in  $\text{kg s}^{-1}$ ), rather than total heat loss and mass (in kg). Their relation was:

$$m_R = \frac{\Phi_{\text{rad}}}{c_p \Delta T + L \Delta \phi}. \quad (4.104)$$

Dimensionally, this is:

$$m_R = \frac{\text{J s}^{-1}}{\frac{\text{J}}{\text{kg K}} \text{K} + \frac{\text{J}}{\text{kg}}} = \frac{\text{J s}^{-1}}{\frac{\text{J}}{\text{kg}} + \frac{\text{J}}{\text{kg}}} = \frac{\text{J s}^{-1}}{\text{J kg}^{-1}} = \text{kg s}^{-1}.$$

In other words, it is the lava mass flux required to balance the heat flux.

To solve this equation, Francis *et al.* (1993) used the heat flux for Erta Ale’s lava lake of 100 MW obtained from a 1986 TM image, plus the heat flux of 84 MW derived for Erebus from a 1985 TM image. For Lascar’s lava dome a heat flux of 110 MW, as obtained from a 1987 TM image, was used. Using  $c_p$  of  $10^3 \text{ J kg}^{-1} \text{ K}^{-1}$  and  $L$  of  $4.2 \times 10^5 \text{ J kg}^{-1}$ , two

end-member models were applied. In model A, lava cooled by 50 °C and crystallized by 25%, so that  $\Delta T = 50$  °C and  $\Delta\phi = 0.25$ . For the three cases this gives the following.

- (1) Ertá Ale (1986),  $m_R = 100 \text{ MW}/[(10^3 \text{ J kg}^{-1} \text{ K}^{-1}) (50 \text{ K}) + (4.2 \times 10^5 \text{ J kg}^{-1}) (0.25)]$   
 $= (100 \times 10^6 \text{ J s}^{-1})/(1.55 \times 10^5 \text{ J kg}^{-1})$   
 $= 645 \text{ kg s}^{-1}$ .
- (2) Erebus (1985),  $m_R = 84 \text{ MW}/[(10^3 \text{ J kg}^{-1} \text{ K}^{-1}) (50 \text{ K}) + (4.2 \times 10^5 \text{ J kg}^{-1}) (0.25)]$   
 $= (84 \times 10^6 \text{ J s}^{-1})/(1.55 \times 10^5 \text{ J kg}^{-1})$   
 $= 540 \text{ kg s}^{-1}$ .
- (3) Lascar (1987),  $m_R = 110 \text{ MW}/[(10^3 \text{ J kg}^{-1} \text{ K}^{-1}) (50 \text{ K}) + (4.2 \times 10^5 \text{ J kg}^{-1}) (0.25)]$   
 $= (110 \times 10^6 \text{ J s}^{-1})/(1.55 \times 10^5 \text{ J kg}^{-1})$   
 $= 710 \text{ kg s}^{-1}$ .

In model B, lava cooled by 400 °C and crystallized by 100 %, so that  $\Delta T = 400$  °C and  $\Delta\phi = 1$ . For the three cases this gives the following.

- (1) Ertá Ale (1986),  $m_R = 100 \text{ MW}/[(10^3 \text{ J kg}^{-1} \text{ K}^{-1}) (400 \text{ K}) + (4.2 \times 10^5 \text{ J kg}^{-1})]$   
 $= (100 \times 10^6 \text{ J s}^{-1})/(8.20 \times 10^5 \text{ J kg}^{-1})$   
 $= 120 \text{ kg s}^{-1}$ .
- (2) Erebus (1985),  $m_R = 84 \text{ MW}/[(10^3 \text{ J kg}^{-1} \text{ K}^{-1}) (400 \text{ K}) + (4.2 \times 10^5 \text{ J kg}^{-1})]$   
 $= (84 \times 10^6 \text{ J s}^{-1})/(8.20 \times 10^5 \text{ J kg}^{-1})$   
 $= 100 \text{ kg s}^{-1}$ .
- (3) Lascar (1987),  $m_R = 110 \text{ MW}/[(10^3 \text{ J kg}^{-1} \text{ K}^{-1}) (400 \text{ K}) + (4.2 \times 10^5 \text{ J kg}^{-1})]$   
 $= (110 \times 10^6 \text{ J s}^{-1})/(8.20 \times 10^5 \text{ J kg}^{-1})$   
 $= 135 \text{ kg s}^{-1}$ .

**The method of Harris *et al.* (1997a)** Adding heat fluxes due to radiation and convection to the top line, and a heat of crystallization term to the bottom line, Harris *et al.* (1997a) wrote the relation,

$$V_R = \frac{A [\varepsilon\sigma(T_c^4 - T_a^4) + h_c(T_c - T_a)]}{\rho(c_p\Delta T + L\Delta\phi)} \quad (4.105)$$

For use with AVHRR data. Take, for example, our typical heat flux measurement of  $2.21 \times 10^9 \text{ J s}^{-1}$  obtained from the AVHRR images of lava active acquired for Etna during 17–18 November 2006, as considered previously in this section. For this eruption, Harris *et al.* (2009) found a good relation between heat flux and volume flux using a dense rock density of  $2700 \text{ kg m}^{-3}$ , a specific heat capacity of  $1130 \text{ J kg K}^{-1}$ , 100 °C cooling and 20 %

post-eruption crystallization. Correcting the density and specific heat capacity for a vesicularity of 22 %

$$\text{i.e., } \rho = (1 - 0.22) \times 2700 \text{ kg m}^{-3} = 2100 \text{ kg m}^{-3},$$

and

$$c_p = (1 - 0.22) \times 1130 \text{ J kg K}^{-1} = 880 \text{ J kg K}^{-1},$$

this yields,

$$V_R = \frac{2.21 \times 10^9 \text{ J s}^{-1}}{2100 \text{ kg m}^{-3} [(880 \text{ J kg}^{-1}\text{K}^{-1})(100\text{K}) + (0.2)(3.5 \times 10^5 \text{ J kg}^{-1})]} \\ = 6.7 \text{ m}^3\text{s}^{-1}.$$

The result of  $6.7 \text{ m}^3 \text{ s}^{-1}$  compares with a LIDAR-measured lava volume of  $5.68 \times 10^5 \text{ m}^3$  erupted over the 25 hour period spanning the three images, to give a time-averaged discharge rate over the same period of  $6.3 \text{ m}^3 \text{ s}^{-1}$ . There is thus good agreement between the satellite-based volume flux measurement and the independent measure for this case.

**Some important points** This approach has become a commonly used method in thermal remote sensing to convert spectral radiances obtained for volcanic hot spots in AVHRR-class data to volume fluxes. It is thus important to understand the limits, and assumptions, behind the application. We first consider the assumptions. Three of the main assumptions, have already been stated, these being

- (1) eruption temperature is constant;
- (2) flow is cooling-limited;
- (3) when flow motion ceases, the final plan area is attained.

To which we can add seven further conditions:

- (4) in terms of topography, the relation needs to be set on a case-by-case basis. A relation set for a case where lava is emplaced on steep slopes, cannot be applied to lavas emplaced on gentle slopes;
- (5) flow conditions need to have reached steady-state, so that the flow front has cooled to  $T_f$ , and maximum flow length and plan area has been attained;
- (6) most of the heat loss takes place by radiation and convection. If not, a term for basal conduction needs to be added to the total heat flux assessment, or for rain;
- (7) the selected surface temperature is roughly constant across the flow, and must be set according to appropriate insulation conditions (i.e., hot and poorly crusted, or cold and well-crusted);
- (8) the ambient temperature needs to be negligible with respect to the lava surface temperature;
- (9) heat produced by crystallization needs to be adequately accounted for, and the cooling condition ( $\Delta T$ ) set appropriately;

- (10) lava is incompressible, and density, specific heat capacity, and emissivity are constant across the flow.

Wright *et al.* (2001) added that the approach relies on an assumption that the active lava area needs to be controlled by the volume flux averaged over some period prior to image acquisition, and that changes in the lava flow area must be proportional to the changes in this precedent flux value. Thus, the method does not give the instantaneous volume flux from the vent at the time of satellite overpass (i.e., effusion rate), but instead gives a time-averaged volume flux (i.e., a time-averaged discharge rate) responsible for feeding the flow area active at the time of image acquisition. This is best viewed by envisaging the following scenario. Lava discharge at the vent doubles. However, it will take some time for this increased discharge to be transmitted to the flow front. It will thus take time for the flow area to respond to the increase in supply. Thus, a satellite overpass at the point of effusion increase will not record this new level of effusion. Instead, a satellite overpass at the time when the flow area has completed its areal response to the new discharge rate will record the increase.

Wright *et al.*'s (2001) argument also points out a final assumption. Any change in discharge must be reflected in a change in flow width and/or length, and no volume can be lost to flow thickening or inflation. The approach will thus not work for flows that become topographically entrapped (in pits or hollows), so that they are not free to spread, or for flows which are inflation dominated. In the inflating case, if too much of the supplied volume goes into flow thickening, any change in volume flux will not be expressed by a change in plan area.

#### *4.5.1.5 A linear, empirical relation as a basis for conversion*

Given the limits of AVHRR-data, where we usually have just one band of unsaturated TIR data (the MIR band being saturated), the three-component TIR solution of [Equation \(4.2b\)](#) is usually applied to obtain the pixel portion occupied by active lava ( $p_c$ ) from the pixel-integrated spectral radiance [ $M(\lambda_{\text{TIR}}, T_{\text{int}})$ ], using

$$p_c = \frac{M(\lambda_{\text{TIR}}, T_{\text{int}}) - M(\lambda_{\text{TIR}}, T_a)}{M(\lambda_{\text{TIR}}, T_c) - M(\lambda_{\text{TIR}}, T_a)}. \quad (4.106a)$$

As described in [Section 4.3.1.2](#), this is solved by using an assumed value (or value range) for the lava surface temperature ( $T_c$ ) and a value to characterize the temperature of surrounding ambient surfaces ( $T_a$ ). Multiplying  $p_c$  by pixel area ( $A_{\text{pixel}}$ ) gives the “active” lava area in the pixel ( $A_{\text{lava}}$ ),

$$A_{\text{lava}} = p_c A_{\text{pixel}}. \quad (4.106b)$$

Heat flux ( $M_{\text{tot}}$ ) is then obtained using Stefan–Boltzmann ( $\sigma$ ) and the convective heat-transfer coefficient ( $h_c$ ) in,

$$\Phi_{\text{tot}} = A_{\text{lava}} [\sigma \varepsilon (T_c^4 - T_a^4) + h_c (T_c - T_a)], \quad (4.106c)$$

a result which can be used to obtain volume flux, or time-averaged discharge rate, in Equation (4.104).

$$V_R = \frac{\Phi_{\text{tot}}}{\rho(c_p \Delta T + L \Delta \phi)}. \quad (4.106d)$$

If we look back through these equations, there is only one variable: pixel-integrated spectral radiance. All other values are assumed.

In effect, we have set up a linear relation between lava area and the time-averaged discharge rate feeding the flow. This can be seen in [Figure 4.24a](#), where we set a relation between lava volume flux and area using AVHRR TIR data for Etna's 1999 lava flows fed by October–November fire fountaining from the Bocca Nuova. We define four relations using assumed lava surface temperatures of 200 °C, 250 °C, 350 °C and 500 °C. In each case, we take the area obtained for each temperature condition and convert to heat and volume flux using

- $\varepsilon = 0.9887$ ,
- $T_a = 25$  °C,
- $h_c = 10$  W m<sup>-2</sup> K<sup>-1</sup>,
- $\rho = 2100$  kg m<sup>-3</sup>,
- $c_p = 880$  J kg<sup>-1</sup> K<sup>-1</sup>,
- $\Delta T = 100$  °C,
- $\Delta \phi = 0.45$ .

In all, 35 images were acquired over 18.5 days. These data, when plotted, define four linear relations between lava area (in km<sup>2</sup>) and volume flux (m<sup>3</sup> s<sup>-1</sup>). There is one relation for each temperature condition,

Condition 1,  $T_c = 200$  °C:

$$V_R = 8.8136 A_{200}.$$

Condition 2,  $T_c = 250$  °C:

$$V_R = 12.466 A_{250}.$$

Condition 3,  $T_c = 350$  °C:

$$V_R = 22.622 A_{350}.$$

Condition 4,  $T_c = 500$  °C:

$$V_R = 47.901 A_{500}.$$

From [Figure 4.24a](#), we see that the four relations span the range of field measurements, where conditions one and two fit the six data points that fall on the line,

$$V_R = 7.2634 A + 2.3091 \quad (R^2 = 0.89),$$

and conditions three and four fit the four data points that define a second relation,

$$V_R = 17.756 A + 7.3662 \quad (R^2 = 1.00).$$

**Solution ranges** Because of uncertainty in the value of the lava surface temperature, and the exact relation between volume flux and lava area, we solve over a range of temperatures and relations. For the Etna 1999 data set, if we assume a lower bound of 100 °C for the lava surface temperature assumption, and an upper bound of 1000 °C, we obtain a minimum bound on  $V_R$  using the lava area at 100 °C ( $A_{100}$ ):

$$V_R = 3.5507 A_{100} (\text{km}^2) \text{ (cubic meters per second)}$$

and a maximum bound using the active lava area obtained using the 1000 °C temperature condition ( $A_{1000}$ ):

$$V_R = 303.55 A_{1000} (\text{km}^2) \text{ (cubic meters per second)}.$$

The field-measured value is assumed to lie between the two results. This, as plotted for our Etna 1999 case in [Figure 4.24b](#), is generally the case.

**The relation** This approach can thus be reduced to a best-fitting method, whereby an empirical relation is set between the active lava area (i.e.,  $A_{\text{lava}}$  summed for all pixels across the anomaly) and time-averaged discharge rate ( $TADR$ ), i.e.,

$$TADR = a A_{\text{lava}} \quad (4.107a)$$

or between total heat flux (again summed for all pixels across the anomaly) and  $TADR$ , i.e.,

$$TADR = b \Phi_{\text{tot.}} \quad (4.107b)$$

In each case,  $a$  and  $b$  are the coefficients that define the slope of a linear relation between the two parameters. This has to be set on a case-by-case basis depending on the spectral band used, as well as values intrinsic to maintaining the underlying assumption of an empirical relation between  $TADR$  and final flow area plan view. That is, the relation will vary depending on rheological, slope and/or thermal insulation conditions. For example, at a given volume flux, a low-viscosity, well-insulated lava spreading on a steep slope may be expected to spread to cover a greater area than a high-viscosity, poorly insulated lava spreading on a shallow slope. The relation thus needs to be set on a case-by-case basis. Given good fits between satellite-data-derived discharge rates and lava flow volumes in the many cases tested to date, if the relation is set appropriately, then reliable results that span a similar range of uncertainty as can be found in field-based measurements can be obtained.

**Setting the relation** Coefficients for Equations (4.107) can be set in one of three ways: (i) theoretically, (ii) through best-fitting with independent  $TADR$  data, or (iii) best-fitting with field-measured lava flow volumes.

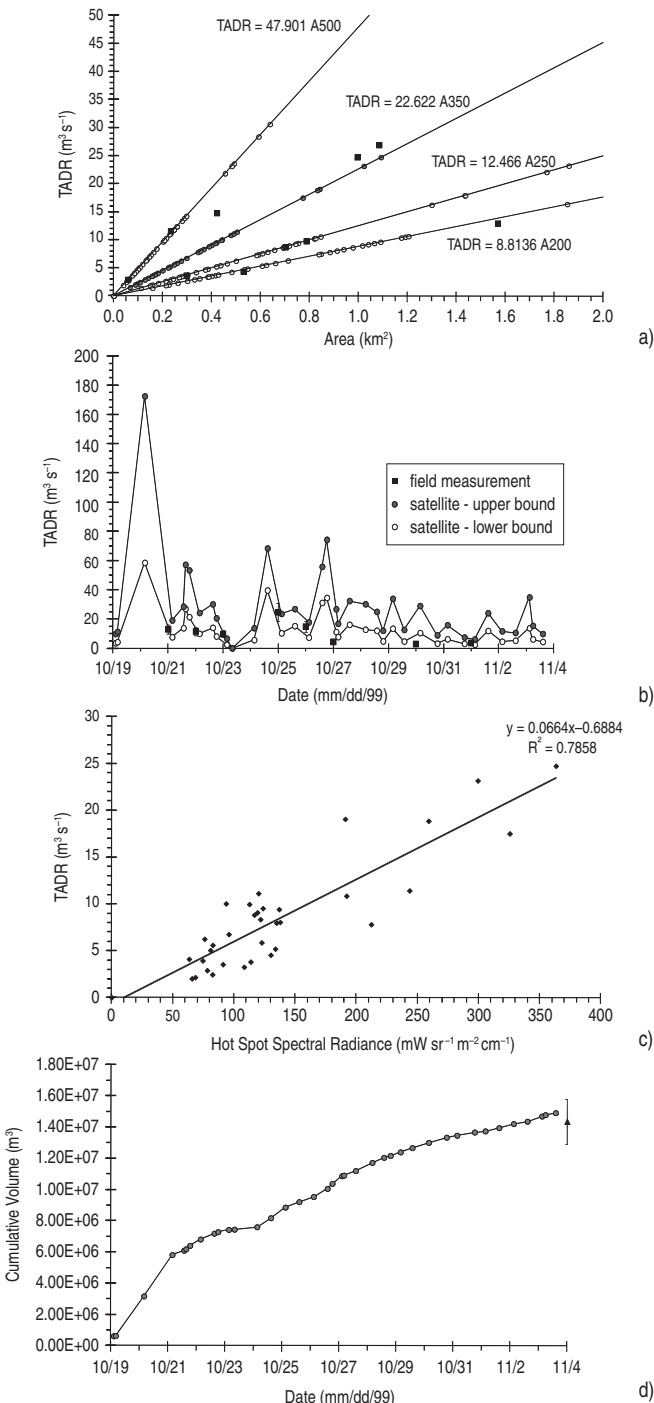


Figure 4.24 AVHRR conversion to TADR during Etna’s October–November fire fountaining events from the Bocca Nuova. Field measurements used for best fitting are given as black squares. (a) Relations between lava area at 200 °C, 250 °C, 350 °C and 500 °C (as extracted from AVHRR TIR data using three-component TIR solution of Section 4.3.1.2) and TADR. (b) Time variation in the upper and lower bounds placed on TADR by application of the 200 °C and 500 °C relations of (a). (c) Relation between hot spot spectral radiance in the TIR, summed for all anomalous pixels, and TADR. (d) Cumulative volume obtained from the 350 °C relation of (a) and field-measured final flow field volume.

### (i) Theoretical

If we are confident that the relations are valid, then we can estimate the conversion values using appropriate values for  $\rho$ ,  $c_p$ ,  $\Delta T$ ,  $L$  and  $\Delta\phi$ . For example, applying Equation (4.106d) to the Etna 2006 test case, we obtain a good fit between volume flux and satellite-derived heat flux using  $\rho = 2100 \text{ kg m}^{-3}$ ,  $c_p = 880 \text{ J kg}^{-1} \text{ K}^{-1}$ ,  $\Delta T = 100 \text{ K}$ ,  $L = 3.5 \times 10^5 \text{ J kg}^{-1}$  and  $\Delta\phi = 0.2$ . In this case, these constants multiply to

$$(2100 \text{ kg m}^{-3})[(880 \text{ J kg}^{-1} \text{ K}^{-1})(100 \text{ K}) + (3.5 \times 10^5 \text{ J kg}^{-1})(0.2)] = 3.32 \times 10^8 \text{ J m}^{-3}$$

this being constant  $b$  in Equation (4.107b), so that

$$TADR = \frac{A_{\text{lava}} M_{\text{tot}}}{b} = \frac{\Phi_{\text{tot}}}{b} = \frac{\Phi_{\text{tot}}}{3.32 \times 10^8 \text{ J m}^{-3}}.$$

In addition,  $M_{\text{tot}}$  can be described using a constant ( $m$ ), so that the relation reduces to:

$$\Phi_{\text{tot}} = m A_{\text{lava}}.$$

For a lava surface temperature assumption of 100 °C,

$$\begin{aligned} m &= \sigma \varepsilon (T_c^4 - T_a^4) + h_c (T_c - T_a) \\ &= (5.67 \times 10^{-8} \text{ W m}^{-2} \text{ K}^{-1})(0.98)[(373 \text{ K})^4 - (298)^4] + (10 \text{ W m}^{-2} \text{ K}^{-1})[373 \text{ K} - 298 \text{ K}] \\ &= 1387 \text{ W m}^{-2} \end{aligned}$$

so that

$$TADR = A_{100} \frac{m}{b} = A_{100} \frac{1387 \text{ W m}^{-2}}{3.32 \times 10^8 \text{ J m}^{-3}} = (4.18 \times 10^{-6} \text{ m s}^{-1}) A_{100},$$

$A_{100}$  being the lava area obtained with the 100 °C temperature assumption. In other words, coefficient  $a$  in Equation (4.107a) has a value of  $4.18 \times 10^{-6} \text{ m s}^{-1}$  for this case. For a lava surface temperature assumption of 1000 °C,

$$\begin{aligned} m &= \sigma \varepsilon (T_c^4 - T_a^4) + h_c (T_c - T_a) \\ &= (5.67 \times 10^{-8} \text{ W m}^{-2} \text{ K}^{-1})(0.98)[(1273 \text{ K})^4 - (298)^4] + (10 \text{ W m}^{-2} \text{ K}^{-1})[1273 \text{ K} - 298 \text{ K}] \\ &= 155 200 \text{ W m}^{-2}, \end{aligned}$$

so that

$$TADR = A_{1000} \frac{m}{b} = A_{1000} \frac{155 200 \text{ W m}^{-2}}{3.32 \times 10^8 \text{ J m}^{-3}} = (4.68 \times 10^{-4} \text{ m s}^{-1}) A_{1000},$$

$A_{1000}$  being the lava area obtained with the 1000 °C temperature assumption. Note that each coefficient can only be used with the temperature condition for which it is derived. That is, the 1000 °C coefficient can only be used with the lava area obtained from TIR data using the 1000 °C lava surface assumption.

**(ii) Best fit with field-measured TADR**

The conversion coefficient may also be obtained by virtue of best fit with field-derived values, as done in [Figure 4.24](#). In this case, lava area and/or heat flux is obtained from the satellite data and coefficients  $a$  and/or  $b$  are adjusted until the best-fit between output  $TADR$  and the independently measured  $TADR$  is obtained.

Harris and Ripepe ([2007a](#)) and Coppola *et al.* ([2009](#)) chose to carry out such a best-fit directly between satellite-derived spectral radiance and  $TADR$ , using,

$$TADR = c L_{\lambda-\text{flow}}, \quad (4.108)$$

in which  $L_{\lambda-\text{flow}}$  is the spectral radiance in band  $\lambda$  for a hot spot pixel, minus that of its background, summed for all hot pixels. Coppola *et al.* ([2009](#)) applied this to MIR pixels acquired by MODIS during the May–July 2003 eruption of Piton de la Fournaise, obtaining

$$TADR = 0.128 L_{\text{MIR-flow}}.$$

Attempting this with our AVHRR data for Etna’s October–November 1999 data, provides

$$TADR = 0.0664 L_{\text{TIR-flow}} - 0.6884.$$

But, as can be seen in [Figure 4.24c](#), the fit is not good, with an  $R^2$  of 0.79.

**(iii) Best fit with field-measured volume**

If, instead of a field-measured  $TADR$ , we have an estimate of volume, the best-fit can be made on the basis of volume. In this case,  $TADRs$  are first obtained using the satellite data in the empirical conversion using a starting conversion coefficient in

$$TADR = a A_{\text{lava}}.$$

The individual  $TADRs$  are then integrated through time (using the trapezium rule) to obtain a total volume. This is then compared with the field-measured volume, and the conversion coefficient adjusted until the two volumes are approximately equal, as done in [Figure 4.24d](#). At this point, we assume that all of the component  $TADRs$  that go into generating the best-fit volume are valid. In our test case of [Figure 4.24](#), best fit between the two volumes is when we assume a lava surface temperature condition of 350 °C and apply the conversion coefficient of

$$V_R = 22.622 A_{350}.$$

This relation gives a total volume of  $14.9 \times 10^6 \text{ m}^3$ , a result which is based on the integration of 39 data points over 18.5 days, and compares with a field-measured volume of  $14.3 \times 10^6 \text{ m}^3 \pm 1.3 \times 10^6 \text{ m}^3$ .

#### 4.5.1.6 Summary

A summary of thermal parameters that have been extracted from time series data acquired by satellite IR sensors is given in [Figure 4.25](#). During an eruption, spectral radiances have been converted to active lava areas, heat fluxes, mass and volume fluxes. At the eruption end,

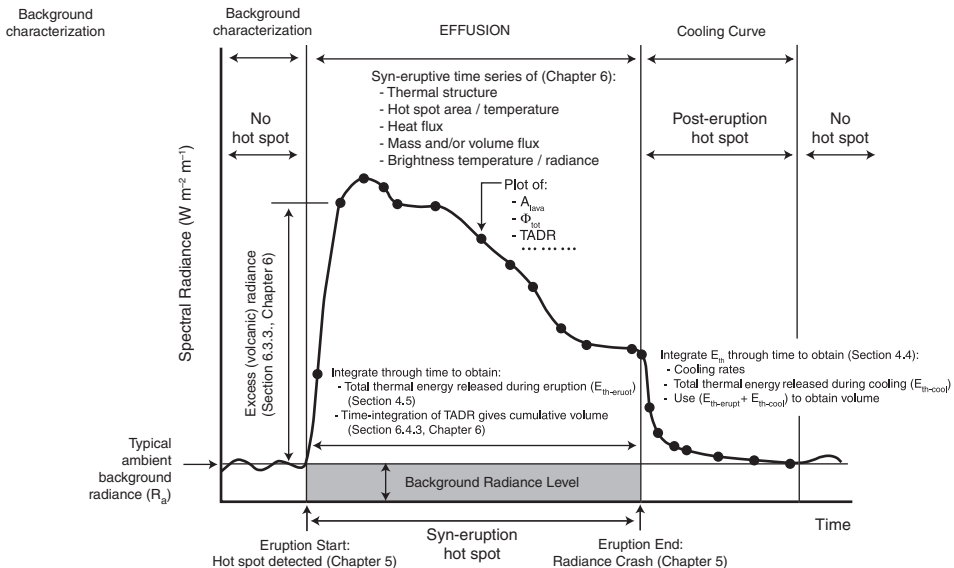


Figure 4.25 Summary of thermal parameters that can be extracted from time series data acquired by satellite IR sensors.

identification of a cooling curve allows cooling rates to be constrained. Integration of heat fluxes through time, to yield total heat loss, can then potentially be converted to total mass or volume flux. Execution of all thermal and mass parameters are based on our ability to construct and apply pixel mixture models that adequately characterize the thermal structure of the lava surface.

**Worked example** An example of the application of the methodologies described in this chapter is given in Electronic Supplement 7. This five-step methodology begins with selection of hot pixels to which a thermal mixture will be applied. The next step (step 2) involves radiance correction (for atmospheric and emissivity effects) of all selected pixels. This is followed by step 3, selection and application of an appropriate thermal mixture model. Step 4 involves lava area and heat flux extraction, which is followed by the fifth and final step, application of the volume flux conversion.

# 5

## Hot spot detection

Real-time detection of volcanic hot spots in satellite infrared data is its logical operational role. We also need to identify, and extract radiance information from, anomalous pixels if we are to use them for quantitative purposes (as in the previous chapter) or time series, classification, and mapping applications (as in the following chapter). We thus now consider the issue of hot spot detection in IR data.

Satellite data are available in real time, if access to a receiving station is possible, and provide data for all surfaces across an entire volcano or volcanic region, allowing timely detection for any point within the imaged zone. In addition, the repeat periods for the AVHRR- and GOES-class sensors, allow hot spot activity to be tracked on a daily-to-hourly basis. Consequently it is now a well-used argument that, at remote or poorly equipped volcanoes, the satellite perspective can contribute to monitoring and tracking volcanic activity, and measuring the associated heat and volume flux. Even at well-monitored volcanoes, satellite data available at temporal resolutions of 15 minutes can fill gaps in the record and narrow down eruption onset times. To achieve this operationally, a level of automated notification is required, to allow timely early warning of the onset of new activity. This is especially true if data loads are high as, for example, is the case of GOES-class data where 96 images a day are available for all volcanoes beneath its hemisphere-wide footprint. Automated spectral radiance extraction also allows efficient time series analysis, especially when examining high-temporal-resolution data sets for eruptions lasting months or years. To manually extract spectral radiance data for all hot spots in all images acquired over the past two years by GOES would, for example, be a daunting task if done manually. Thus, automated algorithms play a role in ensuring (i) timely detection and tracking of eruption-related hot spots, and (ii) efficient generation of long-term thermal data sets for time series analysis. After considering the physical basis of hot spot detection, we focus on detection issues, methods and algorithms currently available, as well as their capabilities and applications.

### 5.1 Detection by eye

By looking repeatedly at a given area under a variety of observing conditions (night-time, day-time, nadir, scan edge, hazy, scattered cloud, cirrus-covered, stratus-covered, etc.),

together the eye and brain can quite quickly become an extremely effective hot spot detection system, capable of pin-pointing the most subtle of anomaly in the most challenging of conditions. The experienced operator may have developed their eye through looking at hundreds, even thousands, of images so that a subtle temporal change in the spectral radiance from a particular point, the persistence of a tiny anomaly and/or a slight increase in spectral radiance at a single point, is immediately noticed. Effectively by examining multiple images of the same volcano target we train a powerful neural network for hot spot detection. In some subtle detection cases it may even be difficult for the operator to describe the detection algorithm they have subconsciously developed. The easiest response when asked “how do you know it is a thermal anomaly?” is often “look at these” and showing the inquirer the image data base, so that the inquirer develops the same pattern recognition system and is able to see the same subtle change as the analyst. Another response may be “I’ve seen that before” or “that’s strange, I’ve not seen that before.” The challenge is to define an automated detection system that is as effective in detecting even the most subtle of thermal anomalies, and detecting all required pixels while not choosing any false, non-anomalous pixels.

## 5.2 Detection: physical basis

The physical basis of hot spot detection has already been covered in [Chapter 2](#), as well as Electronic Supplement 1. These principles now need to be applied to understand which wavebands are best used to detect a volcanic hot spot, and the likely problems that will be encountered when trying to detect a thermal anomaly. First, though, we need to clarify some definitions.

### 5.2.1 Thermal anomaly: a definition

Resolving power can be defined as an *instrument's ability to distinguish very small or very close objects*. In our case we need to resolve very small, hot objects in a larger pixel and the thermal anomaly that they create. In this regard, an anomaly can be defined as an *irregularity* so that we are dealing with a thermal irregularity. A thermal anomaly can thus be defined as an object or feature that differs in temperature when compared, spatially or temporally, with typical surface temperatures for other objects. That is, the surface temperature may be irregular between one point and another (to form a spatial thermal anomaly) or between one image and the next (to form a temporal thermal anomaly). It can also be defined spectrally, in that (in both the spatial and temporal cases) it requires the presence of an object which is significantly brighter or hotter than other objects present in the same spatial or temporal dimension. Thus, to be resolvable, the object has to be sufficiently different in terms of its spectral radiance (i.e., be sufficiently bright or hot), as to be distinguishable, or resolvable, from other surfaces in the spatial or temporal neighborhood.

### **5.2.2 Which wavebands?**

The waveband used to detect a thermal anomaly will depend on the size and temperature of the volcanic feature, as well as the dynamic range of the sensor used. In short, the waveband has to be sufficiently sensitive to allow a small, but anomalous, sub-pixel object to be resolved. From a review of Electronic Supplement 1, we can conclude the following:

#### *5.2.2.1 For the NIR and SWIR*

TM-class (30 m pixel) data acquired in the NIR and SWIR will be suited to detecting the hottest volcanic phenomena (active lava flows, lakes, domes and vents). However, if the feature is too small (as in the case of a fumarole vent) or the pixel too large (as with an AVHRR- or GOES-class pixel) the anomaly may not be resolvable in these wavebands.

#### *5.2.2.2 For the MIR*

This is often the ideal waveband for detection, with even quite small hot spots being resolvable in AVHRR- and GOES-class data. It has thus become labeled the “fire channel,” owing to its extensive use by the fire monitoring community. However, it can be too sensitive. That is, for many sensors it is usually rather too easy to exceed the MIR dynamic range so that TM-, AVHRR- and GOES-class data collected in the MIR over active lava flows are often saturated.

#### *5.2.2.3 For the TIR*

Because of the poor sensitivity of this waveband to sub-pixel hot spots, small but hot sub-pixel targets may not cause an anomaly in the TIR. However, the coincidence of this waveband with the peak emission from surfaces at ambient temperatures means that it may be useful for detecting subtle thermal anomalies associated with crater lakes or geo-thermal anomalies, especially in TM-class data. In AVHRR- and GOES-class data, smaller active lava features will not be detectable, but lavas of sufficient size and temperature to saturate the MIR usually provide a resolvable anomaly in the TIR.

### **5.2.3 Can we resolve the hot spot?**

Whether the anomaly is resolvable thus depends on (i) the waveband, (ii) the size and temperature of the sub-pixel hot spot, and (iii) the degree to which the spectral radiance of the target pixel is elevated above that of its surroundings. In effect, the background is not a flat, black background against which the target pixel forms a nice clean, white spot. Instead, the background comprises a range of temperature and/or reflectance levels above which the hot spot pixel must become suitably elevated so as to allow it to be distinguished, or resolved, from that of the background.

In an extreme but illustrative example, the presence of a 2 m radius sub-pixel vent at 950 °C at the summit of a snow-capped volcano with a typical surface temperature of 0 °C, will give a pixel integrated temperature in AVHRR-class (1 km) MIR data of 11 °C. Solar

heating of snow-free, barren, lava fields that fill lower-elevation pixels surrounding the summit pixel will mean, however, that those pixels may register temperatures of between 40 °C and 50 °C. Thus the hot spot will not be resolvable. In fact, in this case, it will appear colder than the lower-elevation, snow-free pixels that surround it.

The issue is similar in the NIR or SWIR, but here the problem is one of reflection. The pixel-integrated radiance from the hot-spot-containing pixel must be suitably elevated above that of the spectral radiance for the surrounding pixels if it is to form a detectable anomaly. The same 2 m radius vent in a 1 km AVHRR-class pixel will give a pixel-integrated temperature in the SWIR of 114 °C (or a spectral radiant exitance of  $4.39 \times 10^5 \text{ W m}^{-2} \text{ m}^{-1}$ ). If we take a typical lava surface with an emissivity of 0.95, so that the reflection is 0.05, putting this reflection into the equations of [Appendix B<sup>1</sup>](#) yields a spectral radiant exitance of  $8.02 \times 10^5 \text{ W m}^{-2} \text{ m}^{-1}$ . This converts to a brightness temperature equivalent of 130 °C. The vent will thus not be resolvable, the spectral radiance of the hot spot pixel being lower than that of the surrounding pixels.

To assess the size and temperature a hot spot needs to attain in order to elevate the pixel brightness temperature above that of the surrounding background, we can apply a mixture model. This is done in [Figure 5.1](#). For this modeled case, we see that in the SWIR, a sub-pixel hot spot at 250 °C has to occupy more than 0.7% of the pixel to elevate the night-time detection threshold, this being ~100 °C for TM's SWIR band 7 ([Figure 5.1a](#)). The area that needs to be occupied decreases with increased temperature, so that a 500 °C hot spot only needs to occupy 0.01% of the pixel to attain the same detection threshold. However, the hot spot size will have to be higher if the detection threshold is higher; we see in [Figure 5.1a](#) that the 250 °C hot spot has to occupy more than 5.5% of the pixel if the detection threshold increases to 150 °C. In the MIR, the 250 °C hot spot will have to occupy more than 0.008% of the pixel (by night) to elevate the pixel-integrated temperature above a background in which temperatures vary by 10 °C ([Figure 5.1b](#)). The poorer sensitivity of the TIR means that the pixel portion covered by the 250 °C hot spot has to occupy more than 2% of the pixel to become resolvable from the same, thermally heterogeneous, background in the TIR ([Figure 5.1c](#)). We also see that, in each case, a point is reached where the sensor will saturate. Between the detection and saturation temperatures lie, define the range of hot spot sizes and temperatures that (i) can be detected, and (ii) yield unsaturated (useable) data.

The line defining our detection limit can be moved up or down depending on the temperature levels in surrounding pixels, thereby increasing or decreasing the size a sub-pixel hot spot has to attain before it can be detected. For example, if our hot spot pixel is set against a uniformly cold background of 0 °C, then detection of smaller, cooler sub-pixel hot spots may be possible. For an Erebus-style hot spot, where a small, hot, sub-pixel target is active against a uniformly cold background, detection will be easier than for an Etna-summit-style hot spot, where the same small target may be active against surfaces at a variety of temperatures. For our

<sup>1</sup> Calculation is made for the following conditions: Wavelength 2.25 μm; Day No. 15; Time 15:00; Latitude 37.73°.

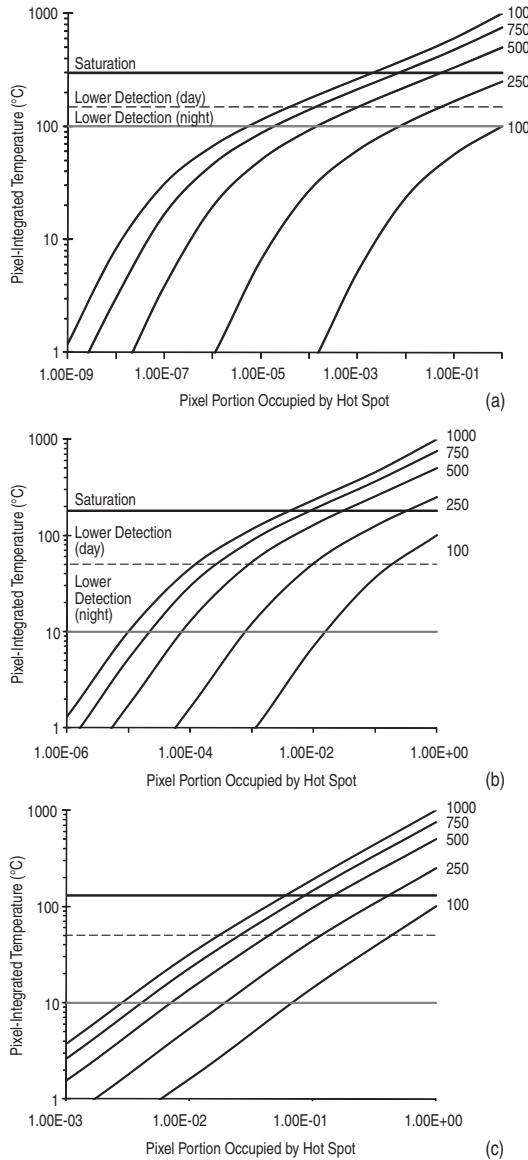


Figure 5.1 Increase in pixel-integrated temperature with sub-pixel hot spot size for a range of hot spot temperatures in (a) the SWIR, (b) the MIR and (c) the TIR. In each case, typical detection and saturation levels are marked to allow assessment of the size and temperature a sub-pixel hot spot needs to attain to (i) be detected, or (ii) saturate the sensor. Generally, as we move from the SWIR to the TIR, the hot spot needs to be increasingly large to be detected or to force saturation. Detection limits in the MIR and TIR assume a cool night-time background at  $10\text{ }^{\circ}\text{C}$ , and a worst case scenario (solar-heated barren rock surface) at  $50\text{ }^{\circ}\text{C}$  by day.

case, the area that an active lava at 250 °C, 500 °C and 1000 °C needs to attain to achieve our detection requirements in TM-class data is:

- 6.6 m<sup>2</sup>, 0.1 m<sup>2</sup> and 0.005 m<sup>2</sup> in the SWIR;
- 0.7 m<sup>2</sup>, 0.06 m<sup>2</sup> and 0.01 m<sup>2</sup> in the MIR;
- 17 m<sup>2</sup>, 6.4 m<sup>2</sup> and 2.5 m<sup>2</sup> in the TIR.

For AVHRR-class data this increases to:

- 7320 m<sup>2</sup>, 140 m<sup>2</sup> and 5.4 m<sup>2</sup> in the SWIR;
- 775 m<sup>2</sup>, 72 m<sup>2</sup> and 9.8 m<sup>2</sup> in the MIR;
- 19 100 m<sup>2</sup>, 7110 m<sup>2</sup> and 2815 m<sup>2</sup> in the TIR.

For GOES-class data this increases to:

- 120 000 m<sup>2</sup>, 2250 m<sup>2</sup> and 85 m<sup>2</sup> in the SWIR;
- 12 400 m<sup>2</sup>, 1150 m<sup>2</sup> and 155 m<sup>2</sup> in the MIR;
- 305 500 m<sup>2</sup>, 114 000 m<sup>2</sup> and 45 000 m<sup>2</sup> in the TIR.

#### 5.2.4 Delta-T ( $\Delta T$ )

Our detection capabilities can be enhanced by using combinations of wavebands. From [Section 4.1](#) of [Chapter 4](#), we know that the differing sensitivities of the MIR and TIR to a sub-pixel hot spot will mean that the pixel-integrated temperature for the hot spot pixel will be higher in the MIR than in the TIR. In our worked example, where a 2-m radius vent at 950 °C is set against a 0 °C background in a 1000 m AVHRR-class pixel, the MIR pixel-integrated temperature will be 11 °C. However, in the TIR it is 0.04 °C, i.e., not resolvable. However, if we subtract the brightness temperature in the TIR ( $T_{\text{TIR}}$ ) from that in the MIR ( $T_{\text{MIR}}$ ) we have a difference ( $\Delta T = T_{\text{MIR}} - T_{\text{TIR}}$ ) of  $\sim 10$  °C. If we take the surrounding solar heated pixels at 40 °C, the temperature should be the same in both wavebands, so that  $\Delta T$  is  $\sim 0$  °C. Now the hot spot that was unresolvable using one waveband of data becomes resolvable using  $\Delta T$ . That is, it shows up as a value of 10 °C against a flat background of near-zero values.

Thus, use of  $\Delta T$  is a good way of finding, or confirming, the presence of subtle thermal anomalies, as well as for checking, rejecting and flattening solar heated areas. Solar heating is a common problem over barren volcanic surfaces. In the summer, solar heating of barren lava surfaces on Etna, for example, can push pixel brightness temperatures in the MIR, as well as in the TIR, to saturation. Likewise, broad swaths across the Sahara are often saturated in both the MIR and TIR bands of the same AVHRR images due to solar heating of large areas of sand. Worse, over a volcano the solar-heated regions are the barren lava flow fields, their solar-heated areas often assume the correct location, shape and size of an active lava flow. However, use of  $\Delta T$  will turn such solar-heated anomalies off, as they will have similarly high temperatures in both the MIR and TIR. Because a real thermal anomaly will have a much higher temperature in the MIR than in the TIR, the same  $\Delta T$  will turn the real anomalies on, as shown in [Figure 5.2](#).

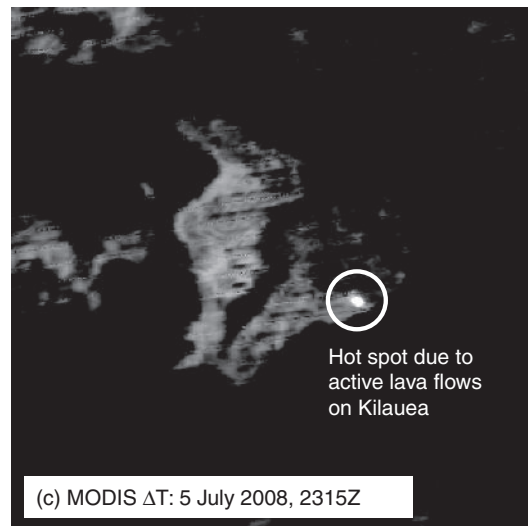
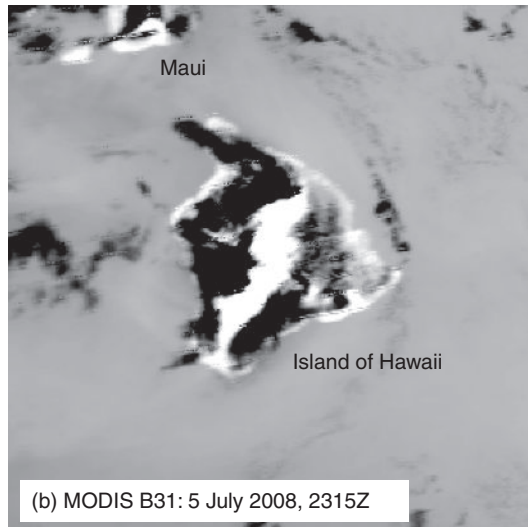
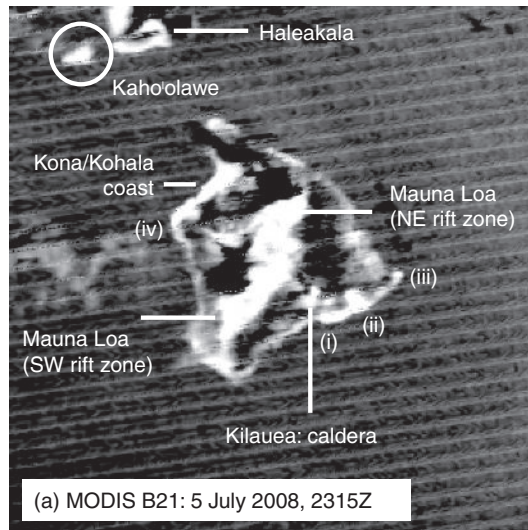


Figure 5.2

### 5.2.4.1 Atmospheric and reflection problems

Unfortunately differential atmospheric and reflection effects between the MIR and TIR wavebands will also cause the brightness temperatures in the two wavebands to differ. If we examine [Table 2.6b](#) of [Chapter 2](#) we see that differential atmospheric and reflection effects between the MIR and TIR mean that a surface at 15 °C yields a brightness temperature of 23 °C in the MIR and 10 °C in the TIR. As a result,  $\Delta T$  obtained for a pixel containing such a homogeneous ambient surface, but subject to differential atmospheric, reflection and emissivity effects, will be far more than zero (i.e.,  $\Delta T$  for this case = 13 °C). Over highly reflective surfaces, such as clouds, the problem can be even worse, with the reflective component adding further to the MIR brightness temperature, and hence increasing the  $\Delta T$  differential. By night, the reflected component goes away, but differential atmospheric effects still mean that the 15 °C surface of [Table 2.6b](#) yields a brightness temperature of ~12 °C in the MIR and ~10 °C in the TIR, for a  $\Delta T$  of ~2 °C. Thus,  $\Delta T$  based on brightness temperature differences will typically be non-zero and can be highly variable. However, appropriate cloud-screening, with band tailored atmospheric and reflection corrections can ameliorate such problems.

### 5.2.4.2 Emissivity problems

Because emissivity will force different radiation temperatures to be recorded at different wavebands (see [Chapter 2](#)), emissivity creates further complications. Take, for example, the Etna 'a'a emissivity of [Table 5.1](#). This has an emissivity of 0.96 in both AVHRR's MIR and TIR band (bands 3 and 4). Although the emissivity is the same in both wavebands, if we use this emissivity to convert from kinetic temperature to radiative temperature in the two bands, we find that the radiative temperature recorded by the two detectors is different. Take, for example, a surface with a kinetic temperature of 15 °C, this converts to a radiative temperature of 14.1 °C in the MIR band and 12.5 °C in the TIR band, to yield a  $\Delta T$  of 1.6 °C. The problem increases as emissivity decreases. A surface with an emissivity of 0.8 will yield radiative temperatures of 10.3 °C and 1.8 °C in the MIR and TIR, respectively; hence yielding a  $\Delta T$  of 8.4 °C.

The problem is exacerbated by the fact that emissivities are often different between the two wavebands. Take the gneiss sample of [Table 5.1](#), for example. This has a MIR emissivity of 0.75 and a TIR emissivity of 0.95, yielding a radiative temperature in the MIR of 8.9 °C, and 11.9 °C in the TIR. This now actually yields a negative  $\Delta T$  of -2.9 °C. The relation between emissivity and  $\Delta T$  is plotted in [Figure 5.3](#), where we see that  $\Delta T$

Caption for Figure 5.2

Islands of Hawaii, Maui and Kaho'olawe imaged on 5 July 2008 at 23:15Z by MODIS in (a) the MIR (band 21) and (b) the TIR (band 32), with (c) the  $\Delta T$  image also being given. In the MIR and TIR we see extensive (apparent) thermal anomalies due to solar heating of vegetation-free surfaces, especially at the summit and coasts of Haleakala volcano (Maui), across the island of Kaho'olawe, along the Kona/Kohala coast of Hawaii, and along both of Mauna Loa's rift zones. Anomalies marked (i), (ii), (iii) and (iv) are apparent thermal anomalies due to solar heating of Mauna Ulu's 1967–72 flow field, Kilauea's post-1983 flow field, Kilauea's 1959 (Kapoho) flow field and Hualalai's 1800 flow field. In the  $\Delta T$  image all "apparent" solar heated anomalies are turned off, and only that associated with active lava flow activity on Kilauea remains.

**Table 5.1** Emissivities for a variety of terrestrial surface types in AVHRR's MIR and TIR bands, bands 3 and 4 ( $\varepsilon_3$  and  $\varepsilon_4$ ). These are used to calculate the brightness temperature in each band [ $T_3$  and  $T_4 = \varepsilon_\lambda M_{BB}(\lambda, T_\lambda)$ ] for a surface with a kinetic temperature of 15 °C. Differential emissivities thus yield different brightness temperatures in each band, and hence  $\Delta T (= T_3 - T_4)$ . The final column gives the range of  $\Delta T$  to be expected from emissivity, rather than sub-pixel hot spot, effects.

Surface type	$\varepsilon_3$	$\varepsilon_4$	$T_3$	$T_4$	$\Delta T$
Basalt	0.91	0.89	13.0	8.0	5.0
Slabby pahoehoe basalt (Etna) (a)	0.94	0.93	13.7	10.6	3.1
Glassy pahoehoe basalt (Hawaii) (a)	0.92	0.86	13.2	6.0	7.2
'A'a basalt (Etna & Hawaii) (a)	0.96	0.96	14.1	12.5	1.6
Basaltic scoria (Etna & Stromboli) (a)	0.94	0.95	13.7	11.9	1.8
Andesite	0.92	0.91	13.2	9.3	3.9
Rhyolite	0.84	0.9	11.3	8.6	2.6
Yellow sulfurous-fumarole sublimate (a)	0.86	0.91	11.8	9.3	2.5
Rhyolite with fumarolically altered coating (a)	0.97	0.98	14.3	13.8	0.6
Obsidian	0.95	0.89	13.9	8.0	5.9
Granite	0.9	0.92	12.7	9.9	2.8
Gneiss	0.75	0.95	8.9	11.9	-2.9
Schist	0.74	0.92	8.6	9.9	-1.3
Slate	0.89	0.95	12.5	11.9	0.6
Limestone	0.91	0.93	13.0	10.6	2.4
Sandstone	0.82	0.96	10.8	12.5	-1.7
Shale	0.92	0.97	13.2	13.1	0.1
Soil	0.8	0.97	10.3	13.1	-2.9
Green foliage	0.96	0.97	14.1	13.1	1.0
Senescent foliage	0.85	0.9	11.5	8.6	2.9
Ice	0.95	0.98	13.9	13.8	0.1
Snow (b)	0.97	0.99	14.3	14.4	0.0
Water bodies	0.97	0.99	14.3	14.4	0.0
Min.	0.74	0.86	8.65	5.98	-2.9
Max.	0.97	0.99	14.34	14.38	7.2
Mean	0.90	0.94	12.63	11.09	1.5

Emissivities are all from Salisbury and D'Aria (1992; 1994), unless marked (a), in which case they have been calculated from reflectance spectra of the sample, or (b) which is from Wiscombe and Warren (1980).

potentially increases from -8 °C (for a situation where  $\varepsilon_{MIR}=0.7$ ;  $\varepsilon_{TIR}=1.0$ ) to +21 °C ( $\varepsilon_{MIR}=1.0$ ;  $\varepsilon_{TIR}=0.7$ ). However, the terrestrial surfaces given in Table 5.1 have a narrower range of emissivities, and hence  $\Delta T$ , than the full range plotted in Figure 5.3, yielding a typical range of  $\Delta T$  of -3 °C to +7 °C. However,  $\Delta T$  of the order of 10 °C can still

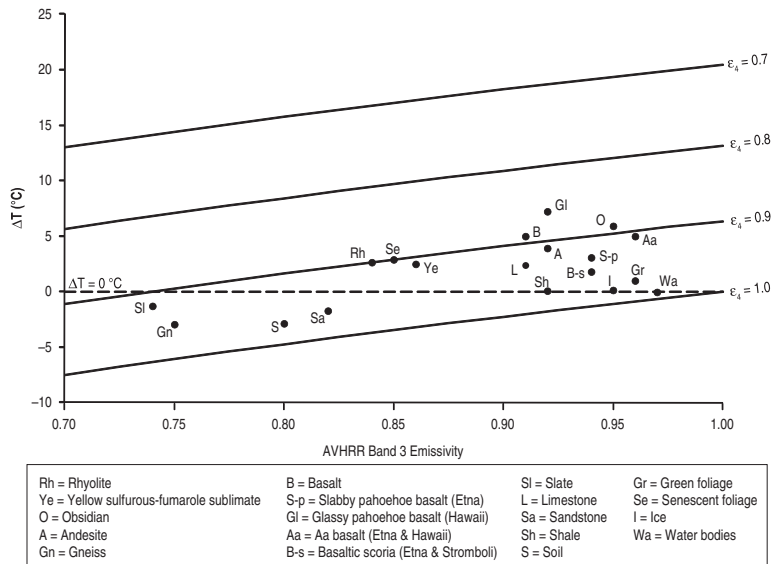


Figure 5.3 Effect of differential emissivity in AVHRR bands 3 ( $\varepsilon_3$ ) and 4 ( $\varepsilon_4$ ) on  $\Delta T$ . Non-unity emissivity will result in brightness temperatures that are different between the two wavebands, and will thus affect  $\Delta T$ . The effect on  $\Delta T$  is plotted using a blackbody temperature of 15 °C,  $\varepsilon_3$  in the range 0.7 to 1.0, and  $\varepsilon_4$  of 0.7, 0.8, 0.9 and 1.0. The effect of emissivity on  $\Delta T$  is also plotted for a number of typical volcanic and Earth surfaces (taken from Table 5.1).

be forced by emissivity, rather than hot spot, effects. This problem can be greatly reduced by correcting each pixel-integrated brightness temperature for the spectral emissivities appropriate for the surface contained within the pixel.

#### 5.2.4.3 Saturation problems

As described in Chapter 3, the sensor will be capable of recording only within a limited temperature range defined by the sensor's dynamic range. The upper limit of that range, i.e., the maximum recordable temperature, is termed *saturation*. At this temperature only one, fixed temperature (equal to the saturation temperature of the sensor) will be recorded, even though the size and temperature of the sub-pixel hot spot may mean that a much higher brightness temperature should be recorded. This effectively caps the brightness temperature at the saturation level. Because of the greater sensitivity of the MIR to sub-pixel hot spots, the MIR will usually saturate well before the TIR. As a result, as the hot spot size and/or temperature increases, the MIR will quickly become saturated and capped, but the TIR will remain unsaturated and will continue to record an increase in brightness temperature as the hot spot size increases. This effectively allows the brightness temperature in the TIR to gain on the brightness temperature in the MIR. This will begin to reduce  $\Delta T$  once the MIR saturation point has been reached.

We see this effect in [Figure 5.4](#). In the modeled case, the sub-pixel hot spot at 250 °C (against a background of 0 °C) attains a saturation temperature of 50 °C in the MIR once the hot spot attains a pixel fraction of ~0.009 (0.9%). At this point, the brightness temperature in the TIR is around 5 °C and  $\Delta T$  is ~45 °C. However, the MIR brightness temperature is now capped at 50 °C, but the TIR brightness temperature can continue to increase as the hot spot fraction increases. Thus  $\Delta T$  begins to fall away from its maximum recordable value of ~45 °C. Eventually a point is reached when the pixel-integrated temperature in the TIR has increased to 50 °C, so that it is equal to the MIR saturation temperature, at which point  $\Delta T$  declines to zero. For this model, this point is reached when the hot spot attains a pixel fraction of ~0.113 (11.3%). Because we use a TIR saturation temperature of 60 °C, the TIR pixel-integrated temperature can actually increase beyond this point, so that the pixel-integrated temperature in the TIR now exceeds that in the MIR, and  $\Delta T$  becomes negative, decreasing to a minimum recordable value of -10 °C, this being equal to the difference between the saturation temperature in the two wavebands. This point is reached when the hot spot attains a pixel fraction of ~0.142 (14.2%). Of course, if the saturation levels are higher, then the problem is reduced.

#### 5.2.4.4 Use of $\Delta T$ for detection

[Figure 5.5](#) shows the increase in  $\Delta T$  with pixel portion occupied by the hot spot for a range of hot spot temperatures. If we assume there is background variation (noise) in  $\Delta T$  of up to 10 °C (due to uncorrected differential atmospheric effects), then the pixel portion a sub-pixel hot spot at 250 °C, 500 °C and 1000 °C needs to attain in order to achieve our minimum detection requirement (i.e.,  $\Delta T > 10$  °C) is:

- $0.0008$ ,  $7.19 \times 10^{-5}$  and  $7.19 \times 10^{-6}$ .

This equates to the following lava areas in TM-class data:

- $0.73\text{ m}^2$ ,  $0.06\text{ m}^2$  and  $0.01\text{ m}^2$ .

For AVHRR-class data this increases to:

- $815\text{ m}^2$ ,  $70\text{ m}^2$  and  $10\text{ m}^2$ ,

and for GOES-class data to:

- $13\,040\text{ m}^2$ ,  $1151\text{ m}^2$  and  $155\text{ m}^2$ .

Comparison with the values given for the same model to allow detection in single SWIR, MIR or TIR bands given previously shows that (if  $\Delta T$  is not corrected adequately for atmospheric and emissivity effects) its ability to resolve a hot spot is about the same as if the MIR brightness temperature is used alone.

If we are able to correct our MIR and TIR data for differential reflection, atmospheric and emissivity effects, and have no saturation, then use of  $\Delta T$  should allow the hot spot to be detected as a bright point ( $\Delta T > 0$  °C) against a uniformly black background ( $\Delta T = 0$  °C). In reality, we may not be able to correct perfectly, and we see problems (i.e., non-zero

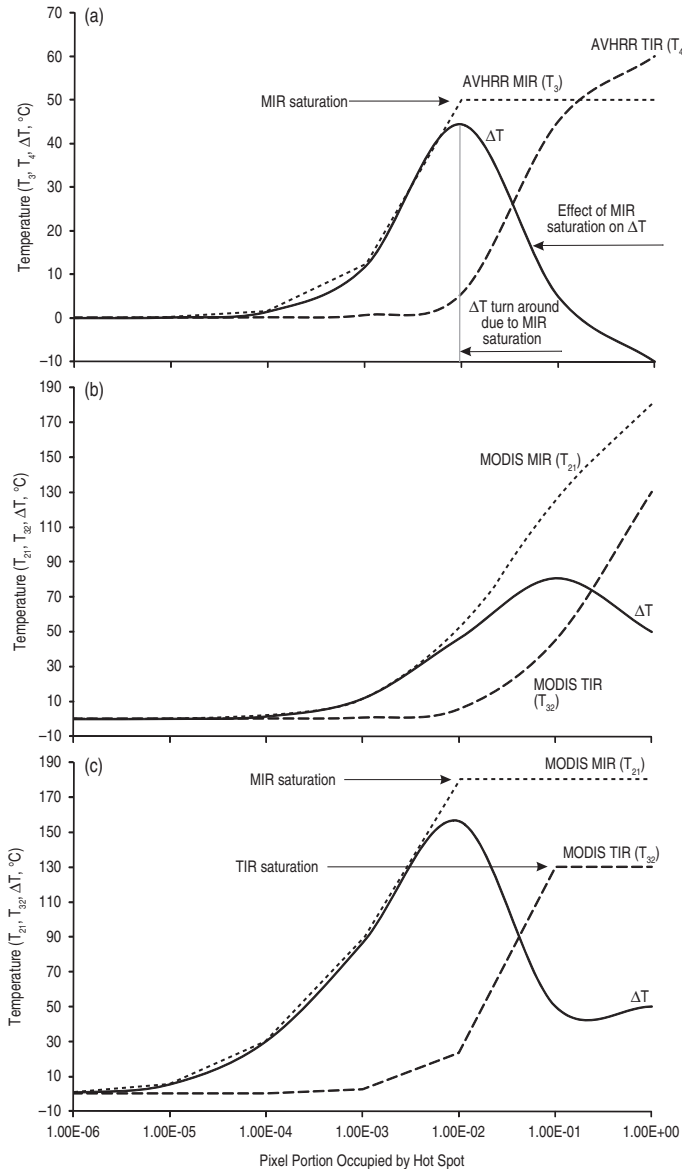


Figure 5.4 Effect of increasing sub-pixel hot spot size on pixel-integrated temperature recorded in (a) AVHRR's MIR (band 3,  $T_3$ ) and TIR (band 4,  $T_4$ ) bands, (b) MODIS' MIR (band 21,  $T_{21}$ ) and TIR (band 32,  $T_{32}$ ) bands. Modeled sub-pixel hot spot is at 250 °C against a background at 0 °C. (c) Same as (b) but for sub-pixel hot spot at 750 °C. In all cases, the resulting  $\Delta T$  is also given. The capping effect of saturation in AVHRR's MIR band is apparent in (a), as is the effect of saturating first MODIS' MIR band, and then the TIR band, in (c). In (b), the modeled hot spot is insufficiently hot or large to cause saturation. Note that, in (b), after a certain point the pixel-integrated temperature in the TIR begins to move towards that recorded in the MIR, a point marked by a turn around in  $\Delta T$ . Likewise, premature capping of the pixel-integrated temperature in the TIR, due to saturation, causes  $\Delta T$  to turn around, as marked on (a).

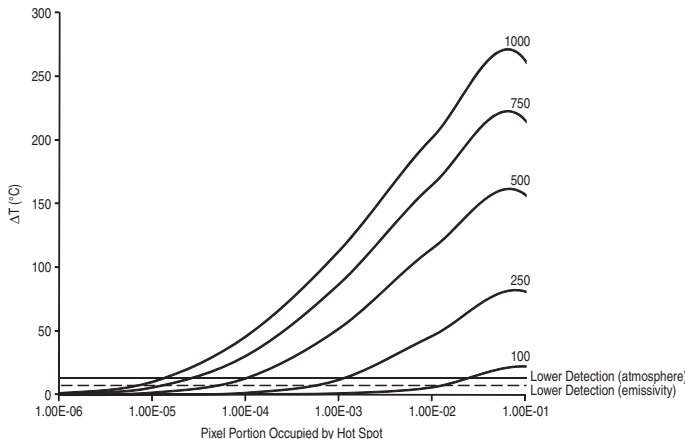


Figure 5.5 Change in  $\Delta T$  with hot spot size for a range of hot spot temperatures. The lower detection levels are defined by  $\Delta T$  levels potentially forced by atmospheric or emissivity effects. If brightness temperature is used, differential atmospheric effects can result in  $\Delta T$  of 13 °C; non-unity emissivity can cause  $\Delta T$  of 7 °C (see Figure 5.3; Table 5.1). Thus the hot spot has to force  $\Delta T$  to a higher point than these levels if it is to be resolved from the background  $\Delta T$  noise. If highly reflective surfaces, such as cloud, are present the problem will be worse, and  $\Delta T$  over “ambient” surfaces may reach 20 °C or 30 °C by day (21 °C is the maximum  $\Delta T$  recorded over cloud contaminated portions of Figure 5.2; 110 °C is the maximum recorded over the lava flow related hot spot).

$\Delta T$  values in the hot spot background) in the example given in Figure 5.2. However, as also seen in Figure 5.2, use of  $\Delta T$  allows us to confirm that a hot spot is present.

#### 5.2.4.5 A normalized $\Delta T$ index

A variant on  $\Delta T$  is the normalized thermal index ( $NTI$ ). This uses:

$$NTI = \frac{R_{MIR} - R_{TIR}}{R_{MIR} + R_{TIR}}, \quad (5.1)$$

in which  $R_{MIR}$  and  $R_{TIR}$  are the pixel spectral radiances in the MIR and TIR, respectively. It works on the same principle as the  $\Delta T$  approach, i.e., it uses the sensitivity difference between the MIR and TIR to a sub-pixel hot spot, but normalizes the result (following the lead of the normalized difference vegetation index) so that values are in the range -1.0 to +1.0. It is based on the principle that spectral radiances for surfaces at terrestrial temperatures are less in the MIR than in the TIR, but are greater in the MIR than in the TIR for high-temperature surfaces (see the Planck curves of Figure 2.1). It thus relies on the spectral radiance behavior defined by Wein’s Displacement Law (see Section 2.1.1 of Chapter 2). A surface with a temperature of -50 °C will have a point of peak emission at 13 μm. However, a surface at 1000 °C will experience peak emission at 2.3 μm. As a result, the Planck curve for the -50 °C surface will ascend between 2.3 μm and 13 μm, so that the spectral radiance in the MIR will be less than that in the TIR (i.e.,  $R_{MIR} < R_{TIR}$ ). In fact, the surface will have a

spectral radiant exitance of  $1.71 \times 10^4 \text{ W m}^{-2} \text{ m}^{-1}$  in AVHRR's MIR band (band 3), but  $6.62 \times 10^6 \text{ W m}^{-2} \text{ m}^{-1}$  in AVHRR's TIR band (band 4). Hence, for such a surface, we have a negative *NTI* with a value of

$$\begin{aligned} NTI &= \frac{1.71 \times 10^4 \text{ W m}^{-2} \text{ m}^{-1} - 6.62 \times 10^6 \text{ W m}^{-2} \text{ m}^{-1}}{1.71 \times 10^4 \text{ W m}^{-2} \text{ m}^{-1} + 6.62 \times 10^6 \text{ W m}^{-2} \text{ m}^{-1}} \\ &= \frac{-6.60 \times 10^6 \text{ W m}^{-2} \text{ m}^{-1}}{+6.64 \times 10^6 \text{ W m}^{-2} \text{ m}^{-1}} = -0.99. \end{aligned}$$

However, for a  $1000^\circ\text{C}$  surface the Planck curve will descend between  $2.3 \mu\text{m}$  and  $13 \mu\text{m}$ , so that the spectral radiant exitance in the MIR will be greater than that in the TIR (i.e.,  $R_{\text{MIR}} > R_{\text{TIR}}$ ). The surface at  $1000^\circ\text{C}$  will have a spectral radiant exitance of  $2.60 \times 10^{10} \text{ W m}^{-2} \text{ m}^{-1}$  in AVHRR's MIR band, and  $1.29 \times 10^9 \text{ W m}^{-2} \text{ m}^{-1}$  in AVHRR's TIR band, so that the *NTI* is now positive with a value of:

$$\begin{aligned} NTI &= \frac{2.60 \times 10^{10} \text{ W m}^{-2} \text{ m}^{-1} - 1.29 \times 10^9 \text{ W m}^{-2} \text{ m}^{-1}}{2.60 \times 10^{10} \text{ W m}^{-2} \text{ m}^{-1} + 1.29 \times 10^9 \text{ W m}^{-2} \text{ m}^{-1}} \\ &= \frac{+2.47 \times 10^{10} \text{ W m}^{-2} \text{ m}^{-1}}{+2.73 \times 10^{10} \text{ W m}^{-2} \text{ m}^{-1}} = +0.91. \end{aligned}$$

Thus, as we move from a cold surface to a hot surface, the *NTI* will move from  $-1.0$  to  $+1.0$ , as shown in [Figure 5.6a](#).

If we place a sub-pixel hot spot inside an otherwise cool pixel, as the size of the hot spot increases, so too will the pixel-integrated temperature. As a result, the difference between the spectral radiance recorded in the MIR and TIR will also change, forcing the *NTI* towards higher values. In [Figure 5.6b](#) we plot the increase in *NTI* with pixel portion occupied by the hot spot for a range of hot spot temperatures. If we assume an *NTI* threshold of  $-0.8$ , then the pixel portion a sub-pixel hot spot at  $250^\circ\text{C}$ ,  $500^\circ\text{C}$  and  $1000^\circ\text{C}$  needs to attain to achieve our minimum detection requirement (i.e.,  $NTI > -0.8$ ) is

- $0.0057$ ,  $5.08 \times 10^{-4}$  and  $6.83 \times 10^{-5}$ .

This equates to the following lava areas in TM-class data:

- $5 \text{ m}^2$ ,  $0.46 \text{ m}^2$  and  $0.06 \text{ m}^2$ .

For AVHRR-class data this increases to:

- $5750 \text{ m}^2$ ,  $510 \text{ m}^2$  and  $70 \text{ m}^2$ ,

and for GOES-class data to:

- $92\,000 \text{ m}^2$ ,  $8100 \text{ m}^2$  and  $1100 \text{ m}^2$ .

Comparison with the values given for the same model to allow detection using  $\Delta T$  shows that the ability of *NTI* to resolve a hot spot is actually poorer than using set  $\Delta T$  thresholds. However, this would improve if the *NTI* threshold was lowered. Lowering to an *NTI*

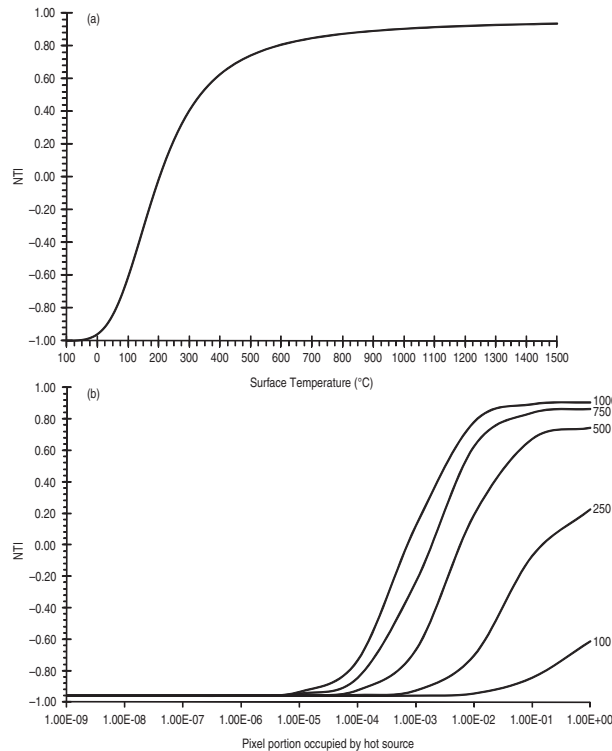


Figure 5.6 (a) Increase in  $NTI$  with surface temperature, and (b) with size of sub-pixel hot spot. Pixel mixture model for (b) assumes one of five hot spot temperatures (as marked) against a background at  $0\text{ }^{\circ}\text{C}$ .

threshold of  $-0.9$  reduces the pixel portion the hot spot at  $250\text{ }^{\circ}\text{C}$ ,  $500\text{ }^{\circ}\text{C}$  and  $1000\text{ }^{\circ}\text{C}$  needs to attain to:

- $0.0020$ ,  $1.78 \times 10^{-4}$  and  $4.01 \times 10^{-5}$ .

The size the hot spot needs to attain to be resolvable is still greater than in the  $\Delta T$  example, but it is an improvement.

### 5.2.5 Scatter plots and histograms

If the size and/or temperature of a sub-pixel hot spot is sufficient to elevate the pixel-integrated temperature for the hot spot pixel above that of its surroundings, then scatter plots and histograms of brightness temperatures,  $\Delta T$  and/or  $NTI$  recorded across the image are a good way of identifying and isolating thermally anomalous pixels. They are also an effective means of:

- (i) illustrating the main points of [Section 5.2](#) regarding use and the physical basis of  $T_{\text{MIR}}$ ,  $T_{\text{TIR}}$ ,  $\Delta T$  and  $NTI$ ;
- (ii) defining the resolving power of each parameter;
- (iii) identifying  $T_{\text{MIR}}$ ,  $T_{\text{TIR}}$ ,  $\Delta T$  and  $NTI$  values that distinguish ambient pixels from hot spot pixels; and hence
- (iv) setting thresholds required by the algorithm types of the following section.

#### 5.2.5.1 $T_{\text{MIR}}$ versus $T_{\text{TIR}}$

In [Figure 5.7a](#), we plot the pixel-integrated temperatures in the MIR ( $T_{\text{MIR}}$ ) and TIR ( $T_{\text{TIR}}$ ) for all pixels within a  $25 \times 23$  AVHRR sub-image centered on Mt. Etna and acquired on 24 December 1991. This image is given in [Appendix G](#). An active lava was present within the image, and was apparent from a 34-pixel thermal anomaly, with a particularly hot core of 14 pixels. In the scatter plot, the ambient pixels form a cluster of black plots with relatively low  $T_{\text{MIR}}$  and  $T_{\text{TIR}}$ . Hot spot pixels mostly have elevated  $T_{\text{MIR}}$ , and thus are apparent as a scatter of points above the ambient cluster (i.e., separated from the ambient cluster in the  $y$ -axis direction). Six points also have elevated  $T_{\text{TIR}}$ , and are thus apparent to the right of the ambient cluster (i.e., they are also separated from the ambient cluster in the  $x$ -axis direction). For this case, a  $T_{\text{MIR}}$  threshold equal to the maximum temperature within the ambient cluster ( $19^{\circ}\text{C}$ ) would isolate 19 of the 34 anomalous pixels, and all of the 14 hottest pixels. However, a  $T_{\text{TIR}}$  threshold set in the same way would only isolate six of the hottest pixels.

Another way of identifying such thermally anomalous “outliers,” and of setting appropriate thresholds, is by using the frequency distribution for the brightness temperatures within the image, or sub-image, as done in [Figure 5.8a](#) for the MIR waveband of this image, and in [Figure 5.8b](#) for the TIR waveband. Here we see that the thermally anomalous pixels are apparent as a low-frequency tail of high-temperature values. This is easily separated from the main distribution formed by the ambient pixels group, which forms a coherent distribution around a well-formed mode.

#### 5.2.5.2 $T_{\text{MIR}}$ versus $\Delta T$

In [Figure 5.7b](#), we plot the scatter for  $T_{\text{MIR}}$  versus  $\Delta T$  for the same image. The same  $T_{\text{MIR}}$  threshold will thus still apply. However, many more pixels are now separated from the ambient cluster in the  $\Delta T$  ( $x$ -axis) direction. For this case, a  $\Delta T$  threshold of  $6^{\circ}\text{C}$  isolates all but three of the anomalous pixels. Again, this separation is apparent from the frequency distribution of  $\Delta T$ , as given in [Figure 5.8c](#), where the anomalous pixels are marked by a series of low-frequency outliers at higher  $\Delta T$  values from the main cluster marking the ambient pixels.

#### 5.2.5.3 $T_{\text{MIR}}$ versus $NTI$

Plotting  $T_{\text{MIR}}$  versus  $NTI$ , as done in [Figure 5.7c](#), collapses the ambient cluster into a tight cloud within which  $NTI$  increases with  $T_{\text{MIR}}$ . This distribution lies along the trend,

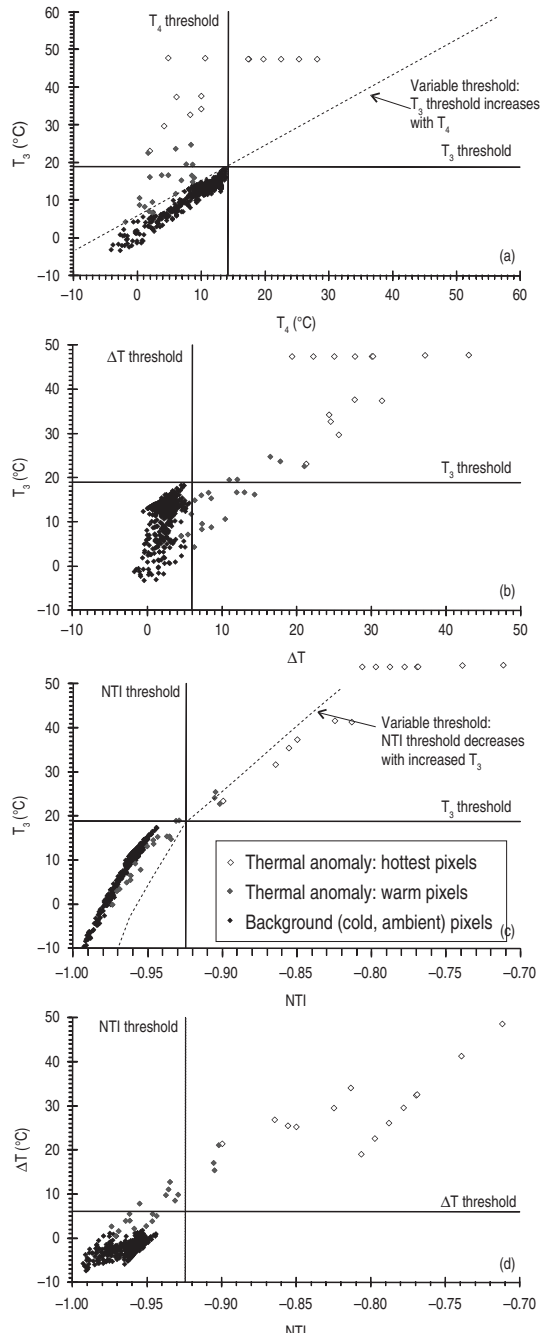


Figure 5.7 Scatter plots of AVHRR MIR (band 3) brightness temperature ( $T_3$ ), TIR (band 4) brightness temperature ( $T_4$ ),  $\Delta T$  and NTI taken from an image of Mt. Etna acquired on 24 December 1991. Image contains a hot spot due to active lava. Thermally anomalous and cold background pixels are identified (see key), and thresholds are set using the limits defined by the cloud of cold background pixels. Two types of threshold are marked: (i) fixed (flat line) thresholds, and (ii) thresholds which vary with  $T_3$ .

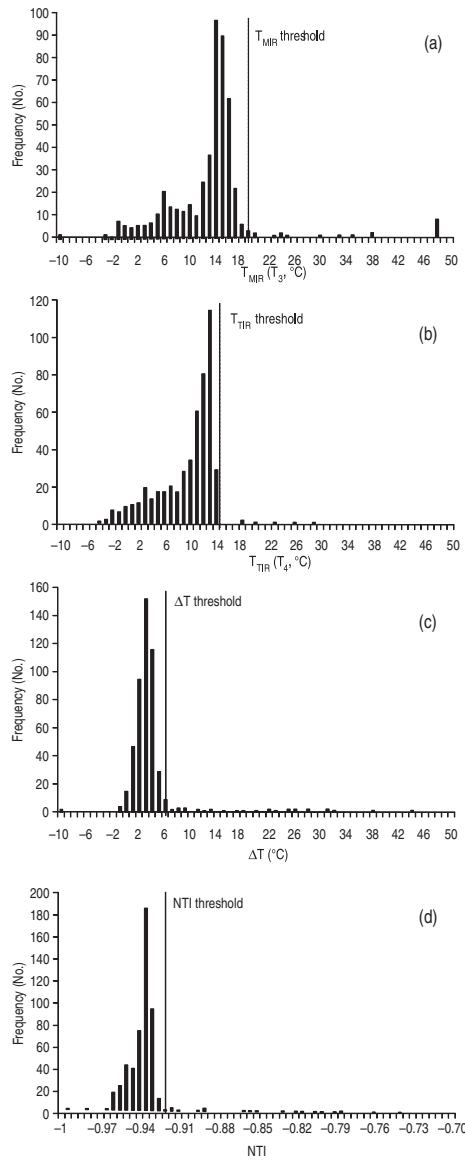


Figure 5.8 Histograms of AVHRR (a) MIR (band 3) brightness temperature ( $T_3$ ), (b) TIR (band 4) brightness temperature ( $T_4$ ), (c)  $\Delta T$  and (d) NTI taken from an image of Mt. Etna acquired on 24 December 1991. Image contains a hot spot due to active lava. The main body of the distribution defines the cold background pixels, so that thresholds can be set using the limits defined by the “cold pixel” distribution. Thermally anomalous pixels are apparent as up-axis outliers from this main body.

$$T_{\text{MIR}} = 544.06(NTI) + 523.61 \quad (R^2 = 0.97).$$

Hot spot pixels fall along a second trend defined by

$$T_{\text{MIR}} = 233.26(NTI) + 230.78 \quad (R^2 = 0.96).$$

Using the maximum  $NTI$  value from the ambient cluster we can set an  $NTI$  threshold for this image of  $-0.925$ , which can also be identified from the frequency distribution of  $NTI$  in [Figure 5.8d](#). Taking all pixels with an  $NTI$  greater than this value isolates 22 of the 34 anomalous pixels, and all of the hottest pixels. However, we also see that  $NTI$  points for anomalous pixels do fall out of the ambient cloud, at values less than  $-0.925$ , being lifted slightly out of the ambient cloud in the up- $x$ -axis ( $NTI$ ) direction. Thus, a threshold that varies the  $NTI$  threshold as a function of  $T_{\text{MIR}}$ , as marked on [Figure 5.7c](#), would stand a chance of isolating all anomalous pixels. For example, using a  $NTI$  threshold of  $-0.94$  for pixels with  $T_{\text{MIR}}$  in the range  $8.4\text{--}9.6\text{ }^{\circ}\text{C}$  would isolate the three anomalous pixels apparent in this temperature range, but not trapped by the  $NTI > -0.925$  condition.

#### 5.2.5.4 $NTI$ versus $\Delta T$

In the scatter plot of  $NTI$  versus  $\Delta T$ , given in [Figure 5.7d](#), we see that our  $\Delta T$  threshold (of  $6\text{ }^{\circ}\text{C}$  for this image) is capable of identifying more anomalous pixels than an  $NTI$  threshold of  $-0.8$ . While the  $\Delta T$  threshold identifies 31 (91%) of the 34 anomalous pixels, the  $NTI$  threshold identifies just five (15%). However, decreasing the  $NTI$  threshold to  $-0.925$  (set using the  $NTI$  frequency distribution for this image given in [Figure 5.8d](#)) increases the number of detected pixels to 22 (65%). In comparison, the  $T_{\text{MIR}}$  and  $T_{\text{TIR}}$  thresholds identified 19 (56%) and 6 (18%) of the anomalous pixels, respectively.

#### 5.2.5.5 Fixed thresholds

In terms of resolving power for this image, use of a  $\Delta T$  threshold would therefore be the most effective approach, followed by fixed thresholds set using  $NTI$ ,  $T_{\text{MIR}}$  and  $T_{\text{TIR}}$ . However, different thermal conditions experienced by different images, acquired (for example) under different solar heating or cloud conditions, or acquired at different times of the day or year, would mean that such a fixed threshold will likely fail on another image, or when applied to a different location. Setting a threshold that works for all images, obtained from all locations at all times, is the challenge of, and problem facing, the designers of automated hot spot detection algorithms.

### 5.3 Automated hot spot detection algorithms

As argued at the outset of this chapter, automated detection of volcanic hot spots in satellite data potentially serves as an early warning for the onset of volcanic effusive (and sometimes also explosive) eruptions. Efforts to develop, test and implement algorithms capable of such

a role have thus been one theme in thermal remote sensing of volcanic hot spots. Efforts to develop such algorithms were reported in 16 (13%) of the 120 papers collated in the [Appendix A](#) data base. Such efforts have been especially important in operational settings where activity at many volcanoes needs to be tracked, but where sites are poorly instrumented or unobserved from the ground, as is the case across the Alaskan, Aleutian and Kamchatkan volcanoes that underlie major air traffic routes between the United States and Japan. Hence, design and implementation of such automated hot spot and plume tracking algorithms has been a major emphasis at the Alaska Volcano Observatory since the mid-1990s.

However, it was the fire community that realized the hot spot detection capability of thermal infrared sensors flown on satellite platforms well before the volcanological community. Algorithms to allow timely detection of wild fires using data from sensors flown on polar orbiting and geostationary platforms were developed from the mid-1980s onwards. The first automated detection algorithm developed by the fire community was that of Flannigan and Vonder Haar ([1986](#)), and by the time of the 1994 publication of the working paper of the International Geosphere Biosphere Programme (IGBP), entitled “IGBP-DIS Satellite Fire Detection Algorithm Workshop Technical Report” ([Justice and Dowty, 1994](#)), eight different fire detection algorithms designed to work with AVHRR or GOES-VAS data could be detailed. A review of progress made by the fire community in developing automated detection algorithms over the decade spanning 1985 to 1995 is given in [Table 5.2](#), where we see that, by 1995, 11 different algorithms had been developed to allow fire detection in both AVHRR- and GOES-class data from local to regional scales.

The first volcano hot spot detection algorithm (VAST) was published in 1995 ([Harris \*et al.\*, 1995a](#)), by which time at least 14 studies had addressed fire detection issues in satellite data. Over the following decade, though, 15 studies were published presenting new, or modified versions of, algorithms to detect hot spots in satellite data due to volcanic activity (see [Appendix A](#)). Like the fire-detection algorithms, many of the automated volcano hot spot detection algorithms were also equipped with cloud-screening, atmospheric correction and parameter extraction routines, allowing the parameter extractions and conversions of [Chapter 4](#) to be executed, and the time series of [Chapter 6](#), to be constructed in an efficient manner.

Steffke and Harris ([2011](#)) provide a review, classification and appraisal of algorithms designed for volcano hot spot detection. They split the algorithms used by the fire and volcanological community into three classes depending on whether the algorithm defines a hot spot, as follows.

- (i) *Spatial context* (contextual algorithms). In other words, is the pixel brightness significantly different from that of its surrounding pixels? This class of algorithms assesses whether a pixel is thermally anomalous in a spatial sense. The parental algorithm (i.e., the first algorithm to be tested specifically for volcano hot spot detection) for this class was the VAST algorithm of [Harris \*et al.\* \(1995a\)](#).
- (ii) *Temporal context* (temporal algorithms). In other words, is the pixel brightness significantly different from that of its preceding history? Thus, this class of algorithms assesses

Table 5.2. Automated fire detection algorithms published in peer-reviewed literature between 1985 and 1995. Algorithms are listed in chronological order of publication.

Study	Algorithm type	Tests executed	Data type (Application region)
Flannigan & Vonder Haar (1986)	Contextual	See Electronic Supplement 8	AVHRR (Forest fires – Canada)
Kaufman <i>et al.</i> (1990) <sup>a</sup>	Fixed (generic)	$T_{\text{MIR}} \geq 316 \text{ K}$ $\Delta T > 10 \text{ K}$ $T_{\text{TIR}} > 250 \text{ K}$ (cloud test)	AVHRR (Fires – Brazil)
Lee and Tag (1990)	Contextual	See Electronic Supplement 8	AVHRR (Wild fires – Yellowstone) (Gas flares – Persian Gulf) (Structure fires – California)
Setzer and Pereira (1991) <sup>b</sup>	Fixed (generic)	$T_{\text{MIR}} > 319 \text{ K}$ Plus: manual detection of smoke	AVHRR (Fires – Brazil)
Brustet <i>et al.</i> (1991)	Fixed (specific)	MIR and TIR thresholds set manually on a case-by-case basis using frequency distributions and $T_{\text{TIR}}$ versus $T_{\text{MIR}}$ scatter plots.	AVHRR (Wild fires – West Africa)
Kennedy <i>et al.</i> (1994)	Fixed (generic)	$T_{\text{MIR}} > 320 \text{ K}$ $\Delta T > 15 \text{ K}$ $T_{\text{TIR}} > 250 \text{ K}$ (cloud test) and/or $R_{\text{NIR}} < 16 \%$ (cloud test)	AVHRR (Wild fires – West Africa)
Langaas (1993)	Contextual	See Electronic Supplement 8	AVHRR (Wild fires – West Africa)
Chuvieco and Martin (1994)	Fixed (generic)	$T_{\text{MIR}} > 317 \text{ K}$ (day) $T_{\text{MIR}} > 295 \text{ K}$ (night) (applied only within forest mask to reject false detections due to solar heated soil, which could approach saturation).	AVHRR (Forest fires – Spain)

Prins and Menzel (1994)	Contextual	See Electronic Supplement 8	GOES-VAS (Burning – S. America)
Arino and Melinotte (1995)	Fixed (generic)	$T_{\text{MIR}} > 320 \text{ K}$ (saturation test); $T_{\text{MIR}} > T_{\text{TIR}} + 15$ ; $T_{\text{TIR}} > 245 \text{ K}$ (cloud test); $R_{\text{VIS}} < 25\%$ (reflection test); $R_{\text{VIS}} - R_{\text{NIR}} > 1\%$ (sunglint test).	AVHRR (Fires – Africa)
Franca <i>et al.</i> (1995)	Fixed (generic)	$T_{\text{MIR}} > 320 \text{ K}$ $\Delta T > 15 \text{ K}$ $T_{\text{TIR}} > 287 \text{ K}$ $0 \leq T_{10\mu\text{m}} - T_{12\mu\text{m}} \geq 5 \text{ K}$ $R_{\text{VIS}} < 9\%$	AVHRR (Wild fires – West Africa)

<sup>a</sup> The algorithm was also applied for fire detection in AVHRR data for West Africa by Kennedy *et al.* (1994).

<sup>b</sup> Another algorithm was published with a similar basis, but using DN criteria (fire if DN < 10 or 8, i.e., if DN are close to AVHRR saturation), by Pereira and Setzer (1993).

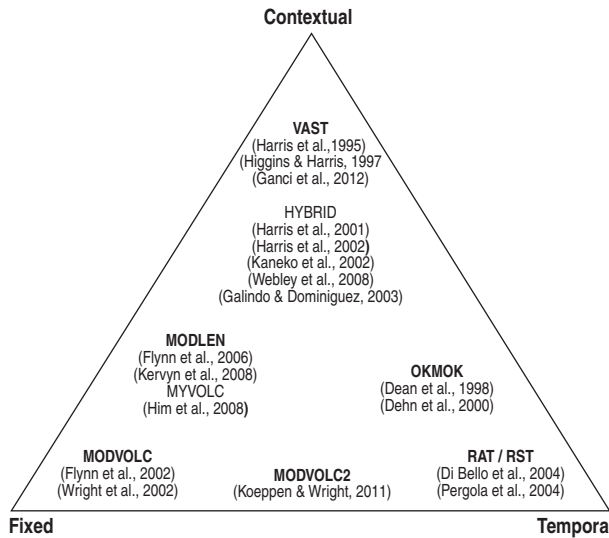


Figure 5.9 Ternary classification of algorithms used to detect volcanic hot spots of Steffke and Harris (2011) [with kind permission from Springer Science and Business Media].

whether a pixel is thermally anomalous in a temporal sense. The parental volcano hot spot detection algorithm for this class was the RAT algorithm of Tramutoli (1998).

- (iii) *Spectral character* (fixed threshold algorithms). That is, does the pixel have spectral properties, i.e., a sufficiently high brightness temperature,  $\Delta T$  and/or  $NTI$ , to define it as hot? This class of algorithms tends to apply single or multiple, but essentially fixed, thresholds to determine whether a pixel is hot or not. The parental volcano hot spot detection algorithm within this class was the MODVOLC algorithm of Wright *et al.* (2002a).

By placing each algorithm into one of these three classes, the ternary classification of Figure 5.9 can be drawn up. In this classification we see that a number of hybrid algorithms also exist which combine elements of the contextual, fixed and temporal approaches, and thereby fall between the points of the triangle defined by each of the three end-member classes. As argued by Steffke and Harris (2011), each of these algorithms operates in a different way, have differing strengths and weaknesses, and may be applied (or adapted) depending on the requirements of the user. Each algorithm has been shown to serve a purpose either in an operational monitoring environment, or by efficiently allowing extraction of time series data for analysis of thermal trends, in a research environment.

#### 5.3.0.1 A note on fire detection algorithms

Because detection algorithm developments by the fire community pre-dated those of the volcanological community by ten years, many of the advances on which the volcanological algorithms are based were made in the fire community. Thus, our review and examination

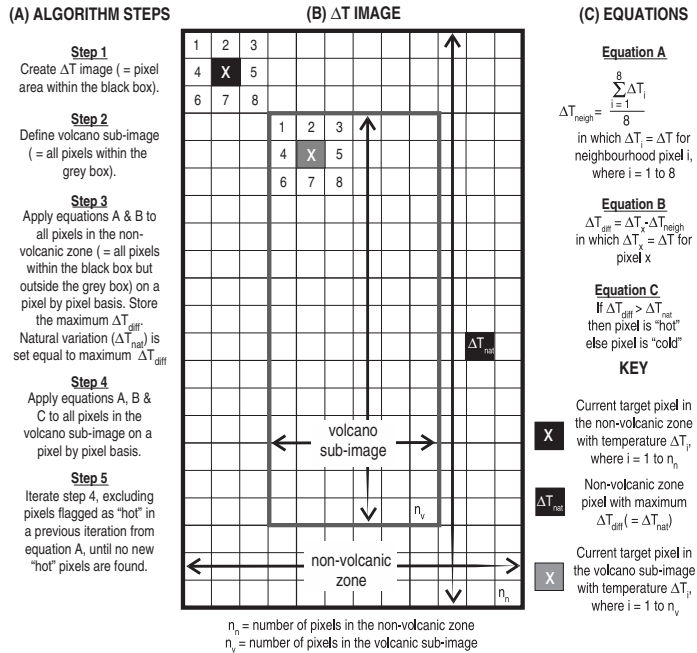


Figure 5.10 Schematic summarizing implementation of the VAST hot spot detection algorithm [from Higgins and Harris (1997, Fig. 3): with permission from Elsevier].

must, by necessity, include consideration of fire, as well as volcano, hot spot detection algorithms, for the two are intimately linked and many ideas from the fire community have pollinated the volcanological community, and vice versa. A review of the main fire detection algorithms of 1985–1995 is given in Electronic Supplement 8.

### 5.3.1 Contextual algorithms

Contextual algorithms apply tests that assess whether or not a pixel is anomalous in a spectral and spatial sense using thresholds set from thermal and brightness statistics obtained from the immediate background of a target pixel. Typically, the background is defined by the eight pixels surrounding a central target pixel, as in Figure 5.10. Next, a number of spectral parameters are defined and used to test whether the central pixel is anomalous or not. Six algorithms developed by the fire community between 1985 and 1996 introduced increasingly sophisticated contextual tests, thereby defining the essential elements for a contextual hot spot detection algorithm. A consideration of these six algorithms is given in Electronic Supplement 8, which provides a good grounding as to (i) the contextual parameters that can be used to test a target pixel for anomalous signal, and (ii) how these parameters can most effectively be defined and calculated.

Given the philosophy of the contextual algorithm, calculation of the spectral levels used to assess whether a pixel is anomalous or not is carried out on an image-to-image, and sometimes pixel-to-pixel, basis so that thresholds are set appropriate for an individual pixel's immediate thermal setting. That is, the thresholds are different for every pixel in every image, being defined on the basis of the pixel's current (and local) thermal background.

### 5.3.1.1 VAST

Influenced by advances made in the fire community, VAST was an automated contextual algorithm designed for local (site-specific) volcano hot spot detection. Its initial version was reported by Harris *et al.* (1995a). It was initially tested using AVHRR images for Etna's 1991–1993 eruption, and later also using AVHRR data for wild fires burning around Sydney during January 1994 by Harris *et al.* (1996). It introduced the concept of “*natural variation*.” This was defined as the difference between a pixel's brightness temperature, or  $\Delta T$ , and that of its surroundings – as defined by the eight pixels immediately surrounding the target pixel. Over thermally homogeneous surfaces, such as the sea, natural variation should be close to zero. However, over thermally heterogeneous surfaces, such as snow covered volcanoes with active lava flow fields, the natural variation should be highly variable. We see this in the example given in Appendix G, where natural variation around the hot spot is of the order of 10 °C, with a maximum of 24 °C, whereas away from the hot spot it typically ranges between −0.02 and +0.01 °C. The VAST algorithm involved the following ten steps and two tests, as summarized in Figure 5.10.

- Step 1. To minimize processing time a sub-image centered on the volcano of interest was extracted. For Etna, 50 × 50 pixel AVHRR sub-images centered at 37.37° N, 15.00° E were sufficient to cover the entire 32 km by 43 km volcano, although 25 × 24 pixel sub-images were also used.
- Step 2. Band 1 and 2 spectral radiances were converted to albedo ( $A_1$  and  $A_2$ ), and band 3 and 4 radiances to brightness temperature ( $T_3$  and  $T_4$ ).
- Step 3. Cloud masking was next completed, where a simple test following Saunders and Kriebel (1988) was applied to day-time images in which pixels were flagged as cloud contaminated if  $A_2/A_1 > 1.6$ .
- Step 4. A  $\Delta T (= T_3 - T_4)$  image was created, using cloud-free pixels to estimate the “natural variation” for each pixel. Natural variation ( $\varpi$ ) was defined as the difference between the  $\Delta T$  of each central pixel and the mean of the eight pixels in a 3 × 3 pixel box surrounding that pixel.
- Step 5. An image-specific natural variation threshold ( $\varpi_{\text{thresh}}$ ) was set from the “non-volcanic” portion of the sub-image. The non-volcanic portion was defined by a three-to-five pixel wide zone around the edge of the sub-image, and  $\varpi_{\text{thresh}}$  was set equal to the maximum  $\varpi$  found within this zone.
- Step 6. The “volcano” portion of the sub-image was defined. Given a 5 × 5 pixel “non-volcanic” zone around a 25 × 25 pixel sub-image, this comprised the central 20 × 20 pixel zone (see Figure 5.10). Anomalously cold sensor recovery pixels in the “volcano” portion of the sub-image were also masked in this step.

- Step 7. The following test was now applied to each pixel in the volcano portion of the sub-image.
- Test 1. If pixel  $\varpi > \varpi_{\text{thresh}}$ , then flag as anomalous.
- Step 8. Because saturated pixels in the MIR may have  $\Delta T$  that are low due to “capping” effects (see [Section 5.2.4](#)) any pixel that was (i) saturated in band 3, and (ii) adjacent to a pixel flagged as anomalous in this first run was also flagged as anomalous.
- Step 9. For pixels at the center of a large anomaly with high  $\Delta T$   $\varpi$  might be quite low due to all surrounding  $\Delta T$  also being high. Also, moderately hot pixels at the periphery of the anomaly may have  $\varpi$  which are low, or even strongly negative, due to the presence of even hotter pixels in the target pixels background. Thus, a final test was added whereby:
- (i) anomalous pixels located in the first run were masked,
  - (ii)  $\varpi$  for each pixel was recalculated excluding any masked pixels, and
  - (iii) the test was re-run.
- Step 10. Step 9 was iterated until no new pixels were found.

By way of illustration, these steps are carried out on the example image given in [Appendix G](#). The algorithm was later developed into the VAST (Volcanic Anomaly SoftWare) code of Higgins and Harris (1997). This was written in ANSI C and made generally available through download from the *Computers & Geosciences* website.

#### 5.3.1.2 Correlation-based approaches

The correlation approach of Wright *et al.* (2002b) carried out a contextual test, that correlated the spectral radiance of a pixel with that of its background. Tested using GOES data for Popocatépetl, selection of anomalous pixels was based on the assumption that two ambient pixels in the same region should heat up and cool down in a similar way during any 24 hour period, as shown in [Figure 5.11a](#). Hence the spectral radiances for the two pixels should be well correlated. However, if a hot spot is introduced into one of the two pixels, the thermal behavior of the hot spot pixel will diverge from the steady diurnal heating and cooling behavior of the background, as shown in [Figure 5.11b](#). Hence the spectral radiances for the two pixels should now be poorly correlated. Under cloudy conditions, the smooth cyclic heating and cooling pattern will be lost, but in the absence of a hot spot the thermal behavior of two adjacent pixels should still be well correlated, as shown in [Figure 5.11c](#). Thus, the correlation between a target pixel and its background should be a valid tool for hot spot detection, where lack of correlation will be indicative of the presence of a hot spot. We see this in [Figure 5.11d](#), where the correlation between the Popocatépetl target pixel and its background breaks down during a period of lava dome extrusion.

For detection purposes the methodology of Wright *et al.* (2002b) can be best set up as follows.

- Step 1. Define a  $10 \times 10$  pixel box centered on the target volcano.
- Step 2. Extract the peak MIR radiance value ( $P_r$ ), and calculate the mean MIR for all pixels within the box. The latter value is used to characterize the background radiance ( $B_r$ ).

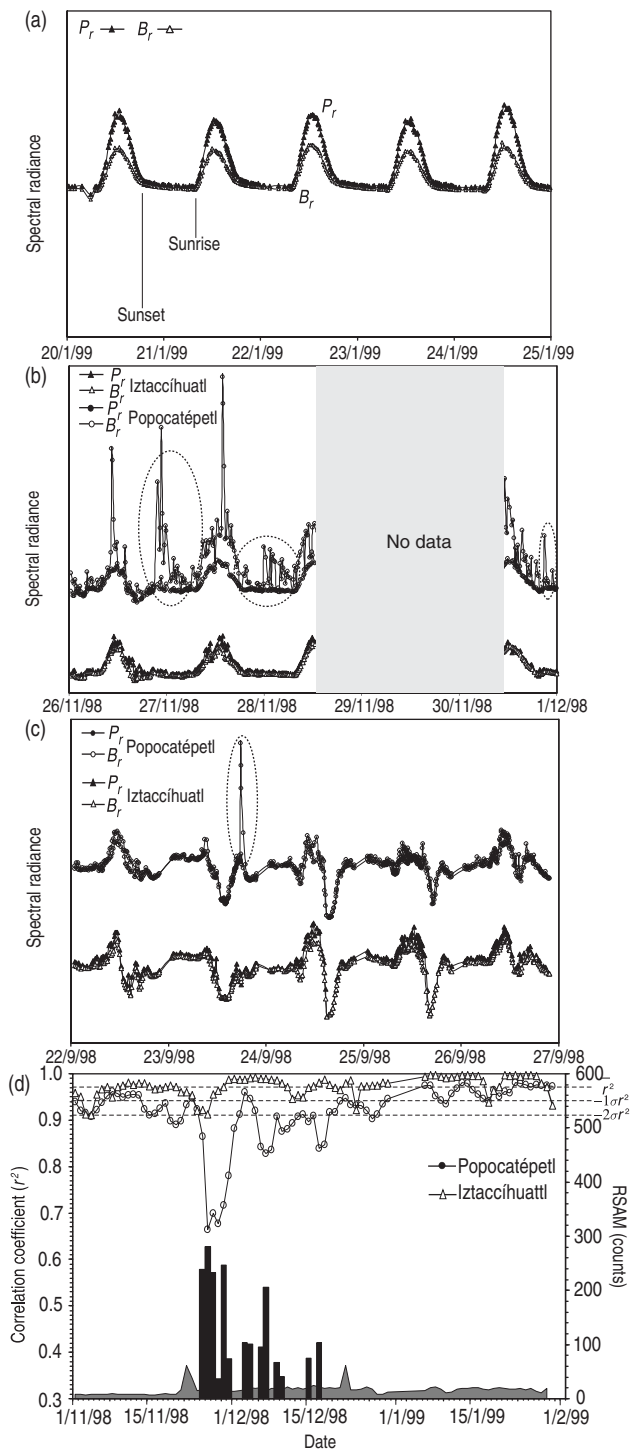


Figure 5.11 (a) Diurnal variation in spectral radiance recorded in the GOES MIR band (band 2) under cloud-free, and hot spot-free, conditions at Popocatépetl:  $P_r$  is the radiance for the hottest pixel from a  $10 \times 10$  pixel box centered on the summit of Popocatépetl and  $B_r$  is the mean radiance for all pixels in the same box. (b) Introduction of a hot spot into the box (in this case due to emplacement of a lava

Step 3. Calculate the correction ( $r^2$ ) coefficient between  $P_r$  and  $B_r$ .

Step 4. If  $r^2$  diverges by more than two standard deviations from the mean, then the pixel where the peak radiance is recorded likely contains a hot spot.

As pointed out by Wright *et al.* (2002b), variation in  $r^2$  due to ambient causes can also cause this threshold to be exceeded. Wright *et al.* (2002b) thus also considered the correlation between the peak and background radiances for an ambient test box, this being a  $10 \times 10$  pixel box centered on the nearby summit of Iztaccíhuatl, a volcano with a similar elevation to Popocatépetl but which is inactive. In Figure 5.11d, we see that  $r^2$  for Iztaccíhuatl is coupled with that recorded at Popocatépetl during all times, except when activity occurs at Popocatépetl. Thus a final step should be as follows.

Step 5. Compare the  $r^2$  trend at the target site with that recorded for an ambient test site.

Such a process was executed successfully by Piscopo (2010) to identify subtle hot spots on Stromboli in MODIS data. In this case the peak radiance from a region of interest centered on Stromboli was correlated with that from a region of interest centered on the nearby island of Salina, an inactive volcanic island with roughly the same altitude as Stromboli. To an extent this correlation-based contextual method also uses temporal information, and so begins to move towards a hybrid algorithm that uses both contextual and temporal information. We next consider such temporally based algorithms.

### 5.3.2 Temporal algorithms

If sufficient data are available, images can be stacked up and the statistics (notably the mean and standard deviation spectral radiance or brightness temperature for each pixel) defined. Once defined, these statistics can be evaluated to assess whether pixels in new images are thermally similar to their previous history or not. If they are significantly different from the thermal norm, in a positive direction, then they are thermally anomalous.

---

Caption for Figure 5.11 (cont.)

dome) causes the smooth diurnal variation in  $P_r$  to break down (as circled). However, the  $B_r$  trend, as well as those for  $P_r$  and  $B_r$  recorded for a  $10 \times 10$  pixel box centered on the summit of the neighboring (inactive) volcano (Iztaccíhuatl), remain smoothly oscillating. (c) The same values plotted during cloudy conditions show that, although the diurnal variation is lost in the  $P_r$  and  $B_r$  trends for both Popocatépetl and Iztaccíhuatl, the  $P_r$  and  $B_r$  values remain coupled, except during an explosive event that deposits a hot spatter field within the Popocatépetl summit pixel (as circled). (d) Comparison of real-time seismic amplitude measurements and the  $r^2$  correlation between  $P_r$  and  $B_r$  for Popocatépetl. While the gray curve gives the RSAM daily average for Popocatépetl, vertical bars give the total amount of seismic energy recorded per day. Three clusters of hot spot activity are apparent as marked by periods when the  $r^2$  value diverges by more than two standard deviations from the mean for the period; each of which coincide with peaks in the seismic measurements [from Wright *et al.* (2002b, Figs. 5, 6, 8 and 16a): reproduced by permission of American Geophysical Union].

### 5.3.2.1 Okmok

The Okmok algorithm developed at the Alaska Volcano Observatory to aid with operational hot spot detection in AVHRR data is a good example of the temporal approach. By comparing the typical surface temperature for the regional background with the maximum temperature obtained from an analysis box centered over an active volcano, the Okmok algorithm provided a graphical assessment of the thermal state of the volcano. As shown in the example taken from Dehn *et al.* (2000) and given in Figure 5.12, divergences between the regional background and local (volcano) maxima are excellent indicators of new, increased, or on-going thermal activity. Annual variations in ambient heating will cause the pixel-integrated temperature for the region to wax and wane through the year, with some noise resulting from differences in cloud cover from day to day which affects the actual level of heating during any day. Arrival of a hot spot causes the pixel brightness temperature to diverge from the steady (annual) heating and cooling trend. Thus thermally anomalous pixels can be isolated because they exceed the typical ambient temperature range defined for any given location on any particular day.

### 5.3.2.2 RAT

Parallel with these efforts, a body of hot spot detection work evolved around the “Robust AVHRR Techniques,” or RAT algorithm, for thermal change detection. Also called the “robust approach” (e.g., Tramutoli *et al.*, 2001), it being “robust in a statistical sense” (Tramutoli, 1998), it was developed at the Universita della Basilicata (Italy) beginning in the late 1990s. Initially proposed by Tramutoli (1998) at the EUROPTO conference on Remote Sensing for Geology during September 1998, the algorithm used time series of satellite TIR and MIR data to define the normal temperature conditions (in terms of diurnal and seasonal ambient heating) for a pixel. The normal condition statistics were then used to assess divergence from normal behavior, where one cause of divergence would be the development of a sub-pixel hot spot due to active lava or fire activity (Tramutoli, 1998). Its use for detecting volcanic ash plumes at Etna, as well as its potential for detecting thermal anomalies associated with earthquakes in southern Italy, was later demonstrated by Pergola *et al.* (2001) and Tramutoli *et al.* (2001), who both tested the algorithm using the 1979–1998 archive of AVHRR data held by the University of Dundee (Scotland). Application of RAT for detection of volcanic hot spots was first demonstrated by Di Bello *et al.* (2004), who demonstrated the algorithm results for a 13 July 2001 scene of Mt. Etna. In this image, hot pixels due to lava flow activity at the summit were detected, as well as a lower intensity anomaly within which an effusive fissure opened four days later. Subsequently Pergola *et al.* (2004a; 2004b) presented the results from running RAT for hot spot and plume detection at Etna. Referred to as RAT through 2006, e.g., by Filizzola *et al.* (2004) and Lacava *et al.* (2006), Pergola *et al.* (2008; 2009) began to use the label Robust Satellite Technique (RST) for the same algorithm around 2008. Mostly, the algorithm’s use for data beyond that supplied by AVHRR (e.g., MODIS and SEVIRI, as well as microwave) made

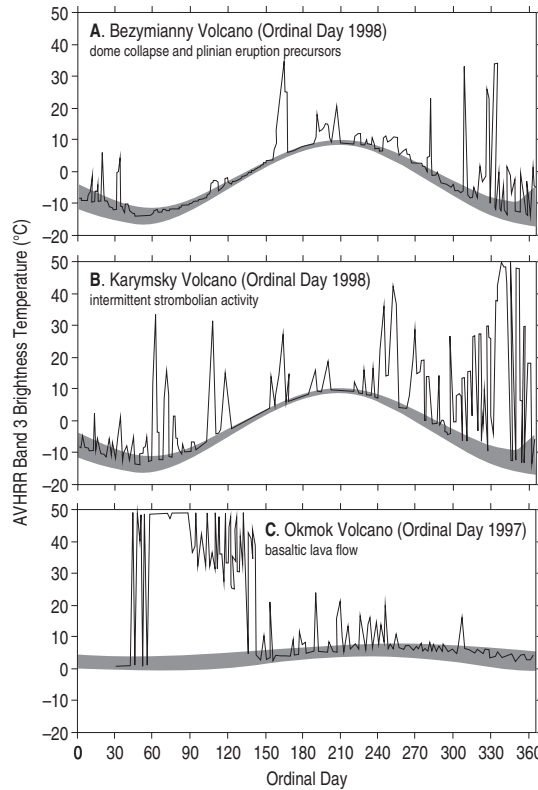


Figure 5.12 Okmok algorithm as applied to three volcanoes. AVHRR band 3 brightness temperatures are plotted. To remove solar reflection effects, only night-time images were used; temperatures below  $-20^{\circ}\text{C}$  were also removed to limit the effect of cold clouds over the region. The range of temperatures for the regional background of each volcano is plotted as a gray band, which shows annual heating and cooling. The maximum brightness temperature recorded at each volcano is plotted in black, where positive spikes that exceed the background range are defined as volcanic thermal anomalies. At Bezymianny, anomalies were associated with lava dome extrusion and plinian explosions (as marked by intermittent spikes). At Karymsky, anomalies were associated with constant strombolian activity, resulting in regular thermal spikes. At Okmok, lava flow effusion rapidly saturated the sensor. Such time series are explained more fully in Chapter 6 [from Dehn *et al.* (2000, Fig. 3)].

use of a new generic title more suitable. However, we here keep with the more commonly used RAT acronym.

RAT relies on a data archive of MIR data to create an Absolutely Local Index of Change of Environment [*ALICE* ( $x,y,t$ )]. This provides an estimate of how much a pixel brightness temperature diverges from its normal conditions as determined from the data time series, normalized by its natural variability in the time domain. *ALICE* can be mathematically defined as (Tramutoli, 1998):

$$ALICE(x, y, t) = [V(x, y, t) - V_{\text{REF}}(x, y)] / [\sigma_V(x, y)], \quad (5.2)$$

in which

$V(x, y, t)$  = brightness temperature recorded by the satellite sensor at location  $(x, y)$  and time  $t$ ;

$V_{\text{REF}}(x, y)$  = mean brightness temperature for the same location and time;

$\sigma_V(x, y)$  = standard deviation in brightness temperature for the same location and time.

A pixel can now be assessed as being anomalous depending on whether  $ALICE$  is greater than a certain value or not. Choosing a value for the  $ALICE$  threshold corresponds to the number of standard deviations away from the mean that a value needs to be in order to be considered anomalous. Thresholds of 2.0, 2.6 and 3.0, for example, will correspond to statistical confidences of 95.4%, 99.0% and 99.7% that the value is outside of the normal distribution of radiances for the given location and time. The algorithm can thus be executed by implementing the following seven steps.

- Step 1. Select the region of interest.
- Step 2. Radiometrically calibrate and precisely geo-locate the data (cloud masking may also be carried out).
- Step 3. Use an “events mask” to remove outliers associated with thermal anomalies in the reference data set.
- Step 4. Define the reference fields, i.e., define the mean and standard deviation for each pixel in the time domain. This can be calculated from a time series of images acquired during the same time of day from, for example, a month of data.
- Step 5. Take the image to be analyzed, and apply Equation (5.2), using the reference fields for the appropriate time of day and year, to calculate  $ALICE$ .
- Step 6. Assess whether  $ALICE$  is greater than the user-defined standard deviation.
- Step 7. If the final case is met, flag the pixel as thermally anomalous.

#### 5.3.2.3 Yuhaniz and Vladimirova (2009)

Yuhaniz and Vladimirova (2009) proposed a method whereby pixel radiances across an image area can be compared with those from the same area in a reference image to determine whether a change has occurred or not. Although, as yet, untested for volcano hot spot scenarios, the method offers a means of applying a temporally based threshold, on the basis of a temporal change in the spectral properties of a pixel, using just two (rather than a time series of) images.

Yuhaniz and Vladimirova (2009) proposed the use of correlation coefficients and differences in means in the radiances between a pair of images to allow an “onboard automatic change detection system for disaster monitoring.” The method, designed for rapid, onboard processing and download of data tiles in which a change was detected, was specifically aimed at efficient tasking of small Earth Observing (EO) satellites that used limited-space on-board recorders and downloaded just once during each orbit. To achieve this, the approach of Yuhaniz and Vladimirova (2009) was to assess the degree of change across

sequential regions of interest, or tiles, from within an image. If the degree of change was sufficiently high, the routine flagged the tile for storage and transmission. Three options were given by Yuhaniz and Vladimirova (2009) for assessing the degree of change in each tile, with each option involving a comparison of values recorded in the acquired image (tile S) with values from a reference image of the same area (tile R).

**Option 1. Percent of changed pixels within each pair of image tiles ( $X_{D1}$ )**

This is calculated using the ratio of the number of “changed” pixels ( $a$ ) to the total number of pixels in the tile ( $n$ ), so that

$$X_{D1} = a/n. \quad (5.3a)$$

To qualify as “changed” the pixel has to pass the following test

$$|x_S - x_R| > T \quad (5.3b)$$

$x_S$  being the pixel value in tile S,  $x_R$  the pixel value in tile R, and T being a threshold. Effectively, if the change experienced by the pixel between the two acquisitions is greater than a fixed threshold, then the pixel is flagged.

**Option 2. Correlation coefficient for each pair of image tiles ( $X_{D2}$ )**

This is calculated by summing the difference between each pixel value and the mean value for the tile in both the reference tile (tile R) and tile S:

$$X_{D2} = \frac{\sum_{k=1}^n (x_{Rk} - \bar{x}_R)(x_{Sk} - \bar{x}_S)}{\sqrt{\sum_{k=1}^n (x_{Rk} - \bar{x}_R)^2 (x_{Sk} - \bar{x}_S)^2}} \quad (5.4)$$

in which

$n$  = the number of pixels in the tile;

$x_{Rk}$  = the value for the  $k$ th pixel in tile R;

$\bar{x}_R$  = the mean of all pixels in tile R;

$x_{Sk}$  = the value for pixel  $k$  in tile S;

$\bar{x}_S$  = the mean of all pixels in tile S.

**Option 3. Difference of means for each pair of image tiles ( $X_{D3}$ )**

This is determined by calculating the mean for each tile, and then subtracting the two means:

$$X_{D3} = \left| \sum_{k=1}^n \left( \frac{x_{Rk}}{n} \right) - \sum_{k=1}^n \left( \frac{x_{Sk}}{n} \right) \right|. \quad (5.5)$$

Although tested on images acquired before and after flooding by Yuhaniz and Vladimirova (2009), the method could equally well be adapted to assess whether a tile contains a zone of thermally anomalous pixels, or not, using SWIR, MIR or TIR spectral radiances. It could also be adapted to work on a pixel-by-pixel basis and applied to volcanic hot spot detection by executing the following five steps.

- Step 1. Complete calibration, image registration and cloud screening.
- Step 2. Extract the region of interest centered on the target volcano in a reference image (image R). In our case, this may be the previous image acquired, or an image known to contain no hot spots.
- Step 3. Extract the same region of interest in the image to be checked for hot spots (image S).
- Step 4. Calculate the correlation coefficient (CC) for each pixel by using the difference between the pixel radiances in the reference image ( $R_R$ ) and the current image ( $R_S$ ) as follows:

$$CC = \frac{(R_{Rk} - \bar{R}_R)(R_{Sk} - \bar{R}_S)}{\sqrt{(R_{Rk} - \bar{R}_R)^2(R_{Sk} - \bar{R}_S)^2}},$$

in which

$R_{Rk}$  = spectral radiance for the  $k$ th pixel in the image R tile;

$\bar{R}_R$  = mean spectral radiance for all pixels in the image R tile;

$R_{Sk}$  = spectral radiance for pixel  $k$  in the image S tile;

$\bar{R}_S$  = mean spectral radiance for all pixels in the image S tile.

- Step 5. Use the results to determine whether a pixel is anomalous or not on the basis of temporal correlation between the current pixel radiance and the previous (or non-active) radiance.

### 5.3.3 Fixed threshold algorithms

Fixed threshold algorithms apply a series of tests designed to determine whether the spectral character of the pixel is consistent with the presence of a sub-pixel thermal anomaly. This is achieved by assessing whether the spectral radiance of the pixel exceeds a fixed, or number of fixed, limits above which the spectral radiance is sufficiently high that it can only be the result of an extremely hot source residing within the pixel. Other thresholds are often applied to assess whether the pixel is cloud-containing or contains a highly reflective source. Thresholds can be generic (i.e., set at one time and applied to multiple images) or case-specific (i.e., set on a case-by-case basis using statistics taken from the image in hand).

#### 5.3.3.1 Fixed threshold algorithm: typical form

Six generic fixed threshold algorithms developed by the fire community between 1985 and 1995 are listed in [Table 5.2](#). They take a similar form, and the most complex execute up to five spectral tests to check for hot, low-reflectance and cloud-free conditions. Thus the following tests are carried out using a series of thresholds.

##### Test 1. Hot spot test

Is the MIR temperature sufficiently high for it to contain a high temperature source? Many of the algorithms in [Table 5.2](#) execute a test that assesses whether or

not the pixel is at, or close to, AVHRR's channel 3 saturation temperature to assess whether a pixel passes this test or not.

#### Test 2. Background thermal state

If the background is solar heated, then the pixel will be equally hot in the TIR. Thus, this test uses the similarity between the pixel-integrated temperature in the MIR and TIR to assess solar heating effects, in effect the closer  $\Delta T$  is to zero, the more likely it is that the MIR is hot simply due to solar heating. Thus, for example, Arino and Melinotte (1995) used a test that  $T_{\text{MIR}}$  had to be greater than  $T_{\text{TIR}}$  by + 15 °C in order to be considered anomalous.

#### Test 3. Cloud test

If the band 4 temperature is very low, then high cold cloud may be present. The reflection from such clouds could cause  $T_{\text{MIR}}$ , and  $\Delta T$  to be anomalously high. Thus a cloud trap can include a  $T_{\text{TIR}}$  temperature test, where Kaufman *et al.* (1990), for example, threw away all pixels with brightness temperatures of less than -23 °C by way of a rudimentary cloud screen.

#### Test 4. Reflection test

Highly reflective conditions may also be indicative of clouds, as well as of high-reflection day-time conditions that may elevate the MIR brightness temperature through large reflection contributions to the MIR integrated radiance. Thus, a final test can be to throw away all pixels above a certain reflectance threshold, with this test being applied to the VIS and/or NIR.

Examples of three multi-step, fixed threshold algorithms designed to detect volcanic hot spots are given in Electronic Supplement 9. Here we focus on the MODVOLC fixed threshold approach.

##### 5.3.3.2 MODVOLC – generic form

MODVOLC was developed in a series of papers by Flynn *et al.* (2002), Wright *et al.* (2002a) and Wright *et al.* (2004). It was a generic fixed threshold algorithm designed to detect volcanic hot spots. The key characteristic of MODVOLC was that it was designed to provide a global detection capability using MODIS data. Developed as part of the EOS-IDS volcanology team effort (see Chapter 1), it became operational following the launch of MODIS on the Terra platform in February 2000. Running on the MODIS data stream at the Goddard Space Flight Center (GSFC) Distributed Active Archive Center (DAAC), MODVOLC was restricted to eight mathematical operations, a requirement imposed to minimize the drain on computer resources at the DAAC. Thus, Wright *et al.* (2002a) developed the *NTI* concept which required use of the MIR and TIR pixel radiances ( $R_{\text{MIR}}$  and  $R_{\text{TIR}}$ ) in just three mathematical operations:

$$\text{Operation (1): } R_{\text{MIR}} - R_{\text{TIR}} = X$$

$$\text{Operation (2): } R_{\text{MIR}} + R_{\text{TIR}} = Y$$

$$\text{Operation (3): } X/Y = NTI$$

and one test:

Test: if  $NTI > \text{Threshold}$ , THEN pixel is hot.

To set the threshold, Wright *et al.* (2002a) completed a histogram analysis of MODIS data similar to the example given here in Figure 5.8d. With data for a variety of volcano hot spot types and sizes, from a variety of environmental settings spanning arctic, temperate, tropical and hot desert, Wright *et al.* (2002a) used the histogram analysis to obtain an appropriate, global value for the *NTI* threshold. This value for the threshold was set to  $-0.8$ , and used to separate ambient pixels ( $NTI < -0.8$ ) from hot spot pixels ( $NTI > -0.8$ ). This global threshold has proved to operate with a very low rate of false detections (Wright *et al.*, 2004), and was increased to  $-0.6$  for day-time images. The resulting MODVOLC algorithm steps are given in Figure 5.13, and executed on our Etna test image in Appendix G.

#### 5.3.3.3 A locally calibrated (case-specific) MODVOLC

The MODVOLC approach has proved a simple yet effective method for detecting hot spots in global satellite IR data sets. However, because MODVOLC's global threshold is set conservatively high, so as to allow global detection with a minimum rate of false detection, more subtle thermal anomalies will be missed.

However, *NTI* histograms can be used to set thresholds that vary on a case-by-case basis, or that can be set regionally-to-locally, to make the algorithm more sensitive and site specific. For example, the *NTI* plot for Etna given in Figure 5.8d shows that  $-0.9$  may be a better threshold for this case, detecting 17 pixels rather than the 4 pixels detected using the  $-0.8$  threshold (see Appendix G). Such an adaptive approach was taken by Kervyn *et al.* (2008) who found that MODVOLC's global threshold was too severe if all of the hot spots apparent at Oldoinyo Lengai were to be detected. Following histogram analysis of hundreds of scenes for this location spanning all seasons, a locally adapted threshold of  $-0.83$  was thus selected as a threshold more appropriate for this local case.

Thus two options are available to adapt MODVOLC, thereby allowing it to be more sensitive and case specific.

- (i) To set an *NTI* threshold on an image-to-image basis, one option being to set the threshold equal to the maximum *NTI* obtained from a region adjacent to the volcanic target on the image under consideration.
- (ii) To use composite histograms from multiple images collected for a given target over all seasons to set a single, site-specific, *NTI* threshold.

#### 5.3.4 Hybrid algorithms

Hybrid algorithms are those which combine elements of pure contextual, temporal and fixed threshold algorithms. In a sense, the correlation-based detection methodologies of Wright *et al.* (2002b) and Yuhaniz and Vladimirova (2009) are two such algorithms, because they use contextual and temporal elements. Two examples of hybrid detection algorithms that have been proposed for volcano hot spot detection are:

- MODLEN, which combines a fixed-threshold approach with a second contextual step, and
- MODVOLC-RAT, which combines a fixed-threshold approach with a second temporal step.

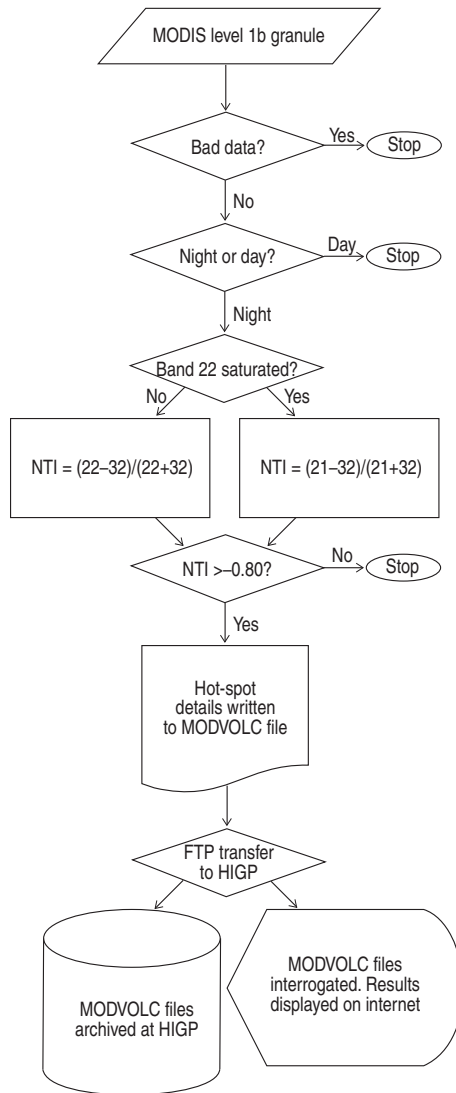


Figure 5.13 Flow diagram illustrating the implementation of the MODVOLC algorithm. Hot spot details written to the MODVOLC text file included time of hot spot detection (year/month/day/time), location (latitude/longitude), spectral radiance recorded in MODIS Bands 21, 22, 28, 31 and 32 (in  $\text{W m}^{-2} \text{sr}^{-1} \mu\text{m}^{-1}$ ), plus satellite zenith, satellite azimuth and solar zenith angles (all in degrees) [from Wright *et al.* (2002a, Fig. 10): with permission from Elsevier].

In both cases, the first step involves application of a low sensitivity algorithm with minimal processing steps. This can be used to scan the larger data set to identify locations for which a second, more complex and sensitive algorithm, can be applied to allow improved detection at individual, anomalous sites.

#### 5.3.4.1 MODLEN

Developed by Kervyn *et al.* (2008), MODLEN combined elements of MODVOLC with a modified form of VAST. Operating with night-time MODIS data, application involved two main steps.

##### Step 1: Fixed threshold step

As with MODVOLC, the algorithm calculated  $NTI$  using spectral radiances either from MODIS' MIR band 22 ( $R_{22}$ ) and TIR band 32 ( $R_{32}$ ), so that

$$NTI = \frac{R_{22} - R_{32}}{R_{22} + R_{32}},$$

or MODIS' MIR band 21 ( $R_{21}$ ) if band 22 was saturated:

$$NTI = \frac{R_{21} - R_{32}}{R_{21} + R_{32}}.$$

MODLEN then used a locally-defined threshold of  $-0.83$  so that a pixel was defined as a “hot spot” if  $NTI > -0.83$ .

This allowed location of more subtle anomalies than achieved when running the global night-time threshold of  $-0.8$ . However, it still did not allow all anomalous pixels to be detected. Thus a second contextual step was added.

##### Step 2: Contextual threshold step

Natural variation in  $NTI$  ( $\sigma_{NTI}$ ) was calculated from:

$$\sigma_{NTI} = \frac{NTI_{\text{target}}}{NTI_{\text{neigh}}}$$

in which  $NTI_{\text{target}}$  was the  $NTI$  of the central pixel in each  $3 \times 3$  pixel enquiry box, and  $NTI_{\text{neigh}}$  was the mean  $NTI$  from the eight pixels surrounding the central target pixel. The resulting  $\sigma_{NTI}$  was then divided by  $NTI_{\text{neigh}}$  to give the spatial derivative of  $NTI$  ( $\Delta NTI / \Delta x \Delta y$ ), i.e.:

$$\frac{\Delta NTI}{\Delta x \Delta y} = \frac{\sigma_{NTI}}{NTI_{\text{neigh}}}.$$

Hot spots were flagged if  $NTI > -0.88$  and  $\Delta NTI / \Delta x \Delta y \leq -0.02$ .

#### 5.3.4.2 MODVOLC-RAT

Koeppen *et al.* (2011) combined MODVOLC and RAT with the aim of improving the detection rate of MODVOLC when applied to a global data set. Application involved two main steps.

##### Step 1. Fixed threshold step

MODVOLC was run using its global threshold of  $-0.8$  for night-time data, and detected pixels were passed on to Step 2. In effect, MODVOLC was used as a filter

to identify locations where a more computationally complex and data hungry algorithm could be focused.

#### Step 2. *Temporal threshold step*

Image time series were created for each location using up to nine years of MODIS data all from the same time of day and month. The images were “cleaned” of hot spots by removing pixels flagged by MODVOLC, and the reference fields required by *ALICE* (i.e., the temporal mean and standard deviation in radiance for each pixel) were defined. Koeppen *et al.* (2011) found that use of at least ~20 images was required to avoid large (bad) standard deviations, although by ~80 images the standard deviation envelope was stable. The location was then tested using *ALICE*. That is, the radiance of each pixel in the image to be tested was compared with the reference values for that pixel through calculation of *ALICE*, so that:

IF *ALICE* > threshold, THEN pixel is anomalous.

Koeppen *et al.* (2011) found that  $\sigma$  thresholds of 2.6 and 3.0 were required to flag hot spots with no false detections at Anatahan and Kilauea, respectively, and that the hybrid approach allowed ~15 % more thermal anomalies to be detected than when using just MODVOLC (set with its global threshold), with very few (“if any”) false detections.

### 5.3.5 Use of NIR and SWIR

#### 5.3.5.1 NIR

Images acquired by AVHRR’s NIR band (band 2) are generally black at night because there is no reflected energy to detect, and ambient heat emissions are too feeble to register recordable energy at these wavelengths. The exception is when particularly large effusion events are captured, so that sufficient radiance is generated to be detectable in the NIR (see Electronic Supplement 1). This led Flynn and Mouginis-Mark (1994) to suggest that the occurrence of a NIR anomaly “could be used to detect extremely vigorous (lava) flows that represent the greatest local hazards.” The incidence of thermal anomalies in AVHRR NIR data is rare, being limited to just three reports in the 1990s: by Flynn and Mouginis-Mark (1994), Harris *et al.* (1995b) and Dean *et al.* (1998) during eruptions at Kilauea, Krafla and Okmok. One unpublished incidence of NIR emission was also found in a nighttime AVHRR image acquired during the first days of Etna’s 1991–1993 eruption. Thus, detection would be rare, but would only include the most major effusive events. Of course, TM-class sensors could also be used, but an hourly, even daily, detection capability would not be possible with any sensor operating in this class.

#### 5.3.5.2 SWIR

SWIR data are likewise black at night. However, because hot spots do not have to be as hot or large to be detectable in the SWIR (see Electronic Supplement 1), this waveband potentially offers more frequent detection than the NIR. Wooster and Rothery (1997a,b),

for example, were successful in showing how AVHRR-class data collected in the SWIR by ATSR could successfully, and frequently, detect hot spots associated with lava domes and flows. Wooster and Rothery (1997a) thereby executed the following scheme for hot spot detection in night-time SWIR data (a scheme which would also work for night-time data collected in the NIR).

- Step 1. Locate the volcano, and extract the region of interest centered on this location (for Wooster and Rothery (1997a) this was a  $5 \times 5$  pixel grid centered on Lascar).
- Step 2. Extract noise statistics (mean and standard deviation radiances for the “dark” image,  $R_{\text{mean}}$  and  $\sigma_R$ ) for a larger  $50 \times 50$  pixel area centered on the region of interest.
- Step 3: Select all pixels within the region of interest with radiances that are more than two standard deviations above the background noise level.

### **5.3.6 Hot spot detection algorithms: relative merits**

Lee and Tag (1990) summed up the philosophy behind contextual approaches stating that, by considering a local neighborhood, “the algorithm computes appropriate background temperatures for each area analyzed.” Likewise, a temporal approach “computes appropriate background temperatures for each area analyzed” and looks for correlations, or lack of correlation, between the current and normal thermal behavior at a given point. That is, in contextual and temporal algorithms, thresholds are set specific to the pixel being tested, and may be different for each pixel in each image. This makes these types of algorithm highly flexible.

The fixed threshold algorithms of Table 5.2, for example, are set for specific regions and hence may not work in another (colder or hotter) region. Take our small, 2-m radius vent atop Etna at 950 °C against an icy winter background of 0 °C. This will give a pixel-integrated temperature in the MIR of 11 °C. Against a solar heated, summer background of 40 °C the MIR pixel-integrated temperature for the same pixel will be 43 °C. Hence, a fixed threshold algorithm that flags all MIR pixels with a temperature of greater than 10 °C will work in the winter, but not the summer. Alternatively, although a threshold of 40 °C may work in the summer, in the winter a very obvious hot spot will be rejected. In contrast, contextual and temporal thresholds are not fixed and will vary depending on location, time of day and time of year. Because the background surface temperatures against which a thermal anomaly may be set will vary in space (between tundra and tropical environments, or with altitude) and time (i.e., surface temperature will vary diurnally and annually) this makes use of a threshold set from the pixel’s spatial or temporal neighborhood a powerful means to generate a flexible, portable and sensitive algorithm. By setting the threshold from the image in question, the contextual approach sets a threshold appropriate to the local ambient thermal conditions at the time of analysis. However, contextual and temporal algorithms are computationally complex and difficult to execute on large data sets, hence the use of MODVOLC for real time analysis of a global data set with limited computing resources.

#### 5.3.6.1 Algorithm reliability

Steffke and Harris (2011) carried out a comparison of the main contextual, temporal and fixed threshold algorithms used in volcanology: VAST, RAT and MODVOLC. The test involved visually examining all AVHRR and MODIS images acquired for five volcano hot spot test cases of varying intensity to assess: (i) how many visually identified hot spots were found by each algorithm, (ii) how many pixels were missed, and (iii) how many false detections occurred. The conclusion was that no algorithm was perfect. All algorithms detected, and missed, anomalous pixels. All algorithms also experienced false detections, and performed differently for different hot spot cases. The message was, an automated algorithm can be used to flag useful images, but if the user requires identification of all anomalous pixels, with the certainty that there are no false positives, manual cross-checking always needs to be carried out.

#### 5.3.6.2 Advantages and disadvantages

Each algorithm type also has a number of advantages and disadvantages that need to be considered.

- Contextual algorithms can operate on a single image, but can be computationally greedy and may be difficult to apply to global data sets.
- Temporal algorithms require availability of a large image archive and exacting geolocation; if a pixel is slightly mis-located the statistics will be affected. This may necessitate access to such an archive, plus considerable storage and processing power while the statistics are being generated.
- Fixed threshold algorithms can be applied to single images, require little computational or processing power, and can thus be applied easily and quickly to any single image. It is quite easy, for example, to use the *band math* tool in ENVI to create a  $\Delta T$  or  $NTI$  image and then apply a fixed threshold using the *masking* procedures. The same simplicity means that it is an efficient way to deal with global data sets.

The user also needs to assess the importance of the number of detections versus the number of missed and false cases. While MODVOLC, for example, will yield a low-to-zero rate of false detection, VAST and RAT will flag many more hot spot images, and flag many more pixels within those images, but with a higher rate of false positives. We explore these issues next.

#### 5.3.7 Which algorithm?

Numerous methodologies have been given in this chapter to allow hot spot detection in satellite imagery. Those proposed for volcano hot spot detection in satellite data are summarized in Table 5.3, where we see that 13 algorithms were proposed between 1995 and 2005, spanning contextual, temporal and fixed threshold approaches. Each algorithm has been designed with different objectives in mind, allowing local, regional or global monitoring using SWIR, MIR and/or TIR data.

Table 5.3. Automated volcano hot spot detection algorithms published in the peer-reviewed literature between 1995 and 2005. Algorithms are listed in chronological order of publication.

Study	Algorithm type	Notes	Data type (Application region)
Harris <i>et al.</i> (1995a)	Contextual	Testing of the detection algorithm that was used by VAST. Based on natural variation in $\Delta T$ , and comparison between natural variation in the volcano sub-image and the surrounding region. (see <a href="#">Section 5.3.1.1</a> )	AVHRR (Etna)
Higgins and Harris (1997)	Contextual	VAST (see <a href="#">Section 5.3.1.1</a> )	AVHRR (Etna, Stromboli & Vulcano)
Dean <i>et al.</i> (1998)	Fixed	Early Okmok algorithm with a fixed threshold (flag if $T_{MIR} > 35$ °C) that issued “many non-volcanic alerts”	AVHRR (Kamchatka, Aleutians & Alaska)
Wooster and Rothery (1997a)	Fixed	Not classified as “automated hot spot detection” in <a href="#">Appendix A</a> because mainly executed to extract data for a specific study, rather than being the focus of a study aimed at testing a general detection algorithm. Uses mean and standard deviation of sub-image radiance to test for anomalous behavior. (see <a href="#">Section 5.3.5.2</a> )	ATSR (Lascar)
Dehn <i>et al.</i> (2000)	Temporal	Okmok (see <a href="#">Section 5.3.2.1</a> )	AVHRR (Kamchatka, Aleutians & Alaska)
Harris <i>et al.</i> (2000a)	Fixed	(i) Apply cloud mask ( $R > 5\%$ );	GOES
Harris <i>et al.</i> (2001, 2002a)		(ii) Calculate $\Delta T$ mean and $\sigma$ for sub-image	(Hawaii)
		(iii) Flag all pixels with $T_{MIR} > 50$ °C	GOES
		(iv) Flag all pixels with $\Delta T > 3.3 \sigma$ above the mean;	(Pacific Rim)
		(v) Mask these pixels, and recalculate $\Delta T$ mean and $\sigma$	
		(vi) Loop until no new pixels are flagged	

Pergola <i>et al.</i> (2001; 2004a) Di Bello <i>et al.</i> (2004)	Temporal	Application of the Robust AVHRR technique (RAT) of Tramutoli (1998) to a volcanic target (See <a href="#">Section 5.3.2.2</a> )	AVHRR (Etna and Stromboli)
Flynn <i>et al.</i> (2002)	Fixed	MODVOLC global hot spot detection algorithm (uses fixed $NTI$ threshold) (see <a href="#">Section 5.3.3.2</a> )	MODIS (global)
Wright <i>et al.</i> (2002)			
Galindo and Dominguez (2002; 2003)	Fixed	Flag if difference in $T_{MIR}$ between target pixel (at volcano summit) and ambient temperature measured at in-situ meteorological station is $> 2$ °C (see Section 5.7)	AVHRR (Colima)
Harris <i>et al.</i> (2002a)	Fixed	Probabilistic approach (see Electronic Supplement 9)	GOES (Pacific Rim)
Kaneko <i>et al.</i> (2002a)	Fixed	Fixed $\Delta T$ thresholds (set using statistics from the image) (see Electronic Supplement 9)	AVHRR (Japan)
Wright <i>et al.</i> (2002b)	Contextual/ Temporal	Use of $R^2$ (Correlation-based approach). Not classified as “automated hot spot detection” in <a href="#">Appendix A</a> because mainly executed to extract data for a specific study, rather than being the focus of a study aimed at testing a general detection algorithm (see <a href="#">Section 5.3.1.2</a> )	GOES (Popocatépetl)
Ramsey and Dehn (2004)	Temporal	Use of OKMOK running on AVHRR data to target and integrate ASTER data (see <a href="#">Section 5.6.2</a> )	AVHRR-ASTER (Bezymianny)

The question is: which algorithm to use? The response to this question is three other questions:

- (i) What are my objectives (local, regional or global monitoring)?
- (ii) What is the nature of my target (lava flow, lake, dome, open vent)?
- (iii) What data do I have (i.e., is it SWIR, MIR and/or TIR, single image or multi-temporal)?

When these questions have been answered, then an algorithm best suited to the user's goals can be selected. Alternatively a number of algorithms can be selected, tested, adapted and combined to make a tailor-made algorithm that meets the user's requirements, or may be tailored to suit the combination of available data, feature type and location.

#### *5.3.7.1 Global-to-Earth-Disk monitoring*

If Global-to-Earth-Disk monitoring is the goal, then we may not be too worried about missing subtle anomalies. The user will not want to be overwhelmed with false detections and we will need a simple, fast and efficient algorithm capable of coping with a global data set several times a day. To reduce processing time, a computationally simple, fixed threshold algorithm (such as MODVOLC) may thus be the user's best option. Data or computationally heavy algorithms (such as VAST or RAT) may simply not be able to keep up with the rate at which data flows through the system, or the computing power may have to be enormous to cope with the algorithm operations, placing strains on limited or finite resources which may also have to be tasked to other processes.

#### *5.3.7.2 Single-site monitoring*

If monitoring of a single volcano is the aim for event detection and warning, then we will want to catch all anomalies in a timely fashion. In such a case we may not be too concerned about the frequent false detections that a sensitive algorithm will create, but which can be filtered using a manual decision making step. In fact, it may be better to have many false detections, than to miss the all-important real detection. In such a case, more complex and sensitive contextual and temporal algorithms may be the user's choice. The actual type of thresholding scheme executed will then depend on the data type available, access to archives, and available computing or processing power.

The algorithm designed for hazard monitoring has succeeded if just one out of ten pixels comprising an anomaly has been detected and used to raise an automated flag triggering rapid response. In effect, the hot spot has been detected and that's all we need to do, we just need to be sure to detect it. If, on the other hand, the objective is to map or parameterize the entire anomaly, then the same algorithm has failed, and a more sensitive algorithm is required that ensures selection of most, if not all, of the anomalous pixels.

#### *5.3.7.3 Tailor-made, hybrid algorithms*

When monitoring a single volcano target, we have an advantage. Unlike the fire community, where multiple hot spots of random and unpredictable location will need to be detected over

a large region, and against a variety of backgrounds, we are interested in just a single volcano, or group of volcanoes, at which hot spots will be active over a small and predictable area, i.e., the area of the volcanic edifice. Thus we can focus our algorithm on a small image area of unchanging location that contains the volcano. This allows us to implement computationally and data hungry algorithms that, due to the small size of the area analyzed, are still executable with minimal computing and processing time. Many routines reviewed above thus often apply to small, selected sub-images from within the main image, or even tiles which can be as small as  $10 \times 10$  pixels in size, centered on the target volcano. The most useful way forward is thus to set algorithms on a case-by-case basis, and design powerful hybrid algorithms capable of maximum detection performance with minimal failure rates. This case-by-case adaptation is reflected in the number of algorithms that have been used by, and are now available to, the hot spot (fire and volcano) tracking community.

#### 5.3.7.4 User interaction

Our other advantage is that there may not be so many volcanic targets so as to preclude at least a degree of user interaction. The best way to treat any automated selection routine is as a guide: a notice of potential hot spot activity within an image. The user can then check the veracity of the notice by examining the image over which the flag has been raised to make a decision as to “accept, and pass on or use the information” or “reject, and continue looking.” If the image is accepted, the user wanting to do further analysis can then check that all pixels needed for higher level analysis have been included, and select any pixels that may have been missed by the automated routine (while rejecting any spurious inclusions). As suggested at the beginning of this chapter, there is likely no better detection system than the combination of human eye and brain. The almost instant pattern recognition and change detection capability of the human brain is likely the ultimate, hybrid, neural network algorithm, and thus should be viewed as the best and only algorithm to really trust.

Automated algorithm output should be a guide, and output should always be checked before being used, passed on or published. Given the difficulty in really detecting all hot pixels across a volcanic anomaly, no one can ever stand by an unchecked piece of algorithm output and say “yes, I have all the hot pixels,” and be sure that the statement is correct. The only sure way to obtain all anomalous pixels is to do it manually, i.e., selection by eye.

## 5.4 How can we detect eruption termination?

Whether from a monitoring point-of-view, or from the perspective of a researcher putting together an eruption time series or extracting a total heat loss estimate, it is equally important that we define the end of effusion, as well as the start. Thus, not only do we need to be able to detect eruption onset, we also need to identify the termination.

Once activity has ceased, lava surfaces will cool rapidly. We have already seen in [Chapter 4](#) (Section 4.3.1.6) that, once exposed to the sky, lava surface temperature will decay logarithmically with time. Following Equation (4.32a), for example, a lava surface

should cool from 1000 °C to ~500 °C during the first minute of exposure, reaching ~300 °C after one hour. The decay in temperature across the surface of a cooling lava flow should thus show a logarithmically decaying trend defining a “cooling curve.” Thus, thermally, the termination of activity should be detectable by:

- (i) a sudden and rapid decrease in recorded surface temperature, and
- (ii) the establishment of a logarithmically decaying cooling curve.

Thus, a sub-pixel lava flow that ceases to be active should force the same trend on the spectral radiance recorded by the pixel, or group of pixels, i.e., a sudden crash in spectral radiance followed by a cooling curve. We can see this behavior in three high-temporal-resolution spectral radiance time series constructed for effusive eruptions of durations spanning a few hours to a few days or weeks, as produced using GOES and SEVIRI data for effusive eruptions at Kilauea, Cerro Azul and Etna. The trends defined in each of these time series can be considered definitive of phases of (i) effusive onset, (ii) active effusion and, most importantly for this section, (iii) effusion cessation.

#### 5.4.0.1 Kilauea (GOES-case)

The GOES MIR spectral radiance time series recorded during the January 1997 effusive eruption at Kilauea’s Napau crater is given in Figure 5.14. The eruption was marked by four short periods of lava effusion. In the time series each period is marked by a rapid increase in spectral radiance, which reaches saturation levels during three of the four effusive phases. Termination of effusive activity for each of the phases is also clear from a sudden decline in spectral radiance. After each phase, smoothly decaying cooling curves can be made out, which last for around an hour – especially after the termination of the first and second eruptive phases.

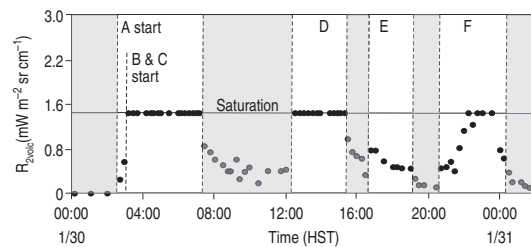


Figure 5.14 Time series of volcanic radiance recorded in GOES MIR band (band 2,  $R_{2\text{volc}}$ ) as obtained for the hot spot associated with Kilauea’s 1997 eruption at Napau crater (see Chapter 6 for the definition of volcanic radiance). White zones define active periods characterized by low fountains along a series of fissures (A to F) which fed active lava flows covering a total area of 0.239 km<sup>2</sup>. Gray zones define inactive periods. Saturation causes the flat tops to the time series recorded during active periods [from Harris et al. (1997b, Fig. 3b); Reproduced by permission of American Geophysical Union].

#### 5.4.0.2 Cerro Azul (GOES-case)

Figure 5.15 gives the GOES MIR spectral radiance time series recorded during Cerro Azul's 1998 effusive eruption. During the two days preceding the eruption we see the classic diurnal variation recorded for cloud-free ambient conditions (Figure 5.15a). The onset of effusion is marked by a rapid ascent to saturated levels, which are maintained for the duration of the eruption. The eruption end is marked by a crash in the spectral radiance between 05:28 and 07:28 on 21 October. A cooling curve is then apparent until the early hours of 24 October (Figure 5.15b).

#### 5.4.0.3 Etna (SEVIRI-case)

The SEVIRI MIR spectral radiance time series recorded during the 9–10 July 2011 fountain-fed effusive eruption at Etna's SE crater, as given in Figure 5.16, shows the same rapid increase in spectral radiance at the eruption onset as witnessed at the onset of the Kilauea and Cerro Azul events. The situation is complicated by obscuration of the hot spot by a cold ash plume which rose above the fountains during the peak of activity. However, once this clears we witness saturation followed by a sudden decline in spectral radiance (to unsaturated levels). This coincides with termination of the main effusive phase around 16:45 on 9 July. Thereafter we see a smooth, logarithmically decaying cooling curve which can be traced until around 00:30 on the morning of 10 July, at which point the cooling curve becomes obliterated by (lost to) the ambient signal.

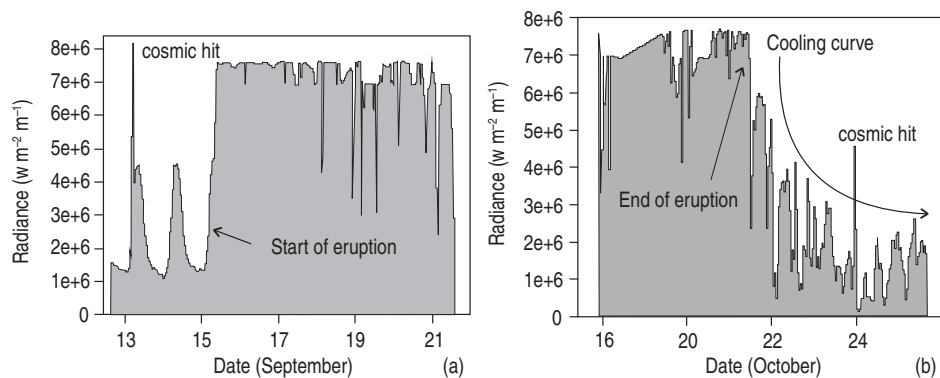


Figure 5.15 Time series of GOES MIR (band 2) data recorded during (a) the opening and (b) closing phases of Cerro Azul's 1998 eruption. Prior to the eruption, a cyclic trend is observed due to diurnal heating and cooling under cloud-free conditions. The onset of effusion is marked by a jump to saturation. During effusion, the plot is generally flat (due to saturation) with valleys being due to cloud contamination. The end of the eruption is marked by a crash in recorded radiances and a cooling curve. Spikes marked "cosmic hit" are false anomalies due to high energy solar particles passing through the (poorly shielded) detector [from Mouginis-Mark *et al.* (2000b, Figs. 3 and 7): with kind permission from Springer Science and Business Media].

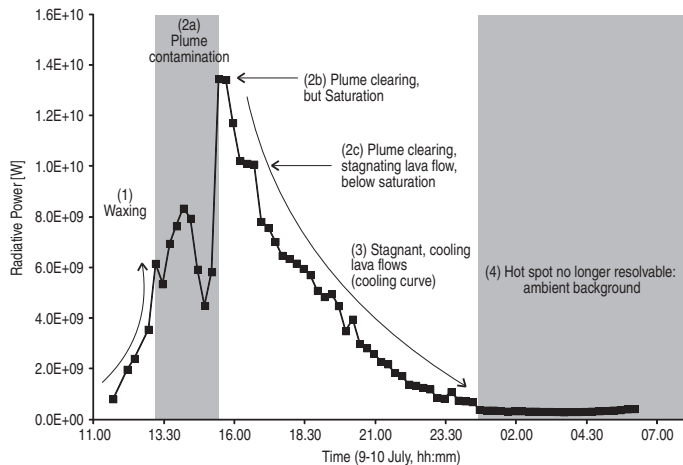


Figure 5.16 Radiative power calculated by applying the method of Wooster *et al.* (2003) to SEVIRI MIR (IR3.9) data during Etna's 9–10 July 2011 lava fountain (see Section 4.4.1.1 of Chapter 4 for method of Wooster *et al.* (2003)), with main phases of fountaining activity – as can be defined by the shape of the heat flux curve – marked.

#### 5.4.0.4 Aries *et al.* (2001)

Aries *et al.* (2001) presented graphs of AVHRR-derived MIR and TIR spectral radiance constructed across the termination of six effusive eruptions at Krafla and Etna, as given here in Figure 5.17. Each time series showed a marked decrease in MIR spectral radiance at the cessation of effusive activity, with the last syn-eruption MIR pixel usually being saturated, and the first post-eruption MIR pixel being unsaturated. Several of the cases given in Figure 5.17 also display a post-eruption cooling curve in both the MIR and TIR data. Thus Aries *et al.* (2001) suggested that, because eruption termination was marked by a rapid transition from high radiances to low radiances, with a short (hour-to-day-long) transition during which the lava flow surface undergoes rapid cooling, eruption termination can be detected “by a sudden and marked decrease in 3.9 μm radiance.” In the case of AVHRR (and GOES) this often means a switch from saturated to unsaturated data.

However, in cases where the lava flow field is particularly large or where remnant activity continues past the termination of effusion, then MIR data, with low saturation levels, may continue to be saturated after the end of effusion. An example of the former case was the cessation of Etna's 1991–1993 eruption which built a 7.6 km<sup>2</sup> flow field over ~16 months of continuous effusive activity. The final flow field was so large that saturation of AVHRR's MIR band continued for around two months after the cessation of activity, as can be seen in Figure 5.17f. As pointed out by Aries *et al.* (2001), for such large-scale lava flow fields, the crash in spectral radiance that marks the cessation of effusion is impossible to detect in data with low saturation levels. An example of such a case was the 1997 eruption of Okmok, as examined by Patrick *et al.* (2003). In this case, although the main phase of effusion ended

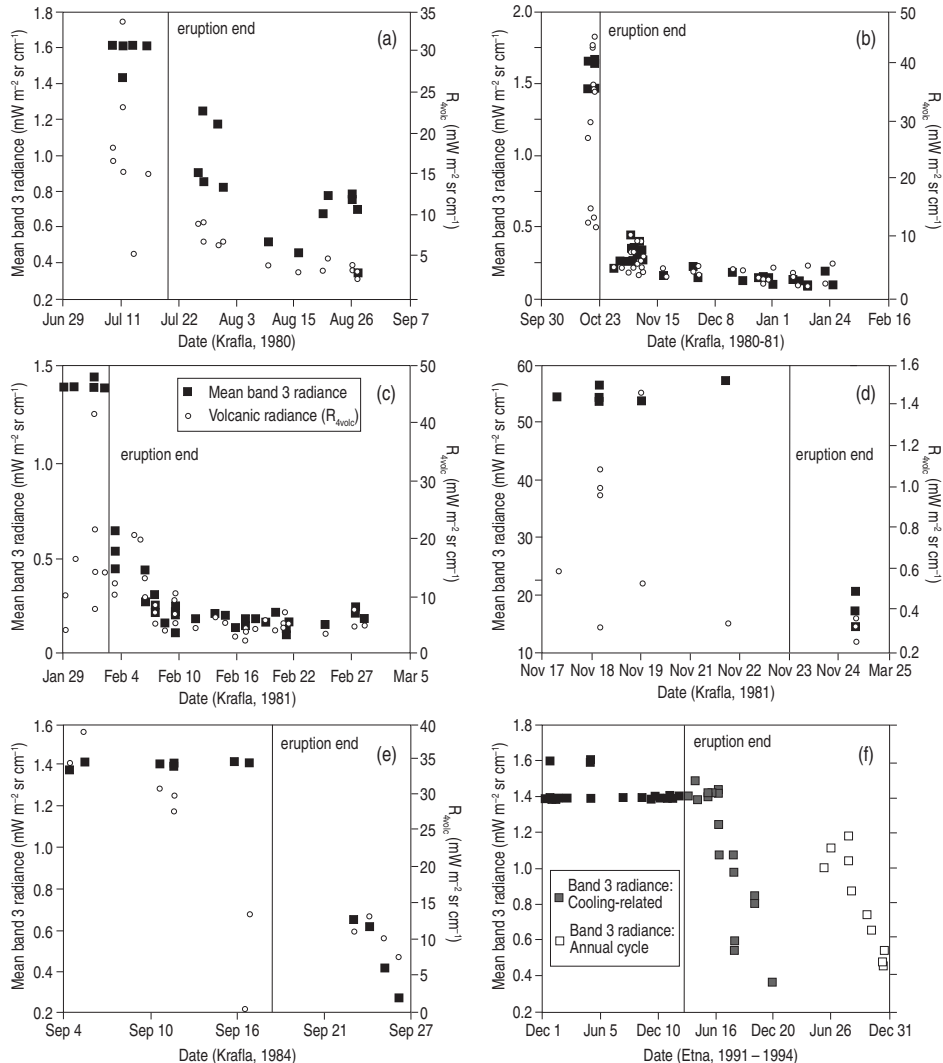


Figure 5.17 AVHRR MIR (band 3) and TIR (band 4) radiance trends through the end of effusive eruptions at Krafla (a – e) and Etna (f), showing the characteristic crash in radiance and onset of a cooling curve recorded at the end of effusion. The exception is (f) where the extent and thickness of the lava flow field meant that saturation was maintained for about four months after effusion ceased [from Aries *et al.* (2001, Figs. 2 and 3); reproduced by permission of American Geophysical Union].

around 25 March, minor “near-vent” activity continued at one of the feeder cones until around 10 April. This caused the AVHRR-recorded radiance to remain saturated until that point. In this case, while a crash in TIR radiance marked the end of the major effusive phase, a crash in MIR radiance marked the end of the eruption. This suggests that, in cases where the MIR radiance is forced to remain high due to the sheer size of the lava flow field, or due

to remnant activity, the TIR trace should be used to search for signs of termination, as suggested by Patrick *et al.* (2003).

### 5.5 Cool anomalies

Even if detectable, subtle thermal anomalies, due to fumarolic activity, geothermal heating or heat conduction/convection across the rocks overlying a shallow intrusion, may be lost as a result of solar heating or stronger spatial variations in ambient surface temperature due, for example, to surface cooling with altitude. On most thermal images of volcanoes which span a wide range of altitudes, strong temperature gradients can often be observed due to adiabatic effects (i.e., cooling with altitude, which causes temperature to decrease between sea-level and the volcano summit). For example, a difference of  $\sim 20$  °C can be witnessed between coastal and summit pixels (at an altitude of  $\sim 3000$  m) on Etna. In addition, atmospheric effects will vary with altitude, with transmissivity and up-welling decreasing with altitude, as the atmosphere becomes thinner. Together, these effects can produce greater variations in satellite-recorded brightness temperatures than those induced by fumarolic activity, geothermal heating or conduction/convection above shallow intrusions, thereby masking any potential thermal anomalies associated with such low temperature active volcanic phenomena.

To overcome these problems, Bonneville *et al.* (1985) proposed a methodology that effectively flattens the thermal image, so that all pixel-integrated temperatures are given in terms of their sea-level equivalent. The methodology represents a detection approach potentially capable of picking out subtle thermal anomalies, suppressing altitudinal-forced effects. The detection procedure uses night-time images only, so as to eliminate solar heating problems, and follows these four steps.

- Step 1. Extract the TIR band sub-image for the target volcano, and fit it to a digital elevation model (DEM).
- Step 2. Correct each pixel-integrated brightness temperature for transmissivity (and atmospheric up-welling) effects using atmosphere correction values appropriate for the altitude of the pixel in question.
- Step 3. Calculate the adiabatic cooling gradient. Bonneville *et al.* (1985) achieved this by using scatter plots of atmospherically corrected temperature versus altitude. These showed a linear decrease in temperature with altitude at Etna, the trend having the correlation and regression coefficients of Table 5.4. This allowed a gradient for the adiabatic cooling rate to be defined at around  $\sim 6$  °C km $^{-1}$ .
- Step 4. Correct each pixel for adiabatic effects by applying the following correction

$$T_{\text{corr-ad}} = T - \frac{\delta T}{\delta z} z$$

or, for this case,

$$T_{\text{corr}} = T + 0.006z ,$$

in which

$T_{\text{corr-ad}}$  = surface temperature corrected for adiabatic effects;

$T$  = atmospherically corrected pixel temperature;

$\frac{\delta T}{\delta z}$  = adiabatic cooling gradient;

$z$  = altitude.

In other words, for this Etna case, pixels at altitudes of 1000 m, 2000 m and 3000 m have corrections of 6 °C, 12 °C and 18 °C added to them, respectively, to take into account adiabatic cooling with height.

Because the presence of vegetation and snow will alter the radiation budget, Bonneville and Kerr (1987) recommended applying vegetation and snow masks, and then obtaining the adiabatic correction from (and then applying the same correction to) vegetation- and snow-free zones. The masks should probably also be used to execute a surface-dependent emissivity correction to the pixel brightness temperatures. However, the cooling gradients obtained for Etna using this extended method, as given in Table 5.4, were similar to those obtained by Bonneville *et al.* (1985) without application of the masking steps.

Table 5.4 Adiabatic cooling rate for Etna estimated from scatter plots of AVHRR-derived temperature versus altitude by Bonneville *et al.* (1985), plus those obtained by Bonneville and Kerr (1987) using vegetation and snow masked images, i.e., snow-free regions above 2000 m in altitude.

AVHRR image (Date)	Correlation coefficient	Regression coefficient (°C m <sup>-1</sup> )	Reference
14-Nov-81	0.98	-0.0063	Bonneville <i>et al.</i> (1985)
21-Dec-81	0.95	-0.0070	Bonneville <i>et al.</i> (1985)
5-Jan-82	0.84	-0.0045	Bonneville <i>et al.</i> (1985)
13-Jan-82	0.94	-0.0068	Bonneville <i>et al.</i> (1985)
7-Jan-83	0.71	-0.0054	Bonneville and Kerr (1987)
19-Jan-83	0.87	-0.0061	Bonneville and Kerr (1987)
26-Jan-83	0.8	-0.0073	Bonneville and Kerr (1987)
10-Feb-83	0.87	-0.0061	Bonneville and Kerr (1987)
12-Feb-83	0.89	-0.0066	Bonneville and Kerr (1987)
5-Mar-83	0.87	-0.0057	Bonneville and Kerr (1987)
14-Mar-83	0.74	-0.0075	Bonneville and Kerr (1987)
21-Mar-83	0.79	-0.0055	Bonneville and Kerr (1987)
22-Mar-83	0.87	-0.0073	Bonneville and Kerr (1987)
23-Mar-83	0.87	-0.0057	Bonneville and Kerr (1987)
Mean	—	-0.0062	Bonneville <i>et al.</i> (1985)
Mean	—	-0.0063	Bonneville and Kerr (1987)
Mean	—	-0.0063	Both data sets

### 5.5.0.1 Results

The method was applied to AVHRR TIR data for Etna by Bonneville and Kerr (1987), and Bonneville *et al.* (1985), as well as to AVHRR and TM TIR data for Etna by Bonneville and Gouze (1992). In addition Gaonac'h *et al.* (1994) applied the approach to TM data for Stromboli and Vulcano to reveal subtle thermal anomalies at both locations, the retrieved anomaly at Vulcano being due to fumarolic activity of relatively low intensity. The results of Bonneville and Kerr (1987) and Bonneville *et al.* (1985) are reviewed in Chapter 1 (see Section 1.3.1.1) and appear effective in bringing out low-temperature anomalies. These included the identification of low-temperature thermal anomalies potentially associated with pre-eruptive intrusions, such as the example given in Figure 1.10 of Chapter 1. In this case, the methodology picked out a low-temperature thermal anomaly along the line of Etna's south rift zone between the summit and the site of the 28 March 1983 south flank eruption. The eruption began around three months after the image was acquired. Bonneville and Kerr (1987) argued that the anomaly was due to intrusion of a dyke in the weeks prior to the eruption, which supplied heat to the surface through permeable convection thereby causing a slight elevation in surface temperature across the area above the intrusion.

Bonneville and Gouze (1992) found a similar anomaly along Etna's south rift zone in adiabatically corrected TIR data acquired by AVHRR and TM on 23 October 1986, a location from which an eruption began seven days later on 30 October 1986. The anomaly was not visible before correction, but after correction had an amplitude of  $\sim 2$  °C. The coincidence of the anomaly with volcano structural features, the absence of similar anomalies on the western and northern flanks of the volcano, and the disappearance of an anomaly (coincident with the cooling 1981 flow field) apparent in the 1983 data, convinced Bonneville and Gouze (1992) that the anomaly was real, and that another “thermal fore-runner” to a flank eruption had been detected.

Although there was some debate over the meaning and cause of these thermal anomalies (Archambault and Tanguy, 1993; Bonneville and Gouze, 1993), the results remain intriguing, and the association of the 1983 and 1986 thermal anomalies found on Etna with eruptions that followed their detection by days-to-weeks is compelling. As pointed out by Bonneville and Gouze (1993), if correctly treated following the methodology outlined above, TM- and AVHRR-class TIR data appear capable of highlighting subtle (low intensity) thermal anomalies not otherwise apparent in untreated data. The method, applied to night-time data, can also distinguish such thermal anomalies from solar heating of barren lava flow fields that often blight day-time images, sometimes even masking high-temperature thermal anomalies and creating “false” hot spots.

## 5.6 Operational volcano hot spot detection systems

A number of hot spot monitoring systems are now operational, each based on the methodologies and algorithms reviewed in this chapter. These include those run at the Alaskan

Volcano Observatory, Hawaii Institute of Geophysics and Planetology, and Istituto Nazionale di Geofisica e Vulcanologia (Catania, Italy).

#### 5.6.0.1 Alaska Volcano Observatory

The first operational satellite-based volcano hot spot detection system was implemented at the Alaska Volcano Observatory (AVO) during the 1990s. Algorithms to aid in the processing of satellite data for hot spot monitoring were initially developed to contribute to AVO's 24-hour monitoring efforts using AVHRR data. These algorithms generated calibrated and georectified  $512 \times 512$  pixel sub-images centered on each active volcano identified across the AVO-monitoring region, which covered Alaska, the Aleutians and Kamchatka. These browse images were used for manual inspection purposes, i.e., the images were manually checked for the presence of volcanic hot spots and plumes (Dean *et al.*, 1996). Later, the Okmok algorithm was developed to aid with automated detection. Subsequently used to trigger targeting of ASTER to hot spots detected by AVHRR (Ramsey and Dehn, 2004), the algorithm remains the foundation of automated, near-real-time satellite-based hot spot monitoring at AVO.

#### 5.6.0.2 The MODVOLC system

In 1998, the first widely accessible hot spot detection and product dissemination system was built at the Hawaii Institute of Geophysics and Planetology (HIGP, University of Hawaii). This ran with GOES data received every 15 minutes for Kilauea, and was initially driven by the fixed threshold algorithm given in Table 5.3 and later by that given in Electronic Supplement 9. Generation of this capability followed an initial proof of concept detection study of GOES hot spots detected during Kilauea's January 1997 eruption at Napau Crater (Harris *et al.*, 1997b). Within a few months of this eruption, a web-based hot spot dissemination system had been generated, with a hot spot email notice running on GOES images of Hawaii being distributed to staff members at HIGP and the Hawaiian Volcano Observatory whenever a hot spot was detected (Harris *et al.*, 2000a; 2001). Extended during 1998 and 1999 to cover all active volcanoes within the GOES footprint, the algorithm detected hot pixels and then generated hot spot location maps, enhanced quick-look images and movies that were posted on an open access website within 12–60 minutes of image acquisition. Emails sent to a controlled distribution list linked the user to the imagery and products which had triggered the notice, to allow rapid manual checking. The software also extracted and plotted various hot spot radiance parameters (Harris *et al.*, 2002a). Results were posted on the World Wide Web and updated every 15 minutes, i.e., with each new image acquisition; old data were placed into an open access archive. With the launch of MODIS in late 1999, the website was expanded to include the MODVOLC feed during 2000, an example page being given in Figure 5.18. Both the real-time, web-based GOES and MODIS resources were used to aid in tracking multiple eruption crises. Mouginis-Mark *et al.* (2000b), for example, described how GOES were used to detect and warn of the onset of a new effusive eruption on Cerro Azul in 1998.

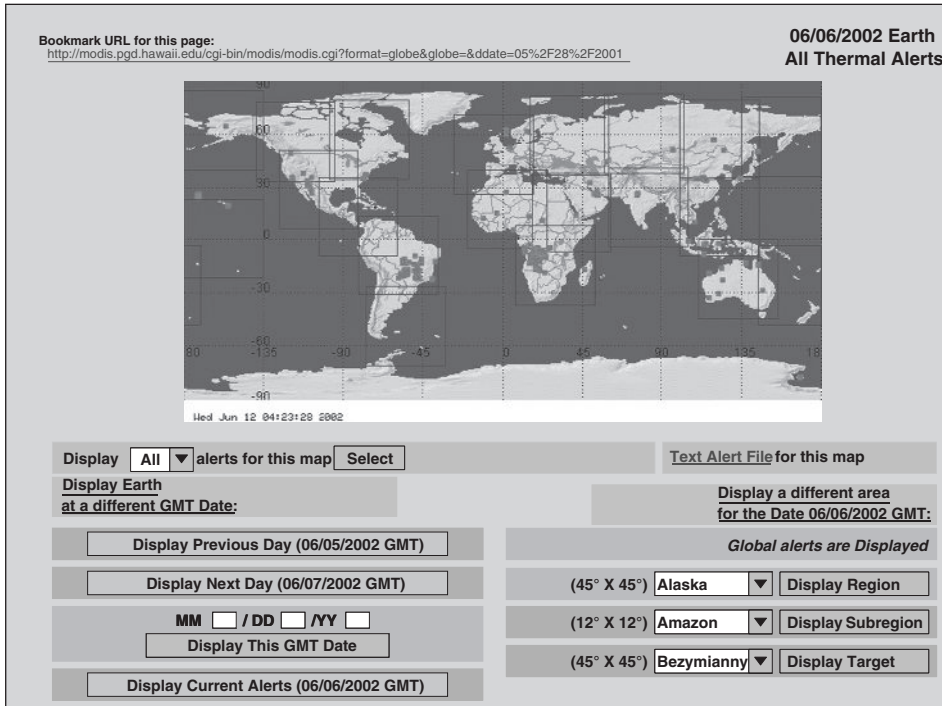


Figure 5.18 The Hawaii Institute of Planetology and Geophysics (HIGP) “hotspots” (MODVOLC) website for global hot spot monitoring as of 6 June 2002. The global hot spot map for that day is given by default, but the data base could be searched for any selected region, sub-region, volcanic target and/or date (by using the appropriate selection windows and buttons), with the map and data for the user-selected parameter combination being displayed within a few seconds. This allowed full data base enquiry, as well as download of data recorded by the algorithm as space delimited text files. See also color plates section.

#### 5.6.0.3 Central America and Japan

Further developments in an operational setting occurred at the Universidad de Colima. These were based around the AVHRR ground station installed at Colima in 1996 to allow satellite-based hot spot and ash monitoring of the Mexican volcanoes of Popocatépetl and Colima (Galindo and Dominguez, 2002; 2003). To support this monitoring effort, a semi-automated approach was developed for hot spot detection in AVHRR data at Colima. Similarly, Kaneko *et al.* (2002a) described an AVHRR-based monitoring tool for Japanese volcanoes using night-time data directly received at a ground station in Tokyo, which used the fixed threshold algorithm given in Electronic Supplement 9. Likewise, Webley *et al.* (2008) described a web-based system for AVHRR hot spot detection in Central America. This ran using data acquired by the Instituto Nicaraguense de Estudios Territoriales (INETER) PC-based satellite receiver in Nicaragua.

#### 5.6.0.4 Italy and France

Since the launch of MSG, at least two systems have been developed to detect volcano hot spots in SEVIRI data, these being HOTSAT, developed at the Istituto Nazionale di Geofisica e Vulcanologia (Catania, Italy), and HOTVOLC, developed at the observatoire de physique du Globe de Clermont-Ferrand (Université Blaise Pascal, Clermont Ferrand, France).

HOTSAT targets Etna and was based, initially, on a modified version of VAST (Vicari *et al.*, 2009). The current version is reported by Ganci *et al.* (2011) in *Annals of Geophysics*, and was used to track hot activity in SEVIRI data, and extract heat and volume fluxes during Etna's 12–13 January 2011 fountaining event (Vicari *et al.*, 2011), plus all 19 fountaining events at Etna through January 2012 (Ganci *et al.*, 2012a). As part of the HOTSAT system, hot spot detection is incorporated into a GIS (LAV@HAZARD) that projects the located pixels into a Google Earth base and allows real-time lava flow simulations, driven by SEVIRI- and MODIS-extracted lava volume fluxes, which can also be viewed over the Google Earth base (Ganci *et al.*, 2012b).

Developed during 2007–2009 (Guéhenneux, 2008), HOTVOLC was tested during eruptions at Eyjafjallajökull, Grimsvötn and Etna and went on-line during 2011. Also used to track Etna's 12–13 January 2011 fountaining event (Gouhier *et al.*, 2012), it uses a direct SEVIRI data feed. The system processes MIR and TIR data for selected volcanic targets to post gas and ash cloud products, as well as hot spot products, on an open access website in near-real-time, as described by Labazuy *et al.* (2012).

#### 5.6.1 What do you need for an effective detection system?

To be of use in a operational detection and response scenario, the detection system needs to have the following properties.

##### 5.6.1.1 Fast

To be of use for rapid, operational response, notice of a new event needs to be made within minutes of detection. Delays of hours or days will be too long; the event will either have been noticed by other sources, or it will be too late to respond.

##### 5.6.1.2 Based on high-temporal-resolution data

Algorithms running on 15 minute GOES-class data are most effective if we are to meet the “fast” requirement. Even algorithms running on AVHRR-class data received every 6 hours may trigger a warning that is too late, or may miss short but high intensity (e.g., lava fountain) events altogether.

##### 5.6.1.3 Quick notice

To reduce response delay, notices need to arrive quickly. That is, immediately the detection is made a notice needs to be distributed either using automated emails or other forms of immediate electronic/digital communication. In this way we notify the responder to the

likelihood of an event in as timely fashion as possible. It is unlikely that the provider can look through up to 96 images per day, every day, in a timely fashion, so that some form of on-reception, automated processing and notice dissemination is necessary.

#### *5.6.1.4 No-spam email notices*

Email notices should be designed so as to reduce spam. For example, a persistent lava flow under cloud-free conditions will trigger 96 GOES detections per day, quickly spamming an email inbox. One solution is to trigger an email notice only if (i) a hot spot is detected, and (ii) the hot spot spectral radiance has increased over the maximum encountered for all detected hot spots at the target over the previous 24 hours, thereby notifying the user only if there is an activity increase.

#### *5.6.1.5 Real-time access*

Products should be placed online immediately to allow user checking and appraisal. Relevant products (i.e., those generated by the image that triggered the email notice) should be linked to the email notice, allowing the recipient to simply click on the links contained within the email and check the veracity of the notice by examining the products.

#### *5.6.1.6 User-customized output products*

Users will be unlikely to want raw data, they do not have the time, or maybe the capability, to process the data. They will more likely want answers to questions such as: when, where, how long, how intense? It is the job of the user to define the desired quick-look product that is most useful in a response situation. It is the job of the remote sensor to then design, test and provide the product, improving the product subject to user feed-back.

#### *5.6.1.7 Post products and answers online (data secondary)*

All products need to be posted on an open access website, in an easy-to-access and examine form, so that the user is in a position to check and assess the current information within the context of past images and products. Raw data need to be archived for cross-checking and follow-up analysis, using easy-to-use tools that access the archive.

#### *5.6.1.8 Operate within defined reporting protocols*

Most crisis situations have well-defined communication protocols that define the information provider, responder and population at risk. They also define the route of information dissemination from the scientists, through the monitoring agency to civil protection, local – regional – national authorities, the media and, finally, to the population at risk. These communication protocols are defined so as to reduce mis-communication and panic, being designed to ensure an appropriate response and population reaction. Such protocols are given by, for example, Peterson (1988), Tilling (1989) and Bertolaso *et al.* (2009). Generally, the remote sensor is likely at the beginning of the communication route, and

should be careful to pass timely but sensitive information to the correct recipient, and not to short-circuit carefully designed hazard communication and response protocols.

#### 5.6.1.9 Operator checking

As already discussed, no algorithm is perfect and an element of operator checking and expert appraisal is essential. Mouginis-Mark *et al.* (2000b) discuss the communication protocols following issue of an email notice of a hot spot in a GOES image of Cerro Azul (Galapagos) in 1998 by the detection system running at the University of Hawaii (see Section 5.6.0.2). In this case, the analyst (upon checking the email notice) discussed the notice with his manager in Hawaii. Upon waiting for a second positive image showing both a hot spot and a plume, the monitoring agency (in this case the Darwin Research Center on the Galapagos Islands) was notified by telephone of a potential eruption on Cerro Azul. Field crews were dispatched, and the eruption confirmed. Helicopters were subsequently sent out to evacuate Galapagos Giant Tortoises who were in the path of the lava flow. This rescue mission latter become the theme of an episode of Barbapapa (Tison, 2000), thanks to an automated hot spot notice tripped by the fixed threshold hot spot detection algorithm of Electronic Supplement 9.

### 5.6.2 Algorithm output: applications

As stated at the beginning of this chapter, automated algorithm output can have two roles:

- (i) to aid in timely event detection and monitoring, and
- (ii) to allow efficient time series creation for scientific enquiry, plus a third role
- (iii) to target other sensors (i.e. sensor tasking).

We here briefly review roles (ii) and (iii), having covered role (i) in previous sections. As regards role (ii), the MODVOLC algorithm, for example, has been building a global inventory of volcanic hot spots since 2000 and is a well used resource. It has contributed data that allowed Wright and Flynn (2004) to build a global heat budget for all volcanoes active across the globe during 2001 and 2002. It has also been widely used to contribute activity reports by the Smithsonian Institute's Global Volcanism Network, as well as to identify hot spots and produce radiance time series during effusive episodes at Anatahan (Wright *et al.*, 2005), Mt. Belinda (Patrick *et al.*, 2005b), Melanesia (Rothery *et al.*, 2005), Stromboli (Ripepe *et al.*, 2005a), Semeru and Merapi (Harris and Ripepe, 2007a), and Fuego (Lyons *et al.*, 2010).

Other detection algorithms have been designed to detect the hot spot, and then apply the methodologies of the previous chapter to apply various forms of the dual-band method, and then to estimate heat and volume flux. While MODVOLC, for example, generated hot spot spectral radiance data capable of producing time series, or converting to heat and volume flux, the VAST code of Higgins and Harris (1997) and the MYVOL/MYMOD algorithm of Hirn *et al.* (2008) also completed these conversions. In regard to role (iii), algorithms have used detection in low-spatial-resolution, but high-temporal-resolution, data (such as

AVHRR or MODIS) to then target the hot spot with high-spatial-resolution sensors such as ASTER (e.g., Ramsey and Dehn, 2004; Duda *et al.*, 2009) or ALI and Hyperion on EO-1 (Chien *et al.*, 2004; Davies *et al.*, 2006a), an idea first proposed by Mouginis-Mark *et al.* (1989; 1991). Alternatively, algorithms running on the spacecraft themselves can be used to “task” the sensor when on-board data storage capacity is limited, as was the intent of Yuhaniz and Vladimirova’s (2009) algorithm. In such cases, data are downloaded once every orbit, and the amount of data that can be saved prior to download is limited, so that targets for which data are to be saved have to be carefully selected. On-board hot spot detection algorithms can automate selection of such appropriate data, as was the role of the Autonomous Sciencecraft experiment on EO-1 whereby an onboard hot spot detection algorithm flagged Hyperion data containing volcanic thermal anomalies, data that were then downloaded to the ground within 3 hours of detection (Davies *et al.*, 2006b).

#### *5.6.2.1 Where next?*

In this chapter we have examined the detection roles of satellite infrared data. In the previous chapters we considered means to extract sub-pixel thermal structures and to convert spectral radiances to surface temperatures and thermal feature area, plus heat, mass and/or volume fluxes. Having detected and quantified the hot spot, useful questions that can be raised are spatial and temporal. Such questions include (i) where is the hot spot, (ii) what is its size, (iii) what is its orientation, as well as, (iv) with which type of activity is it associated? Two further questions are (i) what is the intensity and/or magnitude of the hot spot, and (ii) what is the temporal trend in hot spot intensity or magnitude (steady, increasing or decreasing)? It thus remains to examine the spatial and temporal applications of thermal infrared data in tracking volcanic hot spots.

# 6

## Mapping, classification, time series and profiles

Once a hot spot has been detected, a logical hazard-related follow-up question is: where is the hot spot and in which direction is it extending? The second question may be: what type of activity is the hot spot associated with? Thus, in the first two sections of this chapter, we review methods to map and classify volcanic hot spots. In the final sections, we consider how these data can be used to generate time series for any derived parameter. The predictable, frequent and repeat nature of the satellite overpass means that data from satellite-based sensors are ideal for creating time series which can then be used for tracking the evolution of the targeted hot spot. This is reflected by the fact that ~50 % of the literature collated in [Appendix A](#) used satellite IR data to generate and examine syn-eruptive thermal time series for all manner of eruption-related hot spots, including lava domes, lava lakes, lava flows, open degassing vents, fumarole fields, pyroclastic flows and lahars. In fact, time series analysis forms the modal group (by number of publications) in our literature collation (see Table A2, [Appendix A](#)).

### 6.1 Hot spot maps

A map can be defined as “a representation, on plane surface, of all (or part of) the Earth’s surface, showing positions of, and boundaries around, physical and political features etc.” with the task of mapping being to “represent features on a map” or (in a mathematical sense) to “associate each element of a data set with elements of another set” (Sykes, 1982). In our case, we are associating measurements of spectral radiance, and its derivatives, with  $x,y$  positions, as represented by the pixels from which the measurements are derived, on the Earth’s surface, thereby providing a map of spectral radiance, temperature or heat flux. Thus an image is in every sense of the word a map, being a spatial representation of the distribution of spectral radiance, surface temperature and/or heat as mapped across a plane surface, with the scanning operation of the sensor allowing us to thermally map that surface.

Given that we have a thermal map of the Earth’s surface, we can use this to achieve all of the roles of a traditional map, these being:

- to precisely locate a feature;
- to define the area, extent, boundaries and dimensions of that feature;

- to reveal the shape and orientation of that feature, “orientation” being the bearing that describes the strike of the feature as defined by the direction of the long axis;
- to plot the feature in relation to other physical and cultural features;
- to allow distances between two features to be measured;
- to allow the spatial distribution of thermal radiance to be viewed.

Volcanic hot spots are dynamic features whose locations, extents, orientations and spatial distributions may change over a matter of minutes, as new vents open and existing vents shut down, or as lava flows advance and bifurcate. The advantage we have here is that the repeat mapping capability of the satellite sensor allows the map to be updated with each cloud-free overpass. This allows our map to be updated on a regular, and potentially frequent, basis. While the current map produced from the current image is as up-to-date as the overpass, previous maps provide a history of the spatial progression of the hot spot development, recording, for example,

- the spatial emplacement history of a lava flow field, lava lake system or dome, or the spatial evolution (establishment, growth and/or decay) of a geothermal area.

### **6.1.1 The image as a map**

Our definition of a *map* means that *any image is a map*. This means that any publication containing a ground- or satellite-based image of a volcanic thermal phenomenon is a publication of a hot spot map. The first published map of a volcanic hot spot was thus the HRIR image of Kilauea given by Gawarecki *et al.* (1965), which located the hot spot associated with effusive activity at Kilauea in 1965. Grainy as it was, the image met the basic role of a map in locating a feature, in this case a hot spot associated with effusive volcanic activity. By this definition, the second published map was the HRIR image of Williams and Friedman (1970) which located the hot spot due to effusive activity at Surtsey, just off the SE coast of Iceland in 1966 (as given in Figure 1.1a of Chapter 1). The literature is full of such examples of satellite-sensor-derived hot spot maps due to active lava lakes, domes and flows.

#### **6.1.1.1 What to map and how to map it?**

The basic parameter level that can be mapped is the distribution of spectral radiance. This is an effective, but simple and easy-to-execute, means of locating, mapping and, thereby, viewing a hot spot, requiring little processing other than display of the image, along with selection of appropriate band combinations, plus some contrast enhancement, to bring out the maximum detail across (or contrast between) the hot spot and its background.

**Single-band (black and white) spectral radiance map** The most simple spectral radiance map type can be produced by using a single band of data, with the band containing the maximum amount of hot spot information being selected for display. An example of such a map is given in Figure 6.1 and is a contrast enhanced AVHRR MIR (band 3)

image of Mt. Etna acquired at 01:09Z on 23 July 2001. It locates a main elongate hot spot with a N–S orientation extending for about 8 pixels (~9 km) down Etna’s south flank, plus a second two pixel anomaly orientated E–W just to the northeast of the main anomaly. A cold plume is apparent with its source within the upper portion of the main anomaly and extending SE through the routes usually taken by aircraft ascending out of Catania airport. These hot spots can be located in relation to the higher elevations of Etna’s summit, apparent from the colder temperatures (darker tones) identifiable in Figure 6.1, as well as the coast, where the water is apparent from warmer temperatures (lighter tones). This single band MIR spectral radiance map effectively locates a complex of channel-fed lava flow fields that had been active since 17 July 2001, the south flank hot spot being related to five lava flow fields emplaced with a N–S orientation over a distance of ~9 km south of Etna’s SE crater. The smaller hot spot to the northeast of the main hot spot relates to two shorter (~2 km long E–W orientated) lava flow fields that were emplaced to the northeast of the SE crater.

**Multiple-band (color) spectral radiance map** Combining multiple bands of data increases the spectral radiance information content of the map. This is now a multi-band spectral radiance map. To produce such a map, appropriate bands need to be selected and displayed. For example: MIR or SWIR data may provide information regarding high-temperature phenomena within the image, and so may be displayed on the hot (red) gun of a red–green–blue (RGB) composite. TIR data may provide information for cooler, ambient, and crusted-lava surfaces, and so may be displayed in the cooler (green) gun.

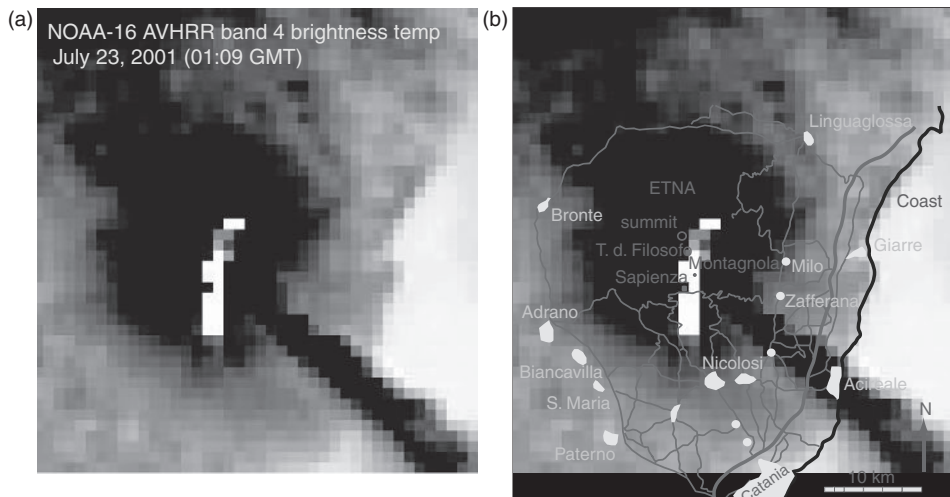


Figure 6.1 (a) Nighttime AVHRR MIR (band 4) image acquired on 23 July 2001 during an eruption at Mt. Etna showing a multiple-pixel hot spot due to the presence of channel-fed active lava, as well as a cold plume extending to the southeast (darker tones = colder temperatures). In (b) the main towns, roads and coast have been overlain on the image (pixel size = 1 km). See also color plates section.

Reflected data acquired in the NIR or VIS may then be displayed using the coolest (blue) gun to provide a sense of location for other physical features such as snow, cloud, lava and tephra fields, forest, fields, roads, and towns.

An example of such a map is given in [Figure 6.2a](#) and shows the spatial distribution of emitted and reflected spectral radiance as recorded by TM across a tube-fed pahoehoe lava flow field active on Kilauea on 23 July 1991. To make an effective map, we have assigned TM's SWIR bands 7 and 5 to the red and green guns, respectively, and assigned a visible band (band 3) to the blue gun. This gives a roughly true color map, in which vegetation is green, cold lava is black, and active lava is yellow-to-red. In this combination, the color of the active lava varies from yellow if the surface is relatively hot, so that there is thermal emission in bands 5 and 7, to red if the surface is relatively cool (so that there is emission just in band 7). [Flynn et al. \(1994\)](#) used this spectral radiance map to produce the feature map of [Figure 6.2c](#). The resulting map shows the location, extent, dimensions, shapes and orientations of:

- (i) eight zones of active pahoehoe;
- (ii) an active lava lake within the main vent at Pu'u 'O'o;
- (iii) a frozen (roofed-over) lava lake, apparent from an anomaly in the TIR, at Kupaianaha;
- (iv) the line of the lava tube, as apparent from a warm, linear feature in the TIR;
- (v) three hot skylights in the lava tube that links Kupaianaha and the active pahoehoe zones;
- (vi) two zones of lava entering the ocean (ocean entries).

It also shows the location of these features in relation to the coast, zones of barren lava and forested land, as well as the inhabited area of the Royal Gardens sub-division, which is apparent as a grid-pattern of roads in the green forest. Thus, the color composite image of [Figure 6.2a](#) fulfils all the roles of a traditional map, doing an excellent job of mapping this active feature.

#### *6.1.1.2 Maps of higher level (derived) parameters*

Using the methodologies of [Chapter 4](#) we can convert our spectral radiance maps to maps of higher level (derived) parameters. [Flynn et al. \(1994\)](#), for example, converted their simple spectral radiance map of [Figure 6.2a](#) to a heat flux map. The resulting heat flux map is given in [Figure 6.2b](#). Such a conversion requires a little more processing, including application of mixture models and their associated assumptions, followed by the appropriate heat flux conversions, as described in [Chapter 4](#). To create the heat flux map of [Figure 6.2](#), [Flynn et al. \(1994\)](#) executed the following steps.

- (1) Run the data through the “Kilauea: two bands of saturated and unsaturated TM data” hot spot identification and pixel mixture model execution routine of Electronic Supplement 6 to (i) locate hot pixels containing active lava, and (ii) extract the thermal structure for each pixel.
- (2) Complete the radiation conversion routine for a two-component active lava surface as given in Equation (4.37) of [Section 4.4.1.1 \(Chapter 4\)](#).

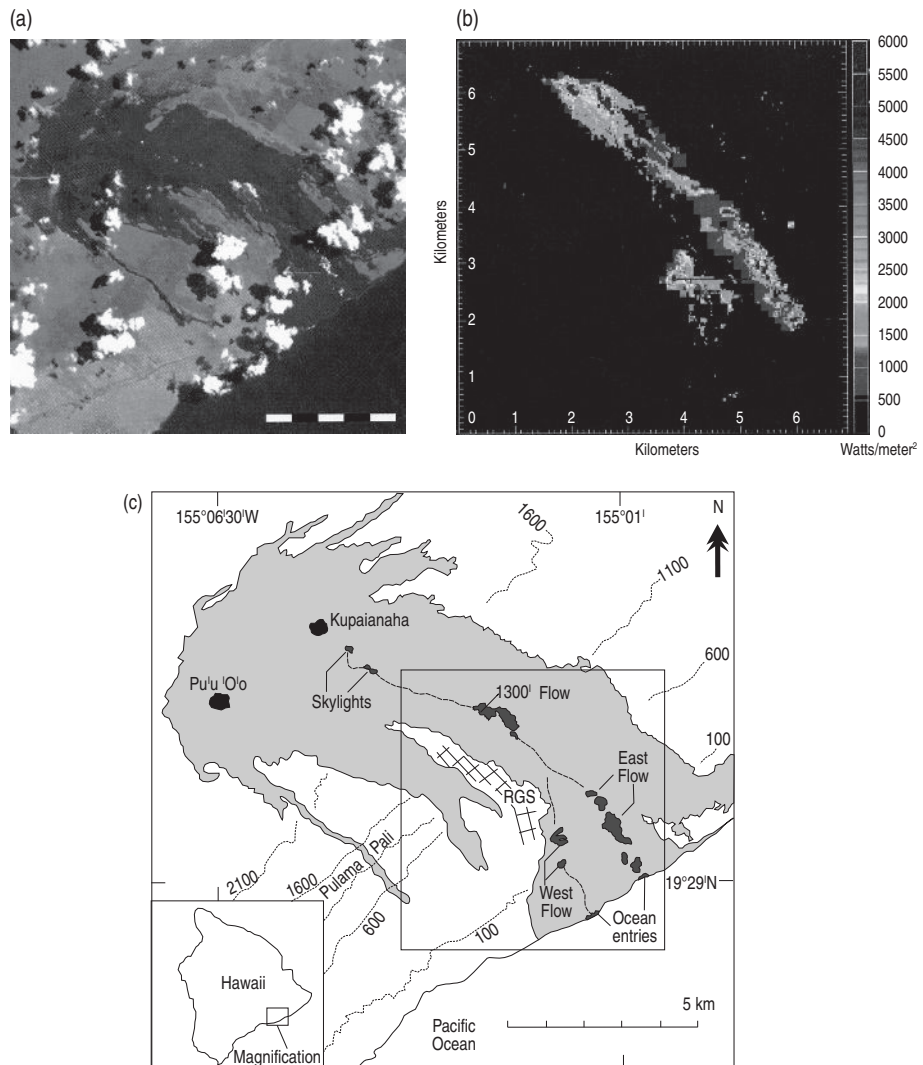


Figure 6.2 (a) TM color composite of bands 7 (red), 5 (green) and 3 (blue) acquired on 23 July 1991 over Kilauea volcano showing the location of active lava flows (red-yellow hot spots), the extent of the lava flow field emplaced since 1983 (black) and vegetated areas (green). The grid of roads comprising the Royal Gardens sub-division (RGS) can also be made out [from Flynn *et al.* (1994, Fig. 2a)]. (b) Map of radiant flux density for the active lava flow zone of (a) [from Flynn *et al.* (1994), Fig. 2b]. (c) Flow field map derived from the image: box = location of the radiant flux density map of (b) [from Flynn *et al.* (1994), Fig. 1] (Figures reproduced with kind permission from Springer Science and Business Media). See also color plates section.

- (3) Define the minimum and maximum radiation fluxes recorded, and split this range into  $n$  classes.
- (4) Assign each class a color from white (for the pixels with the maximum radiation flux) to blue (for the pixels with the minimum radiation flux), and assign all background pixels black.
- (5) Display color coded radiation flux image as a map.

This map shows the same distribution as seen in the original map of spectral radiation, as we can see from comparing [Figure 6.2a](#) with [Figure 6.2b](#). However, while the spectral radiation map may be of great use for basic location and spatial interpretation purposes, converting to higher-level parameters allows the map to be presented in terms of more “useable” parameters. Display of the map in terms of heat flux or thermal structure will likely increase the utility of the map for understanding physical processes. Lava flow heat fluxes and thermal structures, for example, are much easier to ingest into cooling-limited lava flow emplacement models than spectral radiance maps. Likewise, mapping of the way in which thermal structures on an active lava flow, lake or dome vary with distance from the vent, or with variations in topography, are much easier to interpret and use in physical models, or to support arguments regarding the emplacement of a lava body, than maps of spectral radiance. For example, a lava flow moving onto steeper slopes may increase in velocity, so that the surface crust breaks up to change the resulting thermal structure, and increase the heat flux.

#### *6.1.1.3 Single higher-level (derived) parameter map*

We can identify two types of higher-level (derived) parameter map: single or multiple parameter. The heat flux map of Flynn *et al.* (1994) is a single (higher-level) parameter map because it plots just one parameter: heat flux. In this case, the pixel tone or color is simply a function of the parameter value. Other higher-level parameters that could be used to derive such maps include calculated crust temperature, crust area, effective radiation temperature or lava interior temperature. Thus another example of a single (higher-level) parameter map is the TM-derived lava flow interior temperature map given for a lava flow active on Etna during June 1984 by Pieri *et al.* (1990), as reproduced in [Figure 1.11](#) of [Chapter 1](#). Likewise, the maps of crack coverage, crust and crack temperature created by Lombardo *et al.* (2009) by applying the dual-band models of [Chapter 5](#), and as given here in [Figure 6.3](#), are nice examples of higher-level (derived) parameter maps. In this case, we see how the flow thermal structure for a channel-fed flow field varies with distance from vent, with the crust extent increasing rapidly with distance from the vent, and crust temperatures decreasing to low but stable levels over much of the length of this channel-contained 'a'a flow.

#### *6.1.1.4 Multiple-parameter maps*

Multiple-parameter maps involve plotting two or more parameters on the same map. One way to project multiple parameters onto a single map may be to assign the pixel a symbol, shape and/or color depending on the numeric value of each parameter to be mapped.

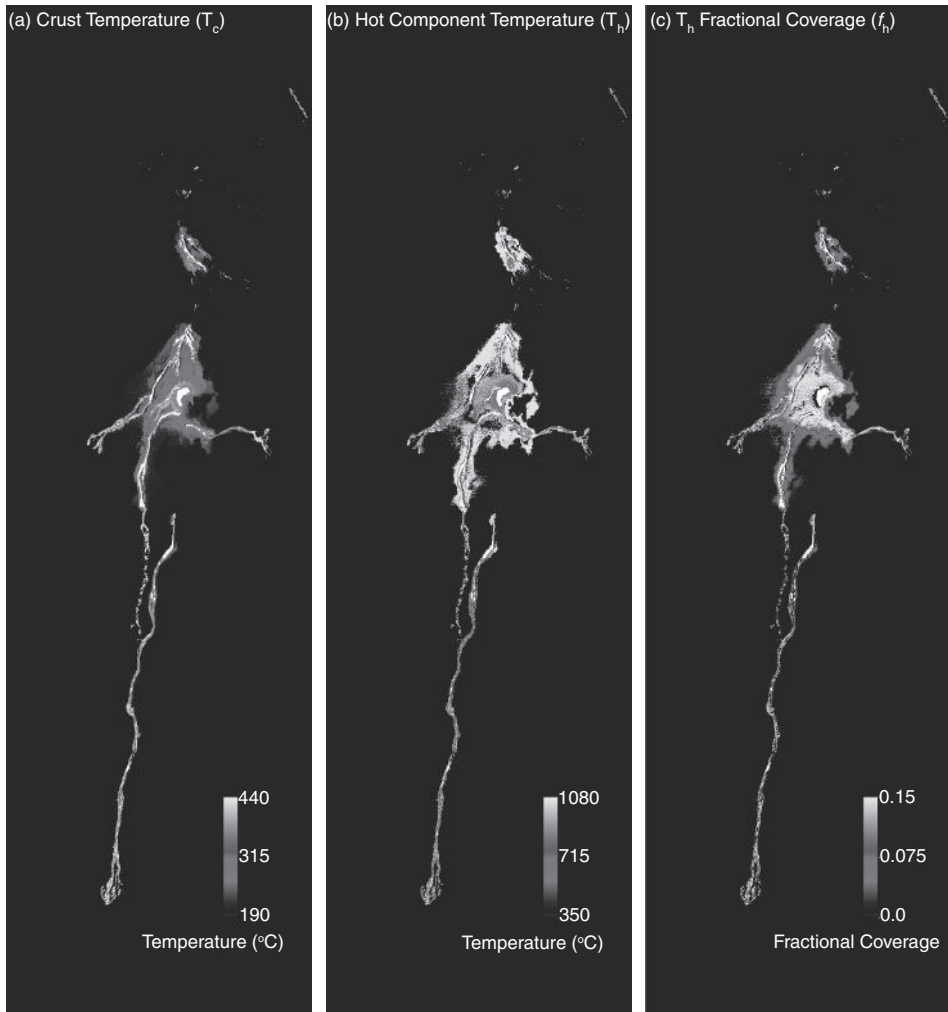


Figure 6.3 Maps of (a) crust component temperature, (b) hot-component temperature (c) hot-component fractional coverage as extracted by applying the dual-band method to high-spatial-resolution airborne sensor data for the same active lava flow field as that imaged in Figure 6.1a. Data: multispectral infrared and visible imaging spectrometer (MIVIS), an airborne sensor equipped with 72 SWIR bands and 10 TIR bands, spatial resolution was 6–12 m depending on surface elevation [from Lombardo *et al.* (2009, Fig. 5); reproduced by permission of American Geophysical Union]. See also color plates section.

Wooster *et al.* (2000), for example, mapped TM-derived thermal structures on a pixel-by-pixel basis across Unzen's lava dome surface by displaying each pixel across the thermal anomaly as a circle, the size and color of which was a function of the hot surface area and temperature, respectively. As reproduced here in Figure 6.4, the mapped variation in thermal structure could be associated with various effusive styles. Application of such a mapping

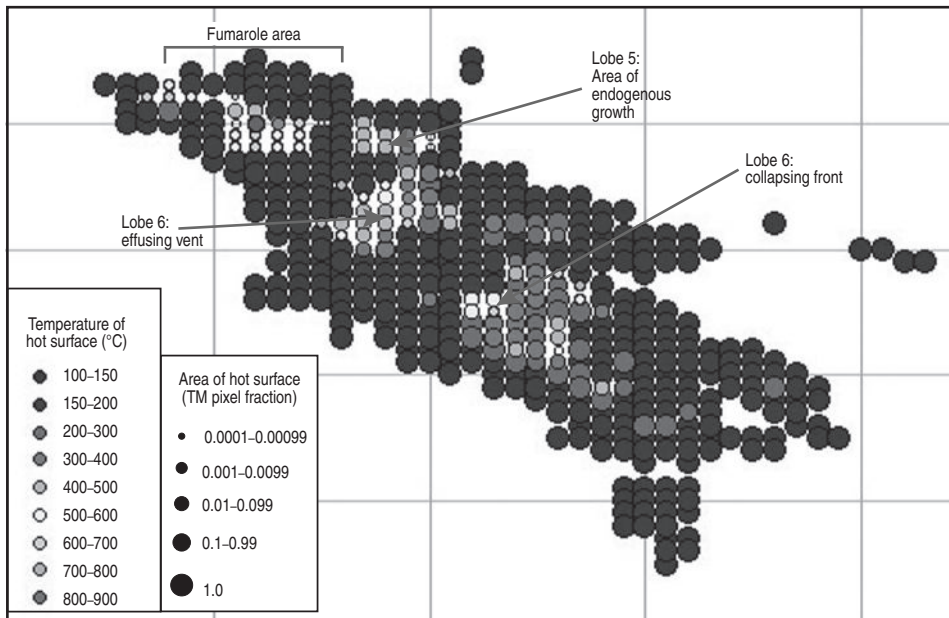


Figure 6.4 Map of hot surface fractional coverage and temperature as extracted through pixel-by-pixel application of the dual-band method to TM data for Unzen's active lava dome: the use of balls allows the two extracted parameters (size and temperature) to be mapped together. Image date: 10 January 1992 [from Wooster *et al.* (2000, Fig. 6), with permission from Elsevier]. See also color plates section.

methodology thus allows multiple parameters to be displayed on a single map to allow the variation in thermal structures and/or heat flux across an active lava body, or geothermal feature, to be viewed and interpreted.

#### 6.1.1.5 Location

So far we have argued that the image is the map. Consequently we have just displayed the image, or parameters derived from the image, to give the hot spot location, distribution and spatial setting. However, we can improve the quality of the hot spot map by either:

- (i) projecting other spatial information onto the image, or
- (ii) extracting pertinent hot spot information from the image and projecting this onto a base map of other physical and cultural features.

Base maps used as part of the second approach include maps of topographic features (such as shaded relief, geomorphologic, or contour maps), traditionally mapped features (road and/or town map), anthropological features (population densities, land use/type, land value, population character, etc.), land use classification (agricultural use/type, industrial, commercial, residential, natural habitat, etc.), geological features (e.g., faults, rift zones, vents, pit craters, cinder cones, historic lava flow fields, etc.) or results of model simulations for lava flow emplacement.

In effect, the result is a geographical information system (GIS) where the location and intensity of the hot spot can be assessed in relation to all other spatial parameters defined for the same location or pixel. Such approaches allow improved assessment of the location, extent and distribution of the hot spot radiance in relation to other physical, natural and anthropogenic features.

A simple example is given in [Figure 6.1b](#). In this case, the image is the base map and supplementary geographical information has been overlain on it. This improves our ability to assess the location and extent of the hot spot in relation to volcano-geomorphic and anthropogenic features such as active vents, cinder cones, roads and towns. In this example, the addition of supplementary information allows us to confirm that the location of the smaller hot spot really is to the northeast of Etna's summit craters, and that the larger hot spot extends from a location between the Torre del Filosfo and Montagnola cone, through the Sapienza ski station and its associated road network, to end three pixels ( $\sim 3.3$  km) short of the town of Nicolosi. We can also see that the orientation of the hot spot points in the direction of Nicolosi, as well as Belpasso, so that the hot spot orientation suggests a real problem for these two towns, if extension of the hot spot (and the associated lava flow) continues.

### **6.1.2 Map scale and data spatial resolution**

Scale is defined as the relative dimensions of a map in regard to the dimensions of the actual surface, or ratio of reduction or enlargement in a map. While large-scale maps will have the least degree of reduction, and will show the greatest degree of spatial detail, small-scale maps will have the greatest degree of reduction, and will show the smallest degree of spatial detail. The scale, or spatial detail, of the hot spot map is determined by the spatial resolution of the data used to generate the map.

- TM-class data can be used to generate large-scale maps with spatial resolutions of tens of meters (typically 30 m).
- AVHRR-class data can be used to generate smaller-scale maps with spatial resolutions of hundreds of meters (typically 500–1000m).
- GOES-class data can be used to generate small-scale maps with spatial resolutions of thousands of meters (typically 1000–4000 m).

In each case, the location precision and spatial detail of variation in any mapped parameter will be of the same order as the sensor spatial resolution. Thus, the spatial detail of the map decreases as we move from TM-class to GOES-class. Maps produced from TM-class data allow the detailed distributions of radiant flux density within the hot spot to be mapped, as done in [Figure 6.2](#). Use of AVHRR- and GOES-class data allow little more than an unimpressive large square to be projected onto a base map, as in the example given in [Figure 6.1](#). In many well-observed cases projecting a large square onto a base map may not be of much added value, because the ground-based observer can, quite quickly, give a much more

precise idea of the eruption location (vent site), plus location, direction and extent of individual lava flows. In addition, the square extracted by an automated algorithm may not give the full anomaly extent (because some pixels will be missed: see [Section 5.3.7 of Chapter 5](#)). However, it can still give kilometre-scale spatial information which may be of value for unobserved cases, or in providing information before the ground-based observers can arrive. It may even influence the destination of those observers. Field teams have (for example) been deployed on the basis of GOES-based hot spot emails that can indicate that effusive activity is increasing and can reveal the approximate location (near-vent, medial, distal-coastal) of that increase in an extensive, active lava flow field comprising multiple units.

#### 6.1.2.1 Sharpening tools

Sharpening tools allow the spatial precision of large-scale spectral radiance maps to be increased, focusing the main sources of spectral radiance into their most likely sub-pixel locations. Such a sharpening tool was developed in [Harris \(1992\)](#). It is effectively a weighted average technique that uses digital number, spectral radiance or heat flux data from the host pixel, plus that from the eight pixels immediately surrounding the host pixel, to assess the most likely distribution of radiance within the host pixel. Take, for example, the hypothetical lava distribution of [Figure 6.5a](#) where the edge of an active lava flow cuts a group of nine pixels diagonally. This distribution of radiant emittance on the ground will result in three pure pixels containing ambient ground (cold) pixels in the NW sector of the group and three pure pixels containing active lava (hot) pixels in the SE sector; separated by a diagonal line of three mixed (warm) pixels, as given in [Figure 6.5a](#). The intent of the sharpening method is to define the most likely sub-pixel spectral radiance distribution for the mixed pixels, approximately locating the boundary of the two features (ambient ground and active lava) within the mixed pixel, as shown in [Figure 6.5](#).

To achieve this, the sharpening method divides each coarse pixel (Pixels A to I in [Figure 6.6](#)) into nine smaller sub-pixels (sub-pixels Spx1 to Spx9), as shown in [Figure 6.6](#). The value (whether expressed in terms of DN, spectral radiance or heat flux) for each of the nine sub-pixels within each coarse (host) pixel is then calculated from:

$$V_{\text{Spx1}} = (V_A + V_B + V_D + V_E)/4 \quad (6.1a)$$

$$V_{\text{Spx3}} = (V_B + V_C + V_E + V_F)/4 \quad (6.1b)$$

$$V_{\text{Spx7}} = (V_D + V_E + V_G + V_H)/4 \quad (6.1c)$$

$$V_{\text{Spx9}} = (V_E + V_H + V_F + V_I)/4 \quad (6.1d)$$

$$V_{\text{Spx2}} = (V_B + V_E + V_{\text{Spx1}} + V_{\text{Spx4}})/4 \quad (6.1e)$$

$$V_{\text{Spx4}} = (V_D + V_E + V_{\text{Spx1}} + V_{\text{Spx7}})/4 \quad (6.1f)$$

$$V_{\text{Spx6}} = (V_E + V_F + V_{\text{Spx3}} + V_{\text{Spx9}})/4 \quad (6.1g)$$

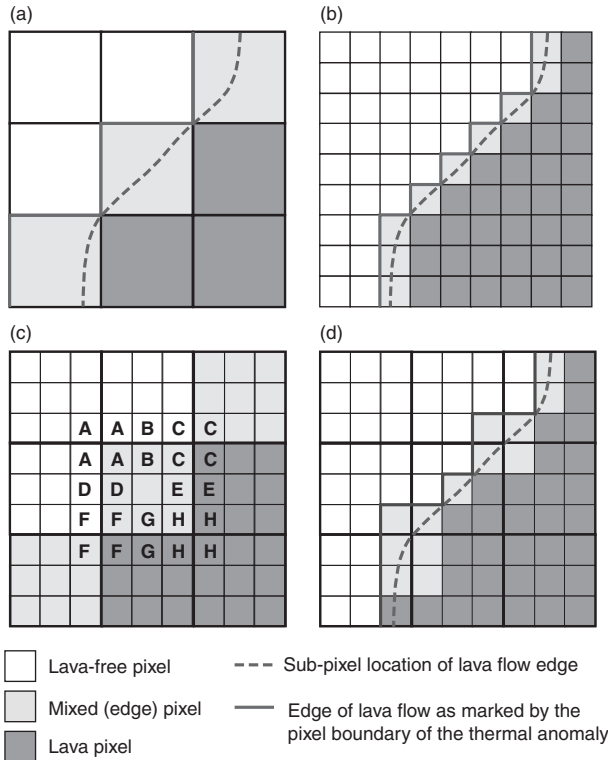


Figure 6.5 (a) Schematic of sub-pixel placement of the edge of an active lava flow in a “large” pixel, where pure lava pixels will be the hottest (orange), pure background pixels the coldest (white) and mixed “edge” pixels at a temperature in between the two (yellow). (b) The same active lava flow, but imaged with a spatial resolution that is three times superior, hence improving the location precision of the flow edge. (c) The sharpening methodology of Section 6.1.2.1. cuts each large pixel into nine sub-pixels, and executes the algorithm of Equation (6.1). This results in sub-pixels with identical letters having the same value. (d) Results of sharpening image (a): the product gives a lava flow edge location that is sub-pixel and narrows down the actual sub-pixel position of the lava flow edge. See also color plates section.

$$V_{\text{Spx}8} = (V_E + V_H + V_{\text{Spx}7} + V_{\text{Spx}9})/4 \quad (6.1\text{h})$$

$$V_{\text{Spx}5} = (V_{\text{Spx}1} + V_{\text{Spx}2} + V_{\text{Spx}3} + V_{\text{Spx}4} + V_{\text{Spx}6} + V_{\text{Spx}7} + V_{\text{Spx}8} + V_{\text{Spx}9})/8 \quad (6.1\text{i})$$

in which  $V_A$  through  $V_I$  are the values for pixels A through I, and  $V_{\text{spx}1}$  through  $V_{\text{spx}9}$  are the values for sub-pixels 1 through 9. As shown in Figure 6.6, the image sub-sampled in this way can then be re-displayed to provide a “sharper” (spatially more precise) map of the spatial distribution of spectral radiance than was possible using the original data. The methodology, can thus be applied as follows.

- Step 1. Isolate the hot spot, plus a one-pixel-wide rim of pixels around the hot spot.
- Step 2. Split each pixel into nine equally-sized sub-pixels.

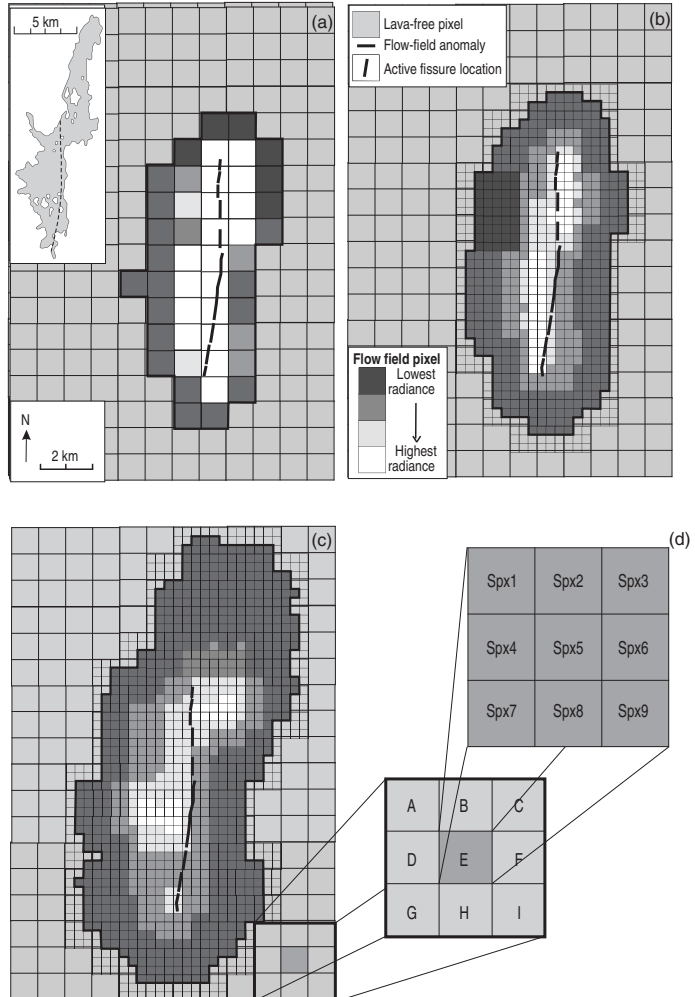


Figure 6.6 (a) Density-sliced 1-km AVHRR image of Krafla (Iceland) obtained at 04:47Z on 5 September 1984, five hours after an effusive eruption began. At the time lava fountaining was occurring along an 8.5 km fissure (as fitted to the image), with activity emplacing the lava flow field as inset. (b) Sharpening focuses the zone of highest radiance onto the actual fissure line. (c) The sharpened thermal map for the following day, when activity was confined to two vents along the original fissure: one on the northern end, the second just south of center. In both cases the image has been geometrically registered to a map of Iceland and the active fissure location from ground-based mapping (inset) overlain (discontinuous black line). Both images have been sharpened by cutting each original “large” pixel into nine sub-pixels, as shown in (d), and applying Equation (6.1) to these pixels [modified from Harris *et al.* (1997a, Fig. 5)]. See also color plates section.

- Step 3. For each pixel, first calculate the sub-pixel spectral radiances for the corner pixels (i.e., apply Equations (6.1a), (6.1b), (6.1c) and (6.1d) to sub-pixels 1, 3, 7 and 9 of [Figure 6.6](#)).
- Step 4. Calculate the sub-pixel radiances for each “side” sub-pixel (i.e., apply Equations (6.1e), (6.1f), (6.1g) and (6.1h) to sub-pixels 2, 4, 6 and 8 of [Figure 6.6](#)).
- Step 5. Calculate the sub-pixel radiance for the central pixel (i.e., apply Equation (6.1i) to sub-pixel 5 of [Figure 6.6](#)).
- Step 6. Set a threshold spectral radiance below which spectral radiances are assumed to be associated with ambient (lava-free) ground. Use this to identify all lava sub-pixels, i.e., if spectral radiance is greater than threshold, then mark sub-pixel as “lava”. This will identify the sub-pixel boundary of the lava.
- Step 7. Density slice the sharpened image by identifying the highest spectral radiances within the lava area, and divide the image into discrete spectral radiance classes between the threshold value and the highest value. Assign each class a color and use this to slice the sharpened image into a number of classes, i.e., assign each pixel a color depending on the class within which its sub-pixel spectral radiance places it.

By way of illustration, these application steps are executed in Electronic Supplement 10 on the image used to produced the *sharpened* spectral radiance map of [Figure 6.6](#). We see that the resulting map tightens up the zone of maximum radiance, in this case focussing it on to the field-mapped line of the lava fountains centred in an active lava flow field spreading in all directions. It also sharpens up the boundary of the flow field, bringing it closer into line with that mapped on the ground.

### 6.1.3 Map time series

The map can be updated with each satellite overpass, allowing map time series to be constructed. The time series will have the temporal resolution of the sensor chosen so that

- TM-class data can be used to generate maps with spatial resolutions of tens of meters, but with temporal resolutions of tens of days (typically 16 days);
- AVHRR-class data can be used to generate maps with spatial resolutions of hundreds of meters, but with temporal resolutions of hours (typically 6–24 hours);
- GOES-class data can be used to generate maps with spatial resolutions of thousands of meters, but with temporal resolutions of minutes (typically 15 minutes).

Thus, although of small scale, the GOES-based maps are capable of mapping the highest degree of temporal detail. We next examine three illustrative examples revealing the spatial and temporal detail available from each map time series class.

#### 6.1.3.1 TM-class map time series

Between 1987 and 2000, 18 cloud-free TM images were acquired of Guatemala’s Santiaguito lava dome complex. These showed hot spots and spectral radiance distributions associated with extrusion of silicic lava, and emplacement of viscous lava flows on the dome

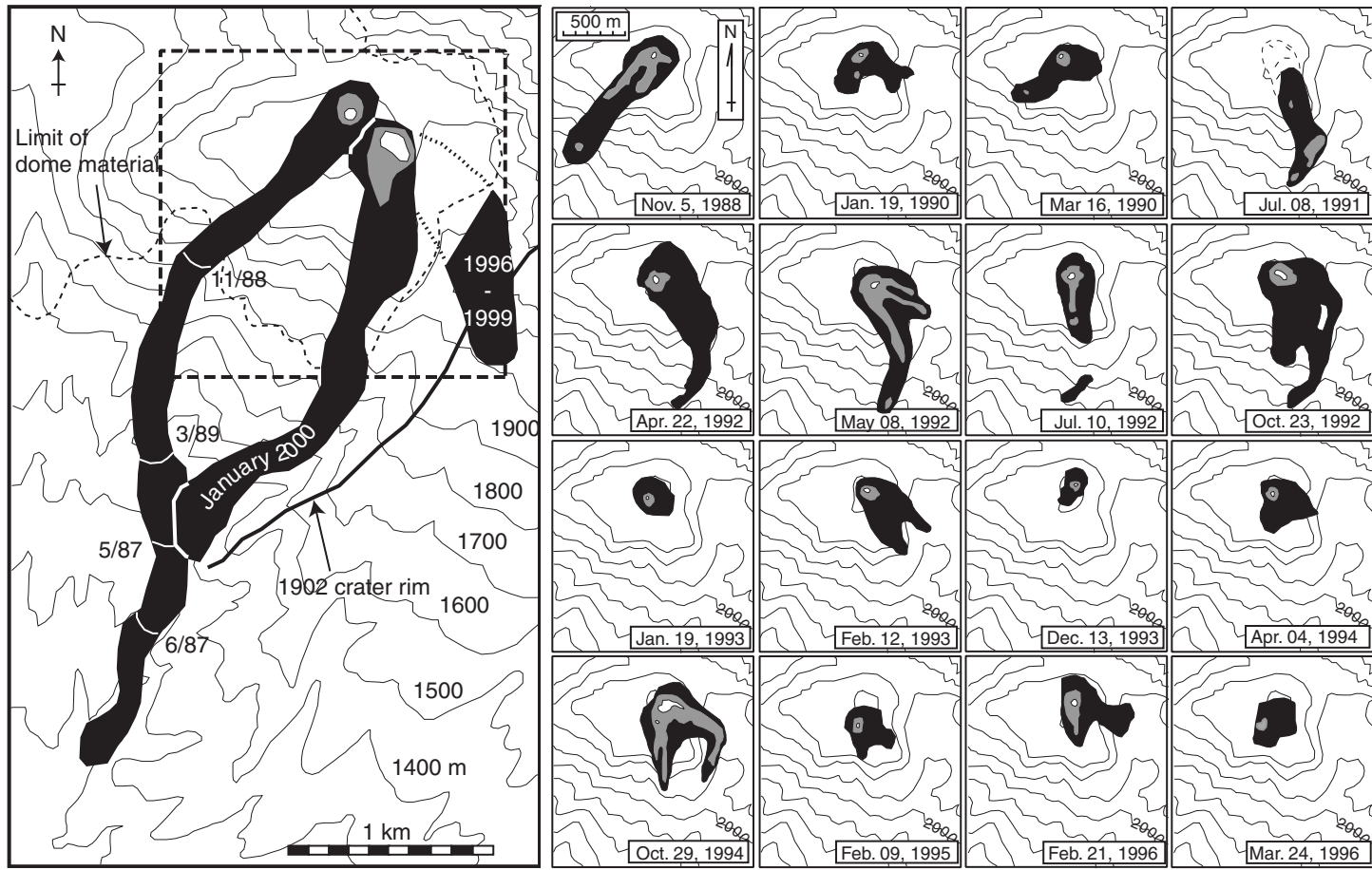


Figure 6.7 Main panel (left): active silicic lava flow units and flow front positions for the Santiaguito lava dome complex during 1987–1989, 1996–1999, and January 2000 as mapped using Landsat TM data. Small panels (right): location of active lava mapped using TM images acquired during 1988–1996. All maps are fitted to a contour map of Santiaguito. Black, gray and white tones locate thermally anomalous surfaces in TM band 6 (pixel-integrated temperatures  $>55^{\circ}\text{C}$ ), band 7 (pixel-integrated temperatures  $>120^{\circ}\text{C}$ ), and band 5 (pixel-integrated temperatures  $>220^{\circ}\text{C}$ ), i.e., cool, warm and hot zones, respectively [modified from Harris *et al.* (2003a, Figs. 2 & 3)].

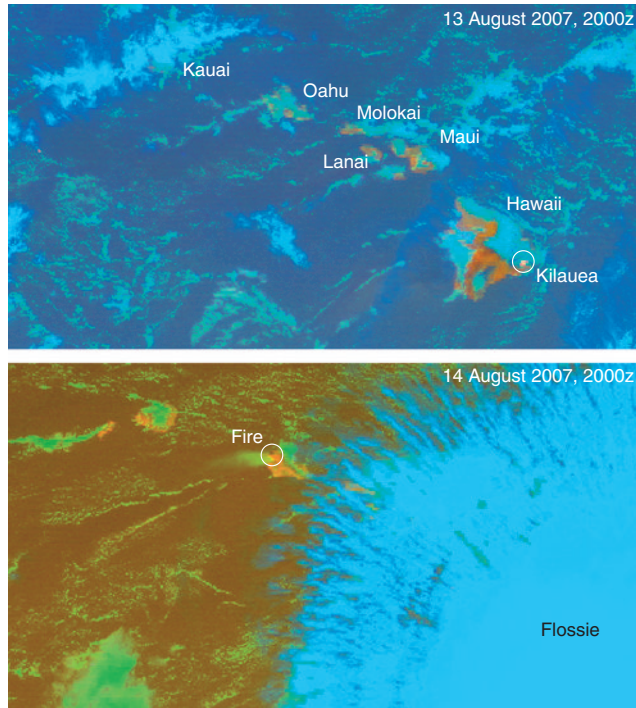


Figure 1.5 See caption in text (p. 34).

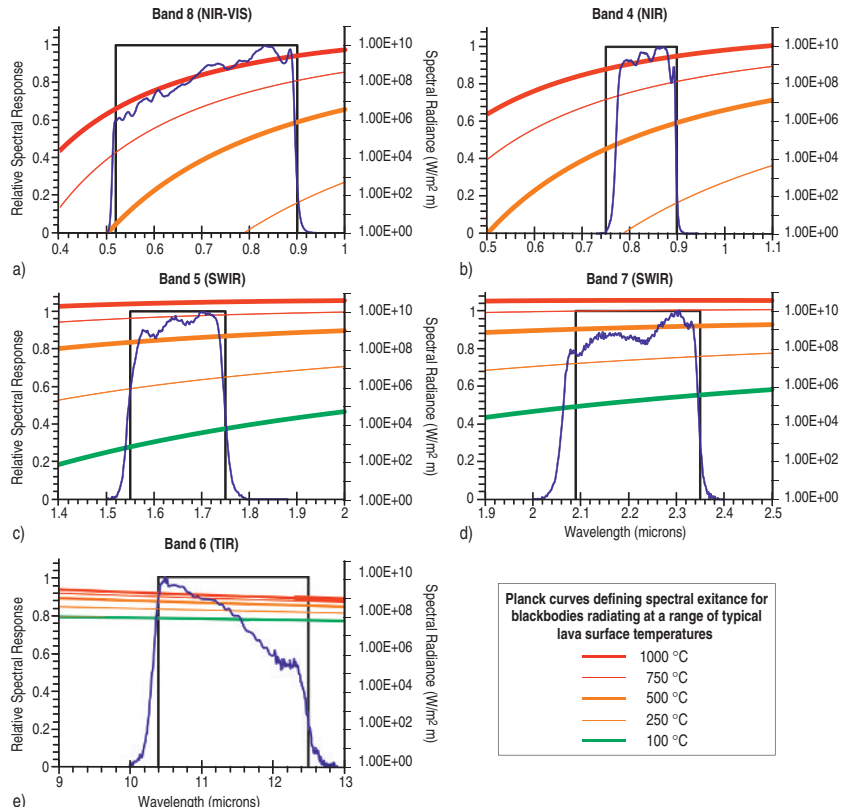
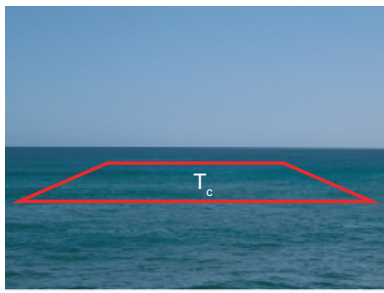


Figure 3.16 See caption in text (p. 149).

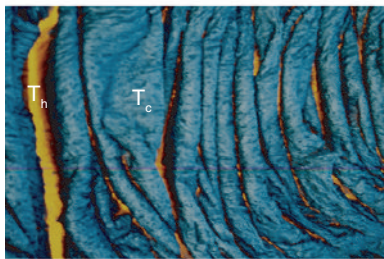


(a) Pixel Case 1: One thermal component

So that:

Pixel Integrated Temperature = Surface Temperature

$$\text{i.e., } M(\lambda, T_{\text{int}}) = pM(\lambda, T_c)$$

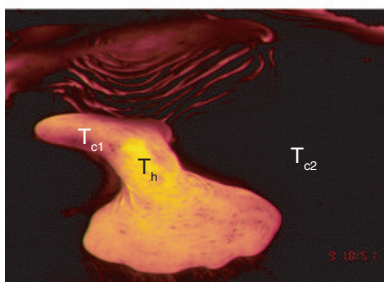


(b) Pixel Case 2: Two thermal components

So that:

Pixel Integrated Temperature < Hottest Temperature

$$\text{i.e., } M(\lambda, T_{\text{int}}) = pM(\lambda, T_c) + (1-p) M(\lambda, T_h)$$

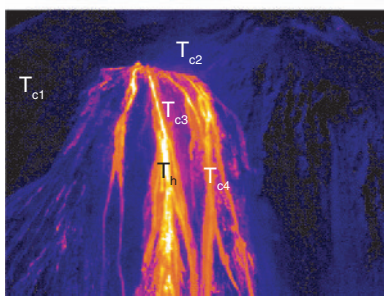


(c) Pixel Case 3: Three thermal components

So that:

Pixel Integrated Temperature << Hottest Temperature

$$\text{i.e., } M(\lambda, T_{\text{int}}) = p_{c1} M(\lambda, T_{c1}) + p_{c2} M(\lambda, T_{c2}) + (1-p_{c1}-p_{c2}) M(\lambda, T_h)$$



(d) Pixel Case 4: Many thermal components

So that:

Pixel Integrated Temperature << Hottest Temperature

$$\text{i.e., } M(\lambda, T_{\text{int}}) = p_{c1} M(\lambda, T_{c1}) + \dots + (1-p_{c1}-p_{cn}) M(\lambda, T_n)$$

Figure 4.6 See caption in text (p. 177).

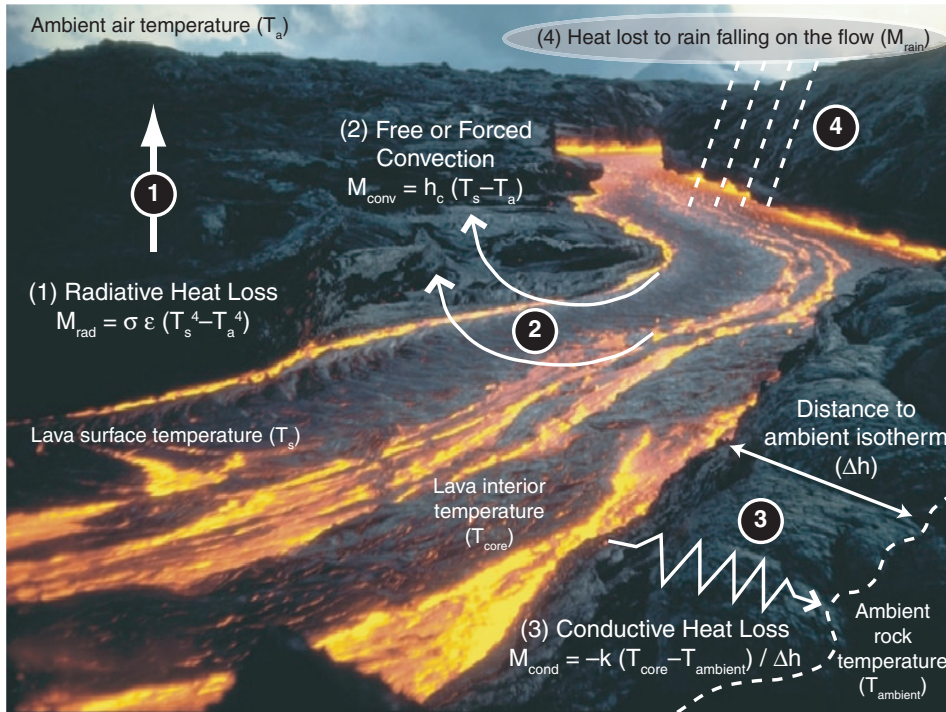


Figure 4.15 See caption in text (p. 215).

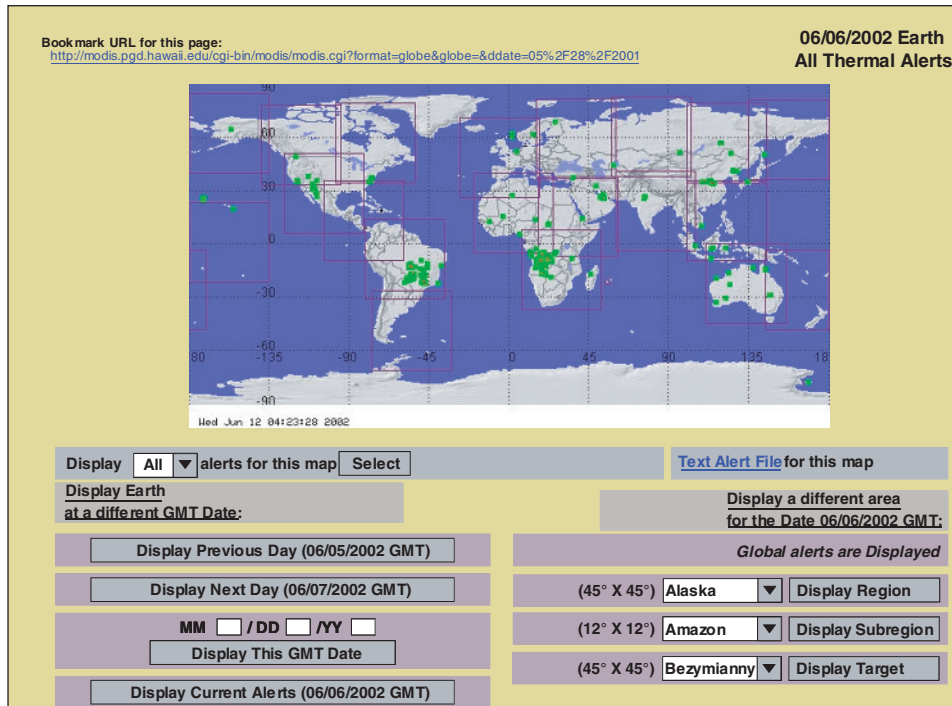


Figure 5.18 See caption in text (p. 328).

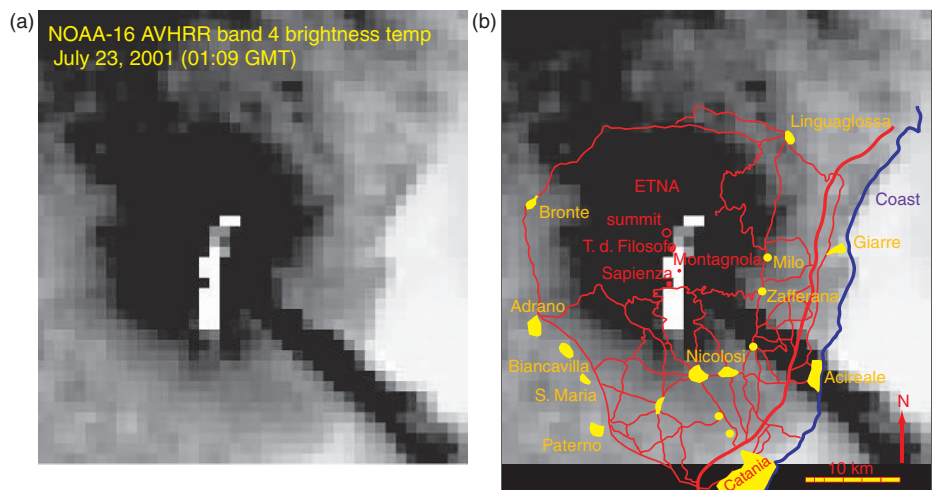


Figure 6.1 See caption in text (p. 335).

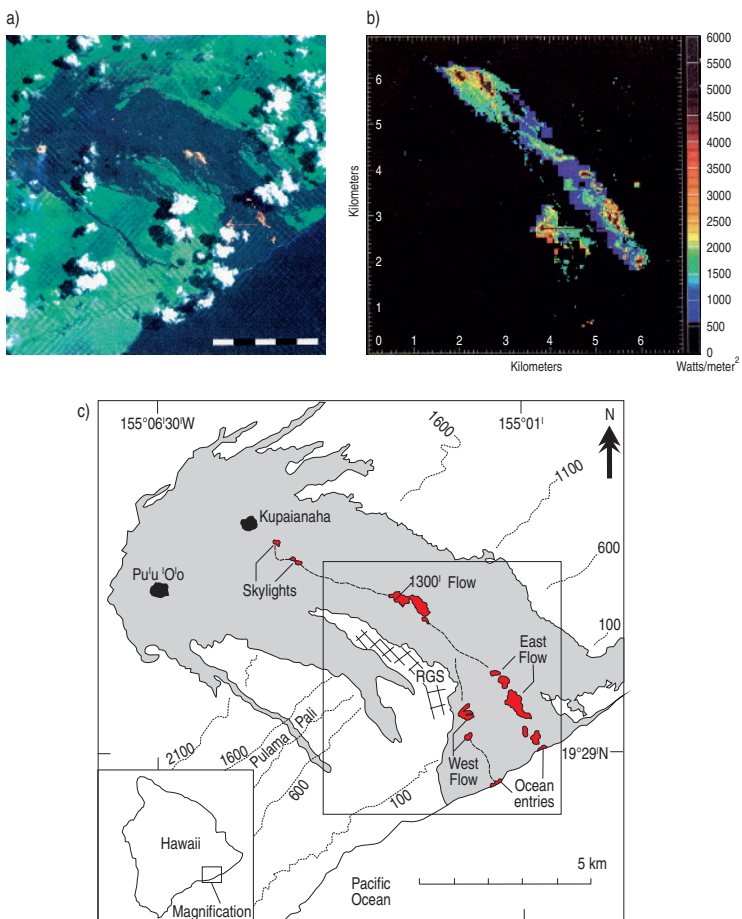


Figure 6.2a, b, c See caption in text (p. 337).

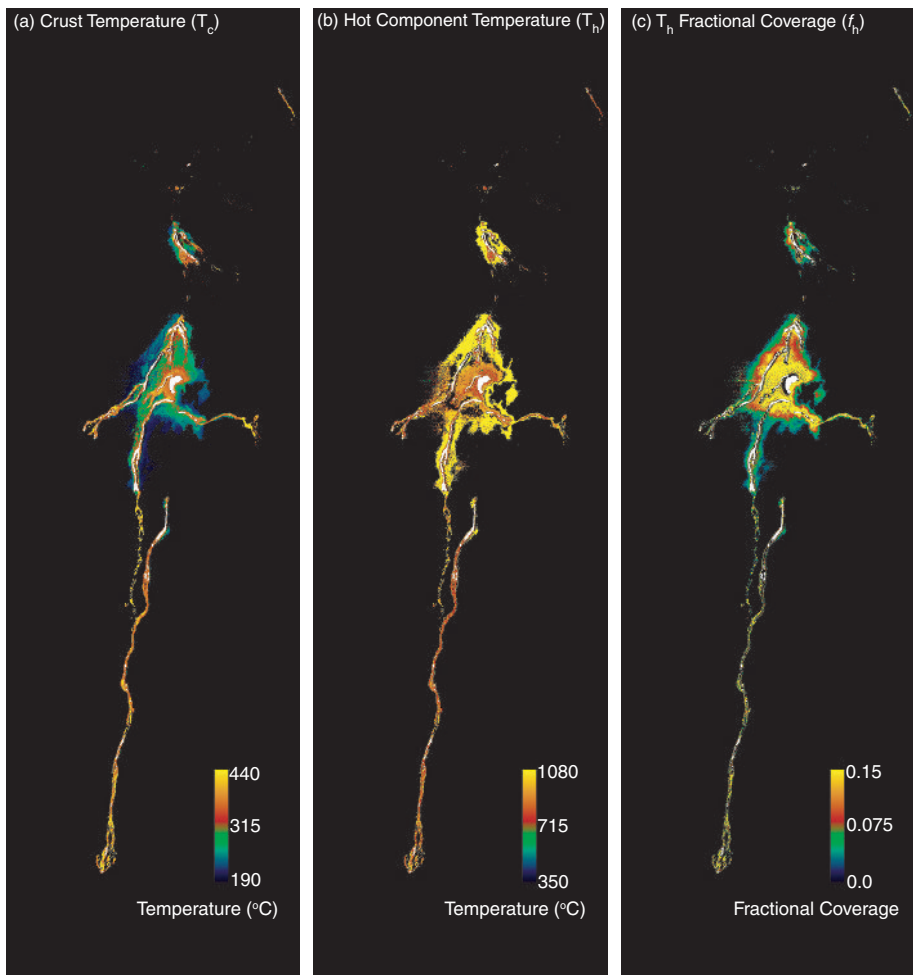


Figure 6.3 See caption in text (p. 339).

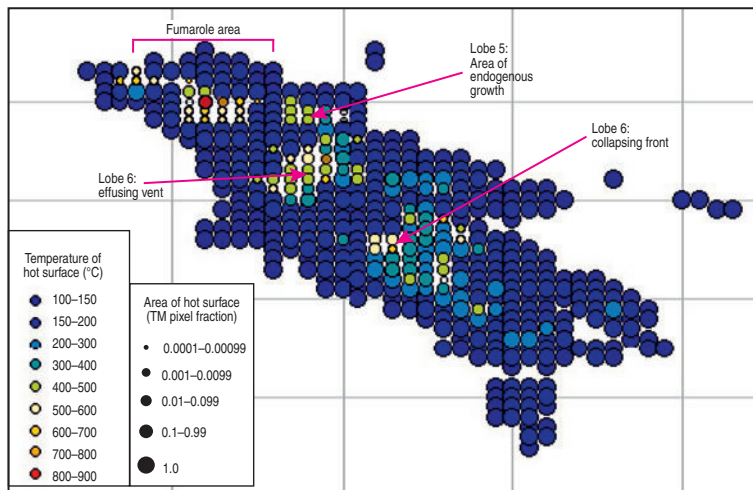


Figure 6.4 See caption in text (p. 340).

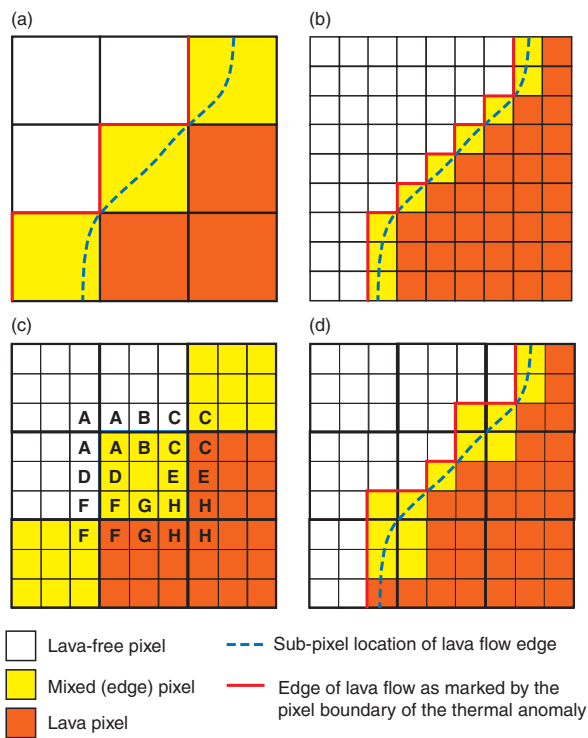


Figure 6.5 See caption in text (p. 343).

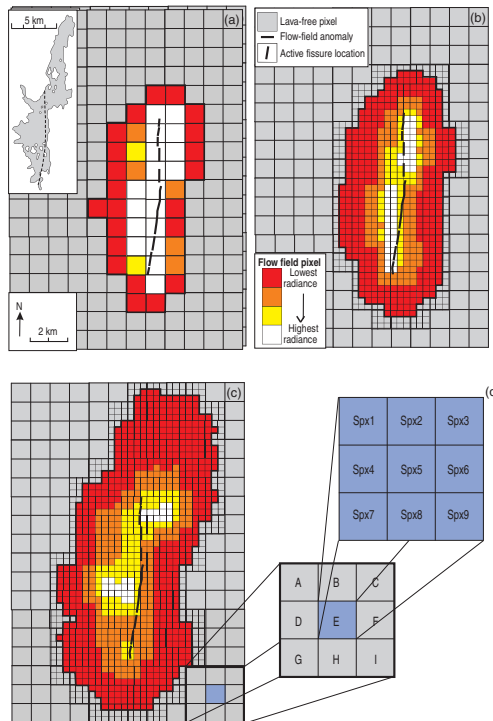


Figure 6.6 See caption in text (p. 344).

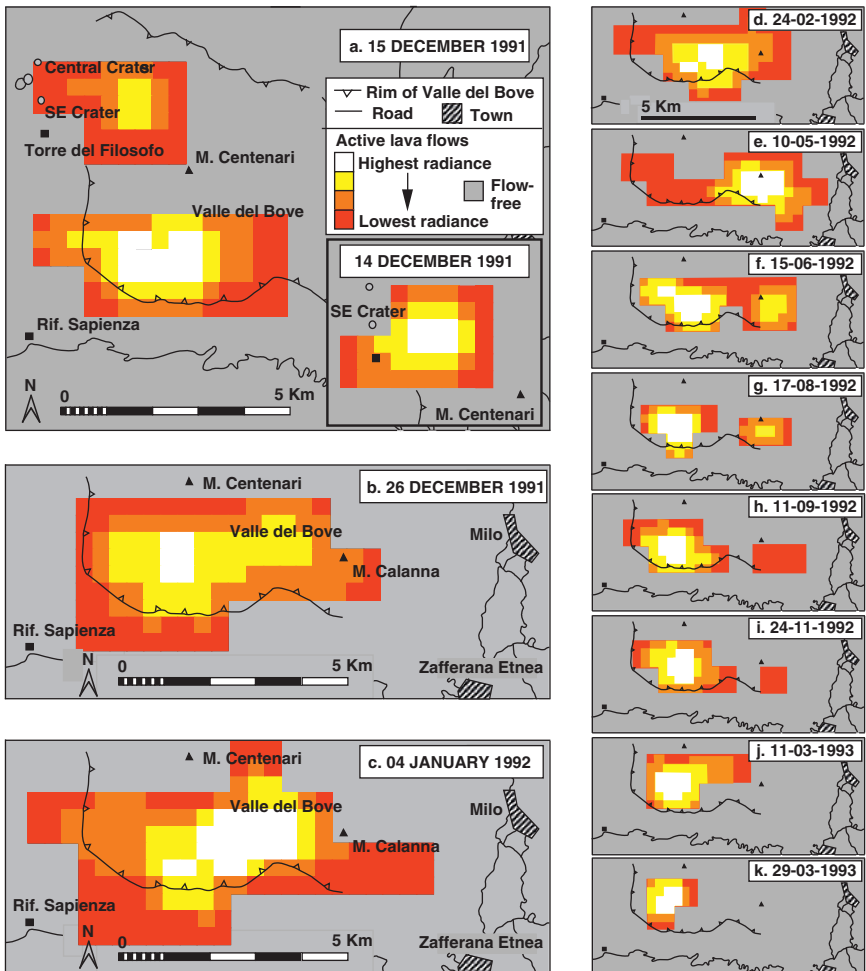


Figure 6.8 See caption in text (p. 348).

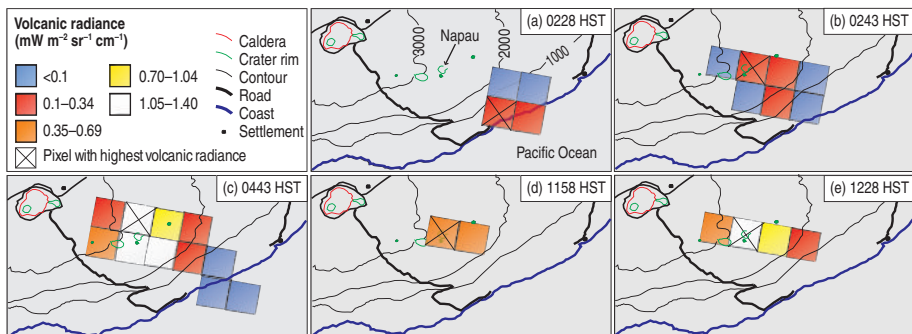


Figure 6.9 See caption in text (p. 349).

(a) Band 5

	195	222				
	300	331	288			
265	282	<b>367</b>	<b>360</b>	222		
	343	345	337	298		

(b) Band 7

	183	210	188			
148		243	<b>274</b>	211		
	194	234	<b>276</b>	<b>275</b>	221	
	214	248	>279	<b>276</b>	211	
		226	240	245	220	

Figure 6.10 See caption in text (p. 349).



a)



b)



c)



d)

Figure 8.1 See caption in text (p. 456).

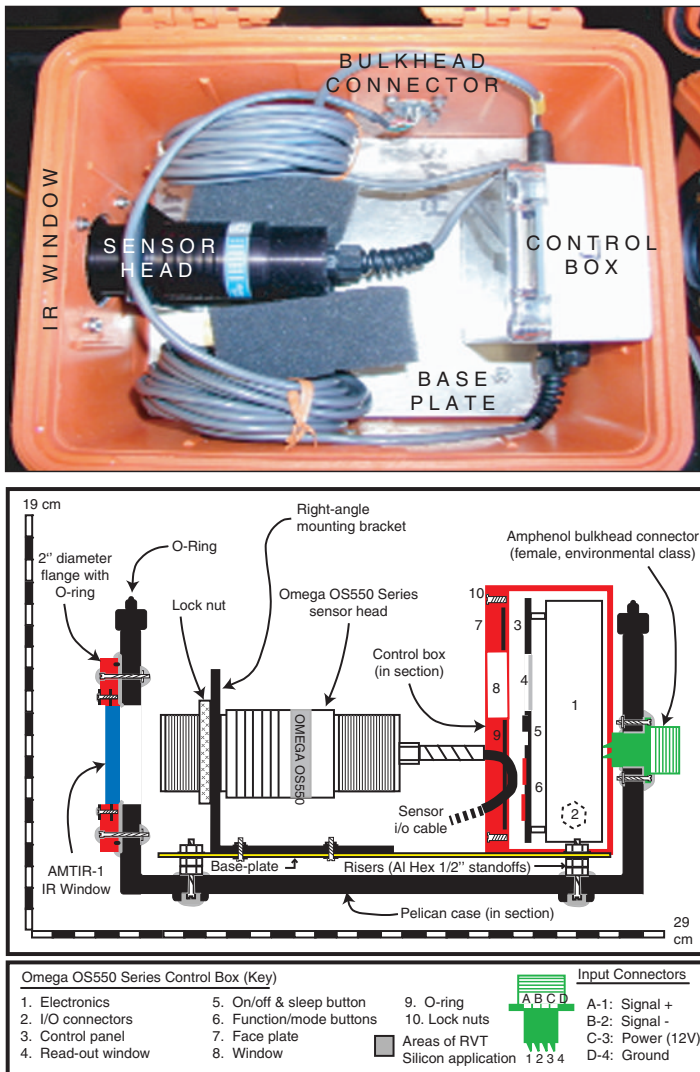


Figure 7.17 See caption in text (p. 453).

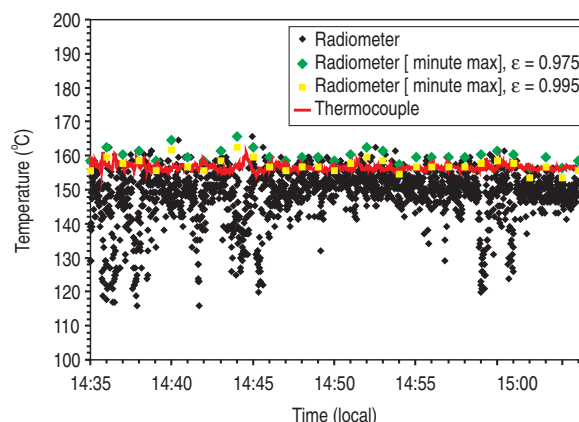


Figure 8.4 See caption in text (p. 468).

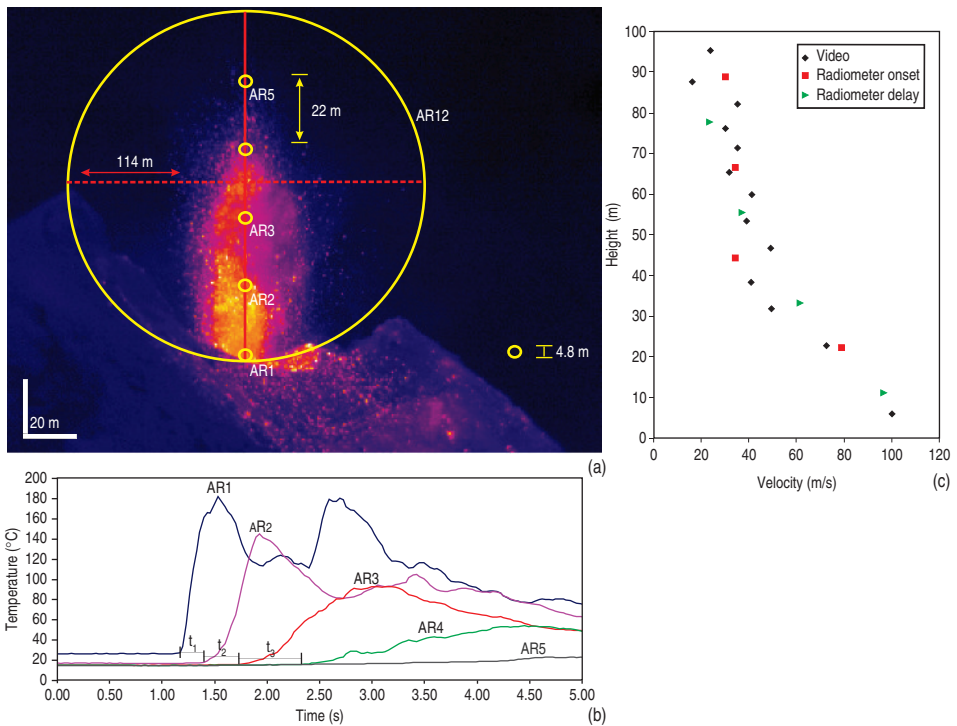


Figure 8.12 See caption in text (p. 488).

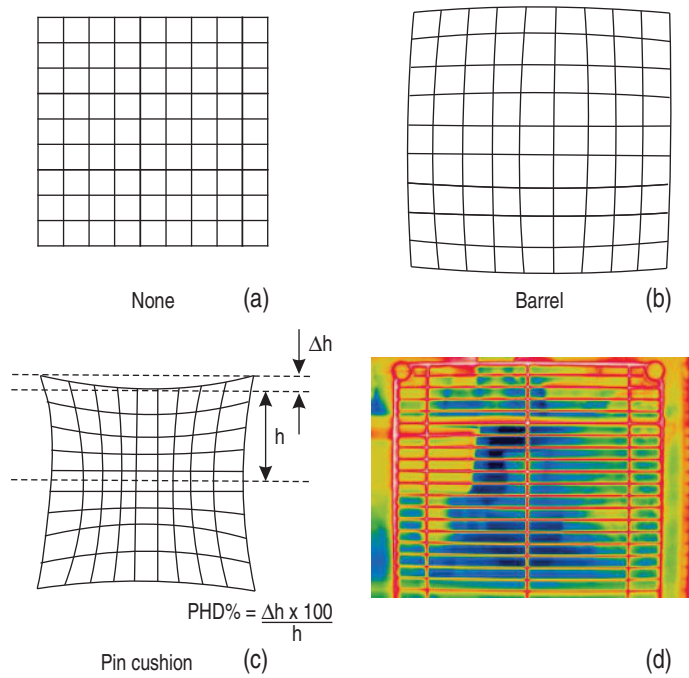


Figure 9.4 See caption in text (p. 530).

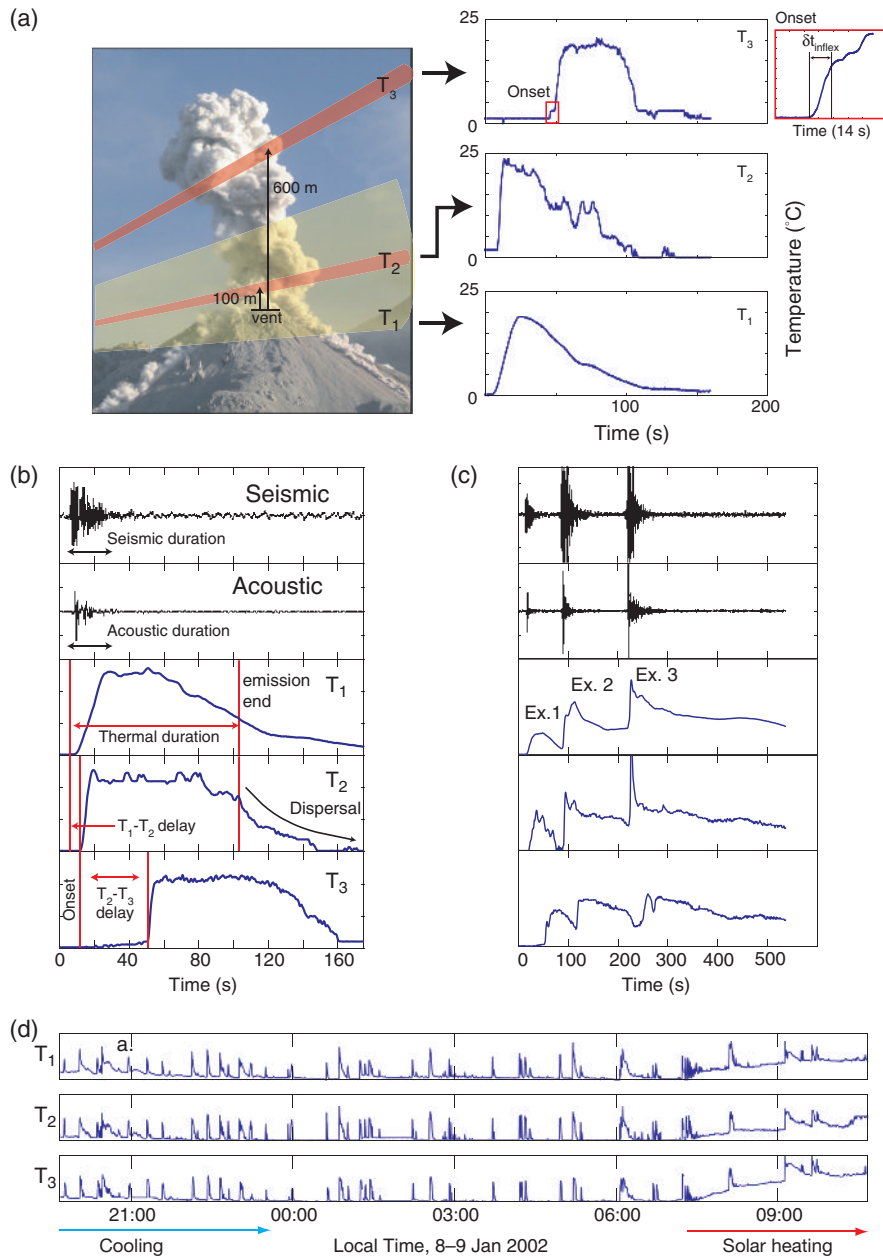


Figure 8.14 See caption in text (p. 493).



Figure 9.22 See caption in text (p. 581).

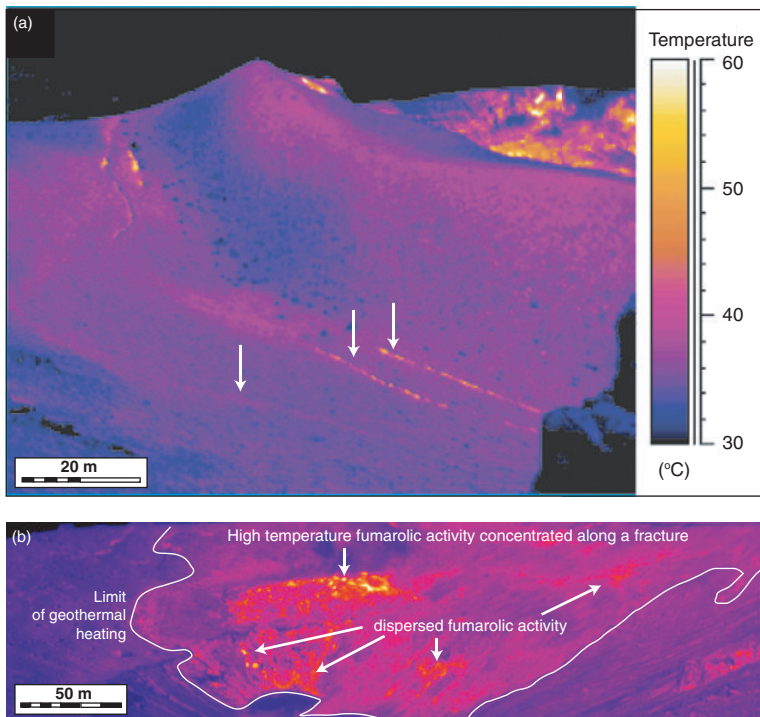


Figure 9.24 See caption in text (p. 590).

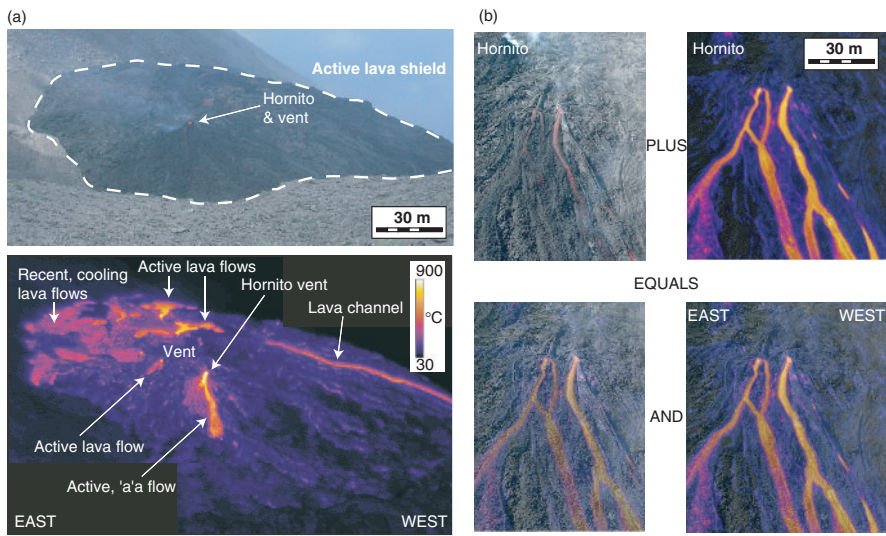


Figure 9.25 See caption in text (p. 591).

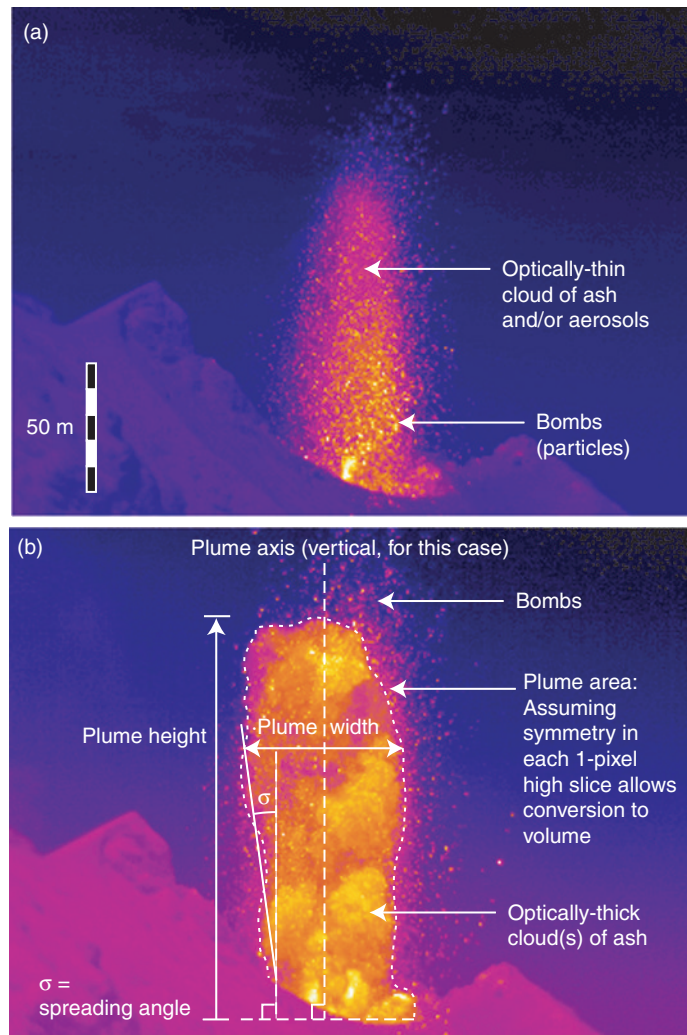


Figure 9.26 See caption in text (p. 593).

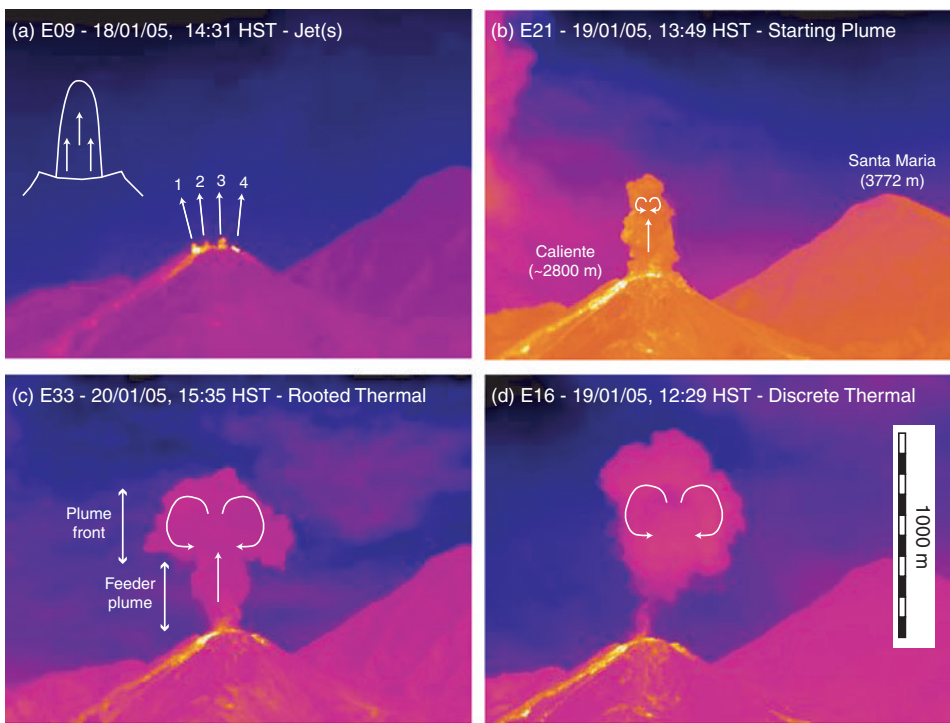


Figure 9.27 See caption in text (p. 594).

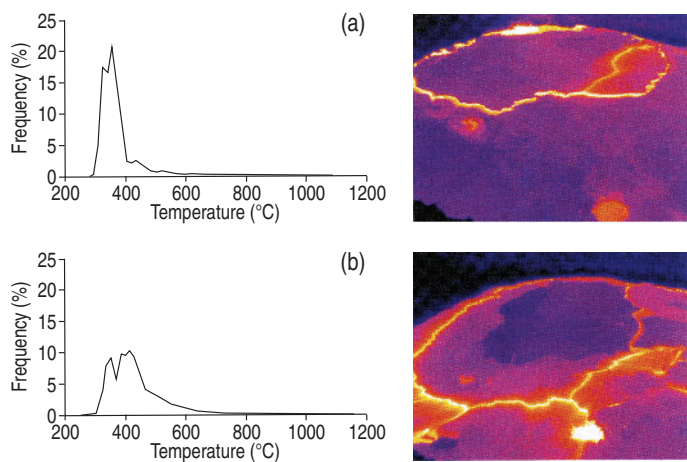


Figure 9.29 See caption in text (p. 598).

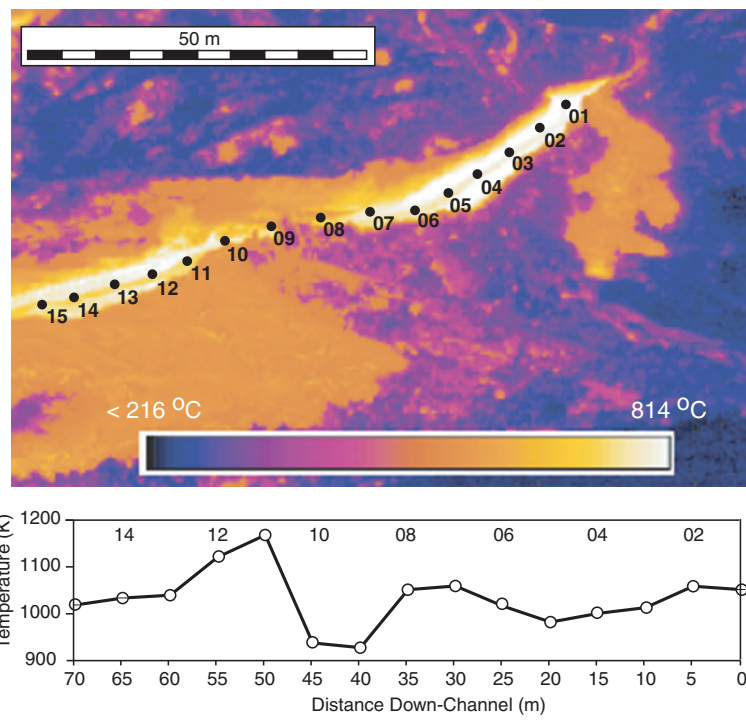


Figure 9.30 See caption in text (p. 601).

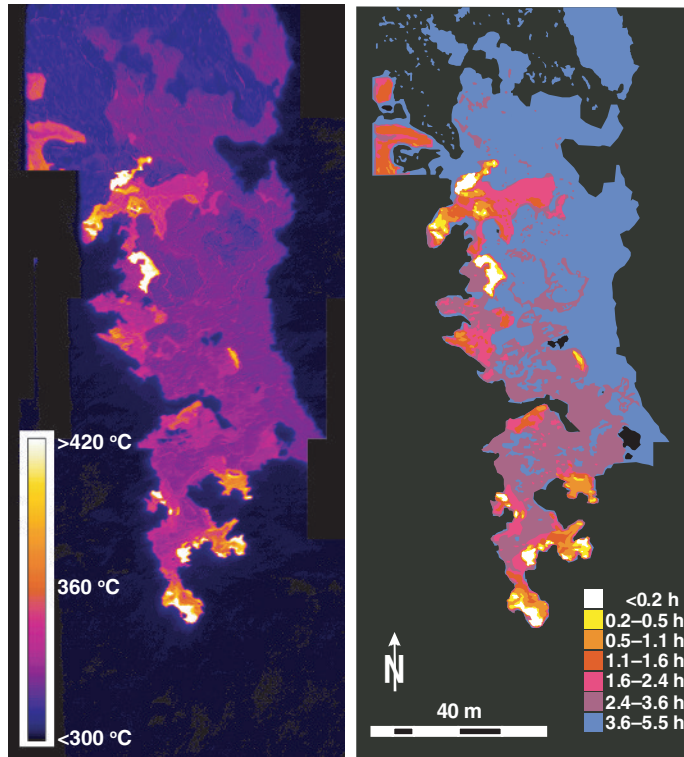


Figure 9.32 See caption in text (p. 608).

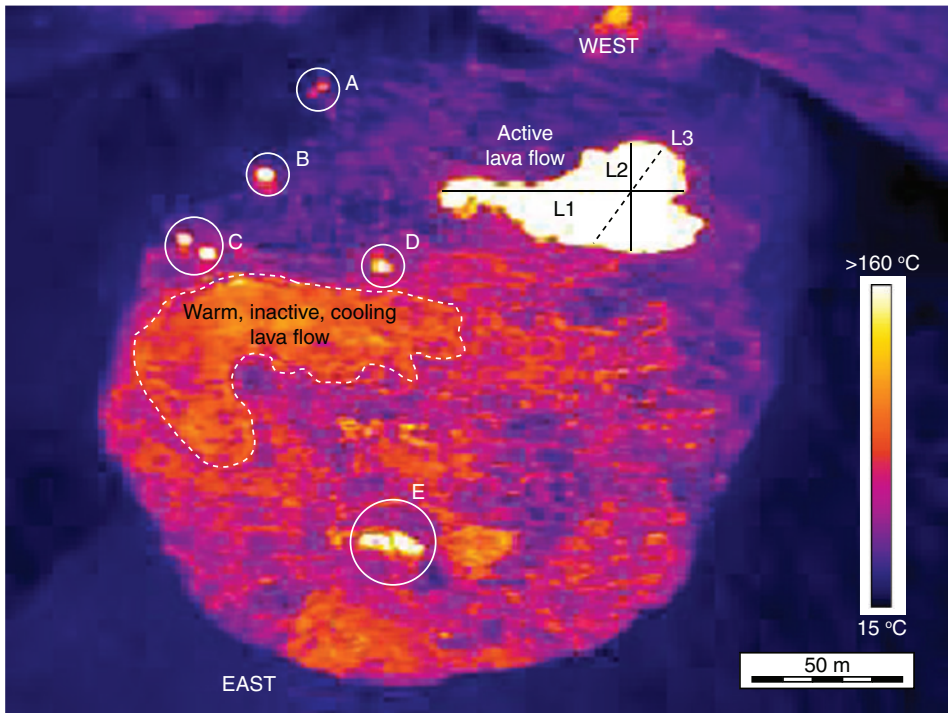


Figure 9.33 See caption in text (p. 610).

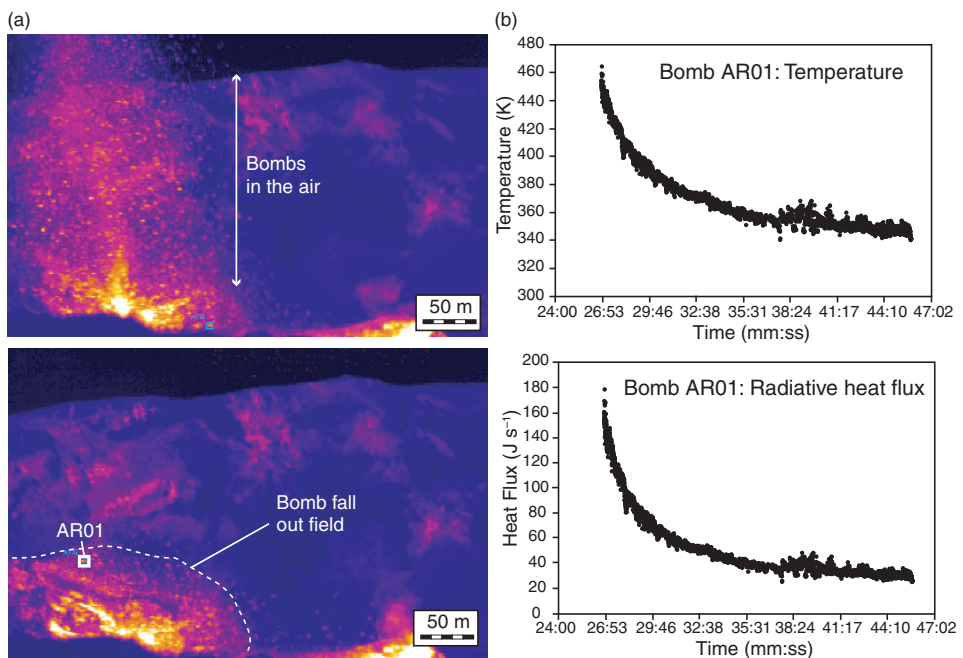


Figure 9.35 See caption in text (p. 624).

flanks. Between one and four maps per year could be produced showing the location, area and orientation of new lava flows, as given in [Figure 6.7](#). This shows a flow direction to the SW during 1987–1988, with flow lengths declining with time. Lava flow activity had shifted to the NE by 1992, with activity during 1993–1996 being confined to near-vent regions. However, emplacement of a longer flow extending to the south, and entering the head waters of the Rio Nima II, was apparent by January 2000.

#### 6.1.3.2 AVHRR-class map time series

During Etna's December 1991 to March 1993 eruption, 308 AVHRR images were acquired on which hot spots were detected. Eleven of these images were sharpened and overlaid on a base map of Etna's eastern flank, as given in [Figure 6.8](#). They show initial emplacement of a small lava flow to the east of the SE Crater, with a main lava flow field active in the southern sector of the Valle del Bove and extending east from the back wall of the valley. With time, the upper (western) segment of the flow field hot spot becomes cooler, and the zone of most intense radiance moves east. This relates to the upper segment of the flow field becoming tube-contained, while the eastern shift of the intense radiance zone marks the extension of tubes in this direction to feed surface flow at increasing distances from the vent, which pond in the basin to the south of Monte Calanna. A barrier had been built at the narrow exit to this basin above the town of Zafferana to contain flow in this location. Human intervention to result in successful breaching of the master tube in the upper segment of the flow field (see Barberi *et al.* (1993) for details regarding this intervention), cut supply to the distal segment in May 1992. This is apparent from a break up of the radiance distribution beginning in June 1992. At this point the zone of most intense radiance, which marks the location of active surface flow, is located in the upper segment of the flow field hot spot. With time, the distal segment is seen to form a separate anomaly which cools, and eventually disappears, marking the cessation of supply to the distal zone in the vicinity of Monte Calanna with lava flows in this zone cooling from May 1992 onwards.

#### 6.1.3.3 GOES-class map time series

In the [Figure 6.9](#) example we have located all visually detected anomalous pixels in GOES images onto a base map of Hawaii during the eruption at Kilauea's Napau crater during 30 January 1997. We see a shift in the location of maximum radiance from a pixel at Kilauea's coast, to an inland location in the vicinity of Napau Crater between 02:28 and 02:43 (local time), consistent with the onset of eruption at the new Napau site. Previously magma had moved down Kilauea's East rift zone to the Pu'u 'O'o vent, and then into a tube system, which fed flow at the coastal, ocean entry, site. Establishment of activity at the new inland site, and shut down of activity at the coastal site, is confirmed by establishment of the Napau hot spot, and disappearance of the coastal hot spot, over the ensuing hours. Thus, even using the GOES-class data we can map a rapid shift in the geographic location of lava flow activity, so that a surprising amount of spatial information is available even in the largest-scale satellite-data-derived spectral radiance maps.

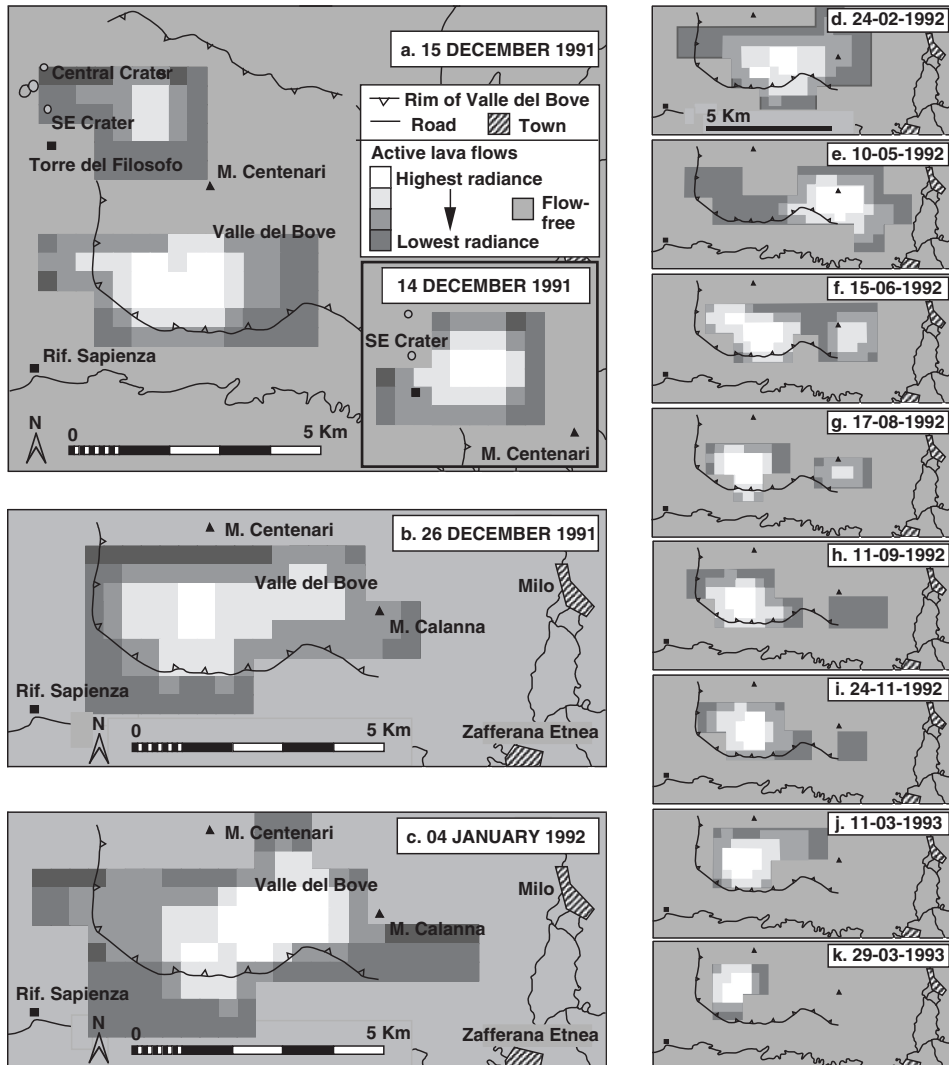


Figure 6.8 Sharpened and density sliced AVHRR band 4 radiance images obtained during Etna's 1991–1993 eruption. The sharpened radiance maps have been fitted to a base-map of Etna's SE flank [modified from Harris *et al.* (1997c, Fig. 4)]. See also color plates section.

## 6.2 Hot spot classification

For “blind” cases where we have no ground truth, hot spot classification has been a problem since early interpretations. How, for example, at an unobserved target, can we determine whether a cross-shaped group of five TM pixels at a volcano summit with radiance in the TIR, MIR, and SWIR, is due to the presence of a large, hot, open vent, a high-temperature fumarolic area, or a small lava lake or dome? Francis and Rothery (1987) had just such a problem with their early TM-data for Lascar (Chile). The distribution of bands 5 and 7 pixel-integrated temperatures given in Figure 6.10 was, not

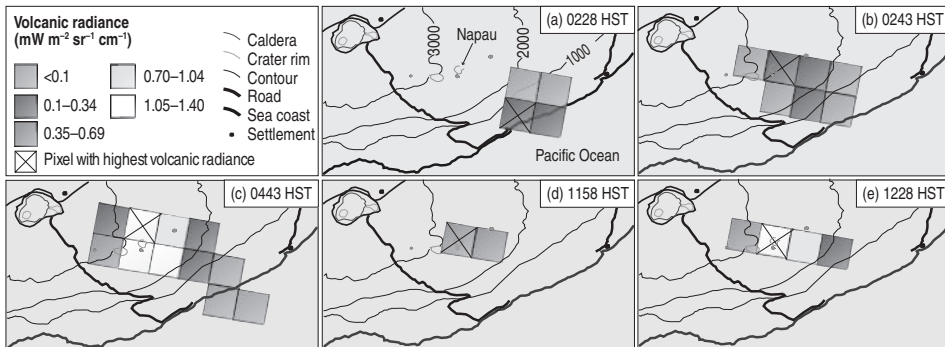


Figure 6.9 Density sliced GOES band 2 volcanic radiance images obtained during Kilauea's January 1997 eruption at Napau Crater. The radiance maps have been fitted to a base map of Kilauea's E rift zone [Modified from Harris *et al.* (1997b, Fig. 1): reproduced by permission of American Geophysical Union]. See also color plates section.

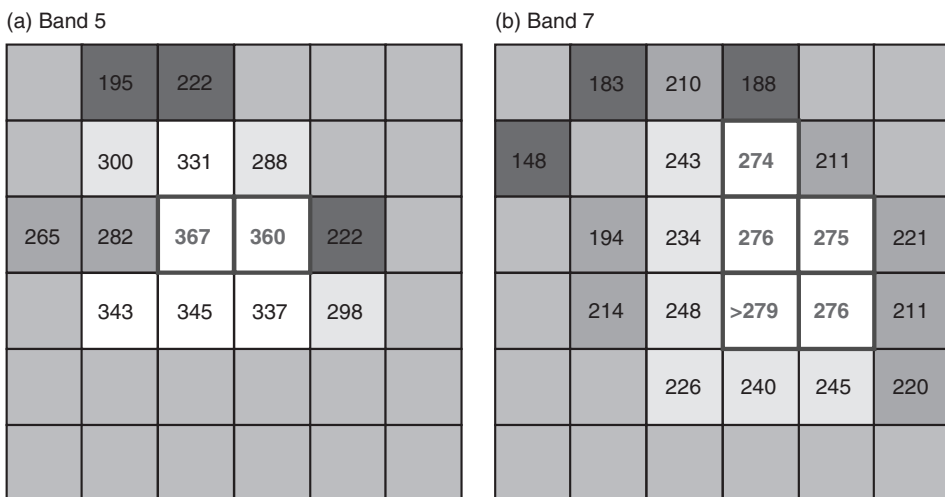


Figure 6.10 Brightness temperatures in (a) TM band 5 and (b) TM band 7 over a thermal anomaly found by Francis and Rothery (1987) in a 21 July 1985 image of Lascar [modified from Francis and Rothery (1987, Fig. 5)]. See also color plates section.

unreasonably, argued to be due to the presence of "a lava lake, located at the bottom of a deep pit crater." This conclusion was reached on the basis of the similarity between the size and radiance of the Lascar hot spot in TM data, and that observed at Erta Ale (and Erebus) where a similar radiance distribution in TM data was known to be due to the presence of a lava lake. The interpretation was echoed by Rothery *et al.* (1988), who added that absence of emission in the SWIR at other sites in the central Andes characterized by known fumarole emission, suggested that Lascar's hot spot was not associated with fumarolic activity. Although Francis and Rothery (1987) stated that "it is not possible to determine fully the cause of a thermal anomaly from remotely sensed data alone," because

Lascar was associated with eruption of basaltic andesite to andesite lavas, the probability of the hot spot being associated with the presence of a dacitic lava dome was considered “rather small.” Later, ground-based observations by Oppenheimer *et al.* (1993a), and then Matthews *et al.* (1997), confirmed the presence of a lava dome. So how can we best make judgments as to the nature of the feature that generates the observed hot spot when ground truth or validation is unavailable?

### **6.2.1 Feature characterization (an air photo interpretation approach)**

Following the methodology applied to air photo interpretation, an obvious qualitative route to determining the feature type with which the hot spot is associated is to assess the basic hot spot dimension and brightness (radiance). A range of hot spot dimension and radiance characteristics can be assessed to make an interpretation and assign the hot spot a label. Following Lillesand and Kiefer (1987), seven feature characteristics need to be assessed when applying a classic air photo interpretation.

- *Shape.* This is the configuration, form, or outline of the feature. Qualitative descriptors for volcanic thermal features may include circular, oval, elongate, lobate, stubby, linear, sinuous, en-echelon, thin or broad. In image data, the pixelated nature of the image may cause small circular-to-oval features to actually take on a square or cross shape (see Chapter 3). A quantitative measure of shape can be made using aspect ratio ( $\alpha$ ), obtained by dividing the feature width by length. Using the aspect ratio, long thin shapes (lava flows) will have  $\alpha < 1$ , and circular shapes (lava lakes and domes) will have  $\alpha \sim 1$ .
- *Size.* This is defined by the characteristic dimensions of the feature, as given by the measured width, length and/or diameter, with qualitative descriptors being huge, large or big, little or small, and tiny, the measurement unit being number of pixels, meters or square meters.
- *Pattern.* This is the design, plan or spatial arrangement of the component parts of the feature. These can show characteristic arrangements which define the way the feature is made-up. The thermal surface may, for example, be characterized by a specific lay-out of the constituent thermal components or a characteristic spatial variation in the radiant intensity, shape and/or dimensions of the components. Can we, for example, detect a trend of cooling with distance from the source characteristic of a lava flow?
- *Tone.* For our case, this is the brightness of the feature, so that qualitative descriptions such as bright or dull may be appropriate. Quantitative measures of tone are radiant spectral exitance, radiant intensity or the presence of emission in the NIR (extremely intense), SWIR (intense) or TIR only (weak).
- *Texture.* This is the arrangement or distribution of the constituent parts that make up the feature or the detail of the way in which those parts are arranged. For our case, it may be defined by the way in which tone changes across the feature, or the frequency of that change, which can range from uniform (no change across the feature) to highly variable or mottled for a high frequency of change.

- *Shadows.* Shadows provide supplementary information regarding the three dimensional shape of the feature, allowing the feature height to be assessed. Shadows in VIS, NIR or SWIR data can confirm the presence of levees or location of a feature within a pit crater, which is helpful in the final, contextual, set of interpretation rules.
- *Association and site.* Certain features will occur in partner with other features, lava tubes, for example, can contain skylights, and fountains will feed channel-fed lava flows. Thus, the feature can be defined, and assessed, in terms of its relation to other features and the way these features are arranged spatially. Likewise, certain features tend to form in predictable locations, so that the setting, site or location of the thermal feature can be used to help clarify its nature.

#### 6.2.1.1 Characteristics of volcanic hot spots

Typical shapes, sizes, patterns and tones that define the main volcanic hot spot types are given in [Table 6.1](#), and characteristic textures, associations and sites are given in [Table 6.2](#). Using such tables as interpretive keys, and by comparing an observed hot spot with archived hot spots associated with known features, it may be possible to place the hot spot within a unique category. The most effective approach uses a combination of spatial attributes (shape, size, pattern, texture, site and/or association) and/or spectral attributes (brightness) to classify the feature.

The typical spatial character of the hot spot can be derived directly from a qualitative analysis of the image or the image-derived radiance map. The feature can then be ascribed a label based on its similarity with, as well as divergence from, the typical characteristics of each feature type given in our interpretation matrix, with the logged evidence used to defend and support the assigned feature label.

Although two or more features may have several spatial characteristics in common, there are usually one or two characteristics that set them apart. A vigorously convecting lava lake and a lava fountain forming at a summit vent may have identical shapes, sizes, patterns, intensities and sites. They will both be relatively small and localized, but extremely bright, point sources within the volcano's summit crater. The fountain, however, will be associated with extensive channel-fed lava flow which it is feeding; the lava lake will be an isolated point source of radiance. The characteristic size, shape, radiance intensity, pattern and, most importantly, association of the component parts, allow most of the features to be identified and distinguished at a glance by the trained eye.

#### 6.2.2 Spectral character

The hot spot spectral character, i.e., the magnitude and intensity of the spectral radiance, as well as its variation at different wavebands, can also be used to support feature classification.

A review of Electronic Supplement 1 shows that different volcanic hot spots will have characteristic thermal structures, and thus also thermal signatures. This, coupled with the differing sensitivities of sensors in the SWIR, MIR and TIR to sub-pixel hot spots, means

Table 6.1. Shape, size, pattern and tone characteristics used for interpretation of volcanic hot spot types.

Feature	Shape: feature configuration (aspect ratio, $\alpha$ )	Size: feature dimensions	Pattern: spatial arrangement	Tone: feature brightness (radianc intensity)
'A'a lava flow	Linear-to-sinuous, elongated downhill, lobate margins. Moderate $\alpha$ (1–0.1)	W: tens to hundreds of m  L: tens of m to tens of km	Elongated lobe of radiance, stretched in the down-flow direction. May bifurcate and braid to feed multiple lobes, with complexity of the pattern (number of lobes) increasing with distance from the vent. May contain central bright zone (especially in proximal-to-medial section) if channel fed	Bright (high radiance: intense)
Active fissure	Elongate, linear or en-echelon. Low $\alpha$ (0.1–0.01)	W: meters to tens of m  L: hundreds of m to tens of km	Long, thin, continuous line of high radiance, possibly arranged in an en-echelon fashion	Very bright (very high radiance: extremely intense)
Active vent	Roughly circular (square in pixel space). Equant $\alpha$ (~1)	Diameter: meters to tens of m	Small, localized point source, likely with bright core and dim halo	Bright to dull (high to low radiance depending on temperature: intense to weak)
Block lava flow	Sinuous, elongated downhill, stubby. Moderate $\alpha$ (1–0.2)	W: tens to thousands of m  L: tens of m to kilometers	Elongate, but broad, lobe of radiance, typically single unit (unbraided), brighter flow front (due to exposure of core by rock fall) and vent zone. Possible bright zones scattered along the levees, and trending at right angles to the line of flow – as defined by elongation of the main anomaly – due to levee failures / rock falls to expose hotter subsurface	Dull (low radiance: weak)

Crater lake	Roughly oval to circular. Equant $\alpha$ (~1)	W: tens of m to hundreds of m  L: tens of m to hundreds of m	Larger (than vent feature), but similarly localized, point source	Dull (extremely low radiance: extremely weak)
Fumarole field	May be linear (if aligned along a fissure) or broad (if a Vulcanic field of many scattered vents)	W: tens of m to hundreds of m  L: tens of m to hundreds of m	Possibly highly dispersed, diffuse anomaly, scattered hot spots dispersed across a wide area. Spatially discontinuous	Dull. (The small size of vents means that the fumarole will be a very small sub-pixel source leading to a low pixel-integrated radiance, hence: weak)
Lava channel	Linear to sinuous, elongated downhill. Extremely low $\alpha$ (0.01–0.0002)	W: meters to tens of m  L: tens of m to tens of km	Long, thin, continuous, probably sinuous line of high radiance. May bifurcate and braid to feed multiple branches, with complexity of the pattern (number of channels) increasing with distance from the vent	Very bright to bright (very high to high radiance depending on degree of crust cover and age/thickness/extent of crust, hence extremely intense to intense)
Lava dome	Roughly circular to oval. Equant $\alpha$ (~1)	Diameter: tens of m to thousands of m	Larger (than vent feature), but similarly localized, point source	Bright to dull (high to low radiance, depending on degree of crust cover: may be intense if the carapace is extensively cracked during vigorous extrusion, or weak if there is extensive, mature crust cover during low extrusion rate phases or subsidence)
Lava fountain	Circular (if vent fed); linear (if fissure fed). Equant $\alpha$ (~1, if vent fed); low $\alpha$ (< 0.1, if fissure fed)	Diameter: meters to hundreds of m	Point source (if vent fed.) continuous (if fissure fed)	Very bright (very high radiance: extremely intense)
Lava lake	Roughly circular to oval (square in pixel space). Equant $\alpha$ (~1)	Diameter: tens of m to hundreds of m	Larger (than vent feature), but similarly localized, point source	Very bright (if overturning). Dull (if heavily crusted). Hence: very high radiance; extremely intense (if overturning). High to low radiance; intense to weak (if heavily crusted)

Table 6.1. (cont.)

Feature	Shape: feature configuration (aspect ratio, $\alpha$ )	Size: feature dimensions	Pattern: spatial arrangement	Tone: feature brightness (radiant intensity)
Lava tube	Linear to sinuous, elongated downhill Extremely low $\alpha$ (0.05–0.0002)	W: meters L: tens of m to tens of km	Long, thin, continuous probably sinuous line of low radiance. May bifurcate and braid to feed multiple branches, with complexity of the pattern (number of tubes) increasing with distance from the vent	Extremely dull / faint (extremely low radiance: weak to extremely weak)
Pahoehoe flow	Lobate. Equant $\alpha$ (~1)	Individual pads: 0.01–0.1 km. Flow field: 1–tens of km	Multiple pads each with bright front and less intense up-flow zone. Possibly highly dispersed, diffuse anomaly, scattered low radiance hot spots dispersed across a wide area. Spatially discontinuous	Bright at active toes, dull over cooling zones. High radiance (intense) at active toes; High to low radiance, (intense to weak over cooling zones)
Pyroclastic flow	Elongated downhill, possibly lobate. Moderate to low $\alpha$ (1–0.04)	W: tens of m to hundred of m L: tens of m to tens of km	Spatially extensive lobe elongated in flow direction, possibility of multiple lobes extending in different directions	Bright to dull (high to low radiance: intense to weak depending on surface temperature and time since deposition)
Skylights	Roughly circular (square in pixel space). Equant $\alpha$ (~1)	Diameter: meters	Very small, localized, point source of high radiance	Bright (high radiance: intense, could be: extremely high radiance – extremely intense – if the 1100 °C skylight source fills the pixel, but they are usually sub-pixel features, which dampens their full intensity potential)

Note: W = feature width; L = feature length; aspect ratio ( $\alpha$ ) = W/L.

Table 6.2. *Texture, association and location characteristics used for interpretation of volcanic hot spot types.*

Feature	Texture: tone change frequency	Association: relation to other features	Location: geographical location
'A'a lava flow	Uniform to mottled, down-flow tone decrease, darker (cooler) tones distally due to down-flow surface cooling. Mottled if highly cracked (high radiance in lower radiance background)	Fissure, vent, channel or tube fed (thus these feature types may be found proximally, or feeding the flow)	Within caldera and on volcano flanks
Active fissure	Little or no tonal variation along-fissure: uniform distribution of high radiance	Lava flow field extending in all directions (thus lava flow – high-temperature sheet flow and/or multiple channel fed flows surround the fissure)	Rift zones & calderas
Active vent	Regular tone increase towards anomaly core	Lava fountain, lake or dome (may occur in the vent). Lava flow source (so that flows may extend from the vent)	Within craters (can be summit or flank)
Block lava flow	Down-flow tone decrease, with uniform, dark tones across medial to distal sections due to extensive surface cooling and lack of cracks	Vent or lava dome at source	Volcano flanks, may extend into surrounding valleys
Crater lake	Uniformly dark (cool) surface with possible localized brighter (warmer) spots due to zones of upwelling	Possible fumarolic activity surrounding the lake	Within craters (generally at summit)
Fumarole field	Scattered but small and isolated bright (high-radiance) sources, against a dark (low-radiance, near-ambient) background leading to mottled (discontinuous) thermal texture	Gas plume, with field as its source	Within calderas and on volcano flanks and across geothermal areas

Table 6.2. (cont.)

Feature	Texture: tone change frequency	Association: relation to other features	Location: geographical location
Lava channel	Generally uniformly bright (high radiance), with possible down-channel tone decrease if crusts become cooler and/or more extensive. On a very fine scale edges will be characterized by bright, high-radiance zones (across highly cracked shear zones) surrounding a central darker (cooler) zone (across the central plug, where crust is unsheared, lacking in cracks, more stable and cooler)	Fed by vent, fountain or fissure, feeds 'a'a or pahoehoe (thus the former feature types may be found proximally, or feeding the flow, while the latter feature types may be found distally, i.e., fed by the channel)	Within calderas and on volcano flanks
Lava dome	May be composed of single to multiple bright points if carapace is a cool crust with a network of hot cracks, or uniformly dark if covered by a homogeneous cool crust. Both may have dark (low-radiance) rims if surrounded by a collar of cool talus from dome collapse	Block lava flows, pyroclastic flows. These will extend away from the dome, possibly in a radial (or directed, unidirectional) fashion	Within craters, typically in summit crater or caldera
Lava fountain	Uniform, intensely bright (high-radiance) core with little or no tonal variation	Source of channel-fed flows, will have associated tephra plume	Within craters (summit or flank) or along rift zones
Lava lake	Uniformly bright (high-radiance) if highly active (overturning and convecting) or uniformly dark (low-radiance) if heavily crusted (stagnant). On a fine scale, bright surface may be broken by even brighter spots if cracks, bubble bursting or small fountains are active on the surface	Lava flows if overflow has occurred	Crater / pit confined (can be summit or flank if at head of lava flow field or formed by lava entrapment in pre-existing pit crater)

Lava tube	Uniform, dark (high-radiance) line with little or no tonal variation	Fed by vent or lava lake, feeds surface lava flows or ocean entry and may contain skylights	On caldera floors and on volcano flanks
Pahoehoe flow	Mottled, blotchy: multiple bright spots locating active breakouts, separated by broader darker zones locating older (cooler) crusts	Tube or lava lake as source	On caldera floors and on volcano flanks
Pyroclastic flow	Possible smooth down-flow tone decrease, although likely uniformly bright to dark (homogeneous thermal structure) depending on surface age	Vent, dome or crater at source, ash clouds above vent and/or flow if feature is active	Extending away from domes, summit vents and/or block flow fronts
Skylights	Bright point of uniformly intense radiance	Lava tube	On caldera floors and on volcano flanks

that different features will attain different radiant emission levels in each waveband depending on the temperature of the crust and proportion of hot cracks at each feature. Take, for example, a cracked lava lake with a crust at 250 °C and a non-cracked lava dome with a crust at the same temperature. Due to the poor sensitivity of the TIR to the sub-pixel cracks, both may have the same pixel-integrated temperature in the TIR. In this case, if the lava lake surface fills the pixel, and cracks at 1000 °C occupy 0.1% of the pixel, the pixel-integrated temperature will be 251 °C. The TIR pixel-integrated temperature for the uncracked dome will also be 250 °C. However, in the SWIR the pixel-integrated temperature for the lava lake will be 279 °C, and that of the uncracked lava dome still 250 °C. Thus, features may be placed by their position in *spectral feature space*, a placement that relies on each feature having a different and characteristic thermal structure.

This theory is tested in [Figure 6.11a](#) where we plot the SWIR versus TIR integrated temperatures for the typical hot spot thermal structures collated in Electronic Supplement 1. We see that the integrated temperatures in the SWIR ( $T_{\text{SWIR}}$ ) and TIR ( $T_{\text{TIR}}$ ) fall along a linear trend defined by

$$T_{\text{TIR}} = 1.0551(T_{\text{SWIR}}) - 43.192.$$

Lava lakes cluster at the low end of this trend, having relatively low  $T_{\text{TIR}}$  and  $T_{\text{SWIR}}$ ; lava channels and skylights are located at the high end, having relatively high  $T_{\text{TIR}}$  and  $T_{\text{SWIR}}$ . There is, though, a great deal of overlap between each feature type. However, we can also take advantage of the characteristic size of each feature, where lava flows are typically larger than lava lakes and skylights, and so will fill a larger portion of an AVHRR-class pixel. We see this effect in the SWIR versus TIR, and SWIR versus MIR plots of [Figures 6.11b](#) and [6.11c](#), respectively, where lava flow feature space is now distinct from the channel, lake and skylight feature space, with the SWIR versus MIR plot also beginning to define a lava channel feature space.

Flynn and Mouginis-Mark (1995) used such an approach to distinguish fires from active lava flows. This classification is given in [Figure 6.12a,b](#). Fires are dominated by a high-temperature flame component, and lavas by a moderate-temperature crust component. As a result, while fires plot in a feature space characterized by high SWIR radiances ([Figure 6.12a](#)), lavas plot in a distinct space characterized by high TIR radiances ([Figure 6.12b](#)). Harris *et al.* (1997c) used such an approach to attempt a spectrally based classification within volcanic hot spot types. Developed further by Carn and Oppenheimer (2000) and Rothery *et al.* (2001), the classification scheme, as given in [Figure 6.12c](#), takes advantage of the characteristic size and thermal structure of different volcanic phenomena. By plotting actual AVHRR MIR and TIR radiances ( $R_{\text{MIR}}$  and  $R_{\text{TIR}}$ ) for a range of features, [Figure 6.12c](#) shows that a number of spectral feature spaces can be defined, including:

- degassing vents: having low  $R_{\text{MIR}}$  and low  $R_{\text{TIR}}$ ,
- lava lakes: having high  $R_{\text{MIR}}$  and low  $R_{\text{TIR}}$ ,
- short lava flows: having moderate  $R_{\text{MIR}}$  and moderate  $R_{\text{TIR}}$ ,
- long lava flows : having high  $R_{\text{MIR}}$  and high  $R_{\text{TIR}}$ .

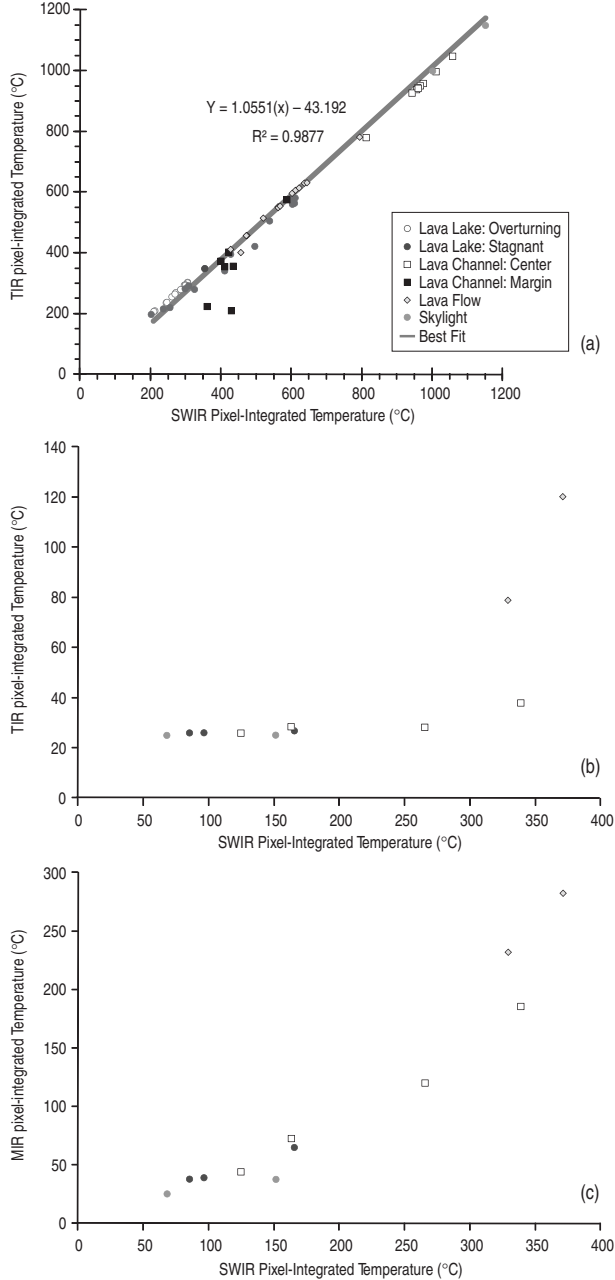


Figure 6.11 (a) Synthetic pixel-integrated TIR and SWIR brightness temperatures for pixel-filling lava bodies with the thermal structures collated in Electronic Supplement 1. Thermal structures and brightness temperatures used are given in Tables E1.4 (for the lava lake case), E1.6 (for the lava channel), E1.8 (for the skylight) and E1.9 (for the lava flow) of Electronic Supplement 1. (b) Synthetic pixel-integrated TIR and SWIR brightness temperatures for sub-pixel lava bodies centered in AVHRR-class (1 km) pixels and with the thermal structures of Electronic Supplement 1. (c) Synthetic pixel-integrated MIR and SWIR brightness temperatures for sub-pixel lava bodies centered in AVHRR-class (1 km) pixels and with the thermal structures of Electronic Supplement 1. Lava body sizes, thermal structures and brightness temperatures used are given in Tables E1.5 (for the lava lake case), E1.7 (for the lava channel), E1.8 (for the skylight) and E1.10 (for the lava flow) of Electronic Supplement 1.

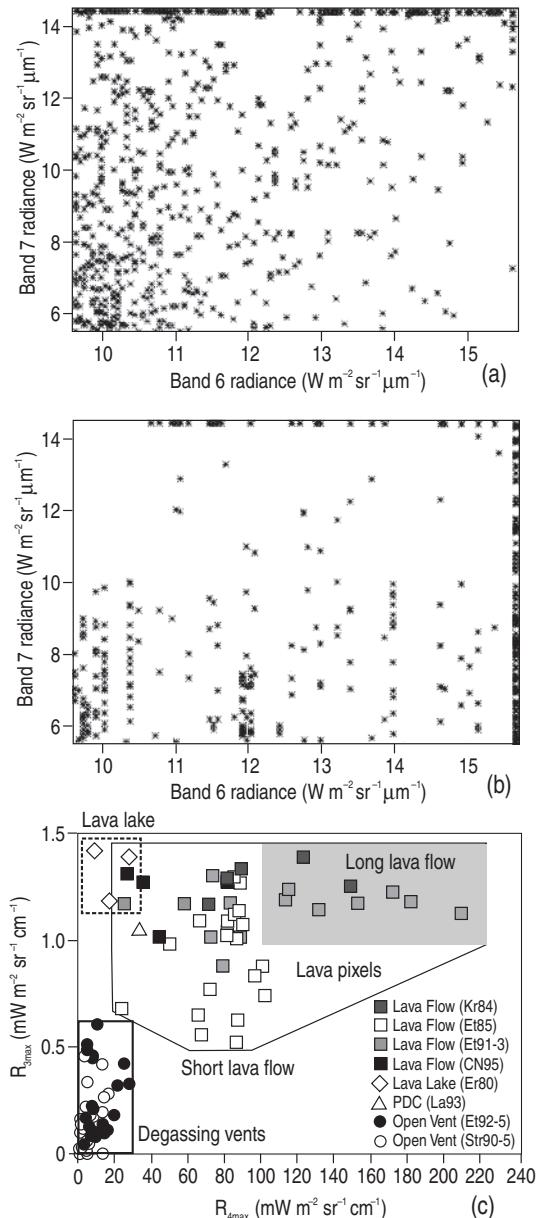


Figure 6.12 (a) TM SWIR (band 7) versus TIR (band 6) spectral radiances for pixels over a fire (Yellowstone, imaged on 8 September 1988). Extensive saturation of band 7 causes plots to spread across the top of the plot. (b) TM SWIR (band 7) versus TIR (band 6) spectral radiances for pixels over an active lava (Kilauea, imaged on 23 July 1991). Here, extensive saturation of band 6 cause plots to spread up the right hand side of the plot [from Flynn and Mouginis-Mark (1995, Fig. 3); reproduced by permission of American Geophysical Union]. (c) Spectral feature space scheme developed by Harris *et al.* (1997c) using maximum hot spot radiances recorded by AVHRR in the MIR (band 3,  $R_{3\text{max}}$ ) and TIR (band 4,  $R_{4\text{max}}$ ). Data are plotted for hot spots associated with a range of known activity types at a number of locations, where Kr = Krafla, Et = Etna, CN = Cerro Negro, Er = Erebus, La = Lascar and Str = Stromboli; number after each volcano abbreviation gives the year of activity/observation. [from Harris *et al.* (1997c, Fig. 14), with kind permission from Springer Science and Business Media].

The single plot for a pyroclastic flow falls in the lava flow feature space of Figure 6.12c. There is, thus, some degree of overlap, but broad groupings of features of characteristic temperature and size can be distinguished. The basic distinctions are between small and cool features (low  $R_{\text{MIR}}$  and  $R_{\text{TIR}}$ ), small and hot features (high  $R_{\text{MIR}}$  and low  $R_{\text{TIR}}$ ), and large and hot features (high  $R_{\text{MIR}}$  and high  $R_{\text{TIR}}$ ). Likely combinations of feature size and radiant intensity for a range of hot spots are given in Table 6.3.

### 6.2.3 Temporal character

Given repeat over passes, we can use temporal information to aid in the classification attempt. Different features will undergo changes in shape, size, pattern, texture, site and/or association, that will vary in different ways depending on the variations in the type of activity with which the hot spot is associated. For example, an extruding lava dome and an active lava lake may both be summit-crater-contained point sources of radiance, but the latter may grow with time, covering an increasing number of pixels and/or increasing in total radiance, whereas the latter will remain of broadly stable size. Likewise a lava flow will move, changing shape, area and pattern with time, with the changes giving information to support the eruption chronology, as in the time series example of Figure 6.8. For example, while waxing lava discharge will give a hot spot that expands in area, waning output will be associated with a shrinking hot spot; changes from channel- to tube-fed flow change the pattern, tone and texture of the feature, as well as the association of its component parts.

#### 6.2.3.1 Temporal character of the spectral radiance

The temporal spectral signature of a hot spot can be defined by generating time series. Different types of activity often have characteristic trends, shapes and time scales to their time series, which can be used to classify the event. Depending on the effusive, extrusive or explosive process driving the eruption, different hot spot types will be characterized by a different spectral radiance time series that

- (i) may or may not display peaks;
- (ii) will display different levels of steady and peak radiance;
- (iii) will wax and wane at different rates and over different time scales depending on the type of activity to which the hot spot is tied.

In the following sections we will consider time series generation and provide case-study examples of some time series shapes that can be sampled by satellite sensors. Here, we provide hypothetical curves based on the general character of each eruption type, which can be used to classify the hot spot. These are summarized in Table 6.4, in which we define 12 types of hot spot on the basis of their temporal character.

Table 6.3. Feature size and radiance characteristics to allow volcanic hot spot classification in TM-class data.

Feature	Shape/dimensions	Radiance level: intensity ( $\text{W m}^{-2}$ )				Case type example [Source]
		NIR	SWIR	MIR	TIR	
'A'a lava flow	W: A few pixels L: Hundreds of pixels	No	Strong	Strong	Strong	Etna [Wright <i>et al.</i> , 2001] <sup>1</sup>
Active fissure	W: A few pixels L: Tens to hundreds of pixels	Strong	Strong	Strong	Strong	Krafla <sup>a</sup> [Harris <i>et al.</i> , 1995b]
Active vent	Diameter: one to a few pixels	No	Strong	Strong	Weak	Stromboli [Harris and Stevenson, 1997a] <sup>2</sup>
Block lava flow	W: Tens of pixels L: tens to hundreds of pixels	No	No	No	Weak	Santiaguito [Harris <i>et al.</i> , 2001] <sup>3</sup>
Crater lake	Diameter: a few to tens of pixels	No	No	No	Weak	Poas [Oppenheimer, 1993b] <sup>4</sup>
Fumarole field	W: a few to tens of pixels L: a few to tens of pixels	No	No	No	Weak	Vulcano [Harris and Stevenson, 1997a]
Lava Channel	W: one or two pixels L: a few to hundreds of pixels	Strong	Strong	Strong	Strong	Etna [Wright <i>et al.</i> , 2001] <sup>1</sup>
Lava dome	Diameter: a few to tens of pixels	No	Moderate	Moderate	Moderate	Lascar [Oppenheimer <i>et al.</i> , 1993a]
Lava fountain	Diameter: a few pixels	Strong	Strong	Strong	Strong	Etna [Wright <i>et al.</i> , 2001] <sup>1</sup>
Lava lake	Diameter: a few pixels	Possible	Strong	Strong	Strong	Erta Ale [Harris <i>et al.</i> , 1999] <sup>5</sup>
Lava tube	W: one or two pixels L: tens to hundreds of pixels	No	No	No	Weak	Kilauea [Flynn <i>et al.</i> , 1994] <sup>6</sup>
Pahoehoe flow	Diameter: a few to tens of pixels	No	Strong	Strong	Moderate	Kilauea [Flynn <i>et al.</i> , 1994] <sup>6</sup>
Pyroclastic flow	W: a few to tens of pixels L: tens to hundreds of pixels	No	Strong	Strong	Moderate	Augustine [Rothery <i>et al.</i> , 1988]
Skylights	Diameter: one or two pixels	No	Strong	Strong	Weak	Kilauea [Flynn <i>et al.</i> , 1994] <sup>6</sup>

<sup>a</sup> Only documented, to date, in AVHRR-class data (see Figure 6.6).

<sup>1</sup> See Figure S1.7 of Electronic Supplement 1 for example.

<sup>2</sup> See Figure S1.14 of Electronic Supplement 1 for example.

<sup>3</sup> See Figure S1.13 of Electronic Supplement 1 for example.

<sup>4</sup> See Figure S1.15 of Electronic Supplement 1 for example.

<sup>5</sup> See Figure S1.4 of Electronic Supplement 1 for example.

<sup>6</sup> See Figure 6.2 of Chapter 6 for example.

Table 6.4. Shape, level and peak duration for time series used to classify volcanic hot spot types.

Feature	Shape of curve	Level of radiance	Duration of peak(s)	Case type example [source] and figure location in this book
Type I Lava Flow – Pressurized Source	Rapid waxing period, followed by longer waning period (as pressurized source is tapped). Longer waning period gives way to Type II lava flow curve once source is depressurized; existence of, and length of, waning and Type II phases depends on duration of eruption	High at peak, declining to moderate-to-low (depending on lava discharge rate in waning period)	Days	Etna and Krafla [Harris <i>et al.</i> , 2000b] <a href="#">Figure 6.16, Chapter 6</a>
Type II Lava Flow – Unpressurized Source	Unchanging / flat, but noisy as unpressurized lava overflows or is released from central conduit	Moderate-to-low (depending on lava discharge rate)	No peak	Etna [Harris <i>et al.</i> , 2000b]
Type III Lava Flow – Batch-Like Supply	Highly variable and peaky, with number of peaks depending on the number of batches ascending the conduit and arriving at the effusive vent	Large changes between low-radiance levels during low-discharge rate phases and high-to-extremely-high during the arrival of a batch	Hours-to-days	Etna 1999 [Harris and Neri, 2002]
Type I Lava Lake – Convecting/OVERTURNING	Highly variable and peaky	Large changes between low-radiance levels during periods of sluggish convection and high-to-extremely-high during vigorous convection and overturn	Minutes	Erta Ale and Erebus [Wright <i>et al.</i> , 2004]

Table 6.4. (cont.)

Feature	Shape of curve	Level of radiance	Duration of peak(s)	Case type example [source] and figure location in this book
Type II Lava Lake – Stagnant	Unchanging / flat	Moderate-to-very-low depending on age and thickness of crust	No peak	Erta Ale and Erebus [Wright <i>et al.</i> , 2004]
Lava Dome	Steadily waxing and waning	Moderate levels during high extrusion phases, decaying to low during low extrusion rate phases ... and then building again.	Weeks-to-months (Lascar-Type) Months-to-years (Santiaguito-Type)	Lascar [Oppenheimer <i>et al.</i> , 1993c] Santiaguito [Harris <i>et al.</i> , 2003a]
Open Vent – Degassing	Unchanging / flat, but noisy	Low-to-moderate depending on size and temperature of degassing vent, possibly varying if magma levels oscillate.	No peak	Stromboli [Harris and Stevenson, 1997a]
Explosive – Fire Fountain	Rapidly waxing, short peak (possibly obscured by cold fountain-fed tephra column) followed by sudden decline followed by cooling-curve as fountain-fed flows cool	High-to-extremely-high (due to high discharge rate of lava)	Hours	Etna [Gouhier <i>et al.</i> , 2012] Figure 5.16, Chapter 5
Explosive – Strombolian	Spike (during explosive emission of hot particles) followed by cooling curve as particles cool. Repeat nature of strombolian activity will mean this waveform is repeated every few minutes.	Low (due to small area of hot deposit)	Seconds	Karymsky [Dehn <i>et al.</i> , 2000] Figure 5.12, Chapter 5 Stromboli [Harris and Stevenson, 1997a] Figure 6.20a, Chapter 6

	Time series will be dominated by steady low-level thermal emission from the persistently active hot vent			
Explosive – Vulcanian	Spike (during explosive emission of hot particles) followed by cooling curve as deposit cools. Repeat nature of vulcanian activity will mean this waveform is repeated every few hours	Moderate (due to moderate area of hot deposit)	Minutes	Pavlof [Roach <i>et al.</i> , 2001] <a href="#">Figure 6.18, Chapter 6</a>
Explosive – Plinian	Spike (during explosive emission of hot particles) followed by cooling curve as deposit cools	High (due to large area of hot deposit)	Hours	None recorded to date*
Pyroclastic Flow	Spike (during emplacement of flow) followed by cooling curve as deposit cools	High-to-extremely-high (depending on extent of flow)	Minutes	Bezymianny [Schneider <i>et al.</i> 2000] <a href="#">Figure 6.17, Chapter 6</a>

\* Although Dehn *et al.* (2002) give a time series recorded during and following a sub-plinian event at Shishaldin (see Figure 6.20 of Chapter 6).

### 6.2.4 Classification scheme: implementation and problems

Tables 6.1 through 6.4 provide conceptual frameworks for classifying hot spots in satellite IR data which use the full range of spatial, spectral and temporal data available from satellite sensors for volcanic hot spots. Spatial–spectral schemes have been implemented by Flynn *et al.* (1994) to classify components of a tube-fed pahoehoe flow field, as well as Wooster *et al.* (2000) to classify features at an active lava dome.

#### 6.2.4.1 Flynn et al. (1994): size, tone, pattern

The classification of Flynn *et al.* (1994) applied to a tube-fed pahoehoe flow field active on Kilauea in 1991 (the image being given here in Figure 6.2). The classification, given in Table 6.5, uses a measure of size and tone, plus an assessment of the feature pattern, as follows:

- feature size was assessed in terms of an area;
- tone was assessed in terms of the bands in which the feature was emitting (emission only in TIR band 6 would be the weakest class, and emission in all SWIR bands would be the most intense class).

Table 6.5. Feature characteristics used to discriminate (label) activity styles at Kilauea's active lava flow field using TM SWIR and TIR data by Flynn *et al.* (1994). Five features (numbered one through five) were defined by Flynn *et al.* (1994). Added (as feature six) is the stagnant (heavily crusted / roofed over) lava lake at Kupaianaha.

Feature	Active bands (Tone 1)	Area (pixels) (size)	Magnitude (Tone 2)	Boundary/sharpness (pattern)
(1) Lava lake (Pu'u 'O'o)	4, 5, 7 6	Tens 4 (at most)	High High	Non-distinct hazy Sharp
(2) Lava tubes	6	One pixel wide	Low	Non-distinct
(3) Skylight	3, 4, 5, 7 6	Few (< 10) 1–3	High Low	Variable hazy Non-distinct
(4) Ocean entry	5, 7 6	Few	Moderate	Sharp
		Few	Moderate	Non-distinct
(5) Lava flows				
(a) Breakouts	4, 5, 7 6	Tens Tens	High High	Sharp Variable
(b) Active flows	5, 7	Tens–hundreds Hundreds	Moderate–high	Variable non-distinct
(c) Inactive flows	5, 7 6	Few Tens–hundreds	Low Low–high	Non-distinct Non-distinct
(6) Lava lake (Kupaianaha)	6	Few	Low	Sharp

- magnitude was assessed in terms of “the relative abundance of radiant flux from the anomaly when compared to that of non-anomalous pixels”;
- pattern was assessed using the feature boundary character, this being a qualitative description of the change in radiant signal between the anomalous area and the surrounding non-anomalous area. Within this assessment *non-distinct* was used to describe cases where there was no easily discerned boundary, and *sharp* was if there was a marked and distinct boundary.

This allowed Flynn *et al.* (1994) to distinguish and classify eight components within the flow field system.

#### 6.2.4.2 Wooster *et al.* (2000): texture, tone, pattern and association

The scheme of Wooster *et al.* (2000) applied the dual-band approach to an active lava dome at Unzen. Assuming a relatively low temperature of the dome carapace (<120 °C), the one-component (non-radiant background) solution of Chapter 4 (Section 4.2.1.2) was applied to extract statistics for the hot-component temperature and area. Also used were ground validation information that allowed pixel regions associated with endogenous and exogenous growth, as well as collapse and fumarolic activity, to be identified and characterized. This allowed the classification scheme of Table 6.6 to be drawn up. This classifies four features on the basis of texture, tone, pattern and association.

#### 6.2.4.3 Hybrid classification scheme

Spatial–spectral classification schemes can be tailored to specific cases, and when correctly set using ancillary ground-truth data to confirm the location and area of actual features within the image, appear quite powerful. However, the best scheme for distinguishing feature types with precision is one that combines spatial, spectral and temporal information.

With lack of hind-sight and ground truth it would have been extremely difficult to determine whether the anomaly of Figure 6.10 was due to a lava lake or lava dome on the basis of spatial and spectral information alone. It was unfortunate for the Lascar case that dome extrusion occurred at a basaltic andesite to andesite system, a piece of ancillary evidence that led Francis and Rothery (1987) to lean towards the lava lake label. Maybe their experience shows that, in cases where we cannot place a hot spot into a single, unique, class within our classification scheme with complete certainty, we should opt for an “uncertain” or “non-unique” class. In this case we would maybe opt for the label *uncertain: lava lake / lava dome / fumarolic*, listing the choices in terms of analyst preference (lava lake being the most preferred interpretation, fumarolic the least). However, time series may be examined after this initial, first image appraisal, to allow a temporal check. In terms of spatial time series, while the area of a lava lake hot spot should remain stable, because it will remain confined within a pit of unchanging dimensions, the lava dome is free to expand, contract, develop new points of extrusion, collapse, explode and regenerate. The associated hot spot will likely show a different variation in size, as well as pattern, with time when

Table 6.6. Feature characteristics used to discriminate (label) activity styles at Unzen lava dome using TM SWIR and TIR data by Wooster et al. (2000) [with permission from Elsevier].

Dome activity style (feature type)	Sub-pixel hotspot characteristics determined by dual-band analysis of pixel radiance in TM bands 5 and 7 (texture)				Spatial structure and surroundings (pattern and association)
	Frequency distribution of temperatures	Mean hot-component temperature	Hot-component size distribution	TM band 6 signal (tone)	
Fumaroles	Corresponds to normal distribution	Hotter than areas of active dome growth	Hot-component areas generally smaller than on actively growing regions	Weak thermal anomalies due to small hot- component area	Minimal surrounding of collapse deposit signature
Exogenous growth	Distribution skewed towards low temperatures	Cooler than fumaroles but inseparable from endogenous areas	Hot-component areas generally larger than in fumarolically active region	Strong thermal anomalies. Maybe strongest at the location of a collapsing lobe front	Possesses identifiable effusing vent and collapsing lobe front, having the highest temperatures. Cooler between these locations. Likely source of any collapse deposition signature
Endogenous growth	Distribution skewed towards low temperatures	Cooler than fumaroles but inseparable from exogenous area	Hot-component areas generally larger than in fumarolically active region	Strong thermal anomalies	No vent or collapsing lobe front signatures
Collapse deposit	Distribution skewed towards low temperatures	Cooler than fumaroles but similar to exogenous and endogenous area	Hot-component areas generally the largest of any activity style. Hot- component areas generally cover almost all of the pixel	Strong thermal anomalies	Decreasing hot- component temperature with distance from active growth region. Possible elongation of thermal anomalies in flow/collapse direction

compared with a persistently active lava lake. A lava lake undergoing cycles of convection and overturn would have left a very different temporal signature.

If such a temporal check is possible (i.e., data of sufficient temporal resolution to create the necessary time series are available), then the temporal check may be used to fix the precise label within the uncertain, non-unique classes defined using the hot spot spatial and spectral character. Thus, in the hybrid classification scheme we use all of the data attributes (spectral, spatial and temporal) so that the initial spectral–spatial check is confirmed, rejected and/or refined by a second (later) temporal check.

### 6.3 Types of time series

Time series can be generated from repeat measurements of a thermal anomaly. Ideally, the measurement is made repeatedly using a data type of unchanging, standard, calibrated format (in our case, the basic format is spectral radiance), as well as spectral and spatial resolution. Parameters used to plot a time series also need to be extracted using a fixed, unchanging methodology, applied using assumptions that remain constant across the entire time series. This allows continuity of measurement, parameter extraction and display. The latter point is extremely important, i.e., assumptions and values used in conversions must remain fixed to allow direct comparison between each point in the series, and so as to avoid data-processing induced steps in the time series. The type of time series that can be generated will be defined by the parameter used to create the times series. Thus, we first define the main parameter groups or types that can be used to generate a time series.

#### 6.3.1 Types of measurement

A measure of the level of activity associated with a volcanic hot spot can be made in terms of three basic groups of measurement type. Each measurement type can, in turn, be used for time series construction.

- (i) The size of the hot spot. This is best expressed in terms of hot spot area, so that the number of anomalous pixels comprising the hot spot, or an estimate for the hot, sub-pixel feature area, in  $\text{m}^2$ , are appropriate measures.
- (ii) The intensity or strength of the hot spot. This is best expressed in terms of the hot spot power, mass or volume flux (per unit time), so that spectral radiance ( $\text{J s}^{-1} \text{m}^{-2} \mu\text{m}^{-1}$ ), heat flux density ( $\text{J s}^{-1} \text{m}^{-2}$ ) or mass flux ( $\text{kg s}^{-1}$ ) and/or volume flux ( $\text{m}^3 \text{s}^{-1}$ ) are appropriate measures.
- (iii) The magnitude or level of radiance associated with the hot spot. This is best expressed in terms of a flux integrated over the hot spot area, so that summed spectral radiance and/or heat flux integrated over the anomaly area ( $\text{J s}^{-1}$ ) may be appropriate measures.

For a single point within a given time series the measure of magnitude can only be produced from integrating the measurement over space (area), there being no temporal dimension to

allow time integration. Thus we consider spectral radiance or heat flux, which combine information regarding the hot spot area and intensity to be proxies for the *instantaneous hot spot magnitude*.

#### 6.3.1.1 Cumulative plots

Magnitude can also be expressed in terms of a quantity integrated over the hot spot area and then also through time, so that total energy (J), mass (kg) or volume ( $\text{m}^3$ ) are appropriate measures. Such a measure can be achieved at the end of an eruption, or eruptive phase, when a sufficient time period is available to allow time integration. It can also be used to generate cumulative plots of energy, mass or volume. This is achieved by integrating values through time between two sequential flux measurements, and then summing each value in sequence. Thus the cumulative volume at the end of time step 2 is obtained from the sum of the volumes obtained during time steps 1 and 2; the volume at time step 3 is then obtained from the sum of the volumes obtained for steps 1, 2 and 3, and so on until the plot is completed. If this runs to the end of the eruption, the final point will give the total energy, mass or volume emitted during the eruption.

#### 6.3.2 Parameter levels

Across these measurement groupings, we can identify three parameter levels, each defined on the basis of the number of processing steps required to generate the parameter, the number of processing steps (and assumptions applied) increasing as we move through the levels.

##### 6.3.2.1 Level zero

The first level of parameters (level zero) that can be extracted simply requires calibration of the raw digital number and conversion to a spectral radiance or brightness temperature. Thus only one processing step (calibration) is required. This parameter level thus effectively represents a measure of the hot spot intensity as expressed by the raw data, before any manipulation. Such level zero parameters thus include spectral radiance (maximum or summed), brightness temperature (maximum or average) and number of anomalous pixels (as a count or multiplied by pixel area to give a result in  $\text{m}^2$  or  $\text{km}^2$ ).

##### 6.3.2.2 First-order parameters

Extraction of higher-order parameters involves applying models or assumptions to convert the raw data (spectral radiance values) to parameters such as sub-pixel lava area or heat flux. Extraction of first-order parameters involves application of a first level of assumptions and/ or use of pixel-mixture models. Estimation of sub-pixel lava area, for example, involves selection of an appropriate mixture model and, usually, assumption of a temperature to solve the mixture model (see Sections 4.2 and 4.3 of Chapter 4). Conversion to heat flux is then dependent on the extracted area and assumed temperature (see Section 4.4 of Chapter 4).

Such first-order parameters thus include estimates of hot feature area (in m<sup>2</sup>) and heat flux (in W). As discussed in Chapter 4, application of the assumptions and mixture models that allow these parameters to be extracted may begin to bias or influence the output, especially if the assumption is incorrect. However, they do allow the time series to be presented in terms of parameters, such as feature area and/or heat flux, that are more accessible to the non-remote sensing expert.

#### 6.3.2.3 Second-order parameters

Extraction of second-order parameters involves applying a second level of assumptions, relations or conversion factors to the first-order parameters. Examples include the application of a conversion factor to a lava area and/or heat flux to allow conversion to mass flux, volume flux or cooling rate. In effect the spectral radiance value has now been through two levels of conversion requiring application of two sets of assumptions. As already discussed at the end of Chapter 4, this often results in a linear conversion between parameter levels, and all we complete is a unit conversion to allow the output to be expressed in a form that is easier to digest or use. Such second-order parameters thus include mass flux (in kg s<sup>-1</sup>), volume flux (in m<sup>3</sup> s<sup>-1</sup>) or cooling rate (in °C s<sup>-1</sup>).

#### 6.3.3 Volcanic radiance

Because a pixel will usually be a mixture of signals from the hot volcanic surface and the surrounding ambient surfaces, some of the variation in the integrated spectral radiance or brightness temperature may be due to the influence of the ambient background. If, for example, a barren, but inactive and cold, lava surface undergoes solar heating by day and cooling by night the pixel will be hotter by day and cooler by night. I have measured variations of 60 °C in a 12-hour period at the summit of Etna during May, where scoria surfaces can heat to ~55 °C by day and cool to -5 °C on a frosty night. If such a surface is present in the background of a mixed pixel containing a small volcanic hot spot, then it will introduce a diurnal variation into the integrated radiance. Likewise, surfaces may be solar heated to higher levels in summer than during winter to also introduce an annual variation. Indeed, the ambient portion of a pixel at the summit of Etna may be filled by solar-heated scoria in summer, but covered by cold snow and ice during the winter.

Simple corrections can be applied to reduce the influence of the unwanted ambient component of the signal. One way of doing this is to subtract an estimate for the radiance of the ambient background ( $M_{\text{back}-\lambda}$ ) from the integrated radiance ( $M_{\text{int}-\lambda}$ ) to isolate the excess radiance due to the volcanic component, a measure termed *volcanic spectral radiance* ( $M_{\text{volc}-\lambda}$ ) by Harris *et al.* (1997b):

$$M_{\text{volc}-\lambda} = M_{\text{int}-\lambda} - M_{\text{back}-\lambda}. \quad (6.2)$$

This measure is, in effect, a proxy for relative radiation.

### 6.3.3.1 An example

We demonstrate this effect using a 10-m radius circular lava lake centered in a 1-km AVHRR pixel. During the day-time satellite overpass the lake is undergoing sluggish activity with a surface crust temperature of 265 °C. During the night-time pass the lake is undergoing vigorous activity with a surface crust temperature of 385 °C. Thus, the radiant intensity for the target (i.e., the lava lake) should increase between the two overpasses. However, by day the lake is set against a solar-heated background at 55 °C, which cools to −5 °C at night. The dominant contribution of the background radiance to the pixel-integrated value means that the pixel-integrated spectral radiance in the MIR (and TIR) actually decreases between the two passes, with the pixel-integrated temperature decreasing from 61 °C during the day-time pass to 14 °C by night. This effect can be seen in the spectral radiance bar graph for this pixel given in [Figure 6.13](#) where, although the radiant contribution from the lava lake increases between the two passes, the decrease in the background contribution between night and day is much greater, forcing an overall decrease on the integrated radiance. Thus a decreasing trend is recorded by the pixel-integrated spectral radiance, when the radiant intensity of the sub-pixel volcanic target actually underwent an increase.

If we now take the radiance of a background pixel (with a pixel-integrated temperature of 55 °C by day and −5 °C by night) and subtract that from the integrated value, we remove the background component of the signal, as done in the final two columns of [Figure 6.13](#). This now isolates the volcanic component. As a result we see an increase in the volcanic radiance between the day-time and night-time overpasses, consistent with the increased radiant intensity for the modeled lava lake. In effect, we have removed the dominant ambient effect (due to diurnal heating) and isolated the radiance from the volcanic (lava lake) source.

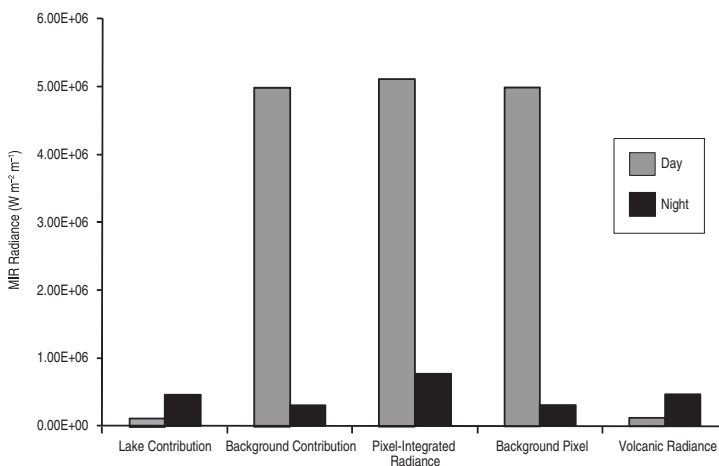


[Figure 6.13](#) Modeled MIR radiance contributions, pixel-integrated radiances and volcanic radiances for a 1 km AVHRR-class pixel containing a 10 m radius circular hot spot. The “day-time” hot spot has a temperature of 265 °C and is against a background at 60 °C. The “night-time” hot spot has a temperature of 385 °C and is against a background at −5 °C. Volcanic radiance is obtained by subtracting the background radiance from the pixel-integrated radiance.

### 6.3.4 Time series classification

A classification of the time series types can now be completed on the basis of the parameter level used to generate each time series, as done in [Figure 6.14](#). This classification is organized on the basis of the level of parameter type plotted, and moves from the most basic parameter level (level 0) through to the highest level (level 2). The classification is illustrated using time series of each parameter generated from 374 MODIS images obtained during Etna's 2008–2009 effusive eruption. Methodologies used to derive each of the parameters plotted are detailed in Electronic Supplement 11, in which all data tables used for each time series plot, and large format versions of each time series plot, are also given.

#### 6.3.4.1 Time series Type I

The first type of time series uses level 0 parameters. The resulting group of time series that can be generated are given at the top of [Figure 6.14](#). There are three sub-levels within this type.

The most basic parameter level that can be plotted as a time series is maximum spectral radiance or brightness temperature, this representing a proxy for hot spot intensity. Use of the pixel with the highest value will be utterly unbiased by user-applied assumptions or the manual (or automated) decision making processes that selects pixels to contribute to the measurement. This parameter thus forms this first (lowest) sub-level.

The next sub-level is a plot of the number of pixels comprising the thermal anomaly. This can give a crude proxy for the hot spot area. We place this time series type at a slightly higher level than maximum spectral radiance or brightness temperature plots because generation requires a decision making process (either automated or manual) to determine whether a pixel is part of the thermal anomaly or not. This selection may differ from user to user, or program to program. The number of pixels flagged as anomalous may thus vary depending on the operator or the hot spot detection algorithm used, so that the total pixel count may vary depending on the process applied. We may thus begin to introduce some bias.

The third sub-level involves summing the spectral radiances for all pixels across the anomaly. This combines area and intensity information to provide a proxy for the instantaneous hot spot magnitude. Time series of volcanic radiance are included at the end of the Type I classification grouping because it requires some data manipulation beyond simple calibration, counting or summing, i.e., it requires a background value to be assumed or selected and subtracted from the raw value. Thus the level of operator interference increases.

#### 6.3.4.2 Time series Type II

The second time series type involves use of first-order parameters. Plots that can be categorized within this type are given in the middle of the [Figure 6.14](#) classification and include estimates of hot feature area and heat flux. We now force assumptions regarding the thermal structure of the pixel on the result, increasing the level of operator interference further.

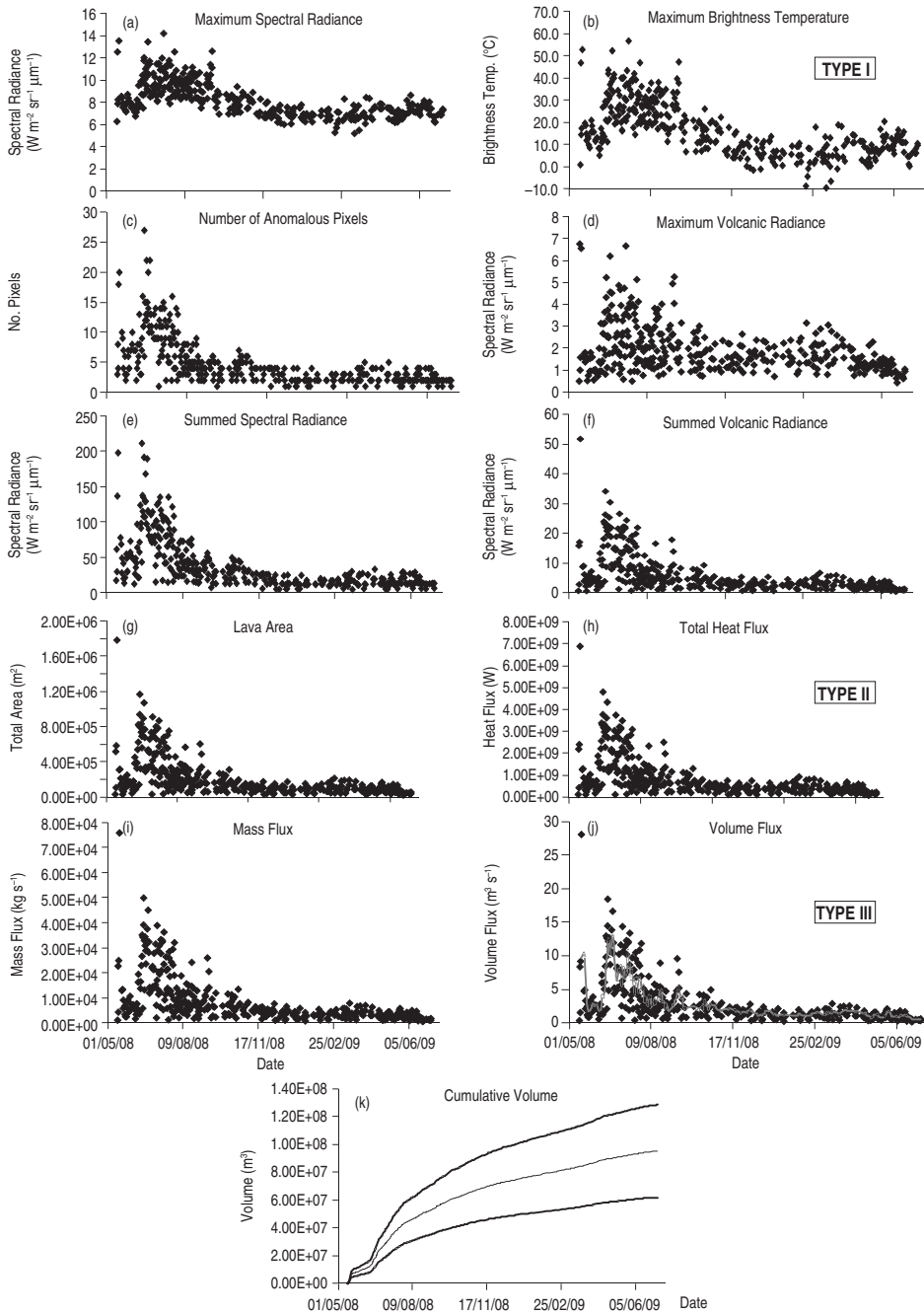


Figure 6.14 Classification of the time series types made on the basis of the parameter level used to generate each time series, illustrated using MODIS data collected during Etna's 2008–2009 eruption. The gray line plotted in the volume flux time series is a five-point moving average. Three cumulative volume curves are given. These are obtained from the minimum and maximum bounds estimated for the volume flux, plus the mid-point value (see Electronic Supplement 11 for details regarding extraction and calculation of each value for this demonstration case, plus enlarged versions of each plot in which trends and spikes referred to in the text are easier to locate).

### 6.3.4.3 Time series Type III

The third time series type involves use of second-order parameters to generate the plots. Plot types within this final category are given at the bottom of the [Figure 6.14](#) classification, where we see that they now allow the time series to be plotted in terms of units of kilograms per second or cubic meters per second, these being units which are measures of the hot spot intensity; useful in tracking, understanding and predicting the progression, or impact, of an eruptive event. However, a further layer of operator interference has been forced onto the result.

## 6.4 Time series generation

So what are the steps required to generate each time series plot? We can attain these steps by applying the theory and methodology laid out so far. In doing so, we can also explore some of the advantages and disadvantages of each time series type.

### 6.4.1 Type I time series – spectral radiance and brightness temperature

The simplest plot type within this category is a time series of maximum spectral radiance or brightness temperature. These plots are given in [Figures 6.14a](#) and [6.14b](#) and are produced by applying the following steps.

- (i) Calibrate the image by converting DN to spectral radiance (while applying any necessary non-linearity corrections) (see [Electronic Supplement 2](#)).
- (ii) Locate all hot spot pixels, and record the pixel with the maximum spectral radiance.
- (iii) To express output in terms of brightness temperature, rather than spectral radiance, solve the inverted form of the Planck equation (see [Chapter 2](#)).

Production of such time series is quick and simple, and provides a measure of the *maximum radiant intensity* or *maximum strength* of the hot spot. For example, a heavily crusted lava lake in overpass 1 that undergoes a major fountaining event during overpass 2 will have a much higher radiant intensity in the second overpass, a result of higher temperatures associated with the fountain of molten lava as opposed to those of the chilled lava crust during the heavily crusted period. Thus a time series of maximum spectral radiance or brightness temperature may reveal peaks and troughs coincident with high and low intensity activity.

We note, however, that maximum radiance and brightness temperature time series will likely suffer diurnal and annual heating effects. For example, maximum radiance and brightness temperature time series given in [Figures 6.14a](#) and [6.14b](#) suffer from an annual effect (as well as likely diurnal effects). This is because we are plotting a measure of both the volcanic and ambient components of the signal. Note, for example, the systematic decline in pixel-integrated brightness temperature plotted in [Figure 6.14a](#) as we move from the summer months to the winter months, then a steady increase as we move back into the

summer months. Note also some particularly low values during February, no doubt due to particularly cold ambient conditions at Etna's snow and ice covered summit at that time. As already shown, such annual and diurnal effects may distract from, or mask, any variation due to changes in thermal intensity experienced by the sub-pixel volcanic component.

#### *6.4.1.1 Maximum volcanic radiance*

Output of volcanic radiance can be attempted, to remove ambient effects and to isolate the volcanic component, as given in [Figure 6.14d](#). To do this we can execute the following steps.

- (i) Calibrate the image by converting DN to spectral radiance, while applying any necessary non-linearity corrections.
- (ii) Locate all hot spot pixels, and record the pixel with the maximum spectral radiance ( $M_{\text{int-MAX-}\lambda}$ ).
- (iii) Locate the nearest ambient pixel (i.e., non-anomalous) pixel and use this to characterize the background radiance ( $M_{\text{back-}\lambda}$ ).
- (iv) Subtract  $M_{\text{back-}\lambda}$  from  $M_{\text{int-MAX-}\lambda}$  to obtain the maximum volcanic radiance ( $M_{\text{volc-MAX-}\lambda}$ ), i.e.,

$$M_{\text{volc-MAX-}\lambda} = M_{\text{int-MAX-}\lambda} - M_{\text{back-}\lambda}.$$

This should begin to remove the influence of the ambient component, and in the plot of maximum volcanic radiance given in [Figure 6.14d](#) we do see that the annual effects evident in [Figure 6.14b](#) are gone, and the “cold” values of February 2009 are removed. Instead we highlight four or five spikes, such as during 9–12 September 2008, when intensities were relatively high.

For a multiple-pixel anomaly, information regarding the size or magnitude of the anomaly will also be missing from such plots of maximum intensity. An expanding lava lava flow field, for example, may have the same maximum spectral radiance value in consecutive images (especially if that value is saturated). Expansion of the flow field will, though, cause the anomaly to spread across an increasing number of pixels so that the total spectral radiance for the anomaly (i.e., summed spectral radiance for all pixels) shows an increase that reflects expansion of the phenomena. This information is lost in the maximum intensity plot.

#### *6.4.1.2 Number of hot pixels*

Output of the number of pixels within an anomaly may give a proxy for the area of the hot spot, such as done in [Figure 6.14c](#). To do this we can execute the following steps.

- (i) Run any of the hot spot detection algorithms reviewed in [Chapter 5](#) or identify anomalous pixels manually.
- (ii) Count and plot the number of pixels flagged as anomalous.

The size of the anomaly can now be tracked as it expands to fill more pixels or contracts to fill fewer pixels. The plot, however, contains no information regarding the intensity of the anomaly and is also limited by the spatial resolution of the sensor. The development of a second 10-m radius lava lake 100 m from the lava lake model of [Figure 6.13](#) will, if centered

in a 1 km pixel still cause the anomalous pixel count to sum to one. The total area of active lava lake(s) has, however, doubled; as has the radiant intensity for the pixel. However, in [Figure 6.14c](#) we do pick out a phase of high area coverage, a waning phase of decreasing area, and a relatively stable phase of low area coverage.

#### 6.4.1.3 Summed spectral radiance

A more useful plot within this category is that of total spectral radiance, a measure which involves summing the spectral radiances for all pixels within the anomaly, as follows.

- (i) Calibrate the image by converting DN to spectral radiance, while applying any necessary non-linearity corrections.
- (ii) Locate all hot spot pixels, and record the spectral radiances for all pixels.
- (iii) Sum the spectral radiance for all hot pixels to yield  $\sum M_{\lambda}$ .

This value is difficult to plot as a brightness temperature, so tends to be left as a spectral radiance. However, it now combines both area and intensity information to give a proxy for the magnitude of the event. We see the effect in [Figure 6.14e](#) where a clearer trend is now apparent when compared with the maximum spectral radiance plot. However, because this value includes summing of pixel-integrated values it may be influenced by temperature changes felt by ambient surfaces within the pixel.

#### 6.4.1.4 Summed volcanic radiance

To clean out potential contamination due to diurnal or annual effects, we can also plot total volcanic radiance, as follows.

- (i) Calibrate the image by converting DN to spectral radiance, while applying any necessary non-linearity corrections.
- (ii) Locate all hot spot pixels, and record the spectral radiances for all pixels.
- (iii) Locate the nearest ambient pixel (i.e., non-anomalous) pixel to each hot pixel and use this to characterize the background radiance ( $M_{\text{back-}\lambda}$ ).
- (iv) Calculate the volcanic radiance for each hot spot pixel by subtracting  $M_{\text{back-}\lambda}$  from  $M_{\text{int-}\lambda}$  to obtain the pixel volcanic radiance ( $M_{\text{volc-}\lambda}$ ), i.e.,

$$M_{\text{volc-}\lambda} = M_{\text{int-}\lambda} - M_{\text{back-}\lambda}.$$

- (iv) Sum the volcanic radiance for all hot pixels to yield  $\sum M_{\text{volc-}\lambda}$ .

To be as close as possible to the actual spectral radiance for ambient surfaces within the hot spot pixels, those ambient pixels that are the closest to the target pixel should be used in setting  $M_{\text{back-}\lambda}$ , with selection considerations being similar to those required for setting background temperatures for use in the dual-band method as discussed in [Section 4.3.1.6](#) of [Chapter 4](#). The resulting plot of  $\sum M_{\text{volc-}\lambda}$  for the 2008–2009 example used here is given in [Figure 6.14f](#). It cleans up the summed spectral radiance plot further, showing a steadily waning phase until November 2008, followed by a low, but relatively stable level

of  $\sum M_{\text{volc}-\lambda}$  until May 2009 after which  $\sum M_{\text{volc}-\lambda}$  levels are particularly low. It also highlights a few spikes that are lost in hot pixel count and summed spectral radiance time series, such as that of 9–12 September 2008.

#### **6.4.2 Type II time series – feature area and heat flux**

The next type of time series involves converting to lava area or heat flux following the methodologies of [Chapter 4](#). The results in terms of lava area and radiative heat flux time series are given in [Figures 6.14g](#) and [6.14h](#). Trends revealed in these plots mirror the trends and spikes of the summed volcanic radiance plot of [Figure 6.14f](#).

This is a particularly nice case type event because: (i) it spans all seasons so that we can check for removal of ambient effects, (ii) there is a large amount of data so that any trend is supported by multiple data points, (iii) a nice trend is apparent with, (iv) a few spikes, so that (v) it illustrates well the advantages and disadvantages of each time series type.

#### **6.4.3 Type III time series – mass, volume flux and cumulative volume**

Generation of the final type of time series involves converting the lava area or heat flux time series to plots of mass or volume flux. This can be achieved following the methodologies detailed in [Section 4.5](#) of [Chapter 4](#). The results for mass flux are given in [Figure 6.14i](#), and for volume flux in [Figure 6.14j](#).

A final type of magnitude time series can be generated by integrating the volume flux through the time separating each volume flux measurement. This allows generation of a cumulative volume plot. One way to achieve this is by applying the trapezium rule to the volume flux time series. In this way a volume can be produced for each time increment following:

$$V_n = t_{n+1} - t_n \left( \frac{TADR_2 + TADR_1}{2} \right). \quad (6.3)$$

Here,  $TADR_1$  is the time-averaged discharge rate (in  $\text{m}^3 \text{s}^{-1}$ ) recorded during the first satellite overpass at time  $t_n$ , and  $TADR_2$  is the time-averaged discharge rate recorded during the next satellite overpass at time  $t_{n+1}$ , so that  $t_{n+1} - t_n$  is the time difference (in seconds) between the two measurements. Thus, if we take the first two time-averaged discharge rates of the time series ( $0.5 \text{ m}^3 \text{s}^{-1}$  and  $8.5 \text{ m}^3 \text{s}^{-1}$ ), as acquired at 09:50Z on 13 May 2008 and 01:10Z on the following day, we obtain:

$$V_n = 55\,200 \text{ s} \left( \frac{(0.5 \text{ m}^3 \text{s}^{-1}) + (8.5 \text{ m}^3 \text{s}^{-1})}{2} \right) = 2.46 \times 10^5 \text{ m}^3.$$

Summing these values through time yields a plot for cumulative volume, i.e., the volume emplaced between the eruption onset and any given point in the eruption. These results for Etna's 2008–2009 eruption are given in [Figure 6.14k](#).

#### 6.4.4 Temporal detail

The temporal detail of the time series depends on the temporal resolution of the data used to generate the plot.

- The temporal resolution of TM-class data (16 days) means that they suit tracking of eruptive trends that develop over weeks to months;
- the temporal resolution of AVHRR-class data (12 hours) allows eruptive trends that develop over days to weeks to be tracked;
- the temporal resolution of GOES-class data (15 minutes) allows eruptive trends that develop over hours to be tracked.

To identify a trend we need three or more data points, so that the eruption duration needs to be at least  $n + 1$  times longer than the satellite return period,  $n$  being the minimum number of data points required. Thus, if a time series is to be produced from TM data an eruption needs to exceed 64 days, for AVHRR the eruption needs to exceed 48 hours (24 hours if two satellites are available to reduce the return period to 6 hours), and has to be in excess of 60 minutes if time series are to be produced from GOES data.

## 6.5 Case studies

A collation and review of satellite-data-derived time series published through 2005 is given in [Tables 6.7](#) and [6.8](#). This collation summarizes:

- (i) the type of data used to generate each time series,
- (ii) the time series temporal resolution,
- (iii) the type of parameter plotted,
- (iv) the type (and location) of the volcanic thermal phenomena tracked,
- (v) the duration of each time series, and
- (vi) the typical number of data points available for time series analysis using TM-, AVHRR- and GOES-class data.

From [Table 6.7](#) we see the following.

- (i) AVHRR-class data have been the most popular class for time series production. Thirty-nine (65%) of the 60 time series studies collated in [Table 6.7](#) have used AVHRR-class data. Of these, AVHRR contributed 25 studies, ATSR contributed 8, and MODIS 6. Of the remaining studies, TM-class data have supported 13, and GOES-class data 8.
- (ii) All parameter types have been used, although plots of spectral radiance have been the most popular form of time series. Indeed, Type I time series account for 58 % of the 85 time series graphs that can be counted in [Table 6.7](#), with Type II and III plots making up 16 % and 26 % of this total, respectively. The total number of graphs for each parameter type is given at the foot of [Table 6.7](#).

**Table 6.7.** Collation of satellite-data-derived time series studies of volcanic hot spots published in the mainstream literature through 2005 (excluding review articles) giving data type and parameters used by the time series, as well as feature type examined. Studies are listed in chronological order. The divide between 1999 and 2000 is marked with a dashed line. Note that the “open vent” feature type includes open vents undergoing degassing and explosive (e.g., strombolian) activity. PF = Pyroclastic flow; CL = hot crater lakes.

Authors	Year	Primary data type used	Parameter(s) plotted	Feature type examined
Glaze <i>et al.</i>	1989	TM	$\Phi_{\text{rad}}$	Lava dome
Oppenheimer <i>et al.</i>	1993	TM	$M_\lambda$	Lava dome
Harris and Stevenson	1997a	AVHRR	$M_{\text{volc-}\lambda}, \Phi_{\text{rad}}$	Open vents
Harris <i>et al.</i>	1997a	AVHRR	$A_{\text{lava}}, \Phi_{\text{rad}}, TADR, V$	Lava flow
Harris <i>et al.</i>	1997b	AVHRR	$A_{\text{lava}}, \Phi_{\text{rad}}, TADR, V$	Lava flow
Harris <i>et al.</i>	1997c	GOES	$M_{\text{volc-}\lambda}$	Lava flow
Oppenheimer and Francis	1997	TM	$\Phi_{\text{rad}}$	Lava lake
Wooster and Rothery	1997a	ATSR	$M_\lambda$	Lava dome
Wooster and Rothery	1997b	ATSR	$A_{\text{lava}}$	Lava flow
Wooster <i>et al.</i>	1997	ATSR	$\Phi_{\text{rad}}$	Lava flow
Dean <i>et al.</i>	1998	AVHRR	No., $T$	Lava flow
Oppenheimer and Francis	1998	TM	$\Phi_{\text{rad}}$	Lava lake
Wooster and Kaneko	1998	ATSR	$M_{\lambda, T}, M_{\text{volc-}\lambda}$	Lava dome
Wooster <i>et al.</i>	1998b	ATSR	$M_\lambda$	Lava dome
Wooster <i>et al.</i>	1998b	ATSR	$M_\lambda$	Lava dome
Harris and Thornber	1999	GOES	$M_{\text{volc-}\lambda}$	Lava flow
Harris <i>et al.</i>	1999	AVHRR	$A_{\text{lava}}$	Lava lake
Kaneko and Wooster	1999	TM	$M_\lambda, A_{\text{anomaly}}$	Lava dome
Dehn <i>et al.</i>	2000	AVHRR	$T$	Lava dome, flow and open vent
Carn and Oppenheimer	2000	AVHRR	$\Delta T$	Lava domes, flows, PFs, CLs
Harris <i>et al.</i>	2000a	AVHRR	$TADR, V$	Lava flows
Harris <i>et al.</i>	2000b	GOES	$M_\lambda$	Lava flows and domes
Mouginis-Mark <i>et al.</i>	2000b	GOES	$M_\lambda$	Lava flow
Schneider <i>et al.</i>	2000	AVHRR	$T$	PFs, lava dome
Urai	2000	TM	$A_{\text{anomaly}}$	Lava dome
Wooster <i>et al.</i>	2000	TM	Maps	Lava dome
Wright <i>et al.</i>	2000	TM	Maps	Lava flow

Table 6.7. (cont.)

Authors	Year	Primary data type used	Parameter(s) plotted	Feature type examined
Aries <i>et al.</i>	2001	AVHRR	$M_\lambda, M_{\text{volc}-\lambda}$	Lava flow
Harris <i>et al.</i>	2001	GOES	$M_{\text{volc}-\lambda}$	Lava flow
Roach <i>et al.</i>	2001	AVHRR	No.	Open vent, PFs?
Rothery <i>et al.</i>	2001	ATSR	$M_\lambda$	Open vent and lava flow
Lachlan-Cope <i>et al.</i>	2001	AVHRR	$A_{\text{lava}}$	Lava lake
Wooster	2001	ATSR	$M_\lambda$	Lava dome
Wright <i>et al.</i>	2001	ETM+	Maps	Lava flow field
Dehn <i>et al.</i>	2002	AVHRR	$T, A, \Phi_{\text{rad}}$	Open vent
Dean <i>et al.</i>	2002	AVHRR	No., $T$	Lava Flow, lava dome
Galindo and Dominguez	2002	AVHRR	$T$	Lava dome
Harris and Neri	2002	AVHRR	$A_{\text{lava}}, TADR, V$	Lava flow and fountains
Harris <i>et al.</i>	2002a,b	GOES	$M_{\text{volc}-\lambda},$	Lava flow, open vents, fountain.
Kaneko <i>et al.</i>	2002a	TM	$M_\lambda, A_{\text{anomaly}}$	Lava dome
Kaneko <i>et al.</i>	2002b	AVHRR	$M_\lambda$	Open vents
Wright <i>et al.</i>	2002b	GOES	$M_\lambda, T$	Lava dome
Galindo and Dominguez	2003	AVHRR	$\Delta T$	Lava dome
Harris <i>et al.</i>	2003a	TM	$A_{\text{lava}}, TADR, V$	Lava dome
Ortiz <i>et al.</i>	2003	GOES	$M_\lambda$	Open vent and lava lake
Patrick <i>et al.</i>	2003	AVHRR	$T, TADR$	Lava flow field
Rowland <i>et al.</i>	2003	ATSR	$TADR$	Lava flow
Calder <i>et al.</i>	2004	GOES	$M_\lambda$	Open vent and lava lake
Dean <i>et al.</i>	2004	AVHRR	$T$	Lahars, lava flow, open vent
Harris <i>et al.</i>	2004	ETM+	$A_{\text{lava}}, \Phi_{\text{rad}}, TADR, V$	Silicic lava flow
Lautze <i>et al.</i>	2004	AVHRR	$TADR$	Lava flow
Ramsey and Dehn	2004	AVHRR	$T$	Lava dome
Wright and Flynn	2004	MODIS	$\Phi_{\text{rad}}$	All
Wright <i>et al.</i>	2004	MODIS	$M_\lambda$	Lava lakes, domes and flows
Calvari <i>et al.</i>	2005	AVHRR	$TADR$	Lava flow
Kaneko and Wooster	2005	TM	$T$	Lava flow
Patrick <i>et al.</i>	2005a	AVHRR	$T$	Lava flow (cooling)
Patrick <i>et al.</i>	2005b	MODIS	$\Phi_{\text{rad}}$	Lava flow, lava lake

Table 6.7. (cont.)

Authors	Year	Primary data type used	Parameter(s) plotted	Feature type examined
Ripepe <i>et al.</i>	2005b	MODIS	TADR	Lava flow and open vent
Rothery <i>et al.</i>	2005	MODIS	$M_\lambda$ , No.	All
Wright <i>et al.</i>	2005	MODIS	$\Phi_{\text{rad}}$	Lava dome

**Parameter key, with total number of graphs for each parameter type (given as no. graphs = XX):** $M_\lambda$ =spectral radiance ( $\text{W m}^{-2} \text{ sr}^{-1} \mu\text{m}$ ): no. graphs = 16 $T$ =brightness temperature (K or  $^{\circ}\text{C}$ ): no. graphs = 13 $\Delta T$ =brightness temperature difference ( $=T_{\text{MIR}} - T_{\text{TIR}}$ , in K or  $^{\circ}\text{C}$ ): no. graphs = 2 $M_{\text{volc-}\lambda}$ =volcanic radiance ( $\text{W m}^{-2} \text{ sr}^{-1} \mu\text{m}$ ): no. graphs = 11

No.=number of hot pixels: no. graphs = 4

 $A_{\text{anomaly}}$ =anomaly area obtained from multiplying the number of hot pixels by pixel area ( $\text{m}^2$ ): no. graphs = 3 $A_{\text{lava}}$ =hot feature area extracted using the dual-band technique ( $\text{m}^2$ ): no. graphs = 2 $\Phi_{\text{rad}}$ =radiative heat flux (W): no. graphs = 12TADR=time-averaged discharge rate ( $\text{m}^3 \text{ s}^{-1}$ ): no. graphs = 11 $V$ =cumulative volume ( $\text{m}^3$ ): no. graphs = 11

- (iii) Time series have been used to support studies covering the full range of volcanic thermal phenomena from lava flows, domes and lakes, to open vents and fumarole fields. However, studies of active lava flows and domes have been the most popular, with the number of time series generated by feature type being: 32 for lava flow, 25 for lava dome, 12 for open vents and 9 for lava lakes.

A review of Table 6.8 reveals that TM-class data have typically been capable of generating between 2 and 12 data points per year, thus being used to track trends developing over time scales of weeks-to-months in data sets spanning 1 to 12 years. AVHRR-class data on the other hand can give up to  $\sim$ 10 data points per week, and typically several points per month. They have thus been used to focus on single eruptions lasting a few days to a few months, as well as activity spanning years to decades. Finally, GOES-class data, giving up to 96 data points per day, have been used to plot trends developing over a few hours.

We next review these studies to illustrate, through case studies:

- (i) the type of activity that can be tracked through time series analysis using each data class;
- (ii) the temporal detail, and time scales of change, that each data class can reveal;
- (iii) inferences regarding eruption dynamics and processes that can be drawn from time series analysis of volcanic hot spots.

Table 6.8. Collation of satellite-data-derived time series studies of volcanic hot spots published in the mainstream literature through 2005 giving volcano targeted, the duration of the time series and the number of data points used. Studies are grouped by data class, and then listed chronologically within each class. Those marked with an asterisk within the AVHRR-class group are time series produced from ATSR data, which has a return period of 3–35 days, as opposed to the 6–12 hour capability of AVHRR.

Authors	Year	Target volcano	Period: date range (duration)	Number of images (data points per unit time)
(1) Time series using TM-class data				
Glaze <i>et al.</i>	1989	Lascar (Chile)	1984–1987 (3.2 years)	10 (3.1 /year)
Oppenheimer <i>et al.</i>	1993a	Lascar (Chile)	1984–1992 (7.2 years)	15 (2.1 /year)
Oppenheimer and Francis	1997	Erta Ale (Ethiopia)	1984–1986 (3 years)	10 (3.3 /year)
Oppenheimer and Francis	1998	Erta Ale (Ethiopia)	1984–1986 (3 years)	10 (3.3 /year)
Kaneko and Wooster	1999	Unzen (Japan)	10/91–11/92 (1.2 years)	8 (6.9 /year)
Urai	2000	Unzen (Japan)	1991–1996 (4.25 years)	23 (5.4 /year)
Wooster <i>et al.</i>	2000	Unzen (Japan)	12/91–11/92 (1 year)	3 (3.0 /year)
Wright <i>et al.</i>	2000	Etna (Italy)	12/91–06/93 (0.6 years)	0 (12 /year)
Wright <i>et al.</i>	2001	Etna (Italy)	27–28 October 1999 (2 days)	1 (12 /year)
Kaneko <i>et al.</i>	2002a	Unzen (Japan)	10/91–01/93 (1.3 years)	10 (7.5 /year)
Harris <i>et al.</i>	2003a	Santiaguito (Guatemala)	11/87–01/00 (12.2 years)	18 (1.5 /year)
Harris <i>et al.</i>	2004	Santiaguito (Guatemala)	01/00–01/02 (2 years)	3 (1.5 /year)
Kaneko and Wooster	2005	Izu-Oshima (Japan)	12/86–06/87 (0.5 years)	6 (12 /year)
(2) Time series using AVHRR-class data				
Harris and Stevenson	1997a	Stromboli (Italy)	1990–1994 (4.5 years)	34 (7.6 /year)
		Stromboli (Italy)	1985–1986 (1.5 years)	20 (13.3 /year)
		Vulcano (Italy)	1985–6 + 1990–4 (7 years)	39 (5.6 /year)
Harris <i>et al.</i>	1997a	Etna (Italy)	14/12/91–30/03/93 (1.3 years)	308 (4.6 /week)
Harris <i>et al.</i>	1997b	Etna (Italy)	12/03/85–13/07/85 (0.3 year)	16 (3.9 /month)
		Cerro Negro (Nicaragua)	25/11/95–6/12/95 (11 days)	4 (2.5 /week)

Table 6.8. (cont.)

Authors	Year	Target volcano	Period: date range (duration)	Number of images (data points per unit time)
Wooster and Rothery	1997a	Lascar (Chile)	1992–1995 (3.0 years)	64 (1.8 /month)*
Wooster and Rothery	1997b	Fernandina (Galapagos)	01/95–04/95 (10 weeks)	8 (2.7 /month)*
Wooster <i>et al.</i>	1997	Etna (Italy)	16/12/91–18/05/93 (1.4 years)	29 (1.7 /month)*
Dean <i>et al.</i>	1998	Okmok (Alaska)	31/1/97–16/05/97 (3.5 months)	~300 (2.9 /day)
Wooster and Kaneko	1998	Unzen (Japan)	01/92–07/94 (2.6 years)	31 (1.0 /month)*
Wooster <i>et al.</i>	1998a	Unzen (Japan)	11/92–07/94 (1.8 years)	26 (1.2 /month)*
		Lascar (Chile)	04/92–11/95 (3.7 years)	55 (1.2 /month)*
Wooster <i>et al.</i>	1998b	Galeras (Colombia)	10/91–11/91 (2 months)	5 (2.5 /month)*
Harris <i>et al.</i>	1999	Erebus (Antarctica)	12–13 January 1980 (2 days)	5 (2.5 /day)
Dehn <i>et al.</i> (a)	2000	Bezymianny (Kamchatka)	1998 (12 months)	~4380 (~12 /day)
		Karymsky (Kamchatka)	1998 (12 months)	~4380 (~12 /day)
		Okmok (Aleutians)	1997 (12 months)	~4380 (~12 /day)
Carn and Oppenheimer (a)	2000	Indonesian volcanoes <sup>1</sup>	01/01/96–01/11/97 (1.8 years)	690 (~1 /day)
Harris <i>et al.</i>	2000b	Etna (Italy)	1983 (4.4 months)	54 (12.4 /month)
		Etna (Italy)	1984 (5.7 months)	45 (7.8 /month)
		Etna (Italy)	1985 (4.1 months)	17 (4.1 /month)
		Etna (Italy)	1986–1987 (4.0 months)	23 (5.8 /month)
		Etna (Italy)	1991–1993 (15.7 months)	33 (2.1 /month)
		Etna (Italy)	1996 (1 month)	19 (19.7 /month)
		Krafla (Iceland)	1980 (8 days)	7 (6.1 /week)
		Krafla (Iceland)	1984 (14 days)	6 (3.0 /week)
Schneider <i>et al.</i>	2000	Bezymianny (Kamchatka)	1/12/97–7/12/98 (37 days)	26 (4.9 /week)

Aries <i>et al.</i>	2001	Etna (Italy)	10/07/80–27/08/80 (1.6 months)	17 (2.5 / week)
		Etna (Italy)	18/10/80–24/01/81 (3.3 months)	46 (3.3 / week)
		Etna (Italy)	30/01/81–28/02/81 (1 month)	35 (8.4 / week)
		Etna (Italy)	17–25 November 1981 (8 days)	11 (9.6 / week)
		Etna (Italy)	4–27 September 1984 (23 days)	11 (3.3 / week)
		Etna (Italy)	12/91–12/93 (2 years)	47 (1.9 / month)
		Krafla (Iceland)	10/07/80–27/08/80 (1.6 months)	19 (2.8 / week)
Roach <i>et al.</i>	2001	Pavlof (Alaska)	6/09/96–25/11/96 (2.6 months)	50 (4.4 / week)*
Lachlan-Cope <i>et al.</i> (a)	2001	Saunders Island <sup>2</sup>	03/95–02/98 (2.9 years)	~5000 (~5 / day)
Rothery <i>et al.</i>	2001	Etna (Italy)	1996–1999 (4 years)	117 (2.4 / month)
Wooster	2001	Lascar (Chile)	1995–2000 (5.75 years)	252 (3.65 / month)
Dehn <i>et al.</i> (a)	2002	Shishaldin (Alaska)	09/02/99–30/04/99 (3 months)	960 (12 / day)
Dean <i>et al.</i> (a)	2002	Okmok (Alaska)	31/1/97–16/05/97 (3.5 months)	~300 (2.9 / day)
		Bezymianny (Kamchatka)	1998(12 months)	~4380 (~12 / day)
Galindo and Dominguez (a)	2002	Colima (Mexico)	1997–2000 (3 years)	4380 (4 / day)
Harris and Neri	2002	Etna (Italy)	17/10/99–05/11/99 (19 days)	38 (2 / day)
Kaneko <i>et al.</i>	2002b	Miyakejima (Japan)	01/07/00–31/12/00 (6 months)	26 (1 / week)
Galindo and Dominguez	2003	Colima (Mexico)	03/02–08/02 (5 months)	296 (1.9 / day)
Patrick <i>et al.</i>	2003	Okmok (Alaska)	13/02/97–25/03/97 (1.3 months)	14 (2.5 / week)
Rowland <i>et al.</i>	2003	Fernandina (Galapagos)	25/01/95–08/04/95 (2.4 months)	8 (3.3 / month)
Dehn <i>et al.</i>	2004	Cleveland (Alaska)	30/01/01–20/04/01 (2.6 months)	42 (3.7 / week)
Lautze <i>et al.</i>	2004	Etna (Italy)	01/01/01–09/08/01 (7.3 months)	207 (6.6 / week)
Ramsey and Dehn (a)	2004	Bezymianny (Kamchatka)	2000 (12 months)	~4380 (~12 / day)
Wright and Flynn	2004	Global (all volcanic hot spots)	2001–2002 (2 years)	Hundreds (1 / day) (a)
Wright <i>et al.</i>	2004	Erta Ale (lava lake)	2001–2003 (2 years)	~300 (1 / day) (a)
		Erebus (lava lake)	2001–2003 (2 years)	~300 (1 / day) (a)
		Etna (lava flow)	17/07/01–07/08/01 (21 days)	21 (1 / day)

Table 6.8. (cont.)

Authors	Year	Target volcano	Period: date range (duration)	Number of images (data points per unit time)
		Stromboli (lava flow)	01/11/02–01/03/03 (4 months)	36 (2.1 / week)
		Popocatepetl (lava dome)	01/06/01–01/06/02 (1 year)	110 (2.1 / week)
		Colima (lava dome)	01/01/02–01/06/02 (5 months)	36 (1.7 / week)
		Montserrat (lava dome)	01/09/00–01/01/03 (2.3 years)	108 (3.8 / month)
		Shiveluch (lava dome)	01/09/00–01/01/03 (2.3 years)	~200 (7.1 / month)
		Karymsky (lava dome)	01/01/02–01/01/03 (1 year)	125 (10.4 / month)
Calvari <i>et al.</i>	2005	Stromboli (Italy)	28/12/02–22/07/03 (6.8 months)	25 (3.7 / month)
Patrick <i>et al.</i>	2005a	Okmok (Alaska)	24/03/97–02/11/07 (5.3 months)	18 (3.4 / month)
Patrick <i>et al.</i>	2005b	Mts. Belinda & Micheal <sup>2</sup>	01/10/01–01/05/04 (2.6 years) 06/01–06/03 (2 years)	71 (2.3 / month) 13 (6.5 / year)
Ripepe <i>et al.</i>	2005a,b	Stromboli (Italy)	01/12/02–01/11/03 (11 months)	25 (2.3 / month)
Rothery <i>et al.</i>	2005	Melanesia	01/01 – 03/03 (2.2 years)	Hundreds (1 / day) (a)
Wright <i>et al.</i>	2005	Anatahan (Mariana Islands)	01/04/04–30/06/04 (3 months)	19 (1.5 / week)
		(3) Time series using GOES-class data		
Harris <i>et al.</i>	1997c	Kilauea (Hawaii)	30–31 January 1997 (22 hours)	76 (83 / day)
Harris and Thornber	1999	Kilauea (Hawaii)	19/06/97–24/08/97 (71 days)	3987 (56 / day)
Harris <i>et al.</i> (a)	2000a	Kilauea (Hawaii)	July 1998 (31 days)	2976 (96 / day)
		Popocatepetl (Mexico)	May–December 1998 (8 months)	23 040 (96 / day)
		Colima (Mexico)	Nov–Dec 1998 (8 months)	23 040 (96 / day)
Mouginis-Mark <i>et al.</i>	2000b	Cerro Azul (Galapagos)	15/09/98–21/10/98 (36 days)	851 (23.6 / day)
Harris <i>et al.</i> (a)	2001	Kilauea (Hawaii)	1997 (12 months)	34 944 (96 / day)
Harris <i>et al.</i> (a)	2002a,b	Kilauea (Hawaii)	7–8 November 1999 (24 hours)	96 (96 / day)
		Cerro Negro (Nicaragua)	5–6 August 1999 (48 hours)	192 (96 / day)

		Pacaya (Guatemala)	23/12/99–24/01/00 (32 days)	3072 (96 / day)
		Lascar (Chile)	29/06/98–08/03/99 (252 days)	24 192 (96 / day)
Wright <i>et al.</i> (a)	2002b	Popocatepetl (Mexico)	01/09/98–01/02/99 (153 days)	14 688 (96 / day)
Ortiz <i>et al.</i> (a)	2003	Villarrica (Chile)	19/10/00–11/11/00 (23 days)	3519 (96 / day)
Calder <i>et al.</i>	2004	Villarrica (Chile)	1999 (12 months)	34 944 (96 / day)

\* This count is actually for the number of days on which a hot spot was observed in an AVHRR image, and is not the total number of images.

**Note.** Most image counts include just those useable (cloud-free) images available during each study period. Those marked (a) include all available images during the time period (cloud-covered and cloud-free) and hence yield a higher image count, being simply the number of satellite overpasses (passes per day) multiplied by duration of the data set (in days). The former count gives a better feel for the true temporal resolution that can be expected from a time series extracted for a volcanic hot spot using each class of data.

<sup>1</sup>18 volcanoes with hot spots.

<sup>2</sup>South Sandwich Islands.

### 6.5.1 Time series analysis using TM-class data

Although TM data were used to generate the first satellite-based IR time series study of an extrusive volcanic eruption (see [Table 6.7](#)), time series studies using TM data suffer from the poor frequency of data acquisition. TM data are of high spatial resolution (30 m pixels), but are only available once every 16 days, and only a few cloud-free scenes may be available per year. In the case of Santiaguito (Guatemala), just 18 cloud-free images were available over a 12.2 year period spanning 1986 to 1999. It is similarly difficult to obtain entirely cloud-free data at Kilauea. Note that even the *cloud-free* TM image given for Kilauea in [Figure 6.2](#) contains localized cloud, some over the active lava hot spot in which we are interested. This is one of only two *cloud-free* TM images obtained for Kilauea during the 1990s. However, those time series that have been derived from TM and ETM+ data have been shown capable of revealing thermal trends developing over weeks to months.

#### 6.5.1.1 TM-derived time series for Lascar's lava dome

The Chilean volcano of Lascar provided the location for the first demonstration of how a thermal time series could be constructed for, and related to, activity at a volcanic system using satellite IR data. Glaze *et al.* (1989) published a radiation flux time series for Lascar comprising ten data points spanning 1984–1987, each obtained from a Landsat-TM image. The time series, as given in [Figure 6.15a](#), revealed a decline in energy flux prior to the 16 September 1989 explosive eruption of Lascar, followed by a recovery to the pre-explosion levels. Oppenheimer *et al.* (1993a) added data from five new TM images to the time series, extending it to 1992, plotting instead spectral radiance. This time series, given in [Figure 6.15b](#), revealed a second cycle of activity which, like the first, was terminated by an explosive eruption, on 20 February 1990. These cycles were inferred to be the result of cyclic lava dome extrusion and cooling, culminating in an explosive eruption. The time series was brought to conclusion by Wooster and Rothery (1997a), who added data from a further TM image and 64 ATSR images, thereby extending the time series through 1995 and identifying a third cycle, which again ended in a major explosive eruption, in April 1993 ([Figure 6.15c](#)). In a companion paper, Matthews *et al.* (1997) provided the working model whereby the cycles identified in the spectral radiance time series could be related to dome growth followed by degassing and devolatilization to cause the dome to subside into the conduit. In the period of extrusion, satellite-measured radiance levels would be high, followed by a decline during subsidence. Blocking of the conduit by the subsiding dome, and a decline in the shallow system permeability, would inhibit degassing, cause pressurization, and result in a vulcanian explosion, thereby terminating the extrusion–subsidence cycle. Extrusion and recovery of the satellite-measured radiance would herald the onset of the next cycle. The end point to this study sequence was a 252-image time series of ATSR-derived spectral radiance spanning from 1995 to September 2000 by Wooster (2001), with Aguilera (2004) adding data from a further two ETM+ images acquired in February 2000 and October 2001.

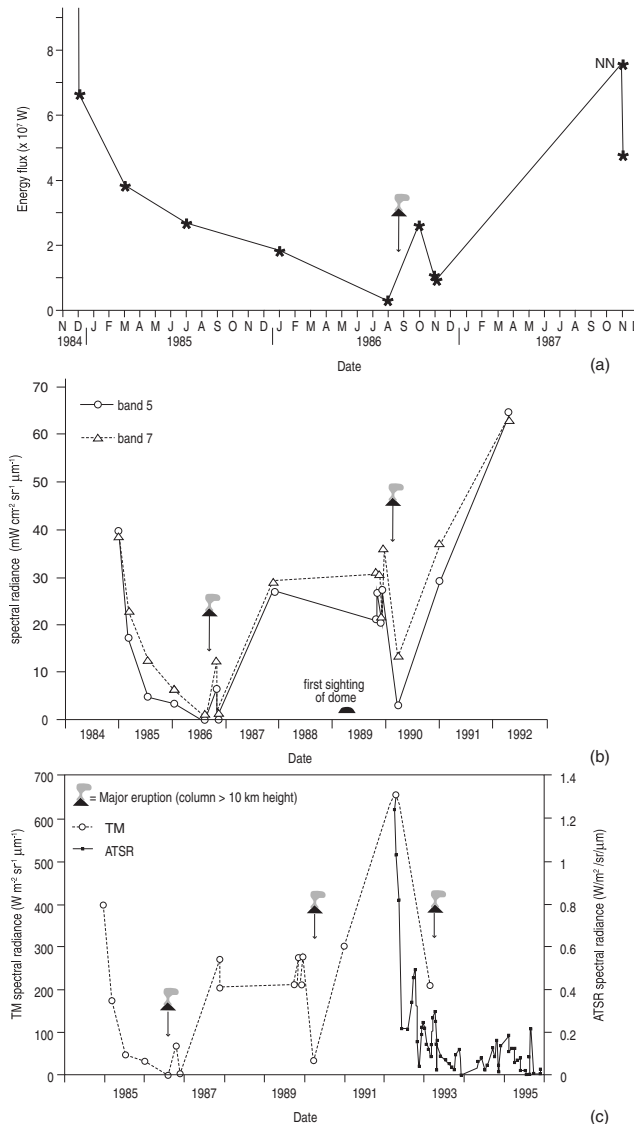


Figure 6.15 a) TM-derived heat flux time series derived by Glaze *et al.* (1989) for Lascar's lava dome for the period 1984 through 1987, showing decline prior to an explosive event, and recovery thereafter [Glaze *et al.* (1989, Fig. 2); reprinted by permission from Macmillan Publishers Ltd]. (b) Same time series expressed as TM bands 5 and 7 radiance and extended through the beginning of 1992 by Oppenheimer *et al.* (1993a) showing further cycles of radiance decay, explosion and recovery [Oppenheimer *et al.* (1993a, Fig. 18); reproduced by permission of American Geophysical Union]. (c) Time series updated to 1995 by Wooster *et al.* (1997) using TM and ATSR spectral radiance data collected in the SWIR (at  $1.6 \mu\text{m}$ ) [from Wooster *et al.* (1997, Fig. 1); with kind permission from Springer Science and Business Media].

### 6.5.1.2 Other dome studies

Subsequently, five other studies have used high-spatial-resolution TM data to produce time series capable of tracking activity cycles at active lava domes. Kaneko and Wooster (1999) used eight Landsat TM images to track the spectral radiance for, and area of fumarolic activity at, Unzen's lava dome during extrusion between 1991 and 1992. Their results showed a declining trend in TM-derived spectral radiance and fumarolic area that mimicked the field-measured trend in extrusion rate. Urai (2000) extended the time series to cover the period 1990–1994 using 23 TM images. The time series showed the variation in area of thermal emission at Unzen's activity during 1989–1995, with changes in the area again correlating with changes in field-measured extrusion rate. In the same year, Wooster *et al.* (2000) used three images from within the same time series to map changes in activity location and style between December 1991 and November 1992. Kaneko *et al.* (2002b) later used ten TM images from the 1989–1995 TM data set for Unzen (spanning October 1991 to January 1993) to track shifts between exogenous and endogenous dome growth styles during extrusion. For the lava dome and associated silicic lava flow activity at Santiaguito, Harris *et al.* (2003a) used 18 TM and ETM+ images during 1987–2000 to produce time series of lava area, time-averaged discharge rate and cumulative volume. This was used to extend the record of cyclic extrusion, documented by Rose (1987) for 1922–1980, through 2000, thereby identifying an eighth cycle of extrusive activity during the 80-year-long extrusive eruption.

### 6.5.1.3 Lava lakes

For Erta Ale's lava lake, Oppenheimer and Francis (1997) used two MSS images, acquired during 1972 and 1973, and ten TM images, acquired during 1984–1986, to track an otherwise undocumented period in the lava lake's history. Activity was recorded using radiative heat flux time series derived from the TM portion of the time series, as well as lake level estimates obtained using shadow data obtained from Landsat TM and SPOT data (Landsat MSS data were of insufficient spatial resolution to allow measurements of crater shadow). The same data were used in a paper of the following year by the same authors (Oppenheimer and Francis, 1998) to suggest that the sustained heat fluxes at Erta Ale's lava lake of 100–400 MW, in concert with minimal surface growth rates (the rate of emplacement of lava onto the surface of the edifice being  $10 \text{ kg s}^{-1}$  time-averaged over the period 1968–1995), implied edifice growth by injection of magma (as dykes and sills) into the underlying crust. This supported the model of Francis *et al.* (1993) whereby at non-eruptive, but degassing systems, the following process operates. Fresh, gas-rich magma ascends the conduit, to lose heat, degas and crystallize near (or at) the surface. This dense material then sinks to become emplaced at depth, following the density-driven conduit convection model of Kazahaya *et al.* (1994). As a result, such systems account for their degassed and cooled magma masses by endogenous growth, i.e., intrusion of degassed, crystallized magma within the volcanic edifice or underlying basement (e.g., Allard *et al.*, 1994; Allard, 1997). Thus, Oppenheimer and Francis (1997) showed how satellite-based IR time series could be used to identify, and parameterize, the style and rate of edifice growth during such styles of activity when heat losses are high, but extruded lava mass fluxes are close to zero.

#### 6.5.1.4 Lava flows (*basaltic, clastogenic and silicic*)

For lava flow activity, Wright *et al.* (2000) used seven DEM-draped Landsat TM images acquired before, during, and after Etna's 1991–1993 eruption to show how variations in the style and location of effusive activity could be visualized. The time series charted a progression from channel- to tube-fed activity by virtue of characteristic spatial distributions of high- and low-radiance areas, as revealed by the mapped spectral radiances. Kaneko and Wooster (2005) used a series of ten TM images acquired after an effusive eruption at Izu-Oshima in which the cooling, but still hot, and recently emplaced lava units could be identified from thermal anomalies in TM bands 6 and 7. This allowed production of a band 6 (TIR) brightness temperature time series to aid in understanding the emplacement and cooling mechanisms of two fountain-fed, clastogenic lava flows at Izu-Oshima.

Harris *et al.* (2004) used three ETM+ scenes to document the evolution of the channel-fed, silicic, lava flow field active at Santiaguito between 1999 and 2002. The TIR data were used to obtain extrusion rates ( $0.5\text{--}1.6 \text{ m}^3 \text{ s}^{-1}$ ) as the flow extended to 3.85 km, at velocities of just  $2\text{--}13 \text{ m day}^{-1}$ , over the three-year period. However, the 15-m spatial resolution data available from the ETM+ panchromatic (VIS) band were the backbone of the study, where these data were used to map flow dimensions and thicknesses ETM+ (from shadow data) for the three snap shots provided by each of the images. Channel widths, for this high viscosity ( $10^9\text{--}10^{10} \text{ Pa s}$ ) and perfectly formed channel-fed silicic lava flow system, were recorded at 45–375 m, with levee heights being up to 120 m.

#### 6.5.1.5 Lava flow field emplacement time series from a single image

Wright *et al.* (2001) used a single ETM+ image containing active and cooling lava flow units, emplaced during Etna's 1999 Bocca Nuova eruption, to show how a single image could be used to infer the time evolution of a complex emplacement event involving multiple lava flow units emplaced sequentially over several hours. Even though only one image was used (as given in Figure S1.7 of Electronic Supplement 1), this was a time series study because it used the thermal data from the single image to extract time series data and make temporal inferences.

Surfaces for lava flows emplaced at different times will have undergone different amounts of cooling, so that they will have different surface temperatures and levels of radiant emission depending on their age. The oldest flow will likely have the coolest surface temperature, and the most recent (or currently active) flow the hottest. Thus, for an effusive eruption where a sequence of lava flow units are emplaced over a few hours, the difference in surface temperature between each unit apparent in the image can be used to reconstruct the sequence of events that constructed the flow field. In effect we can use the spectral radiance data for each unit to create a time series for areal expansion of the flow.

The surface temperature of each unit can be used to assign each unit an age (in terms of hours since initial surface exposure) following the empirical relation of Hon *et al.* (1994a,b).

This, as given in Equation (4.32a) of Chapter 4, can be rearranged so that time ( $t$  in hours) since exposure can be obtained from the surface temperature ( $T$ ) following:

$$t = 10^{\left(\frac{T-303}{-140}\right)}. \quad (6.4)$$

This method was applied by Harris *et al.* (1998) to estimate flow areas emplaced over discrete time periods spanning the 30 hours previous to image acquisition using two TM images containing active pahoehoe at Kilauea. The method was applied as follows:

- (i) apply the dual-band method of Flynn *et al.* (1994) to estimate a lava surface temperature for each pixel (see Electronic Supplement 6 for method);
- (ii) convert the surface temperature to an age using Equation (6.4);
- (iii) count the number of pixels with an age less than or equal to a given age threshold to obtain the total area of lava emplaced over each time period.

The results, as given in Table 6.9, allowed five temporal data points to be extracted from the single image, giving a proxy for the rate at which the lava flow field expanded during the 30 hours prior to image acquisition.

*Table 6.9. Mean surface temperature and pixel area to which that average applies for two TM images of Kilauea containing active pahoehoe. Temperatures are converted to a time required for a pahoehoe surface to cool to that temperature following Equation (6.4). Areas are obtained by multiplying the number of pixels by pixel area (900 m<sup>2</sup>), and expansion rate is given in terms of the number of pixels covered per minute.*

Temperature (°C)	Age (hours)	Pixels (no.)	Area (m <sup>2</sup> )	Area (km <sup>2</sup> )	Expansion rate (pixels min <sup>-1</sup> )
<b>TM Image: 23 July 1991</b>					
97	29.6	10885	9.80E+06	9.796	6
198	5.6	1641	1.48E+06	1.477	5
266	1.8	1241	1.12E+06	1.117	11
392	0.2	103	9.23E+04	0.092	7
425	0.1	13	1.17E+04	0.012	2
<b>TM Image: 11 October 1991</b>					
114	22.4	6907	6.22E+06	6.216	5
193	6.1	2347	2.11E+06	2.112	6
248	2.5	1421	1278 450	1.278	10
385	0.3	64	57 600	0.058	4
425	0.1	1	900	0.001	0.1

Note that area estimates are cumulative, because the flow area emplaced within the last 0.2 hours also includes that emplaced within the last 0.1 hours. Likewise, the flow area emplaced within the last 1.8 hours includes that emplaced within the last 0.2 hours . . . . and so on. Thus, areas emplaced within a given time period can be obtained by subtracting one area from another, so that the area emplaced between 0.1 and 0.2 hours is 0.092 km<sup>2</sup> minus 0.012 km<sup>2</sup> = 0.08 km<sup>2</sup>.

We note that, in this case, areas have been obtained simply by multiplying pixel area by the number of pixels with a pixel-integrated temperature equal to, or greater than, each temperature, or time, threshold. This will likely result in an over-estimate of actual lava area. Simply, the active lava likely occupies a fraction of the pixel, when the whole of each pixel has been considered lava filled. Thus, area estimates are a maximum possible. Dividing each area estimate by the time over which the area was emplaced could provide a lava coverage or areal expansion rate. However, the results appear unrealistically large:  $\sim 100 \text{ m}^2$  per second (!), when  $10\text{--}40 \text{ m}^2$  per minute is likely more typical for spreading pahoehoe pads fed at  $\sim 0.5 \text{ m}^3 \text{ s}^{-1}$  at Kilauea (Harris *et al.*, 2007). This confirms that lava inundation areas obtained from simple pixel-counting methods are hugely over-estimated. Thus, in this case, I prefer to give the coverage rate in terms of pixels per minute, suggesting that lava may spread into, but not necessarily fill, a given number of pixels per unit time, as entered in the final column of Table 6.9.

In the case of Wright *et al.* (2001) three lava flow units were identified. Unit B was the coolest and oldest, was only radiant in band 7, had surface temperatures in the range 120–180 °C, and had a calculated age of 8–20 hours. Unit A was warmer and younger, but was still only radiant in band 7, with surface temperatures in the range 120–260 °C; it had ceased to move, having attained a distance of 4.3 km, and had a calculated age of 2–3 hours. Unit C was the hottest, being radiant in bands 4, 5 and 7, as well as in the panchromatic band of ETM+, and covered the proximal sections of A and B. It was therefore interpreted as a channel-fed flow active at the time of image capture (see Electronic Supplement 1).

#### 6.5.1.6 ASTER

ASTER is a TM-class sensor with a temporal resolution of up to 2–7 days – if operated in pointable mode. Otherwise, the nominal temporal resolution is 16 days at the Equator, decreasing polewards (see Chapter 3 and Appendix C). Thus, ASTER promises time series of the typical TM-class temporal resolution, unless operated in pointable mode, in which case a temporal resolution of a few days is possible. By the time of the cut-off date for the Table 6.7 collation, only one time series study of a volcanic target had been published using ASTER data. However, since 2005 this has changed, with 11 ASTER-based time series for volcano targets being published between 2005 and 2010. These are reviewed in Table 6.10.

Ramsey and Dehn (2004) were the first to present an ASTER time series collected as part of ASTER's *rapid response* volcano targeting program. This was used to track activity at Bezymianny during 2000–2001. The time series was presented in terms of a series of maps showing evolution of the TIR hot spot at Bezymianny's lava dome, and the extent of hot pyroclastic flow deposits. Carter *et al.* (2008) also used a time series of seven ASTER images collected as part of the *rapid response* program to reveal a further eruption sequence at Bezymianny's dome. The seven images were collected between 8 October 2006 and 18 March 2007, with a further 17 having been collected in the 10 months following an explosive eruption of 11 January 2005 (Carter *et al.*, 2007).

Urai *et al.* (2007) submitted an emergency acquisition request following the April 2007 effusive eruption and crater collapse events at Piton de la Fournaise. Six images were acquired over 16 days, and used, with the 20 images that had been collected for this target

Table 6.10. Collation and review of ASTER-data-derived time series studies, as published in the mainstream literature between 2004 and 2010. Studies are listed chronologically. We note that our time series definition is a little looser here than that used for the Table 6.7 collation, in that we consider any study that uses ASTER NIR, SWIR and/or TIR data, from two or more images, to track changes in volcanic activity or morphology. The collation of Table 6.7 considers just those studies containing temporal plots of quantitative parameters as defined as comprising quantitative time series in Section 6.3. Studies not containing temporal plots of extracted parameters are marked with an asterisk.

Authors	Year	Target volcano	Period: date range (duration) (dd/mm/yy)	Number of images (data points per unit time)
Ramsey and Dehn	2004	Bezymianny (Russia)	29/04/00–11/01/01 (0.7 years)	20 (28.3 / year)
*Pieri and Abrams	2004	Chikurachki (Kuriles)	29/01/03–14/02/03 (16 days)	2 (45.5 / year)
*Carter <i>et al.</i>	2007	Bezymianny (Russia)	01/05–10/05 (0.8 years)	17 (20.4 year)
*Urai <i>et al.</i>	2007	Piton de la Fournaise (Reunion)	20/04/07–06/05/07 (16 days)	6 (137 / year)
Carter <i>et al.</i>	2008	Bezymianny (Russia)	8/10/06 – 18/03/07 (0.4 years)	7 (15.8 / year)
Hirn <i>et al.</i>	2008	Kilauea (Hawaii)	01/12/00–31/12/05 (5 years)	15 (3 / year)
Vaughan <i>et al.</i>	2008	Oldoinyo Lengai (Chile)	23/1/07–9/11/07 (0.6 years)	9 (14.2 / year) <sup>a</sup>
Carter and Ramsey	2009	Bezymianny (Russia)	10/06–12/07 (1.2 years)	30 (25.6 / year)
Duda <i>et al.</i>	2009	Kliuchevskoi (Russia)	04/01/07–07/06/07 (0.4 years)	18 (42.5 / year)
*Norini <i>et al.</i>	2009	Etna (Italy)	12/08/06–14/07/07 (0.9 years)	5 (5.4 / year)
Rose and Ramsey	2009	Kliuchevskoi (Russia)	15/01/05–16/05/05 (0.3 years)	14 (42.1 year)
Carter and Ramsey	2010	Shiveluch (Russia)	19/05/01–19/01/09 (7.7 years)	27 (3.5 / year)
Wessels <i>et al.</i>	2010	Augustine (Alaska)	20/12/05–15/10/06 (0.8 years)	11 (13.4 / year)

<sup>a</sup> Only useable, cloud-free images of Vaughan *et al.*'s (2008) Table 1 are counted.

\* Study does not contain a parameter plot, and so does not fit within the time series classification of Section 6.3.

since 2000, to track the morphological changes associated with the April 2007 activity. Likewise, Norini *et al.* (2009) used five ASTER images to track morphological changes, and emplacement of new deposits, at Etna's SE Crater spanning the 16 November 2006 flank collapse at the same crater.

We note here that most of these studies until 2008 presented time series in terms of map sequences which, as reviewed in Section 6.1, can be used to draw inferences regarding temporal patterns in volcanic activity from the changes in the spatial distribution of the thermal radiance.

Carter *et al.* (2008) was one of the first studies of this group to present a time series plot, this being of SWIR- and TIR-derived maximum temperatures. With this exception, these studies were not, therefore, true quantitative time series studies as defined in this chapter, and are thus flagged as such in Table 6.10. They do, though, allow study of temporal changes and trends, while revealing the improved temporal capability of ASTER. Their inclusion also allows a complete review of ASTER-based volcano applications to date.

Vaughan *et al.* (2008) produced a true, 12-image, quantitative ASTER time series for hot spot activity associated with natrocarbonatite lava flow emplacement at Oldoinyo Lengai. The data set spanned a ~9 month time period (23 January–9 November 2007) and comprised nine cloud-free images which were used to produce a pixel-integrated temperature time series showing an increasing trend (consistent with increased effusive and explosive activity during the study period). The ASTER-derived trend supported trends observed in a higher-temporal-resolution MODIS-data-derived time series. Hirn *et al.* (2008) also combined 15 ASTER images with MODIS data to generate a time-averaged discharge rate time series for lava flows active at Kilauea between December 2005 and January 2006. The remaining quantitative ASTER time series of Table 6.10 all involved plots of brightness temperature, thus being Type I time series within our classification scheme.

- Carter and Ramsey (2009), who produced a TIR maximum brightness temperature plot for Bezymianny's lava dome spanning October 2006 to December 2007.
- Duda *et al.* (2009), who plotted maximum TIR, SWIR and NIR pixel-integrated temperatures to track activity during Kliuchevskoi's 2007 eruption.
- Rose and Ramsey (2009), who used 14 scenes collected over four months to produce time series of maximum TIR, SWIR and NIR pixel-integrated temperatures during Kliuchevskoi's 2005 eruption.
- Carter and Ramsey (2010), who plotted background ( $T_{\text{back}}$ ) and maximum ( $T_{\text{max}}$ ) TIR pixel-integrated temperatures during 7.7 years of activity at Shiveluch. Maximum temperature corrected for background, i.e., “ $T_{\text{max}}$  above background” was actually plotted. This, in effect, was a proxy for volcanic radiance.
- Wessels *et al.* (2010), who produced time series of both temperature maps and plots of pixel-integrated temperature in the SWIR and TIR (maximum, average and  $T_{\text{max}}$  above background) to track activity during Augustine's 2006 eruption.

ASTER-derived time series thus offer some improvements in the temporal resolution offered by TM-class time series. If operated in rapid response mode, time series with temporal resolutions of up to one data point every 12 hours to 3 days are possible over short, targeted

periods. However, cloud-cover still limits the number of useable data points. Pieri and Adams (2004) pointed out, for example, that cloud-free ASTER images of the volcanoes of the Kurile Islands are rare, so that their analysis involved just two cloud-free images acquired in January and February 2003 in which thermal anomalies preceding the April 2003 eruption of Chikurachki were apparent. As a result the typical temporal resolution of those ASTER time series studies published to date is typically between 1 and 4 images per month, with time series typically spanning periods of 3–11 months, so that the data are suited to tracking trends at hot spots developing over weeks. For time series of better temporal resolution we have to turn to AVHRR- and GOES-class data.

### 6.5.2 Time series analysis using AVHRR-class data

Data available at higher temporal, but lower spatial, resolution have tended to form the focus of time series construction. The more frequent the overpass the more likely that overpass is to coincide with a break in the cloud, or short period of activity. The higher-temporal-resolution capability can be especially useful if a satellite goes over once during the night and once during the day. During Guatemala's dry season, for example, cloud tends to build rapidly from 10:00 am (local time) at the Santiaguito lava dome, meaning that a 10:30 am TM or ASTER overpass will often be cloud contaminated. However, cloud typically clears during the evening, so that conditions are more likely to be clear by the 01:30 am overpass time of the MODIS flown aboard Aqua.

The temporal resolution of AVHRR-class data mean that these data have been used for tracking trends in lava area, heat flux and/or discharge rate developing over time scales of days to weeks, rather than the typical monthly time-scale of TM-class time series. The results have, in turn, been applied to track and assess changes in system dynamics, levels of activity and lava flow emplacement evolving over the same time scales, i.e., days to months. We review these AVHRR-class time series studies chronologically.

#### 6.5.2.1 Year: 1997

This was a big year for AVHRR-class time series studies. It did not just witness the first publication of an AVHRR-class time series, but six of them. These spanned time series for tracking the evolution of lava flow fields, domes and open vents.

For tracking the time evolution of active lava flow fields, Harris *et al.* (1997a) used AVHRR data to produce time series of active lava area, heat flux, *TADR* (i.e. time-averaged discharge rate or volume flux), and cumulative volume from 308 images acquired during Etna's 1991–1993 eruption. The *TADR* time series, as given here in Figure 6.16, was used to identify trends in volumetric output developing over a few days and to argue that the eruption was fed by a pressurized source, resulting in the characteristic discharge trend described by Wadge (1981) for eruptions fed by such a source. That is, the eruption began with a short waxing phase during which *TADR* climbed to an initial peak over a few days. This was followed by a longer phase, spanning weeks to months, during which *TADR* slowly

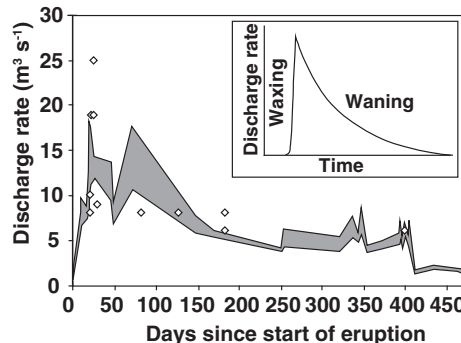


Figure 6.16 Time series of AVHRR-derived lava discharge rate ( $TADR$ ) during Etna's 1991–1993 eruption. Gray zone marks range of AVHRR-based estimate, and diamonds give field-based measurements for comparison. Inset is the hypothetical discharge trend expected for effusive eruptions from a pressurized source [from Harris *et al.* (1997a, Fig. 9a): Reproduced by permission of American Geophysical Union].

declined, as the source was increasingly depressurized, to reach a steady, lower level by the summer of 1992. Wooster *et al.* (1997) followed up with an energy balance inventory for the same eruption, generated from 29 cloud-free ATSR images. This not only covered the duration of the eruption, but also the first two months of flow field cooling in April and May 1993.

Wooster and Rothery (1997b) also examined the thermal evolution of the lava flow field emplaced during Fernandina's 1995 eruption using eight cloud-free ATSR images. Plots for total crusted lava flow area, as well as the fraction of that area comprising hot cracks, were generated. Both plots suggested steadily waning levels of effusive activity, with the area of crusted lava showing a steady decline, and the area of exposed core showing logarithmic decay with time. Harris *et al.* (1997c) also produced time series plots of active lava area, heat flux,  $TADR$  and cumulative volume for effusive eruptions at Etna and Cerro Negro, with Wooster and Rothery (1997a) presenting the ATSR-based plot of spectral radiance for Lascar's lava dome, spanning 1991–1995, already detailed as part of Section 6.5.1.1 and given in Figure 6.15c. Finally, Harris and Stevenson (1997a) produced AVHRR-derived volcanic radiance and heat flux time series to document changes in activity (i) at Stromboli during a period of normal explosive and open vent degassing activity spanning 1990–1994, (ii) before, during and after Stromboli's effusive eruption of 1985–1986, and (iii) for fumarolic activity at Vulcano during 1985–1994.

#### 6.5.2.2 Two years: 1998–1999

These two years saw further AVHRR-class time series developed for tracking activity at active lava domes, as well as lava lakes. Dean *et al.* (1998), for example, used more than 300 AVHRR images to track the increase in thermal anomaly size related to emplacement of a lava flow field at Okmok during 1997.

For lava domes, Wooster and Kaneko (1998) used 31 cloud-free ATSR images (from a total archive of 159 images obtained between January 1992 and July 1994), to plot time series of summed 1.6  $\mu\text{m}$  spectral radiance, 11  $\mu\text{m}$  brightness temperature and background corrected 11  $\mu\text{m}$  brightness temperature (a proxy for volcanic radiance) for Unzen's lava dome. These plots showed how variations in thermal flux from the dome, during its 1992–1994 growth, could be related to variations in the extrusion rate and gas flux. In addition, Wooster *et al.* (1998b) used an ATSR-derived spectral radiance time series, comprising five data points obtained over two months, to show a generally declining trend in radiance at Galeras' newly extruded lava dome.

In the following year, Harris *et al.* (1999) used seven AVHRR images obtained in January, February and November of 1980 to estimate the sub-pixel lava lake area at Erebus. Converging orbits towards the Poles and cloud-free conditions meant that five images were available on 12 and 13 January 1980 alone. This short time series contributed to a longer, integrated time series of TM and ground-reported data to track a decline in activity at the lake during 1980–1990.

#### 6.5.2.3 Year: 2000

By 2000, AVHRR-class time series had thus been produced for most feature types (lava flows, domes, lakes and vents) using most derivable parameter types (i.e., time series of level I, II and III parameters had all been generated). This can be seen by glancing down columns four and five of Table 6.7. Attention now turned to producing time series using data sets of increased temporal resolution and duration, and on further expanding our library of time series case studies for volcanic hot spots.

- Dehn *et al.* (2000) used three year-long AVHRR data sets, with a temporal resolution of ~12 images per day, to produce AVHRR band 3 (MIR) brightness temperature time series for volcanoes undergoing (i) dome collapse and plinian explosive events (at Bezymianny), (ii) intermittent strombolian activity (at Karymsky) and (iii) lava flow activity (at Okmok) (as reproduced here in Chapter 5: Figure 5.12).
- Carn and Oppenheimer (2000) used a 690-image AVHRR data set to complete a thorough inventory of volcanic activity across the Indonesian island arc between 1996 and 1997, producing hot spot inventories, activity calendars and  $\Delta T$  time series for 18 volcanoes at which hot spots were found.
- Harris *et al.* (2000b) used 218 AVHRR, plus 27 ATSR images and six TM images, to produce *TADR* and cumulative volume time series for eight effusive eruptions at Etna, two at Krafla, and one at Stromboli during the period 1980–1999. These time series were used to define effusive eruptions fed by pressurized and depressurized (open vent) sources.
- Schneider *et al.* (2000) considered AVHRR time series for a single eruption, producing a brightness temperature time series from 26 AVHRR images to show how hot spot temperature varied before and during the December 1997 explosive eruption of Bezymianny. The maximum band 3 (MIR) brightness temperature was plotted, with an

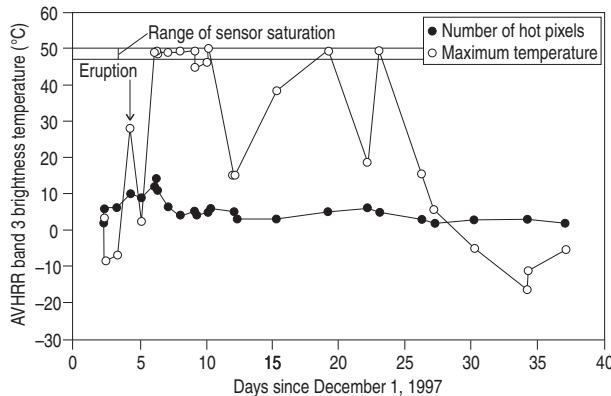


Figure 6.17 Time series for number of anomalous pixels and maximum brightness temperature recorded in AVHRR MIR (band 3) data during eruptive activity at Bezymianny in December 1997 [from Schneider *et al.* (2000, Fig. 6): reproduced by permission of American Geophysical Union].

initial spike marked “eruption” in Figure 6.17 recording the emplacement of hot pyroclastic deposits erupted during a 4 December explosive event. This was followed by a series of saturated values that marked a subsequent phase of dome extrusion until 25 December, after which time the intensity of the anomaly declined, with saturated values no longer being recorded.

#### 6.5.2.4 Year: 2001

Five papers were published in 2001 presenting AVHRR-class time series. That of Lachlan-Cope *et al.* (2001) involved the examination of more than 5000 AVHRR images to discover a previously unknown lava lake at Saunders Island (South Sandwich Islands). Lachlan-Cope *et al.*’s use of a time series for the lava lake area to track variations in its activity during 1995–1998 was a nice example of how satellite thermal data can be used to track activity in remote, unmonitored regions. Later, Patrick *et al.* (2005b) used a MODIS time series, along with ASTER and ETM+ data, to extend the analysis of the lava lake activity at Saunders Island. In addition, Patrick *et al.* (2005b) produced radiative heat flux time series to record the development of an effusive eruption at the neighboring South Sandwich Island volcano of Mt. Belinda during 2001–2004.

Also in 2001, Roach *et al.* (2001) published the results of using AVHRR hot spot time series, along with AVHRR-derived ash plume parameters and ground-based seismicity, to track Pavlof’s 1996 eruption, as reviewed in Chapter 1. The chronology of the eruption derived from the time series is given in Table 1.5, and plotted here in Figure 6.18 in terms of the number of hot pixels recorded. The increasing size of the thermal anomaly through 18 October was presumably due to increasingly large areas of hot pyroclastic flow deposit being emplaced during each successive (plume producing) explosive event. Rothery *et al.* (2001) also published a time series of total radiance in ATSR’s 1.6  $\mu\text{m}$

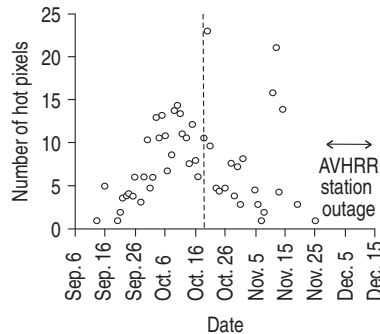


Figure 6.18 Time series for number of anomalous pixels recorded in AVHRR MIR (band 3) data during eruptive activity at Pavlov in 1996 [from Roach *et al.* (2001, Fig. 8): with kind permission from Springer Science and Business Media].

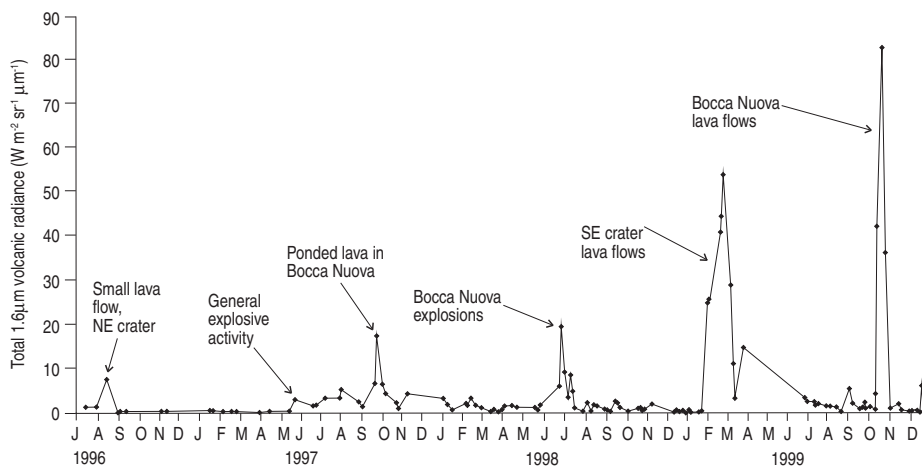


Figure 6.19 Time series of total volcanic radiance in ATSR's 1.6  $\mu\text{m}$  band recorded for Etna between 1996 and 1999 [from Rothery *et al.* (2001, Fig. 6): with kind permission from Springer Science and Business Media].

band recorded for Etna using ~120 images obtained during 1996 to 1999. This time series is reproduced here in Figure 6.19 and shows how six peaks in summed spectral radiance related to periods of explosive activity, lava flow and lava pond activity, providing a record of Etna's activity during these four years. Finally, Aries *et al.* (2001) used a time series analysis of volcanic radiances spanning a few days to two years, and straddling the termination of seven effusive eruptions at Etna and Krafla, to determine whether, and how, such time series could be used to set a stop date/time for effusive activity, as detailed in Section 5.4 of Chapter 5 (see Figure 5.17).

#### 6.5.2.5 Four years: 2002–2005

Between 2002 and 2005 a further 19 studies were published containing time series derived from AVHRR-class data (see [Table 6.7](#)). The main trend at this point was the increasing incidence of time series studies using MODIS data. Again, time series were generated from tens, hundreds, or even thousands of images. However, the global detection capability of the MODVOLC system (as detailed in Section 5.6.0.2 of Chapter 5) meant that time series could be generated for single eruptions, multiple eruptions at different volcanoes, all eruptions over entire regions, or for all volcanic hot spots across the globe. For example, while Wright *et al.* ([2005](#)) used 23 MODVOLC hot spot detections to produce a chronology of the May–June 2003 Anatahan eruption, Wright *et al.* ([2004](#)) produced time series for lava lake, flow and dome activity at nine different volcanoes. At a regional scale, Rothery *et al.* ([2005](#)) used MODVOLC-derived time series to produce an inventory of volcanic hot spot activity across Melanesia during 2001–2003, and at a global scale Wright and Flynn ([2004](#)) produced a time series for total heat flux from all volcanic hot spots detected by MODVOLC during 2001 and 2002.

#### 6.5.2.6 Thermal precursors to explosive activity, and explosive activity

Dehn *et al.* ([2002](#)) showed how a number of time series types could be combined to monitor explosive activity, and precursors to that activity. Using AVHRR data acquired during Shishaldin's 1999 eruption, Dehn *et al.* ([2002](#)) began with a time series plot of AVHRR brightness temperature, as given in [Figure 6.20a](#). Dehn *et al.* ([2002](#)) argued that the spiky appearance of this plot was due to intermittent strombolian eruptions, each eruption causing a short-lived hot spot associated with the emplacement of hot spatter on the snow around the vent. This activity culminated in a large sub-plinian eruption, during which emplacement of extensive, hot, pyroclastic deposits led to a longer-term (flat-topped, saturated) spike at the end of the time series. Dehn *et al.* ([2002](#)) argued that an increase in brightness temperature prior to the sub-plinian event was the result of increasing magma levels in the conduit. Assuming a constant conduit area, which was set equal to the sub-pixel hot spot area, this allowed the sub-pixel temperature of the volcanic hot source to be estimated. This, as plotted in [Figure 6.20b](#), steadily increased to attain impossible levels, i.e., temperatures were higher than magmatic temperatures, during 13–24 March. At this point it was argued that the stable anomaly assumption had failed, a result of hot tephra sheets now being emplaced around the vent so that the sub-pixel hot spot was now also increasing in area. This was supported by a coincident increase in the pixel area of the anomaly ([Figure 6.20c](#)) and a peak in the hot spot radiative flux ([Figure 6.20d](#)). All trends were argued to be a precursory ramp to the sub-plinian event of 19 April.

#### 6.5.3 Time series analysis using GOES-class data

Very-high-temporal-resolution data, such as are available every 15 minutes from GOES, can increase the detail of satellite-derived time series from days (as in the cases reviewed above for AVHRR-class data) to minutes. To illustrate this capability, Harris *et al.* ([1997b](#))

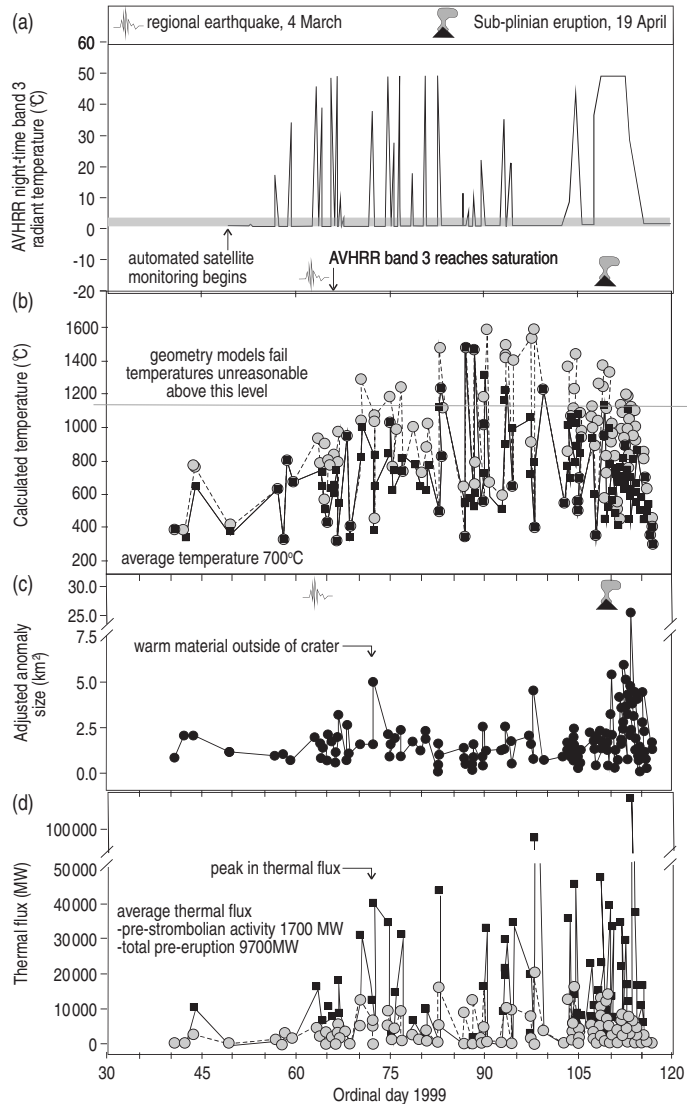


Figure 6.20 Time series of (a) AVHRR MIR (band 3) brightness temperature, (b) dual-band-derived sub-pixel hot spot temperature, (c) anomaly size (given in terms of total pixel area adjusted for scan-angle variation in pixel size) and (d) thermal flux during eruptive activity at Shishaldin in 1999. In (b), the dual-band method is solved for a two-component model that estimates hot spot temperature using background temperature (obtained from adjacent non-hot-spot pixels) and assuming that the hot spot (i) has the same area as the conduit (vent) area (gray circles), or (ii) has the same area as the conduit area plus 20% to take into account warm material thrown out of the vent (black circles). These end-member solutions are converted to end-member thermal fluxes in (d). Spiky appearance of (a) is thought to be indicative of intermittent strombolian activity that emplaced sheets of hot tephra on the surrounding snow pack [from Dehn *et al.* (2002, Figs. 4 & 5); with kind permission from Springer Science and Business Media].

Table 6.11. Start and stop times for fissure segments active during Kilauea's Episode 54 eruption at Napau crater; all times are in Hawaiian Standard Time (hhmm) and are for 30 January 1997, unless otherwise noted. Following the eruption there was a hiatus in activity that lasted until 24 February 1997. The timing for the return of lava to Pu'u 'O'o on that day is also given, as recorded by the appearance of a new hot spot in GOES data. Start times recorded from the ground for fissure A are from reports from campers spending the night at the Napau camp ground. Hawaiian Volcano Observatory field crew did not arrive until later, so that timings for the onset of activity at segments B and C can only be estimated at sometime after 0240. Ranges for GOES-based start times are obtained from the time of pixel acquisition (see [Chapter 3](#)) for the image preceding any increase in the hot spot radiance (lower bound) and the first image in which enhanced radiance was recorded (upper bound). The reverse is true for the stop time ranges. This gives an onset time spanning of 15 minutes and which typically straddles the ground-based time. GOES-derived stop times typically lag ground-based stop times by 15–30 minutes, probably due to the time needed for lava flows to cease moving and begin to cool, so as to register the crash in the GOES radiance time series that we use to define the termination of effusion (see [Section 5.4](#) of Chapter 5). The ground-based timing of the activity onset at Pu'u 'O'o is from the first helicopter over flight of the day, during which time lava was already present within Pu'u 'O'o. The GOES timing puts the arrival of the new lava at almost an hour earlier [from Harris et al., (1997b): reproduced by permission of American Geophysical Union].

Fissure	Ground		GOES	
	Start	Stop	Start	Stop
A	0240	0530	0228–0243	0713–0728
B	>0240	0716	0258–0313	0713–0728
C	>0240	0630	0258–0313	0713–0728
D	1239	1450	1158–1228	1513–1528
E	1639	1840	1628–1643	1858–1913
F	2043	0033 (31/01/97)	2028–2043	2328–0033
Pu'u 'O'o	0740 (24/02/97)		0643–0658	

examined the January 1997 eruption at Kilauea's Napau crater. The eruption lasted just under 22 hours during which time the activity was apparent from hot spots in 76 consecutive GOES images. From the variation in hot spot radiance, as given in [Figure 5.14](#) of [Chapter 5](#), it was possible to determine the start and stop times for activity at each of the six fissure segments that were active during the short eruption (see [Section 5.4.0.1](#) of [Chapter 5](#) for discussion regarding identification of effusion start and stop times using such plots). The start and stop times for effusive activity at each fissure segment could thereby be timed to plus or minus 7.5 minutes, as given in [Table 6.11](#).

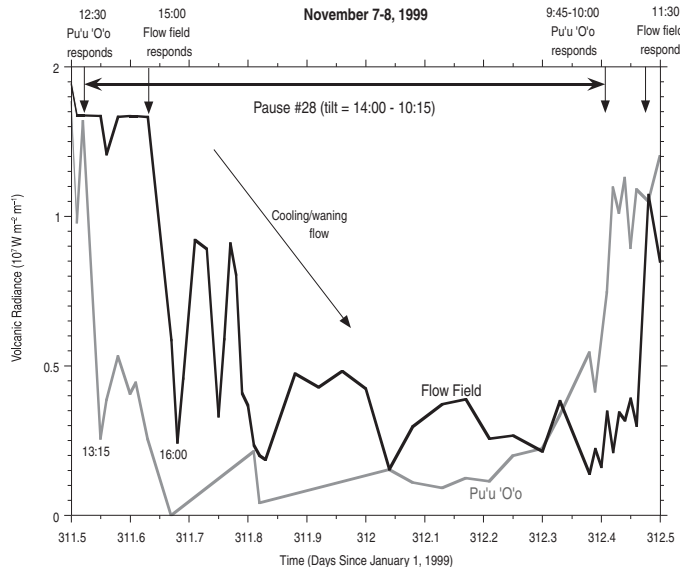


Figure 6.21 Time series of GOES MIR (band 2) volcanic radiance for the vent (Pu'u 'O'o) sector of the hot spot (gray line) and flow field (black line), showing a lagged response in the flow field trend. This is due to the time needed to drain, and then refill, the tube systems linking the vent with the flow field during a pause in supply.

Harris and Thornber (1999) further explored the temporal detail that can be obtained from very-high-temporal-resolution GOES-class data by comparing thermal time series obtained from 3987 GOES images acquired for Kilauea's Pu'u 'O'o vent between 19 June and 24 August 1997 with remote video camera data. A complex and detailed event chronology was generated, within which almost every peak and trough in the GOES-derived time series could be related to an actual event on the ground. An example of how such temporal detail allows complex effusive events to be tracked and documented at a sub-hour scale is given in Figure 6.21. The plot gives a MIR volcanic radiance time series for Kilauea during 7–8 November 1999. The hot spot has been divided into a northern sector, containing the Pu'u 'O'o vent, and a southern flow field sector which contained active lava flows fed by a 2–3 km-long tube extending southeast from Pu'u 'O'o. The time period covered by the time series spanned a pause in supply from the summit magma chamber to Pu'u 'O'o. Based on tilt records maintained by the Hawaiian Volcano Observatory, the pause began at around 14:00 (all times are local) on 7 November and ended at ~10:15 the following day. The Pu'u 'O'o (vent) sector of the hot spot responded to the pause first, the radiant intensity of the hot spot at Pu'u 'O'o crashing between 12:30 and 13:15, 45 minutes before the tilt began to change. This was followed 2.75 hours later by a crash in the radiance recorded for the flow field sector. This is consistent with the time needed to drain the tube system feeding the surface lava flow activity, so that the pause at

Pu'u 'O'o was followed by a pause at the active lava flows it fed. The termination of the pause is apparent from an increase in radiance first at Pu'u 'O'o and then, ~1.5 hours later, at the flow field. Again, this is consistent with a delay as lava enters and flows down the tube system to break out as surface flows 2–3 km from the vent area.

As we can see from the collation in [Table 6.8](#), GOES-based time series can potentially draw on information from thousands, even tens of thousands, of images. This means that not only can detailed time series be built for short events lasting just a few hours or days, but it also increases the chances of the image acquisition coinciding with cloud-free conditions. Thus if, for example, the maximum radiance from any day is plotted (i.e., the maximum volcanic radiance recorded for the hot spots in each of the 96 images collected over each 24-hour period), it can provide a reliable time series of volcanic radiance, the assumption being that the maximum value represents the least cloud-contaminated measure in any 24-hour period. In such a plot trends developing over time scales of days, weeks and months can be used to monitor and track the level, extent and style of effusive activity, and to identify any activity changes.

Such a plot is given in [Figure 6.22](#) and shows how the levels of, and trends in, the GOES-derived daily maximum volcanic radiance for Kilauea during 1997 matched the changes in the observed style and extent of effusive activity. We see six periods of activity each marked by characteristic volcanic radiance levels, these being as follows.

- Period 1, low levels of  $M_{\text{volc}-\lambda}$ : tube-fed flow to the coast.

Because surface flow areas are small, with most of the lava being sent directly to the sea by the tube system, radiant intensities are low. Note, this period ends with a spike due to the eruption of lava at Napau on 30 January 1997, a short phase of effusive activity as detailed in the GOES-based  $M_{\text{volc}-\lambda}$  time series of [Figure 5.14](#) of [Chapter 5](#).

- Period 2, no  $M_{\text{volc}-\lambda}$ : pause in the eruption.

No hot spot, due to no effusive activity.

- Period 3, very low levels of  $M_{\text{volc}-\lambda}$ : lava lake activity confined to the vent.

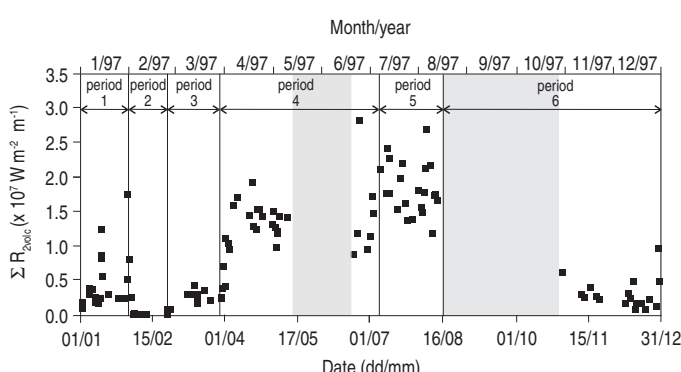


[Figure 6.22](#) Time series of daily maximum volcanic radiance for Kilauea during 1997 obtained from GOES MIR (band 2) data. Gray zones are data gaps [from Harris *et al.* (2001, Fig. 9)].

In this case, the area of active lava within the pixel is very small and thus the radiant intensity is also very low.

- Period 4, moderate levels of  $M_{\text{volc-}\lambda}$ : lava flows extending beyond the vent area.  
In this scenario, the area of active lava within the pixel is larger, and hence so too is the radiant intensity.
- Period 5, increasing and high levels of  $M_{\text{volc-}\lambda}$ : lava flows of increasing extent.  
With the area of active lava within the pixel increasing, the radiant intensity also increases.
- Period 6, low levels of  $M_{\text{volc-}\lambda}$ : return to tube-fed flow to the coast.  
Now areas of surface flow are small once more, so that the radiant intensity is also low.

#### *6.5.3.1 Waveform for a fire fountain event collected using SEVIRI: the way forward*

There are just a few time series for hot spots evolving during and after explosive events, or records of cooling of pyroclastic (fall or flow) deposits. Such events have typically been too short-lived to capture. However, a nice example of how 15-minute IR data from a geostationary platform can be used to track an explosive event, and the resulting waveform that can be generated, is given in [Figure 5.16](#) of [Chapter 5](#) for Etna's July 2011 fountaining event. The duration of the short fountaining phase is well-defined, as is a shorter, precursory, build up of strombolian activity and lava ponding in the vent. A short-lived, but well-developed, cooling curve is also recorded for the cooling deposits.

#### **6.5.4 Time series: waveform typology**

The large body of literature for time series production and analysis using satellite IR data now gives at least 85 waveforms associated with a variety of volcanic hot spot scenarios. This library now allows us to produce the typology of [Table 6.4](#). In this typology we see 12 case-type hot spot waveforms spanning effusive to explosive activity. Each waveform type can be linked to different eruption styles, durations of eruption, effusive conditions (e.g., pressurized versus non-pressurized; batch versus explosive), frequency of eruption and deposit cooling rates. The classic waveform associated with each type, as given in this book, is referenced from [Table 6.4](#). The text associated with each case-type example waveform already describes each case-type waveform, so that these descriptions will not be repeated here; their being mostly contained within the literature review of this section.

## **6.6 Trends and smoothing**

As data sets become more extensive, so the inclusion of spurious points becomes more of a problem, as does the requirement to identify and quantify trends. Trends can be confirmed and brought out by curve fitting. Fits need to be selected, applied, accepted and/or rejected using standard curve fitting routines and an assessment of the quality of the fit (e.g.,  $R^2$ ). For example, Wooster *et al.* (1998b) applied a second-order polynomial to bring out the increasing-decreasing temporal trend in their five-point spectral radiance time series for

Galeras. Application of a logarithmic trend to *TADR* time series produced from AVHRR-data for Krafla's 1984 eruption by Harris *et al.* (2000b), yielded a logarithmic fit of

$$TADR = -30.144\ln(d) + 126.08,$$

in which  $d$  was days since the start of the eruption. The relation had an  $R^2$  of 0.9899. Application of running means may also help to bring out trends, but can begin to suppress real peaks and troughs in the data. We can see this problem in Figure 6.14j, where a five-point running mean has been applied to the data set, which suppresses the apparent waning trend and misses the peak point.

#### 6.6.0.1 Spurious points and the maximum value approach

Trends may also be biased by the presence of spurious points. Harris *et al.* (1997a), for example, noted unexpected peaks and troughs in their AVHRR-derived lava flow area time series for the opening two months of Etna's 1991–1993 eruption. These points were all either due to inclusion of cloud-contaminated data or associated with data collected at extreme scan angles, as indicated in Figure 6.23.

Spurious measurements from data collected at extreme scan angles have long been known to occur in AVHRR-derived Normalized Difference Vegetation Index (NDVI) data (Holben and Fraser, 1984; Singh, 1988). This led Tucker *et al.* (1984) and Goward *et al.* (1991) to suggest filtering (rejection) of images collected at scan angles of greater than 30°, a cut-off selected on the basis of increased distortion, pixel size, and overlap beyond this point (see Chapter 3). Frulla *et al.* (1995) was more generous and recommended that data outside of a scan angle of ±50° should be removed “because it has poor observation geometry.” A harsh angular filter may destroy many valid data points in a thermal time series for a volcanic hot spot, and further reduce the utility of a time series already handicapped by loss of images due to cloud cover. For the Etna 1991–1992 case of Figure 6.23, identifying and removing data collected at scan angles of greater than 50° improved the fit between the satellite-derived and field-measured trend in active flow field area. However, application of even such a liberal scan-angle filter may still remove some valid data, such as the point marked “valid?” in Figure 6.23b.

A different solution is to apply the maximum value approach. Initially applied to AVHRR-derived NDVI images to reduce errors due to cloud contamination, atmospheric and scan angle effects, the approach uses the maximum NDVI value obtained for any pixel over a series of images. This maximum pixel value is then used to produce a maximum value time composite image (Holben, 1986). Applying such an approach to a time series plot involves placing all data points into sequential groups; the trend is then plotted through the maximum value of each group. In the case of Figure 6.23c, all cloud-free data at any scan angle have been placed into six sequential groups, each three data points in size (these groups are marked A through F in Figure 6.23c). The trend plotted through the maximum of each group now matches the field-derived trend.

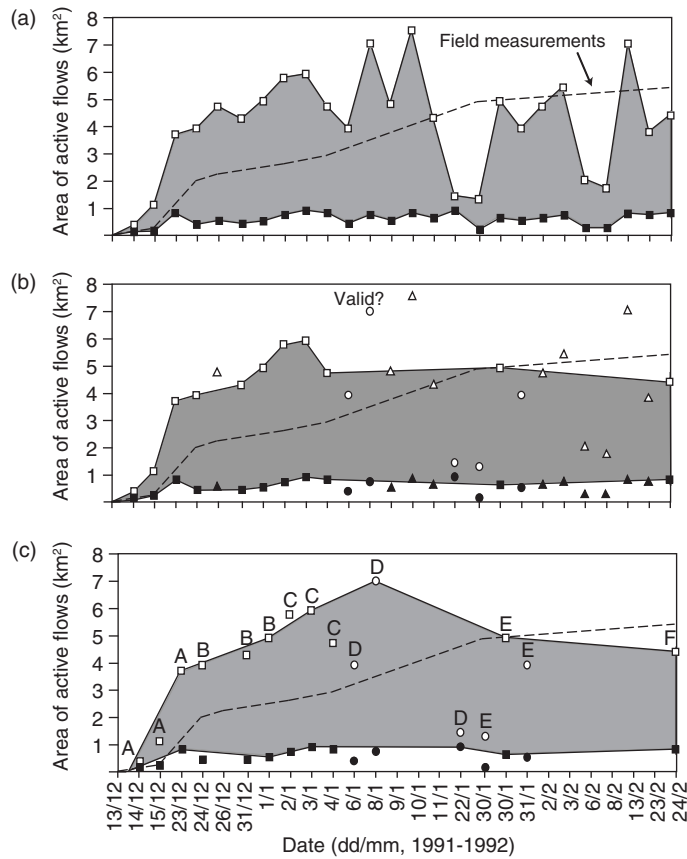


Figure 6.23 AVHRR-derived time series for active lava flow area during the first 2.5 months of Etna’s 1991–1993 eruption. Maximum area is extracted by assuming a lava flow surface temperature of 100 °C (white squares) and minimum area by assuming a lava flow surface temperature of 500 °C (black squares) [see Section 4.3.1.2 of Chapter 4]. The range of possible solutions between these two end members is marked by the gray zone. In (a) all data are plotted, along with the field-measured total flow field area. In (b) data collected at extreme scan angles (triangles) and cloud contaminated data (circles) have been identified and excluded. However, some extreme scan angle measurements may still remain valid, as marked. In (c) all data have been placed into groups of three (group A, B, C, etc.), and the trend plotted through the maximum value of each group. The field measurement is now roughly centered in the range defined by our end-member solutions, and follows the same trend until 8 January 1992. At that point, the two trends begin to diverge (the field measurement continuing to increase, while the satellite trend begins to decline). This is a result of the satellite being a measure of currently active area, and the field measure being for all lava erupted since the beginning of the eruption [from Harris *et al.* (1997a, Fig. 7); reproduced by permission of American Geophysical Union].

### 6.6.0.2 No lines?

It is always tempting to link data points scattered through time with lines, so as to bring out temporal trends, but can this give a false impression? For example, in [Figure 6.23c](#) a data point of 9 January is linked to the next point, acquired 21 days later on 30 January 1992, by a straight line. This leads the reader to believe that the flow area declined steadily between these two dates, and that the turn around to a declining trend occurred on 9 January. Did it? In truth we do not know; all we can say is that the active lava flow area was lower on 30 January than on 9 January. We do not know when this change occurred, whether the decline was steady, rapid or slow, or whether there were any peaks and troughs within the data-free period.

Maybe it is best to leave any two points which are separated by more than a day or so in time free of such a link? Use of the line may also lead to the feeling that the trend so revealed is constrained by data, and thus real, when it is not: it is just a line drawn between two points and so, of course, will be straight. Certainly, a line-free data plot of all the data should be given, along with information regarding the data quality for each point (e.g., scan angle and local cloud-cover information). This allows the reader to make an objective assessment as to the likelihood that any trends exist and, if they do, what the probable form of the trend is. The same reader is then free to make unbiased decisions as to what data should be included or excluded, what trends the plot may, or may not, be capable of revealing, as well as the time scale of trend that can be resolved. In other words, the reader's eye is left to draw its own conclusions.

## 6.7 Spatial profiles

The concept of the spatial profile is simple: it is a plot of the variation in the chosen parameter with distance along a line (or lines) taken across, or down, the center line of a feature. In our case the parameter plotted will likely be surface temperature, spectral radiance, or heat flux, and the plot may be taken down the center line of an active lava flow, or across the flow, to define and show the characteristic spatial distribution of surface temperature. Likewise, profiles may be taken across a lava dome, lava lake or crater lake to allow an examination of the spatial distribution of thermal structures across such features.

Because of the spatial resolution of AVHRR- and GOES-class data, extracting profiles that show temperature trends across an active lava, which may be just a few meters to hundreds of meters across, is close to impossible. However, profiles taken across an entire image, or image portion, can reveal the presence of a hot spot from a spike in the profile. The first use of such a GOES-class profile was by Williams and Friedman ([1970](#)) who plotted the brightness temperature along one scan line of 8-km resolution HRIR data to reveal the hot spot due to the 1966 effusive activity at Surtsey. This first example of a satellite image-derived spatial profile is given in [Chapter 1](#) (see [Figure 1.1b](#)). Another example, this time using AVHRR-class data, is also given in [Chapter 1](#) where the Erebus

lava lake can be seen as a one- to three-pixel spike in the spatial profile made across the location of the lava lake in an AVHRR image of 1980 (see [Figure 1.8 of Chapter 1](#)).

TM-class data are of sufficient spatial resolution to allow extraction of temperature profiles that can reveal the character, or distribution, of actual temperatures across or within an active lava. Three examples are given in [Figure 6.24](#). This shows the pixel-by-pixel surface temperature down a silicic lava flow active at Santiaguito between 2000 and 2002. It shows a characteristic logarithmic decline in the surface temperature with distance from the source, consistent with down-flow cooling of a stable crust with distance from the vent (and hence also time since eruption). Such a trend is characteristic of channel fed blocky and 'a'a lava flows and was apparent in spatial profiles produced from MSS data for active lava flows at Sierra Negra by Rothery *et al.* ([1988](#)) and Lonquimay by Oppenheimer ([1991](#)). These profiles are given in [Figure 1.9 of Chapter 1](#) and [Figure 4.11c of Chapter 4](#), respectively.

## **6.8 Use of multiple platform data for validation**

We have considered generation of time series from individual data classes: TM-, AVHRR-, or GOES-class. However, classes can be combined in multi-platform time series studies, and a number of studies have done this. Such an approach gives us the best of both worlds, combining the temporal detail of the AVHRR- and/or GOES-class data with the spatial detail of the TM-class data.

Patrick *et al.* ([2005b](#)), for example, used 71 MODIS-derived measurements of radiative heat flux during an effusive eruption at Montagu Island (South Sandwich Islands) to identify four phases of activity on the basis of the level of the emitted heat flux. The MODIS-derived time series was cross-checked with an analysis of ASTER, ETM+ and RADARSAT imagery. This allowed Patrick *et al.* ([2005b](#)) to check the style of activity associated with each radiance level, allowing the phases to be defined as follows.

- Phase 1: minor thermal anomalies:  
due to lava flow of limited extent.
- Phase 2: high-radiance thermal anomalies:  
not due to increased lava flow area, but due to improved viewing conditions.
- Phase 3: high radiance thermal anomalies:  
no high-spatial-resolution data were available to check whether this level was due to larger flow areas or excellent viewing conditions.
- Phase 4: high-radiance thermal anomalies:  
Confirmed to be due to the presence of longer lava flows.

In this way, trends and levels apparent in the coarser-spatial-resolution, but higher-temporal-resolution, AVHRR- and/or GOES-class time series can be validated by more detailed observations, or precise parameter extractions, from rarer TM-class data within the time period studied.

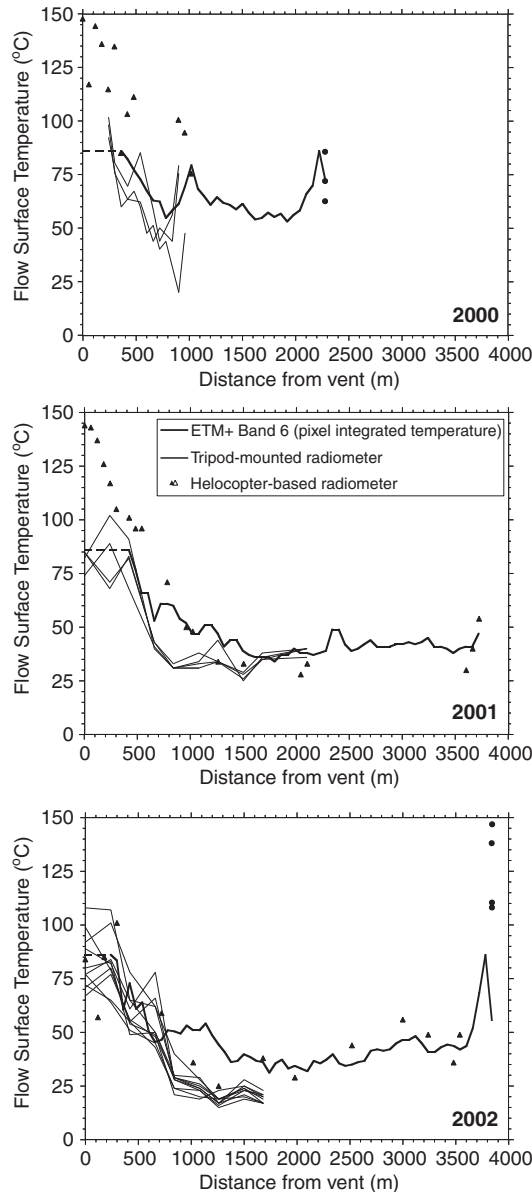


Figure 6.24 Down-flow profiles of surface temperature obtained for an active silicic lava flow at Santiaguito. ETM+ derived profiles are for TIR (band 6) pixel-integrated temperature (corrected for emissivity and atmospheric effects) taken down the center line of the lava flow thermal anomaly. Images were acquired on 23 January 2000, 25 January 2001 and 19 January 2002. Radiometer-based measurements were made on, or around, the same time as the satellite overpass. Saturated ETM+ values are given by the thinner line filled circles give ground-based radiometer measurements made at the flow front [from Harris *et al.* (2004, Fig. 12), with permission from Elsevier].

### **6.9 Inventories: the current status of satellite remote sensing**

As of 2012, satellite remote sensing of volcanic hot spots was at a point where both long-term and temporally detailed thermal emission inventories for volcanic activity were available. By 2012 some TM-, AVHRR- and GOES-class spectral radiance data bases were continuous over decades, with data bases for MODIS/ASTER, GOES, TM/ETM+ and AVHRR spanning 13, 18, 30 and 34 years, respectively. In addition, sensors flown on GOES, MSG, and MTSAT allowed coverage in the MIR and TIR with temporal resolutions of 15 minutes. These data sets allowed detailed time series to be produced for short-lived and transient events, such as lava fountains active for just a few hours, as well as the thermal characterization of long-lived extrusive and degassing episodes. Such long and/or temporally detailed data bases came with a full range of data processing methodologies, and were available for a range of activity types, spanning crater lakes of water and lava, through lava flows and domes, to degassing, fountaining and strombolian activity. Decade-scale data sets were also available for single volcanoes, entire volcanically active regions, and even global volcanism, as was the case for the MODVOLC data base. Chapters up to this point have been littered with illustrative examples and case studies that sum up the state-of-the-art for volcano radiometry from space as of 2012, and highlight these capabilities. We now move on to consider ground-based options for detecting, measuring and tracking volcanic thermal phenomena.

## **Part III**

Ground-based volcano radiometry and thermography



# 7

## Broad-band radiometers I: instrumentation and application

A broad-band radiometer can be defined as an instrument that measures electromagnetic radiation emitted across a given waveband from a single spot on a targeted surface. They differ from traditionally used optical pyrometers in that they detect and measure incoming radiation. Instead, an optical pyrometer uses the brightness or color of the surface to determine the temperature (see [Appendix H](#)). Most commercially available broad-band radiometers operate in a similar manner, having the basic design of [Figure 7.1](#). That is, radiation emitted from the targeted surface across a given waveband causes the detector to register a change in voltage. This is amplified and converted to a digital signal by an analog-to-digital converter. The change in voltage is proportional to the emitted spectral radiance, so that factory calibration converts the voltage to a spectral radiance through an onboard calibration. Through inversion of the Planck Function, this is converted to a brightness temperature that is displayed on the instrument read-out.

### 7.1 Detector types

Two detector types are used to detect optical radiation: photo-detectors and thermal detectors. The difference between the two types is as follows.

- In photo- (or photon-) detectors, light arriving at the detector causes a change in the resistance, inductance, voltage, or current of the detector. This is a result of a certain number of photons being converted into a number of electrons.
- In thermal detectors, optical radiation incident upon the detector causes a temperature change in the detector. This produces an electrical change at the detector, such as a change in voltage or resistance.

Photo-detectors and thermal detectors can be used to manufacture small, light-weight and thus portable, broad-band radiometers capable of hand-held use. However, selection of detector type will influence the waveband sampled and, hence, the temperature sensitivity of the instrument, as well as the response time and need for detector cooling. Dereniak and Boreman (1996) provide a thorough and detailed review of photo-detectors and thermal detectors on which the following summary is based.

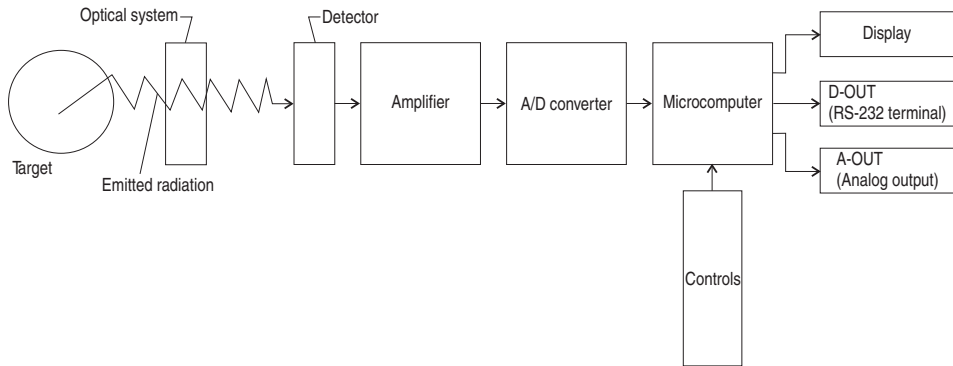


Figure 7.1 Schematic showing the main components of a broad-band radiometer, and the passage of the signal through those components [from Minolta/Land (9222-1860-21, p. 50)].

### 7.1.1 Detector sensitivity

In photo-detectors, detector sensitivity is limited by the wavelength at which the lowest energy photon can be detected, this being termed the cut-off wavelength ( $\lambda_c$ ). The energy that a photon must achieve to be detected has to exceed the energy gap of the detector material ( $\varepsilon_g$ ). This is the energy range in which no electron states exist, and is defined by:

$$\varepsilon_g = hc/\lambda_c, \quad (7.1a)$$

$h$  being the Planck constant ( $6.6 \times 10^{-34}$  J s) and  $c$  being the speed of light ( $\sim 3 \times 10^8$  m s $^{-1}$ ). Re-arranging Equation (7.1a), substituting for the constants and correcting for units so that wavelength is in microns and energy gap is in electron volts, Dereniak and Boreman (1996) rewrite Equation (7.1a) as

$$\lambda_c = 1.238/\varepsilon_g. \quad (7.1b)$$

This shows that, as the energy gap increases, the cut-off wavelength decreases. As a result, small-energy-gap materials can detect radiation further into the infrared than high-energy-gap materials.

High-energy-gap materials also require cooling, the reason being as follows. A population of thermally generated electrons ( $n_e$ ) can be related to temperature ( $T$ ) by:

$$n_e \propto \exp(-\varepsilon_g/kT), \quad (7.1c)$$

$k$  being the Boltzmann constant ( $1.38 \times 10^{-23}$  J K $^{-1}$ ). Hence, holding temperature constant, as the energy gap decreases, the number of thermally generated electrons increases. These dark-current-generated electrons are prevented from outnumbering the photo-generated electrons by cooling the detector, where detectors with lower energy gaps (and hence longer cut-off wavelengths) require cooling to lower temperatures. The presence of any thermally generated electrons will create dark-current noise.

### 7.1.2 Photo-detectors

Dereniak and Boreman (1996) review three types of photo-detector, which operate as follows.

- Photo-voltaic: Record light change as a change in VOLTAGE.
- Photo-conductors: Record light change as a change in RESISTANCE.
- Photo-emissive: Record light change as a change in CURRENT.

Broad-band radiometers tend to use either photo-voltaic detectors or photo-conductors. The key is, to be portable, the use of detectors that require cooling needs to be avoided.

In photo-voltaic detectors, optical radiation incident upon the detector produces a voltage or current. In this case, the voltage is proportional to the radiation incident upon the detector or photon flux, i.e., the voltage increases with the photon flux. Two types of photo-voltaic detector, InSb (indium–antimony) and HgCdTe (mercury–cadmium–tellurium), have relatively small energy gaps (0.225 and 0.113 eV, respectively) and hence have relatively long  $\lambda_c$  of 5.5 and 11  $\mu\text{m}$ , respectively. Operation at these wavelengths means such detectors are capable of measuring ambient temperatures. However, operating temperatures of 77 K mean that both detectors require cooling.

Photo-voltaic detectors with relatively high-energy gaps include silicon (1.125 eV) and germanium (0.688 eV). These do not require cooling (having room-temperature operating temperatures). However, these detectors have  $\lambda_c$  of 1.1 and 1.8  $\mu\text{m}$ , respectively. Measurements at these wavelengths mean that only high-temperature targets will be detectable.

For photo-conductors, radiation incident upon the detector produces a resistance or conductance. In this case, the resistance is inversely proportional to the incident radiation or photon flux, i.e., resistance decreases with increased photon flux. PbS (lead–sulfur) and PbSe (lead–selenium) photo-conductors have  $\lambda_c$  of 3 and 5  $\mu\text{m}$ , respectively, with nominal operating temperatures of 300 K. Detection at such wavelengths means that temperatures below  $\sim$ 300 °C may not be measured.

### 7.1.3 Thermal detectors

Dereniak and Boreman (1996) review four types of thermal detector.

- Bolometers: Record temperature change as a change in RESISTANCE.
- Thermopiles: Record temperature change as a change in VOLTAGE.
- Pyroelectric: Record temperature change as a change in CAPACITANCE.
- Superconductor: Record temperature change as a change in RESISTANCE.

Bolometers are widely used for ground-based thermal imaging, and so will be covered in Chapter 9. Thermopiles are the most commonly used detector type for hand-held broad-band radiometers used for volcanic studies. A thermopile is a series connection of thermocouples. The thermocouple is composed of a cold junction which is kept stable at a reference temperature, and a hot junction which is exposed to the heat source. As the temperature at

the hot junction changes, so does the voltage carried by the thermocouple, with the voltage being proportional to the difference in temperature between the hot and cold junction. Because the hot junction must absorb radiation, this junction is typically coated with a thermally absorptive (black) substance. The series connection is used to increase the voltage output. All the hot junctions in the series are exposed to the source and all the cold junctions to the reference. The voltages of the individual thermocouples add up, creating a larger voltage that can be generated by electronic amplification. The advantage of a thermopile is that it covers a broad spectral range (200 nm–30 µm) and can thus be used for temperature measurement across a wide range (typically –30 to 1200 °C) thereby spanning ambient to molten lava temperatures. This explains why it is the most widely used detector for volcano applications.

Pyroelectric detectors are also used in broad-band radiometers. In pyroelectric detectors, the change in temperature creates a change in polarization. A current is produced if the detector experiences a temperature change, so that if temperature is constant no current is produced. As opposed to thermopiles, which tend to have relatively slow responses, pyroelectric detectors offer high levels of sensitivity at room temperature and fast response times.

#### 7.1.4 Nomenclature

A number of generic terms have been used to provide a general instrument descriptor for all of the detector types listed in Sections 7.1.2 and 7.1.3, including “thermal infrared thermometer” and “pyrometer.” To be precise the exact detector type should be used in referring to the instrument within which the detector resides [e.g., photo-voltaic (Si) photo-detector]. However, we here use the generic term “broad-band radiometer” for all instruments containing the detector types reviewed above.

#### 7.1.5 Response time

Detector response time is determined by how fast the detector can respond to a change in radiation incident upon it. In the case of a photon-detector, this is the time the electrons take to be generated and re-arranged following a change in light incident upon the detector. In the case of the thermal detector, this is the time the detector takes to heat up or cool down following a change in heat incident upon it. The speed of response thus depends on the detector’s electrical response, or how fast the change in electron concentration in the detector ( $\Delta n$ ) can occur in response to a change in light or radiation.

For an instantaneous increase in radiation incident upon a thermal detector, Dereniak and Boreman (1996) show that output response as a function of time ( $t$ ) depends on the electron recombination time ( $\tau_r$ ). This is proportional to photon irradiance ( $E_q$ ):

$$\Delta n = \eta E_q \propto \tau_r (1 - e^{-t/\tau_r}), \quad (7.2)$$

$\eta$  being a measure of photon efficiency. Photon efficiency is typically expressed as a percentage and can be viewed as the ratio of the number of electrons produced ( $n_e$ ) to

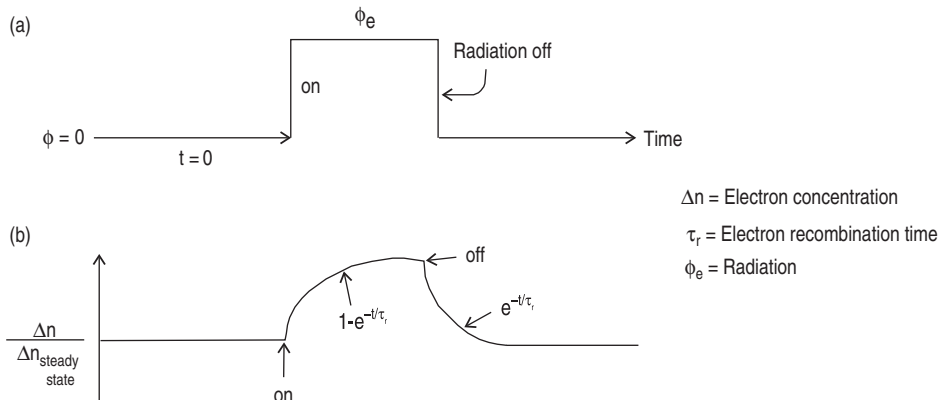


Figure 7.2 (a) Box-shaped pulse of radiation onto a detector and (b) the output waveform for a detector with a response time of  $\Delta n$  [from Dereniak and Boreman (1996, Fig. 5.18): this material is reproduced with permission of John Wiley & Sons, Inc]. The rate of change in the output waveform is dictated by  $\Delta n$ , the speed at which the detector's electron concentration changes in response to switching the radiation source on or off. Response time  $\Delta n$  is, in turn, a function of the time needed for electrons to recombine ( $\tau_r$ ) following the change in the incident radiation. This means that the detector moves from one radiation level to another over a period of time (i.e., full response is not instantaneous), forcing an exponentially increasing, or decaying, form onto the output waveform.

number of photons absorbed ( $n_p$ ) when light arrives at the detector, so that  $\eta = n_e/n_p$ . For photo-voltaic detectors and photoconductors,  $\eta$  typically has a value of  $\sim 60\%$  (Dereniak and Boreman, 1996). This implies that the greater the irradiance, the higher the recombination time and, thus, the response time. Likewise, when the radiation source is turned off, the detector will need time to respond. This response also has an exponentially decaying form which follows (Dereniak and Boreman, 1996):

$$\Delta n = \tau_r e^{-t/\tau_r}. \quad (7.3)$$

The resulting sensor response to a discrete radiation pulse will thus have the form shown in Figure 7.2, where an exponentially increasing voltage is registered as the radiation source is turned on, followed by an exponentially decaying voltage once the source is turned off.

Butterworth (1968) showed how the spectral peak of an input signal with a Gaussian shape will be distorted when the response time of the detector is comparable to, or greater than, the half-width of the distribution. Distortion appears as a decrease in pulse height, displacement of the peak to a later time, and some asymmetry, as plotted in Figure 7.3. The waveform of the response-time-modified pulse, i.e. the output voltage ( $V_0$ ) as a function of time ( $t$ ) [ $V_0(t)$ ], depends on the input pulse amplitude ( $A$ ), width ( $m$ ), and detector response time ( $\tau_r$ ), following:

$$V_0(t) = \frac{A\pi^{1/2}}{2m\tau_r} \exp\left(\frac{1}{4m^2\tau_r^2} - \frac{t}{\tau_r}\right) \{1 + \operatorname{erf}[mt - 1/(2m\tau_r)]\}. \quad (7.4)$$

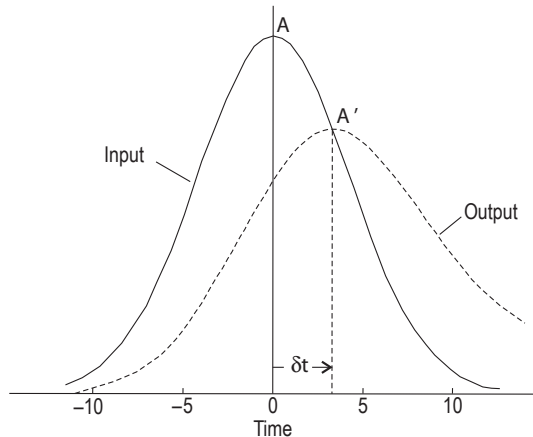


Figure 7.3 Input and output pulse shapes for a pulse with a half-width of ten time units received by a detector with a response time of five time units [from Butterworth (1968, Fig. 1)]. The onset of both pulses is simultaneous, but the output pulse peaks ( $A'$ ) after the peak in the input pulse ( $A$ ). The response time effect thus causes the recorded time of peak radiation to lag behind the actual time of peak emission (by  $\delta t$ ). Also, the recorded peak level of radiation is lower than the input, and the output pulse continues to decay after the input pulse has reached zero.

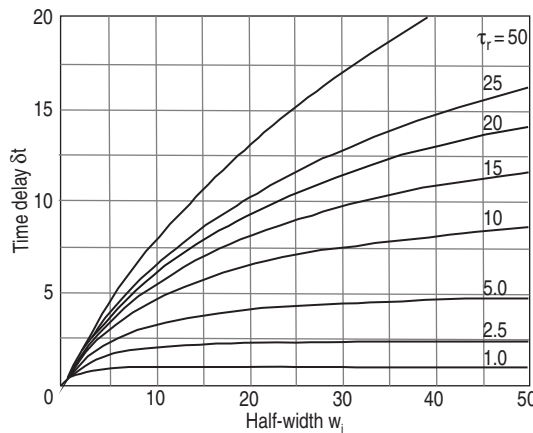


Figure 7.4 Time delay of the output peak ( $\delta t$  in Figure 7.3) as a function of initial pulse half-width ( $w_i$ ) and response time ( $\tau_r$ ), plotted for response times varying between 1 and 50 time units [from Butterworth (1968, Fig. 3)]. The delay increases with pulse width and delay time.

Given a Gaussian distribution to the input pulse, the time delay for arrival of the peak signal ( $\delta t$ ) can be calculated from:

$$e^{[m\delta t - 1(2m\tau_r)]^2} \{1 + \operatorname{erf}[m\delta t - 1(2m\tau_r)]\} = 2m\tau_r/\pi^{1/2}. \quad (7.5)$$

The time delay thus depends on the half-width of the input pulse and the response time, with  $\delta t$  increasing with pulse width and response time, following the relations of Figure 7.4.

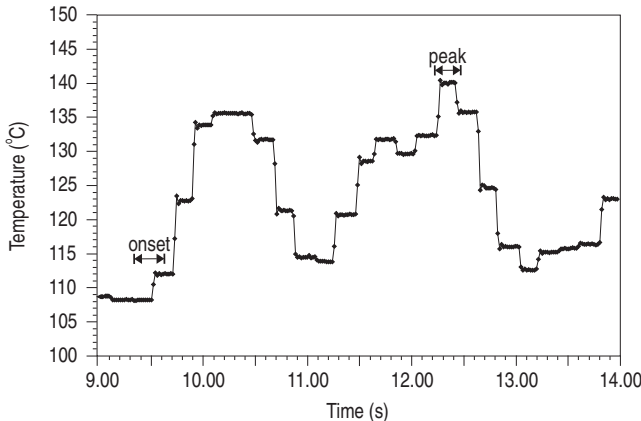


Figure 7.5 Effect of chopping on the output signal of a radiometer. A steadily varying radiation source is transformed into a series of steps of equal radiation (in this case converted to brightness temperature). In this case, the output of a Minolta/Land Cyclops 300, the signal is chopped at the same frequency as the response time, i.e., 0.25 s (so that each step is 0.25 s in duration). Each oscillation records a hot puff of gas exiting an active vent on Stromboli, and we see that the precision with which we can pick the time for the onset and peak of the associated waveform is limited by the chopping effect. The onset, for example, is sometime between 9.3768 s and 9.6268 s.

Thus, although the detector will begin to respond to a discrete change in radiation immediately, the full response will not be recorded until after a certain time period (see Figure 7.2). Response times for most commercially available broad-band radiometers are 0.1–0.5 s, depending on the detector type.

Response time effects are important if continuous measurements are being made at high sampling frequencies, and the input signal is varying over a time scale that is less than, or equal to, the response time. In this case, the output waveform will suffer distortion. For example, following Figure 7.4, if an instrument with a response time of 2.5 s records an oscillation with a half-width of 5 s, then the arrival of the peak will be delayed by  $\sim 2$  s.

Thermopiles respond slowly, so that they are typically used with chopped radiance at frequencies less than 25 Hz (Dereniak and Boreman, 1996). Chopping results in an output voltage that shows a step-like form, as shown in Figure 7.5. Each step is composed of a series of roughly identical voltages, with the step length approximating the duration of the response time. Chopping the output voltage effectively forces the instrument to record no variation shorter than the response time. It hence removes distortion effects, but also reduces the temporal resolution making the picking of exact onset and peak times less precise, their being marked by a step rather than a point (as marked on Figure 7.5).

## 7.2 Broad-band radiometers: capabilities and operation

As with the volcanological application spin-off of weather satellites, the volcanologist benefits from the widespread need for, and use of, portable hand-held radiometers by the mechanical

and electrical maintenance industries, power and utility services, as well as the paper, food, chemical, petrochemical, glass and metal industries. Because of the high demand for precision hand-held radiometers, choice is wide and levels of customer service high, with excellent access to help-desks, instrument engineers and calibration services. As a result, a great range of portable hand-held radiometers are available, some at quite low cost. Examples of commercially available instruments suitable for volcanological applications are given in Tables 7.1 and 7.2. None requires cooling, and all are small, light weight and portable. However, they vary in price and spectral capability depending on the detector used and quality of the viewing optics.

We split the instruments into two groups, hand-held ([Table 7.1a,b](#)), and fixed mount ([Table 7.2a,b](#)). Hand-held instruments, as the name implies, are suitable for hand-held (or tripod-mounted) use during temporary deployments. Such instruments, as pictured in [Figure 7.6a,b](#), are small and light weight (typically not exceeding 1 kg). We define a third instrument category in [Table 7.1c](#): light weight hand-held instruments. These are particularly small and light weight (typically <0.2 kg) and are also, usually, available at low cost. However, these instruments typically have more limited specifications than their more expensive counterparts. For example, no lightweight instrument listed in [Table 7.1c](#) is capable of measuring temperatures above 540 °C.

All hand-held and light weight instruments have minimal power requirements, typically requiring between two and six AA batteries that can power continuous recording for up to 60 hours. Sighting capabilities range from laser to optical. The laser spot tends to become lost over longer distances, but can be very effective at pinpointing near-field targets (i.e., targets within 10 m of the instrument). Optical sighting allows target checking over greater distances. However, errors in co-location of the measurement circle as given in the viewing optics with the actual measurement area can increase with distance, where errors over ~250 m can be half of the field of view (FOV) diameter or more. Thus, optical sighting should usually be used to provide a pointing guide, and fine-tuning should then be achieved by nudging the instrument up and down, and side to side until maximum temperature is recorded. In short, although an incandescent vent may be centered in the viewfinder measurement circle, the maximum temperature may not be recorded until the vent appears to be somewhat outside of the measurement circle.

Fixed-mount instruments are listed in [Table 7.2a,b](#) and are more suitable for permanent installation. As pictured in [Figure 7.6c](#), they lack targeting optics, but are typically small, light weight, and installed in robust, weather-proof enclosures. This makes them appropriate for mounting in a fixed position, from which they are able to record the same spot in a continuous manner. This, with their low power consumption, suits them to permanent field deployment.

Within both the hand-held and fixed mount groups, we split the instruments between photon detectors and thermal detectors. Because of their low cut-off wavelengths, all photon-detector-based instruments operate in the short-wave infrared, typically between 1 μm and 2 μm (see [Table 7.1a](#) and [7.2a](#)). This sets a limit on the minimum temperature that can be measured, most hand held photon-detector-based instruments not allowing measurements below 300–600 °C. Thus, such instruments are not suited to measurement of cooler volcanic phenomena. However, the upper measurement range extends well beyond the

Table 7.1  
EXAMPLES OF COMMERCIALLY AVAILABLE HAND-HELD RADIOMETERS SUITABLE FOR VOLCANOLOGICAL APPLICATIONS, WITH DETECTOR TYPE WHERE KNOWN.

**Table 7.1a. Hand-held radiometers: short-wave infrared (<2 µm) photon-detectors.**

Manufacturer:	Chino	Chino	Micro Photonics	Mikron	Minolta/Land
Model	IR-AHS	IR-HI	TI315	MI-GA 8+	Cyclops 153 (152)
Sensor type:	Si	InGaAs	—	—	Si
Operating temp. range (°C):	0–50	0–50	0–50	0–50	0–50
Waveband (µm):	0.96	1.55	2.1–2.4	1.45–1.8	0.8–1.1
Temperature range (°C):	600–3000	300–1000	400–1800	300–1300	500–3200
Output (analog):	—	—	—	—	1 mV/°C or F
Output (digital):	RS232	RS232	—	RS232	RS232
Accuracy:	±0.5%	±6 °C	±1%	1%	±0.5%
Response time (s):	0.5	0.25	0.2	0.001	0.13
Field of View (FOV, °):	0.57	0.25	0.5	0.5	½
Size (mm):		148 × 100 × 70	185 × 200 × 50	210 × 75 × 175	223 × 78 × 170
Weight (kg):	0.7	0.35	0.6	1.2	1
Power supply:	4 × AA batteries	2 × AA batteries	2 × 6F229V batteries	6 × 1.5 V batteries	6 × AA batteries
Power consumption:	—	—	—	—	20 mA
Battery life (h):	20	50	—	35	—
Optical system:	Focusable view finder	Fixed focus view finder	Telescope	10° FOV w/measurement circle	8° FOV w/½° measurement circle
Price (US\$) (date):	—	—	1430 (07/08)	—	2995 (02/02)

Table 7.1b. Hand-held radiometers: Broad-band (8–14  $\mu\text{m}$ ) thermal detectors.

Manufacturer:	Chino	Fluke	Micro Photonics	Micro Photonics	Mikron
Model:	IR-AHT	574	TI200	TI213EL	M90G
Sensor type:	Thermopile	Thermopile	—	—	—
Operating temp. range ( $^{\circ}\text{C}$ ):	0–50	0–50	0–50	–18.5–50	0–50
Waveband ( $\mu\text{m}$ ):	8–13	8–14	8–14	8–14	8–14
Temperature range ( $^{\circ}\text{C}$ ):	–50–1000	–30–900	–20–700	–25–1200	0–500
Output (analog):	—	1 mV/ $^{\circ}\text{C}$ or F	—	—	1 mV/ $^{\circ}\text{C}$ or F
Output (digital):	RS232	RS232	—	—	RS232
Accuracy:	$\pm 1\%$	$\pm 0.75\%$	$\pm 1\%$	$\pm 1\%$	$\pm 0.8\%$
Response time (s):	1	0.25	0.4	0.2	1
Field of View (FOV, $^{\circ}$ ):	1.4	1	1.64	0.72	2.5
Size (mm):	—	170 $\times$ 120 $\times$ 42	185 $\times$ 170 $\times$ 50	165 $\times$ 187 $\times$ 76	—
Weight (kg):	0.7	0.48	0.2	0.5	1.1
Power supply:	4 $\times$ AA batteries	2 $\times$ AA batteries	2 $\times$ 6F229V	2 $\times$ 6F229V	Rechargeable
Power consumption:	—	—	—	—	—
Battery life (h):	20	13	—	—	8
Optical system:	Cassegrain focusable mirror type	Laser	Laser	Coaxial laser	View finder w/9 $^{\circ}$ FOV
Price (US\$) (date):	—	1091 (07/08)	500 (07/08)	1140 (07/08)	—

Manufacturer:	Mikron	Minolta/Land Compac 3	Minolta/Land Cyclops 300	Omega OS523-1	Omega OS651
Model:	M90B	Thermopile	Thermopile	—	—
Sensor type:	—	Thermopile	Thermopile	—	—
Operating temp. range (°C):	0–50	0–50	0–50	0–50	4–43
Waveband (μm):	8–14	8–14	8–13	8–14	8–14
Temperature range (°C):	−50–1000	−50–500	−50–1000	−18–1370	−29–1093
Output (analog):	1 mV/°C or F	1 mV/°C or F	1 mV/°C or F	1 mV/°C or F	1 mV/°C or F
Output (digital):	RS232	RS232	RS232	—	—
Accuracy:	±0.8%	±1%	±1%	±1%	±1%
Response time (s):	0.75	0.2	0.5	0.25	1
Field of view (FOV, °):	1.5	1.7	1	1.9	1.9
Size (mm):	165 × 187 × 76	90 × 82 × 126	146 × 90 × 111	—	150 × 230 × 60
Weight (kg):	1.1	0.72	0.83	—	0.9
Power supply:	Rechargeable	6 × AA batteries	4 × AA batteries	4 × AA batteries	9 V alkaline battery
Power consumption:	—	25 mA	50 mA	—	—
Battery life (h):	8	24	40	60	20
Optical system:	View finder w/9° FOV	Optical w/8° FOV w/ 1° & 1.7 ° measurement circles	Focusable mirror optical system, $f = 60 \text{ mm}$ , 8° FOV w/1° measurement circle	Laser	V-groove
Price (US\$) (date):	—	—	2910 (02/02)	1095 (1999)	795 (1999)

Table 7.1b. (*cont.*)

Manufacturer:	Omega	Omega	Omega	PIC*	Raytek
Model:	OS86	OSP1000	OS3701	PRT-5	3i LTSC
Sensor type:	—	—	—	Bolometer	Thermopile
Operating temp. range (°C):	0–50	–5–55	0–50	–20–40	0–50
Waveband (μm):	8–14	8–14	8–14	8–14	8–14
Temperature Range (°C):	–20–900	–30–1000	–50–1000	–50–150	–30–1200
Output (analog):	—	1 mV/°C or F	1 mV/°C or F	1 v.d.c.	1 mV/°C or F
Output (digital):	RS232	RS232	RS232	—	RS232
Accuracy:	±0.8%	±1%	±1–8%	±0.5 °C	±1%
Response time (s):	0.5	—	1	0.005, 0.05 & 0.5	0.7
Field of view (FOV, °):	1.9	0.57	0.33, 0.67 & 1.5	0.14, 2 & 20	1
Size (mm):	—	200 × 180 × 80	187 × 165 × 76	483 × 134 × 254	244 × 257 × 71
Weight (kg):	—	0.8	1.1	10.9	0.794
Power supply:	Rechargeable	Rechargeable	4 × AA batteries	115 or 230 V	4 × AA batteries
Power consumption:	—	—	—	—	200 mA
Battery life (h):	20	18	16	—	—
Optical system:	Laser	Scope or laser	Optical w/9° FOV	Scope	Scope w/measurement circle
Price (US\$) (date):	995 (1999)	2080 (1999)	2875–4900 (1999)	—	1895 (08/97)

\* The Pyrometer Instrument Company.

Table 7.1c. Hand-held radiometers: light-weight and low-cost.

Manufacturer:	Chino	Fluke	Micro Photonics	Omega	Raytek
Model:	IR-TA	62	TI120EL	OS520L	MiniTemp MT6
Sensor type:	Thermopile	Thermopile	—	—	—
Operating temp. range (°C):	0–50	0–50	0–50	0–50	—
Waveband (μm):	8–14	6.5–18	8–14	8–14	—
Temperature range (°C):	−40–500	−30–500	−20–500	−18–540	−30–500
Output (analog):	—	—	—	1 mV/°C or F	—
Output (digital):	—	—	—	—	—
Accuracy:	±1%	±1%	±1%	±1%	±2%
Response time (s):	0.8	0.5	0.4	0.25	0.5
Field of view (FOV, °):	2.6	5.7	7.2	5.7	5.7
Size (mm):	—	152 × 101 × 82	170 × 89 × 42	—	“Pocket size”
Weight (kg):	0.18	0.2	0.17	—	—
Power supply:	3 × AA batteries	9V battery	2 × AAA 1.5 V	4 × AA batteries	—
Power consumption:	—	—	—	—	—
Battery life (h):	50	12	—	60	—
Optical system:	Laser	Laser	Laser	Laser	Laser
Price (US\$) (date):	—	83 (07/08)	280 (07/08)	295 (1999)	99 (07/08)

Table 7.2

EXAMPLES OF COMMERCIALLY AVAILABLE FIXED-MOUNT RADIOMETERS  
SUITABLE FOR VOLCANOLOGICAL APPLICATIONS, WITH DETECTOR TYPE WHERE  
KNOWN.

Table 7.2a. *Fixed-mount radiometers: short-wave (<2 µm) and mid-infrared (4–5 µm) photon-detectors.*

Manufacturer:	Chino	Mikron	Omega	Omega
Model:	IR-CAI	MI-K740-HS	OS1561	OS1532-R3
Sensor type:	InGaAs	—	Lead Selenide	Lead Selenide
Operating temp. range (°C):	0–50	0–40	10–50	10–50
Waveband (µm):	1.55	1.58–1.8 & 1.58–2.5	4.5–5.15	4.5–5.15
Temperature range (°C):	200–1000 & 300–1600	300–1400 & 160–1000	600–2400	215–1225
Output (analog):	4–20 mAADC	—	1mV/°C or F	—
Output (digital):	—	—	—	—
Accuracy:	0.5%	±0.75%	±1%	—
Response time (s):	0.003	0.009	0.01	0.003
Field of view (FOV, °):	0.3, 0.2 & 1.2	0.14	1.1	4.5
Size (mm):	—	170 × 70 × 70	69 × 102 × 305	68 × 102 × 282
Weight (kg):	1.3	1.2	3.6	1.8
Power supply:	24 V DC	24 VAC	15 V DC	—
Power consumption:	2.4 VA	—	—	—
Battery life (h):	—	—	—	—
Optical system:	Viewfinder	Viewfinder	—	—
Price (US\$) (date):	—	—	2340 (1999)	4995 (1999)

Table 7.2b. *Fixed-mount radiometers: broad-band (8–14 µm) thermal detectors.*

Manufacturer:	Chino	Chino	Omega	Omega
Model:	IR-CAB	IR-BAT1P & BAXL1	OS554	OS43H
Sensor type:	Pyroelectric	Thermopile	—	—
Operating temp. range (°C):	0–50	0–50	−18–85	−40–110
Waveband (µm):	8–13	8–14 & 3.43	8–14	8–14
Temperature range (°C):	−50–100 / 200–1000	0–600 & 400–1300	−18–1370	−40–1200
Output (analog):	4–20 mAADC	4–20 mAADC	1 mV/°C or F	1 mV/°C or F
Output (digital):	—	—	RS232	—
Accuracy:	0.1%	±1%	±1%	—

Table 7.2b. (cont.)

Manufacturer:	Chino	Chino	Omega	Omega
Model:	IR-CAB	IR-BAT1P & BAXL1	OS554	OS43H
Sensor type:	Pyroelectric	Thermopile	—	—
Response time (s):	2 & 0.2	0.05 & 1	0.25	0.25
Field of view (FOV, °):	1.55 & 2.1	4.6	~1, ~2, ~3 & ~10	2, 15 & 60
Size (mm):	—	—	Head: 106 × 41 Electronics: 133 × 91	51 × 79
Weight (kg):	1.3	0.22	Head: 0.45 Electronics: 1.2	0.45
Power supply:	24 V DC	12–24 V DC	7–24 V DC	5–26 V DC
Power consumption:	5 VA	60 mA	—	—
Battery life (h):	—	—	—	—
Optical system:	Laser	—	—	—
Price (US\$) (date):	—	—	750 (1999)	1090 (1999)

maximum temperature expected at a volcanic system (i.e., ~1200 °C) so that saturation will not occur. Photon-detector-based instruments also have faster response times than thermal-detector-based instruments, some offering response times as fast as 1 millisecond. This is an attractive feature if measuring high velocity volcanic phenomena, such as explosive events. The explosive event must, however, register a temperature greater than the instrument's lower detection limit (i.e., 300–600 °C). Thus, lower-temperature emissions, or emissions that do not fill the field of view with hot material, may not be detected.

Most thermal-detector-based instruments use thermopiles and detect in the 8–14 μm waveband. This allows detection of cooler surfaces, i.e., surfaces at ambient temperatures. However, the upper limit to the measurement range is not so high, with most detectors being capable of measuring temperatures from –30 to –50 °C up to 500 to 1000 °C. This means that for the highest-temperature volcanic phenomena (at temperatures greater than 500–1000 °C) saturation will occur. A few instruments, though, operate up to the maximum expected temperatures for volcanic systems (i.e., 1200 °C). Being thermopile-based, most have slow response times (of 0.25–1 s), which complicates measurements of high-velocity phenomena where the temperature of the material passing through, or cooling in, the field of view can change faster than the response time, i.e., faster than 0.25 s.

Choice of instrument will depend upon the situation to which the instrument is going to be applied. This requires consideration of the temperature range that the instrument is capable of detecting, and response time (if high-speed phenomena are to be captured), plus size, weight, power consumption and environmental protection if the instrument is to be field-deployed.

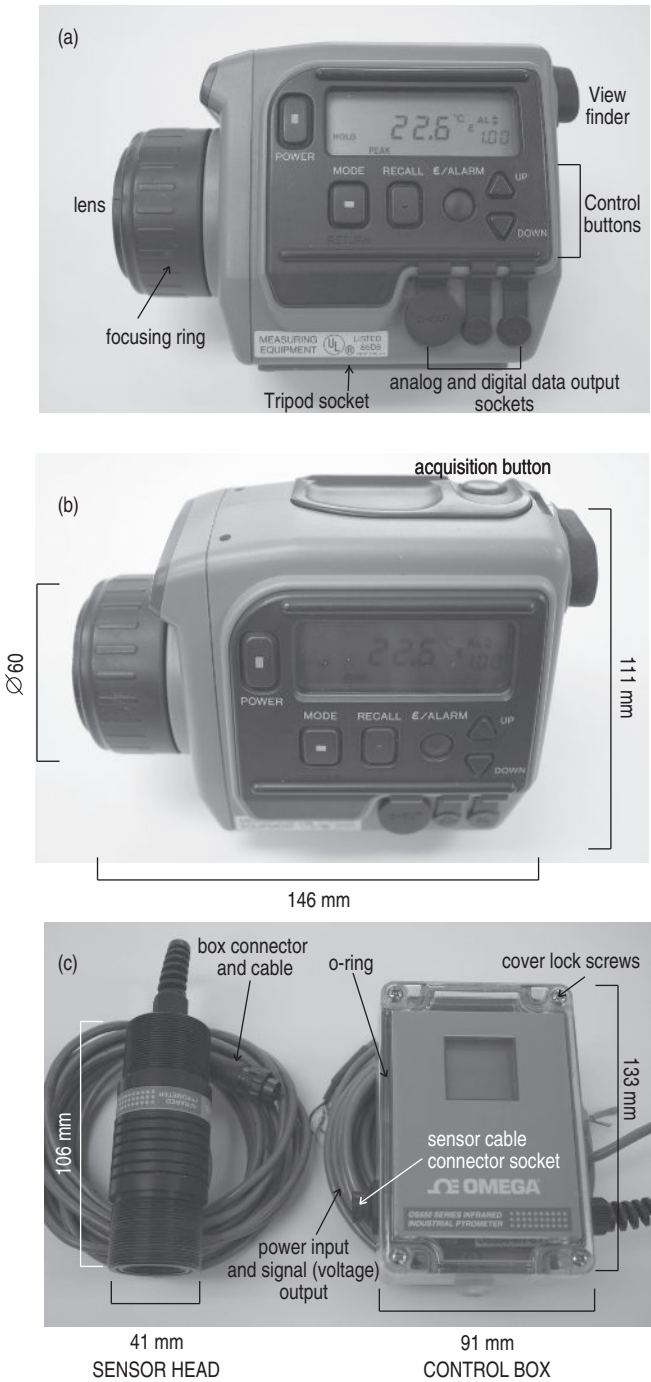


Figure 7.6 Side (a) and oblique view (b) of a hand-held radiometer (Minolta/Land Cyclops 300), showing the control buttons, readout-scree and output terminals, and (c) a fixed-mount radiometer

### 7.2.1 Data output, response time, emissivity and atmospheric effects

All instruments in Tables 7.1 and 7.2 are factory calibrated, allowing temperature measurement to an accuracy of  $\pm 1\%$ . Most instruments display the recorded temperature and provide the option of recalling (in the instrument display) the minimum, maximum and, sometimes, mean acquired over a given measurement session, i.e., for the period for which the trigger has been depressed. The maximum temperature recall feature is particularly useful because it allows scanning of a zone until the highest-temperature feature has been found, or measurement of a fixed point through time until the highest temperature event, or clearest line-of-sight condition (and hence optimum viewing conditions) has been attained.

Data are also output as a continuous voltage that can be sampled at any frequency. For analog output, the output voltage changes by 1 mV for every degree ( $^{\circ}\text{C}$  or  $^{\circ}\text{F}$ ) change in temperature, so that (for example)  $100\ ^{\circ}\text{C} = 100\ \text{mV}$ . This makes for ease of conversion from output voltage to temperature. If connected to a data logger, this allows continuous measurements for tracking short-time-scale (10 ms to 1 s) variations in temperature. However, although the onset time of a temperature change can be measured with a precision of 10 ms, if the temperature of the source is varying at a rate that is faster than the detector response time, then the actual variation in temperature that follows the onset will be complicated by response time effects. That is, for a response time of 0.25 s, the detector will be responding to the current change in temperature as well as all changes that occurred within the previous 0.25 s, and the full response for the current event will not be registered until after 0.25 s.

As with a satellite sensor, the actual temperature recorded by the instrument will be a brightness temperature ( $T^*$ , see Chapter 2). To obtain surface temperature ( $T_{\text{surf}}$ ) the brightness temperature must be corrected for emissivity and atmospheric effects, as well as reflection. For measurements in the short-wave infrared, brightness temperature will have to be converted to a radiance using the Planck Function [ $L(\lambda, T)$ ], and corrected for target emissivity ( $\varepsilon_\lambda$ ), radiation reflected by the target [ $L_R(\lambda)$ ], and atmospheric transmissivity ( $\tau_\lambda$ ). That is, the at-instrument radiance at wavelength  $\lambda$  will be the result of

$$L(\lambda, T^*) = \varepsilon_\lambda \tau_\lambda L(\lambda, T_{\text{surf}}) + L_R(\lambda). \quad (7.6a)$$

To obtain surface temperature, brightness temperature must be corrected as follows:

$$L(\lambda, T_{\text{surf}}) = [L(\lambda, T^*) - L_R(\lambda)] / \varepsilon_\lambda \tau_\lambda. \quad (7.6b)$$

---

Caption for Figure 7.6 (cont.)

(Omega OS554). For the fixed-mount radiometer, all operating controls are inside the weather-proof control box. For the Minolta/Land Cyclops 300 the temperature readout can also be seen in the view finder, where a circle also visible within the view finder defines the measurement area. Although the temperature readout can often obliterate the eye's perception of low-level glow by night, and the viewfinder circle and actual measurement area are not perfectly co-located, they aid enormously with ease of targeting (see Chapter 8 for targeting issues and methodologies).

For detectors operating in the thermal infrared ( $8\text{--}14\ \mu\text{m}$ ) reflected radiation can be ignored, but there will be a contribution from atmospheric emission [ $L_{\text{U}}(\lambda)$ ], so that:

$$L(\lambda, T^*) = \varepsilon_{\lambda}\tau_{\lambda}L(\lambda, T_{\text{surf}}) + L_{\text{U}}(\lambda). \quad (7.7\text{a})$$

In this case, the correction must be modified to correct for  $L_{\text{U}}(\lambda)$  rather than  $L_{\text{R}}(\lambda)$ ,

$$L(\lambda, T^*) = [L(\lambda, T_{\text{bright}}) - L_{\text{U}}(\lambda)]/\varepsilon_{\lambda}\tau_{\lambda}. \quad (7.7\text{b})$$

As with a satellite-based measurement, the amount of up-welling radiance and the value of transmissivity will decrease with path length and altitude, as plotted in Figure 7.7. Thus, measurements made over shorter path lengths and/or at higher altitude will suffer less from atmospheric effects. However, as discussed in Chapter 2, for high-temperature sources ( $>500\ ^{\circ}\text{C}$ ) the contribution of  $L_{\text{U}}(\lambda)$  to the total radiance detected by the sensor operating in the  $8\text{--}14\ \mu\text{m}$  radiance will be negligible. Thus, at these temperatures, the correction can be simplified to:

$$L(\lambda, T^*) = L(\lambda, T_{\text{bright}})/\varepsilon_{\lambda}\tau_{\lambda}. \quad (7.7\text{c})$$

However, even at an altitude of 3 km over a path length of 500 m,  $\tau_{\lambda}$  is still 0.95 (see Figure 7.7b). Thus, if actual surface temperature is required, then the correction must be

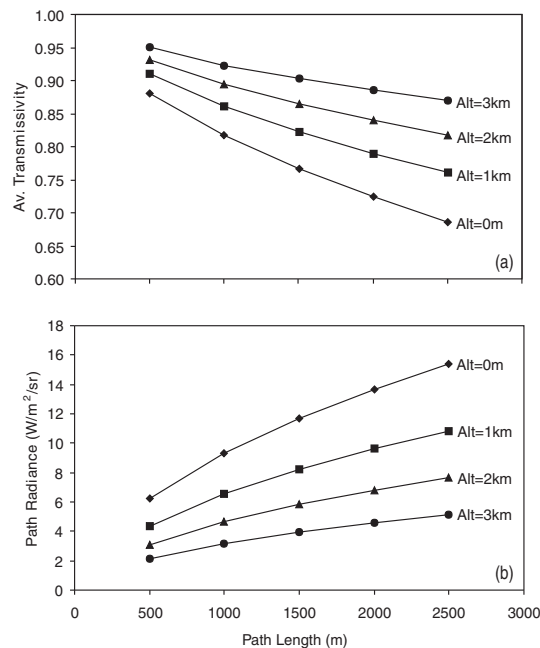


Figure 7.7 Variation in (a) atmospheric transmissivity and (b) up-welling radiation for measurements made over a range of horizontal path lengths and altitudes (between 0 and 3 km) at  $8\text{--}14\ \mu\text{m}$  (this being the typical waveband used by most commercially available thermopiles, see Tables 7.1 and 7.2). Values were obtained using MODTRAN with 1976 US Standard atmosphere and a  $\text{CO}_2$  mixing ratio of 380 ppm·v (see Electronic Supplement 4 for a definition of MODTRAN).

applied. Note, though, for extremely short path lengths (a few meters) we can simplify further to

$$L(\lambda, T^*) = L(\lambda, T_{\text{bright}})/\varepsilon_\lambda. \quad (7.7d)$$

### 7.2.1.1 Detector heating and cooling

A final external effect has been noted during measurements of active lava at high sample rates using an exposed sensor head. That is, when gusts of wind blow over the sensor, the output can vary by a few degrees centigrade due to the cooling effect on the sensor. Likewise, heating of the sensor head by the Sun can cause the output temperature to drift. To minimize this effect, the sensor can be placed in an enclosure or shelter that shields the sensor head from the wind and Sun. Alternatively, use of a model where the sensor head is already well protected inside an instrument body reduces this effect.

### 7.2.2 Field of view

Broad-band radiometers measure the temperature of a single spot on the targeted surface. The instrument angular field of view ( $\text{FOV}_\alpha$ ) defines a measurement cone that opens at angle  $\alpha$ , with line-of-sight distance ( $D_{\text{LOS}}$ ) from the instrument. Where the cone intersects the targeted surface it will define a measurement spot of diameter ( $W_{\text{FOV}}$ ). Thus, the measurement spot size is defined by the instrument's angular field of view and the instrument-to-target distance. For a surface orientated at right angles to the instrument line of sight, the diameter of this spot can be calculated following the simple trigonometry of Figure 7.8:

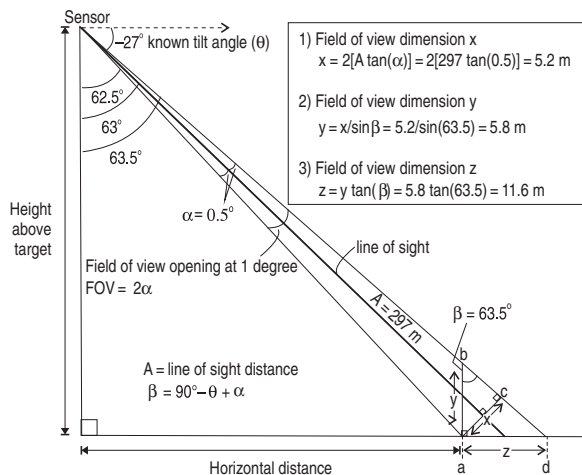


Figure 7.8 Trigonometry for the calculation of measurement spot of diameter ( $W_{\text{FOV}}$ ). The sketch is for a field of view opening at  $\alpha$  degrees, and for an instrument-to-target distance  $A$ , which is tilted downwards at angle  $\theta$ . Solutions are given for a surface orientated: (i) at right-angles to the line of sight, dimension  $x$ , (ii) vertically with respect to the line-of-sight distance, dimension  $y$ , and (iii) horizontally with respect to the line-of-sight distance, dimension  $z$ .

$$W_{\text{FOV}} = 2[D_{\text{LOS}} \tan(\alpha/2)]. \quad (7.8a)$$

If  $\alpha$  is small ( $< 10^\circ$ ), and in radians, this relationship can be approximated by

$$W_{\text{FOV}} \approx D_{\text{LOS}}(\alpha). \quad (7.8b)$$

Hence, the diameter of the measured spot increases with distance and angular field of view: the closer the instrument is to the target, and the smaller the  $\text{FOV}_\alpha$ , the smaller the area measured, as plotted in [Figure 7.9a](#).

For surfaces that are not orientated at right angles to the line of sight, i.e., during oblique targeting, the spot size will have to be calculated following, for example, the relationships given in [Figure 7.8](#). In all cases, for calculation of measurement area using the instrument  $\text{FOV}_\alpha$ , the following parameters need to be known, and therefore measured in the field:

- (i) horizontal and/or slant-line distance from the instrument to the target,
- (ii) vertical distance above the target, and/or
- (ii) instrument tilt angle.

The effect of the field of view area on the temperature retrieved for the target will depend on the area of the target in relation to that of the FOV. The portion of the field of view that the target will occupy ( $p$ ) can be calculated using the area of the target ( $A_{\text{target}}$ ) and the area of the FOV [ $A_{\text{FOV}} = \pi(W_{\text{FOV}}/2)^2$ ] in  $p = A_{\text{target}}/A_{\text{FOV}}$ . As the area of the FOV becomes larger, either due to increasing instrument-to-target distances or increases in the size of the angular FOV used, so (for a stable target area)  $p$  will decrease.

In cases where target area is less than the FOV area (i.e.,  $p < 1$ ), the integrated temperature for the FOV ( $T_{\text{int}}$ ) will be described by a two-component thermal model. In such a case, the target at temperature  $T_h$  will be surrounded by a cooler background at  $T_b$ . This background source will occupy the remainder ( $1 - p$ ) of the FOV, so that the FOV-integrated temperature can be described by:

$$L(\lambda, T_{\text{int}}) = pL(\lambda, T_h) + (1 - p)L(\lambda, T_b). \quad (7.9)$$

This relationship can be used to solve for:

- (i) target temperature, if target size and background temperature are known, or
- (ii) target area ( $A_{\text{target}}$ ) if target and background temperature are known.

The relationship in Equation (7.9) also shows that, for a stable target temperature and area, as instrument-to-target distance or the size of the  $\text{FOV}_\alpha$  increases, so the recorded integrated temperature will decrease as  $p$  also decreases (as plotted in [Figure 7.9b,c](#)).

### 7.3 Review of radiometer measurements of volcanic phenomena

One of the first field-based thermal measurement campaigns at an active volcano was completed by Thomas A. Jaggar in 1917 ([Jaggar, 1917a,b](#)). Jaggar's measurements were a classic example of the perceptive adaptation of technology used in other disciplines to

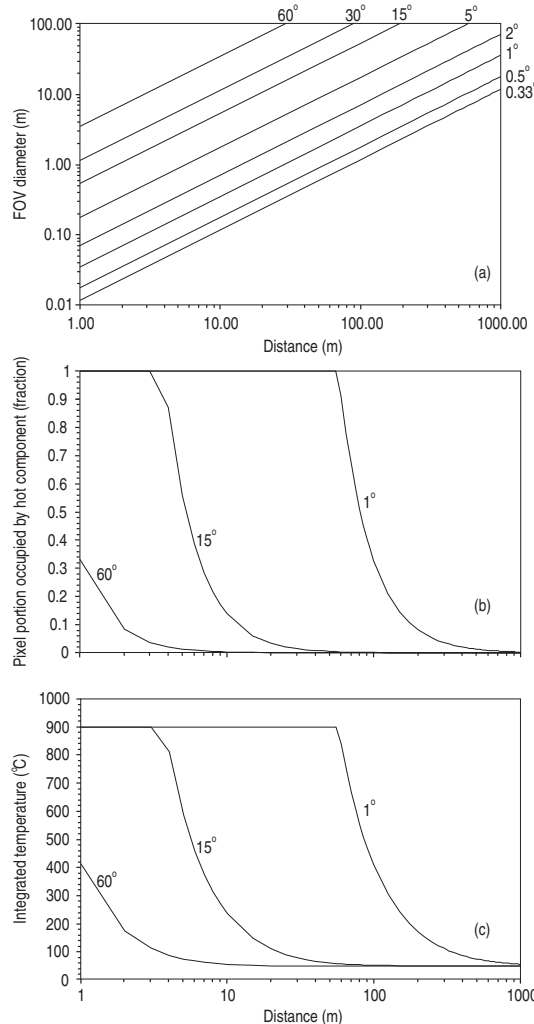


Figure 7.9 (a) Increase in FOV area defined by the instrument angular field of view ( $\text{FOV}_a$ ) for a range of instrument-to-target distances up to 1 km and for a range of typical  $\text{FOV}_a$  used by most commercially available radiometers (see Tables 7.1 and 7.2). (b) Decrease in pixel portion occupied by the target (hot component) with increasing instrument-to-target distance for a 1 m radius circular target centered in a 1°, 15° and 60° FOV. (c) Decrease in pixel-integrated temperature recorded for a 1 m radius circular target at 900 °C set against a 50 °C background and centered in a 1°, 15° and 60° FOV. In all cases, the target temperature is recorded as long as the target fills the field of view, so that the portion occupied by the target is one. Once a distance is reached whereby the target no longer fills the FOV, the portion occupied by the target decreases and the pixel-integrated temperature becomes less than the actual (sub-spatial-resolution) hot target as, following Equation (7.9), increasing amounts of cool background contribute to the integration. This relation can be used to estimate the maximum distance over which a measurement of a small target can be made, and still ensure a “pure” temperature measurement, i.e.,  $p = 1$  so that  $L(\lambda, T_{\text{int}}) = L(\lambda, T_h)$ .

volcanology, where Jaggar used a device commonly used to measure the temperature in potters' kilns (Seger cones) to obtain lava lake temperatures. Jaggar's experiment, which involved driving Seger cones (mounted in steel pipes) through the surface of the Halemaumau lava lake (Kilauea), also illustrates why remote thermal measurements are somewhat less taxing than contact measurements. Jaggar (1917a) states that conditions were "arduous, and the thrusting of a one-inch (2.54 cm) steel pipe into the lava and withdrawing it are by no means simple operations." Underfoot conditions were "hot enough to burn shoe leather, but one could stand on it with hob-nailed boots, by keeping in motion." Radiated heat from the lake surface was extreme and "could be endured for a few minutes, but not for an unlimited time." It was also difficult to penetrate the lake crust, so that optimum conditions for insertion had to be identified. Withdrawal was similarly problematic, where it "commonly took the united strength of four or five men to withdraw a pipe." Finally, there was always the threat that increased lava lake activity would destroy the equipment (and personnel), so that measurements had to be made quickly and watchfully. Such conditions are familiar to anyone who has become uncomfortably hot waiting for a K-type thermocouple plunged into a lava flow to equilibrate, and then been frustrated when the device is destroyed before a reliable measurement is made.

In spite of the measurement difficulties, over five days spanning 11–26 January 1917, Jaggar managed to obtain 37 temperature measurements with a precision of 40 °C. These revealed temperatures of between 590 and 1150 °C, and allowed Jaggar (1917a) to conclude that lake magma just below the surface was relatively cool (750–850 °C), lava in the fountains was hotter (1100–1200 °C), and oxidizing gases at "flaming orifices" gave temperatures of 1350 °C or higher.<sup>1</sup> Jaggar (1917b) was also able to use the data to construct a temperature profile through the uppermost 15 m of the lava lake. This showed lake temperatures increasing from 700–950 °C in the uppermost 5 m of the lake, to 1160 °C at a depth of 11 m.

Today, light-weight, power-efficient hand-held radiometers are capable of providing at least one measurement per second for a targeted surface, allowing temperature measurements with an accuracy of  $\pm 1\%$  from comfortable and safe distances. The distant vantage point also allows measurement of unapproachable features. The drawback is that only surface temperature is measured, so that the lava lake thermal profile obtained by Jaggar (1917b) could not be reproduced using broad-band radiometers. However, contact measurements require contact and discomfort, and so will not be considered in a remote sensing text such as this, which strictly deals with non-contact and high degrees of comfort. The pros and cons of thermocouples are discussed by Macdonald (1972), Archambault and Tanguy (1976) and Pinkerton (1993).

One of the earliest attempts to measure surface temperature at an active volcanic feature using a non-contact instrument actually pre-dates Jaggar's campaign. Daly (in 1909) and then Day and Shepherd (in 1912) both used optical pyrometers to gain temperatures of 940 °C and 1185 °C from lava fountains active at the Halemaumau lava lake (as reported in Jaggar, 1917a). Later Zies, in 1940, used an optical pyrometer from a distance of several miles to

<sup>1</sup> This being a flame temperature.

obtain a temperature of 725 °C for the dacite dome at Santiaguito (Zies, 1941). Optical pyrometers were again used to measure the surface temperature of the lava lake that formed in Kilauea's Makaopuhi crater in March 1965 by Wright *et al.* (1968). Poor weather conditions and fumes hampered measurements, but temperatures obtained from distances of 3–6 m for freshly exposed pahoehoe on the rising lake yielded maximum temperatures of 1085–1190 °C. These were 25–120 °C less than the melt temperature expected from glass chemistry (Wright *et al.*, 1968). This was likely because of the extremely rapid cooling that lava undergoes upon being exposed to the atmosphere, as well as the relatively cool nature of the upper section of an active lava lake, as initially discovered by Jaggar (1917a).

Moxham *et al.* (1965) reported one of the first volcanological uses of a fixed-mount broad-band radiometer, when a Barnes Engineering Co. IT-2 infrared (8–13 μm) radiometer with a 3° field of view was flown on a plane to obtain a temperature profile across the summit of Mt. Rainier. The overflights were made between 15:51 and 15:57 (local time) on 11 July 1964, and revealed thermal anomalies within the summit crater due to fumarolic activity, as marked in the brightness temperature transect of Figure 7.10.

The first ground-based use of a broad-band radiometer at an active volcano was reported by Decker and Peck (1967). They used a Stoll-Hardy HL4 radiometer to obtain surface temperature profiles across the surface of a cooling, inactive lava lake within Kilauea's Alae pit crater, their results being given in Figure 7.11. Measurements were made in November and December 1964 (15–16 months after the 1963 eruption that fed the lake had ended and shortly

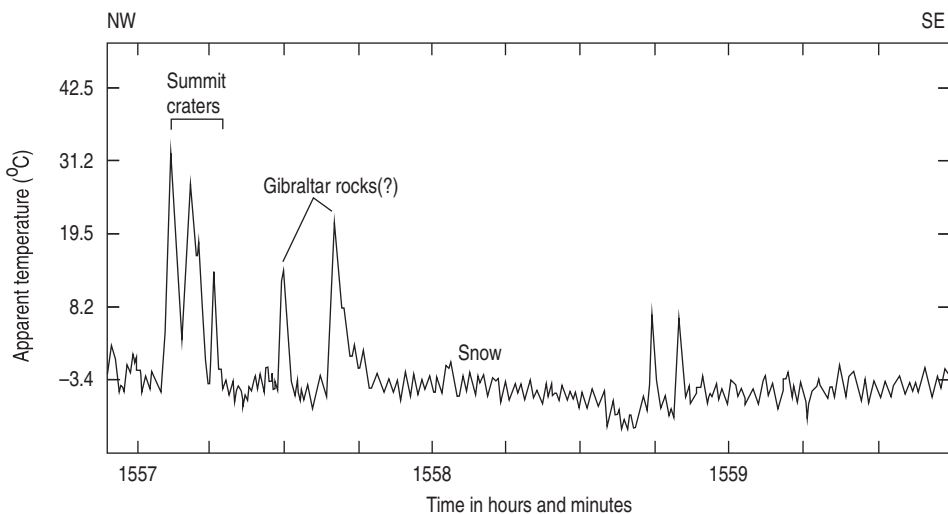


Figure 7.10 Brightness temperature record from an airborne-mounted fixed-mount radiometer flown across the summit of Mt. Rainier, elevation 4392 m (Flight 3, July 11, 1964, time 15:57 Pacific daylight time, altitude 4511 m) [from Moxham *et al.* (1965, Fig. 3)]. Thermal anomalies are apparent as high temperature spikes against a cold (snow/ice) background, and are due to fumarolic activity at the summit craters and snow/ice free surfaces at Gibraltar Rock.

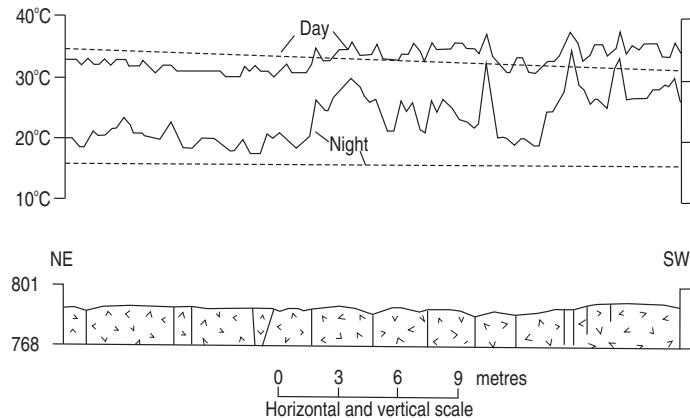


Figure 7.11 Profile showing joint cracks (bottom) and brightness temperature profiles (top) along a line across the center of Kilauea's Alea lava lake [from Decker and Peck (1967, Fig. 3)]. Dashed line marks the temperature levels recorded by base stations at the NE and SW edges of the lake (on ambient ground). We see that, by day, solar heating causes loss of some of the subtle surface thermal anomaly caused by the lava lake's cooling interior (i.e., some temperatures recorded for the lake surface temperature are lower than surrounding ambient surfaces, falling below the dashed line defining the ambient background). By night, the whole transect is anomalous (i.e., all temperatures recorded across the lake surface are higher than surrounding ambient surfaces, falling above the dashed line defining the ambient background). Day-time transect was recorded on November 17, 1964; the night-time transect on December 18, 1964. The lava lake had been active in August 1963.

after the lava body had completely solidified) to estimate the surface-leaving radiative energy flux for the cooling body. A few years later, between December 1969 and March 1970, Birnie (1973) used a Barnes PRT-5 (8–14  $\mu\text{m}$ ) radiometer over distances of 500 to 4000 m to obtain surface temperatures for points across Santiaguito's active lava dome and the surface of Pacaya's McKinney cone (both in Guatemala). These were used to produce thermal contour maps and to estimate radiated heat fluxes, as well as geothermal gradients within Santiaguito's dome. Following this "mapping" method, during August 1972, Lange and Avent (1974) used a Barnes Engineering PRT-5 radiometer ( $\text{FOV} = 0.14^\circ$ , waveband = 9.5–11.5  $\mu\text{m}$ ) to scan the west flank of MT. Rainier, thereby deriving thermal contour maps.

The first attempt to run a radiometer continuously during an explosive event, thereby obtaining a thermal waveform for the emission, was completed by Shimozuru (1971) during strombolian to vulcanian eruptions at Japan's Akita-komaga-take on 2 October 1970. The experiment used a detector sensitive between 1.8 and 2.5  $\mu\text{m}$ , with the output being recorded using a pen-writing milli-voltmeter running at a paper speed of  $3 \text{ mm s}^{-1}$ . The recorded waveforms could be split into two main groups: (i) single eruptions ejecting lava fragments, ash and/or gas to give single-peaked waveforms, and (ii) successive eruptions to give multi-peaked waveforms, as reproduced in Figure 7.12.

In the previous year, Tazieff (1970) had also published thermal waveforms acquired using a continuously recording radiometer during persistent degassing (gas puffing) from a

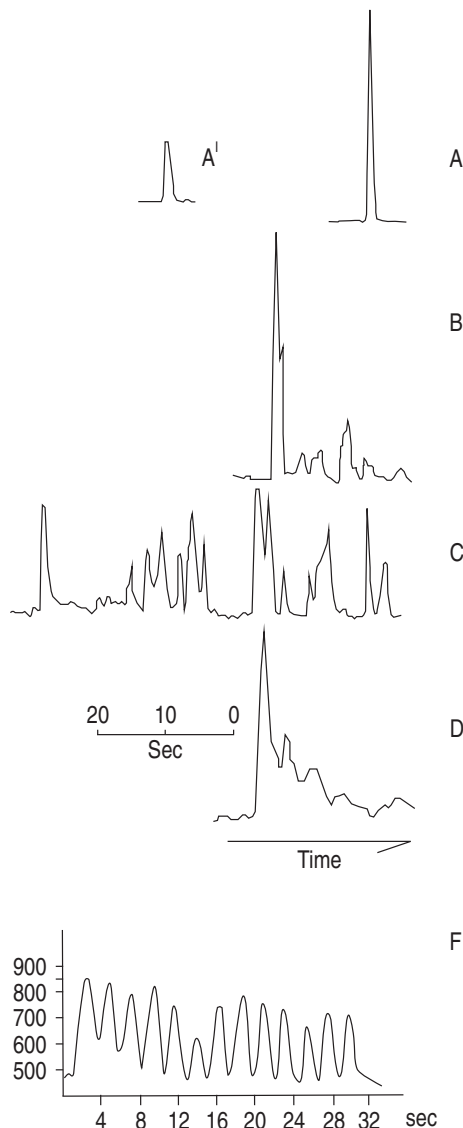


Figure 7.12 Waveforms obtained from continuous radiometer measurements of explosive emissions by Shimozuru (1971) [reprinted by permission from Macmillan Publishers Ltd] and for a degassing (puffing) vent by Tazieff (1970) [reproduced with kind permission from Springer Science and Business Media]. Shimozuru (1971) classified his waveforms between Type A, “single eruption ejecting lava fragments and ash”; Type A’, “small single eruption, mostly of gas”; Type B, “single eruption followed by successive minor eruptions ( $B = A + A'$ )”; Type C, “successive minor eruptions ( $C = nA'$ )”; and Type D, “ejection of lava fragments”. Note that the number of peaks, peak temperature, and form of the recording depends on the number of explosive bursts, and type of material erupted, with the Type D waveform being similar to that typically recorded during a ballistic-dominated explosion at Stromboli, as given in Figure 8.11 of Chapter 8. The Type F waveform is that recorded by Tazieff (1970) at a persistently degassing vent and shows an oscillating signal, with each oscillation recording the passage of a hot burst of gas (see Section 8.3.1 of Chapter 8).

degassing vent on Mt. Etna in 1969. This waveform, as also reproduced in Figure 7.12, was the first published waveform recorded by a continuously recording radiometer. Prior to this, Tazieff and Jatteau (1969) had published (in French) gas puffing waveforms in the *Comptes Rendus Académie des Sciences Paris* using results collected on Etna by a continuously-recording radiometer operating in the 2–5.5 μm region during September 1968. Later, Le Guern *et al.* (1982a) published time series of gas ascent velocity, dynamic pressure and radiometer-derived temperature for gas puffing during the 1969 experiment in the *Journal of Volcanology and Geothermal Research*.

Between 1965 and the end of 2007, at least 60 studies reported results obtained using ground-based broad-band radiometers for explosions, fumaroles and geothermally heated surfaces as well as lava flows, lakes and domes (as reviewed in Table 7.3). Since 2000 there has been a marked increase in the application of ground-based radiometry, with 36 of the 67 studies collated in Table 7.3 occurring over the 35 years prior to 2000 (~1 study per year), and 31 occurring in the seven years since 2000 (4.4 studies per year). This reflects the increased availability of cheap, robust and portable instruments since the mid-1990s.

All studies completed during 1965–2000 can be split into five types, each of which share the theme of the six seminal studies reviewed above.

- Type 1. Measurement of spot temperature (e.g., Wright *et al.*, 1968).
- Type 2a. Spatial surveys using spot temperature measurements (e.g., Birnie, 1973).
- Type 2b. Thermal profile construction (e.g., Moxham *et al.*, 1965).
- Type 3. Time series studies (e.g., Tazieff, 1970; Shimozuru, 1971).
- Type 4. Construction of energy budget inventories (e.g., Decker and Peck, 1967).

### 7.3.1 Type 1: spot temperature measurements

These studies follow the approach of Wright *et al.* (1968) and use broad-band radiometers to obtain the surface temperature of the observed (usually inaccessible) phenomena. As pointed out by Archambault and Tanguy (1976) remote temperature measurements using broad-band radiometers are extremely useful when “approach of magma itself is impossible.” As a result, thermal infrared radiometers have been used to measure the temperature and heat flux of inaccessible features such as:

- lava lake surfaces at Niragongo (Le Guern, 1987) and Erta Ale (Burgi *et al.*, 2002);
- small fountains/strombolian activity at Piton de la Fournaise (Le Guern *et al.*, 1982b);
- active lava fountains and standing waves in lava channels during Mauna Loa’s 1984 eruption (Lipman and Banks, 1987);
- lava dome surface temperatures at Lascar (Oppenheimer *et al.*, 1993a);
- lava channel surface and 'a'a flow front temperatures at Etna (Bailey *et al.*, 2006);
- tube-contained lava visible at skylights on Kilauea (Witter and Harris, 2007);
- incandescent vent temperatures at Stromboli (Harris and Stevenson, 1997a).

Table 7.3. Summary of published ground-based broad-band radiometer deployments, observations, measurements and analyses at active volcanoes, 1965–2007. List does not include ground-based spectrometers, imagers, contact (e.g., thermocouple) measurements, thesis chapters or conference abstracts. Those marked \* were initially reviewed by Francis (1979), and those marked <sup>A</sup> involve use of an aircraft-mounted radiometer. Dashed line separates pre- and post-2000 studies. Studies are listed chronologically with the primary activity type targeted also indicated.

Citation	Volcano	Exp	Fum	LF	LL	LD	Srf	Journal details
Moxham <i>et al.</i> (1965) <sup>A</sup>	Mt. Rainier						✓	USGS Prof. Pap. <b>525-D</b> , D93–D100
Decker and Peck (1967)*	Kilauea				✓			USGS Prof. Pap. <b>575-D</b> , D169–D175
Fujita <i>et al.</i> (1968)	Fuji						✓	Satellite & Mesometeorology Res. <b>72</b> , 32 p
Williams <i>et al.</i> (1968)	Surtsey				✓			Surtsey Res. Prog. Report IV
Wright <i>et al.</i> (1968)	Kilauea					✓		J. Geophys. Res. <b>73</b> (10), 3181–3205
Tazieff and Jatteau (1969)	Etna		✓					C.R. Acad. Sc. Paris, t. <b>268</b> , Serie D, 767–770
Tazieff and Jatteau (1969)*	Erta Ale			✓				C. Hebd. Seanc. Acad. Sci. Paris D <b>268</b> , 767–770
Tazieff (1970)	Etna		✓					Bull. Volcanol. <b>35</b> , 421–438
Shimozuro (1971)	Akita-Komaga-Take	✓						Nature <b>234</b> , 457–459
Zettwoog and Tazieff (1972)	Italy		✓					Bull. Volcanol. <b>36</b> , 1–19
Birnie (1973)*	Pacaya & Santataguito			✓	✓	✓		Bull. Volcanol. <b>37</b> , 1–36
Lange and Avent (1974)*	Mt. Rainier						✓	Bull. Volcanol. <b>38</b> , 929–943
Sekioka and Yuhara (1974)	Owakudani			✓				J. Geophys. Res. <b>79</b> (14), 20530–2058
Archambault and Tanguy (1976)	Etna			✓				J. Volc. Geothem. Res. <b>1</b> , 113–125
Perry and Crick (1976) <sup>A</sup>	Rabaul		✓				✓	In: Volcanism in Australasia, 211–219 <sup>a</sup>
Shimozuru and Kagiyama (1978)	Kusatsu-shirane		✓					J. Volc. Geothem. Res. <b>4</b> , 251–264
Le Guern <i>et al.</i> (1979)	Erta Ale			✓				J. Volc. Geothem. Res. <b>6</b> , 27–48
Brivio <i>et al.</i> (1980)	Vulcano			✓				Bull. Bur. Rech. Geol. Min. Sect. IV, <b>2</b> , 161–168
Kieffer <i>et al.</i> (1981)	Mt. St. Helens					✓		USGS Prof. Pap. <b>1250</b> , 257–277
Kagiyama (1981)	Kirishima			✓				J. Volc. Geotherm. Res. <b>9</b> , 87–97
Le Guern <i>et al.</i> (1982a)	Etna		✓					J. Volc. Geothem. Res. <b>12</b> , 161–166
Le Guern <i>et al.</i> (1982b)	Piton de la Fournaise		✓					J. Volc. Geothem. Res. <b>12</b> , 167–175

Table 7.3. (cont.)

Citation	Volcano	Exp	Fum	LF	LL	LD	Srf	Journal details
Le Guern (1987)	Niragongo		✓					<i>J. Volc. Geotherm. Res.</i> <b>31</b> , 17–31
Lipman and Banks (1987)	Mauna Loa		✓					<i>USGS Prof. Pap.</i> <b>1350</b> , 1527–1567
Brivio <i>et al.</i> (1989)	Vulcano	✓						<i>Volcanic Hazards</i> , Springer-Verlag, 357–371
Oppenheimer and Rothery (1991)	Vulcano	✓						<i>J. Geol. Soc. Lond.</i> <b>148</b> , 563–569
Oppenheimer <i>et al.</i> (1993a)	Lascar			✓				<i>J. Geophys. Res.</i> <b>98</b> , 4269–4286
Oppenheimer <i>et al.</i> (1993c)	Vulcano							<i>J. Volc. Geotherm. Res.</i> <b>55</b> , 97–115
Hon <i>et al.</i> (1994b)	Kilauea		✓					<i>USGS Open File Report 93-342A</i> , 5 p
Hon <i>et al.</i> (1994a)	Kilauea		✓					<i>Geol. Soc. Am. Bull.</i> <b>106</b> , 351–370
Harris <i>et al.</i> (1996)	Stromboli	✓		✓				<i>Acta Vulc.</i> <b>8</b> , 57–62
Keszthelyi and Denlinger (1996)	Kilauea		✓					<i>Bull. Volcanol.</i> <b>58</b> , 5–18
Harris and Stevenson (1997b)	Stromboli & Vulcano	✓	✓					<i>Geophys. Res. Lett.</i> <b>24</b> , 1043–1046
Harris and Stevenson (1997a)	Stromboli & Vulcano	✓	✓					<i>J. Volc. Geotherm. Res.</i> <b>76</b> , 175–198
Harris <i>et al.</i> (1997c)	Etna	✓						<i>Bull. Volcanol.</i> <b>59</b> , 49–64
Harris <i>et al.</i> (1998)	Kilauea		✓					<i>Bull. Volcanol.</i> <b>60</b> , 52–71
Harris and Maciejewski (2000)	Vulcano		✓					<i>J. Volc. Geotherm. Res.</i> <b>102</b> , 119–147
Ripepe <i>et al.</i> (2001)	Stromboli	✓						<i>J. Geophys. Res.</i> <b>106</b> , 8713–8727
Burgi <i>et al.</i> (2002)	Ert Aile			✓				<i>Bull. Volcanol.</i> <b>64</b> , 472–485
Harris <i>et al.</i> (2002)	Santiaguito		✓					<i>Geol. Soc. Am. Bull.</i> <b>114</b> , 533–546
Pinkerton <i>et al.</i> (2002)	Kilauea			✓				<i>J. Volc. Geotherm. Res.</i> <b>113</b> , 159–176
Ripepe <i>et al.</i> (2002)	Stromboli	✓						<i>J. Volc. Geotherm. Res.</i> <b>118</b> , 285–207
Urbanski <i>et al.</i> (2002)	Stromboli	✓						<i>Int. J. Earth Sci.</i> <b>91</b> , 712–721
Harris <i>et al.</i> (2003b)	Kilauea							<i>EOS Trans. AGU</i> <b>84</b> , 409–418
Keszthelyi <i>et al.</i> (2003)	Kilauea			✓				<i>Geophys. Res. Lett.</i> <b>30</b> , 1989
Astier <i>et al.</i> (2004)	Erebus	✓			✓			<i>EOS Trans. AGU</i> <b>85</b> , 97–101
Gottsmann <i>et al.</i> (2004)	Kilauea				✓			<i>Earth &amp; Planet. Sci. Res. Lett.</i> <b>228</b> , 343–353
Gresta <i>et al.</i> (2004)	Etna							<i>J. Volc. Geotherm. Res.</i> <b>137</b> , 219–230

Harris <i>et al.</i> (2004)	Santiaguito	✓						
Johnson <i>et al.</i> (2004)	Santiaguito	✓						
Lautze <i>et al.</i> (2004)	Etna	✓						
Rippey <i>et al.</i> (2004)	Stromboli	✓						
Saherty-Engel <i>et al.</i> (2004)	Santiaguito	✓						
Harris <i>et al.</i> (2005a)	Ert Aile	✓						
Harris <i>et al.</i> (2005b)	Kilauea & Stromboli	✓	✓					
Harris <i>et al.</i> (2005d)	Etna	✓	✓					
Johnson (2005)	Stromboli	✓	✓					
Johnson <i>et al.</i> (2005)	Kilauea	✓	✓					
Rippey <i>et al.</i> (2005b)	Stromboli	✓	✓					
Rippey <i>et al.</i> (2005a)	Stromboli	✓	✓					
Bailey <i>et al.</i> (2006)	Etna		✓					
Jones <i>et al.</i> (2006)	Ert Aile		✓					
Rosi <i>et al.</i> (2006)	Stromboli		✓					
Harris and Rippey (2007)	Stromboli		✓					
Harris and Rippey (2007c)	Stromboli		✓					
Lagios <i>et al.</i> (2007)	Nisyros		✓					
Witter and Harris (2007)	Kilauea		✓					
TOTAL		26	15	16	7	5	5	67

Exp. = Explosions (includes degassing vents, gas puffing, gas pistonning and fountainning), Fum = Fumaroles, LF = Lava Flows & Tubes, LL = Lava Lakes, LD = Lava Domes, Srf. = Surface Temperature.

<sup>a</sup>Full reference = In: *Volcanism in Australasia*, ed. R. W. Johnson. Amsterdam: Elsevier, pp. 211–219.

### 7.3.2 Type 2: spatial surveys (Type 2a) and thermal profiling (Type 2b)

Spatial surveys follow the method of Birnie (1973) and use multiple broad-band radiometer temperature measurements, made across a broad area, to allow thermal mapping. A variant on this is thermal profiling, where the instrument is used to take regular temperature measurements along a line to produce a temperature profile across the surface. This follows the method of Moxham *et al.* (1965), where the characteristic temperature profile is recorded by moving the radiometer at a steady speed across the active phenomena while sampling the temperature at a regular temporal interval. In both cases, making many measurements over the width and breadth of the entire feature allows the spatial variation in thermal structure to be obtained.

Due to aircraft flight speeds, use of an airborne-mounted radiometer in such a way can result in problems. Perry and Crick (1976) noted that the broad-field of view ( $2^\circ$ ) and response time (50 milli-seconds) of the radiometer that they used during overflights of Rabaul during May 1973 resulted in averaging of surface temperatures over small thermal areas. Thus, especially over small thermal features, the velocity at which the radiometer is passed over the phenomena should be minimized.

At fumarole fields, Kagiyama (1981) and Oppenheimer *et al.* (1993c) made multiple radiometer measurements to produce temperature contour maps for an entire fumarolically active area and individual fumaroles, respectively. The fumarole “isotherm” map produced by Oppenheimer *et al.* (1993c) using ground-based Minolta/Land Cyclops instruments (a Cyclops 33 and 52) at Momotombo is reproduced in Figure 7.13. Oppenheimer *et al.* (1993c) also took profiles across individual fumaroles, along lines symmetrical about the vent, to show the spatial gradients in temperature across fumaroles at Momotombo and Vulcano. Profiles typically showed steep decreases in temperature at the vent lip, with a plateau of high temperatures within the vent (see Figure 7.14).

At lava flows, Pinkerton *et al.* (2002) combined the profiling and spatial survey approaches by making six profiles of surface temperature, using a Minolta/Land C52, across a 2.8-m-wide lava stream exiting a tube on Kilauea. Profiles were made every 10 m downstream and used to generate a thermal contour map of the stream surface, as reproduced in Figure 7.15. This map showed a wedge-shaped central zone of high temperatures, contained between an upstream-widening zone of cooler temperatures, a thermal structure consistent with gradual inwards growth of lateral levees to form a tube in a “zipper” fashion.

### 7.3.3 Type 3: time series studies

These studies follow the methods of Tazieff (1970) and Shimozuru (1971) and involve pointing the instrument at a fixed spot and then recording the temperature at high frequencies to record either:

- (i) the thermal history for a static feature, i.e., an object that is stationary within the field of view but which is changing in temperature with time, or
- (ii) the waveform for a dynamic feature, i.e., an object that is moving through the field of view.

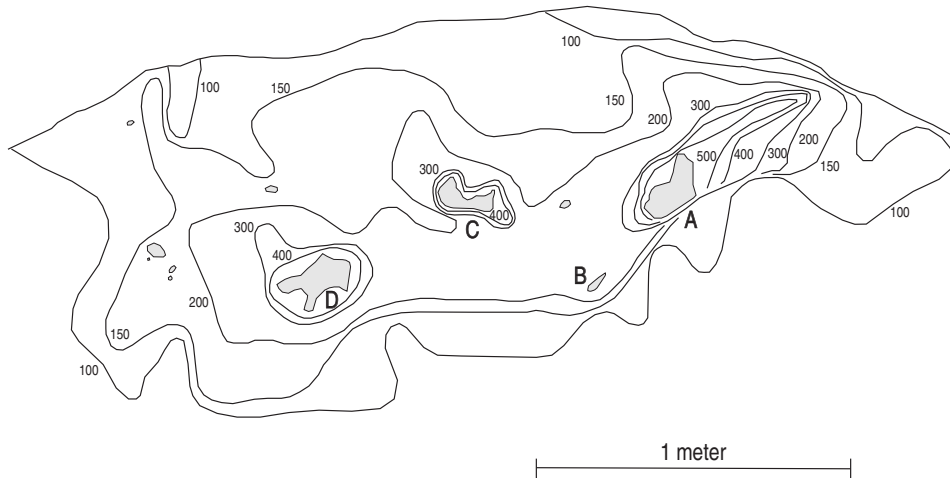


Figure 7.13 Temperature isotherm map of a fumarole at Momotombo produced from multiple radiometer measurements [from Oppenheimer *et al.* (1993c, Fig. 5): with permission from Elsevier] showing the distribution of temperatures around four vents: A ( $880\text{ }^{\circ}\text{C}$ ), B ( $870\text{ }^{\circ}\text{C}$ ), C ( $779\text{ }^{\circ}\text{C}$ ) and D ( $716\text{ }^{\circ}\text{C}$ ).

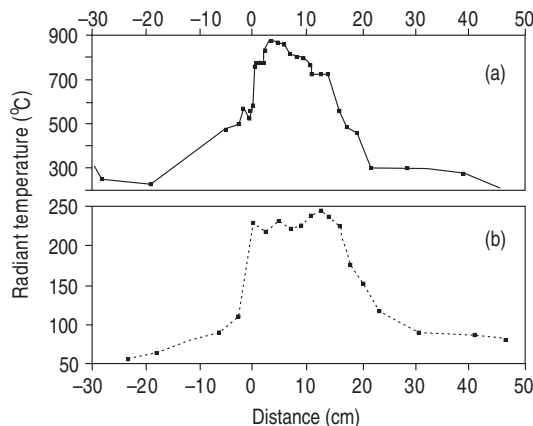


Figure 7.14 Radiometer-derived temperature profiles collected across fumarole vents at (a) Momotombo (measured at  $0.8\text{--}1.1\text{ }\mu\text{m}$  and  $8\text{--}14\text{ }\mu\text{m}$ ) and (b) Vulcano (measured at  $8\text{--}14\text{ }\mu\text{m}$ ) [from Oppenheimer *et al.* (1993c, Fig. 7): with permission from Elsevier]. The higher temperatures at Momotombo allow measurement using a radiometer measuring in the SWIR when measurements in the TIR are saturated.

A nice example of the use of time series measurements for a fixed point to obtain the thermal history of a static feature is the pahoehoe cooling study of Hon *et al.* (1994a,b). As part of this study a Minolta Cyclops 330 was pointed at a fixed point on the surface of a cooling pahoehoe flow. Measurements were made for a period of around 100 hours,

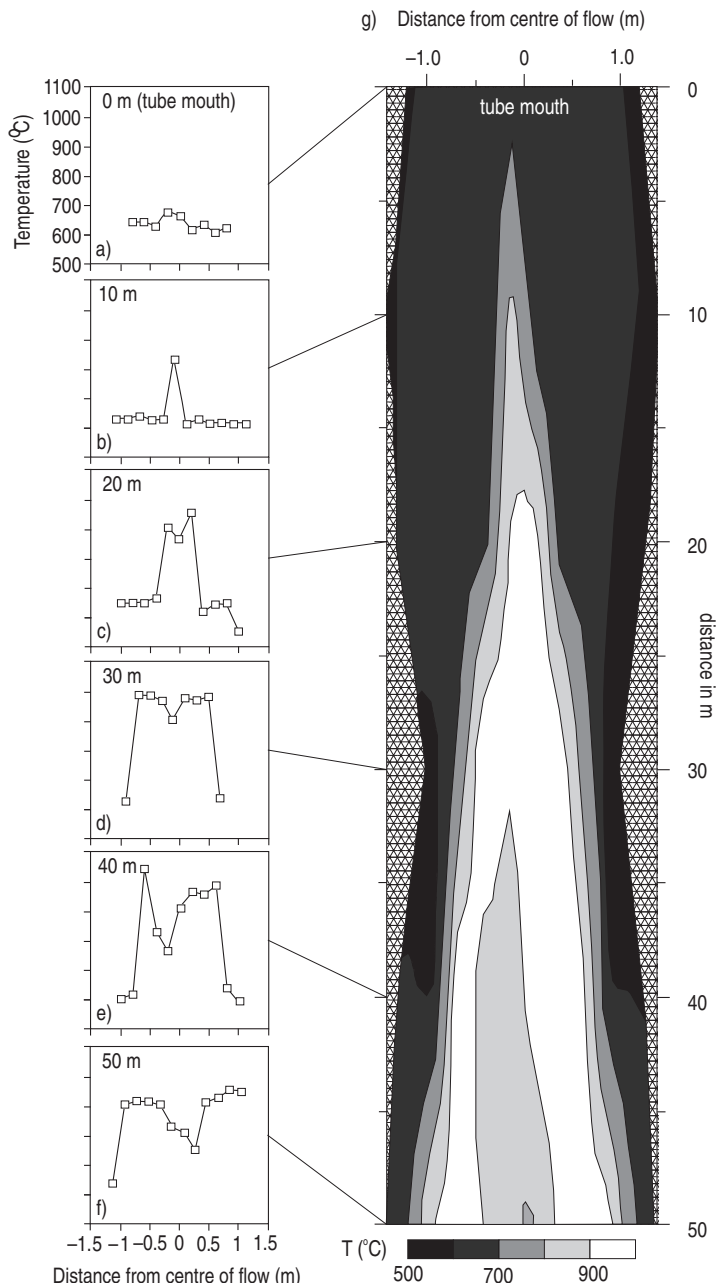


Figure 7.15 Radiometer-derived surface temperature profiles (a–f) produced every 10 m down a lava stream active on Kilauea in January–February 1990, between the stream source (tube mouth = 0 m) and a point 50 m downstream. On the right (in g) is the surface temperature isotherm map produced from those profiles, with the location of each profile marked [modified from Pinkerton *et al.* (2002, Fig. 8): with permission from Elsevier]. Flow direction in (g) is from the top to the bottom of the map.

beginning almost immediately after flow emplacement. The resulting cooling curve showed a logarithmic decay, and has already been used in Chapter 4 (see Figure 4.11a). In a variant on the experiment of Hon *et al.* (1994a,b), Keszthelyi *et al.* (2003) targeted a cooling pahoehoe surface using a tripod-mounted Raytek Raynger 3i as the surface cooled between 1000 °C and 300 °C. Radiometer measurements were completed simultaneously with wind speed measurements made by anemometers suspended 10–30 cm above the flow surface (i.e., within the thermal boundary layer). These data were used to determine the effect of wind on the cooling rate of the flow surface, where gusts of wind were shown to cause enhanced cooling by forced convection, especially during cooling between 550 °C and 400 °C.

In the true spirit of Shimozuru (1971), an increasing number of studies have targeted exploding vents and sampled the radiometer analog output at frequencies of up to ~100 Hz to examine the source and emission dynamics. Strangely, there was a 23-year gap between the inception of the concept of making continuous thermal measurements to understand the dynamics of explosive emissions, and the full development and utilization of this promising approach. The first of these follow up studies did not occur until three experiments on Stromboli during the 1990s, the first being in 1994 by Ripepe *et al.* (2001), the second in 1995 by Harris *et al.* (1996), and a third in 1999 by Ripepe *et al.* (2002). Following the lead of Tazieff (1970) and Shimozuru (1971), such “modern” studies have also been used to understand the dynamics of degassing and explosive activity spanning a range of eruption intensities including:

- gas-puffing (Harris and Ripepe, 2007b; Branan *et al.*, 2008; Gurioli *et al.*, 2008),
- gas-pistoning (Johnson *et al.*, 2005; Marchetti and Harris, 2008),
- strombolian eruptions (Ripepe *et al.*, 2001, 2002, 2005b),
- more powerful strombolian explosions, such as the 5 April 2003 paroxysm at Stromboli (Rosì *et al.*, 2006; Ripepe and Harris, 2008; Harris *et al.*, 2008), and
- ash-rich explosions at Santiaguito (Johnson *et al.*, 2004; Sahetapy-Engel *et al.*, 2008).

#### 7.3.3.1 Lava lake and flow dynamics

Broad-band radiometers can also be pointed at lava lake or flow surfaces as the surface moves through the field of view to reveal the rates and dynamics of the surface motions. At lava tubes, radiometers targeting a fixed point on the tube-contained stream (visible through skylights) have been used to show stability in stream surface temperature (Pinkerton *et al.*, 2002). Harris *et al.* (2005a) used radiometer data collected for a fixed point on the surface of Erta Ale’s lava lake to define two styles of activity: (i) vigorous periods characterized by formation of hot, short-lived, plastic crusts, and during which plates of crust, moved across the lake surface at velocities of 0.1–0.4 m s<sup>-1</sup>, and (ii) sluggish periods characterized by cooler, longer lived, brittle crusts, with slower (0.01–0.08 m s<sup>-1</sup>) surface motions. Likewise, Bailey *et al.* (2006) targeted an active lava channel on Mount Etna with a tripod-mounted Minolta/Land Cyclops 300. The time

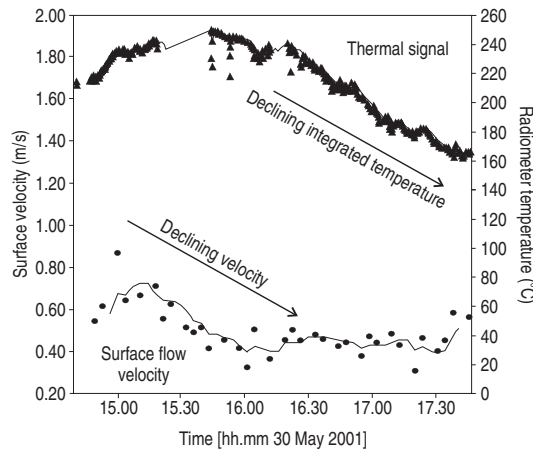


Figure 7.16 Surface temperature time series for the surface of an active lava channel obtained by targeting a  $\sim 2.43 \text{ m}^2$  spot centered in the channel and sampling every 5 seconds using tripod-mounted Minolta/Land Cyclops 300. The velocity plot at the base of the figure shows the relation between surface thermal state and simultaneously measured velocity [modified from Bailey *et al.* (2006, Fig. 7c)].

series revealed how the thermal state of the surface varied with time depending on the surface velocity of lava flowing down the channel, as shown in Figure 7.16.

### 7.3.4 Type 4: construction of energy budget inventories

Decker and Peck (1967) used data from thermal profiles obtained across the surface of the cooling lava lake within Alae to estimate radiative heat flux density ( $M_{\text{rad}}$ ) using measurements of the warm lava surface ( $T_1$ ) and cold (ambient) lava surface ( $T_0$ ) measured at a control (reference) base station at the lake margin in:

$$M_{\text{rad}} = \varepsilon\sigma(T_1^4 - T_0^4). \quad (7.10a)$$

From this, Decker and Peck (1967) concluded that “an approximate solution can be obtained for the night-time radiation heat loss (along) the profile in excess of the ‘normal’ radiative heat loss at the cold base station by using the average radiation temperature along the profile for  $T_1$  (296.5 K) and the constant cold base station temperature (289 K) for  $T_0$ .” This, with a Stefan – Boltzman constant ( $\sigma$ ) of  $1.354 \times 10^{-12} \text{ cal cm}^{-2} \text{ K}^{-4} \text{ s}^{-1}$  and an emissivity ( $\varepsilon$ ) of 0.95 gave:

$$M_{\text{rad}} = (0.95)(1.354 \times 10^{-12})[(296.5)^4 - (289)^4] = 968 \times 10^{-6} \text{ cal cm}^{-2} \text{ s}^{-1}.$$

Because the power function was not linear, Decker and Peck (1967) suggested a better solution could be obtained from integration of the radiation heat flux density from each station along the profile:

$$M_{\text{rad}} = \varepsilon\sigma/n \sum_{i=1}^n (T_1^4 - T_0^4) = 957 \times 10^{-6} \text{ cal cm}^{-2} \text{ s}^{-1}, \quad (7.10\text{b})$$

in which  $n$  was the number of stations along the profile. This method can also be used with spatial survey and single point data, as well as time series data. For example:

- Birnie (1973) used Equation (7.10b) with his spatial survey data to estimate radiative heat flux densities at Santiaguito and Pacaya;
- Oppenheimer *et al.* (1993c) used Equation (7.10a) with point measurements of fumaroles at Momotombo to calculate the radiative heat flux density at fumaroles of differing temperature;
- Keszthelyi and Denlinger (1996) used time series data for cooling pahoehoe flows at Kilauea to calculate the variation in radiative heat flux density with time.

Such broad-band radiometer measurements can also be used to generate more complex heat budget inventories. Such inventories add, for example, convective and conducted heat losses.

#### 7.3.4.1 Heat flux density, heat flux and inventories

Spatial data also allow integration of heat fluxes across the entire feature area, to provide a heat loss estimate in units of watts (rather than watts per meter squared). That is, Equation (7.10a) gives  $M_{\text{rad}}$  in units of radiative energy flux density (in calories per second) per square centimeter. Multiplying by area ( $A$ ) gives radiated energy in units of calories per second [i.e.,  $\Phi_{\text{rad}} = A \varepsilon \sigma (T_1^4 - T_0^4)$ ]. Harris and Stevenson (1997a), for example, used spot temperature and vent dimension measurements for Stromboli's active vents to construct a heat budget for a hot vent that considered radiative, convective and conductive heat losses. The model is given in Table 7.4 and was applied at Stromboli using vent temperatures of 870–940 °C, obtained using a Minolta/Land Cyclops 152 during October 1995, and a typical vent radius of 2 m, measured with a laser range finder.

Likewise, Keszthelyi and Denlinger (1996) provided a complete heat budget for an active pahoehoe lava flow, constrained using broad-band radiometer measurements, and Sekioka and Yuhara (1974) provided a fumarole field heat budget that was constrained using radiometer-based data. However, because portable thermal imaging cameras allow integration of the heat flux over the entire surface of an active feature, thereby permitting a more thorough (i.e., spatially complete) analysis, we consider such inventories in more detail in Chapter 9.

## 7.4 Permanent deployment

Permanent installation of optical instruments to measure vent temperatures was promoted by Zettwoog and Tazieff (1972) following collaborative tests by the French CNRS and Italian CNR on Etna during 1967. In addition, potential acquisition options, deployment possibilities and radiometers for permanent deployments were presented by Moxham in his 1971

Table 7.4. Vent and conduit heat loss model applied to Stromboli using broad-band radiometer spot temperature measurements of incandescent vents by Harris and Stevenson (1997a). Heat is lost from the vent by radiation and convection. Heat is also lost from the empty section of the conduit, between the magma surface and the vent, by conduction.

Term	Derivation	Input value and units	Parameter definition, source and results
Heat radiated from the vent ( $Q_{\text{rad}}$ )	$Q_{\text{rad}} = \pi r^2 \varepsilon \sigma (T_v^4 - T_a^4)$	$r = 2 \text{ m}$ $\varepsilon = 0.9887$ $\sigma = 5.67 \times 10^{-8} \text{ W m}^{-2} \text{ K}^{-4}$ $T_v = 1143\text{--}1213 \text{ K}$ $T_a = 273\text{--}303 \text{ K}$	Measured vent radius at Stromboli Basalt (8–14 μm) emissivity from Salisbury & D'Aria (1992) Stefan–Boltzmann constant Vent temperature measured in October 1995 Night-time ambient temperature measured in October 1995
	$Q_{\text{rad}} (1) = (3.14) (2)^2 (0.9887) (5.67 \times 10^{-8}) [(1143)^4 - (298)^4]$ $Q_{\text{rad}} (2) = (3.14) (2)^2 (0.9887) (5.67 \times 10^{-8}) [(1213)^4 - (298)^4]$	$Q_{\text{rad}} (1) = 1.20 \times 10^6 \text{ W}$ $Q_{\text{rad}} (2) = 1.52 \times 10^6 \text{ W}$	
Heat lost by convection ( $Q_{\text{conv}}$ )	$Q_{\text{conv}} = \pi r^2 h_c (T_v - T_a)$	$r = 2 \text{ m}$ $h_c = 19 \text{ W m}^{-2} \text{ K}^{-1}$ $T_v = 1143\text{--}1213 \text{ K}$ $T_a = 273\text{--}303 \text{ K}$	Measured vent radius at Stromboli Convective heat transfer coefficient calculated from values in Kays & Crawford (1980) Vent temperature measured in October 1995 Night-time ambient temperature measured in October 1995
	$Q_{\text{conv}} (1) = (3.14) (2)^2 (19) [(1143) - (298)]$ $Q_{\text{conv}} (1) = (3.14) (2)^2 (19) [(1213) - (298)]$	$Q_{\text{conv}} (1) = 0.20 \times 10^6 \text{ W}$ $Q_{\text{conv}} (2) = 0.22 \times 10^6 \text{ W}$	

Heat lost by conduction ( $Q_{\text{cond}}$ )	$Q_{\text{cond}} = [2 \pi k L (T_g - T_a)] / \ln (r_a/r_c)$	$k = 3 \text{ W m}^{-2} \text{ K}^{-1}$ $L = 10\text{--}180 \text{ m}$	Wall rock conductivity from Giberti <i>et al.</i> (1992) Empty conduit length, which is the same as the depth to magma surface (from Ripepe <i>et al.</i> , 2001)
		$T_g = (1273+1143)/2 = 1208 \text{ K}$ $T_g = (1273+1213)/2 = 1243 \text{ K}$	Average conduit temperature, obtained from $(T_{\text{magma}}+T_v)/2$ , in which $T_{\text{magma}}$ is the magma surface temperature ( $1000 \text{ }^{\circ}\text{C}$ )
		$T_a = 273\text{--}303 \text{ K}$	Night-time ambient temperature measured in October 1995
		$r_a = 150 \text{ m}$	Distance to ambient temperatures, obtained from the radius of the summit hydrothermal system at Stromboli (from Finizola <i>et al.</i> , 2002)
		$r_c = 2 \text{ m}$	Conduit radius (assumed equal to vent radius)
	$Q_{\text{cond}} (1) = \{(2) (3.14) (3) (85) [(1208) - (298)]\} / \ln [(150)/(2)]$	$Q_{\text{cond}} (1) = 0.34 \times 10^6 \text{ W}$	
	$Q_{\text{cond}} (2) = \{(2) (3.14) (3) (85) [(1243) - (298)]\} / \ln [(150)/(2)]$	$Q_{\text{cond}} (2) = 0.35 \times 10^6 \text{ W}$	

---

review for UNESCO (Moxham, 1971). However, permanent thermal installations at active volcanoes were initially hampered by harsh conditions and equipment bulk. Moxham *et al.* (1973), for example, described deployment of temperature transducers on Mt. Rainier during 1970. The instrument package was encased in an insulated plywood box, with power provided from a solar panel and data transmitted via satellite telemetry. Severe weather conditions caused breakdown after about five weeks. Upon retrieval, although the antenna was free of ice, the wind generator had been destroyed, the solar panel blown over, and the instrument package buried in snow. The interior of the housing was “wet and there was severe corrosion to some hardware.” Moxham *et al.* (1973) concluded, optimistically, that the experiment “though of less-than-desired duration, has demonstrated the feasibility of utilizing satellites for telemetry of volcanic temperatures.”

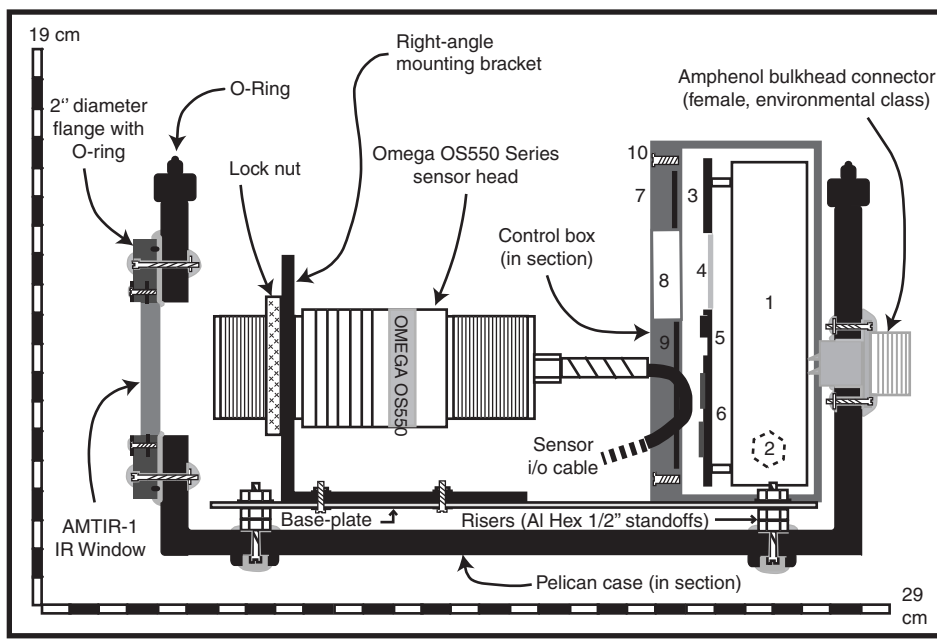
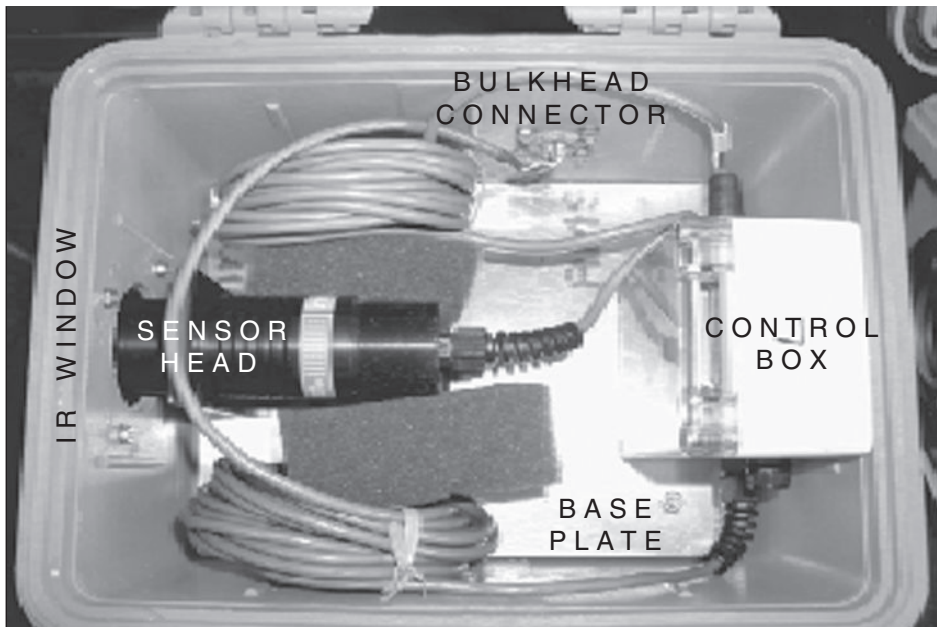
Brivio and Tomasoni (1980) also reported installation of an infrared radiometer at Vulcano during April 1978. They had to modify a (normally manually operated) Barnes Instatherm model 14–220–4. This operated in the 6.5–20  $\mu\text{m}$  waveband, had a sensitivity of  $-10^\circ\text{C}$  to  $60^\circ\text{C}$  and a  $28^\circ$  FOV. The instrument was mounted on a 2.5-m high pillar overlooking the fumarole field, and data were transmitted 5 km back to a reception center on Lipari. However, after a few months, corrosion in the “severe environment” characterized by high salinity, humidity, wind, rain and fumarolic gas, caused the system to fail. The pillar, however, remains in place today.

Advances in equipment and material design, especially the advent of robust, cheap, low-power-consumption, off-the-shelf radiometers, has allowed the successful installation of permanent systems in recent years. Radiometers have been installed in a range of environments, including Kilauea (Harris *et al.*, 2003b), Stromboli (Ripepe *et al.*, 2004) and Erebus (Aster *et al.*, 2004). In the latter two deployments, continuously-acquiring radiometers formed part of multi-component geophysical arrays, also including infrasonic sensors and seismometers.

The DUCK design of Harris *et al.* (2005b) involves an Omega OS554 radiometer mounted in a Pelican case, and viewing the target through a selenium-germanium-arsenide (AMTIR-1) window, as sketched in Figure 7.17. The absorption effect of the window was assessed through blackbody tests, so that a correction to take into account the window’s transmissive properties was derived. This converts temperature obtained by targeting the sensor through the window ( $T_{\text{window}}$ ) to a window-free brightness temperature ( $T_b$ ) following:

$$T_{\text{window}} = 0.745T_b + 11. \quad (7.11)$$

The first deployment involved installation of three sensors on the rim of Kilauea’s Pu’u ‘O'o crater during November 2000. Initial problems involved water-logging due to third-party interference, with visitors either opening the instrument box or the power hub enclosure. The visitor who opened the instrument box kindly closed it again, but only after allowing  $\sim 10$  cm of rain water to collect in the box. The instrument slowly degraded over the following week and required complete replacement. The power hub box probably suffered from being otherwise known as a beer cooler. Thirsty hikers, likely annoyed by finding car batteries



Omega OS550 Series Control Box (Key)

1. Electronics	5. On/off & sleep button	9. O-ring	Input Connectors
2. I/O connectors	6. Function/mode buttons	10. Lock nuts	A-1: Signal + B-2: Signal -
3. Control panel	7. Face plate		C-3: Power (12V)
4. Read-out window	8. Window		D-4: Ground
		Areas of RVT Silicon application	1 2 3 4

Figure 7.17 Plan view picture and schematic cross-section showing the design of radiometer units installed on the rim of Kilauea's Pu'u 'O'o crater between March 2001 and December 2003, and on Stromboli since May 2002 [from Harris *et al.* (2005b, Fig. 5): with permission from Elsevier]. The Stromboli units were still operating as of November 2012. See also color plates section.

rather than ice-cold beer within the cooler, refused to replace the lid out of protest. One of the worst rain storms since records began arrived a few days later, filling the power box with water and causing the power supply to fail. Both problems were fixed, cleverly, by locking the boxes. The use of environmentally designed (plastic) connectors, thoroughly covered in plastic and silicon coatings, also ensured no corrosion or ingress of water into the connectors. After these upgrades, the simple design proved extremely effective, with the Pelican cases successfully keeping out moisture and gas, the interiors and instruments remaining pristine throughout the 2–3 year deployment, despite being within tens of meters of the degassing vents.

The design thus proved reliable and robust, capable of surviving a volcanic environment. The initial target operation period for the Pu'u 'O'o system of one year was easily exceeded, running continuously for a total of 34 months between March 2001 and December 2003, and then only terminating when lack of funds prohibited upgrade of the telemetry system. A sister system has been running continuously on Stromboli between May 2002 and the time of writing (April 2012). This system survived (indeed recorded through) two major explosive events in 2003 and 2006, in spite of being subject to heavy bomb fall and passage of a pressure wave. Again the only problem has been third-party interference, with one visitor dismounting a unit to “borrow” the tripod for his own camera to take photos of the eruptions. The unit, however, missed the explosions that the visitor photographed, recording, instead, ground temperature (for a while) before being remounted by the happy photographer to stare (usefully) at the Mediterranean sea for three days, until the non-expert-installed targeting error was realized.

The DUCK system was also cheap, with the sensor (\$750), mounting bracket (\$50), protective case (\$31) and window (\$240) costs resulting in a total unit cost of \$1071. The units were also light and portable, the complete unit (with internal battery pack and data logger) measuring 28 × 25 × 15 cm and weighing 3.1 kg. The low power requirements and analog data output of the OS554 allowed easy incorporation as part of a multi-parameter instrument hub linked to a master data logger. Such deployments are capable of supporting an increasingly powerful range of monitoring and scientific objectives. However, for installations at insecure and frequently visited sites, the problem of interference by visitors is a real one which needs to be taken into account when designing, installing and protecting a permanently deployed system.

# 8

## Broad-band radiometers II: data collection and analysis principles

Modern broad-band radiometers are cheap, robust and field portable, and can be used either hand-held or tripod-mounted, with some deployment examples being pictured in [Figure 8.1](#). They are quick to set up and easy to operate, making them extremely versatile, as demonstrated by the range of instrument options and applications reviewed in [Chapter 7](#). We next consider some general measurement and analysis considerations that allow data to be appropriately collected and reduced, to support a variety of volcanological applications.

### 8.1 Lava flows and lakes

Targeting an active lava surface from a close, but safe, distance, and recording the maximum temperature can provide a good estimate of actual surface temperature. As Archambault and Tanguy ([1976](#)) pointed out, if emissivity is known and atmospheric effects are minimized by recording many readings and retaining the maximum, then apparent temperatures that approach the true surface temperature can be obtained.

In making such measurements at an active lava flow, it must be remembered that surface temperatures are being collected, and that these may not be equal to the core or interior temperature due to thermal stratification, rapid surface cooling and the presence of a complex surface thermal structure. Thus, temperature differences of between 50 °C and 100 °C were found between surface and interior temperatures for sluggishly moving (<1 km h<sup>-1</sup>) flows on Mt. Etna by Archambault and Tanguy ([1976](#)). It also explains why Wright *et al.*'s ([1968](#)) measurements of Makaopuhi's lava lake were a little lower than expected from glass-chemistry-derived melt temperatures (see [Section 7.3](#) of [Chapter 7](#)). Likewise, emissivity-corrected surface temperatures obtained for active pahoehoe at Kilauea using a Minolta/Land Cyclops 152 by Harris *et al.* ([1998](#)) gave maximum temperatures of 870–1040 °C, compared with a K-type thermocouple interior measurement of 1130 °C. Harris *et al.* ([1998](#)) noted that this was due to the presence of a mesh of filaments forming on the incandescent surface of the flow through which the molten core was exposed. The mesh was caused by stretching of vesicle walls across the inflating surface. Pinkerton *et al.* ([2002](#)) also recorded, using a Minolta/Land Cyclops 52, maximum flow surface temperatures of 1000 °C on an active channel on Kilauea, with newly exposed interior lava rapidly forming a skin at ~900 °C. Such



Figure 8.1 (a) Hand-held use of a Minolta/Land Cyclops 300 to measure fumarole vent temperatures at Vulcano (Italy). (b) Tripod-mounted DUCK-design radiometer deployed to measure temperatures of a tube-contained lava stream passing beneath a skylight at Kilauea. Note: tripod is heavily secured by lava blocks, and cable leads to data logger and power supply. (c) Radiometer array targeting four active vents at Stromboli, where each radiometer is targeting a different vent. Radiometers, from left to right, are: (i) a Raytek 3i LTSC, (ii) a Minolta/Land Cyclops 300, (iii) a Minolta/Land Compac 3, and (iv) a Minolta/Land Cyclops 152. Note: to ensure that the Compac 3 records continuously, a small stone has been forced against the acquisition button using (red) insulating tape. All cables lead to a common data acquisition system. (d) Two Omega OS554s set, with an angular separation of  $5^\circ$  using an aluminum brace, to measure two points vertically stacked within an ascending eruption column. See also color plates section.

features make obtaining an interior temperature by way of a surface temperature measurement difficult. Thus, if measurements of lava lake or flow interior temperature are required, then thermocouple (e.g., Hon *et al.*, 1994a,b), drill based (i.e., drill a hole through the crust and measure the interior temperature using the hole, e.g., Peck, 1978), and geochemical methodologies (e.g., Helz and Thornber, 1987) are more appropriate.

All the same, Pinkerton *et al.* (2002) showed that radiometer-based surface measurements for a high-effusion-rate flow at Kilauea using Land/Minolta C52 were within  $20\text{ }^\circ\text{C}$  of the thermocouple-measured interior temperature. Likewise, the measurements of Witter and Harris (2007) for tube-contained lava streams, targeted through skylights, were within  $30\text{--}40\text{ }^\circ\text{C}$  of the thermocouple-derived interior temperature for nearby pahoehoe flows. Bailey *et al.* (2006) recorded a maximum surface temperature of  $1074\text{ }^\circ\text{C}$  at an Etnean 'a'a flow front, almost  $10\text{ }^\circ\text{C}$

higher than the thermocouple-derived interior temperature of 1065 °C. However, this was a day-time measurement made using an instrument measuring in the shortwave infrared (a Land/Minolta Cyclops 152), so that the measurement was likely contaminated by reflected radiation. Pinkerton *et al.* (2002) noted that temperatures measured in sunlight using such shortwave instruments could be 8 °C to 36 °C higher than the stable temperature (of 1087 °C) measured when the Sun was obscured by cloud. Hence radiometer measurements made in the shortwave infrared may have an additional reflected contribution by day, thereby giving an overestimate of surface temperature. Thus Pinkerton *et al.* (2002) concluded that “if appropriate emissivities are used, the viewing distance is minimized, and the measurements are carried out in the absence of sunlight, then temperatures obtained with the C52 (shortwave) radiometer are within ±10 °C of the maximum surface temperatures of the measured area.”

To obtain the best possible surface temperature measurement using a broad-band radiometer the following suggestions should be considered.

- Reduce the line-of-sight distance to a minimum, so as to minimize the area of the measurement spot and number of thermal components filling the field of view. This will also minimize fume and atmospheric effects, as will recording the maximum obtained over a period of several seconds, even minutes, with the recording period increasing with poorer viewing conditions.
- Measurements in the shortwave infrared should be made in night time or low-light conditions, to cut out contamination from reflected radiation.
- To obtain maximum lava temperatures, the hottest (most active) part of the flow should be scanned for a period of several seconds (even minutes) and the maximum held so as to capture the molten interior at the instant of exposure before complex thermal structures and radiative cooling have had chance to take effect. The maximum temperature measurement of Bailey *et al.* (2006), for example, took around 30 minutes of near-continuous measurement, from an uncomfortable location ~2 m from the flow front, to obtain.
- Temperatures should be corrected using an appropriate emissivity. This can be achieved by converting the brightness temperature to a radiance and dividing by emissivity:

$$L(\lambda, T_{\text{surf}}) = L(\lambda, T_{\text{bright}})/\varepsilon_\lambda. \quad (8.1)$$

Emissivity can be set using broad-band emissivities appropriate for the feature measured, with appropriate values being given in [Table 8.1](#).

- Temperature measurements made over distances greater than ~10 m (at sea-level) should also be corrected for atmospheric effects (see [Chapters 7 and 9](#)).

### **8.1.1 Thermal profiles and contour maps**

To obtain thermal profiles, or sets of points for use in construction of temperature contour maps, measurements can be made at set distances marked out along a measured line. As pictured in [Figure 8.1a](#), the operator stands on a marked spot of known distance from the

Table 8.1. Broad-band (8–14  $\mu\text{m}$ ) emissivity for a range of volcanic surface types. Sample reflectance spectra from which these emissivities are obtained were measured between 2.08 and 14  $\mu\text{m}$  using a Nicolet system FTIR spectrometer by J. Salisbury (Johns Hopkins University) during December 1995. Samples ascribed to Moxham (1971) are taken from Table 1 of Moxham (1971).

Sample	Location	Type	Emplaced	Collected	Description	8–14 $\mu\text{m}$ Emissivity
MU1	Kilauea	Basalt: pahoehoe	1974	10/95	Pahoehoe with glassy surface from 1969–74 Mauna Ulu flow field	0.901
MU2	Kilauea	Basalt: Aa	1969	10/95	'A'a from 1969–1974 Mauna Ulu flow field	0.954
Haw83	Kilauea	Basalt: pahoehoe	10/95	10/95	Glassy pahoehoe ropes from 1983–95 Pu'u 'O'o flow field	0.943
Haw83a	Kilauea	Basalt: pahoehoe	10/95	10/95	Pahoehoe with smooth, glassy surface from 1983–95 Pu'u 'O'o flow field	0.900
Haw83b	Kilauea	Basalt: pahoehoe	10/95	10/95	Pahoehoe with vesicular surface from 1983–95 Pu'u 'O'o flow field	0.909
Etna1	Etna	Basalt: pahoehoe	05/92	09/95	Slaby (spiny) pahoehoe from toe of 1991–93 flow	0.957
Etna2	Etna	Basalt: Aa	05/92	09/95	'A'a clasts from toe of 1991–93 flow just above Zafferana Etna	0.971
Etna3	Etna	Basalt: Scoria	1990	09/95	Scoria from 1990 air-fall field W of summit craters	0.968
Strom	Stromboli	Basalt: Spatter	09/95	09/95	Spatter collected within 50 m of active vent	0.953
StromA	Stromboli	Basalt: Scoria	09/95	09/95	Scoria collected within 50 m of active vent	0.960
StromB	Stromboli	Basalt: Aa	1986	10/94	'A'a clasts from 1985–86 flow field on the Sciara del Fuoco	0.963

Vulc1	Vulcano	Trachyte/ Rhyolite	1888–90	09/95	Trachytic-rhyolitic block erupted during 188–90 eruption	0.975
Vulc2fsh	Vulcano	Sulfur	–	09/95	Yellow sulfur from fumarole within Fossa fumarole field: Fresh surface	0.860
Vulc2wth	Vulcano	Sulfur	–	09/95	Yellow sulfur from fumarole within Fossa fumarole field: Weathered surface	0.909
Moxham (1971)		Andesite			From: Daniels, D. L. (1968)	0.912–0.942
Moxham (1971)		Rhyolite			Integrated 8–14 $\mu$ emissivities of rocks from Mono Craters region (USGS Open File Report)	0.937–0.951
Moxham (1971)		Obsidian (Rhyolitic)				0.868–0.896
Moxham (1971)		Tuff (Rhyolitic)				0.847–0.969

profile zero point, points the radiometer straight down, records for a short period of time, holds the maximum and then moves to the next point, which is a known – measured – distance from the first. Where the surface is unapproachable (as on an active lava channel) there are two options: airborne and oblique measurements. In the airborne approach, the radiometer is pointed vertically, or obliquely, downwards out of a helicopter or aircraft flying over the target. For each measurement, the craft position is recorded using a GPS, the pointing angle of the radiometer is taken and the altitude noted (using, for example, the craft altimeter). These parameters can then be used in simple trigonometric relationships, such as those sketched in [Figure 7.8](#) of [Chapter 7](#), to calculate the location of each measurement point. In the oblique method, the radiometer is tripod-mounted and moved in steps of known angle across, or up and down, the profile. For each measurement the tilt angle of the instrument is recorded, as well as the line-of-sight distance (using a laser range finder) to the measurement point. Horizontal distance is then obtained from the sine of the tilt angle multiplied by the line-of-sight distance.

### **8.1.2 Fixed-point time series**

For obtaining a time series for a fixed point on a lava flow or lake surface, the instrument has to be tripod-mounted, thereby ensuring measurement of a fixed and stable area. Especially when a light weight tripod is used, the tripod should be buried in rocks to ensure stability, and that the instrument does not get blown over, as in [Figure 8.1b](#). If the surface is stationary, as at a stagnant, cooling lava flow or lake, then a time series of the cooling, or heating, of that surface will be obtained. In such a case, the rate of change of the integrated temperature ( $\delta T_{\text{int}}/\delta t$ ) will equate (if variations in atmospheric absorption and emission, or surface reflection and emissivity, can be discounted) to the rate at which the surface temperature ( $\delta T_{\text{surf}}/\delta t$ ) is changing.

#### *8.1.2.1 Mixed pixels and surface motion*

For a mixed field of view such as a surface composed of relatively cool crust (at temperature  $T_{\text{crust}}$ ) broken by high-temperature cracks (at temperature  $T_{\text{crack}}$ ), the integrated temperature (corrected for emissivity and atmospheric effects,  $T_{\text{int}}$ ) can be written:

$$L(\lambda, T_{\text{int}}) = pL(\lambda, T_{\text{crack}}) + (1 - p)L(\lambda, T_{\text{crust}}), \quad (8.2a)$$

where  $p$  is the field of view (FOV) portion occupied by the hot crack. Thus, the integrated temperature will change depending on the crack area ( $p = A_{\text{crack}}/A_{\text{FOV}}$ , where  $A_{\text{crack}}$  is the crack area), crust temperature and/or crack temperature.

Now take two consecutive measurements from a field of view centered on an active lava channel (or lake) through which lava with a cracked crust is moving, with the two measurements separated by a time difference of  $\Delta t$  ( $= t_2 - t_1$ ). At time 1 ( $t_1$ ),  $T_{\text{int}}$  can be written

$$L(\lambda, T_{\text{int}1}) = p_1L(\lambda, T_{\text{crack}1}) + (1 - p_1)L(\lambda, T_{\text{crust}1}). \quad (8.2b)$$

At time 2 ( $t_2$ ) a new set of crust and crack conditions may be appropriate for the field of view, i.e.,

$$L(\lambda, T_{\text{int}2}) = p_2 L(\lambda, T_{\text{crack}2}) + (1 - p_2) L(\lambda, T_{\text{crust}2}). \quad (8.2c)$$

The time derivative for the two measurements can be obtained from subtracting the two measurements and dividing by the time difference between the two (i.e.,  $\delta T_{\text{int}}/\delta t = T_{\text{int}1} - T_{\text{int}2} / \Delta t$ ). In short, for a two-component surface passing through a FOV the integrated temperature will change as one (or all of)  $T_{\text{crack}}$ ,  $T_{\text{crust}}$ , or  $p$  changes. We now take three simple cases to illustrate the way in which the rate of change in the thermal signal can be related to the dynamics of the flow.

### 8.1.2.2 Case 1: stagnant and cooling surface

For a stagnant lava flow or lake surface, the crust will be stationary and cooling. In this case, the presence of an ageing crust, where crust temperatures are declining following Equation (4.32a) and crust coverage is becoming increasingly extensive (i.e., cracks are becoming sparser and  $p$  is declining), will cause the integrated temperature to decline with time. When the crust becomes complete ( $p = 0$ ),  $T_{\text{int}}$  will equal  $T_{\text{crust}}$ . In the case of Hon *et al.* (1994a,b), where a stagnant pahoehoe lobe was targeted with a broad-band radiometer, a cooling curve was obtained for the condition  $p = 0$  so that the rate of decline in crust temperature was recorded, i.e.,  $\delta T_{\text{crust}}/\delta t = \delta T_{\text{int}}/\delta t$  (see Figure 4.11a of Chapter 4).

Crust foundering, overturn and/or crack opening will thermally renew the surface, i.e., it will destroy old, cooled crust and will replace it with fresh, hot material of the exposed upper layer of the molten lava body. While these processes will cause  $T_{\text{crust}}$  to increase, they will also cause  $p$  to increase as new zones of hot material are created. Thus, integrated temperature will also increase as the crust becomes more broken and/or replaced by hotter material from the interior of the flow or lake. If all crust is removed ( $p = 1$ ),  $T_{\text{int}}$  will equal  $T_{\text{crack}}$ . Such thermal renewal will be followed by a new cooling curve as the exposed surface immediately begins to cool.

### 8.1.2.3 Case 2: an ageing crust on a moving surface

We next take a case where a crust of increasing age, and hence (logarithmically) decaying temperature, is moving through a field of view. This will also cause the integrated temperature to change. As crust moves away from the source, it will cool so that the recorded crust temperature depends on distance from the source and flow velocity. The recorded temperature at this fixed point will thus be modified if the velocity changes. For example, take a spreading center at a lava lake. Such centers are sources of crust where up-welling lava from the lake interior arrives at the surface to create new crust. As the crust moves away from the spreading center it increases in age and cools, surface temperature decaying logarithmically with time following Equation (4.32a) of Chapter 4. If the radiometer FOV remains fixed at a given distance from the spreading center and the rate of spreading remains constant, then the temperature should remain stable because crust of the same age (and hence temperature) will always be passing through the FOV. If the spreading center begins to move away from the FOV then crust of increasing age (and

hence decreasing temperature) will enter the FOV, the crust having had to travel a greater distance and hence having had a greater amount of time to cool. Likewise, if the velocity at which the crust moves away from its source decreases, the crust will take longer to reach the FOV. It will thus again have had a greater amount of time to cool so that lower temperatures will be recorded.

Following Harris *et al.* (2005a), the expected crust temperature at distance ( $D_S$  in m) from the source can be calculated by substituting  $t$  in the Equation (4.32a) relationship with  $D_S/V$ ,  $V$  being the velocity at which the crust is moving, so that:

$$T_{\text{crust}} = -140\log(t) + 303 = -140\log(D_S/V) + 303. \quad (8.3a)$$

Note that time is in hours, thus velocity must be input in units of meters per hour. Now, take a measurement point located 100 m down-channel from the source. By the time stable (non-renewing) crust, moving at a velocity of  $0.5 \text{ m s}^{-1}$  ( $1800 \text{ m h}^{-1}$ ) reaches the field of view, it will be 200 s (0.056 h) old and will have a surface temperature of  $\sim 480^\circ\text{C}$ . If velocity increases to  $1 \text{ m s}^{-1}$  ( $3600 \text{ m h}^{-1}$ ), the more rapid transit over the 100 m distance will mean that it will be younger (100 s or 0.028 h), and thus hotter ( $\sim 520^\circ\text{C}$ ), by the time it reaches the FOV. If we move the measurement zone to a distance of 1000 m from the source, transit time (at  $1 \text{ m s}^{-1}$ ) will increase to 1000 seconds (0.278 h) and the surface will have time to cool to  $\sim 380^\circ\text{C}$ . Consequently, crust temperature will decline with distance from the source and transit time, as plotted in Figure 8.2. Simply, for a set distance from the source, the faster the transit time the shorter the cooling time, and so the higher the recorded temperature. If distance from the source increases, or velocity decreases, so recorded temperature will decrease.

Take a second example, where velocities for lava flowing down an active lava channel begin to decline. Given crust formation at the channel source, declining velocity will cause the crust transit time to the FOV (at a fixed position down-channel from the source) to increase. Hence increasingly mature and thick (i.e., older and cooler) crusts will arrive in the FOV, causing integrated temperature to decline. An increase in flow velocity will reverse the trend. Increases in flow velocity may also enhance foundering, tearing and other process that serve to increase the portion of the FOV occupied by the high-temperature (uncrusted) component, so as to thermally renew the surface and thus increase the recorded integrated temperature further. Nevertheless, the Equation (8.3a) relation may be used to assess the cooling and velocity conditions, and any changes in these conditions, where we have a stable, uncracked crust moving away from the source.

#### *8.1.2.4 Case 3: a cracked crust on a moving surface*

We now take a simple case where the flow is moving through the FOV, the crust and crack temperatures are constant, i.e., in Equation (8.2)  $T_{\text{crack}1} = T_{\text{crack}2}$  and  $T_{\text{crust}1} = T_{\text{crust}2}$ . The rate of change in the integrated temperature is now a function of  $\delta p/\delta t$  (see Equation (8.2)). Thus, for a thermal source entering (or leaving) the field of view, the rate of change in integrated temperature will depend on the rate (or velocity) at which the hot component (i.e., the crack) travels into, and then out of, the field of view. That is, the rate of change of the fractional

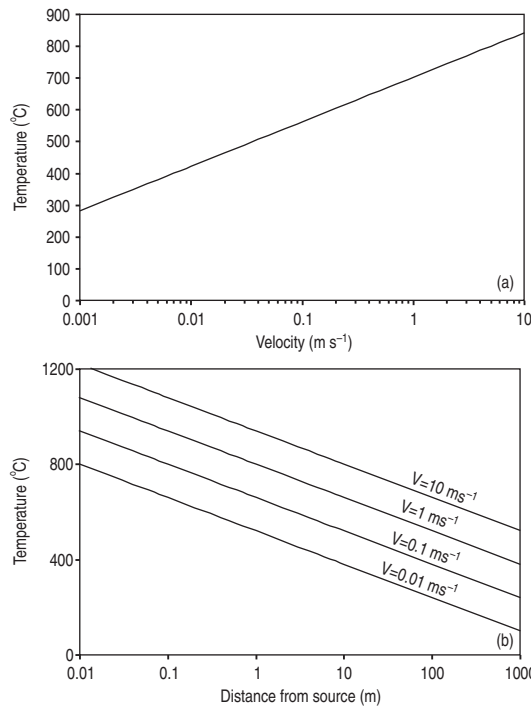


Figure 8.2 (a) Theoretical increase in crust temperature for a measurement point located 5 m from the lava emission source. Increase is plotted in terms of velocity at which the surface is moving away from the source. (b) Theoretical decrease in crust temperature with distance from source. Decrease is plotted for surfaces moving away from the source at a range of velocities between 0.01 and 10 m s<sup>-1</sup>. At any given point, the faster the transit time, the less time for cooling and, hence, the hotter the surface.

coverage of cracks ( $p$ ). For faster-moving sources, the rate at which the integrated temperature will rise and fall as a crack passes in and out of the field of view will thus be faster.

Picture entry of an isothermal high-temperature crack into the field of view. As this hot surface enters the field of view, it increases the FOV fractional coverage for the hot component in Equation (8.2) at the expense of the lower-temperature component that is leaving it, so that the integrated temperature increases. The integrated temperature will increase at a rate dependent on the velocity at which the hot component is entering the FOV, to reach a peak when the hot component fills the FOV (in terms of Equation (8.2),  $p$  will have increased to one, so that  $T_{\text{int}} = T_{\text{crack}}$ ). The time taken to reach the peak will equate to the time the leading edge of the hot crack took to cross the field of view. Thus, if the width of the field of view is known ( $W_{\text{FOV}}$ ), then the velocity at which the crack moved across the field of view ( $V$ ) can be obtained from dividing by the time taken to move from background to peak signal ( $\delta t_{\text{peak}}$ ), i.e.,

$$V = W_{\text{FOV}} / \delta t_{\text{peak}}. \quad (8.3b)$$

### 8.1.2.5 Case Study: Erta Ale

The example taken from Erta Ale lava lake and given in [Figure 8.3](#) illustrates these concepts well. During the experiment a  $1^\circ$  FOV Omega OS554 was pointed at the lake surface and left to record for a period of  $\sim 72$  h while the lake cycled through periods of vigorous and sluggish activity. Over the  $\sim 130$  m line-of-sight distance, this meant that the integrated temperature for a  $\sim 2.3$  m diameter spot was recorded.

Vigorous and sluggish activity, recorded and confirmed using simultaneous video and photographic records, resulted in two distinctive sets of thermal properties, one associated with high surface motions, the second with low velocity conditions. The typical time series recorded during a vigorous period is given in [Figure 8.3a](#). Surface motions were rapid and rates of surface renewal high, so that crust temperatures (and hence  $T_{\text{int}}$ ) were relatively high (mean  $T_{\text{int}} = 540$  °C). Cracks passing through the field of view at relatively high velocities resulted in many narrow spikes in the thermal signal. Examination of the spikes showed that they had a relatively short waxing phase, the typical  $\delta t_{\text{peak}}$  of 24–69 s yielding velocities of 3.4–12.4 cm s $^{-1}$  (see [Figure 8.3c](#)). The typical time series recorded during a sluggish period is given in [Figure 8.3b](#). During sluggish periods, surface motions decreased, as did rates of surface renewal, so that crust temperatures (and hence  $T_{\text{int}}$ ) were relatively low (mean  $T_{\text{int}} = 340$  °C). Cracks passing through the field of view at relatively low velocities resulted in rarer, wider, spikes in the thermal signal, with the spikes having a long waxing phase, the typical  $\delta t_{\text{peak}}$  of 104–117 s yielding lower velocities of 2.2–3.2 cm s $^{-1}$  (see [Figure 8.3c](#)).

These characteristic thermal properties for vigorous and sluggish flow are summarized in [Table 8.2](#). This table also summarizes the thermal properties, and associated lava flow dynamics, for a radiometer time series collected during periods of high- and low-velocity flow in a lava channel, this being the time series given in [Figure 7.16](#) of [Chapter 7](#).

## 8.2 Vents and fumarole fields

Although the presence of condensed gas, often in variable amounts, complicates measurements at degassing vents, the measurement principle at active vents and fumaroles is nearly identical to those applied at active lava flows. Simply, line-of-sight distances need to be minimized, maximum temperature recorded over a period of several seconds, or even minutes, should be held, and brightness temperatures must be corrected for emissivity and atmospheric effects.

The main problem is that gas being emitted by the source will condense and reduce the radiometer-recorded vent temperature by causing path-length absorption of the signal. Variations in wind speed and condensation will thus cause the recorded temperature to vary over short time periods ([Oppenheimer \*et al.\*, 1993c](#)). As a result, variation of several tens of degrees centigrade over a few seconds can be recorded at a vent whose temperature may actually be stable, as can be seen in the vent temperature record of [Figure 8.4](#). However, given a stable vent temperature, then the maximum temperature obtained during continuous measurements over periods of several seconds can approximate the contact (thermocouple-derived) temperature for the vent. This is illustrated by the 30-minute record of simultaneous

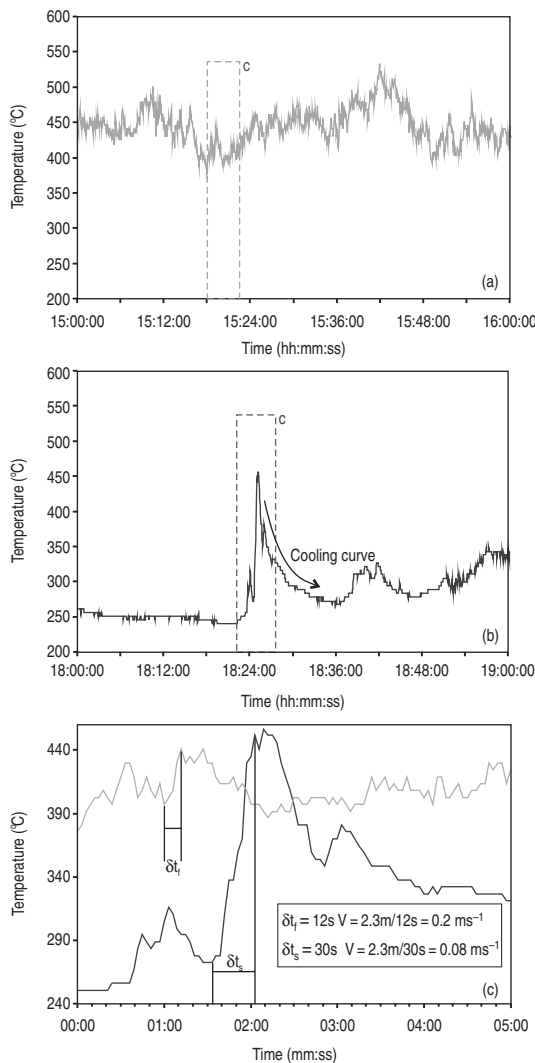


Figure 8.3 Omega OS554 time series for the temperature of a fixed point on the surface of Erta Ale's lava lake. Visual observations confirm that spikes in the record are due to passage of hot cracks across the radiometer field of view. Parts (a) and (b) give hour-long records for the lake surface during (a) a period of relatively fast surface movement ("vigorous" activity), and (b) a period of relatively slow surface movement ("sluggish" activity). In (c) five-minute-long segments of the hour-long records have been magnified to show that (i) thermal levels are higher, but spike amplitudes are lower, during periods of relatively fast surface movement, and (ii) the onset of each spike is shorter and the spike width narrower during the fast period. The spike magnified for the slow surface movement period of (b) is followed by a well-developed cooling curve. Time windows magnified in (a) and (b) are located using the labelled dashed-line box in (a) and (b).

Table 8.2. *Expected thermal conditions for (I) an active lava lake and (II) an active channel-contained lava flow during vigorous (high-velocity) and sluggish (low-velocity) flow. Recorded flow conditions for the lava lake case are those measured during operation of a broad-band radiometer at Erta Ale by Harris et al. (2005a); those for the lava channel were those measured during the broad-band radiometer deployment of Bailey et al. (2006) at Mt. Etna.*

(I) LAVA LAKE

Parameter	Expected			Conditions: recorded
	Vigorous	Sluggish	Vigorous	
<b>Relative flow rates</b>				
Volume flux	High	Low	$0.1\text{--}0.8 \text{ m}^3 \text{ s}^{-1}$	$< 0.1 \text{ m}^3 \text{ s}^{-1}$
Surface velocity	High	Low	$0.034\text{--}0.124 \text{ m s}^{-1}$	$0.022\text{--}0.032 \text{ m s}^{-1}$
<b>Flow dynamics and crust characteristics</b>				
Degree of foundering	High	Low	Vigorous surface motions maximize the rate at which high temperature cracks move through the FOV. Crust renewed at active spreading centers at high rates which maximizes surface thermal renewal	Sluggish surface motions minimize the rate at which high-temperature cracks move through the FOV. Low rates of spreading minimize surface thermal renewal
Surface thermal renewal rate	Rapid	Slow		
Degree of crust tearing	High	Low		
Crack coverage ( $p$ )	High	Low		
<b>Thermal signal characteristics</b>				
Crust temperature	High	Low	Young, thin, high-temperature crusts	Mature, thick, low-temperature crusts
Integrated temperature	High	Low	540 °C	340 °C
Rate of signal change	Fast	Slow	Signal rises rapidly: oscillations have steep slopes and narrow peaks	Signal rises slowly: oscillations have gentle slopes & broad peaks
$\delta t_{\text{peak}}$	Short	Long	24–69 s	104–117 s

Table 8.2 (cont.)

Parameter	(II) CHANNEL-CONTAINED LAVA FLOW			
	Expected		Conditions: recorded	
	Vigorous	Sluggish	Vigorous	Sluggish
<b>Relative flow rates</b>				
Volume flux	High	Low	0.7 m <sup>3</sup> s <sup>-1</sup>	0.1 m <sup>3</sup> s <sup>-1</sup>
Surface velocity	High	Low	0.29 m s <sup>-1</sup>	0.05 cm s <sup>-1</sup>
<b>Flow dynamics and crust characteristics</b>				
Degree of foundering	High	Low	Fast transit times lead to relatively high crust temperature in the FOV, and rapid passage of cracks. Crust renewed at shear zones, where tearing leads to high rates of surface thermal renewal	Slow transit times lead to relatively low crust temperature in the FOV, and slow passage of cracks. Low degrees of tearing and surface thermal renewal
Surface thermal renewal rate	Rapid	Slow		
Degree of crust tearing	High	Low		
Crack coverage ( $p$ )	High	Low		
<b>Thermal signal characteristics</b>				
Crust temperature	High	Low	Young, thin, high temperature crusts	Mature, thick, low-temperature crusts
Integrated temperature	High	Low	220–280 °C	160–200 °C
Rate of signal change	Fast	Slow	Signal rises rapidly: oscillations have steep slopes and narrow peaks	Signal rises slowly: oscillations have gentle slopes and broad peaks
$\delta t_{\text{peak}}$	Short	Long	Short	Long

thermocouple and radiometer measurements for a fumarole of stable temperature given in Figure 8.4. The radiometer (a Land/Minolta Cyclops 300) was tripod-mounted (for stability) and aimed at a fumarole over a line-of-sight distance of  $\sim 3$  m. A K-type thermocouple was placed in the same fumarole and, after the thermocouple signal had stabilized, both instruments were sampled at a rate of one reading every second. The vent temperature recorded by the thermocouple was broadly stable, with a mean of  $157^\circ\text{C}$  and a standard deviation of  $1^\circ\text{C}$ . Fluctuations were likely the result of wind. Given that the thermocouple was placed in the fumarole mouth, gusts of wind would have temporarily cooled the exposed bare wires of the thermocouple. The radiometer showed much greater variability, with temperature declining to  $115\text{--}120^\circ\text{C}$  for short periods. This reduced the mean for the radiometer-derived time series to  $148^\circ\text{C}$  and increased the standard deviation to  $8^\circ\text{C}$ . This was the result of variations in condensation, wind blowing fume away (to improve line-of-sight conditions) or fume gathering above the fumarole in windless conditions (to cause line-of-sight conditions to deteriorate). However, the maximum recorded during clearest conditions by the radiometer ( $165^\circ\text{C}$ ) compares well the thermocouple recorded maximum ( $161^\circ\text{C}$ ). In fact, if we plot the radiometer-recorded maximum for each minute-long segment of the record we obtain a stable time series that compares excellently with that recorded by the thermocouple (see Figure 8.4).

The radiometer-recorded maximum temperature in Figure 8.4 is actually a little higher than the thermocouple-recorded maximum, with the mean of the radiometer maximum for each minute-long window ( $\pm 1\sigma$ ) being  $160 \pm 2^\circ\text{C}$ , compared with the thermocouple mean ( $\pm 1\sigma$ ) of  $157 \pm 1^\circ\text{C}$ . This could be the result of two factors: error in the emissivity correction

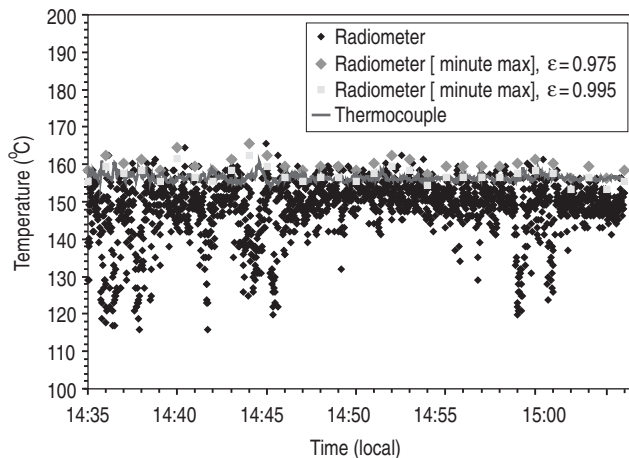


Figure 8.4 Thirty-minute record of fumarole vent temperature at Vulcano. Black plots give the temperature recorded by a fixed, tripod-mounted Minolta/Land Cyclops 300 sampled once a second. Red line gives the temperature recorded by K-type thermocouple placed in the vent mouth and within the radiometer field of view. Green and yellow plots mark the maximum recorded by the radiometer in sequential one-minute-long windows when corrected for an emissivity of 0.975 (green plots) and 0.995 (yellow plots). Black plots are corrected for an emissivity of 0.975 (the emissivity for trachytic-rhyolitic surfaces, as given in Table 8.1). See also color plates section.

applied to the radiometer data or variable temperatures across the vent. Because the vent walls were comprised of sulfur-free trachyte/rhyolite, an 8–14  $\mu\text{m}$  emissivity of 0.975 was used (from [Table 8.1](#)) to correct the brightness temperature. Increasing the emissivity to 0.996 provides an exact fit between the radiometer maximum and thermocouple time series (see [Figure 8.4](#)), with the mean of the radiometer maximum for each minute-long window ( $\pm 1\sigma$ ) now being  $157 \pm 2$  °C. However, temperature may also be variable across the vent so that the difference may reflect a slightly lower temperature at the location of the thermocouple compared with that at the location of the radiometer FOV.

Thus, fumarole vent temperatures can be obtained to within a few degrees of the thermocouple-measured control if:

- measurement distance is minimized so that the fumarole (vent) fills the radiometer field of view;
- the maximum temperature, recorded under best line-of-sight conditions is obtained. In the case reviewed above, this involved holding the maximum recorded over one minute;
- the fumarole is swept repeatedly by the radiometer so that the point of maximum temperature within the vent is located; and
- brightness temperature is corrected using an appropriate emissivity.

A comparison of 25 sets of simultaneous radiometer and thermocouple measurements of vent temperature are given in [Figure 8.5](#). These tests involved a comparison of the differences between simultaneous radiometer- and K-type thermocouple measurements for fumaroles at Vulcano during 1998 and 1999. Differences were between –10 °C and 18 °C, with a mean of 2.5 °C. Negative differences indicated a thermocouple-derived temperature that was higher than that obtained by the radiometer. Only three of the 25 comparisons were negative, i.e., the thermocouple temperature was higher than the radiometer temperature (see [Figure 8.5b](#)). Twenty-one of the comparisons were positive, i.e., the radiometer temperature was higher than the thermocouple temperature. As discussed above, this may be a result of (i) the radiometer, through its ability to cover the whole vent area, finding the highest temperature point within the vent, and/or (ii) temperatures being corrected for an emissivity that was a little too low [0.975 having been used to correct the radiometer-recorded brightness temperature].

### **8.2.1 Vent temperatures and gas emissivity**

For a field of view centered in an open vent subject to a constant stream of hot gas and surrounded by hot wall rock heated by that gas, just what are we measuring the temperature of? The answer depends on the emissivity of the gas component within the field of view.

#### *8.2.1.1 The emissivity of gas*

The emissivity of carbon dioxide and water vapor depends on gas temperature, partial pressure and beam length (Hottel, 1954; Holman, 1992), with emissivity increasing with partial pressure ( $P_{\text{gas}}$ ) and/or mean beam length ( $L_e$ ), as plotted in [Figure 8.6](#). Mean beam length

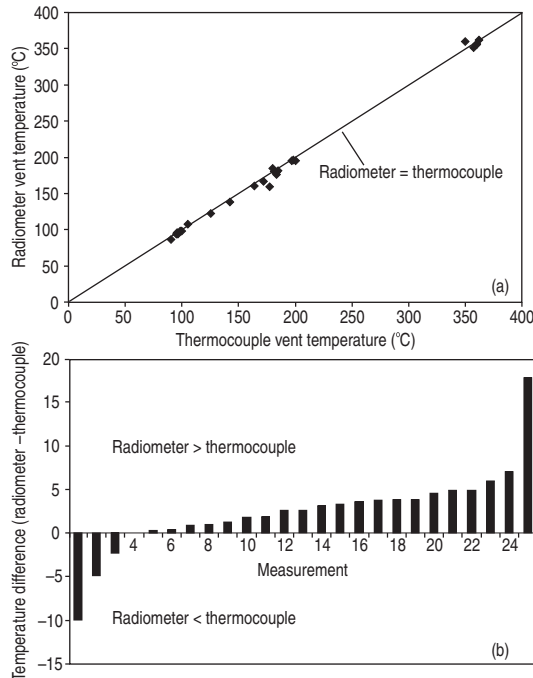


Figure 8.5 Comparison of 25 simultaneous Minolta/Land Cyclops 300 and K-type thermocouple measurements made at fumarole vents on Vulcano. (a) Comparison of each measurement pair (for points falling on the black 45° line, the two temperatures are identical), and (b) difference between the radiometer and thermocouple measurement for each measurement pair. Data are ordered by difference magnitude, and difference is expressed in °C.

can be approximated using the total gas volume ( $V_{\text{gas}}$ ) and area ( $A_{\text{gas}}$ ) following (Holman, 1992):

$$L_e = 3.6V_{\text{gas}}/A_{\text{gas}}. \quad (8.4)$$

Thus for a given gas volume, mean beam length (and hence emissivity) will increase as the area covered by the gas decreases. Or, for a given area, mean beam length (and hence emissivity) will increase with gas volume.

Following the ideal gas law, partial pressure depends on the number of moles of gas ( $n$ ), gas volume and temperature ( $T_{\text{gas}}$ ):

$$P_{\text{gas}} = nRT_{\text{gas}}/V_{\text{gas}}, \quad (8.5a)$$

$R$  being the ideal gas constant ( $8.314\,472\, \text{m}^3\, \text{Pa}\, \text{K}^{-1}\, \text{mol}^{-1}$ ). The number of moles, in turn, depends on the gas mass ( $M_{\text{gas}}$ ):

$$n = M_{\text{gas}}/Mw_{\text{gas}}, \quad (8.5b)$$

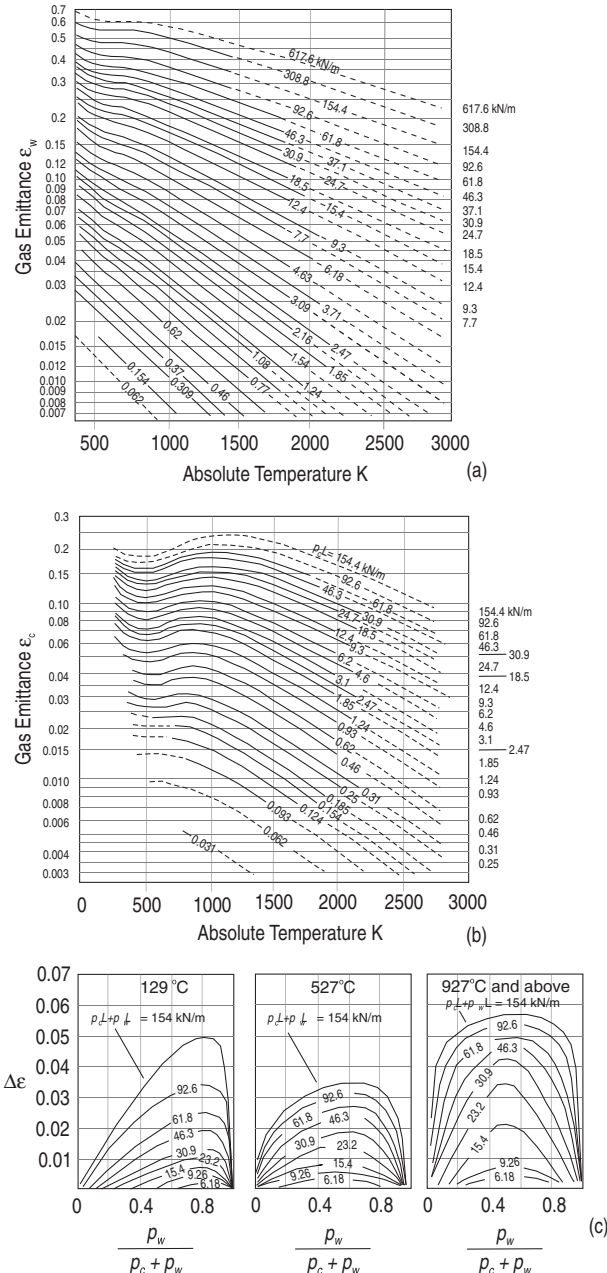


Figure 8.6 Variation in the emissivity of (a) water vapor ( $\varepsilon_w$ ) and (b) carbon dioxide ( $\varepsilon_c$ ) with vapor temperature for a range of partial pressure and beam length combinations ( $L_e P_g$ , in  $\text{kN m}^{-1}$ ) [after Hottel (1954) and as reproduced in Figs. 8–34 and 8–35 of Holman (1992)]. (c) Look-up tables of Hottel (1954) providing  $\Delta\varepsilon$  corrections applied when calculating the emissivity of a mixture of water vapor and carbon dioxide [Fig. 8–38 of Holman (1992)].

$Mw_{\text{gas}}$  being the gas molecular weight in grams per mole. Equations (8.5a) and (8.5b) show that if the hot gas mass per unit volume increases, partial pressure will also increase and, hence, so too will the emissivity of the gas.

For mixtures of water vapor and carbon dioxide, the mixture emissivity ( $\varepsilon_g$ ) may be obtained using the product of beam length and partial pressure ( $L_e P_g$ ). Using the appropriate gas temperature and  $L_e P_g$ , emissivities can now be looked up using the graphs of Hottel (1954), as given in Figure 8.6. At atmospheric pressure, the emissivity of the gas mixture can be obtained by addition of the values for water vapor ( $\varepsilon_w$ ) and carbon dioxide ( $\varepsilon_c$ ) and applying a small correction ( $\Delta\varepsilon$ ) (Holman, 1992):

$$\varepsilon_g = \varepsilon_w + \varepsilon_c - \Delta\varepsilon. \quad (8.6)$$

The correction value depends on the mixture temperature and the ratio of the water vapor partial pressure ( $P_w$ ) to the combined partial pressure of the carbon dioxide and water vapor ( $P_c + P_w$ ), and is given in Figure 8.6c. At non-atmospheric pressures, a correction also needs to be applied to the water vapor and carbon dioxide emissivities (see Holman (1992) or Hottel (1954)).

Take, for simplicity, a spherical gas cloud of radius ( $r_{\text{gas}}$ ) at source. Being at source, we assume that the gas has not yet cooled, expanded or entrained air. We take a radius for the cloud of 0.5 m. At source, the gas volume will be  $4/3\pi r_{\text{gas}}^3 = 0.52 \text{ m}^3$  and area will be  $\pi r_{\text{gas}}^2 = 0.79 \text{ m}^2$ . This gives a beam length of:

$$L_e = (3.6) [(0.52 \text{ m}^3)(0.79 \text{ m}^2)] = 2.4 \text{ m.}$$

Measurements of Stromboli's gas composition during persistent degassing by Burton *et al.* (2007) reveal that  $\text{H}_2\text{O}$  and  $\text{CO}_2$  account for 82.9 % and 13.6 % of the total gas volume, respectively. For such a mixture, the volumes of water vapor ( $V_w$ ) and carbon dioxide ( $V_c$ ) will be:

$$V_w = (0.829)(0.52 \text{ m}^3) = 0.43 \text{ m}^3, \text{ and}$$

$$V_c = (0.136)(0.52 \text{ m}^3) = 0.07 \text{ m}^3.$$

The densities of water vapor and carbon dioxide at 600–850 K can be looked up from Tables in Holman (1992) and are  $0.2579 \text{ kg m}^{-3}$  and  $0.8938 \text{ kg m}^{-3}$ , respectively. Using these densities, the two volumes convert to masses of:

$$M_w = (0.43 \text{ m}^3)(0.2579 \text{ kg m}^{-3}) = 0.112 \text{ kg} = 112 \text{ g, and}$$

$$M_c = (0.07 \text{ m}^3)(0.8938 \text{ kg m}^{-3}) = 0.064 \text{ kg} = 64 \text{ g.}$$

Using the molecular weight of water vapor ( $22 \text{ g mol}^{-1}$ ) and carbon dioxide ( $44 \text{ g mol}^{-1}$ ) we can convert these masses to number of moles of each gas:

$$n_w = (112 \text{ g})[(1 \text{ mol})/(22 \text{ g})] = 5.1 \text{ mol, and}$$

$$n_c = (64 \text{ g})[(1 \text{ mol})/(44 \text{ g})] = 1.4 \text{ mol.}$$

We can now apply the ideal gas law to find that the partial pressures for the two gases ( $P_w$  and  $P_c$ ) at 1000 °C (1273 K) are:

$$P_w = (5.1 \text{ mol})(8.314\ 472 \text{ m}^3 \text{ Pa K}^{-1} \text{ mol}^{-1})(1273 \text{ K})/(0.52 \text{ m}^3) = 103 \text{ kPa, and}$$

$$P_c = [(1.4 \text{ mol})(8.314\ 472 \text{ m}^3 \text{ Pa K}^{-1} \text{ mol}^{-1})(1273 \text{ K})]/(0.52 \text{ m}^3) = 29 \text{ kPa.}$$

Remembering that a pascal can be written as the force (in newtons) applied per unit area (i.e., 1 Pa = 1 N m<sup>2</sup>) we obtain:

$$L_e P_w = (2.4 \text{ m})(103 \text{ kN m}^2) = 247 \text{ kN m, and}$$

$$L_e P_c = (2.4 \text{ m})(29 \text{ kN m}^2) = 70 \text{ kN m.}$$

Using Figures 8.6a and 8.6b as look-up tables, for a gas temperature of 1273 K and these  $L_e P_w$  we have a water vapor emissivity of ~0.45 and a carbon dioxide emissivity of ~0.2. Now taking the value for  $P_w/P_c+P_w$ :

$$(103 \text{ kPa}) [(103 \text{ kPa}) + (29 \text{ kPa})] = 0.78,$$

we can use Figure 8.6c to obtain a  $\Delta\varepsilon$  correction of 0.055. Thus, we arrive at an emissivity for the gas mixture of:

$$\varepsilon_g = (0.45) + (0.2) - (0.055) = 0.6.$$

Thus, when highly concentrated and hot, volcanic gas may have an emissivity close to 0.6.

However, rapid expansion, air ingestion, and cooling will mean that this ideal situation is moved away from quite rapidly. If, for example, we assume that the cloud volume used above is composed of 90% air, then our calculated emissivity drops to 0.33. By also reducing the hot gas temperature to 250 °C, emissivity declines further to ~0.30. For smaller gas masses, the emissivity will be smaller still.

For low partial pressures (i.e., low gas masses) and beam lengths (i.e., at  $L_e P_g$  less than 0.2 for water vapor, and less than 6.18 for carbon dioxide) emissivity falls to less than 0.1 (see Figure 8.6). If emissivity drops to such low values, and high temperatures are still recorded, then another source must be responsible for the emission. A gas temperature of 1000 °C and emissivity of 0.1, for example, can only yield a brightness temperature of ~170 °C at 8–14 μm. The same gas at 500 °C will give a brightness temperature of just ~70 °C. Thus, if a brightness temperature of 500 °C is recorded under such low emissivity gas conditions, what is causing the emission?

#### 8.2.1.2 What are we measuring?

If the water vapor condenses, then the above discussion is moot because we are dealing with a cloud of gas and water droplets. Given that water is effectively a blackbody, then the emissivity of an opaque cloud of water droplets will be 1 and we will be measuring the water cloud temperature.

If we are dealing with low-emissivity, non-condensed gas conditions then most of the radiometer-recorded signal must be generated by emission from heated wall rock around the

vent. Given a constant gas flux of stable temperature, the gas will heat the wall rock to the same temperature as the gas. This relationship was apparent during observations of a 4-m-wide degassing vent on Stromboli during May 2001. Degassing at the active vent was apparent from the emission of a stream of gas puffs at a rate of one puff every 1–2 s. When observed at night, diminished degassing (puffing) caused glow to fade until the vent was completely dark. During such periods, vent temperatures measured with a Minolta/Land 152 declined from  $\sim 690$  °C to  $\sim 600$  °C. As puffing re-established so the glow turned back on, and increased in intensity until glowing brightly once more. At the same time vent temperature climbed from  $\sim 640$  °C to  $\sim 740$  °C.

In non-condensed cases, where gas emissivity is low, we are thus measuring the gas-heated wall rock temperature through a largely thermally transparent gas stream. This is the case in our example from Vulcano given in [Figure 8.4](#), where a stable gas temperature measured by a thermocouple suspended in the fumarole mouth was identical to the vent wall rock temperature measured by the radiometer. That we are detecting emission from the wall rock is consistent with the radiometer-recorded brightness temperature which, when corrected for an emissivity appropriate for the wall rock (0.975), converts to a temperature ( $\sim 160$  °C) approximately equal to that of the thermocouple ( $\sim 157$  °C). If we assume we are recording emission from the gas, then the lower emissivity that we have to use (<0.6), causes the excellent fit between the emissivity-corrected radiometer temperature and the thermocouple temperature to disappear, with the corrected brightness temperature becoming unrealistically high ( $\sim 240$  °C for  $\varepsilon_g$  of 0.6, and  $\sim 400$  °C for  $\varepsilon_g$  of 0.3). By virtue of best-fit, we therefore conclude that, in this case, the gas was non-emissive and the recorded emission was from the heated fumarole wall rock.

### **8.2.2 Fumarole field surveys**

At fumaroles, the radiometer has several advantages over the thermocouple. The fact that insertion into the fumarole is not required, coupled with the portability and rapid response of the radiometer mean that many fumaroles can be visited in quite a short time. Under good conditions, a vent temperature can be acquired in less than five seconds. As a result, a fumarole-field-wide vent temperature inventory can easily be built.

The method developed at Vulcano by Harris and Maciejewski ([2000](#)) allows several hundred (typically between 500 and 1200) vent temperature measurements to be made in between three and four hours. Measurements are made by moving across the fumarole field along set transects that are walked to ensure representative coverage of the entire fumarole field. Hand-held GPS points are taken every 5–10 m to allow location of measurement clusters for mapping. The radiometer is hand-held, with the operator lingering at each fumarole for up to 10 seconds and scanning the vent until the maximum temperature has been reached. Path length is kept to a minimum by making measurements from eye height (or lower), i.e., over a line-of-sight of  $\leq 2$  m (as pictured in [Figure 8.1a](#)). The operator also uses the radiometer viewing optics to ensure that the vent fills the field of view. Sub-FOV

vents are rejected because an integrated temperature from the vent and vent background will have been collected, rather than pure vent temperature. For this task the Minolta/Land Compac 300 has proved reliable and robust over multiple (13) surveys at Vulcano between 1994 and 2007, with the clarity of the viewing optics allowing excellent targeting.

Survey data can then be used to produce:

- (1) vent temperature maps (by contouring GPS-located values, e.g., [Figure 8.7a](#)),
- (2) vent temperature statistics for the entire fumarole field (e.g., [Figure 8.7b](#)) and/or,
- (3) vent temperature statistics for different zones within the field (e.g., [Figure 8.7c](#)).

The first product on this list was first derived by Kagiyama (1981), who produced a surface temperature map for a fumarole field active in Kirishima's Ohachi crater in 1977 [see [Figure 4](#) of Kagiyama (1981)]. Vent temperatures used to generate such maps can be used to statistically define and compare the thermal character of different zones within the fumarole field, or to assess temporal changes if a time series of surveys is available. As a zone cools, for example, the vent temperature frequency distribution tends to develop a prominent low-temperature mode at the expense of high-temperature tails. As a result, the shape of the histogram changes from a relatively flat distribution, associated with a widely dispersed vent temperature population, to a peaked distribution associated with clustering of values around a low-temperature mode. As a result, the kurtosis shifts from positive (flat) to negative (peaked). At the same time the distribution loses its asymmetry, characterized by a skew towards high temperature, so that the skewness also moves from positive (skewed in the positive direction) to negative (skewed in the negative direction).

### 8.2.3 Sources of survey error

Given that fumarole temperatures likely remain stable between the two consecutive days, any difference in survey statistics from surveys repeated in short succession (less than a few days apart) will likely result from changes in viewing conditions or sampling bias. Two such tests were made at Vulcano during October 1994 (Harris and Maciejewski, 2000) and June 2004 (Harris *et al.*, 2009). The two tests showed that sampling bias, rather than viewing conditions, are likely to be the greatest source of error in the resulting statistics.

#### 8.2.3.1 Test 1: good conditions, change in sample size

During October 1994 two surveys were completed four days apart. Viewing conditions were optimum on both days (low humidity, high air temperatures, light plume condensation). However, the sample size was around twice as high during the first survey (no. = 150) as during the second (no. = 83). During the first survey, a maximum of 457 °C was obtained, and the mean was 173 °C. However, during the second (smaller) survey the maximum had decreased to 385 °C, but the mean had increased to 177 °C. In addition, the modal group and median were both ~20 °C higher for the second (smaller) survey. As a result the kurtosis and skewness both changed, the kurtosis declining from 1.57 for the larger survey to 0.67 for the

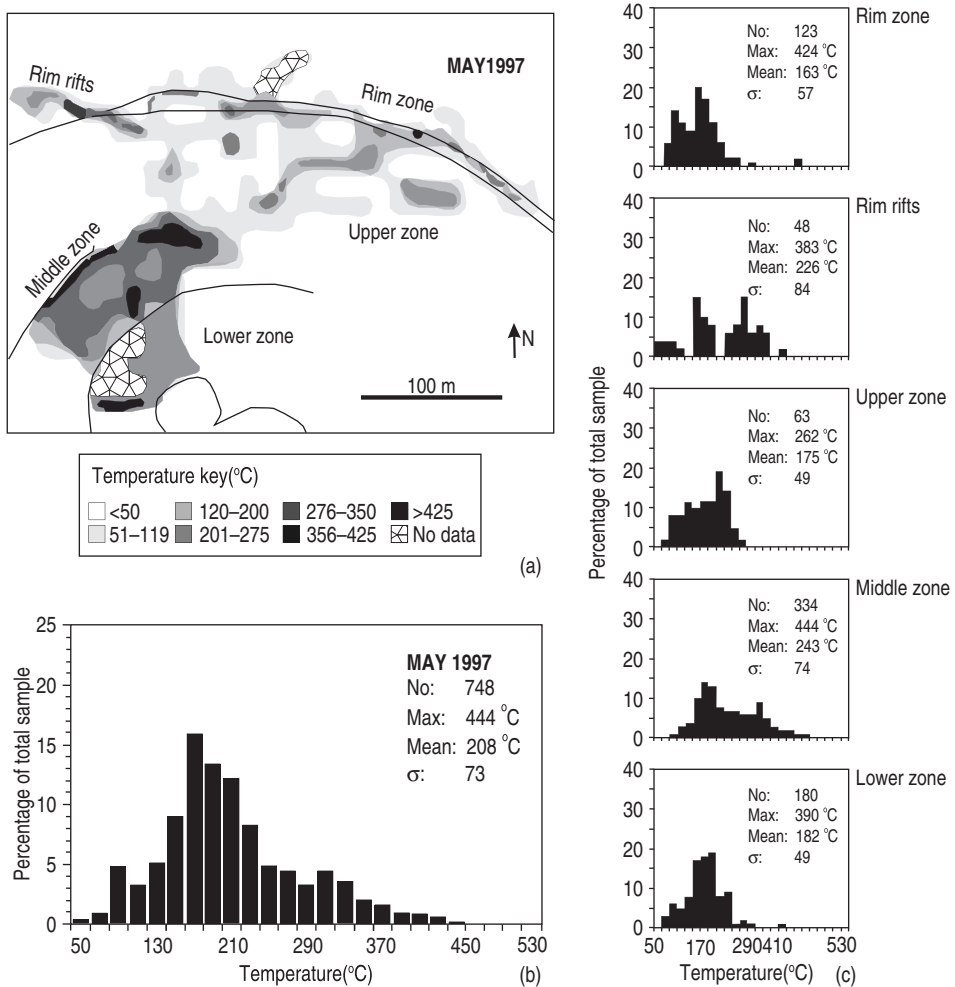


Figure 8.7 (a) Vent temperature map produced from a May 1997 Minolta/Land Cyclops 300 survey of Vulcano's Fossa fumarole field, with (b) whole-field vent temperature statistics, and (c) statistics broken down by zone within the field. (c) shows the different frequency distribution shapes for hotter zones (e.g., the broader and flatter distributions of the rim rifts and middle zones) and cooler zones (e.g., the narrower distributions with more prominent modes of the rim and lower zones). Map and statistics were produced from 748 vent temperature measurements distributed across the field.

smaller survey, and the skewness declining from 3.93 to 2.12. These differences resulted from the maximum temperature fumarole being missed in the smaller survey. However, the smaller survey also neglected the dominant population of cooler fumaroles and concentrated on the rarer, higher-temperature fumaroles, so that the mean, mode and median of the smaller sample were all higher.

#### 8.2.3.2 Test 2: stable sample size, change in conditions

During June 2004 measurements were made on consecutive days. This time sample sizes were similar (Day 1: 63 measurements, Day 2: 70 measurements). However, conditions were poor on the first day (high humidity, low air temperatures, heavy plume condensation), and good on the second day (low humidity, high air temperatures, light plume condensation). Under poor conditions, a mean of 110 °C and a maximum of 223 °C was obtained. On the following day, under improved conditions, the mean had increased only slightly to 114 °C, as had the maximum (225 °C). In addition the kurtosis (Day 1: 0.6, Day 2: 0.9) and skewness (Day 1: 1.3, Day 2: 1.5) were not as greatly affected as when the sample size was changed.

#### 8.2.3.3 Lens problems

Under harsh, acidic conditions, a scratched lens can degrade rapidly, developing a uniform white fog across the entire lens, or white lines along any scratches in the lens. This results in reduction of the signal, so that brightness temperature is under-estimated. When a severely degraded (completely fogged) lens was used during a 2004 survey at Vulcano, lens fogging resulted in recorded temperatures being  $51 \pm 11$  °C lower than under clear-optic conditions. In such cases, the lens must be replaced. However, calibration can be achieved. By heating an element through a series of temperature steps, and making 50 simultaneous thermal camera, thermocouple and radiometer measurements as the element heated from 80 °C to 500 °C, comparison between element temperature ( $T$ ) and radiometer temperature obtained with the fogged lens ( $T_{\text{fog}}$ ) allowed correction. For the 2004 case, a correction was obtained whereby  $T = 0.9308T_{\text{fog}} + 61.895$ ,  $R^2 = 0.995$ .

#### 8.2.3.4 Summary

For radiometer-based fumarole surveys, the following data collection requirements should be noted.

- Keep sample sizes similar and avoid sampling bias.
- Surveys should be made under conditions of low humidity and/or high air temperature so that dew point is low and viewing conditions are optimum (plume condensation is minimal).
- If conditions are poor, the measurement time for each fumarole must be increased to catch the best possible viewing conditions.
- Viewing optics must be kept clean, or well calibrated if fogging occurs.

### 8.3 Explosive eruptions

As pointed out by Shimozuru (1971), three types of explosive emission can be detected with a radiometer, these being:

- eruptions ejecting only gas (gas-dominated emission),
- eruptions ejecting gas and coarse fragments (bomb-dominated emission), and
- eruptions ejecting gas and fine fragments (ash-dominated emission).

In all cases, to record the thermal waveform associated with the emission, the radiometer should be tripod-mounted so that a fixed and stable field of view is maintained, located just above the vent, as in the set-up pictured in [Figure 8.1c](#). Now the variation in thermal emission can be recorded as the emitted cloud of gas, bombs and/or ash passes upwards through the field of view. In this way a temporal record of the thermal emission associated with cloud ascent is obtained. Because at-vent ascent velocities are usually fast (tens to hundreds of meters per second), transit time for hot particles through the field of view will also be fast so that high sampling rates (20–100 Hz) should be used to capture the detail of the waveform.

### **8.3.1 Thermal waveforms associated with gas-dominated emission**

Gas-dominated emissions can be split into two sub-types: puffing and pistonning.

- Originally recorded in radiometer data for a degassing vent at Mt. Etna by Tazieff ([1970](#)), gas puffing is typically associated with persistent degassing activity where repeated bursting of relatively small bubbles feeds a stream of gas puffs that exit the vent. Bursting bubbles do have an over-pressure, even if small ([Ripepe et al., 1996](#)), and the emission does display a (very) short gas-thrust phase, making it an extremely low energy style of explosive emission ([Harris and Ripepe, 2007b](#)). Such emissions have been recorded using continuously recording radiometers at Etna ([Tazieff, 1970](#); [Lautze et al., 2004](#)), Stromboli ([Ripepe et al., 2002](#); [Harris and Ripepe, 2007b](#)), Masaya ([Branan et al., 2008](#)), Villarrica ([Gurioli et al., 2008](#)) and Kilauea ([Marchetti and Harris, 2008](#)).
- Gas pistonning has been commonly recorded for lava lakes and degassing vents at Kilauea ([Swanson et al., 1979](#); [Barker et al., 2003](#)). On the basis of events observed at Mauna Ulu (Kilauea) by [Swanson et al. \(1979\)](#), gas-piston activity was first ascribed to gases accumulating under a relatively impermeable magma layer to cause a rise in the level of the magma. Once the strength of the over-burden had been exceeded, release of the trapped, over-pressurized gas occurred by sustained jetting. It results in a characteristic thermal waveform that has been analyzed using radiometer data by [Johnson et al. \(2005\)](#) and [Marchetti and Harris \(2008\)](#).

We next consider the waveforms associated with each event type, and the emission dynamics that can be inferred from the waveform.

#### **8.3.1.1 Gas puffing**

Because gas puffs are usually just a few meters in diameter, and disperse at a height of a few tens of meters above the vent, measurements are best made by targeting a narrow field of view instrument immediately above the vent. Passage of a stream of puffs through the radiometer FOV will then be apparent as an oscillating waveform. As shown in [Figure 8.8a](#), each oscillation records the passage of a single puff. By counting the number of peaks in the time series (each of which relates to the passage of a discrete gas puff) the puffing frequency can thus be obtained. For example, the time series of [Figure 8.8a](#) for vent CC-W shows

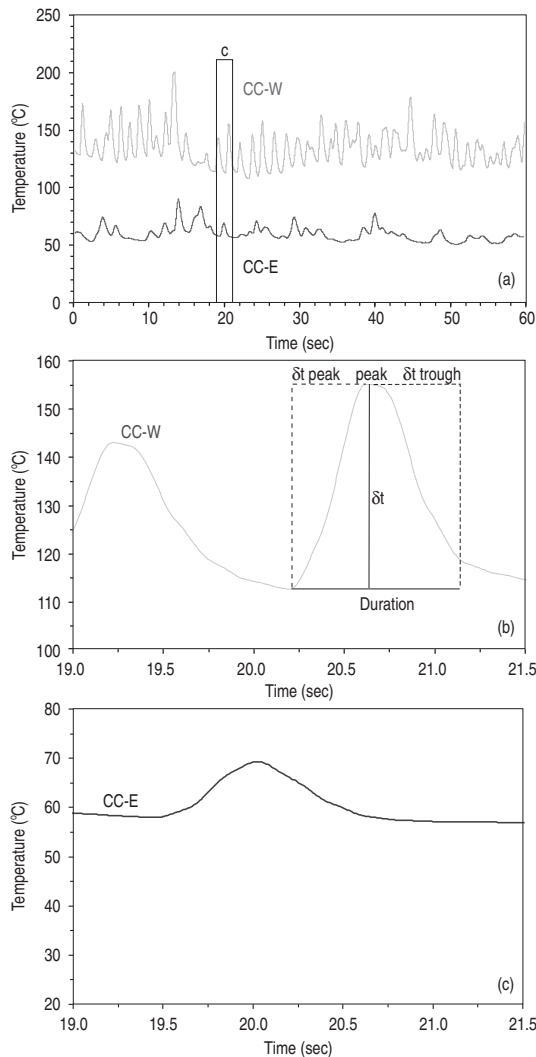


Figure 8.8 (a) One-minute-long Omega OS554 record for two degassing vents on Stromboli (CC-W and CC-E). At both vents, oscillations in the data record ascent of hot gas puffs upwards through the radiometer field of view. While puffing at CC-W is vigorous (puff ascent velocity is relatively high), that at CC-E is less vigorous (puff ascent velocity is relatively low). (b) and (c) highlight two 1.5-second-long periods from the CC-W and CC-E records, showing that (i) thermal levels and oscillation amplitudes are higher for the vigorously puffing case, and (ii) the onset of each oscillation ( $\delta t_{\text{peak}}$ ) is shorter for the vigorously puffing case. Quantitative parameters used to describe the waveform, and to constrain puff ascent dynamics, are marked in (b); and window extracted in (b) and (c) is marked on (a) using the box marked “c”.

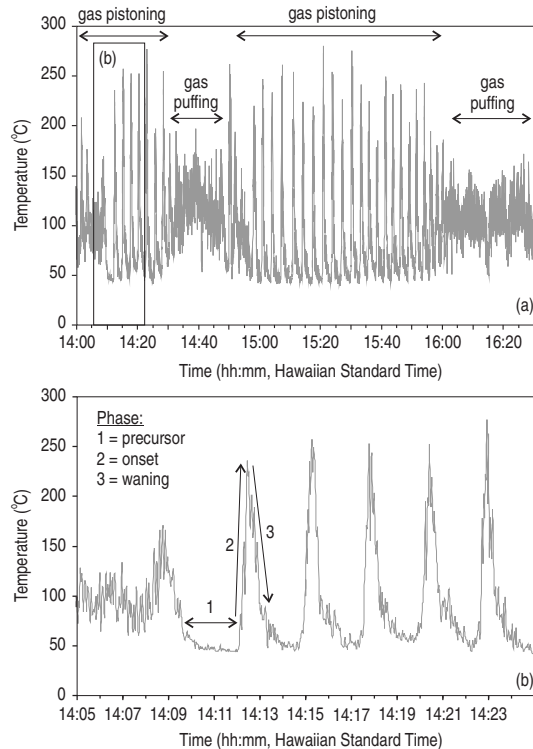


Figure 8.9 (a) Two-and-a-half-hour-long Omega OS554 record for a degassing vent within Kilauea's Pu'u 'O'o crater that is switching between gas pistonning and gas puffing. (b) Thirty-minute-long extract showing the characteristic and repetitive thermal waveform associated with gas pistonning.

47 peaks over the one minute long thermal record. This equates to an intermittency of 1 puff every 1.3 s, or a frequency of 0.78 Hz.

To understand the waveform associated with the passage of an individual puff through the radiometer field of view, and the dynamics that can be inferred from its shape, we again turn to a two-component thermal model for the FOV-integrated temperature. In this model the hot gas puff, assumed to be at a uniform temperature of  $T_{\text{puff}}$ , occupies portion  $p$  of the FOV, with the remainder being occupied by a cooler background at  $T_{\text{back}}$ , so that the integrated temperature ( $T_{\text{int}}$ ) recorded at the radiometer recording at wavelength  $\lambda$  can be written:

$$L(\lambda, T_{\text{int}}) = pL(\lambda, T_{\text{puff}}) + (1 - p)L(\lambda, T_{\text{back}}). \quad (8.7)$$

In the instant before the puff enters the field of view,  $p = 0$  so that  $L(\lambda, T_{\text{int}}) = L(\lambda, T_{\text{back}})$ . As the puff ascends through the field of view, the FOV portion occupied by the hot puff will increase; thus so, too, will the integrated temperature. As in the case of a cracked lava flow surface moving through the field of view, if puff temperature remains stable during ascent

through the field of view, then the rate at which the integrated temperature increases will be a proxy for the velocity at which the puff is moving through the field of view. Rapidly ascending puffs will fill the FOV more quickly than slowly ascending puffs. Hence  $p$  and  $T_{\text{int}}$  will increase more quickly in the fast ascent case than in the slow ascent case, and a steeper ascending limb to the waveform will be apparent, as can be seen by comparing Figures 8.8b and 8.8c. These two figures give the waveforms for puffs ascending at relatively high and low velocities, respectively.

Peak temperature will be reached as the puff leading edge reaches the top of the FOV. At this point the FOV has become filled with the hot source, so that  $p = 1$  and  $L(\lambda, T_{\text{int}}) = L(\lambda, T_{\text{puff}})$ . In this case, the time taken to reach peak temperature ( $\delta t_{\text{peak}}$ ) is the time the puff leading edge takes to move from the bottom to the top of the FOV of width  $W_{\text{FOV}}$ , so that puff front velocity, or FOV-entry velocity, can be calculated from

$$V_{\text{lead}} = W_{\text{FOV}} / \delta t_{\text{peak}}. \quad (8.8a)$$

As the puff leaves the FOV, so the FOV will be steadily emptied of the hot source, and  $p$  and  $T_{\text{int}}$  will decline to cause a waning limb. The factors controlling the rate and duration of the temperature change are the same for the waning limb as they are for the waxing limb, i.e.:

- a rapidly ascending puff will leave the FOV more quickly than a slowly ascending puff, so that the rate of decline will be more rapid and the slope of the waning limb will be steeper for the fast case;
- the time taken to move from peak temperature to background temperature ( $\delta t_{\text{trough}}$ ) will be the time the puff back-edge takes to move from the bottom to the top of the FOV of width  $W_{\text{FOV}}$ , so that puff back-edge, or FOV-exiting, velocity can be calculated from

$$V_{\text{back}} = W_{\text{FOV}} / \delta t_{\text{trough}}; \quad (8.8b)$$

- $\delta t_{\text{trough}}$  will be shorter for a rapidly ascending puff than for a slowly ascending puff.

Given a stable ascent velocity over the FOV, the waveform will be symmetrical with the waxing and waning limbs having the same slopes and durations, so that  $\delta t_{\text{peak}} = \delta t_{\text{trough}}$  meaning that  $V_{\text{lead}} = V_{\text{back}}$ . This is the case for the fast ascending puff of Figure 8.8b. If ascent velocity declines during passage through the FOV, then the waveform will be asymmetrical with a shorter, steeper waxing limb and a longer, shallower waning limb. In this case  $\delta t_{\text{peak}} < \delta t_{\text{trough}}$  meaning that  $V_{\text{lead}} > V_{\text{back}}$ . Such a waveform shape (i.e., generation of a longer tail) can also be forced if the puff is cooling due to expansion and entrainment of air. This is the case for the slowly ascending puff of Figure 8.8c.

Duration of the waveform ( $t_{\text{waveform}}$ ) will record the time that the puff, of length  $L_{\text{puff}}$ , took to enter, ascend through, and clear the FOV. Hence, given the puff ascent velocity, puff length can be approximated from

$$L_{\text{puff}} = t_{\text{waveform}}[(V_{\text{lead}} + V_{\text{back}})/2]. \quad (8.8c)$$

If the width of the puff ( $w_{\text{puff}}$ ) can be assumed, length can be converted to volume. If puff width (measured at the vent exit) is controlled by the radius of the vent ( $r_{\text{vent}}$ ) puff volume ( $\varpi_{\text{puff}}$ ) can be calculated from:

$$\varpi_{\text{puff}} = \pi r_{\text{vent}}^2 L_{\text{puff}}. \quad (8.8d)$$

In the case of puffs at Masaya, measurements by Branan *et al.* (2008) were made higher in the puff stream, so that puffs had formed discrete thermals which could be approximated by a spherical shape so that:

$$\varpi_{\text{puff}} = 4/3\pi(L_{\text{puff}}/2)^3. \quad (8.8e)$$

Multiplying by puff density ( $\rho_{\text{puff}}$ ) allows puff mass ( $m_{\text{puff}}$ ) to be calculated ( $m_{\text{puff}} = \varpi_{\text{puff}} \rho_{\text{puff}}$ ). If we can assume the puff is dominated by water vapor, puff density can be estimated, using an appropriate temperature, from look-up tables for steam density in, for example, Holman (1992). However, the derived mass will be the mass for a mixture of volcanic gas and entrained air. Branan *et al.* (2008) provide a method for estimating puff dilution ( $d$ ) by air entrainment for a puff of spherical geometry and radius  $r_{\text{puff}}$  passing through the radiometer FOV, whereby,

$$d = 3eV_{\text{lead}}/Br_{\text{puff}}. \quad (8.8f)$$

Here,  $e$  is the entrainment constant for the thermal (0.25),  $V_{\text{lead}}$  is the puff ascent velocity, and  $B$  is buoyancy. Buoyancy can be calculated from the density difference ( $\Delta\rho$ ) between the puff (at density  $\rho_{\text{puff}}$ ) and the surrounding air (at density  $\rho_{\text{air}}$ ), in

$$B = g\Delta\rho/\rho_{\text{air}}, \quad (8.8g)$$

in which  $g$  is acceleration due to gravity.

Measured and calculated puff parameters for the two case type puffs of Figures 8.8b and 8.8c are given in Table 8.3. Such an analysis assumes that:

- (1) the puff is isothermal during passage through the field of view, is optically thick and does not change in emissivity, and
- (2) the puff is at least as wide as the FOV, so that it fills the FOV in the fashion of a vertically ascending piston (rather than a radially expanding body).

To achieve this the diameter of the field of view must be kept as narrow as possible so that:

- (1) gas cooling and air entrainment during passage through the FOV is minimized, and
- (2) the FOV width is narrower than the puff width, so that the puff completely fills the FOV during passage through it.

### 8.3.1.2 Gas flux estimation?

Both Harris and Ripepe (2007b) and Branan *et al.* (2008) have suggested that gas puff statistics, and the application of the above sequence of Equations (8.8a) – (8.8g) can be used

Table 8.3. Measured and calculated puff parameters for the two case type puffs of Figure 8.8.

Parameter	Fast puff vent CC-W (Figure 8.8b)	Slow puff vent CC-E (Figure 8.8c)	Notation/derivation
Puff onset time (s)	20.20	19.45	Time $t_1$
Peak start time (s)	20.63	20.01	Time $t_2$
Peak stop time (s)	20.71	20.01	Time $t_3$
Puff end time (s)	21.15	20.58	Time $t_4$
Duration of waxing limb (s)	0.43	0.56	$\delta t_{\text{peak}} = t_2 - t_1$
Peak width (s)	0.07	0.00	Peak width = $t_3 - t_2$
Duration of waning limb (s)	0.44	0.57	$\delta t_{\text{trough}} = t_4 - t_3$
FOV width (m)	5.4	5.4	$W_{\text{FOV}}$
Puff leading edge velocity ( $\text{m s}^{-1}$ )	12.4	9.7	$V_{\text{lead}} = W_{\text{FOV}} / \delta t_{\text{peak}}$
Puff back edge velocity ( $\text{m s}^{-1}$ )	12.2	9.4	$V_{\text{back}} = W_{\text{FOV}} / \delta t_{\text{trough}}$
Puff duration (s)	0.95	1.13	$t_{\text{waveform}} = t_4 - t_1$
Puff length (m)	11.7	10.8	$L_{\text{puff}} = t_{\text{waveform}} [(V_{\text{lead}} + V_{\text{back}})/2]$
Puff radius (m)	2	2	$r_{\text{vent}}$
Puff volume ( $\text{m}^3$ )	147	136	$\varpi_{\text{puff}} = \pi r_{\text{vent}}^2 L_{\text{puff}}$
Puff density ( $\text{kg m}^{-3}$ )	0.35	0.35	$\rho_{\text{puff}}$ for steam at 650 K
Puff mass (kg)	52	48	$m_{\text{puff}} = \varpi_{\text{puff}} \rho_{\text{puff}}$
Background temperature ( $^{\circ}\text{C}$ )	113	58	$T_{\text{back}}$
Peak temperature ( $^{\circ}\text{C}$ )	155	69.5	$T_{\text{peak}}$
Amplitude ( $^{\circ}\text{C}$ )	42	11.5	$\delta T = T_{\text{back}} - T_{\text{peak}}$
No. puffs per minute	47	29	$f_{\text{puff}}$
Total daily volume ( $\text{m}^3 \text{ day}^{-1}$ )	$9.96 \times 10^6$	$5.67 \times 10^6$	$\varpi_{\text{daily}} = f_{\text{puff}} \varpi_{\text{puff}} (60 \times 24)$
Total daily gas mass ( $\text{kg day}^{-1}$ )	$3.49 \times 10^6$	$1.98 \times 10^6$	$m_{\text{daily}} = f_{\text{puff}} m_{\text{puff}} (60 \times 24)$
Total daily gas mass ( $t \text{ day}^{-1}$ )	3500	2000	$t/\text{day} = m_{\text{daily}}/1000$
Fraction SO <sub>2</sub> in total gas	0.06	0.06	$f_{\text{SO}_2}$
Dilution	None = 1	None = 1	$d$
Total daily SO <sub>2</sub> mass ( $t \text{ day}^{-1}$ )	210	120	$\varpi_{\text{SO}_2} = d f_{\text{SO}_2} m_{\text{daily}}/1000$

to estimated gas flux. By way of example, take the typical radiometer-recorded puff parameters from data collected by Branan *et al.* (2008) at Masaya during February 2002. Waveforms typically reached peak temperature in 2.7 s which, for a 8.5 m diameter FOV, yields a velocity (using Equation (8.8a)) for the puff leading edge of:

$$V_{\text{lead}} = (8.5 \text{ m}) / (2.7 \text{ s}) = 3.1 \text{ m s}^{-1}.$$

Waveforms were typically symmetrical (i.e.,  $\delta t_{\text{peak}} = \delta t_{\text{trough}}$  and  $V_{\text{lead}} = V_{\text{back}}$ ), so that puff length can be obtained by using  $V_{\text{lead}}$  and the typical puff duration (9.5 s) in Equation (8.8c), i.e.:

$$L_{\text{puff}} = (9.5 \text{ s})(3.1 \text{ m s}^{-1}) = 30 \text{ m.}$$

Puff volume is now obtained using puff radius ( $= L_{\text{puff}}/2$  for this spherical case) in:

$$\varpi_{\text{puff}} = (4/3)\pi(15)^3 = 14\,000 \text{ m}^3.$$

Using a density for the gas prior to entrainment of air ( $0.65 \text{ kg m}^{-3}$ ) this volume converts to a mass of:

$$m_{\text{puff}} = (14\,000 \text{ m}^3)(0.65 \text{ kg m}^{-3}) = 9100 \text{ kg.}$$

Using an air density of  $1.25 \text{ kg m}^{-3}$ , buoyancy can now be calculated as:

$$B = (9.8 \text{ m s}^{-2})[(1.25 \text{ kg m}^{-3}) - (0.65 \text{ kg m}^{-3})]/1.25 \text{ kg m}^{-3} = 5 \text{ m s}^{-2}$$

so that dilution can be calculated using puff velocity and radius as:

$$d = [(3)(0.25)(3.1 \text{ m s}^{-1})]/[(5 \text{ m s}^{-2})(15 \text{ m})] = 0.11.$$

This means that the puff had been diluted to a point where it comprised 11% volcanic gas, the remainder of the volume being entrained air. Thus, the total volcanic gas mass emitted per puff ( $m_{\text{puff-gas}}$ ) can be calculated as:

$$m_{\text{puff-gas}} = (9100 \text{ kg})(0.11) = 960 \text{ kg per puff.}$$

Given that puffs were typically emitted at a rate of six puffs per minute, the total daily flux of volcanic gas ( $m_{\text{gas}}$ ) can be obtained from multiplying the typical mass of volcanic gas in each puff by the number of puffs emitted in one day:

$$m_{\text{gas}} = (960 \text{ kg per puff})(6 \text{ puffs per min})(60 \text{ min})(24 \text{ hours}) = 8.3 \times 10^6 \text{ kg per day.}$$

Given that Masaya's gas is typically composed of 4.5% SO<sub>2</sub>, this converts to a daily SO<sub>2</sub> flux ( $m_{\text{SO}_2}$ ) of:

$$m_{\text{SO}_2} = [(8.3 \times 10^6 \text{ kg per day})(0.045)]/(1000) = 375 \text{ t/d.}$$

This value is well within error of the simultaneously measured SO<sub>2</sub> flux using conventional (COSPEC-style) techniques of  $470 \pm 190 \text{ t/d}$  (Branan *et al.*, 2008). The same series of calculations are given in Table 8.3, completing the radiometer-based parameterization of the puffing case at Stromboli, and lead us to arrive at a total daily SO<sub>2</sub> flux from the two vents of 330 t/d.

### 8.3.1.3 Gas pistonning

The waveform recorded during gas pistonning has a different shape to that recorded during puffing, as given in Figure 8.9. In this case, more prolonged jetting of hot gas leaves a

characteristic thermal transient in the time series. Repeated gas jetting events cause the time series to take on a “spikey” form, as can be seen in [Figure 8.9a](#).

An analysis of ~4000 gas piston events recorded by radiometers located at Pu'u 'O'o between March 2001 and December 2003 by Marchetti and Harris ([2008](#)) showed the typical waveform to be characterized by three phases:

- (1) a precursory period of low temperatures, possibly due to a reduced gas flux preceding the gas-jetting event,
- (2) an impulsive onset during which the signal climbs rapidly to an initial peak, and associated with passage of the initial jet, followed by
- (3) a long (50–300 s) waning limb during which gas emission steadily declines.

The result is an asymmetrical waveform, as given for a sequence of five gas jets in [Figure 8.9b](#). As with gas puffs, the waveform can be used to record the number of gas piston events, their duration, dynamics and recurrence. These parameters can be extracted through application of the same methodologies as just described for gas puffs. These include primary measurements, made directly from the waveform, i.e.,

- frequency and duration,
- peak temperature and onset time,

and secondary calculations that use these measurements, with a number of assumptions, to calculate,

- ascent velocity;
- emission volume and/or mass;
- air entrainment and gas mass;
- gas mass flux integrated over the duration of the emission.

## 8.4 Thermal waveforms associated with bomb-dominated emission

As with gas-dominated emissions, the passage of a cloud composed of a mixture of gas, sulfite aerosols, water vapor and bombs will cause the FOV-integrated temperature to rise as the cloud enters the field of view, and decline as the cloud leaves the field of view. However, waveforms are somewhat more complicated due to two factors: the complexity of the event and the non-isothermal character of the emission.

### 8.4.1 Waveform types during strombolian eruptions

Bomb-dominated, or strombolian type, thermal emissions, can be split into two sub-classes:

- simple, single peak events [Type A events of Shimozuru ([1971](#)), [Figure 7.12](#)], and
- complex, multi-peaked events [Type D events of Shimozuru ([1971](#)), [Figure 7.12](#)].

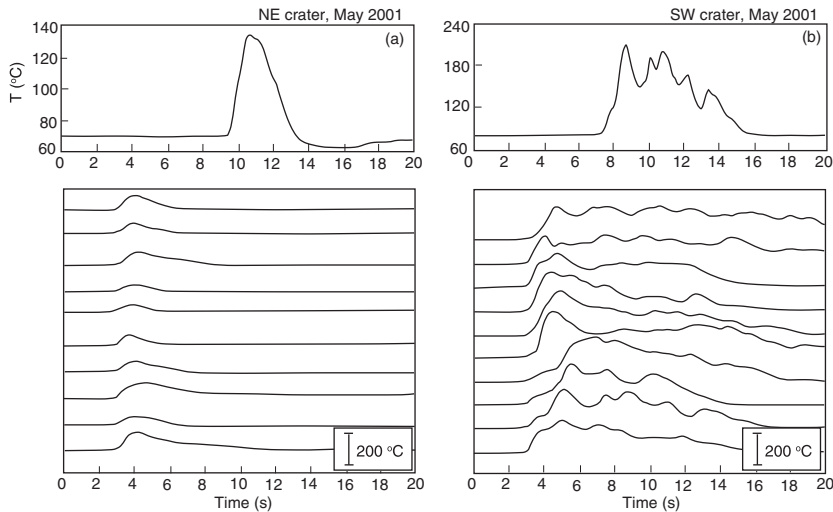


Figure 8.10 Two types of thermal waveform recorded during explosive events at Stromboli: (a) simple, short, single-peaked – Type A – events, and (b) complex, longer-lasting, multi-peaked – Type D – events [from Ripepe *et al.* (2005b, Fig. 2): reproduced by permission of American Geophysical Union]. Waveforms recorded using an Omega OS554 located 250 m horizontally from the plumes and sampling at 54 Hz. Lower panels give signals from multiple events.

Both event types have been well documented through radiometer deployments at Stromboli, where eruptions from the NE crater tends to give simple, shorter, single peaked – Type A – thermal waveforms (Figure 8.10a). Eruptions from the SW crater, however, tend to generate complex, longer-lasting – Type D – waveforms with multiple peaks (Figure 8.10b).

In both cases, passage of the hot cloud of gas and particles is propelled upwards through the field of view by the explosion to result in a waveform with a number of characteristic phases. As marked on Figure 8.11, these are:

- a rapidly ascending limb during passage of the initial jet into, and through, the field of view. If the radiometer is aimed at the vent, the at-vent onset of emission will be recorded by a rapid increase from stable background temperatures, as in inset in Figure 8.11;
- periods of elevated temperature within the waveform will mark discrete bursts of hot gas and fragments that pass through the field of view. If there is just one burst, one peak will be recorded, multiple bursts will leave multiple peaks and more complex waveforms as in Figure 8.11;
- periods of sustained high temperatures will mark sustained emission;
- waning limbs will mark declining emission; and
- a post-explosion cooling curve will be recorded as hot material that landed within the FOV cools.

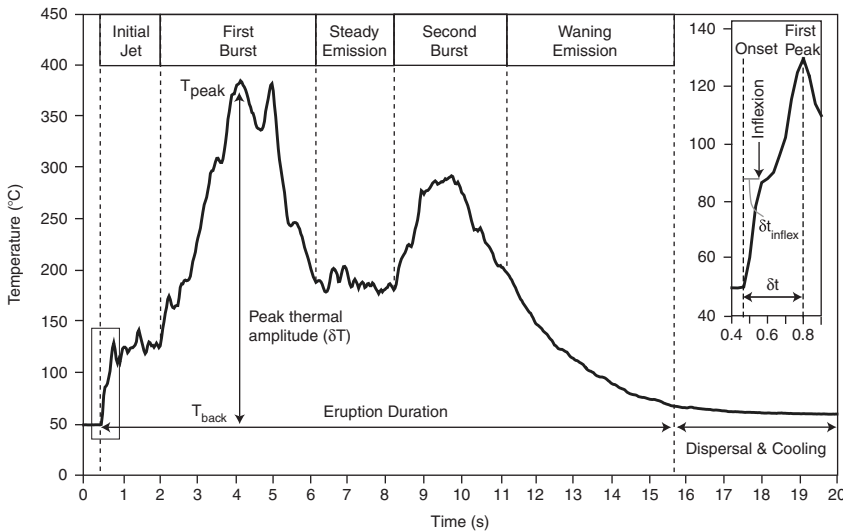


Figure 8.11 Case type waveform for a discrete Stromboli-type eruption. The onset phase is enlarged. Parameters used to describe the waveform, and to constrain plume emission and ascent dynamics, are marked [modified from Harris and Ripepe (2007b, Fig. 11): with permission from Elsevier].

#### 8.4.1.1 Velocity

Although the initial passage of material through the field of view will cause the integrated temperature to increase, with the rate of increase being a function of the velocity at which the FOV is filled, increase will also be recorded after the FOV has become completely filled. This is a result of the cloud temperature increasing with time as the emission becomes more heavily loaded with bombs, or if hotter, larger bombs are emitted following the initial jet. For example, an initial high-velocity spray of bombs will cause the integrated temperature to increase rapidly as the FOV becomes filled with the hot source. However, the following mass of slower, larger, hot bombs will cause continued increase in the FOV-integrated temperature as the size, and temperature, of the hottest sources (the bombs) passing through the FOV increases. However, the rate of increase will likely decline, so that the change from an initial condition where the increase in temperature is driven by a hot cloud expanding within the field of view, to one where the increase is driven by increases in the size and temperature of the hottest (bomb) components will be marked by an inflection, as marked on Figure 8.11. This inflection usually marks the point at which the leading edge of the cloud attains the top of the field of view. As with the gas puff, the time difference between the onset of the thermal waveform and the first inflection ( $\delta t_{\text{inflex}}$ ) can be used to estimate ascent velocity if the FOV diameter is known (i.e.,  $V_{\text{lead}} = W_{\text{FOV}}/\delta t_{\text{inflex}}$ ).

Velocity can also be obtained by stacking radiometer FOVs vertically above the vent, as sketched in Figure 8.12. In this method, the distance to the target, which in this case is the active vent ( $D_{\text{vent}}$ ), and angular separation ( $\alpha_{\text{sep}}$ ) between the lower and upper radiometers

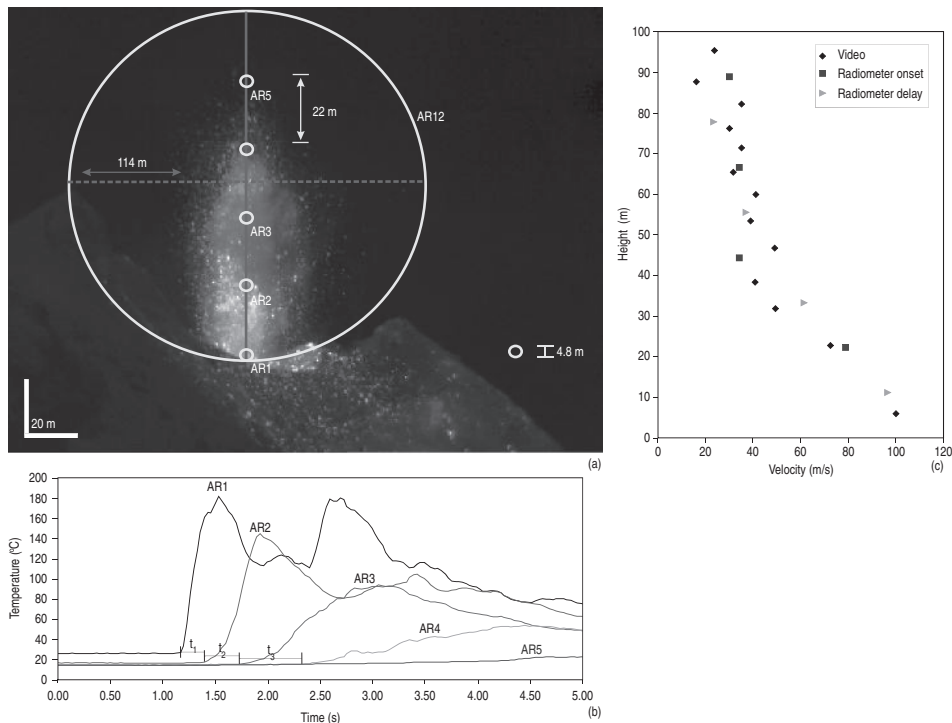


Figure 8.12 (a) Thermal image of an eruption plume at Stromboli overlain with the locations of five vertically-stacked 1° field of view radiometers (AR1-AR5). Also given is the field of view covered by a 15° FOV radiometer (AR12). (b) The waveforms recorded by each radiometer in the stack during the explosive emission, with the time delay in onset between each. (c) Velocities estimated from (i) the time delays, (ii) the onset time apparent in the waveform recorded by each radiometer in the stack ( $\delta t_{\text{inflex}}$  of Figure 8.11), and (iii) particle tracking in simultaneously recorded thermal video. See also color plates section.

needs to be known. Such a set-up is photographed in Figure 8.1d, where the two radiometers are separated by a carefully controlled and known angle. The vertical distance between the lower and upper FOVs ( $\Delta d$ ) can then be calculated from  $2[D_{\text{vent}} \tan(\alpha_{\text{sep}}/2)]$ . Arrival of the plume front in the lower FOV will cause the signal for this sensor to respond first, the later arrival of the plume front in the higher FOV causing this sensor to respond second. The time difference between the onset of the signal recorded by the lower and upper FOVs ( $\Delta t$ ) will be the time it takes the cloud leading edge to travel the distance  $\Delta d$  that separates the two FOVs above the vent. Thus velocity can be estimated from  $\Delta d/\Delta t$ . Use of multiple sensors stacked above the vent allows a plume velocity profile to be built vertically, as done in Figure 8.12c.

Comparison between velocities obtained from the onset and stacking methods, as well as with those from tracking the leading edge in thermal video data during tests at Stromboli, show good agreement. For example, take the time difference between the onset of the signal recorded by the lowermost FOV in the Figure 8.12 stack (FOV AR1), and the next in the

sequence (FOVAR2). The onset time for the AR1 signal ( $t_1$ ) is 1.17 s. For AR2 it is 1.40 s ( $t_2$ ). Thus, the time difference is:

$$\Delta t = t_2 - t_1 = (1.40 \text{ s}) - (1.17 \text{ s}) = 0.23 \text{ s}.$$

For the FOVs higher in the stack (e.g., AR3 and AR4),  $\Delta t$  is longer:

$$\Delta t = t_4 - t_3 = (2.43 \text{ s}) - (1.83 \text{ s}) = 0.60 \text{ s}.$$

Now, given a separation between each FOV ( $\Delta d$ ) of 22.2 m, these convert to velocities between AR1 and AR2 of:

$$V_{\text{AR1-AR2}} = (22.2 \text{ m}) / (0.23 \text{ s}) = 96.5 \text{ m s}^{-1}$$

and between AR3 and AR4 of:

$$V_{\text{AR3-AR4}} = (22.2 \text{ m}) / (0.60 \text{ s}) = 37.0 \text{ m s}^{-1}.$$

The sampling frequency (~33 Hz or 1 sample every 0.03 s) is not fast enough to capture the onset of the rapidly (~100 m s<sup>-1</sup>) ascending front in the lowest FOV (i.e., the front is moving three times faster than the sampling rate). However, for AR2, AR3, and AR4 the first inflection ( $\delta t_{\text{inflex}}$ ) occurs after 0.061 s, 0.141 s and 0.141 s, respectively. Given a distance of 500 m from the target ( $D_{\text{ist}}$ ) and a FOV <sub>$\alpha$</sub>  of 0.5°, the FOV width is:

$$W_{\text{FOV}} = 2[D_{\text{ist}} \tan(\alpha/2)] = 2[(500 \text{ m}) \tan(0.25^\circ)] = 4.8 \text{ m}.$$

So that the velocities from the first inflexions are, for AR2,

$$V_{\text{AR2}} = (4.8 \text{ m}) / (0.061 \text{ s}) = 79 \text{ m s}^{-1}$$

for both AR03 and AR04,

$$V_{\text{AR3}} \text{ and } V_{\text{AR4}} = (4.8 \text{ m}) / (0.141 \text{ s}) = 34 \text{ m s}^{-1}.$$

As plotted in [Figure 8.12c](#), the two sets of velocities show good agreement which, in turn, compare well with video-based estimates obtained from particle tracking.

As with gas puffing, to make such velocity measurements the field of view must be kept as narrow as possible. This ensures that the plume front will ascend vertically through the FOV, rather than expand radially within it. In addition, the FOV needs to be placed carefully: if ambient velocity is required the FOV should be placed immediately above the vent. For FOVs placed higher in the plume, deceleration will cause lower velocities to be recorded, as shown in [Figure 8.12c](#).

#### 8.4.1.2 Large field of view measurements, thermal amplitude and plume area

Use of a larger field of view tends to dampen the signal, a result of an increased background contribution from the cold sky, so that much of the waveform detail apparent in the narrower FOV data are lost, as shown in [Figure 8.13a](#). For measurements using larger FOV data,

however, there is a good correlation between plume area and FOV-integrated temperature, with integrated temperature increasing as the area of the hot eruption cloud within the FOV increases, to reach a peak as the areal coverage of the plume peaks (see Figure 8.13b). Thus, variations in the rate of change in temperature recorded for a FOV that encompasses the entire eruption plume will be related to changes in the aerial expansion rate of the plume in

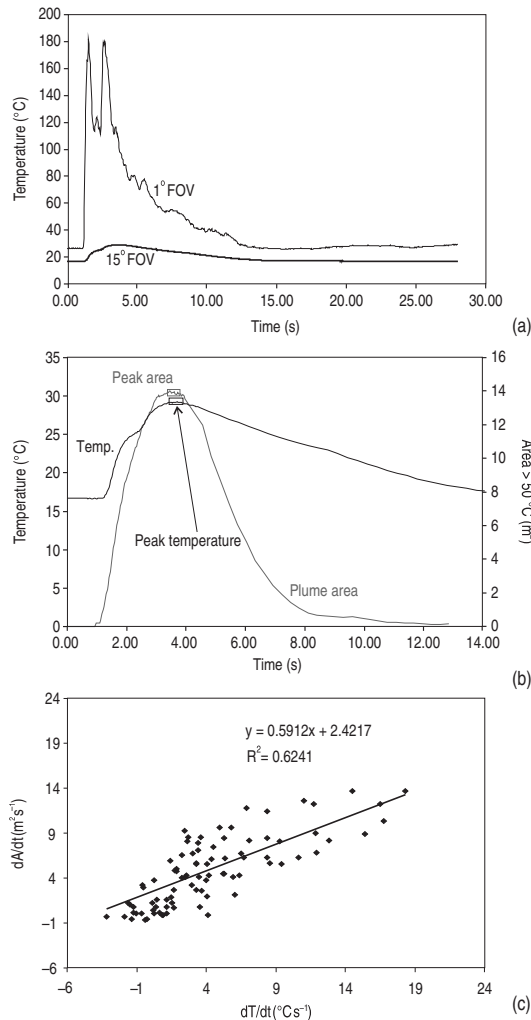


Figure 8.13 (a) Syn-eruption waveform recorded by the near-vent one-degree FOV radiometer of Figure 8.12 (AR1) and the 15° FOV radiometer (AR12). (b) Relationship between the 15° FOV radiometer waveform and plume area, as obtained from simultaneous thermal video, showing coincidence between peak temperature recorded by the radiometer and peak plume area measured in the video. (c) Relation between the rate of change in plume area measured using the thermal video ( $dA/dt$ ) and the rate of change in the radiometer-recorded temperature ( $dT/dt$ ). Boxes in (b) locate the point of peak temperature and plume area.

the FOV (see [Figure 8.13c](#)). In such a case, higher peak thermal amplitudes ( $\delta T$ ) may be associated with greater plume areas. Thermal amplitude is defined in [Figure 8.11](#) and can be calculated from the background temperature ( $T_{\text{back}}$ ) recorded immediately before the eruption and the peak temperature recorded during the eruption ( $T_{\text{peak}}$ ), i.e.,

$$\delta T = T_{\text{back}} - T_{\text{peak}}. \quad (8.9)$$

#### 8.4.1.3 Waveform shapes

We note that the waveforms for strombolian eruptions are somewhat more asymmetric than those recorded during puffing (c.f., [Figures 8.8](#) and [8.11](#)). This is a result of the puff rising completely out of the narrow field of view, whereas the strombolian plume can stall and disperse within the wide field of view causing a long, waning limb as the plume disperses. For narrow field of view records of strombolian eruptions long waning limbs (such as that in [Figure 8.11](#)) are a result of

- (1) steadily waning emission at the vent,
- (2) ejecta falling back down through the field of view,
- (3) gas/aerosols lingering/dispersing over the vent, and/or
- (4) ejecta that has fallen to the ground around the vent and is lying within the field of view, cooling slowly with time.

This latter effect can add a cooling curve to the end of the explosion-related waveform. As a result, waveform durations may actually be somewhat longer than the emission itself. That is, at-vent emission can end, but a thermal signal will still be apparent due to these four effects.

#### 8.4.2 Thermal waveforms associated with ash-dominated emission

Waveforms associated with ash-dominated emissions show the same characteristics as those associated with bomb-dominated emissions. Consequently, the same parameters can be extracted as explored in the previous sections. From the example given in [Figure 8.14](#), we see the following.

- The eruption is apparent as a thermal transient as the hot cloud of ash and gas passes through the field of view ([Figure 8.14a](#)).
- Waveforms can be simple (Type A) if associated with a single explosion (e.g., [Figure 8.14b](#)) or complex (Type D) when ash clouds from multiple explosions pass through the FOV (e.g., [Figure 8.14c](#)).
- Repeated eruptions are apparent as a series of spikes in a time series, each spike recording the passage of an ash cloud through the field of view (e.g., [Figure 8.14d](#)). These are the classic Type B and C sequences of Shimozuru (1971) (see [Figure 7.12](#) of [Chapter 7](#)), and is typical of thermal time series recorded during repeated, discrete strombolian or vulcanian explosions.

- Changing coverage of the FOV by the cloud, as well as increasing emission temperature, will result in an ascending (onset) limb which initially has a steep slope. This slope is maintained until the FOV is filled, at which point the signal may continue to increase. However, the rate of increase now declines as the changing integrated temperature becomes just a function of changing cloud temperature, rather than changing cloud temperature and FOV coverage, the FOV coverage now being 100%. This influence on the onset of the waveform is inset in [Figure 8.14a](#).
- The onset time, as given by the time to first inflection ( $\delta t_{\text{inflex}}$ , [Figure 8.14a](#)), as well as the delay in response between stacked radiometers (e.g., [Figure 8.14b](#)), can be used to obtain ascent velocity of the cloud's leading edge.
- The waveform is typically asymmetrical with a waning limb that is much longer than the waxing limb (e.g., [Figure 8.14a](#)). For larger FOVs, asymmetry is often accentuated by the fact that the cloud will need time to drift out of the FOV once the emission has ended.
- Detail recorded for the waveform diminishes with the size of the FOV: compare the  $15^\circ$  FOV ( $T_1$ ) waveform of [Figure 8.14](#), with the  $1^\circ$  FOV ( $T_2$  and  $T_3$ ) waveforms.

Cloud detachment and dispersal within the FOV will cause elevated signal in the radiometer record as long as there is some warm cloud component within the field of view. This causes thermal event durations, recorded by the radiometer, to be longer than the actual explosion duration, as recorded by seismometers or infrasonic sensors, or emission duration: compare the durations of seismic, acoustic and thermal waveforms in [Figures 8.14b](#) and [8.14c](#). Dispersion may, however, be identified in the thermal time series from a waning, cooling-curve-like, limb to the waveform, as marked on [Figure 8.14b](#), with the onset of the waning limb marking emission termination.

#### 8.4.2.1 Radiated heat flux

An ash emission is usually easier to deal with in a temperature retrieval sense, because a fairly uniform ash body of known emissivity will fill the field of view with optically opaque material, as shown in [Figure 8.14a](#). As a result, we can work with absolute, as well as relative, temperature. The means we can, for example, estimate heat fluxes associated with, or carried by, the plume.

The radiated heat flux density for the plume ( $M_{\text{plume}}$ ), i.e., heat flux per unit area, will be given by

$$M_{\text{plume}} = \sigma \varepsilon [T_{\text{plume}}(t)^4 - T_b^4] \quad (\text{J s}^{-1} \text{ m}^{-2}). \quad (8.10a)$$

in which  $T_{\text{plume}}$  is the plume temperature,  $T_b$  is the ambient, background (sky) temperature,  $\varepsilon$  is the emissivity of the ash comprising the plume, and  $\sigma$  is the Stefan–Boltzmann constant. By integrating the heat flux density through time, a measure of the total radiated flux can be obtained. This provides a measure of the total energy (in

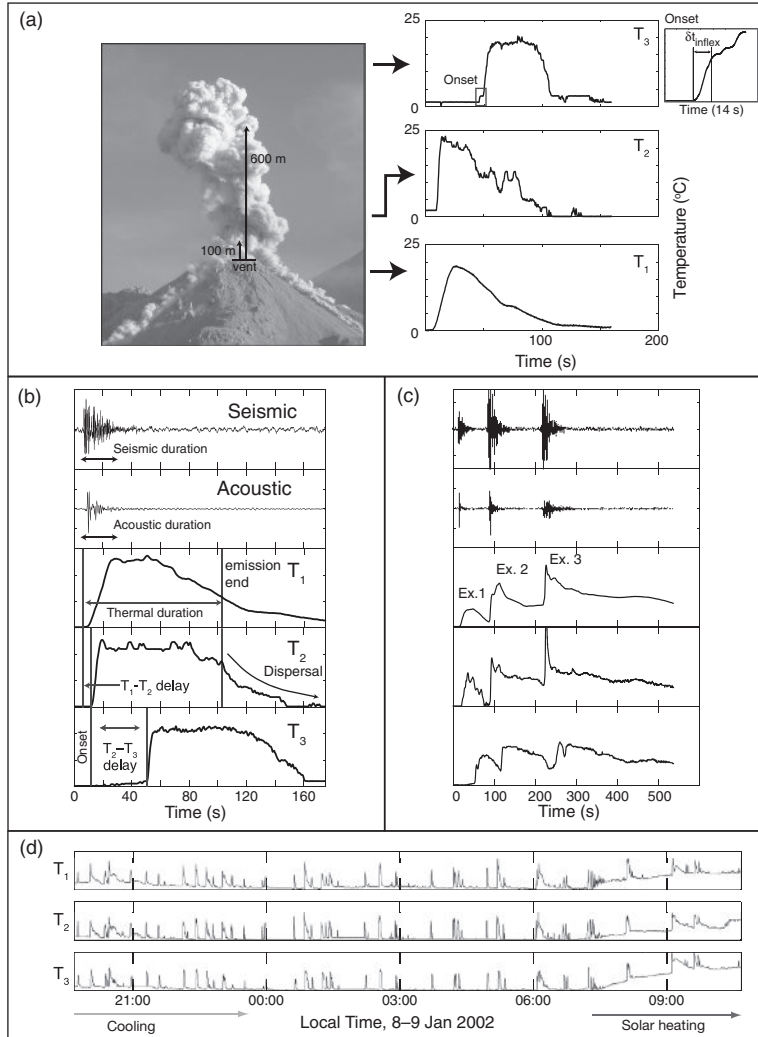


Figure 8.14 (a) Radiometer array deployed at Santiaguito (Guatemala) to track ash cloud emission and ascent dynamics by Sahetapy-Engel *et al.* (2008), comprising three Omega OS554 radiometers, one with a 15° FOV ( $T_1$ ), and two 1° FOVs ( $T_2$  and  $T_3$ ) in a vertical stack within the 15° FOV. Typical waveforms recorded by the three radiometers are displayed to the right, with the onset phase of the  $T_3$  waveform enlarged. Below, seismic, acoustic and thermal waveforms are given for (b) a single explosive event and (c) a sequence of three explosive events (Ex. 1, Ex. 2 and Ex. 3). Delays used to estimate ascent velocities, emission duration and plume dispersal phase are marked on (b). (d) Fourteen-hour-long radiometer record showing spikes due to explosive events superimposed on a background trend of night-time cooling of ambient surfaces in each FOV and day-time (solar) heating. See also color plates section.

joules per meter squared) radiated by the plume, and will increase with plume temperature and emission duration. It can be obtained by integrating the heat flux record obtained from the onset of plume emission (at  $t = 0$ ) through the end of cooling (at  $t = \text{end}$ ) following:

$$E_{\text{plume}} = \int_{t=0}^{t=\text{end}} \sigma \epsilon [T_{\text{plume}}(t_i)^4 - T_b^4] \delta t \text{ (J m}^{-2}\text{)}, \quad (8.10\text{b})$$

in which  $T_{\text{plume}}(t_i)$  is the plume temperature recorded at time  $t_i$ ,  $T_b$  is the background temperature recorded immediately before the eruption and  $\delta t$  is the sampling increment. Multiplying by FOV area ( $A_{\text{FOV}}$ ) gives the result in joules, for the FOV area ( $Q_{\text{FOV}}$ ):

$$Q_{\text{FOV}} = \int_{t=0}^{t=\text{end}} \sigma \epsilon A_{\text{FOV}} [T_{\text{plume}}(t_i)^4 - T_b^4] \delta t \quad (\text{joules}). \quad (8.10\text{c})$$

A number of caveats need to be placed on this estimation, and  $Q_{\text{FOV}}$  may not equate to the actual energy radiated by the plume ( $Q_{\text{plume}}$ ).

- (1) If the plume rises out of the field of view, before it cools to ambient, the total energy radiated by the plume during cooling to ambient will not be measured, and  $Q_{\text{FOV}}$  will be less than  $Q_{\text{plume}}$ .
- (2) Where the plume is the same width as the FOV,  $Q_{\text{FOV}} \approx Q_{\text{plume}}$ . However, if the plume is larger than the FOV, the full plume will not be captured and the total radiated energy will not be recorded; again  $Q_{\text{FOV}}$  will be less than  $Q_{\text{plume}}$ .
- (3) If the plume does not fill the field of view, an under-estimate will result because the contribution of the cooler background will mean that the integrated temperature (used as a proxy for  $T_{\text{plume}}$ ) will be lower than the actual sub-FOV plume temperature. Consider our familiar mixture model:

$$L(\lambda, T_{\text{int}}) = pL(\lambda, T_{\text{plume}}) + (1-p)L(\lambda, T_b). \quad (8.11)$$

In this case,  $p$  is less than 1 and  $T_b$  is less than  $T_{\text{plume}}$ , so  $T_{\text{int}}$  will also be less than  $T_{\text{plume}}$  so that, again,  $Q_{\text{FOV}}$  will be less than  $Q_{\text{plume}}$ . Here,  $M_{\text{FOV}}$  and  $E_{\text{FOV}}$  will both also be less than  $M_{\text{plume}}$  and  $E_{\text{plume}}$ .

- (4) If the FOV size is too small, an anomalously hot portion of the plume may be measured, resulting in an over-estimate of the total radiative flux, so that now  $M_{\text{FOV}}$  and  $E_{\text{FOV}}$  will both also be greater than  $M_{\text{plume}}$  and  $E_{\text{plume}}$ .

Because of uncertainty as to how variations in the FOV size, in relation to the plume area, may be affecting the integrated temperature, it may thus be difficult to compare heat fluxes obtained at different volcanoes, or between fluxes obtained for multiple measurements made at a single volcano but from different distances from the target or using different FOV sizes, or where the plume size (width) varies markedly from eruption to eruption. Take, for

example, a 10 000 m<sup>2</sup> plume at 500 °C targeted with a 15° FOV instrument placed at a distance of 500 m. The field of view will be 13 600 m<sup>2</sup> in area, so that the FOV portion occupied by the plume is 0.73. Assuming, for convenience, an emissivity of one, a background sky temperature of –25 °C gives a FOV-integrated temperature of 400 °C. Using  $T_{\text{int}}$  for  $T_{\text{plume}}$  in Equation (8.10a) gives a radiated heat flux density of:

$$M_{\text{plume}} = (5.67 \times 10^{-8} \text{ W m}^{-2} \text{ K}^{-4})(1) \left[ (673)^4 - (248)^4 \right] = 11.4 \times 10^3 \text{ J s}^{-1} \text{ m}^{-2}.$$

Now, take a measurement of the same plume with a 15° FOV instrument but from a distance of 2500 m. The field of view increases to 340 000 m<sup>2</sup>, but the plume area remains the same, so that the FOV portion occupied by the plume decreases to 0.03, and the integrated temperature to 20 °C. Now the heat flux density shows an apparent decline to:

$$M_{\text{plume}} = (5.67 \times 10^{-8} \text{ W m}^{-2} \text{ K}^{-4})(1) \left[ (293)^4 - (248)^4 \right] = 0.2 \times 10^3 \text{ J s}^{-1} \text{ m}^{-2}.$$

Thus, decline in calculated heat flux density is purely a result of increasing the measurement distance so that the plume becomes an increasingly small sub-resolution feature. In fact, because the plume is smaller than the measurement area in both cases, both calculations under-estimate the true plume heat flux density which should be:

$$M_{\text{plume}} = (5.67 \times 10^{-8} \text{ W m}^{-2} \text{ K}^{-4})(1) \left[ (773)^4 - (248)^4 \right] = 20 \times 10^3 \text{ J s}^{-1} \text{ m}^{-2}.$$

Measurements of heat flux density, heat flux, or energy made in such a way should thus be viewed as a relative, rather than absolute, measure.

#### 8.4.2.2 Measurement examples

In spite of these caveats, radiometer-based estimated  $E_{\text{plume}}$ , from fixed points on a single volcano, have shown promising results.

- Johnson *et al.* (2004) showed a correlation between  $E_{\text{plume}}$  and convective velocities, indicating that higher energies enhance buoyancy and result in greater convective ascent velocities.
- Sahetapy-Engel *et al.* (2008) showed good positive correlations between  $E_{\text{plume}}$  and total seismic and infrasonic energies at Santiaguito, indicating that  $E_{\text{plume}}$  may be used as a proxy for eruption power.
- Marchetti *et al.* (2009) showed good positive correlations between the ratio of  $E_{\text{plume}}$  to seismic and infrasonic energy at Villarrica, Stromboli, Fuego and Santiaguito, indicating that  $E_{\text{plume}}$  may be used, with infrasonic energy, to track changes in eruption power as well as style.
- Scharff *et al.* (2008) showed positive correlations between  $E_{\text{plume}}$  and total radar-reflected energies at Stromboli.

Thus, the use of  $E_{\text{plume}}$  to assess the radiant energy of an eruption should be used with caution. However, when time series measurements are made from a fixed position with a

fixed field of view, variations should provide a record of relative changes in the eruption thermal energy.

### 8.5 Slope of the waveform and velocity

When a hot source moves through a field of view at velocity  $V$ , it should be possible to calculate the velocity from the rate at which the integrated radiance increases. For two measurements separated by a time difference of  $\Delta t (= t_2 - t_1)$ , the time derivative for the two radiance measurements ( $R_{\text{int}1}$  and  $R_{\text{int}2}$ ) can be obtained from subtracting the two measurements and dividing by the time difference between the two, so that the rate of change in recorded radiance is:

$$\Delta R_{\text{int}}/\Delta t = \frac{R_{\text{int}1} - R_{\text{int}2}}{\Delta t}. \quad (8.12a)$$

If the temperature of the background (at  $T_b$ ) and target (at  $T_h$ ) are constant between the two measurements, then the rate of change in integrated radiance depends on the rate at which the FOV portion covered by the high temperature component changes ( $\Delta p/\Delta t$ ):

$$\Delta R_{\text{int}}/\Delta t = \Delta p/\Delta t L(\lambda, T_h) + (1 - \Delta p/\Delta t) L(\lambda, T_b). \quad (8.12b)$$

The rate at which the FOV portion occupied by the hot component changes will, in turn, depend on the rate at which the area of the hot source changes ( $\Delta A_{\text{hot}}/\Delta t$ ):

$$\Delta p/\Delta t = \frac{\Delta A_{\text{hot}}/\Delta t}{A_{\text{FOV}}}, \quad (8.12c)$$

$A_{\text{FOV}}$  being the FOV area. If the hot source is wider than the FOV, and moving vertically through it, Equation (8.12c) simplifies to:

$$\Delta p/\Delta t = \frac{\Delta h_{\text{hot}}/\Delta t}{h_{\text{FOV}}}, \quad (8.12d)$$

$h_{\text{hot}}$  being the height of the hot source and  $h_{\text{FOV}}$  being the height of the FOV. Note that, for simplicity, we have assumed a square FOV. In the case of a circular FOV,  $\Delta h_{\text{hot}}$  will not be proportional to  $\Delta A_{\text{hot}}$ , so that the underlying assumption behind the move from Equation (8.12c) to (8.12d) cannot be made.

For the square FOV case, parameter  $\Delta h_{\text{hot}}/\Delta t$  is otherwise the vertical ascent velocity of the hot source (i.e., plume ascent velocity,  $V$ ), so that Equation (8.12d) further simplifies to:

$$\Delta p/\Delta t = \frac{\Delta h_{\text{hot}}/\Delta t}{h_{\text{FOV}}} = \frac{V}{h_{\text{FOV}}}. \quad (8.12e)$$

Inserting into Equation (8.12a) gives:

$$\Delta R_{\text{int}}/\Delta t = \frac{V}{h_{\text{FOV}}} L(\lambda, T_h) + \left(1 - \frac{V}{h_{\text{FOV}}}\right) L(\lambda, T_b), \quad (8.12f)$$

so that,

$$V = h_{\text{FOV}} \left[ \frac{\Delta R_{\text{int}}/\Delta t - L(\lambda, T_b)}{L(\lambda, T_h) - L(\lambda, T_b)} \right] \quad (8.12g)$$

In short, this describes a situation where the change in recorded radiance will be faster with increased velocity of the hot source moving through the FOV. In this case, velocity can be calculated from  $\Delta R_{\text{int}}/\Delta t$  using Equation (8.12g), if  $T_h$ ,  $T_b$ , and  $h_{\text{FOV}}$  are known. However, in practice the theory is difficult to apply because it requires:

- exact knowledge of the high-temperature-component temperature, and the assumption that it is stable and constant during passage through the FOV;
- knowledge of the background-temperature-component temperature, and the assumption that it is stable;
- assumption that the width of the emission is constant, vertically orientated, and moves as a front, that is wider than the FOV, upwards through the FOV; and
- that the FOV is square (although we could force this case on the radiometer by viewing the emission through a square mask whose diameter is smaller than the FOV width).

For an expanding plume of ejecta, gas and aerosol at unknown temperature against a background gas cloud at unknown temperature and emissivity, application of Equation (8.12g) is extremely difficult to justify.

## 8.6 Response time and slew rate

As discussed in Chapter 7, signals which develop faster than the instrument's response time (see Section 7.1.5 of Chapter 7 for definition) will result in waveforms which suffer from distortion. Examination of Figure 7.3 (Chapter 7) shows that changes in temperature that occur over time periods that are shorter than the response time will result in late measurement of the peak temperature. Late arrival of the peak will mean that measurements (e.g., velocities) that use the peak time arrival will be under-estimates. However, as long as the rate of change in the signal is less than the instrument slew rate, i.e., the maximum rate of change of the output voltage, the start of the thermal event should be recorded at the correct time. So, too, should the timings for changes in the rate of change, i.e., inflexions in the waveform.

An analysis of the effect of the typical 0.25 s response time of a thermopile on the recorded form of a thermal pulse is given in Figure 8.15. In cases where the onset and duration of the input pulse are much longer than the response time, the differences between the input and output pulses are minimal. As the pulse onset time and duration approaches the

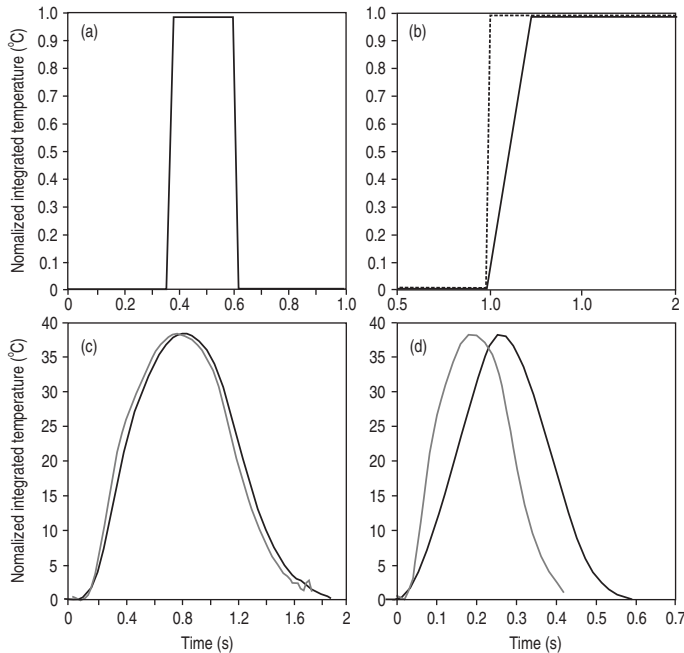


Figure 8.15 (a) Radiometer response function simulated using a box-car function with the same duration as the 0.25 s instrument response time. (b) Assuming a sharp thermal transient as a step function (dashed line), convolution of the transient with the box-car function will result in a 0.25-second-long ramp. (c) Response-time-free thermal waveform obtained from thermal video of an ascending gas puff at Stromboli (gray line) and the same waveform with the calculated effect of the 0.25 s response time applied (black line). In this case the duration of the onset time and puff are both longer than 0.25 s, and differences between the two waveforms are minimal. (d) Same comparison but for a waveform where the onset time and puff durations are of the order of the 0.25 s instrument response time, showing a simulated waveform with no response time effect (black line) and waveform with response time effect (gray line). The peak time is displaced, and the onset time is longer, in the case affected by response time [from Harris and Ripepe, 2007b, Fig. 7].

instrument response time, so the arrival of the peak becomes increasingly delayed and the duration of the recorded waveform exceeds that of the input pulse by an increasing amount. As a result, errors on the velocities calculated from the difference in the pulse start and peak times (i.e., onset time) increase as the onset time decreases, as plotted in Figure 8.16, being around –20% for an onset time that is equal to the response time of, in this case, 0.25 s. There are two solutions to this problem:

- (1) use plots such as that of Figure 8.16 to estimate the likely error on the calculation, or
- (2) do not use waveforms that have onsets that are less than, or equal to, the instrument response time.

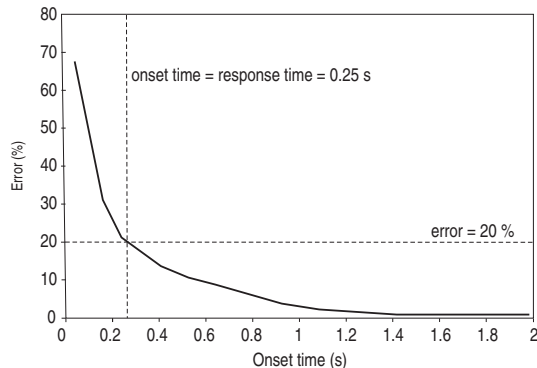


Figure 8.16 Error on the measurement of pulse onset time introduced by the instrument response time plotted as a function of the pulse onset time. Instrument response time (0.25 s) is marked with the vertical dashed line. Errors greater than 20% are introduced when the onset time is shorter than 0.25 s, as marked by the horizontal dashed line, but decline to around 1% for thermal variations developing over 1.25 s.

### 8.6.1 Checking the time scale of response and response time

The time scale of the waveform increase (onset time) can be compared with that of the instrument response time to check whether the waveform can be used for velocity calculation. Take the likely maximum emission velocity at Stromboli of  $\sim 100 \text{ m s}^{-1}$ , with a  $1^\circ$  FOV instrument with a 0.25 s response time, located 300 m from the vent. For this case, FOV diameter ( $W_{\text{FOV}}$ ) will be given by Equation (7.8a) as

$$W_{\text{FOV}} = 2[D_{\text{LOS}} \tan(\alpha/2)] = 2[(300) \tan(1^\circ/2)] = 5.2 \text{ m.}$$

For a front of (isothermal) hot material ascending across such a FOV, peak signal will be recorded after ( $\delta t_{\text{peak}}$ ):

$$\delta t_{\text{peak}} = (5.2 \text{ m}) / (100 \text{ m s}^{-1}) = 0.052 \text{ s.}$$

This is much shorter than the instrument response time, and so the onset will suffer heavy distortion.

### 8.6.2 Appropriate experiment set up

The same calculation can be used to set the FOV diameter to ensure that the recorded waveform develops over a time scale that is slower than the response time. If the signal is to develop at a time scale of the order of the response time ( $\tau_r$ ), then expected emission velocity ( $V$ ) can be used to estimate the optimum FOV diameter ( $W_{\text{optimum}}$ ) in:

$$W_{\text{optimum}} = V\tau_r \quad (8.13a)$$

which in this case is:

$$W_{\text{optimum}} = (100 \text{ m s}^{-1})(0.25 \text{ s}) = 25 \text{ m.}$$

Such a FOV diameter can be obtained by increasing the line of sight distance until it is greater than, or equal to, the optimum targeting distance ( $D_{\text{optimum}}$ ) of:

$$D_{\text{optimum}} = [W_{\text{optimum}}/2] \tan(\alpha/2)^{-1} \quad (8.13b)$$

being, for the case of a  $1^\circ$  FOV,

$$D_{\text{optimum}} = [25 \text{ m}/2] \tan(1^\circ/2) = 1430 \text{ m.}$$

Alternatively, the instrument can be located at the same position, but a larger angular field of view will need to be used, the optimal FOV (FOV<sub>optimum</sub>) being:

$$\text{FOV}_{\text{optimum}} = 2[\tan^{-1}(r_{\text{optimum}}/D_{\text{LOS}})], \quad (8.13c)$$

$r_{\text{optimum}}$  being the optimum FOV radius (i.e.,  $W_{\text{optimum}}/2$ ). For our case, this gives:

$$\text{FOV}_{\text{optimum}} = 2[\tan^{-1}(12.5 \text{ m}/300 \text{ m})] = 5^\circ.$$

An instrument with a shorter response time could also be used. The optimum response time ( $\tau_{\text{optimum}}$ ) is obtained from

$$\tau_{\text{optimum}} = W_{\text{FOV}}/V, \quad (8.13d)$$

which gives, for a  $1^\circ$  field of view instrument located 300 m from the target,

$$\tau_{\text{optimum}} = (5.2 \text{ m})/(100 \text{ m s}^{-1}) = 0.052 \text{ s.}$$

In this case, such short response times would require use of photon detectors, some of which have response times as low as 0.001 s (see [Tables 7.1a](#) and [7.2a](#)).

## 8.7 Radiometers versus imagers

The advent of portable thermal imagers capable of sampling at frame rates of up to 120 Hz, even 1000 Hz, will be reviewed in the next chapter, and potentially could be argued to make the deployment of radiometers obsolete. However, radiometers present a number of advantages that still make them attractive for many tasks.

- They are portable, quick and easy to use, and are power efficient; they can be operated continuously for up to 50 hours using six AA batteries.
- They are relatively cheap; low-cost models are < US\$ 100, with even the most expensive models being of the order of US\$ 3000.

- Being a voltage rather than a series of images, the data are easy to deal with and process (i.e., less data = less processing). This also facilitates simultaneous collection, and direct use, with infrasonic and seismic data.
- Data rates and file sizes are small. For example, 15 minutes of radiometer data collected at 54 Hz has a file size of ~800 kilo-bytes , which compares with a single thermal image file size of ~150 kilo-bytes, meaning a thermal image data set of the same duration and temporal resolution would be 7.29 GB.
- Because radiometers are cheap and robust, they are more amenable to use in environments where they may become damaged or lost. That is, they may be considered a “disposable” option whose loss can be absorbed and accepted as a cost whose benefit is outweighed by the potential data, monitoring and science gain, whereas thermal imagers with price tags of up to US\$ 50 000 and higher may not.

We will consider the application of thermal imagers to volcano thermography next, in [Chapter 9](#).

# 9

## Broad-band thermal imaging cameras

Like the radiometer, a broad-band thermal camera can be defined as an instrument that measures electromagnetic radiation emitted across a given, and wide, waveband typically in the thermal infrared. However, rather than collecting the radiation emitted from a single spot on a targeted surface, they sample an array of pixels distributed as a grid across the surface to allow generation of a thermal image. Use of the word *camera* also distinguishes such instruments from thermal scanners, which build the image by scanning the surface, assembling the image line-by-line, as is the case for many of the devices reviewed under the *airborne remote sensing* section of [Chapter 1 \(Section 1.4.2\)](#). Instead, as with a digital camera operating at visible wavelengths, the thermal camera captures the entire pixel grid at once, without recourse to scanning. In addition, because of their compact and light design, such instruments have become labeled *hand-held thermal cameras*, a result of their portability and operation like a standard hand-held camcorder. These facets have meant that their use in volcanology has become popular over the past decade.

### 9.1 Thermal camera: general texts

At least three books have been published dealing specifically with the functioning, operation and application of broad-band thermal cameras, these being (in chronological order):

- *Common Sense Approach to Thermal Imaging*, by Gerald C. Holst (Holst, [2000](#));
- *Thermal Imaging Cameras: Characteristics and Performance*, by Thomas L. Williams (Williams, [2009](#));
- *Infrared Thermal Imaging: Fundamentals, Research and Applications*, by Michael Vollmer and Klaus-Peter Möllmann (Vollmer and Möllmann, [2011](#)).

Williams ([2009](#)) focuses on the camera and its component parts, including types of lenses and detectors, and covers thermal camera performance, testing, calibration and measurement issues. Vollmer and Möllmann ([2011](#)) provide chapters covering the physical principles of thermal imaging and heat transfer, as well as the properties of thermal cameras and detectors, plus six chapters devoted to applications. Holst's book ([2000](#)), even though more than ten years old now, is another excellent consideration of thermal imaging principles, camera design and performance, and includes two chapters covering camera selection and observer

training, as well as ten chapters detailing industrial and surveillance applications, including professional inspection procedures and report writing requirements. In addition, many thermal camera manufacturers supply operation and application manuals for their cameras, such as:

- FLIR Systems *ThermaCAM™ Operator's Manual* (FLIR Systems, 2003);
- The Fluke Corporation and Snell Groups *Introduction to Thermography Principles* (Fluke Corporation, 2009).

While tending to focus on operation and key (solely industrial) applications of individual camera systems they are essential reading for the camera operator.

## 9.2 The hand-held thermal camera

The development of small, uncooled detectors that can be combined to form a focal plane array (FPA) has allowed the thermal camera to become hand-held. An essential definition at the outset is therefore that of the FPA.

### 9.2.0.1 The focal plane array

The FPA allowed the development of a staring system as opposed to a scanning system. While the scanning system uses a single detector and a scanning mirror to build an image line by line (scan by scan), as is the case for most satellite-based systems (see [Section 3.2 of Chapter 3](#)), a staring system uses detectors arranged in an array of columns and rows to obtain the entire image in a single shot. This is the focal plane array, which is, in effect, a grid of detectors, with each pixel having its own detector capturing energy at the same time as all the other detectors in the array to form an image within which the number of pixels is equal to the number of detectors. No moving parts are involved, so reducing bulk, weight, power requirements and maintenance issues.

### 9.2.1 Hand-held thermal cameras: a brief history

Holst (2000) traces the first infrared line scanner to a military-developed system deployed in 1946. However, the thermal image (or thermogram) acquired by this system took one hour to produce, a time that had been reduced to five minutes by 1960 (Holst, 2000). The first high-temporal-resolution system, operating at 20 images per second, was produced in 1965 (FLIR Systems, 2003). Thus Holst (2000) comments that 1965 can be “considered the year that thermal imaging systems, as we know them today, were created.” However, these early systems still relied on scanning, were heavy, and required equally bulky supporting material such as oscilloscopes, generator sets and liquid nitrogen dewars, which made them not particularly portable. However, as Holst (2000) also points out, because such systems could look in the forward direction, they became called *Forward Looking Infrared (Radiometer) Systems*, or FLIRs. This is a name now also associated with the primary manufacturer of

hand-held thermal cameras used in volcanology (FLIR Systems<sup>TM</sup>, SE-182 11 Danderyd, Sweden<sup>1</sup>), but is also a name which continues to be used interchangeably with *thermal camera* to label the modern, forward staring, hand-held thermal imaging system.

Although the high frame rates offered by the early systems were suited to tracking highly dynamic, active volcanic phenomena, the challenge was to produce an uncooled staring system. Within such a system the lack of moving parts and absence of a cooling requirement both reduces power consumption and negates the need for use of bulky coolant systems; thereby making manufacture of a hand-held system viable. The realization of a hand-held system thus came with the introduction of high-spatial-resolution focal plane arrays (FPAs) in the 1990s. FLIR Systems<sup>TM</sup> dates the first FPA for predictive maintenance (PM) and research and development (R&D) applications as coming on-line in 1993. The first camcorder style FPA infrared (staring) system, the ThermaCAM<sup>TM</sup> series, then entered the market in 1995, with the first uncooled micro-bolometer-based system being available in 1997 (FLIR Systems, 2003). These developments, coupled with advances in high-speed digital electronics that allowed imagery to be stored on small memory disks and, later, cards was a process which, in Holst's (2000) words, "revolutionized the commercialization of thermal imaging systems," and brought in the era of hand-held thermal camera deployments on active volcanoes.

### **9.2.2 Hand-held thermal cameras: basic design and operation**

Current thermal camera design makes them, externally, much like a standard camcorder in shape, weight and basic operation. By way of example, scaled diagrams of the FLIR Systems ThermaCAM<sup>TM</sup> S40 are given in Figure 9.1. Powered by internal, rechargeable batteries, basic operation requires pressing of an "on" (power) button, and then a "record" (or acquisition) button to capture an image, or series of images. While battery and memory status are given in a window placed on the side of the camera, higher level operating parameters can be entered using options available from pull-down menus visible in the view finder and selectable using buttons mounted on the camera exterior.

Internally, the thermal camera works much like the radiometer, as given in the schematic of Figure 7.1 (Chapter 7), the difference being that incoming IR radiation is sensed by an array of detectors, this being the FPA, rather than a single detector, to allow instantaneous acquisition of an image. Upon arriving at the optical system, IR radiation is focused by the lens onto the FPA where a voltage is registered at each detector in the array, the voltage being a function of the radiance incident upon the detector. This continuous voltage is sampled by an analog-to-digital converter, which quantizes the continuous voltage into a series of digital numbers. These digital numbers are converted to spectral radiance and then, via Planck's Law, to a pixel-integrated brightness temperature for each detector. The control system may allow factors such as the gain setting, distance to the target, emissivity or atmospheric parameters to be entered, as well as the color mapping scheme to be selected (i.e., selection of the color palette for image display) plus sampling rate and acquisition duration. These settings are then taken into account in the camera's

<sup>1</sup> Web address as of July 2011: <http://www.flir.com>

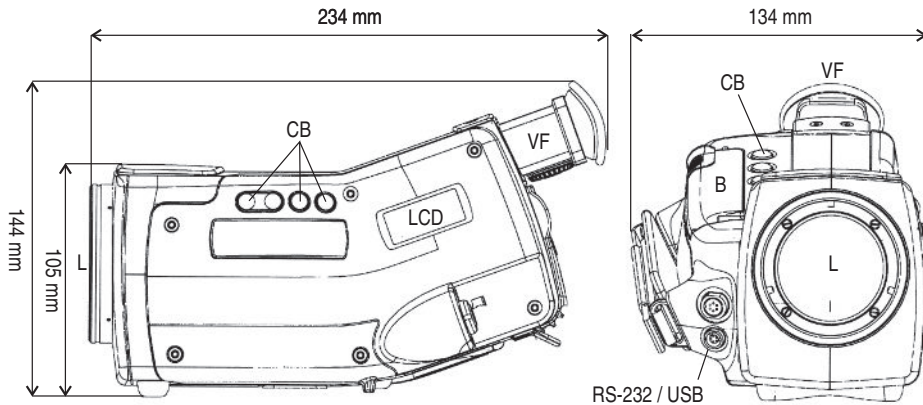


Figure 9.1 Scaled diagrams of the FLIR Systems ThermaCAM™ S40: side and front view. Labeled are the lens (L), view finder (VF), control buttons (CB), camera status window (LCD), data output sockets (RS-232 / USB), and rechargeable battery compartment (B) [modified from FLIR Systems (2003, Fig. 12.10)].

internal processing stream. The image is then reconstructed and either output in an analog and/or digital form to be saved on internal disks or streamed (typically via firewire) to a PC, while also being streamed to the view finder (or fold-out, camcorder-style viewing window).

Output images come with header information giving details such as image date and time, file name, camera model, serial number, and lens type, plus any parameters entered by the operator (such as emissivity, air temperature, humidity and distance to target). In the newest models, GPS information is also provided. Each pixel in the image will have a brightness temperature, which may or may not have been corrected for emissivity and atmospheric effects. In many cases, manufacturer-dependent software is required to read the images and export to a public format (e.g., jpg, bmp, mat). The same software allows a degree of image processing and analysis.

### 9.2.3 Hand-held thermal cameras: common detectors used for the FPA

The most commonly used detector in a focal plane array is the bolometer or micro-bolometer, this being a type of thermal detector (see Chapter 7 for definition). However, other detector types, mostly photo-detectors comprising platinum silicide (PtSi), have also been used. This second group of detectors require cooling. Thus, although the micro-bolometer-based camera can usually be used immediately, the photo-detector-based system requires time to cool down. For example, while the start-up time for the micro-bolometer-based ThermaCAM™ 545–675–695 range is less than 25 s, the photo-detector-based Merlin camera requires ~ 10 min cool-down time, during which time the detector is cooled to the operating temperature of 77 K.

#### 9.2.3.1 Bolometers

The bolometer registers changes in emitted power in the 1.6  $\mu\text{m}$  to millimeter waveband from a change in the electrical resistance of a semiconductor material (Dereniak and Boreman, 1996).

Generally used for measurements in the TIR, especially between 7  $\mu\text{m}$  and 14  $\mu\text{m}$ , increases in the incoming radiation cause the detector temperature to increase. This produces a resistance change in the detector bolometer. A second bolometer is linked to the detector by a bridge circuit. This second bolometer is shielded from radiation so that its resistance is stable. When there is no radiation incident upon the detector bolometer, the bridge between the detector and stable bolometer is balanced and no current flows through the resistor between the two. If the detector is exposed to radiation, while the resistance of the detector bolometer decreases, that at the stable bolometer remains unchanged, so that the bridge circuit between the two bolometers is unbalanced and a voltage crosses the bridging circuit, the voltage being proportional to the radiation received by the sensor.

As with detector types reviewed in [Chapter 7](#), the bolometer will have a response time. That is, if exposed to an instantaneous pulse of heat, the bolometer will take time to heat up and fully respond to that pulse. Likewise, when the source is turned off, the bolometer will take time to cool down. For a bolometer, this detector response time is  $\sim 4$  ms (Vollmer and Möllmann, 2011). The bolometer will also have a spectral response function that is not a top-hat shape (see [Section 3.4.1](#) of [Chapter 3](#)). Thus, following the temperature retrieval methodology of Electronic Supplement 3, to obtain precise pixel-integrated temperature measurements, the response function needs be convolved with the spectral radiance arriving at the sensor, as well as with the spectral responses for emissivity, transmissivity and atmospheric up-welling radiance, to retrieve precise temperatures.

#### *9.2.3.2 Platinum silicide*

Platinum silicide (PtSi) has also been used in the construction of hand-held thermal cameras that record in the MIR, especially between 3  $\mu\text{m}$  and 5  $\mu\text{m}$ . The now discontinued FLIR Systems Prism DS hand-held thermal camera, for example, used a  $224 \times 320$  FPA of PtSi detectors to record images in the MIR. Likewise, Yeh *et al.* (2000) described a “new man-portable thermal imager,” the Seagle-1, that comprised a  $256 \times 244$  FPA of PtSi detectors in a thermal camera that weighed 3 kg and recorded between 3.4  $\mu\text{m}$  and 5  $\mu\text{m}$ . Developed during the early 1990s, such PtSi-based devices comprised a Schottky barrier detector array (Platinum Metals Review, 1991). This is a photo-detector which comprises a metal film (the barrier) at the base of a semiconductor. For infrared detectors, silicon (Si) is used as the semiconductor and platinum (Pt) as the metal or barrier (Dereniak and Boreman, 1996). The photons enter the detector and first pass through the Si layer, but are absorbed by the silicide (PtSi) film at the base of the Si layer, with only a portion of the photons crossing the barrier. This records a current that is a function of light (number of photons) arriving on the detector, so that this is a photo-emissive detector with the current being dependent on the level of photo-emission experienced by the barrier.

#### *9.2.3.3 Other photo-detector types and on-board-cooling*

Other detector materials used in thermal cameras that operate in the SWIR and MIR include indium-antimony (InSb), and indium-gallium-arsenide (InGaAs) (see [Table 9.1a](#)). These

materials allow construction of photodiodes and Quantum Well Infrared Photodetectors, respectively (see Dereniak and Boreman (1996) for definition). These produce currents or voltages as a function of the light energy incident on the detector. However, all such detectors require cooling to 77 K to remove dark-current noise (see [Section 7.1.1 of Chapter 7](#)). Thus, all cameras operating photo-detectors must contain a cooling system. This usually involves Stirling Cycle coolers or Thermoelectric (Peltier) coolers. While the Stirling Cycle coolers operate on the same principle as the household refrigerator, thermoelectric coolers make use of the Seebeck or Peltier effect, whereby an electric current passing through a junction of two dissimilar materials produces cooling when the current flows in one direction, and heating when it travels in the other. Both are compact, low weight and low power consumption electrical solutions to detector cooling, requiring just a few amps to run. As a result both cooler types have become widespread in small, compact, portable and battery operated thermal camera systems that use photon detectors (see Williams 2009; Vollmer and Möllmann, 2011).

#### ***9.2.4 Thermal camera options***

A number of manufacturers currently produce commercially available broad-band thermal cameras, including Infratek, E2V Technologies, FLIR Systems<sup>TM</sup>, Fluke, Land, Mikron, NEC Avio Infrared Technologies, and Thermoteknix (see [Appendix I](#) for listing). As a result, a variety of thermal camera options are available. A selection of thermal cameras with potential for volcano surveillance and research applications are collated in [Table 9.1](#), as well as in [Appendix I](#). We can see that most commercial thermal cameras currently operate in the 7–14  $\mu\text{m}$  window using FPAs of micro-bolometers. As with radiometers, commercially available thermal cameras can be split into two types: hand-held cameras and fixed-mount systems. A selection of commonly used hand-held cameras as of 2008 are listed in [Table 9.1b](#). These camera systems include optics and an image viewing capability. This involves either a view finder and/or flip-out LCD screen mounted on the camera side or top, on which the in-coming stream of thermal images can be viewed in real time. The screen also allows menu-driven control of the camera functions. This makes hand-held cameras more expensive than fixed-mount systems, but allows for easy targeting and use in the field. Fixed-mount systems are listed in [Table 9.1c,d](#) and lack a viewing capability. This makes them less expensive, more robust and useful for long-term-to-permanent deployments. As a result they usually come with a variety of mount points to allow versatility in the installation process. The FLIR Systems SC645 and SC655 fixed-mount cameras, for example, have tripod mounts, as well as threads to take screws, on three sides. Usually, the operating parameters (e.g., control of the sampling rate or temperature gain settings) have to be set via external control through connection to a PC on which the connection and control software has been installed. Once the operation parameters are set, the camera will operate in the defined configuration once powered up. Fixed-mount systems also usually lack internal batteries and thus have to be supplied with an external power source.

Table 9.1. Examples of commercially available broad-band thermal imaging cameras suitable for volcanological applications, with detector type where known, as commonly used through 2008 (SEE APPENDIX I FOR COMPLETE MARKET SURVEY AS OF APRIL 2012).

Table 9.1a. Thermal cameras operating with: SWIR and MIR thermal-detectors.

Manufacturer:	CSIST <sup>a</sup>	Indigo Systems	FLIR Systems
Model:	Seagle-1	Pheonix-Near	ThermoVision SC6000 MWIR
Sensor type:	PtSi	InGaAs	InSb
Waveband (μm)	3.4–5	0.9–1.7	3–5 (optional: 1.5–5 μm)
Cooling	Stirling Cycle cooler	Thermo-electric (TEC) stabilization	
Array dimensions (H × V)	256 × 244	320 × 256	640 × 512
Pixel size		30 μm	25 μm
FOV (degrees)	4.6 × 3.5 (with 100 mm lens)	5.5 × 4.4 (with 100 mm lens)	
Temperature range (°C)			
Accuracy			
Thermal sensitivity (NEΔT)	0.067 °C		0.025 °C
Image frequency		345 Hz	120 Hz (digital)
Image and video output	12 bit digital data (external video connector)		Analog video @30 Hz (windowing capability for increased frame rates)
Weight	3 kg	7 lbs	10 lbs
Size (H × W × L)	10.8 × 18.5 × 11.6 cm	7.5" × 4.4" × 5.2"	7.7" × 5" × 6"
Tripod Mounting		¼" × 20" plate	
Source (date)	Yeh <i>et al.</i> (2000)	Indigo Systems (2002)	FLIR Systems (2005)
Price (date)			

<sup>a</sup> Chung Shan Institute of Science and Technology, Lung Tan, Taoyuan Taiwan.

#### 9.2.4.1 Hand-held thermal cameras: past and current options

One of the first commercially available hand-held thermal cameras used to examine a high-temperature volcanic target was a ThermaCAM™ 595. The ThermaCAM™ 545–595–675–695 range used a micro-bolometer FPA to collect 320 × 240 pixel radiometric images at one of three (standard) gain settings: low, medium or high (FLIR Systems, 2001).

Table 9.1a. (cont.)

Manufacturer:	FLIR Systems <sup>b</sup>	FLIR Systems
Model:	Merlin MWIR	Star SAFIRE HD / III
Sensor type:	InSb	InSb
Waveband ( $\mu\text{m}$ )	1.5–5.5 3–5 $\mu\text{m}$ set by cold filter	3–5
Cooling	Integral Stirling or $\text{LN}_2$ to 77 K; cool down time: 10 mins	
Array dimensions (H $\times$ V)	$320 \times 256$	$640 \times 512 / 680 \times 480$
Pixel size	30 $\mu\text{m}$	
FOV (degrees)	5.5 $\times$ 4.1 (with 100 mm lens)	30–0.25 / 25–0.35
Temperature range ( $^{\circ}\text{C}$ )	0–350 $^{\circ}\text{C}$ or: 300–2000 $^{\circ}\text{C}$	
Accuracy	$\pm 2 ^{\circ}\text{C}$ , $\pm 2\%$ of reading	
Thermal sensitivity ( $NE\Delta T$ )	0.025 $^{\circ}\text{C}$	
Image frequency	60 Hz	
Image and video output	Analog video @60 Hz S-video Digital video 60 Hz (12-bit) Digital video output: RS-422	NTSC/PAL
Weight	9 lbs	10.4 kg
Size (H $\times$ W $\times$ L)	5.5" $\times$ 5.0" $\times$ 9.0"	25.4 $\times$ 19.1 $\times$ 31.8 cm
Tripod Mounting	1/4" $\times$ 20" plate	Aircraft mounted
Source (date)	FLIR Systems (2004) Indigo Systems (2002)	FLIR Systems (2006)
Price (date)	\$60 000 (08/02)	

<sup>b</sup> Formerly by Indigo Systems.

While the PM 545 low gain setting covered –20 to 120  $^{\circ}\text{C}$ , that of the PM 675 and 695 spanned –40 to 120  $^{\circ}\text{C}$ , with the medium gain setting spanning 55 to 350  $^{\circ}\text{C}$  (PM 545), 80 to 500  $^{\circ}\text{C}$  (PM 675) and 0 to 500  $^{\circ}\text{C}$  (PM 695). High gain settings spanning 200 to 1000  $^{\circ}\text{C}$  could be selected for the PM 545 and PM 675, increasing to 350 to 1500  $^{\circ}\text{C}$  or 350 to 2000  $^{\circ}\text{C}$  for the PM 695. Including a standard camera tripod mount on its base and powered by a single rechargeable NiMh battery, which had an operating time of 2 h and recharge time of 1 h, its volume ( $\sim 4000 \text{ cm}^3$ ) and weight (2.4 kg, with battery) made the ThermaCAM<sup>TM</sup> range both hand-held and field-portable. It also set the standard for the typical thermal camera field of view (24  $\times$  18 degrees) and pixel size (1.3 mrad). The range was actually the second generation of micro-bolometer-based thermal camera systems developed by FLIR Systems and grew out of the AGEMA<sup>TM</sup> 570 thermal camera, which went on-line during 1997. This, in

Table 9.1b. Hand-held thermal cameras: TIR uncooled microbolometer thermal-detectors. Cameras are listed in chronological order, i.e., by year of data sheet download.

Manufacturer:	FLIR Systems	Indigo Systems	FLIR Systems	FLIR Systems
Model:	545/595/675/695	TVS-620	S40	S45
Sensor type:	Bolometer	Bolometer	Bolometer	Bolometer
Waveband ( $\mu\text{m}$ )	7.5–13	8–14	7.5–13	7.5–13
Array or image dimensions (pixels)	320 × 240	320 × 240	320 × 240	320 × 240
Pixel size	1.3 mrad	1.4 mrad	1.3 mrad	1.3 mrad
FOV (degrees)	24 × 18	26.2 × 19.3 (35 mm lens)	24 × 18	24 × 18
Temperature range ( $^{\circ}\text{C}$ )				
Low	–40 to 120	–20 to 550	–40 to 120	–40 to 120
Mid	80 to 500	–	0 to 500	0 to 500
High	200 to 1000 <sup>a</sup>	–20 to 900	350 to 1500 <sup>b</sup>	350 to 1500 <sup>b</sup>
Accuracy	$\pm 2^{\circ}\text{C}$ , $\pm 2\%$ of reading	$\pm 2^{\circ}\text{C}$ , $\pm 2\%$ of reading	$\pm 2^{\circ}\text{C}$ , $\pm 2\%$ of reading	$\pm 2^{\circ}\text{C}$ , $\pm 2\%$ of reading
Thermal sensitivity ( $NE\Delta T$ )	0.1 $^{\circ}\text{C}$ (695 = 0.07 $^{\circ}\text{C}$ )	0.15 $^{\circ}\text{C}$	0.08 $^{\circ}\text{C}$ (@ 30 $^{\circ}\text{C}$ )	
Image frequency	50/60 Hz	30 Hz	60 Hz	60 Hz
Image and video output	60 Hz (RS170) 50 Hz (S-video, 695 only)	Images in *.tif format	Radiometric images: 15 Hz by firewire	Radiometric images: 60 Hz by firewire
Weight	2.4 kg (w/battery)	2.0 kg	1.4 kg (w/battery)	1.4 kg (w/battery)
Size (H × W × L)	22 × 13 × 14 cm	21.7 × 14.2 × 11.5 cm	22 × 10 × 12 cm	22 × 10 × 12 cm
Tripod mounting	¼" × 20" plate		¼" × 20" plate	¼" × 20" plate
Batteries (and life)	NiMh battery (2 h)	Standard lithium ion (2.5 h)	Li-ion (recharge) (2 h)	Li-ion (recharge) (2 h)
Source (date)	FLIR Systems (2001)	Indigo Systems (2002)	FLIR Systems (2002)	FLIR Systems (2005)
Price (date)		\$40 000 (08/02)		

<sup>a</sup> Ranges for PM675 are given, where the high range is an optional range for PM545 and 675, and 350 to 1500  $^{\circ}\text{C}$  for the 695 model. Low and mid-ranges for PM545 are –20 to 120  $^{\circ}\text{C}$  and 55 to 350  $^{\circ}\text{C}$ , and for PM695 are –40 to 120  $^{\circ}\text{C}$  and 0 to 500  $^{\circ}\text{C}$ .

<sup>b</sup> Optional range to 2000  $^{\circ}\text{C}$ .

Manufacturer:	FLIR Systems	Mikron	Mikron	FLIR Systems
Model:	SC640	M7640	M7604F/G	SC660
Sensor type:	Bolometer	Bolometer	Bolometer	Bolometer
Waveband ( $\mu\text{m}$ )	7.5–13	8–14	8–14 plus 3.9 $\mu\text{m}$ (7640F) or 4.8–5.2 $\mu\text{m}$ (7640G)	7.5–13
Array or image dimensions (pixels)	640 × 480	640 × 480	320 × 240	640 × 480
Pixel size	0.65 mrad	0.6 mrad	1.2 mrad	0.65 mrad
FOV (degrees)	24 × 18	21.7 × 16.4	21.7 × 16.4	24 × 18
Temperature range (°C)				
Low	–40 to 120	–20 to 60	–40 to 120	–40 to 120
Mid	0 to 500	–40 to 120	0 to 500	0 to 500
High	350 to 1500 <sup>b</sup>	0 to 500 <sup>c</sup>	400 to 1600 <sup>c</sup>	350 to 1500 <sup>b</sup>
Accuracy	±2 °C, ±2% of reading	±2 °C, ±2% of reading	±2 °C, ±2% of reading	±1 °C, ±1% of reading
Thermal sensitivity ( $NE\Delta T$ )	0.06 °C (@ 30 °C)	0.06 °C (@ 30 °C)	0.06 °C (@ 30 °C)	0.045 °C (@ 30 °C)
Image frequency	30 Hz	30 Hz	60 Hz	Up to 120 Hz
Image and video output	30 Hz (IEEE-1394 firewire)	Compact flash memory card NTSC/PAL via S-video	Compact flash memory card NTSC/PAL via S-video	30 Hz (IEEE-1394 firewire)
Weight	1.7 kg (w/battery)	1.7 kg (w/battery)	3.5 lbs (w/battery)	1.7 kg (w/battery)
Size (H × W × L)	22 × 12 × 14.5 cm	21 × 11 × 11 cm	7.4 × 4.3 × 4.5"	22 × 12 × 14.5 cm
Tripod mounting	¼" × 20" plate	¼" × 20" plate	¼" × 20" plate	¼" × 20" plate
Batteries (and life)	Li-ion (recharge) (3 h)	7 W (2.5 h)	6 W (2.5 h)	Li-ion (recharge) (3 h)
Source (date)	FLIR Systems (2006)	Mikron Infrared (2008)	Mikron Infrared (2008)	FLIR Systems (2008)
Price (date)	€ 30 000 (05/09)	\$37 995 (5/09)	\$35 000 (5/09)	€ 30 000 (05/09)

<sup>c</sup> Optional range to 2000 °C.

Manufacturer:	FLIR Systems	FLIR Systems	FLIR Systems	FLIR Systems
Model:	B660	P620/640/660	T360/400	i-series
Sensor type:	Bolometer	Bolometer	Bolometer	Bolometer
Waveband (μm)	7.5–13	7.5–13	7.5–13	7.5–13
Array or image dimensions (pixels)	640 × 480	640 × 480	320 × 240	120 × 120 (i40) 140 × 140 (i50) 180 × 180 (i60)
Pixel size	0.65 mrad	0.65 mrad	1.36 mrad	—
FOV (degrees)	24 × 18	24 × 18	25 × 19	25 × 25
Temperature range (°C)				
Low	−40 to 120 <sup>d</sup>	−40 to 120	−20 to 120	−20 to 350
Mid		0 to 500 <sup>e</sup>	0 to 350 <sup>e</sup>	
High				
Accuracy	±1 °C, ±1% of reading	±2 °C, ±2% of reading	±2 °C, ±2% of reading	±2 °C, ±2% of reading
Thermal sensitivity (NEΔT)	0.045 °C (@ 30 °C)	0.065 °C (@ 30 °C)	0.06 °C (@ 30 °C)	<0.1 °C (@ 25 °C)
Image frequency	30 Hz	30/60 Hz	—	—
Image and video output	Removable SD-card (1GB) for saving radiometric movies; MPEG-4 (non-radiometric) video streaming via firewire	Removable SD-card (1GB) for saving radiometric movies Radiometric images @ 2 Hz via USB	Removable SD-card (1GB, 1000 JPEG images) NTSC video output	Removable SD-card (1GB, 1000 images) MPEG-4 video via USB
Weight	1.7 kg (w/battery)	1.7 kg (w/battery)	0.88 kg	0.6 kg
Size (H × W × L)	22 × 12 × 14.5 cm	22 × 12 × 14.5 cm	20.1 × 10.6 × 12.5 cm	23.5 × 0.81 × 17.5 cm
Tripod mounting	¼" × 20" plate	¼" × 20" plate	¼" × 20" plate	
Batteries (and life)	Li-ion (recharge) (>3 h)	Li-ion (recharge) (3 h)	Li-ion (recharge) (4h+)	Li-ion (recharge) (5h)
Source (date)	FLIR Systems (2008)	FLIR Systems (2008)	FLIR Systems (2008)	FLIR Systems (2008)
Price (date)			€ 18 000 (05/09)	€ 995 (i3, 2011)

<sup>d</sup> Two optional extended ranges up to 1500 °C and 2000 °C.

<sup>e</sup> Extended range up to 2000 °C optional.

Table 9.1c. *Fixed-mount thermal cameras: TIR uncooled microbolometer thermal-detectors by FLIR Systems. Cameras are listed in chronological order; i.e., by year of data sheet download.*

Manufacturer:	FLIR Systems	FLIR Systems
Model:	ThermoVision A10 <sup>f</sup>	A320G/SC325
Sensor type:	Bolometer	Bolometer
Waveband (μm)	7.5 – 13.5	7.5 – 13
Array or image dimensions (pixels)	160 × 120	320 × 240
Pixel size	4.64, 2.83, 1.7 mrad <sup>g</sup>	
FOV (degrees)	40 × 30 25 × 19 15 × 11 <sup>g</sup>	25 × 18.8
Temperature range (°C)		
Low	to 150	–20 to 120
Mid	to 400 <sup>h</sup>	0 to 350
High		Optional: 200 to 1200
Accuracy	–	±2 °C, ±2 % of reading
Thermal sensitivity (NEΔT)	0.085 °C	0.05 °C (@ 30 °C)
Image frequency	30 Hz	60 Hz (for full frame)
Image and video output	Firewire allows digital video acquisition without a framegrabber	RJ-45 Gigabit Ethernet connection supplies 16-bit 320 × 240 images at 60 Hz with linear temperature data
Weight	0.12 kg	0.7 kg
Size (H × W × L)	1.45 × 1.35 × 1.9"	7 × 7 × 17 cm
Tripod Mounting		¼" × 20" plate on 3 sides
Power	< 1.5 W	24 W
Source (Date)	FLIR Systems (2005) Indigo Systems (2002)	FLIR Systems (2007)
Price (date)		\$17 950 (05/09) <sup>i</sup>

<sup>f</sup>Formerly the Omega camera of Indigo Systems.

<sup>g</sup>At 11, 18 and 30 mm focal lengths.

<sup>h</sup>With optional auto-gain mode.

<sup>i</sup>€ 16 900 (11/10).

Table 9.1c. (cont.)

Manufacturer:	FLIR Systems	FLIR Systems
Model	SC645	SC655
Sensor type:	Bolometer	Bolometer
Waveband ( $\mu\text{m}$ )	7.5–13	7.5–13
Array or image dimensions (pixels)	640 $\times$ 280	640 $\times$ 280
Pixel size		
FOV (degrees)	25 $\times$ 18.8	25 $\times$ 18.8
Temperature range ( $^{\circ}\text{C}$ )		
Low	–20 to 150	–20 to 150 $^{\circ}\text{C}$
Mid	0 to 650	0 to 650 $^{\circ}\text{C}$
High	Optional: up to 2000	Optional: up to 2000
Accuracy	2 $^{\circ}\text{C}$ , $\pm 2\%$ of reading	2 $^{\circ}\text{C}$ , $\pm 2\%$ of reading
Thermal sensitivity ( $NE\Delta T$ )	0.05 $^{\circ}\text{C}$ (@ 30 $^{\circ}\text{C}$ )	0.05 $^{\circ}\text{C}$ (@ 30 $^{\circ}\text{C}$ )
Image frequency	25 Hz	50 Hz 100/200 Hz with windowing
Image and video output	Ethernet & USB: 16-bit 640 $\times$ 480 pixels at 25 Hz, temperature linear & radiometric	16-bit 640 $\times$ 480 pixels at 25 Hz, up to 100 Hz (USB) or 200 Hz (Ethernet) with windowing
Weight	0.7 kg	0.7 kg
Size (H $\times$ W $\times$ L)	7.5 $\times$ 7.3 $\times$ 21.6 cm	7.5 $\times$ 7.3 $\times$ 21.6 cm
Tripod Mounting	$\frac{1}{4}$ " $\times$ 20" plate & threads <sup>j</sup>	$\frac{1}{4}$ " $\times$ 20" plate & threads <sup>j</sup>
Power	24 W	24 W
Source (Date)	FLIR Systems (2010)	FLIR Systems (2010)
Price (date)	€ 23 950 (11/10)	

<sup>j</sup> On three sides.

turn, was based on the first FPA camera system, the AGEMA 550. The AGEMA 550 used a Stirling Cycle cooled array of PtSi photo-detectors to acquire 320  $\times$  240 pixel images in the MIR (3.6 – 5.0  $\mu\text{m}$ ) and was launched in 1993.

The ThermaCAM™ range also featured a 14 bit analog-to-digital converter which allowed conversion of the analog signal from the detector into a digital format with 16 384 levels, as opposed to 256 levels provided by previous 8-bit systems. Each of the 768 000 detectors in the FPA were individually calibrated for accuracy, allowing conversion to pixel brightness temperature across the image with a  $NE\Delta T$  of 0.1  $^{\circ}\text{C}$  and an accuracy of  $\pm 2\%$  of the reading. However, although non-radiometric video could be output

Table 9.1d. Fixed-mount thermal cameras: TIR uncooled microbolometer thermal-detectors.

Manufacturer:	Thermoteknix
Model:	Miricle 110K-25
Sensor type:	Bolometer
Waveband ( $\mu\text{m}$ )	7–14
Array or image dimensions (pixels)	384 × 288
Pixel size	0.78 mrad
FOV (degrees)	3.1 × 2.3 to 37.2 × 28.4
Temperature range ( $^{\circ}\text{C}$ )	Multiple autogain modes
Accuracy	—
Thermal sensitivity ( $NE\Delta T$ )	<50 mK
Image frequency	50/60 Hz (up to 240 Hz)
Image and video output	NTSC/PAL (RS232 + USB2)
Weight	105 g
Size (H × W × L)	4.6 × 4.5 × 5.25 cm
Tripod mounting	—
Power	<3.2 W
Source (Date)	Thermoteknix (2008)
Price (Date)	—

at up to 60 Hz (60 Hz for NTSC format, 50 Hz for PAL format), radiometric (calibrated) images had to be saved onto an internal memory card. This limited the storage capacity to the size of the memory card. Given the  $\sim$  150 kilobyte image size, while the 16 Mb PCMCIA flash card of the PM545 could store  $\sim$  106 images, the 160 Mb card of the PM 675–695 could store  $\sim$  1060 images. The time required to save a single 14-bit image was  $\sim$  1.5 s, meaning that radiometric images could be stored at a rate of  $\sim$  0.5 Hz (i.e., one image every 2 s), which would fill the 16 Mb card after 3.5 min, and the 160 Mb card after  $\sim$  35 min.

Around 2002, FLIR systems launched the ThermaCAM™ S40. This was essentially the same as the ThermaCAM™ 695, with the upper limit of the high gain setting being 1500  $^{\circ}\text{C}$  or 2000  $^{\circ}\text{C}$ , and the lower limit of the mid gain being 0  $^{\circ}\text{C}$  (see Table 9.1b). These adjustments made the camera even more useful for analysis of high-temperature volcanic phenomena, providing data which would previously have been out of range given the gain settings of the PM 545 or 595. The camera was also less shoe-box in design, and had a reduced weight of 1.4 kg (including battery). More importantly, the S40 also permitted radiometric images to be transferred to a PC via firewire (IEEE 1394), where the ThermaCAM™ Researcher software could collect data at a rate of 15 Hz (i.e., 15 frames per second), a rate which was increased to 60 Hz with the S45, and allowed video-style imaging of fast moving or rapidly evolving volcanic phenomena.

The launch of the ThermaCAM<sup>TM</sup> S60 around 2006 saw an increase in spatial resolution, with the field of view being maintained at  $24 \times 18$  degrees but the FPA array size increasing to  $640 \times 480$  detectors, yielding an image of the same dimensions but halving the pixel size to 0.65 mrad. However, this also halved the rate at which images could be output, reducing the acquisition rate to 30 Hz. Around 2008, Mikron launched a range of cameras with similar specifications, as did Fluke and a number of other manufacturers, with FLIR Systems continuing to expand their number and variety of commercially available models (see [Table 9.1b](#)). As a result, there are now a wide range of models on the market offering a variety of styles, sizes, weights, dynamic ranges, spatial resolutions and sampling rates to suit almost any thermal application, as summarized in [Appendix I](#). The FLIR Systems i-series, for example, features a low cost pistol grip model weighing just 0.365 kg. Likewise, Fluke's pistol grip TiS thermal camera weighed just 0.726 kg was available, on amazon.com, for \$2495 as of 13 August 2011. PCE instruments also offered a pistol grip option (the PCE-TC4) which weighed 0.75 kg, was capable of acquiring a  $160 \times 120$  image at 7.5 Hz and cost €3528.20 (including tax, 18 April 2012). Other cameras, such as the FLIR Systems P- and T-series come not only with a simultaneous visible and thermal digital image acquisition capability, but also a fusion capability allowing on-the-fly merge of visible and thermal images. While the T-series has a touch screen capability, the P660 also comes with built-in Geographical Positioning System (GPS) to allow location tagging of each image.

#### *9.2.4.2 Fixed-mount options*

The fixed-mount thermal cameras of [Table 9.1c](#) have similar specifications to the hand-held models of [Table 9.1b](#). That is, they allow collection of images of between 76 800 ( $320 \times 240$ ) and 179 200 ( $640 \times 280$ ) pixels in size over a  $25 \times 18.8$  degree field of view with temperature ranges spanning  $-20^{\circ}\text{C}$  to  $2000^{\circ}\text{C}$ . Frame rates are also similar, offering repeat imaging at up to 25 to 60 Hz. By using cooled photo-detectors, the fixed-mount cameras of [Table 9.1a](#) also allow imaging at shorter wavelengths, in the MIR and SWIR. They are also small, light and of relatively low power consumption. The smallest, the ThermoVision A10, has a volume of just  $3.7\text{ cm}^3$  and weighs 0.12 kg, easily fitting in the palm of a hand.

#### *9.2.4.3 Multi-waveband options*

Cameras are now becoming available with two band options. For example, Defense Technology International ([2010](#)) described the Condor II. This was developed by Selex Galileo for the UK Defense Ministry to allow dual-waveband imaging in the MIR and TIR using a single cadmium-mercury-telluride detector and a  $640 \times 512$  pixel array of  $24\text{ }\mu\text{m}$  pixels. Images could be collected simultaneously in both wavebands which, given the differential response to sub-pixel hot spots between the MIR and TIR (see [Chapter 4](#)), offers enormous potential to volcanological applications.

Prata and Bernardo ([2009](#)) also described a bolometer-based camera, the Cyclops, which collected  $320 \times 240$  pixel images in the  $7\text{--}14\text{ }\mu\text{m}$  range. Images at five different wavebands within the  $7\text{--}14\text{ }\mu\text{m}$  waveband could be collected by use of a series of filters. These were mounted on a wheel which allowed any of the five filters to be rotated into position. Once in

position the filter limited imaging to wavebands centered at 7.34, 8.55, 10, 11 or 12  $\mu\text{m}$ , with each band having a width of 1  $\mu\text{m}$ . The design of the system indicates how filters may be used to home in on a wavelength of interest using a narrow waveband filter placed in front of a detector operating over a broader waveband.

### 9.2.5 Selection of a suitable model for volcanological applications

As with radiometers, selection of an appropriate camera will depend on the application to which the instrument is going to be applied. Questions that need to be asked when selecting a camera include the following.

- How small is the object I need to detect?
- How hot is the object?
- How close can I approach the target?
- What will my pixel size, and resulting pixel-integrated temperature, be?
- How fast will any changes in temperature be at the target?
- How fast will the target move?

Answers to these questions need to be squared with the performance of available models, allowing a camera of suitable dynamic range, spatial- and temporal-resolution to be selected. The choice between a hand-held model and a fixed-mount system will then depend on how long the measurement period will last (i.e., short-term campaign style or long-term monitoring style). Prices vary between \$1k and \$50k, with typical prices being within the range \$30k to \$40k. Broad-band thermal cameras are thus not cheap, so that the selection process should be made carefully.

#### 9.2.5.1 Dynamic range

Most thermal cameras listed in [Table 9.1](#) can measure the full range of temperatures encountered at an active volcanic scenario (i.e., 0  $^{\circ}\text{C}$  to 1200  $^{\circ}\text{C}$ ). Unfortunately, some of the lower-cost models saturate at 120  $^{\circ}\text{C}$ , 350  $^{\circ}\text{C}$  or 500  $^{\circ}\text{C}$ . However, the cost of such models can be quite low. For example, the FLIR-Systems i-series, although saturating at 350  $^{\circ}\text{C}$ , could be purchased for €995 as of Spring 2011.

However, for thermal work at a variety of hot spot types, cameras with adjustable gain settings are the most versatile and useful, if expensive, option. Given such a camera function, a temperature measurement range can be selected depending on the thermal character of the feature to be targeted, maximizing the amount of useable (unsaturated) data that can be collected. For most thermal camera models, one of three temperature measurement levels or gain settings can be selected, these being: low (-40  $^{\circ}\text{C}$  to 120  $^{\circ}\text{C}$ ), mid (0  $^{\circ}\text{C}$  to 500  $^{\circ}\text{C}$ ) and high (350  $^{\circ}\text{C}$  to 1500  $^{\circ}\text{C}$ ) (see [Table 9.1](#)). However, because images at two settings cannot be collected at the same time, and because none of these settings spans the full range of temperatures expected at, for example, an active lava flow, some thought needs to go into which gain setting to use. With low- and mid-gain settings, there may be saturation issues over higher-temperature volcanic

targets. Conversely, with the higher-gain settings there may be inverse-saturation issues. This occurs when pixels with a temperature less than the lower cut-off of the measurement range (i.e.,  $\sim 350^\circ\text{C}$  for most high gain settings) are assigned the minimum recordable value. Thus, high-temperature surfaces will be mapped at the cost of lower-temperature surfaces.

Generally, for most degassing and eruption plume analyses, the mid-gain setting is often appropriate, with the high gain setting being useful at active lava bodies. For cooler, more subtle, geothermal anomalies, hot fissures and fumarole fields, the lowest gain setting may be appropriate. However, thought does need to go into which setting is used when in the field, because it cannot be changed after the data have been collected; there is nothing more frustrating than getting home and finding that all data were saturated, or that the emission was not hot enough to register in the selected gain setting. One option is to first collect a test image, or image series, in the low- or mid-gain mode, check the recorded temperature range and then adjust the gain setting accordingly.

#### 9.2.5.2 Spatial resolution

Spatial resolution needs to be selected depending on the expected spatial scale of thermal variation across the surface in question, and the distance over which the measurement can be made. As detailed in [Section 3.3 of Chapter 3](#), spatial resolution (or pixel dimension,  $L_p$ ) will depend on the detector instantaneous field of view (IFOV), which is defined by a cone opening at angle  $\beta_{\text{IFOV}}$ , and the distance to the target ( $D$ ), so that pixel diameter is given by

$$L_p = 2[D \tan(\beta_{\text{IFOV}}/2)]. \quad (9.1)$$

Thus spatial resolution will be set by the detector IFOV. We see from [Table 9.1](#) that there are essentially two spatial resolutions for currently available thermal cameras: low ( $\beta_{\text{IFOV}} = 1.3$  mrad) and high ( $\beta_{\text{IFOV}} = 0.65$  mrad). Over a distance of 1 m, these two IFOVs yield pixel diameters of:

$$L_p = 2[1 \text{ m} \tan(0.00065)] = 2 \tan(0.00065) = 0.0013 \text{ m} = 0.13 \text{ cm}$$

and

$$L_p = 2[1 \text{ m} \tan(0.000325)] = 2 \tan(0.000325) = 0.00065 \text{ m} = 0.065 \text{ cm}.$$

In other words, for a distance of 1 m, the spatial resolution (in cm) can be obtained by multiplying the IFOV (in radians) by 100.

Unlike with satellite-flown sensors where distance  $D$  between the detector and the target is fixed by the satellite height, the camera operator is free to get as close to, or as far away from, the target as he or she likes. Thus  $D$  is variable. In [Figure 9.2](#) we plot the increase in pixel size with distance from the target for a typical thermal camera IFOV of 1.3 mrad and 0.65 mrad. We see that pixel size increases linearly with distance, with the slope being that defined by the IFOV, so that [Equation \(9.1\)](#) can be reduced to:

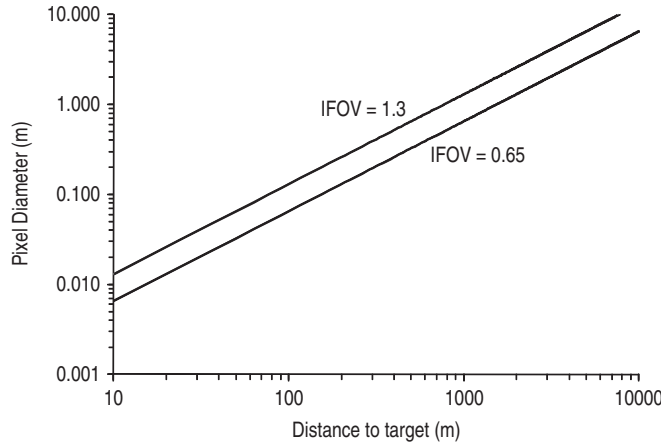


Figure 9.2 Increase in pixel diameter with distance to target for two commonly used thermal camera IFOVs (0.65 and 1.3 mrad).

$$L_p = \beta_{\text{IFOV}} \times D. \quad (9.2)$$

Thus, over a line of sight of 250 m, we will have a pixel diameter of

$$L_p = 0.0013 \text{ rad (Distance)} = 0.0013 \text{ rad (250 m)} = 0.325 \text{ m}$$

$$L_p = 0.00065 \text{ rad (Distance)} = 0.00065 \text{ rad (250 m)} = 0.16 \text{ m}$$

and over 5 km

$$L_p = 0.0013 \text{ rad (Distance)} = 0.0013 \text{ rad (5000 m)} = 6.5 \text{ m}$$

$$L_p = 0.00065 \text{ rad (Distance)} = 0.00065 \text{ rad (5000 m)} = 3.25 \text{ m}.$$

This simple relation allows us to quickly assess the best IFOV and/or the distance we need place the camera from the target to obtain the required spatial resolution. For a 2-m-wide hot vent at 950 °C, for example, the 250 m line-of-sight would guarantee that the target fills the pixel (if the vent is circular):

$$\pi r^2 / L_p^2 = \pi 1^2 / 0.325^2 = \pi / 0.1056 = \sim 30 \text{ pixels}$$

or

$$\pi r^2 / L_p^2 = \pi 1^2 / 0.16^2 = \pi / 0.0256 = \sim 123 \text{ pixels.}$$

From the 5 km distance, however, even the high-spatial-resolution option will not allow the hot spot to fill the pixel, the pixel diameter (3.25 m) being greater than the vent diameter (2 m). Thus, we either have to accept that we have a mixed pixel, or move the camera closer

to the target until the pixel dimension becomes smaller than the target dimension. With the thermal camera we always have this flexibility, depending on the safety and topographic possibility of close approach.

#### *9.2.5.3 Can we resolve the target?*

Holst (2000) gives a simple calculation that can be used to assess the maximum distance at which a target of known dimensions can be resolved ( $R_{\max}$ ) at a given angular IFOV ( $\beta_{\text{IFOV}}$ ), this being

$$R_{\max} = \frac{\text{Target Diameter}}{\beta_{\text{IFOV}}} . \quad (9.3)$$

Thus, for our 2-m-wide vent and a  $\beta_{\text{IFOV}}$  of 0.0013 rad, we can measure at a maximum range of 1540 m, increasing to 3080 m for a  $\beta_{\text{IFOV}}$  of 0.00065 rad. That is, at this range, if the target is centered on the pixel, it will exactly fill the pixel. Any closer, and the target will begin to fill multiple pixels, any further and the target will become a sub-pixel feature. This now fixes the maximum distance we can back away from the target for a camera of given spatial resolution, and still ensure that the target fills the pixel (given perfect placement of the pixel in relation to the target).

Holst (2000) also gives the Airy-disk-based measure of optical resolution. This is “the bright center of the diffraction pattern produced by an ideal optical system” (Holst, 2000) and, when expressed as an angle, has a diameter of

$$\theta_{\text{Airy}} = 2.44 \frac{\lambda_{\text{ave}}}{D_{\text{lens}}} , \quad (9.4)$$

in which  $\lambda_{\text{ave}}$  is the average wavelength of the detector and  $D_{\text{lens}}$  is the lens diameter. Thus for a lens diameter of 5 cm and a measurement in the 7.5–13  $\mu\text{m}$  waveband we have

$$\theta_{\text{Airy}} = 2.44 \frac{10.25 \times 10^{-6} \text{ m}}{0.05 \text{ m}} = 0.0005 \text{ radians.}$$

Now the minimum size of a target that can be resolved over a given range can be obtained from:

$$\text{Target size} = (\theta_{\text{Airy}})(\text{Range}) = \left( 2.44 \frac{\lambda_{\text{ave}}}{D_{\text{lens}}} \right) \text{Range} \quad (9.5)$$

so that, for a range of 1500 m, the minimum target diameter is:

$$\text{Target size} = 0.0005 \text{ rad} \times 1500 \text{ m} = 0.75 \text{ m}$$

reducing, for a range of 250 m, to

$$\text{Target size} = 0.0005 \text{ rad} \times 250 \text{ m} = 0.125 \text{ m.}$$

Thus the Airy-disk approach means that we may be able to back off further, with the maximum range over which our 2-m-diameter target can be resolved now increasing to:

$$\text{Target size}/\theta_{\text{Airy}} = 2 \text{ m} / 0.0005 \text{ rad} = \sim 4000 \text{ m.}$$

However, we now run into mixed-pixel problems, in that the hot source may be resolvable, but will be smaller than the pixel area. Thus, for quantitative measurements of temperature that rely on a pixel being thermally pure, the Equation (9.3) approach is best for assessing the maximum distance over which we can image a target at a given spatial resolution and obtain at-least one thermally “pure” pixel (i.e., a pixel filled by the target, if the pixel placement is opportune).

#### 9.2.5.4 Array size and spatial resolution

Many cameras have been upgraded to allow a higher spatial resolution while maintaining the image FOV at the same size, this typically being  $24 \times 18$  degrees. The array dimension can be related to the field of view through (Williams, 2009),

$$\text{FOV} = 2 \tan^{-1} \frac{\text{Array dimension}}{2 \text{ focal length}}. \quad (9.6)$$

Thus, if we increase the array dimension we will increase the FOV diameter. However, if we increase the focal length to maintain the FOV, we can achieve a smaller pixel size. Thus increased spatial resolution has been achieved by doubling the image size in terms of pixels, while maintaining the FOV. By doing this, the number of pixels that make up that field of view can be increased from 76 800 pixels (for a  $320 \times 240$  pixel image) in the low-spatial-resolution option to 307 200 pixels (for a  $640 \times 480$  pixel image) in the high-spatial-resolution option. This can be allows an increase in the spatial resolution from an IFOV of 1.3 mrad for the  $320 \times 240$  pixel images to 0.65 mrad for the  $640 \times 480$  pixel image (see Table 9.1).

#### 9.2.5.5 Temporal resolution

The temporal resolution that we need will depend on how fast the feature we wish to record is moving, or how fast its temperature is changing. For more slowly evolving features (active lava bodies and fumarole fields) most, if not all models will suffice, all being capable of saving a radiometric image at least once every 5–10 s. For one-off surveys, e.g., production of a thermal map of a lava flow or geothermally heated surface, temporal resolution may not even be an issue. However, for faster moving features (mostly pyroclastic plumes and flows) models capable of saving data at a sufficiently fast rate are less common.

We need to be careful here because, although many models can image at between 25 and 60 Hz, some even extending up to 120 Hz (and higher using windowing modes), not all models can save and output the radiometric data at the same rate. For example, a camera may be able to image at up to 60 Hz, but it may only be capable of saving those radiometric images to an internal memory card or exporting them through a USB or firewire connection to a PC at 2 Hz.

The FLIR S660 could save images onto an internal memory card at high rates, but it first recorded onto the camera memory, recording no more than 80 frames. Then, to continue the recording, these files had to be downloaded onto the internal memory card, a process that took several minutes. Several other cameras, such as the FLIR SC640 and the Mikron M7640 have such a “burst” mode facility, where images can be saved to the memory card at rates of 30 frames per second, but only for image sequences of several seconds to several minutes in duration. It then requires about the same amount of time to save the sequence to the card.

Many cameras (as identified in [Table 9.1](#)) can, though, collect full-speed (non-radiometric) movies of the observed phenomena, often in NTSC/PAL or MPEG-4 format using a video output, or internally onto a memory card (although storage capacity will be limited for the internal storage case). This will mean that the absolute temperature detail will be lost, but relative temperature will be retained and the full temporal resolution will be utilized, which is useful for fast moving features, or thermal phenomena that undergo rapid changes in temperature.

#### *9.2.5.6 Data rates*

There is a pay-off here between temporal resolution and spatial resolution. The maximum achievable frame rate at which radiometric images can be recorded will be limited by the speed of data transfer and storage. [Vollmer and Möllmann \(2011\)](#) give the following example.

- If we take a detector with a frame integration time of 1  $\mu$ s, then a frame rate of 1 MHz is theoretically possible.
- For a dynamic range of 14 bits, this multiplies to 14 Mbits  $s^{-1}$  for a single detector or pixel.
- Thus, for a  $320 \times 240$  image, the data rate will be

$$14 \text{ Mbits } s^{-1} \text{ per pixel} \times 76\,800 \text{ pixels} = \sim 10^{12} \text{ bits } s^{-1}.$$

As [Vollmer and Möllmann \(2011\)](#) point out, the current maximum data readout that electronics can achieve is much lower than this value, typically being  $\sim 2$  Gbits  $s^{-1}$ .

Hence, an increase in spatial resolution comes at the expense of a decrease in temporal resolution. Take, for example, a camera recording 14 bit data for a  $320 \times 240$  pixel image at a rate of 60 Hz. This gives a data rate of:

$$14 \text{ bits} \times 76\,800 \text{ pixels} \times 60 \text{ frames } s^{-1} = \sim 65 \text{ Mbits } s^{-1}.$$

If we increase the size of the image to  $640 \times 480$  pixels (an increase in the number of pixels by a factor of four) then, to maintain the data rate, we have to quarter the imaging frequency, that is

$$65 \text{ Mbits } s^{-1} / (14 \text{ bits} \times 307\,200 \text{ pixels}) = \sim 15 \text{ frames } s^{-1}.$$

Alternatively, the data rate has to be increased to:

$$14 \text{ bits} \times 307\,200 \text{ pixels} \times 30 \text{ frames } s^{-1} = \sim 129 \text{ Mbits } s^{-1},$$

or

$$14 \text{ bits} \times 307\,200 \text{ pixels} \times 120 \text{ frames s}^{-1} = \sim 516 \text{ Mbits s}^{-1}.$$

Hence, currently, cameras recording larger (higher-spatial-resolution) images tend to record at lower frequencies.

#### 9.2.5.7 Windowing to increase temporal resolution

To allow higher temporal resolutions, some cameras allow a windowing capability whereby a smaller sub-image selected from within the larger image is selected and recorded at a faster rate. Reducing the size of the exported pixel array brings the data rate to within the capability of the readout electronics, allowing high speed imaging of small, selected areas within the master image. The FLIR SC6000 has such a windowing capability, whereby the full  $640 \times 512$  image can be recorded at a maximum rate of 126 frames per second, that is

$$14 \text{ bits} \times 327\,680 \text{ pixels} \times 126 \text{ frames s}^{-1} = \sim 578 \text{ Mbits s}^{-1}.$$

Now, if we reduce the size of the exported image by applying the user-defined windowing capability, we can increase the frame rate, while maintaining the data rate, as follows:

- (1)  $320 \times 256$  pixel window =  $14 \text{ bits} \times 81\,920 \text{ pixels} \times 433 \text{ fps} = 497 \text{ Mbits s}^{-1}$
- (2)  $288 \times 180$  pixel window =  $14 \text{ bits} \times 51\,840 \text{ pixels} \times 651 \text{ fps} = 472 \text{ Mbits s}^{-1}$
- (3)  $192 \times 100$  pixel window =  $14 \text{ bits} \times 19\,200 \text{ pixels} \times 1504 \text{ fps} = 404 \text{ Mbits s}^{-1}$
- (4)  $64 \times 64$  pixel window =  $14 \text{ bits} \times 4\,096 \text{ pixels} \times 3884 \text{ fps} = 223 \text{ Mbits s}^{-1}$
- (5)  $4 \times 64$  pixel window =  $14 \text{ bits} \times 256 \text{ pixels} \times 36\,000 \text{ fps} = 129 \text{ Mbits s}^{-1}$ .

In which Fps is frames (or images) per second. This capability has the potential for very-high-speed imaging, extending to hundreds or thousands of Hertz for small image zones.

#### 9.2.5.8 Portability / battery life / accessories / duration of deployment

All cameras listed in [Table 9.1](#) are portable, weighing 2.4 kg or less and having maximum dimensions of less than 23 cm, with those hand-held models of [Table 9.1b](#) also being powered by internal, rechargeable batteries, meaning that no supplementary power supply has to be carried. The deployment time will, though, be limited by battery lifetime, which is typically  $\sim 3$  hours. However, multiple batteries can be purchased, charged and carried, or the camera can be connected to an external battery, extending the measurement period. To prevent data loss, battery exchange should be done before the old battery completely fails. To allow high-frame-rate acquisition of radiometric images, connection via firewire to a laptop is necessary, from which the data acquisition is controlled using the camera software. Thus, a laptop with sufficient battery power and cables needs to be added to the equipment pile to be carried to the field if high-frame-rate acquisition is desired. Such high-speed acquisitions also require camera stability, so that the camera should be mounted on a stable tripod. Thus, the full accessory list includes: camera, tripod, connector cables, and laptop PC (with sufficient hard-disk space for image storage), plus spare camera (and laptop) batteries.

### 9.2.5.9 Final, pre-purchase questions

When selecting and purchasing a thermal camera, Holst (2000) lists seven questions that should be posed, all of which are relevant when choosing a camera for a volcanological application. These are as follows.

- *In a harsh environment, the window will become dirty. If a window is contaminated with a pollutant such as soot (in our case ash, grit, or dry deposition of sulfur), how easy is it to clean?* (Holst, p. 132, 2000)
- *Will the calibration be valid at extreme temperatures and does it drift?* (Holst, p. 133, 2000)
- *How long do the batteries last?* (Holst, p. 139, 2000).
- *How often does the system require (Factory) recalibration?* (Holst, p. 145, 2000).
- *What is the repeatability and drift?* (Holst, p. 145, 2000).
- *What is the cost of recalibration?* (Holst, p. 145, 2000).
- *How is the data transferred to the computer?* (Holst, p. 146, 2000).

To this list, we should add the following.

- Is the temperature range capable of measuring the full range of temperatures I expect to encounter?
- What is the pixel IFOV and image dimensions?
- Is the camera capable of saving radiometric data at a sufficiently fast rate?
- Will I need a dedicated laptop to run the camera and save data, and what are the minimum specifications that the laptop requires?

And, given that scratching and etching of the lens will occur,

- how much would a replacement window cost?

### 9.2.6 Detector and lens performance

The thermal camera system comprises three main components: the lens, the detector, and the electronic system. Most detector performance issues, such as point-spread function issues, have already been covered in Chapter 3. In Chapter 3 the focus was on satellite-flown infrared detectors, and many of the issues considered in that chapter (such as point-spread function problems) apply equally to thermal cameras. We here consider five groups of detector and lens performance issues that specifically affect measurements made using a hand-held thermal camera, or radiometer, these being: (i) turn-on and detector shock effects, (ii) signal-to-noise considerations, (iii) focal-length considerations, (iv) veiling glare and the narcissus effects, and (v) lens distortion.

#### 9.2.6.1 Detector turn-on and thermal shock issues

Upon turn-on, the detectors may not yet be in thermal equilibrium with the surrounding environment and so will undergo a response as they warm up or cool down. They may also

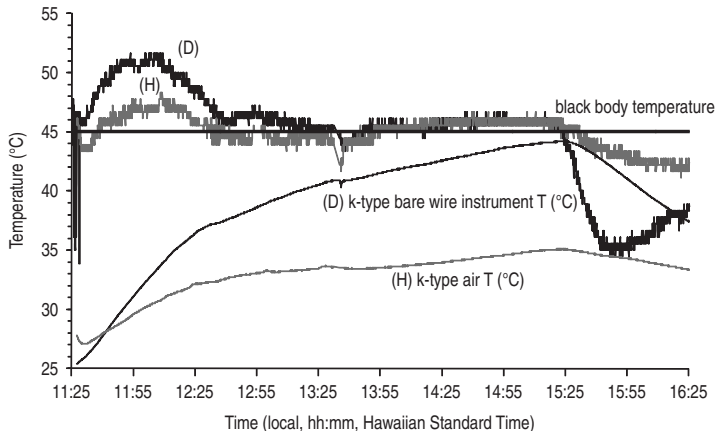


Figure 9.3 Turn on and thermal shock effects experienced by a thermal detector (in this case a thermopile). Two thermopiles (both Omega OS554s) are targeting a blackbody at a fixed and stable temperature of 45 °C (horizontal line). One thermopile (D) is exposed the Sun, the second (H) is protected in a pelican case. Bare wire thermocouples record the temperature of the exposed sensor exterior, and the air temperature in the box. We see both detectors undergo turn-on effects, which are less severe for the protected detector. At 15:25 both detectors were placed in the shade. Both underwent thermal shock effects, which were again less severe for the protected detector. A perfect response would have the detectors recording the same temperature as the blackbody throughout the measurement period.

undergo “thermal shock” if they experience a sudden change in environmental temperature. These effects can be seen in Figure 9.3 where two radiometers, both Omega OS554s, were placed in sunlight with an ambient air temperature of 33 °C. One radiometer was shielded from the direct effect of solar heating through placement of the sensor in a pelican case, the second was directly exposed to the Sun. They both viewed a blackbody emitting at 45 °C. Both sensors underwent a turn-on effect lasting 1 hour and 20 minutes, after which the recorded temperature stabilized at 45.5 °C,  $\pm 0.5$  °C (this being the expected accuracy for the radiometer used, i.e.,  $\pm 1\%$ ). The turn-on effect was marked by a positive oscillation in temperature, with a peak amplitude of 6 °C for the exposed sensor (sensor D) and 3 °C for the shielded sensor (sensor H). Similar tests made on bolometer- and photo-detector-based cameras by Vollmer and Möllmann (2011) showed similar results, with the time taken to reach thermal equilibrium by both cameras being more than 90 minutes, during which time the temperature drifted downwards by  $\sim 3$  °C. However, Vollmer and Möllmann (2011) found that both cameras achieved their specified temperature accuracies of  $\pm 2$  °C after about 10 minutes. Thus, a device should probably be warmed up (i.e., turned on) at least 10 minutes before measurements begin.

We also witness a thermal shock in the test of Figure 9.3. At 15:25, the two radiometers were shaded. Following shading, the recorded temperature drifted downwards, a trend which continued through the termination of the test as the external temperature of the sensor cooled from 44.2 °C to 36.3 °C. Again, the effect was more strongly felt with the exposed sensor, with the recorded temperature crashing to 35 °C over a period of 25 minutes as the

external temperature cooled to 42.2 °C. Thereafter, the temperature recorded by the exposed sensor began to recover, but only to 38.9 °C. The protected sensor drifted downwards to record a stable level of  $42.2 \pm 0.5$  °C after  $\sim 1$  hour of cooling. Again, Vollmer and Möllmann (2011) carried out a similar experiment on both a bolometer- and a photo-detector-based camera, moving the cameras from a 13 °C environment to a 23 °C environment, and then switching them on. Although the photo-detector-based camera recorded within its specified accuracy immediately, the bolometer-based camera recorded temperatures that were between 3 and 4 °C too high. Recorded temperatures drifted downwards over  $\sim 60$  minutes, with the camera reaching its  $\pm 2$  °C accuracy after 20–30 minutes. Thus, thermal shock situations should be avoided, which can be achieved by bringing the camera to environmental temperature well before operation. The camera should then be shielded from abrupt temperature changes environmental (i.e., the temperature of the instrument's environment should be kept as stable as possible). The same applies to radiometer operation.

#### 9.2.6.2 Signal-to-noise

Both the target and the atmosphere will emit radiance (see Chapter 2). Because the atmospheric path radiance does not contain any target information, it can be considered noise. Holst (2000) gives an equation for signal-to-noise ratios (SNR) which uses the atmospheric transmission ( $\tau$ ), the path length ( $R$ ) and difference in temperature between the target and the background ( $\Delta T_{t-b}$ ), divided by the sensor's noise-equivalent-differential-temperature ( $NE\Delta T$ ), to assess the expected SNR:

$$\text{SNR} = \frac{\tau^R \Delta T_{t-b}}{NE\Delta T}. \quad (9.7)$$

Thus, for a typical 8–14 μm transmissivity over a path length of 500 m at sea-level (i.e.,  $\tau = 0.88$ ), a target temperature of 500 °C, a background temperature of 25 °C, and typical thermal camera  $NE\Delta T$  of 0.1 °C (see Table 9.1) we have:

$$\text{SNR} = \frac{0.88^{0.5 \text{ km}} 475 \text{ °C}}{0.1 \text{ °C}} = 4456.$$

That is, there is much more signal than noise. Even with a transmissivity of 0.7 over a path length of 5 km and a temperature difference between the target and background of 10 °C, the SNR is still  $\sim 17$ . That is, we still have 17 times more signal than noise.

By re-arranging Equation (9.7) we can estimate the path length at which the SNR declines to one, that is:

$$R = \frac{\log\left(\frac{NE\Delta T}{\Delta T}\right)}{\log(\tau)}. \quad (9.8)$$

Essentially, this marks the point at which the hot spot is no longer detectable. At this point the noise level is the same as the variation in signal caused by the presence of the hot source. For the conditions given above we find that this point is reached at a range of,

$$R = \frac{\log\left(\frac{0.1\text{ }^{\circ}\text{C}}{475\text{ }^{\circ}\text{C}}\right)}{\log(0.88)} = 66 \text{ km}$$

and

$$R = \frac{\log\left(\frac{0.1\text{ }^{\circ}\text{C}}{10\text{ }^{\circ}\text{C}}\right)}{\log(0.77)} = 13 \text{ km.}$$

Thus, the low  $NE\Delta T$  of most commercially available thermal cameras should allow detection of hot targets over quite long ranges. The problem is, over such ranges pixel size will be large. For example, at a distance of 10 km the pixel diameter, for a 1.3 mrad detector, will be 13 m.

#### 9.2.6.3 Lens focal length, image field of view and magnification

For an object at infinity, the focal length ( $f$ ) is approximately equal to the distance from the lens to the FPA. Focal length controls the dimensions of the FOV, following,

$$\tan(\phi) = \frac{h/2}{f}, \quad (9.9a)$$

in which  $\phi$  is half the angular field of view (FOV) and  $h$  is linear dimension of the FPA. The full angular dimension of the FOV is thus given by (Williams, 2009):

$$\text{FOV} = 2\phi = 2 \tan^{-1} \left[ \frac{h/2}{f} \right]. \quad (9.9b)$$

From these equations we see that, for a given FPA dimension, if we increase  $f$  we will decrease the angular FOV. Thus, for a set camera-to-target distance, we will begin to image a smaller and smaller area as we increase the focal length. However, because the size of the FPA does not change, we will be fitting the same number of pixels into a smaller and smaller area, so that the spatial resolution for the imaged area will increase. That is, the size of the pixels in the smaller image will also be smaller.

This is the function of zoom and wide angle lenses. With a zoom lens,  $f$  is increased to allow a narrower, but higher spatial resolution, FOV to be recorded. With a wide-angle lens,  $f$  is decreased to allow acquisition of a wider, but lower-spatial-resolution, FOV. Most thermal cameras come with a variety of lens options which can be fitted to the camera to allow higher-spatial-resolution (zoomed) imaging of smaller areas, or acquisition of lower-spatial-resolution (wide-angle) images of larger areas. Typical zoom and wide-angle lens options currently available for commercial cameras are given in [Table 9.2](#), where we can see the effect of changing the focal length on the dimensions of, and pixel dimension within, the imaged area as we move downwards through the table from zoom lenses to wide-angle lenses.

Table 9.2. *Lens specifications given by FLIR Systems (2001) with the image horizontal and vertical dimensions (HFOV and VFOV) that each angular FOV will give for a camera-to-target distance of 500 m. Also given are the IFOVs specified by FLIR Systems (2001) for each lens, and the pixel dimension to which this relates for the 500 m camera-to-target distance. “Weight” is weight of the lens (this is zero for the standard lens as it comes fitted to the camera, and is thus included in the total camera weight of 2.4 kg\*), and magnification factor is assessed in relation to the spatial resolution provided by the standard 24° lens.*

Lens (degrees)	Lens (type)	HFOV (degrees)	VFOV (degrees)	HFOV (m) @ 500 m	VFOV (m) @ 500 m	IFOV (mrad)	IFOV (m) @ 500 m	Weight (kg)	Magnification factor
80	Zoom	80	60	839	577	5.2	2.60	0.74	4
45	Zoom	45	34	414	306	2.6	1.30	0.31	2
24	Standard	24	18	213	158	1.3	0.65	—	1
12	Wide	12	9	105	79	0.7	0.35	0.55	0.5
7	Wide	7	5.3	61	46	0.4	0.20	1.6	0.3

\*Weight is for the ThermaCAM™ PM 545–675–695 series and includes battery. Weight is 2.0 kg without battery.

#### 9.2.6.4 Veiling glare and the narcissus effect

Veiling glare is caused by unwanted stray radiation that reaches the FPA and may result from lens scatter and/or reflection (or radiation) from the lens and camera body (Williams, 2009). It serves to reduce image contrast. The narcissus effect is one type of veiling glare usually apparent as an area of reduced temperature at the center of the thermal image. Williams (2009) describes its cause as being “the result of one or more of the optical surfaces reflecting an approximately in-focus image of the cooler detector back to the FPA.” In the case of a bolometer, reflection of the relatively warm detector can also cause a bright or warm spot (narcissus) in the center of the image. Solutions to the problem suggested by Holst (2000) and Vollmer and Möllmann (2011) include tilting the lens window (Holst, 2000) or changing the viewing angle (Vollmer and Möllmann, 2011) so that there is no incident radiation from the detector array on the camera lens.

#### 9.2.6.5 Lens and image distortion

Image distortion can be induced by the lens. Lens distortion introduces two types of effect, barrel and pin cushion distortion (as illustrated in Figure 9.4). The degree of picture height distortion (PHD) can be expressed in terms of a ratio between the degree of distortion suffered by the top of the image ( $\Delta h$ ) to the height of the undistorted center of the image ( $h$ ), as shown in Figure 9.4c. The degree of distortion can be assessed by imaging a regular grid, or distribution of points. The degree of distortion suffered by the recorded geometry can then be used to measure the PHD, an example of this process being given in Figure 9.4c. Williams (2009) states that “levels of relative distortion of up to about 0.03 (i.e., 3%) are normally not noticeable, and larger amounts may be cosmetically acceptable.” However, for precise dimensional measurements using an image, the degree (or lack) of distortion should be checked and, if significant, will need to be corrected for.

### 9.3 Thermal camera applications in volcanology: history and classification

One of the first deployments of an “infrared camera” at a volcano was that of Shimozuru and Kagiyama (1978). The “camera” was used to complete ground-based infrared surveys after eruptive episodes at the Japanese volcanoes of Kusatsu-shirane and Mihara-yama during 1976. However, the camera was actually a broad-band (8–12.5  $\mu\text{m}$ ) bolometer-based radiometer attached to a scanning device. The “image” was obtained by tripod-mounting the radiometer, fixing the vertical pointing angle and taking a horizontal profile across the targeted surface. The vertical angle was then changed, and the next “image line” collected. This improved on the previously deployed (radiometer-based) method of thermal mapping which involved taking a “polaroid picture” of the area concerned and choosing control points across that picture. Radiometer measurements were then made at those points and used to determine the spatial temperature distribution across the picture (Shimozuru and Kagiyama (1978), pp. 251–252). This, in effect, is the Type 2a radiometer-based spatial survey methodology of Chapter 7.

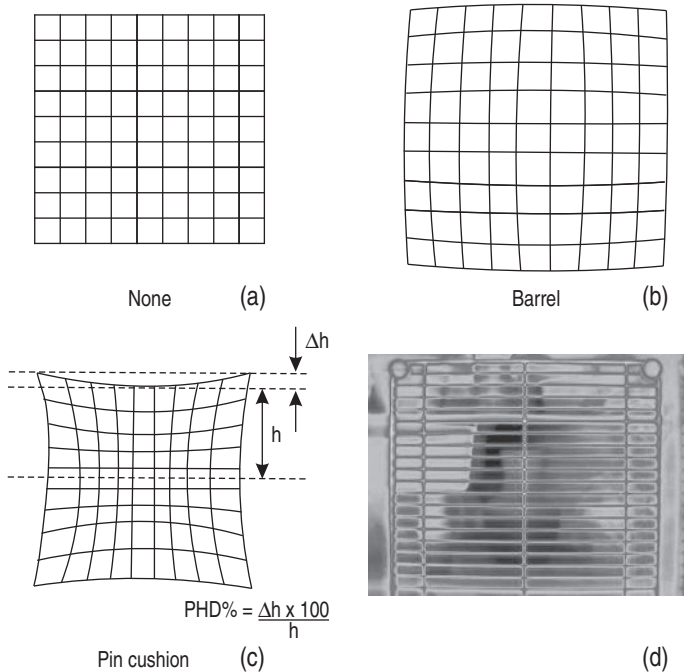


Figure 9.4 Comparison of (a) an undistorted image of a grid with the same image suffering (b) barrel and (c) pin cushion effects [modified from Williams (2009, Fig. 4.8)]. The means to assess the degree of picture height distortion, as given by Fig. 4.12 of Williams (2009), is marked on (c). In (d) we show an image of a cold freezer shelf obtained using a FLIR Systems ThermaCAM™ S40 showing a slight barrel effect, apparent from outward bowing of the shelf edges. See also color plates section.

Yuhara *et al.* (1981) used a true thermal camera to complete a helicopter-based survey of Unzen in 1978. The “camera” was, however, a scanning system that gave “a thermal image of television type” on the “display unit,” with data being “recorded on magnetic tape for reproduction in the laboratory” (Yuhara *et al.* (1981), pp. 101–102). Ballestracci and Nougier (1984) also reported deployment of a “thermo-video” camera system at the Kerguelen archipelago. However, it was again a scanning system which used a In-Sb detector that required liquid nitrogen for cooling and an external 24 V power supply, with the IR signal being “amplified and visualized on an oscilloscope screen” which was then recorded onto magnetic tape.

Kieffer *et al.* (1981) and Friedman *et al.* (1981) report the use of uncalibrated FLIR Systems video (acquired using an AGA Thermovision 750) to track surface temperature prior to, and after, the 18 May 1980 eruption of Mount St. Helens. However, this (as discussed above) was the predecessor to the true camcorder style (uncooled micro-bolometer-based) thermal camera that went on-line in 1997. The first report of use of such a thermal camera to target volcanic activity is generally cited as the abstract presented at the AGU Fall 1999 meeting by McGimsey *et al.* (1999). Utilizing a FLIR Systems SAFIRE

model mounted on the underbelly of an Alaska State Troopers twin-engine aircraft, McGimsey *et al.* (1999) imaged eruptive activity at Pavlov and Shishaldin volcanoes during their 1997 and 1999 eruptive phases. Roach *et al.* (2001) later noted that thermal video collected by Alaska State Troopers had aided in tracking Pavlov's 1996 activity in their *Bulletin of Volcanology* paper, marking the entry of the thermal camera into the mainstream literature. To be fair, the SAFIRE was an aircraft mounted, rather than hand-held, thermal camera and operated using a cooled FPA of photo-detectors, rather than an FPA of uncooled bolometers (see Table 9.1a). We had to wait another year to see the entry of data gained by camera systems based on FPAs of uncooled micro-bolometers into the literature, with 2002 seeing the publication of eight papers in the peer-reviewed literature that used data from hand-held thermal cameras for volcanic targets (see Table 9.3). This year can thus be viewed as the entry of what we define here as the *hand-held thermal camera* into the volcanological literature.

The popularity of the hand-held thermal camera as both a research and surveillance tool is apparent from the constant stream of publications post-2001 (as collated in Table 9.3), so that at least 113 publications using hand-held (or fixed-mount) thermal camera data for active volcanic targets had been published in the peer-reviewed literature by the end of 2010. This is quite an astonishing publication rate, with papers being published at a rate of 12 per year over the ten year period spanning 2002–2011, increasing to almost 16 per year for the five year period spanning 2005–2009, reaching a peak of 27 publications in 2009 (see Figure 9.5). This peak was helped by widespread citing of thermal-camera-derived information in a special issue of the *Journal of Volcanology and Geothermal Research* devoted to Stromboli's 2007 eruption, in which no less than eight papers (out of a total of 14) mentioned the use of thermal camera data to aid in detecting, timing, tracking and understanding activity patterns. Either side of this peak, the years 2008 and 2010 saw 19 and 14 publications, respectively.

If the publication trend continues, the total number of publications detailing hand-held thermal camera applications in volcano radiometry should reach 140 around the end of 2012, likely overtaking the size of the publication data base provided by satellite-based volcano radiometry (which numbered 120 publications as of 2005 – see Appendix A). Within this growth, we see that cameras manufactured by FLIR Systems have really opened the door to ground-based volcanological enquiry, with the FLIR systems cameras contributing data to at least 77 (or ~70 %) of the 113 studies.

### 9.3.1 Classification of applications

In 2011, Spampinato *et al.* (2011) published a review of volcano surveillance using broad-band thermal cameras, detailing the applications and volcanological science achieved using hand-held thermal cameras up until 2011.

Table 9.3. Summary of published broad-band thermal camera deployments, observations, measurements and analyses at active volcanoes, 2000–2010. List does not include institutional internal reports, thesis chapters or conference abstracts. Listing does include publications that involve “mention” of a thermal camera-based observation (i.e., a single line or phrase containing information derived from thermal camera data), but does not include publications in which thermal camera information is cited from another article. Dashed line separates pre- and post-2005 studies.

Citation	Volcano	Camera	Exp	Fum	LF	LL	LD	Srf	Journal details
Roach <i>et al.</i> (2001)	Pavlov	—		✓					<i>Bull. Volcanol.</i> , <b>62</b> , 385–399
Dehn <i>et al.</i> (2002)	Shishaldin	FLIR 595		✓					<i>Bull. Volcanol.</i> , <b>64</b> , 525–534
Honda and Nagai (2002)	Mayon	—						✓	<i>ISPRS J. Photogram. &amp; Rem. Sens.</i> , <b>57</b> , 159–168
Kaneko <i>et al.</i> (2002)	Usu	LAIRD 3A		✓					<i>Adv. Environ. Monitoring &amp; Model.</i> , <b>1</b> (1), 153–166
Nye <i>et al.</i> (2002)	Shishaldin	FLIR 595		✓					<i>Bull. Volcanol.</i> , <b>64</b> , 507–519
Ohba <i>et al.</i> (2002)	Usu	—		✓					<i>J. Volc. Geotherm. Res.</i> , <b>115</b> , 33–42
Oppenheimer and Yirgu (2002)	Erta Ale	Agema 550					✓		<i>Int. J. Remote Sensing</i> , <b>23</b> (22), 4777–4782
Stelling <i>et al.</i> (2002)	Shishaldin	FLIR 595		✓					<i>Bull. Volcanol.</i> , <b>64</b>
Wright <i>et al.</i> (2002)	Popocatepetl	—		✓					<i>J. Geophys. Res.</i> , <b>107</b> , doi: 10.1029/2000JB000125
Bonaccorso <i>et al.</i> (2003)	Stromboli	FLIR 695						✓	<i>Geophys. Res. Lett.</i> , <b>30</b> , 1941–1944
Caplan-Auerbach and McNutt (2003)	Shishaldin	FLIR 595		✓					<i>Bull. Volcanol.</i> , <b>65</b> , 405–417
Kauahikaua <i>et al.</i> (2003)	Kilauea	—			✓				<i>USGS Prof. Pap.</i> , <b>1676</b> , 63–88
Keszthelyi <i>et al.</i> (2003)	Kilauea	FLIR SC2000			✓				<i>Geophys. Res. Lett.</i> , <b>30</b> , doi:10.1029/2003GL017994
Matsushima <i>et al.</i> (2003)	Iwodake	Agema 470			✓				<i>J. Volc. Geotherm. Res.</i> , <b>126</b> , 285–301
Seidl <i>et al.</i> (2003)	Galeras	FLIR 595						✓	<i>J. Volc. Geotherm. Res.</i> , <b>125</b> , 1–12
Wright and Flynn (2003)	Kilauea	FLIR 595				✓			<i>Geology</i> , <b>31</b> (10), 893–896

Calvari and Pinkerton (2004)	Etna	FLIR 695		✓	<i>J. Volc. Geotherm. Res.</i> , <b>132</b> , 225–239
Dehn <i>et al.</i> (2004)	Mt. Cleveland	FLIR 595	✓	✓	<i>J. Volc. Geotherm. Res.</i> , <b>135</b> , 51–73
Lautze <i>et al.</i> (2004)	Etna	FLIR 595	✓		<i>J. Volc. Geotherm. Res.</i> , <b>137</b> , 231–246
Oppenheimer <i>et al.</i> (2004)	Erta Ale	Agema 550		✓	<i>Geology</i> , <b>32</b> (6), 509–512
<hr/>					
Andronico <i>et al.</i> (2005)	Etna	FLIR 695	✓		<i>Bull. Volcanol.</i> , <b>67</b> , 314–330
Burton <i>et al.</i> (2005)	Etna	FLIR 695	✓		<i>Geophys. Res. Lett.</i> , <b>32</b> , L09303
Calvari <i>et al.</i> (2005)	Stromboli	FLIR 695	✓		<i>J. Geophys. Res.</i> , <b>110</b> , doi:10.1029/2004JB003129
Chiodini <i>et al.</i> (2005)	Solfatara, Campi Flegrei	NEC TS7302	✓		<i>J. Geophys. Res.</i> , <b>110</b> , doi:10.1029/2004JB003542
Coppola <i>et al.</i> (2005)	Piton de la Fournaise	FLIR 695	✓		<i>Geol. Soc. Am., Spec. Pap.</i> , <b>396</b> , 103–123
Harris <i>et al.</i> (2005)	Etna	FLIR 595	✓		<i>Geol. Soc. Am., Spec. Pap.</i> , <b>396</b> , 125–146.
Harris <i>et al.</i> (2005)	Stromboli	FLIR 595+695	✓		<i>Bull. Volcanol.</i> , <b>68</b> , 107–117
Matsushima (2005)	Miyakejima	Avio TVS-650	✓		<i>Geophys. Res. Lett.</i> , <b>32</b> , doi:10.1029/2005GL023217
Nakada <i>et al.</i> (2005)	Anatahan	FLIR		✓	<i>J. Volc. Geotherm. Res.</i> , <b>146</b> , 226–240
Saito <i>et al.</i> (2005)	Aso	Sony Handycam	✓		<i>Earth Planets Space</i> , <b>57</b> , e5–e8
Vaughan <i>et al.</i> (2005)	Mt. St. Helens	FLIR S40		✓	<i>Geophys. Res. Lett.</i> , <b>32</b> , doi:10.1029/2005GL024112
Andò and Pecora (2006)	Etna	FLIR 160	✓		<i>Computers &amp; Geosciences</i> , <b>32</b> , 85–91
Ball and Pinkerton (2006)	Etna	FLIR S40+S2000	✓		<i>J. Geophys. Res.</i> , <b>111</b> , doi:10.1029/2005JB003829
Calvari <i>et al.</i> (2006)	Stromboli	FLIR 695	✓		<i>J. Volc. Geotherm. Res.</i> , <b>149</b> , 160–175
Bailey <i>et al.</i> (2006)	Etna	FLIR 595	✓		<i>Bull. Volcanol.</i> , <b>68</b> , 492–515
James <i>et al.</i> (2006)	Etna	FLIR S40	✓		<i>Bull. Volcanol.</i> , <b>69</b> , 105–108
Power <i>et al.</i> (2006)	Augustine	FLIR 595	✓	✓	<i>EOS</i> , <b>87</b> (37), 373+377

Table 9.3. (cont.)

Citation	Volcano	Camera	Exp	Fum	LF	LL	LD	Srf	Journal details
Sawyer and Burton (2006)	Stromboli	FLIR 695	✓						<i>Geophys. Res. Lett.</i> , <b>33</b> , doi:10.1029/2005GL025320
Wilson <i>et al.</i> (2006)	Kilauea	FLIR S40	✓						<i>EOS</i> , <b>89</b> , 203
Carter <i>et al.</i> (2007)	Bezymianny	FLIR S40					✓		<i>Bull. Volcanol.</i> , <b>69</b> , 811–815
Chiodini <i>et al.</i> (2007)	Solfatara, Campi Flegrei	NEC TS7302		✓					<i>J. Geophys. Res.</i> , <b>112</b> , doi:10.1029/2007JB005140
Coppola <i>et al.</i> (2007)	Piton de la Fournaise	FLIR 695			✓				<i>J. Geophys. Res.</i> , <b>112</b> , doi:10.1029/2006JB004659
Harris and Ripepe (2007)	Stromboli	FLIR 595+S40	✓						<i>J. Geophys. Res.</i> , <b>112</b> , doi:10.1029/2006JB004393
Harris and Ripepe (2007)	Stromboli	FLIR S40	✓						<i>Chemie der Erde</i> , <b>67</b> , 1–35
Harris <i>et al.</i> (2007)	Kilauea	FLIR S40		✓					<i>Geophys. Res. Lett.</i> , <b>34</b> , doi:10.1029/2007GL030791
Hernández <i>et al.</i> (2007)	Santa Ana	—					✓		<i>Pure Applied Geophys.</i> , <b>164</b> , 2507–2522
Huggel <i>et al.</i> (2007)	Iliamna	FLIR		✓					<i>J. Volc. Geotherm. Res.</i> , <b>168</b> , 114–136
Lodato <i>et al.</i> (2007)	Stromboli	FLIR 695			✓				<i>Bull. Volcanol.</i> , <b>69</b> , 661–679
James <i>et al.</i> (2007)	Etna	FLIR S40			✓				<i>G<sup>3</sup></i> , <b>8</b> (3), doi:10.1029/2006GC001448
Lagios <i>et al.</i> (2007)	Nisyros	NEC TS7302		✓					<i>ISPRS J. Photogram. &amp; Rem. Sens.</i> , <b>62</b> , 447–460
Patrick (2007)	Stromboli	FLIR S40	✓						<i>J. Geophys. Res.</i> , <b>112</b> , doi:10.1029/2006JB004387
Patrick <i>et al.</i> (2007)	Stromboli	FLIR 595+S40	✓						<i>Bull. Volcanol.</i> , <b>69</b> , 769–784
Witter and Harris (2007)	Kilauea	FLIR 595			✓				<i>J. Geophys. Res.</i> , <b>112</b> , doi:10.1029/2005JB003800
Andronico <i>et al.</i> (2008)	Etna	FLIR A40	✓						<i>J. Volc. Geotherm. Res.</i> , <b>173</b> , 325–328
Andronico <i>et al.</i> (2008)	Etna	FLIR A40	✓						<i>J. Volc. Geotherm. Res.</i> , <b>176</b> , 541–550

Burton <i>et al.</i> (2008)	Stromboli	FLIR 695	✓		<i>AGU Geophysical Monograph</i> <b>182</b> , 93–104
Calkins <i>et al.</i> (2008)	Erebus	Agema 550		✓	<i>J. Geotherm. Res.</i> , <b>177</b> , 695–704
Davies <i>et al.</i> (2008)	Erebus	FLIR P65		✓	<i>J. Volc. Geotherm. Res.</i> , <b>177</b> , 705–724
Del Negro <i>et al.</i> (2008)	Etna	FLIR 695	✓		<i>Bull. Volcanol.</i> , <b>70</b> , 805–812
Ball <i>et al.</i> (2008)	Kilauea	FLIR S40	✓		<i>J. Volc. Geotherm. Res.</i> , <b>173</b> , 148–156
Berthelote <i>et al.</i> (2008)	Lab / Kilauea	FLIR S40	✓		<i>Bull. Volcanol.</i> , <b>70</b> , 813–824
Gersy <i>et al.</i> (2008)	Erebus	–	✓		<i>J. Volc. Geotherm. Res.</i> , <b>177</b> , 648–660
Gurioli <i>et al.</i> (2008)	Villarrica	FLIR S40	✓		<i>J. Geophys. Res.</i> , <b>113</b> , doi:10.1029/2007JB005328
Harris <i>et al.</i> (2008)	Stromboli	FLIR 695	✓		<i>AGU Geophysical Monograph</i> <b>182</b> , 39–48
Lodato <i>et al.</i> (2008)	Vulcano	FLIR A40	✓		In: Marzocchi and Zollo (2008)*, pp. 427–434
Pioli <i>et al.</i> (2008)	Stromboli	FLIR 695	✓		<i>AGU Geophysical Monograph</i> <b>182</b> , 105–116
Ripepe <i>et al.</i> (2008)	Stromboli	FLIR S40	✓		<i>AGU Geophysical Monograph</i> <b>182</b> , 39–48
Spampinato <i>et al.</i> (2008)	Erta Ale	FLIR P65		✓	<i>G<sup>3</sup></i> , <b>9</b> (12), doi:10.1029/2008GC002164
Spampinato <i>et al.</i> (2008)	Etna	FLIR 695	✓		<i>J. Volc. Geotherm. Res.</i> , <b>177</b> , 301–312
Spampinato <i>et al.</i> (2008)	Stromboli	FLIR 695		✓	<i>AGU Geophysical Monograph</i> <b>182</b> , 201–211
Stevenson and Varely (2008)	Colima	–	✓		<i>J. Volc. Geotherm. Res.</i> , <b>177</b> , 911–924
Tank <i>et al.</i> (2008)	Siena Graben	Agema 570	✓		<i>J. Volc. Geotherm. Res.</i> , <b>177</b> , 515–524
Vilardo <i>et al.</i> (2008)	Solfatara, Campi Flegrei	NEC TS7302	✓		In: Marzocchi and Zollo (2008)*, pp. 481–495
Andonico <i>et al.</i> (2009)	Etna	–	✓		<i>J. Volc. Geotherm. Res.</i> , <b>180</b> , 123–134
Antoine <i>et al.</i> (2009)	Piton de la Fournaise	FLIR 695			<i>J. Volc. Geotherm. Res.</i> , <b>183</b> , 228–244
Barberi <i>et al.</i> (2009)	Stromboli	–	✓	✓	<i>J. Volc. Geotherm. Res.</i> , <b>182</b> , 123–130

Table 9.3. (cont.)

Citation	Volcano	Camera	Exp	Fum	LF	LL	LD	Srf	Journal details
Behncke <i>et al.</i> (2009)	Etna	FLIR A40	✓						<i>J. Geophys. Res.</i> , <b>114</b> , doi:10.1029/2008JB005882
Bertolaso <i>et al.</i> (2009)	Stromboli	—		✓	✓				<i>J. Volc. Geotherm. Res.</i> , <b>182</b> , 269–277
Carapezza <i>et al.</i> (2009)	Stromboli	—		✓					<i>J. Volc. Geotherm. Res.</i> , <b>182</b> , 231–245
Carter and Ramsey (2009)	Bezymianny	FLIR S40					✓		<i>Remote Sensing Environ.</i> , <b>113</b> , 2142–2151
Casagli <i>et al.</i> (2009)	Stromboli	—		✓	✓				<i>J. Volc. Geotherm. Res.</i> , <b>182</b> , 182–200
Giordano and Porreca (2009)	Stromboli	—		✓	✓				<i>J. Volc. Geotherm. Res.</i> , <b>182</b> , 145–154
Harris <i>et al.</i> (2009)	Vulcano	FLIR S40		✓					<i>Bull. Volcanol.</i> , <b>71</b> , 441–458
James <i>et al.</i> (2009)	Etna	FLIR S40			✓				<i>Geophys. Res. Lett.</i> , <b>36</b> , doi:10.1029/2009GL040701
Kelfoun <i>et al.</i> (2009)	Tungurahua	—		✓	✓				<i>Bull. Volcanol.</i> , <b>71</b> , 1057–1075
Marchetti <i>et al.</i> (2009)	Stromboli	FLIR A40			✓				<i>J. Volc. Geotherm. Res.</i> , <b>182</b> , 155–161
Marchetti <i>et al.</i> (2009)	Stromboli	FLIR A20	✓						<i>EPSL</i> , <b>279</b> , 273–281
Mori and Burton (2009)	Stromboli	—		✓					<i>J. Volc. Geotherm. Res.</i> , <b>188</b> , 395–400
Oppenheimer <i>et al.</i> (2009)	Erebus	Agema 550				✓			<i>EPSL</i> , <b>284</b> , 392–398
Prata and Bernard (2009)	Rabaul	Cyclops	✓						<i>J. Volc. Geotherm. Res.</i> , <b>186</b> , 91–107
Rose and Ramsey (2009)	Kliuchevskoi	FLIR S40				✓			<i>J. Volc. Geotherm. Res.</i> , <b>184</b> , 367–380
Ripepe <i>et al.</i> (2009)	Stromboli	FLIR A20	✓		✓				<i>J. Volc. Geotherm. Res.</i> , <b>182</b> , 131–136
Sahetapy-Engel and Harris (2009)	Santiaguito	FLIR S40				✓			<i>Bull. Volcanol.</i> , <b>71</b> , 15–28
Sahetapy-Engel and Harris (2009)	Santiaguito	FLIR S40	✓						<i>Bull. Volcanol.</i> , <b>71</b> , 827–830
Schneider <i>et al.</i> (2009)	Mt. St. Helens	FLIR 595					✓		<i>USGS Prof. Pap.</i> , <b>1750</b> , 347–359
Staudacher <i>et al.</i> (2009)	Piton de la Fournaise	—					✓		<i>J. Volc. Geotherm. Res.</i> , <b>184</b> , 126–137

Vallance <i>et al.</i> (2009)	Mt. St. Helens	FLIR 595		✓	<i>USGS Prof. Pap.</i> , <b>1750</b> , 169–208
Yokoo (2009)	Sakurajima	—	✓		<i>Earth Planets Space</i> , <b>61</b> , 1345–1350
Zanon <i>et al.</i> (2009)	Stromboli	FLIR A40	✓		<i>Geol. Mag.</i> , <b>146</b> , 591–601
Andronico and Pistolesi (2010)	Stromboli	FLIR	✓		<i>J. Volc. Geotherm. Res.</i> , <b>196</b> , 120–125
Applegarth <i>et al.</i> (2010)	Etna	FLIR S40		✓	<i>Bull. Volcanol.</i> , <b>72</b> , 641–656
Calvari <i>et al.</i> (2010)	Stromboli	FLIR 595	✓		<i>J. Geophys. Res.</i> , <b>115</b> , doi:10.1029/2009JB006478
Coppola <i>et al.</i> (2010)	Piton de la Fournaise	FLIR 695		✓	<i>Bull. Volcanol.</i> , <b>72</b> , 341–356
Fee <i>et al.</i> (2010)	Tungurahua	FLIR	✓		<i>J. Volc. Geotherm. Res.</i> , <b>193</b> , 67–81
James <i>et al.</i> (2010)	Etna	FLIR S40		✓	<i>Bull. Volcanol.</i> , <b>72</b> , 671–676
Lyons <i>et al.</i> (2010)	Fuego	Infratec Variocam		✓	<i>Bull. Volcanol.</i> , <b>72</b> , 1–15
Martin <i>et al.</i> (2010)	Masaya	—	✓		<i>J. Geophys. Res.</i> , <b>115</b> , doi:10.1029/2010JB007480
Spampinato <i>et al.</i> (2010)	Poas	—		✓	<i>Rev. Geol. Am. Cent.</i> , <b>43</b> , 171–190
Staudacher (2010)	Piton de la Fournaise	FLIR 695		✓	<i>J. Volc. Geotherm. Res.</i> , <b>191</b> , 60–68
Steffke <i>et al.</i> (2010)	Tungurahua	FLIR	✓		<i>J. Volc. Geotherm. Res.</i> , <b>193</b> , 143–160
Stroberg <i>et al.</i> (2010)	Laboratory	FLIR A3280	✓		<i>J. Volc. Geotherm. Res.</i> , <b>194</b> , 214–219
Vaughan <i>et al.</i> (2010)	Erebus / Yellowstone	FLIR P45		✓	<i>J. Volc. Geotherm. Res.</i> , <b>189</b> , 225–237
Wessels <i>et al.</i> (2010)	Augustine	FLIR 595	✓	✓	<i>USGS Prof. Pap.</i> , <b>1769</b> , 527–552
TOTAL			48	12	37 7 10 9 113

Exp. = Explosions (includes degassing vents, gas puffing, gas pistoning, lava fountaining & pyroclastic flows), Fum = Fumaroles, LF = Lava Flows & Tubes, LL = Lava Lakes, LD = Lava Domes, Srf. = Surface Temperature (includes fractures, cones and crater lakes).

\*In: *Conception, Verification and Application of Innovative Techniques to Study Active Volcanoes*, Marzochi, W. and Zollo, A. (Eds.), INGV (Roma), ISBN 978-88-89972-09-0

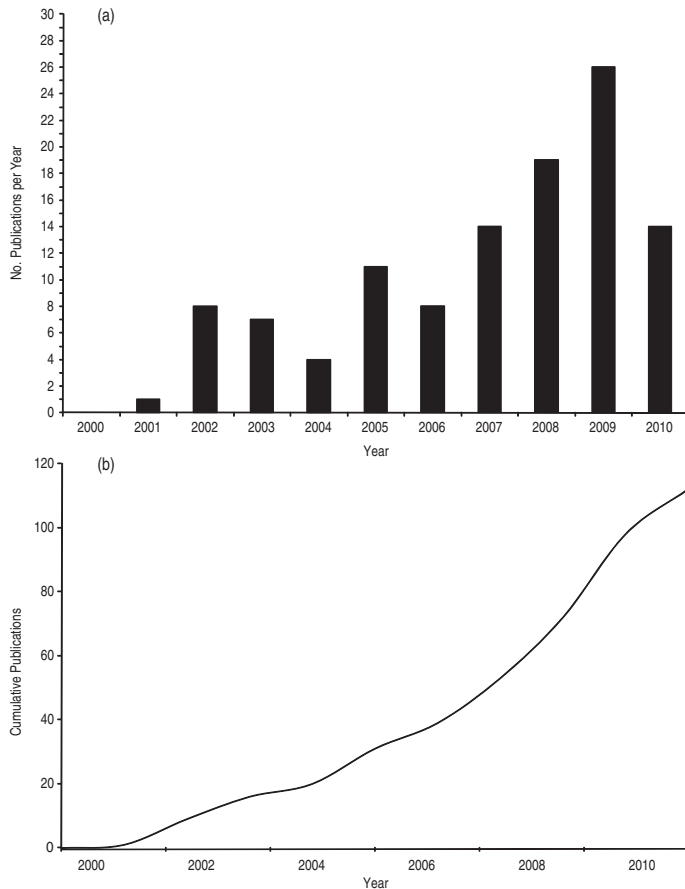


Figure 9.5 Publications per year that use hand-held thermal cameras to target volcanic phenomena, 2000–2010 given as (a) a frequency distribution and (b) cumulative publications. The graphs use the publications collated in [Table 9.3](#).

The Spampinato review placed volcanological applications into five main groups:

- (i) hydrothermal areas and fumarole fields;
- (ii) lava bodies;
- (iii) explosive activity and volcanic plumes;
- (iv) pyroclastic flow deposits;
- (v) fracturing and cracking.

We use more or less the same groupings to classify the literature data base of [Table 9.3](#), and see that one of the most popular areas of study has been explosive activity. Studies within this theme account for 48, or 42%, of the 113 studies published between 2001 and 2011. We see, too, that explosive eruptions were the theme of six of the nine papers that led the way in 2001 and 2002.

We can split the lava bodies group into three sub-groups: studies of lava flows, lakes and domes. These sub-groups respectively contribute 37 (33%), 7 (6%) and 10 (9%) papers to the

data base, for a total of 54 papers, or 48% of all thermal camera publications in volcanology. This group is thus the most popular. The lava lake of Erta Ale was the first lava body to be targeted using a hand-held thermal camera, as reported by Oppenheimer and Yirgu (2002). There followed three papers using thermal camera data to address lava flow issues in 2003 (Kauahikaua *et al.*, 2003; Keszthelyi *et al.*, 2003; Wright and Flynn, 2003), all three reporting thermal camera applications and results from deployments at Kilauea.

The hydrothermal areas and fumarole fields category accounts for 12 (11%) of the 113 papers, with the first study to use hand-held thermal camera data to target a fumarole field being that of Matsushima *et al.* (2003). To date, studies of pyroclastic flow deposits using hand-held thermal cameras have tended to be secondary themes within a study, and are thus not indicated in Table 9.3 which just classifies according to primary theme. However, they include the following.

- Thermal imaging of hot, recently emplaced, pyroclastic flow deposits at Stromboli by Calvari *et al.* (2005; 2010) and Pioli *et al.* (2008), as well as at Bezymianny by Carter *et al.* (2007). However, while the three Stromboli studies are listed within the lava flow category of Table 9.3, the Bezymianny study is listed within the lava dome category.
- Thermal imaging of phoenix clouds ascending over active pyroclastic flows at Stromboli by Calvari *et al.* (2006), as also detailed by Harris *et al.* (2008); both of which are listed within the explosions category of Table 9.3.

The fracturing and cracking category features just two papers in which it forms the primary theme, a study of crack development on a cinder cone by Calvari and Pinkerton (2004), and on the NE flank of Stromboli during 2002–2003 by Bonaccorso *et al.* (2003). I have included these studies in our “surface temperature” category of Table 9.3 because, due to the low magnitude of the associated thermal anomaly, such studies typically require precise measurement and mapping of surface temperatures. Thus, also included in this category is the study by Antoine *et al.* (2009) who used thermal camera data to examine subtle temperature differences between cinder cone rims and flanks to constrain a convective air flow model within the unconsolidated deposits of the imaged cone.

### 9.3.2 Role of the hand-held thermal camera in volcanological enquiry

Table 9.3 shows that volcanological applications in all theme areas were well developed by the end of 2003, i.e., within 36 months of the first publication. We may argue that this was because initial studies were based on three decades of advances in satellite- and ground-based infrared remote sensing of, and radiometry at, hot volcanic targets (as detailed in the first eight chapters of this book). Indeed, there is little need to detail many of the principles and methodologies applied to thermal camera data in this chapter, for they have already been covered in our consideration of identical applications using satellite- and ground-based radiometer data during between the 1960s and 1990s.

What the thermal camera added was flexibility, plus high temporal and spatial resolution, explaining its popularity – especially with a generation of volcanologists who had been working within the limits of 100–120 m TIR pixels collected by satellite-based sensors every 12 hours to 16 days. The key advance has been the ability to collect thermal video with spatial resolutions of a few centimeters and sampling frequencies of up to 120 Hz, with the operator being free to choose and modify the dynamic range, sampling rate, field of view, and targeted area, as well as acquisition start and stop times. Thus, among the first studies that used thermal camera data were those that required flexibility for aircraft-based rapid response and eruption surveillance, such as the studies of McGimsey *et al.* (1999), Nye *et al.* (2002) and Kauahikaua *et al.* (2003), or high-spatial-resolution analyses of thermal structures and heat losses at active lava bodies, such as the studies of Oppenheimer and Yirgu (2002) and Wright and Flynn (2003).

Early studies were also quick to take advantage of the video capability of the thermal camera to capture rapidly evolving, or fast-moving, eruption dynamics, such as those occurring during the explosive emission of plumes loaded with ash and ballistics. In this regard, some of the first progress reports made to the volcanological community were those detailing applications of the FLIR Systems ThermaCam™ 595, operating at its maximum sampling rate of ~0.25 Hz, to track the dynamics of strombolian eruption plumes, such as the abstract presented at the AGU Fall meeting in December 2001 by Dehn *et al.* (2001). Applications of the ThermaCam™ S40 operating at up to 30 Hz to study high-speed lava flow thermal processes, as well as eruption plume dynamics, were presented at the same meeting three years later, in 2004 – the S40 only having come on-line in 2002. Presentations involving hand-held thermal camera data included those of Harris (2004), Schneider *et al.* (2004), Pinkerton *et al.* (2004), Patrick *et al.* (2004) and Witter and Harris (2004); the presentations of Pinkerton *et al.* (2004) and Patrick *et al.* (2004), in particular, used data collected at 30 Hz to examine lava flow and plume emplacement processes, respectively.

While the camera itself was off-the-shelf and easy-to-use, approaches were also based on three decades of methodological, processing and interpretation developments made using satellite-sensor and ground-based radiometer IR data. This may explain why the thermal camera literature did not go through an experimental, test or proofing phase. Indeed, many of the publications listed in Table 9.3 simply used thermal-camera-derived data and observations to support a wider analysis. That is, studies did not focus on the thermal camera itself and/or methodologies to extract information, but instead used the data to furnish or support observations. The first paper to use thermal camera data listed in Table 9.3., i.e., Roach *et al.* (2001), included a simple statement that “... airborne video observations made by Alaska State Troopers with a Forward-Looking Infrared Radiometer” (p. 380) were used to aid in making observations of Pavlof’s 1996 eruption.

In effect, the technology was accepted immediately as a valid surveillance and monitoring tool. Thus, it was not until four years after the take-off studies of 2002 that Ball and Pinkerton (2006) rigorously tested the performance of the cameras that had already been integrated into routine monitoring and research, with Sawyer and Burton (2006) examining

the effects of volcanic gas on hand-held thermal camera measurements. Could this trend to the history of hand-held thermal camera application in volcanological research, surveillance and monitoring represent the establishment and acceptance of thermal remote sensing as an operational tool in volcanology by 2002?

## 9.4 Measurement principles

As with thermal IR data collected by satellite-based sensors, there are both atmospheric, emissivity, and geometric corrections that need to be made before the data can be used for quantitative thermal or dimensional measurements. However, because hand-held camera images are usually taken of uneven surfaces from an oblique vantage point, the geometric issues are somewhat more complex than in the satellite-based case. At an active volcanic target safe approach considerations and topographic barriers, such as the presence of deep, sheer-sided pit craters, fast-moving braided streams of lava or fall-out from ballistic plumes, mean that the perfect face-on viewing geometry may not always be possible. In addition, the volcanic surface will likely be rough and uneven, so that simple geometric corrections may not be applicable.

### 9.4.1 Field of view: geometry and dimensions

The camera angular field of view ( $\beta$ ) and distance to the target ( $D$ ) will determine the dimensions of imaged area. We start by considering the simple condition whereby the targeted surface is orientated at right angles to the FPA, as in [Figure 9.6a](#). With this simple geometry the horizontal field of view (HFOV) and vertical field of view (VFOV) can be estimated using the relation,

$$\text{HFOV} = 2[D \tan(\beta_H/2)] \quad (9.10\text{a})$$

and

$$\text{VFOV} = 2[D \tan(\beta_V/2)], \quad (9.10\text{b})$$

$\beta_H$  being the angular field of view in the horizontal dimension;  $\beta_V$  being the angular field of view in the vertical dimension. Hence, for a camera with a  $\beta_H \times \beta_V$  of  $24 \times 18^\circ$  viewing a vertical surface over a horizontal line-of-sight of 250 m, the imaged area will be

$$\text{HFOV} = 2[250 \text{ m} \tan(0.419 \text{ rad}/2)] = 106 \text{ m}$$

by

$$\text{VFOV} = 2[250 \text{ m} \tan(0.314 \text{ rad}/2)] = 79 \text{ m}.$$

Over short distances, this can be approximated by

$$\text{HFOV} = \beta_H \times \text{Distance} = (0.419 \text{ rad})(250 \text{ m}) = 105 \text{ m}$$

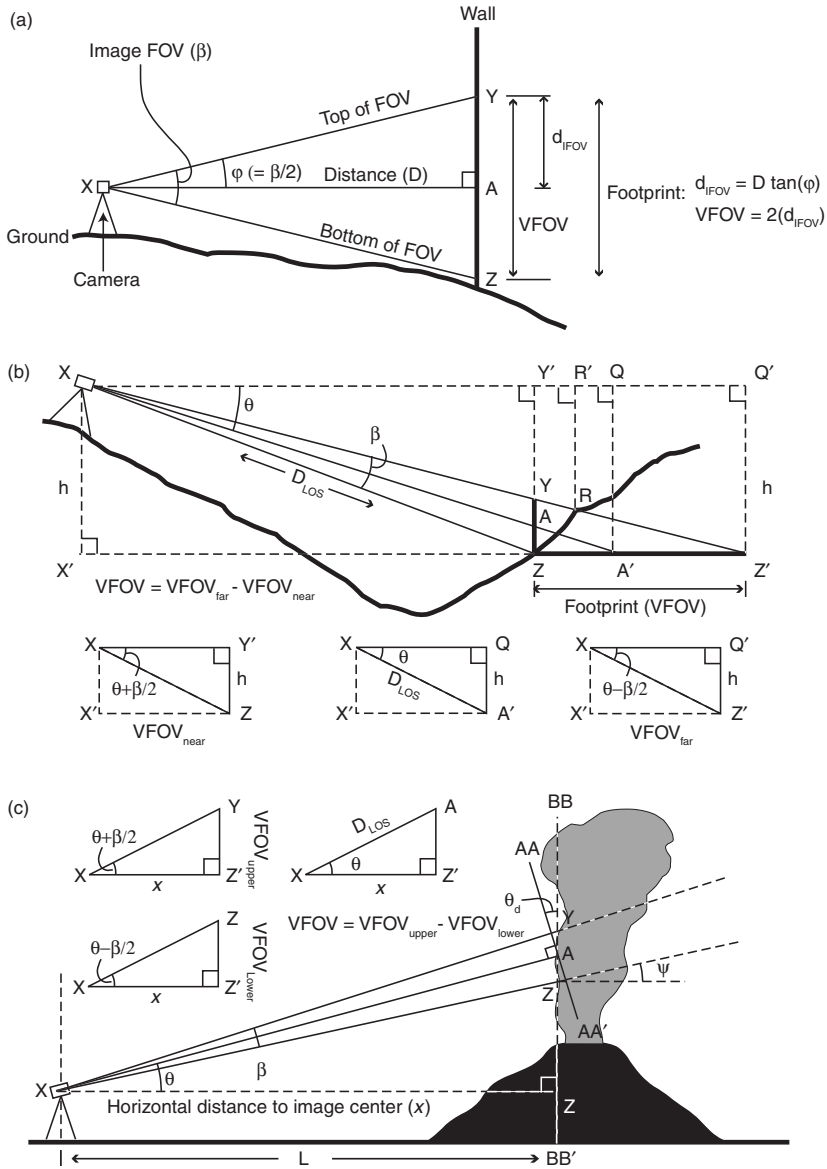


Figure 9.6 (a) Trigonometry to calculate image field of view for a “head-on” view of a flat, vertically orientated, surface. The camera is at point X, and is directly opposite the center point of the imaged surface area (point A). (b) Trigonometry to calculate image field of view for an image acquired when the camera is tilted downwards at angle  $\theta$ . Triangles extracted here, and solution in text, are for a downward looking view onto a horizontal surface, with the footprint spanning distance Z–Z'. For a vertically orientated surface the footprint will span distance Z–Y, and for a surface sloping away from the camera distance Z–R. For both cases solution using the appropriate triangles will need to be applied. (c) Trigonometry to calculate image field of view for an image acquired when the camera is tilted upward at angle  $\theta$ . For a vertically orientated feature points along line BB–BB' will be projected onto the image plane (line AA–AA').

and

$$\text{VFOV} = \beta_V \times \text{Distance} = (0.314 \text{ rad})(250 \text{ m}) = 79 \text{ m.}$$

In reality, the perfect geometry of [Figure 9.6a](#) is unlikely to apply; it is more likely that the camera will be pointed downwards, or upwards, at the target and/or the surface will not be orientated at right angles to the line-of-sight. In these cases, calculation of the FOV dimensions needs to take into account the viewing angle,  $\theta$ . For a camera pointing downwards onto a flat, horizontal, surface that is  $h$  meters vertically below the camera, we have the geometry of [Figure 9.6b](#). For this case, the line of sight distance to the image center is

$$D_{\text{LOS}} = \frac{h}{\sin(\theta)}, \quad (9.11)$$

the horizontal distance to the FOV near edge is

$$\text{VFOV}_{\text{near}} = \frac{h}{\tan(\theta + \frac{\beta_V}{2})} \quad (9.12a)$$

and the horizontal distance to the FOV far edge is

$$\text{VFOV}_{\text{far}} = \frac{h}{\tan(\theta - \frac{\beta_V}{2})}. \quad (9.12b)$$

The difference between the two is now the height of the image, i.e.,

$$\text{VFOV} = \text{VFOV}_{\text{far}} - \text{VFOV}_{\text{near}} = h \left[ \frac{1}{\tan(\theta - \frac{\beta_V}{2})} - \frac{1}{\tan(\theta + \frac{\beta_V}{2})} \right] \quad (9.12c)$$

so that, for a camera 113.5 m above the targeted surface and pointing downwards at an angle of 27°, a  $\beta_V$  of 18° gives,

$$D_{\text{LOS}} = \frac{113.5 \text{ m}}{\sin(0.471)} = 250 \text{ m}$$

and

$$\begin{aligned} \text{VFOV} &= 113.5 \text{ m} \left[ \frac{1}{\tan(0.471 - \frac{0.314}{2})} - \frac{1}{\tan(0.471 + \frac{0.314}{2})} \right] = 349.3 \text{ m} - 156.2 \text{ m} \\ &= 193.1 \text{ m.} \end{aligned}$$

We see that the FOV diameter will increase with height above the imaged surface, as well as with depression angle. Thus, for a given height, the image footprint will decrease in size as

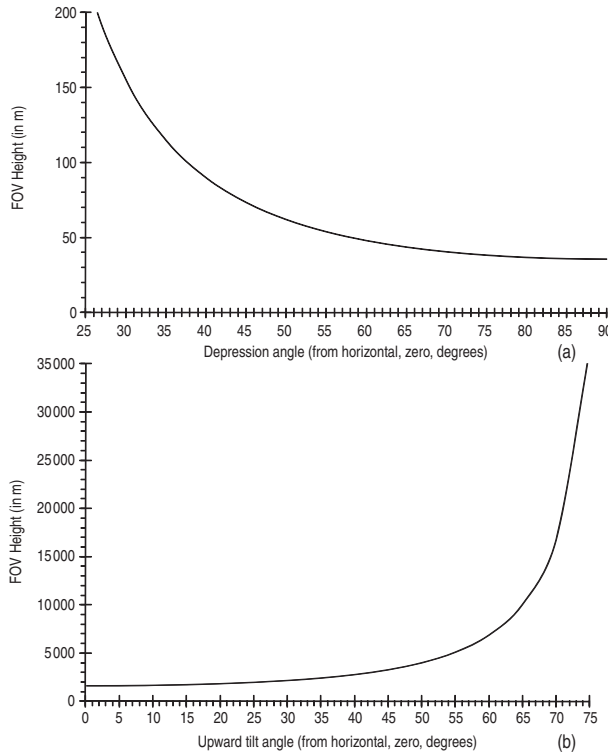


Figure 9.7 Change in height of imaged area (FOV) with (a) downward depression angle and (b) upward tilt angle. Both plots are for a camera with an  $18^\circ$  vertical FOV, with that of (a) being for a camera located 113.5 m above a flat surface and pointed downwards onto it, and (b) being for a camera located 5000 m horizontally from a vertical surface and pointed upwards onto it.

the operator increases the depression angle, i.e., tilts the camera downwards, the effect being plotted in Figure 9.7a.

For a camera pointing upwards onto a target that is  $x$  meters horizontally away from the camera we have the geometry of Figure 9.6c. For this case, the line-of-sight distance to the image center is

$$D_{\text{LOS}} = \frac{x}{\cos(\theta)}, \quad (9.13)$$

the horizontal distance to the FOV upper edge is

$$\text{VFOV}_{\text{upper}} = x \tan\left(\theta + \frac{\beta_V}{2}\right) \quad (9.14a)$$

and the horizontal distance to the FOV lower edge is

$$\text{VFOV}_{\text{lower}} = x \tan\left(\theta - \frac{\beta_V}{2}\right). \quad (9.14\text{b})$$

The difference between the two is now the height of the image, i.e.,

$$\text{VFOV} = \text{VFOV}_{\text{upper}} - \text{VFOV}_{\text{lower}} = x \left[ \tan\left(\theta + \frac{\beta_V}{2}\right) - \tan\left(\theta - \frac{\beta_V}{2}\right) \right] \quad (9.14\text{c})$$

so that, for a camera 5 km away from the targeted surface and pointing upwards at an angle of  $27^\circ$ , a  $\beta_V$  of  $18^\circ$  gives

$$D_{\text{LOS}} = \frac{5000 \text{ m}}{\sin(0.471)} = 5612 \text{ m}$$

and

$$\begin{aligned} \text{VFOV} &= 5000 \text{ m} \left[ \tan\left(0.471 + \frac{0.314}{2}\right) - \tan\left(0.471 - \frac{0.314}{2}\right) \right] \\ &= 3632.7 \text{ m} - 1624.6 \text{ m} = 2008 \text{ m}. \end{aligned}$$

For this case, FOV diameter will increase with distance from the imaged surface, as well as with inclination angle. Thus, for a given distance, the image footprint will increase in size as the operator increases the inclination angle, i.e., tilts the camera upwards, the effect being plotted in [Figure 9.7b](#).

Thus to accurately calculate FOV (or image footprint) dimensions, the operator needs to record

- (1) the angle at which the camera is tilted downwards or upwards,
- (2) the height above the targeted surface, and/or
- (3) the horizontal distance between the camera and the targeted surface.

While the downward-looking geometry may apply to measurements made from helicopters, or staring down into active craters, the upward-looking geometry may apply to cases where the camera is pointed up at a volcano summit or at an ascending plume.

#### 9.4.2 Pixel dimensions

The same geometric issues apply to calculation of pixel dimensions within the image FOV. Again, the simple “head-on” geometry of [Figure 9.6a](#) will apply to a situation where the targeted surface is orientated at right angles to FPA. However, the “head-on” geometry will only apply to the central pixel in the image. For pixels away from the image center point, pixel dimensions can be calculated using the geometry of [Figure 9.8](#). To complete this calculation, we first need to estimate the angle between the image center point and the pixel in question. We can do this as follows.

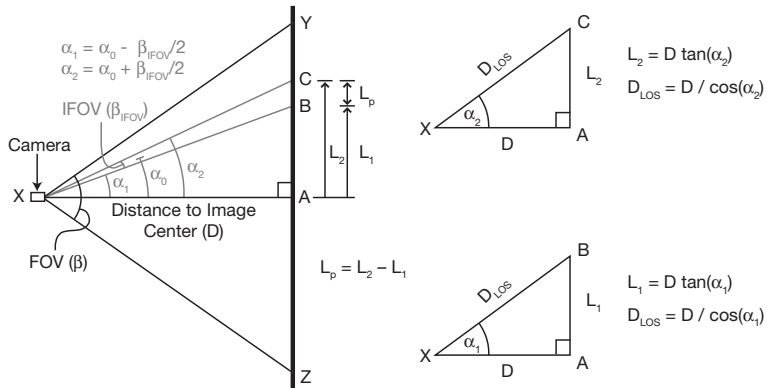


Figure 9.8 Trigonometry to calculate pixel dimensions for a “head-on” view of a flat, vertically orientated surface. Camera is at point X, and is directly opposite the center point of the imaged surface area (point A). The image FOV, opening at angle  $\beta$ , is defined by triangle XZY. The pixel IFOV, opening at angle  $\beta_{\text{IFOV}}$  and for a pixel at angle  $\alpha_0$  from the image center, is defined by triangle XBC. The pixel dimension ( $L_p$ ), and line-of-sight distance to the pixel ( $D_{\text{LOS}}$ ), can be estimated from the distance to the image center ( $D$ ) and pixel viewing angles ( $\alpha_0$ ,  $\alpha_2$  and  $\alpha_1$ ) using the trigonometric solutions given for triangles XAC (to obtain distance  $L_2$ ) and XAB (to obtain distance  $L_1$ ). Now  $L_p = L_2 - L_1$ .

- First, locate the pixel and determine the pixel distance, in terms of number of pixels, from the image center point. If, for example we have a pixel located at image coordinate  $x = 10$  or  $y = 10$ , in a  $320 \times 240$  pixel image, this point will be 150 pixels from the image center in the  $x$  direction, or 110 pixels from the center point in the  $y$  direction. Note that we are using the upper left corner of the image as the origin ( $x = 0, y = 0$ ).
- Second, estimate the pixel-increment angle ( $\alpha_l$ ). This can be estimated by dividing  $\beta$  by the number of pixels in the image. If the FOV is  $24 \times 18^\circ$ , then the increment angle will be:

$$24^\circ/320 \text{ pixels} = 0.075^\circ \text{ per pixel in the } x \text{ direction, and}$$

$$18^\circ/240 \text{ pixels} = 0.075^\circ \text{ per pixel in the } y \text{ direction.}$$

- Third, multiply the pixel-increment angle ( $\alpha_l$ ) by the distance (in pixels) from the image center to the target pixel ( $D_{\text{pixels}}$ ). This gives the angle between the center of the image and the target pixel ( $\alpha_0$ ) where, in our case, we have:

$$\alpha_0(x) = 150 \text{ pixels} \times 0.075^\circ \text{ per pixel} = 11.25^\circ \text{ in the } x \text{ direction, and}$$

$$\alpha_0(y) = 110 \text{ pixels} \times 0.075^\circ \text{ per pixel} = 8.25^\circ \text{ in the } y \text{ direction.}$$

We can now use this angular pixel position to estimate the ground distance to the pixel from the image center using the geometry laid out in Figure 9.8. Within this geometry, while the ground distance to the pixel outer edge ( $L_2$ ) will be:

$$L_2 = D \left[ \tan \left( \alpha_0 + \frac{\beta_{\text{IFOV}}}{2} \right) \right], \quad (9.15a)$$

$\beta_{\text{IFOV}}$  being the pixel opening angle or IFOV (in radians), the ground distance to the pixel inner edge ( $L_1$ ) can be obtained from,

$$L_1 = D \left[ \tan \left( \alpha_0 - \frac{\beta_{\text{IFOV}}}{2} \right) \right]. \quad (9.15b)$$

Now, the pixel dimension ( $L_p$ ) can be obtained by subtracting the two distances, i.e.,

$$L_p = L_2 - L_1 = D \left[ \tan \left( \alpha_0 + \frac{\beta_{\text{IFOV}}}{2} \right) - \tan \left( \alpha_0 - \frac{\beta_{\text{IFOV}}}{2} \right) \right]. \quad (9.15c)$$

We can also calculate the line-of-sight ( $D_{\text{LOS}}$ ) distance to the center of the pixel from,

$$D_{\text{LOS}} = \frac{D}{\cos(\alpha_0)}. \quad (9.15d)$$

For our case, given a line-of-sight distance of 250 m to the image center, the line-of-sight distance to the pixel at  $11.25^\circ$  from the image center in the horizontal ( $x$ ) dimension is

$$D_{\text{LOS}} = \frac{250 \text{ m}}{\cos(0.196)} = 254.9 \text{ m}.$$

For the same pixel, the horizontal ground distance between the pixel outer edge and the image center will be

$$L_2 = 250 \text{ m} \left[ \tan \left( 0.196 + \frac{0.0013}{2} \right) \right] = 49.897 \text{ m}$$

and for the pixel inner edge,

$$L_1 = 250 \text{ m} \left[ \tan \left( 0.196 - \frac{0.0013}{2} \right) \right] = 49.559 \text{ m},$$

so that the pixel diameter is:

$$\begin{aligned} L_p &= 250 \text{ m} \left[ \tan \left( 0.196 + \frac{0.0013}{2} \right) - \tan \left( 0.196 - \frac{0.0013}{2} \right) \right] = 49.9 \text{ m} - 49.56 \text{ m} \\ &= 0.338 \text{ m}. \end{aligned}$$

In the vertical ( $y$ ) dimension, for our pixel at  $\alpha_0 = 8.25^\circ$ , we obtain

$$L_2 = 250 \text{ m} \left[ \tan\left(0.144 + \frac{0.0013}{2}\right) \right] = 36.414 \text{ m}$$

$$L_1 = 250 \text{ m} \left[ \tan\left(0.144 - \frac{0.0013}{2}\right) \right] = 36.082 \text{ m}$$

so that the pixel diameter is

$$\begin{aligned} L_p &= 250 \left[ \tan\left(0.144 + \frac{0.0013}{2}\right) - \tan\left(0.144 - \frac{0.0013}{2}\right) \right] = 36.41 \text{ m} - 36.01 \text{ m} \\ &= 0.332 \text{ m.} \end{aligned}$$

These dimensions ( $0.338 \times 0.332 \text{ m}$ ) compare with the diameter for the central pixel of

$$L_p = 0.0013 \text{ rad(Distance)} = 0.0013 \text{ rad}(250 \text{ m}) = 0.325 \text{ m.}$$

Thus, even for a flat surface viewed head-on over quite a short line-of-sight, the pixel size will increase a little with distance from the image center, so that variations in the spatial resolution resulting from the angular variation in the pixel position across the image will need to be taken into account when making precise, dimension-based, measurements such as object width, height, area, distance and velocity, especially for fast moving and/or small objects.

#### 9.4.2.1 Downwards and upwards viewing

For a camera tilted downwards or upwards at a target the pixel dimensions will increase with distance, as sketched in [Figure 9.9](#). Pixels will also become increasingly stretched with distance from the camera. For a downward pointed view, the dimensions for pixels within such a grid can be calculated using the geometry of [Figure 9.10a](#). Within this geometry, the line-of-sight distance to the middle of the central pixel in the image is given by

$$D_{\text{LOS}} = h / \cos(\theta_0), \quad (9.16)$$

$h$  being the elevation difference between the higher camera and lower target, and  $\theta_0$  being the elevation angle (= 90 minus the depression angle,  $\theta$ ). The distance to the inner edge of the central pixel in this image ( $L_1$ ) can be obtained from:

$$L_1 = h \tan\left(\theta_0 - \frac{\beta_{\text{IFOV}}}{2}\right) \quad (9.17a)$$

and the distance to the outer edge ( $L_2$ ) from

$$L_2 = h \tan\left(\theta_0 + \frac{\beta_{\text{IFOV}}}{2}\right) \quad (9.17b)$$

so the pixel dimension ( $L_p$ ) becomes

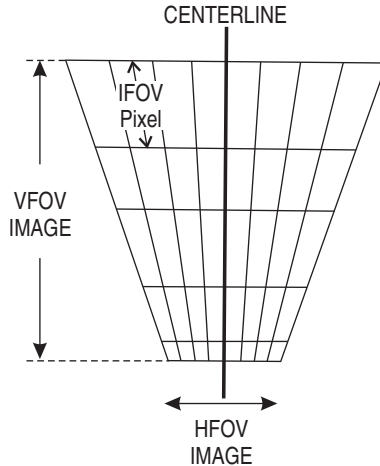


Figure 9.9 Image and pixel distortion experienced in an obliquely acquired image. This applies to cases where the camera is looking down onto a flat surface, or upwards onto a vertically-orientated surface [modified from Holst (2000, Fig. 8.4)].

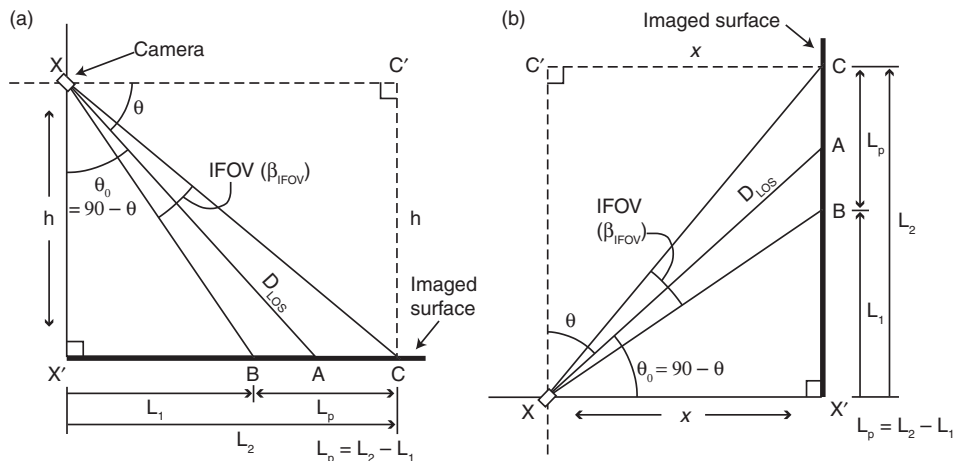


Figure 9.10 (a) Trigonometry to calculate pixel dimensions for the central pixel in an image where the camera is pointed downwards at angle  $\theta$  to image a flat surface  $h$  meters below the camera. (b) Trigonometry to calculate pixel dimensions for the central pixel in an image where the camera is pointed upwards at angle  $\theta_0$  to image a vertical surface  $x$  meters away from the camera.

$$L_p = L_2 - L_1 = h \left[ \tan\left(\theta_0 + \frac{\beta_{\text{IFOV}}}{2}\right) - \tan\left(\theta_0 - \frac{\beta_{\text{IFOV}}}{2}\right) \right]. \quad (9.17c)$$

To carry out these calculations for pixels in the near field (i.e., between the image center and the image inner-edge), we need to subtract the pixel increment angle ( $\alpha_l$ ) from the elevation angle, so that

$$\theta_n = \theta_0 - \alpha_l. \quad (9.18a)$$

For the far field (i.e., between the image center and the image outer-edge), we to add the pixel increment angle to the elevation angle, so that

$$\theta_n = \theta_0 + \alpha_l. \quad (9.18b)$$

These angles can then be used in the Equations (9.17) to obtain the pixel dimension at pixel  $n$ . For the center point of our image obtained looking downwards at an angle of  $27^\circ$  (so that  $\theta_0 = 90^\circ - 27^\circ = 63^\circ = 1.1$  rad) from a height of 113.5 m above the target we obtain

$$D_{\text{LOS}} = 113.5 \text{ m} / \cos(1.1) = 250 \text{ m}$$

$$\begin{aligned} L_p &= 113.5 \text{ m} \left[ \tan\left(1.1 + \frac{0.0013}{2}\right) - \tan\left(1.1 - \frac{0.0013}{2}\right) \right] = 222.399 \text{ m} - 223.115 \text{ m} \\ &= 0.716 \text{ m}, \end{aligned}$$

so that the dimension of the central pixel has increased somewhat over the 0.325 m pixel obtained for the “head-on” case. The pixel angle for, and dimension of, our pixel towards the edge of the image (i.e., at pixel 10) becomes

$$\theta_n = 63^\circ + (110 \text{ pixels} \times 0.075^\circ \text{ per pixel}) = 71.25^\circ = 1.24 \text{ radians},$$

so that

$$\begin{aligned} L_p &= 113.5 \text{ m} \left[ \tan\left(1.24 + \frac{0.0013}{2}\right) - \tan\left(1.24 - \frac{0.0013}{2}\right) \right] \\ &= 333.648 \text{ m} - 335.076 \text{ m} = 1.428 \text{ m}. \end{aligned}$$

This is considerably larger than the diameter obtained assuming a “head-on” geometry, i.e., 0.335 m. In our reference frame, the nearest pixel to the camera will be 120 pixels from the image center, so that the viewing angle to this pixel will be

$$\theta_n = 63^\circ - (120 \text{ pixels} \times 0.075^\circ \text{ per pixel}) = 54^\circ = 0.942 \text{ radians}$$

so that the minimum pixel dimension in the near-field will be:

$$\begin{aligned} L_p &= 113.5 \text{ m} \left[ \tan\left(0.942 + \frac{0.0013}{2}\right) - \tan\left(0.942 - \frac{0.0013}{2}\right) \right] \\ &= 156.006 \text{ m} - 156.433 \text{ m} = 0.427 \text{ m}. \end{aligned}$$

The variation in pixel dimension with viewing angle for these geometric conditions is given in [Figure 9.11](#), where we can see how the pixel dimension increases as we move from the front to the back of the image.

For an upward pointed view the pixel dimensions can be estimated using the geometry sketched in [Figure 9.10b](#). For this case the upward inclination angle of the camera is used for

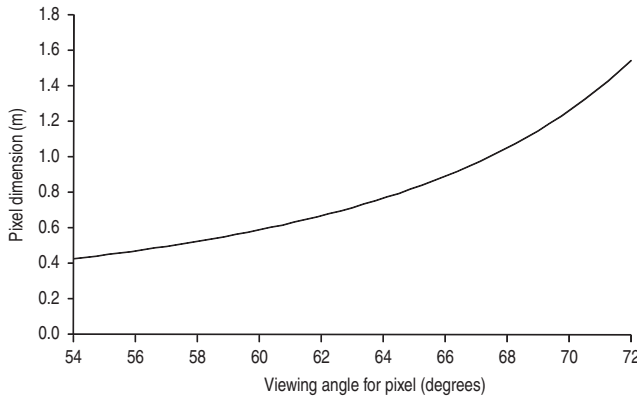


Figure 9.11 Increase in pixel dimension with viewing angle for an oblique image acquired by a camera pointed downwards to target a flat surface. The camera is pointed downwards at an angle of  $27^\circ$  (so that  $\theta_0 = 63^\circ$ ) from a height of 113.5 m. IFOV is  $0.075^\circ$  and the image extends 120 pixels either side of the center point, so that the near edge of the image is viewed at an angle of  $54^\circ$ , and the far edge at  $72^\circ$ .

$\theta_0$  and the horizontal distance between the camera and the base of the vertical surface is used for  $x$ . To obtain the distance to the lower edge of the central pixel ( $L_1$ ) we now have:

$$L_1 = x \tan\left(\theta_0 - \frac{\beta_{\text{IFOV}}}{2}\right) \quad (9.19\text{a})$$

and to the pixel upper edge ( $L_2$ ):

$$L_2 = x \tan\left(\theta_0 + \frac{\beta_{\text{IFOV}}}{2}\right). \quad (9.19\text{b})$$

For an upward inclination angle of  $27^\circ$  and a range of 5 km,  $L_p$  for the central pixel in the image becomes

$$\begin{aligned} L_p &= 5000 \text{ m} \left[ \tan\left(0.471 + \frac{0.0013}{2}\right) - \tan\left(0.471 - \frac{0.0013}{2}\right) \right] = 2551.7 \text{ m} - 2543.5 \text{ m} \\ &= 8.2 \text{ m}. \end{aligned}$$

For our point 10 pixels from the top of the image we have,

$$\theta_n = 27^\circ + (110 \text{ pixels} \times 0.075^\circ \text{ per pixel}) = 35.25^\circ = 0.615 \text{ radians}$$

so that

$$\begin{aligned} L_p &= 5000 \text{ m} \left[ \tan\left(0.615 + \frac{0.0013}{2}\right) - \tan\left(0.615 - \frac{0.0013}{2}\right) \right] \\ &= 3538.5 \text{ m} - 3528.8 \text{ m} = 9.7 \text{ m}. \end{aligned}$$

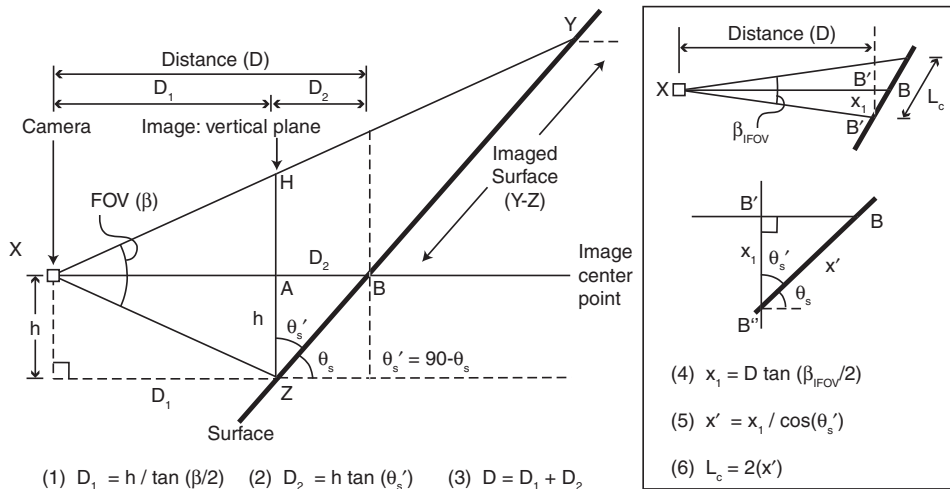


Figure 9.12 Trigonometry to calculate pixel dimensions in an image where the camera is pointed horizontally onto a surface sloping away from the camera.

Finally, a point at the bottom of the image will be at angle,

$$\theta_n = 63^\circ - (120 \text{ pixels} \times 0.075^\circ \text{ per pixel}) = 18^\circ = 0.314 \text{ radians}$$

so that

$$L_p = 5000 \text{ m} \left[ \tan\left(0.314 + \frac{0.0013}{2}\right) - \tan\left(0.314 - \frac{0.0013}{2}\right) \right] = 1628.2 \text{ m} - 1621.0 \text{ m} \\ = 7.2 \text{ m.}$$

Again, the pixel dimension increases between the image bottom and the image top.

#### 9.4.3 Topographic effects

Calculation of pixel dimension becomes more complicated if the surface within the FOV is sloping. This may be the case when imaging, for example, a lava flow front or the flank of a cone. There are several geometric solutions to this problem. One simple solution is given in Figure 9.12.

##### (1) Solution if horizontal distance between the camera and FOV base is known

This solution uses the distance between the camera and the base of the FOV ( $D_1$  in Figure 9.12) to estimate pixel diameter. This horizontal distance can also be obtained if the camera is orientated horizontally and the camera height above the FOV base is known (height  $h$  in Figure 9.12). For our demonstration case the camera is sited 39.6 m

above the FOV base so that, for a FOV of  $18^\circ$  in the  $y$  (vertical) dimension, we have a horizontal distance between the camera location and the image vertical plane (i.e., distance  $D_1$ ) of

$$D_1 = h \tan(90 - 0.5 \beta) = (39.6 \text{ m}) \tan(1.41 \text{ rad}) = 250 \text{ m}.$$

Now, to estimate the dimension of the central pixel the solution of [Figure 9.12](#) involves six calculation steps.

- Step 1. Use  $h$  to calculate the distance to the image plane orientated vertically in relation to the camera (Equation 1, [Figure 9.12](#)).
- Step 2. Use dimension  $h$  with the ground slope ( $\theta_s$ ) to estimate  $D_2$ , i.e., the horizontal distance between the center of the image vertical plane and the actual ground position at the image center (Equation 2, [Figure 9.12](#)).
- Step 3. Sum  $D_1$  and  $D_2$  to obtain  $D$ , i.e., the distance between the camera and the image center point (Equation 3, [Figure 9.12](#)).
- Step 4. Use  $D$  with the pixel IFOV ( $\beta_{\text{IFOV}}$ ) to calculate  $x_1$ , i.e., the pixel half-width if the surface were orientated at right angles to the image plane (Equation 4, [Figure 9.12](#)).
- Step 5. Correct pixel dimension  $x_1$  using the topographic slope ( $\theta_s$ ) to obtain  $x'$ , i.e., the actual radius of the ground-area covered by the pixel opening with an IFOV of  $\beta_{\text{IFOV}}$  (Equation 5, [Figure 9.12](#)).
- Step 6. Multiply  $x'$  by two to obtain  $L_p$ , i.e., the pixel diameter (Equation 6, [Figure 9.12](#)).

For the image geometry of [Figure 9.12](#) and the following image properties:

- a camera height above the FOV base of ( $h$ ) 39.6 m;
- a  $\text{FOV}(\beta)$  opening with an angle of  $18^\circ$  ( $0.314 \text{ rad}$ );
- a ground slope ( $\theta_s$ ) of  $35^\circ$  (so that  $\theta_s' = 90^\circ - 35^\circ = 55^\circ = 0.96 \text{ rad}$ );
- a pixel IFOV ( $\beta_{\text{IFOV}}$ ) of  $1.3 \text{ mrad}$ ,

we have the following solution.

- Step 1. Distance to FOV vertical plane ( $D_1$ ):

$$D_1 = \frac{h}{\tan(\beta/2)} = \frac{39.6 \text{ m}}{\tan(0.314/2)} = 250 \text{ m}.$$

- Step 2. Distance between the center of the vertical plane and the ground position at the center of the image ( $D_2$ ):

$$D_2 = h \tan(\theta_s') = 39.6 \text{ m} \tan(0.96) = 56.6 \text{ m}.$$

- Step 3. Distance between the camera and the image center point

$$D = D_1 + D_2 = 250 \text{ m} + 56.6 \text{ m} = 306.6 \text{ m}.$$

Step 4. Pixel size for surface orientated at right angles to the image plane:

$$x_1 = D \tan(\beta_{\text{IFOV}}/2) = 306.5 \text{ m} \tan(0.0013/2) = 0.2 \text{ m.}$$

Step 5. Pixel dimension corrected using the topographic slope ( $\theta_s$ ):

$$x_1' = x_1 / \cos(\theta_s') = 0.2 \text{ m} \cos(0.96) = 0.35 \text{ m.}$$

Step 6. Pixel diameter projected onto the sloping surface ( $L_p$ ):

$$L_p = 2 \times 0.35 \text{ m} = 0.7 \text{ m.}$$

Above this center point position, the increasing range due to the terrain sloping away from the camera perspective will cause the pixel dimension to increase with distance from the image center. Below the center point, the decreasing range (due to the terrain sloping towards the camera) will cause the pixel dimension to decrease with distance from the image center.

#### (2) Solution if horizontal distance between the camera and FOV center is known

Where the distance to the center of the image is known, we can go straight to Step 4 of the solution given above, where the half-width for a pixel in the vertically orientated plane ( $x_1$ , [Figure 9.12](#)) can be calculated using the ground slope ( $\theta_s$ ), pixel instantaneous field of view ( $\beta_{\text{IFOV}}$ ) and range ( $D$ ). For a center point range of 250 m and a pixel IFOV of 1.3 mrad we have,

$$x_1 = D \tan(\beta_{\text{IFOV}}/2) = (250 \text{ m}) \tan(1.3 \text{ mrad} / 2) = 0.1625 \text{ m.}$$

The pixel diameter for such a geometry, i.e., if the surface was orientated vertically, would be

$$L_p = 2(x_1) = 2(0.1625 \text{ m}) = 0.325 \text{ m.}$$

Correcting the pixel dimension for the slope effect we have, for a slope ( $\theta_s$ ) of 35°,

$$x' = x_1 / \cos(90 - \theta_s) = 0.1625 \text{ m} / \cos(0.96 \text{ rad}) = 0.283 \text{ m}$$

so that the slope-adjusted  $L_p$  is,

$$L_p = 2(x') = 2(0.283 \text{ m}) = 0.567 \text{ m.}$$

That is, the slope effect has, for this 35° case, increased the pixel size by 74%.

Pixel dimension will increase as the slope decreases. The relation between pixel size and ground slope is plotted in [Figure 9.13](#), in which we see that the relation between pixel diameter and ground slope follows a power law with the form,

$$L_p = 16.259 \theta_s^{-0.9167}. \quad (9.20)$$

This relation results from the effective incidence angle (as defined by  $\theta_s'$ ) increasing as the slope angle ( $\theta_s$ ) decreases, so that the relation between slope and pixel dimension is inverse. In effect, the projection of the pixel footprint onto the surface becomes increasingly glancing

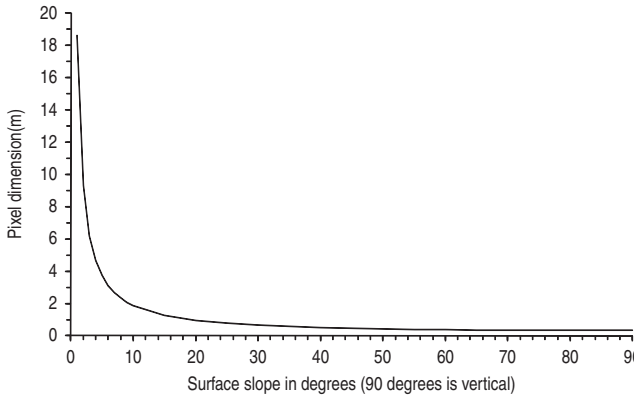


Figure 9.13 Decrease of pixel dimension with increased ground slope. Model for a pixel in the image center. Image center is viewed head-on and is 250 m horizontally from the camera and the pixel has an IFOV of 1.3 mrad.

as the slope decreases, so that the pixel becomes increasingly stretched in the  $y$  direction as we move from a surface that is orientated at right angles in relation to the camera FPA to one which is parallel with it.

**(a) Pixels between the FOV center point and upper edge** For the geometric case where the surface is sloping away from the camera, the distance between the camera and the imaged ground point will increase with height in the FOV, so that the pixel dimension will decrease towards the base of the image, and increase towards the top. This effect can be calculated using the geometry sketched in Figure 9.14. Given the distance to the image center (distance  $D$ , Figure 9.14), we can estimate the vertical distance between the image center and any point vertically above the center (distance  $m$ , Figure 9.14) using:

$$m = D \tan(\alpha_0), \quad (9.21)$$

$\alpha_0$  being the angle between horizontal and the line-of-sight to the pixel center. Now, we can estimate the ground surface distance between the image center point and the pixel center (distance  $l$ , Figure 9.14) using triangle XBR" of Figure 9.14 and the trigonometric relation

$$\frac{m}{\sin(\alpha_3)} = \frac{l}{\sin(\alpha_2)} = \frac{t}{\sin(\theta_s')}. \quad (9.22a)$$

As shown in Figure 9.14, all angles in this system of triangles can be calculated using the pixel viewing angle ( $\alpha_0$ ), the slope of the terrain ( $\theta_s$ ), and/or  $\theta_s'$  ( $= 90 - \theta_s$ ), so that

$$l = \sin(\alpha_2) \frac{m}{\sin(\alpha_3)}. \quad (9.22b)$$

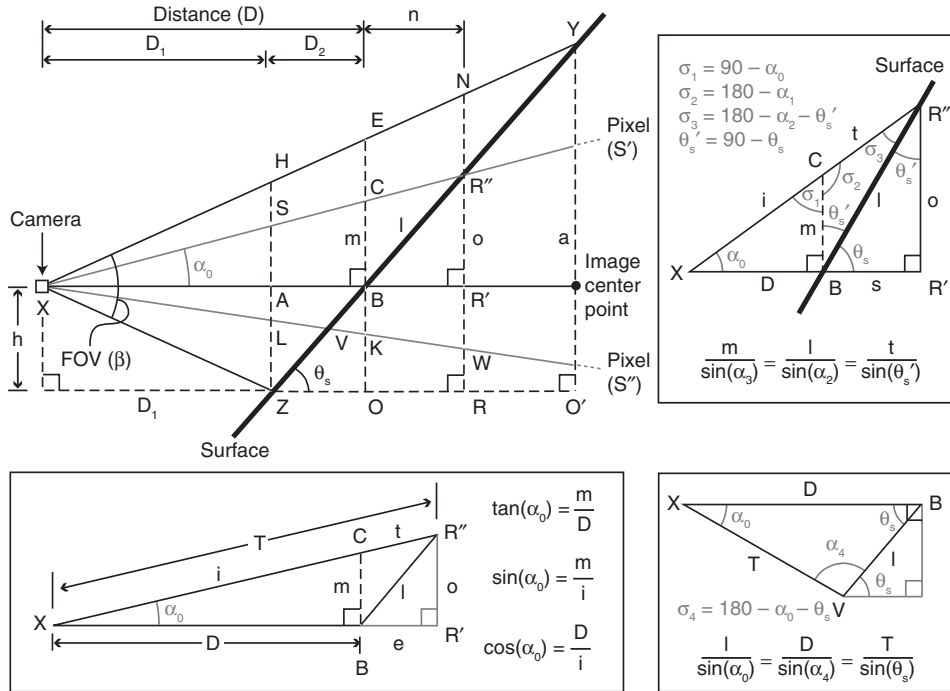


Figure 9.14 Trigonometry to calculate pixel dimensions for pixels in an image where the camera is pointed horizontally onto a surface sloping away from the camera. Inset bottom left and top right are the triangles and relations needed to constrain the viewing geometry for pixels in the upper half of the image. Inset bottom right are the triangles and relations needed to constrain the viewing geometry for pixels in the lower half of the image. Lower case letters give line lengths, upper-case identify triangles.

To obtain the line-of-sight distance from the camera to the pixel center, we need to add the distance between the camera and the center of the vertical plane (distance  $i$ , Figure 9.14) to the distance between the vertical plane and the actual ground surface (distance  $t$ , Figure 9.14). Distance  $i$  can be obtained using  $m$  and  $\alpha_0$  in the relation

$$i = \frac{m}{\sin(\alpha_0)} \quad (9.23a)$$

and  $t$  from

$$t = \sin(\theta_s') \frac{m}{\sin(\alpha_3)}. \quad (9.23b)$$

Now, the range to our pixel on the sloping terrain is

$$\text{Range} = T = i + t. \quad (9.23c)$$

For terrains with a slope of  $35^\circ$  (sloping away from the camera mid-point) the distance to the center of our pixel located ten pixels from the top of the image (at pixel angle,  $\alpha_0$ , of  $8.25^\circ$ ) we have, for an image mid-point located 250 m from the camera,

$$m = (250 \text{ m}) [\tan (0.144)] = 36.25 \text{ m}$$

so that

$$i = (36.25 \text{ m}) / [\sin (0.144)] = 252.61 \text{ m}.$$

Now, angle  $\alpha_1$  in triangle XCB of [Figure 9.14](#) is,

$$\alpha_1 = 180^\circ - 90^\circ - \alpha_0 = 90^\circ - 8.25^\circ = 81.75^\circ$$

so that the angles in triangle BCR" are

$$\alpha_2 = 180^\circ - \alpha_1 = 180^\circ - 81.75^\circ = 98.25^\circ$$

$$\theta_s' = 90^\circ - \theta_s = 90^\circ - 35^\circ = 55^\circ$$

and

$$\alpha_3 = 180^\circ - \alpha_2 - \theta_s' = 180^\circ - 98.25^\circ - 55^\circ = 26.75^\circ.$$

Now,

$$t = \sin (0.96) \frac{36.25}{\sin (0.467)} = 65.97 \text{ m},$$

so that

$$\text{Range} = T = i + t = 252.61 \text{ m} + 65.97 \text{ m} = 318.58 \text{ m}$$

and

$$l = \sin(1.715) \frac{36.25}{\sin(0.467)} = 79.70 \text{ m}.$$

To estimate the pixel dimension, we can use the angle to the pixel lower edge ( $\alpha_L$ ), where

$$\alpha_L = \alpha_0 - (\beta_{\text{IFOV}}/2). \quad (9.24a)$$

We now substitute  $\alpha_0$  in Equations [\(9.21\)](#) and [\(9.22\)](#) with  $\alpha_L$  to estimate the slant line distance between the FOV center and the lower edge of pixel  $n$  [ $x(n)_L$ ]. Next, we estimate the angle to the pixel upper edge ( $\alpha_U$ )

$$\alpha_U = \alpha_0 + (\beta_{\text{IFOV}}/2). \quad (9.24b)$$

Likewise, we now substitute  $\alpha_0$  in Equations [\(9.21\)](#) and [\(9.22\)](#) with  $\alpha_U$  to estimate the slant line distance between the FOV center and the upper edge of pixel  $n$  [ $x(n)_U$ ]. Now the pixel dimension projected onto the sloping terrain can be calculated from

$$L_p = x(n)_U - x(n)_L. \quad (9.24c)$$

Thus, for our pixel at angle  $8.25^\circ$  above the image center and with an IFOV of 1.3 mrad, we have,

$$\alpha_L = (0.1440 \text{ rad}) - (0.0013/2 \text{ rad}) = 0.1433 \text{ rad}$$

and

$$\alpha_U = (0.1440 \text{ rad}) + (0.0013/2 \text{ rad}) = 0.1446 \text{ rad.}$$

For the lower edge of this pixel we have

$$m = (250 \text{ m}) [\tan(0.1433)] = 36.082 \text{ m.}$$

Now, using

$$\alpha_1 = 90^\circ - \alpha_L = 1.5708 \text{ rad} - 0.1433 \text{ rad} = 1.4275 \text{ rad}$$

$$\alpha_2 = 180^\circ - \alpha_1 = 3.1416 \text{ rad} - 1.4275 \text{ rad} = 1.7141 \text{ rad}$$

and

$$\alpha_3 = 90^\circ - \alpha_L - \theta_s' = 1.5708 \text{ rad} - 0.1433 \text{ rad} - 0.9599 \text{ rad} = 0.4676 \text{ rad}$$

we obtain

$$x(n)_L = \sin(1.7141) \frac{36.082}{\sin(0.4676)} = 79.23 \text{ m.}$$

For the pixel upper edge we have,

$$m = (250 \text{ m}) [\tan(0.1446)] = 36.414 \text{ m.}$$

Next, using

$$\alpha_1 = 90^\circ - \alpha_U = 1.5708 \text{ rad} - 0.1446 \text{ rad} = 1.4262 \text{ rad}$$

$$\alpha_2 = 180^\circ - \alpha_1 = 3.1416 \text{ rad} - 1.4262 \text{ rad} = 1.7154 \text{ rad}$$

and

$$\alpha_3 = 90^\circ - \alpha_U - \theta_s' = 1.5708 \text{ rad} - 0.1446 \text{ rad} - 0.9599 \text{ rad} = 0.4663 \text{ rad}$$

we obtain

$$x(n)_U = \sin(1.7154) \frac{36.414}{\sin(0.4663)} = 80.15 \text{ m}$$

so that the pixel dimension is

$$L_p = x(n)_U - x(n)_L = 80.15 \text{ m} - 79.23 \text{ m} = 0.92 \text{ m.}$$

**(b) Pixels between the FOV center point and lower edge** Below the center point the slope of the terrain will cause the range to each pixel to decrease as we move towards the FOV base, so that the pixel dimension becomes smaller with distance from the center point. For this case, the geometry is more simple so that the range ( $T$ ) can be obtained from (Figure 9.14),

$$T = \sin(\theta_s) \frac{D}{\sin(\alpha_4)}, \quad (9.25)$$

in which

$$\alpha_4 = 180^\circ - \alpha_0 - \theta_s.$$

Now, the ground distance between the pixel at angle  $\alpha_0$  and the image center point is

$$l = \sin(\alpha_0) \frac{D}{\sin(\alpha_4)}. \quad (9.26)$$

Thus, given ground sloping at an angle of  $35^\circ$  towards the camera, for a pixel at the base of the image (i.e., at pixel 120, angle  $90^\circ$ ), we have

$$\theta_s = 35^\circ = 0.6109 \text{ rad}$$

and

$$\alpha_4 = 180^\circ - 90^\circ - 35^\circ = 136^\circ = 2.374 \text{ rad}$$

so that the range is

$$T = \sin(0.6109) \frac{250 \text{ m}}{\sin(2.374)} = 206.42 \text{ m.}$$

Now, using the angle to the pixel lower edge ( $\alpha_L$ ) instead of  $\alpha_0$ , we can estimate the pixel dimension as before. For this case we have, to the pixel lower edge,

$$\alpha_L = (0.1571 \text{ rad}) - (0.0013/2 \text{ rad}) = 0.1564 \text{ rad}$$

so that

$$\alpha_4 = 3.1416 \text{ rad} - 0.1564 \text{ rad} - 0.6109 \text{ rad} = 2.3743 \text{ rad}$$

and

$$x(n)_L = \sin(0.1564) \frac{250 \text{ m}}{\sin(2.3743)} = 56.106 \text{ m.}$$

For the pixel upper ( $\alpha_U$ ) edge we have,

$$\alpha_U = (0.1571 \text{ rad}) + (0.0013/2 \text{ rad}) = 0.1577 \text{ rad}$$

so that

$$\alpha_4 = 3.1416 \text{ rad} - 0.1577 \text{ rad} - 0.6109 \text{ rad} = 2.3730 \text{ rad}$$

and

$$x(n)_U = \sin(0.1577) \frac{250 \text{ m}}{\sin(2.3730)} = 56.492 \text{ m.}$$

This gives a pixel dimension of

$$L_p = x(n)_L - x(n)_U = 56.106 \text{ m} - 56.492 \text{ m} = 0.386 \text{ m.}$$

Using the [Figure 9.14](#) geometry (i.e., a terrain that is sloping away from all points above the image center point, and towards all points below the image center point) we thus have a range that decreases from the image top to the image base, as plotted in [Figure 9.15a](#). Consequently the pixel dimension also decreases from the image top to the image base, as plotted in [Figure 9.15b](#).

#### 9.4.4 Complex viewing geometries

To complicate matters further, we can have both an oblique viewing geometry and a sloping surface, as in [Figure 9.6b](#). Worse still, natural (especially lava) surfaces usually have highly irregular topographies, slopes changing over spatial scales of a meter or so, so that the viewing geometry and incidence angle will change from pixel-to-pixel. In this case the ground slope and geometry used will have to be changed on a pixel-by-pixel basis. A number of solutions are available to correct for such complex viewing geometry and topographic combinations.

One solution is to geometrically correct the image by fitting the slave (the image) to a master ground-control image, such as a Digital Elevation Model (DEM) for the imaged area. This can be done using standard image processing software. Because the ground-based views can be quite oblique, this is a little more complicated than geo-rectification of satellite images. Very oblique views from the ground-based vantage point can, for example, cause great variation in the pixel size across the image. It will also introduce foreshortening and shadowing effects, i.e., some objects will be hidden by higher objects in front of them, and the reverse slope may not be visible. James *et al.* (2006) provided a photo-grammetric solution for such a situation that involves fitting the obliquely acquired image of a topographically uneven thermal surface to a digital elevation model of the same surface. In their

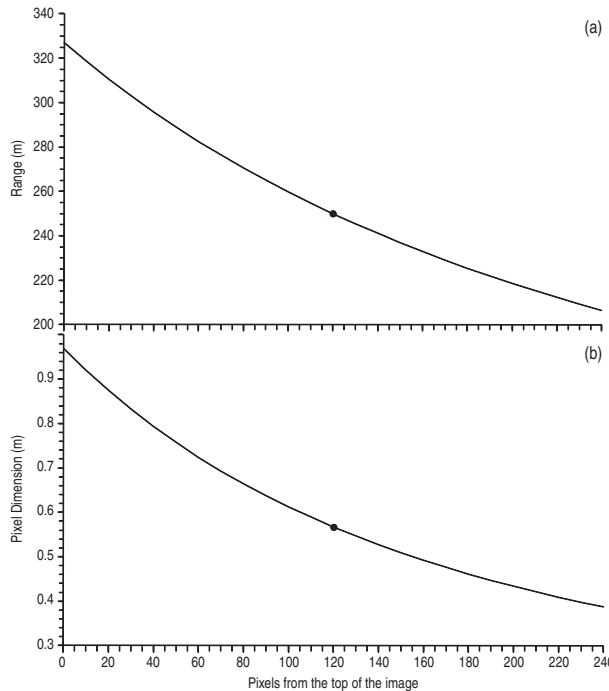


Figure 9.15 Decrease in (a) range to the pixel, and (b) pixel diameter, from the top to bottom of an image acquired for a surface that is sloping away from the camera: point marks image center point. Image is 240 pixels high, with pixel zero being at the top of the image. Pixel IFOV is  $0.0745^\circ$  (1.3 mrad), horizontal distance to image center is 250 m and ground slope is  $35^\circ$ .

case the surface was an active lava flow, imaged from a position slightly higher than the location of the flow front.

Formenti *et al.* (2003) provide, in an Appendix to their paper, the geometric transformations required for a situation where the camera is staring upward at a vertically orientated feature, i.e., the situation sketched in Figure 9.6c. The methodology can equally well be applied to a downward looking view of a vertically-orientated feature. Applying the same geometrical principles as considered above, the method of Formenti *et al.* (2003) allows transformation of the  $x$ ,  $y$  and  $z$  coordinates of the image plane (plane AA-AA' in Figure 9.6c) to the real coordinates of a targeted surface orientated at angle  $\theta_d$  from the image plane (plane BB-BB' in Figure 9.6c). The transformation allows the calculation of the true  $y$ -coordinate ( $y_b$ ) for a point using the  $y$ -coordinate of the same point in the image ( $y_a$ ) following:

$$y_b = \frac{y_a L \tan(\theta_h)}{X \cos(\theta_v + \psi) - y_a \tan(\theta_h) \sin(\theta_v + \psi)}, \quad (9.27a)$$

in which

- $L$  = distance between the camera and the base of the FOV (m);
- $\theta_h$  = half the angular FOV in the horizontal dimension (i.e.,  $\beta_H/2$ );
- $\theta_v$  = half the angular FOV in the vertical dimension (i.e.,  $\beta_V/2$ );
- $X$  = half the width of the projected image on the read-out monitor (m); and
- $\Psi$  = angle between the line-of-sight and horizontal (see [Figure 9.6c](#)).

Now, the true  $x$ -coordinate ( $x_b$ ) can be obtained from the image  $x$ -coordinate ( $x_a$ ) following:

$$x_b = \frac{x_a L \tan(\theta_h)}{X \cos(\theta_v + \psi) - y_a \tan(\theta_h) \sin(\theta_v + \psi)}. \quad (9.27b)$$

Finally the true  $z$ -coordinate (i.e., line-of-sight distance),  $z_b$ , can be obtained using

$$z_b = \frac{y_a L \tan(\theta_h) \tan(\theta_v + \phi)}{X \cos(\theta_v + \psi) - y_a \tan(\theta_h) \sin(\theta_v + \psi)}. \quad (9.27c)$$

This solution is useful for dynamic features ascending vertically through an upward- or downward-looking FOV, as may be the case when imaging ash and ballistic plumes.

Both the James *et al.* (2006) and Formenti *et al.* (2003) solutions require exacting geometric control and/or the availability of a simultaneously derived DEM, which may not be available or possible to collect. The Formenti *et al.* (2003) solution, for example, requires precise viewing angles and distances to the imaged surface to be measured during image acquisition. In addition, with an active lava flow, the DEM will be out-of-date as quickly as the lava flow moves, so that a DEM has to be made for each image. James *et al.* (2006) achieved a solution by running a tripod-based LIDAR next to the thermal camera. Probably the most simple solution is to ensure that the camera is set up such that the observed surface is at an angle which is approximately at right angles to the FPA, or at least set at an angle that allows the simple geometrical corrections considered here for downward- and upward-looking views to be applied.

#### 9.4.5 Accuracy of temperature retrieval

The manufacturer-published temperature measurement accuracy for most thermal cameras reviewed in [Table 9.1](#) is  $\pm 2^\circ\text{C}$  or  $\pm 2\%$  of the reading, whichever is greater. This means that the absolute accuracy of the temperature measurement will decrease with increased temperature. Accuracy being:

- $\pm 2^\circ\text{C}$  at  $100^\circ\text{C}$
- $\pm 5^\circ\text{C}$  at  $250^\circ\text{C}$
- $\pm 10^\circ\text{C}$  at  $500^\circ\text{C}$
- $\pm 15^\circ\text{C}$  at  $750^\circ\text{C}$

- $\pm 20$  °C at 1000 °C
- $\pm 24$  °C at 1200 °C.

Ball and Pinkerton (2006) tested the accuracy of a ThermaCam™ S40 thermal camera when targeting surfaces at high temperatures, finding that the camera measured 2 °C higher than the target temperature at 855 °C. This is well within the  $\pm 2\%$  range specified by the manufacturer, where an accuracy of  $\pm 17$  °C is expected at this temperature. Noise levels measured by Ball and Pinkerton (2006) were  $\pm 0.4$  °C, and there were some pixel-to-pixel differences, with hot surfaces at 845 °C and 1035 °C undergoing variation by up to  $\pm 0.8\%$  (but typically less than 0.6%) depending on which detector in the FPA was used. Thus confidence in the measurement at 1000 °C is around  $\pm 8$  °C, increasing to  $\pm 4$  °C at 500 °C and  $\pm 2$  °C at 250 °C.

#### **9.4.6 Atmospheric effects and corrections**

Thermal data collected in the SWIR, MIR and TIR will be subject to the same atmospheric and emissivity conditions as described in Chapter 2 for satellite-based observations. The difference is, the atmospheric path length for a thermal camera measurement will likely be horizontal, or at best oblique, rather than vertical (as is the case for a satellite-based measurement), and the camera will be located within the atmosphere, rather than above the top of it.

As with the satellite-based sensor, measurements of high-temperature targets in the TIR will mostly be affected by atmospheric absorption (as described by the transmissivity of the atmosphere,  $\tau$ ). Atmospheric up-welling radiance ( $R_U$ ), will also contaminate the signal (see Section 2.3 of Chapter 2). Because we may be viewing along a horizontal line-of-sight, these effects will be more problematic than with a satellite-based observation, especially over long path lengths. The problem is, with a thermal camera measurement made horizontally, the atmospheric properties will be the same along the entire path length, that is the atmosphere will remain equally “thick” over the entire path length. For the satellite-based case, where the view is vertical to near-vertical the atmosphere will thin upwards, so that the absorption for a 5 km line-of-sight looking vertically downwards will be less than for a 5 km line-of-sight looking horizontally. Take a horizontal line-of-sight distance of 5 km at sea-level compared to one at 3 km. At sea-level, the transmissivity will be 0.52, so that almost half of the signal is absorbed; at 3 km  $\tau$  is 0.78, so that 22% of the signal is absorbed. If we look vertically downwards onto these two surfaces from a height of 5 km above them, transmissivity is 0.7 for the sea-level case, i.e., only 30% of the signal is absorbed, declining to 0.85 for the 3 km case, i.e., only 15% of the signal is absorbed. Thus, atmospheric effects will be a significant source of error to the temperature measurement using a thermal camera over long lines-of-sight, and must be removed if we are to measure actual surface temperature. The high values for transmissivity encountered along the horizontal path length are not helped by the fact that the broad-band covered by the thermal camera begins to stray into the water vapor window that spans 4.13–8.6 μm (see Chapter 2).

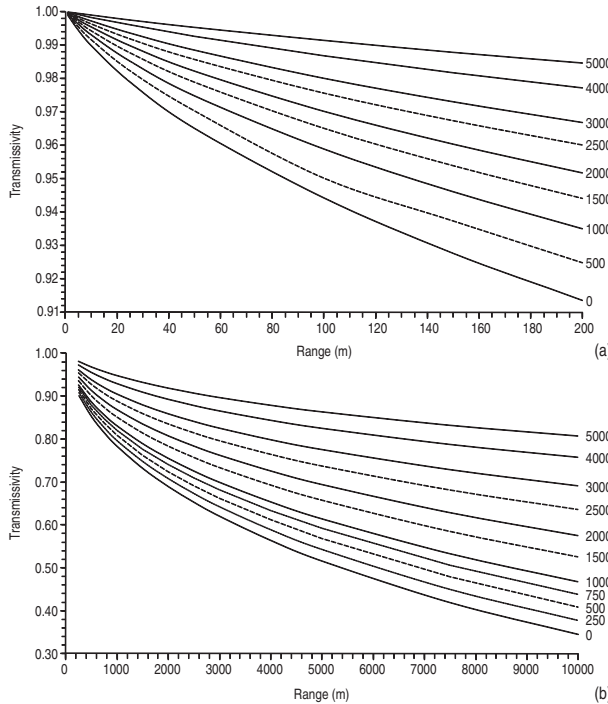


Figure 9.16 Increase in atmospheric transmissivity over a horizontal line-of-sight for a measurement at a range of altitudes between 0 m and 5000 m for (a) a short line of sight (range 0 m to 200 m), and (b) greater distances (out to 10 km) (line labels are in meters). Values were obtained using MODTRAN with 1976 US Standard atmosphere and a CO<sub>2</sub> mixing ratio of 380 ppm·v across the 7.5 μm to 13 μm waveband (see Electronic Supplement 4 for definition of MODTRAN).

#### 9.4.6.1 Absorption and transmissivity along a horizontal path length

For a horizontal path length at any given altitude, atmospheric absorption will increase with path length, as shown in Figure 9.16a for near-field measurements, and in Figure 9.16b for the far field. The increased atmospheric thickness encountered at longer horizontal path lengths will mean that the amount of absorption increases with range, so that transmissivity decreases with path length. For example, absorption for a worst (sea-level) case scenario is 6% over a range of 100 m (i.e.,  $\tau = 0.94$ ) increasing to 65% ( $\tau = 0.35$ ) over a range of 10 km. Owing to the thinner atmosphere at higher elevations, the degree of absorption decreases with altitude. For any given path length absorption effects are thus less strongly felt at higher altitudes. Take the 200 m line-of-sight of Figure 9.16a, for example. While at sea-level 19% of the signal will be absorbed ( $\tau = 0.91$ ), the thinner atmosphere at 3000 m above sea-level means that only 3% of the signal is absorbed ( $\tau = 0.97$ ) over the same horizontal line-of-sight.

The advantage of the thermal camera is that we can minimize atmospheric effects by getting as close as possible to the target. As we can see from Figure 9.16a, for

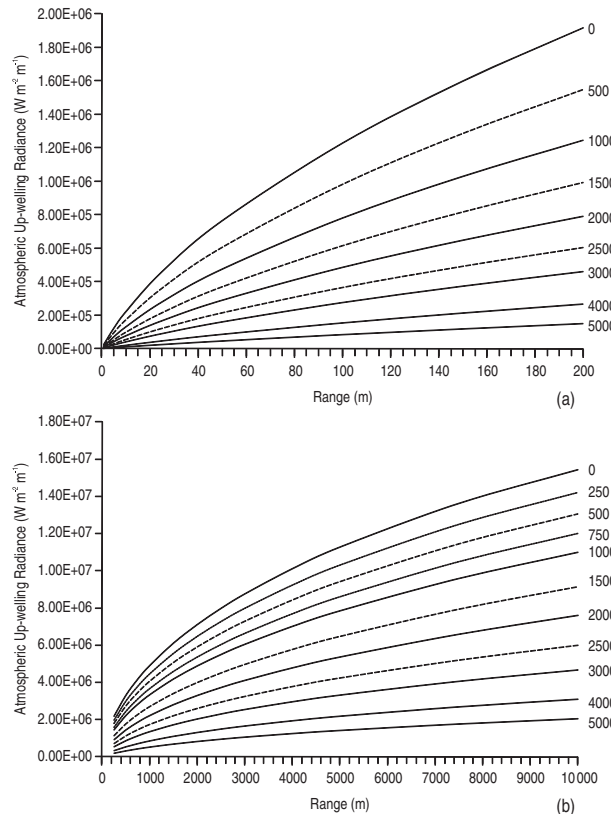


Figure 9.17 Increase in atmospheric up-welling radiance over a horizontal line of sight for a measurement at a range of altitudes between 0 m and 5000 m for (a) a short line of sight (range 0 m to 200 m), and (b) greater distances (out to 10 km) (line labels are in meters). Values were obtained using MODTRAN with 1976 US Standard atmosphere and a  $\text{CO}_2$  mixing ratio of 380  $\text{ppm}\cdot\text{v}$  across the 7.5  $\mu\text{m}$  to 13  $\mu\text{m}$  waveband (see Electronic Supplement 4 for definition of MODTRAN).

close-up viewing, absorption is minimized. Even at sea-level, less than 1% of the signal will be absorbed if we place the camera within 10 m of the target ( $\tau$  being greater than 0.99 for all elevation cases). However, by a range of 200 m absorption has increased to 5% for measurements made at or below an altitude of 2000 m, i.e.,  $\tau$  has dropped to 0.95. Thereafter, absorption increases with camera-to-target distance to a maximum of 65% (i.e.,  $\tau = 0.35$ ) for a measurement at sea-level over a range of 10 km (Figure 9.16b).

#### 9.4.6.2 Up-welling radiance along a horizontal path length

Likewise, the contribution of atmospheric up-welling radiance to the at-sensor measurement will increase with path length and decrease with altitude, as plotted in Figure 9.17. However, as explained in Chapter 2, the relative contribution of the up-welling component will

decrease with target temperature. For a blackbody, we can approximate the at-sensor radiance ( $R_{\text{in}}^*$ ) in the TIR (from [Chapter 2](#)) as

$$R_{\text{in}}^* = \tau(\lambda) L_S(\lambda) + L_U(\lambda) \quad (9.28)$$

in which

- $\tau(\lambda)$  is the atmospheric transmissivity,
- $L_S(\lambda)$  is the spectral radiance emitted by the surface, and
- $L_U(\lambda)$  is the spectral radiance emitted by (i.e., up-welling from) the atmosphere.

Thus, the contribution of the up-welling component can be assessed from

$$\text{Contribution } L_U(\lambda) = L_U(\lambda) / R_{\text{in}}^*. \quad (9.29)$$

If we plot the contribution of  $L_U(\lambda)$  for a worst case (sea-level) scenario, as done in [Figure 9.18a,b](#), we see that the contribution increases with range. That is, as the atmospheric column becomes longer, so more spectral radiance is emitted by that column. However, the relative contribution of the atmosphere to the at-sensor radiance decreases as the temperature of the target increases. At a range of 200 m, for example, the 7.5–13  $\mu\text{m}$  spectral radiance emitted by a target at 25 °C is  $30.1 \times 10^6 \text{ W m}^{-2} \text{ m}^{-1}$ , while that emitted by the atmosphere is  $1.92 \times 10^6 \text{ W m}^{-2} \text{ m}^{-1}$ ; thus the atmospheric up-welling radiance contributes 9.7% of the total at-sensor radiance. However, if the target temperature increases to 500 °C, although the spectral radiance emitted by the surface increases to  $642 \times 10^6 \text{ W m}^{-2} \text{ m}^{-1}$ , the atmospheric contribution remains  $1.92 \times 10^6 \text{ W m}^{-2} \text{ m}^{-1}$ ; thus the up-welling contribution to the total is now just 0.08%. From [Figure 9.18a](#) we see that, at ranges of less than 200 m, for surfaces >100 °C, upwelling radiance will contribute less than 2% to the signal, and typically much less than 1%. The problem becomes worse with path length. We see from [Figure 9.18b](#) that, by the time we reach a range of 2 km, upwelling contributes at least 10% of the at-sensor radiance for surfaces at temperatures of around 100 °C. By a range of 5 km, 3% of the at-sensor radiance for a surface at 500 °C comprises up-welling radiance. While the up-welling contribution to the 100 °C source at 2 km increases the brightness temperature to 109 °C, that for the 500 °C source at 5 km increase the brightness temperature to 506 °C. With thinner atmospheres at higher altitudes, the absolute and relative contributions of the upwelling component diminishes. We see from [Figure 9.18c](#) that, by the time we reach an altitude of 3000 m, over ranges of less than 200 m, the upwelling contribution is typically less than 1% at all temperatures, and less than 0.1% for surfaces at >150 °C. The effect over greater ranges is plotted in [Figure 9.18d](#), where we see that the upwelling contribution is less than 10% for all surfaces at temperatures >75 °C, and typically less than 5% for surfaces >150 °C.

#### 9.4.6.3 Error

Because of increasingly severe absorption effects along a horizontal path length, recorded brightness temperatures quickly become under-estimates of the actual surface temperature

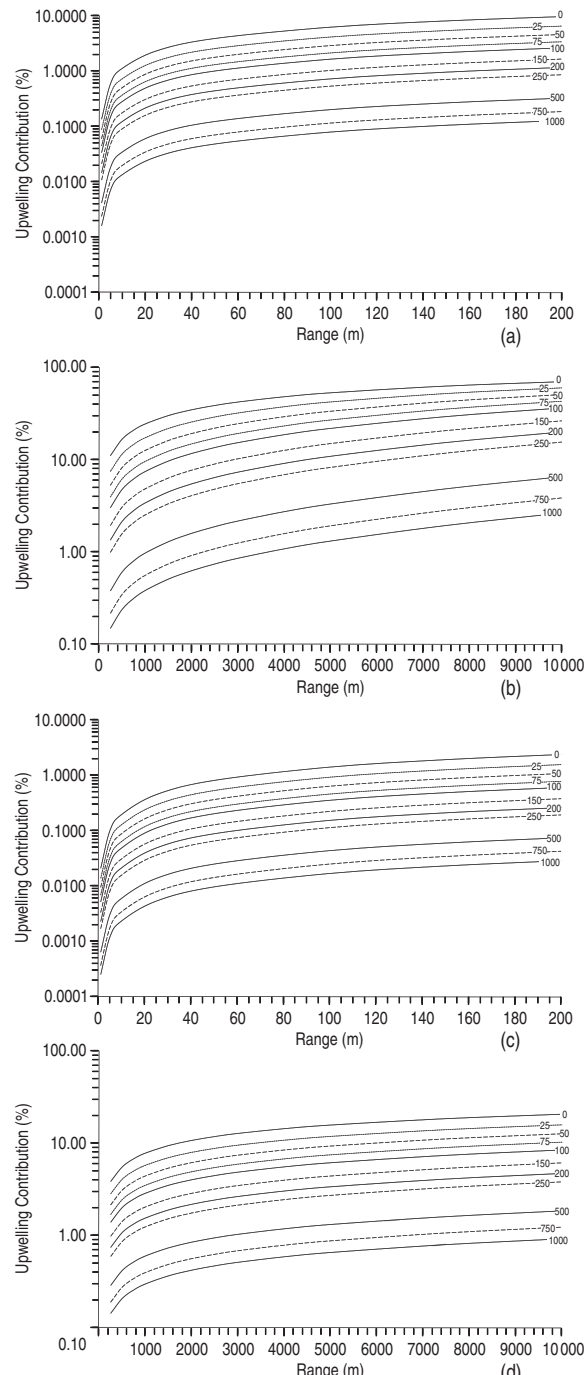


Figure 9.18 Percent contribution of up-welling radiance to the at-sensor radiance for surfaces emitting at temperatures of 0 °C to 1000 °C over horizontal paths with ranges of (a) 0 m to 200 m and (b) 0 m to 10 km at sea-level (line labels are in °C). (c) and (d) give the same relations, but for an elevation of 3000 m (atmospheric model is that of Figure 9.17).

as the distance to the target increases. We plot this effect, for surfaces at sea-level, in [Figure 9.19a](#). We see that, for ranges of less than 5 m, the error due to atmospheric effects is less than 1 °C for surfaces at temperatures less than 250 °C. However, the error for surfaces at 500 °C, 750 °C and 1000 °C is already 2 °C, 3 °C and 4 °C, respectively. That is, the recorded brightness temperature is up to 4 °C less than the actual surface temperature. The error then increases with range, more rapidly so for high-temperature surfaces, so that, by the time we reach a range of 200 m, errors for surfaces at 25 °C to 50 °C are between 1 °C and 5 °C, and for surfaces at 1000 °C errors are up to 66 °C. As plotted in [Figure 9.19b](#), the error continues to increase through 5 km, by which point the errors for surfaces at 25 °C to 50 °C are between 7 °C and 27 °C, and 384 °C for surfaces at 1000 °C. Owing to reduced absorption at higher altitudes, errors are reduced for measurements at higher elevations, as plotted in [Figure 9.19c](#). However, although errors in the near range are reduced, over the range of 200 m at 3000 m above sea-level, errors for surfaces at 25 °C to 50 °C are still between 1 °C and 2 °C. For surfaces at 1000 °C errors are up to 25 °C. For more distant measurements, as plotted in [Figure 9.19b](#), errors for the 5 km range are still up to 7 °C for surfaces at 25 °C and 15 °C for surfaces 50 °C, increasing to 174 °C for surfaces at 1000 °C.

Thus absorption of the signal by the atmosphere along horizontal or oblique paths can result in measured brightness temperatures that can be up to 530 °C less than the actual surface temperature (for a 1000 °C surface imaged at sea-level along a 10 km horizontal path). Error increases with decreased altitude, increased range and/or increased target temperature. Thus, atmospheric correction is essential to obtain reliable surface temperature measurements over ranges greater than 10 m. Even over a 10 m line-of-sight, higher-temperature (500 °C to 1000 °C) surfaces may be in error by up to 4 °C.

#### 9.4.6.4 On-board corrections

Some cameras allow on-board correction of recorded pixel-integrated spectral radiance for atmospheric and emissivity effects. FLIR Systems ([2003](#)) describes the correction routine that they apply as follows. The total spectral radiation received by the detector is composed of radiance emitted and reflected by the surface, plus radiance emitted by the atmosphere between the target and the camera. Thus, following [Chapter 2](#) (see [Section 2.3.2](#)), the total spectral radiation received by the detector ( $R_{\text{in}}^*$ ) can be written

$$R_{\text{in}}^* = [\varepsilon(\lambda)\tau(\lambda) L_S(\lambda)] + L_R(\lambda) + L_U(\lambda) \quad (9.30)$$

in which

- $\varepsilon(\lambda)$  is the emissivity of the surface averaged across the camera waveband,
- $\tau(\lambda)$  is the atmospheric transmissivity for altitude  $z$  and path length  $y$
- $L_S(\lambda)$  is the spectral radiance emitted by the surface itself,
- $L_R(\lambda)$  is the spectral radiance reflected by the surface, and
- $L_U(\lambda)$  is the spectral radiance emitted by (i.e., up-welling from) the atmosphere.

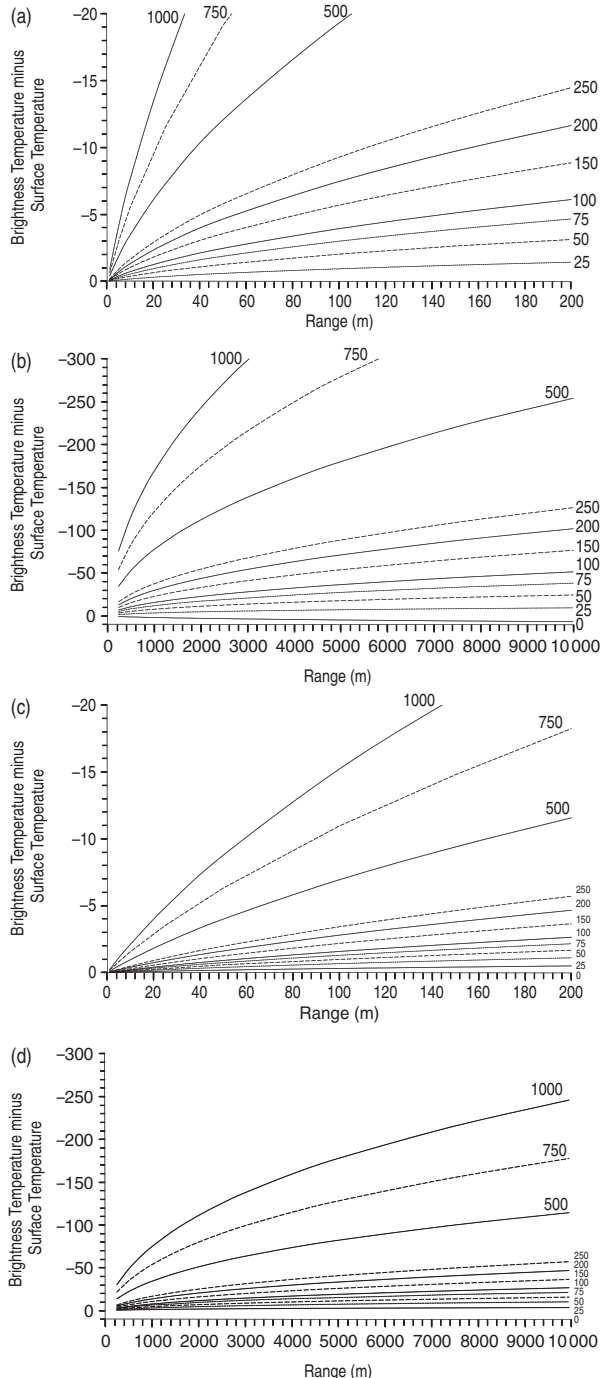


Figure 9.19 Difference between sensor-recorded brightness temperature and surface temperature for surfaces emitting at temperatures of  $0\text{ }^{\circ}\text{C}$  to  $1000\text{ }^{\circ}\text{C}$  over horizontal paths with ranges of (a)  $0\text{ m}$  to  $200\text{ m}$  and (b)  $0\text{ m}$  to  $10\text{ km}$  at sea-level (line labels are in  $^{\circ}\text{C}$ ). Note, the effect of increased absorption outweighs the effect of increased atmospheric contribution, so that the difference is negative (i.e., brightness temperature is less than actual surface temperature). Parts (c) and (d) give the same relations, but for an elevation of  $3000\text{ m}$  (atmospheric model is that of Figures 9.16 and 9.17).

Hence, to isolate the measurement that we want ( $L_S(\lambda)$ ) we must estimate and remove the unwanted parameters. FLIR Systems (2003) do this by re-arranging Equation (9.30) so that,

$$L_S(\lambda) = \frac{R_{\text{in}}^* - L_R(\lambda) - L_U(\lambda)}{\varepsilon(\lambda)\tau(\lambda)}. \quad (9.31)$$

The camera software solves this equation (i.e., completes the correction) by using an operator-input emissivity, and software-based estimates for  $\tau(\lambda)$ ,  $L_R(\lambda)$  and  $L_U(\lambda)$ . These estimates are achieved using a MODTRAN-based estimate for range-dependent atmospheric effects and user-input measurements of:

- (1) the distance between the camera and the target,
- (2) relative humidity, and
- (3) the temperature of the atmosphere.

#### *9.4.6.5 Corrections that vary with range and altitude*

Ball and Pinkerton (2006) warn that on-board corrections use a range (distance between the camera and the target) that is uniform across the image. Thus, for images where there is variation in range, the correction will be in error for locations further from, or closer to, the camera than the input range. Take, for example, a situation where the camera is placed at an altitude of 1000 m to view a lava flow that is moving down a 12° slope. The camera is placed 250 m in front of the lava flow front, so that the flow front is viewed over a line-of-sight of 250 m. However, the upper section of the lava flow, which in our demonstrative case will be at a horizontal distance of 2.35 km behind the flow front, is 500 m higher than the flow front. It will thus be viewed over an upward pointing line-of-sight with an elevation angle of 11.1° and range of 2650 m. If we set the atmospheric correction for the flow front range of 250 m and altitude of 1000 m we obtain, from Figure 9.16b, a transmissivity of 0.925. This is now applied by the camera to the flow front pixels, as well as all other pixels across the image. However, the range to the lava in the upper portion of the image is ~2.5 km. Figure 9.16b shows that a surface viewed over a range of 2.5 km will experience a transmissivity of 0.725, if at an altitude of 1000 m. However, surfaces in the upper portion of the image are also ~500 m higher than those in the foreground, placing them at an altitude of 1500 m so that the transmissivity at the source is 0.757 (see Figure 9.16b). The median transmissivity for the camera and upper image locations (which approximates the transmissivity of the atmosphere between the two points) is 0.741. Now, whereas the brightness temperature for a surface at 250 °C and experiencing the short path transmissivity for this case ( $\tau = 0.925$ ) will be 236 °C, that for the 250 °C surface experiencing the long path transmissivity ( $\tau = 0.741$ ) will be 200 °C. Of course, if we correct the radiance equivalent of the 236 °C brightness temperature for the short path transmissivity, we will retrieve the surface temperature (i.e., 250 °C). However, applying the same correction to the 200 °C pixel yields a temperature of 212 °C, causing an under-estimate by ~40 °C. Thus, the single-range atmospheric correction does not, in this case, work for the more distant points.

Owing to the large variation in transmissivity and up-welling radiance with range, using a correction fixed for a single range will yield large errors. At sea-level, even moving the camera from a location 10 m from the surface to one 25 m from the surface will decrease the transmissivity from 0.99 to 0.98 (see [Table 9.4](#)). We see from the same table that the atmospheric correction should also be set for the appropriate pixel altitude. So a correction set for sea-level, for example, will over-correct a measurement made at an altitude of 500 m, and one set for an altitude of 500 m will under-correct the sea-level brightness temperature. Thus, for cases where the range varies over more than a few tens of meters, or altitudes over a few hundred meters, atmospheric corrections should be executed on a pixel-by-pixel basis using the appropriate range to (and altitude difference between) the camera and the pixel.

Thus the most effective atmospheric correction for an obliquely viewed volcanic surface is

$$L_S(\lambda) = [R_{in}^*(x, y, z) / \tau(\lambda, z, a)] - L_U(\lambda, z, a), \quad (9.32)$$

in which

- $R_{in}^*(x, y, z)$  is the uncorrected radiance for the pixel at image location  $x, y$ , and range  $z$ ,
- $\tau(\lambda, z, a)$  is the atmospheric transmissivity for the pixel at range  $z$  with a characteristic path altitude  $a$ , where  $a$  can be approximated from the elevation of the camera plus the elevation of the targeted surface divided by 2, and
- $L_U(\lambda, z, a)$  is the atmospheric up-welling radiance for the pixel at range  $z$  with characteristic altitude  $a$ .

Given the  $x, y, z$  location of the pixel, the geometries already discussed allow us to estimate the range to all points, as well as the difference in altitude between the measurement point and the camera ( $h'$ ). For example, the difference in height between the camera point and the observed point can, for a camera pointed upwards to view a surface that is at a higher elevation than the camera, be calculated from

$$h' = \text{Range} \sin(\alpha_0) \quad (9.33)$$

in which Range is the slant line distance to the pixel and  $\alpha_0$  is the angle to the pixel. Adding this to the camera altitude gives the altitude of points in the image, so that

$$\text{Pixel altitude} = \text{camera altitude} + h'. \quad (9.34)$$

[Table 9.4](#) then provides values for transmissivity and atmospheric up-welling over a range of distances (from 1 m to 10 km) and altitudes (from sea-level to 5000 m) for a MODTRAN US-Standard (1976, rural-summer, visibility = 23 km) atmosphere. These potentially serve as look-up tables for such range- and altitude-based corrections to thermal camera data collected in the 7.5–13  $\mu\text{m}$  range, and are the values plotted in [Figures 9.16](#) and 9.17.

#### 9.4.6.6 Emissivity correction

Because lava is not a blackbody, spectral radiances need to be corrected for emissivity to extract surface temperature (see [Chapter 2](#)). Emissivities for the wavebands at which the

Table 9.4. Atmospheric properties between  $7.5 \mu\text{m}$  and  $13 \mu\text{m}$  for horizontal line-of-sight distances of 1 m to 10 km and altitudes ranging from sea-level to 5000 m. To obtain these values MODTRAN was run for a 1976 US Standard atmosphere (rural, visibility = 23 km) with a horizontal path length from the observation point to a target point at the same altitude. Modeling used a  $\text{CO}_2$  mixing ratio of 380  $\text{ppm}\cdot\text{v}$

(A) TRANSMISSIVITES OVER SHORT RANGES (1 M TO 200 M)

Altitude (m): Range (m)	0	250	500	750	1000	1500	2000	2500	3000	4000	5000
1	0.9988	0.9989	0.9990	0.9991	0.9992	0.9994	0.9995	0.9996	0.9997	0.9998	0.9999
5	0.9944	0.9949	0.9954	0.9959	0.9963	0.9970	0.9975	0.9981	0.9985	0.9991	0.9995
10	0.9898	0.9907	0.9916	0.9924	0.9931	0.9943	0.9954	0.9964	0.9972	0.9983	0.9990
25	0.9789	0.9806	0.9823	0.9838	0.9852	0.9877	0.9898	0.9919	0.9936	0.9960	0.9975
50	0.9650	0.9678	0.9703	0.9726	0.9748	0.9789	0.9822	0.9857	0.9885	0.9926	0.9953
100	0.9442	0.9482	0.9502	0.9556	0.9589	0.9651	0.9702	0.9756	0.9801	0.9868	0.9914
150	0.9276	0.9327	0.9374	0.9419	0.9461	0.9539	0.9604	0.9673	0.9731	0.9817	0.9878
200	0.9135	0.9194	0.9249	0.9301	0.9350	0.9441	0.9518	0.9600	0.9669	0.9772	0.9846

(B) TRANSMISSIVITES OVER LONG RANGES (250 M TO 10 000 M)

Altitude (m):	0	250	500	750	1000	1500	2000	2500	3000	4000	5000
Range (m)											
250	0.9010	0.9076	0.9138	0.9196	0.9251	0.9354	0.9441	0.9534	0.9613	0.9730	0.9816
500	0.8515	0.8609	0.8697	0.8780	0.8858	0.9005	0.9130	0.9266	0.9383	0.9556	0.9685
750	0.8139	0.8253	0.8360	0.8461	0.8556	0.8735	0.8888	0.9056	0.9201	0.9415	0.9577
1000	0.7827	0.7953	0.8079	0.8195	0.8304	0.8509	0.8685	0.8880	0.9049	0.9295	0.9483
1500	0.7314	0.7471	0.7618	0.7758	0.7889	0.8137	0.8350	0.8588	0.8796	0.9094	0.9324
2000	0.6891	0.7071	0.7239	0.7398	0.7547	0.7831	0.8074	0.8348	0.8588	0.8927	0.9189
2500	0.6527	0.6725	0.6911	0.7087	0.7252	0.7567	0.7836	0.8141	0.8410	0.8782	0.9072
3000	0.6202	0.6417	0.6620	0.6811	0.6990	0.7332	0.7624	0.7958	0.8253	0.8655	0.8968
4000	0.5639	0.5883	0.6112	0.6329	0.6534	0.6924	0.7257	0.7642	0.7983	0.8435	0.8787
5000	0.5159	0.5424	0.5676	0.5915	0.6140	0.6571	0.6941	0.7371	0.7753	0.8248	0.8632
7500	0.4192	0.4494	0.4785	0.5063	0.5329	0.5843	0.6286	0.6814	0.7285	0.7870	0.8317
10 000	0.3452	0.3771	0.4082	0.4385	0.4676	0.5249	0.5751	0.6360	0.6906	0.7568	0.8065

(C) UP-WELLING RADIANCE ( $\text{W M}^{-2} \text{ m}^{-1}$ ) OVER SHORT RANGES (1 M TO 200 M)

Altitude (m):	0	250	500	750	1000	1500	2000	2500	3000	4000	5000
Range (m)											
1	2.65E+04	2.30E+04	2.00E+04	1.73E+04	1.50E+04	1.12E+04	8.33E+03	5.89E+03	4.17E+03	2.10E+03	1.04E+03
5	1.20E+05	1.05E+05	9.16E+04	7.99E+04	6.96E+04	5.22E+04	3.93E+04	2.81E+04	2.00E+04	1.01E+04	5.05E+03
10	2.20E+05	1.93E+05	1.69E+05	1.48E+05	1.30E+05	9.80E+04	7.43E+04	5.36E+04	3.84E+04	1.97E+04	9.92E+03
25	4.59E+05	4.06E+05	3.59E+05	3.16E+05	2.79E+05	2.14E+05	1.65E+05	1.21E+05	8.78E+04	4.63E+04	2.38E+04
50	7.64E+05	6.79E+05	6.04E+05	5.36E+05	4.75E+05	3.70E+05	2.88E+05	2.14E+05	1.58E+05	8.58E+04	4.52E+04
100	1.23E+06	1.10E+06	9.81E+05	8.76E+05	7.80E+05	6.15E+05	4.85E+05	3.66E+05	2.74E+05	1.54E+05	8.38E+04
150	1.60E+06	1.43E+06	1.29E+06	1.15E+06	1.03E+06	8.16E+05	6.48E+05	4.93E+05	3.73E+05	2.13E+05	1.18E+05
200	1.92E+06	1.72E+06	1.55E+06	1.39E+06	1.25E+06	9.92E+05	7.91E+05	6.05E+05	4.60E+05	2.67E+05	1.51E+05

(D) UP-WELLING RADIANCE ( $\text{W M}^{-2} \text{ m}^{-1}$ ) OVER LONG RANGES (250 M TO 10 000 M)

Altitude (m):	0	250	500	750	1000	1500	2000	2500	3000	4000	5000
Range (m)											
250	2.20E+06	1.98E+06	1.78E+06	1.60E+06	1.44E+06	1.15E+06	9.21E+05	7.08E+05	5.40E+05	3.17E+05	1.81E+05
500	3.33E+06	3.01E+06	2.72E+06	2.46E+06	2.22E+06	1.79E+06	1.45E+06	1.13E+06	8.69E+05	5.26E+05	3.10E+05
750	4.19E+06	3.80E+06	3.45E+06	3.12E+06	2.82E+06	2.29E+06	1.86E+06	1.46E+06	1.13E+06	6.96E+05	4.19E+05
1000	4.92E+06	4.47E+06	4.05E+06	3.68E+06	3.33E+06	2.71E+06	2.21E+06	1.74E+06	1.35E+06	8.43E+05	5.15E+05
1500	6.12E+06	5.57E+06	5.06E+06	4.60E+06	4.18E+06	3.42E+06	2.80E+06	2.21E+06	1.73E+06	1.09E+06	6.79E+05
2000	7.12E+06	6.48E+06	5.90E+06	5.37E+06	4.88E+06	4.01E+06	3.29E+06	2.60E+06	2.04E+06	1.30E+06	8.19E+05
2500	7.99E+06	7.28E+06	6.63E+06	6.04E+06	5.49E+06	4.52E+06	3.72E+06	2.94E+06	2.31E+06	1.48E+06	9.42E+05
3000	8.76E+06	7.99E+06	7.28E+06	6.64E+06	6.04E+06	4.97E+06	4.10E+06	3.25E+06	2.55E+06	1.65E+06	1.05E+06
4000	1.01E+07	9.24E+06	8.43E+06	7.69E+06	7.00E+06	5.78E+06	4.78E+06	3.78E+06	2.96E+06	1.93E+06	1.25E+06
5000	1.13E+07	1.03E+07	9.42E+06	8.60E+06	7.84E+06	6.48E+06	5.36E+06	4.24E+06	3.32E+06	2.18E+06	1.42E+06
7500	1.36E+07	1.25E+07	1.15E+07	1.05E+07	9.58E+06	7.94E+06	6.58E+06	5.21E+06	4.07E+06	2.68E+06	1.76E+06
10 000	1.54E+07	1.42E+07	1.31E+07	1.20E+07	1.10E+07	9.14E+06	7.59E+06	6.00E+06	4.68E+06	3.10E+06	2.05E+06

thermal cameras typically operate are given in [Table 9.5](#). As discussed in [Chapter 2](#), emissivity varies with composition and surface roughness, so that an appropriate emissivity should be selected depending on the surface type. We see, for example, that emissivity varies (at 3–5  $\mu\text{m}$ ) between 0.90 for a smooth glassy (Kilauea) pahoehoe surface, and 0.95 for a rough vesicular (Kilauea) pahoehoe surface, and is as high as 0.97 for a rhyolitic surface.

The problem with thermal camera measurements is that the direction of emission may not be perpendicular to (i.e., directly at) the detector. As shown by Dozier and Warren ([1982](#)), Labed and Stoll ([1991](#)), and Sobrino and Cuenca ([1999](#)), for snow and soil surfaces emissivities may vary with viewing angle, potentially decreasing rapidly at extreme angles. Such an effect was demonstrated for a volcanic surface by Ball and Pinkerton ([2006](#)), whose measurements for a smooth basalt surface, given here in [Figure 9.20](#), show a sharp drop-off in emissivity once the incidence angle increases above 30° from the nadir view. Although the effect was not as extreme for rough samples (Ball and Pinkerton, [2006](#)), to ensure that standard emissivity measurements are valid, incidence angles should be kept to within 30° of “head-on,” otherwise a correction for the incidence angle will need to be applied to the emissivity. Given that such correction data are rare, being limited to the correction provided for perfectly smooth basalt from Etna by Ball and Pinkerton ([2006](#)) ([Figure 9.20](#)), such a correction may be difficult to apply and needs provision of improved look-up tables.

#### *9.4.6.7 Effects of volcanic gas*

Atmospheric correction routines use standard atmospheric conditions without volcanic gas. Gas drifting into the FOV will change both the transmissivity and up-welling properties of the atmospheric path between the observer and the target. These effects can be estimated, but the composition and path length concentration of the gas needs to be known (see [Section 8.2.1](#) of [Chapter 8](#)).

The modeling and field tests of Sawyer and Burton ([2006](#)) showed that the presence of volcanic gas will absorb a significant amount of the radiation emitted by the targeted surface, so that derived surface temperatures may be under-estimated. This is a result of three effects:

- (1) a strong increase in absorption by  $\text{SO}_2$  at 8.7  $\mu\text{m}$ , and by  $\text{SiF}_4$  at 9.7  $\mu\text{m}$ ,
- (2) a broad absorption over the entire 7.5–13  $\mu\text{m}$  window, a result of absorption by aerosols, and
- (3) absorption by water vapor in the 7.5–13  $\mu\text{m}$  window.

The result was a 29% reduction in the detected radiance over normal conditions, of which 2% was the result of  $\text{SO}_2$  absorption, 2% due to  $\text{H}_2\text{O}$  absorption and 25% due to aerosol and  $\text{SiF}_4$  absorption. Effects are not as severe in the 3–5  $\mu\text{m}$  window within which an 18% reduction in detected radiance was observed.

By converting the target temperature to spectral radiance, reducing the radiance by these amounts, and converting the reduced radiance back to a brightness temperature, we can assess the absolute effects of gas absorption. This is plotted in [Figure 9.21a](#). We see that the non-linear relation between temperature and spectral radiance (as defined by the Planck Function) causes an under-estimate in temperature which increases with target temperature so that:

Table 9.5. *Band-averaged emissivities for a range of volcanic surface types. Emissivities are averaged over the thermal camera wavebands of Table 9.1. See Table 8.1 of Chapter 8 for sample details.*

Sample	Location	Type	Emissivity				
			3.4–5 $\mu\text{m}$	3–5 $\mu\text{m}$	7.5–13 $\mu\text{m}$	7.5–13.5 $\mu\text{m}$	8–14 $\mu\text{m}$
MU1	Kilauea	Basalt: pahoehoe	0.927	0.934	0.905	0.908	0.901
MU2	Kilauea	Basalt: 'A'a	0.950	0.955	0.955	0.956	0.954
Haw83	Kilauea	Basalt: pahoehoe – ropey	0.958	0.958	0.949	0.949	0.943
Haw83a	Kilauea	Basalt: pahoehoe – smooth, glassy	0.903	0.903	0.909	0.910	0.900
Haw83b	Kilauea	Basalt: pahoehoe – vesicular	0.951	0.951	0.918	0.919	0.909
Etna1	Etna	Basalt: pahoehoe – slabby (spiny)	0.946	0.946	0.960	0.960	0.957
Etna2	Etna	Basalt: 'A'a	0.968	0.969	0.972	0.972	0.971
Etna3	Etna	Basalt: Scoria	0.937	0.944	0.970	0.970	0.968
Strom	Stromboli	Basalt: Spatter	0.939	0.944	0.957	0.958	0.953
StromA	Stromboli	Basalt: Scoria	0.956	0.959	0.964	0.964	0.960
StromB	Stromboli	Basalt: 'A'a	0.955	0.955	0.965	0.965	0.963
Vulc1	Vulcano	Trachyte/Rhyolite	0.970	0.974	0.976	0.977	0.975
Vulc2fsh	Vulcano	Sulfur	0.768	0.796	0.855	0.856	0.860
Vulc2wth	Vulcano	Sulfur	0.857	0.864	0.907	0.907	0.909

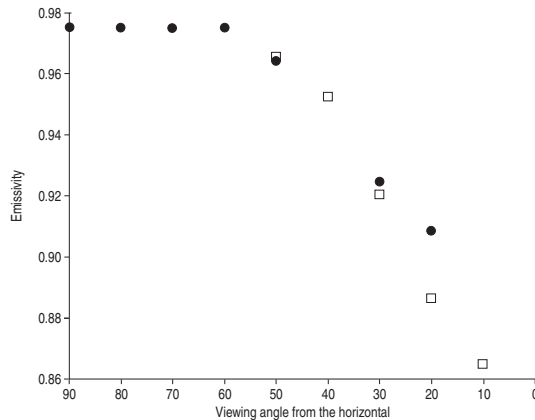


Figure 9.20 Decrease in 7.5–13  $\mu\text{m}$  emissivity with viewing angle recorded by Ball and Pinkerton (2006) for a smooth surfaced basalt. Emissivity is estimated from the difference between the actual kinetic (surface) temperature of the sample and the recorded brightness temperature (see Chapter 2 for methodology). Results from two experiments are given, using black dots and open squares, respectively [from Ball and Pinkerton (2006, Fig. 14); reproduced by permission of American Geophysical Union].

- for 18% absorption at 3–5  $\mu\text{m}$ , the under-estimate is 8 °C for a surface at 100 °C, and 79 °C for a surface at 1000 °C;
- for 25% absorption at 7.5–13  $\mu\text{m}$ , the under-estimate is 26 °C for a surface at 100 °C, and 196 °C for a surface at 1000 °C;
- for 29% absorption at 7.5–13  $\mu\text{m}$ , the under-estimate is 31 °C for a surface at 100 °C, and 229 °C for a surface at 1000 °C.

These estimates are for those gas compositions and path length compositions measured at Stromboli during 2001–2002. As shown by Sawyer and Burton (2006) the problem will increase with path length concentration of  $\text{H}_2\text{O}$  and  $\text{SO}_2$ . Of these, increasing the concentration of  $\text{H}_2\text{O}$  has a greater effect than increasing  $\text{SO}_2$  concentration, as can be seen in Figures 9.21b and 9.21c. In a worst case scenario, in the 7.5–13  $\mu\text{m}$  waveband and for a target at 1200 K, while absorption by  $\text{H}_2\text{O}$  alone potentially increases the under-estimate to 227 K, absorption by  $\text{SO}_2$  has the potential to cause a maximum under-estimate of 84 K.

As Sawyer and Burton (2006) point out, though, for gas-free conditions, such as at an active lava flow front, these considerations will not apply. In gassy conditions, however, absolute temperatures should be treated with caution or a suitable correction applied. Correction is problematic, requiring simultaneous measurement of path-length gas composition and concentration which may, in turn, vary over a period of seconds with wind and plume ascent speed and direction, as well as rate of emission of the plume itself. However, routines described in Section 8.2 of Chapter 8, such as recording for long time periods and holding the maximum temperature (assumed to be the temperature acquired in the clearest conditions, and thereby

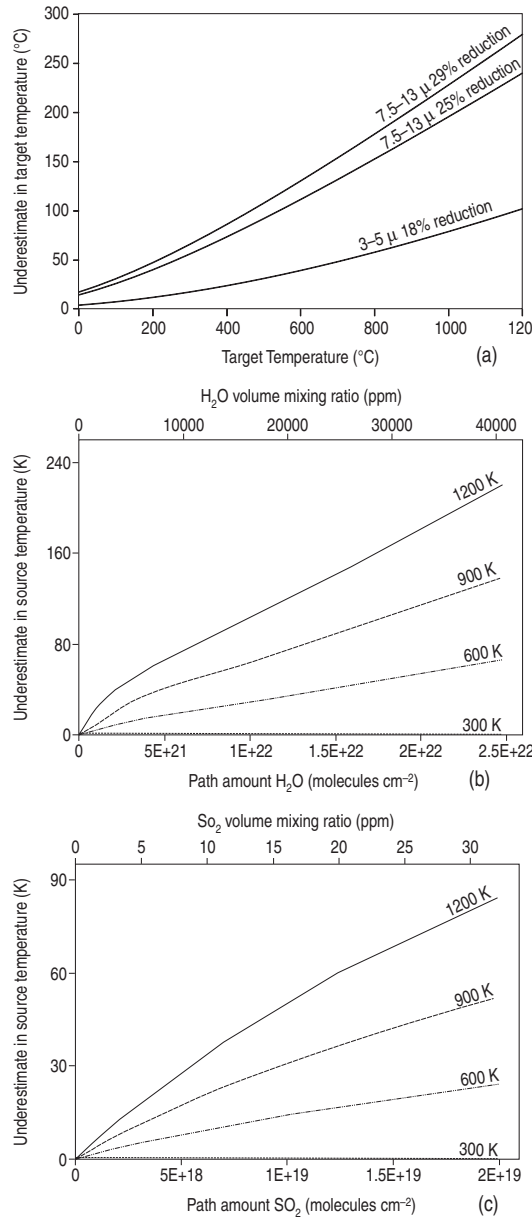


Figure 9.21 (a) Increase in under-estimate in brightness temperature recorded at 7–13.5  $\mu\text{m}$  with surface temperature for situations where volcanic gas absorbs 29%, 25% and 18% of the emitted radiance. (b) Increase in under-estimate of surface temperature (for four surface temperature cases) with increased path amount of H<sub>2</sub>O [from Sawyer and Burton (2006, Fig. 3b): reproduced by permission of American Geophysical Union]. (c) Increase in under-estimate of surface temperature (for four surface temperature cases) with increased path amount of SO<sub>2</sub> [from Sawyer and Burton (2006, Fig. 3c): reproduced by permission of American Geophysical Union].

the temperature suffering the smallest degree of under-estimate), can be applied to reduce such effects.

## 9.5 Deployment principles: making the measurement

Thermal cameras are typically deployed in one of two styles: roving survey style or fixed-point campaign style, as shown in [Figure 9.22](#). The style of survey deployed will depend on the nature of the target and the objectives of the deployment.

### 9.5.1 Survey-style deployment

The aim of survey-style deployments is to thermally characterize large surface areas, as is the case when a thermal camera is used for thermal mapping of a lava flow field, fumarole field or geothermal zone. In such cases, the target is usually viewed from a number of points and angles so as to cover all thermally anomalous zones across the active area. The survey network is set out in such a way that data of a reasonably high spatial resolution are available for the entire surface, including outer and inner flanks of any craters, and/or blind sides of any topographic ridges, so that no shadow zones remain. Images can then be geometrically corrected, geo-referenced, stitched together and/or draped over a secondary spatial data set, such as a digital elevation model and/or digital photo mosaic of the same area, to produce a thermal map of the entire area. While single surveys can be used to generate one-off thermal maps of a thermal surface, repeating the survey allows a time series of thermal maps to be generated so that changes in the thermal character, location and size of hot spots can be tracked and examined.

Such surveys may involve touring the survey area on foot, stopping at each survey point to collect images from a sufficient number of angles so as to allow acquisition of a mosaic of overlapping images covering the entire surface. Survey points need to be selected so that they allow all of the thermal surface to be covered using a series of overlapping images. Such surveys are often best made from the air. Use of an aircraft allows an areally extensive or remote feature to be surveyed much more quickly and efficiently than from the ground, and at better (vertical) look angles. Such surveys have typically been helicopter-based, use of a helicopter allowing flexibility in the overpass velocity, allowing acquisition from a stationary, hovering position, as well as flexibility in location of the survey point.

### 9.5.2 Campaign-style deployment

The aim of a campaign-style deployment is usually to collect data allowing the emission or emplacement history of a highly dynamic thermal feature to be defined. In a volcanic sense, such features include lava flowing in active lava channels or tubes, crust moving across the surface of an active lava lake, changes in the structure of an extruding or collapsing lava dome, or plumes emitted during an explosive eruption. To measure such rapidly evolving and/or fast moving features, repeat coverage at high frame rates is required, as is camera stability so that pixels in each successive image record the thermal character of the same unchanging area within the FOV.

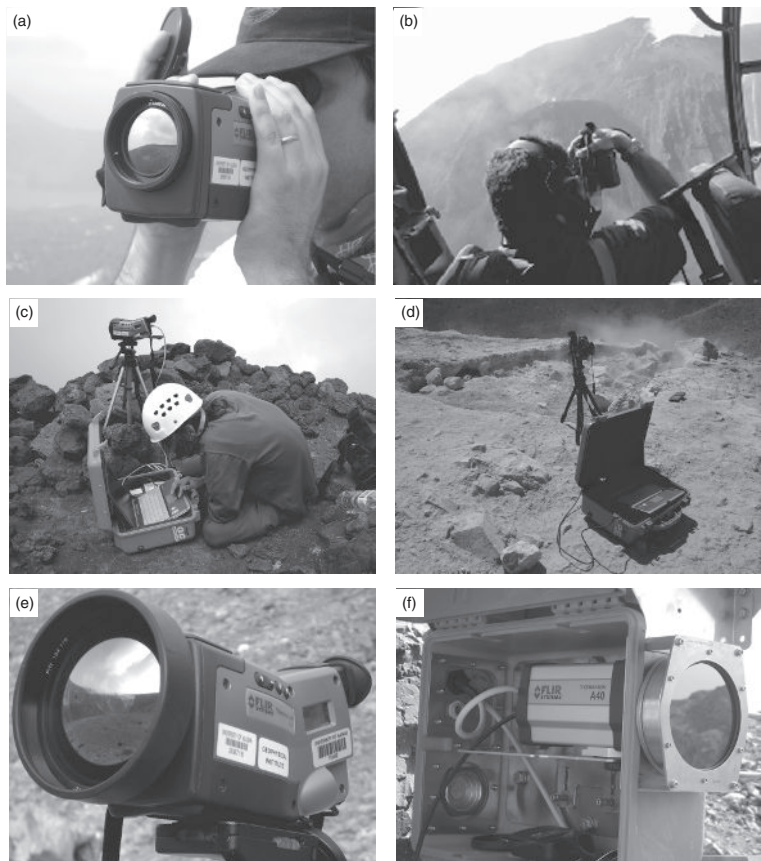


Figure 9.22 Roving survey style, fixed-point campaign style and permanent thermal camera installations to track volcanic thermal phenomena. (a) Roving use of a FLIR S40 to build a thermal map of the inner flanks of Vulcano's Fossa crater. (b) Operator targets the active lava flow field at Stromboli during June 2003 with a FLIR S40 from a helicopter hovering over a GPS-fixed survey position. (c) Targeting of explosions at Stromboli during June 2004 using a FLIR S40 sampling at 30 Hz through firewire connection to a laptop: operator is controlling the acquisition from the laptop. (d) Targeting an active fumarole pit on Vulcano during July 2005 using a FLIR S40 sampling at 30 Hz through firewire connection to a laptop: the laptop is shut in a pelican case during acquisition for protection from the corrosive atmosphere. A thermocouple is being used to measure the temperature of a control fumarole within the thermal camera field of view. (e) Targeting of degassing fumaroles across the lower section of Vulcano's Fossa fumarole field during July 2005 using a FLIR S40 fitted with a 12 degree magnification lens. Camera is saving one image every 30 seconds onto the internal memory card. (f) Permanent installation of a FLIR A40 at Vulcano on 27 June 2006. See also color plates section.

Campaign-style deployments are thus made from fixed, unmoving positions, with the camera best being tripod-mounted to ensure stability of the FOV and pixel positions. The camera FOV is thus carefully targeted at the beginning of the deployment, and then left absolutely untouched throughout the deployment, with the camera recording at an appropriate and pre-set frame rate

during the acquisition. The result is a time series of images covering the same FOV to provide data capable of showing rapid changes in the thermal character, position and area of features within that FOV.

### 9.5.3 What else do I need to measure and consider?

In both survey- and campaign-style surveys a number of ancillary parameters need to be measured at the time of image acquisition to allow adequate geometric and atmospheric correction. As sketched in [Figure 9.23](#), these include:

- hand-held GPS ( $x,y,z$ , UTM) position for the camera location at the time of image acquisition;
- downward (or upward) pointing angle of the camera, with the sign being negative for downward pointing and positive for upward pointing;
- camera azimuth (i.e., viewing direction as a bearing in degrees from North);
- height of columnation (i.e., tripod height or operator feet-to-eye height);
- slant line and/or horizontal distance to the targeted surface, as well as distance (and vertical + horizontal angle) to any other distinctive ground-control points within the FOV. A distance measurement to the surface that falls in the center of the FOV is the easiest to work with.

If the images are being collected survey style, a waypoint needs to be collected at each survey point, and a track log should be recorded to check the survey coverage. The following two topographic measurements should also be made:

- height above, or below, the targeted surface;
- slope of the imaged surface, and orientation of the surface with respect to the FPA.

If the camera depression or elevation angle is measured, then any of the following

- the height of the camera above (or below) the targeted point,
- the horizontal distance to the target, or
- the slant line distance

can be estimated, if one of the other three listed distances have been measured (see [Table 9.6](#)). In addition, to allow suitable atmospheric and emissivity corrections to be made we need to measure:

- path length (slant distance to each pixel), air temperature and humidity;
- time, altitude (of both the camera and the target) and viewing angle;
- surface type (so as to be able to apply appropriate emissivity corrections); while making
- qualitative notes on viewing conditions plus activity styles and levels.

Within this final list, the first group of parameters should be measured, and/or entered into the camera's internal software, at least every 15 minutes. Because of the importance of relative humidity in the atmospheric correction procedure when applied to thermal camera data, especially for surfaces at high temperatures, Ball and Pinkerton (2006) recommend making relative humidity and atmospheric temperature measurements in two locations: one

Header Information:	
(i) Field location + operator name (plus any companion data sets / operators)	
(ii) Date + acquisition start time & stop time	
(iii) Sampling rate; or time & GPS location of each image acquistion	
(1) Camera position (x,y,z location) Collect GPS point & set time (note time zone used for time synchronization)	(6) Air temperature, humidity (every few minutes) plus notes on surface type (for ε correction)
(3) Height of columnation	(2) Camera tilt angle (downwards = -ve, upwards = +ve), and viewing angle (degrees from North)
(4) Height above target (h), line-of-sight distance ( $D_{LOS}$ ) and/or horizontal distance (L), plus camera details (including FOV and IFOV & details of any zoom or wide angle lenses used)	(5) Slope of imaged surface ( $\theta_s$ ) and/or DEM, map of (or GPS points-ground control points-across) the imaged area
Footer Information:	
(iv) Notes on target nature, deployment objectives & activity	

Figure 9.23 Parameters to be measured at the time of image acquisition to allow adequate geometric and atmospheric correction.

at the camera site and a second as close to the target as possible (as well as as many other locations as possible along the line of sight). Because of uncertainties regarding on-board atmospheric correction for surfaces that fall over a range of distances and/or altitudes within a single image (see [Section 9.4.6](#)), it may also be best to correct pixel brightness temperatures for atmospheric transmissivity and up-welling effects calculated for the appropriate camera-to-target path length and altitude for each pixel of interest using the geometric and atmospheric corrections detailed previously in this chapter.

#### 9.5.3.1 Frame rate, data transfer rates, data storage, and battery life

The frame rate needs to be set depending on the velocity of the target and the diameter of the FOV. If, for example, the targets are fragments of lava crust moving down a channel at  $0.1 \text{ m s}^{-1}$  and across a 1-m-wide field of view, then the fragments will take 10 s to move across the field of view. Thus, a frame rate between 1 Hz and 0.5 Hz should be adequate to capture their dynamics and record velocities, i.e., the fragments should be imaged between 5 and 10 times

Table 9.6. Simple trigonometric relations to allow the elevation difference between the camera and the target, the horizontal distance to the target, or the slant line distance to the target to be calculated using the simple right-angle triangle trigonometry of Figure 9.23.

For a downward looking view, if depression angle ( $\theta$ ) is measured	For an upward looking view, if elevation angle ( $\theta$ ) is measured
(1) If the slant line distance to the targeted surface ( $H$ ) is measured: Elevation above the targeted surface ( $A$ ) = $CAH = \cos(\theta) = A/H$ $A = H \cos(\theta)$ Horizontal distance to the targeted surface ( $O$ ) = $SOH = \sin(\theta) = O/H$ $O = H \sin(\theta)$	(1) If the slant line distance to the targeted surface ( $H$ ) is measured: Elevation above the targeted surface ( $O$ ) = $SOH = \sin(\theta) = O/H$ $O = H \sin(\theta)$ Horizontal distance to the targeted surface ( $A$ ) = $CAH = \cos(\theta) = A/H$ $A = H \cos(\theta)$
(2) If elevation above the targeted surface ( $A$ ) is measured: Slant line distance to the targeted surface ( $H$ ) = $CAH = \cos(\theta) = A/H$ $H = A / \cos(\theta)$ Horizontal distance to the targeted surface ( $O$ ) = $TOA = \tan(\theta) = O/A$ $O = A \tan(\theta)$	(2) If elevation above the targeted surface ( $O$ ) is measured: Slant line distance to the targeted surface ( $H$ ) = $SOH = \sin(\theta) = O/H$ $H = O / \sin(\theta)$ Horizontal distance to the targeted surface ( $A$ ) = $CAH = \cos(\theta) = A/H$ $A = O \cos(\theta)$
(3) If horizontal distance to the targeted surface ( $O$ ) is measured: Slant line distance to the targeted surface ( $H$ ) = $SOH = \sin(\theta) = O/H$ $H = O / \sin(\theta)$ Elevation above the targeted surface ( $A$ ) = $TOA = \tan(\theta) = O/A$ $A = O / \tan(\theta)$	(3) If horizontal distance to the targeted surface ( $A$ ) is measured: Slant line distance to the targeted surface ( $H$ ) = $CAH = \cos(\theta) = A/H$ $H = A / \cos(\theta)$ Elevation above the targeted surface ( $O$ ) = $TOA = \tan(\theta) = O/A$ $O = A \tan(\theta)$

during their transit across the FOV. If we back the camera off, so that the FOV is now 100 m wide, the same fragments now take 1000 s to move across the FOV. For this case, a frame rate of one image every 10 s should be adequate, allowing the fragments to be imaged 100 times during their passage across the FOV. Now, take a ballistic fragment exiting a vent at  $100 \text{ m s}^{-1}$ . This will travel across a 10 m-high FOV in 0.1 s, and across a 100 m-wide FOV in 1 s. Thus, frame rates of four images every tenth of a second, or 40 frames per second, are required, so that imaging frequencies of 40 Hz, or more, are required for this case. Again, if we back off to 5 km and angle the camera up at  $27^\circ$ , the FOV diameter increases to 2008 m and the time for the fragments to move across the FOV declines to  $\sim 20$  s, so that a frame rate of  $\sim 1$  Hz may suffice, allowing 20 images to be acquired during transit of the fragment. Because the particle will decelerate upon leaving the vent due to gravity, these are approximations and give the maximum imaging frequencies required.

Once a suitable frame rate has been selected, we need to check that we can record sufficiently fast. Currently, many (or most) models have a limit of around 1–2 Hz for the rate at which radiometric data can be saved onto internal memory cards. Use of the memory card makes deployment straightforward as all we need is the camera and a card. However, higher frame rate acquisition will have to be via firewire onto a laptop computer, or through use of “burst” mode (see [Section 9.2.5.5](#)). If deployed with the camera, the laptop will have to be loaded with the camera operating software, and suitably protected, as in the campaign-style set-up of [Figure 9.22](#).

The next question is, do I have sufficient memory or storage space available? A back-of-the-envelope calculation allows us to estimate the space we need using the frame rate, intended duration of the measurement and typical image size, i.e.,

$$\text{space needed} = \text{frame rate} \times \text{duration} \times \text{image size}.$$

Given a typical size of  $\sim 150$  kBytes for a  $320 \times 240$  pixel image, space needed to record at 1 Hz for 15 minutes will be

$$1 \text{ image per second} \times 900 \text{ seconds} \times 150 \text{ kBytes} = 135 \text{ MB}.$$

If we increase the frame rate to 50 Hz we obtain

$$50 \text{ images per second} \times 900 \text{ seconds} \times 150 \text{ kBytes} = 6.75 \text{ GB}.$$

Decreasing the frame rate to 1 image every 10 seconds or 1 image every minute, we reduce the storage requirement to

$$0.1 \text{ images per second} \times 900 \text{ seconds} \times 150 \text{ kBytes} = 13.5 \text{ MB}$$

for the first case, and

$$0.0167 \text{ images per second} \times 900 \text{ seconds} \times 150 \text{ kBytes} = 2.25 \text{ MB}$$

for the second case.

We can re-arrange our calculation to determine how long it will take to fill a memory card of given size at the selected frame rate. This will be,

$$\text{Duration} = \text{space available} / (\text{frame rate} \times \text{image size}).$$

Now, given a 1 GB card and running at a frame rate of 2 frames per second, we will fill the card in

$$1 \text{ GB} / (2 \text{ images per second} \times 150 \text{ kBytes}) = 55.6 \text{ minutes}$$

and so can run the experiment for just less than one hour at the required frame rate. Likewise, we can select the opportune sampling rate for a chosen recording period. Given, for example, a 1 GB card and the necessity to record for 1.75 hours, then the maximum frame rate that we can record at will be

$$\text{Frame rate} = \text{space available} / (\text{duration} \times \text{image size})$$

so that

$$\text{Frame rate} = 1 \text{ GB} / (150 \text{ kb} \times 6300 \text{ s}) = \text{around 1 image per minute.}$$

We can now use these quick calculations to adjust the frame rate to maximize acquisition time, or to buy and take (into the field) a sufficient number of extra memory cards so as to extend data collection at an opportune frame rate. Given that data cards are now quite cheap, it is a good idea to take a handful of cards into the field, packing several more than are thought to be needed is a good idea.

However, there will also be a limit imposed by battery life, which is typically 2–3 hours for most commercially-available thermal cameras (see [Table 9.1](#)). Again, we can always take supplementary batteries into the field to allow extended data collection, with the number carried depending on the duration we wish to run for (while remembering to take sufficient batteries for the laptop too, if a laptop is to be used).

To ensure that no data are lost, and that data files are closed properly, acquisition should always be stopped before the camera or laptop battery completely dies, and/or before the memory card completely fills. In addition, when collecting images as sessions (i.e., multiple images saved together as a single image sequential file), it is best to collect multiple short sessions rather than one long one. The reasons being:

- (1) if a data file corrupts or fails to save properly, then only a portion of the data will be lost if only a short duration file has been recorded;
- (2) it prevents data files from becoming too large, where we find the maximum file size that can often be handled by the camera software is usually around

$$15 \text{ minutes} \times 50 \text{ Hz} \times 150 \text{ kBytes} = 6.75 \text{ GB},$$

so that we typically stop, save and restart a session every 15 minutes when running at such a frame rate.

### *9.5.3.2 Other acquisition issues*

Other questions to think about when acquiring imagery are as follows.

- Is the camera clock set to GPS time in UTC?  
If not, there may be problems when precise time synchronization is needed, or when comparisons with ancillary data sets are attempted.
- Is the image in focus?  
If not, the data will be difficult to use in a quantitative fashion due to smearing.
- If the camera is to be flown on a helicopter, are the doors off and/or can the windows be opened during flight?  
If the measurement is made through glass the temperature of the glass will be measured, not that of the target.
- If the survey is being made from a helicopter, is the craft speed sufficiently slow as to avoid blur and data gaps?  
If the craft is moving too fast, then the image will be blurred, and areas may be missed.
- If a survey is being made with an auto-save rate of one image every two seconds, is the camera being moved sufficiently slowly so as to avoid blur, while moving sufficiently fast so as to achieve a full panorama of the surface with no gaps between adjacent images?  
Ideally, to achieve a sequence of overlapping images the operator should slowly pan the camera, type writer fashion, from the top left corner of the area to be surveyed to the bottom right corner. If auto-save is not being used, an image needs to be saved at each step across an overlapping grid of images that fully covers the surveyed area.  
Auto-save makes the process easier by removing the requirement of manually saving, but sufficient memory must be available to square with the survey duration and auto-save frequency.
- Has a suitable gain setting been selected?  
This needs to be set to a level that (i) ensures minimal saturation, while ensuring that (ii) temperatures are not below the minimum gain setting.
- Is my GPS on and recording?  
For helicopter operations it is particularly useful to run a GPS track log, and have the camera time sync-ed to the GPS time, so that camera location can be obtained from the track log using the image acquisition time if necessary.

## **9.6 Methodologies**

The hand-held thermal camera image can be used simply as a thermal map to make qualitative observations and appraisals regarding the location, intensity and dimensions of thermal features, and any changes in these properties. However, while the image also comprises calibrated temperature data allowing quantification of thermal levels and heat fluxes, the digital (pixilated) data also facilitate precise measurements regarding target dimensions and hence, also, areas and volumes. When collected as video sequences, the imagery also allow dynamics to be assessed and quantified, including rates of change in

temperature (i.e., cooling) and position (i.e., velocity) and hence, also, mass or volume flux. Thus a number of methodologies have been derived to extract quantitative thermal and dynamic information.

### **9.6.1 Qualitative applications (basic image interpretation)**

There are, potentially, hundreds of examples of how interpretation of hand-held thermal camera images, and application of the basic rules of air photo interpretation, can be used to allow a qualitative assessment of the style, location and time-evolving nature of volcanic activity to be assessed, thereby contributing to the documentation of activity at a volcanic system.

Qualitative analysis involves simple visual appraisal of images to identify, describe, locate and/or track a feature. This process involves application of the basic rules of air photo and image interpretation, as have already been detailed in [Chapter 6](#). Following these considerations, the most important descriptors in registering a volcanic hot spot in hand-held thermal camera data include the following:

- Location of the hot spot in an absolute sense (i.e., definition of the hot spot's geographic coordinates).
- Appraisal of feature location in relation to the edifice, i.e., is it the summit or on the flank, and what is its aspect and elevation?
- Appraisal of the feature in relation to other volcanic structures, i.e., what is the association of the feature in relation to known fissures and fissure systems, rifts and rift zones, pit craters, cones, valleys, ridges, etc?
- Description of the feature shape, e.g., is it equant, elongate, circular, linear, en echelon, sinuous, curved, narrow, wide?
- Assessment of the orientation of the feature in relation to associated structures and local slope, e.g., does it run down slope, across the slope or is it orientated with the slope?
- Description of the feature size, including sub-features such as local hot spots within the broader thermal anomaly.
- Description of any thermal tone (or intensity), texture and/or pattern.

Together, these observations allow the feature to be classified and described in a consistent manner, providing a basis for any subsequent changes to be assessed.

#### *9.6.1.1 Fractures, fumaroles and geomethermal areas: interpretation examples*

The first studies that used thermal camera imagery to assess thermal patterns across active volcanic cones and craters included examination of “lineaments (fumarole alignments)” developing following the 18 May 1980 eruption of Mount St. Helens by Friedman *et al.* (1981). Likewise, Shimozuru and Kagiyama (1978), Kieffer *et al.* (1981), Yuhara *et al.* (1981) and Ballestracci and Nougier (1984) all used thermal

camera imagery to identify fracture patterns, zones of fumarolic activity and geothermal activity by virtue of their characteristic thermal expression. Thus, all of the first thermal camera papers in volcanology focused on interpretation of *fractures, fumaroles and geomethermal areas*.

Later, targeting of the unbuttressed NE flank of Stromboli by Bonaccorso *et al.* (2003) during the beginning of Stromboli's 2002–2003 eruption, and of an Etnean cinder cone constructed during Etna's 2001 eruption by Calvari and Pinkerton (2004), revealed thermally defined lineaments. In both cases warm, narrow and arcuate features running across a slope were convincingly given as evidence for fractures opening in zones of instability, with an example from Stromboli being given in Figure 9.24a. In comparison, warm, but diffuse and broad anomalous zones can be interpreted as evidence for fumarolic activity and geothermal heating. An example of the shapes and patterns for thermal features expected at fractured, fumarolic and geothermally heated zones is given in Figure 9.24b. This image collected at Vulcano's

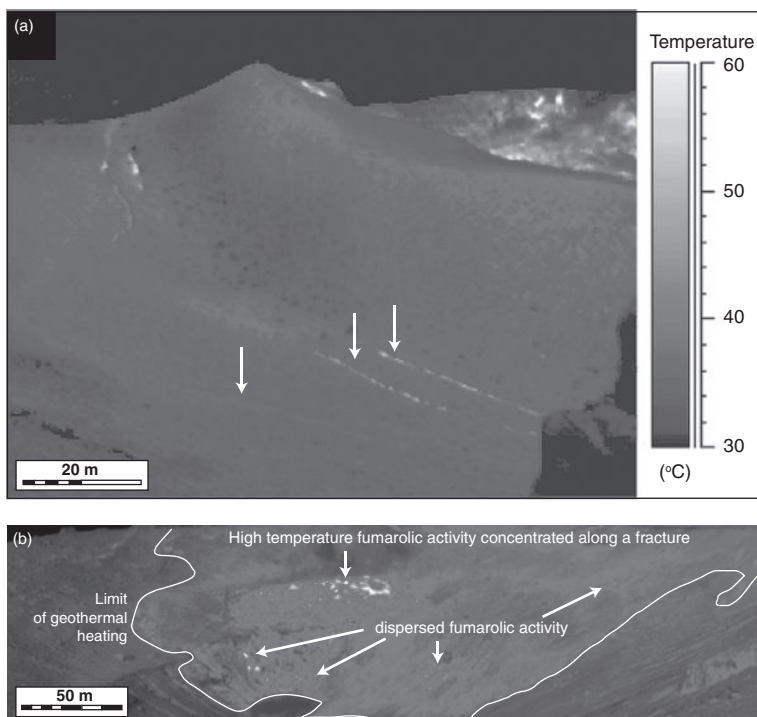


Figure 9.24 (a) Arcuate sets of concentric fractures, apparent from their subtle to strong thermal expression, running around Stromboli's SW cratera imaged on 8 June 2003 (arrows mark main fractures: there are three, of which the outermost is the coolest). Surface is imaged by day, but under overcast conditions, so as to minimize solar heating which can obliterate such subtle thermal anomalies. (b) Mosaic of thermal images acquired for Vulcano's Fossa fumarole field during July 2005 showing thermal anomalies due to (i) high-temperature fumaroles aligned along fractures, (ii) dispersed and clustered fumarolic activity, and (iii) zones of geothermal heating. See also color plates section.

fumarole field just before dawn (so that solar heating effects are minimized) shows the following.

- (1) Concentrated high-temperature fumarolic activity along fractures, apparent from their linear, narrow, elongate distribution of uniformly high-intensity tone.
- (2) Localized areas of dispersed fumarolic activity apparent from broad areas across which the temperature is warm, or the texture mottled. Temperatures are spatially variable, with relatively high- and low-intensity pixels occurring side by side, each high intensity pixel marking an open vent or roughly circular fumarole pit/cluster.
- (3) Areas of geothermal heating apparent from a broader, larger area of smoother (but brighter than the surrounding) tones, within which the dispersed zone of fumarolic activity lies.

#### *9.6.1.2 Lava bodies: interpretation examples*

Application of the basic rules of air photo interpretation to thermal camera images of active lava bodies can be used to identify, describe, map and track active units. An example is given in [Figure 9.25a](#), where visible and thermal images of a lava shield active at the head of an active lava flow field on Stromboli during June 2003 are given. In the visible view we see just a black compound lava flow field of possibly active and possibly inactive pahoehoe and 'a'a units, with a single point of incandescence marking a hot vent atop a hornito. The thermal view, though, shows a long, narrow, high-intensity feature trending west–east and extending off the image at its eastern edge. This marks the line of an active lava channel. We also see a high-intensity lobate feature on the camera-facing flank of the hornito. This delimits the extent of a short, but active, 'a'a flow fed by the active vent atop the hornito. Two other intense point sources feed bright lobate features at the top of the image. These mark two other active vents, one feeding the channel and the second feeding a lava flow which departs the FOV over the SW skyline. A third point source to the SW of the hornito feeds a very small, moderate intensity, lobate feature. This marks a fourth small vent that is feeding a lava flow of extremely limited extent. All other moderate- to low-intensity lobate features not associated with bright spots (vents) are recent, but now inactive and cooling, lava flows. We see that the remainder of the shield is marked by low thermal intensities (i.e., blue colors), which are cold and inactive (although some warm spots mark cracks in the cool crust meaning the shield interior is still hot). None of this was visible to the naked eye or in the visible image.

In [Figure 9.25b](#) we merge the visible and thermal images for the braided, channel-fed lava flow field, thereby increasing the level of detail available for the mapped phenomena. In this map we are able to define the full extent of the flow from its thermal expression, and confirm the phenomena to which the thermal anomaly is associated, in this case: channel-fed 'a'a lava flows. Some recent thermal camera models allow simultaneous acquisition of visible and

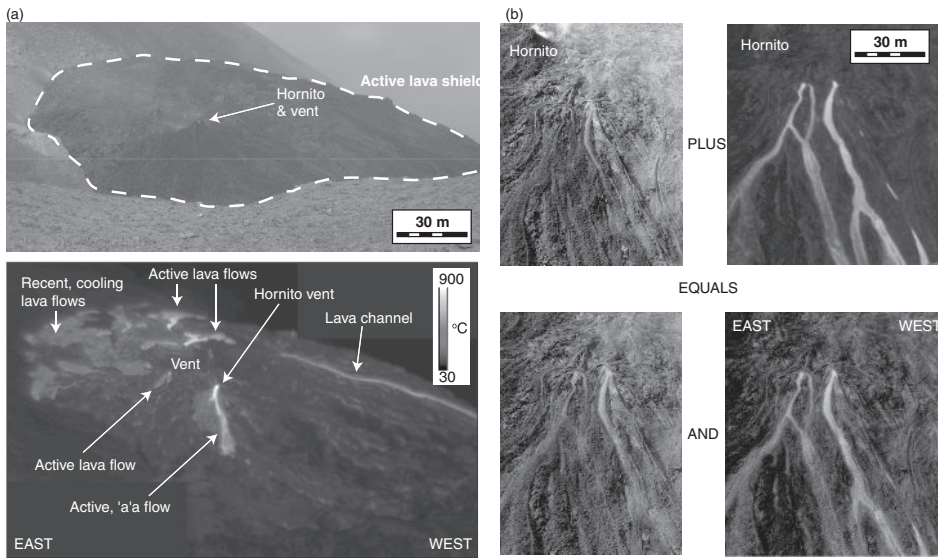


Figure 9.25 (a) Visible digital photo and thermal camera image of a lava shield active at Stromboli on 1 June 2003, with (b) a digital photo and thermal image for the proximal portions of the channel-fed lava flows active on steep slopes to the west of the same shield on 7 June 2003. In (b) the visible–thermal merge of the same two images is given, where the merge is weighted towards the visible (bottom left) or thermal (bottom right). See also color plates section.

thermal images, along with image merging software, a useful feature allowing interpretation on the basis of combined visible and thermal detail.

#### 9.6.1.3 Image interpretation for plume classification

Image interpretation can be used to distinguish between the three main components of volcanic plumes: ash, gas and bombs/blocks. This has allowed classification of the nature of the plume in terms of these three main components, so that we have:

- Type 1 plumes: bomb-rich;
- Type 2 plumes: ash-rich;
- Type 3 plumes: gas-rich;
- Type n(a,b,c) plumes: mixed.

In the last case, an appraisal as to the relative proportions of the components that comprise the mixture can be made to set sub-classes, so that a number is assigned to n according to the dominant component. For example;

- Type 1a: bomb-dominated with gas,
- Type 1b: bomb-dominated with minor ash,
- Type 2a: ash-dominated with minor bombs,

- Type 2b: ash-dominated with no bombs,
- Type 3a: gas-dominated with minor bombs,
- Type 3b: gas-dominated with minor ash,
- Type 3c: gas-dominated with minor bombs + ash.

This was the basis of the plume typology made using thermal camera data by Patrick *et al.* (2007), who used the data to distinguish:

- Type 1 plumes – dominated by coarse ballistic particles, and
- Type 2 plumes – consisting of an optically-thick, ash-rich plume with (Type 2a) or without (Type 2b) large numbers of ballistic particles.

Images of these two end-member plume types are given in Figures 9.26a and 9.26b, respectively. These show how the texture of the image, as well as tone or intensity, can be used to distinguish each of the components. While areas of ash tend to give broadly continuous tones and smoother textures with a distinct "billowing", "bulbous" pattern, discrete hot bombs produce an irregular texture comprising a scatter of many discrete, but bright, points. Like ash, areas of gas and aerosol tend to have smooth textures, but have much lower intensities than areas of ash and, if not condensing, will be semi-transparent so that we can see the background topography through the warm gas plume area.

We can also use plume shape to distinguish the four main plume types defined, on the basis of morphology, by Turner (1969). These, as imaged in Figure 9.27, are as follows.

#### (1) Jets

These being high velocity plumes driven by initial momentum which, in the example given here, are characterized by a well-collimated form which shows little upward spreading and contains no shapes associated with formation of thermals.

#### (2) Starting plumes

These are buoyant plumes in which the circulating plume front begins to form a thermal. The plume front thus begins to take on a bulbous form, below which a longer feeder column is apparent, with the plume beginning to show signs of spreading with height.

#### (3) Rooted thermals

In the rooted thermal the convecting thermal at the plume front becomes particularly well formed. The plume shape becomes that of the classic mushroom-shaped cloud.

#### (4) Discrete thermals

Such plumes are no longer fed by, or associated with, a steady feeder plume; they have detached and/or emission of the steady plume has died out. However, the thermal is still able to convect and ascend under its own buoyancy. Thus all we now see is the detached rolling, broadly spherical form of the thermal, with no associated feeder plume.

Figure 9.27 shows how each plume morphology can be identified from their characteristic shapes, as well as a characteristic arrangement of their component parts. Such basic interpretation and classification steps are important because different plume types will

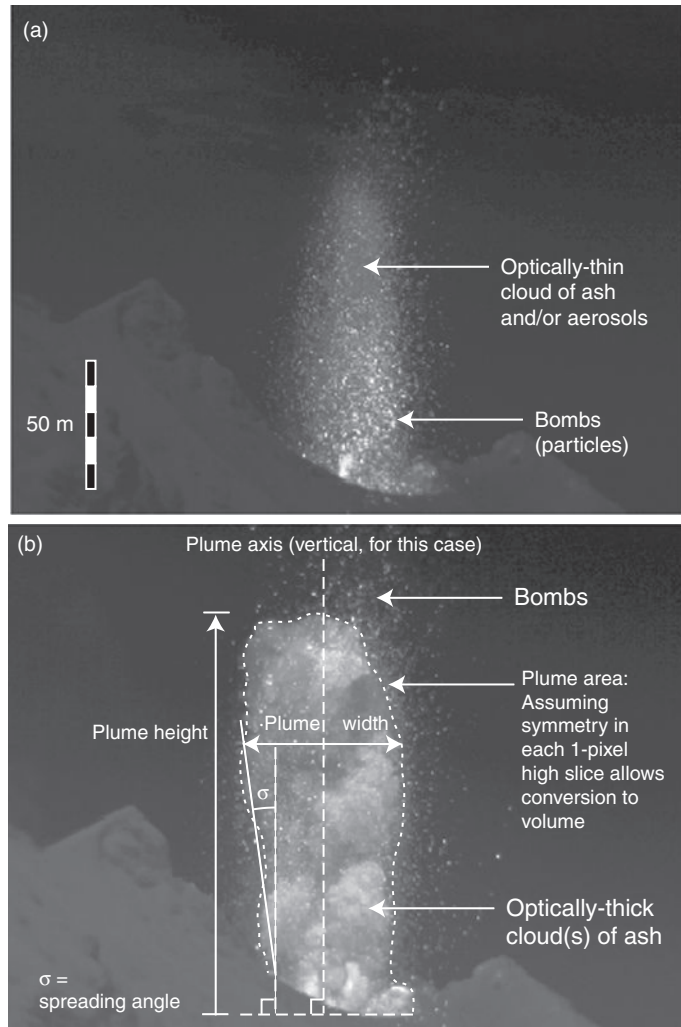


Figure 9.26 Plumes imaged at Stromboli during July 2004 showing (a) a Type 1 plume, dominated by coarse ballistic particles, and (b) a Type 2 plume consisting of an optically thick, ash-rich plume with, in this case, large numbers of ballistic particles. Bombs are apparent as point source hot spots in both images, distinguishing them from the warm to hot “cloud” of ash and aerosols. Part (b) is labeled with the main plume parameters that can be extracted from the imagery. See also color plates section.

experience different dynamics. Whereas particles in a bomb- or block-rich emission, for example, will follow ballistic trajectories, ascent dynamics of ash and/or gas rich emissions will be driven by gas thrust and buoyancy. Likewise, while jets will be associated with gas thrust dynamics, thermals will undergo ascent by buoyancy at a slower rate.

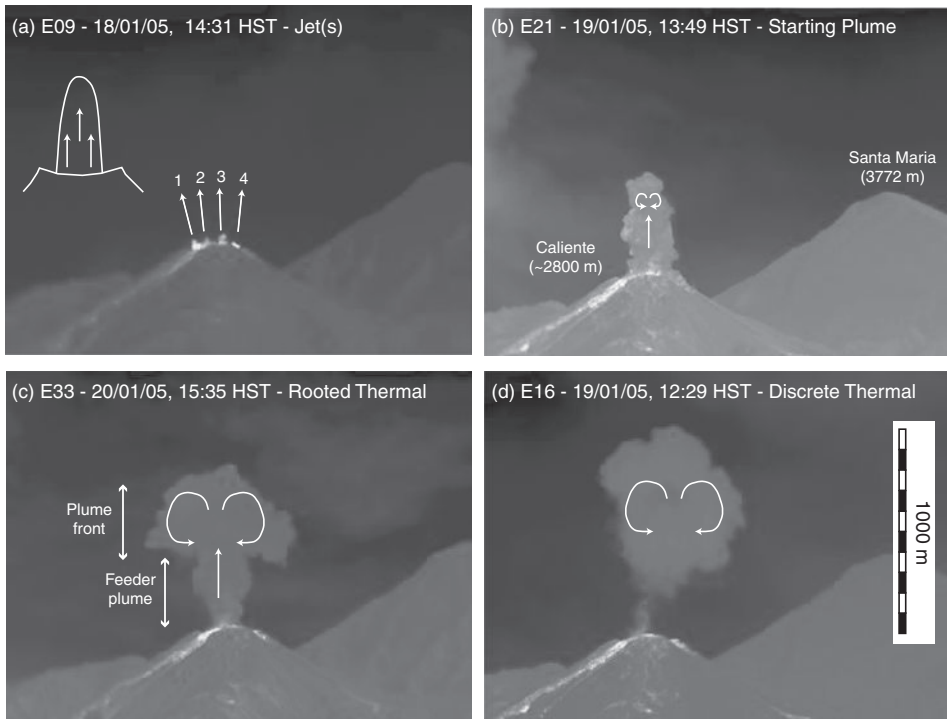


Figure 9.27 The four main plume types of Turner's (1969) classification as imaged at Santiaguito in 2005. In (a) we see four sets (as labelled 1 through 4) each having the form as enlarged. Arrows give sense of motion in each plume or plume component. In (a) four jets are apparent, as numbered. Date format is dd/mm/yy and time is Hawaiian Standard Time (HST). See also color plates section.

## 9.7 Methodologies II: temperature measurements

A major advantage of the thermal camera is that we can usually make a close approach to the object, sometimes being able to approach to within 100 m, even within 5–10 m. This maximizes the spatial resolution, reducing pixel scales to mm or cm, so that we may avoid the mixed pixel issues encountered with satellite data where pixels have scales of tens to thousands of meters. We may thus avoid a whole level of processing and mixture model application.

However, in some cases absolute temperatures can still be quite difficult to obtain due to gas and atmospheric, or mixed pixel, issues. Two examples include measurements of bombs in flight, and small (cm-scale) fumarole vents. With the example of the bomb, the eruption plume usually has to be viewed (for safety reasons) from some distance so that the pixels may be relatively large in relation to the size of the bomb, meaning that the bombs are sub-pixel features, so that the pixel-integrated temperature will be less than the actual bomb

surface temperature. Also, the bombs will be moving quite rapidly, so that their pixel location and mixture properties will always be changing. For example, in the first acquisition the bomb may fall across two pixels, in a second at the intersection of four pixels, in a third between two pixels. This would cause the apparent, integrated temperature for the bomb pixel(s) to decrease and increase as the energy becomes divided between four and then two pixels. In the case of the fumarole, the mm to cm-scale vent will likely be a sub-pixel feature, and variable amounts of gas will serve to contaminate the measurement, increasing and decreasing the degree of signal attenuation as gas drifts in and out of the IFOV. Thus care should be taken in retrieving temperatures acquired under such conditions, and the two-component one-band mixture models of [Chapter 4](#) may need to be applied, as will careful consideration, and correction for, atmospheric path length effects.

#### *9.7.0.1 Temperature distributions*

As already reviewed in [Section 8.2.2](#) of [Chapter 8](#), frequency distributions of temperature can be used to thermally characterize a surface. They are useful in that they use brightness statistics, rather than absolute temperature, to characterize the thermal character of the surface, and so may be used with pixel-integrated brightness temperature data. Harris and Maciejewski ([2000](#)) used frequency distributions derived from radiometer surveys of Vulcano's fumarole field to characterize hot, cool and moderate temperature fumarole zones. Each was apparent from characteristic frequency distributions of temperature.

- Low-temperature zones were characterized by a distribution that was relatively tightly and symmetrically clustered around a low-temperature mode, so that the standard deviation was also relatively small.
- High-temperature zones were characterized by a wider spread of temperatures, which was usually asymmetric about a less prominent mode and skewed in the high-temperature direction.
- Mixed (low and high) temperature zones showed frequency distributions that were a mixture of the two end-member distributions.

The advantage of the thermal camera is that, with a  $320 \times 240$  pixel image, we potentially have 76 800 data points for our frequency distribution, increasing to 307 200 points for a  $640 \times 480$  image. Frequency distributions produced for high- and low-temperature fumarole zones at Vulcano using a ThermaCam™ S40 situated 100 m from the vents had the following character.

- Ambient surfaces have the most tightly clustered distribution, with the most prominent mode, as shown in [Figure 9.28a](#).
- Mixing ambient pixels with pixels containing low-temperature fumaroles causes the amplitude of the mode to decrease and the distribution to spread a little, as shown in [Figure 9.28b](#).

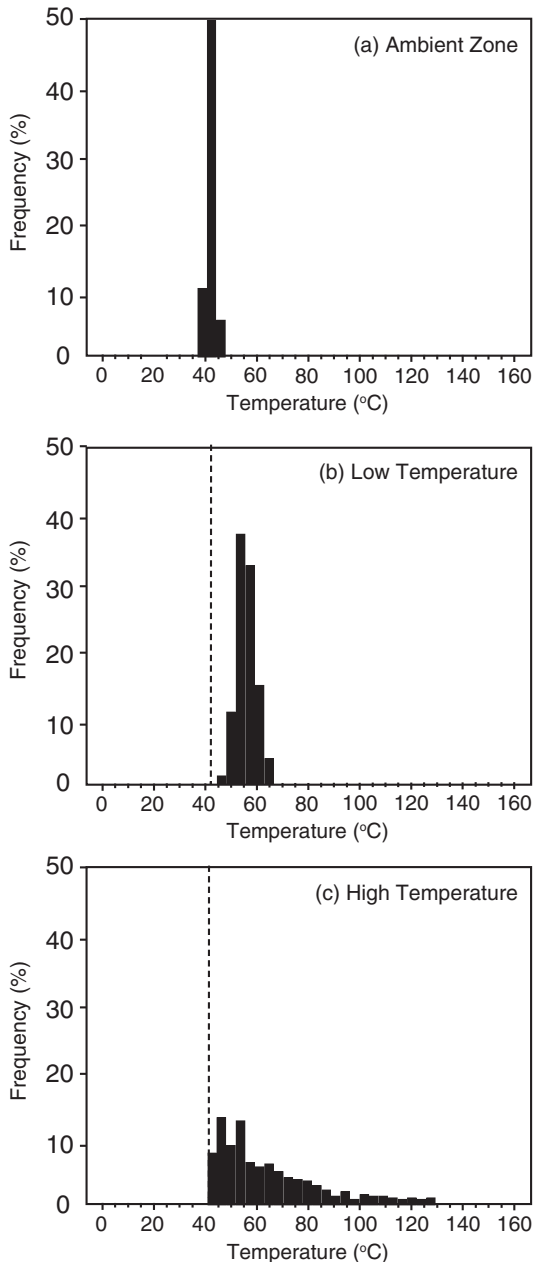


Figure 9.28 Frequency distributions of pixel-integrated temperature taken from a thermal camera image of Vulcano's Fossa fumarole field for (a) a fumarole-free zone, (b) a zone containing low-temperature ( $100\text{ }^{\circ}\text{C}$ ) fumaroles and (c) a zone containing high-temperature ( $>250\text{ }^{\circ}\text{C}$ ) fumaroles. Vertical dashed line marks location of the mode in the ambient distribution of (a).

- Mixing in pixels containing high-temperature fumaroles causes the distribution to flatten, and become skewed towards higher temperatures, the distribution taking on the asymmetrical and widely spread character of a high-temperature fumarole zone, as shown in [Figure 9.28c](#).

The same rules appear to apply to active lava surfaces. Oppenheimer and Yirgu ([2002](#)), Oppenheimer *et al.* ([2004](#)), Calkins *et al.* ([2008](#)) and Spampinato *et al.* ([2008](#)) all give thermal-camera-derived frequency distributions of temperature for lava lake surfaces displaying various thermal states, and Wright and Flynn ([2003](#)) provide the same for active pahoehoe surveys. The distributions derived for Erta Ale's lava lake by Oppenheimer and Yirgu ([2002](#)) are given here in [Figure 9.29](#) and show that, as the lava lake becomes more active, the distributions evolve from

- a low-temperature distribution, with a prominent low-temperature mode, through
- a moderate-temperature distribution, which is flatter, with a less prominent low-temperature mode and a high-temperature skewed limb, to
- a high-temperature distribution, in which secondary modes develop at higher temperatures.

This frequency distribution characterization of high- and low-temperature surfaces thus appears valid for both fumarolic surfaces and active lava bodies and allows us to thermally characterize the surface, the end-members being

- relatively quiet and cool, with the characteristic low-temperature distribution, and
- active and hot, with the characteristic high-temperature distribution.

While such distributions can thus be used to define the “thermal state” of a surface, they can also be used to track the thermal evolution of a surface through time. While a surface showing a distribution that evolves from a low- to a high-temperature distribution is, for example, becoming more active, one evolving in the opposite direction is becoming less active.

#### *9.7.0.2 Heat flux*

Following the methods given in [Section 4.4](#) of [Chapter 4](#), we can convert our temperature map to a map of heat flux density (in  $\text{W m}^{-2}$ ). Multiplying by pixel area will yield the heat flux (in W) for each pixel, and summing the flux for each pixel across the imaged feature will yield the total heat flux. A simple and quick way to do this is to use the frequency distribution of temperature for the feature, as follows.

- Convert the distribution to one of heat flux density. To do this for radiative heat flux density simply involves raising the temperature of each bin to the power of four, subtracting the background temperature raised to the power of four, and multiplying the result by emissivity and the Stefan–Boltzmann constant.
- Multiply the result by pixel area to convert the distribution to one of heat flux (in Watts).
- Multiply the heat flux of each bin by the number of occurrences to obtain the total heat flux in each bin.
- Summing the heat flux for all bins now yields the total heat flux for the feature.

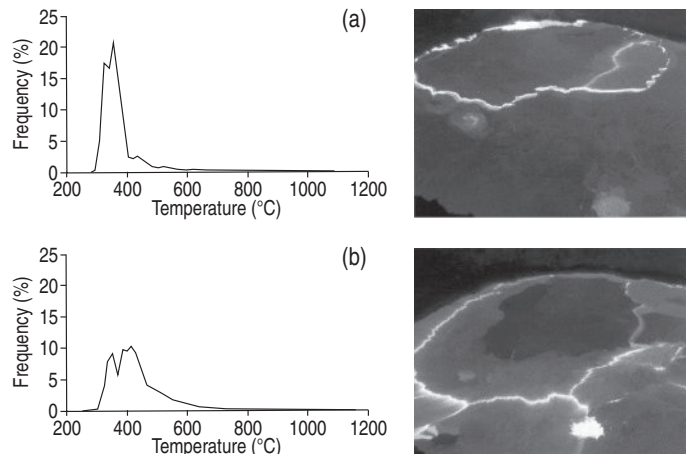


Figure 9.29 Frequency distribution of surface temperature, and thermal camera image from which each distribution was obtained, for Erta Ale's lava lake during (a) relatively quiet and (b) relatively vigorous activity during February 2001 [from Oppenheimer and Yirgu (2002, Fig. 3)]. See also color plates section.

The result, however, will be an approximation, because temperatures will be rounded to the mid-point temperature of each bin. It will also not take into account any variations in pixel area or background temperature across the image. The most precise method is to calculate the heat fluxes on a pixel-by-pixel basis which can be achieved by running a simple conversion algorithm across the image. The heat flux conversion used, as well as necessary ancillary measurements that need to be made, will vary depending on the nature of the target (active lava body, crater lake, geothermal field). The location of appropriate conversion routines and measurement methodologies in this book, as well as the main ancillary measurements required to complete each heat flux calculation, are given in [Table 9.7](#).

### 9.7.1 Time series and profiles

As with satellite and radiometer data, repeat image collection allows time series to be generated. The advantage of the thermal camera perspective is that the temporal resolution of the time series can be greatly increased. Plotting, for example, the heat flux from a degassing vent using data recorded at 33 Hz provides a time series of the same temporal resolution, i.e., 33 data points per second. This allows time series to be produced for extremely fast, rapidly evolving, or short-lived events. Parameters that can be extracted from such time series have already been explored in detail in [Chapter 8](#).

Likewise the improved spatial resolution greatly enhances our ability to produce spatial profiles down and across targeted thermal features, as done using satellite data in Section 6.7 of [Chapter 6](#). With the thermal camera it is possible to produce transects across a feature that may only be centimeters to meters wide, something that is impossible even using the

**Table 9.7. Processing, location of conversion equations, and ancillary measurements required to convert thermal camera temperature data to heat flux density. In all cases, to move from heat flux density to a heat flux requires multiplication by pixel area; total heat flux is obtained by summing heat flux for all pixels across the thermal surface in question.**

Target	Processing	Location of heat flux conversion equations	Ancillary calculations and measurements
Lava flow	Extract area containing hot pixels across	<a href="#">Section 4.4.1 of Chapter 4</a>	Ambient temperature <sup>a</sup> ;
Lava dome	the active surface		convective heat transfer coefficient.
Lava lake			
Lava tube	Extract surface temperature profile above tube and down the line of the tube	<a href="#">Section 4.4.1.6 of Chapter 4</a>	Tube dimensions and roof thickness.
Skylights	Extract skylight area and lava surface temperature	<a href="#">Section 4.4.1.7 of Chapter 4</a>	Velocity of air blowing out of skylight; ambient air temperature.
Crater lakes	Extract area containing lake surface pixels	<a href="#">Section 4.4.1.10 of Chapter 4</a>	Air temperature and humidity; wind speed.
Open vents (including fumaroles)	Extract pixels containing open vents	<a href="#">Section 4.4.1.11 of Chapter 4</a>	A mixture model may have to be applied if the fumarole vent is smaller than the pixel; air temperature.
Geothermal fields	Extract geothermally heated area	<a href="#">Section 4.4.1.12 of Chapter 4</a>	Ambient ground temperature <sup>a</sup> Air temperature and relative humidity

<sup>a</sup>Can be obtained from nearby pixel outside of heated zone.

highest spatial-resolution satellite data. For example, imaging a fumarole from a vertical viewing point 1 m above the fumarole will yield pixels that, given an IFOV of 1.3 mrad, will be 0.065 cm wide. Thus, if the fumarole is only 3 cm across, the transect will still have  $\sim 46$  points. A lava channel imaged from a distance of 50 m will have a spatial resolution of 3.25 cm, so that if the channel is just 1 m wide there will still be  $\sim 30$  data points along a profile taken across the channel. As described in [Chapter 8](#), this can be done using an appropriately targeted radiometer, but profiles are much easier to produce using thermal camera data. It simply involves placement of a line across the image down or across the axis of the feature for which the profile is to be produced, and plotting the pixel temperature or heat flux for each pixel along the line. Repeating the same process, along the same line, on multiple images can be used to determine how the thermal state is changing with time, as well as with distance along the transect. An example is given in [Figure 9.30](#), which is a surface temperature transect for a 70-m-long stretch of active lava channel.

### 9.7.2 Cooling rates, surface age and crust thickness

Surface cooling can be defined in a spatial or temporal sense using a thermal image. This can then be used to estimate cooling of the flow interior as well as the thickness of the thermal boundary layer between the flow interior and the surface. The latter parameters can be derived from the heat flux, as already described in [Section 4.4 of Chapter 4](#) (see section 4.4.1.4).

#### 9.7.2.1 Surface cooling with distance (flows and plumes)

Placing a profile down the centerline of a lava flow, or up the center axis of an ascending plume, will provide a plot of surface temperature with distance down flow, or with height in the plume. We can use this to determine the cooling rate of that surface with distance from the source. This is done by taking the temperature difference between any two points along a transect ( $\Delta T_{\text{surf}}$ ), and dividing them by the distance between the two points ( $\Delta x$ ). This yields cooling per unit distance ( $\Delta T_{\text{surf}}/\Delta x$ ).

In [Table 9.8](#) we use this approach to estimate the down-flow surface cooling for the surface temperature profile plotted for an active lava channel in [Figure 9.30](#). The second and third columns give the distance and temperature at that distance, respectively. The fourth column gives the temperature difference between each step, so that dividing by the distance between each measurement (which in this case is 5 m for each step) yields surface cooling rate, as given in column five. From these data we see that, at the head of the channel, we have a surface temperature of 790 °C, compared with 660 °C at a distance of 70 m down channel. Thus, down the entire channel, we have surface cooling by 130 °C, so that we have a temperature decline of

$$\frac{\Delta T_{\text{surf}}}{\Delta x} = \frac{130 \text{ } ^\circ\text{C}}{70 \text{ m}} = -1.9 \text{ } ^\circ\text{C m}^{-1},$$

the minus sign indicating that, overall, surface temperature has declined down the channel. However, such a cooling rate will be for the surface of the body, and not the interior. For a

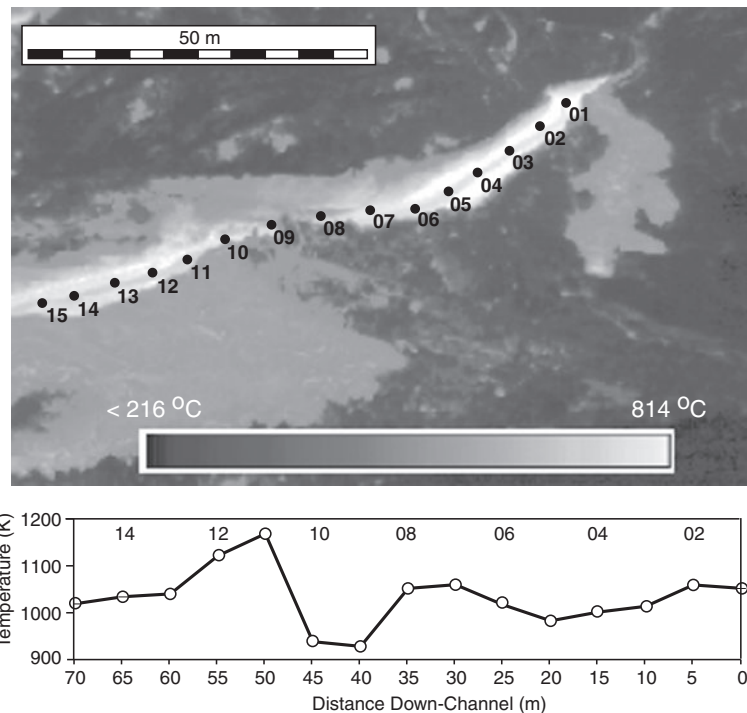


Figure 9.30 Thermal camera image of the proximal section of a lava channel active on Etna on 30 May 2001, with the points used to construct the down-flow surface temperature profile. The extracted profile is given at the base of the figure. See also color plates section.

lava flow we can use the surface-leaving heat loss to estimate the cooling of the interior per unit distance ( $dT/dx$ ) by applying Equation (4.65k) of Chapter 4. That is,

$$\frac{dT}{dx} = \frac{M_{\text{tot}}}{U_{\text{flow}} d\rho (c_p + C_L \frac{d\phi}{dT})}, \quad (9.35)$$

where

- $M_{\text{tot}}$  = the heat flux density ( $\text{J s}^{-1} \text{m}^{-2}$ );
- $U_{\text{flow}}$  = flow velocity ( $\text{m s}^{-1}$ );
- $\rho$  = lava density ( $\text{kg m}^{-3}$ );
- $c_p$  = lava specific heat capacity ( $\text{J kg}^{-1} \text{K}^{-1}$ );
- $C_L$  = latent heat of crystallization ( $\sim 3.5 \times 10^5 \text{ J kg}^{-1}$ ); and
- $d\phi/dT$  = mass fraction of crystallization per degree cooling ( $\text{K}^{-1}$ ).

Thus, first we have to convert our temperature to a heat flux density, which we do in column six of Table 9.8 by raising the temperature (in kelvin) to the power of four and multiplying

Table 9.8. Down-channel surface temperatures plotted in Figure 9.30 and conversion to cooling rates. Values used to solve Equations (9.35) and (9.36) were, for this Etnean case: flow velocity ( $U_{flow}$ ) =  $0.1 \text{ m s}^{-1}$ ; channel width = 3 m, channel/flow depth (d) = 1.5 m; bulk density =  $2030 \text{ kg m}^{-3}$ ; bulk specific heat capacity =  $960 \text{ J kg}^{-1} \text{ K}^{-1}$ ; heat of crystallization ( $C_L$ ) =  $3.5 \times 10^5 \text{ J kg}^{-1}$ ; crystallization rate =  $0.003 \text{ K}^{-1}$ .

Profile	Surface Cooling ( $\text{^{\circ}\text{C m}^{-1}}$ )				Interior cooling ( $\text{^{\circ}\text{C m}^{-1}$ ) (Equation 9.35)			Interior cooling ( $\text{^{\circ}\text{C s}^{-1}}$ ) (Equation 9.36)			
	Point	Distance	$T_{surf}$ ( $^{\circ}\text{C}$ )	$\Delta T$ ( $^{\circ}\text{C}$ )	$\Delta T/\Delta x$ ( $^{\circ}\text{C m}^{-1}$ )	$M_{rad}$ ( $\text{W m}^{-2}$ )	$dT/dx$ ( $^{\circ}\text{C m}^{-1}$ )	$dT/dx$ ( $^{\circ}\text{C km}^{-1}$ )	$\Phi_{rad}$ (W)	$dT/dt$ ( $^{\circ}\text{C s}^{-1}$ )	$dT/dt$ ( $^{\circ}\text{C h}^{-1}$ )
SP1	0	790				7.10E+04	0.116	116			
SP2	5	760	-30	-6		6.33E+04	0.103	103	9.50E+05	0.013	48
SP3	10	760	0	0		6.33E+04	0.103	103	9.50E+05	0.013	48
SP4	15	750	-10	-2		6.09E+04	0.099	99	9.13E+05	0.013	46
SP5	20	720	-30	-6		5.41E+04	0.088	88	8.11E+05	0.011	41
SP6	25	610	-110	-22		3.38E+04	0.055	55	5.07E+05	0.007	25
SP7	30	620	10	2		3.54E+04	0.058	58	5.30E+05	0.007	27
SP8	35	580	-40	-8		2.94E+04	0.048	48	4.42E+05	0.006	22
SP9	40	570	-10	-2		2.81E+04	0.046	46	4.21E+05	0.006	21
SP10	45	630	60	12		3.70E+04	0.060	60	5.55E+05	0.008	28
SP11	50	720	90	18		5.41E+04	0.088	88	8.11E+05	0.011	41
SP12	55	710	-10	-2		5.19E+04	0.085	85	7.79E+05	0.011	39
SP13	60	680	-30	-6		4.59E+04	0.075	75	6.88E+05	0.010	35
SP14	65	640	-40	-8		3.86E+04	0.063	63	5.80E+05	0.008	29
SP15	70	660	20	4		4.21E+04	0.069	69	6.32E+05	0.009	32
Average:		680	-130	-1.9		4.59E+04	0.075	75	9.63E+06	0.010	35

by emissivity and the Stefan–Boltzmann constant. Using the typical surface temperature for the channel in Equation (9.35) we thus have,

$$\frac{dT}{dx} = \frac{(0.98)(0.000\,000\,0567 \text{ W m}^{-2} \text{ K}^{-4})(953 \text{ K})^4}{(0.1 \text{ m s}^{-1})(1.5 \text{ m})(2030 \text{ kg m}^{-3})[960 \text{ J kg}^{-1} \text{ K}^{-1} + (3.5 \times 10^5 \text{ J kg}^{-1})(0.003 \text{ K}^{-1})]} \\ = \frac{4.59 \times 10^4 \text{ W m}^{-2}}{6.12 \times 10^5 \text{ W m}^{-1} \text{ K}^{-1}} = 0.075 \text{ K m}^{-1} = (0.075 \text{ K m}^{-1})(1000 \text{ m}) = 75 \text{ K km}^{-1}.$$

Because surface temperature varies from point to point, the heat flux density, and thus also the cooling rate, varies from point to point. Lower surface temperatures lead to decreased rates of heat loss and, hence, decreased cooling rates. We can thus use the image-derived surface temperature profile to estimate the down-flow variation in the rate of interior cooling, as done in column eight of [Table 9.8](#).

#### 9.7.2.2 Surface cooling with time (flows and plumes)

By tracking the temporal evolution in the temperature of an object in thermal video, we can also estimate the cooling rate per unit time. To do this we identify the object we wish to track, a piece of crust or pyroclastic particle, and obtain its pixel temperature in image 1 ( $T_1$ ). We then locate the same object in the next image ( $T_2$ ) and subtract the second temperature from the first, so that the temperature difference between the two images ( $\Delta T = T_2 - T_1$ ) is obtained. For a stationary object, this is simple and just requires tracking the pixel temperature with time, for a moving object it requires that we track the object. Now, dividing by the difference in time between the two images ( $\Delta t$ ), we obtain the rate of surface cooling per unit time ( $\Delta T/\Delta t$ ).

#### 9.7.2.3 Interior cooling with time (lava flows)

For a lava flow, by applying Equation (4.65f) of [Chapter 4](#), we can use the surface-leaving heat loss to estimate the cooling of the interior per unit time ( $dT/dt$ ),

$$\frac{dT}{dt} = \frac{\Phi_{\text{tot}}}{V\rho(c_p + C_L \frac{d\phi}{dT})}, \quad (9.36)$$

where

- $\Phi_{\text{tot}}$  = the heat flux ( $\text{J s}^{-1}$ )
- $V$  = lava volume ( $\text{m}^3$ );
- $\rho$  = lava density ( $\text{kg m}^{-3}$ );
- $c_p$  = lava specific heat capacity ( $\text{J kg}^{-1} \text{ K}^{-1}$ );
- $C_L$  = latent heat of crystallization ( $\sim 3.5 \times 10^5 \text{ J kg}^{-1}$ );
- $d\phi/dT$  = mass fraction of crystallization per degree cooling ( $\text{K}^{-1}$ ).

To apply this equation we thus need to convert our heat flux density measurements to heat flux. We can do this by multiplying the heat flux density by the feature surface area. For our case,

where we have a 70 m length of channel that is 3 m wide, the surface area is  $70 \text{ m} \times 3 \text{ m} = 210 \text{ m}^2$ . We also need to estimate the volume of lava involved. For our channel, which is 1.5 m deep, this is  $70 \text{ m} \times 3 \text{ m} \times 1.5 \text{ m}$ , which, given a vesicularity of 22%, gives a dense rock volume of

$$[70 \text{ m} \times 3 \text{ m} \times 1.5 \text{ m}] [1 - 0.22] = 245.7 \text{ m}^3.$$

Thus we have

$$\begin{aligned} \frac{dT}{dt} &= \frac{(210 \text{ m}^2)(0.98)(0.000\,000\,0567 \text{ W m}^{-2}\text{K}^{-4})(953 \text{ K})^4}{(245.7 \text{ m}^3)(2030 \text{ kg m}^{-3})[960 \text{ J kg}^{-1} \text{ K}^{-1} + (3.5 \times 10^5 \text{ J kg}^{-1})(0.003 \text{ K}^{-1})]} \\ &= \frac{9.63 \times 10^6 \text{ Js}^{-1}}{1.00 \times 10^9 \text{ JK}^{-1}} = 0.01 \text{ K s}^{-1} = (0.01 \text{ K s}^{-1})(3600 \text{ s}) = 36 \text{ K h}^{-1}. \end{aligned}$$

Again, because surface temperature varies from point to point, the heat flux, and thus also the cooling rate, varies from point to point, as we see from the point-by-point calculations in [Table 9.8](#). To achieve these calculations, we multiply the heat flux density at each step by the area of lava within each step, this being the channel width multiplied by the step length, i.e.,  $3 \text{ m} \times 5 \text{ m} = 15 \text{ m}^2$ . The resulting heat flux is given in column nine of [Table 9.8](#). Now we need to estimate the volume of lava contained within the channel across each step, this being  $5 \text{ m} \times 3 \text{ m} \times 1.5 \text{ m}$ , which, given a vesicularity of 22%, gives a bulk volume of

$$[5 \text{ m} \times 3 \text{ m} \times 1.5 \text{ m}] [1 - 0.22] = 17.55 \text{ m}^3.$$

Using this value in Equation (9.36) we can estimate the cooling rate (per unit time) across each step, as done in the final two columns of [Table 9.8](#).

#### 9.7.2.4 Surface age (lava flows)

Given the temperature of a cooling lava surface, the time required to cool to the observed value can be calculated. So far in this book we have used the empirical relation of Hon *et al.* (1994a) to calculate this time ( $t$ ). This relation was derived from thermal data acquired for inflating pahoehoe on Kilauea. It thus applies best to Hawaiian pahoehoe and gives

$$t = 145.98 \exp^{(-0.0164 T_{\text{surf}})}, \quad (9.37)$$

$T_{\text{surf}}$  being the current, measured, surface temperature (in  $^{\circ}\text{C}$ ) and  $t$  being the time (in hours) since exposure. However, time-dependent surface cooling can also be calculated theoretically, thus allowing such relations to be derived for situations where different thermal gradients and thermal properties apply.

Following the Stefan (1891) cooling problem, surface temperature ( $T_{\text{surf}}$ ) can be expressed as a function of time ( $t$ ) using

$$T(t) = T_{\text{surf}} = \left[ \frac{M}{\sigma} + T_a^4 \right]^{0.25}, \quad (9.38)$$

where  $\sigma$  is the Stefan–Boltzmann constant ( $5.67 \times 10^{-8} \text{ W m}^{-2} \text{ K}^{-4}$ ),  $T_a$  is the ambient temperature and  $M$  is the heat flux density. For this solution, heat flux can be calculated from

$$\varphi = \frac{T_h - T_a}{R_k + \left(\frac{R_c R_r}{R_c + R_r}\right)}, \quad (9.39)$$

$T_h$  being the temperature from which the lava cooled.  $R_k$ ,  $R_c$  and  $R_r$  are the thermal resistance terms for conduction, convection and radiation, respectively, where

$$R_k = \frac{y}{k}, \quad R_c = \frac{1}{h_c}, \quad R_r = \frac{T_h - T_a}{\varepsilon \sigma (T_h^4 - T_a^4)}, \quad (9.40)$$

$y$  being crust thickness,  $k$  being thermal conductivity and  $h_c$  being the convective heat transfer coefficient. Given that all heat supplied to the surface must be lost by radiation and convection,  $\varphi$  can also be written

$$M = \varepsilon \sigma (T_{\text{surf}}^4 - T_a^4) + h_c (T_{\text{surf}} - T_a), \quad (9.41)$$

$\varepsilon$  being emissivity and  $h_c$  being the convective heat transfer coefficient. Now, writing  $R_k$  in full in Equation (9.38),

$$\varepsilon \sigma (T_{\text{surf}}^4 - T_a^4) + h_c (T_{\text{surf}} - T_a) = \frac{T_h - T_a}{\frac{y}{k} + \left(\frac{R_c R_r}{R_c + R_r}\right)}. \quad (9.42)$$

We can now re-arrange to calculate crust thickness ( $y$ ) as a function of  $T_{\text{surf}}$ , from

$$y = \left[ \frac{T_h - T_a}{\varepsilon \sigma (T_{\text{surf}}^4 - T_a^4) + h_c (T_{\text{surf}} - T_a)} - \frac{R_c R_r}{R_c + R_r} \right] k. \quad (9.43)$$

Crust thickness can also be written as

$$y = (2\lambda\sqrt{\kappa t}) \div 1000, \quad (9.44)$$

in which  $\lambda$  is a dimensionless scaling value,  $\kappa$  is thermal diffusivity (in  $\text{mm}^2 \text{ s}^{-1}$ ) and  $t$  is time (in s); dividing by 1000 places  $y$  in units of meters. We can now combine Equations (9.43) and (9.44) to eliminate  $y$ , i.e.,

$$1000 \left[ \frac{T_h - T_a}{\varepsilon \sigma (T_{\text{surf}}^4 - T_a^4) + h_c (T_{\text{surf}} - T_a)} - \frac{R_c R_r}{R_c + R_r} \right] k = 2\lambda\sqrt{\kappa t}. \quad (9.45)$$

Re-arranging allows us to estimate the time required ( $t$ ) for a surface to cool to  $T_{\text{surf}}$ , if  $\lambda$  is known, from

$$t = \left\{ \left[ \left( \frac{T_h - T_a}{\varepsilon \sigma (T_{\text{surf}}^4 - T_a^4) + h_c (T_{\text{surf}} - T_a)} - \frac{R_c R_r}{R_c + R_r} \right) k \right] 1000 \frac{1}{2\lambda} \right\}^2 \frac{1}{\kappa}. \quad (9.46)$$

Using the lambda value given for basalt by Turcotte and Schubert (2002) of 0.421, after 60 s Equation (9.46) balances with a surface temperature of 558 °C (831 K). Our solution, for Kilauea, is,

$$R_c = \frac{1}{50} \text{ W m}^{-2} \text{K}^{-1} = 0.02 \text{ W m}^{-2} \text{K}^{-1},$$

$$R_r = \frac{(1273 \text{ K}) - (298 \text{ K})}{(0.98)(5.67 \times 10^{-8} \text{ W m}^{-2} \text{K}^{-4})[(831 \text{ K}^4) - (298 \text{ K}^4)]} = 0.037 \text{ W m}^{-2} \text{K}^{-1},$$

$$\begin{aligned} \epsilon\sigma(T_{\text{surf}}^4 - T_a^4) &= (0.98)(5.67 \times 10^{-8} \text{ W m}^{-2} \text{K}^{-4})[(831 \text{ K}^4) - (298 \text{ K}^4)] \\ &= 2.61 \times 10^4 \text{ W m}^{-2} \end{aligned}$$

and

$$h_c(T_{\text{surf}} - T_a) = (50 \text{ W m}^{-2} \text{K}^{-1})[(831 \text{ K}) - (298 \text{ K})] = 2.67 \times 10^4 \text{ W m}^{-2}$$

so that

$$\begin{aligned} y &= \left( \frac{(1273 \text{ K}) - (298 \text{ K})}{2.61 \times 10^4 \text{ W m}^{-2} + 2.67 \times 10^4 \text{ W m}^{-2}} - \frac{(0.02 \text{ W m}^{-2} \text{K}^{-1})(0.037 \text{ W m}^{-2} \text{K}^{-1})}{(0.02 \text{ W m}^{-2} \text{K}^{-1}) + (0.037 \text{ W m}^{-2} \text{K}^{-1})} \right) k \\ &= [(0.0185 \text{ W m}^{-2} \text{K}^{-1}) - (0.013 \text{ W m}^{-2} \text{K}^{-1})](1 \text{ W m}^{-1} \text{K}^{-1}) = 0.0055 \text{ m}. \end{aligned}$$

Now,

$$\begin{aligned} t &= \left[ (0.0055 \text{ m})(1000)(0.842)^{-1} \right]^2 \left[ 1/(0.7 \text{ mm}^2 \text{s}^{-1}) \right] = (42.7 \text{ mm}^2)(1.429 \text{ mm}^2 \text{s}^{-1}) \\ &= 61 \text{ s}. \end{aligned}$$

That is, it takes ~60 s for the surface to cool from 1000 °C to 558 °C under these thermal conditions. Solution at 60 s is consistent with the surface temperature predicted by the empirical relationship of Hon *et al.* (1994a) for Hawaiian pahoehoe which predicts 552 °C after 60 seconds. Solutions for other times, along with comparisons with field data and the results of application of the Hon *et al.* (1994a) relation, are given in Table 9.9. As plotted in Figure 9.31, these tests suggest that both the theoretical and empirical approaches can be used to estimate lava surface age (and crust thickness) from surface temperature to within a few minutes (mm for surface crust thickness), if the relation has been set correctly. Values used to set the relation for Kilauea are:

- thermal conductivity ( $k$ ): 1 W m<sup>-1</sup> K<sup>-1</sup>;
- starting temperature ( $T_h$ ): 1000 °C;
- emissivity ( $\epsilon$ ): 0.98;
- convective heat transfer coefficient ( $h_c$ ): 50 W m<sup>-2</sup> K<sup>-1</sup>;
- thermal diffusivity ( $\kappa$ ): 0.7 mm<sup>2</sup> s<sup>-1</sup>;
- ambient temperature ( $T_a$ ): 25 °C;
- *lambda* ( $\lambda$ ): 0.421.

Table 9.9. Comparison of lava surface temperatures measured for a cooling pahoehoe lobe during 40 minutes of surface cooling, with those predicted by (1) the relation of Hon et al. (1994a), and (2) the Equation (9.46) model.

Time (s)	$T_{\text{surf}}$ (°C): Measured	$T_{\text{surf}}$ (°C): Hon et al. (1994a)	$T_{\text{surf}}$ (°C): Eqn (9.46) model
1	825	801	801
10	614	661	674
20	598	619	631
30	592	594	605
40	581	577	586
50	570	563	571
60	563	552	558
120	524	510	510
180	497	485	481
240	467	468	461
300	455	454	444
600	373	412	393
1200	335	370	342
1800	312	345	312
2400	304	328	292

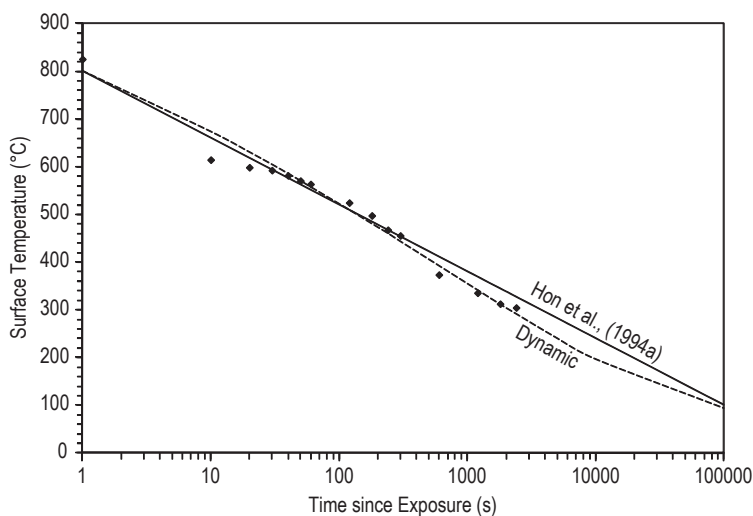


Figure 9.31 Thermal camera-derived surface temperature plotted as a function of time since exposure (diamonds), with the theoretical surface cooling relation of Equation (9.46), labeled “Dynamic,” and the empirical relation of Hon et al. (1994a). Data are for a cooling pahoehoe surface imaged at Kilauea in February 2004.

This provides a methodology by which lava surface temperature in a thermal image can be converted to age. Running the empirical relation of Hon *et al.* (1994a), or the theoretical relation of Equation (9.46), across an image on a pixel-by-pixel basis allows the surface temperature for each pixel to be converted to a time since the lava surface in that pixel was exposed to the atmosphere. We do this in Figure 9.32, where we convert the temperature map of the left hand image to the age map of the right hand image. Now, by summing the number of pixels within each age range, the aerial coverage at each time step can be obtained. By dividing the area covered during each time step ( $\Delta A$ ), by the duration of that time step ( $\Delta t$ ), areal coverage rate can be obtained, (i.e.,  $\Delta A / \Delta t$ ). For example,

- in the map of Figure 9.32, the surface area at temperatures greater than 300 °C is 2351 m<sup>2</sup>;
- this temperature converts to a time since exposure of 64 minutes, so that all lava within the threshold is younger than 64 minutes.
- areal coverage rate is thus 2351 m<sup>2</sup> / 64 minutes = 36.7 m<sup>2</sup> per minute over the last 64 minutes.

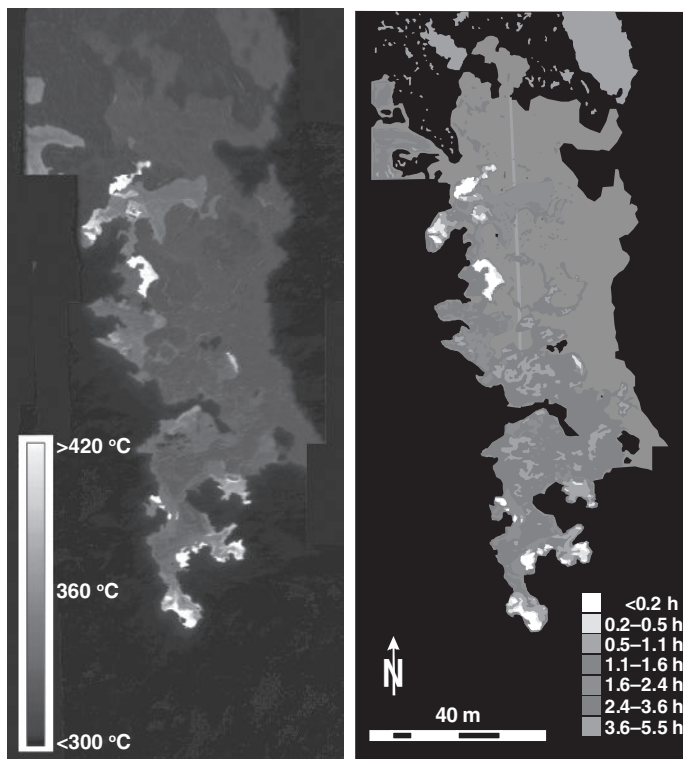


Figure 9.32 Thermal camera image mosaic of a pahoehoe lava flow active on Kilauea during 24 February 2006 (left) with derived surface age map (right). Images were acquired vertically from a helicopter hovering 750 m above the flow. The mosaic comprises five images [from Harris *et al.* (2007, Fig. 2): reproduced by permission of American Geophysical Union]. Surface temperatures have been converted to ages using the *surface age* methodology of Section 9.7.2.4 (i.e., Equation 9.46). See also color plates section.

## **9.8 Methodologies III: dimensional and volume/mass measurements**

As well as the thermal character of a targeted surface, a number of dimensional parameters can be quantified using hand-held thermal camera images. These dimensional measurements can be split into two groups:

- (i) basic dimensional measurements, such as length, width and height; and
- (ii) rates, such as velocity and spreading rate, which are derived from spatial or temporal changes in the basic dimensional measurements.

Because the dynamics and rates of plume ascent differ from the dynamics and velocities associated with motions at an active lava body, the measurements and methodologies applied differ between the two eruption styles (explosive versus effusive). In addition, the plume usually ascends in a vertical to near-vertical plane, whereas the lava body is emplaced on a surface that is closer to a horizontal plane. This also makes the plane of the dimensional measurement different in the two cases. Thus we consider measurements of lava bodies and explosion plumes separately.

### **9.8.1 Lava bodies**

The basic dimensional measurements that can be made using a hand-held thermal camera image of an active lava body are marked on [Figure 9.33](#) and include:

- location;
- distance and/or length;
- diameter, width and/or radius;
- perimeter length and/or area;
- direction and/or orientation; and
- height or level.

Direction or orientation may be defined by the long axis of the flow, or may be the angle of a straight line drawn between the source and the flow front. It may also include the orientation of components within the flow. In fact, all of these measurements can be applied to the parental feature, as well as component features within it. For example, the area of a lava lake can be measured, as can the dimensions and motions of plates of crust within the lake, or the width of a channel can be measured, as well as the width of the shear and plug zones within the channel, if they can be resolved.

In all cases, making the measurement is simple. Lines or regions of interest can be drawn, and their lengths or areas (in pixels) read off to define the required dimension. Multiplying the measurement in pixels by pixel dimension converts the measurement to units of meters. Distances can also be estimated by selecting two points that define the beginning and end of the segment to be measured. In the case where the line is horizontal or vertical, obtaining the line length involves a straightforward subtraction. Take, for example, the image of a lava flow active on the floor of Pu'u 'O'o crater taken using a ThermaCam S40 on 10 January 2004, as [Figure 9.33](#). The horizontal distance, L1, starts at  $x, y$  point 147,63 ( $x = 167, y = 63$ )

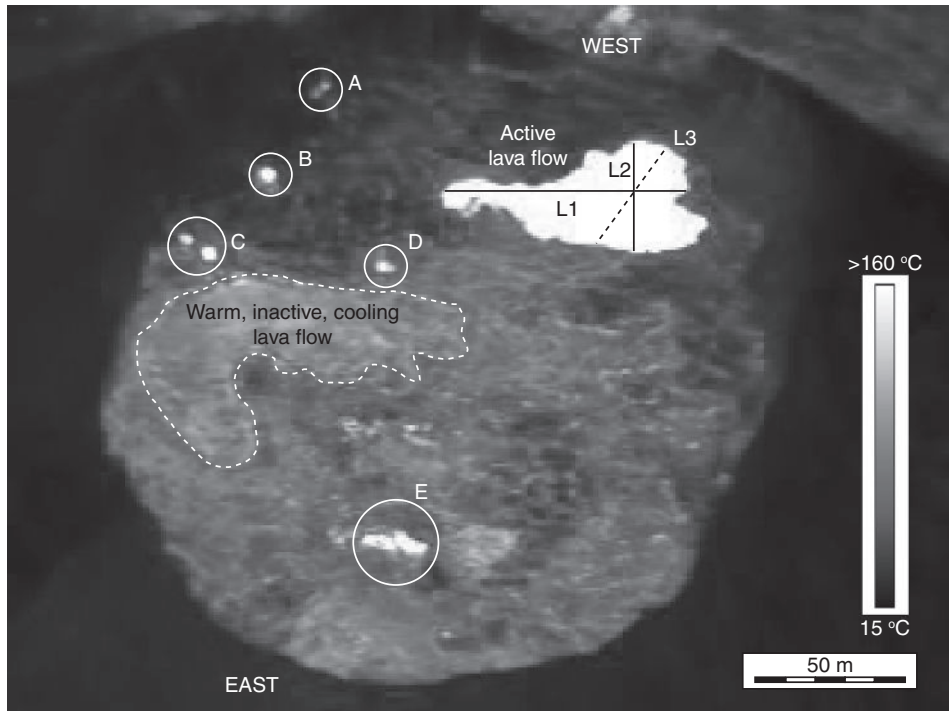


Figure 9.33 Oblique thermal camera image of the floor of Pu'u 'O'o crater (kilauea) obtained from a helicopter hovering 440 m above the surface, on 10 January 2004. Image contains an active pahoehoe lava flow, where the dimensions along the lines marked L1, L2 and L3 are calculated in the text. Also indicated, is the perimeter and area of a warm, inactive lava flow (dashed line), plus the location of eight hot vents (circled; labeled A through E). See also color plates section.

and ends at 227,63. It is thus  $227 - 147 = 80$  pixels long. Given a helicopter position  $\sim 440$  m above the surface and a downward-looking angle of  $45^\circ$ , the pixel dimension (calculated following Equation (9.17)) is approximately 1.15 m, so that the horizontal distance is 92 m. Vertical distance, L2, starts at  $x, y$  point 213,46, and ends at 213,84, so that this line is  $84 - 46 = 38$  pixels or  $\sim 44$  m long.

The distance for slant lines, such as L3 in Figure 9.33, can be obtained from the simple geometric relation

$$a^2 = b^2 + c^2.$$

Thus this line starts at  $x, y$  point 196, 81 and ends at 223, 50. These points define a right-angled triangle that has a horizontal base that is 27 pixels long, and a height of 31 pixels, meaning that the slant-line distance is

$$a^2 = (27 \text{ pixels})^2 + (31 \text{ pixels})^2 = \sqrt{1690} \text{ pixels},$$

so that slant distance  $a$  is 41 pixels or 47 m.

### 9.8.1.1 Rates

If measured on consecutive images, the dimensions listed above can be used to estimate a number of rates that characterize emplacement and motions at active lava bodies, including:

- change in location or position with time = velocity;
- change in distance and/or length with time = extension rate;
- change in diameter, width and/or radius with time = expansion rate;
- change in perimeter length and/or area with time = areal spreading rate;
- direction and/or orientation of movement = vector of movement;
- change in height or level = filling (or drainage) rate.

All values are obtained simply by subtracting the dimension measured on the current image from that obtained from the previous image and dividing by the time difference between the two images. For an object in motion, such as a piece of crust moving down a lava channel or across a lava lake surface, if the line of that motion is not orientated perfectly horizontally or vertically, then the difference in its  $x,y$  position in the current and previous image will have to be used in  $a^2 = b^2 + c^2$  to estimate the distance traveled by the object in the time between the two images. The bearing of that line will give the vector of the motion. The vector ( $\omega$ ) for Line 1 in [Figure 9.33](#), for example is  $90^\circ$ , that of line 2 is  $45^\circ$ , while line 3 is

$$\omega = \tan(\varpi) \frac{O}{A} = \tan(\varpi) \frac{31}{27} = \tan^{-1}(1.15) = 49^\circ.$$

An obvious application of vector analysis is in tracking the rates, styles and patterns of motion on a lava lake surface, or for the motions of objects in an explosion plume.

### 9.8.1.2 Discharge rates

One key parameter that can be extracted from thermal camera data is the volumetric rate of lava discharge in cubic meters per second, i.e., time-averaged discharge rate (*TADR*). There are three potential methods that can be applied to extract *TADR*. The first uses changes in the lava body dimensions to estimate the lava volume at two points in time. The difference in volume between the two measurements divided by the period of time separating the two measurements yields the volumetric rate of discharge time-averaged between the two measurement points. The second method uses measured dimensions and velocities to obtain the rate at which lava is flowing through a cross-section area, the result being the volume flux down a channel. The third method uses thermal data to apply the heat-budget-based mass and volume conversion methods of [Chapter 4](#) (see [Section 4.5](#)).

**(1) Dimensional approach** As with many field-based approaches that use mapped lava body area to convert to volume, the dimensional approach is the most straightforward to apply, but will likely involve a thickness assumption. It involves measuring feature area and

multiplying by thickness to obtain volume. If we can do this on two images of the same, growing feature, then the volume difference between the two images, divided by the time separating them, yields the discharge rate averaged over the period separating the two image acquisitions.

The problem is assuming a thickness. A reasonable range may have to be assumed, but this can induce significant error. In [Figure 9.33](#) we image a hot lava area that covers 2090 pixels. Given a pixel area of  $1.32 \text{ m}^2$  this converts to an area of  $2760 \text{ m}^2$ . However, what to assume for a thickness? A value of between 0.5 m and 3.0 m seems plausible for an inflating pahoehoe flow on Kilauea, but this yields a volume range of  $1380 \text{ m}^3$  to  $8280 \text{ m}^3$ . Given that the surface temperature is at least  $160^\circ\text{C}$ , the flow has been active for at least 10.5 hours (see the previous section for surface temperature to time-since-exposure conversion). This yields a *TADR* over this period of  $0.04\text{--}0.2 \text{ m}^3 \text{ s}^{-1}$ . This is an uncertainty of  $\pm 71\%$ . Thus, fixing a plausible and narrow thickness value is the key to this approach.

Where we have a level marker, the problem is solved. We could also make an independent measurement of flow thickness in the field, but it is sometimes difficult to apply a single thickness to an entire lava flow unit. One method attempted on Kilauea by Harris *et al.* ([2007](#)) used the predictable cooling and inflation properties of Hawaiian pahoehoe to obtain a series of discharge rates from a single image. This was done as follows.

- (1) Take the thermal camera image, and convert each pixel temperature to an age following the methodology of [Section 9.7.2.4](#).
- (2) For each pixel, use the age ( $t$  in hours) to estimate the lava thickness ( $H$  in meters) using the empirically-derived relationship between thickness and time for an inflating pahoehoe flow of Hon *et al.* ([1994a](#)):

$$H = 0.649 t^{0.217}. \quad (9.47)$$

- (3) Multiply pixel area by  $H$  to obtain the volume of lava in each pixel.
- (4) Define a series of time periods and sum the pixel volumes for each time period to obtain the volume emplaced during each period.
- (5) Divide by the duration of the period to obtain the discharge rate time-averaged over each period.

Results from applying this methodology to the image of [Figure 9.32](#) are given and explained in [Table 9.10](#). For our  $2760 \text{ m}^2$  lava flow in the Pu'u 'O'o image of [Figure 9.33](#) the probable emplacement time (10.5 h) yields a thickness of 1.1 m, narrowing down the probable time-averaged discharge rate to

$$TADR = [(2760 \text{ m}^2)(1.1 \text{ m})]/[(10.5 \text{ h})(60 \text{ min})(60 \text{ s})] = 0.08 \text{ m}^3 \text{ s}^{-1}.$$

- (2) Cross-sectional area and velocity** This methodology works best when thermal video is obtained from lava flowing in a conduit of fixed and measurable dimensions, such as a channel or tube. The methodology involves the following steps.

Table 9.10. Temperature threshold applied to the image of Figure 9.32. Each threshold is converted to a time required to cool the surface to the given temperature, following the methodology of [Section 9.7.2.4](#). This is then used to estimate spreading rate and TADR.

Threshold (°C)	Time (h)	Time (min)	Step (min)	Cumulative area (m <sup>2</sup> )	New area (m <sup>2</sup> )	Areal spreading rate (m <sup>2</sup> min <sup>-1</sup> )	Thickness (m)	Volume (m <sup>3</sup> )	Eruption rate (m <sup>3</sup> s <sup>-1</sup> )	TADR (m <sup>3</sup> s <sup>-1</sup> )
425	0.137	8.2	8.2	211	96	35	0.42	89	0.18	0.3
400	0.207	12.4	7.5	365	154	37	0.46	168	0.23	0.3
375	0.311	18.7	11.2	588	223	35	0.50	296	0.26	0.3
350	0.469	28.2	17.0	934	346	37	0.55	514	0.30	0.4
325	0.707	42.4	25.4	1463	529	37	0.60	881	0.35	0.4
300	1.066	63.9	38.5	2351	888	41	0.66	1547	0.40	0.5

#### Explanation

- (1) The area within each temperature threshold is given as “cumulative area”; it is cumulative because as the threshold becomes cooler new lava, plus the lava included in the previous, hotter threshold, is added.
- (2) The area added during each time window is obtained from subtracting the current cumulative area from the previous cumulative area, and is given as “new area.”
- (3) The areal spreading rate for each time step is obtained by dividing the new area by the duration of the time step.
- (4) Thickness is calculated using the threshold temperature in Equation (9.47) and multiplying by the cumulative area to yield the volume emplaced since time zero (i.e., this works off of cumulative area and so is a cumulative volume).
- (5) By dividing each cumulative volume by the elapsed time (as given in columns 2 and 3) we obtain the eruption rate.
- (6) By calculating the new volume added in each step, and dividing by the duration of that step (column 4) we obtain the discharge rate time-averaged over each step duration.

- (1) Estimate the velocity of the lava surface by the transit time of cool clots of crust moving down a channel length of known distance.
- (2) Convert the velocity to a mean velocity by multiplying by 0.67. Note that flow velocity will increase from a minimum at the conduit margin to a maximum at the flow center, with the mean velocity being two-thirds of the maximum velocity. At an active lava channel, the easiest approach is to measure the center-line velocity, this being the maximum velocity ( $v_{\max}$ ). Thus, if maximum (center-line) velocity has been measured, this will have to be reduced by one-third to obtain mean velocity (see Calvari *et al.* (2003)).
- (3) Measure the channel width from the image, and estimate the depth. Depth may be measured in the field (e.g., by pushing a length of rebar into the flow until the base is encountered) or by making a shape assumption (e.g., assume that the flow is semi-circular so that radius = depth, or square so that diameter = depth). Level changes apparent in the thermal imagery can then be used to update the depth measurement.
- (4) Use the shape assumption, and measured channel dimensions, to estimate the cross-sectional area of flow ( $A_{\text{cross}}$ ).
- (5) Multiply by the mean velocity to obtain bulk effusion rate.

Thus the instantaneous bulk (lava and bubbles) volume flux ( $E_{\text{bulk}}$ ) can be obtained from:

$$E_{\text{bulk}} = 0.67 (v_{\max} A_{\text{cross}}) \quad (9.48a)$$

in which, for a semi-circular channel,

$$A_{\text{cross}} = \pi r^2, \quad (9.48b)$$

$r$  being the channel radius.

**(3) Heat flux approach** This approach is based on that commonly applied to satellite thermal data, as detailed in [Section 4.5 of Chapter 4](#). As argued in [Chapter 4](#), this approach reduces to an empirical relation between active flow area and discharge rate. That is, active flow area is assumed to increase linearly with discharge rate. We tested this methodology using thermal camera data acquired during daily surveillance flights over Stromboli's active lava flow field during May and June 2003. The methodology was described by Harris *et al.* ([2005c](#)). It was applied as follows:

- (1) identify all pixels containing active lava;
- (2) for those pixels, use the pixel temperature to calculate the heat flux densities:  $M_{\text{rad}}$  and  $M_{\text{conv}}$ ;
- (3) convert to pixel heat flux ( $\Phi_{\text{rad}}$  and  $\Phi_{\text{conv}}$ ) by multiplying each heat flux density by pixel area;
- (4) sum  $\Phi_{\text{rad}}$  and  $\Phi_{\text{conv}}$  for all pixels to yield the total heat flux ( $\Phi_{\text{tot}}$ ) from all active lava zones;
- (5) use this in the relation  $TADR = x \Phi_{\text{tot}}$  to convert to discharge rate.

Because of uncertainty in setting the  $TADR = x \Phi_{\text{tot}}$  relation,  $TADRs$  were obtained using two end-member relations to output upper and lower bounds on the probable  $TADR$  range. For this case, the relations

$$TADR(\text{min}) = 2 \times 10^{-9} \text{ m}^3 \text{J}^{-1} \Phi_{\text{tot}} \quad (9.49\text{a})$$

$$TADR(\text{max}) = 1 \times 10^{-9} \text{ m}^3 \text{J}^{-1} \Phi_{\text{tot}}, \quad (9.49\text{b})$$

yielded  $TADRs$  that were in agreement with independent measurements.  $TADR$  output using these relations were compared to  $TADRs$  estimated from channel dimensions and flow velocity. Measurements made on 31 May 2003 gave a dimensionally derived  $TADR$ , i.e.,  $TADR$  based on channel cross-sectional area and velocity, in the range  $0.14\text{--}1.6 \text{ m}^3 \text{s}^{-1}$  (mid-point =  $0.87 \text{ m}^3 \text{s}^{-1}$ ). This compared with a range of  $0.23\text{--}0.87 \text{ m}^3 \text{s}^{-1}$  (mid-point =  $0.55 \text{ m}^3 \text{s}^{-1}$ ) obtained from this heat-flux-based approach.

### **9.8.2 Explosion plumes**

The basic dimensional measurements that can be extracted from a thermal camera image of an ascending plume of bombs, ash and/or aerosols are marked on [Figure 9.26b](#). These include:

- location of emission;
- plume height;
- plume diameter, width and/or radius;
- plume (vertical) plan area;
- direction and/or orientation of emission (vertical, lateral, directed or bent-over);
- spreading angle.

As at a lava body, these measurements may apply to the parental plume, as well as to components within it. For example, we may be able to measure the height and diameter of the plume front, as well as the width, height and orientation of its feeder plume and any identifiable large particles within that plume (such as individual blocks or bombs). As with a lava body, such measurements are also easy to make, simply involving:

- (1) drawing a line that defines the dimension to be measured;
- (2) summing the number of pixels that fall along that line;
- (3) multiplying by pixel dimension to convert the line distance to the required dimension in units of meters.

#### *9.8.2.1 Rates*

If measured on consecutive images, or at different points in the plume, the dimensions listed above can be used to estimate a number of rates that characterize plume ascent. These include:

- change in plume front location or position with time = plume front velocity;
- change in particle location or position with time = particle velocity;

- change in diameter, width and/or radius with height = spreading rate;
- change in diameter, width and/or radius with time = lateral spreading velocity;
- direction and/or orientation of movement = vector of movement.

The spatial and temporal resolution provided by the thermal camera means that such rate-based measurements can be made to a high degree of temporal and/or spatial precision. For example, [Figure 9.34](#) gives plume front location (height), diameter, and temperature as extracted from thermal video collected at a rate of 30 Hz for 25 explosive emissions at Santiaguito (Guatemala). Measurements were made every 10 m over a 900 m-long line centered on the plume axis. In the bottom panels each of the dimensions have been converted to their associated rates. This is achieved by dividing the dimension by the time increment between each image, so that the height plot converts to plume front ascent velocity, the plume front diameter plot converts to lateral spreading velocity, and the temperature plot converts to cooling rate per unit time.

Rates that rely on time (such as velocity) can thus be obtained by subtracting the dimension measured on the current image from that obtained on the previous image and dividing by the time difference between the two images. For those rates that rely on change in dimension with height (such as spreading), the same dimension can be measured at a series of heights and the difference in the measurement between each step in height divided by the step distance to obtain the rate of change (in units of  $\text{m}^{-1}$ ).

In ballistic plumes, it is particularly easy to use the thermal video to track individual particles. Tracking is a simple task which involves following a particle from image to image and noting its coordinates in each image. In this way we can define the ballistic trajectory, launch angle, velocity, height and range. Most particles will likely not move perfectly horizontally or vertically, so that application of the  $a^2 = b^2 + c^2$  geometry is particularly important to extract distance traveled from one image to the next. Take, for example, the following particle identified exiting the vent in a thermal video sequence for the onset of an explosion at Stromboli. In the first frame its  $x,y$  location is 197, 201. By the time of the next frame it is at point 199,181. Thus, it has moved a vertical ( $y$ -dimension) distance of 20 pixels, and a horizontal ( $x$ -dimension) distance of two pixels. Thus the slant line distance traveled by the particle is

$$a^2 = (2 \text{ pixels})^2 + (20 \text{ pixels})^2, \quad \text{so that } a = \sqrt{404} \text{ pixels},$$

giving a travel distance of 20.1 pixels. The camera was pointed face-on to the plume over a distance of 450 m. Thus we can apply the simple geometry of [Equation \(9.15\)](#) so that a 1.3 mrad IFOV yields a pixel that is 58.5 cm across. The pixel distance traveled by the ballistic thus converts to 11.76 m. The time difference between the two images, 0.066 s, can now be used to define the particle velocity from

$$11.76 \text{ m}/0.066 \text{ s} = 178 \text{ m s}^{-1}.$$

Repeating this process while tracking the particle or plume front allows profiles of velocity with height to be generated for the ascending particle or plume.

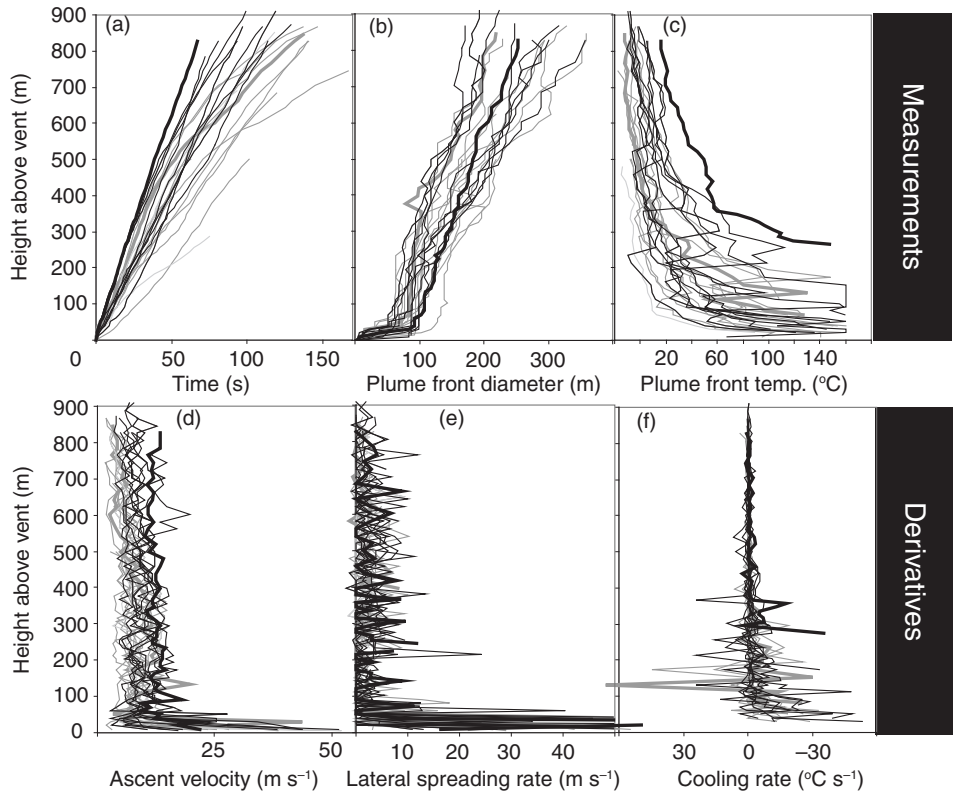


Figure 9.34 Plume front parameters as measured using thermal video of plumes ascending above Santiguito's Caliente vent during January 2005. The top line of plots gives the measurements, i.e., (a) plume front position with time, (b) plume front radius, and (c) plume front apparent temperature (all plotted versus height). The bottom line gives the first order derivative of parameters given in (a) to (c), respectively, i.e., (d) plume front ascent rate, (e) lateral spreading rate and (f) cooling rate [from Sahetapy-Engel and Harris (2009, Fig. 2): with kind permission from Springer Science and Business Media].

It must be noted, though, that this approach assumes that the particle is moving in the image plane, which it probably isn't. The 2D projection is only a constraint on the 3D motion of the particle, so that the extracted velocity is also only a constraint. This is a very important issue with quantitative measurements of particle motion in images, requiring stereo-imaging techniques to resolve.

#### 9.8.2.2 Entrainment, spreading and plume form

The rate of entrainment of air into the plume is typically expressed by an equation with the form:

$$\frac{dm_a}{dt} = A u_v \epsilon \rho_{\text{air}}, \quad (9.50)$$

in which

- $dm_a/dt$  = the mass flux of air into the plume;
- $A$  = the entrainment surface area;
- $u_v$  = the bulk upward velocity;
- $\varepsilon$  = the entrainment coefficient;
- $\rho_{\text{air}}$  = the density of air.

Of these variables,  $A$  and  $u_v$  can be calculated quite easily from the thermal image (see preceding sections).

The air entrainment coefficient can also be estimated from thermal image data following the method of Patrick (2007). Air entrainment directly controls the lateral spreading rate of the plume: the spreading angle increases with the degree of air entrainment. The degree of entrainment is thus also related to plume shape, with discrete thermals having much greater spreading angles, and thus experiencing much greater degrees of air entrainment, than jets. Patrick (2007) thus chose to use his thermal camera data for ascending ash plumes at Stromboli to define the spreading properties of the plume and solve for the entrainment coefficient by applying the following, plume-form-dependent, equations of Morton (1956) and Turner (1962, 1973):

$$\text{jet} \quad \frac{db}{dh} = 2\varepsilon \quad (9.51\text{a})$$

$$\text{steady (buoyant) plume} \quad \frac{db}{dh} = \frac{6}{5}\varepsilon \quad (9.51\text{b})$$

$$\text{discrete thermal} \quad \frac{db}{dh} = \varepsilon. \quad (9.51\text{c})$$

In these equations  $b$  is the plume radius and  $h$  is the height at which the radius measurement is made, so that  $db/dh$  is the degree of spreading per unit height. The measured radius will be a “top hat” measurement, top hat measurements being ones that assume all plume properties, such as velocity, temperature and density, to be constant across the plume, so that they can be described by a single bulk value. This compares with Gaussian models in which velocity is assumed to decay in a Gaussian fashion around a maximum value at the plume center. The models of Equations (9.51a – c) are for a top hat situation. As Patrick (2007) points out, the visible radius ( $r$ ) measured from the thermal imagery will not equal the Gaussian radius ( $R$ ) or top hat radius ( $b$ ) used by Equations (9.51a – c). Thus Patrick first converted his measured radii to Gaussian radii following the conversion of Turner (1962), this being:

$$\text{for thermals} \quad R = 0.63r \quad (9.52\text{a})$$

$$\text{for steady plumes} \quad R = 0.5r. \quad (9.52\text{b})$$

The Gaussian radii were then converted to top hat radii following a second conversion given by Turner (1973), this being:

$$b = \sqrt{2}R. \quad (9.53)$$

Combining these two steps allowed the top hat radius ( $b$ ) to be obtained directly from the measured radius ( $r$ ) following:

$$\text{for thermals} \quad b = 0.9r \quad (9.54\text{a})$$

$$\text{for steady plumes} \quad b = 0.71r. \quad (9.54\text{b})$$

Now, given variations in the plume radii with height for both the plume front (a thermal) and the feeder plume (a steady plume), Patrick (2007) converted his visual spreading rates ( $dr/dh$ ) to top hat equivalent spreading rates ( $db/dh$ ) to solve Equations (9.51a – c), obtaining typical entrainment rates of

- 0.06 (for jets);
- 0.07 (for steady, buoyant plumes);
- 0.12 (for thermals at the plume front with velocities greater than  $15 \text{ m s}^{-1}$ );
- 0.22 (for thermals at the plume front with velocities less than  $15 \text{ m s}^{-1}$ ).

The *Journal of Geophysical Research* paper of Patrick (2007) from which this methodology is taken currently serves as a manual for application of those measurements that need to be, and can be, made using thermal camera imagery for ascending plumes. It can also be used as a guide as to how the thermal camera-derived plume data can be analyzed, applied and plotted to define, quantify and interpret plume dynamics.

#### 9.8.2.3 Volume and mass fluxes

As with estimation of discharge rates at lava flows, a number of methodologies are available that allow the volume or mass flux of material exiting the vent, or involved in an explosive emission, to be calculated. There are three potential methodologies that can be applied to extract the volume or mass exiting the vent. The first method uses the plume dimensions to estimate the plume volume and, by dividing by the duration of emission, yields the flux. The second method uses measured plume dimensions and ascent or vent exit velocities to obtain the flux of material through a defined cross-section. The third method uses the thermal data to apply the heat budget-based mass and volume conversion methods of Chapter 4. Two further methodologies are available to convert volumetric flux measurements to mass fluxes, one being thermally based, the other being based on the plume dynamics.

**(1) Dimensional approach** The dimensional approach involves measuring the volume of the entire plume, and dividing by emission duration to obtain volume flux. This will give the

bulk volume and volume flux for all components of the plume, including ash, bombs, gas and any entrained air. Patrick (2005) provides such a dimensionally based approach in Chapter 4, *Automated analysis of small volcanic explosions using thermal (FLIR) imagery*, of his PhD dissertation. This method involves a four-step process, as follows.

- Step 1. Generate a background image during a plume-free period. Any change over this background image will be due to injection of new material into the field of view, so that extraction of the plume area in the plume image can be achieved by subtracting the background image and running a simple threshold across the result.
- Step 2. Divide the extracted plume area into slices of thickness  $h_{\text{slice}}$  and radius  $r_{\text{slice}}$ , assume radial symmetry and estimate the volume of each slice from  $h_{\text{slice}} \pi r_{\text{slice}}^2$ . Now the volumes of all slices can be summed to obtain total plume volume.
- Step 3. Summing plume volumes obtained from all images will lead to a massive degree of double counting as the same slice is considered multiple times. Thus, following the image processing approach of Ripepe *et al.* (1993), we can take the maximum value obtained from any single frame during the emission and assume that it approximates the total plume volume.
- Step 4. Divide by emission duration to obtain the volume flux time-averaged over the duration of the emission.

#### 9.8.2.4 Conversion to mass

Conversion to mass can be achieved by solving, for each slice, the heat budget for the slice. The total heat in the combined mass of air, gas and ash comprising the plume ( $m_{\text{final}}$ ) should equal the heat originally supplied by the mass of gas and ash at their initial temperatures ( $m_{\text{initial}}$ ), so that

$$m_{\text{final}} = m_{\text{initial}} \quad (9.55\text{a})$$

$$[m_{\text{air}}c_{\text{air}} + m_{\text{ash}}c_{\text{ash}} + m_{\text{gas}}c_{\text{gas}}]\Delta T_{\text{bulk}} = m_{\text{ash}}c_{\text{ash}}\Delta T_{\text{ash}} + m_{\text{gas}}c_{\text{gas}}\Delta T_{\text{gas}}. \quad (9.55\text{b})$$

Here,

- $m_{\text{ash}}$ ,  $m_{\text{air}}$  and  $m_{\text{gas}}$  are the respective masses of ash, air and gas comprising the plume;
- $c_{\text{ash}}$ ,  $c_{\text{air}}$  and  $c_{\text{gas}}$  are the respective specific heat values for the same parameters;
- $\Delta T_{\text{bulk}}$  is the bulk temperature of the slice above background;
- $\Delta T_{\text{ash}}$  and  $\Delta T_{\text{gas}}$  are the respective initial temperatures of the ash and gas components.

There are rather too many unknowns in Equations (9.55a,b). However, if we assume the plume is ash-and-air dominated we can solve to provide an end member solution using the balance,

$$[m_{\text{air}}c_{\text{air}} + m_{\text{ash}}c_{\text{ash}}]\Delta T_{\text{bulk}} = m_{\text{ash}}c_{\text{ash}}\Delta T_{\text{ash}}. \quad (9.56\text{a})$$

By rearranging this simplified balance we can isolate the ash mass ( $m_{\text{ash}}$ ), i.e.,

$$m_{\text{air}}c_{\text{air}}\Delta T_{\text{bulk}} = m_{\text{ash}}[c_{\text{ash}}\Delta T_{\text{ash}} - c_{\text{ash}}\Delta T_{\text{bulk}}] \quad (9.56\text{b})$$

so that

$$m_{\text{ash}} = \frac{m_{\text{air}}c_{\text{air}}\Delta T_{\text{bulk}}}{c_{\text{ash}}(\Delta T_{\text{ash}} - \Delta T_{\text{bulk}})}. \quad (9.56\text{c})$$

To solve this equation, air mass ( $m_{\text{air}}$ ) can be estimated from the volume of each slice, multiplied by the air density ( $\rho_{\text{air}}$ ), so that

$$m_{\text{air}} = \rho_{\text{air}}[\pi r_{\text{slice}}^2 h_{\text{slice}}]. \quad (9.56\text{d})$$

Now the mass of each slice can be plotted with height, summed over the entire plume to obtain total mass in the image, or summed across the various component plume parts to obtain, for example, the mass of the feeder plume versus the mass of the thermal at the plume leading edge.

Take, for example, a jet of 19 m radius with a leading edge 130 m above the vent. Given a horizontal line of sight distance of 450 m onto the vertically orientated jet and an IFOV of 1.3 mrad, then the pixel dimension is 0.585 m, so that we can divide the jet into 222 slices, each with a thickness of 0.585 m. For this case,

$$m_{\text{air}} = (1.05 \text{ kg m}^{-3})[\pi(19 \text{ m}^2)(0.585 \text{ m})] = (1.05 \text{ kg m}^{-3})(663.5 \text{ m}^3) = 697 \text{ kg}$$

so that, given a plume bulk temperature of 70 °C against an ambient air temperature at 0 °C, we have

$$m_{\text{ash}} = \frac{(697 \text{ kg})(1000 \text{ J kg}^{-1}\text{K}^{-1})(70 \text{ K})}{(1100 \text{ J kg}^{-1}\text{K}^{-1})[(1000 \text{ K}) - (70 \text{ K})]} = 47.7 \text{ kg}.$$

That is, our slice contains ~ 48 kg of ash. If all slices that comprise the jet are of the same dimension and temperature, then the slices sum to a total mass of (222 slices × 47.7 kg per slice =)  $10.6 \times 10^3$  kg, this being the mass of ash in the jet. If dimension and/or temperature is changing with height, then the mass will have to be calculated separately for each slice.

#### 9.8.2.5 Gas-only

A similar methodology was given by Matsushima (2005) who used the heat balance approach to estimate the gas flux for plumes comprising solely gas. The key equation in the Matsushima (2005) method relates the mass flow rate of saturated water vapor in the plume ( $m_{\text{plume}}^{\text{w,v}}$ ) to the thermal-camera-derived upward velocity, radius and temperature of the plume in,

$$m_{\text{plume}}^{\text{w,v}} = \frac{e_{\text{plume}}^{\text{w,v}} u \pi r^2}{R_{\text{w,v}} T_{\text{plume}}}, \quad (9.57)$$

in which

- $e_{\text{plume}}^{\text{w,v}}$  is the saturation vapor pressure (i.e.,  $e_s$ , Chapter 4);
- $u$  is the upward velocity;
- $r$  is the plume radius;
- $R_{\text{w,v}}$  is the specific gas constant of water vapor ( $461.5 \text{ J kg}^{-1} \text{ K}^{-1}$ );
- $T_{\text{plume}}$  is the plume temperature.

A widely used empirical expression to obtain saturation vapor pressure from temperature has already been given in Chapter 4 (Section 4.4.1.12) and is given as,

$$e_s = c_1 \exp\left(\frac{a_1 T}{b_1 + T}\right) \quad (9.58)$$

in which the coefficients are,

- $a_1 = 17.625$
- $b_1 = 243.04 \text{ }^\circ\text{C}$
- $c_1 = 610.94 \text{ Pa}$ .

This allows air temperature to be converted to  $e_s$  with an error of less than 4% between  $-40 \text{ }^\circ\text{C}$  and  $+50 \text{ }^\circ\text{C}$  (Lawrence, 2005).

Given a gas plume temperature of  $18.9 \text{ }^\circ\text{C}$ , an ascent velocity of  $5.6 \text{ m s}^{-1}$  and a plume diameter of  $293 \text{ m}$ , these being the values derived from thermal camera data during degassing at Miyakejima by Matsushima (2005), we have,

$$e_s = (610.94 \text{ Pa}) \exp\left(\frac{(17.625)(18.9 \text{ }^\circ\text{C})}{(243.04 \text{ }^\circ\text{C}) + (18.9 \text{ }^\circ\text{C})}\right) = 2179 \text{ Pa}$$

so that

$$m_{\text{plume}}^{\text{w,v}} = \frac{(2179 \text{ Pa})(5.6 \text{ m s}^{-1})\pi(146.5)^2}{(461.5 \text{ J kg}^{-1} \text{ K}^{-1})(292 \text{ K})} = 6105 \text{ kg s}^{-1}.$$

This multiplies up to  $(6105 \text{ kg s}^{-1} \times 60 \text{ s} \times 60 \text{ min} \times 24 \text{ h}) = 5.27 \times 10^8 \text{ kg}$ , or 527 kilo-tons, of gas (in the form of water vapor) emitted each day.

It is important to note that this approach only works with optically thick plumes where we are actually measuring the temperature of the plume surface. Because of the potential for problems induced by the plume not being optically thick, so that the camera looks through the plume and does not give a correct plume surface temperature, it is important to compare results to other measurements, say through  $\text{SO}_2$  emission rates, and conversion to  $\text{H}_2\text{O}$  flux using the  $\text{SO}_2:\text{H}_2\text{O}$  ratio, as done by Witter *et al.* (2012). This needs to be done at least once to confirm that the results are reasonable.

**(2) Cross-sectional area and velocity** The cross-sectional area through which the ash–gas mixture is moving, multiplied by the velocity at which the mixture is moving, can be

used to estimate volume flux. Thus, if we know the vent geometry and the velocity at which the plume is exiting the vent, we can estimate the volume flux. Take, for example, a 2-m-radius vent and a plume exit velocity of  $178 \text{ m s}^{-1}$ . The volume flux for this moment is,

$$E_{\text{plume}} = (178 \text{ m s}^{-1}) [\pi(2 \text{ m})^2] = 2240 \text{ m}^3 \text{ s}^{-1}.$$

Integrating the flux through time yields the total volume erupted.

Again, this will be a volume flux for all plume components (ash, bombs and gas). However, because we are making the measurement at the vent, we may be able to assume there has been no air entrainment. Another advantage of this approach is that we have no double counting issues. Input parameters are also relatively simple to extract from the thermal imagery. A measurement of the plume radius at the source, for example, can be used to approximate the vent radius, and the exit velocity may be obtained from tracking features in the plume just above the vent. These can be particles or isotherms: a hot packet of material will, for example, have a characteristic temperature which can be tracked. Thus, as the packet ascends, its thermal signature will move. Obtaining the distance moved by a particular thermal structure between two images, as defined by the isotherms plotted for the plume surface, and dividing by the time difference between the two images, thus gives the velocity at which the feature with the given thermal signature is moving. This is the approach of Delle Donne and Ripepe (2012).

**(3) Heat flux approach** The heat flux approach can be applied to a hot deposit cooling on the ground. An example is given in [Figure 9.35a](#) where a hot deposit is emplaced around the vent by the explosion. If we track the cooling of this deposit with the thermal video, we can construct a cooling curve for each pixel, an example of which is given in [Figure 9.35b](#). This cooling curve is plotted in terms of temperature but, using the relations of [Chapter 4](#) ([Section 4.4](#)), it can be converted to heat flux. Now, following the principles laid out in [Section 4.5](#) of [Chapter 4](#), integrating the heat flux through time, to the point at which the deposit cools to ambient, can be used to estimate the total thermal energy released by the mass ( $E_{\text{th}}$ ) in cooling. This, in turn, can be squared with the mass of the body ( $m$ ) from

$$m = \frac{E_{\text{th}}}{c_p(T_{\text{dep}} - T_a)}, \quad (9.59)$$

in which  $c_p$  is the deposit heat capacity,  $T_{\text{dep}}$  is the deposit emplacement temperature and  $T_a$  is the ambient temperature. In the case of the [Figure 9.35](#) example, radiative and convective heat losses integrated through time for the single bomb tracked yield a total thermal energy released in cooling of  $0.43 \times 10^6 \text{ J}$ . This gives,

$$m = \frac{0.43 \times 10^6 \text{ J}}{(1510 \text{ J kg}^{-1} \text{ K}^{-1})[(1000 \text{ }^\circ\text{C}) - (25 \text{ }^\circ\text{C})]} = 0.29 \text{ kg}.$$

The total energy released by the entire deposit for this case was between 13.8 GJ and 16.1 GJ, so that for the entire deposit we obtain a mass of between

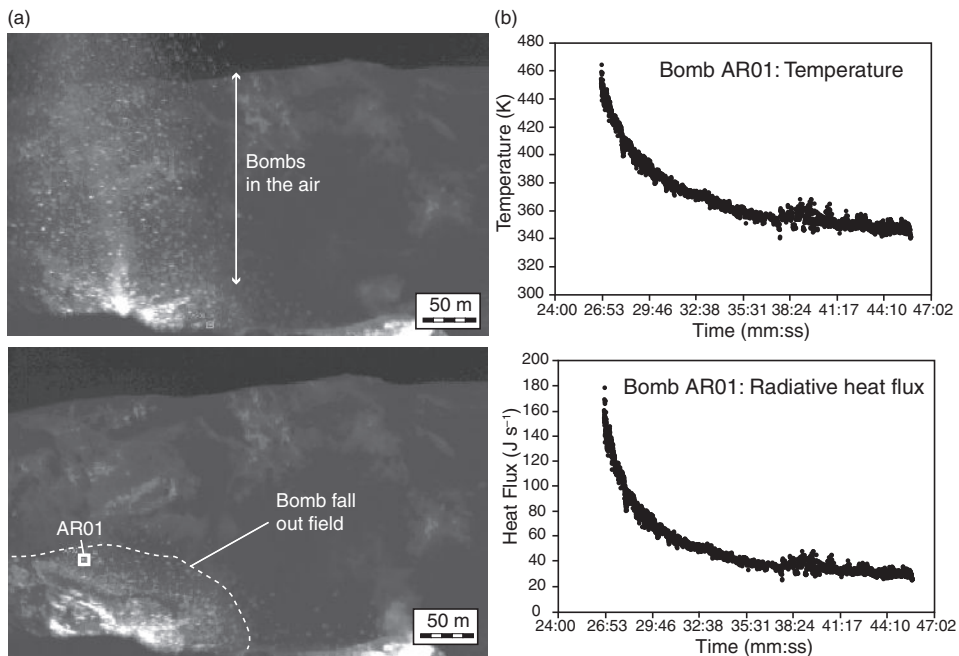


Figure 9.35 (a) Thermal camera image of a bomb-loaded (Type 1) eruption from Stromboli's SW Crater on 1 June 2008 (at 14:26:30 UTC) during (top) and after (bottom) the eruption. Bomb emission and cooling was imaged at 7.5 Hz, allowing bomb cooling to be tracked at the same frequency, as given in (b). The cooling curve recorded for the bomb marked AR01 in (a) is given in terms of pixel-integrated temperature (top) and converted to radiative heat flux (bottom). See also color plates section.

$$m = \frac{13.8 \times 10^9 \text{ J}}{(1510 \text{ J kg}^{-1} \text{ K}^{-1})[(1000 \text{ }^\circ\text{C}) - (25 \text{ }^\circ\text{C})]} = 9400 \text{ kg}$$

and

$$m = \frac{16.1 \times 10^9 \text{ J}}{(1510 \text{ J kg}^{-1} \text{ K}^{-1})[(1000 \text{ }^\circ\text{C}) - (25 \text{ }^\circ\text{C})]} = 10900 \text{ kg.}$$

Given that this deposit was entirely bombs with a typical density of  $1230 \text{ kg m}^{-3}$  this converts to a total erupted bomb volume of between  $7.6$  and  $8.9 \text{ m}^3$ . The total duration of the emission, as observed in the thermal video, was  $\sim 6$  s so that the mass flux of bombs time-averaged across the emission was between

$$9400 \text{ kg/6 s} = 1570 \text{ kg s}^{-1}$$

and

$$10\,900 \text{ kg}/6 \text{ s} = 1820 \text{ kg s}^{-1}.$$

**(4) Conversion of volume to mass using plume density** A number of the methodologies given above yield the plume volume or volume flux, when mass or mass flux may be required. In the first methodology the heat balance was used to convert the plume volume to a mass. However, the dynamics of the plume ascent, as recorded by the thermal camera, may also allow the plume bulk density to be estimated and used to convert the volume of the ascending thermal to a mass. The basis of this approach is the equation which relates the rise rate, due to buoyancy ( $u_b$ ), of a sphere, to its density ( $\rho_b$ ) and radius ( $r$ ),

$$u_b = \sqrt{-\frac{8r(\rho_b - \rho_a)g}{3\rho_a C}}, \quad (9.60)$$

in which:

- $r$  is the radius of thermal;
- $\rho_b$  is the bulk density of the thermal;
- $\rho_a$  is the density of the air through which the thermal is rising;
- $C$  is the drag coefficient, which has a value of 0.5 for a sphere.

Given that we can measure the rise rate and radius of an ascending thermal using the thermal camera, we can rearrange Equation (9.60) to solve for the density of the thermal, i.e.,

$$\rho_b = -\left(\frac{3\rho_a Cu_b^2}{8rg}\right) + \rho_a. \quad (9.61)$$

This can now be multiplied by the thermal camera-derived volume for the thermal to convert to mass. For example, take a thermal of radius 2 m ascending buoyantly at  $7 \text{ m s}^{-1}$ , this being one of the gas puffs of Table 8.3 of Chapter 8 (note velocities in Table 8.3 are for the at-vent, gas-thrust phase of ascent, not the phase of buoyant ascent). Using these measurements we obtain

$$\rho_b = -\left(\frac{3(1.18 \text{ kg m}^{-3})(0.5)(7 \text{ m s}^{-1})^2}{8(2 \text{ m})(9.8 \text{ m s}^{-2})}\right) + (1.18 \text{ kg m}^{-3}) = 0.63 \text{ kg m}^{-3}.$$

The volume of the thermal estimated from its plan area in thermal imagery was  $\sim 136 \text{ m}^3$ . Given a density of  $0.63 \text{ kg m}^{-3}$  this converts to a mass of 86 kg. Using the emission duration of this small burst (1.13 s) we obtain a mass flux, time averaged over the duration of the emission, of

$$86 \text{ kg}/1.13 \text{ s} = 76 \text{ kg s}^{-1}.$$

## 9.9 Surveillance and monitoring

Because of its ability to identify, track and measure active volcanic effusive and explosive phenomena, the hand-held thermal camera has become a widely used observatory tool. Instances of use of hand-held thermal cameras, typically operated during helicopter over-flights, to contribute to monitoring efforts actually predated the upswing in publications using thermal camera data in the volcanological literature that began around 2002. Kauahikaua *et al.* (2003) described how, beginning in 1993, the Hawaiian Volcano Observatory (HVO) used a hand-held thermal camera several times a year, from plane and helicopter, to map areas of active lava at Kilauea. The Alaska Volcano Observatory (AVO) purchased a ThermaCAM™ 595 in 2000, and Italy's Istituto Nazionale di Geofisica e Vulcanologia (INGV, Catania section) acquired a ThermaCAM™ 695 the following year. While AVO upgraded to a ThermaCAM™ S40 in 2003, INGV-Catania subsequently purchased at least two other cameras for portable (non-fixed) use. These have been used to aid in monitoring of all of Etna's eruptions since 2001. The INGV portable cameras were also deployed to track Stromboli's 2002–2003 and 2007 eruptive crises, as documented by Calvari *et al.* (2005) for the 2002–2003 eruption and by Calvari *et al.* (2010) for the 2007 eruption.

A thermal camera was deployed by the US Geological Survey's (USGS) Cascades Volcano Observatory (CVO) during 2004 to aid with monitoring of the eruptive crisis at Mt. St. Helens, results were presented at the AGU Fall meeting in San Francisco of the same year, and later documented by Schneider *et al.* (2008) in a USGS professional paper dedicated to the eruption. A thermal camera (initially the ThermaCAM™ S40 of the University of Hawaii) was used routinely by HVO for foot- and air-based surveillance on a weekly to daily basis beginning November 2007, where HVO currently maintains a ThermaCAM™ SC620. Since the beginning of this routine deployment at kilauea, results – in the form of stills and movies – have been regularly used to communicate eruptive events via HVO's public website, a website designed for public outreach and communication purposes. These postings have generated positive responses, one example being:<sup>2</sup>

I have been a regular visitor to your site and commend you on doing daily updates even when things are relatively quiet: it must get boring at times. However, you have really hit on something with this infrared camera. If it is new or just been sitting on the shelf it is a great addition and if not too costly to operate it goes a long way to telling someone like myself where to potentially expect more activity. I hope you can use it more often. Thank you.

Clearly the insightful, yet colorful and spectacular, images provided by a thermal camera are an effective means not just of surveillance, but also of communicating activity levels, styles and hazards, as well as the associated volcanic processes, to the general public, where HVO's website, currently at <http://hvo.wr.usgs.gov>, serves as a blueprint for such outreach efforts.

<sup>2</sup> Matthew Patrick and Tim Orr, written communication, 2008.

### 9.9.1 Permanent installations

Installation of permanently sited thermal cameras to aid in monitoring paralleled the growth in portable deployments to aid in observatory surveillance efforts. One of the first permanent thermal camera installations occurred in 2000. As described by Kaneko *et al.* (2002c), a Nikon thermal vision infrared camera was installed to track activity at Usu volcano in Japan, with imagery being transmitted in real time, and disseminated via the internet, for a few months following mid-April 2000.

In 2003, the Università di Firenze installed an Indigo Omega (see Table 9.1c) fixed-mount thermal camera on Stromboli. This has since been upgraded to a FLIR A20 (Maurizio Ripepe, written communication, December 2012). Data are transmitted in real time to the Civil Protection Operations Center on Stromboli (COA) on Stromboli, as well as on to offices in Rome and Florence, allowing activity to be viewed at frame rates of 4 Hz (Dario Delle Donne, written communication, December 2012). There have been a series of such installments at Italian volcanoes for surveillance purposes. Andò and Pecora (2006) describe installation of a FLIR 160M on Etna during 2002, as well as strategies to transmit, receive and view the data stream. Likewise, Vilardo *et al.* (2008) describe the set-up of two NEC Thermo Tracer TS7302 cameras, one at Solfatara (Campi Flegrei) and one on Vesuvius, in 2004. Lodato *et al.* (2008) then described installation and operation of a FLIR A40 at Vulcano in 2006, whose installation is pictured here in [Figure 9.22f](#).

As of July 2010, at least 11 thermal cameras had been installed permanently to aid in surveillance efforts at seven different volcanoes, these being the following:

- Stromboli: one camera operated by Università di Firenze, two by INGV-Catania;
- Vulcano: one camera operated by INGV-Catania;
- Etna: two cameras operated by INGV-Catania;
- Vesuvius: one camera operated by the Vesuvius Observatory, INGV-Naples;
- Solfatara: one camera operated by the Vesuvius Observatory, INGV-Naples;
- Montserrat (Soufriere Hills): one camera operated by Università di Firenze;
- Kilauea: four cameras operated by HVO (number as of April 2012).

The installation set-up and design for a permanently deployed thermal camera is essentially the same as that required for the permanently installed radiometer of [Chapter 7](#), and involves four components:

- (1) the camera, which needs to be adequately protected from adverse weather and gas conditions, housed in a pelican case, viewing through a selenium-germanium-arsenide window;
- (2) power supply (battery-hub linked to a solar panel array);
- (3) transmission, which needs to be capable of handling  $320 \times 240$  pixel images captured at rates of 1–2 Hz, meaning that data rates for 14 bit data have to be between 1 and 2 Mbits per second;
- (4) reception, which needs to include a facility to automatically enhance, display and archive the image stream, as well as allow basic and rapid image processing and parameter calculation for display, reporting and response purposes.

### 9.9.2 Use of low-cost, uncalibrated cameras

A permanently installed ground-based thermal monitoring system need not be expensive. If surveillance and checking of sizes and levels of activity is the priority, and the need for precise calibrated thermal data is secondary, then a number of low-cost options are available. For example, Saito *et al.* (2005) describe operation of a Sony digital camcorder (a DCR-PC120 or Handycam) to track a volcanic hot spot. The Handycam was used in both normal and nightshot modes to detect, track and measure “glow” at Aso volcano in Japan during 2001 and 2002. Use of such systems reduces camera prices to less than \$1000.

In addition a number of commercially available uncalibrated models are available for installation for civil surveillance purposes. Such cameras can be cheaper than calibrated thermal cameras, and provide streaming thermal video which can be used for interpretive and measurement purposes. Most models also allow pointing and zooming and come with control software which allows tilting, panning and zooming by the remote operator, as well as environmental protection (including windscreen wipers), as with Raytheon’s Nightsight 2000 thermal camera range, which were available for \$11 500. Likewise, the Bosch MIC 412 thermal camera series are capable of providing  $324 \times 256$  pixel images at  $7.5\text{--}13.5\text{ }\mu\text{m}$ . These cameras are built to conform with industrial, safety and weatherproofing standards, come with a control system, and cost \$28 800. Cheaper options include the ACTi’s KCM-5311 thermal camera, which has a  $35\times$  zoom, and is a two-Megapixel camera operating between  $0.7\text{ }\mu\text{m}$  and  $1.1\text{ }\mu\text{m}$  with a resolution of  $1920 \times 1080$  pixels, a frame rate of 15 fps and a cost of between \$742 and \$912.

Although not calibrated, the pixel sizes and FOVs of such low-cost cameras are still well-defined, allowing detection, interpretation and precise dimensional analysis of the targeted thermal features. Although data may not be calibrated, conversion of recorded pixel brightness to temperature may be possible. Saito *et al.* (2005) provide one methodology to allow conversion. This conversion involves making temperature measurements for a number of points apparent within the image for which differing brightness can be identified in the corresponding image. The relation between recorded brightness and in-situ temperature can then be used to set a brightness-to-temperature conversion through a best-fit relation between the two properties.

## 9.10 End note

The utility of hand-held thermal imaging to volcano science and surveillance has meant that the thermal camera has rapidly become a widely accepted and used tool in volcanology. Widespread use for surveillance, science and methodology development by the volcanological community has been witnessed by the take-off in thermal-camera-based publications over the past 10 years in the volcanological literature, the thermal camera library already exceeding 100 publications. A major advantage is that the IR perspective can often allow us to see through haze, fog and gassy conditions, allowing hot objects,

obscured by the path length conditions from the naked eye, to be resolved. To illustrate this capability, Holst (2000) gives an image of a sleeping woman in a smoke filled room (see Figure 18–7 of Holst (2000), p. 270). As a result, Williams (2009), in his book *Thermal Imaging Cameras*, points out that thermal cameras have proved “very useful” in fire fighting. The same can now also be said for volcano fighting, and the hand-held thermal camera can be placed next to the satellite-based sensor and radiometer in our thermal armory.

## Appendix A

### Collation and summary of satellite-volcano radiometry: a literature data base

The [Appendix A](#) data base considers journal-published articles that deal with satellite-based thermal data for the detection and analysis of active volcanic thermal phenomena (i.e., satellite-volcano radiometry). This collation considers all peer-reviewed literature until the end of 2005, but does not include conference abstracts, white papers, agency or survey reports, theses or review articles. [Table A1](#) gives the reference detail, a brief summary of each study content, and the volcano (or region) targeted by each study. [Table A2](#) identifies the feature type considered, satellite sensor used, key theme area addressed, and parameters extracted by each study. We identify five main theme areas which can be used to categorize all of the literature listed here, as follows.

- (1) Examination and demonstration of satellite sensor detection capabilities,
- (2) examination of mixed pixel issues, sub-pixel thermal structures, and application of the dual-band technique,
- (3) derivation of heat loss and erupted (effusive) mass or volume flux rates,
- (4) automated hot spot event detection, and
- (5) generation of eruption chronologies and time series analysis.

These themes can be linked to the generation of the following four parameters.

- (1) Quantitative assessment of detection capabilities and limits.
- (2) Surface thermal structure – i.e., number of thermal components characterizing a surface, their temperature and area.
- (3) Heat (radiative and convective) flux.
- (4) Lava discharge rate, lava volume and/or mass flux.

Summary graphs showing, for 1985 to 2005, annual number of publications, in total as well as broken up by sensor-type and theme, are given in [Chapter 1](#) ([Figure 1.4](#)). Here, for the same period, we also give the cumulative number of studies broken up by journal type ([Figure A1a](#)), feature type studied ([Figure A1b](#)) and main parameters extracted ([Figure A1c](#)).

Table A1. Data base of international (peer-reviewed) journal-published articles that deal with satellite-based thermal data for the detection and analysis of active volcanic thermal phenomena up until the end of 2005. Given in chronological order, the collation gives author, year and journal location for each contribution, summarizes the main themes addressed by each study, and lists the volcano (or region) targeted by each study.

Reference	Content	Volcanoes
Gawarecki <i>et al.</i> [Am. Astr. Soc., <b>4</b> , 1965]	Lava flow hot spot detection	Kilauea
Williams and Friedman [J. Br. Int. Soc., <b>23</b> , 1970]	Lava flow hot spot detection & heat flux	Surtsey
Brandli [PE&RS, <b>44</b> , 1978]	Lava flow detection	Kilauea
Wiesnet and D'Aguanno [Ant. J., 1982]	Lava lake hot spot detection	Erebus
Bonneville <i>et al.</i> [JVGR, <b>24</b> , 1985]	Low temperature anomalies	Etna
Scorer [Weather, <b>41</b> (12), 1986]	Lava flow hot spot detection	Etna
Bonneville and Kerr [J. Geodynamics, <b>7</b> , 1987]	Low temperature anomalies	Etna
Francis and Rothery [Geology, <b>15</b> , 1987]	Lava dome hot spot detection	Lascar
Rothery <i>et al.</i> [JGR, <b>98</b> (B7), 1988]	Thermal structures at active lavas	Lascar, Erta Ale, Erebus, Augustine and Sierra Negra
Glaze <i>et al.</i> [Nature, <b>338</b> , 1989]	Lava lake and dome heat loss	Lascar, Erebus, Erta Ale
Glaze <i>et al.</i> [BV, <b>51</b> , 1989]	Lava dome thermal structure	Lascar
Pieri <i>et al.</i> [Geology, <b>18</b> , 1990]	Lava flow effective temperature and heat loss	Etna
Rothery and Francis [IJRS, <b>11</b> (10), 1990]	Hot spot detection	Erebus
Abrams <i>et al.</i> [BV, <b>53</b> , 1991]	Lava dome thermal structure	Colima
Oppenheimer [JGR, <b>96</b> (B13), 1991]	Lava flow thermal structure and heat loss	Lonquimay
Oppenheimer and Rothery [J. Geol. Soc. Lond., <b>148</b> , 1991]	Volcano hot spot thermal structures	Stromboli, Masaya, Erebus, Vulcano
Bonneville and Gouze [GRL, <b>19</b> (7), 1992]	Low temperature anomalies	Etna
Rothery <i>et al.</i> [IJRS, <b>13</b> (15), 1992]	Hot spot detection	Etna
Bhattacharya <i>et al.</i> [PE&RS, <b>59</b> (8), 1993]	Lava flow thermal structure	Barren Island
Francis <i>et al.</i> [Nature, <b>366</b> , 1993]	Lava lake mass flux	Erta Ale
Gupta and Badarinath [IJRS, <b>14</b> (16), 1993]	Vent area and temperature	Barren Island
Oppenheimer [JVGR, <b>55</b> , 1993]	Crater lake area and temperature	Poas
Oppenheimer <i>et al.</i> [JVGR, <b>55</b> , 1993]	Thermal structures fumarole fields	Momotombo and Vulcano
Oppenheimer <i>et al.</i> [JGR, <b>98</b> (B3), 1993]	Lava dome extusion cycles	Lascar
Reddy <i>et al.</i> [IJRS, <b>14</b> (4), 1993]	Lava flow thermal structure	Barren Island
Flynn and Mouginis-Mark [BV, <b>56</b> , 1994]	Lava channel heat flux	Kilauea

Table A1. (cont.)

Reference	Content	Volcanoes
Flynn <i>et al.</i> [BV, 56, 1994]	Lava flow heat flux mapping	Kilauea
Gaonac'h <i>et al.</i> [JGR, 99, 1994]	Low temperature anomalies	Stromboli
Mouginis-Mark <i>et al.</i> [RSE, 48, 1994]	Lava flows	Kilauea
Rothery and Oppenheimer [AGU Res. Ser., 66, 1994]	Lava lake	Erebus
Andres and Rose [PE&RS, 61(6), 1995]	Lava dome and flow thermal structure	Santiaguito and Pacaya
Flynn and Mouginis-Mark [GRL, 22(19), 1995]	Lava versus fire radiance	Kilauea
Harris <i>et al.</i> [IJRS, 16(6), 1995]	Hot spot detection	Krafla
Harris <i>et al.</i> [IJRS, 16(18), 1995]	Hot spot detection	Etna
Harris <i>et al.</i> [IJRS, 16(1), 1995]	Hot spot detection	Krafla and Etna
Denniss <i>et al.</i> [IJRS, 17(11), 1996]	Lava dome and pyroclastic flow	Lascar
Oppenheimer [GRL, 23(14), 1996]	Crater lake heat loss	Poas, Ruapehu and Kawah Ijen
Harris and Stevenson [JVGR, 76, 1997]	Open vent & fumarole heat / mass flux	Vulcano and Stromboli
Harris <i>et al.</i> [BV, 59, 1997]	Hot spot detection	Etna, Krafla, Cerro Negro, Fogo, Lascar, Erebus
Harris <i>et al.</i> [JGR, 102(B4), 1997]	Lava flow field emplacement	Etna
Harris <i>et al.</i> [GRL, 24(24), 1997]	Hot spot chronology	Kilauea
Higgins and Harris [Comp & Geosci., 23(6), 1997]	Hot spot detection	Etna and Vulcano
Oppenheimer [IJRS, 18(1), 1997]	Crater lake temperature and color	Ruapehu-Taal-Kawah-Ijen-Kelut-Poas-Apoyeque-Jiloa
Oppenheimer and Francis [IJRS, 18(8), 1997]	Lava lake heat and mass flux	Erta Ale
Wooster <i>et al.</i> [GRL, 24(24), 1997]	Lava flow thermal budget and volume	Etna
Wooster and Rothery [RSE, 62, 1997]	Lava flow emplacement	Fernandina
Wooster and Rothery [BV, 58, 1997]	Lava dome extrusion cycles	Lascar
Dean <i>et al.</i> [EOS, 79(35), 1998]	Hot spot detection	Alaska & Aleutians
Denniss <i>et al.</i> [IJRS, 19(5), 1998]	PF and dome thermal structure/mapping	Lascar
Harris <i>et al.</i> [BV, 60, 1998]	Lava flow heat loss and effusion rate	Kilauea
Oppenheimer [IJRS, 19(1), 1998]	Hot spot detection	Ol Doinyo Lengai
Oppenheimer [IJRS, 19(15), 1998]	Hot spot detection	Kilauea, Etna and Erebus
Oppenheimer and Francis [JVGR, 80, 1998]	Lava lake heat and mass flux	Erta Ale

Table A1. (cont.)

Reference	Content	Volcanoes
Wooster and Kaneko [ <i>JGR</i> , <b>103</b> (B9), 1998]	Lava dome extrusion rates	Unzen
Wooster <i>et al.</i> [ <i>IJRS</i> , <b>19</b> (13), 1998]	Lava dome	Lascar
Wooster <i>et al.</i> [ <i>Adv. Space Res.</i> , <b>21</b> (3), 1998]	Lava dome	Galeras and Lascar
Harris and Thomsen [ <i>BV</i> , <b>61</b> , 1999]	Vent and flow activity and permanent video	Kilauea
Harris <i>et al.</i> [ <i>IJRS</i> , <b>20</b> (15–16), 1999]	Lava lake detection and mass flux	Erebus
Harris <i>et al.</i> [ <i>JGR</i> , <b>104</b> (B4), 1999]	Lava lake heat loss and mass flux	Erebus, Erta Ale, Pu'u 'O'o and Nyiragongo
Kaneko and Wooster [ <i>JVGR</i> , <b>89</b> , 1999]	Dome extrusion rates and gas fluxes	Unzen
Wright <i>et al.</i> [ <i>GRL</i> , <b>26</b> (12), 1999]	Simulated sensor response	Theoretical
Dehn <i>et al.</i> [ <i>Geology</i> , <b>28</b> (8), 2000]	Hot spot detection	Alaska and Aleutians
Carn and Oppenheimer [ <i>IJRS</i> , <b>21</b> (5), 2000]	Hot spot detection	Indonesia
Harris <i>et al.</i> [ <i>JVGR</i> , <b>102</b> , 2000]	Lava flow effusion rates (time series)	Etna, Krafla and Stromboli
Harris <i>et al.</i> [ <i>AGU Spec. Mon.</i> , <b>116</b> , 2000]	Hot spot detection	Pacific Rim
Mouginis-Mark <i>et al.</i> [ <i>BV</i> , <b>62</b> , 2000]	Hot spot chronology	Cerro Azul
Schneider <i>et al.</i> [ <i>AGU Spec. Mon.</i> , <b>116</b> , 2000]	Hot spot detection and chronology	Bezymianny
Urai [ <i>IJRS</i> , <b>21</b> (5), 2000]	Lava dome time series	Unzen
Wooster <i>et al.</i> [ <i>JVGR</i> , <b>102</b> , 2000]	Dome thermal structure/mapping	Unzen
Wright <i>et al.</i> [ <i>BV</i> , <b>62</b> , 2000]	Lava flow emplacement	Etna
Aries <i>et al.</i> [ <i>GRL</i> , <b>28</b> (9), 2001]	Hot spot detection	Etna and Krafla
Flynn <i>et al.</i> [ <i>RSE</i> , <b>78</b> , 2001]	Lava flow thermal structure	Kilauea and Etna
Harris <i>et al.</i> [ <i>IJRS</i> , <b>22</b> (6), 2001]	Hot spot detection	Kilauea
Roach <i>et al.</i> [ <i>BV</i> , <b>62</b> , 2001]	Hot spot time series & seismic monitoring	Pavlof
Rothery <i>et al.</i> [ <i>BV</i> , <b>63</b> , 2001]	Lava flow	Etna
Lachlan-Cope <i>et al.</i> [ <i>JVGR</i> , <b>112</b> , 2001]	Lava lake	Saunders Island
Pergola <i>et al.</i> [ <i>Ann. Geofisc.</i> , <b>44</b> , 2001]	Hot spot detection	Stromboli and Etna
Wooster [ <i>GRL</i> , <b>28</b> (5), 2001]	Lava dome extrusion cycles and PF cooling	Lascar
Wooster and Kaneko [ <i>JGR</i> , <b>106</b> (B7), 2001]	Solar reflection correction	Unzen
Wright <i>et al.</i> [ <i>BV</i> , <b>63</b> , 2001]	Lava flow emplacement	Etna
Wright <i>et al.</i> [ <i>EPSL</i> , <b>192</b> , 2001]	Effusion rates	Etna / theoretical
Dehn <i>et al.</i> [ <i>BV</i> , <b>64</b> , 2002]	Magma levels	Shishaldin

Table A1. (cont.)

Reference	Content	Volcanoes
Dean <i>et al.</i> [AEMM, 1(3), 2002]	Hot spot monitoring	Alaska and Aleutians
Flynn <i>et al.</i> [AEMM, 1(3), 2002]	Hot spot detection	Global
Galindo and Dominguez [JVGR, 117, 2002]	Lava dome	Colima
Harris and Neri [JVGR, 116, 2002]	Fountain-fed lava flows	Etna
Harris <i>et al.</i> [GSA Bull., 114(5), 2002]	Block lava flow thermal structure and heat loss	Santiaguito
Harris <i>et al.</i> [AEMM, 1(3), 2002a]	Hot spot detection	Pacific Rim
Harris <i>et al.</i> [AEMM, 1(3), 2002b]	Hot spot detection	Pacific Rim
Kaneko <i>et al.</i> [AEMM, 1(3), 2002]	Hot spot detection	Japan
Kaneko <i>et al.</i> [JVGR, 116, 2002]	Dome extrusion rates and heat flux	Unzen
Wright <i>et al.</i> [RSE, 82, 2002]	Hot spot detection	Global
Wright <i>et al.</i> [JGR, 107(B8), 2002]	Dome growth time series and RSAM	Popocatepetl
Galindo and Dominguez [AGU Mon., 139, 2003]	Lava dome thermal and seismic	Colima
Harris <i>et al.</i> [BV, 65, 2003]	Lava dome thermal structure and extrusion rate	Santiaguito
Patrick <i>et al.</i> [JVGR, 127, 2003]	Lava flow field emplacement	Okmok
Rowland <i>et al.</i> [BV, 65, 2002]	Lava flow field emplacement	Fernandina and Cerro Azul
Bello <i>et al.</i> [Analys Geophys., 47(1), 2004]	Lava flow – detection	Etna
Calder <i>et al.</i> [R. Geol. Chile, 31(2), 2004]	Lava lake activity and RSAM	Villarrica
Dean <i>et al.</i> [JVGR, 135, 2004]	Eruption chronology	Cleveland
Donegan and Flynn [JVGR, 135, 2004]	Lava flow thermal structures	Etna
Harris <i>et al.</i> [JVGR, 135, 2004]	Silicic lava flow emplacement	Santiaguito
Hellman and Ramsey [JVGR, 135, 2004]	Hot springs	Yellowstone
Lautze <i>et al.</i> [JVGR, 137, 2004]	Lava flow effusion rates (time series)	Etna
Lombardo <i>et al.</i> [JVGR, 134, 2004]	Lava flow, lake and vent thermal structure	Etna
Patrick <i>et al.</i> [JVGR, 131, 2004]	Heat loss for mud volcanoes	Copper River Basin Mud Volcanoes
Pergola <i>et al.</i> [RSE, 93, 2004]	Hot spot detection	Etna and Stromboli
Pieri and Adams [JVGR, 135, 2004]	Hot spot detection	Global
Ramsey and Dehn [JVGR, 135, 2004]	Hot spot detection	Bezymianny
Wright and Flynn [Geology, 32(3), 2004]	Volcanic heat flux inventory	Global
Wright <i>et al.</i> [JVGR, 135, 2004]	Hot spot detection	Global
Calvari <i>et al.</i> [JGR, 110, 2005]	Lava flow tracking	Stromboli
Kaneko and Wooster [JVGR, 148, 2005]	Lava flow cooling	Izu-Oshima

Table A1. (*cont.*)

Reference	Content	Volcanoes
Patrick <i>et al.</i> [ <i>JGR</i> , <b>110</b> , 2005]	Lava flow modeling	Okmok
Patrick <i>et al.</i> [ <i>BV</i> , <b>67</b> , 2005]	Hot spot chronology	Belinda
Pieri and Adrams [ <i>RSE</i> , <b>99</b> , 2005]	Hot spot preceding an eruption	Chikurachki
Ripepe <i>et al.</i> [ <i>Geology</i> , <b>33</b> , 2005]	Volume flux coupled infrasound-seismic-gas	Stromboli
Rothery <i>et al.</i> [ <i>BV</i> , <b>67</b> , 2005]	Hot spot activity patterns	Melanisa
Vaughan <i>et al.</i> [ <i>GRL</i> , <b>32</b> , 2005]	Lava dome extrusion	Mt. St. Helens
Wright <i>et al.</i> [ <i>JVGR</i> , <b>146</b> , 2005]	Hot spot chronology	Anatahan

Note. The collation does not include reviews (as listed in Chapter 0). These add a further 11 publications to the 1965–2005 total. Neither does it include conference abstracts (short or extended), technical or agency (e.g., USGS) reports and publications, regional publications, undergraduate, masters or PhD dissertations.

Table A2. Content summary for the publication data base given in Table A1. Summary identifies active volcanic feature type considered, satellite sensor used, key theme areas addressed, and the main parameters extracted by each study. From 1985, horizontal dashed lines break up studies into five year-long groups.

Key.

Feature type:

F = Lava flow, D = Lava dome, L = Lava lake, Pf = Pyroclastic flow, Ov = Open vent, Fu = Fumaroles, cL = Crater Lake, LT = Low-temperature thermal anomaly.

Sensor type:

Av = AVHRR, Mo = MODIS, At = ATSR, Go = GOES, Tm = TM, As = ASTER, O = Other (HRIRS, DMSP, OPS & ALI).

Theme:

1 = Detection, 2 = Pixel mixture model / dual-band technique, 3 = Derivation of heat loss and/or mass-volume flux, 4 = Time series production and/or analysis, 5 = Automated hot spot detection.

Parameters:

D = Basic detection, Ts = Thermal structure, HF = Heat flux, Er = Mass / volume flux.

Reference	Year	Active feature type considered								Satellite sensor used						Theme area					Parameters							
		F	D	L	Pf	Ov	Fu	cL	LT	Av	Mo	At	Go	Tm	As	O	1	2	3	4	5	D	Ts	HF	Er			
Gawarecki <i>et al.</i>	1965	✓															✓	✓					✓					
Williams and Friedman	1970	✓															✓	✓	✓				✓		✓			
Brandli	1978	✓															✓	✓					✓					
Wiesnet and D'Aguzzano	1982				✓											✓		✓					✓					
<hr/>																												
Bonneville <i>et al.</i>	1985								✓	✓							✓	✓										
Scorer	1986	✓									✓							✓						✓				
Bonneville and Kerr	1987										✓	✓							✓						✓		✓	
Francis and Rothery	1987		✓															✓		✓				✓				
Rothery <i>et al.</i>	1988	✓	✓	✓	✓	✓											✓		✓						✓			
Glaze <i>et al.</i>	1989		✓	✓													✓		✓	✓	✓			✓	✓	✓	✓	

Table A2. (cont.)

Reference	Year	Active feature type considered								Satellite sensor used						Theme area					Parameters							
		F	D	L	Pf	Ov	Fu	cL	LT	Av	Mo	At	Go	Tm	As	O	1	2	3	4	5	D	Ts	HF	Er			
Glaze <i>et al.</i>	1989	✓															✓						✓					
Pieri <i>et al.</i>	1990	✓																✓	✓	✓			✓	✓				
Rothery and Francis	1990			✓														✓						✓				
Abrams <i>et al.</i>	1991		✓																✓						✓			
Oppenheimer	1991	✓																✓	✓	✓	✓			✓	✓			
Oppenheimer and Rothery	1991			✓	✓	✓											✓	✓					✓					
Bonneville and Gouze	1992						✓			✓								✓							✓			
Rothery <i>et al.</i>	1992	✓																✓						✓				
Bhattacharya <i>et al.</i>	1993	✓																✓						✓				
Francis <i>et al.</i>	1993		✓															✓			✓						✓	
Gupta and Badarinath	1993				✓													✓						✓				
Oppenheimer	1993						✓											✓			✓						✓	
Oppenheimer <i>et al.</i>	1993						✓											✓			✓						✓	
Oppenheimer <i>et al.</i>	1993							✓										✓			✓						✓	
Reddy <i>et al.</i>	1993	✓																✓			✓						✓	
Flynn and Mouginis-Mark	1994	✓								✓								✓										✓
Flynn <i>et al.</i>	1994	✓																✓			✓						✓	
Gaonac'h <i>et al.</i>	1994	✓							✓									✓			✓						✓	
Mouginis-Mark <i>et al.</i>	1994	✓								✓								✓			✓						✓	
Rothery and Oppenheimer	1994		✓								✓							✓			✓						✓	
Andres and Rose	1995	✓																✓			✓						✓	
Flynn and Mouginis-Mark	1995	✓																✓			✓						✓	
Harris <i>et al.</i>	1995	✓																	✓	✓							✓	
Harris <i>et al.</i>	1995	✓																	✓								✓	
Harris <i>et al.</i>	1995	✓																	✓								✓	
Denniss <i>et al.</i>	1996		✓		✓														✓		✓	✓				✓		✓
Oppenheimer	1996																		✓		✓							✓

Reference	Year	Active feature type considered								Satellite sensor used					Theme area					Parameters							
		F	D	L	Pf	Ov	Fu	cL	LT	Av	Mo	At	Go	Tm	As	O	1	2	3	4	5	D	Ts	HF	Er		
Harris and Stevenson	1997				✓	✓				✓			✓				✓	✓	✓			✓	✓	✓			
Harris <i>et al.</i>	1997	✓								✓							✓					✓	✓	✓			
Harris <i>et al.</i>	1997	✓								✓								✓	✓	✓			✓	✓	✓		
Harris <i>et al.</i>	1997	✓											✓				✓	✓					✓				
Higgins and Harris	1997	✓					✓			✓							✓	✓				✓	✓	✓			
Oppenheimer	1997							✓					✓					✓									
Oppenheimer and Francis	1997			✓						✓			✓		✓			✓	✓	✓			✓	✓	✓		
Wooster <i>et al.</i>	1997	✓										✓						✓	✓	✓			✓	✓	✓		
Wooster and Rothery	1997	✓										✓							✓	✓							
Wooster and Rothery	1997		✓									✓						✓	✓	✓							
Dean <i>et al.</i>	1998	✓								✓							✓			✓	✓	✓		✓			
Denniss <i>et al.</i>	1998		✓							✓								✓	✓					✓			
Harris <i>et al.</i>	1998	✓								✓			✓					✓	✓				✓	✓	✓		
Oppenheimer	1998	✓								✓			✓										✓				
Oppenheimer	1998	✓		✓						✓								✓	✓					✓			
Oppenheimer and Francis	1998		✓							✓				✓				✓	✓	✓			✓	✓	✓		
Wooster and Kaneko	1998		✓									✓						✓	✓	✓			✓	✓	✓		
Wooster <i>et al.</i>	1998		✓									✓							✓	✓							
Wooster <i>et al.</i>	1998		✓									✓						✓	✓	✓							
Harris and Thornber	1999	✓											✓						✓					✓			
Harris <i>et al.</i>	1999		✓							✓				✓				✓	✓	✓			✓	✓	✓		
Harris <i>et al.</i>	1999			✓									✓					✓	✓				✓	✓	✓		
Kaneko and Wooster	1999		✓										✓					✓	✓	✓			✓	✓	✓		
Wright <i>et al.</i>	1999	✓	✓	✓													✓	✓				✓					
Dean <i>et al.</i>	2000	✓	✓		✓					✓							✓		✓	✓		✓					
Carn and Oppenheimer	2000	✓	✓			✓				✓							✓		✓			✓					
Harris <i>et al.</i>	2000	✓								✓			✓		✓				✓	✓							
Harris <i>et al.</i>	2000	✓	✓			✓				✓			✓						✓	✓			✓	✓	✓		
Mouginis-Mark <i>et al.</i>	2000	✓											✓						✓				✓				

Table A2. (cont.)

Reference	Year	Active feature type considered							Satellite sensor used					Theme area					Parameters									
		F	D	L	Pf	Ov	Fu	cL	LT	Av	Mo	At	Go	Tm	As	O	1	2	3	4	5	D	Ts	HF	Er			
Schneider <i>et al.</i>	2000	✓								✓										✓		✓						
Urai	2000	✓											✓					✓		✓				✓				
Wooster <i>et al.</i>	2000	✓											✓					✓	✓	✓				✓	✓			
Wright <i>et al.</i>	2000	✓											✓							✓				✓				
Aries <i>et al.</i>	2001	✓								✓								✓		✓				✓				
Flynn <i>et al.</i>	2001	✓											✓					✓	✓					✓		✓	✓	
Harris <i>et al.</i>	2001	✓											✓							✓	✓			✓				
Pergola <i>et al.</i>	2001	✓								✓										✓	✓			✓				
Roach <i>et al.</i>	2001								✓	✓										✓				✓				
Rothery <i>et al.</i>	2001	✓									✓									✓				✓				
Lachlan-Cope <i>et al.</i>	2001			✓						✓									✓				✓					
Wooster	2001	✓									✓		✓						✓	✓				✓	✓	✓		
Wooster and Kaneko	2001	✓											✓						✓					✓				
Wright <i>et al.</i>	2001	✓											✓							✓				✓				
Wright <i>et al.</i>	2001	✓								✓									✓					✓	✓	✓	✓	
Dehn <i>et al.</i>	2002								✓	✓								✓	✓	✓			✓		✓			
Dean <i>et al.</i>	2002									✓									✓					✓				
Flynn <i>et al.</i>	2002	✓	✓	✓	✓	✓							✓							✓				✓	✓	✓		
Galindo and Dominguez	2002		✓							✓									✓	✓	✓			✓				
Harris and Neri	2002	✓								✓				✓					✓	✓	✓				✓	✓		
Harris <i>et al.</i>	2002	✓											✓						✓						✓	✓		
Harris <i>et al.</i>	2002	✓	✓										✓						✓	✓					✓			
Harris <i>et al.</i>	2002	✓	✓											✓						✓					✓			
Kaneko <i>et al.</i>	2002	✓	✓							✓										✓	✓			✓				
Kaneko <i>et al.</i>	2002	✓											✓						✓	✓					✓			
Wright <i>et al.</i>	2002	✓											✓						✓	✓				✓	✓			
Wright <i>et al.</i>	2002	✓												✓						✓					✓			

Reference	Year	Active feature type considered							Satellite sensor used					Theme area					Parameters									
		F	D	L	Pf	Ov	Fu	cL	LT	Av	Mo	At	Go	Tm	As	O	1	2	3	4	5	D	Ts	HF	Er			
Galindo and Dominguez	2003	✓								✓									✓	✓			✓					
Harris <i>et al.</i>	2003		✓											✓				✓	✓	✓				✓	✓	✓		
Patrick <i>et al.</i>	2003	✓									✓								✓	✓					✓	✓		
Rowland <i>et al.</i>	2003	✓											✓						✓	✓							✓	
Bello <i>et al.</i>	2004	✓									✓										✓				✓			
Calder <i>et al.</i>	2004			✓										✓							✓				✓			
Dean <i>et al.</i>	2004	✓									✓							✓		✓				✓				
Donegan and Flynn	2004	✓												✓				✓	✓	✓					✓	✓		
Harris <i>et al.</i>	2004	✓											✓						✓	✓	✓				✓	✓	✓	
Hellman and Ramsey	2004								✓					✓			✓							✓				
Lautze <i>et al.</i>	2004	✓									✓							✓	✓	✓							✓	
Lombardo <i>et al.</i>	2004	✓												✓				✓							✓			
Patrick <i>et al.</i>	2004	✓											✓							✓							✓	
Pergola <i>et al.</i>	2004	✓							✓				✓								✓				✓			
Pieri and Adams	2004	✓	✓															✓	✓						✓			
Ramsey and Dehn	2004		✓										✓						✓	✓	✓				✓			
Wright and Flynn	2004	✓	✓	✓										✓					✓	✓								✓
Wright <i>et al.</i>	2004	✓	✓	✓										✓					✓	✓					✓			
Calvari <i>et al.</i>	2005	✓									✓								✓	✓							✓	
Kaneko and Wooster	2005	✓												✓					✓	✓							✓	
Patrick <i>et al.</i>	2005	✓									✓								✓	✓						✓		
Patrick <i>et al.</i>	2005	✓												✓	✓	✓				✓							✓	
Pieri and Adams	2005		✓															✓							✓	✓		
Ripepe <i>et al.</i>	2005	✓												✓					✓	✓								✓
Rothery <i>et al.</i>	2005	✓		✓										✓				✓		✓								
Vaughan <i>et al.</i>	2005		✓															✓										
Wright <i>et al.</i>	2005	✓												✓						✓								
Total	120	68	38	19	2	14	5	3	4	47	8	11	9	51	6	8	35	43	50	59	16	53	38	47	23			

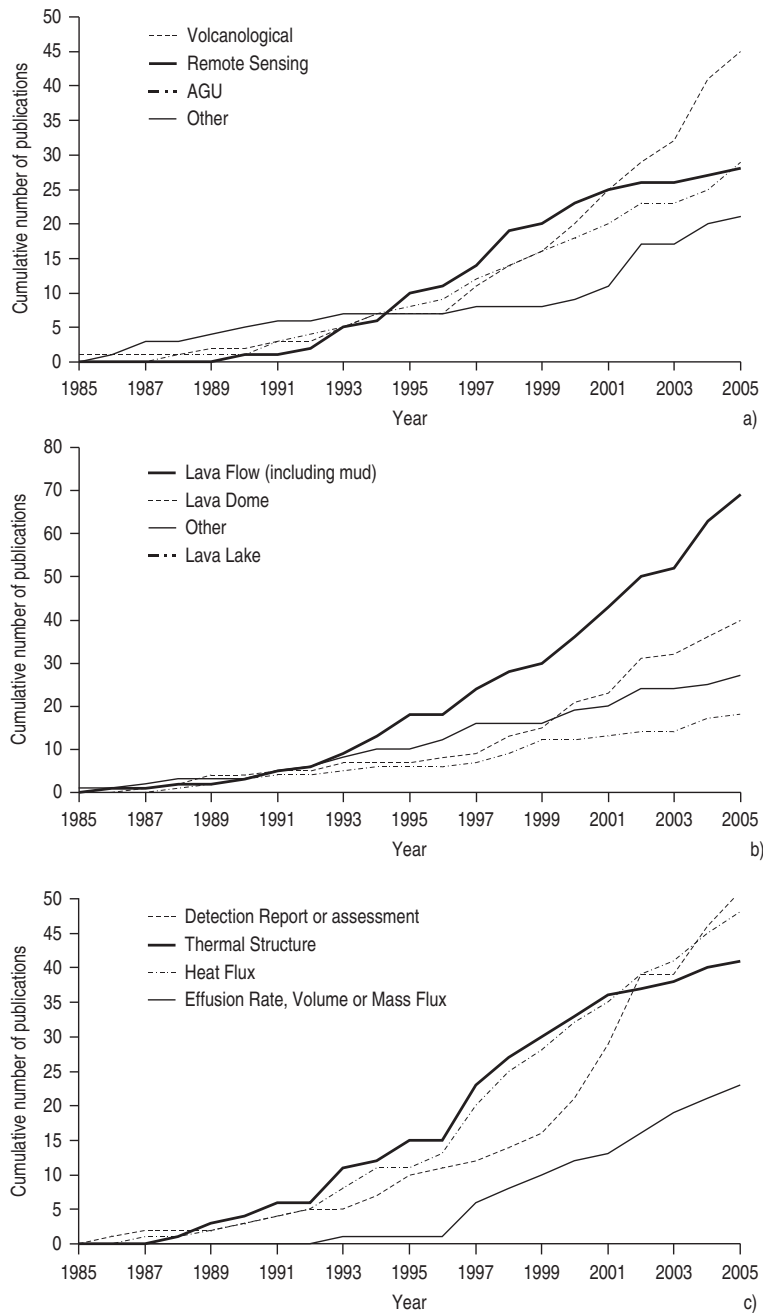


Figure A1 Cumulative number of studies by (a) journal type, (b) feature type studied and (c) main parameters extracted. Tables A1 and A2 provide the data base from which these graphs are plotted.

## Appendix B

### Estimation of solar zenith angle and contribution of reflected radiation to at-satellite radiance

Solar astronomical relationships can be defined and calculated following Iqbal (1983). As given graphically in Figure B1, the relevant solar astronomical definitions made by Iqbal (1983) are given in Table B1. The equations used to calculate each parameter, the variation in solar reflection with solar zenith and its implications for the contribution of solar reflection to at-satellite radiance in the MIR are given in this appendix.

#### Estimation of solar zenith angle

For our purposes, solar zenith angle ( $\theta_z$ ) is the value of interest. This can be calculated (in degrees) using solar declination ( $\delta$ ), geographic latitude ( $\phi$ ) and hour angle ( $\omega$ ) in:

$$\cos\theta_z = \sin\delta \sin\phi + \cos\delta \cos\phi \cos\omega = \sin\alpha,$$

$\alpha$  being the solar altitude. Of these parameters, hour angle (in degrees) can be calculated using the distance moved by the Earth, in degrees, in one hour. Given that the Earth rotates  $360^\circ$  in 24 hours, this value can be simply calculated from  $360^\circ/24$  hours =  $15^\circ$  per hour. Thus 1 hour angle =  $15^\circ$ . Because noon is zero and morning is positive, 10:00 am becomes  $2 \times 15^\circ = 30^\circ$ , 15:00 becomes  $3 \times -15^\circ = -45^\circ$ , and so on. Solar declination (in degrees) can be calculated using day angle ( $\Gamma$ ) in:

$$\delta = (0.006\ 918 - 0.399\ 912 \cos \Gamma + 0.070\ 257 \sin \Gamma - 0.006\ 758 \cos 2\Gamma + 0.000\ 907 \sin 2\Gamma - 0.002\ 697 \cos 3\Gamma + 0.001\ 48 \sin 3\Gamma) (180/\pi).$$

Day angle (in radians) can, in turn, be calculated from:

$$\Gamma = 2\pi(d_n - 1)/365$$

in which  $d_n$  is day number, which ranges from one on 1 January to 365 on 31 December.

Thus, to obtain solar zenith at Etna ( $37.73^\circ$  N) on 15 January ( $d_n = 15$ ) at 15:00 ( $\omega = -45^\circ$ ), firstly the day angle must be calculated. This will be:

$$\Gamma = 2\pi(15 - 1)/365 = 0.241 \text{ radians},$$

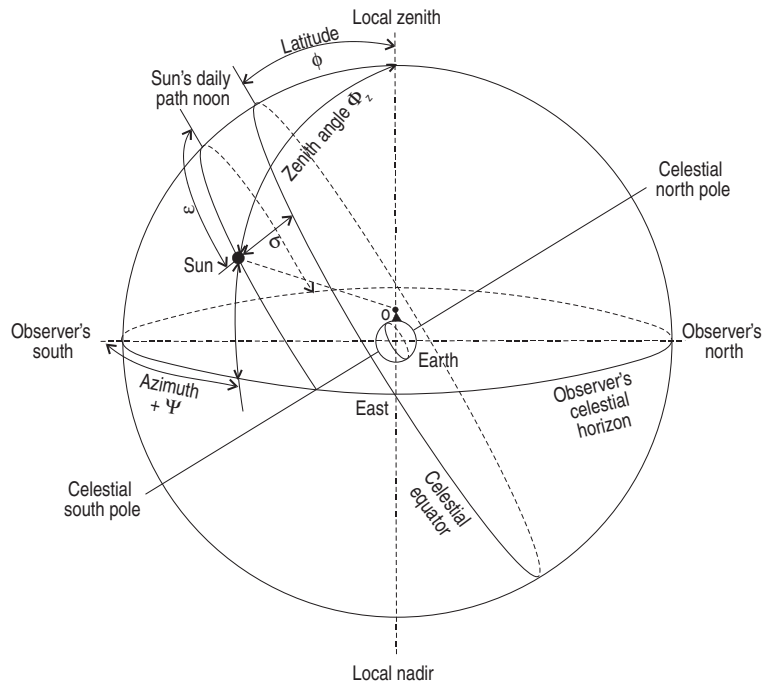


Figure B1 Parameters used in the calculation of surface reflection illustrated using the sketch of the “celestial sphere and Sun’s coordinates relative to observer on Earth at point O” given by Iqbal (1983) [from Iqbal (1983), Fig. 1.5.1].

which converts to

$$\Gamma = [(180)(0.241 \text{ radians})]/\pi = 13.81^\circ.$$

Next, declination is obtained from:

$$\begin{aligned} \delta &= [0.006\ 918 - 0.399\ 912(0.9711) + 0.070\ 257(0.2387) - 0.006\ 758(0.8861) + \\ &\quad 0.000\ 907(0.4636) - 0.002\ 697(0.7498) + 0.001\ 48(0.6616)] (180/\pi) \\ &= -21.3^\circ. \end{aligned}$$

Now solar zenith can be calculated from:

$$\theta_z = \cos^{-1} [(-0.3628)(0.6119) + (0.9319)(0.7909)(0.7071)] = 72.6^\circ.$$

### Estimation of spectral reflectance

Following the methodology given in Chapter 2, we can now use solar zenith to estimate the theoretical at-satellite spectral radiance reflected by the surface at a given wavelength,  $L_{SR}(\lambda)$ . For this worked example we estimate  $L_{SR}(\lambda)$  at 3.5 μm.

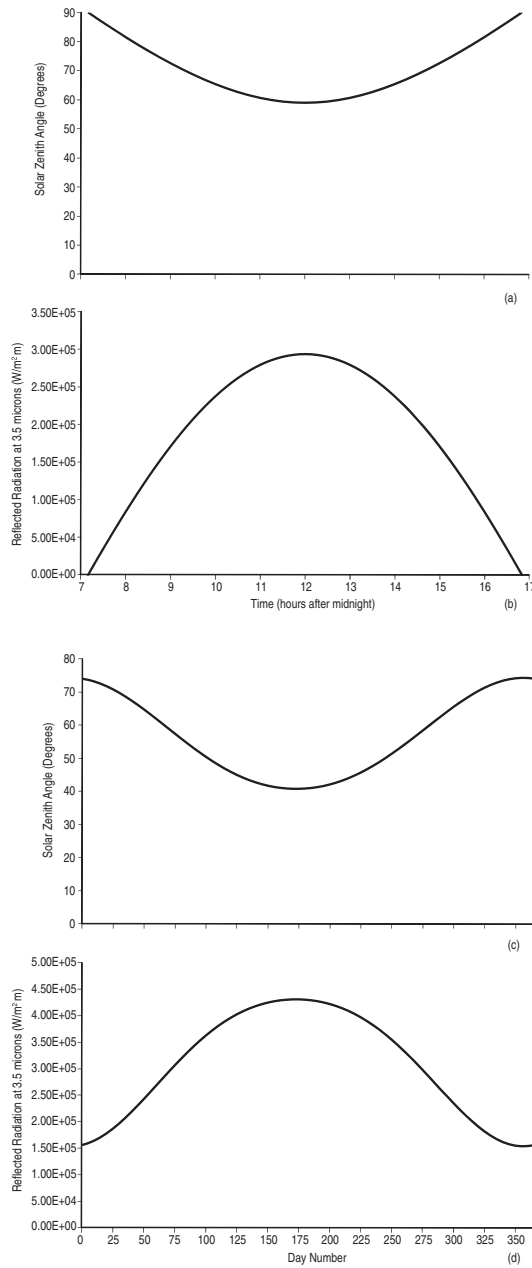


Figure B2 (a) Calculated variation in solar zenith angle at Etna's latitude ( $37.73^{\circ}$  N) for Ordinal Day 15. (b) Diurnal variation in  $3.5\text{ }\mu\text{m}$  reflection for a surface with an emissivity of 0.95 at Etna's latitude on Ordinal Day 15. (c) Annual variation in solar zenith angle and (d) reflection for a surface with an emissivity of 0.95 at Etna's latitude at 15:00. (e) Variation in solar zenith angle with latitude at 15:00 on Ordinal Day 15 and (f) reflection for a surface with an emissivity of 0.95 under the same conditions.

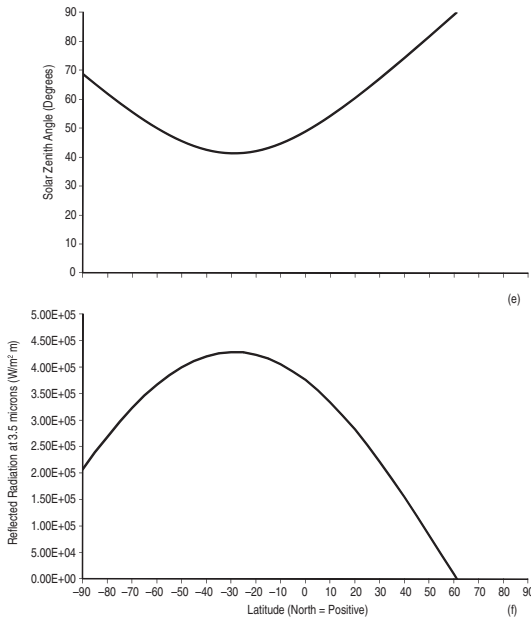


Figure B2 (cont.)

First we need to calculate the solar irradiance arriving at the top of the atmosphere,  $\bar{E}_{\text{TOA}}(\lambda)$ . This is obtained using the radiant exitance from the Sun which, given a temperature of 6000 K in Equation (2.1) of Chapter 2, will be  $7.23 \times 10^{11} \text{ W/m}^2 \text{ m}$ . Now we can use Equation (2.16a) of Chapter 2 to estimate  $\bar{E}_{\text{TOA}}(\lambda)$  at  $3.5 \mu\text{m}$ :

$$\begin{aligned}\bar{E}_{\text{TOA}}(\lambda) &= (7.23 \times 10^{11} \text{ W/m}^2 \text{ m}) [(695.3 \times 10^6 \text{ m}) / (149.6 \times 10^9 \text{ m})]^2 \\ &= 1.5628 \times 10^7 \text{ W/m}^2 \text{ m}.\end{aligned}$$

Correcting for orbital eccentricity using Equation (2.16b) of Chapter 2 we obtain, for 15 January (day 15),

$$E_{\text{TOA}}(\lambda) = (1.56 \times 10^7 \text{ W/m}^2 \text{ m}) \{1 + (0.0167)\cos[2\pi(15 - 3)/365]\}^2.$$

Radiance incident upon the surface can now be calculated using the atmospheric transmissivity (0.85) and solar zenith appropriate for the time, day and latitude ( $72.6^\circ$ ) in Equation (2.17) of Chapter 2:

$$E_{\text{in}}(\lambda) = (0.85)\cos(1.267)(1.6143 \times 10^7 \text{ W/m}^2 \text{ m}) = 4.1045 \times 10^6 \text{ W/m}^2 \text{ m}.$$

For a lava surface with an emissivity of 0.95, and hence a reflectivity of  $1 - 0.95 = 0.05$ ,  $L_{\text{SR}}(\lambda)$  at  $3.5 \mu\text{m}$  can now be estimated from Equation (2.18a) of Chapter 2:

$$L_{\text{SR}}(\lambda) = (0.85)(0.05)(4.1045 \times 10^6 \text{ W/m}^2 \text{ m}) = 1.7444 \times 10^5 \text{ W/m}^2 \text{ m}.$$

### Variation in spectral reflectance by time, date and latitude

Examination of Equation (2.18c) of Chapter 2 shows that the amount of reflected radiation will vary with solar zenith angle. Because solar zenith depends, in turn, on time of day, day of the year and latitude, so too will the amount of reflected spectral radiation.

For the model applied here (i.e., Day = 15, Latitude =  $37.73^{\circ}$  N), the variation in solar zenith through the day is plotted in Figure B2a, with the resulting variation in reflected radiation plotted in Figure B2b. For this date and latitude we find that sunrise will occur just after 7 a.m. (07:00) and sunset will occur just before 5 p.m. (17:00), at which point solar zenith exceeds  $90^{\circ}$  (see Figure B2a), i.e., the Sun will be below the horizon. Thus, between 17:00 and 07:00 reflection will be zero, as plotted in Figure B2b.

Solar azimuth will also vary depending on date, reaching, in this case, a maximum at day 175 (Figure B2c). Hence reflection will also be greatest on this date (Figure B2d). Finally, the variation of solar azimuth with latitude is plotted in Figure B2e. We find that, on this date (15 February) and at this time (15:00) maximum solar azimuth is found around  $30^{\circ}$  S, so that the maximum potential for reflection from the given surface type is found at this latitude on this day and at this time (Figure B2f). On this date and time, for latitudes above  $60^{\circ}$  N, azimuth is greater than  $90^{\circ}$  (Figure B2e), hence the Sun is below the horizon and reflection is zero, as seen from the plot of Figure B2f where reflection plunges to zero around  $60^{\circ}$  N.

### Implications for correction of at-satellite radiance at $3.5\text{ }\mu\text{m}$

The implication is that the contribution of reflected radiation to the  $3.5\text{ }\mu\text{m}$  at-satellite radiance will vary with time of day, date and latitude. In Figure B3 we examine, for this case, the contribution of reflected radiation for three emission scenarios: reflection and emission of spectral radiance for a surface with an emissivity of 0.95 and a kinetic temperature of (1)  $15^{\circ}\text{C}$ , (2)  $50^{\circ}\text{C}$ , and (3)  $175^{\circ}\text{C}$ . Using an atmospheric transmissivity of 0.85, the surface emitted radiance arriving at the satellite,  $L_S(\lambda)$ , for these three surface scenarios will be (1)  $4.48 \times 10^5\text{ W/m}^2\text{ m}$ , (2)  $1.68 \times 10^6\text{ W/m}^2\text{ m}$ , and (3)  $5.86 \times 10^7\text{ W/m}^2\text{ m}$ .

#### (i) Variation with time of day

Considering emission from the surface at  $15^{\circ}\text{C}$ , the contribution of reflected radiation to the total at-satellite radiance will be zero by night. It then increases from zero around 7 a.m. (sunrise) to a maximum of  $\sim 45\%$  by mid-day before declining again to zero by 17:00 (when the Sun sets, Figure B3a).

#### (ii) Variation with date

For any given daylight hour, the percent contribution of reflected radiation will vary by day. In our modeled case (latitude =  $37.73^{\circ}$  N; time = 15:00) we reach a maximum contribution of  $\sim 55\%$  around the middle of the year for the  $15^{\circ}\text{C}$  surface emission scenario (Figure B3b).

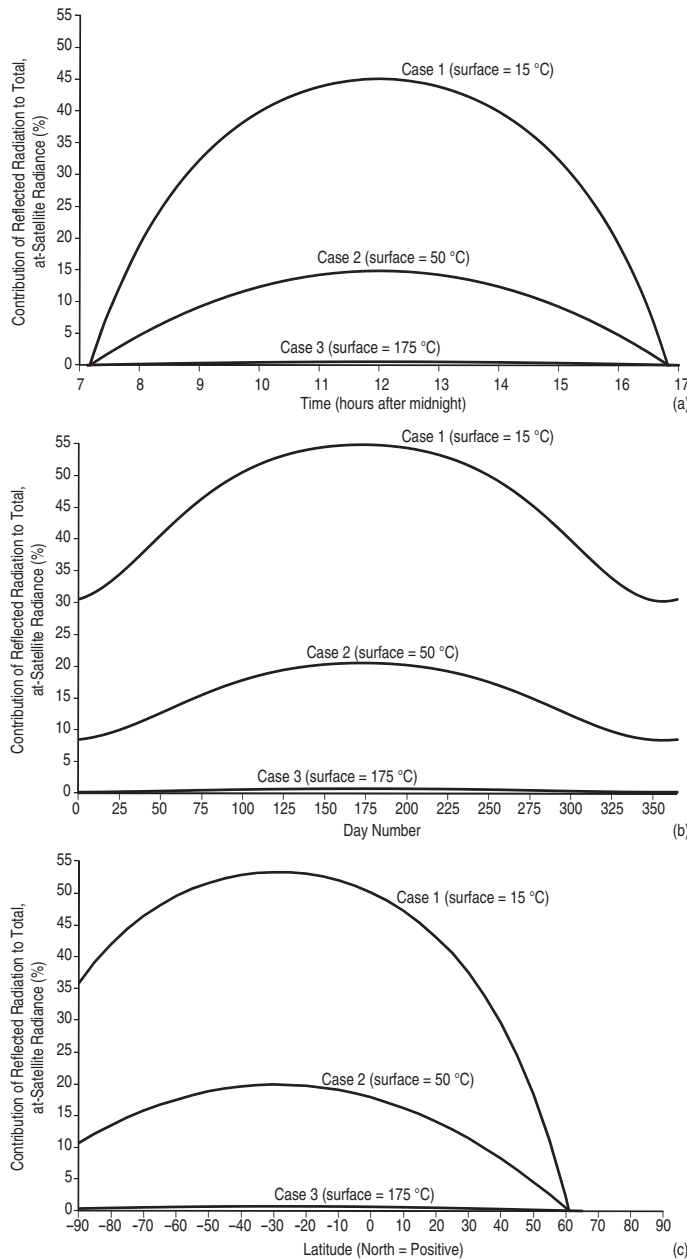


Figure B3 (a) Diurnal variation in the percent contribution of reflected radiance at  $3.5 \mu\text{m}$  to the total at-satellite radiance for latitude =  $37.73^\circ \text{N}$ , Day Number = 15, Emissivity = 0.95. (b) Annual variation in the percent contribution of reflected radiance at  $3.5 \mu\text{m}$  to the total at-satellite radiance for latitude =  $37.73^\circ \text{N}$ , Hour = 15:00, Emissivity = 0.95. (c) Variation in the contribution of reflected radiation with latitude. For all cases, emission from three surfaces are considered at temperatures of (1)  $15^\circ \text{C}$ , (2)  $50^\circ \text{C}$  and (3)  $175^\circ \text{C}$ . All three have an emissivity of 0.95.

Table B1. Definition, notation and sign conventions for the parameters used in the calculation of solar zenith angle (from Iqbal, 1983).

Notation	Parameter	Units	Definition
$\theta_z$	Solar zenith angle	Degrees	Angle between local zenith and the line joining the observer with the Sun: an angle between $0^\circ$ and $90^\circ$ .
$\alpha$	Solar altitude	Degrees	The Sun's angular height above the observer's celestial horizon, $\alpha = 90 - \theta_z$ .
$\delta$	Solar declination	Degrees (North positive)	Angular position of the Sun at solar noon with respect to the plane of the Equator.
$\phi$	Geographic latitude	Degrees (North positive)	Observer position on the planet in the North–South plane.
$\omega$	Hour angle	Degrees (morning positive)	The angle measured at the celestial pole between the observer's meridian and the solar meridian.

### (iii) Variation with latitude

For any given date and time, the contribution of reflected radiation also varies with latitude. For this date (15 January) and time (15:00), the maximum contribution from reflected radiation is found at  $30^\circ$  S, where the contribution of reflected radiation for the  $15^\circ\text{C}$  surface emission scenario reaches  $\sim 55\%$  (Figure B3c).

### (iv) Variation with surface temperature

We note that the reflection contribution varies with temperature. As temperature increases, so the emitted radiance increases. Because the reflected component remains constant, the relative contribution of reflected radiation decreases. Thus, for all modeled cases, the percent contribution of reflected radiation to the total at-satellite radiance decreases as the temperature of the surface increases. Once surface temperatures reach  $\sim 175^\circ\text{C}$ , the contribution of reflected radiation to the total at-satellite radiance is typically less than 1% for any time of day, day in the year or latitude (Figure B3).

# Appendix C

## TM-class sensors

To date, four TM-class sensors have been used for volcanological purposes: MSS, TM, ETM+ and ASTER. These sensors have been placed in this class because they share a spatial resolution of ~30 m. They also provide data in the SWIR and TIR, and have nominal return periods of 16 days. In this appendix we give the main orbit and sensor characteristics for each instrument, as well as the primary information sources from which the details given are largely taken, and from which further sensor and calibration information can be obtained.

### Multispectral Scanner, Thematic Mapper and Enhanced Thematic Mapper Plus (Table C1)

The Landsat satellite series has flown three sensors. These are, in chronological order, the Multispectral Scanner (MSS), the Thematic Mapper (TM) and the Enhanced Thematic Mapper Plus (ETM+). The inception and launch of each sensor in the series has represented a progressive increase in spectral and spatial capabilities. The launch details of each are given in [Table 1.2 of Chapter 1](#), with the orbit and sensor details being given here in [Table C1](#).

MSS had four 80 m pixel bands spanning the VIS-NIR. MSS on Landsat-3 featured a fifth band in the TIR with 240 m pixels, but this failed shortly after launch. Instead, TM was a seven-band sensor which added two SWIR bands to the MSS format. In addition, the spatial resolution of the VIS, NIR and SWIR bands was increased to 30 m and that of the TIR band to 120 m. Finally, ETM+ featured an eighth, panchromatic, band with a resolution of 15 m. All other bands remained at the same wavelengths as TM, but high and low gain settings were added which, importantly for studies of active volcanism, increased the saturation temperature during high gain acquisition (see [Table C1](#)). In addition, the spatial resolution of the TIR band was further reduced to 60 m.

### Primary information sources

- Flynn, L. P., Harris, A. J. L. and Wright, R. (2001). Improved identification of volcanic features using Landsat 7 ETM+. *Remote Sensing of Environment*, **78**, 180–193.
- Lillesand, T. M. and Kiefer, R. W. (1987) *Remote Sensing and Image Interpretation*. New York: John Wiley & Sons, 721 pp.
- Markham, B. L. (1985). The Landsat sensors' spatial responses. *IEEE Trans. Geoscience and Remote Sensing*, **GE-23**(6), 864–875.

Table C1. *Nominal orbit and instrument characteristics of NASA's Multispectral Scanner (MSS), Thematic Mapper (TM) and Enhanced Thematic Mapper Plus (ETM+). Values are for TM, unless otherwise indicated.*

Orbit parameter	Details					
Altitude	705 km					
Orbit period	98.9 minutes					
Repeat cycle	16 days					
Number of orbits per day	14.6					
Equatorial crossing time (at launch)	09:45 and 21:45 (TM), 10:00 and 22:00 (ETM+)					
Sensor characteristics	Details					
Scan angle from nadir	$\pm 7.46^\circ$					
Scan increment angle	0.0425 mrad (TM), 0.0213 mrad (ETM+)					
Swath width	185 km					
Radiometric resolution	8 bits (0 to 255 counts)					
Pixel dwell time	42.5 $\mu$ s					
Infrared band $NE\Delta T$	0.22 K (ETM+)					
Detector type	InSb (Bands 5, 7 & 4), HgCdTe (Band 6)					
	Bands 1 to 4		Bands 5 & 7		Band 6	
TM spatial resolution	Track	Scan	Track	Scan	Track	Scan
(1) Protoflight (PF) instrument flown on Landsat-4						
IFOV (mrad)	0.0455	0.0508	0.0473	0.0508	0.1758	0.2005
Nadir pixel dimension (m)	32	36	33	36	124	141
Scan-edge pixel dimension (m)	32	37	34	37	126	144
(2) Flight (F) instrument flown on Landsat-5						
IFOV (mrad)	0.0455	0.0509	0.0473	0.0505	0.1758	0.2001
Nadir pixel dimension (m)	32	36	33	36	124	141
Scan-edge pixel dimension (m)	32	37	34	37	126	144
(3) Nominal values for ETM+						
IFOV (mrad): bands 1–5 and 7	0.0425					
Nadir pixel dimension (m)	30 m					
IFOV (mrad): band 6	0.0851					
Nadir pixel dimension (m)	60 m					
IFOV (mrad): band 8	0.02128					
Nadir pixel dimension (m)	15 m					

Table C1. (*cont.*)

Band	Spectral region	MSS waveband	TM waveband	ETM+ waveband (μm) (pixel size, m)	Saturation (°C)
		(μm) (pixel size, m)	(μm) (pixel size, m)		TM (ETM+) <sup>b</sup>
1	VIS	0.5 – 0.6 (79/82) <sup>a</sup>	0.45 – 0.52 (30)	0.45 – 0.515 (30)	1490 (1483/1526)
2	VIS	0.6 – 0.7 (79/82) <sup>a</sup>	0.52 – 0.60 (30)	0.525 – 0.605 (30)	1410 (1301/1340)
3	NIR (MSS), VIS (TM)	0.7 – 0.8 (79/82) <sup>a</sup>	0.63 – 0.69 (30)	0.63 – 0.69 (30)	1170 (1119/1156)
4	NIR	0.8 – 1.1 (79/82) <sup>a</sup>	0.76 – 0.90 (30)	0.75 – 0.90 (30)	950 (926/961)
5	SWIR		1.55 – 1.75 (30)	1.55 – 1.75 (30)	415 (417/440)
6	TIR	10.4 – 12.6 (240) <sup>c</sup>	10.4 – 12.5 (120)	10.4 – 12.5 (60)	70 (51/77)
7	SWIR		2.08 – 2.35 (30)	2.09 – 2.35 (30)	280 (258/276)
8	NIR-VIS			0.52 – 0.90 (15)	(1056/1092)

<sup>a</sup> 79 m on Landsat-1 to -3, and 82 m for Landsat-4 and -5.

<sup>b</sup> Saturation temperature in low gain (LG) mode is given first, and in high gain (HG) mode second [format: (LG/HG)]

<sup>c</sup> Only for the MSS carried on Landsat-3, but it failed shortly after launch.

### Advanced Spaceborne Thermal Emission and Reflection Radiometer (Table C2)

The Advanced Spaceborne Thermal Emission and Reflection Radiometer (ASTER) was flown on NASA's EOS-AM1 (Terra) satellite alongside MODIS. ASTER had a total of 14 bands, with the main orbital and instrument characteristics being given in Table C2.

While the three VIS-NIR bands had pixel sizes of 15 m, the six SWIR bands had sizes of 30 m, and the five TIR bands 90 m. The NIR band 3 had both a nadir view (band 3N) and a backward looking view (band 3R). Band 3R, being pointed backwards at an angle of 27.6° allowed a base-height ratio of 0.6 to be achieved, thereby allowing stereo imaging for Digital Elevation Model generation. The SWIR bands featured a high gain setting, whereby the normal gain was increased by a factor of two to allow unsaturated data collection over high-temperature targets. The high gain saturation levels are given in Table C2.

The nominal swath width of 60 km was somewhat less than the equatorial orbit separation (172 km) so that the nominal equatorial return period was 16 days. However, the instrument was pointable, with the pointing range of ±8.55° allowing coverage out to ±116 km of nadir. As Yamaguchi *et al.* (1998) stated, “this capability was added to shorten the potential delay period for a time-critical observation of natural hazards, like volcanic eruptions and floods.” The VIS-NIR subsystem was pointable out to 24° (±318 km). This increased the return

Table C2. Nominal orbit and instrument characteristics of NASA's Advanced Spaceborne Thermal Emission and Reflection Radiometer (ASTER).

Orbit parameter		Details			
Altitude		705 km			
Orbit period		98.9 minutes			
Repeat cycle		16 days (but see notes)			
Number of orbits per day		14.6			
Equatorial crossing time (at launch)		10:30 and 22:30 (AM-1, Terra)			
Sensor characteristics		Details			
Scan angle from nadir		$\pm 2.44^\circ$			
Swath width		60 km			
Radiometric resolution		8 bits (bands 1–9), 12 bits (bands 10–14)			
Infrared band $N\Delta T$		< 0.3 K			
Band	Spectral region	Detector type	Waveband ( $\mu\text{m}$ )	Saturation ( $^\circ\text{C}$ )	Nominal pixel size (m)
1	VIS	Si	0.52–0.60		15
2	VIS	Si	0.63–0.69		15
3N	NIR	Si	0.78–0.86		15
3B	NIR	Si	0.78–0.86		15
4	SWIR	PtSi	1.600–1.700	466	30
5	SWIR	PtSi	2.145–2.185	385	30
6	SWIR	PtSi	2.185–2.225	376	30
7	SWIR	PtSi	2.235–2.285	358	30
8	SWIR	PtSi	2.295–2.365	330	30
9	SWIR	PtSi	2.360–2.430	326	30
10	TIR	HgCdTe	8.125–8.475	97	90
11	TIR	HgCdTe	8.475–8.825	97	90
12	TIR	HgCdTe	8.925–9.275	97	90
13	TIR	HgCdTe	10.25–10.95	97	90
14	TIR	HgCdTe	10.95–11.65	97	90

period at the Equator to between 2 and 7 days. At mid-latitudes, ASTER was capable of return periods of 30 hours, which decreased to 12 hours at higher latitudes. Moreover, in standard mode, ASTER's temporal resolution at high latitudes was 5 days, so that, for example, we could commonly acquire 3 images in less than 3 days in Kamchatka (Mike Ramsey, written communication, April 2012).

The primary operational constraint was the limited data volume allocated to ASTER in EOS-AM1's solid-state recorder memory. Based on a two-orbit data collection cycle, eight minutes of data could be stored per orbit. This was 8% of the 98.9 minute orbit, so the sensor was termed as having an 8% duty cycle. If no data were collected during the preceding or following orbit, this could be increased to 16 minutes for one orbit. Thus, data collection was

prioritized and scheduled to maximize the science return. One of the nine specific ASTER science areas was identified by Kahle *et al.* (1991) as being volcano monitoring. Thus, numerous images of active volcanoes have been scheduled, prioritized and acquired by ASTER.

### Primary information sources

- Fujisada, H. and Ono, A. (1994). Observational performance of ASTER instrument on EOS-AM1 spacecraft. *Adv. Space Res.*, **14**(3), (3)147–(3)150.
- Kahle, A. B., Palluconi, F. D., Hook, S. J., Realmuto, V. J. and Bothwell, G. (1991). The Advanced Spaceborne Thermal Emission and Reflection Radiometer (ASTER). *Int. J. Imaging Systems and Technology*, **3**, 144–156.
- Yamaguchi, Y., Kahle, A. B., Tsu, H., Kawakami, T. and Pniel, M. (1998). Overview of Advanced Spaceborne Thermal Emission and Reflection Radiometer (ASTER). *IEEE Trans. Geoscience and Remote Sensing*, **36**(4), 1062–1071.

# Appendix D

## AVHRR-class sensors

To date, three AVHRR-class sensors have been used for volcanological purposes: AVHRR, ATSR and MODIS. These sensors have been placed in this class because they share a spatial resolution of 1 km. They also provide data in the TIR, MIR, and SWIR (or NIR) and have a return period of 12 h, with the exception of ATSR which instead had a nadir and forward looking capability. This appendix contains the main orbit and sensor characteristics for each instrument, as well as the primary information sources from which the details given are largely taken, and from which further sensor and calibration information can be obtained.

### **Advanced Very High Resolution Radiometer (Table D1)**

The Advanced Very High Resolution Radiometer (AVHRR) was flown on the NOAA satellite series. Between the launch of the first AVHRR sensor on TIROS-N in 1978 and the launch of NOAA-18 in 2005, 15 AVHRR sensors were put (not all successfully) into orbit. The launch details of each are given in [Table 1.1 of Chapter 1](#), with the orbit and sensor details being given here in [Table D1](#).

Sensor and orbit details varied by platform, and there were three versions of the sensor. Version 1 was a four band sensor which recorded data in one MIR waveband and one TIR waveband. Data were also recorded in one NIR waveband and one VIS waveband, as listed in [Table D1](#). Version 2 was a five band sensor featuring a second TIR waveband. Version 1 was flown on TIROS-N, as well as NOAA-6, -8 and -10, with version 2 being flown on NOAA-7 and -9, as well as NOAA-11 through -14, and -18 (see [Table 1.1 of Chapter 1](#)). Version 3 was launched in 1998, being first flown on NOAA-15. It was also flown on NOAA-16 and -17. Version 3 represented a major change, whereby a sixth band was added (band 3A). The new band was shared with the old band 3, which was renamed 3B. Only five bands were transmitted to the ground at any given time, so that bands 3A and 3B could not operate simultaneously. Thus, band 3A operated during daytime passes and band 3B was switched to operate during night-time passes.

### **Primary information sources**

Cracknell, A.P., (1997). *The Advanced Very High Resolution Radiometer*. London: Taylor & Francis, 534 pp.

**Table D1.** *Nominal orbit and instrument characteristics of NOAA's Advanced Very High Resolution Radiometer (AVHRR). Spatial resolution is calculated using the method given in Chapter 3 for a satellite height of 850 km.*

Orbit parameter	Details				
Altitude	833 km (NOAA-6, -8, -10, -12) or 870 km (NOAA-7, -9, -11, -13, -14)				
Orbit period	101.58 (833 km orbit) or 102.37 km (870 km orbit)				
Repeat cycle	12 hours (maintaining a minimum of 2 satellites in orbit ensures a 6 hour repeat cycle)				
Number of orbits per day	14.18 (833 km orbit) or 14.07 (870 km orbit)				
Equatorial crossing time (at launch)	02:30 and 14:30 (NOAA-7, -9) 07:30 and 19:30 (NOAA-6, -8, -10, -12, -15) 01:30 and 13:30 (NOAA-11, -13, -14) 02:00 and 14:00 (NOAA-16, -18) 10:00 and 22:00 (NOAA-17)				
Sensor characteristics	Details				
Scan angle from nadir	$\pm 55.4^\circ$				
Scan increment angle	0.95 mrad				
Swath width	$\sim 3000$ km				
Radiometric resolution	10 bits (0 to 1024 counts)				
Line rate	360 lines per minute				
Pixel dwell time	25 $\mu$ s				
Image width	2048 pixels				
Infrared band $NE\Delta T$	$<0.12$ K for a scene temperature of $27^\circ\text{C}$				
Infrared band saturation	47–50 $^\circ\text{C}$ (band 3), 50–60 $^\circ\text{C}$ (bands 4 and 5) Bands 3B, 4 and 5 on NOAA-15, -16, -17 have 62°C (335 K)				
	Band				
Spatial resolution	1	2	3 (3A)	4	5
IFOV (mrad)	1.39	1.41	1.51 (1.3)	1.41	1.30
Ground resolution at nadir					
Along scan (km)	1.18	1.20	1.28 (1.11)	1.20	1.11
Cross scan (km)	1.18	1.20	1.28 (1.11)	1.20	1.11
Ground resolution at scan edge					
Along scan (km)	7.25	7.36	7.88 (6.78)	7.36	6.78
Cross scan (km)	2.55	2.58	2.77 (2.38)	2.58	2.38

Table D1. (*cont.*)

Band	Spectral region (detector type)	Waveband (μm)					
		TIROS-N	NOAA-6, -8, -10	-12, -14, -18	NOAA-7, -9, -11,	NOAA-13	NOAA-15, -16, -17
1	VIS (silicon)	0.55–0.90	0.58–0.68	0.58–0.68	0.58–0.68	0.58–0.68	
2	NIR (silicon)	0.725–1.1	0.725–1.1	0.725–1.1	0.725–1.1	0.725–1.1	0.725–1.0
3A	SWIR (InGaAs)						1.58–1.64
3 (3B)	MIR (InSb)	3.55–3.93	3.55–3.98	3.55–3.93	3.55–3.93	3.55–3.93	3.55–3.93
4	TIR (HgCdTe)	10.5–11.5	10.5–11.5	10.3–11.3	10.3–11.3	10.3–11.3	10.3–11.3
5	TIR (HgCdTe)	Band 4 repeated		11.5–12.5	11.4–12.4	11.5–12.5	

Kidwell, K. B. (1995). *NOAA polar orbiter data users guide (TIROS-N, NOAA-6, NOAA-7, NOAA-8, NOAA-9, NOAA-10, NOAA-11, NOAA-12, NOAA-13, and NOAA-14).* NOAA POD Guide, Washington DC: National Oceanic and Atmospheric Administration.

Schwalb, A. (1978). The TIROS-N/NOAA A-G satellite series. *NOAA Technical Memorandum NESS*, **95**, 75 p.

### Along Track Scanning Radiometer (Table D2)

The first Along Track Scanning Radiometer (ATSR-1) was launched by the European Space Agency (ESA) on their ERS-1 satellite in July 1991. Although ESA chose to cease data collection from ERS-1 in June 1996, acquisition continued using ATSR-2, launched on ERS-2 in April 1995, and then through operation of the Advanced Along Track Scanning Radiometer (AATSR), which was launched on ENVISAT in March 2002. Details of all ATSR sensors are given in Table D2.

ATSR-1 was a four band instrument, with one band in the SWIR, one in the MIR and two in the TIR, with three bands (two in the VIS and one in the NIR) being added to ATSR-2 and AATSR. The ATSR on ERS-1 used a single pre-amplifier for the 1.6 μm and 3.7 μm bands, causing measurements in these two wavebands to be mutually exclusive. The criterion for selecting which of the two bands was placed in the telemetry was based on the 1.6 μm reflectance, with 1.6 μm data being acquired if it exceeded a threshold value which was set around the detector noise level (i.e., 110 counts or 0.02 W/m<sup>2</sup> sr μm). Usually this value was only achieved in the day-time, causing 1.6 μm data to be preferred by day, and 3.7 μm to be preferred at night. However, over sufficiently hot surfaces (such as at active lavas) the 1.6 μm radiance threshold would also be exceeded by night, thus triggering acquisition of 1.6 μm data over volcanic hot spots by night if they were sufficiently hot (Wooster and Rothery, 1997a,b). With the failure of the 3.7 μm band in May 1992, the threshold was lowered so that all of the 1.6 μm data were kept. A higher threshold of 150 counts was applied to ATSR-2 because it was considered that 3.7 μm data, usually discarded by day, remained useful in low light conditions.

Table D2. Nominal orbit and instrument characteristics of ESA's Along-Track Scanning Radiometer (ATSR).

Orbit parameter	Details	
Altitude	777 km	
Orbit period	100 minutes	
Repeat cycle	ERS-1: 3 days (Jul. 91–Apr. 92 & Dec. 93–Apr. 94) 35 days (Apr. 92–Dec. 93) 168 days (Apr. 94–Mar. 95) ERS-2: 35 days	
Number of orbits per day	14.4	
Equatorial crossing time (at launch)	10:30 and 22:30	
Sensor characteristics	Details	
Scan angle from nadir	$\pm 23.45^\circ$	
Swath width	500 km	
Radiometric resolution	8 bit (12 $\mu\text{m}$ band), 10 bit (1.6 and 3.7 $\mu\text{m}$ band) and 12 bit (10.8 $\mu\text{m}$ band)	
Scan duration	150 ms	
Pixel dwell time	75 $\mu\text{s}$	
Image width	555 pixels (nadir scan) and 371 pixels (forward scan)	
Noise level (1.6 $\mu\text{m}$ )	0.02 W/m <sup>2</sup> sr $\mu\text{m}$	
Infrared band $NE\Delta T$	ATSR-1: Better than 0.05 K for a 27 °C scene temperature ATSR-2: 50 mK, 21 mK & 25 mK for the 3.7, 11.0 and 12.0 bands, respectively	
Infrared band saturation	50 °C (3.8, 10 and 12 $\mu\text{m}$ bands) and 260 °C (1.6 $\mu\text{m}$ band)	
Spatial resolution	Nadir scan	Forward scan
IFOV		
Along scan (mrad)	1.54 mrad	1.54 mrad
Cross scan (mrad)	1.29 mrad	1.29 mrad
Ground Resolution at nadir		
Along scan (km)	1.20 km	1.58 km
Cross scan (km)	1.00 km	3.31 km
Ground Resolution at scan edge		
Along scan (km)	1.38 km	1.51 km
Cross scan (km)	1.07 km	2.95 km

Table D2. (*cont.*)

Band	Spectral region	Detector type	Waveband width (μm)	Dynamic range (W/m <sup>2</sup> sr μm)	ATSR-1	ATSR-2 AASTR
0.55 μm	VIS	Si	0.2 μm		N	Y
0.67 μm	VIS	Si	0.2 μm		N	Y
0.87 μm	NIR	Si	0.2 μm		N	Y
1.6 μm	SWIR	PV InSb	0.3 μm	0.02–0.53	Y	Y
3.7 μm	MIR	PV InSb	0.3 μm	0.0057–0.98	Y	Y
10.8 μm	TIR	PC CMT	1.0 μm	0.96–13	Y	Y
12.0 μm	TIR	PC CMT	1.0 μm	1.1–12	Y	Y

ERS-1 and -2 had an orbit maneuvering capability, so that the orbital period could be adjusted by making slight adjustments in the spacecraft altitude, with repeat cycles of 3, 35 and 168 days being employed. The ATSR featured a conical scanning geometry which enabled the satellite to view the same position on the Earth's surface within two minutes. The scan geometry resulted in a cross-track scan passing through nadir, as well as a second scan forward of the sub-satellite point, with the two scans being curved and separated by 900 km along the sub-satellite track. The scan geometry, and resulting pixel size calculation, is detailed in Prata *et al.* (1990).

#### Relative response with scan distance

Wooster *et al.* (1998b) described the effect of pixel overlap in terms of spreading radiance between pixels with special reference to the ATSR. For the ATSR, the IFOV is 0.074°, with each pixel being constructed from the integration of the signal collected over 75 μs. During the integration period the scan mirror collects radiance for pixel A. The scan mirror then advances 0.074°, or 1 km, and collects radiance for the next pixel, pixel B. Because each integration period is continuous with the previous, the response functions are triangular with a 2 km base and 1 km half-width so that pixels overlap at the half-height (50%) of the response level. Thus, pixels will always contribute radiance to the signal of two surrounding pixels, and will not attain 100% response over the ground cell to which they relate. This potentially leads to over-sampling of the radiance. However, in the case of ATSR, Wooster *et al.* (1998b) pointed out that “the response function profiles indicate that any point is always observed with a cumulative view time of 75 μsec, equating to 100% pixel responsibility if all affected pixels are considered.”

#### Primary information sources

Delderfield, J., Llewellyn-Jones, D. T., Bernard, R. *et al.* (1985). The Along Track Scanning Radiometer (ATSR) for ERS-1. *Proc. SPIE Instrumentation for Optical Remote Sensing from Space*, **589**, 114–120.

- Mutlow, C. (1999). ATSR-1/2 user guide. *European Space Agency (ESA) User's Guide*, 29 pp.
- Prata, A. J. F., Cechet, R. P., Barton, I. J. and Llewellyn-Jones, D. T. (1990). The Along Track Scanning Radiometer for ERS-1 – scan geometry and data simulation. *IEEE Trans. Geosciences & Remote Sensing*, **28**(1), 3–13.
- Wooster, M. J. (1996). ATSR data calibration. *Int. J. Remote Sensing*, **17**, 1069–1074.
- Wooster, M. J., and Rothery, D. A. (1997b). Time-series analysis of effusive volcanic activity using the ERS Along Track Scanning Radiometer: the 1995 eruption of Fernandina Volcano, Galapagos Islands. *Remote Sensing of Environment*, **62**, 109–117.
- Wooster, M. J., Rothery, D. A. and Kaneko, T. (1998a). Geometric considerations for the remote monitoring of volcanoes: studies of lava domes using ATSR and the implications for MODIS. *Int. J. Remote Sensing*, **19**(13), 2582–2591.

### **Moderate Resolution Imaging Spectroradiometer (Tables D3 and D4)**

The initial design specifications for the Moderate Resolution Imaging Spectroradiometer were set by the MODIS instrument panel formed in 1984 and given in Salomonson *et al.* (1989). However, the final instrument specifications were a little different, as given in Barnes *et al.* (1998). The instrument that was launched featured ten VIS bands, six NIR bands, four SWIR bands, six MIR bands and ten TIR bands, giving a total of 36 bands. These, along with the orbit and full sensor details are listed in Table D3, with the launch details of each MODIS sensor being given in Chapter 1, where two MODIS sensors were launched: one on the AM-1 (Terra) platform in December 1999, and one on the PM-1 (Aqua) platform in May 2002.

Pixel sizes ranged from 250 m in bands 1 and 2, to 500 m in bands 3–7, and 1000 m in bands 8–36, with all MIR and TIR bands having a spatial resolution of ~1000 m. The data of Barnes *et al.* (1998) allow us to use Equation (3.5) of Chapter 3 to estimate the exact along scan and cross scan IFOV in each band, as done in Table D4. MODIS featured a 10 km along-track field of view, so that each 1 km band had a 10 element linear detector array, and the 500 and 250 m bands had 20 and 40 element arrays, respectively. Thus, each 2330 km-wide scan was collected in a series of swaths each of which were 10 km (10 pixels at 1 km, 20 at 0.5 km or 40 at 0.25 km) wide.

Required signal-to-noise (S/N) ratios and noise equivalent temperature differences ( $NE\Delta T$ ) are given in Table D3. Xiong *et al.* (2008) showed that, after 7 years and 4.5 years of operation on Terra and Aqua, respectively, both sensors were performing “better than their design requirements, with excellent calibration stability and satisfactory cross-sensor consistency.” The tests of Xiong *et al.* (2008) showed that, for TIR bands 31 and 32, (1)  $NE\Delta T$ s had been continuously below 0.05 K, (2) calibration coefficients had been extremely stable with scan-by-scan variations being less than 0.1%, and (3) calibration differences between the two instruments were less than 0.1 K for both bands.

MODIS data were provided via the internet (see Chapter 0) in a number of well defined and documented standard formats, including geolocated Level 1A format data (Nishihama *et al.*, 1997), and calibrated Level 1B format data (Xiong *et al.*, 2005). Most volcanological applications tended to use the Level 1B format, as it provided calibrated spectral radiance data.

Table D3. *Nominal orbit and instrument characteristics of NASA's Moderate Resolution Imaging Spectroradiometer (MODIS).*

Orbit parameter	Details				
Altitude	705 km				
Orbit period	98.9 min				
Repeat cycle	12 h (at high latitudes) to 48 h (at the Equator)				
Number of orbits per day	14.6				
Equatorial crossing time (at launch)	10:30 and 22:30 (AM-1, Terra); 13:30 and 01:30 (PM-1, Aqua)				
Sensor characteristics	Details				
Scan angle from nadir	$\pm 55^\circ$				
Pixel dwell time	333 $\mu$ s				
Swath width	2330 km				
Radiometric resolution	12 bits				
Scan duration	1.477 s				
Image width	1354 pixels				
Detector type	Photovoltaic silicon dioxide (VIS & NIR), Photovoltaic HgCdTe (SWIR, MIR and TIR bands 27–30), Photoconductive HgCdTe (TIR bands 31–36)				
Infrared band saturation	470 °C (SWIR band 6), 300 °C (SWIR band 7) 180 °C (MIR band 21), 60 °C (MIR band 22), 130 °C (TIR band 32)				
Band	Region	Waveband ( $\mu$ m)	S/N	$NE\Delta T$ (K)	Spatial resolution, nominal: along scan by cross-scan (m)
1	VIS	0.620–0.670	128	250: 300 × 262	
2	NIR	0.841–0.876	201	250: 291 × 254	
3	VIS	0.459–0.479	243	500: 560 × 499	
4	VIS	0.545–0.565	228	500: 546 × 499	
5	SWIR	1.230–1.250	74	500: 540 × 520	
6	SWIR	1.628–1.652	275	500: 540 × 520	
7	SWIR	2.105–2.155	110	500: 538 × 521	
8	VIS	0.405–0.420	880	1000: 1059 × 1007	
9	VIS	0.438–0.493	838	1000: 1043 × 1003	
10	VIS	0.483–0.493	802	1000: 1058 × 1003	
11	VIS	0.526–0.536	754	1000: 1041 × 991	
12	VIS	0.546–0.556	750	1000: 1054 × 984	
13	VIS	0.662–0.672	910	1000: 1038 × 1001	
14	VIS	0.673–0.683	1087	1000: 1043 × 1009	
15	NIR	0.743–0.753	586	1000: 1042 × 1004	
16	NIR	0.862–0.877	516	1000: 1045 × 1007	

Table D3. (*cont.*)

Band	Region	Waveband ( $\mu\text{m}$ )	S/N	$NE\Delta T$ (K)	Spatial resolution, nominal: along scan by cross-scan (m)
17	NIR	0.890–0.920	167		1000: 1049 × 1017
18	NIR	0.931–0.941	57		1000: 1019 × 1002
19	NIR	0.915–0.965	250		1000: 1027 × 998
20	MIR	3.660–3.840		0.05	1000: 1027 × 998
21	MIR	3.929–3.989		2.00	1000: 1081 × 1003
22	MIR	3.929–3.989		0.07	1000: 1081 × 1003
23	MIR	4.020–4.080		0.07	1000: 1036 × 1007
24	MIR	4.433–4.498		0.25	1000: 1057 × 1013
25	MIR	4.482–4.549		0.25	1000: 1042 × 1010
26	SWIR	1.360–1.390	150		1000: 1061 × 1012
27	TIR	6.535–6.895		0.25	1000: 1110 × 1013
28	TIR	7.175–7.475		0.25	1000: 1091 × 1016
29	TIR	8.400–8.700		0.05	1000: 1122 × 1022
30	TIR	9.580–9.880		0.25	1000: 1103 × 1006
31	TIR	10.780–11.280		0.05	1000: 1120 × 1013
32	TIR	11.770–12.270		0.05	1000: 1078 × 1012
33	TIR	13.185–13.485		0.25	1000: 1126 × 1004
34	TIR	13.485–13.785		0.25	1000: 1132 × 990
35	TIR	13.785–14.085		0.25	1000: 1138 × 997
36	TIR	14.085–14.385		0.35	1000: 1128 × 1011

#### A note on the bow-tie effect

A phenomenon peculiar to MODIS was the “bow-tie effect.” This resulted from the MIR and TIR images being acquired in sequential scans that were 10 pixels wide. Although at nadir there was no overlap between adjacent scans, this increased with scan angle to 100% overlap at a scan angle of 55°. This meant that, at a scan angle of 45°, pixel 1 of scan 1 would also appear in pixel 8 of scan 2. Over an active lava this meant that, when the pixels were reprojected to their correct position, the hot spot was duplicated, appearing as a mirrored hot spot separated by two pixels from the real hot spot. At extreme scan angles, the degree of separation for the mirrored hot spot increased. For example, at 55° a hot spot in pixel 5 of scan 1 would also appear in pixel 1 of scan 2. When reprojected this hot spot was apparent as a mirrored hot spot separated by four pixels from the real hot spot. The effect was easy to spot, with the mirror hot spot being separated by a few pixels from the real hot spot and having the same radiance as the real hot spot. The mirrored (duplicated) hot spot just needed to be identified and removed to prevent double counting.

Table D4. Nadir pixel dimensions for each of MODIS' 36 bands calculated, using the pixel-calculation method of Chapter 3, from the IFOVs given by Barnes et al. (1998).

Band	Waveband ( $\mu\text{m}$ )	Pixel dimension (m)	IFOV (mrad)	
1	0.620–0.670	300	262	0.4255
2	0.841–0.876	291	254	0.4128
3	0.459–0.479	560	499	0.7943
4	0.545–0.565	546	499	0.7745
5	1.230–1.250	540	520	0.7660
6	1.628–1.652	540	520	0.7660
7	2.105–2.155	538	521	0.7631
8	0.405–0.420	1059	1007	1.5021
9	0.438–0.493	1043	1003	1.4794
10	0.483–0.493	1058	1003	1.5007
11	0.526–0.536	1041	991	1.4766
12	0.546–0.556	1054	984	1.4950
13	0.662–0.672	1038	1001	1.4723
14	0.673–0.683	1043	1009	1.4794
15	0.743–0.753	1042	1004	1.4780
16	0.862–0.877	1045	1007	1.4823
17	0.890–0.920	1049	1017	1.4879
18	0.931–0.941	1019	1002	1.4454
19	0.915–0.965	1027	998	1.4567
20	3.660–3.840	1027	998	1.4567
21	3.929–3.989	1081	1003	1.5333
22	3.929–3.989	1081	1003	1.5333
23	4.020–4.080	1003	1007	1.4227
24	4.433–4.498	1057	1013	1.4993
25	4.482–4.549	1042	1010	1.4780
26	1.360–1.390	1061	1012	1.5050
27	6.535–6.895	1110	1013	1.5745
28	7.175–7.475	1091	1016	1.5475
29	8.400–8.700	1122	1022	1.5915
30	9.580–9.880	1103	1006	1.5645
31	10.780–11.280	1120	1013	1.5887
32	11.770–12.270	1078	1012	1.5291
33	13.185–13.485	1126	1004	1.5972
34	13.485–13.785	1132	990	1.6057
35	13.785–14.085	1138	997	1.6142
36	14.085–14.385	1128	1011	1.6000

### Primary information sources

- Barnes, W. L., Pagano, T. S. and Salomonson, V. V. (1998). Prelaunch characteristics of the Moderate Resolution Imaging Spectroradiometer (MODIS) on EOS-AM1. *IEEE Trans. Geosciences & Remote Sensing*, **36**(4), 1088–1100.
- Nishihama, M., Wolfe, R., Solomon, D. *et al.* (1997b). MODIS Level 1A earth location: algorithm theoretical basis document version 3.0. *NASA support document prepared by the MODIS Science Data Support Team*, 88 pp.
- Salomonson, V. V., Barnes, W. L., Maymon, P. W., Montgomery, H. E. and Ostrow, H. (1989). MODIS: Advanced facility instrument for studies of the Earth as a system. *IEEE Trans. Geosciences & Remote Sensing*, **27**(2), 145–153.
- Xiong, J., Toller, G., Chiang, V., Sun, J., Esposito, J. and Barnes, W. (2005). MODIS Level 1B algorithm theoretical basis document. NASA support document prepared by the MODIS Characterization Support Team, 40 pp.
- Xiong, X., Wu, A. and Cao, C. (2008). On-orbit calibration and inter-comparison of Terra and Aqua MODIS surface temperature spectral bands. *Int. J. Remote Sensing*, **29**(17–18), 5347–5359.

# Appendix E

## GOES-class sensors

GOES-class sensors share a high temporal resolution of 15–30 minutes, have MIR and TIR capabilities and low spatial resolutions. They also have geostationary orbits. This sensor group includes the GOES-Imager, launched in 1994, plus SEVIRI and MTSAT, both of which were launched in 2005 (see [Chapter 1](#)). In this appendix we give the main orbit and sensor characteristics of these instruments, as well as the primary information sources from which the details given here are largely taken, and from which further sensor and calibration information can be obtained.

### Geostationary Operational Environmental Satellite (GOES) Imager ([Table E1](#))

The GOES Imager was launched on GOES-I in 1994. The Imager had a five band imaging capability:

Band 1, VIS:	0.55–0.75 $\mu\text{m}$
Band 2, MIR:	3.80–4.00 $\mu\text{m}$
Band 3, TIR :	6.50–7.00 $\mu\text{m}$
Band 4, TIR:	10.2–11.2 $\mu\text{m}$
Band 5, TIR:	11.5–12.5 $\mu\text{m}$

The GOES-I Imager details are given in [Table E1](#) and show a spatial resolution to 4.0 km for bands 2, 4 and 5. However, Menzel and Purdom (1994) pointed out that the GOES Imager over-samples the MIR and TIR pixels by a factor of 1.75 in the scan direction. This reduces the EIFOV in the scan direction to 2.3 km (see [Table E1](#)).

Unlike their predecessors, the post-GOES-I satellites did not spin. In the spinning case (i.e., GOES A to H carrying VISSR and VAS), while mirror spin would ensure collection of an E–W swath, the satellite N–S spin would ensure image acquisition in the N–S dimension. Instead GOES Imager data were collected using a two-axis gimbaled mirror scan system mounted on a non-spinning platform. Each image swath was collected by the motion of an E–W/W–E tracking scan mirror rotating at a rate of 20° per second. At the end of each scan the mirror velocity was slowed and reversed over a 0.2 s interval. During this interval the N/S control moved the gimbal assembly 224  $\mu\text{rad}$  to the south and the next swath would start in the opposite direction to the previous swath. The N/S stepping motion continued until the

Table E1. *Nominal orbit and instrument characteristics of NOAA's Imager flown as part of the Geostationary Operational Environmental Satellite (GOES) program.*

Orbit parameter	Details
Altitude	35 790 km
Orbit period	Geostationary
Repeat cycle	Variable: 15–30 min (see <a href="#">Section 3.1.4 of Chapter 3</a> )
Sensor characteristics	Details
Total scan angle	19° (E–W) by 20.8° (N–S)
Scan increment angle	16 µrad (E–W), 8 µrad (N–S)
Swath width	Earth disk (although variable, see <a href="#">Section 3.1.4 of Chapter 3</a> )
Radiometric resolution	10 bits
GVAR image dimensions	6135 × 6125 pixels (full disk, all detectors)
Pixel dwell time	183.3 µs

GOES spatial resolution		
Band	IFOV (km)	EIFOV (km)
1	1.0 × 1.0 km	0.57 × 1.0 km
2	4.0 × 4.0 km	2.30 × 4.0 km
3	8.0 × 8.0 km	2.30 × 8.0 km
4	4.0 × 4.0 km	2.30 × 4.0 km
5	4.0 × 4.0 km	2.30 × 4.0 km

Band	Spectral region	Sensor type	Waveband (µm)	Saturation (°C)	NEΔT	Nominal square IFOV at nadir
1	VIS	Si	0.55–0.75			1 km
2 (GOES I, J, K)	MIR	InSb	3.80–4.00	47 °C	0.15 K @ 300 K	4 km
2 (GOES L, M)			3.80–4.00	62 °C		4 km
3 (GOES I, J, K, L)	TIR	HgCdTe	6.50–7.00	47 °C	0.3 K @ 230 K	8 km
5 (GOES M)			5.80–7.30	47 °C		8 km
4 (GOES I, J, K, L)	TIR	HgCdTe	10.2–11.2	47 °C	0.2 K @ 300 K	4 km
5 (GOES I, J, K, L)	TIR	HgCdTe	11.5–12.5	47 °C	0.2 K @ 300 K	4 km
3 (GOES M)			13.0–13.7	47 °C		4 km

southern limit of acquisition was reached, at which point the mirror would be driven back up to the start of the next scene.

### Primary information sources

- Menzel, W. P. and Purdom, J. F. W. (1994). Introducing GOES-I: The first of a new generation of Geostationary Operational Environmental Satellites. *Bull. Am. Met. Soc.*, **75** (5), 757–761.
- Space Systems / Loral (1996). GOES I-M DataBook. *DRL 101–08*, Revision 1, 197 pp.

### Spinning Enhanced Visible and Infrared Imager (Table E2)

The Spinning Enhanced Visible and Infrared Imager (SEVIRI) was launched, by the European Space Agency in 2002, on the Meteosat Second Generation (MSG) satellite. This placed SEVIRI in a geostationary orbit (see [Table 1.4 of Chapter 1](#)). It offered 12 spectral channels with a nominal spatial resolution of 3 km, except for a high-resolution (1 km) band in the VIS. The 12 bands included one band in the MIR capable of detecting volcanic hot spots, which have been applied to detect, track and measure high-temperature features such as fires burning within its footprint (e.g., Roberts and Wooster, [2008](#)). In addition, SEVIRI featured two TIR bands with relatively high saturation temperatures (IR10.8 and IR12). All bands and main sensor characteristics are listed in [Table E2](#).

Rapid line scan was performed from east to west by the spinning motion of the satellite, spinning on an axis perpendicular to the orbital plane at 100 rotations per minute. Thus, in the 12.5 minute image acquisition period, 1250 lines of data could be acquired. Each spin lasted 600 ms, of which ~30 ms were dedicated to Earth view, so the pixel dwell time was  $30\text{ ms} / 1250\text{ pixels} = 24\text{ }\mu\text{s}$ . Slow scanning was performed by a scan mirror scanning from north to south to build the image in the N–S direction by stepping in increments of  $125.8\text{ }\mu\text{rad}$  at the end of each satellite spin. A total scan angle of  $11^\circ$  (0.19 radians) was sufficient to cover the full Earth disk from a height of 36 000 km. This corresponded to  $0.19\text{ radians} / 125.8\text{ }\mu\text{rad} = 1526$  steps, allowing 1527 scan lines to be acquired (including the first line acquired before the first step occurred at step 0).

### Primary information sources

- EUMETSAT (2006). Pre-launch MSG-1 SEVIRI instrument level 1.0 data. *EUMETSAT Document Number EUM/OPS-MSG/TEN/05/0625*, <http://www.eumetsat.int>.
- Roberts, G. and Wooster, M. J. (2008). Fire detection and fire characterization over Africa using Meteosat SEVIRI. *IEEE Transactions on Geoscience and Remote Sensing*, **46**, 1200–1218, doi: [10.1109/TGRS.2008.915751](https://doi.org/10.1109/TGRS.2008.915751).
- Schmid, J. (2006). The SEVIRI instrument. *EUMETSAT Document*, pdf\_ten\_msg\_seviri\_-instrument.pdf, <http://www.eumetsat.int>.

### Multi-functional Transport Satellite (MTSAT) Imager

With the launch of the Multi-functional Transport Satellite (MTSAT) in 2005, the Japanese Meteorological Agency (JMA) placed a sensor with GOES Imager-like capabilities into a geostationary orbit at  $140^\circ\text{E}$  (see [Table 1.4 of Chapter 1](#)). Previously the satellites flown in

Table E2. *Nominal orbit and instrument characteristics of ESA's Spinning Enhanced Visible and Infrared Imager (SEVIRI) flown on the Meteosat Second Generation satellites.*

Orbit parameter		Details			
Altitude		36 000 km			
Orbit period		Geostationary			
Repeat cycle		15 mins (for full Earth disk)			
Sensor characteristics		Details			
Total scan angle		$\pm 5.5^\circ$ (S–N)			
Scan increment angle		125.8 $\mu$ rad			
Swath width		Earth disk			
Radiometric resolution		10 bits (0 to 1023 DN)			
Image dimensions		1250 scan lines			
Pixel dwell time		24 $\mu$ s			
Band	Spectral region	Waveband ( $\mu$ m)	Saturation ( $^\circ$ C)	$NE\Delta T$	Nominal square IFOV at nadir
HRV	VIS	0.50–0.90		S/N 1.2	1 km
VIS0.6	VIS	0.56–0.71		S/N 10	3 km
VIS0.8	NIR	0.74–0.88		S/N 7	3 km
NIR1.6	SWIR	1.50–1.78		S/N 3	3 km
IR3.9	MIR	3.48–4.36	62 $^\circ$ C	0.35 K	3 km
WV6.2	TIR	5.35–7.15	27 $^\circ$ C	0.28 K	3 km
WV7.3	TIR	6.85–7.85	27 $^\circ$ C	0.25 K	3 km
IR8.7	TIR	8.30–9.10	27 $^\circ$ C	0.37 K	3 km
IR9.7	TIR	9.38–9.94	37 $^\circ$ C	0.75 K	3 km
IR10.8	TIR	9.80–11.80	62 $^\circ$ C	0.75 K	3 km
IR12.0	TIR	11.00–13.00	62 $^\circ$ C	1.50 K	3 km
IR13.4	TIR	12.40–14.40	27 $^\circ$ C	1.80 K	3 km

this location carried a VISSR operating in four bands spanning the VIS and TIR. With the launch of the imager on MTSAT, a fifth MIR band was added, to give the following band configuration:

Band 1, VIS:	0.55–0.80 $\mu$ m
Band 2, TIR:	10.3–11.3 $\mu$ m
Band 3, TIR :	11.5–12.5 $\mu$ m
Band 4, TIR:	6.7–7.5 $\mu$ m
Band 5, MIR:	3.5–4.5 $\mu$ m

The MIR band was equivalent to GOES band 2 and thereby capable of detecting volcanic hot spots. MTSAT Imager data were acquired at 1024 (10 bit) quantization levels, with a 2291 (west–east) by 2201 (north–south) pixel IR image of the full Earth disk, with imaging full disk requiring 22 minutes, and a hemispherical observation taking 11 minutes. With the VIS data having a 1 km resolution at nadir, and the MIR and TIR having 4 km, the MTSAT imager extended the GOES-Imager capability over the volcanoes within its footprint.

#### **Primary information sources**

JMA (1999). MTSAT HiRID Technical Information. *Japan Meteorological Agency Document*, <http://www.jma.go.jp/jma/jma-eng/satellite/mtsat1r/mtsat1r.html>.

# Appendix F

## Scan and satellite location geometry

We here define the main terms used for scan and satellite location geometry. These definitions are given graphically in [Figure F1](#).

### Definition of scan geometry terms

In the case of a scanner-based system, the scan direction is determined by the direction of the mirror rotation, where a new pixel is collected with each increment of the mirror sweep. The image is thus built in the  $x$ -(sample)-dimension by the motion of the mirror sweep and in the  $y$ -(line)-dimension by the motion of the satellite. In this case, scan coordinates can be named either in terms of the direction of the scan, in which case *scan-direction* is the label for the  $x$ -axis (east–west image dimension) and *cross-scan* labels the  $y$ -axis (south–north image dimension). Alternatively, coordinates can be labeled in terms of direction of satellite motion, in which case *cross-track* is the label for the  $x$ -axis, and *track* is the label for the  $y$ -axis. Within this coordinate system, we make the following definitions.

- *Line*. Line of pixels acquired during each Earth-pointed sweep of the scan mirror. Each line contains a total number of pixels equal to  $n_{\text{samples}}$  (for AVHRR,  $n_{\text{samples}} = 2048$ ). While the length of each line defines the dimension of the image in the  $x$ -direction (E–W), the satellite motion builds the image in the  $y$ -direction (N–S).
- *Nadir*. The sub-satellite point, i.e., the Earth surface point vertically below the satellite. The pixel at the nadir point (at pixel  $n_{\text{NADIR}}$ ) will be in the middle of the line of pixels that comprise the image in the  $x$ -direction (for AVHRR this will be at pixel 1024).
- *Satellite height ( $S_h$ )*. Vertical height of the satellite above the ground at nadir. For AVHRR this is  $\sim 850$  km (see Appendix D).
- *Scan increment angle ( $\alpha_l$ )*. The angle by which the scan mirror is stepped between each pixel measurement. This is the step necessary to move the mirror from a position that is centered in the middle of the previous pixel to a position that is centered in the current pixel. For AVHRR  $\alpha_l = 0.95$  mrad.
- *Scan angle ( $\alpha$ )*. The angle between nadir and the pixel being sampled (pixel  $n_x$ ). In our coordinate system, we measure this in terms of an angle from nadir, at which point the view is vertically downwards and scan angle is  $0^\circ$ . For pixels in the down-scan direction, i.e., between the first sample and nadir (i.e.,  $n_x < n_{\text{NADIR}}$ ):

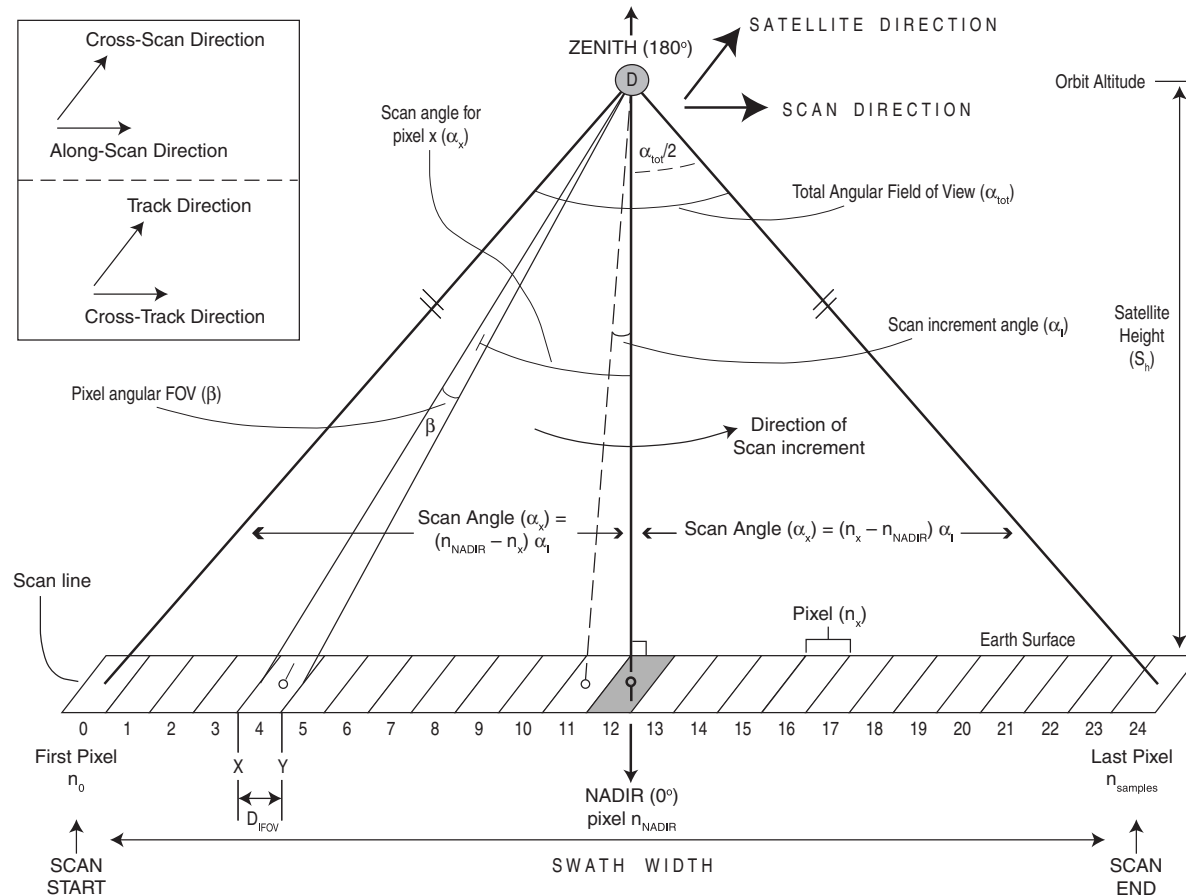


Figure F1 Cartoon showing scan geometry and terminology for an infrared scanner flown on a platform operating at an altitude of  $S_h$ , with a scan direction of W-E and a flight (orbit) direction of S-N.

$$\alpha_x = (n_{\text{NADIR}} - n_x)\alpha_I.$$

Thus, for AVHRR pixel 248

$$\begin{aligned}\alpha_x &= (1024 - 248) 0.95 \text{ mrad} = 0.7372 \text{ radians} \\ &= [(180)(0.7372)]/\pi = 42.2^\circ.\end{aligned}$$

- We may want to place a negative sign in front of this value to indicate that it is in the down-scan direction. For pixels in the up-scan direction, i.e., between the nadir pixel and final pixel in the scan line (i.e.,  $n_x > n_{\text{NADIR}}$ ):

$$\alpha_x = (n_x - n_{\text{NADIR}})\alpha_I.$$

Thus, for AVHRR pixel 1800

$$\alpha_x = (1800 - 1024) 0.95 \text{ mrad} = 0.7372 \text{ radians} = [(180)(0.7372)]/\pi = 42.2^\circ.$$

- *Total angular field of view (FOV,  $\alpha_{\text{tot}}$ )*. The angle covering the full Earth surface scan completed by the sensor. This will be  $n_{\text{samples}}$  multiplied by  $\alpha_I$  (so that  $\alpha_{\text{tot}}/\alpha_I = n_{\text{samples}}$ ). For AVHRR this is  $110.8^\circ$  (or  $55.4^\circ$  either side of nadir).
- *Swath width*. The distance on the ground covered by each full Earth surface scan completed by the sensor. For AVHRR, this is between 2925 km and 3095 km (Table 3.2b of Chapter 3).
- *Angular instantaneous field of view (IFOV,  $\beta$ )*. The angle defining a cone extending from the detector to the surface and which, when projected onto the ground surface, defines the shape and dimensions of the sampled area (i.e., the pixel). For AVHRR,  $\beta$  is  $\sim 1.4$  mrad.
- *Instantaneous field of view ( $D_{\text{IFOV}, xy}$ )*. The Earth surface dimensions (in the  $y$ - and  $x$ -directions) of the ground area defined by the angular instantaneous field of view, i.e., the  $x,y$ -dimensions of the pixel. For AVHRR at nadir ( $S_h = 850$  km and  $\beta = 0.95$  mrad) this is  $1190$  m (Equation 3.5, Chapter 3), so that (for a circular pixel) the sample area is  $\pi r^2 = \pi(595 \text{ m})^2 = 1\ 112\ 202 \text{ m}^2 = 1.112\ 202 \text{ km}^2$ .

# Appendix G

## Automated volcano hot spot detection: worked example

This appendix contains an AVHRR test image containing a volcanic hot spot, completes the processing steps executed by VAST and MODVOLC, and gives the resulting hot spot detection output, i.e., the final image with anomalous pixels flagged as “hot” by the two algorithms. Contents of this Appendix are this as follows.

- (1) Image:  
AVHRR sub-image centered on Mt. Etna, acquired on 24 December 1992.
- (2) DN grids are given in:  
[Table G1](#) for band 3, and  
[Table G2](#) for band 4.
- (3) Brightness temperature conversions are given in:  
[Table G3](#) for band 3 ( $T_3$ ), and  
[Table G4](#) for band 4 ( $T_4$ ).

DN to Radiance conversion is completed using:

	Slope	Intercept
Band 3:	-0.001499	1.482797
Band 4:	-0.177616	176.383399

(See Electronic Supplement 2 for ON-to-Radiance conversion methodology.)

Temperature conversion completed using wavenumbers of:

Band 3:	$2671.4 \text{ cm}^{-1}$
Band 4:	$927.83 \text{ cm}^{-1}$

(See [Section 2.1.4 of Chapter 2](#).)

- (4) The result of subtracting the two brightness temperature images ( $\Delta T = T_3 - T_4$ ) and applying the natural variation kernel (see [Section 5.3.1.1 of Chapter 5](#)) are given in Tables G5 ( $\Delta T$ ) and G6 ( $\omega$ ), respectively.

- (5) NTI (see Equation 5.1 of Chapter 5) calculated for the Etna sub-image is given in Table G7.
- (6) Results from running VAST over the Etna sub-image are given in Table G8 using a natural variation threshold ( $\sigma_{\text{thresh}}$ ) of 1.75 selected from the boundary zone of this image (see Section 5.3.1.1. of Chapter 5 for execution of algorithm).
- (6) Results from running MODVOLC over the Etna sub-image are given in Table G9 using the global night-time MODVOLC NTI threshold of Wright *et al.* (2002) of  $-0.8$  and a locally-calibrated NTI threshold of  $-0.9$  (as derived for this image using the histogram of Figure 5.8d in Chapter 5; see Section 5.3.3 in Chapter 5 for execution of algorithm).

### Key

Hottest pixels:	Bold, white background. Pixels with values of $47^{\circ}\text{C}$ or $48^{\circ}\text{C}$ are saturated.
Warm pixels:	Bold, with gray background.
Sensor recovery:	Dark gray background.
Ambient pixels:	Non-bold, white background.
“R”:	Masked sensor recovery pixels in $\Delta T$ image.

VAST results (as given in Table G8):

A:	Pixel selected during first iteration of VAST.
S:	Saturated pixel added at the end of VAST first iteration.
B:	Pixel selected during subsequent iterations of VAST.

MODVOLC results (as given in Table G9):

X:	Pixel with $\text{NTI} > -0.8$ .
Y:	Pixel with $\text{NTI} > -0.9$ .

Table G1. *AVHRR band 3 digital numbers for Etna sub-image.*

DN3	A	B	C	D	E	F	G	H	I	J	K	L	M	N	O	P	Q	R	S	T	U	V	W	X	Y	
A	736	739	744	762	771	799	816	823	829	843	865	876	883	876	875	860	840	831	807	796	776	763	746	747	770	
B	751	732	737	745	761	790	809	826	833	851	863	873	883	885	879	852	838	830	822	813	795	774	758	754	749	
C	745	736	733	746	749	766	801	831	831	844	859	868	883	880	876	849	836	828	822	808	801	782	758	757	745	
D	721	719	720	739	752	772	801	833	844	851	864	868	881	874	866	837	819	810	806	797	785	781	764	761	758	
E	727	738	753	762	765	781	805	827	833	837	842	866	889	890	879	856	833	811	805	784	773	776	762	746	733	
F	728	744	758	771	775	783	818	845	835	834	833	857	882	867	863	855	831	809	785	773	765	761	765	759	756	
G	712	732	759	778	783	805	818	843	855	853	844	843	843	860	851	846	813	789	771	753	753	751	756	759	761	
H	723	762	783	792	805	822	833	841	838	830	821	811	790	807	824	825	820	787	778	776	777	770	753	748	747	
I	721	740	763	761	779	801	818	826	831	823	800	731	645	637	725	779	799	784	774	764	771	779	756	749	755	
J	728	729	736	751	764	793	816	828	828	852	986	36	47	47	47	38	343	746	782	783	774	754	766	753	757	764
K	744	740	746	763	784	802	815	831	832	837	941	628	47	47	47	46	426	773	779	781	759	762	743	752	773	
L	742	738	745	757	772	783	796	823	822	814	796	725	522	349	460	611	733	769	773	774	759	748	741	756	763	
M	734	729	744	753	766	774	787	799	794	797	766	773	741	688	689	726	759	756	771	766	764	755	753	754	761	
O	736	735	739	744	745	754	765	781	778	773	760	754	770	766	753	757	761	757	769	764	766	758	748	750	759	
N	751	749	748	748	745	756	760	773	757	754	756	747	764	765	762	771	762	763	764	771	770	761	754	761	765	
P	706	725	736	739	749	761	766	770	760	764	759	752	751	749	762	759	755	755	755	754	748	753	759	766	766	
Q	705	706	735	744	754	757	761	763	753	761	760	771	771	758	744	740	748	748	751	751	744	752	754	763	763	
R	740	741	748	747	743	741	738	740	748	751	765	772	765	758	762	747	758	758	761	759	750	752	757	760	757	
S	731	732	738	739	731	738	737	742	747	744	758	754	755	749	750	743	743	754	753	754	742	745	755	758	759	
T	732	714	725	734	733	744	744	752	737	742	751	741	750	745	746	744	741	747	753	753	744	755	757	762	762	

Table G2. *AVHRR band 4 digital numbers for Etna sub-image.*

DN4	A	B	C	D	E	F	G	H	I	J	K	L	M	N	O	P	Q	R	S	T	U	V	W	X	Y
A	492	493	496	502	510	526	539	547	555	570	584	592	593	587	581	567	552	540	526	516	505	498	493	494	499
B	495	491	490	495	505	521	538	552	560	574	589	598	601	596	582	560	545	540	532	523	512	501	496	491	491
C	490	487	488	493	500	516	536	551	558	572	587	598	604	598	580	557	545	540	534	525	515	505	496	491	488
D	485	483	486	493	500	516	537	553	563	574	588	603	608	599	579	558	548	541	534	523	514	504	496	490	487
E	483	488	496	501	507	522	542	557	566	573	586	606	616	606	587	568	551	537	527	516	507	502	494	487	485
F	482	490	499	506	510	525	547	563	569	571	580	602	614	601	586	569	549	535	520	508	500	495	492	488	487
G	483	493	506	514	520	535	550	564	570	571	577	591	600	589	578	562	541	527	514	505	499	493	490	487	486
H	481	495	506	515	526	540	552	562	568	569	573	578	584	584	569	555	538	520	510	505	501	494	488	485	484
I	478	490	498	503	517	535	547	556	565	568	569	572	574	572	558	541	532	518	507	502	499	496	488	484	484
J	481	484	489	497	512	529	544	552	559	564	569	550	446	426	504	509	520	518	512	501	494	492	488	485	485
K	487	488	491	501	516	530	542	550	555	561	564	541	401	348	375	447	509	517	512	501	493	490	485	484	484
L	490	491	496	503	510	520	534	542	545	547	544	550	555	540	523	522	518	513	507	502	495	489	486	485	484
M	486	488	493	498	505	513	525	533	536	532	525	530	534	528	520	521	515	506	503	500	495	490	487	485	484
O	485	486	490	494	497	502	513	521	523	519	514	515	524	525	519	520	514	504	501	498	493	488	485	484	484
N	485	487	490	492	496	500	508	515	514	512	509	510	520	523	518	517	510	503	499	496	492	487	485	484	483
P	480	483	486	489	493	498	503	503	502	503	504	503	505	508	509	508	505	501	496	492	489	487	485	484	483
Q	477	481	485	490	493	496	499	499	498	502	504	506	505	504	502	502	501	497	492	489	488	485	484	483	483
R	479	483	487	489	489	492	493	494	498	501	506	505	502	501	499	499	500	500	496	491	487	485	484	483	483
S	478	482	486	486	488	489	488	491	495	498	499	496	496	496	495	496	498	496	491	486	484	484	483	483	483
T	477	478	482	484	485	487	488	490	489	490	492	491	493	494	494	494	494	496	495	491	485	483	483	483	483

Table G3. *AVHRR band 3 brightness temperatures for Etna sub-image.*

T3	A	B	C	D	E	F	G	H	I	J	K	L	M	N	O	P	Q	R	S	T	U	V	W	X	Y
A	16	16	15	13	13	9.7	7.8	6.9	6.2	4.4	1.1	-0.7	-1.9	-0.7	-0.5	1.9	4.8	5.9	8.8	10	12	13	15	15	13
B	14	16	16	15	14	11	8.6	6.6	5.7	3.2	1.4	-0.2	-1.9	-2.3	-1.2	3.1	5	6.1	7.1	8.1	10	12	14	14	15
C	15	16	16	15	15	13	9.5	5.9	5.9	4.2	2	0.6	-1.9	-1.4	-0.7	3.5	5.3	6.3	7.1	8.7	9.5	12	14	14	15
D	17	17	17	16	14	13	9.5	5.7	4.2	3.2	1.3	0.6	-1.6	-0.3	1	5.2	7.4	8.5	8.9	9.9	11	12	13	14	14
E	17	16	14	13	13	12	9.1	6.4	5.7	5.2	4.5	1	-3	-3.2	-1.2	2.5	5.7	8.4	9.1	11	12	12	13	15	16
F	16	15	14	13	12	11	7.6	4.1	5.4	5.6	5.7	2.4	-1.7	0.8	1.4	2.6	5.9	8.6	11	12	13	14	13	14	14
G	18	16	14	12	11	9.1	7.6	4.4	2.6	2.9	4.2	4.4	4.4	1.9	3.2	3.9	8.1	11	13	14	14	14	14	14	14
H	17	13	11	10	9.1	7.1	5.7	4.6	5	6.1	7.2	8.4	11	8.8	6.8	6.7	7.3	11	12	12	12	13	14	15	15
I	17	15	13	14	12	9.5	7.6	6.6	5.9	6.9	9.6	16	23	23	17	12	9.7	11	12	13	13	12	14	15	14
J	16	16	16	14	13	10	7.8	6.3	6.3	3.1	-56	48	47	47	48	38	15	12	11	12	14	13	14	14	13
K	15	15	15	13	11	9.4	7.9	5.9	5.8	5.2	-16	24	47	47	47	48	34	12	12	12	14	13	15	14	12
L	15	16	15	14	13	11	10	6.9	7.1	8	10	17	30	37	33	25	16	13	12	12	14	15	15	14	13
M	16	16	15	14	13	12	11	9.7	10	9.9	13	12	15	20	20	17	14	14	13	13	14	14	14	14	14
O	16	16	16	15	15	14	13	12	12	12	14	14	13	13	14	14	14	14	13	13	13	14	15	15	14
N	14	15	15	15	15	14	14	12	14	14	14	15	13	13	13	13	13	13	13	13	13	14	14	14	13
P	18	17	16	16	15	14	13	13	14	13	14	14	14	15	13	14	14	14	14	14	15	14	14	13	13
Q	18	18	16	15	14	14	14	13	14	14	14	13	13	14	15	15	15	14	14	15	14	14	13	13	
R	15	15	15	15	15	16	15	15	15	14	13	13	13	14	13	15	14	14	14	14	15	14	14	14	14
S	16	16	16	16	16	16	15	15	15	14	14	14	15	15	15	15	14	14	14	15	15	14	14	14	14
T	16	18	17	16	16	15	15	14	16	15	14	15	15	15	15	15	15	14	14	15	14	14	13	13	

Table G4. *AVHRR band 4 brightness temperatures for Etna sub-image.*

T4	A	B	C	D	E	F	G	H	I	J	K	L	M	N	O	P	Q	R	S	T	U	V	W	X	Y
A	12	12	12	11	9.8	7.9	6.2	5.2	4.1	2.2	0.3	-0.8	-0.9	-0.1	0.7	2.6	4.5	6.1	7.9	9.1	10	11	12	12	11
B	12	12	12	12	10	8.5	6.3	4.5	3.5	1.6	-0.4	-1.6	-2.1	-1.4	0.6	3.5	5.4	6.1	7.1	8.2	9.6	11	12	12	12
C	12	13	13	12	11	9.1	6.6	4.7	3.8	1.9	-0.1	-1.6	-2.5	-1.6	0.8	3.9	5.4	6.1	6.8	8	9.2	10	12	12	13
D	13	13	13	12	11	9.1	6.5	4.4	3.1	1.6	-0.3	-2.3	-3	-1.8	1	3.8	5.1	6	6.8	8.2	9.3	11	12	12	13
E	13	13	12	11	10	8.4	5.8	3.9	2.7	1.8	0	-2.8	-4.2	-2.8	-0.1	2.4	4.7	6.5	7.7	9.1	10	11	12	13	13
F	13	12	11	10	9.8	8	5.2	3.1	2.3	2	0.8	-2.2	-3.9	-2.1	0	2.3	4.9	6.7	8.6	10	11	12	12	13	13
G	13	12	10	9.3	8.6	6.7	4.8	3	2.2	2	1.2	-0.7	-1.9	-0.4	1.1	3.2	6	7.7	9.3	10	11	12	12	13	13
H	13	12	10	9.2	7.9	6.1	4.5	3.2	2.4	2.3	<b>1.8</b>	<b>1.1</b>	<b>0.3</b>	<b>0.3</b>	<b>2.3</b>	4.1	6.3	8.6	9.8	10	11	12	13	13	13
I	14	12	11	11	9	6.7	5.2	4	2.8	2.4	<b>2.3</b>	<b>1.9</b>	<b>1.6</b>	<b>1.9</b>	<b>3.8</b>	<b>6</b>	7.1	8.9	10	11	11	12	13	13	13
J	13	13	12	11	9.6	7.5	5.6	4.5	3.6	3	<b>2.3</b>	<b>4.8</b>	<b>17</b>	<b>20</b>	<b>11</b>	<b>10</b>	<b>8.6</b>	8.9	9.6	11	12	12	13	13	13
K	13	13	12	11	9.1	7.3	5.8	4.8	4.1	3.4	<b>3</b>	<b>6</b>	<b>22</b>	<b>28</b>	<b>25</b>	<b>17</b>	<b>10</b>	9	9.6	11	12	12	13	13	13
L	12	12	12	11	9.8	8.6	6.8	5.8	5.4	5.2	5.6	<b>4.8</b>	<b>4.1</b>	<b>6.1</b>	<b>8.2</b>	<b>8.4</b>	<b>8.9</b>	9.5	10	11	12	12	13	13	13
M	13	13	12	11	10	9.5	8	7	6.6	7.1	8	7.3	<b>6.8</b>	<b>7.6</b>	<b>8.6</b>	<b>8.5</b>	9.2	10	11	11	12	12	13	13	13
O	13	13	12	12	11	11	9.5	8.5	8.2	8.7	9.3	9.2	8.1	8	8.7	8.6	9.3	11	11	11	12	13	13	13	13
N	13	13	12	12	12	11	10	9.2	9.3	9.6	10	9.8	8.6	8.2	8.9	9	9.8	11	11	12	12	13	13	13	13
P	13	13	13	12	12	11	11	11	11	11	11	11	10	10	10	10	10	11	12	12	12	13	13	13	13
Q	14	13	13	12	12	12	11	11	11	11	11	10	10	11	11	11	11	11	12	12	13	13	13	13	13
R	14	13	13	12	12	12	12	12	11	11	11	10	10	11	11	11	11	11	12	12	13	13	13	13	13
S	14	13	13	13	13	12	13	12	12	11	11	12	12	12	12	12	11	12	12	13	13	13	13	13	13
T	14	14	13	13	13	13	13	12	12	12	12	12	12	12	12	12	12	12	12	12	13	13	13	13	13

Table G5.  $\Delta T$  derived for Etna sub-image.

$\Delta T$	A	B	C	D	E	F	G	H	I	J	K	L	M	N	O	P	Q	R	S	T	U	V	W	X	Y
A	3.8	3.6	3.6	2.7	2.8	1.9	1.6	1.8	2.1	2.2	0.8	0.1	-1	-0.6	-1.2	-0.7	0.2	-0.1	1	1	1.7	2.1	3	3.1	1.5
B	2.8	4	3.5	3.4	3.1	2.2	2.3	2	2.2	1.6	1.8	1.5	0.1	-0.9	-1.8	-0.4	-0.4	-0	-0	-0.1	0.6	1.4	2.3	2.1	2.5
C	2.8	3.2	3.6	3	3.6	4	2.9	1.3	2.2	2.3	2.2	2.3	0.6	0.3	-1.5	-0.4	-0.1	0.2	0.2	0.7	0.3	1.1	2.3	1.8	2.5
D	4.2	4.1	4.4	3.6	3.3	3.4	3	1.3	1.1	1.6	1.5	3	1.5	1.4	0	1.4	2.4	2.5	2.1	1.7	1.9	1	1.7	1.3	1.2
E	3.5	3.1	2.8	2.5	3	3.3	3.2	2.6	3	3.4	4.5	3.7	1.2	-0.5	-1.1	0.1	1	1.9	1.3	2.2	2.2	1.3	1.7	2.3	3.2
F	3.3	2.8	2.7	2.3	2.4	3.4	2.4	1	3.1	3.5	4.9	4.5	2.2	2.9	1.4	0.3	1	1.9	2.6	2.3	2.1	1.9	1.2	1.2	1.4
G	4.7	4.2	3.4	2.6	2.8	2.3	2.8	1.4	0.5	0.9	3	5	<b>6.3</b>	2.3	2.1	0.7	2.2	3.1	3.3	3.9	3.1	2.6	1.8	1.1	0.8
H	3.6	1.8	1.1	1.3	1.2	1	1.2	1.4	2.6	3.8	<b>5.4</b>	<b>7.3</b>	<b>10</b>	<b>8.6</b>	<b>4.5</b>	2.6	1	2.4	2.1	1.7	1.1	0.9	1.8	1.9	1.9
I	3.4	3.2	2.1	2.9	2.8	2.8	2.4	2.6	3.1	4.5	<b>7.3</b>	<b>14</b>	<b>21</b>	<b>21</b>	<b>13</b>	<b>5.9</b>	2.6	2.5	2.1	2.5	1.4	0.3	1.5	1.7	1.1
J	3.1	3.4	3.4	3.1	3.7	2.9	2.2	1.8	2.7	0.1	R	<b>43</b>	<b>30</b>	<b>28</b>	<b>37</b>	<b>28</b>	<b>6.3</b>	2.7	1.8	1.4	2.4	1.1	1.8	1.1	0.4
K	2.5	3	2.8	2.4	2.2	2	2.1	1.1	1.7	1.8	R	<b>18</b>	<b>25</b>	<b>19</b>	<b>22</b>	<b>30</b>	<b>24</b>	3.4	2.2	0.7	1.8	1.2	2.3	1.4	-0.6
L	3	3.5	3.5	3.2	2.7	2.8	3.2	1.1	1.6	2.8	4.5	<b>12</b>	<b>26</b>	<b>31</b>	<b>25</b>	<b>16</b>	<b>7.2</b>	3.3	2.2	1.5	2.1	2.4	2.6	1.2	0.4
M	3.2	3.9	3.2	3	2.6	2.8	3	2.8	3.7	2.8	5.1	5.1	<b>8.5</b>	<b>12</b>	<b>11</b>	<b>8.2</b>	4.5	3.7	1.9	2	1.6	1.9	1.7	1.3	0.6
O	2.9	3.1	3.3	3.3	3.6	3.4	3.7	3.1	3.7	3.7	4.3	5	4.6	5.1	5.6	5.3	4.2	3.4	1.9	2	1.2	1.3	1.9	1.6	0.8
N	1.6	2	2.5	2.7	3.5	3	3.6	3.2	4.6	4.6	4.1	5	4.7	5	4.6	3.6	3.6	2.7	2.1	1.1	0.7	0.9	1.3	0.6	0.1
P	4.8	3.6	3.1	3.2	2.8	2.3	2.4	2	2.8	2.6	3.2	3.7	4	4.6	3.5	3.7	3.7	3.2	2.6	2.2	2.4	1.7	0.9	0.1	-0
Q	4.5	4.9	3	2.8	2.3	2.4	2.4	2.2	3	2.7	3.1	2.3	2.2	3.3	<b>4.3</b>	<b>4.6</b>	<b>3.9</b>	3.8	3.1	2.5	2.7	1.9	1.3	0.4	0.3
R	1.9	2.3	2.1	2.5	2.8	3.3	3.7	3.7	3.5	3.5	2.9	2.1	2.4	2.9	2.3	3.7	2.8	2.8	2	1.6	1.9	1.5	0.9	0.6	0.8
S	2.5	2.9	2.9	2.8	3.5	3.2	3.2	3.1	3.2	3.8	2.7	2.7	2.6	3.1	3	3.5	3.7	2.9	2.8	2.1	2.5	2	1.1	0.7	0.6
T	2.3	3.9	3.5	3	3.2	2.5	2.6	2.1	3.3	3	2.5	3.2	2.7	3.2	3.1	3.3	3.6	3.3	2.6	2.2	2.2	1	0.8	0.4	0.4

Table G6. Values of  $\omega$  derived for Etna sub-image.

$\omega$	A	B	C	D	E	F	G	H	I	J	K	L	M	N	O	P	Q	R	S	T	U	V	W	X	Y
A	0.3	0.1	0.1	-0.6	0.1	-0.5	-0.4	-0.3	0.1	0.5	-0.6	-0.5	-1	0.4	-0.3	0	0.6	-0.3	0.8	0.3	0.7	0.3	0.9	0.8	-1
B	-0.7	0.7	0.1	0.1	0.2	-0.6	0.1	0	0.3	-0.4	0.2	0.6	-0.1	-0.3	-1.1	0.3	-0.3	-0.1	-0.4	-0.8	-0.4	-0.3	0.2	-0.3	0.3
C	-0.9	-0.5	-0.1	-0.5	0.3	1	0.5	-0.9	0.5	0.5	0.2	0.8	-0.6	0.3	-1.5	-0.3	-0.8	-0.6	-0.7	-0.1	-0.8	-0.4	0.7	-0.2	0.7
D	0.9	0.7	1.2	0.4	0	0.1	0.3	-1.1	-1.1	-0.9	-1.3	0.8	-0	1.4	0	1.4	1.5	1.4	0.7	0.3	0.5	-0.5	0.1	-0.8	-1
E	-0	-0.3	-0.4	-0.5	-0.1	0.2	0.7	0.3	0.8	0.5	1.2	0.8	-1.2	-1.6	-2	-0.8	-0.4	0.1	-0.8	0.2	0.4	-0.4	0.2	0.7	1.7
F	-0.4	-0.6	-0.3	-0.5	-0.4	0.7	-0.1	-1.4	1.1	0.6	1.3	0.7	-1	1.1	0.6	-0.6	-0.4	-0.2	0.1	-0.3	-0.3	-0.1	-0.6	-0.4	-0.3
G	1.5	1.3	1.1	0.4	0.8	0.2	1	-0.5	-1.7	-2.4	-1.4	-0.5	<b>0.9</b>	-2.5	-0.8	-1.2	0.6	1	0.8	1.6	1.1	0.8	0.2	-0.4	-0.7
H	0.1	-1.4	-1.6	-1.1	-1.1	-1.3	-0.9	-0.7	0.3	0.4	<b>-0.3</b>	<b>-1.8</b>	<b>-0.3</b>	<b>-1.6</b>	<b>-2.5</b>	-1.4	-1.8	0.1	-0.6	-0.8	-1	-0.8	0.3	0.4	0.5
I	0.3	0.5	-0.4	0.5	0.5	0.6	0.4	0.4	0.7	8.6	<b>4.8</b>	<b>6</b>	<b>0.7</b>	<b>2.2</b>	<b>-3.9</b>	<b>-6</b>	-3.7	-0.2	-0	0.7	0	-1.2	0.2	0.2	-0.2
J	0.1	0.5	0.6	0.3	1	0.4	0	-0.4	0.6	7.1	R	<b>38</b>	<b>6.4</b>	<b>4.2</b>	<b>16</b>	<b>10</b>	<b>-6.1</b>	-3	-0.4	-0.5	1.1	-0.5	0.5	-0.1	-0.5
K	-0.7	-0.2	-0.4	-0.6	-0.6	-0.7	-0.1	-0.9	0	9.8	R	<b>9.9</b>	<b>-0.8</b>	<b>-8.6</b>	<b>-4.6</b>	<b>9.4</b>	12	-2.8	0.1	-1.3	0.3	-0.9	0.7	0.3	-1.5
L	-0.2	0.4	0.4	0.4	0	0.2	1	-1.3	-0.6	2.6	1	<b>2.9</b>	<b>9.2</b>	<b>13</b>	<b>5.7</b>	<b>-0.1</b>	<b>-4.6</b>	-2.9	-0.1	-0.3	0.4	0.5	1	-0.1	-0.4
M	-0.1	0.7	-0.2	-0.2	-0.5	-0.3	0.2	-0.1	1	-0.8	0.1	-3.6	<b>-4.1</b>	<b>-2.5</b>	<b>-2.6</b>	<b>-1.7</b>	-1.9	0.1	-0.6	0.2	-0.2	0	-0.1	0	-0.5
O	0.2	0.3	0.3	0.3	0.5	0.2	0.6	-0.4	0.1	-0.4	-0.1	-0.2	-1.7	-1.9	-1.3	-0.3	-0.2	0.3	-0.5	0.4	-0.3	-0.1	0.6	0.6	-0.1
N	-1.7	-1.1	-0.6	-0.4	0.5	-0.2	0.7	-0.1	1.4	1	0.1	0.8	0.1	0.4	0.1	-0.6	-0.1	-0.4	-0.3	-0.8	-0.9	-0.5	0.2	-0.3	-0.5
P	1.5	0.3	-0	0.3	-0	-0.5	-0.2	-1	-0.3	-0.9	-0.3	0.1	0.2	0.6	-0.7	-0.3	0	-0	0	0.1	0.7	0.2	-0.1	-0.5	-0.3
Q	1	1.8	-0	0.1	-0.4	-0.4	-0.4	-0.7	0.1	-0.3	0.2	-0.6	-1	0	0.7	1.2	0.4	0.8	0.5	0.1	0.8	0.2	0.3	-0.2	-0.1
R	-1.6	-0.8	-0.9	-0.3	-0	0.4	0.8	0.6	0.3	0.4	0	-0.5	-0.3	0	-1.3	0.1	-0.8	-0.3	-0.7	-0.8	-0.2	-0.3	-0.3	-0.2	0.3
S	-0.1	0.2	0	-0.1	0.6	0.1	0.2	-0	-0.1	0.7	-0.3	0.1	-0.2	0.3	-0.1	0.3	0.4	-0	0.3	-0.2	0.7	0.5	0.1	0	0.1
T	-0.8	1.1	0.4	-0.2	0.2	-0.7	-0.2	-1	0.3	-0.1	-0.6	0.6	-0.3	0.3	-0.1	-0.1	0.2	0.2	0	-0.3	0.3	-0.7	-0.2	-0.4	-0.2

Table G7. *NTI derived for Etna sub-image (all values are NEGATIVE: –ve sign has been removed to save space).*

NTI	A	B	C	D	E	F	G	H	I	J	K	L	M	N	O	P	Q	R	S	T	U	V	W	X	Y
A	0.93	0.93	0.93	0.94	0.94	0.94	0.95	0.95	0.95	0.95	0.96	0.96	0.96	0.96	0.96	0.95	0.95	0.95	0.94	0.94	0.94	0.93	0.93	0.94	
B	0.94	0.93	0.93	0.93	0.94	0.94	0.95	0.95	0.95	0.96	0.96	0.96	0.96	0.96	0.96	0.95	0.95	0.95	0.95	0.95	0.95	0.94	0.94	0.94	0.94
C	0.93	0.93	0.93	0.93	0.93	0.94	0.94	0.95	0.95	0.95	0.96	0.96	0.96	0.96	0.96	0.96	0.95	0.95	0.95	0.95	0.95	0.94	0.94	0.94	0.93
D	0.93	0.93	0.93	0.93	0.93	0.94	0.94	0.95	0.95	0.96	0.96	0.96	0.96	0.96	0.96	0.95	0.95	0.95	0.95	0.94	0.94	0.94	0.94	0.94	0.94
E	0.93	0.93	0.94	0.94	0.94	0.94	0.94	0.95	0.95	0.95	0.96	0.96	0.96	0.96	0.96	0.95	0.95	0.95	0.94	0.94	0.94	0.94	0.94	0.93	0.93
F	0.93	0.93	0.94	0.94	0.94	0.94	0.95	0.95	0.95	0.95	0.95	0.96	0.96	0.96	0.96	0.95	0.95	0.95	0.94	0.94	0.94	0.94	0.94	0.94	0.94
G	0.93	0.93	0.94	0.94	0.94	0.95	0.95	0.95	0.96	0.96	0.95	0.95	0.95	0.95	0.95	0.95	0.94	0.94	0.93	0.94	0.94	0.94	0.94	0.94	0.94
H	0.93	0.94	0.94	0.94	0.95	0.95	0.95	0.95	0.95	0.95	<b>0.95</b>	<b>0.94</b>	<b>0.93</b>	<b>0.94</b>	<b>0.95</b>	0.95	0.95	0.94	0.94	0.94	0.94	0.94	0.94	0.94	0.94
I	0.93	0.93	0.94	0.94	0.94	0.94	0.95	0.95	0.95	0.95	<b>0.94</b>	<b>0.92</b>	<b>0.89</b>	<b>0.89</b>	<b>0.92</b>	<b>0.94</b>	0.94	0.94	0.94	0.94	0.94	0.94	0.94	0.94	0.94
J	0.93	0.93	0.93	0.94	0.94	0.94	0.95	0.95	0.95	0.96	R	<b>0.74</b>	<b>0.78</b>	<b>0.79</b>	<b>0.76</b>	<b>0.83</b>	<b>0.93</b>	0.94	0.94	0.94	0.94	0.94	0.94	0.94	0.94
K	0.93	0.93	0.93	0.94	0.94	0.95	0.95	0.95	0.95	0.95	R	<b>0.89</b>	<b>0.80</b>	<b>0.81</b>	<b>0.81</b>	<b>0.78</b>	<b>0.85</b>	0.94	0.94	0.94	0.94	0.94	0.93	0.94	0.94
L	0.93	0.93	0.93	0.94	0.94	0.94	0.94	0.95	0.95	0.95	0.94	<b>0.92</b>	<b>0.86</b>	<b>0.82</b>	<b>0.85</b>	<b>0.89</b>	<b>0.93</b>	0.94	0.94	0.94	0.94	0.94	0.93	0.94	0.94
M	0.93	0.93	0.93	0.94	0.94	0.94	0.94	0.94	0.94	0.94	0.94	0.94	<b>0.93</b>	<b>0.91</b>	<b>0.92</b>	<b>0.92</b>	0.93	0.94	0.94	0.94	0.94	0.94	0.94	0.94	0.94
O	0.93	0.93	0.93	0.93	0.93	0.94	0.94	0.94	0.94	0.94	0.94	0.93	0.94	0.94	0.93	0.93	0.94	0.94	0.94	0.94	0.94	0.94	0.94	0.94	0.94
N	0.94	0.94	0.94	0.93	0.93	0.94	0.94	0.94	0.93	0.93	0.93	0.93	0.94	0.94	0.94	0.94	0.94	0.94	0.94	0.94	0.94	0.94	0.94	0.94	0.94
P	0.93	0.93	0.93	0.93	0.93	0.94	0.94	0.94	0.94	0.94	0.94	0.93	0.93	0.93	0.94	0.94	0.94	0.94	0.94	0.94	0.94	0.94	0.94	0.94	0.94
Q	0.93	0.93	0.93	0.93	0.94	0.94	0.94	0.94	0.94	0.94	0.94	0.94	0.94	0.94	0.93	0.93	0.93	0.94	0.94	0.93	0.94	0.94	0.94	0.94	0.94
R	0.93	0.93	0.93	0.93	0.93	0.93	0.93	0.93	0.93	0.94	0.94	0.94	0.94	0.94	0.94	0.93	0.94	0.94	0.94	0.94	0.94	0.94	0.94	0.94	0.94
S	0.93	0.93	0.93	0.93	0.93	0.93	0.93	0.93	0.93	0.94	0.94	0.94	0.93	0.93	0.93	0.93	0.94	0.94	0.94	0.93	0.94	0.94	0.94	0.94	0.94
T	0.93	0.93	0.93	0.93	0.93	0.93	0.93	0.94	0.93	0.93	0.94	0.93	0.94	0.93	0.93	0.93	0.93	0.94	0.94	0.94	0.93	0.94	0.94	0.94	0.94

Table G8. *Pixels detected by VAST.*

$\Delta T$	A	B	C	D	E	F	G	H	I	J	K	L	M	N	O	P	Q	R	S	T	U	V	W	X	Y
A	3.8	3.6	3.6	2.7	2.8	1.9	1.6	1.8	2.1	2.2	0.8	0.1	-1	-0.6	-1.2	-0.7	0.2	-0.1	1	1	1.7	2.1	3	3.1	1.5
B	2.8	4	3.5	3.4	3.1	2.2	2.3	2	2.2	1.6	1.8	1.5	0.1	-0.9	-1.8	-0.4	-0.4	-0	-0	-0.1	0.6	1.4	2.3	2.1	2.5
C	2.8	3.2	3.6	3	3.6	4	2.9	1.3	2.2	2.3	2.2	2.3	0.6	0.3	-1.5	-0.4	-0.1	0.2	0.2	0.7	0.3	1.1	2.3	1.8	2.5
D	4.2	4.1	4.4	3.6	3.3	3.4	3	1.3	1.1	1.6	1.5	3	1.5	1.4	0	1.4	2.4	2.5	2.1	1.7	1.9	1	1.7	1.3	1.2
E	3.5	3.1	2.8	2.5	3	3.3	3.2	2.6	3	3.4	4.5	3.7	1.2	-0.5	-1.1	0.1	1	1.9	1.3	2.2	2.2	1.3	1.7	2.3	3.2
F	3.3	2.8	2.7	2.3	2.4	3.4	2.4	1	3.1	3.5	4.9	4.5	2.2	2.9	1.4	0.3	1	1.9	2.6	2.3	2.1	1.9	1.2	1.2	1.4
G	4.7	4.2	3.4	2.6	2.8	2.3	2.8	1.4	0.5	0.9	3	5	<b>B</b>	2.3	2.1	0.7	2.2	3.1	3.3	3.9	3.1	2.6	1.8	1.1	0.8
H	3.6	1.8	1.1	1.3	1.2	1	1.2	1.4	2.6	3.8	<b>B</b>	<b>B</b>	<b>B</b>	<b>B</b>	<b>B</b>	2.6	1	2.4	2.1	1.7	1.1	0.9	1.8	1.9	1.9
I	3.4	3.2	2.1	2.9	2.8	2.8	2.4	2.6	3.1	4.5	<b>B</b>	<b>B</b>	<b>B</b>	<b>A</b>	<b>B</b>	<b>B</b>	2.6	2.5	2.1	2.5	1.4	0.3	1.5	1.7	1.1
J	3.1	3.4	3.4	3.1	3.7	2.9	2.2	1.8	2.7	0.1	<b>R</b>	<b>A</b>	<b>A</b>	<b>A</b>	<b>A</b>	<b>B</b>	2.7	1.8	1.4	2.4	1.1	1.8	1.1	0.4	
K	2.5	3	2.8	2.4	2.2	2	2.1	1.1	1.7	1.8	<b>R</b>	<b>B</b>	<b>S</b>	<b>S</b>	<b>S</b>	<b>A</b>	<b>A</b>	3.4	2.2	0.7	1.8	1.2	2.3	1.4	-0.6
L	3	3.5	3.5	3.2	2.7	2.8	3.2	1.1	1.6	2.8	4.5	<b>B</b>	<b>A</b>	<b>A</b>	<b>A</b>	<b>B</b>	<b>B</b>	3.3	2.2	1.5	2.1	2.4	2.6	1.2	0.4
M	3.2	3.9	3.2	3	2.6	2.8	3	2.8	3.7	2.8	5.1	5.1	<b>B</b>	<b>B</b>	<b>B</b>	<b>B</b>	4.5	3.7	1.9	2	1.6	1.9	1.7	1.3	0.6
O	2.9	3.1	3.3	3.3	3.6	3.4	3.7	3.1	3.7	3.7	4.3	5	4.6	5.1	5.6	5.3	4.2	3.4	1.9	2	1.2	1.3	1.9	1.6	0.8
N	1.6	2	2.5	2.7	3.5	3	3.6	3.2	4.6	4.6	4.1	5	4.7	5	4.6	3.6	3.6	2.7	2.1	1.1	0.7	0.9	1.3	0.6	0.1
P	4.8	3.6	3.1	3.2	2.8	2.3	2.4	2	2.8	2.6	3.2	3.7	4	4.6	3.5	3.7	3.7	3.2	2.6	2.2	2.4	1.7	0.9	0.1	-0
Q	4.5	4.9	3	2.8	2.3	2.4	2.4	2.2	3	2.7	3.1	2.3	2.2	3.3	4.3	4.6	3.9	3.8	3.1	2.5	2.7	1.9	1.3	0.4	0.3
R	1.9	2.3	2.1	2.5	2.8	3.3	3.7	3.7	3.5	3.5	2.9	2.1	2.4	2.9	2.3	3.7	2.8	2.8	2	1.6	1.9	1.5	0.9	0.6	0.8
S	2.5	2.9	2.9	2.8	3.5	3.2	3.2	3.1	3.2	3.8	2.7	2.7	2.6	3.1	3	3.5	3.7	2.9	2.8	2.1	2.5	2	1.1	0.7	0.6
T	2.3	3.9	3.5	3	3.2	2.5	2.6	2.1	3.3	3	2.5	3.2	2.7	3.2	3.1	3.3	3.6	3.3	2.6	2.2	2.2	1	0.8	0.4	0.4

Table G9. *Pixels detected by MODVOLC*.

NTI	A	B	C	D	E	F	G	H	I	J	K	L	M	N	O	P	Q	R	S	T	U	V	W	X	Y
A	0.93	0.93	0.93	0.94	0.94	0.94	0.95	0.95	0.95	0.95	0.96	0.96	0.96	0.96	0.96	0.95	0.95	0.95	0.94	0.94	0.94	0.93	0.93	0.94	
B	0.94	0.93	0.93	0.93	0.94	0.94	0.95	0.95	0.95	0.96	0.96	0.96	0.96	0.96	0.96	0.95	0.95	0.95	0.95	0.95	0.95	0.94	0.94	0.94	0.94
C	0.93	0.93	0.93	0.93	0.93	0.94	0.94	0.95	0.95	0.95	0.96	0.96	0.96	0.96	0.96	0.95	0.95	0.95	0.95	0.95	0.95	0.94	0.94	0.94	0.93
D	0.93	0.93	0.93	0.93	0.93	0.94	0.94	0.95	0.95	0.96	0.96	0.96	0.96	0.96	0.96	0.95	0.95	0.95	0.95	0.94	0.94	0.94	0.94	0.94	0.94
E	0.93	0.93	0.94	0.94	0.94	0.94	0.94	0.95	0.95	0.95	0.96	0.96	0.96	0.96	0.96	0.95	0.95	0.95	0.94	0.94	0.94	0.94	0.94	0.93	0.93
F	0.93	0.93	0.94	0.94	0.94	0.94	0.95	0.95	0.95	0.95	0.95	0.96	0.96	0.96	0.96	0.95	0.95	0.94	0.94	0.94	0.94	0.94	0.94	0.94	0.94
G	0.93	0.93	0.94	0.94	0.94	0.95	0.95	0.95	0.96	0.96	0.96	0.95	0.95	0.96	0.95	0.95	0.94	0.94	0.93	0.94	0.94	0.94	0.94	0.94	0.94
H	0.93	0.94	0.94	0.95	0.95	0.95	0.95	0.95	0.95	<b>0.95</b>	<b>0.94</b>	<b>0.93</b>	<b>0.94</b>	<b>0.95</b>	0.95	0.95	0.94	0.94	0.94	0.94	0.94	0.94	0.94	0.94	0.94
I	0.93	0.93	0.94	0.94	0.94	0.94	0.95	0.95	0.95	<b>0.94</b>	<b>0.92</b>	Y	Y	<b>0.92</b>	<b>0.94</b>	0.94	0.94	0.94	0.94	0.94	0.94	0.94	0.94	0.94	0.94
J	0.93	0.93	0.93	0.94	0.94	0.94	0.95	0.95	0.95	0.96	R	X	X	X	X	X	<b>0.93</b>	0.94	0.94	0.94	0.94	0.94	0.94	0.94	0.94
K	0.93	0.93	0.93	0.94	0.94	0.95	0.95	0.95	0.95	0.95	R	Y	Y	Y	Y	X	Y	0.94	0.94	0.94	0.94	0.94	0.93	0.94	0.94
L	0.93	0.93	0.93	0.94	0.94	0.94	0.94	0.95	0.95	0.95	0.94	<b>0.92</b>	Y	Y	Y	Y	<b>0.93</b>	0.94	0.94	0.94	0.94	0.94	0.93	0.94	0.94
M	0.93	0.93	0.93	0.94	0.94	0.94	0.94	0.94	0.94	0.94	0.94	0.94	<b>0.93</b>	<b>0.91</b>	<b>0.92</b>	<b>0.92</b>	0.93	0.94	0.94	0.94	0.94	0.94	0.94	0.94	0.94
O	0.93	0.93	0.93	0.93	0.93	0.94	0.94	0.94	0.94	0.94	0.94	0.93	0.94	0.94	0.93	0.93	0.94	0.94	0.94	0.94	0.94	0.94	0.94	0.94	0.94
N	0.94	0.94	0.94	0.93	0.93	0.94	0.94	0.94	0.94	0.93	0.93	0.93	0.94	0.94	0.94	0.94	0.94	0.94	0.94	0.94	0.94	0.94	0.94	0.94	0.94
P	0.93	0.93	0.93	0.93	0.93	0.94	0.94	0.94	0.94	0.94	0.94	0.93	0.93	0.93	0.94	0.94	0.94	0.94	0.94	0.94	0.94	0.94	0.94	0.94	0.94
Q	0.93	0.93	0.93	0.94	0.94	0.94	0.94	0.94	0.94	0.94	0.94	0.94	0.94	0.94	0.93	0.93	0.93	0.94	0.94	0.93	0.94	0.94	0.94	0.94	0.94
R	0.93	0.93	0.94	0.93	0.93	0.93	0.93	0.93	0.93	0.93	0.94	0.94	0.94	0.94	0.94	0.93	0.94	0.94	0.94	0.94	0.94	0.94	0.94	0.94	0.94
S	0.93	0.93	0.93	0.93	0.93	0.93	0.93	0.93	0.93	0.93	0.94	0.94	0.94	0.93	0.93	0.93	0.93	0.94	0.94	0.94	0.94	0.93	0.94	0.94	0.94
T	0.93	0.93	0.93	0.93	0.93	0.93	0.93	0.94	0.93	0.93	0.94	0.93	0.94	0.93	0.93	0.93	0.93	0.94	0.94	0.94	0.93	0.94	0.94	0.94	0.94

# Appendix H

## Optical pyrometers

### Temperature from color

As the temperature of a body changes, so too does its color and/or brightness. As a body is heated, it first begins to glow a dull red color around 475 °C, reaching a bright cherry red color around 700 °C. As the temperature increases further, the body color changes from red to orange around 900 °C, to yellow at 1000 °C, and finally to white at 1250 °C. These color changes indicate that the object is emitting sufficient energy in the visible portion of the spectrum for the eye to detect it. As a result, at temperatures greater than ~475 °C, source temperature can be assessed visually from the emission color of the heated body.

Hence, the temperature of an incandescent volcanic source can be assessed by eye, where color-temperature look-up tables are given in [Table H1](#). One of these look-up tables was derived for the volcanologist by Macdonald (1972), and both can be used to guide visual assessments of lava, vent, or ejecta temperature on the basis of the color of the object. Such visual temperature estimates underlie the most basic remote sensing thermal measurement: temperature assessment of an incandescent or glowing object using the eye. Indeed, a commonly used cartoon, as used by Forsythe (1941), Weber (1950) and Sostmann and Metz (1995), depicts an old, bearded foundry worker peering into a glowing furnace under the title “the first optical pyrometer.” Sostmann and Metz (1995) claim that such “experienced workers in high temperature industries can often estimate temperature by eye to ±50 °C.” Experience with active lavas viewed by night and day (where visual, color-based surface temperature estimates were compared with radiometer measurements of pahoehoe active on Kilauea by day and night) suggests that such a precision from eye-based measurements is about right for surfaces between 800 °C and 1100 °C.

A good example of the application of such a fundamental remote sensing thermal approach was that of Principe and Marini (2008). Principe and Marini (2008), in assessing statements of “fire by night” in treatises written prior to the 1631 eruption of Vesuvius, used the [Table H1](#) look-up table to conclude that “fire by night” indicated that exposed rocks were incandescent and at temperatures greater than 500 °C.

Table H1. *Colors used to assess temperatures of a glowing object as viewed with an unaided eye as given by Macdonald (1972) and Sostmann and Metz (1995). Macdonald (1972) notes that his tabulation is appropriate for objects viewed by night or in dark surroundings.*

*Experience at Kilauea and Etna indicates that the tabulation of Sostmann and Metz (1995) may work in cloudy, day-time conditions.*

Sostmann and Metz (1995)		Macdonald (1972)	
$T$ (°C)	Color	$T$ (°C)	Color
		475	Lowest visible red
530	Dark blood red	550 to 625	Dull red
570	Dark red		
635	Dark cherry red		
675	Medium cherry red	700	Bright cherry red
750	Cherry full red		
850	Light, bright cherry red		
900	Salmon, orange	900	Orange
950	Light salmon orange		
1000	Yellow	1090	Golden yellow
		>1150	White
1180	Light yellow		
1250	White		

### Optical pyrometry

Color-based or brightness-based temperature assessments are the basis of optical pyrometry. An optical pyrometer is thus an instrument that assesses source temperature by comparing “the brightness of the radiation source to some standard (brightness)” (Sostmann and Metz, 1995). The optical pyrometer thus allows the color of the object to be compared with the color of a standard whose temperature is known. To achieve this, a pyrometer includes, in the optical path, a wire, ribbon or lamp filament heated by a variable current. The viewing optics allow the lamp filament to be superimposed upon the view of the radiating source. The radiating source is observed via the optical system while the lamp filament current, and hence its brightness, is varied until the source and filament brightnesses are equal. At this brightness the filament seems to disappear, i.e., if the source is dull red, the dull red filament will become indistinguishable from the background source viewed through the pyrometer telescope. Because the appearance of the filament, as the brightnesses become equal, appears to be extinguished, such instruments can be termed “extinction” type (Sostmann and Metz, 1995). Calibration of the instrument thus

consists of establishing the relationship between temperature, lamp filament color/brightness and current (see Forsythe (1941) and Sostmann and Metz (1995) for a complete description of optical pyrometer design and calibration). For example, optical pyrometer measurements of Santaguito's active lava dome by Zies (1941) involved use of an optical pyrometer within which the color of the filament was varied by manually regulating the current flowing through it until the filament gained the same color as the object. In this case the filament color that matched the red glow of the lava was achieved at a temperature of 700 °C, with duplicate readings agreeing to ±25 °C. Such a procedure is also described by Macdonald (1972) (see Section 1.4.1 of Chapter 1).

Sostmann and Metz (1995) note that pyrometers "may depend upon the observer to note the point at which the image of the reference filament brightness is equal to the brightness of the source, and disappears. Obviously, this won't work at lower temperatures where the radiance is at a wavelength too long for the eye to see. More sophisticated 'automatic' pyrometers use a photodetector to detect the brightness null." Thus, such instruments cannot operate below a lower cut-off temperature, typically between 550 °C and 700 °C (Zies, 1941). Below this cut-off, emitted brightness levels are too low to detect visually. Optical pyrometers also operate using a red filter within the optical path. This is a red-light-transmitting filter which eliminates light at wavelengths shorter than the visible red region of the spectrum, usually constraining the measurement to a narrow waveband centered around 0.65 μm. This helps reduce problems due to the differing emissivity of the lamp filament and the background (i.e., the source/target), and focuses the measurement in the region of the spectrum where the emission will be strongest (i.e., the red end of the VIS).

The Pyrometer Instrument Company's (Windsor, NJ, USA) PYRO Micro-Therm "disappearing filament" type of optical pyrometer has an effective measurement wavelength of 0.655 μm and a standard measurement range of 700 °C to 3200 °C (Pyrometer Instrument Company, 2007). Likewise, HeatWave Labs. (Watsonville, CA, USA) DFP 2000 "disappearing filament" optical pyrometer has an effective measurement wavelength of 0.65 μm and four measurement ranges between 760 °C to 4200 °C (HeatWave Labs., 2002). Zeis' (1941) optical pyrometer also had a cut-off of ~700 °C, but could be calibrated down to 550 °C if all glass filters were removed. However, Zeis (1941) stated that "it is quite difficult at first to match the dull red of the test object at 550 °C with that of the filament; but visual acuity improves with practice, and readings made under test conditions can be duplicated to within ±5 °C. It is doubtful, however, whether it is possible to make brightness matches at this temperature of a natural object such as heated lava."

As charted in Chapter 1, optical pyrometers were commonly used in volcanology up until 1965 (see Table 1.6 of Chapter 1), thereafter the use of broad-band radiometers took over. Between 1965 and 2007, at least 60 studies reported results obtained using ground-based broad-band radiometers at volcanoes, with very few studies using optical pyrometers. The ground-based radiometer thus appears to have become the instrument of choice in volcanology, no doubt due to its low cost, full temperature range coverage (i.e., ambient to magmatic), ease of use, rapidity of obtaining a measurement, minimization of manual

intervention and versatility. We thus focus on ground-based radiometers in Chapters 7 and 8. However, principles and methods described in this book can equally well be applied to optical pyrometer data.

### References

- Forsythe (1941). Optical pyrometry. In *Temperature Its Measurement and Control*. American Institute of Physics, Reinhold Publishing, New York, pp. 1115–1131.
- HeatWave Labs (2002). DFP 2000 disappearing filament optical pyrometer: Manual for operation and maintainance. HeatWave Labs Inc. (Watsonville, CA, USA), DFP 2000 Manual Rev. 1 date 123002, 23 pp.
- Macdonald, G. A. (1972). *Volcanoes*. Prentice Hall (Englewood Cliffs, New Jersey), 510 pp.
- Principe, C. and Marini, L. (2008). Evolution of the Vesuvius magmatic-hydrothermal system before the 16 December 1631 eruption. *J. Volcanol. Geotherm. Res.*, **171**, 301–306.
- Pyrometer Instrument Company (2007). PYRO Micro-Therm. The Pyrometer Instrument Company Inc., Windsor, NJ, USA, 2007 Specifications Sheet, 2 pp.
- Sostman, H. E. and Metz, P. D. (1995). Fundamentals of thermometry part VIII Radiation thermometry and calibration. *Isotech. J. Thermometry*, **6**(2), 74–86.
- Weber, R. L. (1950). *Heat and Temperature Measurement*. Prentice-Hall, New Jersey.
- Zies, E. G. (1941). Temperatures of volcanoes, fumaroles and hot springs. American Institute of Physics. New York: Reinhold Publishing, pp. 1115–1131.

# Appendix I

## Thermal camera options

As discussed in Chapter 9, there are now a wide range of thermal camera options on the market. These span fixed-mount, hand-held and ultra-portable pistol-grip options, and also allow acquisition of a range of image sizes, with a variety of frame rate and dynamic range options and combinations. Those cameras available through 2008, and as initially used for volcanological applications, are detailed in Table 9.1. Provided here is a fuller listing of thermal camera manufacturers, and the main models suitable to volcanological applications available as of 18 April 2012. The market is developing so rapidly that this listing will likely be out of date very quickly, and camera resolutions (spatial, spectral and temporal) and functionality are likely to continue to evolve to meet the needs of the market. However, this appendix provides a summary of thermal camera availability and selected options for the volcanologist at the time of press. The listing spans all camera makes and types used for volcanological applications through 2010, as collated in the literature review of Table 9.3. Details given for each selected camera model are:

waveband, image size, dynamic range, frame rate, dimensions (weight).

Note that the weight includes the battery.

### AGEMA

<http://www.flir.com/legacy/view/?id=51369>

*AGEMA 550 (Hand-held thermal camera, PtSi detector)*

3.6 – 5.0  $\mu\text{m}$ , 320  $\times$  240 pixels, n/a (2.3 kg).

*AGEMA 570 (Hand-held thermal camera, micro-bolometer)*

7.5 – 13  $\mu\text{m}$ , 320  $\times$  240 pixels, n/a (2.3 kg).

These models are now out of production, the replacement product currently being the FLIR Systems P-series, as listed in Table 9.1. The same applies to the old Inframetrics thermal camera range.

## **E2V Technologies**

<http://www.e2v.com/> and <http://www.argus-tics.com/>

E2V Technologies currently offer three types of thermal camera.

TT Type = thermal torch (pistol grip) cameras for “first responder applications.”

P Type = monocular cameras.

F Type = high-sensitivity cameras for “specialist search applications.”

They also offer a range of imaging detectors, detector arrays and cameras spanning the NIR through TIR.

## **FLIR Systems**

<http://www.flir.com/US/>

*SC600 series (Hand-held thermal camera, uncooled micro-bolometer)*

7.5 – 13 µm, 640 × 480 pixels, – 40 to 1500 °C (up to 2000 °C optional), 120 Hz,  
282 × 144 × 147 mm (1.37 kg).

*SC600 series (Fixed-mount thermal camera, uncooled micro-bolometer)*

7.5 – 13 µm, 640 × 480 pixels, – 20 to 650 °C (up to 2000 optional °C), 25 – 200 Hz,  
216 × 73 × 75 mm (0.7 kg).

*i3 Series (Pistol-grip thermal camera, uncooled micro-bolometer)*

7.5 – 13 µm, 140 × 140 pixels, –20 to 250 °C, n/a, 223 × 79 × 85 mm (0.365 kg).

## **Fluke**

<http://www.fluke.com/>

*Ti100 Series (Pistol-grip thermal camera, uncooled micro-bolometer)*

7.5 – 14 µm, 160 × 220 pixels, – 20 to 350 °C, n/a, 284 × 86 × 135 mm (0.726 kg).

*P3 Series (Pistol-grip thermal camera, uncooled micro-bolometer)*

7.5 – 14 µm, 320 × 240 pixels, – 20 to 600 °C, n/a, 277 × 122 × 170 mm (1.05 kg).

## **Infratec**

<http://www.infratec.de/en/thermography>

*VarioCAM® hr inspect series (Hand-held thermal camera, uncooled micro-bolometer)*

7.5 – 14 µm, 320 × 240 or 640 × 480 pixels, – 40 to 1200 °C (> 2000 °C optional),  
50/60 Hz, 133 × 106 × 110 mm (1.5 kg).

*VarioCAM hr head 700 (Fixed-mount thermal camera, uncooled micro-bolometer)*

7.5 – 14 µm, 1280 × 960 pixels, –40 to 1200 °C (> 2000 °C optional), 60 Hz,  
133 × 91 × 110 mm (1.3 kg).

*InfraTec mobileIR E9 (Pistol-grip thermal camera, uncooled micro-bolometer)*

8 – 14 µm, 384 × 288 pixels, –20 to 250 °C (up to 1500 °C optional), 50/60 Hz, 112 × 182 × 252 mm (0.82 kg).

**Land**

<http://www.landinst.com/>

*Arc-Infrared Thermal Imaging Camera (Fixed-mount thermal camera, uncooled micro-bolometer)*

8 – 14 µm, 384 × 288 pixels, –0 to 500 °C or 100 to 1000 °C, 7.5/30 Hz, 85 × 85 × 276 mm (1.8 kg).

**Mikron Infrared**

<http://mikroninfrared.com>

*MikroScan 7600PRO (Hand-held thermal camera, uncooled micro-bolometer)*

8 – 14 µm, 320 × 240 pixels, –40 to 2000 °C, 60 Hz, 109 × 114 × 188 mm (1.57 kg).

*M7800 (Pistol-grip thermal camera, uncooled micro-bolometer)*

8 – 14 µm, 320 × 240 pixels, –40 to 500 °C, 60 Hz, 203 × 229 × 102 mm (1.3 kg).

**NEC Avio Infrared Technologies Co., Ltd.**

<http://www.nec-avio.co.jp/en/products/index.html>

*H2640 (Hand-held thermal camera, uncooled micro-bolometer)*

8 – 13 µm, 640 × 480 pixels, –40 to 500 °C (up to 2000 °C optional), 30 Hz, 110 × 110 × 210 mm (1.7 kg).

*ThermoTracer TS9100 (Fixed-mount thermal camera, uncooled micro-bolometer)*

8 – 14 µm, 320 × 240 pixels, –40 to 500 °C (up to 2000 °C optional), 60 Hz, 99 × 112 × 206 mm (2.6 kg).

*ThermoGEAR G30 (Pistol-grip thermal camera, uncooled micro-bolometer)*

8 – 13 µm, 160 × 120 pixels, –20 to 350 °C, 8.5 Hz, 80 × 209 × 123 mm (0.5 kg).

**Nikon**

<http://ndtnet.com/m/nikon/laird3a/index.htm>

*Thermal Vision LAIRD 3A (Fixed-mount thermal camera, PtSi detector)*

3 – 5 µm, 768 × 494 pixels, –20 to 250 °C, 30 Hz, 140 × 390 × 175 mm (2.5 kg).

**PCE Instruments**

<http://www.pce-france.fr>

*PCE-TC2 (Pistol-grip thermal camera)*

8 – 14  $\mu\text{m}$ , 47  $\times$  47 pixels, –10 to 300 °C, 8 Hz, 130  $\times$  95  $\times$  90 mm (0.85 kg).

**Thermoteknix Systems Ltd**

<http://www.thermoteknix.com/>

*VisIR 640 (Hand-held thermal camera, uncooled amorphous Si micro-bolometer)*

7.5 – 13  $\mu\text{m}$ , 640  $\times$  480 pixels, –20 to 500 °C (0 to 1500 or 2000 °C optional), 60 Hz, 190  $\times$  210  $\times$  110 mm (1.8 kg).

*Miricle series (Fixed-mount thermal camera, uncooled Amorphous (A) Si detector)*

8 – 12  $\mu\text{m}$ , 640  $\times$  480 pixels, 50/60/240 Hz, 46.6  $\times$  45  $\times$  52.5 mm (0.105 kg).

## References

- Abrams, M. J., Bianchi, R. and Buongiorno, M. F. (1997). Next generation spectrometer aids study of Mediterranean. *EOS, Transactions, American Geophysical Union*, **78** (31), 317–322.
- Adams, E. E., Cosler, D. J. and Helffrich, K. R. (1990). Evaporation from heated water bodies: predicting combined forced plus free convection. *Water Resources Research*, **26**(3), 425–435.
- Aguilera, F. (2004). *Volcanic monitoring using remote sensing applications to Lascar Volcano, Chile: Preliminary report*. Universidad Católica del Norte: Departamento de Ciencias Geológicas, 25 p.
- Allard, P. (1997). Endogenous magma degassing and storage at Mount Etna. *Geophysical Research Letters*, **24**(17), 2219–2222.
- Allard, P., Carbonnelle, J., Métrich, N., Loyer, H. and Zettwoog, P. (1994). Sulphur output and magma degassing budget of Stromboli volcano. *Nature*, **368**, 326–330.
- Aloisi, M., D'Agostino, M., Dean, K. G., Mostaccio, A. and Neri, G. (2002). Satellite analysis and PUFF simulation of the eruptive cloud generated by the Mount Etna paroxysm of 22 July 1998. *Journal of Geophysical Research*, **107** (B12), 2373. DOI: 10.1029/2001JB000630.
- Andò, B. and Pecora, E. (2006). An advanced video-based system for monitoring active volcanoes. *Computers & Geosciences*, **32**, 85–91.
- Antoine, R., Baratoux, D., Rabinowicz, M. et al. (2009). Thermal infrared image analysis of a quiescent cone on Piton de la Fournaise volcano: Evidence for convective air flow within an unconsolidated soil. *Journal of Volcanology and Geothermal Research*, **183**, 228–244.
- Archambault, C. and Tanguy, J. C. (1976). Comparative temperature measurements on Mount Etna lavas: problems and techniques. *Journal of Volcanology and Geothermal Research*, **1**, 113–125.
- Archambault, C. and Tanguy, J. C. (1993). Comment on the paper: “Thermal survey of Mount Etna Volcano from Space” by A. Bonneville and P. Gouze. *Geophysical Research Letters*, **20**(10), 999–1000.
- Archambault, C., Stoschek, J. and Tanguy, J. C. (1979). Mise en évidence de zones thermiquement anormales sur le massif de l'Etna. *Proceedings of the 7<sup>e</sup> Réunion Annuelle des Sciences de la Terre*. Lyon (France): 1979. p. 15.
- Aries, S. A., Harris, A. J. L. and Rothery, D. A. (2001). Remote infrared detection of the cessation of volcanic eruptions. *Geophysical Research Letters*, **28**(9), 1803–1807.
- Arino, O. and Melinotte, J. M. (1995). Fire index atlas. *Earth Observation Quarterly*, **50**, 11–16.

- Arya, S. P. S. (1998). *Introduction to Micrometeorology*. Orlando: Academic Press, pp. 1–307.
- Aster, R., McIntosh, W., Kyle, P. et al. (2004). Real-time data received from Mount Erebus Volcano, Antarctica. *EOS*, **85**(10), 97–104.
- Aubert, M. (1999). Practical evaluation of steady heat discharge from dormant active volcanoes: case study of Vulcarolo fissure (Mount Etna, Italy). *Journal of Volcanology and Geothermal Research*, **92**, 413–429.
- Aubert, M. and Alaprone, S. (2005). Variation d'origine sismique du flux de Chaleur convectif dans La Fossa de Vulcano (Italie). *Comptes Rendus Académie des Sciences Paris*, **330**, 1–8.
- Aubert, M., Diliberto, S., Finizola, A. and Chébli, Y. (2008). Double origin of hydrothermal convective flux variations in the Fossa of Vulcano (Italy). *Bulletin of Volcanology*, **70**, 743–751.
- Badarinath, K. V. S., Kharol, S. K. and Chand, T. R. K. (2007). Use of satellite data to study the impact of forest fires over the northeast region of India. *IEEE Geoscience and Remote Sensing Letters*, **4**(3), 485–489.
- Bailey, J. E., Harris, A. J. L., Dehn, J., Calvari, S. and Rowland, S. K. (2006). The changing morphology of an open lava channel on Mt. Etna. *Bulletin of Volcanology*, **68**, 497–515.
- Ball, M. and Pinkerton, H. (2006). Factors affecting the accuracy of thermal imaging cameras in volcanology. *Journal of Geophysical Research*, **111**, B11203. DOI: 10.1029/2005JB003829.
- Ballestracci, R. and Nougier, J. (1984). Detection by infrared thermography and modeling of an icecapped geothermal system in Kerguelen archipelago. *Journal of Volcanology and Geothermal Research*, **20**, 85–99.
- Barberi, F., Carapezza, M. L., Valenza, M. and Villari, L. (1993). The control of lava flow during the 1991–1992 eruption of Mt. Etna. *Journal of Volcanology and Geothermal Research*, **56**, 1–34.
- Barker, S. R., Sherrod, D. R., Lisowski, M., Heliker, C. and Nakata, J. S. (2003). Correlation between lava-pond drainback, seismicity, and ground deformation at Pu'u 'O'o. *United States Geological Survey Professional Paper*, **1676**, 53–62.
- Barnes, W. L., Pagano, T. S. and Salomonson, V. V. (1998). Prelaunch characteristics of the Moderate Resolution Imaging Spectroradiometer (MODIS) on EOS-AM1. *IEEE Trans Geosciences & Remote Sensing*, **36**(4), 1088–1100.
- Bertolaso, G., De Bernardinis, B., Bosi, V. et al. (2009). Civil protection preparedness and response to the 2007 eruptive crisis of Stromboli Volcano, Italy. *Journal of Volcanology and Geothermal Research*, **182**, 269–277.
- Bertrand, C., Clerbaux, N., Ipe, A. and Gonzalez, L. (2003). Estimation of the 2002 Mount Etna eruption cloud radiative forcing from Meteosat-7 data. *Remote Sensing of Environment*, **87**, 257–272.
- Bhattacharya, A., Reddy, C. S. S. and Srivastav, S. K. (1993). Remote sensing for active volcano monitoring in Barren Island, India. *American Society for Photogrammetry and Remote Sensing*, **59**(8), 1293–1297.
- Bianchi, R., Casacchia, R., Coradini, A. et al. (1990a). Remote sensing of Italian volcanos. *EOS, Transactions, American Geophysical Union*, **13** November 1990, 1790–1791.
- Bianchi, R., Casacchia, R., Picchiotti, A., Poscolieri, M. and Salvatori, R. (1990b). Airborne thermal IR survey. In *Mt. Etna: the 1989 Eruption*, ed. F. Barberi, A. Bertagnini and P. Landi. Rome: Giardini, pp. 69–75.
- Birnie, R. W. (1973). Infrared radiation thermometry of Guatemalan volcanoes. *Bulletin of Volcanology*, **37**, 1–36.

- Bizouard, H., Barberi, F. and Varet, J. (1980). Mineralogy and petrology of Erta Ale and Boina volcanic series, Afar Rift, Ethiopia. *Journal of Petrology*, **21**(2), 401–436.
- Bodvarsson, G. (1983). Temperature/flow statistics and thermomechanics of low-temperature geothermal systems in Iceland. *Journal of Volcanology and Geothermal Research*, **19**, 255–280.
- Bonaccorso, A., Calvari, S., Garfi, G., Lodato, L. and Patane, D. (2003). Dynamics of the December 2002 flank failure and tsunami at Stromboli volcano inferred by volcanological and geophysical observations. *Geophysical Research Letters*, **30**, 1941–1944. DOI: 10.1029/2003GL017702
- Bonneville, A. and Gouze, P. (1992). Thermal survey of Mount Etna from space. *Geophysical Research Letters*, **19**(7), 725–728.
- Bonneville, A. and Gouze, P. (1993). Reply to the comments made by Archambault and Tanguy on “Thermal survey of Mount Etna Volcano from Space”. *Geophysical Research Letters*, **20**(10), 1001.
- Bonneville, A. and Kerr, Y. (1987). A thermal forerunner of the 28th March 1983 Mt. Etna eruption from satellite thermal infrared data. *Journal of Geodynamics*, **7**, 1–31.
- Bonneville, A., Vasseur, G. and Kerr, Y. (1985). Satellite thermal infrared observations of Mt. Etna after the 17th March 1981 eruption. *Journal of Volcanology and Geothermal Research*, **24**, 293–313.
- Boynton, G. R. and Moxham, R. M. (1969). A rapid film-density analyzer. *U.S. Geological Survey Professional Paper*, **650-C**, pp. C123–C126.
- Branan, Y. K., Harris, A., Watson, I. M. et al. (2008). Investigation of at-vent dynamics and dilution using thermal infrared thermometers at Masaya Volcano, Nicaragua. *Journal of Volcanology and Geothermal Research*, **169**, 34–47.
- Brandli, H. W. (1978). The night eye in the sky. *Photogrammetric Engineering and Remote Sensing*, **44**(4), 503–505.
- Breaker, L. C. (1990). Estimating and removing sensor-induced correlation from Advanced Very High Resolution Radiometer satellite data. *Journal of Geophysical Research*, **95** (C6), 9601–9711.
- Brivio, P. A. and Tomasoni, R. (1980). Thermal infrared continuous ground measurements in severe environment: A working data collection system. *Proceedings of the 14th International Symposium on Remote Sensing of the Environment*, **III**, 23–30 April 1980, 1731–1740.
- Brivio, P. A., Tomasoni, R. and Zilioli, E. (1980). Vulcano Island: a new method for surficial heat control. *Bull. Bur. Rech. Géol. Minières*, **IV**(2), 161–168.
- Brivio, P. R., Lo Giudice, E. and Zilioli, E. (1989). Thermal infrared surveys at Vulcano Island: an experimental approach to the thermal monitoring of volcanoes. In *Volcanic Hazards*, ed. J. H. Latter. Berlin, Heidelberg: Springer-Verlag, pp. 357–371.
- Brown, G., Rymer, H., Dowden, J. et al. (1989). Energy budget analysis for Poás crater lake: implications for predicting volcanic activity. *Nature*, **339**, 370–373.
- Brustet, J. M., Vickos, J. B., Fontain, J. et al. (1991). Remote sensing of biomass burning in West Africa with NOAA-AVHRR. In *Global Biomass Burning: Atmospheric, Climatic and Biospheric Implications*, ed. J. Levine. MIT Press, pp. 47–52.
- Bryant, R. G. (1996). Validated linear mixture modeling of Landsat TM data for mapping evaporite minerals on a playa surface: methods and applications. *International Journal of Remote Sensing*, **17**(2), 315–330.
- Burgi, P.-Y., Caillet, M. and Haefeli, S. (2002). Field temperature measurements at Erta Ale lava lake, Ethiopia. *Bulletin of Volcanology*, **64**, 472–485.

- Burton, M., Allard, P., Muré, F. and La Spina, A. (2007). Magmatic gas composition reveals the source depth of slug-driven strombolian explosive activity. *Science*, **317**, 227–230.
- Butterworth, G. J. (1968). Effect of detector response time on the distortion of spectral peaks of Gaussian shape. *Journal of Scientific Instruments (Journal of Physics E)*, **1**, 1165–1167.
- Calder, E., Harris, A., Peña, P. et al. (2004). Combined thermal and seismic analysis of the Villarrica volcano lava lake. *Revista Geologica de Chile*, **31**(2), 259–272.
- Calkins, J., Oppenheimer, C. and Kyle, P. R. (2008). Ground-based thermal imaging of lava lakes at Erebus volcano, Antarctica. *Journal of Volcanology and Geothermal Research*, **177**, 695–704.
- Calvari, S. and Pinkerton, H. (2004). Birth, growth and morphologic evolution of the ‘Laghetto’ cinder cone during the 2001 Etna eruption. *Journal of Volcanology and Geothermal Research*, **132**, 225–239.
- Calvari, S., Coltellini, M., Neri, M., Pompilio, M. and Scribano, V. (1994). The 1991–1993 Etna eruption: chronology and lava flow-field evolution. *Acta Vulcanologica*, **4**, 1–14.
- Calvari, S., Neri, M. and Pinkerton, H. (2003). Effusion rate estimations during the 1999 summit eruption on Mount Etna, and growth of two distinct lava flow fields. *Journal of Volcanology and Geothermal Research*, **119**, 107–123.
- Calvari, S., Spampinato, L., Lodato, L. et al. (2005). Chronology and complex volcanic processes during the 2002–2003 flank eruption at Stromboli volcano (Italy) reconstructed from direct observations and surveys with a handheld thermal camera. *Journal of Geophysical Research*, **110**, B02201. DOI: 10.1029/2004JB003129.
- Calvari, S., Spampinato, L. and Lodato, L. (2006). The 5 April 2003 vulcanian paroxysmal explosion at Stromboli volcano (Italy) from field observations and thermal data. *Journal of Volcanology and Geothermal Research*, **149**, 160–175.
- Calvari, S., Lodato, L., Steffke, A. et al. (2010). The 2007 Stromboli eruption: event chronology and effusion rates using thermal infrared data. *Journal of Geophysical Research*, **115**, B04201. DOI: 10.1029/2009JB006478.
- Calvari, S., Salerno, G. G., Spampinato, L. et al. (2011). An unloading foam model to constrain Etna’s 11–13 January 2011 lava fountaining episode. *Journal of Geophysical Research*, **116**, B11207, DOI: 10.1029/2011JB008407.
- Campbell, J. B. (1986). *Introduction to Remote Sensing*. New York: The Guildford Press, 551 p.
- Carn, S. A. and Oppenheimer, C. (2000). Remote monitoring of Indonesian volcanoes using satellite data from the Internet. *International Journal of Remote Sensing*, **21**(5), 873–910.
- Carroll, M. R. and Holloway, J. R. (1994). *Volatiles in Magmas. Reviews in Mineralogy*, **30**, Washington DC: Mineralogical Society of America, 517 p.
- Carslaw, H. W. and Jaeger, J. C. (1959). *Conduction of Heat in Solids*. 2nd edn. Oxford: Clarendon Press, 496 pp.
- Carter, A. J. and Ramsey, M. S. (2009). ASTER- and field-based observations at Bezymianny Volcano: Focus on the 11 May 2007 pyroclastic flow deposit. *Remote Sensing of Environment*, **113**, 2142–2151.
- Carter, A. and Ramsey, M. (2010). Long-term volcanic activity at Shiveluch Volcano: nine years of ASTER spaceborne thermal infrared observations. *Remote Sensing*, **2**, 2571–2583.
- Carter, A. J., Ramsey, M. S. and Belousov, A. B. (2007). Detection of a new summit crater on Bezymianny Volcano lava dome: satellite and field-based thermal data. *Bulletin of Volcanology*, **69**, 811–815.

- Carter, A. J., Girina, O., Ramsey, M. S. and Demyanchuk, Y. V. (2008). ASTER and field observations of the 24 December 2006 eruption of Bezymianny Volcano, Russia. *Remote Sensing of Environment*, **112**, 2569–2577.
- Cassinis, R. and Lechi, G. I. (1974). The use of infrared radiometry in geothermal areas. In *Physical Volcanology*, ed. Civetta, Gasparini, Luongo and Rapolla. Amsterdam: Elsevier, pp. 117–131.
- Chamberlain, J. M., Terndrup, T. E., Alexander, D. T. et al. (1995). Determination of normal ear temperature with an infrared emission detection thermometer. *Annals of Emergency Medicine*, **25**(1), 15–20.
- Chand, T. R. K., Badarinath, K. V. S., Prasad, V. K. et al. (2006). Monitoring forest fires over the Indian region using Defense Meteorological Satellite Program-Operational Linescan nighttime satellite data. *Remote Sensing of Environment*, **103**, 165–178.
- Chien, S., Davies, A., Tran, D. et al. (2004). Using automated planning for sensorweb response. *Proceedings of the 14th International Workshop on Automated Planning and Scheduling for Space*, Whistler (Canada), 3–7 June 2004, 1–8.
- Chioldini, G., Granieri, D., Avino, S. and Costa, A. (2005). Carbon dioxide diffuse degassing and estimation of heat release from volcanic and hydrothermal systems. *Journal of Geophysical Research*, **110**, B08204. DOI: 10.1029/2004JB003542.
- Chuvieco, E. and Martin, M. P. (1994). A simple method for fire growth mapping using AVHRR channel 3 data. *International Journal of Remote Sensing*, **15**(16), 3141–3146.
- Coppola, D., Piscopo, D., Staudacher, T. and Cigolini, C. (2009). Lava discharge rate and effusive pattern at Piton de la Fournaise from MODIS data. *Journal of Volcanology and Geophysical Research*, **184**, 174–192.
- Cracknell, A. P. (1997). *The Advanced Very High Resolution Radiometer*. London: Taylor & Francis, 534 p.
- Cracknell, A. P. and Hayes, L. W. B. (1991). *Introduction to Remote Sensing*. London: Taylor & Francis, 293 p.
- Crisp, J. and Baloga, S. (1990a). A model for lava flows with two thermal components. *Journal of Geophysical Research*, **95**, 1255–1270.
- Crisp, J. and Baloga, S. (1990b). A method for estimating eruption rates of Planetary lava flows. *Icarus*, **85**(2), 512–515.
- Crisp, J., Kahle, A. B. and Abbott, E. A. (1990). Thermal infrared spectral character of Hawaiian Basaltic glasses. *Journal of Geophysical Research*, **95**(B13), 21 657–21 669.
- Curran, P. J. (1985). *Principles of Remote Sensing*, Harlow: Longman Scientific and Technical, 282 p.
- Daniels, D. L. (1968). Integrated 8–14 $\mu$  emissivities of rocks from Mono Craters region. In *Thermal anomalies and geologic features of the Mono Lake area, California, as revealed by infrared imagery*, U.S. Geological Survey Open File Report.
- Davies, A. G. (2008). *Volcanism on Io: a Comparison with Earth*, Cambridge: Cambridge University Press, 355 p.
- Davies, A. G., Chien, S., Wright, R. et al. (2006a). Sensor web enables rapid response to volcanic activity. *EOS, Transactions, American Geophysical Union*, **87**(1), 1–5.
- Davies, A. G., Chien, S., Baker, V. et al. (2006b). Monitoring active volcanism with the Autonomous Sciencecraft experiment in EO-1. *Remote Sensing of Environment*, **101**, 427–446.
- Dean, K., Searcy, C., Wyatt, C., George, S. and Engle, K. (1996). Monitoring volcanoes in the North Pacific Ocean region using satellite imagery, modeling and meteorological

- data. *Proceedings of the Pan Pacific Hazards Conference*. Vancouver (Canada): 27 July – 4 August, 1996, p. 1–29.
- Dean, K., Servilla, M., Roach, A., Foster, B. and Engle, K. (1998). Satellite monitoring of remote volcanoes improves study efforts in Alaska. *EOS, Transactions, American Geophysical Union*, **79**(35), 413–423.
- Dean, K. G., Dehn, J., Engle, K. et al. (2002). Operational satellite monitoring of volcanoes at the Alaska Volcano Observatory. *Advances in Environmental Monitoring and Modeling*, **1**(3), 70–97.
- Dean, K., Dehn, J., Papp, K. R. et al. (2004). Integrated satellite observations of the 2001 eruption of Mt. Cleveland, Alaska. *Journal of Volcanology and Geothermal Research*, **135**, 51–73.
- Decker, R. W. and Peck, D. L. (1967). Infrared radiation from Alae lava lake, Hawaii. *U.S. Geological Survey Professional Paper*, **575-D**, D169–D175.
- Defense Technology International (2010). Image makeover. *Defense Technology International*, December 2010, p. 14.
- Dehn, J., Dean, K. and Engle, K. (2000). Thermal monitoring of North Pacific volcanoes from space. *Geology*, **28**(8), 755–758.
- Dehn, J., Harris, A. and Ripepe, M. (2001). Infrared Imaging of Strombolian Eruptions. *Annual American Geophysical Union Meeting*, San Francisco, CA, USA, December 10–14, 2001, V52C–01.
- Dehn, J., Dean, K. G., Engle, K. and Izbekov, P. (2002). Thermal precursors in satellite images of the 1999 eruption of Shishaldin volcano. *Bulletin of Volcanology*, **64**, 525–545.
- Delderfield, J., Llewellyn-Jones, D. T., Bernard, R. et al. (1985). The Along Track Scanning Radiometer (ATSR) for ERS1. *Proc. SPIE Instrumentation for Optical Remote Sensing from Space*, **589**, 114–120.
- Delle Donne, D. and Ripepe, M. (2012). High-frame rate thermal imagery of strombolian explosions. Implications for explosive and infrasonic source dynamics. *Journal of Geophysical Research*, **117**, 609206, DOI: 10.1029/2011JB008987.
- Denniss, A. M., Harris, A. J. L., Carlton, R. W., Francis, P. W. and Rothery, D. A. (1996). The 1993 Lascar pyroclastic flow imaged by JERS-1. *International Journal of Remote Sensing*, **17**(11), 1975–1980.
- Denniss, A. M., Harris, A. J. L., Rothery, D. A., Francis, P. W. and Carlton, R. W. (1998). Satellite observations of the April 1993 eruption of Lascar volcano. *International Journal of Remote Sensing*, **19**(5), 801–821.
- Dereniak, E. L. and Boreman, G. D. (1996). *Infrared Detectors and Systems*. New York: John Wiley & Sons, 561 p.
- Di Bello, G., Filizzola, C., Lacava, T. et al. (2004). Robust satellite techniques for volcanic and hazards monitoring. *Annals of Geophysics*, **47**(1), 49–64.
- Donegan, S. J. and Flynn, L. P. (2004). Comparison of the response of the Landsat 7 Enhanced Thematic Mapper Plus and the Earth Observing-1 Advanced Land Imager over active lava flows. *Journal of Volcanology and Geothermal Research*, **135**, 105–126.
- Dozier, J. (1980). Satellite identification of surface radiant temperature fields of subpixel resolution. *NOAA Technical Memorandum*, NOAA-81021710, Washington DC: National Earth Satellite Service, 17 p.
- Dozier, J. (1981). A method for satellite identification of surface temperature fields of subpixel resolution. *Remote Sensing of Environment*, **11**, 221–229.
- Dozier, J. and Warren, S. G. (1982). Effect of viewing angle on the infrared brightness temperature of snow. *Water Resource Research*, **18**, 1424.
- Drury, S. A. (2001). *Image Interpretation in Geology*, 3rd edn. Cheltenham: Nelson Thornes.

- Duda, K. A., Ramsey, M., Wessels, R. and Dehn, J. (2009). Optical satellite volcano monitoring: A multi-sensor rapid response system. In *Geoscience and Remote Sensing*, ed. P. Ho. Vukovar (Croatia): In-Tech Press, pp. 473–496.
- Dzurisin, D. (2007). *Volcano Deformation: Geodetic Monitoring Techniques*. Chichester: Praxis Publishing, 441 p.
- Elvidge, C. D., Baugh, K. E., Hobson, V. R. et al. (1997). Satellite inventory of human settlements using nocturnal radiation emissions: a contribution for the global toolchest. *Global Change Biology*, **3**, 387–395.
- Ernst, G. G. J., Kervyn, M. and Teeuw, R. M. (2008). Advances in remote sensing of volcanic activity and hazards, with special consideration to applications in developing countries. *International Journal of Remote Sensing*, **29** (2), 6687–6723.
- EUMETSAT (2006). Pre-launch MSG-1 SEVIRI instrument level 1.0 data. *EUMETSAT Document Number EUM/OPS-MSG/TEN/05/0625*, <http://www.eumetsat.int>.
- Filizzola, C., Pergola, N., Pietrapertosa, C. and Tramutoli, V. (2004). Robust satellite techniques for seismically active areas monitoring: a sensitivity analysis on September 7, 1999 Athens's earthquake. *Physics and Chemistry of the Earth*, **29**, 517–527.
- Finizola, A., Sortino, F., Lenat, J.-F. and Valenza, M. (2002). Fluid circulation at Stromboli volcano (Aeolian Islands, Italy) from self-potential and CO<sub>2</sub> surveys. *Journal of Volcanology and Geothermal Research*, **116**, 1–18.
- Fischer, W. A. et al. (1975). History of Remote Sensing. In *Manual of Remote Sensing*, ed. F. J. Janza. Falls Church (VA): American Society of Photogrammetry, pp. 27–50.
- Fischer, W. A., Moxham, R. M., Polcyn, F. and Landis, G. H. (1964). Infrared surveys of Hawaiian volcanoes. *Science*, **146**, 733–742.
- Flannigan, M. D. and Vonder Haar, T. H. (1986). Forest fire monitoring using NOAA satellite AVHRR. *Canadian Journal of Forest Research*, **16**, 975–982.
- FLIR Systems (2001). *Features/Specifications: ThermaCAM® PM 695/675/545 Handheld infrared cameras*. Danderyd (Sweden): FLIR Systems, 18 p.
- FLIR Systems (2003). *ThermaCAM™ S40 Operator's Manual*. Danderyd (Sweden): FLIR Systems, Publication Number 1 557 539 Rev. C, 136 p.
- Fluke Corporation (2009). *Introduction to Thermography Principles*. Orland Park (IL): American Technical Publishers Inc., 68 p.
- Flynn, L. (1996). Thermal anomaly – low spatial resolution. *EOS Volcanology Team Data Product Document, MOU81-3292*, 13 p.
- Flynn, L. P. and Mouginis-Mark, P. J. (1992). Cooling rate of an active Hawaiian lava flow from nighttime spectroradiometer measurements. *Geophysical Research Letters*, **19** (17), 1783–1786.
- Flynn, L. P. and Mouginis-Mark, P. J. (1994). Temperature measurements of an active lava channel from spectral measurements, Kilauea Volcano, Hawaii. *Bulletin of Volcanology*, **56**, 297–301.
- Flynn, L. P. and Mouginis-Mark, P. J. (1995). A comparison of the thermal characteristics of active lava flows and forest fires. *Geophysical Research Letters*, **22**(19), 2577–2580.
- Flynn, L. P., Mouginis-Mark, P. J., Gradie, J. C. and Lucey, P. G. (1993). Radiative temperature measurements at Kupaianaha lava lake, Kilauea Volcano, Hawaii. *Journal of Geophysical Research*, **98**(B4), 6461–6476.
- Flynn, L. P., Mouginis-Mark, P. J. and Horton, K. A. (1994). Distribution of thermal areas on an active lava flow field: Landsat observations of Kilauea, Hawaii, July 1991. *Bulletin of Volcanology*, **56**, 284–296.

- Flynn, L. P., Harris, A. J. L., Rothery, D. A. and Oppenheimer, C. (2000). Landsat and hyperspectral analyses of active lava flows. *American Geophysical Union Monograph Series*, **116**, 161–177.
- Flynn, L. P., Harris, A. J. L. and Wright R. (2001). Improved identification of volcanic features using Landsat 7 ETM+. *Remote Sensing of Environment*, **78**, 180–193.
- Flynn, L., Wright, R., Garbeil, H., Harris, A. and Pilger, E. (2002). A global thermal alert system using MODIS: initial results from 2000–2001. *Advances in Environmental Monitoring and Modeling*, **1**(3), 37–69.
- Formenti, Y., Druitt, T. H. and Kelfoun, K. (2003). Characterisation of the 1997 vulcanian explosions of Soufrière Hills Volcano, Montserrat, by video analysis. *Bulletin of Volcanology*, **65**, 587–605.
- Forsythe (1941). Optical pyrometry. In *Temperature Its Measurement and Control*. American Institute of Physics, Reinhold Publishing, New York, pp. 1115–1131.
- Fournier, N., Witham, F., Moreau-Fournier, M. and Bardou, L. (2009). Boiling Lake of Dominica, West Indies: high-temperature volcanic crater lake dynamics. *Journal of Geophysical Research*, **114**, B02203. DOI: 10.1029/2008JB005773.
- Franca, J. R. A., Brustet, J.-M. and Fontan, J. (1995). Multispectral remote sensing of biomass burning in West Africa. *Journal of Atmospheric Chemistry*, **22**, 81–110.
- Francis, P. W. (1979). Infra-red techniques for volcano monitoring and prediction – a review. *Journal of the Geological Society London*, **136**, 355–359.
- Francis, P. and Oppenheimer, C. (1992). Applications of satellite remote sensing techniques to volcanology. In *Understanding the Terrestrial Environment – the Role of Observation from Space*, ed. Mather. London: Taylor & Francis, pp. 37–52.
- Francis, P. W. and Rothery, D. A. (1987). Using the Landsat Thematic Mapper to detect and monitor active volcanoes: an example from Lascar volcano, northern Chile. *Geology*, **15**, 614–617.
- Francis, P. and Rothery, D. (2000). Remote sensing of active volcanoes. *Annual Review of Earth and Planetary Sciences*, **28**, 81–106.
- Francis, P., Oppenheimer, C. and Stevenson, D. (1993). Endogenous growth of persistently active volcanoes. *Nature*, **366**, 554–557.
- Francis, P. W., Wadge, G. and Mouglinis-Mark, P. J. (1996). Satellite monitoring of volcanoes. In *Monitoring and Mitigation of Volcano Hazards*, ed. Scarpa and Tilling. Berlin: Springer-Verlag, pp. 257–298.
- Friedman, J. D. (1966). Thermal anomalies and geologic features of the Mono Lake area, California as revealed by infrared imagery. *Proceedings of the Geological Society of America Annual Meeting*: 1966, pp. 73–74.
- Friedman, J. D. (1968). Thermal anomalies and geologic features of the Mono Lake area, California, as revealed by infrared imagery. *Interagency Technical Report, NASA-82* (USGS 68-107), 84 p.
- Friedman, J. D. and Williams, R. S. (1968). Infrared sensing of active geologic features. *Proceedings of the 5th Symposium on Remote Sensing of Environment*. Ann Arbor (Michigan): University of Michigan Institute of Science and Technology, pp. 787–820.
- Friedman, J. D., Williams, R. S., Miller, C. D. and Pálmasón, G. (1967). Infrared surveys in Iceland in 1966. *American Geophysical Union Transactions*, **48**(1), 228.
- Friedman, J. D., Williams, S. R., Pálmasón, G. and Miller, C. D. (1969). Infrared surveys in Iceland – preliminary report. *U.S. Geological Survey Professional Paper*, **650-C**, pp. C89–C105.

- Friedman, J. D., Frank, D., Kieffer, H. H. and Swatzky, D. L. (1981). Thermal infrared surveys of the May 18 crater, subsequent lava domes, and associated volcanic deposits. *United States Geological Survey Professional Paper*, **1250**, pp. 279–293.
- Frulla, L. A., Miolovich, J. A. and Gagliardini, D. A. (1995). Illumination and observation geometry for NOAA-AVHRR images. *International Journal of Remote Sensing*, **16** (12), 2233–2253.
- Fujita, T., Baralt, G. and Tsuchiya, K. (1968). Aerial measurement of radiation temperatures over Mt. Fuji and Tokyo areas and their application to the determination of ground- and water-surface temperatures. *Satellite and Mesometeorology Research Project Report*, **72**, 32 pp.
- Fujisada, H. and Ono, A. (1994). Observational performance of ASTER instrument on EOS-AM1 spacecraft. *Adv. Space Res.*, **14**(3), (3)147–(3)150.
- Galindo, I. and Dominguez, T. (2002). Real-time AVHRR multispectral thermal monitoring and ash emission detection into the atmosphere: the case of Colima Volcano (Mexico). *AGU Geophysical Monograph Series*, **139**, pp. 133–149.
- Galindo, I. and Dominguez, T. (2003). Near real-time satellite monitoring during the 1997–2000 activity of Volcán de Colima (México) and its relationship with seismic monitoring. *Journal of Volcanology and Geothermal Research*, **117**, 91–104.
- Ganci, G., Vicari, A., Fortuna, L. and Del Negro, C. (2011). The HOTSAT volcano monitoring system based on combined use of SEVIRI and MODIS multispectral data. *Annals of Geophysics*, **54**(5), 544–550.
- Ganci, G., Harris, A. J. L., Del Negro, C. et al. (2012a). A year of lava fountaining at Etna: volumes from SEVIRI. *Geophysical Research Letters*, **39**, L06305. DOI: 10.1029/2012GL051026.
- Ganci, G., Vicari, A., Cappello, A. and Del Negro, C. (2012b). An emergent strategy for volcano hazard assessment: from thermal satellite monitoring to lava flow modeling. *Remote Sensing of Environment*, **119**, 197–207.
- Gaonac'h, H., Vandemeulebrouck, J., Stix, J. and Halbwachs, M. (1994). Thermal infrared satellite measurements of volcanic activity at Stromboli and Vulcano. *Journal of Geophysical Research*, **99**(B5), 9477–9485.
- Gawarecki, S. J., Lyon, R. J. P. and Nordberg, W. (1965). Infrared spectral returns and imagery of the Earth from Space and their application to Geologic problems. *American Astronautical Society Science and Technology Series*, **4**, 13–33.
- Gens, R. and Van Genderen, J. L. (1996). SAR interferometry – issues, techniques, applications. *International Journal of Remote Sensing*, **17**(10), 1803–1835.
- Geraci, A. L., La Rosa, G., Caltabiano, T. and Lo Giudice, E. (1985). Monitoring of ground fractures caused by volcanic eruptions using remote sensing techniques. *Proceedings of the EARSeL/ESA Symposium*. Strasbourg (France): 31 March – 3 April 1985, pp. 221–227.
- Giberti, G., Jaupart, C. and Sartoris, G. (1992). Steady-state operation of Stromboli volcano, Italy: constraints on the feeding system. *Bulletin of Volcanology*, **54**, 535–541.
- Glaze, L., Francis, P. W. and Rothery, D. A. (1989). Measuring thermal budgets of active volcanoes by satellite remote sensing. *Nature*, **338**, 144–146.
- Gottsmann, J., Harris, A. J. L. and Dingwell, D. B. (2004). Thermal history of Hawaiian pahoehoe lava crusts at the glass transition: implications for flow rheology and flow emplacement. *Earth and Planetary Science Letters*, **228**, 343–353.
- Gouhier, M., Harris, A., Calvari, S. et al. (2012). Lava discharge during Etna's January 2011 fire fountain tracked using MSG-SEVIRI. *Bulletin of Volcanology*. DOI: 10.1007/s00445-011-0572-y.

- Goward, S. N., Markham, B., Dye, D. G., Dulaney, W. and Yang, J. (1991). Normalized difference vegetation index measurements from the Advanced Very High Resolution Radiometer. *Remote Sensing of Environment*, **35**, 257–277.
- Gower, J. F. R. (1992). Low cost satellite sensor image reception for NOAA HRPT and other compatible data. *International Journal of Remote Sensing*, **14**, 177–181.
- Grassl, H. (1976). The dependence of the measured cool skin of the ocean on wind stress and total heat flux. *Boundary-Layer Meteorology*, **10**, 465–474.
- Greeley, R. and Iverson, J. D. (1987). Measurements of wind and friction speeds over lava surfaces and an assessment of sediment transport. *Geophysical Research Letters*, **14**, 925–928.
- Gresta, S., Ripepe, M., Marchetti, E. et al. (2004). Seismoacoustic measurements during the July–August 2001 eruption of Mt. Etna volcano, Italy. *Journal of Volcanology and Geothermal Research*, **137**, 219–230.
- Guéhenneux, Y. (2008). Développement d'un outil de surveillance temps réel des édifices volcaniques, grâce à l'utilisation des données MSG. Masters Thesis, Université Blaise Pascal: Laboratoire Magmas et Volcans, 50 p.
- Gupta, R. K. and Badarinath, K. V. S. (1993). Volcano monitoring using remote sensing data. *International Journal of Remote Sensing*, **14**(16), 2907–2918.
- Gurioli, L., Harris, A. J. L., Houghton, B. F., Polacci, M. and Ripepe, M. (2008). Textural and geophysical characterization of explosive basaltic activity at Villarrica volcano. *Journal of Geophysical Research*, **113**, B08206. DOI: 10.1029/2007JB005328.
- Hanstrum, B. N. and Watson, A. S. (1983). A case study of two eruptions of Mount Galunggung and an investigation of volcanic eruption cloud characteristics using remote sensing techniques. *Australian Meteorological Magazine*, **31**, 171–177.
- Harris, A. J. L. (1992). *Volcano detection and monitoring using AVHRR: The Krafla eruption, Iceland, 1984*. Masters Thesis, Department of Applied Physics and Electronics and Manufacturing Engineering, University of Dundee, 206 p.
- Harris, A. J. L. (1996). Towards automated fire monitoring from space: semi-automated mapping of the January 1994 New South Wales wild-fires using AVHRR data. *International Journal of Wildland Fire*, **6**(3), 107–116.
- Harris, A. J. L. (2004). Can satellite-based sensors, hand-held thermal imagers and thermal infrared radiometers calculate reliable eruption rates at active lava flows, domes and lakes? *Eos Trans. AGU*, **85**(47), Fall Meeting Supplement, San Francisco (CA), 13–17 December, 2004, V31D-03.
- Harris, A. J. L. and Baloga, S. M. (2009). Lava discharge rates from satellite-measured heat flux. *Geophysical Research Letters*, **36**, L19302. DOI: 10.1029/2009GL039717.
- Harris, A. J. L. and Maciejewski, A. J. H. (2000). Thermal surveys of the Vulcano Fossa fumarole field 1994–1999: evidence for fumarole migration and sealing. *Journal of Volcanology and Geothermal Research*, **102**(1–2), 119–147.
- Harris, A. J. L. and Neri, M. (2002). Volumetric observations during paroxysmal eruptions at Mount Etna: pressurized drainage of a shallow chamber or pulsed supply? *Journal of Volcanology and Geothermal Research*, **116**, 79–95.
- Harris, A. J. L. and Ripepe, M. (2007a). Regional earthquake as a trigger for enhanced volcanic activity: evidence from MODIS thermal data. *Geophysical Research Letters*, **34**, L02304. DOI: 10.1029/2006GL028251.
- Harris, A. and Ripepe, M. (2007b). Temperature and dynamics of degassing at Stromboli. *Journal of Geophysical Research*, **112**, B03205. DOI: 10.1029/2006JB004393.

- Harris, A. J. L. and Ripepe, M. (2007c). Synergy of multiple geophysical approaches to unravel explosive eruption conduit and source dynamics – A case study from Stromboli. *Chemie der Erde*, **67**, 1–35.
- Harris, A. J. L. and Stevenson, D. S. (1997a). Thermal observations of degassing open conduits and fumaroles at Stromboli and Vulcano using remotely sensed data. *Journal of Volcanology and Geothermal Research*, **76**, 175–198.
- Harris, A. J. L. and Stevenson, D. S. (1997b). Magma budgets and steady-state activity of Vulcano and Stromboli volcanoes. *Geophysical Research Letters*, **24**(9), 1043–1046.
- Harris, A. J. L. and Thornber, C. (1999). Complex effusive events at Kilauea as documented by the GOES satellite and remote video cameras. *Bulletin of Volcanology*, **61**(6), 382–395.
- Harris, A. J. L., Swabey, S. E. J. and Higgins, J. (1995a). Automated thresholding of active lavas using AVHRR data. *International Journal of Remote Sensing*, **16**(18), 3681–3686.
- Harris, A. J. L., Vaughan, R. A. and Rothery, D. A. (1995b). Volcano detection and monitoring using AVHRR data: the Krafla eruption, 1984. *International Journal of Remote Sensing*, **16**(6), 1001–1020.
- Harris, A. J. L., Rothery, D. A., Carlton, R. W., Langaas, S. and Mannstein, H. (1995c). Non-zero saturation of AVHRR thermal channels over high temperature targets: evidence from volcano data and a possible explanation. *International Journal of Remote Sensing*, **16**(1), 189–196.
- Harris, A. J. L., Stevens, N. F., Maciejewski, A. J. H. and Röllin, P. J. (1996). Thermal evidence for linked vents at Stromboli. *Acta Vulcanologica*, **8**, 57–62.
- Harris, A. J. L., Blake, S., Rothery, D. A. and Stevens, N. F. (1997a). A chronology of the 1991 to 1993 Etna eruption using AVHRR data: implications for real time thermal volcano monitoring. *Journal of Geophysical Research*, **102**(B4), 7985–8003.
- Harris, A. J. L., Keszthelyi, L., Flynn, L. P. et al. (1997b). Chronology of the Episode 54 eruption at Kilauea Volcano, Hawaii, from GOES-9 satellite data. *Geophysical Research Letters*, **24**(24), 3281–3284.
- Harris, A. J. L., Butterworth, A. L., Carlton, R. W. et al. (1997c). Low cost volcano surveillance from space: case studies from Etna, Krafla, Cerro Negro, Fogo, Lascar and Erebus. *Bulletin of Volcanology*, **59**, 49–64.
- Harris, A. J. L., Flynn, L. P., Keszthelyi, L. et al. (1998). Calculation of lava effusion rates from Landsat TM data. *Bulletin of Volcanology*, **60**, 52–71.
- Harris, A. J. L., Wright, R. and Flynn, L. P. (1999). Remote monitoring of Mount Erebus Volcano, Antarctica, using Polar Orbiters: progress and Prospects. *International Journal of Remote Sensing*, **20**(15&16), 3051–3071.
- Harris, A. J. L., Flynn, L. P., Dean, K. et al. (2000a). Real-time monitoring of volcanic hot spots with satellites. *American Geophysical Union Monograph Series*, **116**, 139–159.
- Harris, A. J. L., Murray, J. B., Aries, S. E. et al. (2000b). Effusion rate trends at Etna and Krafla and their implications for eruptive mechanisms. *Journal of Volcanology and Geothermal Research*, **102**(3–4), 237–269.
- Harris, A. J. L., Pilger, E., Flynn, L. P. et al. (2001). Automated, high temporal resolution, thermal analysis of Kilauea volcano, Hawaii, using GOES-9 satellite data. *International Journal of Remote Sensing*, **22**(6), 945–967.
- Harris, A. J. L., Pilger, E. and Flynn, L. P. (2002a). Web-based hot spot monitoring using GOES: what it is and how it works. *Advances in Environmental Monitoring and Modeling*, **1**(3), 5–36.

- Harris, A. J. L., Pilger, E., Flynn, L. P. and Rowland, S. K. (2002b). Real-time hot spot monitoring using GOES: case studies from 1997–2000. *Advances in Environmental Monitoring and Modeling*, **1**(3), 134–151.
- Harris, A. J. L., Flynn, L. P., Matias, O. and Rose, W. I. (2002c). The thermal stealth flows of Santiaguito: implications for the cooling and emplacement of dacitic block lava flows. *Geological Society of America Bulletin*, **114**(5), 533–546.
- Harris, A. J. L., Flynn, L. P. and Rose, W. I. (2003a). Temporal trends in lava dome extrusion at Santiaguito 1922–2000. *Bulletin of Volcanology*, **65**, 77–89.
- Harris, A., Johnson, J., Horton, K. *et al.* (2003b). Ground-based infrared monitoring provides new tool for remote tracking of volcanic activity. *EOS*, **84**(40), 409–418.
- Harris, A. J. L., Flynn, L. P., Matias, O., Rose, W. I. and Cornejo, J. (2004). The evolution of an active silicic lava flow field: an ETM+ perspective. *Journal of Volcanology and Geothermal Research*, **135**, 147–168.
- Harris, A. J. L., Carniel, R. and Jones, J. (2005a). Identification of variable convective regimes at Erta Ale lava lake. *Journal of Volcanology and Geothermal Research*, **142**, 207–223.
- Harris, A., Pirie, D., Horton, K. *et al.* (2005b). DUCKS: low cost thermal monitoring units for near-vent deployment. *Journal of Volcanology and Geothermal Research*, **143**, 335–360.
- Harris, A. J. L., Dehn, J., Patrick, M. *et al.* (2005c). Lava effusion rates from hand-held thermal infrared imagery: an example from the June 2003 effusive activity at Stromboli. *Bulletin of Volcanology*, **68**, 107–117.
- Harris, A., Bailey, J., Calvari, S. and Dehn, J. (2005d). Heat loss measured at a lava channel and its implications for down-channel cooling and rheology. *Geological Society of America Special Paper*, **396**, 125–146.
- Harris, A. J. L., Dehn, J., James, M. R. *et al.* (2007). Pahoehoe cooling, discharge and coverage rates from thermal image chronometry. *Geophysical Research Letters*, **34**, L19303. DOI: 10.1029/2007GL030791.
- Harris, A. J. L., Ripepe, M., Calvari, S., Lodato, L. and Spampinato, L. (2008). The 5 April 2003 explosion of Stromboli: timing of eruption dynamics using thermal data. *AGU Geophysical Monograph*, **182**, 305–316.
- Harris, A. J. L., Lodato, L., Dehn, J. and Spampinato L. (2009). Thermal characterization of the Vulcano fumarole field. *Bulletin of Volcanology*, **71**, 441–458. DOI: 10.1007/s00445–008–0236–8.
- Harris, A. J. L., Favalli, M., Steffke, A., Fornaciai, A. and Boschi, E. (2010). A relation between lava discharge rate, thermal insulation, and flow area set using lidar data. *Geophysical Research Letters*, **37**, L20308. DOI: 10.1029/2010GL044683.
- Hasse, L. (1963). On the cooling of the sea surface by evaporation and heat exchange. *Tellus*, **15**, 363–366.
- Hasse, L. (1971). The surface temperature derivation and the heat flow at the sea–air interface. *Boundary-Layer Meteorology*, **1**, 368–379.
- HeatWave Labs (2002). DFP 2000 disappearing filament optical pyrometer: Manual for operation and maintainance. HeatWave Labs Inc. (Watsonville, CA, USA), DFP 2000 Manual Rev. 1, date 123002, 23 p.
- Heiken, G. and Pitts, D. E. (1975). Identification of eruption clouds with the Landsat satellites. *Bulletin of Volcanology*, **39**(2), 255–265.
- Helz, R. and Thornber, C. R. (1987). Geothermometry of Kilauea Iki lava lake, Hawaii. *Bulletin of Volcanology*, **49**, 651–668.

- Helz, R., Banks, N. G., Heliker, C., Neal, C. A. and Wolfe, E. W. (1995). Comparative geothermometry of recent Hawaiian eruptions. *Journal of Geophysical Research*, **100** (B9), 17 637–17 657.
- Heppenheimer, T. A. (1997). *Countdown: A History of Space Flight*. New York: John Wiley & Sons, 398 p.
- Hérdervári, P. (1963). On the energy and magnitude of volcanic eruptions. *Bulletin of Volcanology*, **25**, 373–385.
- Higgins, J. and Harris, A. J. L. (1997). VAST: a program to locate and analyse volcanic thermal anomalies automatically from remotely sensed data. *Computers and Geosciences*, **23**(6), 627–645.
- Hirn, B., Di Bartola, C. and Ferrucci, F. (2008). Spaceborne monitoring 2000–2005 of the Pu'u 'O'o-Kupaianaha (Hawaii) eruption by synergetic merge of multispectral payloads ASTER and MODIS. *IEEE Transactions on Geoscience and Remote Sensing*, **46**(10), 2848–2856.
- Holasek, R. E. and Self, S. (1995). GOES weather satellite observations and measurements of the May 18, 1980, Mount St. Helens eruption. *Journal of Geophysical Research*, **100**(B5), 8469–8487.
- Holasek, R. E., Self, S. and Woods, A. W. (1996). Satellite observations and interpretation of the 1991 Mount Pinatubo eruption plumes. *Journal of Geophysical Research*, **101** (B12), 27 635–27 655.
- Holben, B. N. (1986). Characteristics of maximum-value composite images from temporal AVHRR data. *International Journal of Remote Sensing*, **7**(11), 1417–1434.
- Holben, B. and Fraser, R. S. (1984). Red and near-infrared sensor response to off-nadir viewing. *International Journal of Remote Sensing*, **5**(1), 145–160.
- Holman, J. P. (1992). *Heat Transfer*, 2nd edn. London: McGraw Hill, 713 p.
- Holst, G. C. (2000). *Common Sense Approach to Thermal Imaging*. Winter Park (FL): JCD Publishing, 377 p.
- Hon, K., Kauahikaua, J., Denlinger, R. and McKay, K. (1994a). Emplacement and inflation of pahoehoe sheet flows: observations and measurements of active lava flows on Kilauea volcano, Hawaii. *Geological Society of America Bulletin*, **106**, 351–370.
- Hon, K., Kauahikaua, J. and McKay, K. (1994b). Inflation and cooling data from pahoehoe sheet flows on Kilauea Volcano. *United States Geological Survey Open-File Report*, **93-342B**.
- Hottel, H. C. (1954). Radiant heat transmission. In *Heat Transmission*, ed. W. H. McAdams. New York: McGraw-Hill, pp. 55–125.
- Hurst, A. W., Bibby, H. M., Scott, B. J. and McGuinness, M. J. (1991). The heat source of Ruapehu Crater Lake; deductions from the energy and mass balances. *Journal of Volcanology and Geothermal Research*, **46**, 1–20.
- Iqbal, M. (1983). *An Introduction to Solar Radiation*. Academic Press: Toronto, 390 p.
- Italiano, F., Nuccio, P. M. and Valenza, M. (1984). Geothermal energy and mass release at Vulcano, Aeolian Island, Italy. *Rendiconti della Società Italiana di Mineralogia e Petrologia*, **39**, 379–386.
- Jaggar, T. A. (1917a). Volcanologic investigations at Kilauea. *American Journal of Science*, **44**, 161–221.
- Jaggar, T. A. (1917b). Thermal gradient of Kilauea lava lake. *Journal of the Washington Academy of Sciences*, **7**(3), 397–405.
- James, M. R., Robson, S., Pinkerton, H. and Ball, M. (2006). Oblique photogrammetry with visible and thermal images of active lava flows. *Bulletin of Volcanology*, **69**, 105–108.

- Janza, F. J., Blue, H. M. and Johnston, J. E. (1975). *Manual of Remote Sensing, Volume 1: Theory, Instruments and Techniques*. Falls Church (VA): American Society of Photogrammetry, 867 p.
- Jaskolla, F. and Arnason, K. (1989). Applicability of Landsat-TM data for geoscientific purposes in Iceland. *Proceedings of a Workshop in Earth Project on Landsat Thematic Mapper Applications*, **ESA SP-1102**, 127–139.
- Jeffreys, H. (1962). *The Earth*, 4th Edn. Cambridge: Cambridge University Press, 438 p.
- Johnson, J. B. (2005). Source location variability and volcanic vent mapping with a small-aperture infrasound array at Stromboli Volcano, Italy. *Bulletin of Volcanology*, **67**, 1–14.
- JMA (1999). MTSAT HiRID Technical Information. *Japan Meteorological Agency Document*, <http://www.jma.go.jp/jma/jma-eng/satellite/mtsatsat1r/mtsatsat1r.html>.
- Johnson, J. B., Harris, A. J. L., Sahetapy-Engel, S., Wolf, R. E. and Rose W. I. (2004). Explosion dynamics of vertically-directed pyroclastic eruptions at Santiaguito, Guatemala. *Geophysical Research Letters*, **31**, L06610. DOI: 2003GL019079.
- Johnson, J. B., Harris, A. J. L. and Hoblitt, R. (2005). Thermal observations of gas pistonning at Kilauea Volcano. *Journal of Geophysical Research*, **110**, B11201. DOI: 10.1029/2005JB003944.
- Jones, J., Carniel, R., Harris, A. J. L. and Malone, S. (2006). Seismic characteristics of variable convection at Erta Ale lava lake, Ethiopia. *Journal of Volcanology and Geothermal Research*, **153**, 64–79.
- Justice, C. and Dowty, P. (1994). IGBP-DIS Satellite Fire Detection Algorithm Workshop Technical Report. *International Geosphere Biosphere Programme Working Paper*, **9**, Workshop held at NASA/GSFC, Greenbelt (MA), 25–26 February 1997, 88 p.
- Kagiyama, T. (1981). Evaluation methods of heat discharge and their applications to the major active volcanoes in Japan. *Journal of Volcanology and Geothermal Research*, **9**, 87–97.
- Kahle, A. B., Palluconi, F. D., Hook, S. J., Realmuto, V. J. and Bothwell, G. (1991). The Advanced Spaceborne Thermal Emission and Reflection Radiometer (ASTER). *Int. J. Imaging Systems and Technology*, **3**, 144–156.
- Kahle, A. B., Adams, M. J., Abbott, E. A., Mougginis-Mark, P. J. and Realmuto, V. J. (1995). Remote sensing on Mauna Loa. *American Geophysical Union Monograph*, **92**, 145–170.
- Kaneko, T. and Wooster, M. J. (1999). Landsat infrared analysis of fumarole activity at Unzen Volcano: time-series comparison with gas and magma fluxes. *Journal of Volcanology and Geothermal Research*, **89**, 57–64.
- Kaneko, T. and Wooster, M. J. (2005). Satellite thermal analysis of the 1986 Izu-Oshima lava flows. *Journal of Volcanology and Geothermal Research*, **148**, 355–371.
- Kaneko, K., Yasuda, A., Ishimaru, T. et al. (2002a). Satellite hot spot monitoring of Japanese volcanoes: a prototype AVHRR-based system. *Advances in Environmental Monitoring and Modeling*, **1**(3), 125–153.
- Kaneko, T., Wooster, M. J. and Nakada, S. (2002b). Exogenous and endogenous growth of the Unzen lava dome examined by satellite infrared image analysis. *Journal of Volcanology and Geothermal Research*, **116**, 151–160.
- Kaneko, K., Munekane, H., Wooster, M. J. and Kagiyama, T. (2002c). Monitoring eruption plumes at Usu Volcano (Japan) using thermal infrared camera imagery broadcast via the internet 2002. *Advances in Environmental Monitoring and Modeling*, **1**(3), 153–166.
- Kauahikaua, J., Sherrod, D. R., Cashman, K. V. et al. (2003). Hawaiian lava-flow dynamics during the Pu'u 'O'o-Kupaianaha eruption: a tale of two decades. *United States Geological Survey Professional Paper*, **1676**, pp. 63–87.

- Kaufman, Y. J., Setzer, A., Justice, C. *et al.* (1990). Remote sensing of biomass burning in the tropics. In *Fire in the Tropical Biota*, ed. J. Goldammer. Berlin: Springer-Verlag, pp. 371–399.
- Kaufman, Y. J., Kleidman, R. G. and King, M. D. (1998). SCAR-B fires in the tropics: properties and remote sensing from EOS-MODIS. *Journal of Geophysical Research*, **103**(D24), 31,955–31,968.
- Kay, J. M. (1968). *An Introduction to Fluid Mechanics and Heat Transfer*, 2nd edn. Cambridge: Cambridge University Press, 327 pp.
- Kays, W. M. and Crawford, M. E. (1980). *Convective Heat and Mass Transfer*. McGraw-Hill: London, 420 p.
- Kays, W. H. and Perkins, H. C. (1973). Forced convection, internal flow in ducts. In *Handbook of Heat Transfer*, ed. W. M. Rohsenow and J. P. Hartnett. New York: McGraw-Hill, pp. 1–193.
- Kazahaya, K., Shinohara, H. and Saito, G. (1994). Excessive degassing of Izu-Oshima volcano: magma convection in a conduit. *Bulletin of Volcanology*, **56**, 207–216.
- Kennedy, P. J., Belward, A. S. and Grégoire, J.-M. (1994). An improved approach to fire monitoring in West Africa using AVHRR data. *International Journal of Remote Sensing*, **15**(11), 2235–2255.
- Kervyn, M., Kervyn, F., Goossens, R., Rowland, S. K. and Ernst, G. G. J. (2007). Mapping volcanic terrain using high-resolution and 3D satellite remote sensing. *Geological Society Special Publication*, **283**, 5–30.
- Kervyn, M., Ernst, G. G. J., Harris, A. *et al.* (2008). Thermal remote sensing of the low-intensity carbonatite volcanism of Oldoinyo Lengai, Tanzania. *International Journal of Remote Sensing*, **29**, 6467–6499.
- Keszthelyi, L. (1995a). Measurements of the cooling at the base of pahoehoe flows. *Geophysical Research Letters*, **22**(16), 2195–2198.
- Keszthelyi, L. (1995b). A preliminary thermal budget for lava tubes on the Earth and planets. *Journal of Geophysical Research*, **100**(B10), 20 411–20 420.
- Keszthelyi, L. and Denlinger, R. (1996). The initial cooling of pahoehoe flow lobes. *Bulletin of Volcanology*, **58**, 5–18.
- Keszthelyi, L. and Self, S. (1998). Some physical requirements for the emplacement of long basaltic lava flows. *Journal of Geophysical Research*, **103**(B11), 27 447–27 464.
- Keszthelyi, L., McEwen, A. S. and Thordarson, T. (2000). Terrestrial analogs and thermal models for Martian flood lavas. *Journal of Geophysical Research*, **105**(E6), 15 027–15 049.
- Keszthelyi, L., Harris, A. J. L. and Dehn, J. (2003). Observations of the effect of wind on the cooling of active lava flows. *Geophysical Research Letters*, **30**(19), DOI: 10.1029/2003GL017994.
- Kidwell, K. B. (1991). *NOAA polar orbiter data [TIROS-N, NOAA-6, NOAA-7, NOAA-8, NOAA-9, NOAA-10, NOAA-11 & NOAA-12]: Users guide*. Washington DC: National Oceanic and Atmospheric Administration.
- Kidwell, K. B. (1995). *NOAA polar orbiter data [TIROS-N, NOAA-6, NOAA-7, NOAA-8, NOAA-9, NOAA-10, NOAA-11, NOAA-12, NOAA-13, and NOAA-14]: Users guide*. Washington DC: National Oceanic and Atmospheric Administration.
- Kieffer, H. H., Frank, D. and Friedman, J. D. (1981). Thermal infrared surveys at Mount St. Helens – observations prior to the eruption of May 18. *United States Geological Survey Professional Paper*, **1250**, 257–277.

- Koeppen, W. C., Pilger, E. and Wright, R. (2011). Time series analysis of infrared satellite data for detecting thermal anomalies: a hybrid approach. *Bulletin of Volcanology*, **73**, 577–593.
- Koyaguchi, T. and Tokuno, M. (1993). Origin of the giant eruption cloud of Pinatubo, June 15, 1991. *Journal of Volcanological and Geothermal Research*, **55**, 85–96.
- Kreuger, A. F. (1982). Geostationary satellite observations of the April 1979 Soufrière eruptions. *Science*, **216**, 1108–1109.
- Krutikov, V. N. (2002). The history of the development and the present state of radiation receivers as primary converters of optical quantities, signals and images. *Measurement Techniques*, **45**(9), 935–942.
- Labazuy, P., Gouhier, M., Harris, A. et al. (2012). Near real-time monitoring of the April–May 2010 Eyjafjallajökull ash cloud: an example of a web-based, satellite-data-driven, reporting system. *International Journal of Environment and Pollution*, **48**(1–4), 262–272.
- Labed, J. and Stoll, M. P. (1991). Angular variation of land surface spectral emissivity in the thermal infrared: Laboratory investigations on bare soils. *International Journal of Remote Sensing*, **12**, 2299–2310.
- Lacava, T., Di Leo, E. V., Pergola, N. and Tramutoli, V. (2006). Space-time wetness variations monitoring by a multi-temporal microwave satellite records analysis. *Physics and Chemistry of the Earth*, **31**, 1274–1283.
- Lachlan-Cope, T., Smellie, J. L. and Ladkin, R. (2001). Discovery of a recurrent lava lake on Saunders Island (South Sandwich Islands) using AVHRR imagery. *Journal of Volcanology and Geothermal Research*, **112**, 105–116.
- Laigos, E., Vassilopoulou, S., Sakkas, V. et al. (2007). Testing satellite and ground thermal imaging of low-temperature fumarolic fields: The dormant Nisyros Volcano (Greece). *ISPRS Journal of Photogrammetry and Remote Sensing*, **62**, 447–460.
- Langaas, S. (1993). A parametrised bispectral model for savanna fire detection using AVHRR night images. *International Journal of Remote Sensing*, **14**(12), 2245–2262.
- Lange, I. M. and Avent, J. C. (1974). Ground-based thermal infrared surveys of Mount Rainier Volcano, Washington. *Bulletin of Volcanology*, **38**(3), 929–943.
- Lardy, M. and Tabbagh, A. (1999). Measuring and interpreting heat fluxes from shallow volcanic bodies using vertical temperature profiles: a preliminary test. *Bulletin of Volcanology*, **60**, 441–447.
- Lautze, N. C., Harris, A. J. L., Bailey, J. et al. (2004). Evidence for pulsed magma supply at Mount Etna during 2001. *Journal of Volcanology and Geothermal Research*, **137**, 231–246.
- Lawrence, M. G. (2005). The relationship between relative humidity and the dewpoint humidity temperature in moist air. *Bulletin of the American Meteorological Society*, **86**(2), 225–233.
- Le Guern, F. (1987). Mechanism of energy transfer in the lava lake of Niragongo (Zaire), 1959–1977. *Journal of Volcanology and Geothermal Research*, **31**, 17–31.
- Le Guern, F., Carbonelle, J. and Tazieff, H. (1979). Erta Ale lava lake: Heat and gas transfer to the atmosphere. *Journal of Volcanology and Geothermal Research*, **6**, 27–48.
- Le Guern, F., Tazieff, H., Vavasseur C. and Zettwoog, P. (1982a). Resonance in the gas discharge of the Bocca Nuova, Etna (Italy), 1968–1969. *Journal of Volcanology and Geothermal Research*, **12**, 161–166.
- Le Guern, F., Morel, P., Tazieff, H. and Vavasseur, C. (1982b). Volcanic plume thermal radiation: 1972 eruption of Piton de la Fournaise, Réunion Island. *Journal of Volcanology and Geothermal Research*, **12**, 167–175.

- Le Moigne, J., Netanyahu, N. S. and Eastman, R. D. (2011). *Image Registration for Remote Sensing*. Cambridge: Cambridge University Press, 484 p.
- Lee, T. F. and Tag, P. M. (1990). Improved detection of hotspots using the AVHRR 3.7  $\mu\text{m}$  channel. *Bulletin American Meterological Society*, **71**(12), 1722–1730.
- Lillesand, T. M. and Kiefer, R. W. (1987). *Remote Sensing and Image Interpretation*. New York: John Wiley & Sons, 721 p.
- Lipman, P. W. and Banks, N. G. (1987). 'A'ā flow dynamics, Mauna Loa 1984. *United States Geological Society Professional Paper*, **1350**, 1527–1567.
- Lodato, L., Spampinato, L., Harris, A. J. L. et al. (2008). Use of forward looking infrared thermal cameras at active volcanoes. In: *Conception, Verification and Application of Innovative Techniques to Study Active Volcanoes*, ed. W. Marzocchi & A. Zollo, Istituto Nazionale di Geofisica e Vulcanologia (Italy), pp. 427–434.
- Lombardo, V. and Buongiorno, M. F. (2006) Lava flow thermal analysis using three infrared bands of remote-sensing imagery: a study case from Mount Etna 2001 eruption. *Remote Sensing of Environment*, **101**, 141–149.
- Lombardo, V., Harris, A. J. L., Calvari, S. and Buongiorno, M. F. (2009). Spatial variations in lava flow field thermal structure and effusion rate derived from very high spatial resolution hyperspectral (MIVIS) data. *Journal of Geophysical Research*, **114**, B02208. DOI: 10.1029/2008JB005648.
- Lyons, J. J., Waite, G. P., Rose, W. I. and Chigna, G. (2010). Patterns in open vent, strombolian behavior at Fuego volcano, Guatemala, 2005–2007. *Bulletin of Volcanology*, **72**, 1–15.
- Macdonald, G. A. (1963). Physical properties of erupting Hawaiian magmas. *Geological Society of America Bulletin*, **74**, 1071–1078.
- Macdonald, G. A. (1972). *Volcanoes*. Englewood Cliffs, New Jersey: Prentice-Hall, 510 p.
- Marchetti, E. and Harris, A. J. L. (2008). Trends in activity at Pu'u 'O'o during 2001/2003: insights from the continuous thermal record. *Geological Society, London, Special Publications*, **307**, 85–101. DOI: 10.1144/SP307.6.
- Marchetti, E., Ripepe, M., Harris, A. J. L. and Delle Donne, D. (2009). Tracing the differences between vulcanian and strombolian explosions using infrasonic and thermal radiation energy. *Earth and Planetary Science Letters*, **279**, 273–281.
- Markham, B. L. (1985). The Landsat sensors' spatial response. *IEEE Transactions on Geoscience and Remote Sensing*, **GE-23**, 864–875.
- Marsh, S. E., Switzer, P., Kowalk, W. S. and Lyon, R. J. P. (1980). Resolving the percentage of component terrains within single resolution elements. *Photogrammetric Engineering and Remote Sensing*, **46**(8), 1079–1086.
- Mather, P. M. (1987). *Computer Processing of Remotely-Sensed Images*, Chichester: John Wiley & Sons, 352 p.
- Matson, M. and Dozier, J. (1981). Identification of subresolution high temperature sources using a thermal IR sensor. *Photogrammetric Engineering and Remote Sensing*, **47**(9), 1311–1318.
- Matsushima, N. (2005). H<sub>2</sub>O emission rate by the volcanic plume during the 2000–2002 Miyakejima volcanic activity. *Geophysical Research Letters*, **32**, L14307. DOI: 10.1029/2005GL023217.
- Matsushima, N., Kazahaya, K., Saito, G. and Shinohara, H. (2003). Mass and heat flux of volcanic gas discharging from the summit crater of Iwodake volcano, Satsuma-Iwojima, Japan, during 1996–1999. *Journal of Volcanology and Geothermal Research*, **126**, 285–301.
- Matthews, S., Walley, K. and Sharphouse, R. (1994). Weather satellite monitoring of volcanic eruptions by a comprehensive school. *Geoscientist*, **4**(6), 23–25.

- Matthews, S. J., Gardeweg, M. C. and Sparks, R. S. J. (1997). The 1984 to 1996 cyclic activity of Lascar Volcano, northern Chile: cycles of dome growth, dome subsidence, degassing and explosive eruptions. *Bulletin of Volcanology*, **59**, 72–82.
- McCabe, M. F., Balick, L. K., Theiler, J., Gillespie, A. R. and Mushkin, A. (2008). Linear mixing in thermal infrared temperature retrieval. *International Journal of Remote Sensing*, **29**(17–18), 5047–5061.
- McGimsey, R. G., Schnieder, D. J., Neal, C. A. and Roach, A. L. (1999). Use of FLIR observations during eruptive repose at two Alaskan volcanoes. *Annual American Geophysical Union Meeting*, San Francisco, CA, USA, December, 1999, V32A–07.
- Menzel, W. P. and Purdom, J. F. W. (1994). Introducing GOES-I: The first of a new generation of Geostationary Operational Environmental Satellites. *Bull. Am. Met. Soc.*, **75**(5), 757–761.
- Mohr, P. J., Taylor, B. N. and Newell, D. B. (2008). CODATA recommended values of the fundamental physical constants: 2006. *Reviews of Modern Physics*, **80**, 633–730.
- Mongillo, M. A. and Wood, C. P. (1995). Thermal infrared mapping of White Island volcano, New Zealand. *Journal of Volcanology and Geothermal Research*, **69**, 59–71.
- Morton, B. R. (1956). Forced plumes. *Fluid Mechanics*, **5**, 151–163.
- Mouginis-Mark, P. (1992). Volcanology IDS Team meets at Goddard Space Flight Center for eruption plume meeting. *The Earth Observer*, **4**(5), 17–19.
- Mouginis-Mark, P. J. and Domergue-Schmidt, N. (2000). Acquisition of satellite data for volcano studies. In *Remote Sensing of Active Volcanoes*, AGU Geophysical Monograph, **116**, pp. 9–24.
- Mouginis-Mark, P. J. and Francis, P. W. (1992). Satellite observations of active volcanoes: prospects for the 1990's. *Episodes*, **15**(1), 46–55.
- Mouginis-Mark, P. J., Pieri, D. C., Francis, P. W. et al. (1989). Remote sensing of volcanoes and volcanic terrains. *EOS*, **70**(52), 1567–1575.
- Mouginis-Mark, P., Rowland, S., Francis, P. et al. (1991). Analysis of active volcanoes from the Earth Observing System. *Remote Sensing of Environment*, **36**, 1–12.
- Mouginis-Mark, P. J., Garbeil, H. and Flament, P. (1994). Effects of viewing geometry on AVHRR observations of volcanic thermal anomalies. *Remote Sensing of Environment*, **48**, 51–60.
- Mouginis-Mark, P. J., Crisp, J. A. and Fink, J. H. (2000a). Remote sensing of active volcanism, *American Geophysical Union Monograph*, **116**, 272 p.
- Mouginis-Mark, P. J., Snell, H. and Ellisor, R. (2000b). GOES satellite and field observations of the 1998 eruption of Volcan Cerro Azul, Galápagos. *Bulletin of Volcanology*, **62**, 188–198.
- Moxham, R. M. (1967). Changes in surface temperature at Taal Volcano, Philippines. *Bulletin of Volcanology*, **31**, 215–234.
- Moxham, R. M. (1969). Aerial infrared surveys at the Geysers geothermal steam field, California. *U.S. Geological Survey Professional Paper*, **650-C**, pp. C106–C122.
- Moxham, R. M. (1970). Thermal features at volcanoes in the Cascade Range, as observed by Aerial infrared surveys. *Bulletin of Volcanology*, **34**, 77–106.
- Moxham, R. M. (1971). Thermal surveillance of volcanoes. In *The Surveillance and Prediction of Volcanic Activity*. Paris: Unesco, pp. 103–124.
- Moxham, R. M., Crandell, D. R. and Marlatt, W. E. (1965). Thermal features at Mount Rainier, Washington, as revealed by infrared surveys. *U.S. Geological Survey Professional Paper*, **525-D**, D106–D122.
- Moxham, R. M., Boynton, G. R. and Cote, C. E. (1973). Satellite telemetry of fumarole temperatures, Mount Rainier, Washington. *Bulletin of Volcanology*, **36**, 191–199.
- Mutlow, C. (1999). ATSR-1/2 user guide. *European Space Agency (ESA) User's Guide*, **29** p.

- NASA (1996). *GOES I-M DataBook*, Goddard Space Flight Center (Maryland): National Aeronautics and Space Administration. DRL 101–08 (GSFC Specification S-480–21A, Contract NAS5–29500, Reference #S-415–19, Revision 1: 31 August 1996), 196 p.
- NASA (1998). *Landsat 7 Science Data Users Handbook*. [http://landsathandbook.gsfc.nasa.gov/handbook/handbook\\_toc.html](http://landsathandbook.gsfc.nasa.gov/handbook/handbook_toc.html).
- Nimah, M. M., Bshesh, K., Callahan, J. D. and Jacobs, B. R. (2006). Infrared tympanic thermometry in comparison with other temperature measurement techniques in febrile children. *Pediatric Critical Care Medicine*, **7**(1), 48–55.
- Nishihama, M., Wolfe, R., Solomon, D., Fleig, A. and Masouka, E. (1997a). *MODIS Level 1A Earth Location: Algorithm theoretical basis document*. Goddard: NASA (GSFC/Code 922).
- Nishihama, M., Wolfe, R., Solomon, D. et al. (1997b). MODIS Level 1A earth location: algorithm theoretical basis document version 3.0. *NASA support document prepared by the MODIS Science Data Support Team*, 88 p.
- Norini, G., De Beni, E., Andronico, D. et al. (2009). The 16 November 2006 flank collapse of the south-east crater at Mount Etna, Italy: study of the deposit and hazard assessment. *Journal of Geophysical Research*, **114**, B02204. DOI: 10.1029/2008JB005779.
- Nothwang, W. D., Cole, M. W. and Goldberg, A (2004). Cutting edge infrared detector materials enhance Army's night vision and targeting capabilities. *AMPTIAC Quarterly*, **8**(4), 111–117.
- Nye, C. J., Keith, T. E. C., Eichelberger, J. C. et al. (2002). The 1999 eruption of Shishaldin volcano, Alaska: monitoring a distant eruption. *Bulletin of Volcanology*, **64**, 519–707.
- Ohba, T., Hirabayashi, J.-I. and Nogami, K. (1994). Water, heat and chloride budgets of the crater lake, Yugama at Kusatsu-Shirane volcano, Japan. *Geochemical Journal*, **28**, 217–231.
- Oppenheimer, C. (1989). AVHRR volcano hot spot monitoring. *Proceedings of the 4th AVHRR data users' meeting*. Rothenberg (Sweden): 3–5 September 1989, pp. 335–338.
- Oppenheimer, C. (1991). Lava flow cooling estimated from Landsat Thematic Mapper infrared data: the Lonquimay eruption (Chile, 1989). *Journal of Geophysical Research*, **96**(B13), 21 865–21 878.
- Oppenheimer, C. (1993a). Thermal distributions of hot volcanic surfaces constrained using three infrared bands of remote sensing data. *Geophysical Research Letters*, **20**(6), 431–434.
- Oppenheimer, C. (1993b). Infrared surveillance of crater lakes using satellite data. *Journal of Volcanology and Geothermal Research*, **55**, 117–128.
- Oppenheimer, C. (1993c). I spy with my infrared eye. *New Scientist*, **1876**, 26–31.
- Oppenheimer, C. (1996). Crater lake heat losses estimated by remote sensing. *Geophysical Research Letters*, **23**(14), 1793–1796.
- Oppenheimer, C. (1997a). Remote sensing of the colour and temperature of volcanic lakes. *International Journal of Remote Sensing*, **18**(1), 5–37.
- Oppenheimer, C. (1997b). Ramifications of the skin effect for crater lake heat budget analysis. *Journal of Volcanology and Geothermal Research*, **75**, 159–165.
- Oppenheimer, C. (1997c). Surveillance and mapping of volcanoes and their emissions by satellite remote sensing. *Geography*, **82**(4), 317–333.
- Oppenheimer, C. (1998). Volcanological applications of meteorological satellites. *International Journal of Remote Sensing*, **19**(15), 2829–2864.
- Oppenheimer, C. and Francis, P. (1997). Remote sensing of heat, lava and fumarole emissions from Erta Ale volcano, Ethiopia. *International Journal of Remote Sensing*, **18**(8), 1661–1692.

- Oppenheimer, C. and Francis, P. (1998). Implications of longevol lava lakes for geomorphological and plutonic processes at Erta Ale volcano, Afar. *Journal of Volcanology and Geothermal Research*, **80**, 101–111.
- Oppenheimer, C. M. M. and Rothery, D. A. (1991). Infrared monitoring of volcanoes by satellite. *Journal of the Geological Society of London*, **148**, 563–569.
- Oppenheimer, C. and Yirgu, G. (2002). Thermal imaging of an active lava lake: Erta Ale volcano, Ethiopia. *International Journal of Remote Sensing*, **23**(22), 4777–4782.
- Oppenheimer, C., Francis, P. W., Rothery, D. A., Carlton, R. W. T. and Glaze, L. S. (1993a). Infrared image analysis of volcanic thermal features: Lascar Volcano, Chile. *Journal of Geophysical Research*, **98**(B3), 4269–4286.
- Oppenheimer, C., Rothery, D. A., Pieri, D. C., Abrams, M. J. and Carrere, V. (1993b). Analysis of Airborne Visible / Infrared Imaging Spectrometer (AVIRIS) data of volcanic hot spots. *International Journal of Remote Sensing*, **14**(16), 2919–2934.
- Oppenheimer, C., Rothery, D. A. and Francis, P. W. (1993c). Thermal distributions at fumarole fields: implications for infrared remote sensing of active volcanoes. *Journal of Volcanology and Geothermal Research*, **55**, 97–115.
- Oppenheimer, C., McGonigle, A. J. S., Allard, P., Wooster, M. J. and Tsanev, V. (2004). Sulfur, heat, and magma budget of Erta Ale lava lake, Ethiopia. *Geology*, **32**, 509–512.
- Ortiz, R., Moreno, H., Garcia, A. et al. (2003). Villarrica volcano (Chile): characteristics of the volcanic tremor and forecasting of small explosions by means of a material failure method. *Journal of Volcanology and Geothermal Research*, **128**, 247–259.
- Pasternack, G. B. and Varekamp, J. C. (1997). Volcanic lake systematics I. Physical constraints. *Bulletin of Volcanology*, **58**, 528–538.
- Patrick, M. R. (2005). Strombolian eruption dynamics from thermal (FLIR) video imagery. PhD Dissertation, University of Hawaii (Honolulu, USA): Department of Geology and Geophysics, 283 p.
- Patrick, M. R. (2007). Dynamics of strombolian ash plumes from thermal video: motion, morphology, and air entrainment. *Journal of Geophysical Research*, **112**, B06202. DOI: 10.1029/2006JB004387.
- Patrick, M. R., Dehn, J., Papp, K. R. et al. (2003). The 1997 eruption of Okmok Volcano, Alaska: a synthesis of remotely sensed imagery. *Journal of Volcanology and Geothermal Research*, **127**, 87–105.
- Patrick, M., Harris, A., Ripepe, M., Dehn, J. and Rothery, D. (2004). Strombolian thermodynamics from FLIR imagery: new insights on explosive styles and source conditions. *Eos Trans. AGU*, **85**(47), Fall Meeting Supplement, San Francisco (CA), 13–17 December, 2004, V11B–1420.
- Patrick, M. R., Dehn, J. and Dean, K. (2005a). Numerical modeling of lava flow cooling applied to the 1997 Okmok eruption: comparison with advanced very high resolution radiometer thermal imagery. *Journal of Geophysical Research*, **110**, B02210. DOI: 10.1029/2003JB002538.
- Patrick, M. R., Smellie, J. L., Harris, A. J. L., Garbeil, H. and Pilger, E. (2005b). First recorded eruption of Mount Belinda volcano, South Sandwich Islands. *Bulletin of Volcanology*, **67**, 415–422.
- Patrick, M. R., Harris, A. J. L., Ripepe, M. et al. (2007). Strombolian explosive styles and source conditions: insights from thermal (FLIR) video. *Bulletin of Volcanology*, **69**, 769–784. DOI: 10.1007/s00445–006–0107–0.
- Paulson, C. A. and Simpson, J. J. (1981). The temperature difference across the cool skin of the ocean. *Journal of Geophysical Research*, **86**(C11), 11 044–11 054.

- Peck, D. L. (1978). Cooling and vesiculation of Alae lava lake, Hawaii. *United States Geological Survey Professional Paper*, **935-B**, 59 p.
- Pereira, M. C. and Setzer, A. W. (1993). Spectral characteristics of deforestation fires in NOAA/AVHRR images. *International Journal of Remote Sensing*, **14**(3), 583–597.
- Pergola, N., Pietrapertosa, C., Lacava, T. and Tramutoli, V. (2001). Robust satellite techniques for monitoring volcanic eruptions. *Annali di Geofisica*, **44**(2), 167–177.
- Pergola, N., Marchese, F. and Tramutoli, V. (2004a). Automated detection of thermal features of active volcanoes by means of infrared AVHRR records. *Remote Sensing of Environment*, **93**, 311–327.
- Pergola, N., Tramutoli, V., Marchese, F., Scaffidi, I. and Lacava, T. (2004b). Improving volcanic ash cloud detection by robust satellite technique. *Remote Sensing of Environment*, **90**, 1.22.
- Pergola, N., Marchese, F., Tramutoli, V., Filizzola, C. and Ciampa, M. (2008). Advanced satellite technique for volcanic activity monitoring and early warning. *Annals of Geophysics*, **51**(1), 287–301.
- Pergola, N., D'Angelo, G., Lisi, M. et al. (2009). Time domain analysis of robust satellite techniques (RST) for near real-time monitoring of active volcanoes and thermal precursor identification. *Physics and Chemistry of the Earth*, **34**, 380–385.
- Perry, W. J. and Crick, I. H. (1976). Aerial thermal infrared survey, Rabaul area, Papua New Guinea, 1973. In *Volcanism in Australasia*, ed. R. Johnson. Amsterdam: Elsevier, pp. 211–219.
- Peterson, D. W. (1988). Volcanic hazards and public response. *Journal of Geophysical Research*, **93**(B5), 4161–4170.
- Pieri, D. and Adams, M. (2004). ASTER observations of thermal anomalies preceding the April 2003 eruption of Chikurachki volcano, Kurile Islands, Russia. *Remote Sensing of Environment*, **99**, 84–94.
- Pieri, D. C. and Baloga, S. M. (1986). Eruption rate area, and length relationships for some Hawaiian lava flows. *Journal of Volcanology and Geothermal Research*, **30**, 29–45.
- Pieri, D. C., Gillespie, A. R. and Kahle, A. B. (1984). Thermal infrared observations of lava flows during the 1984 Mauna Loa eruption. *Geological Society of America Abstract Program*, **16**, 623.
- Pieri, D. C., Glaze, L. S. and Abrams, M. J. (1990). Thermal radiance observations of an active lava flow during the June 1984 eruption of Mount Etna. *Geology*, **18**, 1018–1022.
- Pinkerton, H. (1993). Measuring the properties of flowing lava. In *Active Lavas*, ed. C. Kilburn & G. Luongo. London: UCL Press, pp. 175–191.
- Pinkerton, H., James, M. and Jones, A. (2002). Surface temperature measurements of active lava flows on Kilauea volcano, Hawaii. *Journal of Volcanology and Geothermal Research*, **113**, 159–176.
- Pinkerton, H., Harris, A., Ball, M. and James, M. (2004). An analysis of the development of surface textures and flow morphology on small lava flows on Kilauea using high frame rate (30 Hz) digital thermal imagery. *Eos Trans. AGU*, **85**(47), Fall Meeting Supplement, San Francisco (CA), 13–17 December, 2004, V31D–05.
- Pioli, L., Rosi, M., Calvari, S. et al. (2008). The eruptive activity of 28 and 29 December 2002. *American Geophysical Union Monograph*, **182**, 105–116.
- Piscopo, D. (2010). *Stromboli MODIS thermal anomalies during strombolian activity*. PhD thesis, Università degli Studi di Torino: Scuola di Dottorato in Scienza e Altra Tecnologia Ciclo XXII, 119 p.
- Platinum Metals Review (1991). Platinum silicide temperature detectors. *Platinum Metals Review*, **35**(4), 208.

- Pollack, J. B., Toon, O. B. and Khare, B. N. (1973). Optical properties of some terrestrial rocks and glasses. *Icarus*, **19**, 372–389.
- Prata, A. J. and Bernardo, C. (2009). Retrieval of volcanic ash particle size, mass and optical depth from a ground-based thermal infrared camera. *Journal of Volcanology and Geothermal Research*, **186**, 91–107.
- Prata, A. J. F., Cechet, R. P., Barton, I. J. and Llewellyn-Jones, D. T. (1990). The Along Track Scanning Radiometer for ERS-1 – scan geometry and data simulation. *IEEE Trans Geosciences & Remote Sensing*, **28**(1), 3–13.
- Principe, C. and Marini, L. (2008). Evolution of the Vesuvius magmatic-hydrothermal system before the 16 December 1631 eruption. *Journal of Volcanology and Geothermal Research*, **171**: 301–306.
- Prins, E. M. and Menzel, W. P. (1994). Trends in South American biomass burning detected with the GOES visible infrared spin scan radiometer atmospheric sounder from 1983–1991. *Journal of Geophysical Research*, **99**(D8), 16 719–16 735.
- Pyrometer Instrument Company (2007). PYRO Micro-Therm. The Pyrometer Instrument Company Inc., Windsor, NJ, USA, 2007 Specifications Sheet, 2 p.
- Ramsey, M. and Dehn, J. (2004). Spaceborne observations of the 2000 Bezymianny, Kamchatka eruption: the integration of high-resolution ASTER data into near real-time monitoring using AVHRR. *Journal of Volcanology and Geothermal Research*, **135**, 127–146.
- Ramsey, M. S. and Fink, J. H. (1999). Estimating silicic lava vesicularity with thermal remote sensing: a new technique for volcanic mapping and monitoring. *Bulletin of Volcanology*, **61**, 32–39.
- Ramsey, M. S. and Flynn, L. P. (2004). Strategies, insights, and the recent advances in volcanic monitoring and mapping with data from NASA's Earth Observing System. *Journal of Volcanology and Geothermal Research*, **135**, 1–11.
- Realmuto, V. J., Hon, K., Kahle, A. B., Abbott, E. A. and Pieri, D. C. (1992). Multispectral thermal infrared mapping of the 1 October 1988 Kupaianaha flow field, Kilauea volcano, Hawaii. *Bulletin of Volcanology*, **55**, 33–44.
- Ripepe, M. and Harris, A. J. L. (2008). Dynamics of the 5 April 2003 explosive paroxysm observed at Stromboli by a near-vent thermal, seismic and infrasonic array. *Geophysical Research Letters*, **35**, L07306. DOI: 10.1029/2007GL032533.
- Ripepe, M., Rossi, M. and Saccorotti, G. (1993). Image processing of explosive activity at Stromboli. *Journal of Volcanology and Geothermal Research*, **54**, 335–351.
- Ripepe, M., Poggi, P., Braun, T. and Gordeev, E. (1996). Infrasonic waves and volcanic tremor at Stromboli. *Geophysical Research Letters*, **23**, 181–184.
- Ripepe, M., Ciliberto, S. and Della Schiava, M. (2001). Time constraints for modeling source dynamics of volcanic explosions at Stromboli. *Journal of Geophysical Research*, **106**(B5), 8713–8727.
- Ripepe, M., Harris, A. J. L. and Carniel, R. (2002). Thermal, seismic and infrasonic evidences of variable degassing rates at Stromboli volcano. *Journal of Volcanology and Geothermal Research*, **118**, 285–207.
- Ripepe, M., Marchetti, E., Poggi, P. et al. (2004). Seismic, acoustic, and thermal network monitors the 2003 eruption of Stromboli volcano. *EOS*, **85**(35), 329–332.
- Ripepe, M., Marchetti, M., Uliveri, G. et al. (2005a). Effusive to explosive transition during the 2003 eruption of Stromboli volcano. *Geology*, **33**(5), 341–344.
- Ripepe, M., Harris, A. J. L. and Marchetti, M. (2005b). Coupled thermal oscillations in explosive activity at different craters of Stromboli volcano. *Geophysical Research Letters*, **32**, L17302. DOI: 10.1029/2005GL022711.

- Roach, A. L., Benoit, J. P., Dean, K. G. and McNutt, S. R. (2001). The combined use of satellite and seismic monitoring during the 1996 eruption of Pavlof volcano, Alaska. *Bulletin of Volcanology*, **62**, 385–399. DOI: 10.1007/s004450000114.
- Roberts, G. and Wooster, M. J. (2008). Fire detection and fire characterization over Africa using Meteosat SEVIRI. *IEEE Transactions on Geoscience and Remote Sensing*, **46**, 1200–1218, doi: 10.1109/TGRS.2008.915751.
- Robock, A. and Matson, M. (1982). Circumglobal transport of the El Chichon volcanic dust cloud. *Science*, **221**, 195–197.
- Rose, S. and Ramsey, M. (2009). The 2005 eruption of Kliuchevskoi volcano: Chronology and processes derived from ASTER spaceborne and field-based data. *Journal of Volcanology and Geothermal Research*, **184**, 367–380.
- Rose, W. I. (1987). Volcanic activity at Santiaguito Volcano, 1976–1984. *Geological Society of America Special Paper*, **212**, 17–28.
- Rosi, M., Bertagnini, A., Harris, A. J. L. et al. (2006). A case history of paroxysmal explosion at Stromboli: timing and dynamics of the April 5, 2003 event. *Earth and Planetary Science Letters*, **243**, 594–606.
- Rothery, D. A. (1989). Volcano monitoring by satellite. *Geology Today*, July–August **1989**, 128–132.
- Rothery, D. A. (1992). Monitoring and warning of volcanic eruptions by remote sensing. In *Geohazards Natural and Man-Made*, ed. McCall, Laming, and Scott. London: Chapman & Hall, pp. 25–32.
- Rothery, D. A. and Lawrence, G. (1992). Remote sensing for the study of volcanoes and earthquakes. *Geoscientist*, **3**(6), 10–11.
- Rothery, D. A. and Pieri, D. C. (1993). Remote sensing of active lava. In *Active Lavas*, ed. C. Kilburn & G. Luongo. London: UCL Press, pp. 203–232.
- Rothery, D. A., Oppenheimer, C. and Bonneville, A. (1995). Infrared thermal monitoring. In *Monitoring Active Volcanoes*, ed. B. McGuire, C. Kilburn and J. Murray. London: UCL Press, pp. 184–216.
- Rothery, D. A., Francis, P. W. and Wood, C. A. (1988). Volcano monitoring using short wavelength infrared data from satellites. *Journal of Geophysical Research*, **93**(B7), 7993–8008.
- Rothery, D. A., Coltelli, M., Pieri, D., Wooster, M. J. and Wright, R. (2001). Documenting surface magmatic activity at Mount Etna using ATSR remote sensing. *Bulletin of Volcanology*, **63**, 387–397.
- Rothery, D. A., Coppola, D. and Saunders, C. (2005). Analysis of volcanic activity patterns using MODIS thermal alerts. *Bulletin of Volcanology*, **67**, 539–556.
- Rowland, S. K., Harris, A. J. L., Wooster, M. J. et al. (2003). Volumetric characteristics of lava flows from interferometric radar and multispectral satellite data. *Bulletin of Volcanology*, **65**, 311–330.
- Sahetapy-Engel, S. T. and Harris, A. J. L. (2009). Thermal-image-derived dynamics of vertical ash plumes at Santiaguito volcano, Guatemala. *Bulletin of Volcanology*, **71**, 827–830. DOI: 10.1007/s00445-009-0284-8
- Sahetapy-Engel, S. T. M., Flynn, L. P., Harris, A. J. L. et al. (2004). Surface temperature and spectral measurements at Santiaguito lava dome, Guatemala. *Geophysical Research Letters*, **31**, L19610, DOI: 10.1029/2004GL020683.
- Sahetapy-Engel, S. T., Harris, A. J. L. and Marchetti, E. (2008). Thermal, seismic and infrasound observations of persistent explosive activity and conduit dynamics at Santiaguito Lava Dome, Guatemala. *Journal of Volcanology and Geothermal Research*, **173**, 1–14.

- Saito, T., Sakai, S., Iizawa, I. *et al.* (2005). A new techniques of radiation thermometry using a consumer digital camcorder: observations of red glow at Aso volcano, Japan. *Earth Planets Space*, **75**, e5–e8.
- Salisbury, J. W. and D'Aria, D. M. (1992). Emissivity of terrestrial materials in the 8–14 µm atmospheric window. *Remote Sensing of Environment*, **42**, 83–106.
- Salisbury, J. W. and D'Aria, D. M. (1994). Emissivity of terrestrial materials in the 3–5 µm atmospheric window. *Remote Sensing of Environment*, **47**, 345–361.
- Salisbury, J. W., Wald, A. and D'Aria, D. M. (1994). Thermal-infrared remote sensing and Kirchoff's law 1. Laboratory measurements. *Journal of Geophysical Research*, **99** (B6), 11 897–11 911.
- Salomonson, V. V., Barnes, W. L., Maymon, P. W., Montgomery, H. E. and Ostrow, H. (1989). MODIS: Advanced facility instrument for studies of the Earth as a system. *IEEE Trans Geosciences & Remote Sensing*, **27**(2), 145–153.
- Saunders, P. M. (1967). The temperature at the ocean-air interface. *Journal of the Atmospheric Sciences*, **24**, 269–273.
- Saunders, R. W. and Kriebel, K. T. (1988). An improved method for detecting clear sky and cloudy radiances from AVHRR data. *International Journal of Remote Sensing*, **9**(1), 123–150.
- Sawada, Y. (1985). GMS observation of eruption clouds of the 1984 September–October Mayon eruption. *Philippine Journal of Volcanology*, **2**, 143–155.
- Sawada, Y. (1989). The detection capability of explosive eruptions using GMS imagery, and the behaviour of dispersing eruption clouds. In *Volcanic Hazards*, ed. J Latter. Berlin, Heidelberg: Springer-Verlag, pp. 233–245.
- Sawyer, G. M. and Burton, M. R. (2006). Effects of a volcanic plume on thermal imaging data. *Geophysical Research Letters*, **33**, L14311. DOI: 10.1029/2005GL025320.
- Scandone, R. (1979). Effusion rate and energy balance of Paricutin eruption (1943–1952), Michoacan, Mexico. *Journal of Volcanology and Geothermal Research*, **6**, 49–59.
- Scharff, L., Hort, M., Harris, A. J. L. *et al.* (2008). Eruption dynamics of the SW crater of Stromboli volcano, Italy – an interdisciplinary approach. *Journal of Volcanology and Geothermal Research*, **176**, 565–570.
- Schlüssel, P., Emery, W. J., Grassl, H. and Mammen, T. (1990). On the bulk-skin temperature difference and its impact on satellite remote sensing of sea surface temperature. *Journal of Geophysical Research*, **95**(C8), 13 341–13 356.
- Schmid, J. (2006). The SEVIRI instrument. *EUMETSAT Document*, pdf\_ten\_msg\_seviri\_instrument.pdf, <http://www.eumetsat.int>.
- Schneider, D. J., Dean, K. G., Dehn, J., Miller, T. P. and Kirilanov, V. Y. (2000). Monitoring and analyses of volcanic activity using remote sensing data at the Alaska Volcano Observatory: case study for Kamchatka, Russia, December 1997. *American Geophysical Union Monograph Series*, **116**, pp. 161–177.
- Schneider, D. J., Wessels, R. and Ramsey, M. S. (2004). Airborne thermal infrared observations during the first month of the 2004 eruption of Mount Saint Helens volcano, Washington. *Eos Trans. AGU*, **85**(47), Fall Meeting Supplement, San Francisco (CA), 13–17 December 2004, V31E-05.
- Schneider, D. J., Vallance, J. W., Wessels, R. L., Logan, M. and Ramsey, M. S. (2008). Use of thermal infrared imaging for monitoring renewed dome growth at Mount St. Helens, 2004. *U.S. Geological Survey Professional Paper*, **1750**, 347–359.
- Schott, J. R. (2007). *Remote Sensing: The Image Chain Approach*, New York: Oxford University Press, 666 p.

- Schowengerdt, R. A. (2007). *Remote Sensing: Models and Methods for Image Processing*, Burlington: Academic Press, 515 p.
- Schwalb, A. (1978). The TIROS-N/NOAA A-G satellite series. *NOAA Technical Memorandum NESS*, **95**, 75 p.
- Scorer, R. S. (1986). Etna: the eruption of Christmas 1985 as seen by meteorological satellite. *Weather*, **41**(12), 378–384.
- Sekioka, M. and Yuhara, K. (1974). Heat flux estimation in geothermal areas based on the heat balance of the ground surface. *Journal of Geophysical Research*, **79**(14), 2053–2058.
- Settle, J. J. and Drake, N. A. (1993). Linear mixing and the estimation of ground cover proportions. *International Journal of Remote Sensing*, **14**(6), 1159–1177.
- Setzer, A. W. and Pereira, M. C. (1991). Amazonia biomass burnings in 1987 and an estimate of their tropospheric emissions. *Ambio*, **20**(1), 19–22.
- Shimozuru, D. (1971). Observation of volcanic eruption by an infrared radiation meter. *Nature*, **234**, 457–459.
- Shimozuru, D. and Kagiyama, T. (1978). A newly devised infra-red ground scanner and its application to geothermal research in volcanoes. *Journal of Volcanology and Geothermal Research*, **4**, 251–264.
- Simpson, J. J. and Paulson, C. A. (1980). Small-scale sea surface temperature structure. *Journal of Physical Oceanography*, **10**, 399–410.
- Singh, S. M. (1988). Simulation of solar zenith angle effect on global vegetation index (GVI) data. *International Journal of Remote Sensing*, **9**(2), 237–248.
- Singh, S. M. and Warren, D. E. (1983). Sea surface temperatures from infrared measurements. In *Remote Sensing Application in Marine Science and Technology*, ed. A. P. Cracknell, D. Reidel Publishing Company, pp. 231–262.
- Sobrino, J. A. and Cuenca, J. (1999). Angular variation of thermal infrared emissivity for some natural surfaces from experimental measurements. *Applied Optics*, **38**, 3931–3936.
- Sostman, H. E. and Metz, P. D. (1995). Fundamentals of thermometry part VIII Radiation thermometry and calibration. *Isotech. J. Thermometry*, **6**(2), 74–86.
- Space Systems / Loral (1996). GOES I-M DataBook. *DRL 101–08*, Revision **1**, 197 p.
- Spampinato, L., Oppenheimer, C., Calvari, S., Cannata, A. and Montalto, P. (2008). Lava lake surface characterization by thermal imaging: Erta Ale volcano (Ethiopia). *Geochemistry Geophysics Geosystems*, **9**(12), Q12008. DOI: 10.1029/2008GC002164.
- Spampinato, L., Calvari, S., Oppenheimer, C. and Boschi, E. (2011). Volcano surveillance using infrared cameras. *Earth-Science Reviews*, **106**, 63–91.
- Sparks, R. S. J., Bursik, M. I., Carey, S. N. et al. (1997). *Volcanic Plumes*. Chichester: John Wiley & Sons, 574 p.
- Stefan, J. (1891). Über die Theorie der Eisbildung, insbesondere über die Eisbildung im Polarmeere. *Annals Physik Chemie*, **42**, 269–286.
- Steffke, A. M. and Harris, A. J. L. (2011). A review of algorithms for detecting volcanic hot spots in satellite infrared data. *Bulletin of Volcanology*, **73**, 1109–1137.
- Stevenson, D. S. (1993). Physical models of fumarolic flow. *Journal of Volcanology and Geothermal Research*, **57**, 139–156.
- Suits, G. H. (1975). The nature of electromagnetic radiation. In *Manual of Remote Sensing*, Volume I, ed. F. J. Janza, H. M. Blue, and J. E. Johnston. American Society of photogrammetry, Falls Church, Virginia, pp. 51–73.
- Swanson, D. A., Duffield, W. A., Jackson, D. B. and Peterson, D. W. (1979). Chronological narrative of the 1969–71 Mauna-Ulu eruption, Kilauea Volcano, Hawaii. *United States Geological Survey Professional Paper*, **1056**, 1–55.

- Symonds, R. B., Rose, W. I., Bluth, G. J. S. and Gerlach, T. M. (1994). Volcanic gas studies: methods, results and applications. *Reviews in Mineralogy*, **30**, 1–66.
- Sykes, J. B. (1982). *The Concise Oxford English Dictionary*. 7th Edition, Oxford University Press, New York, 1260 pp.
- Tabbagh, A. and Trezeguet, D. (1987). Determination of sensible heat flux in volcanic areas from ground temperature measurements along vertical profiles: The case study of Mount Etna (Sicily, Italy). *Journal of Geophysical Research*, **92**(B5), 3635–3644.
- Tabbagh, A., Tabbagh, J. and Dechambenoit, C. (1987). Mapping of the surface temperature of Mount Etna and Vulcanello Island using an airborne scanner radiometer. *Journal of Volcanology and Geothermal Research*, **34**, 79–88.
- Tazieff, H. (1970). New investigations on eruptive gases. *Bulletin of Volcanology*, **34**, 421–438.
- Tazieff, H. and Jatteau, M. (1969). Mesure dans l'infrarouge des paramètres des gaz éruptifs. *Comptes Rendus Académie des Sciences Paris*, **268**, 767–770.
- Tilling, R. I. (1989). Volcanic hazards and their mitigation: progress and problems. *Reviews of Geophysics*, **27**, 237–269.
- Tison, A. (2000). Les Tortus Géant. In *Le Tour du Monde des Barabapapa*, Episode 44, DVD edited and distributed by TF1 vidéo.
- Tramutoli, V. (1998). Robust AVHRR Techniques (RAT) for environmental monitoring: theory and applications. *Proceedings of SPIE*, **3496**, 101–113.
- Tramutoli, V., Di Bello, G., Pergola, N. and Piscitelli, S. (2001). Robust satellite techniques for remote sensing of seismically active areas. *Annali di Geofisica*, **44** (2), 295–311.
- Tucker, C. J., Gatlin, J. A. and Schneider, S. R. (1984). Monitoring vegetation in the Nile delta with NOAA-6 and NOAA-7 AVHRR imagery. *Photogrammetric Engineering and Remote Sensing*, **50**(1), 53–61.
- Turcotte, D. L. and Schubert, G. (2002). *Geodynamics*, 2nd edn. Cambridge: Cambridge University Press, 456 p.
- Turner, J. S. (1962). The ‘starting plume’ in neutral surroundings, *Journal of Fluid Mechanics*, **13**, 356–368.
- Turner, J. S. (1969). Buoyant plumes and thermals. *Annual Reviews of Fluid Mechanics*, **1**, 29–44.
- Turner, J. S. (1973). *Buoyancy Effects in Fluids*. Cambridge: Cambridge University Press, 368 p.
- Urai, M. (2000). Volcano monitoring with Landsat TM short-wave infrared bands: the 1990–1994 eruption of Unzen Volcano, Japan. *International Journal of Remote Sensing*, **21**(5), 861–872.
- Urai, M., Geshi, N. and Staudacher, T. (2007). Size and volume of the caldera collapse on Piton de la Fournaise volcano during the April 2007 eruption using ASTER stereo imagery. *Geophysical Research Letters*, **34**, L22318, DOI: 10.1029/2007GL031551.s.
- Urbanski, N.-A., Voge, M., Seyfried, R. et al. (2002). Fifteen days of continuous activity survey at Stromboli volcano, Italy, in September 2000: Doppler radar, seismicity, infrared, soil humidity, and mapping of the crater region. *International Journal of Earth Science*, **91**, 712–721.
- USGS/NOAA (1984). *Landsat 4 Data Users Handbook*. Alexandria (VA): United States Geological Survey / National Oceanographic and Atmospheric Division (US Government Printing Office), 262 p.
- Vaughan, R. G., Kervyn, M., Realmuto, V., Abrams, M. and Hook, S. J. (2008). Satellite measurements of recent volcanic activity at Oldoinyo Lengai, Tanzania. *Journal of Volcanology and Geothermal Research*, **173**, 196–206.
- Verhoogen, J. (1946). Volcanic heat. *American Journal of Science*, **244**(11), 745–771.

- Vicari, A., Ciraudo, A., Del Negro, C., Herault, A. and Fortuna, L. (2009). Lava flow simulations using discharge rates from thermal infrared satellite imagery during the 2006 Etna eruption. *Natural Hazards*, **50**, 539–550.
- Vicari, A., Ganci, G., Behncke, B. et al. (2011). Near-real-time forecasting of lava flow hazards during the 12–13 January 2011 Etna eruption. *Geophysical Research Letters*, **38**, L13317. DOI: 10.1029/2011GL047545.
- Vilardo, G., Chiodini, G., Augusti, V. et al. (2008). The permanent thermal infrared network for the monitoring of hydrothermal activity at the Solfatara and Vesuvius volcanoes. In *Conception, Verification and Application of Innovative Techniques to Study Active Volcanoes*, ed. W. Marzocchi & A. Zollo, Istituto Nazionale di Geofisica e Vulcanologia (Italy), pp. 481–495.
- Vollmer, M. and Möllmann, K.-P. (2011). *Infrared Thermal Imaging: Fundamentals, Research, Applications*. Weinheim: Wiley-VCH, 593 p.
- Wadge, G. (1981). The variation of magma discharge during basaltic eruptions. *Journal of Volcanology and Geothermal Research*, **11**, 139–168.
- Walter, L. S. and Salisbury, J. W. (1989). Spectral characterization of igneous rocks in the 8- to 12- $\mu\text{m}$  region. *Journal of Geophysical Research*, **94**(B7), 9203–9213.
- Weber, R. L. (1950). *Heat and Temperature Measurement*. Prentice-Hall, New Jersey.
- Webley, P. W., Wooster, M. J., Strauch, W. et al. (2008). Experiences from near-real-time satellite-based volcano monitoring in Central America: case studies at Fuego, Guatemala. *International Journal of Remote Sensing*, **29**(22), 6621–6646.
- Wells, M. A. and Cullinane, T. (2007). Spectral discrimination of dolerite in crushed rock road aggregate, Perth, Western Australia. *International Journal of Remote Sensing*, **28** (23–24), 5299–5314.
- Wessels, R. L., Coombs, M. L., Schneider, D. J., Dehn, J. and Ramsey, M. S. (2010). High-resolution satellite and airborne thermal infrared imaging of the 2006 eruption of Augustine Volcano. *U.S. Geological Survey Professional Paper*, **1769**, 527–552.
- Wiesner, D. R. and D'Aguanno, J. (1982). Thermal imagery of Mount Erebus from the NOAA-6 satellite. *Antarctic Journal of the United States*, **17**, 32–34.
- Williams, T. L. (2009). *Thermal Imaging Cameras: Characteristics and Performance*. Boca Raton (FL): CRC Press, 218 p.
- Williams, R. S. (1972). Terrestrial remote sensing: applications of thermal infrared scanners to the geological sciences. *ISA Transducer Compendium*, Part 3, 219–236.
- Williams, R. S. and Friedman, J. D. (1970). Satellite observation of effusive volcanism. *Journal of the British Interplanetary Society*, **23**, 441–450.
- Williams, R. S., Jr., Friedman, J. D., Thorarinsson, S., Sigurgeirsson, T. and Palmason, G. (1968). Analysis of 1966 infrared imagery of Surtsey, Iceland. In *Surtsey Research Progress Report IV*. The Surtsey Research Society, Reykjavik.
- Williams-Jones, G., Stix, J. and Hickson, C. (2008). *The COSPEC cookbook*. IAVCEI: Methods in Volcanology I, 233 p.
- Williamson Corporation (2004). *Application summary sheet Aluminum Industry – Smelting plants*. Concord (MA): Williamson Corporation, 6 p.
- Wiscombe, W. J. and Warren, S. G. (1980). A model for the spectral albedo of snow. I. Pure snow. *Journal of the Atmospheric Sciences*, **37**, 2712–2733.
- Witter, J. B. and Harris A. J. L. (2004). Heat loss from skylights in lava tube systems. *Eos Trans. AGU*, **85**(47), Fall Meeting Supplement, San Francisco (CA), 13–17 December 2004, V31D-04.

- Witter, J. B. and Harris, A. J. L. (2007). Field measurements of heat loss from skylights and lava tube systems. *Journal of Geophysical Research*, **112**, B01203. DOI: 10.1029/2005JB003800.
- Witter, J. B., Hernandez, P., Harris, A. J. L. and Pérez, N. (2012). Quantification of the mass flux of H<sub>2</sub>O gas (steam) at three active volcanoes using thermal infrared imagery. *Pure and Applied Geophysics*, DOI: 10.1007/s0024-011-0446-4.
- Wooster, M. J. (1996). ATSR data calibration. *Int. J. Remote Sensing*, **17**, 1069–1074.
- Wooster, M. J. (2001). Long-term infrared surveillance of Lascar Volcano: contrasting activity cycles and cooling pyroclasts. *Geophysical Research Letters*, **28**(5), 847–850.
- Wooster, M. J. and Kaneko, T. (1998). Satellite thermal analyses of lava dome effusion rates at Unzen Volcano, Japan. *Journal of Geophysical Research*, **103**(B9), 20 935–20 947.
- Wooster, M. J. and Rothery, D. A. (1997a). Thermal monitoring of Lascar Volcano, Chile, using infrared data from the along-track scanning radiometer: a 1992–1995 time series. *Bulletin of Volcanology*, **58**, 566–579.
- Wooster, M. J. and Rothery, D. A. (1997b). Time-series analysis of effusive volcanic activity using the ERS Along Track Scanning Radiometer: the 1995 eruption of Fernandina Volcano, Galápagos Islands. *Remote Sensing of Environment*, **62**, 109–117.
- Wooster, M. J. and Rothery, D. A. (2002). A review of volcano surveillance applications using the ATSR instrument series. *Advances in Environmental Monitoring and Modeling*, **1**(3), 97–123.
- Wooster, M. J., Wright, R., Blake, S. and Rothery, D. A. (1997). Cooling mechanisms and an approximate thermal budget for the 1991–1993 Mount Etna lava flow. *Geophysical Research Letters*, **24**(24), 3277–3280.
- Wooster, M. J., Rothery, D. A. and Kaneko, T. (1998a). Geometric considerations for the remote monitoring of volcanoes: studies of lava domes using ATSR and the implications for MODIS. *International Journal of Remote Sensing*, **19**(13), 2585–2591.
- Wooster, M. J., Rothery, D. A., Sear, C. B. and Carlton, R. W. T. (1998b). Monitoring the development of active lava domes using data from the ERS-1 Along Track Scanning Radiometer. *Advances in Space Research*, **21**(3), 501–505.
- Wooster, M. J., Kaneko, T., Nakada, S. and Shimizu, H. (2000). Discrimination of lava dome activity styles using satellite-derived thermal structures. *Journal of Volcanology and Geothermal Research*, **102**, 97–118.
- Wooster, M. J., Zhukov, B. and Oertel, D. (2003). Fir radiative energy for quantitative study of biomass burning: derivation from the BIRD experimental satellite and comparison to MODIS fire products. *Remote Sensing of Environment*, **86**, 83–107.
- Wright, R. and Flynn, L. P. (2003). On the retrieval of lava-flow surface temperatures from infrared satellite data. *Geology*, **31**(10), 893–896.
- Wright, R. and Flynn, L. P. (2004) Space-based estimate of the volcanic heat flux into the atmosphere during 2001 and 2002. *Geology*, **32**(3), 189–192. DOI: 10.1130/G20239.1.
- Wright, R., Rothery, D. A., Blake, S., Harris, A. J. L. and Pieri, D. C. (1999). Simulating the response of the EOS Terra ASTER sensor to high-temperature volcanic targets. *Geophysical Research Letters*, **26**(12), 1773–1776.
- Wright, R., Rothery, D. A., Blake, S. and Pieri, D. C. (2000). Visualising active volcanism with high spatial resolution satellite data: the 1991–1993 eruption of Mount Etna. *Bulletin of Volcanology*, **62**, 256–265.
- Wright, R., Blake, S., Harris, A. and Rothery, D. (2001). A simple explanation for the space-based calculation of lava eruptions rates. *Earth and Planetary Science Letters*, **192**, 223–233.
- Wright, R., Flynn, L., Garbeil, H., Harris, A. and Pilger, E. (2002a). Automated volcanic eruption detection using MODIS. *Remote Sensing of Environment*, **82**, 135–155.

- Wright, R., Cruz-Reyna, S. D., Flynn, L., Harris, A. and Gomez-Palacios, J. J. (2002b). Integrated geophysical monitoring at Popocatepetl, Mexico: explosive activity and dome growth processes. *Journal of Geophysical Research*, **107**(B8). DOI: 10.1029/2000JB000125.
- Wright, R., Flynn, L. P., Garbeil, H., Harris, A. J. L. and Pilger, E. (2004). MODVOLC: near-real-time thermal monitoring of global volcanism. *Journal of Volcanology and Geothermal Research*, **135**, 29–49.
- Wright, R., Carn, S. A. and Flynn, L. P. (2005). A satellite chronology of the May–June 2003 eruption of Anatahan volcano. *Journal of Volcanology and Geothermal Research*, **146**, 102–116.
- Wright, T. L., Kinoshita, W. T. and Peck, D. L. (1968). March 1965 eruption of Kilauea volcano and the formation of Makaopuhi lava lake. *Journal of Geophysical Research*, **73**(10), 3181–3205.
- Wyatt, W. C. and Dean, K. (1995). AVHRR observations of thermal anomalies associated with the 1994 eruption of Klyuchevskoi. *AGU Fall Meeting Abstracts*, December 1995, San Francisco, F540.
- Xiong, J., Toller, G., Chiang, V., Sun, J., Esposito, J. and Barnes, W. (2005). MODIS Level 1B algorithm theoretical basis document. *NASA support document* prepared by the MODIS Characterization Support Team, 40 p.
- Xiong, X., Wu, A. and Cao, C. (2008). On-orbit calibration and inter-comparison of Terra and Aqua MODIS surface temperature spectral bands. *Int. J. Remote Sensing*, **29**(17–18), 5347–5359.
- Yamaguchi, Y., Kahle, A. B., Tsu, H., Kawakami, T. and Pniel, M. (1998). Overview of Advanced Spaceborne Thermal Emission and Reflection Radiometer (ASTER). *IEEE Trans. Geoscience and Remote Sensing*, **36**(4), 1062–1071.
- Yeh, R.-N., Lu, F.-F., Hong, H.-M., Cherng, Y. T. and Chang, H. (2000). Seagle-1, A new man-portable thermal imager. *Proceedings of SPIE*, **4080**, 55–61.
- Yokoyama, I. (1956). Energetics in active volcanoes. 1st Paper. (Activities of Volcano Mihara, Oshima Island during period 1953~54). *Bulletin of the Earthquake Research Institute*, **34**, 185–195.
- Yokoyama, I. (1957a). Energetics in active volcanoes. 2nd Paper. *Bulletin of the Earthquake Research Institute*, **35**, 75–97.
- Yokoyama, I. (1957b). Energetics in active volcanoes. 3rd Paper. *Bulletin of the Earthquake Research Institute*, **35**, 99–107.
- Yuhaniz, S. S. and Vladimirova, T. (2009). An onboard automatic change detection system for disaster monitoring. *International Journal of Remote Sensing*, **30**(23–24), 6121–6139.
- Yuhara, K., Ehara, S. and Tagomori, K. (1981). Estimation of heat discharge rates using infrared measurements by a helicopter-borne thermocamera over the geothermal areas of Unzen volcano, Japan. *Journal of Volcanology and Geothermal Research*, **9**, 99–109.
- Zettwoog, P. and Tazieff, H. (1972). Instrumentation for measuring and recording mass and energy transfer from volcanoes to atmosphere. *Bulletin of Volcanology*, **37**, 1–36.
- Zies, E. G. (1941). Temperatures of volcanoes, fumaroles, and hot springs. In *Temperature: Its Measurement and Control in Science and Industry*. New York: Reinhold Publishing, pp. 372–380.
- Zobin, V. M. (2003). *Introduction to Volcanic Seismology. Developments in Volcanology*, **6**, Amsterdam: Elsevier, 290 p.
- Zülicke, C. and Hagen, E. (1998). Impact of skin effect on the near-surface temperature profile. *Physics and Chemistry of the Earth*, **23**(5–6), 531–535.

# Index

- A/D conversion, 126, 127, 130, 414  
Absolutely Local Index of Change of Environment (ALICE), 303, 311  
absorption, by volcanic gases, 575  
active lava, 213, 605  
  areal spreading rate, 605, 608  
  cooling of sub-aqueous flows, 232  
  cooling rates, 230, 597  
  crust thickness, estimation of (using thermal data), 222, 601  
  expansion rate, 608  
  extension rate, 608  
  heat flux, 213, 224  
  pixel mixture model, 174  
radiometer-based measurements at, 438  
surface temperature, 453, 454  
thermal structures, 189, 204  
thermal camera measurements at, 605  
time series analysis of, 394  
  velocity, 455–462, 608  
adiabatic cooling rate, 322–323  
Advanced Very High Resolution Radiometer (AVHRR), 29–31, 651  
advection, 230  
air entrainment, 480, 482  
  coefficient, 615  
  rate, 614  
air photo interpretation, 61, 62, 348, 587  
airborne scanners, 61  
  AGA Thermovision System (AATS), 62  
  Airborne Visible/Infrared Spectrometer (AVIRIS), 68  
  deployment issues, 68  
  deployment of, 62  
  hyper-spectral data, 68  
  literature review, 61–68  
  Multispectral Infrared Visible Imaging Spectrometer (MIVIS), 68  
  Thermal Infrared Multispectral Scanner (TIMS), 68  
  types of study, 69  
  use in volcanology, 60–61, 68  
aircraft campaigns, 68–69  
Airy-disc, 518  
Akita-komaga-take, 57, 436  
Alae crater (Kilauea), 57, 435, 446  
Alaska, 50  
Alaskan Volcano Observatory (AVO), 50, 53, 293, 302, 325, 623, 693, 711  
Aleutians, 50  
ALICE, 303, 311  
Amonton, 54  
Analog/Digital (A/D) converter, 126  
Anatahan, 311, 399  
angular field of view (FOV), 116, 122, 431, 432, 497, 518, 525, 539, 668  
angular instantaneous field of view, 668, 131–132  
area, of sub-pixel hot spot, 198  
Asama, 251  
ascent velocity, 479, 481, 485, 494  
ash plumes, 7, 34, 39  
  air entrainment, 614, 615  
associated thermal waveforms, 436, 438, 445, 475, 476, 478, 480, 482, 484, 489, 491  
Gaussian radius, 615  
heat flux, 490, 492, 493  
particle velocity, 608, 612  
plume front velocity, 485, 486, 487, 612  
spreading angle, 614  
spreading rate, 613  
types, 588–589  
top hat radii, 616  
tracking by geostationary satellites, 37  
tracking of, 50  
mass flux, 616–622  
volumetric flux, 616, 620  
Aso, 625  
atmospheric correction, 91, 105–109, 210  
  for thermal camera data, 560–564, 566–573  
  of radiometer measurements, 429–430  
  of satellite data, 109–111  
atmospheric down-welling radiance, 96

- atmospheric effects, 90  
 and radiometer measurements, 429–430  
 in the MIR, 108–109  
 in the SWIR, 107  
 in the TIR, 108  
 in thermal camera data, 561, 564  
 on sensor-arriving radiance, 91–102  
 variation with path length, 102–105, 430, 561–564
- atmospheric transmissivity, 91  
 and radiometer measurements, 430  
 and thermal camera data, 562  
 correction for, 91  
 definition of, 91  
 effect on satellite measurements, 91  
 variation with path length, 91  
 variation with scan angle, 93  
 variation with surface altitude, 93  
 variation with wavelength, 91
- atmospheric up-welling radiance, 95, 102  
 and radiometer measurements, 430  
 and thermal camera data, 563  
 contribution to at-sensor radiance, 102  
 definition of, 95  
 variation with path length, 103  
 variation with scan angle, 104  
 variation with surface altitude, 104  
 variation with wavelength, 97
- atmospheric windows, 91
- Augustine, 44, 393
- AVHRR-class-sensors, 113, 651–660  
 and cool anomalies, 324  
 and cooling curves, 262  
 and explosive eruptions, 324  
 and hot spot classification, 349  
 and hot spot detection, 276, 277, 284, 286, 293, 312  
 and mapping, 339, 345  
 and spatial profiles, 407–408  
 and TADR extraction, 264–265, 266–271  
 and thermal precursors, 324  
 and time series construction, 343, 376, 380, 394–399  
 and volcanic radiance, 370  
 dual-band application, 169, 173, 185, 203  
 mixed pixel issues, 156, 159, 161–162  
 pros and cons, 152  
 spatail, temporal and spectral resolution, 151  
 use in multi platform approach, 324
- ballistic trajectories, 613
- Barren Island, 182
- Belinda, Mt., 397
- Bezymianny, 391, 393, 396, 537
- blackbody, 78
- Boiling Lake, 236
- bolometer, 60  
 definition, 415, 503  
 invention of, 60  
 use in thermal cameras, 503
- boundary layer, at the surface of a water body, 235
- brightness temperature, 95, 149, 429
- bulk temperature, 234, 235
- buoyancy, 480, 482, 622
- calibration, 110, 126, 128, 130
- camera, 500
- Campi Flegrei, 61
- Cascades, 61
- Cascades Volcano Observatory (CVO), 623
- Cerro Azul, 319, 329
- Cerro Negro, 395
- Chikurachki, 394
- chopping, of output voltage, 419
- Classification (of hot spots), 346–348  
 hybrid classification, 365, 367  
 published schemes, 364–365  
 using air-photo interpretation, 346–348  
 using spectral character, 349, 356–359  
 using temporal character, 359
- Colima, 326
- conduction, 221  
 around a conduit, 239  
 at a crater lake, 238  
 from a lava tube, 227  
 thermal boundary layer, thickness of, 221  
 through the base of a lava body, 221
- conductive heat flux, 221  
 density, 221
- convection, 216  
 at a skylight, 228  
 from a crater lake, 238  
 from a lava tube, 225  
 from an active lava, 216, 220  
 in water, 235
- convective flux, 216  
 density, 216
- convective heat transfer coefficient, 216–221
- cooling curve, 203, 318, 445
- cooling rate, 47, 229–231  
 cooling with time, 459–460, 600–601  
 distance-dependent, 232  
 measurements using a thermal camera, 597  
 radiometer-based measurements of, 443, 459  
 surface cooling with distance, 597–600  
 time-dependent, 231
- crater lakes, 233  
 bulk temperature, 234–236  
 heat fluxes, 236–239  
 satellite-based measurements at, 243  
 surface temperature, 233–234  
 crystallization, heat generated by, 231  
 cut-off wavelength, 414  
 Czemy, 60
- dark current noise, 130, 414, 505
- data rates, 499, 519–520, 521

- data storage space, 582  
deformation, 1, 7  
detectors, 413  
    and FPAs, 501, 503–507  
    and radiometers, 57, 413–418  
    and sensor systems, 125–126  
    and thermal cameras, 60–61, 502, 503–507  
bolometer, 60, 415, 503  
chopping, 419  
cooling, 54, 129, 414, 415, 420, 501, 504  
cut-off wavelength, 414  
definition of, 54–55, 415–416  
detector response function, convolution with spectral radiance, 149  
detector turn-on effect, 522  
energy gap, 414  
germanium, 415  
history of, 55–56  
Indium-Antimony (InSb), 415  
Indium-Antimony (InSb), 504  
Indium-Gallium-Arsenide (InGaAs), 504  
Lead-Selenium (PbSe), 415  
Lead-Sulphur (PbS), 415  
photo-conductors, 415  
photo-detectors, 415  
photo-emissive, 415  
photo-voltaic, 415  
Platinum Silicide (PtSi), 503, 504  
pyroelectric, 415, 416–419  
Quantum Well Infrared Photodetectors, 505  
response time, 416–419  
Schottky barrier, 504  
sensitivity, 146–147, 148  
silicon, 415  
superconductor, 415  
Tellurium-Mercury-Cadmium (HgCdTe), 415  
thermal detectors, 415  
thermal shock, 431, 523  
thermopile, 415, 416  
diffuse radiation, 75  
digital number (DN), 110, 126, 130  
dilution (of an ascending gas cloud), 480, 482  
discrete thermals, 589  
dual-band method, 45, 48, 166, 169, 210  
    assumptions, 214–219  
    one band solution, 182–183  
    graphical solution of, 170  
    history of, 169  
    multiple component solution, 207–210  
    numerical solution of, 170  
    one component solution (in the NIR or SWIR), 215–217  
one band solution (in the TIR), 188–189  
    (in the MIR), 192–193  
point of impossible solution, 177  
requirements for application, 169, 174–177, 210–212  
sum-to-one constraint, 207  
three-component solution, 185  
TIR application of, 182, 188–189  
using bands of differing spatial resolution, 193–195  
use of saturation, 195–196  
using non-response, 195–196  
dynamic range, 150  
Earth Observation Program, 41  
Earth Observing System (EOS), 4, 7, 39, 49  
Earth Observing-1 (EO-1) mission, 40  
Earth Science Enterprise (ESE), 39  
Edison, 60  
effective instantaneous field of view (EIFOV), 144  
effective radiation temperature, 214  
El Chichon, 37, 89  
emissivity, 78  
    and Kirchoff&hairsp;’s law, 80  
    and radiometer measurements, 429, 455  
    and spectral reflectance, 80  
    and surface roughness, 89  
    and temperature measurements, 82  
    angular effects, 573  
    at fumaroles, 467  
    correction of satellite data, 210  
    correction of radiometer data, 455  
    correction of thermal camera data, 569  
    definition of, 78  
    effect of glass and bubbles, 87, 89  
    measurement of, 80, 88  
    of active (basaltic) lava surfaces, 89  
    of basalt, 83, 456, 574  
    of basaltic glass, 85  
    of gas, 467, 471  
    of lava, 83–84, 84–87  
    of rhyolite obsidian, 85  
    of sulphur, 83, 456, 574  
    of terrestrial surface types, 87  
    of trachyte-rhyolite, 83, 456, 574  
    of volcanic surfaces, 455, 456, 574  
    variation with time / surface age, 85, 87  
    variation with wavelength, 83  
Empedocles project, 41  
energy balance box model, 230, 236  
energy budget (For cooling lava), 254–257  
energy gap, 414  
EOS-IDS volcanology team, 307  
Erebus, 29, 43, 44, 47, 120, 264, 396, 407, 450  
Ertá Ale, 44, 47, 182, 264, 388, 444, 462, 463, 537, 594  
Etna, 29, 39, 41, 43, 45, 46, 47, 57, 61, 62, 68, 161, 200, 204, 244, 257, 259, 265, 298, 302, 308, 319, 320, 324, 333, 345, 371, 389, 393, 394, 396, 398, 438, 447, 453, 454, 586, 623, 624  
European Space Agency (ESA), 37, 41  
explosive events, 59, 399, 436, 445, 475, 537, 588, 612

- Fernandina, 261, 395  
 field of view (Fov, satellites), 116, 122, 668  
 field of view (thermal cameras and radiometers), 497, 519, 541  
 and integrated temperature, 432  
 area of, 432, 539–543  
 fire channel, 276  
 fire detection algorithms, 293  
 fires, 29, 42, 45, 214, 356  
 FLIR Systems, 61, 502, 507, 513  
 focal length, 525  
 focal plane array (FPA), 60, 501, 502  
 forced convection, 217, 445  
 Forward Looking Infrared (Radiometer) System (FLIR), 60, 501  
 Fourier's Law, 221, 234, 241, 244  
 fractures, 537, 585  
 frame rate, 580  
 free convection, 216  
 frequency distribution (of surface or vent temperature), 473, 493–496  
 Fuego, 493  
 fumarole fields, 462, 472, 585, 592  
 emissivities at, 84, 456  
 thermal structures at, 158–159  
 satellite measurements at, 212, 241–242  
 heat flux at, 239–240  
 vent temperatures, 466–471  
 surveys of, 473–475  
 thermal camera measurements at, 575–577, 590–592, 585–586  
 radiometer measurements of, 442, 450, 462–467, 474–475  
 Galeras, 396  
 Galunggung, 39  
 gas  
   effects on radiometer measurements, 462, 466–467  
   effects on thermal imaging, 573–575  
   emissivity of, 471–493  
   radiometer-based measurements of, 57, 436, 476–482  
   remote sensing of, 1, 7  
   thermal camera-based measurements, 618  
 gas field flares, 42  
 gas flux, 481, 482, 618  
 gas pistonning, 445, 476, 482  
 gas puffing, 436, 445, 476  
   puff mass, 480, 482  
   puff volume, 480, 482  
 gas thermometer, 54  
 geomethermal areas, 585  
 geometric correction, 139, 140, 558  
 geostationary orbits, 122, 124, 129  
 geothermal fields, 241–242  
   conduction at, 244–245  
   heat transfer coefficient at, 246  
 surface temperature anomalies at, 1–2, 45–46, 245, 324  
 system volume, 248  
 heat loss at, 245–247  
 use of radiometers at, 247  
 use of thermal cameras at, 247  
 use of satellite data at, 247–248, 322–324  
 water flux, 242–244  
 geothermal heating, 45, 242–248  
 GEOTIFF format, 8, 53  
 geysers geothermal field, 61  
 glow (use of, to calibrate thermal cameras) 625  
 GOES-class-sensors, 113, 661–665  
   and cooling curves, 262  
   and hot spot detection, 274, 276, 277, 284, 286, 293, 327  
   and mapping, 339, 348  
   and spatial profiles, 407  
   and time series construction, 343, 377, 380, 399, 401–404  
   dual-band application, 184  
   mixed pixel issues, 156, 160  
   pros and cons, 152  
   spatial, temporal and spectral resolution, 151  
   use in multi platform approach, 390  
   use to detect eruption termination, 318  
 GOES-East, 34  
 GOES-West, 34  
 Grashof number, 217  
 graybody, 79  
 Halemaumau (Kilauea), 57, 434  
 Handycam, 625  
 Hawaiian Volcano Observatory (HVO), 623  
 heat flux, 212  
   and conversion to lava volume, 257  
   conversion to mass flux, 264, 616–619  
   conversion to volume flux, 263–266  
   conversion to volume, 259–262, 619–621  
   derivations from radiometer data, 434–436, 446–447  
   derivations from satellite data, 212, 223–225, 227–228, 229–230, 240–241, 245–248  
   derivations from thermal camera data, 594  
   estimation at active lava, 213–216, 221–222  
   estimation at ash plumes, 490–492  
   estimation at crater lakes, 233, 235–239  
   estimation at fumarole fields, 239–240  
   estimation at geothermal fields, 241–247  
   estimation at hot springs, 239–240  
   estimation at lava tubes, 225–227  
   estimation at open vents, 239–240  
   estimation at sky lights, 227–229  
   lava flowing into water, 231–233  
   relation with lava mass, 250–254  
   relation with rock mass, 248–250  
 heat flux density, 212, 214  
 heat loss, 211

- and lava mass, 249–256  
at degassing vents, 239–241  
at fumarole fields, 241–245  
at geothermal systems, 241–245  
at hot springs, 240–241  
crater lakes, 233–234, 239  
from a lava tube, 225–227, 228  
from a skylight, 227–230  
from an active lava body, 213–214, 215, 220–222, 223–225  
from heated water, 223–233  
measurements using a thermal camera, 594  
radiometer-based inventories, 447  
heat required to vaporize water, 233  
heat transfer coefficient, 216, 217, 220, 221, 240  
Hekla, 61  
Herschel, John, 60  
Herschel, William, 55  
horizontal field of view (HFOV), 539  
hot spot detection algorithms, 292  
a history of, 292  
algorithm choice, 313, 316  
applications, 316, 329–330  
change detection approaches of, 304–306  
classification of, 293, 296  
contextual, 296–299  
correlation-based approaches, 299–301  
effective detection, requirements, 327–329  
fixed threshold, 292, 306–308  
for fire detection, 296–297  
hybrid algorithms, 308–311, 316–317  
onboard change detection, 304  
operational systems, 324–327  
output applications, 329–330  
relative merits 312, 313  
reliability, 313  
requirements, 327–329  
temporal approaches, 301–304  
use of night-time NIR data, 311  
use of night-time SWIR data, 311  
user interaction, 317  
hot spots, 42  
and DeltaT, 281, 284  
atmospheric problems, 281  
refraction problems, 281  
emissivity problems, 281–283  
saturation problems, 282–284  
use in detection, 293, 298–299, 306  
and eruption termination, 317, 318, 319, 320, 321, 322  
and NTI, 284–286, 306–310  
and scatter plots, 287–290, 292  
cool anomalies, 322–324  
definition of, 16, 275  
in the MIR, 276  
in the NIR and SWIR, 276, 311, 312  
in the TIR, 276  
manual detection of, 274  
pixel-intergrated temperature effects, 162–164  
resolvability, 276–278  
HOTSAT, 327  
HOTVOLC, 327  
IAVCEI Remote Sensing Commission, 46  
Iceland, 45  
image blurring, 142, 144  
image distortion, 139, 527  
image processing, 54  
image sharpening, 340  
industrial hot spots, 29, 45  
infrared radiometry, 16  
history of, 54–61  
INGV-Catania, 69, 623, 624  
instantaneous field of view (IFOV), 131–134, 144, 516–519, 543–558, 668  
integrated temperature, 162–164, 167–168, 432, 458  
Io, 10  
Izu-Oshima, 389  
Jagger, 434  
Japanese Meteorological Agency, 37  
jets, 589  
Kamchatka, 50  
Karymsky, 396  
Kerguelen archipelago, 528  
Kilauea, 23, 39, 41, 57, 61, 185, 200, 203, 205, 311, 318, 334, 345, 386, 391, 403, 438, 442, 450, 454, 537, 603, 609, 623  
kinetic temperature, 82  
Kirchoff's Radiation Law, 80  
Kliuchevskoi, 393  
Krafla, 311, 396, 398  
Kupaianaha, 185  
Kurile Islands, 50, 394  
Kusatsu-Shirane, 236, 527  
Lambertian radiation, 75, 76  
Langley, 60  
Lascar, 41, 44, 45, 47, 130, 169, 201, 204, 312, 346, 386, 438  
lateral spreading, of a plume, 615  
launch vehicle, 113  
lava channels, 442, 445–446  
lava domes, 44, 47, 48, 169, 204, 218–219, 250, 264, 300, 303, 337–338, 343–344, 348, 356, 359, 364–365, 386–388, 393, 394, 395, 436, 438  
lava flows, 47–48, 333–336, 340–343, 345, 375–380, 389, 393–394, 407  
cooling, 45, 260  
cooling rates, 230–232, 260–262, 598–599  
core temperature, 200–201, 454–454

- lava flows (cont.)  
   crust temperature, 201–203  
   crust thickness, 222–223, 602  
   crystallization rates, 262  
   down-flow temperature profiles of, 44, 443, 595–599  
   energy budget, 254–256  
   heat budget, 250–253  
   heat loss, 48, 213–215, 220–225, 455–461  
   hot cracks, 159, 203, 386, 476  
   interior cooling, 46–48, 600  
   radiometer deployments at, 442  
   surface cooling with distance, 203  
   surface cooling with time, 203, 595–598  
   thermal camera measurements of, 606  
 lava fountains, 39, 268, 270, 318, 319–320, 327, 342–343, 349, 389, 404, 410, 438  
 lava lakes, 43, 44, 57, 58, 68, 88–89, 182, 185, 211, 218, 253, 264, 333, 346–, 349, 359, 364, 365, 370, 374, 388, 396, 397, 403, 407–408, 432, 435, 438, 453, 454, 462, 476, 529, 594  
 lava tubes, 225–230, 333, 349, 445  
 lens distortion, 527  
 line spread function (LSF), 142  
 Llaima, 8  
 longwave infrared (TIR), definition of, 16  
 Lonquimay, 203, 223, 408  
 Low Earth Orbit (LEO), 115–119  
 low temperature thermal anomalies, 45, 322–324  
 lower detection limit, 177
- Makaopuhi crater (Kilauea), 435, 453  
 maps, 332–, 338–339  
   of fumaroles, 442, 462, 585–586  
   of lava domes, 337  
   of lava Flows, 48, 333, 334, 336, 345, 443, 587–588, 605  
   scale, 339–340  
   sharpening, 340–343  
   types, 332–338  
   using AVHRR data, 333, 345  
   using DMSP data, 42  
   using GOES data, 345  
   using MODVOLC, 317  
   using radiometer data, 436, 438, 442, 443, 455, 462, 473  
   using thermal camera data, 584–, 585–588, 605  
   using TM data, 333, 337, 343
- Masaya, 480, 481, 482  
 mass (of a cooling lava), 250–256  
 mass flux, 254, 264, 616–622  
 mass to energy conversion, 620  
   for a bomb field, 619–621  
   for a gas plume, 618–619  
   for a lava, 262–264  
   for an ash plume, 616–617  
   history of, 249–254  
   principles, 249–250, 254–256
- Mauna Loa, 68, 438  
 Mauna Ulu (Kilauea), 476  
 maximum value approach, 405  
 Mayon, 39  
 Melloni, 55  
 mid-wave infrared (MIR), definition of, 16  
 Mihara-yama, 527  
 Ministry of Land, Infrastructure and Transport (Australia), 37  
 mixed pixel, 46, 155–157  
 mixing equation, 158, 160, 164, 207  
 mixture model, 158, 160–162, 207  
   for crater lakes, 234  
   precision of, 193–195  
   three components, 175, 183  
   two components, 158, 160, 432  
   two-component weighted average, 158, 160
- Miyakejima, 619  
 MODIS Level 1A data, 140  
 MODIS Level 1B data, 8  
 MODLEN, 310  
 MODTRAN, 92  
 MODVOLC, 10, 296, 307, 310, 669–670, 677, 679  
 Momotombo, 442  
 Mono Lake, 61  
 Montagu Island (South Sandwich Islands), 408  
 Montserrat (Soufrière Hills), 624  
 Mount St. Helens, 37, 62, 68, 528, 585, 623  
 Myvatn, 61
- nadir, 132, 666  
 Napau crater (Kilauea), 39, 318, 345, 401  
 Narcissus effect, 527  
 NASA, 4, 33, 39, 49  
 National Oceanic and Atmospheric Administration (NOAA), 29  
 National Space Development Agency (NASDA), 37  
 natural variation, 298  
 near infrared, definition of, 16  
 New Millennium Program (NMP), 40  
 Newton's Second Law of Motion, 114  
 NIR, night-time imaging in, 41, 310  
 Niragongo, 253  
 NOAA, 29, 33  
 Nobili, 55  
 noise equivalent temperature difference ( $NE\Delta T$ ), 111, 150  
 normalized thermal index (NTI), 286, 310  
 normalized vegetation index (NDVI), 405  
 Nusselt number, 216, 217, 227
- Ohachi crater (Kirishima), 473  
 Okmok, 216, 311, 320, 395, 396  
   algorithm, 50, 302  
 Oldoinyo Lengai, 57, 393  
 optical pyrometer, 57, 682, 685  
   definition of, 57, 413, 681–682

- history of, 432, 434  
models, 682  
temperature from color, 680  
use in volcanology, 57
- orbit, 113  
ascending mode, 115  
descending mode, 115  
geostationary, 122  
low-earth orbit (LEO), 115–116  
orbit convergence, 120, 122  
orbital period, 113, 116  
polar orbits, 115–116  
precess, 115
- orbit, definition of, 114  
orbit convergence, 120  
orbital period, 114, 119
- Owakudani geothermal area, 247
- Pacaya, 57, 436  
Paricutin, 252  
particle velocity, 613  
Pavlof, 50, 397, 529, 538  
photo-detectors, 413  
photon radiation detectors, 55  
picture height distortion (PHD), 527  
Pinatubo, 39  
Piton de la Fournaise, 272, 391  
pixel, 125–126, 129–130, 132  
adjustment for a sloping surface, 139, 550–558  
dimension, 129–132  
and scan angle, 132, 133  
example calculation, 132  
nadir, 131  
off-nadir, 132  
thermal camera, 515–518, 543–550
- distortion, 133, 136, 137–140  
overlap, 136, 137, 144  
rotation, 137  
shape, 137–139
- pixel-integrated temperature, 163–164, 166–167, 193–195
- Planck, Max, 70  
Planck curves, 71  
and mixed pixels, 164–167  
and spectral response, 149–150  
and the dual-band method, 169  
effect of emissivity, 80–82  
mixing of, 208–210
- Planck Function, 70, 71  
and detector response function, 149  
convolution with detector response function, 149  
emissivity correction, 80  
example solution, 78  
expressed in terms of spectral radiance, 76  
inversion of, 77, 110  
simplification of, 70  
spectral exitance units, 77
- use to obtain temperature, 77  
Poas, 234  
point spread function (PSF), 142, 144  
Popocatépetl, 299, 326  
Prandtl number, 217, 218, 240  
Profiles, 407–408, 438, 442, 454, 458, 595  
across fumaroles, 443  
across/down lava flows, 203, 408, 442, 595  
across lava lakes, 43, 434–435  
conversion to cooling rate, 595–598  
conversion to heat flux, 446–450  
for explosion plumes, 612  
from AVHRR data, 43  
from HRIR data, 23  
from radiometer data, 57, 203, 409, 435, 443, 454, 455, 595  
from thermal camera data, 527, 595, 611–612  
from TM data, 44, 203, 408  
within an active lava lake, 432
- precursors, 399  
Pu'u O'o (Kilauea), 402, 450, 483, 606
- pyroclastic flows, 44, 537
- Rabaul, 62, 442  
radar, 7  
radiance, spreading/smearing, 144  
radiant energy, 75, 216  
radiant flux, 75, 213, 216  
density, 74, 213, 216  
radiation, 4, 53, 54, 57, 71, 74, 75  
at a lava lake, 446  
at a skylight, 227–229  
from a crater lake, 238  
from a degassing vent, 239  
from an active lava, 213–216  
from an ash cloud, 490–492  
measured using a radiometer, 446  
measured using a thermal camera, 594  
radiation shape factor, 228, 229  
radiation temperature, 82, 88, 89  
radiometer, 413, 416  
body temperature, measurement of, 56  
classification of applications, 438  
commercially available instruments, 420  
field of view, 430–432  
fixed-mount, definition, 420  
generic specifications, 429  
hand-held, definition, 420  
history of, 54–56, 432, 434–438  
industrial use of, 56–57, 413, 416, 438  
lens deterioration, 475  
map generation, 438, 443, 454, 462  
measurement, of explosive plumes, 436, 475  
measurement of gas flux, 480–482  
measurement of gas pistonning, 476, 481–482  
measurement of gas puffing, 436, 438, 476–480  
measurement of heat flux, 446, 490–492

- radiometer (cont.)  
 ash-dominated emission, waveform types, 404, 489–490  
 bomb-dominated emission, waveform types, 482–484, 487–488, 489  
 heat flux, 490–492  
 peak thermal amplitude, 489  
 plume velocity, 484–487, 493–495  
 measurements at open vents, 462–466, 471  
 measurements of spot temperature, 438, 447, 448  
 output voltage, 429  
 permanent installations, 450–452  
 pro's and con's, 498–499  
 profile generation, 438, 443, 454  
 spatial surveys, 438, 442, 446–447  
 thermopile-based systems, 54, 415, 416, 419, 427  
 time series, 436, 443, 445, 455  
 use at fumarole fields, 442, 462–466, 471–473, 473–475  
 use at lava flows, 442, 443–, 445, 455  
 use at lava lakes, 434–436, 453–454, 455–461  
 use in volcanology 56–60, 438–449
- radiometer, models, 419–420  
 Barnes Engineering Co. IT-2 infrared, 435  
 Barnes Instatherm model 14–220–4, 450  
 Barnes PRT-5, 436  
 Land/Minolta CS2, 442, 453, 454, 456–457, 464–468  
 Minolta/Land Compac, 2, 161, 454  
 Minolta/Land Compac, 298, 473  
 Minolta/Land Cyclops, 150, 420, 447, 453, 454, 472  
 Minolta/Land Cyclops, 234, 298, 419, 420, 445, 454, 462, 467, 473  
 Omega OS554, 450, 454, 462, 478, 484, 491, 522, 523  
 Raytek Raynger 3i, 445  
 Stoll-Hordy HL4, 434  
 rain, heat losses due to, 224, 227  
 Rainier, 57, 61, 435, 447  
 Rapid response volcano targeting, 391  
 Robust AVHRR Technique (RAT), 296, 302, 310  
 Rayleigh number, 217, 227  
 receiving stations, 8–10  
 reflected radiation, 96–97, 102, 639–645  
   and solar zenith angle, 105, 643  
   contribution to at-sensor radiance, 102–105  
   correction for, 105–108, 209  
   correction of radiometer data, 429  
   correction of thermal camera data, 566  
   day and night effects, 102–105, 643  
   estimation of, 639–642  
   variation with wavelength, 97–102  
 relative humidity, 246, 566, 579  
 remote sensing, 5  
   applications in volcanology, 7, 21–67  
   benefits of, 8
- classification of volcano hot spot applications, 1–2, 46, 633  
 extra-terrestrial, 10  
 general texts in, 15, 16  
 history of, 5, 21, 67–23  
 history of definition, 4  
 history of volcano hot spot applications, 1–4, 41–49  
 literature collation, 627  
 volcanological review, 6–7  
 waveband definitions, 16  
 repeat coverage, 116, 120–124  
 resolving power, 275  
 response time, for detectors, 54, 416–419, 420, 429, 495–498, 503  
 return period, 116, 120  
 Reynolds number, 217, 240  
 Rinjani, 8  
 Robust Satellite Technique (RST), 302  
 rockets, 21, 113  
 rooted thermals, 589  
 Ruapehu, 236
- Santiaguito, 57, 343, 388, 389, 408, 435, 436, 445, 493  
 satellite, definition of, 113–114  
 satellite height, 114, 666  
 satellites, 23  
   Aqua (EOS PM-1), 4, 39, 653  
   Environmental Science Services Administration (ESSA), 29  
   ENVISAT, 41, 654  
   EO-1, 4, 39  
   European Remote Sensing Satellite (ERS-1), 41, 653  
   Explorer, 21  
   Geostationary Meteorological Satellites (GMS), 34, 39  
   Geostationary Operational Environmental Satellite (GOES), 33, 34, 39, 122–113, 661  
   Improved TIROS Operational System (ITOS-1), 29  
   Japanese Earth Resources Satellite (JERS), 41  
   Landsat, 4, 27, 31–33, 116, 120, 646–647  
   Meteosat Second Generation (MSG), 37, 661  
   Meteosat, 34, 37, 39, 122, 123, 129, 661  
   MTSAT, 37, 39, 122, 661–665  
   Nimbus, 23, 41  
   NOAA, 29–31, 120, 651  
   Sputnik, 21  
   Synchronous Meteorological Satellites (SMS), 33–34  
   Terra (EOS AM-1), 4, 39, 648–649, 656–658  
   TIROS, 2, 21, 29, 651–653  
 saturation, 127, 150, 283  
 saturation vapor pressure, 246, 619  
 Saunders Island, 397  
 scale, 339  
 scan, 666  
   cross scan, 666  
   duration/rate, 120–124  
   line (of pixels), 127–129, 666

- sample time, 124–125  
 scan angle, 132, 666  
 scan direction, 666  
 scan increment angle, 132, 666  
 swath width, 116, 669  
 scanning, 127–128, 666–668  
 scanning mirror, 126, 127, 128, 129, 501  
 Seebeck, 55  
 Seger cones, 434  
 seismology, 1  
 selective radiator, 78–79, 80  
 sensor 114, 125–127  
   beam splitters, 129  
   definition of, 125–127  
   lower detection limit, 413  
   optics, 129  
   scanning, 116–129  
   sensor-arriving radiance, 109–111  
   signal sampling, 129  
   signal-to-noise, 149  
   spatial response, 142–144  
   spectral response, 148–149  
   tasking, 304, 329–330, 394  
   upper detection limit, 150  
 satellite sensors, 125–129  
   Advanced Along Track Scanning Radiometer (AATSR), 41, 653  
   Advanced Land Imager (ALI), 33, 39, 40  
   Advanced Spaceborne Thermal Emission and Reflection Radiometer (ASTER), 39, 119, 150, 648–650  
   Advanced Very High Resolution Radiometer (AVHRR), 8–10, 27, 29–31, 119, 120, 127–128, 132–134, 135–137, 139, 144–146, 150, 651–653  
   Advanced Vidicon Camera System (AVCS), 29  
   Along Track Scanning Radiometer (ATSR), 41, 653–656  
   Coastal Zone Color Scanner (CZCS), 41  
   Defense Meteorological Satellite Program (DMSP), 40–41  
   Enhanced Thematic Mapper Plus (ETM+), 8, 27, 33–34, 39–40, 53–54, 148, 149, 151, 646–648  
   GOES-Imager, 33, 122–125, 129, 130, 661–663  
   High Resolution Infrared Radiometer (HRIR), 23, 24  
   Hyperion, 40  
   Low Resolution IR Radiometer (LRIR), 29  
   Medium Resolution Infrared Radiometer (MRIR), 23  
   Moderate Resolution Imaging Spectroradiometer (MODIS), 8, 33, 39, 53–54, 119, 128–129, 140, 144, 149, 151, 656–658  
   Multispectral Scanner (MSS), 31, 33, 54, 144, 646–648  
   Operational Linescan System, 41  
   Optical Sensor (OPS), 41  
   Scanning Radiometer (SR), 29  
 Spinning Enhanced Visible and Infrared Imager (SEVIRI), 37, 39, 123, 663–664  
 Surface Composition Mapping Radiometer (SCMR), 23  
 Temperature–Humidity Infrared Radiometer (THIR), 23  
 Thematic Mapper (TM), 8, 27, 31–33, 54, 119, 120, 133, 140, 144, 146, 151, 264, 646–648  
 Very High Resolution Radiometer (VHRR), 29  
 Vidicon, 21  
 Visible Infrared Spin Scan Radiometer (VISSR), 37, 661, 662  
 Visible Infrared Spin Scan Radiometer Atmospheric Sounder (VAS), 37  
 Shishaldin, 399, 529  
 shortwave infrared (SWIR), definition of, 16  
 Sierra Negra, 44, 408  
 signal-to-noise ratio (SNR, S/N), 150, 523–524  
 skin (surface) temperature, 234, 235  
 skin effect, 234, 235  
 skylights (in lava tubes), 182, 227–230, 333, 349, 439, 446, 454, 596  
 slew rate, 495  
 solar heating, 241, 247, 277, 292, 306, 322, 324, 436, 492, 587  
 solar radiance, 96, 643  
 solar zenith angle, 96, 639–640  
 Solfatara (Campi Flegrei), 62, 624  
 Soufrière (St. Vincent), 37  
 spatial resolution, 113, 130–134  
 spectral radiance, 71, 76, 113  
   and spectral response function, 148  
   at-detector, 149  
   at sensor, 109–111  
   conversion from ON, 126  
   direct conversion to heat flux, 214–216  
   direct conversion to TADR, 271  
   pixel-integrated, 160, 164, 183, 266  
   units of, 77  
   use in the Planck function, 76–77  
   worked example for derivation, 78  
 spectral radiant exitance, 71  
 spectral resolution, 113, 146  
 spectral response, 148–149  
 spectral response function, 148–150  
 starting plumes, 589  
 Stefan cooling problem, 601  
 Stefan–Boltzmann constant, 74–75  
 steradian, 75  
 Stirling Cycle coolers, 505  
 Stromboli, 46, 57, 61, 68, 159, 301, 395, 396, 438, 445, 447, 450, 470, 484, 493, 537, 575, 586, 587, 611, 615, 623, 624  
 surface age (lava flows), 600–603  
 surface (kinetic) temperature, 82  
   extraction from radiometer data, 429–430  
   extraction from satellite data, 111

- surface (kinetic) temperature (cont.)  
 measurement using a radiometer, 455, 458  
 measurements using a thermal camera, 591  
 rate of change, 455–462, 597
- Surtsey, 21, 23, 61, 253, 407  
 overlap, 120
- Swath width, 119, 133, 666  
 narrow, 120  
 wide, 120
- Taal, 61
- Tasimeter, 60
- temperature profiles, 44, 57, 203, 408, 432, 434, 442, 444, 595, 597, 598
- temporal resolution, 113, 119, 120, 122, 124, 519
- thermal amplitude, 489
- thermal anomaly, 16, 289
- thermal boundary layer, temperature of, 217
- thermal camera, 500  
 accessories, 521  
 and focal plane array, 501  
 and volcano surveillance, 623  
 batteries, 521, 582–583  
 civil surveillance models, 625  
 classification of applications, 529–537  
 data rates, 519–520  
 definition, 500, 501  
 deployment, campaign-style, 577  
 deployment, survey-style, 575, 577  
 design, 502  
 dynamic range, 515  
 Field of View (FOV) dimensions, 539–543  
 fixed-mount, 505, 514  
 focal length, 524–525  
 frame rates, 519, 520–521, 580–583  
 frequency distribution generation, 590–592  
 gain settings, 515  
 general texts, 500–501  
 hand-held, 505–504  
 history of, 60–61, 501  
 image distortion, 525, 527  
 lenses, 525  
 line of sight distance, 539, 541  
 manufacturers, 505  
 measurement accuracy, 560  
 measurements of cooling rates, 597–601  
 measurements of explosive plumes, 589  
   air entrainment rate, 614–615  
   ascent velocity, 612–613  
   density, 622  
   dimension, 611  
   mass flux, 617–621  
   plume classification, 588–590  
   spreading rate, 613, 614  
   volume flux, 616, 619  
 measurements of heat flux, 594
- measurements of lava discharge rate, 607–611
- measurements of surface age, 600–605
- military applications, 54, 60–61
- models, 505
- narcissus effect, 527
- permanent monitoring networks, 624
- picture height distortion, 525, 527
- pixel dimensions, 515–518  
 across image variation, 543–546  
 correction for complex geometries, 558–560  
 topographic effects, 549–558  
 variation with pointing angle, 546–549
- pre-purchase questions, 514, 521–522
- profile generation, 595
- signal-to-noise, 524
- spatial resolution, 518–519
- surveys, 577–579, 583–584
- target detection limits, 517–518, 524
- time series, 595
- thermal shock, 523
- turn-on effects, 522
- two-band options, 514
- use at fumarole fields, 585–587, 590–592
- use at lava flows, 587, 592, 605–607
- use at lava lakes, 592
- use in volcanology, 61, 527–529, 537–538
- veiling glare, 525
- windowing, 520–521
- thermal camera, commercially available systems, 506–514, 684–687  
 AGEMA 550, 512, 684  
 AGEMA 570, 507, 684  
 FLIR S660, 520  
 FLIR SC640, 520  
 FLIR SC6000, 504, 521  
 FLIR Systems i-series, 514, 515  
 FLIR Systems P- and T-series, 514  
 FLIR Systems Prism DS, 504  
 FLIR Systems SC645/SC655, 505  
 FLIR Systems ThermaCAM S60, 512  
 FLIR Systems ThermaCAM S40, 502, 512, 527, 538, 560, 577, 592, 606, 622  
 Fluke, 501, 514, 685  
 Mikron, 514, 685  
 Mikron M7640, 520  
 PCE instruments, 514, 685  
 Seagle-1, 503  
 Star SAFIRE, 61, 527  
 ThermaCAM range, 501, 502, 505, 512  
 ThermaCAM 545–595–675–695, 501, 502, 506, 512, 623  
 ThermoVision A10, 514  
 uncalibrated models, 625  
   Sony PC120 (Handycam), 624  
   Raytheon Nightsight 2000, 624

- Bosch MIC 412, 624  
 ACTi KCM-5311, 624  
 thermal contour maps, 436, 442, 455, 458  
 thermal detectors, 413  
 thermal diffusivity, 221  
 thermal infrared (TIR), definition of, 16  
 thermal radiation detectors, 55  
 thermal sensor technology, history of, 54–55  
 thermal shock (of a detector), 523  
 thermocouple, 55, 415  
     and heat loss measurements, 244  
     invention of, 55  
     use at carter lakes, 233  
     use at fumaroles, 462, 466–468, 472  
     use at lava flows, 201, 432, 454  
     use at lava lakes, 87, 434  
     use in thermopile construction, 415  
     use in volcanology, 57  
 thermodynamics, First Law of, 248, 250  
 thermoelectric (Peltier) coolers, 505  
 thermogram, 501  
 thermograph, 60  
 thermopile, 55, 415–416  
     invention of, 55  
     response, 419, 427  
     use in radiometers, 415  
     use in volcanology, 56  
 time series, 331, 367–369, 404–405, 407  
     for cooling lava flows, 201–203, 320–322, 396, 445  
     for explosive activity, 396, 398, 399, 436, 445, 482–485, 489–490  
     for fountaining, 319  
     for fumaroles, 394  
     for lava domes, 386–388, 396, 399  
     for lava flows, 317, 319, 389, 393–394, 396, 398, 399, 402–404, 445  
     for lava lakes, 388, 396, 397, 399, 462  
     for open vents, 394, 399  
     for precursors, 399  
     for pyroclastic flows, 396  
     from a single image, 389–391  
     literature collation, 376–386  
     maximum value approach, 404  
     of ASTER data, 391–393  
     of ATSR data, 394, 396, 398  
     of AVHRR data, 320–322, 393, 395, 396, 398, 399  
     of brightness temperature, 373  
     of degassing, 436, 445, 476  
     of GOES data, 317, 318, 399, 401, 402–404  
     of maps, 344  
         AVHRR-class, 345  
         GOES class, 345  
         TM-class, 345–362  
     of mass/volume flux, 375–376  
     of maximum volcanic radiance, 373  
     of MODIS data, 396, 399  
     of pixel numbers, 373  
     of radiometer data, 436, 442, 445, 455–460, 462, 476, 482–485, 489–490  
     of SEVIRI data, 318, 404  
     of spectral radiance, 373  
     of summed radiance, 374  
     of summed volcanic radiance, 374  
     of TM/ETM+ data, 386  
     parameter levels, 367–373  
     spurious points, 404  
     temporal detail, 376  
     types, 371, 404  
     use for classification, 359, 361, 365  
 time-averaged discharge rate (TADR), 266, 267, 268, 269, 376, 388, 393, 608, 609  
 TM-class-sensors, 113, 646–650  
     and cool anomalies, 324  
     and cooling curves, 262  
     and crater lakes, 233  
     and heated water detection, 233  
     and hot spot classification, 360  
     and hot spot detection, 276, 277, 284, 286, 310  
     and lava domes, 386–388  
     and lava flows, 389–391  
     and lava lakes, 388  
     and open vents, 241  
     and spatial profiles, 408  
     and thermal map production, 339, 343–345  
     and time series construction, 343, 376, 380, 386  
 ASTER, 391–393  
 dual-band, application, 169, 174–176, 182–185, 196, 203  
 mixed pixel issues, 156, 160, 162–163, 404  
 pros and cons, 151  
 Spatial, temporal and spectral resolution, 150–151  
 use in multi platform approach, 408  
 total angular field of view (of the sensor), 119  
 total energy, 216  
 trapezium rule, 259  
 Università della Basilicata, 302  
 Università di Firenze, 624  
 University of Alaska Fairbanks, 4, 50  
 University of Hawaii, ix 10, 35, 325, 623, 707  
 Unzen, 388, 396, 528  
 USGS Hawaiian Volcano Observatory, 69  
 Usu, 624  
 Vanuatu, 244  
 VAST, 293, 298, 310, 669–670, 675, 676, 678  
 veiling glare, 527  
 vertical field of view (VFOV), 539  
 Vesuvius, 61, 624  
 Vesuvius Observatory, INGV-Naples, 624  
 Villarrica, 493

- virtual temperature, 238  
visible, definition of, 16  
viscous dissipation, 232–253  
volatiles, heat carried by, 252–253, 256  
volcanic radiance, 369  
volcanology interdisciplinary science (IDS), 49  
volume (of a cooling lava), 250–254, 255,  
    256–262, 608  
volume flux (of an active lava), 253, 263–266,  
    267–268, 607–611
- Vulcano, 46, 61, 62, 68, 159, 244, 245, 246, 248, 395,  
    442, 467, 472, 473, 592, 624
- water vapor pressure, 238, 246  
weighted average equation, 158  
Wein’s Displacement Law, 74  
White Island, 68, 397  
windowing, 521  
Yellowstone, 61